Landolt-Börnstein
Numerical Data and Functional Relationships in Science and Technology
New Series / Editor in Chief: W. Martienssen

Group III: Condensed Matter
Volume 27

Magnetic Properties of Non-Metallic Inorganic Compounds Based on Transition Elements

Subvolume J 3

Halide Perovskite-type Layer Structures

Editor: H.P.J. Wijn

Author: R. Geick

Springer

ISSN 1616-9549 (Condensed matter)

ISBN 3-540-41225-5 Springer-Verlag Berlin Heidelberg New York

Library of Congress Cataloging in Publication Data
Zahlenwerte und Funktionen aus Naturwissenschaften und Technik, Neue Serie
Editor in Chief: W. Martienssen
Vol. III/27J3: Editor: H.P.J. Wijn
At head of title: Landolt-Börnstein. Added t.p.: : Numerical data and functional relationships in science and technology.
Tables chiefly in English.
Intended to supersede the Physikalisch-chemische Tabellen by H. Landolt and R. Börnstein of which the 6th ed. began publication in 1950 under title: Zahlenwerte und Funktionen aus Physik, Chemie, Astronomie, Geophysik und Technik.
Vols. published after v. 1 of group I have imprint: Berlin, New York, Springer-Verlag
Includes bibliographies.
1. Physics--Tables. 2. Chemistry--Tables. 3. Engineering--Tables.
I. Börnstein, R. (Richard), 1852-1913. II. Landolt, H. (Hans), 1831-1910.
III. Physikalisch-chemische Tabellen. IV. Title: Numerical data and functional relationships in science and technology.
QC61.23 502'.12 62-53136

This work is subject to copyright. All rights are reserved, whether the whole or part of the material is concerned, specifically the rights of translation, reprinting, reuse of illustrations, recitation, broadcasting, reproduction on microfilm or in other ways, and storage in data banks. Duplication of this publication or parts thereof is permitted only under the provisions of the German Copyright Law of September 9, 1965, in its current version, and permission for use must always be obtained from Springer-Verlag. Violations are liable for prosecution act under German Copyright Law.

Springer-Verlag Berlin Heidelberg New York
a member of BertelsmannSpringer Science+Business Media GmbH

© Springer-Verlag Berlin Heidelberg 2001
Printed in Germany

The use of general descriptive names, registered names, trademarks, etc. in this publication does not imply, even in the absence of a specific statement, that such names are exempt from the relevant protective laws and regulations and therefore free for general use.

Product Liability: The data and other information in this handbook have been carefully extracted and evaluated by experts from the original literature. Furthermore, they have been checked for correctness by authors and the editorial staff before printing. Nevertheless, the publisher can give no guarantee for the correctness of the data and information provided. In any individual case of application, the respective user must check the correctness by consulting other relevant sources of information.

Cover layout: Erich Kirchner, Heidelberg
Typesetting: Fotosatz-Service Köhler OHG, Würzburg, and Redaktion Landolt-Börnstein, Darmstadt
Printing: Computer to plate, Mercedes-Druck, Berlin
Binding: Lüderitz & Bauer, Berlin

SPIN: 10783359 63/3020 - 5 4 3 2 1 0 – Printed on acid-free paper

Editor

H.P.J. Wijn, Institut für Werkstoffkunde der Elektrotechnik der Rheinisch-Westfälischen Technischen Hochschule Aachen, Templergraben, 52056 Aachen, FRG

Author

R. Geick, Physikalisches Institut der Universität Würzburg, Am Hubland, 97074 Würzburg, FRG

Landolt-Börnstein

Editorial Office
Gagernstr. 8, D-64283 Darmstadt, Germany
fax: +49 (6151) 171760
e-mail: lb@springer.de

Helpdesk
e-mail: em-helpdesk@springer.de

Internet
http://science.springer.de/newmedia/laboe/lbhome.htm
http://link.springer.de/series/lb/

Preface

The Landolt-Börnstein Volume 27 deals with magnetic properties of non-metallic inorganic compounds based on transition elements, such as there are pnictides, chalcogenides, oxides, halides, borates, silicates and phosphates. A preliminary survey of the contents of all subvolumes that have already appeared or have been planned to appear in the near future is printed on the inside of the front cover.

The magnetic properties of halides have been compiled in Subvolume III/27J, the third part of which is presented herewith. The first part (Subvolume J1, published in 1994) deals with halides of the general formula MX_n with M being a 3d element and X a halogen element, while the second part (Subvolume J2, published in 1995) covers the halides composed out of three types of elements, A, M and X, where generally A represents an alkali element, M a 3d element and X a halogen element. The present Subvolume J3 contains data on the structural and magnetic properties of halide perovskite-type layer structures of the type A_2MX_4, where X = F^-, Cl^-, Br^- and I^-, M = Mg^{2+}, Cr^{2+}, Mn^{2+}, Fe^{2+}, Co^{2+}, Ni^{2+}, Zn^{2+}, Cd^{2+} etc. and A = K^+, Rb^+ Cs^+ etc. In addition to these monolayer compounds, data are also included for double-layer and triple-layer compounds of the types $A_3M_2X_7$ and $A_4M_3X_{10}$, respectively. For X = Cl^- and Br^-, data are presented on compounds where the alkali ions are replaced by n-alkylammonium chains, i.e. by A = $(n\text{-}C_nH_{2n+1}NH_3)^+$, and by A = $[C_6H_5(CH_2)_mNH_3]^+$. Finally, diammonium compounds are included here where two alkali ions are replaced by divalent alkylene-diammonium ions, i.e. by $A_2 = [NH_3(CH_2)_mNH_3]^{2+}$.

The compounds with paramagnetic ions exhibit as usual magnetic ordering and magnetic phase transitions and many of the above listed compounds undergo structural phase transitions. Because of these phase transitions, the compounds dealt with in this subvolume have been of special interest for about 30 years. They were found to be good realizations and thus prototypes for a number of phase transition models like the 2D Ising model, the 2D XY-model with finite-size effects and the 2D Ising spin glass. For these reasons, it is appropriate to present here a brief sketch of the theory of phase transitions and of the relevant models, and the data in this subvolume comprise not only the magnetic and structural properties in general but also a comprehensive collection of data on critical properties near the phase transitions.

Many thanks are due to the author for the careful selection of data and for the agreeable cooperation, to the Landolt-Börnstein editorial office, especially to Dr. W. Polzin and Frau I. Lenhart for the great help with the editorial work, and to Springer Verlag for their thoughtful help in the final preparation of this volume.

Aachen, May 2001 **The Editor**

Definitions, units and conversion factors

In the SI, units are given for both defining relations of the magnetization, $\boldsymbol{B} = \mu_0(\boldsymbol{H} + \boldsymbol{M})$ and $\boldsymbol{B} = \mu_0\boldsymbol{H} + \boldsymbol{M}$, respectively. $\mu_0 = 4\pi\cdot 10^{-7}$ Vs A^{-1} m^{-1}, A: molar mass, ρ: mass density, $\boldsymbol{P}$: magnetic moment, $\boldsymbol{M}$: magnetic moment per unit volume (magnetization, magnetic polarization).

Quantity	cgs/emu	SI	
$\boldsymbol{B}$	G = (erg cm^{-3})$^{1/2}$	T = Vs m^{-2}	
	1 G $\hat{=}$	10^{-4} T	
$\boldsymbol{H}$	1 Oe = (erg cm^{-3})$^{1/2}$	A m^{-1}	
	1 Oe $\hat{=}$	$10^3/4\pi$ A m^{-1}	
$\boldsymbol{M}$	$\boldsymbol{B} = \boldsymbol{H} + 4\pi\boldsymbol{M}$	$\boldsymbol{B} = \mu_0(\boldsymbol{H} + \boldsymbol{M})$	$\boldsymbol{B} = \mu_0\boldsymbol{H} + \boldsymbol{M}$
	G	A m^{-1}	T
	1 G $\hat{=}$	10^3 A m^{-1}	$4\pi\cdot 10^{-4}$ T
$\boldsymbol{P}$	$\boldsymbol{P} = \boldsymbol{M}V$	$\boldsymbol{P} = \boldsymbol{M}V$	$\boldsymbol{P} = \boldsymbol{M}V$
	G cm^3	A m^2	V s m
	1 G cm^3 $\hat{=}$	10^{-3} A m^2	$4\pi\cdot 10^{-10}$ V s m
σ	$\sigma = M/\rho$	$\sigma = M/\rho$	$\sigma = M/\rho$
	G cm^3 g^{-1}	A m^2 kg^{-1}	V s m kg^{-1}
	1 G cm^3 g^{-1} $\hat{=}$	1 A m^2 kg^{-1}	$4\pi\cdot 10^{-7}$ V s m kg^{-1}
σ_m	$\sigma_\mathrm{m} = \sigma A$	$\sigma_\mathrm{m} = \sigma A$	$\sigma_\mathrm{m} = \sigma A$
	G cm^3 mol^{-1}	A m^2 mol^{-1}	V s m mol^{-1}
	1 G cm^3 mol^{-1} $\hat{=}$	10^{-3} A m^2 mol^{-1}	$4\pi\cdot 10^{-10}$ V s m mol^{-1}
χ	$\boldsymbol{P} = \chi\boldsymbol{H}$	$\boldsymbol{P} = \chi\boldsymbol{H}$	$\boldsymbol{P} = \chi\mu_0\boldsymbol{H}$
	cm^3	m^3	m^3
	1 cm^3 $\hat{=}$	$4\pi\cdot 10^{-6}$ m^3	$4\pi\cdot 10^{-6}$ m^3
χ_v	$\chi_v = \chi/V$	$\chi_v = \chi/V$	$\chi_v = \chi/V$
	cm^3 cm^{-3}	m^3 m^{-3}	m^3 m^{-3}
	1 cm^3 cm^{-3} $\hat{=}$	4π m^3 m^{-3}	4π m^3 m^{-3}
χ_g	$\chi_\mathrm{g} = \chi_v/\rho$	$\chi_\mathrm{g} = \chi_v/\rho$	$\chi_\mathrm{g} = \chi_v/\rho$
	cm^3 g^{-1}	m^3 kg^{-1}	m^3 kg^{-1}
	1 cm^3 g^{-1} $\hat{=}$	$4\pi\cdot 10^{-3}$ m^3 kg^{-1}	$4\pi\cdot 10^{-3}$ m^3 kg^{-1}
χ_m	$\chi_\mathrm{m} = \chi_\mathrm{g} A$	$\chi_\mathrm{m} = \chi_\mathrm{g} A$	$\chi_\mathrm{m} = \chi_\mathrm{g} A$
	cm^3 mol^{-1}	m^3 mol^{-1}	m^3 mol^{-1}
	1 cm^3 mol^{-1} $\hat{=}$	$4\pi\cdot 10^{-6}$ m^3 mol^{-1}	$4\pi\cdot 10^{-6}$ m^3 mol^{-1}

Experimental errors

In this volume, experimental errors are given in parentheses referring to the last decimal places. For example, 1.352(12) stands for 1.352 ± 0.012, and 342.5(21) stands for 342.5 ± 2.1.

9 Magnetic Properties of Halides

(Chap. 9.1–9.5 see Subvol. III/27J1; Chap. 9.6–9.11 see Subvol. III/27J2)

9.12 Halide Perovskite-type Layer Structures

9.12.1 Introduction

9.12.1.1 Characterization of Perovskite-type Layer Structures

This contribution is devoted to halide perovskite-type layer structures and their various physical properties, especially to their magnetic properties and structural phase transitions. These materials are closely related to the perovskite family with the composition AMX_3. There are oxide perovskites like $BaTiO_3$ and halide perovskites like $KNiF_3$. Here, we will concentrate on the halides where $X = F^-$, Cl^-, Br^- etc., where $M = Mg^{2+}$, Mn^{2+}, Fe^{2+}, Co^{2+}, Cu^{2+}, Cd^{2+} etc. and where $A = K^+$, Rb^+ etc. The essential structural unit in AMX_3 compounds with the cubic perovskite structure are MX_6 octahedra where the M-ion is surrounded by six X-ions (see Fig. 1.1). These octahedra form a corner-sharing three-dimensional network. The composition of compounds with a perovskite-type layer structure is A_2MX_4, also with MX_6 octahedra as structural units which form a two-dimensional network in this case. The layers with octahedra are sandwiched between AX layers (cf. Fig. 1.1). There are also oxides of the type A_2MX_4 with the same layered structure, for example Bi_2CuO_4 and La_2CuO_4 which are closely related to the high-T_C superconductors. But these materials are beyond the scope of this contribution and will be mentioned only to show parallels or differences between halides and oxides.*) In addition to the compounds with single perovskite-type layers as shown in Fig. 1.1, there are layered structures with double layers (see Fig. 1.2) or with an even higher number of perovskite-type layers sandwiched between AX layers, e.g. triple layer structures [90J1, 95A1]. The general formula is $A_3M_2X_7$ and $A_4M_3X_{10}$ for double- and triple-layer compounds, respectively. However, most of the halide perovskite-type layer structures studied so far are of the single-layer type, some are of the double-layer type and only few of the triple layer type, e.g. $Rb_4Cd_3Cl_{10}$ [68S1, 90B2]. More examples of the latter type exist among the oxides, e.g. $Sr_4Ti_3O_{10}$ [58R1], $Ca_4Ti_3O_{10}$ [91E] and $Ca_4Mn_3O_{10}$ [67C1].

These layered structures have become famous as model systems for quasi two-dimensional magnets [74J1, 90J1]. When M is a paramagnetic ion, the cubic symmetry of the perovskite structure requires the exchange interaction among nearest neighbours of M-ions to be equal in all three space directions. But in the layer structure, the exchange interaction is strong only between nearest neighbours within the layers and very weak between neighbours in adjacent layers, usually smaller by three orders of magnitude than the intra-layer interaction. For example, K_2CoF_4 and Rb_2CoF_4 have been found to be almost ideal realizations of the two-dimensional Ising model [84H1, 84C1] which can be solved exactly [44O]. In the double layer structures, we have a strong exchange coupling within the layers and also to the neighbouring layer of the double layer system. For chlorides and bromides (X = Cl, Br), it is possible to increase the separation of the perovskite-type layers by preparing compounds with organic n-alkylammonium chains instead of the alkali ions, i.e. $A = (C_nH_{2n+1}NH_3)^+$ or, more precisely, $A = (n\text{-}C_nH_{2n+1}NH_3)^+$. In the following, the "n-" will be dropped, except for some cases where other alkylammonium groups are discussed in comparison to n-alkylammonium chains. In the compounds with these chains, the interlayer distance depends critically on the length n of the chains (number of carbon atoms), and it was the idea that the magnetic properties would be closer to those of an ideal two-dimensional system by increasing this distance. Another type of chlorides or bromides with organic ions are alkylenediammonium compounds with divalent ions $A_2 = [NH_3(CH_2)_nNH_3]^{2+}$ which also provide an increasing layer separation with increasing n. The particular magnetic properties of these halide perovskite-type layer structures will be a major topic to be discussed in several of the following sections.

---

*) For perovskite-type layered cuprates see Landolt-Börnstein, Vol. III/27F2.

The monoammonium and diammonium compounds $(C_nH_{2n+1}NH_3)_2MX_4$ and $[NH_3(CH_2)_nNH_3]MX_4$ undergo a number of structural phase transitions, mainly of the order-disorder type. The molecular symmetry of the organic ions does not fit to the tetragonal symmetry of the ideal A_2MX_4 structure (cf. Fig. 1.1), usually called the K_2NiF_4 structure [55B]. There are several possibilities of hydrogen-bonding between the NH_3-group and the X-ions of the perovskite-type layers which are the dominant mechanism for the phase transitions. This will be outlined in detail in one of the following sections and it will be shown that propyl-compounds $(C_3H_7NH_3)_2MCl_4$ have outstanding properties among these materials with even some incommensurate structural phases. For longer chains (n ≥ 5), structural phase transitions arise also from conformational changes in the hydrocarbon chains. In the low temperature phase, the hydrocarbon chains exhibit an ordered arrangement while they can be considered liquid-like in the high temperature phase where the layers of MX_6 octahedra still behave as a solid.

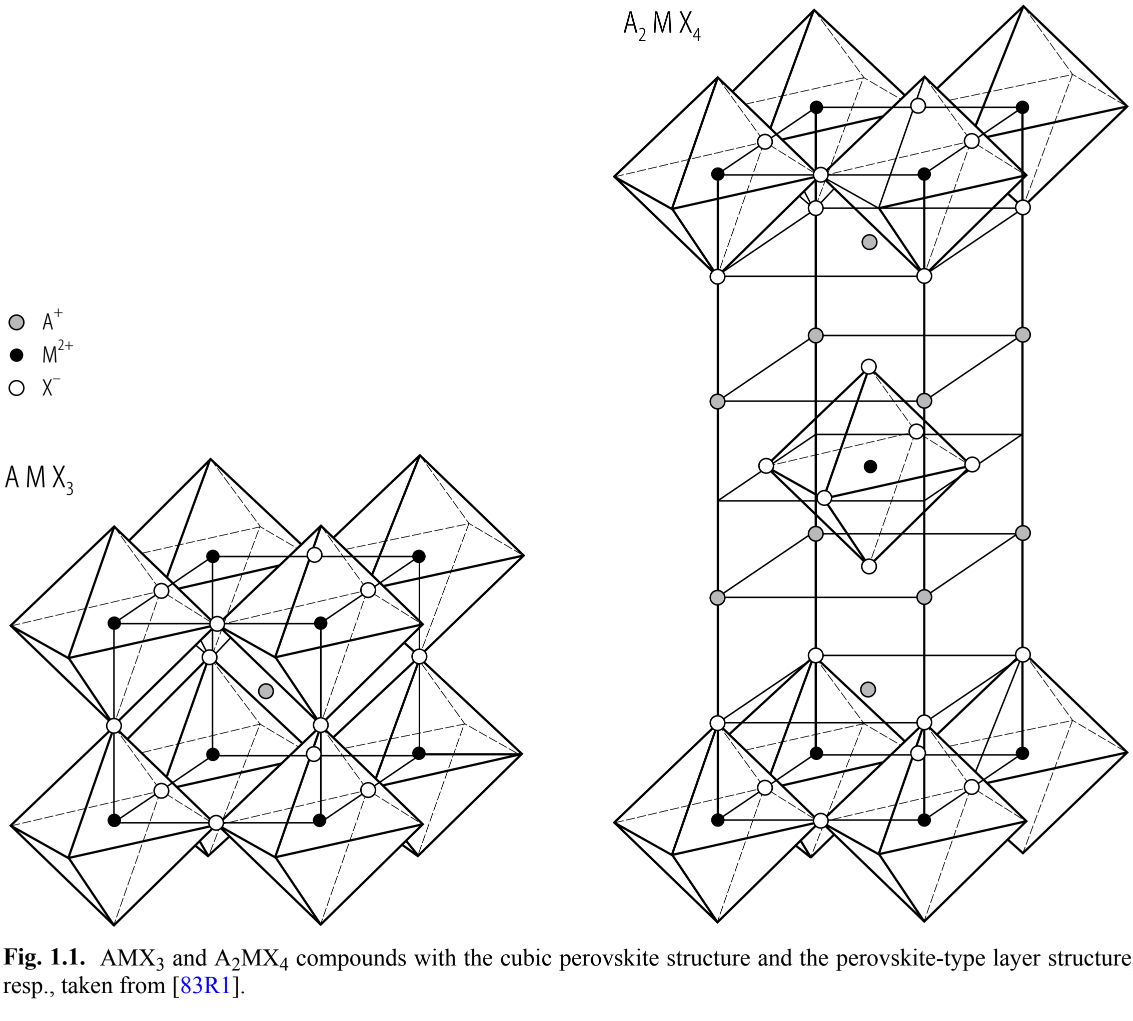

Fig. 1.1. AMX_3 and A_2MX_4 compounds with the cubic perovskite structure and the perovskite-type layer structure, resp., taken from [83R1].

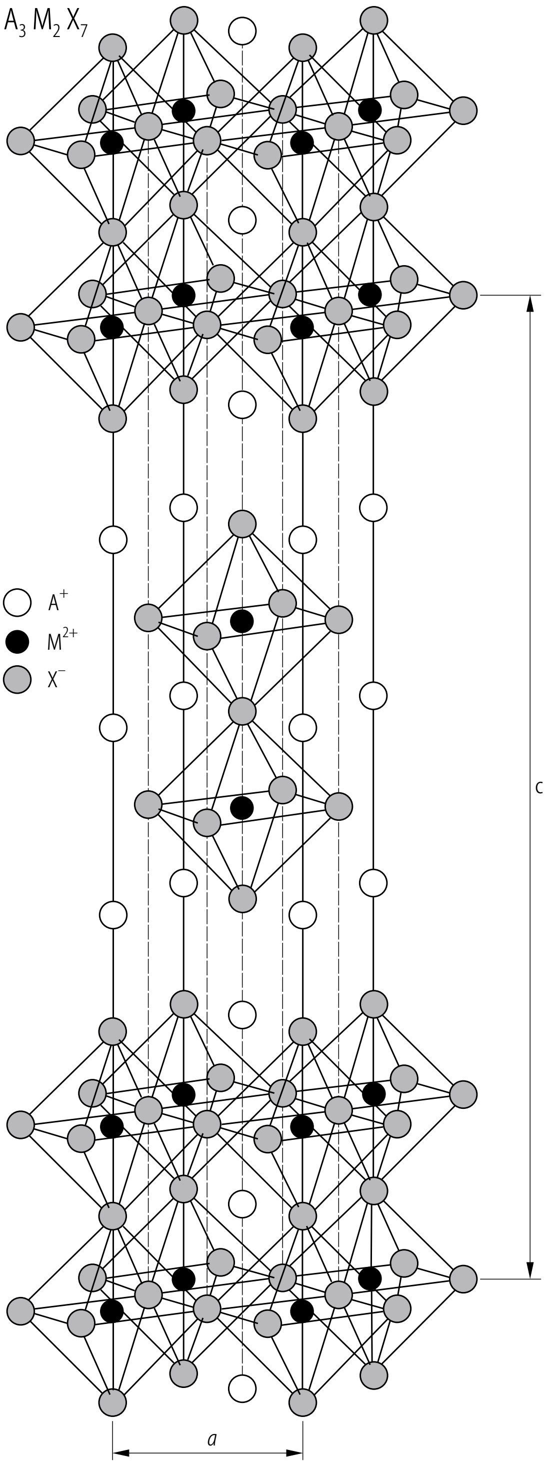

Fig. 1.2. $A_3M_2X_7$ with a double-layer perovskite-type structure, after [76G1].

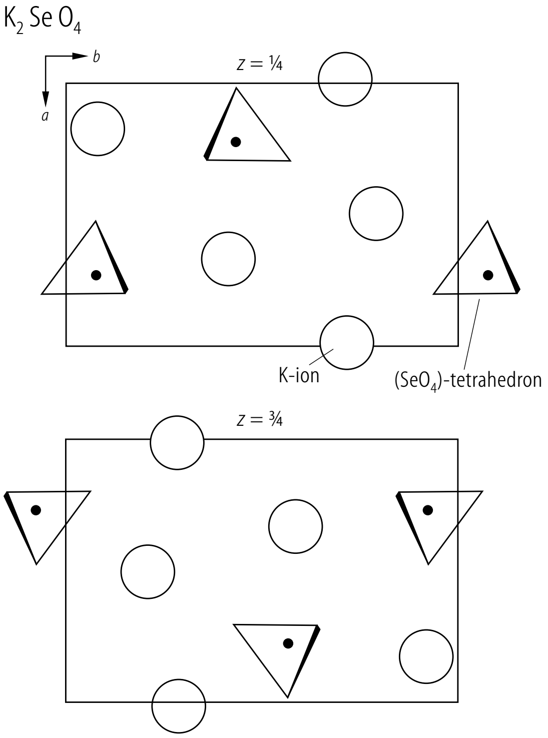

Fig. 1.3. K_2SeO_4. High temperature structure ($T > T_i$ = 130 K), illustrating the isolated SeO_4 ($\hat{=} MX_4$) tetrahedra. Two levels along the *c*-direction at heights $z = \frac{1}{4}$ and $z = \frac{3}{4}$ are shown (taken from [77I1)].

As often occurs in nature, there exist compounds with the same composition A_2MX_4 which are not perovskite-type layer structures in the above defined sense. Their structure is the β-K_2SO_4 structure, for some compounds only at high temperatures above the transition to an incommensurate phase ($T > T_i$). In this structure, the M-ions and the X-ions form isolated tetrahedra as shown for K_2SeO_4 in Fig. 1.3. Examples of this type are Rb_2ZnCl_4 [81D1], Cs_2CoCl_4 [56P], Rb_2FeCl_4, $CsFeCl_4$ [66S1], $(C_nH_{2n+1}NH_3)_2ZnCl_4$ [76M1, 77C1], $(C_nH_{2n+1}NH_3)_2CoCl_4$ [77L1], Cs_2CuCl_4 [52H] and other compounds. With the different structure, they have different physical properties. For example, the magnetic properties of Cs_2CoCl_4 are that of a quasi one-dimensional antiferromagnet and not those of a quasi two-dimensional one [79S1]. Therefore, they do not fit into the framework of this contribution and are not discussed here, except for a few examples where the comparison of the properties of our perovskite-type layer structures with these compounds brings more clarity and a better understanding. We will further not deal with compounds like K_2PtCl_4 and K_2PdCl_4 [22D, 72M1] where the crystal structure contains isolated square planar units of $PtCl_4$ or $PdCl_4$, respectively, which are arranged parallel to each other. However, compounds like $(C_3H_7NH_3)_2PdCl_4$ [77W2] and $[NH_3(CH_2)_2NH_3]PdCl_4$ [76B3] will be included since the $PdCl_4$ units are packed together there in a way that they form an infinite two-dimensional networks of distorted corner-sharing octahedra. Thirdly, we will exclude compounds with trivalent M^{3+}-ions like AMX_4, A_2MX_5. Examples of this type are $KFeF_4$, $KMnF_4$ and K_2FeF_5 *). They are in some aspects similar to the compounds under consideration here. Their structure consists of puckered MX_6 octahedral layers [72H1, 92M1] but for reasons of a well-rounded and complete survey we would have to include also a great number of compounds with trivalent ions like $RbAlF_4$, $LiYF_4$, $LiTbF_4$, $LiHoF_4$ and Tl_2AlF_5 which is beyond the limits of this chapter. Compounds of the type $BaMnF_4$, $BaZnF_4$ will be excluded for similar reasons.

In the last two decades, the compounds under consideration have been reviewed under various aspects, and a number of interesting data have been published in them. In their review on magnetic model systems, de Jongh and Miedema [74J1] included as prototypes for quasi two-dimensional magnetism the halide perovskite-type layer structures. Another review dealt with magnetic resonance experiments on these compounds [83G1]. Within the framework of low dimensional magnetic systems [90J1], they were reviewed with respect to magnetic phase transitions [90R1], field induced phenomena [90G3], spin waves [90A3], neutron scattering experiments [90H] and with respect to electron paramagnetic resonance (EPR) and nuclear magnetic resonance (NMR) investigations in the paramagnetic regime [90B1]. Also the structural phase transitions of perovskite-type crystals have been the subject of reviews [87A1, 95A1].

9.12.1.2 Lattice Dynamics: Intralayer and Interlayer Forces

As already mentioned, the halide perovskite-type layer structures are prototypes for two-dimensional magnetism which will be discussed in detail below. Another question is whether also the lattice dynamics of these compounds exhibits two-dimensional properties, i.e. whether the interlayer forces between the ions are much weaker than the intralayer forces. Since this contribution is mostly devoted to the magnetic properties and to the phase transitions of these compounds and since there will not be enough space for an extra section subjected to the lattice dynamics, it is perhaps advisable to answer the above questions briefly in this part of the introduction. Let us look at the mechanical and lattice dynamical properties of some compounds:

a) perovskite-type layer compounds are easily cleaved parallel to the layers. This easy cleavage could be an indication for weak interlayer forces
b) the second criterion are the elastic constants. Let us compare them for some of our compounds with those of a cubic perovskite and of a typical layer compound with very weak interlayer forces, namely pyrolytic graphite (all elastic constants in GPa). For a similar comparison in more detail: see [79G4]

---

*) See Landolt-Börnstein, Vol. III/27J2 for these compounds.

cubic perovskite $KZnF_3$ [87B5]: $C_{11} = 134.4$, $C_{33} = 134.4$, $C_{66} = 38.3$, $C_{44} = 38.3$

layer structure K_2ZnF_4 [84L1]: $C_{11} = 90.8$, $C_{33} = 74.4$, $C_{66} = 25.0$, $C_{44} = 16.0$

layer str. $(CD_3ND_3)MnCl_4$ [79G4]: $C_{11} = 30.3$, $C_{33} = 18.6$, $C_{66} = 9.5$, $C_{44} = 3.2$

pyrolytic graphite [72N]: $C_{11} = 1440$, $C_{33} = 37.1$, $C_{66} = 460$, $C_{44} = 4.6$

This comparison shows that the ratios C_{11}/C_{33} and C_{66}/C_{44} are of the order 1 for the perovskite-type layer structures in contrast to pyrolytic graphite with $C_{11}/C_{33} = 38.8$ and $C_{66}/C_{44} = 100$ and similar compounds like MoS_2 [75W2]. These data give thus some evidence that the interlayer forces are not much weaker than the intralayer forces in the layer structures under consideration

c) at third let us compare the infrared active lattice modes of the perovskite $KZnF_3$ [67P] and the layer compound K_2ZnF_4 [76B2] which are shown in Fig. 1.4 as oscillator strength $S = \tilde{\nu}_{TO}\,\varepsilon''_{max}\,\gamma$ versus the wavenumber $\tilde{\nu}_{TO}$ of the corresponding transverse optic (TO) branch for $q \to 0$ and where ε''_{max} is the maximum of the imaginary part ε'' of the dielectric constant at this frequency and γ the width of this maximum. An example of such infrared spectra is shown in Fig. 2.25 in Sect. 2.2.1. For reasons of the anisotropy, the infrared spectroscopic measurements are performed on K_2ZnF_4 for $\boldsymbol{E} \perp \boldsymbol{c}$ and $\boldsymbol{E} \parallel \boldsymbol{c}$ where $\boldsymbol{c}$ means the crystalline *c*-axis perpendicular to the layers. The data in Fig. 1.4 reveal that the modes of K_2ZnF_4 for $\boldsymbol{E} \perp \boldsymbol{c}$ occur at nearly the same frequency with nearly the same oscillator strength as the modes of $KZnF_3$, except for one mode which becomes infrared active in the lower symmetry of the layered compound. This is not surprising since the ions K^+, Zn^{2+} and F^- are displaced in these modes within the three-dimensional network of ZnF_6 octahedra in $KZnF_3$ and within the plane of the two-dimensional network of the octahedra in K_2ZnF_4 (cf. Fig. 1.1). The modes of K_2ZnF_4 for $\boldsymbol{E} \parallel \boldsymbol{c}$ mean a displacement of the ions perpendicular to the layers involving also interlayer forces. The three modes for $\boldsymbol{E} \parallel \boldsymbol{c}$ have somewhat different frequencies, but are in the same frequency range and not at much smaller frequencies. Therefore, Fig. 1.4 gives no hint for weaker interlayer forces. Similar results are obtained by comparing the infrared and/or Raman active lattice modes of other perovskite and perovskite-type layered materials [76S6, 77G2].

d) A more direct evaluation of the interlayer and intralayer forces is achieved by comparing the phonon dispersion curves, i.e. the phonon frequencies $\omega_{q,\mu}$ at wavevector $\boldsymbol{q}$ in branch μ, for K_2ZnF_4 [83R1, 85R3] with those of $KZnF_3$ [81G4, 81R4, 82L2] as obtained by neutron inelastic scattering (experimental points in Figs. 1.5 and 1.6). Fig. 1.5 presents $\omega_{q,\mu}$ of K_2ZnF_4 for the directions (0, 0, 1) and (1, 1, 0). Both start at the center Γ of the Brillouin zone and end for (0, 0, 1) at the high symmetry point Z of the Brillouin zone and for (1, 1, 0) at Z of the neighbouring zone. A broken line indicates for (1, 1, 0) the boundary between the two zones. In (0, 0, 1) direction, the lattice modes are longitudinal (L) and doubly degenerate transverse (T) ones (symmetry species $\Lambda_1 - \Lambda_5$) while the modes in (1, 1, 0) direction are mixed transverse and longitudinal and are therefore labelled according to their symmetry species $\Sigma_1 - \Sigma_4$. For the definition of high symmetry points and lines in the Brillouin zones of K_2ZnF_4 (tetragonal structure I4/mmm) and of $KZnF_3$ (cubic structure Pm3m), the reader is referred to [69Z], and for the symmetry species or irreducible representations of the point group of the wavevector along the high symmetry lines to [63K1]. Fig. 1.6 reproduces $\omega_{q,\mu}$ of $KZnF_3$ for the main symmetry directions (1, 0, 0), (1, 1, 0) and (1, 1, 1) starting at Γ and ending at the high symmetry points X, M and R, resp., at the Brillouin zone boundary. For all three directions, the modes are longitudinal (L) and doubly degenerate transverse (T) ones. The symmetry species are $\Delta_1 - \Delta_5$ (1, 0, 0), $\Sigma_1 - \Sigma_4$ (1, 1, 0) and $\Lambda_1 - \Lambda_3$ (1, 1, 1). The experimental data in Figs. 1.5 and 1.6 illustrate that the frequencies of the lattice modes are very similar in both cases indicating that also the forces are very similar. The only difference is that the number of branches is larger for K_2ZnF_4 due to the larger number of particles in the unit cell.

The curves in Figs. 1.5 and 1.6 have been calculated by means of a lattice dynamical shell model. Such a model consists of long-range Coulomb forces between the ions and short-range repulsive forces between them. The shell model allows further to take the polarizability of the ions into account (see for example [62C, 72S2, 82L2, 85R3]). In some shell models, axially symmetric short range forces have been employed with the parameters fitted to the experimental data. But for both compounds, a successful fit was also obtained [81G4, 82L2, 85R3] by calculating the short-range force constants from crystal-independent interionic potentials for the K–F and F–F interactions which were originally derived for alkali halides [77C6, 78S10, 78S11] and also used for calculating various properties of perovskites [81K11, 89B3]. For $KZnF_3$ and K_2ZnF_4, the application of interionic potentials requires only to take the different distances of the ions within the octahedra and for K_2ZnF_4 between the octahedral layers into account. For the three-dimensional network of octahedra as the basic structural element in the perovskites and the two-dimensional network in the perovskite-type layer structure (cf. Fig. 1.1), the forces are nearly equal in both cases and there is no principle difference between the intralayer and interlayer forces in K_2ZnF_4 because of the same interionic potentials and because of the Coulomb forces which are equal in all directions of space depending only on the distance between the ions. The interionic potentials have also successfully been applied to other perovskite-type layer materials like K_2MnF_4, K_2NiF_4 and K_2CuF_4 [82S3]. Further, nonempirical interionic potentials were employed to calculate various properties of $KZnF_3$ and K_2ZnF_4 like lattice constants, ionic positions in the unit cell, elastic constants and phonon dispersion curves which all agree reasonably well with the corresponding experimental data [92M7].

The conclusion from these examples is that the lattice dynamics of the perovskite-type layer structures exhibits three-dimensional behaviour and not a two-dimensional one, in contrast to the magnetic properties. Also the critical exponents (cf. Sect. 4.1.1) obtained at the structural phase transitions confirm this three-dimensional character (cf. Table 6).

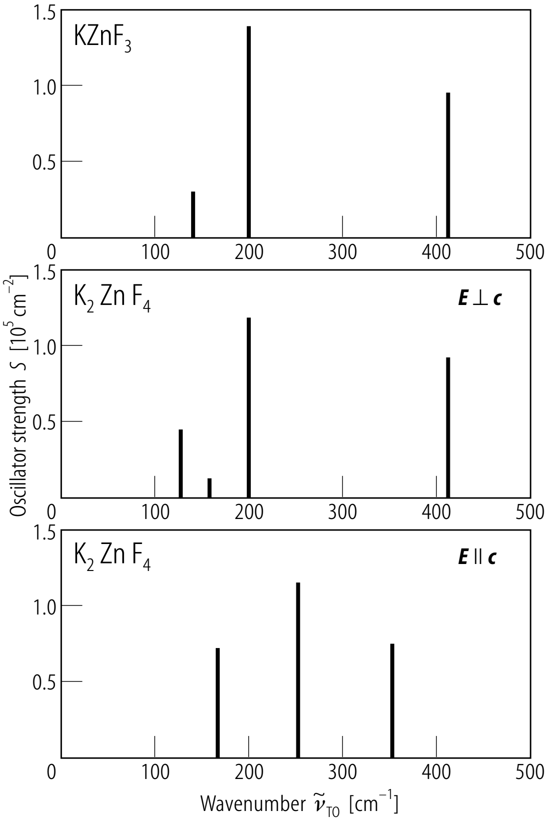

Fig. 1.4. $KZnF_3$ and K_2ZnF_4. Oscillator strength $S = \tilde{\nu}_{TO}\,\varepsilon''_{max}\,\gamma$ versus wavenumber $\tilde{\nu}_{TO}$ of infrared active lattice modes where ε''_{max} is the maximum of the imaginary ε'' part of the dielectric constant and γ its width at the wavenumber $\tilde{\nu}_{TO}$. The infrared data on $KZnF_3$ are taken from [67P], those on K_2ZnF_4 for $\boldsymbol{E} \perp \boldsymbol{c}$ and $\boldsymbol{E} \parallel \boldsymbol{c}$ from [76B2]. For further explanations, see text or [83R1].

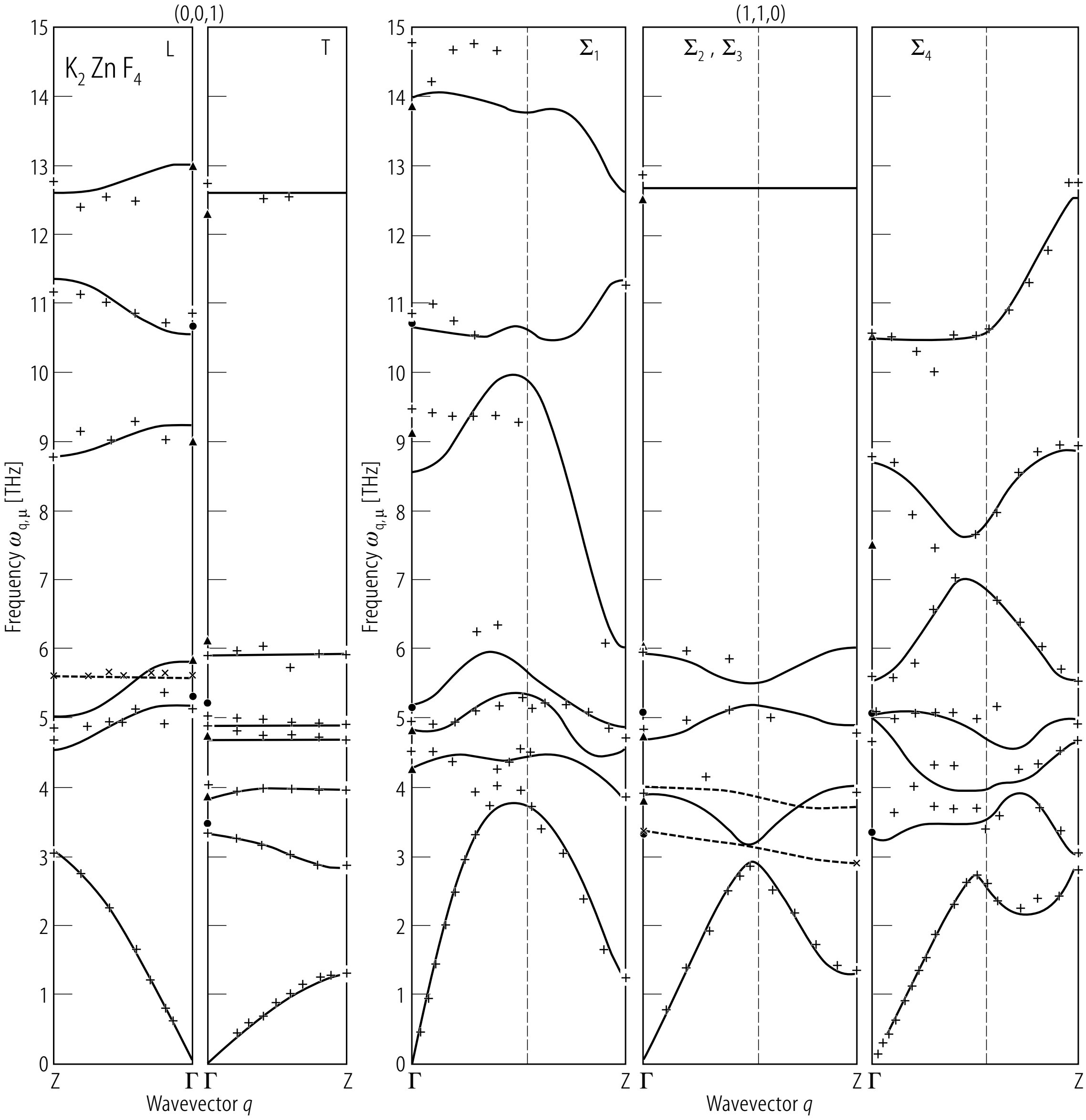

Fig. 1.5. K_2ZnF_4. Phonon dispersion curves, i.e. frequency $\omega_{q,\ \mu}$ (branch μ) versus wavevector $\boldsymbol{q}$, for the directions (0, 0, 1): L [Λ_1 (plusses), Λ_4 (crosses)], T [Λ_5 (plusses)] and for (1, 1, 0) [Σ_1 (plusses), Σ_2 (plusses), Σ_3 (crosses), Σ_4 (plusses)]; also shown: infrared (full triangles) and Raman (full circles) data. The points represent experimental data and the curves (Λ_4, Σ_3: broken lines, all others: full lines) are calculated by means of a lattice dynamical shell model (taken from [85R3]). For further details, see text or [83R1, 85R3].

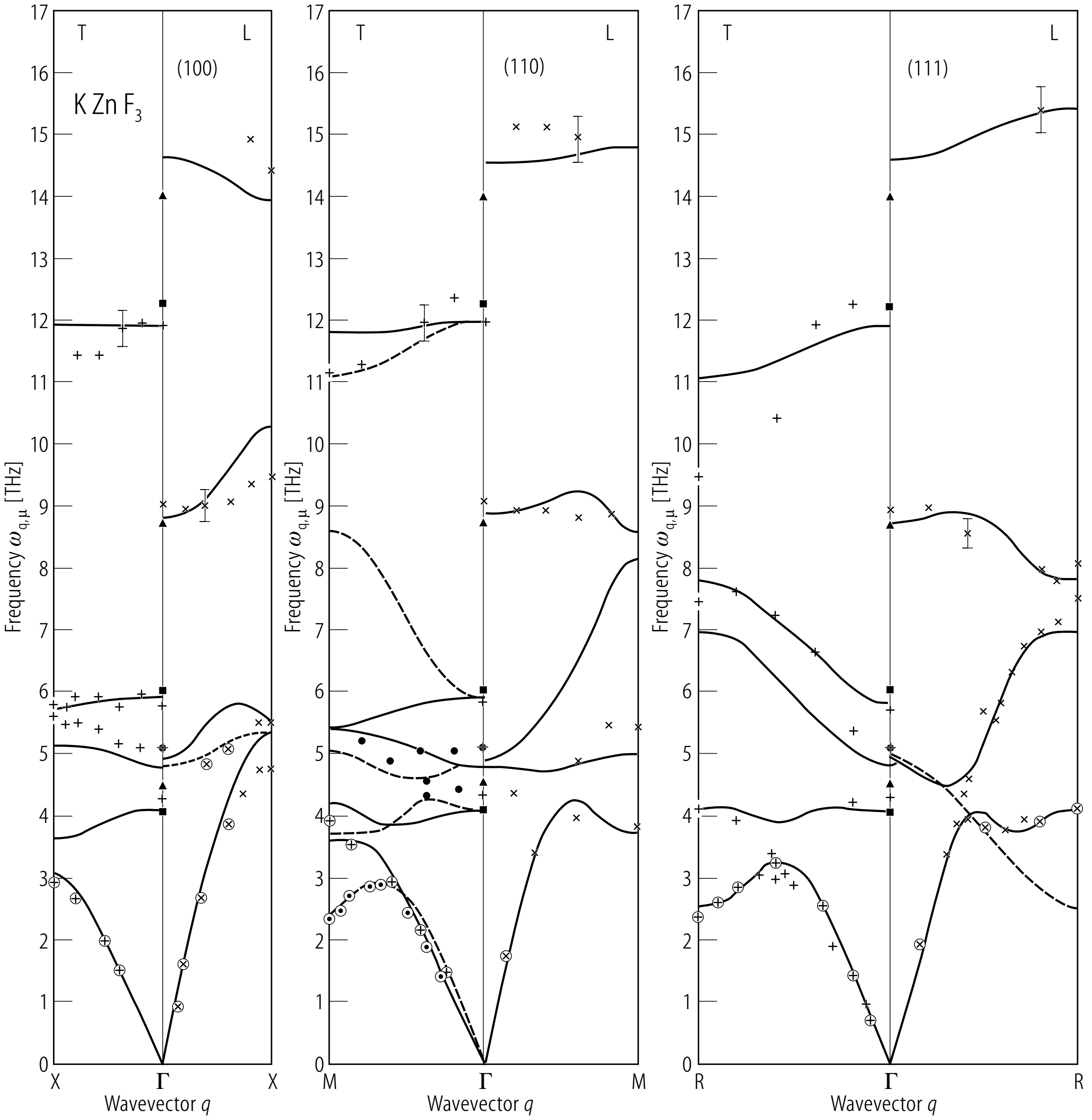

Fig. 1.6. KZnF$_3$. Phonon dispersion curves, frequency $\omega_{q,\mu}$ (branch μ) versus wavevector $\boldsymbol{q}$, for the directions (1, 0, 0): L [Δ_1 (crosses), Δ_2 (full circles)], T [Δ_5 (plusses)]; (1, 1, 0): L [Σ_1 (crosses)], T [Σ_2 (plusses), Σ_3 (full circles), Σ_4 (plusses)]; (1, 1, 1): L [Λ_1 (crosses), Λ_2 (full circles)], T [Λ_3 (plusses)]; also shown: infrared data [LO (full triangles), TO (full squares)]. The points are experimental data and the curves (Δ_2, Σ_3, Λ_2: broken lines, all others: full lines) are calculated by means of a lattice dynamical shell model (taken from [82L2]). Encircled points: taken from [81R4]. For further details, see text.

9.12.1.3 Comments on Notation and Units and Table 1

Let us start with a brief survey over the following sections. This contribution will be organized as follows:

The following Section 2 will be devoted to the structures of halide perovskite-type layer compounds and their structural phase transitions. The structural data are compiled in Table 2 and the distances characterizing the layer structures in Table 3. The text in Section 2 introduces to all symbols and abbreviations used in the Tables and illustrates with some figures the various structures, including the magnetic ones. For the structural phase transitions, experimental data will be discussed as well as group theoretical connections between the phases and model calculations for the transitions. All data about the structural phase transitions are collected in Table 4.

The magnetic properties will be introduced in Section 3, the various magnetic orderings at low temperatures and magnetic interactions. Also, linear and renormalized spin-wave theories will briefly be explained and all other theoretical definitions and connections which are necessary for the understanding of the entries to Table 5 with all data about the magnetic properties like various exchange constants, anisotropy fields. The important experimental methods for exploring the magnetic properties are neutron difraction, neutron inelastic scattering and magnetic resonance experiments.

As already mentioned, perovskite-type layer compounds are with their two-dimensional magnetic properties prototypes and close realizations for certain models of phase transitions like the Ising model, the XY-model or the Heisenberg model. These differ in the critical exponents at the phase transition. Therefore, Section 4 will deal with the critical properties observed near the critical temperature at which the system undergoes the phase transition. Section 4 will further introduce to the critical exponents and critical amplitudes. The corresponding numerical values are listed in Table 6. Not only the static but also the dynamic critical behaviour is of interest and, in this context, also the results of electron paramagnetic resonance at temperatures far above the critical temperature are a subject in Section 4 because of their relation to the correlation function of the system which is responsible for the fluctuations near the critical temperature and also for the typical two-dimensional effects observed at elevated temperatures.

In Tables 2–6, the various data of the perovskite-type layer compounds, i.e. structures, structural phase transitions, magnetic and critical properties, are compiled in the following order:

a) fluorides
b) chlorides, bromides, and iodides with inorganic A^+-ions
c) chlorides and bromides with organic A^+-ions
d) diammonium compounds with $X = Cl^-$, Br^-
e) diluted magnets (magnetic compounds doped with diamagnetic M^{2+}-ions)
f) mixed magnets (magnetic compounds doped with other paramagnetic M^{2+}-ions)

Within these sections, the compounds are ordered according to the atomic number of the divalent M-ion. For all numerical values in Tables 2–6, the error limits (standard deviation or appropiate estimate) are given as a number in parentheses corresponding to the last decimal place. The above listing indicates that it is advantageous to deal separately with mixed crystals and solid solutions of the type $A_2M_x\widetilde{M}_{1-x}X_4$ with two different divalent ions M^{2+} and $\widetilde{M}^{2+}$ because of the special properties of such systems as, for example, spin glass behaviour. Mixed crystals of the type $A_x\widetilde{A}_{1-x}MX_4$ with two different A^+-ions or of the type $A_2M(X_x\widetilde{X}_{1-x})_4$ with two different X^--ions, on the other hand, are dealt with in the sections of the pure materials a)–b). This order applies not only to the tables but also to the text sections.

With respect to the tables, it is further worth noting that some data on perovskite-type layer structures with the composition A_2MX_4 have already been published in this Landolt-Börnstein series about 25 years ago in Vol. III/4a [70G1] and nearly 20 years ago in Vol. III/12a [78N1]. It is unavoidable that there is some overlap between this contribution and the previous ones. However, there have been published so many new and interesting results in the mean time that it is justified to write a new compilation of data and results on these compounds. In the Tables, e.g. on structural and magnetic properties, we refer to the previously published data by [III/4a] or [III/12a], respectively, under remarks in the Tables. In those cases where no new data are available we will also include the "old" data in order to have a complete survey. In the Tables, this will be marked by "[III/4a] rep." and "[III/12a] rep.", respectively ("rep." $\hat{=}$ "reproduced"). This applies mostly to Table 2 since the previous contributions to the Landolt-Börnstein series are usually restricted to structural data and do not list data about structural phase transitions or magnetic properties in detail.

The symbols and abbreviations used in the sections and the tables of this contribution are compiled in Table 1. The units for the various quantities have been mostly chosen according to the international SI-system. That means, for example, that the lattice parameters of the crystal structures are given here in nm and not in Å-units as in the previous contributions in Vol. III/4a and Vol. III/12a. The symbols and the notation for physical quantities is in most cases chosen in accordance with the literature. Where different symbols are used for the same quantity in different references, there has to be a unified and unique choice in this contribution. It is further inevitable to use one symbol or letter for more than one quantity (cf. Table 1). For example, in context with equations of motion and temporal evolutions, "t" is the time and, in context with critical phenomena, "t" is the reduced temperature equal $(T/T_C - 1)$. Some special arrangements are necessary for energy units in context with spectroscopic techniques since it is quite unusual to present the energy of elementary excitations like phonons or magnons in J. Mostly the units used for this purpose depend on the spectroscopic technique. In neutron scattering, THz or meV are frequently used and cm^{-1} in infrared and Raman spectroscopy. For thermodynamic considerations, characteristic energies are expressed in K. In order to make the entries to the Tables comparable, two units, namely cm^{-1} and K, have been chosen for the data collected in this contribution from the number of various units, and the corresponding data have, if necessary, been converted to these units.

A further remark concerning units is for the magnetic field. Unfortunately, the SI-unit for H(A/m) has not found common use. Therefore, we will use here for H the magnetic flux density in vacuum $B = \mu_0 H$ in T as most people do. Older units like kG or kOe will be converted to T. Also the magnetization M will be given in T throughout this contribution and, consequently, the magnetic dipole moment in $\mathrm{Vsm} = \mathrm{Tm}^3$, e.g. $\mu_B = 1.16541 \cdot 10^{-29}$ Vsm. This choice of the units for H, M and μ_B implies that a factor $(\mu_0)^{-1}$ has to be introduced for products like MH, $\mu_B H$ and $(\mu_B)^2$ for obtaining the energy density in Jm^{-3}, the energy in J and the product $(\mu_B)^2$ in Jm^3. In order to present $g\mu_B H$, MH and similar expressions in the form commonly used in the literature we will suppress the unusual factor $(\mu_0)^{-1}$ in the equations containing such expressions. But it is tacitly assumed that in these expressions the units of H are converted from T to A/m, different from our choice, or, equivalently, a factor $(\mu_0)^{-1}$ is added in order to obtain the appropiate energy units. One exception to these rules is concerned with the product $(g\mu_B)^2$, where the factor $(\mu_0)^{-1}$ is explitcitly included in the equations to obtain the correct dimension Jm^3, for example in the Curie constant C which appears in the Curie law and in the Curie-Weiss law and which reads in our notation $C = (N/V) \cdot [(g\mu_B)^2/(3\mu_0 k_B)]$.

As the reader of this contribution will have noticed already, it is Chapter 9.12 within the III/27 volumes of the Landolt-Börnstein series. Thus, each section is labelled accordingly, e.g. 9.12.1.2 or 9.12.2.2.4 (cf. also the Table of Contents and the titles in this section). For reasons of better lucidity and to avoid unwieldy forms, the common prefix 9.12 is dropped when reference is given to another section in the text or on the tables. If, for example, a remark in Sect. 9.12.3.2.1 refers to Sect. 9.12.2.1.2, this is written as: see Sect. 2.1.2. For the same reason, the figures and the equations are numbered within the sections 9.12.1 – 9.12.4 also without 9.12, e.g. Fig. 3.24, i.e. Fig. 24 in Sect. 9.12.3, or Eq. 2.36, i.e. Eq. 36 in Sect. 9.12.2.

Table 1. List of Symbols and Abbreviations

a) Symbols

A, B, C	factors in the internal energy $U\,(n_1, n_2, n_3, n_4)$, cf. Eq. 2.29 (Sect. 2.2.4)
A_2MX_4	perovskite-type layer structure with A^+, M^{2+} and X^- ions, introduced in Sects. 1.1 and 2.1.1
$A_x\widetilde{A}_{2-x}MX_4$, $A_2M_x\widetilde{M}_{1-x}X_4$, $A_2MX_x\widetilde{X}_{4-x}$	mixed crystals of A_2MX_4 with concentration x: a) with two different A^+-ions, b) with two different M^{2+}-ions, c) with two different X-ions X^- and $\widetilde{X}^-$ (cf. Sects. 2.1.1 and 2.1.5)
A^+, A^-, A	specific heat critical amplitude, + for $T > T_C$, – for $T < T_C$, without superscript for $T > T_C$ and for $T < T_C$
A_{DS}	constant factor in $I(q, \Delta x, \mu)$ Eq. 4.105 (Sect. 4.1.11)
A_{EPR} [T]	constant part of the EPR linewidth, see Eq. 4.164 in Sect. 4.2.6 and Eq. 4.186 in Sect. 4.2.8
$\widetilde{A}_{EPR}$	factor of the spin diffusion term of the EPR linewidth, obtained at the magic angle, see Eq. 4.183 in Sect. 4.2.8
A_{LS}	constant factor in $S(\boldsymbol{q}, \omega)$ for T near T_C, cf. Eqs. 4.158 and 4.158a (Sect. 4.2.3)
A_{NMR}	abbreviation for the geometrical factors associated with the hyperfine interaction, see Eq. 4.161 (Sect. 4.2.5)
A_{RF}	amplitude of the Lorentzian part of $S(q)$ in a random field system, see Eq. 4.118 (Sect. 4.1.12)
A_S	amplitude of the Lorentzian part of $S(\omega)$ for diluted system, see Eq. 4.151 (Sect. 4.2.2)
A_{hf}	hyperfine coupling coefficient, see Eq. 3.125 (Sect. 3.3.1)
A_n, A_{ng}, A_{nu}	symmetry species (irreducible representations) of a point group in the Mulliken or chemical notation (n = 1, 2, 3, etc.), the additional subscripts g and u apply to point groups with inversion symmetry and mean even and odd with respect to this point group operation, for details see [64T] and [78B3]
$A_{n\alpha}$	number of ways in which a n-ion cluster of type α can be implemented, cf. Eq. 3.130 in Sect. 3.3.2
A_{theory}	theoretical specific heat critical amplitude for the anisotropic Heisenberg model, see Eq. 4.19 (Sect. 4.1.3)
Abma, I4/mmm, $P4_2$/ncm	symbols for space groups in the international notation [69I, 69Z]
a_3, a_5, a_7	coefficients of the nonlinear part of M (Eq. 4.124) and of the nonlinear susceptibility χ_{nl} (Eq. 4.125, Sect. 4.1.13)
a, b, c [nm]	lattice parameters
a, b, c, d, f, g	factors in the Landau-type internal energy $U(\eta_1, \eta_2, \eta_3)$, cf. Eq. 2.33 (Sect. 2.2.4)
$\boldsymbol{a}, \boldsymbol{b}, \boldsymbol{c}$	basic lattice vectors
$\boldsymbol{a}^*, \boldsymbol{b}^*, \boldsymbol{c}^*$	basic vectors of the reciprocal lattice
a' [nm]	distance between the two layers of a double layer system, as introduced in context with Eqs. 2.6 and 2.7 (Sect. 2.1.1)

Table 1. List of Symbols and Abbreviations *(continued)*

a_{nn} [nm]	nearest neighbour distance of paramagnetic M^{2+}-ions
$a_{\mathrm{nn},0}$ [nm]	reference value of a_{nn} for the model calculation of $J(a_{\mathrm{nn}})$, see Eq. 3.1 in Sect. 3.1.1, $a_{\mathrm{nn},0} = 0.4074$ nm
$\mathrm{a}(T)$	T-dependent critical exponent of $\chi \cdot k_{\mathrm{B}}T$ as function of the number of spins N (finite-size!), cf. Eq. 4.62 (Sect. 4.1.8)
a [cm^{-1} or K]	parameter of the 4th order out-of-plane single-ion anisotropy, tetragonal symmetry, cf. Eq. 3.34 (Sect. 3.1.5)
a_{n}	coefficients in the high-temperature series expansion for the susceptibility χ, see Eq. 3.26 (Sect. 3.1.3), n = 1, 2, 3, ...
$a_{\mathrm{n}}(T)$	coefficients in the expansion of the susceptibility χ with respect to powers of the concentration x in a diluted system, see Eq. 3.131 (Sect. 3.3.2)
$\mathrm{a}_{\mathrm{i}}^{+}, \mathrm{a}_{\mathrm{i}}$	local Bose creation and annihilation operators for spin deviations at lattice site i on sublattice a, cf. Eq. 3.3 (Sect. 3.1.2)
$\mathrm{a}_{\mathrm{q}}^{+}, \mathrm{a}_{\mathrm{q}}$	wavevector dependent creation and annihilation operators on sublattice a, cf. Eq. 3.4a (Sect. 3.1.2)
$B \sim L^{\Psi}$	barrier height in activated dynamics (cf. Sects. 4.1.13, 4.2.2)
$B = b\,(2 - \eta)$	nonuniversal parameter in the exponential law for $\chi(T)$ in the Kosterlitz-Thouless theory, see Eq. 4.44 (Sect. 4.1.8)
B_0, B_1, B_2	coefficients in the expansion of $M(T)/M(0)$ with respect to $t = T/T_{\mathrm{C}} - 1$ in Eq. 4.1 (Sect. 4.1.1), B_0 is the order parameter critical amplitude
B_2^0, B_4^4 [cm^{-1} or K]	factors describing the strength of the uniaxial and the cubic crystalline field, see Eq. 3.33 (Sect. 3.1.5)
$B(\boldsymbol{q}) = B_{\mathrm{q}}$	q-dependent factor in the spin-wave calculations and in the microwave absorption rate for parallel pumping, see Eq. 3.116 (Sect. 3.2.5)
B_{EPR} [$\mathrm{T\,K}^{-1}$]	factor of the term linear in T in the EPR linewidth, see Eq. 4.164 in Sect. 4.2.6 and Eq. 4.186 in Sect. 4.2.8
$B_{\mathrm{EPR,\ antisymmetric\ exchange}}$	theoretical form for B_{EPR}, resulting from antisymmetric exchange, see Eq. 4.187a in Sect. 4.2.8
$B_{\mathrm{EPR,\ anisotropic\ exchange}}$	theoretical form for B_{EPR}, resulting from anisotropic exchange, see Eq. 4.187b in Sect. 4.2.8
B_{RF}	amplitude of the Lorentzian squared in $S(q)$ of a random field system, see Eq. 4.118 (Sect. 4.1.12)
B_{S}	amplitude of the anomalous spin diffusion part of $S(\omega)$ in a diluted system (cf. Eq. 4.151 in Sect. 4.2.2)
B_{hf}	hyperfine coupling coefficient, see Eq. 3.125 (Sect. 3.3.1)
$\mathrm{B}_{\mathrm{n}}, \mathrm{B}_{\mathrm{ng}}, \mathrm{B}_{\mathrm{nu}}$	symmetry species (irreducible representations) of a point group in the Mulliken or chemical notation (n = 1, 2, 3, etc.), the additional subscripts g and u apply to point groups with inversion symmetry and mean even and odd with respect to this point group operation, for details see [64T] and [78B3]
b	nonuniversal parameter in the exponential law for $\xi(T)$ in the Kosterlitz-Thouless theory, see Eq. 4.43 (Sect. 4.1.8)
$\boldsymbol{b}$ [T]	oscillating magnetic flux density of the microwave or millimeter wave in magnetic resonance, see Eq. 3.46 (Sect. 3.1.6)

Table 1. List of Symbols and Abbreviations *(continued)*

b_n	coefficients in the high-temperature series expansion of the reciprocal susceptibility χ^{-1}, see Eq. 3.27 (Sect. 3.1.3), n = 1, 2, 3, ...
$\mathrm{b}_\mathrm{j}^{+}, \mathrm{b}_\mathrm{j}$	local Bose creation and annihilation operators for spin deviations at lattice site j on sublattice b, cf. Eq. 3.3 (Sect. 3.1.2)
$\mathrm{b}_\mathrm{q}^{+}, \mathrm{b}_\mathrm{q}$	wavevector dependent creation and annihilation operators on sublattice b, cf. Eq. 3.4a (Sect. 3.1.2)
C [K]	Curie constant, see Curie-Weiss law Eq. 3.25 (Sect. 3.1.3)
C [m s^{-1}]	factor in the magnon dispersion relation of a Heisenberg antiferromagnet, hydrodynamic description (Eq. 3.139, Sect. 3.3.3)
$C_2(r, \mathrm{x})$	pair connectedness function in diluted magnetic systems, see Eq. 4.90 in Sect. 4.1.11
$C_0^{\pm}, C_1^{\pm}, C_2^{\pm}$	coefficients in the expansion of χ with respect to $t = T/T_\mathrm{C} - 1$ in Eq. 4.8 (Sect. 4.1.2), $C_0^{\pm}$ is the magnetic susceptibility critical amplitude
C_AFMR [T K^{-4}]	factor in T^4-law for the AFMR linewidth, Eq. 3.13 (Sect. 3.1.2)
C_EPR [T]	factor of $t^{-\mathrm{p}}$ in the EPR linewidth (Eqs. 4.164 and 4.165 in Sect. 4.2.6)
C_NMR [T]	factor of $t^{-\mathrm{w}}$ in the NMR linewidth (Eq. 4.160 in Sect. 4.2.5)
C_M [K$^{-3/2}$]	factor in the $T^{3/2}$-dependence of the magnetization of a ferromagnet, cf. Eq. 3.78 (Sect. 3.2.1)
C_broad [T]	factor of the concentration x in $\Delta H_\mathrm{EPR}(\mathrm{x} \neq 0) - \Delta H_\mathrm{EPR}(\mathrm{x} = 0)$, see Eq. 4.189 (Sect. 4.2.9)
C, C_mn [Pa]	elastic (stiffness) constants (m, n = 1, 2, ..., 6) in the Voigt notation, e.g. C_{12}: $12 \mathrel{\hat{=}} x_0 x_0 y_0 y_0$, C_{66}: $66 \mathrel{\hat{=}} x_0 y_0 x_0 y_0$ (cf. [55L]) with x_0, y_0 referring to the (x_0, y_0, z_0) coordinate system of the parent phase I4/mmm throughout this contribution
C_{66}^0 [Pa]	elastic constant C_{66} without coupling to the structural phase transitions, see Eq. 2.36 in Sect. 2.2.4
C_p [J mol^{-1} K^{-1}]	(molar) specific heat (at constant pressure)
$C_\mathrm{p,0}$ [J mol^{-1} K^{-1}]	background specific heat due to lattice vibrations, cf. Eq. 4.81 in Sect. 4.1.10
$C_\mathrm{p}(T)_\mathrm{trans}$, ΔC_p	anomalous part of the specific heat at a phase transition, see Eqs. 2.18a, 2.18b (Sect. 2.2.1) and Eq. 4.81 (Sect. 4.1.10)
C_phonon [J mol^{-1} K^{-1}]	(molar) specific heat, calculated from the spectrum of lattice vibrations, cf. Eq. 2.17 in Sect. 2.2.1
C_magn [J mol^{-1} K^{-1}]	magnetic contribution to the specific heat in a ferro- or antiferromagnetic system
$C_\mathrm{magn}^{(\mathrm{n})}(h_\mathrm{E}')$	n-th derivative of $C_\mathrm{magn}(h_\mathrm{E}')$ with respect to h_E' (cf. Sect. 4.1.9)
$C_\mathrm{magn}^{\mathrm{2D}}, C_\mathrm{magn}^{\mathrm{3D}}$	magnetic specific heat of the system in the 2D and 3D regime, resp., see Eq. 4.76 (Sect. 4.1.9)
$\boldsymbol{c}' \perp \boldsymbol{a}, \boldsymbol{b}$	means that $\boldsymbol{c}'$ is a direction perpendicular to $\boldsymbol{a}$ and $\boldsymbol{b}$ which is different from the direction of $\boldsymbol{c}$ in monoclinic crystals, i.e. $\angle(\boldsymbol{c}, \boldsymbol{c}') = \beta - 90°$
c	velocity of light in vacuum, $c = 2.997924 \cdot 10^8$ m/s
c	nonuniversal parameter in Eq. 4.67 (Sect. 4.1.8), finite-size 2D XY-model, see also Eq. 4.68

Table 1. List of Symbols and Abbreviations *(continued)*

c', c''	constant factors in the relations for the time- and frequency-dependent susceptibilities $\chi'_{\mathrm{ac}}(\omega, T)$ and $\chi''_{\mathrm{ac}}(\omega, T)$, see Eq. 4.150 (Sect. 4.2.2)
c_{n}	coefficients in the high-temperature series expansion for the magnetic specific heat C_{magn}, see Eq. 4.39 (Sect. 4.1.7) n = 1, 2, 3, ...
×-over	crossover, e.g. 2D XY ↔ 3D XY
D [$\mathrm{m}^2\,\mathrm{s}^{-1}$]	diffusion constant, long-time behaviour of the two-spin correlation function (spin diffusion), see Eq. 4.179 in Sect. 4.2.8
$D^{\pm}$, E	coefficients for the background of the specific heat, constant and linear term, see Eqs. 4.16 and 4.17 (Sect. 4.1.3) and Eqs. 4.81 and 4.82 in Sect. 4.1.10
D_{DS}	constant factor for $\kappa(0, \mu)$ in Eqs. 4.109a and 4.109b (Sect. 4.1.11)
$\mathrm{D_f}$	fractal dimension, see Eq. 4.100 (Sect. 4.1.11)
$\boldsymbol{D}_{\mathbf{DM}}$ [cm^{-1} or K]	constant vector $\boldsymbol{D}_{\mathbf{DM}} = (D_{\mathrm{DM,x}}, D_{\mathrm{DM,y}}, D_{\mathrm{DM,z}})$ as parameters of the anti-symmetric exchange, i.e. of the Dzyaloshinskii-Moriya interaction, see Eq. 3.52 (Sect. 3.1.7)
$D_{\mathrm{s}}(r)$, $\widetilde{D}(x, y)$	density profile of a cluster in a diluted magnetic system and associated scaling function, see Eq. 4.99b (Sect. 4.1.11)
D [cm^{-1} or K]	parameter of the 2nd order out-of-plane single-ion anisotropy, tetragonal symmetry, cf. Eqs. 3.16 (Sect. 3.1.2), 3.34 and 3.35 (Sect. 3.1.5)
D_{A}, D_{B} [cm^{-1} or K]	$\mathrm{A_2M_x\widetilde{M}_{1-x}X_4}$: out-of plane anisotropy parameters for M- and $\widetilde{\mathrm{M}}$-ions (virtual crystal model, Eq. 3.142, Sect. 3.3.4)
$\widetilde{D}$ [cm^{-1} or K]	anisotropy parameter in Hamiltonian $\mathscr{H}(1)$ for a canted ferromagnet, cf. Eq. 3.81 (Sect. 3.2.2)
$\mathrm{D}_{2\mathrm{h}}^{18}, \mathrm{D}_{4\mathrm{h}}^{17}, \mathrm{C}_{2\mathrm{h}}^{5}$	symbols for space groups in the Schoenflies notation [69I, 69Z]
d	space dimensionality (cf. Sect. 4.1.1)
d [nm]	interlayer distance, i.e. separation of the perovskite-type layers, perpendicular to the layers
$\boldsymbol{d}$ [$\mathrm{A\,m}^{-2}$]	oscillating electric flux density of the microwave or millimeter wave in AFMR, see Eq. 3.46 (Sect. 3.1.6)
$\langle \Delta\, d \rangle$ [nm]	difference of interlayer distance d for $\Delta\mathrm{n} = 1$, i.e. for one $\mathrm{CH_2}$ group more in the hydrocarbon chain, averaged over a series of compounds $\mathrm{(C_nH_{2n+1}NH_3)_2MCl_4}$ with various chain lengths n
$\boldsymbol{E}$ [$\mathrm{V\,m}^{-1}$]	electric field
E [cm^{-1} or K]	parameter of the 2nd order in-plane single-ion anisotropy, orthorhombic symmetry, cf. Eq. 3.35 (Sect. 3.1.5)
E_{AA}, E_{BB}, $E_{\mathrm{AA,q}}$, $E_{\mathrm{BB,q}}$, $E_{\mathrm{AB,q}}$, $E_{\mathrm{BA,q}}$	energy terms in the secular equation of the mean or virtual crystal model for mixed systems (cf. Eq. 3.143, Sect. 3.3.4)
E_{ex} [J]	excitation energy, in context with the Arrhenius law for the electrical conductivity, cf. Eq. 2.44 (Sect. 2.2.6)
E_{i} [J]	neutron scattering: energy of the incident neutron
E_{f} [J]	neutron scattering: energy of the scattered neutron

Table 1. List of Symbols and Abbreviations *(continued)*

E_n, $E_n(\boldsymbol{q})$, $E_{n,q}$	Ising cluster energies in diluted antiferromagnets, Eqs. 3.140 and 3.141 in Sect. 3.3.3
$E_{n,M}$, $E_{n,C}$	Ising cluster excitations of M- and C-ions for non-collinear ordering in a mixed magnetic system (Eq. 3.153, Sect. 3.3.6)
$\widetilde{E}_n = E_n - \alpha E_n^3$	energy E_n for Co-compounds, modelling the nonlinear dependence on the molecular field in the lowest Kramers doublet as discussed in Sect. 3.3.3 and in [80C1]
E_p [cm^{-1}]	peak energy of the two-magnon Raman line (cf. Figs. 3.4 and 3.5)
E_s [J]	excitation energy of a 2D soliton, see Eqs. 4.170, 4.170a and 4.171 in Sect. 4.2.7
$\mathrm{E_n}$, $\mathrm{E_{ng}}$, $\mathrm{E_{nu}}$	symmetry species (irreducible representations) of a point group in the Mulliken or chemical notation (n = 1, 2, 3, etc.), the additional subscripts g and u apply to point groups with inversion symmetry and mean even and odd with respect to this point group operation, for details see [64T] and [78B3]
e [cm^{-1} or K]	parameter of the 4th order in-plane single-ion anisotropy, tetragonal symmetry, cf. Eqs. 3.34 (Sect. 3.1.5)
$e(h_A)$	temperature-independent renormalization factor in renormalized spin-wave theory, cf. Eq. 3.24a (Sect. 3.1.3)
$\boldsymbol{e}$ [V m^{-1}]	oscillating electric field of the microwave or millimeter wave in magnetic resonance, see Eq. 3.46 (Sect. 3.1.6)
e_m	elastic strain (m = 1, 2, ..., 6) in the Voigt notation, e.g. e_6: $6 \triangleq x_0\, y_0$ in the (x_0, y_0, z_0) coordinate system
F	factor relating the temperature derivative of LMB data to the magnetic specific heat C_{magn}, see Eq. 4.18 (Sect. 4.1.3)
$F \sim L^{\theta}$	typical droplet energy in activated dynamics (cf. Sect. 4.2.2)
$\mathcal{F}(\mathrm{x})$	scaling function for $\chi''_{ac}(\omega, T)$, see Eq. 4.128 (Sect. 4.1.13)
F [Jm^{-3}]	free energy of a system as defined in thermodynamics, per unit volume
$F\,[\sigma_6/(t_1)^{\varphi}]$	scaling function, homogeneous in $\sigma_6/(t_1)^{\varphi}$ where φ is the crossover exponent, see Eq. 4.87 in Sect. 4.1.10
$F(\omega)$	time Fourier transform of the two-spin correlation function $G(\boldsymbol{r}, t)$, see Eqs. 4.180 and 4.181 in Sect. 4.2.8
$F^{\alpha\beta}(\boldsymbol{K}, \omega)$	frequency distribution or spectral shape function, fluctuations of spin components S_α and S_β (α, $\beta = x, y, z$), cf. Eq. 4.23 (Sect. 4.1.5)
$F_{\parallel}(\boldsymbol{K}, \omega)$	spectral shape function for longitudinal critical fluctuations (parallel to the easy axis), cf. Eq. 4.131 (Sect. 4.2.1)
ΔF [Jm^{-3}]	additional term in the free energy, cf. Eq. 2.36 (Sect. 2.2.4)
f [Hz]	frequency
f_{NMR}, Δf_{NMR} [MHz]	NMR frequency or difference of NMR frequency (see e.g. [77A2]), reflecting the internal field acting on the nuclei
$f(\boldsymbol{K})$	magnetic form factor
$f(\boldsymbol{q}) = f_q$	q-dependent term in renormalized spin-wave theory, see Eq. 3.18 (Sect. 3.1.3)

Table 1. List of Symbols and Abbreviations *(continued)*

$f(\nu)$	in EPR: $\Delta H_{\mathrm{EPR}}^{\infty} = f(\nu)$ means that the constant term of the EPR linewidth depends on the frequency ν at which the experiment is performed (cf. Eq. 4.165 in Sect. 4.2.6)
$f(t\text{-range})$	in EPR: $C_{\mathrm{EPR}} = f(t\text{-range})$ means that the factor C_{EPR} is different for different ranges of t since ΔH_{EPR} is to be continuous at an ×-over point (cf. Eq. 4.165 in Sect. 4.2.6)
$G^{\alpha\beta}(\boldsymbol{r}, t)$	spin pair correlation function for fluctuations of spin components S_α and S_β ($\alpha, \beta = x, y, z$), see Eq. 4.22 (Sect. 4.1.5)
$G(\boldsymbol{r}, t)$	simplified form of the two-spin correlation function, see Eq. 4.180 in Sect. 4.2.8
$G(t_1, \sigma_6)$	free energy as a function of reduced temperature t_1 and elastic stress σ_6 in a scale-invariant form, see Eq. 4.87 in Sect. 4.1.10 and also [74A2, 82G1]
$G(\omega)$ [arb. units]	frequency distribution = generalized phonon density of states as a function of the frequency ω
G_0, G_1, G_2, etc.	space groups of the structural phases of a compound, where G_0 is the parent phase ("para"-phase) and G_1, G_2 etc. are usually subgroups of G_0
g	g-factor: in general or isotropic system
g_a, g_b, g_c	g-factor for magnetic fields $\boldsymbol{H_0}$ parallel to the a-, b-, or c-axis, respectively
$g_{\parallel}$, $g_{\perp}$	g-factor for magnetic fields $\boldsymbol{H_0}$ parallel or perpendicular to the c-axis, cf. Eq. 3.125 in Sect. 3.3.1
g_I	g-factor of the nuclear spin $\boldsymbol{I}$, assumed to be isotropic
$g(x)$, $\tilde{g}(x)$	scaling functions for C_{magn} and $\mathrm{d}(\Delta n)/\mathrm{d}T$ in random field systems, cf. Eq. 4.117a, 4.117b (Sect. 4.1.12)
$g(x)$, $\hat{g}(x)$	scaling functions for the nonlinear susceptibility χ_{nl}, see Eq. 4.127 (Sect. 4.1.12)
$\boldsymbol{g_1}$, $\boldsymbol{g_2}$, $\boldsymbol{g_3}$	special set of basic lattice vectors, see Eq. 2.21 (Sect. 2.2.1)
$g(\boldsymbol{q}) = g_q$	q-dependent term in renormalized spin-wave theory, see Eq. 3.15 (Sect. 3.1.2)
$g(\tau)$	distribution of relaxation times τ, see Eq. 4.148 (Sect. 4.2.2)
$\mathcal{H}$, $\mathcal{H}'$	Hamiltonian
$\boldsymbol{H}$ [T]	magnetic field, expressed by the magnetic flux density in vacuum ($1\ \mathrm{T} = 1\ \mathrm{Wb\ m^{-2}}$)
$\boldsymbol{H}_{\mathbf{a,eff}}$, $\boldsymbol{H}_{\mathbf{b,eff}}$ [T]	effective magnetic field acting on sublattices a or b, see Bloch-Bloembergen equation, see Eq. 3.42 (Sect. 3.1.6)
H_0 [T]	applied external magnetic field
$\boldsymbol{H_0} = (H_{0x}, H_{0y}, H_{0z})$ [T]	applied external magnetic field with x-, y- and z-components
$H_0^* = (g_c/g_a)\, H_0$ [T]	modified external magnetic field ($\boldsymbol{H_0} \parallel \boldsymbol{c}$), taking into account the anisotropy of the g-factor, see Eq. 3.97 (Sect. 3.2.3)
H_A [T]	anisotropy field, i.e. the main or out-of-plane anisotropy field
$H_{A,M}$, $H_{A,C}$ [T]	virtual crystal model Eq. 3.151: out-of-plane anisotropy fields of M- and C-ions, respectively (Sect. 3.3.6)

Table 1. List of Symbols and Abbreviations *(continued)*

$\hat{H}_{\mathrm{A,\,M}}, \hat{H}_{\mathrm{A,\,C}}$ [T]	virtual crystal model Eq. 3.151: in-plane anisotropy fields of M- and C-ions, resp., of tetragonal symmetry (Sect. 3.3.6)
$H_{\mathrm{A}}^{\Delta} = (g_{\mathrm{a}}/g_{\mathrm{c}})\, H_{\mathrm{A}}$ [T]	modified anisotropy field for $\boldsymbol{H}_{\mathbf{0}} \parallel \boldsymbol{c}$, taking into account the anisotropy of the g-factor, see Eqs. 3.108–3.109a (Sect. 3.2.3)
$\tilde{H}_{\mathrm{A}}, \hat{H}_{\mathrm{A}}$ [T]	in-plane anisotropy fields corresponding to the in-plane single-ion anisotropies of orthorhombic and tetragonal symmetry, resp., see Eqs. 3.37 (Sect. 3.1.5) and 3.41 (Sect. 3.1.6)
$H_{\mathrm{A1}}, H_{\mathrm{A2}}$ [T]	anisotropy fields corresponding to the anisotropy parameters $\tilde{P}$ and $\tilde{D}$ in Eq. 3.81 (Sect. 3.2.2), see Eq. 3.101 (Sect. 3.2.3)
H_{AD} [T]	anisotropy field, calculated from magnetic dipolar interactions, cf. Eqs. 3.8 and 3.12 (Sect. 3.1.2)
$H_{\mathrm{C}}(T)$ [T]	easy-plane ferromagnets: critical field $\boldsymbol{H} \parallel \boldsymbol{c}$ at which the system undergoes the transition from the ferro- to the paramagnetic state at a temperature $T < T_{\mathrm{C}}$ (cf. Fig. 3.33 in Sect. 3.2.1)
$H_{\mathrm{CF}}^{\mathrm{a}}, H_{\mathrm{CF}}^{\mathrm{b}}, H_{\mathrm{CF}}^{\mathrm{c}}$ [T]	critical magnetic field for $\boldsymbol{H}_{\mathbf{0}} \parallel \boldsymbol{a}$, $\boldsymbol{H}_{\mathbf{0}} \parallel \boldsymbol{b}$ or $\boldsymbol{H}_{\mathbf{0}} \parallel \boldsymbol{c}$, resp., in antiferromagnets with spin canting ($H_{\mathrm{D}} \neq 0$, see Eq. 3.60 in Sect. 3.1.8 for $\boldsymbol{H}_{\mathbf{0}} \parallel \boldsymbol{c}$)
$H_{\mathrm{C.P.}}$ [T]	magnetic field at the critical point in the (H_0, T) phase diagram of an antiferromagnet (see Fig. 3.18 in Sect. 3.1.6)
H_{D} [T]	Dzyaloshinskii-Moriya field, corresponding to antisymmetric exchange (Eq. 3.53 in Sect. 3.1.7) and to special anisotropic exchange in Cu-compounds (Eq. 3.99 in Sect. 3.2.3)
H_{E} [T]	intralayer exchange field
$H_{\mathrm{E,MM}}, H_{\mathrm{E,CC}}, H_{\mathrm{E,MC}}$	virtual crystal model Eq. 3.151: exchange fields for pairs of M–M, C–C, and M–C ions (Sect. 3.3.6)
H'_{E} [T]	interlayer exchange field, see Eq. 3.96 (Sect. 3.2.3)
H_{RF} [T]	random field in a diluted antiferromagnet with $\langle H_{\mathrm{RF}} \rangle = 0$ and $\langle H_{\mathrm{RF}}^{2} \rangle \neq 0$ (cf. Sect. 4.1.12)
H_{hf} [T]	hyperfine field in Mössbauer spectroscopy, cf. Sect. 3.3.2
$H_{\mathrm{int},\alpha}$ [T]	α-component of the internal magnetic field $\boldsymbol{H}_{\mathbf{int}}$, see Eq. 3.92 (Sect. 3.2.3)
H_{res} [T]	magnetic field at resonance (AFMR, EPR, FMR)
$H_{\mathrm{res,fm}}, H_{\mathrm{res,afm}}$ [T]	magn. field at resonance for the FMR-mode and the AFMR-mode of antiferromagnets in the field-induced paramagnetic phase (cf. Sect. 3.1.8)
H_{SF} [T]	antiferromagnet: critical field for the spin-flop transition, see Eqs. 3.38, 3.39 (Sect. 3.1.6) and 3.57 (Sect. 3.1.8)
H_{MF} [T]	molecular field, see Eq. 3.61 (Sect. 3.1.9)
$H_{\mathrm{PM}}^{\mathrm{a}}, H_{\mathrm{PM}}^{\mathrm{b}}, H_{\mathrm{PM}}^{\mathrm{c}}$ [T]	antiferromagnet: critical field for the transition from the AF- or the SF-phase to the PM-phase for $\boldsymbol{H}_{\mathbf{0}} \parallel \boldsymbol{a}$, $\boldsymbol{H}_{\mathbf{0}} \parallel \boldsymbol{b}$ and $\boldsymbol{H}_{\mathbf{0}} \parallel \boldsymbol{c}$, resp., cf. Eqs. 3.57–3.59 (Sect. 3.1.8)
ΔH_{AFMR} [T]	linewidth in antiferromagnetic resonance (AFMR), cf. Eq. 3.13 (Sect. 3.1.2)
$\Delta H_{\mathrm{AFMR}}^{0}$ [T]	AFMR linewidth for $T \to 0$, including instrumental linewidth
ΔH_{EPR} [T]	linewidth of the electron paramagnetic resonance (EPR), see Eqs. 4.164 and 4.165 (Sect. 4.2.6)

Table 1. List of Symbols and Abbreviations *(continued)*

$\Delta H_{\mathrm{EPR,sol}}$ [T]	EPR linewidth due to solitons, cf. Eq. 4.172 in Sect. 4.2.7
$\Delta H_{\mathrm{EPR,sw}}$ [T]	EPR linewidth due to magnons, cf. Eq. 4.173 in Sect. 4.2.7
$\Delta H_{\mathrm{EPR}}^{\infty}$ [T]	noncritical part of the EPR linewidth, Eq. 4.165 (Sect. 4.2.6)
$\Delta H_{\mathrm{EPR}}(\psi)$ [T]	angular dependence of the EPR linewidth, $\psi = \angle(\boldsymbol{H}_{\mathbf{0}}, c\text{-axis})$
$\Delta H_{\mathrm{A}}, \Delta H_{\mathrm{B}}, \Delta H_{\mathrm{C}}$	constants in Eqs. 4.182, 4.184 and 4.185, theoretical forms for $\Delta H_{\mathrm{EPR}}(\psi)$, cf. Sect. 4.2.8
$\Delta H'_{\mathrm{A}}, \Delta H'_{\mathrm{B}}$ [T]	constants in Eq. 4.188, a theoretical form for $\Delta H_{\mathrm{EPR}}(\psi)$, cf. Sect. 4.2.9
$\Delta H_1, \Delta H_2$ [T]	constants in Eq. 4.166, a theoretical form for $\Delta H_{\mathrm{EPR}}(\psi)$, cf. Sect. 4.2.6
$\Delta H'_1, \Delta H'_2$ [T]	constants in Eq. 4.166a, a theoretical form for $\Delta H_{\mathrm{EPR}}(\psi)$, cf. Sect. 4.2.6
ΔH_{FMR} [T]	linewidth in ferromagnetic resonance (FMR)
ΔH_{NMR} [T]	linewidth of the nuclear magnetic resonance (NMR), see Eq. 4.160 (Sect. 4.2.5)
$\Delta H_{\mathrm{NMR}}^{\infty}$ [T]	noncritical part of the NMR linewidth, Eq. 4.160 (Sect. 4.2.5)
ΔH_{q} [T]	linewidth of the spin wave with wavevector $\boldsymbol{q}$, spin-wave relaxation time: $(\gamma_{\mathrm{a}} \Delta H_{\mathrm{q}})^{-1}$
ΔH [J mol^{-1}]	transition enthalpy at a structural phase transition
ΔH_{n} [J mol^{-1}]	transition enthalpy of the n – th structural phase transition
h, k	factors in the additional Landau-type free energy ΔF for the coupling between elastic strain e_6 and the order parameters η_1, η_2, η_3 of the structural phase transitions, cf. Eq. 2.36 in Sect. 2.2.4
$h = 2\mu_{\mathrm{B}} H_0 / k_{\mathrm{B}} T$	reduced magnetic field for the description of the response of a diluted system to an external field H_0 (Eq. 4.95, Sect. 4.1.11)
$h = (g\mu_{\mathrm{B}} S H_0)/(k_{\mathrm{B}} T)$	alternative definition of the reduced field for random field systems, see Eq. 4.117b (Sect. 4.1.12)
$\boldsymbol{h}$ [T]	oscillating magnetic field of the microwave or millimeter wave in magnetic resonance, see Eq. 3.41 (Sect. 3.1.6)
h_0 [T]	amplitude of the oscillating magnetic field $\boldsymbol{h}$, see Eq. 3.115 (Sect. 3.2.5)
$h_{0,\mathrm{C}}$ [T]	threshold amplitude of the microwave field in parallel pumping, see Eq. 3.118 (Sect. 3.2.5)
$h_{\mathrm{A}} = H_{\mathrm{A}} / H_{\mathrm{E}}$	reduced out-op-plane anisotropy field
$\widetilde{h}_{\mathrm{A}} = \widetilde{H}_{\mathrm{A}} / H_{\mathrm{E}}$	reduced in-plane anisotropy field (orthorhombic symmetry)
$h'_{\mathrm{E}} = \mathrm{z}' J' / \mathrm{z} J$	reduced interlayer exchange field
$h_{\mathrm{E2}} = \lvert J_2 / J \rvert$	reduced exchange field for intralayer coupling between next nearest neighbours, see Eq. 3.14 (Sect. 3.1.2)
$h_{0\mathrm{x}} = g_{\mathrm{a}} \mu_{\mathrm{B}} H_{0\mathrm{x}} / 2z\, S \lvert J \rvert$	reduced external magnetic field $\boldsymbol{H}_{\mathbf{0}} \parallel \boldsymbol{x}$, isotropic systems $g_{\mathrm{a}} = g$
$h_{0\mathrm{z}} = g_{\mathrm{c}} \mu_{\mathrm{B}} H_{0\mathrm{z}} / 2z\, S \lvert J \rvert$	reduced external magnetic field $\boldsymbol{H}_{\mathbf{0}} \parallel \boldsymbol{z}$, isotropic systems $g_{\mathrm{c}} = g$
$h_{\mathrm{int,x}} = H_{\mathrm{int,x}} / H_{\mathrm{E}}$	x-component of the reduced internal field

Table 1. List of Symbols and Abbreviations *(continued)*

h_{RF}	reduced form of the random field in diluted antiferromagnets, see Eq. 4.115b (Sect. 4.1.12)
h_{κ}	reduced field defined in Eq. 3.74 (Sect. 3.2.1)
$h_{\kappa,0}$	reduced field h_{κ} for $H_0 = 0$, used in Eq. 4.38 (Sect. 4.1.7)
$(\mathrm{h}_0, \mathrm{k}_0, \mathrm{l}_0)$, $(\mathrm{h}, \mathrm{k}, \mathrm{l})$	indexing of the Bragg reflections with respect to the coordinate system $(q_{\mathrm{x0}}, q_{\mathrm{y0}}, q_{\mathrm{z0}})$ or $(q_{\mathrm{x}}, q_{\mathrm{y}}, q_{\mathrm{z}})$, resp.
h	Planck's constant, $h = 6.62619 \cdot 10^{-34}$ Js
$\hbar = h/2\pi$	Planck's constant divided by 2π, $\hbar = 1.05459 \cdot 10^{-34}$ Js
$\hbar\omega$	energy transfer in a neutron scattering process, cf. Eq. 2.24 (Sect. 2.2.3)
$\hbar\omega_{\mathrm{q}} = \hbar\omega(\boldsymbol{q})$	magnon (or phonon) energy at wavevector $\boldsymbol{q}$
$\hbar\omega_{\mathrm{q}}^{+} = \hbar\omega^{+}(\boldsymbol{q})$	magnon energy at $\boldsymbol{q}$ (+-branch), cf. Eqs. 3.5, 3.6 (Sect. 3.1.2)
$\hbar\omega_{\mathrm{q}}^{-} = \hbar\omega^{-}(\boldsymbol{q})$	magnon energy at $\boldsymbol{q}$ (−-branch), cf. Eqs. 3.5, 3.6 (Sect. 3.1.2)
$\hbar\omega_{\mathrm{BB}}(\mathrm{n}_1, \mathrm{n}_2)$	energy of the magnetic excitation of a pair Ni-ions ("B") surrounded by n_1 and n_2 Mn-ions ("A"), Eq. 3.145 (Sect. 3.3.4)
$\boldsymbol{I} = (I_{\mathrm{x}}, I_{\mathrm{y}}, I_{\mathrm{z}})$	nuclear spin, components with respect to the (x, y, z) coordinate system, see Eq. 3.125 (Sect. 3.3.1)
I, $I(\boldsymbol{q})$, $I(\boldsymbol{K})$	intensity, neutron scattering intensity (counting rate) of a Bragg reflection, e.g. as a function of wavevector $\boldsymbol{q}$ (Eq. 4.101) or quasi-elastic scattering intensity as function of $\boldsymbol{K}$ (Eq. 4.104) (Sect. 4.1.11)
I_{ac}	light intensity, transmitted in ac-configuration by an optically active sample at $T < T_{\mathrm{C}}$ under crossed polarizers, see [80K2]
I_{g}	initial gradient of $T_{\mathrm{C}}(\mathrm{x})/T_{\mathrm{C}}(1)$ for $\mathrm{x} \to 1$, see Eqs. 3.128 and 3.129 in Sect. 3.3.2
J_{ij} [cm^{-1} or K]	exchange constant describing the interaction between the two spins at lattice sites i and j, the exchange constants are presented in this contribution for practical reasons not in J but in spectroscopic units cm^{-1} or in temperature units K
J, J_2 [cm^{-1} or K]	exchange constants describing the intralayer interaction between the spins of two nearest neighbours or of two next nearest neighbours, resp.
$\tilde{J}$ [cm^{-1} or K]	exchange constant describing the intralayer interaction between nearest neighbours in a canted ferromagnet, cf. Eq. 3.81 in Sect. 3.2.2
J_{AA}, J_{BB}, J_{AB} [cm^{-1} or K]	$\mathrm{A_2M_x\tilde{M}_{1-x}X_4}$: exchange parameters for pairs of M–M, $\tilde{\mathrm{M}}-\tilde{\mathrm{M}}$, and $\mathrm{M}-\tilde{\mathrm{M}}$ ions (virtual crystal model, Eq. 3.142, Sect. 3.3.4)
$\hat{J}_{\mathrm{AB}}$ [cm^{-1} or K]	approximation of J_{AB} as the geometric mean of J_{AA} and J_{BB}, see Eq. 3.147 (Sect. 3.3.4)
$J(\boldsymbol{r}_{\mathrm{nn}})$ [cm^{-1} or K]	constant of the exchange between nearest neighbours connected by $\boldsymbol{r}_{\mathrm{nn}}$, within the layers and in adjacent layers (cf. Sect. 4.1.8)
$J(\boldsymbol{q})$ [cm^{-1} or K]	spatial Fourier transform of $J(\boldsymbol{r}_{\mathrm{nn}})$, cf. Eq. 4.54 (Sect. 4.1.8)
J_{calc} [cm^{-1} or K]	value of the exchange parameter J for nearest neighbours in the layers, calculated by means of Eq. 3.1 in Sect. 3.1.1
J_{exp} [cm^{-1} or K]	experimental value of the exchange parameter J (cf. Sect. 3.1.1)

Table 1. List of Symbols and Abbreviations *(continued)*

J_x, J_y, J_z [$\mathrm{cm^{-1}}$ or K]	exchange constants for nearest neighbours intralayer interaction, as defined in Eq. 4.2 (Sect. 4.1.1)
J_A, $\widetilde{J}_A$ [$\mathrm{cm^{-1}}$ or K]	constant of the out-of-plane and of the in-plane anisotropic intralayer exchange, resp.
J' [$\mathrm{cm^{-1}}$ or K]	exchange constant describing the interlayer interaction between neighbouring spins in adjacent layers
$J_{\parallel}$, $J_{\perp}$ [$\mathrm{cm^{-1}}$ or K]	exchange constants in strongly anisotropic antiferromagnets, cf. Eq. 3.62 (Sect. 3.1.9), e.g. Co-compounds [90H, 90N]
J_{VC} [$\mathrm{cm^{-1}}$ or K]	exchange constant in the expression for the 2D Ising model virtual crystal magnetization (cf. Eq. 3.136 in Sect. 3.3.2)
$j' = J'/J$	reduced interlayer exchange parameter in Eq. 4.69 (Sect. 4.1.9)
$K(\mathrm{x})$	mean number of finite clusters in a diluted magnetic system, see Eq. 4.94 in Sect. 4.1.11
$K = \lvert J \rvert / (k_B T)$	variable in high-temperature series expansions, see Eqs. 3.26 and 3.27 (Sect. 3.1.3)
$\widetilde{K} = 2S^2 \lvert J \rvert / (k_B T)$	spin stiffness ρ_s relative to the temperature T, cf. Eq. 4.48a (Sect. 4.1.8)
$\widetilde{K}_{\mathrm{eff}}$	effective relative spin stiffness, renormalized by the presence of vortex-antivortex pairs, see Eq. 4.48b (Sect. 4.1.8)
$\boldsymbol{K}$ [$\mathrm{nm^{-1}}$]	wavevector transfer in a neutron scattering process, cf. Eq. 2.24 (Sect. 2.2.3)
k	extinction coefficient
k_B	Boltzmann's constant, $k_B = 1.380622 \cdot 10^{-23}\ \mathrm{JK^{-1}}$
$\boldsymbol{k}_i$, $\boldsymbol{k}_f$ [$\mathrm{nm^{-1}}$]	neutron scattering: wavevector of the incident neutron and of the scattered neutron, resp.
k_{x0}, k_{y0}, k_{z0}	wavevector of a sound wave defining its direction of propagation, referring to the (x_0, y_0, z_0) coordinate system (Sect. 2.2.1)
k_x, k_y, k_z	wavevector of a sound wave defining its direction of propagation, with respect to the (x, y, z) coordinate system (Sect. 2.2.1)
L	Avogadro's number, $L = 6.0022 \cdot 10^{23}\ \mathrm{mol^{-1}}$
$L = \sqrt{N}$	characteristic length (in lattice constants) of a 2D system with N spins, finite-size 2D XY-model (cf. Sect. 4.1.8)
$L_{\mathrm{eff}} = \xi / a$	effective length in the finite-size 2D XY-model (cf. Sect. 4.1.8)
$\boldsymbol{L}$	orbital angular momentum of a paramagnetic ion
ℓ	C–C bond length in hydrocarbon chains, $l = 0.154$ nm
M [T]	magnetization; ferromagnet: spontaneous magnetization
M_0 [T]	antiferromagnet: ideal sublattice magnetization (Néel state, cf. Eq. 3.18 in Sect. 3.1.3); ferromagnet: magnetization for $T \to 0$ (Eq. 3.75a in Sect. 3.2.1) and demagnetization field (Eq. 3.92 in Sect. 3.2.3)
$M_0^* = (g_c / g_a) M_0$ [T]	modified demagnetization field for $\boldsymbol{H_0} \parallel \boldsymbol{c}$, taking into account the anisotropy of the g-factor, see Eqs. 3.109 (Sect. 3.2.3)
M_0^{θ} [T]	modified demagnetization field, taking into account the anisotropy of the g-factor if the magnetization forms an angle θ with the c-axis, see Eq. 3.108 (Sect. 3.2.3)

Table 1. List of Symbols and Abbreviations *(continued)*

M_{subl} [T]	sublattice magnetization (antiferromagnet)
M_{S} [T]	sublattice magnetization for $T \to 0$
$M_{0,\mathrm{n}}(T)$	local magnetization of the central ion surrounded by n magnetic neighbours, see Eq. 3.136 (Sect. 3.3.2)
$M_{\mathrm{VC}}(T)$ [T]	2D Ising model virtual crystal magnetization (Eq. 3.136 in Sect. 3.3.2)
$\boldsymbol{M} = (M_{\mathrm{x}}, M_{\mathrm{y}}, M_{\mathrm{z}})$	magnetization, e.g. of a ferromagnet (x-, y-, z-components)
$\boldsymbol{M}_{\mathbf{a}} = (M_{\mathrm{a,x}}, M_{\mathrm{a,y}}, M_{\mathrm{a,z}})$	magnetization of sublattice a, e.g. of an antiferromagnet
$\boldsymbol{M}_{\mathbf{b}} = (M_{\mathrm{b,x}}, M_{\mathrm{b,y}}, M_{\mathrm{b,z}})$	magnetization of sublattice b, e.g. of an antiferromagnet
$\boldsymbol{M}_{\mathbf{a,0}}$, $\boldsymbol{M}_{\mathbf{b,0}}$	static part of the magnetization of sublattices a and b, see Eq. 3.44 (Sect. 3.1.6)
$\boldsymbol{M}_{\mathbf{a}}$, $\boldsymbol{M}_{\mathbf{b}}$, $\boldsymbol{M}_{\mathbf{c}}$, $\boldsymbol{M}_{\mathbf{d}}$	the four sublattice magnetizations in the virtual crystal or average model, see Eq. 3.151 (Sect. 3.3.6)
$M_{\parallel}(H_{0\mathrm{z}}, T)$ [T]	magnetization parallel to the easy axis, induced by $H_{0\mathrm{z}}$, as a function of temperature T, cf. Eq. 3.21 (Sect. 3.1.3)
$\langle \hat{M} \rangle$	average magnetization per spin derived as a dimensionless quantity in [76M3], cf. Eq. 4.156 (Sect. 4.2.3)
$\langle \hat{M}^2 \rangle$	average of the square of the magnetization derived as a dimensionless quantity in [78M3], cf. Eq. 4.62 (Sect. 4.1.8)
$\boldsymbol{m}$ [T]	oscillating of precessing part of the magnetization, response of the system to the oscillatory field $\boldsymbol{h}$, cf. Eq. 3.45 (Sect. 3.1.6)
$\boldsymbol{m}_{\mathbf{a}}$, $\boldsymbol{m}_{\mathbf{b}}$ [T]	oscillating or precessing part of the magnetizations of sublattices a and b, resp., see Eqs. 3.42 and 3.44 (Sect. 3.1.6)
$m_{\mathrm{a}}^{(1)}$, $m_{\mathrm{b}}^{(1)}$, $m_{\mathrm{a}}^{(2)}$, $m_{\mathrm{b}}^{(2)}$	components of the oscillating or precessing parts of the magnetizations of sublattices a and b, resp., see Eq. 3.44 (Sect. 3.1.6)
N	total number of spins; in antiferromagnets: in both sublattices ($N/2$ spins per sublattice)
$N_{\mathrm{eff}} = (\xi/a)^2$	effective number of spins (cf. Sect. 4.1.8)
N/V [m^{-3}]	total number of spins per unit volume
$\mathbf{N}$	demagnetization tensor, cf. Eq. 3.98 (Sect. 3.2.3)
N^{x}, N^{y}, N^{z}	demagnetization coefficients with respect to the (x, y, z) coordinate system, see Eq. 3.92 (Sect. 3.2.3)
N^{a}, N^{b}, N^{c}	demagnetization coefficients with respect to the crystal axes
n	refractive index
n	spin dimension (cf. Sect. 4.1.1)
Δn	difference of the refractive indices, e.g. n_{b} (b-axis) minus n_{a} (a-axis), as determined by birefringence
$\Delta n(T_{\mathrm{Cn}})$	1st order jump of Δn at a slightly discontinuous phase transition with critical temperature T_{Cn} (Eq. 4.84a in Sect. 4.1.10)
Δn_{aa}, Δn_{ac}	difference of refractive indices observed by LMB in aa- or ac-configuration, resp., for definition see [80K2]
n_{q}, n_{q}^{+}, n_{q}^{-}	thermal average magnon state occupation number in general, and for +-branch and −-branch, resp., cf. Eq. 3.15 (Sect. 3.1.2)

Table 1. List of Symbols and Abbreviations *(continued)*

n_s(x)	number of clusters with size s in a diluted system with concentration x, see Eqs. 4.96 and 4.97 (Sect. 4.1.11)
n_1, n_2, n_3, n_4	occupation probabilities for the four possible orientations of the $(CH_3NH_3)^+$-group of compounds like $(CH_3NH_3)_2MCl_4$ in the high temperature structure I4/mmm
O_2^0, O_4^0, O_4^4	standard notation of operator equivalents for calculating the energy levels of magnetic ions in the crystalline electric field, see Eq. 3.33 (Sect. 3.1.5) and [64H]
P [cm^{-1} or K]	parameter of the 2nd order in-plane single-ion anisotropy of orthorhombic symmetry, see Eqs. 3.85 and 3.86 (Sect. 3.2.2)
$\widetilde{P}$ [cm^{-1} or K]	anisotropy parameter in Hamiltonian $\mathcal{H}(1)$ for a canted ferromagnet, cf. Eq. 3.81 (Sect. 3.2.2)
P(x)	percolation probability in diluted magnetic systems, see Eq. 4.93 in Sect. 4.1.11
P_C [W]	threshold microwave power in parallel pumping
P_i [W]	incident microwave power (in parallel pumping)
$P_{\parallel}(K^2, \omega)$ [arb. units]	frequency distribution (inelastic neutron scattering data) as a function of frequency ω for average $\boldsymbol{K}$ essentially parallel to the layers
$P_{\perp}(K^2, \omega)$ [arb. units]	frequency distribution (inelastic neutron scattering data) as a function of frequency ω for average $\boldsymbol{K}$ essentially perpendicular to the layers
$\mathrm{P}^{\mathrm{Abma}}_{\mathrm{s}\bar{1}1}$	example of the denotation of a superspace group for an incommensurate structure according to de Wolff, Janssen and Janner [81W1]
p [Pa]	pressure
p_C [Pa]	critical pressure, i.e. the pressure at the transition to a pressure induced phase
p	EPR linewidth exponent, see Eqs. 4.164 and 4.165 in Sect. 4.2.6
p^+, p^-	imbalance of the two sublattice magnetizations induced by a magn. field parallel to the easy axis, cf. Eq. 3.15 (Sect. 3.1.2)
p	diammonium compounds $[NH_3(CH_2)_nNH_3]MCl_4$: probability for twisted $[NH_3(CH_2)_nNH_3]$-chains or the average portions of chains in this state, $(1-p)$ the corresponding probability for all-trans chains (cf. Sect. 2.2.6)
p	parameter describing the deviation of $\chi(T, j')$ from $\chi(T, 0)$ due to the interlayer exchange coupling j', see Eq. 4.70 (Sect. 4.1.9)
p_m, p_n	order parameters in structural phase transitions as defined in context with Eq. 2.35 (Sect. 2.2.4) and in [79K5]
Q	vorticity of a vortex, defined in Eq. 4.40 (Sect. 4.1.8)
$\boldsymbol{Q}$, $\boldsymbol{Q}_0$ [nm^{-1}]	general vector of the reciprocal lattice and a special one, e.g. an ordinary Bragg reflection or an antiferromagnetic superreflection
q	critical exponent in the scaling relation for $\chi''_{ac}(\omega, T)$ see Eq. 4.128 (Sect. 4.1.13)
$\boldsymbol{q}$ [nm^{-1}]	wavevector of a collective excitation, usually in the first Brillouin zone
$\boldsymbol{q}_0$, q_0 [nm^{-1}]	modulation wavevector and its absolute value in modulated or incommensurate structures

Table 1. List of Symbols and Abbreviations *(continued)*

(q_{x0}, q_{y0}, q_{z0})	components of the wavevector $\boldsymbol{q}$, corresponding to the coordinate system (x_0, y_0, z_0) for the I4/mmm structure (cf. Fig. 2.1)
(q_x, q_y, q_z)	components of the wavevector $\boldsymbol{q}$, corresponding to the rotated coordinate system (x, y, z) for F4/mmm (cf. Fig. 2.1 in Sect. 2.1.2) and for low temperature structures
R	reflectivity
R	universal gas constant, $R = 8.31441$ J mol^{-1} K^{-1}
R_0, R_1	T-independent and T-dependent renormalization terms in renormalized spin-wave theory, cf. Eq. 3.15 (Sect. 3.1.2)
$R_A^{(m)}$, $R_M^{(n)}$, R_X	ionic radii of the A- and M-ions with coordination numbers m and n, resp., and of the X-ions in A_2MX_4 compounds, cf. Eqs. 2.15 and 2.16 (Sect. 2.1.5)
R_S	universal relation between critical amplitudes in the 2D Ising model, see Eq. 4.15 (Sect. 4.1.2)
R_s, $\widetilde{R}(x)$	radius of a cluster in a diluted magnetic system and associated scaling function, see Eq. 4.99a (Sect. 4.1.11)
R_{x0}, R_{y0}, R_{z0}	direction of polarization of a sound wave, with respect to the (x_0, y_0, z_0) coordinate system of I4/mmm (cf. Sect. 2.2.1)
R_x, R_y, R_z	direction of polarization of a sound wave, with respect to the (x, y, z) coordinate system of F4/mmm (cf. Sect. 2.2.1)
R′, R″	long-chain compounds $(C_nH_{2n+1}NH_3)_2MCl_4$ with $n > 5$: partial hydrocarbon groups of the long hydrocarbon chain
r	amplitude reflection coefficient
r_1, r_2	characteristic length defined in Eqs. 4.154, 4.155 (Sect. 4.2.3) for the 2D Heisenberg model
r_i, r_j	location of lattice sites i and j with spins S_i and S_j, resp.
$\boldsymbol{r}_{ij} = \boldsymbol{r}_i - \boldsymbol{r}_j$	vector connecting two lattice sites i and j
r_{ip}	in-plane MX bond length, i.e. parallel or nearly parallel to the layers
r_{op}	out-of-plane MX bond length, i.e. perpendicular or nearly perpendicular to the layers
$\boldsymbol{r}_n = (x_n, y_n, z_n)$	location of lattice site no. n, cf. Eq. 3.12 (Sect. 3.1.2)
$\boldsymbol{r}_{nn}$	vector connecting two nearest neighbours
S	value of the electronic spin of a paramagnetic ion
S_A, S_B	$A_2M_x\widetilde{M}_{1-x}X_4$: spin values of paramagnetic M^{2+}- and $\widetilde{M}^{2+}$-ions, resp., (virtual crystal model, Eq. 3.142, Sect. 3.3.4)
$S(x)$	mean size of finite clusters below the percolation threshold in diluted magnetic systems, see Eq. 4.92 (Sect. 4.1.11)
S_x, S_y, S_z	spin components with respect to the (x, y, z) coordinate system
S_ξ, S_η, S_ζ	spin components with respect to the (ξ, η, ζ) coordinate system
$\boldsymbol{S}_i = (S_{i,x}, S_{i,y}, S_{i,z})$	spin of paramagnetic ion at lattice site i, with x-, y- and z-components (operators)

Table 1. List of Symbols and Abbreviations *(continued)*

$\boldsymbol{S}_{\mathbf{a,i}}$, $\boldsymbol{S}_{\mathbf{b,j}}$, $\boldsymbol{S}_{\mathbf{c,i}}$, $\boldsymbol{S}_{\mathbf{d,j}}$	$A_2M_x\widetilde{M}_{1-x}X_4 : M^{2+}$- and $\widetilde{M}^{2+}$-spins on sites i and j in sublattices 1 and 2 (virtual crystal model, Eq. 3.142, Sect. 3.3.4)
S_i^+, S_i^-	raising and lowering operators for the spin at lattice site i, $S_i^+ = S_{i,x} + i\,S_{i,y}$, $S_i^- = S_{i,x} - i\,S_{i,y}$
$\langle S_z \rangle_0$	mean or expectation value of S_z in the ground state, see Eq. 3.61 (Sect. 3.1.9)
$S_D^{\alpha\beta}\,(\boldsymbol{K}, \omega)$	neutron scattering function (diffuse scattering, spin components S_α and S_β (α, $\beta = x, y, z$), momentum transfer $\hbar\boldsymbol{K}$ and energy transfer $\hbar\omega$, cf. Eq. 4.23 (Sect. 4.1.5)
$S(\boldsymbol{q})$	structure factor, definition see [90B3]
$S(\omega)$	neutron scattering function as defined in Eq. 4.151 (Sect. 4.2.2)
$S^{\parallel}(\boldsymbol{K})$, $S^{\perp}(\boldsymbol{K})$	total neutron scattering functions as defined in Eq. 4.103 (Sect. 4.1.11) where "$\parallel$" corresponds to "zz" and "$\perp$" to "xx" or "yy"
$S(\boldsymbol{q}, \omega)$	neutron scattering function for an inelastic scattering process, see Eqs. 4.157–4.159 (Sect. 4.2.3)
$\Delta_0 S$	zero point spin deviation, see Eq. 3.19 (Sect. 3.1.3)
S_{mn} [Pa^{-1}]	elastic compliances (m, n = 1, 2, ..., 6) in the Voigt notation, e.g. S_{12}: 12 $\hat{=} x_0\, x_0\, y_0\, y_0$, S_{66}: 66 $\hat{=} x_0\, y_0\, x_0\, y_0$ (cf. [55L]) with x_0, y_0 referring to the (x_0, y_0, z_0) coordinate system of the parent phase I4/mmm throughout this contribution, see Eqs. 4.78 and 4.79 in Sect. 4.1.10
S_{66}^0 [Pa^{-1}]	elastic compliance S_{66} without coupling to the structural phase transitions, see Eq. 4.78 in Sect. 4.1.10
S_{66}^+ [Pa^{-1}]	critical amplitude of the anomalous part of the elastic compliance S_{66}, see Eq. 4.86 in Sect. 4.1.10
$\Delta S_{66} = S_{66} - S_{66}^0$ [Pa^{-1}]	anomalous part of the elastic compliance S_{66} at the structural phase transition, cf. Eq. 4.86 in Sect. 4.1.10
S [J mol^{-1} K^{-1} or J m^{-3}K^{-1}]	entropy as defined in thermodynamics, per mole (cf. Eq. 2.18 in Sect. 2.2.1 and Eq. 2.41 in Sect. 2.2.5) or per unit volume (cf. Eq. 2.30 in Sect. 2.2.4)
S_{ex} [J mol^{-1} K^{-1}]	excess entropy due to the disorder of twisted and all-trans chains in diammonium compounds, see Eq. 2.43 (Sect. 2.2.6)
ΔS [J mol^{-1} K^{-1}]	transition entropy at a structural phase transition
ΔS_n [J mol^{-1} K^{-1}]	change of entropy in the n – th structural phase transition
ΔS_{tot} [J mol^{-1} K^{-1}]	total change of entropy due to structural phase transitions as defined in Eq. 2.39 (Sect. 2.2.4)
S	long-chain compounds $(C_nH_{2n+1}NH_3)_2MCl_4$ with $n > 5$: nematic order parameter (liquid crystals), describes the nematic order averaged over the segments of the chain and over all chains in such a compound
s	size of a cluster in diluted magnetic systems, i.e. the number of occupied sites in a cluster (cf. Sect. 4.1.11)
$\boldsymbol{s}_1$, $\boldsymbol{s}_2$, $\boldsymbol{s}_3$	special set of basic lattice vectors, see Eq. 2.20 (Sect. 2.2.1)
T [K]	temperature
T_C [K]	critical temperature = phase transition temperature (in context with a structural phase transition)

Table 1. List of Symbols and Abbreviations *(continued)*

T_{Cn} [K]	critical temperature at the n – th of more than one structural phase transition
T_{C} [K]	Curie temperature (in context with a ferromagnet)
$T_{\mathrm{C}}(\mathrm{x})$, $T_{\mathrm{N}}(\mathrm{x})$ [K]	in diluted magnets: critical temperature, i.e. Curie temperature T_{C} (ferromagnet) or Néel temperature T_{N} (antiferromagnet) as a function of concentration x, cf. Eq. 3.128 (Sect. 3.3.2)
$T_{\mathrm{C}}(H_0)$ [K]	transition temperature in a random field system, defined in Eq. 4.121 (Sect. 4.1.12)
$T_{\mathrm{C.P.}}$ [K]	temperature at the critical point in the (H_0, T) phase diagram of an antiferromagnet (see Fig. 3.18 in Sect. 3.1.6)
$T_{\mathrm{M}}(H_0)$ [K]	metastability boundary in a random field system, defined in Eq. 4.120 (Sect. 4.1.12)
T_{N} [K]	Néel temperature (in context with an antiferromagnet)
$T_{\mathrm{N}}^{\mathrm{MF}} = T_{\mathrm{N}} - \mathrm{b}\,H_0^2$ [K]	mean field Néel temperature of a diluted antiferromagnet in a magnetic field, see Eqs. 4.114 and 4.115a (Sect. 4.1.12)
T_{KT} [K]	Kosterlitz-Thouless temperature in the 2D XY-model
T^* [K]	temperature between T_{KT} and T_{C} at which $\eta(\mathrm{T})$ and $\widetilde{K}_{\mathrm{eff}}(\mathrm{T})$ assume their universal values in the finite-size 2D XY-model
$\widetilde{T} = k_{\mathrm{B}}T/(2S^2\|J\|)$	temperature, relative to the spin-wave stiffness (cf. Sect. 4.1.8)
$\widetilde{T}_{\mathrm{KT}}, \widetilde{T}^*, \widetilde{T}_{\mathrm{C}}$	characteristic temperatures of the finite-size 2D XY-model, relative to the spin-wave stiffness (cf. Sect. 4.1.8)
$T_{\mathrm{C}}^{(2)}$ [K]	Stanley-Kaplan temperature (Eq. 3.29, Sect. 3.1.3) for two-dimensional magn. systems, sometimes used as an estimate for T_{C} or T_{N}
$T_{\times}$ [K]	crossover temperature
T_{f} [K]	freezing temperature of a spin glass (cf. Sect. 4.1.12)
T_{p} [K]	temperature at which the deviation of $\chi(T_{\mathrm{p}}, j')$ from $\chi(T_{\mathrm{p}}, 0)$ has the value p, see Eq. 4.70 (Sect. 4.1.9)
$T_{\max}$, $T_{\parallel,\max}$, $T_{\perp,\max}$	temperature $T > T_{\mathrm{N}}$ at which the maximum occurs of the magnetic susceptibility χ, of $\chi_{\parallel}$ and of $\chi_{\perp}$, resp.
T_1 [s]	spin-lattice relaxation time in nuclear magnetic resonance
$\mathrm{T_n}$, $\mathrm{T_{ng}}$, $\mathrm{T_{nu}}$	symmetry species (irreducible representations) of a point group in the Mulliken or chemical notation (n = 1, 2, 3, etc.), the additional subscripts g and u apply to point groups with inversion symmetry and mean even and odd with respect to this point group operation, for details see [64T] and [78B3]
t [s]	time
$t = (T - T_{\mathrm{C}})/T_{\mathrm{C}}$	reduced temperature, ferromagnet: T_{C} = Curie temperature, and structural phase transitions: T_{C} = critical temperature
$t_{\mathrm{n}} = (T - T_{\mathrm{Cn}})/T_{\mathrm{Cn}}$	reduced temperature (n = 1, 2, 3, ...) at the n-th transition for a system with more than one structural phase transition: T_{Cn} = n-th critical temperature, cf. Eq. 4.80 in Sect. 4.1.10
$t = (T - T_{\mathrm{N}})/T_{\mathrm{N}}$	reduced temperature, antiferromagnet: T_{N} = Néel temperature

Table 1. List of Symbols and Abbreviations *(continued)*

t_{CH}	reduced temperature t at which a change-over occurs in the slope of the log-log plot of ΔH_{EPR} for diluted or mixed antiferromagnets, see Eqs. 4.190a and 4.190b (Sect. 4.2.9)
$\tilde{t} = (T - T_{KT})/T_{KT}$	reduced temperature with respect to the Kosterlitz-Thouless transition temperature T_{KT} (cf. Sect. 4.1.8)
$t_C(H_0)$	reduced part of the transition temperature in a random field system, see Eqs. 4.116 and 4.121 (Sect. 4.1.12)
$t_M(H_0)$	reduced part of the metastability boundary in a random field system, see Eq. 4.120 (Sect. 4.1.12)
$\boldsymbol{t}_1, \boldsymbol{t}_2, \boldsymbol{t}_3$	special set of basic lattice vectors, see Eq. 2.19 (Sect. 2.2.1)
U [J mol^{-1} or Jm^{-3}]	internal energy as defined in thermodynamics, per mole (e.g. specific heat $C = \partial U/\partial T$) or per unit volume (e.g. elastic contribution $\frac{1}{2} C_{66}^0 e_6^2$, cf. Eq. 2.36 in Sect.2.2.4)
U_{magn} [J mol^{-1}]	molar energy due to magnetic ordering (2D Ising model), see Eq. 4.4 (Sect. 4.1.2)
U_0, U_C [J mol^{-1}]	U_{magn} for $T = 0$ and for $T = T_C$ (cf. Sect. 4.1.2)
u	energy density, see Eq. 3.41 (Sect. 3.1.6)
u_q, υ_q	wavevector dependent factors in the Bogoliubov transform Eq. 3.4b (Sect. 3.1.2) with $u_q^2 - \upsilon_q^2 = 1$
V_A, V_M	vacancy at A^+- or M^{2+}-sites in A_2MX_4 perovskite-type layer structure, see discussion in Sect. 3.3.1
V_O	vacancy at O^{2-}-site in $SrTiO_3$ (Sect. 3.3.1)
$V_{xx} - V_{yy}$	asymmetry of the electric field gradient (EFG), cf. [78T2, 80T3]
V_{mol} [m^3 mol^{-1}]	volume of 1 mole of the compound under consideration
υ_s [km s^{-1}]	velocity of a sound wave (cf. Sect. 2.2.1)
$W_n(x)$	statistical weight or probability that a paramagnetic M^{2+}-ion is surrounded in a dilution $A_2M_x\tilde{M}_{1-x}X_4$ by n M^{2+}-ions and by (4 – n) diamagnetic $\tilde{M}^{2+}$-ions (Eq. 3.137 in Sect. 3.3.2)
W_p [cm^{-1}]	peak width of the two-magnon Raman line (cf. Figs. 3.4 and 3.5)
dW/dt [W]	net absorption of microwave energy per second in parallel pumping, see Eq. 3.116 (Sect. 3.2.5)
w	NMR linewidth exponent, see Eq. 4.160 (Sect. 4.2.5)
X	universal relation between critical amplitudes in the 2D Ising model, see Eq. 4.14 (Sect. 4.1.2)
X, $\tilde{\mathrm{X}}$, Z	special high symmetry points at the boundary of the Brillouin zone of the structure I4/mmm [69Z]
X_n, $\mathrm{X}_n^{\pm}$, Z_n, $\mathrm{Z}_n^{\pm}$	symmetry species (irreducible representations) of a space group in the Bethe notation (n = 1, 2, 3, etc.) at special points X, Z of the Brillouin zone, the superscripts + and – apply to space groups with inversion symmetry and mean even and odd with respect to this operation, see [63K1] and [78B3]
x	concentration in mixed crystals (Sects. 2.1.1 and 2.1.5)

Table 1. List of Symbols and Abbreviations *(continued)*

$\mathrm{x_p}$	critical percolation concentration for a system with only nearest neighbour interaction, cf. Eq. 3.127 (Sect. 3.3.2)
$\mathrm{x_p}(1, 2)$	critical percolation concentration for a system with first and second neighbour interaction, cf. Eq. 3.127 (Sect. 3.3.2)
(x_0, y_0, z_0)	coordinate system for the tetragonal I4/mmm structure
(x, y, z)	coordinate system for F4/mmm, Acam, Bbcm etc., rotated by 45° about the z-axis with respect to the system (x_0, y_0, z_0)
$z(xx)y$, $z(yx)y$ or $z_0(x_0 x_0)y_0$, $z_0(y_0 x_0)y_0$	Raman scattering configuration in the Porto notation, e.g. incident wave with $\boldsymbol{q} \parallel \boldsymbol{z}$ and polarization $\parallel \boldsymbol{x}$ or $\parallel \boldsymbol{y}$ and the scattered wave with $\boldsymbol{q} \parallel \boldsymbol{y}$ and polarization $\parallel \boldsymbol{x}$, where the coordinate directions refer to the (x, y, z) or to the (x_0, y_0, z_0) system, resp.
z	dynamical critical exponent, cf. Eq. 4.133 (Sect. 4.2.1)
z	number of nearest neighbours in the layer, $z = 4$ in the square lattice
z'	number of nearest neighbours in adjacent layers
z_2	number of next nearest neighbours in the layer, $z_2 = 4$ in the square lattice
z_X	parameter of the atomic position $(0, 0, z_\mathrm{X} c)$ of the X-ion
α, β, γ [deg]	angles between crystallographic axes
$\mathrm{\alpha}$	exponent determining the dependence of the exchange parameter J on the nearest neighbour distance a_nn, see Eq. 3.1 in Sect. 3.1.1
α	parameter determining the width of a relaxation time distribution (Eq. 4.144 in Sect. 4.2.2)
α	sound attenuation, cf. Eq. 4.137 (Sect. 4.2.2)
α_0, α^+	T-independent part and critical amplitude of the sound attenuation α (Eq. 4.137 in Sect. 4.2.2)
α^+, α^-	specific heat critical exponent, + for $T > T_\mathrm{C}$, – for $T < T_\mathrm{C}$
α_2D	specific heat critical exponent for $T > T_\mathrm{C}$ in the 2D regime, cf. Eqs. 4.76 and 4.77 (Sect. 4.1.9)
α_p	percolation critical exponent, defined in Eqs. 4.94 and 4.96a, theoretical value in Eq. 4.102 (Sect. 4.1.11)
α_T	thermal critical exponent like α for $\mathrm{x} = \mathrm{x_p}$ and $T \to 0$ near the percolation multicritical point (cf. Sect. 4.1.11)
$\tilde{\alpha}$, $\tilde{\beta}$, $\tilde{\gamma}$, $\tilde{\nu}$, $\tilde{\eta}$	critical exponents α, β, γ, ν, η for a (3D) random field system, cf. Sect. 4.1.12
α_q^+, α_q	wavevector dependent magnon creation and annihilation operators (+-branch), cf. Eqs. 3.4b–3.6 (Sect. 3.1.2)
$\alpha_{\mu\nu}$	$\mu\nu$-component, $(\mu, \nu = x, y, z)$ of the Raman tensor, where the coordinates refer to the (x, y, z) coordinate system, and analogous for the system (x_0, y_0, z_0) with additional subscript 0
α_sound	absorption (attenuation) coeffient of a sound wave
α, β, γ, δ, ε, ζ, η	denotation for structural phases in compounds with a relatively large number of phase transitions
β	order parameter critical exponent: $T < T_\mathrm{C}$

Table 1. List of Symbols and Abbreviations *(continued)*

β_p	percolation critical exponent of P(x), defined in Eqs. 4.93 and 4.96b, theoretical value in Eq. 4.102 (Sect. 4.1.11)
β_T	thermal critical exponent like β for $x = x_p$ and $T \to 0$ near the percolation multicritical point (cf. Sect. 4.1.11)
β [deg]	azimuthal angle between external field $\boldsymbol{H}_0$ and the a-axis (x-axis)
β_q^+, β_q	wavevector dependent magnon creation and annihilation operators (−-branch), cf. Eqs. 3.4b–3.6 (Sect. 3.1.2)
Γ	center of the Brillouin zone [$\boldsymbol{q} = (0, 0, 0)$]
Γ	critical exponent in the scaling relation for the nonlinear susceptibility χ_{nl} (cf. Eq. 4.127 in Sect. 4.1.12)
$\Gamma = \tau^{-1}$ [s^{-1}]	relaxation rate, characteristic frequency or frequency width, cf. Eq. 4.136 (Sect. 4.2.2)
$\Gamma_{\parallel}(\boldsymbol{K})$, $\Gamma_{\parallel}(q, \omega)$	relaxation rate or characteristic frequency of the longitudinal critical spin fluctuations, see Eq. 4.132 (Sect. 4.2.1)
$\Gamma_q = \Gamma(q)$	special damping (relaxation) for the magnons at $T > T_C$ in the 2D Heisenberg model (Eqs. 4.159 and 4.159a in Sect. 4.2.3)
Γ_n, Γ_n^+, Γ_n^-	symmetry species (irreducible representations) of a point group or of a space group at Γ in the Bethe notation (n = 1, 2, 3, etc.), the superscripts + and – apply to groups with inversion symmetry and mean even and odd with respect to this operation, for details, see [63K1] and [78B3]
$\gamma = g\mu_B/\hbar$	gyromagnetic ratio, in general or with isotropic g-factor
$\gamma_a = g_a\mu_B/\hbar$	gyromagnetic ratio for $\boldsymbol{H}_0 \parallel \boldsymbol{a}$, mostly more general for $\boldsymbol{H}_0 \perp \boldsymbol{c}$
$\gamma_c = g_c\mu_B/\hbar$	gyromagnetic ratio for $\boldsymbol{H}_0 \parallel \boldsymbol{c}$
$\gamma(\boldsymbol{q}) = \gamma_q$	wavevector dependent term in magnon dispersion relations for nearest neighbours intralayer exchange interaction, cf. Eqs. 3.6 (Sect. 3.1.2) and 3.71a (Sect. 3.2.1)
$\gamma'(\boldsymbol{q}) = \gamma'_q$	q-dependent term in magnon dispersion relations for nearest neighbours interlayer exchange interaction, cf. Eq. 3.71a (Sect. 3.2.1)
γ_{q2}	q-dependent term for next nearest neighbours intralayer exchange interaction, cf. Eq. 3.14 (Sect. 3.1.2)
$\gamma_q^{1,2}$, $\gamma_q^{3,4}$	q-dependent term for nearest neighbour intralayer exchange interaction in double-layer compounds, cf. Eq. 3.31 (Sect. 3.1.4)
γ^+, γ^-	susceptibility critical exponent, + for $T > T_C$, – for $T < T_C$
γ_{2D}	susceptibility critical exponent for $T > T_C$ in the 2D regime, cf. Eqs. 4.71 and 4.72 (Sect. 4.1.9)
γ_p	percolation critical exponent of S(x), defined in Eqs. 4.92 and 4.96c, theoretical value in Eq. 4.102 (Sect. 4.1.11)
γ_T	thermal critical exponent like γ for $x = x_p$ and $T \to 0$ near the percolation multicritical point (cf. Sect. 4.1.11)
$\Delta = \beta + \gamma$	critical exponent in scaling relations Eqs. 4.12a and 4.12b (Sect. 4.1.2)
$\Delta_p = \beta_p + \gamma_p = \beta_p\delta_p$	percolation critical exponent in scaling relations analogous to Eqs. 4.12a and 4.12b, see also Eq. 4.98 (Sect. 4.1.11)

Table 1. List of Symbols and Abbreviations *(continued)*

δ	critical exponent of $M(H)$ on the critical isotherm
$\delta(T)$	T-dependent critical exponent of $M(H_{\text{int}})$ in the theory of the 2D XY-model for $T < T_C$, see Eq. 4.46 (Sect. 4.1.8)
δ_p	percolation critical exponent of $\mu_C(h)$ for $x = x_p$, defined in Eqs. 4.95 and 4.96d, theoretical value in Eq. 4.102 (Sect. 4.1.11)
δ_T	thermal critical exponent like δ for $x = x_p$ and $T \to 0$ near the percolation multicritical point (cf. Sect. 4.1.11)
$\pm\,\delta$ [deg]	canting angle of the two sublattices a and b ($\boldsymbol{M}_\mathbf{a}$ and $\boldsymbol{M}_\mathbf{b}$) with respect to the a-axis, e.g. in Rb_2CrCl_4 (cf. Fig. 3.34 in Sect. 3.2.2)
δ_a, δ_b [deg]	azimuthal angle between sublattice magnetization $\boldsymbol{M}_\mathbf{a}$ or $\boldsymbol{M}_\mathbf{b}$ and the a-axis (x-axis)
δ_a, δ_b, δ_c, δ_d [deg]	azimuthal angles between the four sublattice magnetizations $\boldsymbol{M}_\mathbf{a}$, $\boldsymbol{M}_\mathbf{b}$, $\boldsymbol{M}_\mathbf{c}$, $\boldsymbol{M}_\mathbf{d}$ and the a-axis in the virtual crystal model, see Eq. 3.149 (Sect. 3.3.5)
δ_{MM}, δ_{MC}, δ_{CC} [deg]	angles between the equilibrium spin orientations of pairs of M–M, M–C and C–C ions in a mixed magnetic systems with non-collinear ordering, see Eq. 3.153 (Sect. 3.3.6)
$\delta(\boldsymbol{r})$	direction of a spin at point $\boldsymbol{r}$, i.e. its angle of orientation with the a-axis
$\delta_i = \delta(\boldsymbol{r}_i)$	orientation angle δ of the spin at $\boldsymbol{r}_\mathbf{i}$
δ, κ	factors for the terms with space derivatives in the Landau-type free energy, cf. Eq. 2.37 (Sect. 2.2.4)
δ, σ	irrational factors describing the modulation in an incommensurate structure, e.g. $\boldsymbol{q}_0 = \delta \cdot \boldsymbol{a}^* + \sigma \cdot \boldsymbol{b}^*$
$\varepsilon = \varepsilon' + i\varepsilon''$	dielectric constant, real and imaginary part
$\boldsymbol{\varepsilon}$	tensor of the dielectric constant with components ε_{xx} ε_{yy} and ε_{zz}, assuming orthorhombic lattice symmetry
ζ, ζ_{x0}, ζ_x, ζ_z	reduced wavevector ($\zeta_{x0} = q_{x0}/a^*$, $\zeta_x = q_x/a^*$, $\zeta_z = q_z/c^*$)
ζ_1, ζ_2	values of ζ_{x0} indicating the crossover 3D XY $\leftrightarrow$ 2D XY and 2D XY $\leftrightarrow$ 2D Heisenberg, cf. Sect. 3.2.1
η	critical exponent: pair correlation function $G(r) \sim \lvert r \rvert^{-(d-2+\eta)}$
η_p, η_T	percolation and thermal critical exponent η, resp., see Eq. 4.89, theoretical value of η_p in Eq. 4.102 (Sect. 4.1.11)
$\eta(T)$	T-dependent critical exponent of $G(\boldsymbol{r})$ in the theory of the 2D XY-model for $T < T_C$, see Eq. 4.47 (Sect. 4.1.8)
η	order parameter for the orientation of $[NH_3(CH_2)_nNH_3]^{2+}$-ions in diammonium compounds, for the definition see [81K3]
η_1, η_2, η_3	order parameters in the structural phase transitions of monoammonium compounds (cf. Sect. 2.2.4)
η_0	constant part of order parameter in a modulated or incommensurate structure, cf. Eq. 2.38 (Sect. 2.2.4)
Θ	reduced temperature, defined in Eq. 3.74 (Sect. 3.2.1)
Θ	parameter for dimensional reduction in random field systems, see Eq. 4.113 in Sect. 4.1.12

Table 1. List of Symbols and Abbreviations *(continued)*

Θ_C [K]	Curie-Weiss temperature in the Curie-Weiss law, cf. Eq. 3.25 (Sect. 3.1.3)
θ	time reversal operator
θ	stiffness exponent in the droplet model for spin glasses (see Sect. 4.2.2)
θ_a, θ_b [deg]	polar angle between sublattice magnetization $\boldsymbol{M}_\mathbf{a}$ and $\boldsymbol{M}_\mathbf{b}$ and the *c*-axis
θ_a, θ_b, θ_c, θ_d [deg]	polar angles between the four sublattice magnetizations $\boldsymbol{M}_\mathbf{a}$, $\boldsymbol{M}_\mathbf{b}$, $\boldsymbol{M}_\mathbf{c}$, $\boldsymbol{M}_\mathbf{d}$ and the *c*-axis in the virtual crystal model, see Eq. 3.149 (Sect. 3.3.5)
$\theta\ (\theta_a = \theta_b)$ [deg]	joint inclination of the two sublattices a and b ($\boldsymbol{M}_\mathbf{a}$ and $\boldsymbol{M}_\mathbf{b}$) by an angle θ with respect to the *c*-axis
ϑ	long-chain compounds $(C_nH_{2n+1}NH_3)_2MCl_4$ with $n > 5$: smectic order parameter (liquid crystals), measures the average tilt angle of the chains with respect to the layer normal
ϑ	exponent of (k_BT/J) in Eq. 3.135 (Sect. 3.3.2)
κ [nm^{-1}]	inverse correlation length
$\kappa_0^\pm$ [nm^{-1}]	inverse correlation length critical amplitude, + for $T > T_C$, – for $T < T_C$ (cf. Sect. 4.1.1)
$\kappa_\perp^-$ [nm^{-1}]	uncritical *T*-independent inverse correlation length in $\chi_\perp(q, t)$ for $T < T_N$, cf. Eq. 4.35 (Sect. 4.1.5)
$\kappa(\Delta x, \mu)$	inverse correlation length in a diluted magnetic system as a function of $\Delta x = x_p - x$ and of μ(T), cf. Eq. 4.106 (Sect. 4.1.11)
κ_G [nm^{-1}]	inverse geometrical correlation length in diluted magnetic systems, cf. Eqs. 4.90 and 4.91 (Sect. 4.1.11)
κ_G^0	critical amplitude of the geometrical inverse correlation length, see Eq. 4.107 (Sect. 4.1.11)
κ_{1D}	inverse correlation length for a 1D model system, Eq. 4.108 (Sect. 4.1.11)
κ_{1D}^I, κ_{1D}^H	κ_{1D} for the 1D Ising model and for the 1D Heisenberg model (Fig. 4.32, Sect. 4.1.11)
$\kappa_{1D}^{\|}$, $\kappa_{1D}^{\perp}$	1D anisotropic Heisenberg model: κ_{1D} for a direction parallel or perpendicular to the anisotropy axis (Fig. 4.32, Sect. 4.1.11)
κ_l	*T*-independent part of κ of the easy-axis antiferromagnet $Rb_2Co_{0.88}Cu_{0.12}F_4$ with competing exchange interactions, see Eq. 4.129 (Sect. 4.1.13)
κ_z	*T*-independent part of κ of an easy-plane ferromagnet in the 3D XY-regime, cf. Eq. 4.56 (Sect. 4.1.8)
Λ	critical exponent of the relaxation time τ in ac measurements, see Eq. 4.142 (Sect. 4.2.2)
$\mathit{\Lambda}$ [s^{-1}]	damping constant in the Bloch-Bloembergen equation, see Eq. 3.42 (Sect. 3.1.6)
λ [cm^{-1} or K]	constant of the spin-orbit coupling
$\lambda = (J - J_A)/J$	parameter of the anisotropic exchange in Eq. 4.59 (Sect. 4.1.8)
λ_C	value of the parameter λ at the stability limit for purely in-plane vortices (cf. Sect. 4.1.8)
λ	parameter in the denominator of $\chi_{TF}(q, t)$, see Eq. 4.31 (Sect. 4.1.5)

Table 1. List of Symbols and Abbreviations *(continued)*

μ_0	induction constant, $\mu_0 = 4\,\pi \cdot 10^{-7}$ V s A^{-1} m^{-1}
μ_B	Bohr magneton, $\mu_B = 1.16541 \cdot 10^{-29}$ V s m
μ_N	nuclear magneton, $\mu_N = 6.34719 \cdot 10^{-33}$ V s m
μ_{Cr} [V s m]	magnetic moment of the Cr^{2+}-ion
$\mu(\mathrm{x}, h)$	magnetic moment per site in external field H_0 as a function of concentration x and reduced field $h = 2\mu_B H_0 / k_B T$, see Eq. 4.95 in Sect. 4.1.11
$\mu_C(h)$	magnetic moment $\mu(\mathrm{x}, h)$ for $\mathrm{x} = \mathrm{x_p}$ (Eq. 4.95, Sect. 4.1.11)
ν^+, ν^-	correlation length critical exponent, + for $T > T_C$, – for $T < T_C$
ν_p	percolation critical exponent of $\xi_G(\mathrm{x})$, defined in Eqs. 4.91, theoretical value in Eq. 4.102 (Sect. 4.1.11)
ν_T	thermal critical exponent like ν for $\mathrm{x} = \mathrm{x_p}$ and $T \to 0$ near the percolation multicritical point (cf. Sect. 4.1.11)
ν [Hz]	frequency
$\tilde{\nu}$ [cm^{-1}]	wavenumber, the unit most frequently used in spectroscopy, instead of frequency $\nu = c\tilde{\nu}$ or of excitation energy $h\nu = hc\tilde{\nu}$
ν_{AFMR} [GHz]	frequency of the antiferromagnetic resonance (AFMR), preferably for $H_0 = 0$ (antiferromagnetic spin wave gap, corresponds to the magnon energy for $\boldsymbol{q} = 0$)
$\nu^{\pm}_{AFMR}$ [GHz]	AFMR frequency for $H_0 \neq 0$ (+-branch and –-branch), see Eq. 3.9 (Sect. 3.1.2)
$\nu_{\mathrm{AFMR,\,out\text{-}of\text{-}pl.}}$	out-of-plane AFMR mode, cf. Eq. 3.37 (Sect. 3.1.5)
$\nu_{\mathrm{AFMR,\,in\text{-}plane}}$	in-plane AFMR mode, cf. Eq. 3.37 (Sect. 3.1.5)
ν_{AR} [GHz]	antiresonance frequency, see Eq. 3.114 (Sect. 3.2.4)
ν_{BZB} [GHz]	double-layer compounds: magnon frequency (quadruply degenerate) at the Brillouin zone boundary (Eq. 3.32b in Sect. 3.1.4)
ν_{FMR} [GHz]	frequency of the ferromagnetic resonance (FMR)
ν_{gap} [GHz]	ferromagnetic spin-wave gap at $\boldsymbol{q} = 0$, its square proportional to the product of in-plane and out-of-plane anisotropy field, see Eqs. 3.89 (Sect. 3.2.2) and 3.107 (Sect. 3.2.3)
ν_{max} [GHz]	maximum magnon frequency for $\boldsymbol{q}$ at the Brillouin zone boundary, see Eqs. 3.7 (Sect. 3.1.2) and 3.90 (Sect. 3.2.2)
$\Delta\tilde{\nu}$ [cm^{-1}]	Raman shift, i.e. the wave number difference between the scattered light and the exciting laser light
ξ [nm]	correlation length
ξ_G [nm]	geometrical correlation length in diluted magnetic systems, see Eq. 4.91 in Sect. 4.1.11
ξ	factor in the Landau-type free energy U for the term coupling the elastic stress σ_6 and the order parameters η_1, η_2 of the THT $\leftrightarrow$ ORT phase transition, cf. Eq. 4.78 (Sect. 4.1.10)

Table 1. List of Symbols and Abbreviations *(continued)*

(ξ, η, ζ)	coordinate system with the ζ-axis parallel to the preferred spin axis in an ordered ferromagnet (cf. Sect. 3.2.1) or a canted ferromagnet with additional subscripts a or b for sublattices a or b (cf. Sect. 3.2.2)
$\rho = 2\,\varphi + \alpha - 2$	critical exponent of the anomalous part of the elastic compliance S_{66} at a structural phase transition (Eqs. 4.86 and 4.87a in Sect. 4.1.10)
$\widetilde{\rho} = \rho + z\,\nu$	critical exponent of the sound attenuation near a structural phase transition (cf. Eq. 4.137 in Sect. 4.2.2)
ρ [gcm^{-3}]	mass density
ρ_s [cm^{-1} or K]	spin stiffness, equals $2S^2J$ in our notation, cf. Eq. 4.43a in Sect. 4.1.8
σ [(Ω cm)$^{-1}$]	electric conductivity
σ_0 [(Ω cm)$^{-1}$]	factor in the Arrhenius law for the electric conductivity, see Eq. 2.44 in Sect. 2.2.6
σ_m [Pa]	elastic stress (m = 1, 2, ..., 6) in the Voigt notation, e.g. σ_6: 6 $\hat{=}$ $x_0\,y_0$ in the (x_0, y_0, z_0) coordinate system
$\sigma_p = \Delta_p^{-1}$	percolation critical exponent in scaling relations for $n_s(x)$, R_s and $D_s(r)$, see Eqs. 4.97, 4.99a and 4.99b (Sect. 4.1.11)
$d^2\sigma / d\Omega\, d\omega$	double-differential neutron scattering cross section
τ [s]	relaxation time
τ_0^+	critical amplitude of the relaxation time τ near a structural phase transition, see Eq. 4.138 (Sect. 4.2.2)
τ_c [s]	mean or centre relaxation time, see Eq. 4.144 (Sect. 4.2.2)
τ_0 [s]	a microscopic time ($\approx 10^{-13}$ s), see Eqs. 4.128 (Sect. 4.1.13) and 4.147 (Sect. 4.2.2)
$\tau_p = 2 + \delta_p^{-1}$	percolation critical exponent for $n_s(x_p)$ (Eq. 4.97, Sect. 4.1.11)
$\boldsymbol{\tau}$	vector of a nonprimitive translation, connected with a symmetry operation
τ_0	order parameter in a modulated structure: amplitude of the modulation, cf. Eq. 2.38 (Sect. 2.2.4)
τ_m	dimensionless factor relating the temperature T_{max} of the susceptibility maximum to the exchange constant J, cf. Eq. 3.28 (Sect. 3.1.3)
$\chi, \chi_{\parallel}, \chi_{\perp}$	magnetic susceptibility: in general and in antiferromagnets for $\boldsymbol{H}_0$ parallel and perpendicular to the preferred spin direction, $\chi = \partial M / \partial H$ dimensionless in our units (M and H in T), sometimes also presented as molar susceptibility in [cm^3/mol]
$\chi_{\parallel c}, \chi_{\perp c}$	magnetic susceptibility for $\boldsymbol{H}_0 \parallel \boldsymbol{c}$ and $\boldsymbol{H}_0 \perp \boldsymbol{c}$ (cf. Fig. 3.71)
$\chi = \chi' + i\chi''$	complex magnetic susceptibility with real and imaginary part
$\chi_0 = C/T$	magnetic susceptibility of a noninteracting system (Curie law) with the Curie constant C, cf. Eq. 3.25 (Sect. 3.1.3)
χ_H	magnetic susceptibility in the 2D Heisenberg model, extracted and interpolated from experimental data (cf. Sect. 4.1.7)
$\chi_{app}^{\alpha\alpha}$	apparent susceptibility ($\alpha = x, y, z$), i.e. the measured value before application of the demagnetization corrections Eqs. 3.94a and 3.94b (Sect. 3.2.3)

Table 1. List of Symbols and Abbreviations *(continued)*

$\chi_{ac}^{\alpha\alpha} = \chi'_{ac} + \chi''_{ac}$	ac susceptibility ($\alpha = x, y, z$) with real and imaginary part, see Eqs. 3.95 (Sect 3.2.3) and 4.139 (Sect. 4.2.2)
χ_{ad}	adiabatic susceptibility $\hat{=}\ \chi_{ac}(\omega \to \infty, T)$, see Eqs. 4.140a and 4.140b (Sect. 4.2.2)
χ_{it}	isothermal susceptibility $\hat{=}\ \chi_{ac}(\omega \to 0, T)$, see Eqs. 4.140a and 4.140b (Sect. 4.2.2)
$\chi_{nl} = 1 - M/\chi_0 H_0$	nonlinear magnetic susceptibility, see Eq. 4.126 (Sect. 4.1.12)
$\tilde{\chi}$	idealized susceptibility factor in Eq. 3.28a (Sect. 3.1.3)
$\hat{\chi}$	reduced susceptibility, defined as a dimensionless quantity in [78M3], cf. Eq. 4.62 in Sect. 4.1.8
$\boldsymbol{\chi}_{\mathbf{dyn}}$	dynamic magn. susceptibility tensor, cf. Eq. 3.45 (Sect. 3.1.6)
$\chi^{\alpha\beta}$, e.g. χ^{xx}, χ^{yy} ($\alpha, \beta = x, y, z$)	components of the tensor of magnetic susceptibility χ, with respect of the (x, y, z) system of the magnetic unit cell; dynamic χ: see Eqs. 3.48, 3.50 (Sect. 3.1.6); staggered $\chi(q)$: see Eq. 4.24 (Sect. 4.1.5)
$\chi_{OZ}(q, t)$	Ornstein-Zernike form for $\chi(q, t)$, see Eq. 4.28 (Sect. 4.1.5)
$\chi_F(q, t)$	Fisher approximant for $\chi(q, t)$, see Eq. 4.29 (Sect. 4.1.5)
$\chi_{FB}(q, t)$	Fisher-Burford approximant for $\chi(q, t)$, 4.30 (Sect. 4.1.5)
$\chi_{TF}(q, t)$	Tarko-Fisher approximant for $\chi(q, t)$, Eq. 4.31 (Sect. 4.1.5)
χ_{max}, $\chi_{\parallel,max}$, $\chi_{\perp,max}$	maximum of the susceptibility χ, of $\chi_{\parallel}$ and of $\chi_{\perp}$, resp., observed at $T_{max} > T_N$
χ'_m	dimensionless factor relating the susceptibility maximum χ_{max} to the exchange constant J, cf. Eq. 3.28 (Sect. 3.1.3)
$\chi_{n\alpha}(T)$	magnetic susceptibility per ion of a particular n-ion cluster of type α, see Eq. 3.130 in Sect. 3.3.2
$\chi^{(n)}(j')$	n-th derivative of the susceptibility $\chi(j')$ with respect to j', cf. Eq. 4.71 (Sect. 4.1.9)
χ_{1D}	magnetic susceptibility of a 1D system (linear chain), appropriate for diluted magnets near x_p (Eq. 3.135 in Sect. 3.3.2)
χ_{2D}, χ_{3D}	magnetic susceptibility in the 2D and the 3D regime, resp., see Eq. 4.74 (Sect. 4.1.9)
$\boldsymbol{\Phi}$	factor in the numerator of $\chi_{FB}(q, t)$, see Eq. 4.30 (Sect. 4.1.5)
$\boldsymbol{\Phi}$ [deg]	C–C–C bond angle in hydrocarbon chains, $\boldsymbol{\Phi} = 112°$
ϕ	crossover critical exponent, see Eqs. 4.69 in Sect. 4.1.9 and 4.89 in Sect. 4.1.11
φ	factor in the numerator of $\chi_{TF}(q, t)$, see Eq. 4.31 (Sect. 4.1.5)
$\pm\ \varphi$ [deg]	canting angle of the two sublattices a and b ($\boldsymbol{M}_a$ and $\boldsymbol{M}_b$), with respect to the c-axis (Eq. 3.54 in Sect. 3.1.7)
φ_c [deg]	canting angle of the sublattice magnetizations $\boldsymbol{M}_a$ and $\boldsymbol{M}_b$ for $\boldsymbol{H}_0 \parallel \boldsymbol{c}$, e.g. in antiferromagnets with covert spin canting, see Eq. 3.100a (Sect. 3.2.3)
$\Psi_\pm(u)$, $\hat{\Psi}_\pm(u)$, $\tilde{\Psi}_\pm(\upsilon)$	homogeneous functions of u and υ in scaling relations Eqs. 4.12a, 4.12b and 4.12c (Sect. 4.1.2)
ψ	barrier exponent with $0 \le \psi \le 1$ (cf. Sect. 4.1.13)

Table 1. List of Symbols and Abbreviations *(continued)*

ψ [deg]	polar angle between the applied field $\boldsymbol{H_0}$ and the c-axis
ψ	phase shift of the reflected wave, phase angle of the amplitude reflection coefficient $r = \sqrt{R}\, e^{i\psi}$, cf. Eq. 2.22 (Sect. 2.2.1)
$\Omega^{\pm}(q/\kappa)$, $\tilde{\Omega}^{\pm}(q/\kappa)$	universal scaling functions, homogeneous in q/κ, + for $T > T_N$ and – for $T < T_N$, cf. Eq. 4.133 (Sect. 4.2.1)
$\Omega_0 = \Omega^{\pm}(q, 0)$	critical amplitude for $q \rightarrow 0$ at $T = T_N$, cf. Eq. 4.135 in Sect. 4.2.1
ω [s^{-1}]	frequency
ω_0 [s^{-1}]	inverse τ_0^{-1} of a microscopic time, typically 10^{13} s^{-1}, see Eq. 4.150 (Sect. 4.2.2)
ω_E [s^{-1}]	exchange frequency as defined in Eq. 4.178a in Sect. 4.2.8
ω_F [s^{-1}]	rms frequency of the dipolar contributions to the fluctuations, see Eq. 4.178 in Sect. 4.2.8 and [90B1]
ω_p [s^{-1}]	microwave pumping frequency in parallel pumping experiments
$\omega(\boldsymbol{q}) = \omega_q$ [s^{-1}]	frequency of magnons at wavevector $\boldsymbol{q}$ within the first Brillouin zone
$\omega_\mu(\boldsymbol{q}) = \omega_{q,\mu}$ [s^{-1}]	frequency of the phonon in branch μ at wavevector $\boldsymbol{q}$ within the first Brillouin zone
$\Delta\omega_{EPR}$	EPR linewidth (in frequency space) due to the exchange interaction (exchange narrowing), cf. Eq. 4.178 in Sect. 4.2.8

b) Abbrevations

0.4653(8)	data are presented with the error limits (standard deviations or appropriate estimate) of the last decimal place in parentheses
1D	one-dimensional
1st r_{op}, 2nd r_{op}	in doubler-layer compounds: two different values of the out-of-plane M-X bond length r_{op}, the first is for the bridging X^--ion between two M^{2+}-ions in neighbouring layers (cf. Eq. 2.7, Sect. 2.1.1), and the second one is for the terminal X^--ion
1-magn. Raman sp.	one-magnon Raman spectroscopy, determination of ν_{AFMR} or other magnon frequency
2D	two-dimensional
2 v. r_{ip} $\hat{=}$ def. oct.	2 values presented for r_{ip} which result from a deformation of the MX_6 octahedra due to orbital ordering and a collective Jahn-Teller effect
2 v. r_{ip} $\hat{=}$ c. sym.	2 values presented for r_{ip} which result from the reduced symmetry of the structure under consideration, usually accompanied by a slight deformation and tilt of the octahedra
2-magn. Raman L.	two-magnon Raman line
2nd d.: Acam	second crystallographic domain is Acam, but the structure has been refined in and the lattice parameters correspond to the first domain, namely Bbcm for this example
3D	three-dimensional

Table 1. List of Symbols and Abbreviations *(continued)*

[III/4a], [III/12a]	materials which have already been listed in Vol. III/4a or Vol. III/12a for which new data are presented here
[III/4a] rep.	data from Vol. III/4a have been reproduced due to the lack of more recent data
[III/12a] rep.	data from Vol. III/12a have been reproduced due to the lack of more recent data
AF-phase	antiferromagnetic phase (cf. Fig. 3.16 in Sect. 3.1.6)
AFMR	antiferromagnetic resonance
AFMR LW	antiferromagnetic resonance linewidth
abbr.	abbreviation
ac cal.	ac calorimetry, cf. [80H4]
ad. cal.	adiabatic calorimetry
add.	additional
afm.	antiferromagnet or antiferromagnetic
anal.	analysis
∠-dependence	angular dependence
approx.	approximately
arb. units	arbitrary units
basic str.	basic structure which is the basis of an incommensurate modulated structure
birefr.	(studies with) birefringence
CMB	circular magnetic birefringence, details see for example [80P4]
$C_p(T)$ by ad. cal.	specific heat measured by the adiabatic calorimeter method
$C_p(T)$ by d.s.c.	specific heat measured with a differential scanning calorimeter
calc.	calculation, calculated
c.f.a.p., e.g. r_{ip}	calculated from the atomic positions, for example r_{ip}
c.s.g.	chemical or crystallographical space group, disregarding the magnetic order
c.u.c.	chemical unit cell, in contrast to the antiferromagnetic one
coeff.	coefficients
coll. JTE	collective Jahn-Teller effect
comp.	comparison, compared
c.s.d.	complete structure determined including atomic positions and thermal parameters, see given reference
const.	constant
cont.	continuous phase transition (2^{nd} order phase transition)
×-over	crossover, e.g. lattice dimensional 2D ↔ 3D or spin dimensional XY ↔ Heisenberg
c. sym.:	crystal symmetry (when space group is not known)
DMI	Dzyaloshinskii-Moriya (antisymmetric exchange) interaction, cf. Sect. 3.1.6
d det. dir.	interlayer separation d has been determined directly, mostly by powder x-ray diffraction, without determining the complete set of lattice parameters

Table 1. List of Symbols and Abbreviations *(continued)*

determ.	determination (of)
def.	deformation
dens. of states	(magnon or phonon) density of states
diel. c.	dielectric constant measurements
diffr.	(studies with) diffraction, by means of elastic x-ray and/or neutron scattering
diff. x-ray sc.	diffuse x-ray scattering
dipolar interact.	(magnetic) dipolar interactions
disc.	discontinuous phase transition (1st order transition)
d.s.c.	differential scanning calorimetry
EISF	elastic incoherent scattering factor (neutron scattering)
EPR	(studies with) electron paramagnetic resonance
EPR LW	electron paramagnetic resonance linewidth
eff. spin 1/2 Ham.	effective spin 1/2 Hamiltonian, Co-compounds (Eq. 3.62 in Sect. 3.1.8)
elast. const.	elastic (stiffness) constants
elast. c.	elastic constants measurements, by means of sound velocity studies or by means of Brillouin scattering
el. + quasi-el. n-scatt.	elastic and quasi-elastic neutron scattering (experiments)
electr.	electric
exam.	examination
exp.	experiment, experimental
exp. data included	experimental data on which a spin-wave analysis is bases
expl.	explained
F_I	out-of-plane (axial, terminal) F^--ion (cf. Fig. 3.7, Sect. 3.1.3)
F_{II}	in-plane (bridging, equatorial) F^--ion (cf. Fig. 3.7, Sect. 3.1.3)
Fig., Figs.	Figure, Figures (with appropriate numbers)
fct.	function, e.g. spin correlation function (see Fig. 4.65 in Sect. 4.2.8)
fm.	ferromagnet or ferromagnetic
H_0-dependence	dependence on applied magnetic field H_0
$\boldsymbol{H_0} \parallel \boldsymbol{a}, \parallel \boldsymbol{b}, \parallel \boldsymbol{c}$	means that $\boldsymbol{H_0}$ has been applied parallel to the *a*-axis, to the *b*-axis and also parallel to the *c*-axis in the experiment under consideration. Sometimes the crystallographic directions are specified by (1, 0, 0) (1, 1, 0) etc. instead of *a*, *b*, *c*
(H_0, T) phase diagram	diagram of magnetic phase boundaries, especially for afm., as applied field H_0 versus temperature T
HAUP	high accuracy universal polarimeter method, for measuring simultaneously optical activity and birefringence [83K1, 86K1, 88K1]
Heis., Heisenb.	Heisenberg (model)
HP	high pressure structural phase
HT	high temperature structural phase
h.m.f. exp.	high magnetic field experiments

Table 1. List of Symbols and Abbreviations *(continued)*

high press. exp.	high pressure experiments
h.t.s.	high temperature series expansion
IM	intermediate temperature structural phase
IM1, IM2	1st and 2nd intermediate temperature structural phase
INC	incommensurate structural phase
inc.	transition to an incommensurate phase
inc. str.	incommensurate structure
incoh. n.s.	incoherent neutron scattering
ind. in Bbcm	indexing of the diffraction data was successful in the space group Bbcm as an example, but there are doubts whether this is the correct space group for the structure under consideration
inel. n-scatt.	inelastic neutron scattering
in-plane anis.	in-plane anisotropy (energy), cf. Eqs. 3.35 (Sect. 3.1.4) and 3.40 (Sect. 3.1.5)
inv.	inverse, e.g. inverse susceptibility χ^{-1} (cf. Fig. 3.10 in Sect. 3.1.3 and inverse correlation length κ (cf. Fig. 3.78 in Sect. 3.3.6)
ir spectr.	(studies with) infrared spectroscopy
LMB	linear magnetic birefringence
LRO	long range order
LT	low temperature structural phase
LW	linewidth
linear spin-w. th.	linear spin-wave theory, without Oguchi corrections [60O1]
MCD	magnetic circular dichroism
MHT	monoclinic high temperature structural phase
MLT	monoclinic low temperature structural phase
MME	method of matching the matrix elements, see [74L2, 76L3]
MRT	monoclinic room temperature structural phase
magn.	magnetic
magn. pt.	magnetic phase transition
m.u.c.	magnetic unit cell
major, minor pt.	major or minor structural phase transition with the larger or smaller transition enthalpy ΔH, resp.
max. χ	maximum (of χ as an example)
meas. X	measurement of quantity X; $X = M$: measurement of magnetization M; $X = \chi$: measurement of susceptibility χ
meas. ν_{AFMR}	measurement of ν_{AFMR} by AFMR, ir spectr. or 1-magn. Raman sp.
meas. and anal. of χ	measurement of susceptibility χ and analysis of the exp. data with respect to the exchange constant J etc.
min. $\chi_\perp$	minimum (of $\chi_\perp$ as an example)
NIR	near infrared (spectral range)

Table 1. List of Symbols and Abbreviations *(continued)*

NMR	(studies with) nuclear magnetic resonance
NMR LW	nuclear magnetic resonance linewidth
NQR	(studies with) nuclear quadrupole resonance
n-diffr.	neutron diffraction (experiments)
n-scatt.	neutron scattering (experiments)
n-scatt., diff. cooling pr.	neutron scattering experiments after different cooling procedures
OHT	orthorhombic high temperature structural phase
OLT	orthorhombic low temperature structural phase
ORT	orthorhombic room temperature structural phase
only u.c.p. (*d*) by diffr.	only the unit cell parameters (interlayer distance *d*) have been determined by diffraction
opt. m.	optical methods with or without microscope and with or without polarizers to study by visual observation the domain structure of the sample and the optical anisotropy within the plane of the perovskite-type layer
opt. spectr.	optical spectroscopy (near infrared, visible, ultraviolet)
orb. order	orbital order, orbital ordering
orthorh.	orthorhombic
out-of-pl. anis.	out-of-plane anisotropy (energy), cf. Eqs. 3.35 (Sect. 3.1.4) and 3.40 (Sect. 3.1.5)
PM-phase	paramagnetic phase of an antiferromagnet at sufficiently high temperatures or high magn. fields (cf. Fig. 3.16 in Sect. 3.1.6)
p.p.	peak pumping, with microwaves in quasi-2D ferromagnets, see Sect. 3.2.5 and [74Y1]
peak pos.	peak position, e.g. of the two-magnon Raman line
ph.	phase, for example ORT-phase, δ-phase
pref.	preferably
$\boldsymbol{Q}_0 \mathrel{\hat{=}} (\mathrm{h}, \mathrm{k}, \mathrm{l})$	abbr. for $\boldsymbol{Q}_0 = \mathrm{h}\boldsymbol{a}^* + \mathrm{k}\boldsymbol{b}^* + \mathrm{l}\boldsymbol{c}^*$, referring to a Bragg reflection or an antiferromagnetic superreflection
$\boldsymbol{Q}_0 \mathrel{\hat{=}} (\mathrm{h}, \mathrm{k}, \mathrm{l}+\zeta_z)$	abbr. for $\boldsymbol{Q}_0 = \mathrm{h}\boldsymbol{a}^* + \mathrm{k}\boldsymbol{b}^* + (\mathrm{l} + \zeta_z)\boldsymbol{c}^*$, referring to a location on an afm. or fm. Bragg rod
$\boldsymbol{q} \mathrel{\hat{=}} (\zeta, \zeta, 0)$	abbr. for $\boldsymbol{q} = \zeta\boldsymbol{a}^* + \zeta\boldsymbol{b}^*$, referring to a magnon wavevector or to a scan across a Bragg rod
Raman sp.	(studies with) Raman scattering spectroscopy
REIM	random exchange Ising model (cf. Sect. 4.1.12)
RFIM	random field Ising model (cf. Sect. 4.1.12)
RMS (distance)	root mean square value (of the distance), see Eq. 4.91 (Sect. 4.1.11)
red.	reduced, e.g. reduced temperature T/T_N (cf. Fig. 3.3 in Sect. 3.1.2) and reduced magnetization $M_{\mathrm{subl}}(T)/M_{\mathrm{subl}}(0)$ (cf. Fig. 3.15 in Sect. 3.1.5)
reentr.	reentrant phase transition

Table 1. List of Symbols and Abbreviations *(continued)*

ref. in I4/mmm	the lattice parameters have been obtained by refining the structure in the space group I4/mmm although the actual structure may be different, possibly a subgroup of I4/mmm. This is the case when only the main Bragg reflections are taken into account and not the (weaker) superreflections
refl., refls.	reflection, reflections, e.g. Bragg reflection(s)
renorm. spin.-w. th.	renormalized spin-wave theory, with Oguchi corrections [60O1]
resid. single-ion anis.	residual single-ion anisotropy (energy), cf. [84U]
resp.	respectively
Sect., Sects.	Section, Sections (with appropriate numbers)
SF-phase	spin-flop phase of an antiferromagnet for $\boldsymbol{H}_0$ applied parallel to the easy axis (cf. Fig. 3.16 in Sect. 3.1.6)
s. also	see also
s.g.:	space group in the notation and with the corresponding number of the International Tables for X-Ray Chrystallography [69I], but often in a non-standard setting in order to have the *c*-axis perpendicular to the layers (unique *c*-axis)
spin-w. th.	spin-wave theory
struct.	structure
struct. pt.	structural phase transition
str. diff. ph. not st. in det.	structures of the different (structural) phases have not been studied in detail
struct. pt.('s) studied by:	structural phase transition(s) have been studied by: then following the methods with the appropriate references
subthr. p.p.	subthreshold parallel pumping (see Sect. 3.2.5)
symm. log. sing.	symmetric logarithmic singularity, in the magnetic specific heat of the 2D Ising model, cf. Eq. 4.6 (Sect. 4.1.2)
TCP	tricritical point
T-dependence, *T*-dep.	temperature dependence
THT	tetragonal high temperature structural phase
TLT	tetragonal low temperature structural phase
theor. calc.	theoretical calculation
therm. m.	thermal (calorimetric) methods, e.g. differential scanning calorimetry or studies with an adiabatic calorimeter [84W1]
therm. e.	thermal expansion measurements
ultrason.	ultrasonic
u.c.p.	unit cell parameters
λ-anomaly	special type of spike in the specific heat at a phase transition

9.12.1.4 References for 9.12.1

22D Dickinson, R.G.: J. Am. Chem. Soc. 44 (1922) 2404.

44O Onsager, L.: Phys. Rev. 65 (1944) 117.

52H Helmholz, L., Kruh, R.F.: J. Am. Chem. Soc. 74 (1952) 1176.

55B Balz, D., Plieth, K.: Z. Elektrochem. 59 (1955) 545.

55L Leibfried, G.: Gittertheorie der mechanischen und der thermischen Eigenschaften der Kristalle in: Encyclopedia of Physics, Flügge, S. (ed.), Berlin: Springer-Verlag, 1955, Vol. VII/1, p.104.

56P Porai-Koshits, M.A.: Kristallografiya 1 (1956) 291.

58R1 Ruddlesden, S.N., Popper, P.: Acta Crystallogr. 11 (1958) 54.

60O1 Oguchi, T.: Phys. Rev. 117 (1960) 117.

62C Cowley, R.A.: Proc. R. Soc. (London) A268 (1962) 121.

63K1 Koster, G.F., Dimmock, J.O., Wheeler, R.G., Statz, H.: Properties of the Thirty-Two Point Groups, Cambridge/Massachusetts: M.I.T. Press, 1963.

64H Hutchings, M.T.: Point charge calculations of energy levels of magnetic ions in crystalline electric fields, in: Solid State Physics, Seitz, F., Turnbull, D. (eds.), New York: Academic Press, 1964, Vol. 16, p. 227.

64T Tinkham, M.: Group Theory and Quantum Mechanics, New York: McGraw-Hill, 1964.

66S1 Seifert, H.J., Klatyk, K.: Z. Anorg. Allg. Chemie 342 (1966) 1.

67C1 MacChesney, J.B., Williams, H.J., Potter, J.F., Sherwood, R.C.: Phys. Rev.164 (1967) 779.

67P Perry, C.H., Young, E.F.: J. Appl. Phys. 38 (1967) 4616.

68S1 Seifert, H.J., Koknat, F.W.: Z. Anorg. Allg. Chemie 357 (1968) 314.

69I International Tables for X-Ray Crystallography, Vol. 1, Henry, N.F.M., Lonsdale, T. (eds.), Birmingham: The Kynoch Press, 1969.

69Z Zak, J. (ed.), Casher, A., Glück, M., Gur, Y.: The Irreducible Representations of Space Groups, W.A. Benjamin, New York 1969.

70G1 Goodenough, J.B., Longo, J.M., in: Landolt-Börnstein, New Series, Hellwege, K.H., Hellwege, A.M. (eds.), Vol. III/4a, Berlin: Springer-Verlag, 1970, p. 126.

72H1 Heger, G., Geller, R.: Phys. Status Solidi (b) 53 (1972) 227.

72M1 Mais, R.H.B., Owston, P.G., Wood, A.M.: Acta Crystallogr. B 28 (1972) 393.

72N Nicklow, R., Wakabayashi, N., Smith, H.G.: Phys. Rev. B5 (1972) 4951.

72S2 Stirling, W.G.: J. Phys. C: Solid State Phys. 5 (1972) 2711.

74A2 Aharony, A., Bruce, A.: Phys. Rev. Lett. 33 (1974) 427.

74J1 de Jongh, L.J., Miedema, A.R.: Adv. Phys. 23 (1974) 1.

74L2 Lindgard, P.A., Danielsen, O.: J. Phys. C: Solid State Phys. 7 (1974) 1523.

74Y1 Yamazaki, H.: J. Phys. Soc. Jpn. 37 (1974) 667.

75W2 Wakabayashi, N., Smith, H.G., Nicklow, R.M.: Phys. Rev. B 12 (1975) 659.

76B2 Bürger, H., Strobel, K., Geick, R., Müller-Lierheim, W.: J. Phys. C: Solid State Phys. 9 (1976) 4213.

76B3 Berg, R.W., Søtofte, I.: Acta Chem. Scand. A 30 (1976) 843.

76G1 Gurewitz, E., Makovsky, J., Shaked, H.: Phys. Rev. B 14 (1976) 2071.

76L3 Lindgard, P.A., Kowalska, A.: J. Phys. C: Solid State Phys. 9 (1976) 2081.

76M1 Morosin, B., Emerson, K.: Acta Crystallogr. B 32 (1976) 294.

76S6 Strobel, K., Geick, R.: J. Phys. C: Solid State Phys. 9 (1976) 4223.

77A2 Arts, A.F.M., van Uijen, C.M.J., de Wijn, H.W.: Phys. Rev. B 15 (1977) 4360.

77C1 Ciajolo, M.R., Corradini, P., Pavone, V.: Acta Crystallogr. B 33 (1977) 553.

77C6 Catlow, C.R.A., Diller, K.M., Norgett, M.J.: J. Phys. C: Solid State Phys. 10 (1977) 1395.

77G2 Geick, R., Lehner, N., Strobel, K.: Nuovo Cimento B 38 (1977) 309.

77I1 Iizumi, M., Axe, J.D., Shirane, G., Shimaoka, K.: Phys. Rev. B 15 (1977) 4392.

77L1 Landi, E., Salerno, V., Vacatello, M.: Gazz. Chim. Ital. 107 (1977) 27.

77W2 Willett, R.D., Willett, J.J.: Acta Crystallogr. B 33 (1977) 1639.

78B3 Burns, G., Glazer, A.M.: Space Groups for Solid State Scientists, New York: Academic Press, 1978.

78L1 Lehner, N.: Progr. Rep. KfK 2720, Karlsruhe 1978.

78N1 Nomura, S., in: Landolt-Börnstein, New Series, Hellwege, K.H., Hellwege, A.M. (eds.), Vol. III/12a, Berlin: Springer-Verlag, 1978, p. 368.

78S10 Sangster, M.J.L., Schröder, U., Atwood, R.M.: J. Phys. C: Solid State Phys. 11 (1978) 1523.

78S11 Sangster, M.J.L., Atwood, R.M.: J. Phys. C: Solid State Phys. 11 (1978) 1541.

78T2 Thurlings, M.P.H., Hendriks, E.M., de Wijn, H.W.: Solid State Commun. 27 (1978) 1289.

79G4 Geick, R., Strobel, K.: J. Phys. C: Solid State Phys. 12 (1979) 27.

79K5 Kind, R., Blinc, R., Zeks, B.: Phys. Rev. B 19 (1979) 3743.

79S1 Smit, J.J., de Jongh, L.J.: Physica 97B (1979) 224.

80C1 Cowley, R.A., Birgeneau, R.J., Shirane, G., Guggenheim, H.J., Ikeda, H.: Phys. Rev. B 21 (1980) 4038.

80H4 Hatta, I., Ikeda, H.: J. Phys. Soc. Jpn. 48 (1980) 77.

80K2 Kleemann, W., Schäfer, F.J.: J. Magn. Magn. Mater. 21 (1980) 143.

80P4 Popov, E.A., Kotlyarski, M.M.: Sov. Phys. Solid State 22 (1980) 1763.

80T3 Thurlings, M.P.H., van Diepen, A.M., de Wijn, H.W.: J. Magn. Magn. Mater. 15-18 (1980) 637.

81D1 Dvorak, V., Kind, R.: Phys. Status Solidi (b) 107 (1981) K109.

81G4 Geick, R., Rauh, H., Lehner, N., Bouillot, J., Stirling, W.G., Heger, G.: J. Phys. (France) 42 (1981) C6-713.

81K3 Kind, R., Plesko, S., Günter, P., Roos, J., Fousek, J.: Phys. Rev. B 23 (1981) 5301. Erratum: Phys. Rev. B 24 (1981) 4910.

81K11 Kilner, J.A.: Philos. Mag. A, Phys. Condens. Matter Defects Mech. Prop. 43 (1981) 1473.

81R4 Rousseau, M., Gesland, J.Y., Hennion, B., Heger, G., Renker, B.: Solid State Commun. 38 (1981) 45.

81W1 de Wolff, P.M., Janssen, T., Janner, A.: Acta Crystallogr. A 37 (1981) 625

82G1 Goto, T., Yoshizawa, M., Tamaki, A., Fujimura, T.: J. Phys. C: Solid State Phys. 15 (1982) 3041.

82L2 Lehner, N., Rauh, H., Strobel, K., Geick, R., Heger, G., Bouillot, J., Renker, B., Rousseau, M., Stirling, W.G.: J. Phys. C: Solid State Phys. 15 (1982) 6545.

82S3 Strobel, K., Geick, R.: J. Phys. C: Solid State Phys. 15 (1982) 2105.

83G1 Geick, R., Strobel, K.: Magnetic resonances in perovskite-type layer structures, in: Reviews of Infrared and Millimeter Waves, Button, K.J. (ed.), New York: Plenum Press, 1983, Vol. 1, p. 249.

83K1 Kobayashi, J., Uesu, Y.: J. Appl. Crystallogr. 16 (1983) 204.

83R1 Rauh, H., Geick, R., Lehner, N., Bouillot, J., Eckold, G.: Phys. Status Solidi (b) 115 (1983) 463.

84C1 Cowley, R.A., Hagen, M., Belanger, D.P.: J. Phys. C: Solid State Phys. 17 (1984) 3763.

84H1 Hagen, M., Paul, D.McK.: J. Phys. C: Solid State Phys. 17 (1984) 5605.

84L1 Lukin, S.N.: Sov. Phys. Solid State 26 (1984) 771.

84U van Uijen, C.M.J., de Wijn, H.W.: Phys. Rev. B 30 (1984) 5265.

84W1 White, M.A.: Thermochim. Acta 74 (1984) 55.

85R3 Rauh, H., Geick, R.: Phys. Status Solidi (b) 127 (1985) 55.

86K1 Kobayashi, J., Kumoni, H., Saito, K.: J. Appl. Crystallogr. 19 (1986) 377.

87A1 Aleksandrov, K.S., Beznosikov, B.V., Misyul, S.V.: Phys. Status Solidi (a) 104 (1987) 529.

87B5 Burriel, R., Bartolomé, J., González, D., Navarro, R., Ridou, C., Rousseau, M., Bulou, A.: J. Phys. C: Solid State Phys. 20 (1987) 2819.

88K1 Kobayashi, J., Asahi, T., Takahashi, S., Glazer, A.M.: J. Appl. Crystallogr. 21 (1988) 479.

89B3 Becher, R.R., Sangster, M.J.L., Strauch, D.: J. Phys.: Condens. Matter 1 (1989) 7801.

90A3 Arts, A.F.M., de Wijn, H.W.: Spin waves in two-dimensional magnetic systems, theory and applications, in: Magnetic Properties of Layered Transition Metal Compounds, de Jongh, L.J. (ed.), Dordrecht: Kluwer Academic, 1990, p. 191.

90B1 Benner, H., Boucher, J.P.: Spin dynamics in the paramagnetic regime, NMR and EPR in two-dimensional magnets, in: Magnetic Properties of Layered Transition Metal Compounds, de Jongh, L.J. (ed.), Dordrecht: Kluwer Academic, 1990, p. 323.

90B2 Bovina, A.F., Kokov, I.T., Melnikova, S.V., Misyul, S.V.: Sov. Phys. Solid State 32 (1990) 1552.

90B3 Birgeneau, R.J.: Phys. Rev. B 41 (1990) 2514.

90G3 de Groot, H.J.M., de Jongh, L.J.: Field-induced phenomena in two-dimensional weakly anisotropic Heisenberg antiferromagnets, in: Magnetic Properties of Layered Transition Metal Compounds, de Jongh, L.J. (ed.), Dordrecht: Kluwer Academic,1990, p. 379.

90H Hirakawa, K., Ikeda, H.: Neutron scattering experiments on two-dimensional Heisenberg and Ising magnets, in: Magnetic Properties of Layered Transition Metal Compounds, de Jongh, L.J. (ed.), Dordrecht: Kluwer Academic, 1990, p. 231.

90J1 de Jongh, L.J.: Introduction to low-dimensional magnetic systems, in: Magnetic Properties of Layered Transition Metal Compounds, de Jongh, L.J. (ed.), Dordrecht: Kluwer Academic, 1990, p. 1.

90N Navarro, R.: Application of high- and low-temperature series expansions to two-dimensional magnetic systems, in: Magnetic Properties of Layered Transition Metal Compounds, de Jongh, L.J. (ed.), Dordrecht: Kluwer Academic,1990, p. 105.

90R1 Regnault, L.P., Rossat-Mognod, J.: Phase transitions in quasi two-dimensional planar magnets, in: Magnetic Properties of Layered Transition Metal Compounds, de Jongh, L.J. (ed.), Dordrecht: Kluwer Academic, 1990, p. 271.

91E Elcombe, M.M., Kisi, E.H., Hawkins, K.D., White, T.J., Goddman, P., Matheson, S.: Acta Crystallogr. B 47 (1991) 305.

92M1 Morón, M.C., Palacio, F., Rodriguez-Carvajal, J.: Physica B 180&181 (1992) 125.

92M7 Mazurenko, V.G., Nikiforov, A.E., Shashkin, S.Yu.: Sov. Phys. Solid State 34 (1992) 300.

94A Aleksandrov, K.S., Bartolomé, J.: J. Phys.: Condens. Matter 6 (1994) 8219.

95A1 Aleksandrov, K.S.: Crystallogr. Rep. 40 (1995) 251.

9.12.2 Structural Properties

(For figures and tables of this section see p. 78 ff.)

9.12.2.1 Structures

9.12.2.1.1 General Aspects

For a great number of perovskite-type layer compounds, the structures have been determined by x-ray diffraction or by neutron scattering. The results of such measurements have been compiled in Table 2 according to the order introduced in Sect. 1.3. There are listed the lattice parameters a, b, and c together with the space group in the notation according to the International Tables for X-Ray Crystallography [69I], provided the space group is known. Otherwise, only the crystal symmetry is given. Also the angles α, β, and γ between the crystallographic axes are listed in Table 2 when they are different from 90°, i.e. in monoclinic and triclinic structures. All crystallographic data are presented in Table 2 with their error limits, i.e. the uncertainty of the last decimal place in parentheses as introduced in Sect. 1.3. Space groups are usually denoted by the international symbol, e.g. I4/mmm or Abma. In some cases however, also the Schoenflies symbol will be presented, i.e. D_{4h}^{17} and D_{2h}^{18} for these two examples. It was already pointed out that we are dealing with layer structures here. In order to make the lattice parameters for the various compounds comparable with each other, it is necessary and more convenient for the reader when we introduce for all compounds a unique coordinate system in which the c-axis is perpendicular or, in monoclinic or triclinic crystals, almost perpendicular to the perovskite-type layers. Therefore, the standard setting of the International Tables can often not be used but a setting has to be used which results from the standard setting by interchanging and relabelling the lattice vectors $\boldsymbol{a}$, $\boldsymbol{b}$, and $\boldsymbol{c}$. For such nonstandard settings, the international notation for space groups is the more appropriate one. Below, a number of space groups will be considered with a nonstandard setting.

In cubic perovskites, the octahedra are regular as is required by symmetry. Such a requirement does no longer hold in the layer structures even in the socalled K_2NiF_4 structure (I4/mmm, cf. Fig. 2.1) with the highest symmetry among the layer-type compounds. In many compounds, however, the octahedra are almost regular also in tetragonal or lower symmetry. For demonstrating this, the M-X bond lengths are compiled for many compounds in Table 3. Two types have to be distinguished. One is the in-plane bond length r_{ip} for bridging X^--ions between two M^{2+}-ions within the layers. Thus, r_{ip} is parallel or nearly parallel to the plane of the layer. For the K_2NiF_4 structure, we have (see Fig. 2.1)

$$r_{\mathrm{ip}} = a/2 \tag{2.1}$$

where a is the in-plane lattice parameter. The other M-X bond length is the out-of-plane one r_{op} for terminal X^--ions with only one neighbouring M^{2+}-ion, and r_{op} is perpendicular or nearly perpendicular to the plane of the layer. It has to be calculated from the atomic position parameters and the lattice parameters which yields for the K_2NiF_4 structure:

$$r_{\mathrm{op}} = z_{\mathrm{x}} \cdot c \tag{2.2}$$

where $(0, 0, z_{\mathrm{x}})$ and $(0, 0, 0)$ are the atomic positions of the X^-- and the M^{2+}-ion, respectively. The difference between r_{ip} and r_{op} shows us for the tetragonal K_2NiF_4 structure the deviations from a regular octahedron. This deviation increases when the crystal symmetry is lowered, for example as a consequence of structural phase transitions. In orthorhombic or lower symmetry, it is further possible that there are two different values for r_{ip}. The values of r_{ip} and r_{op} depend essentially on the chemical nature of the X^--ion, and typical values for M-F, M-Cl, and M-Br bonds are 0.20–0.22 nm, 0.25–0.26 nm and 0.27–0.28 nm, resp., (cf. Table 3). There is only a slight dependence on the M-ion. The bridging X^--ions mediate the magnetic superexchange in case of paramagnetic M^{2+}-ions, and also from this point of view, the M-X bond length r_{ip} is of interest. In addition to the bond lengths r_{ip} and r_{op}, the interlayer separation d is a characteristic measure for the layer structures under consideration which is in the K_2NiF_4 structure (cf. Fig. 2.1)

$$d = c/2 \tag{2.3}$$

This distance between the layers is an especially interesting quantity for compounds with hydrocarbon chains $(C_nH_{2n+1}NH_3)_2MX_4$. The data in Table 3 show that the layer separation d increases with n while the in-plane M-X bond length r_{ip} and thus the size of the whole perovskite-type layer are almost independent of n. For some long-chain compounds, there are not all data available necessary for the calculation of r_{ip} and r_{op}. In such a case it is useful to define an average in-plane length $\langle r_{\mathrm{ip}}\rangle$ as a measure for the size of the octahedral layer system. If the parameters a, b, c of the orthorhombic lattice are known but not the atomic positions for more detailed calculations, the average value for r_{ip} is

$$\langle r_{\mathrm{ip}}\rangle = \tfrac{1}{2}\sqrt{a\cdot b/2} \tag{2.4}$$

where the factor 2 under the square root accounts for the change of coordinate systems as discussed below. In some cases only the layer separation d has been determined directly from diffraction data and not the whole set of lattice parameters. If then the volume V_{mol} of 1 mole of the compound under consideration is known, the average value of r_{ip} can be defined in the following way

$$\langle r_{\mathrm{ip}}\rangle = \tfrac{1}{2}\sqrt{V_{\mathrm{mol}}/(L\cdot d)} \tag{2.5}$$

where L is Avogadro’s number and V_{mol}/L the volume of one molecule.

For double-layer structures (cf. Fig. 1.2), two values for the layer separation have to be considered. At first there is the distance between the two layers of a double-layer set. This will be denoted a' because it should ideally be equal to the lattice parameter a. The second distance is the separation d of two double-layer sets from each other. In this case, we obtain

$$d = c/2 - a' \tag{2.6}$$

because $c/2$ measures half of the whole unit cell in Fig. 1.2 from which the width a' of double-layer set has to be subtracted. For the out-of-plane M-X bond length, we have also two values in the double-layer structure. The first one is that for the bridging X^--ion connecting two M^{2+}-ions in neighbouring layers of the double-layer set. The corresponding value is

$$r_{\mathrm{op}} = a'/2 \tag{2.7}$$

while the second one is again that for a terminal X^--ion, and this value for r_{op} can only be calculated from the atomic positions and the lattice parameters. No simple formula can be presented in this case since the calculations depend on the origin which can be chosen in two different ways for the double-layer structure. The origin should be in the middle between the two layers (see Fig. 1.2) at a center of inversion. But there, it can be chosen either at the position of an A^+-ion [65S, 78G] or at that of an X^--ion [80H1, 82B2].

With respect to structural and also magnetic phase transitions, there is usually a reduction of the symmetry from tetragonal to orthorhombic and/or monoclinic. In case of the K_2NiF_4 structure, this requires a change of the coordinate system. The x- and y-axes are rotated by 45° about the $z = z_0$-axis as shown for the tetragonal K_2NiF_4 structure in Fig. 2.1, where the usual body-centered unit cell (I4/mmm) is presented together with the unusual face-centered cell (F4/mmm) and the rotated coordinate system. This face-centered structure is the starting point for a number of orthorhombic structures resulting from phase transitions. The coordinate system for the space group I4/mmm is denoted (x_0, y_0, z_0) because it refers to the high temperature parent space group G_0 while that for F4/mmm is denoted (x, y, z) since it is also appropriate for all the space groups G_n of lower symmetry which are subgroups of G_0. In the discussion of the structural and magnetic properties of the perovskite-type layer structures, the (x, y, z) system will be more important than (x_0, y_0, z_0), in particular with respect to low temperatures. F4/mmm is a further example for a non-standard setting of a space group. The change of the coordinate system can as well be described as a change of basic lattice vectors $(\boldsymbol{a}, \boldsymbol{b}, \boldsymbol{c}) \rightarrow (\boldsymbol{a} + \boldsymbol{b}, \boldsymbol{b} - \boldsymbol{a}, \boldsymbol{c})$ where we use

$$\boldsymbol{a} = (a, 0, 0), \qquad \boldsymbol{b} = (0, a, 0) \qquad \text{and} \qquad \boldsymbol{c} = (0, 0, c) \tag{2.8}$$

as an orthogonal set for I4/mmm in accordance with the International Tables [69I]. The coordinates in Eq. 2.8 refer to the system (x_0, y_0, z_0). A similar set of basic vectors is obtained for the system (x, y, z) with $a_{(x,y,)} = \sqrt{2} \cdot a_{(\mathrm{x0,\,y0,\,z0})}$ and $c_{(x,y,z)} = c_{(x0,y0,z0)}$. In Table 2 with the crystallographic data, it is not possible to indicate for each entry the coordinate system, whether (x_0, y_0, z_0) or (x, y, z) is used for the description of that particular crystal structure. This would be too space-consuming. It is, however, relatively easy to identify the coordinate system because of the factor $\sqrt{2}$ between the in-plane lattice parameters (a and b) of the two systems.

9.12.2.1.2 Easy-Axis Antiferromagnets

Many compounds with paramagnetic divalent M-ions become antiferromagnetic. Below their Néel temperature T_N, the spins are aligned parallel or antiparallel to the c-axis in antiferromagnets of the easy-axis type. The doubling of the unit cell in the transition to the antiferromagnetic state requires a change to the face-centered unit cell (cf. Fig. 2.1) and to the (x, y, z) coordinate system. However, the crystal symmetry is reduced to orthorhombic because the antiferromagnetic order destroys the four-fold symmetry of the space group F4/mmm. Therefore, we obtain two antiferromagnetic domains in these materials (see Fig. 2.2) which can be described as the space groups Acam and Bbcm. For Rb_2MnCl_4, an elaborate structure determination has confirmed these space groups for the antiferromagnetic phase ($T < T_N$) [97T2]. Acam and Bbcm are again examples of non-standard settings of crystallographic space groups. In this case, the standard setting found in the International Tables is Cmca (No. 64). The complete notation for the magnetic space groups is Acam + Acam $\times (\theta \,|\, \boldsymbol{\tau})$ and Bbcm + Bbcm $\times (\theta \,|\, \boldsymbol{\tau})$, resp., [70E, 76D1, 80J]. These magnetic space groups are type IV Shubnikov groups [69C2]. The operation of time inversion θ is combined here with the nonprimitive translation $\boldsymbol{\tau} = (a/2, a/2, 0)$ which connects an up- and a down-spin within the same plane z = const. in the antiferromagnetic structure (cf. Fig. 2.2). The vector $\boldsymbol{\tau}$ refers to the system (x, y, z) with $a_{(x,y,z)} = \sqrt{2} \cdot a_{(x0,\,y0,\,z0)}$. The difference between the two domains is that the orientation of the spins in the plane $z = \frac{1}{2}$ is reversed in Bbcm with respect to Acam. Both domains can be distinguished by neutron diffraction since they give rise to different antiferromagnetic superreflections. This was first reported for K_2NiF_4 [62L1, 64P]. The equivalence of the two domains results from the fact that the interlayer exchange interaction is negligibly small and that the reversing of the spin in the plane $z = \frac{1}{2}$ requires only an extremely small amount of energy. Detailed considerations show further that the interactions almost cancel between the spins in the plane $z = \frac{1}{2}$ and those in the neighbouring planes $z = 0$ and $z = 1$. The cancellation is complete for the I/4mmm tetragonal structure, but not quite complete in lower symmetry. Thus, the interlayer interaction is essentially between next-nearest layers. It is ferromagnetic, but extremely small. In this sense, these antiferromagnets can be called two-dimensional although their magnetic ordering is three-dimensional.

The small interlayer interaction can also be antiferromagnetic. In this case, magnetic Bragg reflections are observed at half-integer values of l_0 or l indicating a magnetic unit cell with lattice parameter $2c$ instead of c as for the K_2NiF_4 structure (cf. Fig. 2.3a). In such a magnetic structure, an antiferromagnetic interaction between next nearest layers causes the spins in the plane $z = 1$ to be oriented antiparallel to those in the planes $z = 0$ and $z = 2$. This type of magnetic ordering was first described for Ca_2MnO_4 [69C1] and is therefore called Ca_2MnO_4-type (Fig. 2.3a) in contrast to the K_2NiF_4-type ordering with ferromagnetic interaction between next nearest layers where the spin orientation is parallel in the planes

$z = 0$ and $z = 1$ (cf. Fig. 2.3b). Ca_2MnO_4-type ordering has mainly been observed for Rb_2MnF_4 [70B1] and Cs_2MnF_4 [94I1]. In these compounds, the two types of ordering coexist below T_N. In Rb_2MnF_4, magnetic Bragg reflections with small intensity have also been found for $l = \frac{1}{3}$ and for $l = \frac{1}{6}$ [87I, 89I1], in addition to the largest peak at $l = \frac{1}{2}$ and the one at $l = 0$. Under hydrostatic pressure, the peak at $l = \frac{1}{2}$ decreases and finally disappears while a number of new reflections appear at $l = \frac{2}{7}, \frac{2}{9}, \frac{2}{15}, \frac{1}{4}$ in Rb_2MnF_4 and at $l = \frac{2}{7}, \frac{3}{8}, \frac{3}{7}$ in Cs_2MnF_4 [94I1]. This behaviour is ascribed to the subtle balance of ferro- and antiferromagnetic interlayer interactions which is affected by the reduction of the interlayer separation due to the hydrostatic pressure. For most of the other compounds like K_2MnF_4 [73B1, 73J1], K_2CoF_4 [74S1], Rb_2MnCl_4 [70G2], the K_2NiF_4-type ordering is stable and the only one. In $Rb_2Mn_{1-x}Co_xF_4$ [89I1] mixed crystals, the antiferromagnetic Bragg reflection at $(1, 0, \frac{1}{2})$ is the strongest one for $x = 0$ (Rb_2MnF_4). With increasing Co-concentration x, diminishes and vanishes for $x = 0.9$. Only the peak at $(1, 0, 0)$ remains for $0.9 \le x \le 1$ indicating the ferromagnetic interlayer interaction as the only one there. However, there are a few reports where ordering of the Ca_2MnO_4-type (cf. Fig. 2.3a) was found in compounds other than Rb_2MnF_4, e.g. in a single sample of K_2MnF_4 [72I]. For Rb_2MnCl_4 [70G2], the two types of ordering have been observed not coexisting in the same sample as in Rb_2MnF_4 but separately in samples grown by different techniques, namely only the K_2NiF_4-type one (cf. Fig. 2.3b) in samples grown from the melt while samples grown from aqueous solutions showed only the Ca_2MnO_4-type ordering.

When the antiferromagnetic ordering requires a reduction of the symmetry of the crystal it is possible that magneto-elastic or magnetostrictive effects cause a small deformation of the crystal. This was observed first in antiferromagnets of the type MnO, NiO etc. [58R2] where the symmetry is reduced from cubic to trigonal in the antiferromagnetic state. For K_2MnF_4 and Rb_2MnCl_4, the results of magnetic resonance experiments [92G1] indicate that there is a small orthorhombic distortion in the antiferromagnetic phase of these materials. Fig. 2.2 illustrates that the ordered spins form ferromagnetic sheets, alternate along the ($+z$)-direction and along the ($-z$)-direction. An orthorhombic deformation could actually be due to the attractive forces between these sheets and thus due to magneto-elastic or magnetostrictive effects. Fig. 2.2 shows also that the ferromagnetic sheets are perpendicular to the x-axis for Acam and perpendicular to the y-axis for Bbcm. This deformation is small but in a high-resolution neutron diffraction experiment it was possible to determine it to be $(a - b)/a = 8 \cdot 10^{-4}$ at temperatures below T_N [97T1, 98T]. An earlier estimate of $5 \cdot 10^{-5}$ [64P] agrees quite well with this value. Because of the smallness of $(a - b)$, the lattice parameters a and b are not listed separately in Table 2 in these cases but as $a \approx b = \dots$.

Completely analogous considerations apply to the antiferromagnetic order of double-layer perovskite-type compounds like $K_3Mn_2F_7$ [79U] or $Rb_3Mn_2Cl_7$ [76G1]. There are also two domains as shown in Fig. 2.4. Again the symmetry is reduced from tetragonal (I4/mmm) to orthorhombic (Acaa or Bbcb, resp.). This means also that the coordinate system is changed from (x_0, y_0, z_0) to (x, y, z). For this case, the magnetic space groups are Acaa + Acaa × $(\theta\,|\,\boldsymbol{\tau})$ and Bbcb + Bbcb × $(\theta\,|\,\boldsymbol{\tau})$, also type IV Shubnikov groups [69C2], where θ is again the time reversal operator and $\boldsymbol{\tau}$ the vector connecting an up- and an down-spin as discussed above. The standard setting of the ordinary (unitary) part of these magnetic space groups is Ccca (No. 68). Also in this case, the distribution of the spins over the two domains can be determined by neutron diffraction experiments. Unfortunately, the notation for the antiferromagnetic superreflections is not unique and may be confusing since they are denoted in some papers according to the reciprocal lattice of the paramagnetic (chemical) unit cell (h_0, k_0, l_0) with half-integer values for h_0 an k_0 and in others according to the magnetic unit cell (h, k, l) with integer values of h and k. The comparison of such two sets is complicated because of the change of the coordinate system as explained above. Therefore it seems necessary to discuss the relevant relations of the reciprocal lattice in detail, at first for the single-layer structures A_2MX_4. For the paramagnetic or chemical unit cell with coordinate system (x_0, y_0, z_0) in real space, we denote the reciprocal lattice points by (h_0, k_0, l_0) and the components of the wavevector by (q_{x0}, q_{y0}, q_{z0}) and for the antiferromagnetic unit cell with coordinate system (x, y, z) by (h, k, l) and (q_x, q_y, q_z), respectively. Fig. 2.5a shows the (q_{x0}, q_{y0}) or (q_x, q_y) reciprocal lattice plane together with the two reciprocal space coordinate systems. Fig. 2.5b presents the (q_x, q_z)-plane. In both parts of Fig. 2.5, the reciprocal lattice points are shown for the nuclear Bragg reflections and for the superreflections arising from the two antiferromagnetic domains. In addition, thick lines indicate in Fig. 2.5b the Bragg rods which are due to strong two-dimensional correlations of the spins and which are usually observed at temperatures slightly above T_N. This phenomenon will be discussed in more detail in context with the magnetic phase transitions. The lattice points in reciprocal space are in general given by

$$\boldsymbol{Q} = \mathrm{h}_0\, \boldsymbol{a}^* + \mathrm{k}_0\, \boldsymbol{b}^* + \mathrm{l}_0\, \boldsymbol{c}^* \tag{2.9}$$

for the (q_{x0}, q_{y0}, q_{z0})-system. The reciprocal lattice vectors $\boldsymbol{a}^*$, $\boldsymbol{b}^*$, and $\boldsymbol{c}^*$ are defined here in accordance with the International Tables [69I]. They are an orthogonal set corresponding to the lattice vectors Eq. 2.8 for the K_2NiF_4 structure:

$$\boldsymbol{a}^* = (a^*, 0, 0) \qquad \boldsymbol{b}^* = (0, b^*, 0) \qquad \boldsymbol{c}^* = (0, 0, c^*) \tag{2.10}$$

with $a^* = b^* = 2\pi/a$ and $c^* = 2\pi/c$. For the (q_x, q_y, q_z)-system, we obtain a similar expression with (h, k, l). The conditions limiting possible reflections are for the single-layer structures A_2MX_4 (cf. Fig. 2.5).

1) nuclear Bragg reflections $(\mathrm{h}_0, \mathrm{k}_0, \mathrm{l}_0)$: $\mathrm{h}_0 + \mathrm{k}_0 + \mathrm{l}_0 = 2\mathrm{n}$

2) antiferromagnetic superreflections domain 1 (Acam):
   $(\mathrm{h}_0, \mathrm{k}_0, \mathrm{l}_0)$ [h_0, k_0 with half-integer values!]: $\mathrm{h}_0 + \mathrm{k}_0 + \mathrm{l}_0 = 2\mathrm{n} + 1$;
   (h, k, l): $\mathrm{h} + \mathrm{k} = 2\mathrm{n} + 1$, $\mathrm{k} + \mathrm{l} = 2\mathrm{n}$.

3) antiferromagnetic superreflections domain 2 (Bbcm):
   $(\mathrm{h}_0, \mathrm{k}_0, \mathrm{l}_0)$ [h_0, k_0 with half-integer values!]: $\mathrm{h}_0 + \mathrm{k}_0 + \mathrm{l}_0 = 2\mathrm{n}$;
   (h, k, l): $\mathrm{h} + \mathrm{k} = 2\mathrm{n} + 1$, $\mathrm{h} + \mathrm{l} = 2\mathrm{n}$.

The units in Fig. 2.5 are a^*, b^* for both systems where $2\pi/a_{(x,y,z)} = \sqrt{2}\pi/a_{(x0,y0,z0)}$ for the (q_x, q_y, q_z) system and, in addition, c^* in Fig. 2.5b. For the double-layer structures $A_3M_2X_7$, we obtain the same rules for the nuclear reflections and for the antiferromagnetic superreflections from the two domains Acaa and Bbcb, for the latter with one difference: No superreflections are observed for $\mathrm{l}_0 = \mathrm{l} = 0$, but only for $\mathrm{l} \neq 0$. Therefore, Fig. 2.5 applies also to $A_3M_2X_7$ compounds if we consider it as the illustration of a plane l = const. in reciprocal space with $\mathrm{l} = 2\mathrm{n} \neq 0$. In practical structure determinations, often only the strong nuclear reflections are taken into account and the superreflections are disregarded. This leads then to the paramagnetic or chemical unit cell, i.e. I4/mmm in our example. In Table 2, these cases show the remark "refined in I4/mmm" which means that the actual structure is obtained by including the superreflections in the structure determination. This actual structure is then in general a subgroup of the space group I4/mmm. For studying antiferromagnetic phenomena, it is necessary to measure the antiferromagnetic superreflections in detail, e.g. the temperature dependence of their intensity.

9.12.2.1.3 Easy-Plane Ferromagnets and Antiferromagnets

Besides the easy-axis antiferromagnets of the K_2NiF_4-type discussed so far, there are easy-plane antiferromagnets like K_2FeF_4 and Rb_2FeF_4 with the preferred spin direction perpendicular to the c-axis [68W1, 69L1]. The paramagnetic or chemical structure of these Fe-compounds is also I4/mmm. In the antiferromagnetic phase, the spins are aligned parallel or antiparallel to the x- or the y-axis in the basal plane combined with a doubling of the unit cell which means again a change of the coordinate system from (x_0, y_0, z_0) to (x, y, z). The ordering of the spins in the plane $z = \frac{1}{2}$ leads again to an A-centered or a B-centered lattice. Thus, one would expect four antiferromagnetic domains in this case [79B2] as shown in Fig. 2.6. The positions (h, k, l) of the antiferromagnetic superreflections obey for A- or B-centering the same rules as described above, but their intensities depend on the spin orientation. And in a neutron scattering study [82T1], it was found that only two of the four domains actually exist in K_2FeF_4, namely b) and c) in Fig. 2.6, and that there is a unique stacking of nearest neighbour layers in K_2FeF_4 in contrast to the easy-axis antiferromagnets like K_2MnF_4 and Rb_2MnCl_4. If we define sheets as the planes spanned by the spin orientation and the *c*-axis, the sheets exhibit antiferromagnetic order of the spins (cf. Fig. 2.6) in domains a) and d) and ferromagnetic order in domains b) and c). Thus, the domains observed in K_2FeF_4 exhibit ferromagnetic order of the sheets. These results indicate further that the formation of ferromagnetic sheets is energetically more favourable and that there exists a coupling between the layers. For the two domains observed in K_2FeF_4 [b) and c) in Fig. 2.6], the magnetic space groups are similar to those for the easy-axis antiferromagnets, namely Abma + $(\theta\,|\,\boldsymbol{\tau}) \times$ Abma and Bmab + $(\theta\,|\,\boldsymbol{\tau}) \times$ Bmab, respectively. Both are again type IV Shubnikov groups [69C2].

In compounds with $M = Cu^{2+}$, Cr^{2+}, the MX_6 octahedra are considerably deformed because of a collective Jahn-Teller effect in these ions with orbital degeneracy in their ground state. This collective Jahn-Teller effect is accompanied by an orbital ordering of the M^{2+}-ions as first pointed out by Khomskii and Kugel [73K1]. The alternate ordering of the $d_{z^2-x^2}$ and $d_{z^2-y^2}$ orbitals in K_2CuF_4 is illustrated in Fig. 2.7. It was observed experimentally by polarized neutron diffraction [76I1]. The Jahn-Teller distortion of the octrahedra and the orbital ordering induce ferromagnetic coupling between nearest Cu^{2+}-neighbours, and below the Curie temperature T_C, K_2CuF_4 orders ferromagnetically with the preferred spin direction in the basal plane (easy-plane ferromagnet). The Jahn-Teller distortion means an elongation of the octahedra in x_0- or y_0-direction as shown in Fig. 2.7. X-ray diffraction studies [74H1] were used to determine the in-plane Cu-F bond length r_{ip}, namely the smaller one (0.192 nm) which is equal to the out-op-plane bond length r_{op} (cf. Fig. 2.7) and the larger one (0.222 nm) resulting from the elongation of the octahedra. Because of this elongation, the crystal structure (above T_C) is no longer I4/mmm but a structure of lower symmetry (cf. Fig. 2.8). The reduction of symmetry is here the result of the Jahn-Teller distortion and not due to the antiferromagnetic ordering as in the previous examples. Also in this case, the coordinate system (x, y, z) must be used instead of the (x_0, y_0, z_0) system as indicated in Fig. 2.8. For K_2CuF_4, two crystal structures have been observed with the space groups $\mathrm{I\bar{4}c2}$ (No. 120) [74H1] and Acam or Bbcm (No. 64) [79H1, 83H1]. This is analogous to $KCuF_3$ where also two structures, namely P4/mbm and I4/mcm, have been found [72T1]. For both Cu-compounds, the two structures are nearly identical, only the orientation of the Jahn-Teller distortion is different in some of the layers. This is sketched in Fig. 2.8 for the layers within a unit cell of the two structures of K_2CuF_4 where the elongation of the octahedra is depicted in an exaggerated way. For $\mathrm{I\bar{4}c2}$, the elongation pattern is rotated by 90° about the *c*-axis (perpendicular to the planes in Fig. 2.8) in the planes at $z = 1.27$ nm and $z = 1.91$ nm with respect to the planes at $z = 0$ and $z = 0.64$ nm. For Acam on the other hand, the ordering is parallel for these two sets of planes. The lattice parameters *a* and *b* are equal for both structures within the limits of experimental error while the parameters *c* differ by a factor of two ($c = 1.27$ nm for Acam and $c = 2.54$ nm for $\mathrm{I\bar{4}c2}$) as a consequence of the different stacking of the layers. For reasons of this difference of the lattice parameters *c*, the planes have been labelled by the *z*-coordinate in nm in Fig. 2.8. A theoretical study has further shown that both structures are equally possible for K_2CuF_4 with virtually the same lattice energy [95N2]. The different Jahn-Teller ordering in the two domains Acam and Bbcm will be discussed in the next paragraph for Rb_2CrCl_4 instead of K_2CuF_4.

Rb_2CrCl_4 is a second compound with orbital ordering, collective Jahn-Teller effect and with ferromagnetic coupling of the Cr^{2+}-ions. Its room temperature structure with the space group Bbcm (No. 64) is shown in Fig. 2.9, also with the change of the coordinate system from (x_0, y_0, z_0) to (x, y, z) due to the symmetry reduction. In complete analogy to the antiferromagnetic ordering of A_2MX_4 (cf. Fig. 2.2), there are two crystallographic domains (Bbcm and Acam) [83J1, 86D1] depending on the antiferrodistortive order of the $CrCl_6$ octahedra in the plane $z = \frac{1}{2}$ as illustrated in Fig. 2.10. There is no difference of this order in the plane $z = 0$ between the two domains but there is one in the plane $z = \frac{1}{2}$. In Fig. 2.10, the Jahn-Teller distortion is shown for the two planes, also in an exaggerated way. In the magnetically ordered state, Rb_2CrCl_4 is a slightly canted easy-plane ferromagnet. If the crystallographic domain is Acam and the magnetization parallel to the *x*-axis, we obtain for the magnetic space group of Rb_2CrCl_4 $\mathrm{A2_1/c11} + \theta \times (\mathrm{Acam} - \mathrm{A2_1/c11})$ [87A3] or Aca′m′, a type III Shubnikov group [69C2], where the primed symmetry operations have to be combined with θ, the operation of time inversion. In case of the second crystallographic domain Bbcm, assuming the magnetization parallel to the *y*-axis, we obtain $B12_1/c1 + \theta \times (Bbcm - B12_1/c1)$ or Bb′cm′ for the magnetic space group. The orbital ordering and the collective Jahn-Teller effect have not only been observed in K_2CuF_4 and Rb_2CrCl_4 but also in Cu-compounds of the type $(C_nH_{2n+1}NH_3)_2CuCl_4$ [89J, 90D1] and $[NH_3(CH_2)_nNH_3]CuCl_4$ [76P1, 78T1, 90G1] and in Cr-compounds like $(C_nH_{2n+1}NH_3)_2CrCl_4$ [78B1, 82S1] and $(C_6H_5CH_2NH_3)_2CrX_4$ (X = Cl, Br) [86B1, 87B1]. A similar elongation of the octahedra is found in corresponding Pd-compounds [76B3, 77W2]. Their structures can be interpreted either as containing square planar $PdCl_4$ units or as a two-dimensional network of distorted corner-sharing $PdCl_6$ octahedra [78S3] in complete analogy to the above mentioned Cu- and Cr-compounds.

9.12.2.1.4 Structures resulting from Structural Phase Transitions

As already mentioned in the introduction, the compounds $(C_nH_{2n+1}NH_3)_2MX_4$ with hydrocarbon chains undergo a number of structural phase transitions. These result from the order or disorder of the alkylammonium groups $(C_nH_{2n+1}NH_3)^+$. Fig. 2.11 shows as an example three structural phases of $(CH_3NH_3)_2MnCl_4$ with the shortest possible hydrocarbon chain (n = 1). The phases are the tetragonal high temperature phase (THT), the orthorhombic room temperature phase (ORT) and the tetragonal low temperature phase (TLT). Here in the text and in Tables 2 and 3, the notation for the structural phases is that usually used in the literature. Of course, terms like "low temperature" and "high temperature" are relative and make sense only in context with the phase transition sequence of the compound under consideration and the transition temperatures which will be discussed below. For compounds with a large number of phase transitions like $(C_3H_7NH_3)_2MCl_4$ with M = Mn, Cu and Cd, the various phases are labelled with lower case greek letters α, β, γ etc. in accordance with the literature. For the THT-phase of $(CH_3NH_3)_2MnCl_4$ with structure I4/mmm, it is obvious that the (CH_3NH_3) molecules do not fit into the tetragonal lattice. A structure refinement succeeds only when a disorder is assumed for these molecules [75H1]. For all particles which cannot be located on a site with fourfold symmetry, we have to choose four or eight equivalent positions with occupation probability 0.25 or 0.125, respectively. That means, for example, that the three H-atoms of the CH_3 group are distributed on 12 equivalent positions around the fourfold axis with an occupation probability of 0.25. In Fig. 2.11, the H-atoms are therefore depicted as rings for demonstrating this disorder in the THT-phase. In the ORT-phase with structure Abma, the (CH_3NH_3) groups are no longer disordered. Fig. 2.11 shows them with the C- and the N-atoms and one H-atom of CH_3 and NH_3 on sites with mirror plane symmetry while the two other H-atoms of these groups are arranged symmetrically to this plane. This order of the (CH_3NH_3) groups is accompanied by a tilting of the $MnCl_6$ octahedra around the *y*-axis so that the whole structure Abma means a *x*-orientation of the particles. This tilting is connected with the hydrogen-bonding between the NH_3 groups and the $MnCl_6$ octahedra which will be discussed in context with the phase transitions in more detail below. The other possible crystallographic domain Bmab is obtained by an interchange of the *x*- and *y*-axes and means a *y*-orientation of the particles. In the TLT-phase with structure $P4_2/ncm$ (cf. Fig. 2.11), this orientation is along the $(1,1,0)$ and $(\bar{1},1,0)$ directions in the (x,y,z)-system. There is no second crystallographic or twin domain for $P4_2/ncm$. But two antiphase domains have been distinguished in this structure in context with model considerations for the structural phase transitions [77K1, 83M2]. These two are denoted (+)-domain and (–)-domain. They belong to the same space group $P4_2/ncm$ but differ in the origin by a vector $(0,\frac{1}{2},\frac{1}{2})$. For the definition of antiphase domains in contrast to twin or crystallogaphic domains, the reader is referred to the literature [76W2]. For the monoclinic low temperature phase (MLT) of $(CH_3NH_3)_2MnCl_4$, there are again two twin domains, namely $A2_1/b11$ and $B12_1/a1$ or, equivalently, $A2_1/c11$ and $B12_1/c1$. These non-standard settings with A- or B-centering are used in order to have nearly the same values of the lattice parameters as in the three other phases and the monoclinic angle α or β with values close to 90°. But in the monoclinic system, a number of alternative descriptions of the same structure can be chosen, e.g. $P2_1/b11$ and $P12_1/a1$ in this case. Examples of such alternatives are listed in Table 2. Neutron diffraction data of $(CH_3NH_3)_2MnCl_4$ in the MLT-phase offer the opportunity to identify the signatures of the two domains [90A1]. Fig. 2.12a presents a $(1,0,l)$-scan with the peaks of various Bragg reflections. The data taken at 5.5 K ($T < T_N$) and at 77 K ($T > T_N$) allow further to distinguish between nuclear and magnetic reflections. These data can be explained by means of Fig. 2.12b where the (c^*, a^*)-plane of the reciprocal lattice is shown with the points for the nuclear and magnetic Bragg reflections. For a better understanding of Fig. 2.12b, let us recall that the lattice and the reprocal lattice of domain 1 ($A2_1/b11$) are given by

$$\begin{array}{lll} \boldsymbol{a} = (a, 0, 0) & \boldsymbol{b} = (0, b, 0) & \boldsymbol{c} = (0, c\cos\alpha, c\sin\alpha) \\ \boldsymbol{a}^* = (\frac{2\pi}{a}, 0, 0) & \boldsymbol{b}^* = (0, \frac{2\pi}{b}, -\frac{2\pi}{b}\,\mathrm{ctg}\,\alpha) & \boldsymbol{c}^* = (0, 0, \frac{2\pi}{c\sin\alpha}) \end{array} \tag{2.11}$$

with $a = 0.725$ nm, $b = 0.707$ nm, $c = 1.900$ nm, and $\alpha = 92.5°$ ([90A1], cf. Table 2). For domain 2 ($B12_1/a1$), the corresponding data are

$$\begin{array}{lll} \boldsymbol{a} = (a, 0, 0) & \boldsymbol{b} = (0, b, 0) & \boldsymbol{c} = (c\cos\beta, 0, c\sin\beta) \\ \boldsymbol{a}^* = (\frac{2\pi}{a}, 0, -\frac{2\pi}{a}\,\mathrm{ctg}\,\beta) & \boldsymbol{b}^* = (0, \frac{2\pi}{b}, 0) & \boldsymbol{c}^* = (0, 0, \frac{2\pi}{c\sin\beta}) \end{array} \tag{2.12}$$

with $a = 0.707$ nm, $b = 0.725$ nm, $c = 1.900$ nm, and $\beta = 92.5°$. At first, Eq. 2.11 and 2.12 illustrate in detail, as already mentioned before, that the two domains are related to each other by an interchange of the x- and y-axes or the a- and b-axes. Secondly, the a^*-axis of domain 1 is perpendicular to the c^*-axis while the a^*-axis of domain 2 subtends an angle of 92.5° (monoclinic angle β) with the c^*-axis. Since there are two ways of deriving the monoclinic structure from the higher temperature structures, we observe a monoclinic splitting, i.e. two a^*-axes for domain 2 in Fig. 2.12b. This splitting can be used to identify the two domains in the (1, 0, l)-scan (cf. Fig. 2.12a) where the reflections with even values of l refer to domain 1 (a^*-axis $\perp$ c^*-axis) and the reflections with odd values of l show the monoclinic splitting as expected for domain 2. In this way, the experimental data provide an evidence for the two domains.

The structures of the compounds $(C_nH_{2n+1}NH_3)_2MX_4$ with organic A^+-ions are usually of the staggered type as shown in detail for the examples of such structures in the preceding paragraph and in Fig. 2.11. The perovskite-type layer in the plane $z = \frac{1}{2}$ is shifted by $(\frac{1}{2}, 0, 0)$ or by $(0, \frac{1}{2}, 0)$ with respect to the neighbouring layers in the planes $z = 0$ and $z = 1$. The diammonium compounds with $A_2 = NH_3(CH_2)_nNH_3$, on the other hand, are of the eclipsed type without such a shift as shown schematically in Fig. 2.13. In both cases, the NH_3 groups are coupled to the perovskite-type layers by hydrogen-bonds. In the diammonium compounds, the chains are thus coupling neighbouring layers as shown in Fig. 2.13 to the right. In the monoammonium compounds, the hydrocarbon chains provide not such a direct coupling. The CH_3 end groups can only mediate a van-der-Waals coupling between the layers, in addition to long-range Coulomb forces resulting from the ionic character of the octahedral network and from the polar NH_3 groups. Especially in compounds with shorter chains, the Coulomb forces play probably an important role in the binding of these crystals. The differences of the two types of structures are illustrated in more detail in Fig. 2.14 by a comparison of the room temperature structures of $(CH_3NH_3)_2MnCl_4$ (ORT-phase Abma) and of $[NH_3(CH_2)_2NH_3]MnCl_4$ ($P12_1/a1$). For an easier comparison, two unit cells of the monoclinic eclipsed structure are shown which can be thought to be derived from the other one (cf. Fig. 2.14) by removing the staggering of the layers and by bonding two (CH_3NH_3) groups together at their CH_3 ends to $NH_3(CH_2)_2NH_3$ where two H-atoms become superfluous. In the monoclinic structure [78T1] of $[NH_3(CH_2)_2NH_3]MnCl_4$, there is no disorder of the organic molecules. The $MnCl_6$ octahedra are tilted and also slightly deformed which gives rise to two slightly different values of the in-plane Mn-Cl bond length r_{ip} (0.2556 and 0.2578 nm, cf. Table 3). This difference is smaller than that resulting from the collective Jahn-Teller effect in Cu-compounds and is merely the result of the low crystal symmetry. The out-of-plane value is $r_{op} = 0.2488$ nm. In the monoclinic structure, it is further difficult to identify an orientation of the particles as was done in the ORT- and TLT-phases of $(CH_3NH_3)_2MnCl_4$ (cf. Figs. 2.11 and 2.14).

Let us now turn to the compounds $(C_nH_{2n+1}NH_3)_2MX_4$ with long hydrocarbon chains $(n > 5)$. As already pointed out, the interlayer separation d increases with the number n of carbon atoms, i.e. with the length of the chain. This increase is almost linear as shown in Fig. 2.15 for the example $(C_nH_{2n+1}NH_3)_2MnCl_4$ with n = 1 – 17. The sice of the two-dimensional network of corner-sharing $MnCl_6$ octahedra is practically independent of n as demonstrated in Fig. 2.15 where the in-plane Mn-Cl bond length r_{ip} or its average value $\langle r_{ip} \rangle$ is shown versus n. For short chains $(n < 5)$, the structural phase transitions are dominated by the hydrogen bonding to the perovskite-type layers. As the chains become longer the phase transitions of the compounds are more and more due to conformational changes within the n-alkyl-ammonium chains. The conformation of a chain results from trans or gauche configurations at the different C-atoms. These configurations are sketched in Fig. 2.16. In the socalled low temperature (LT) phase which is usually observed at room temperature, the chains form an ordered arrangement in an all-trans configuration except for the first or second C-atom at the polar NH_3 head where gauche bonds provide a better adaption of the chain for the H-bonding to the MX_6 octahedral network. For long chain compounds, only a few complete structure determinations have been performed, e.g. for $(C_{10}H_{21}NH_3)_2CdCl_4$ (structure: P12/n1 [79K1]) and $(C_{14}H_{29}NH_3)_2CdCl_4$ (structure: $P\bar{1}$ [88S1]). For the discussion of more details of the long chain compounds, we introduce abbreviations, namely C_nMX for $(C_nH_{2n+1}NH_3)_2MX_4$. The ordered arrangement of the chains at room temperature is shown for $C_{10}CdCl$ and $C_{14}CdCl$ as a projection of the structure to the (b, c)-plane in Fig. 2.17. The chains with nearly alltrans configuration are arranged parallel. They subtend an angle of nearly 45° with the b-axis. This inclination of the chains is achieved by the gauche bond near the NH_3 group as shown in Fig. 2.17. In $C_{10}CdCl$, there are two inequivalent hydrocarbon chains [79K1], the A-chains with the gauche bond between the first and the second C-atom and the B-chains with it between the second and the third C-atom. In $C_{10}MnCl$, on the other hand, only the B-chains are found [76C1]. A major difference between the structures for $C_{10}CdCl$ and $C_{14}CdCl$ is that the center of inversion is at the Cd site in the $CdCl_6$ layer in $C_{14}CdCl$ and in the van-der-Waals bonding layer between the CH_3 groups in $C_{10}CdCl$. The space made available for the chains by the layers with tightly fixed distances is not wide enough to allow an intercalation of the chains which would reduce the interlayer separation d considerably (2.580 nm and 3.2484 nm in $C_{10}CdCl$ and $C_{14}CdCl$, resp., cf. Table 3). Such an intercalation, however, is possible in compounds without a tight two-dimensional network of MX_6 octahedra but with isolated MX_4 tetrahedra as found in Zn- and Co-compounds. As an example, the intercalated ordered arrangement of the chains in $(C_{13}H_{27}NH_3)_2ZnCl_4$ is also presented in Fig. 2.17 (structure at room temperature: $P12_11$ [85Z1]). The distances between the isolated tetrahedra are large enough that there is sufficient space for the intercalation of the chains in $C_{13}ZnCl$ where d is reduced to 2.20 nm [85Z1].

For the ordered low-temperature phases (LT, T near 295 K) of the long-chain compounds, it is useful to define the quantity $\langle \Delta d \rangle$ per $\Delta n = 1$, i.e. per additional CH_2 group, because of the linear increase of the interlayer distance with n (cf. Fig. 2.17). The experimental values of $\langle \Delta d \rangle$ are for $(C_nH_{2n+1}NH_3)_2MCl_4$ compounds

M:	Mn	Cu	Cd	Co	Zn
$\langle \Delta d \rangle$ [nm]:	0.169	0.162	0.176	0.118	0.125

These values for the LT-phases have been determined from the data in Table 3 (Mn-, Cu-, and Cd-compounds) where also the references are found and from the literature (Co- and Zn-compounds) [77L1]. The above experimental data may be compared to a theoretical estimate for the ordered chains [79B1]

$$\langle \Delta d \rangle \geq \ell \sin(\Phi/2) = 0.128 \text{ nm} \qquad (2.13)$$

of the structures with isolated MX_4 tetrahedra and with the chains oriented perpendicular to the layers of tetrahedra. In Eq. 2.13, $\ell = 0.154$ nm is the C–C bond length and $\Phi = 112°$ the C–C–C bond angle in the hydrocarbon chains. If the chains are inclined with respect to the layer normal as, for example, in $C_{13}ZnCl$ (cf. Fig. 2.17) by $\alpha \approx 20°$, $\langle \Delta d \rangle$ is reduced by a factor $\cos \alpha \approx 0.94$ which explains the experimental values of $\langle \Delta d \rangle$ for Co- and Zn-compounds. For structures with an octahedral network (Mn-, Cu-, and Cd-compounds) and with non-intercalated chains oriented at an angle $\alpha \approx 45°$ with respect to the layer normal [79K1, 88S1], the theoretical estimate is for $\alpha \approx 45°$ [79B1, 81V]

$$\langle \Delta d \rangle \geq 2\,\ell \sin(\Phi/2)\cos\alpha = 0.181 \text{ nm} \tag{2.14}$$

in reasonable agreement with the experimental data for the ordered LT-phases of the Mn-, Cu-, and Cd-compounds. In the high temperature phase (HT, near 370 K) of the long-chain compounds, the MX_6 octahedra still form a solid 2-dimensional network, but the chains are more in a liquid-like state with a high degree of dynamical disorder. The chains are found almost perpendicular to the layers. The consequence is a drastic increase of the interlayer separation *d* by nearly 10%, e.g. from 2.938 nm at 293 K to 3.216 nm at 360 K in $C_{12}CdCl$ [85C1]. In many compounds, there are several phase transitions and intermediate phases between the LT- and the HT-phase.

9.12.2.1.5 Mixed Crystals

Perovskite-type layers with an octahedral network exist only in compounds with chains $CH_3–(CH_2)_n–NH_3$ or $NH_3–(CH_2)_n–NH_3$ and with special organic molecules like $C_6H_5–(CH_2)_n–NH_3$ [76D2, 86B1, 87B1, 90W1, 92Z2], $CH_2OH–CH_2–NH_3$ [87L1], $COOH–(CH_2)_2–NH_3$ [81W2, 83W2] and with $C_5N_2H_8$ = 3-ammoniumpyridinium instead of a diammonium chain [88W1]. But if, for example, an isopropylammonium group $(CH_3)_2–CH–NH_3$ replaces the n-propylammonium group, a structure results in $[(CH_3)_2CHNH_3]_2CuCl_4$ which has isolated $CuCl_4$ units of distorted tetrahedral symmetry [81B2] and which is no longer a perovskite-type layer structure. The same is true for compounds like $[(CH_3)_4N]_2NiCl_4$ [67W1] and $[(C_2H_5)_4N]_2NiCl_4$ [67S1] with tetramethylammonium and tetraethylammonium groups which form not chains but tetrahedral molecules. That means perovskite-type layer structures exist only with organic molecules which need sufficiently narrow space that the two-dimensional octahedral network is not broken up. As already mentioned in the introduction, there are also A_2MX_4 compounds with inorganic A^+-ions like Rb_2ZnCl_4 which crystallize in the β-K_2SO_4 structure and form isolated MX_4 tetrahedra instead of layers with corner-sharing octahedra. Beznosikov and Aleksandrov [85B2] have performed a crystal-chemical analysis for halide A_2MX_4 compounds. Their analysis yields conditions for the ionic radii of the ions which limit the range of existence of a certain type of structure (see also [79G7]). For the K_2NiF_4 structure, these conditions are

$$R_A^{(9)} \geq 0.73\,R_X \qquad 0.41\,R_X \leq R_M^{(6)} \leq 0.73\,R_X$$
$$R_M^{(6)} < 0.48\,R_A^{(9)} + 0.11 \tag{2.15}$$

where R_A, R_M and R_X are the ionic radii of the A-, M-, and X-ions, respectively. The superscripts denote the coordination number of the ions (cf. the tables for ionic radii [70S2, 76S1]). The corresponding conditions for β-K_2SO_4 are

$$R_A^{(10)} \geq 0.73\,R_X \qquad 0.225\,R_X \leq R_M^{(4)} \leq 0.41\,R_X \tag{2.16}$$

On the basis of these conditions, it is not only possible to explain why a particular compound crystallizes in the K_2NiF_4 or in the β-K_2SO_4 structure but also to predict compounds with these or other structures which have not yet been observed experimentally.

Within the A_2MX_4 family of perovskite-type layer structures, there are three types of mixed crystals or solid solutions according to the number of different ions in these compounds, namely $A_x\tilde{A}_{2-x}MX_4$, $A_2MX_x\tilde{X}_{4-x}$ and $A_2M_x\tilde{M}_{1-x}X_4$. An example of the first type is $Rb_xK_{2-x}MnF_4$ with the K_2NiF_4 structure (I4/mmm) for all values of x. In this system, Rb^+ has a larger ionic radius than K^+ by about 7% [69S1, 76S1] and the results of x-ray diffraction studies show an increase of the lattice parameters *a* and *c* with the concentration x, *a* increases linearly with x while *c* deviates slightly from a linear function of x [64C1], cf. Table 2. For the second type of mixed crystals, the ionic radii increase from Cl^- to Br^- and to I^- by 9% and 13%, resp., [69S1, 76S1]. While the A^+-ions occupy sites between the layers in the K_2NiF_4 structure (cf. Fig. 2.1), the X^--ions are an essential part of the layers of MX_6 octahedra. They occupy two crystallographically inequivalent sites, the "in-plane" sites between two M^{2+}-ions within the layers and the "out-of-plane" sites (cf. the discussion in context with Eqs. 2.1 and 2.2). Generally, the ions in the mixed crystals will be arranged in such a way that the distortions are minimized which are caused by replacing some of the X^--ions by $\widetilde{X}^-$-ions. $Rb_2MgCl_{4-x}Br_x$ with x = 0, 1, 2 is an example of this type (all members with K_2NiF_4 structure). This system has been studied by doping the samples with less than 1% Mn^{2+} and by performing EPR measurements [73W1]. The result of this investigation revealed for x = 0, as expected, O_h-symmetry around the Mn^{2+}-ion ($MnCl_6$ octahedra). For x = 2, i.e. for $Rb_2MgCl_2Br_2$, the Mn^{2+}-dopant has D_{4h}-symmetry indicating the formation of $MnCl_4Br_2$ octahedra. This can be explained by assuming that the Br^--ions with the larger ionic radius occupy preferably the out-of-plane sites. And for x = 1 (Rb_2MgCl_3Br), both symmetries were found and thus a mixture of the two types of octahedra. There was no evidence for $MnCl_5Br$ octahedra. Such an ordering of the X^--ions was also concluded for a number of similar mixed crystal systems, namely for $Rb_2MnCl_{4-x}X_x$, $(NH_4)_2MnCl_{4-x}X_x$ with X = Br, I and of $Cs_2MnCl_{4-x}Br_x$ [74W1]. Structural investigations of these systems have shown that the relative changes of the lattice parameter *c* is considerably larger than that of the lattice parameter *a*. For *c*, the increase is about 10% for $Rb_2MnCl_2I_2$ and $(NH_4)_2MnCl_2I_2$ in comparison to Rb_2MnCl_4 and $(NH_4)_2MnCl_4$, respectively. The corresponding increase of *a* is only 1–2% (cf. Table 2). For mixed crystals of this type with the Jahn-Teller ions Cr^{2+} and Cu^{2+}, the collective Jahn-Teller effect and the orbital ordering have to be taken into account, in addition to the ordering of the X^--ions which was also reported for systems of this type like $Rb_2CrCl_{4-x}X_x$ with X = Br, I [83W1, 85F1], $Rb_2CuCl_{4-x}Br_x$ [74W2] and $(CH_3NH_3)_2CuCl_{4-x}Br_x$ [79K2, 83S1]. For $Rb_2CrCl_{4-x}X_x$ and $Rb_2CuCl_{4-x}Br_x$, structure refinements in Bbcm (cf. Table 2) revealed in increase of the out-of-plane Cr-X bond length r_{op} (cf. Table 3) corresponding to an ordering of the Br^-- and I^--ions. For $Rb_2CrCl_{4-x}X_x$, r_{op} increases from 0.241 nm in Rb_2CrCl_4 to 0.257 nm in $Rb_2CrCl_2Br_2$ and to 0.277 nm in $Rb_2CrCl_2I_2$ (cf. Table 3). The smaller value of r_{ip} is nearly independent of the concentration x while the larger value increases with x according to the increase of *a* and *b*. A special structure investigation was performed for $(CH_3NH_3)_2CuCl_2Br_2$. In the fit for the refinement in Acam, the occupation of the in-plane and out-of-plane sites by Cl^- or Br^- was varied as new parameters [91W1] with the result that the in-plane sites are occupied by Cl^- with a probability of $p = 0.88$ and by Br^- with $p = 0.12$, and the out-of-plane sites by Cl^- with $p = 0.24$ and by Br^- with $p = 0.76$. These results demonstrate in a rather convincing way the preferable occupation of the out-of-plane sites by the X^--ions with the larger ionic radius.

In the third type of mixed crystals, the M-ion in the center of the octrahedra (cf. Fig. 2.1) is partly replaced by a different $\widetilde{M}$-ion. With respect to their magnetic properties, these mixed crystals are most interesting because they are magnetic dilutions if one partner is a diamagnetic ion and magnetic mixtures with competing interactions if both partners are paramagnetic ions. One example of such a dilution is $K_2Ni_xZn_{1-x}F_4$ [79K2, 81R1]. According to structure investigations, the samples have the K_2NiF_4 structure for all values of x and both lattice parameters *a* and *c* decrease linearly from K_2ZnF_4 to K_2NiF_4 (cf. Table 2) since Ni^{2+} has a slightly smaller ionic radius than Zn^{2+} [69S1, 70S2, 76S1]. In the systems $Rb_2Co_xMg_{1-x}F_4$ [80C1] and $Rb_2Mn_xCd_{1-x}Cl_4$ [82P1], the ionic radii of the M-ions and $\widetilde{M}$-ions are almost equal and the variation of the lattice parameters with the concentration x is rather small for *c* and a little larger for *a*. In the system $K_2Cu_xZn_{1-x}F_4$, the end members K_2CuF_4 and K_2ZnF_4 have different crystal structures. The structure of K_2ZnF_4 is the usual K_2NiF_4 structure I4/mmm. For K_2CuF_4 with collective Jahn-Teller effect and orbital ordering, there are two equivalent structures, namely $I\bar{4}c2$ [74H1, 81H1, 81R1] and Acam or Bbcm [79H1, 83H1], depending on the orbital order in different layers (cf. Fig. 2.8 and [95N2]). An interesting problem is how far the collective deformation of the octahedra extends with decreasing Cu^{2+}-concentration x towards K_2ZnF_4. Because of the different structures of the two end members, it is useful to describe the mixed system $K_2Cu_xZn_{1-x}F_4$ and their crystallographic data (cf. Fig. 2.18) uniquely in the (*x*, *y*, *z*) coordinate system and thus K_2ZnF_4 in the unusual setting F4/mmm (cf. Fig. 2.1). Structure refinements of these mixed crystals [79K2, 81R1, 83H1, 86H1] have revealed that the variation of the lattice parameters with the Cu^{2+}-concentration x is rather drastic in the range

$0.4 \le x \le 1$ where $a \approx b$ decreases while c increases as shown in Fig. 2.18. In the range $0 \le x \le 0.4$, on the other hand, the change of the lattice parameters with x is considerably smaller. This behaviour is ascribed to the collective orbital ordering and its variation with the Cu^{2+}-concentration x and the conclusion is that this collective order persists down to $x \approx 0.4$. In addition, it was observed [83H1] that the superreflections corresponding to Acam and Bbcm are spot-like in the range $0.9 \le x \le 1$ and rod-like in the range $0.6 \le x \le 0.85$. This means that for $x \ge 0.9$ the elongation of the CuF_6 octahedra is three-dimensionally correlated (structure: Acam or Bbcm) but correlated only two-dimensionally for $0.6 \le x \le 0.85$, i.e. uncorrelated along the c-axis. Similar results have been obtained for the system $Rb_2Mn_xCr_{1-x}Cl_4$ where Rb_2CrCl_4 exhibits the collective Jahn-Teller effect and orbital ordering while Rb_2MnCl_4 has the structure I4/mmm in its paramagnetic state. Weak superreflections have been observed for x = 0.01, 0.08, 0.13, and 0.31 [80M3, 81M1], and, by means of these diffraction data, the displacement has been evaluated for the Cl^--ions from their symmetric position between two M^{2+}-ions (deformation of the octahedra). From EPR measurements [79K2, 83Y1, 83Y2] and from the study of phonons by Raman scattering in the mixed system $K_2Cu_xZn_{1-x}F_4$ [83N1, 85N, 89T4, 91F1], also information can be obtained about the collective orbital ordering and its variation with concentration x. For the phonon measurements, a group theoretical analysis yields that a number of lattice modes is Raman active in both structures I4/mmm and Acam or Bbcm. But other modes are Raman active only in the structure with the lower symmetry (Acam or Bbcm). In the mixed crystals, these latter modes are observed in the Raman spectra over the range $1 \ge x \ge 0.4$ [83N1, 85N, 91F1], and these results thus indicate that the collective orbital ordering extends down to $x \approx 0.4$. The disappearance of these Raman lines near $x \approx 0.4$ has been discussed in connection with the percolation problem on a square lattice [85N] since the collective Jahn-Teller effect and the ordering will disappear at the percolation limit like other collective phenomena. From the experimental results, it was further concluded that not only neares neighbour interactions but also those of next nearest neighbours are involved in this process since on a square lattice the critical percolation probability is $x_p = 0.59$ for only nearest neighbour interaction and $x_p = 0.41$ for interactions including first and second neighbours [64S2, 66D1]. And for $x < 0.41$, there will still be elongated octahedra due to the Jahn-Teller effect but a collective order is no longer possible. Results similar to those for $K_2Cu_xZn_{1-x}F_4$ have been obtained for the system $Rb_2Cu_xZn_{1-x}F_4$ [79K2, 81R1].

9.12.2.2 Structural Phase Transitions

9.12.2.2.1 Experimental Investigations

All available information about the structural phase transitions of halide perovskite layer structures is compiled in Table 4. The most important and instructive information is the diagram of the sequence of phase transitions with the different structures and with the character of the transition, e.g. a continuous, a discontinuous, a reentrant or a lock-in transition. Further, Table 4 presents the values of the transition temperatures T_{Cn} and of the thermodynamic parameters connected with the phase transition, namely the transition enthalpy ΔH_n and the transition entropy ΔS_n where n refers to the n-th phase transition. Of course, the subscript "n" is missing if there is only one structural phase transition for a particular compound. Finally, a complete survey is given in Table 4 about the experimental methods which have been used to study the phase transition (see "struct. pt's studied by:", i.e. "structural phase transitions studied by:" in Table 4). There is a great variety of experimental techniques which have been employed for the investigation of structural phase transitions:

a) thermal methods (differential scanning or adiabatic calorimetry)
b) diffraction experiments (x-ray or neutron elastic scattering)
c) optical methods like polarizing microscopy etc. and linear birefringence
d) infrared spectroscopy and Raman scattering
e) elastic constants by sound velocity measurements or by Brillouin scattering
f) nuclear magnetic resonance (NMR) or nuclear quadrupole resonance (NQR),

$0.4 \le x \le 1$ where $a \approx b$ decreases while c increases as shown in Fig. 2.18. In the range $0 \le x \le 0.4$, on the other hand, the change of the lattice parameters with x is considerably smaller. This behaviour is ascribed to the collective orbital ordering and its variation with the Cu^{2+}-concentration x and the conclusion is that this collective order persists down to $x \approx 0.4$. In addition, it was observed [83H1] that the superreflections corresponding to Acam and Bbcm are spot-like in the range $0.9 \le x \le 1$ and rod-like in the range $0.6 \le x \le 0.85$. This means that for $x \ge 0.9$ the elongation of the CuF_6 octahedra is three-dimensionally correlated (structure: Acam or Bbcm) but correlated only two-dimensionally for $0.6 \le x \le 0.85$, i.e. uncorrelated along the c-axis. Similar results have been obtained for the system $Rb_2Mn_xCr_{1-x}Cl_4$ where Rb_2CrCl_4 exhibits the collective Jahn-Teller effect and orbital ordering while Rb_2MnCl_4 has the structure I4/mmm in its paramagnetic state. Weak superreflections have been observed for x = 0.01, 0.08, 0.13, and 0.31 [80M3, 81M1], and, by means of these diffraction data, the displacement has been evaluated for the Cl^--ions from their symmetric position between two M^{2+}-ions (deformation of the octahedra). From EPR measurements [79K2, 83Y1, 83Y2] and from the study of phonons by Raman scattering in the mixed system $K_2Cu_xZn_{1-x}F_4$ [83N1, 85N, 89T4, 91F1], also information can be obtained about the collective orbital ordering and its variation with concentration x. For the phonon measurements, a group theoretical analysis yields that a number of lattice modes is Raman active in both structures I4/mmm and Acam or Bbcm. But other modes are Raman active only in the structure with the lower symmetry (Acam or Bbcm). In the mixed crystals, these latter modes are observed in the Raman spectra over the range $1 \ge x \ge 0.4$ [83N1, 85N, 91F1], and these results thus indicate that the collective orbital ordering extends down to $x \approx 0.4$. The disappearance of these Raman lines near $x \approx 0.4$ has been discussed in connection with the percolation problem on a square lattice [85N] since the collective Jahn-Teller effect and the ordering will disappear at the percolation limit like other collective phenomena. From the experimental results, it was further concluded that not only neares neighbour interactions but also those of next nearest neighbours are involved in this process since on a square lattice the critical percolation probability is $x_p = 0.59$ for only nearest neighbour interaction and $x_p = 0.41$ for interactions including first and second neighbours [64S2, 66D1]. And for $x < 0.41$, there will still be elongated octahedra due to the Jahn-Teller effect but a collective order is no longer possible. Results similar to those for $K_2Cu_xZn_{1-x}F_4$ have been obtained for the system $Rb_2Cu_xZn_{1-x}F_4$ [79K2, 81R1].

9.12.2.2 Structural Phase Transitions

9.12.2.2.1 Experimental Investigations

All available information about the structural phase transitions of halide perovskite layer structures is compiled in Table 4. The most important and instructive information is the diagram of the sequence of phase transitions with the different structures and with the character of the transition, e.g. a continuous, a discontinuous, a reentrant or a lock-in transition. Further, Table 4 presents the values of the transition temperatures T_{Cn} and of the thermodynamic parameters connected with the phase transition, namely the transition enthalpy ΔH_n and the transition entropy ΔS_n where n refers to the n-th phase transition. Of course, the subscript "n" is missing if there is only one structural phase transition for a particular compound. Finally, a complete survey is given in Table 4 about the experimental methods which have been used to study the phase transition (see "struct. pt's studied by:", i.e. "structural phase transitions studied by:" in Table 4). There is a great variety of experimental techniques which have been employed for the investigation of structural phase transitions:

a) thermal methods (differential scanning or adiabatic calorimetry)
b) diffraction experiments (x-ray or neutron elastic scattering)
c) optical methods like polarizing microscopy etc. and linear birefringence
d) infrared spectroscopy and Raman scattering
e) elastic constants by sound velocity measurements or by Brillouin scattering
f) nuclear magnetic resonance (NMR) or nuclear quadrupole resonance (NQR),

and many other techniques which cannot all be listed here. In Table 4, the information about phase transitions has been limited to the most important data like sequence of the phase transitions and the thermodynamical quantities. Not all of the numerous experimental results can be compiled there which have been obtained with the various techniques. Instead of aiming for completeness only some examples of such results will be presented in the following paragraphs.

The thermal measurements are performed either with a differential scanning calorimeter, very often with a commercial one like a Perkin-Elmer DSC-2 or DSC-4, or with an adiabatic calorimeter. For a review on these techniques, see [79G1]. A critical comparison of both methods with respect to structural phase transitions in solids was published by M.A. White [84W1]. As an example served the compound $(C_{18}H_{37}NH_3)_2CdCl_4$ which undergoes four structural phase transitions in the narrow temperature range 349 K–366 K. These were found to be fully resolved by adiabatic calorimetry and could well be characterized while the results were not so satisfactory for the other method. For $(C_{14}H_{29}NH_3)_2CdCl_4$ with also four structural phase transitions in the even narrower range 341 K–351 K, two data sets obtained with differential scanning calorimetry [84N, 88S1] are presented in Table 4. The comparison shows that not all of these transitions are well resolved. An essential result of such thermal studies is the specific heat C_p (at constant pressure) as a function of temperature T. As an example, $C_p(T)$ of $(CH_3NH_3)_2MnCl_4$ is shown in Fig. 2.19 for the range $4\ \text{K} \le T \le 410\ \text{K}$ [78S2, 79S4]. For $T \le 100$ K, the experimental data (open circles in Fig. 2.19) have been obtained with adiabatic calorimetry [79G1] and those for $T \ge 100$ K with the differential scanning method.

The ordinary specific heat is due to the lattice vibrations and superimposed on this ordinary part are anomalies of the specific heat due to the structural phase transitions. In Fig. 2.19, the structural phases of $(CH_3NH_3)_2MnCl_4$ are indicated by abbreviations THT etc. as introduced in Sect. 2.1.4 and Table 4. In the temperature range $10\ \text{K} \le T \le 295\ \text{K}$, the specific heat of $(CH_3NH_3)_2MnCl_4$ has also been measured by White et al. [82W2]. Their data agree with those in Fig. 2.19 within the limits of experimental error. Solely the anomalies were also measured at the phase transitions near 257 K [77T1] and near 394 K [75B1], resp., shown as full circles in Fig. 2.19. These data represent well the anomalies but the ordinary part is considerably lower than the complete data in Fig. 2.19 and also than those of White et al. [82W2]. Finally, the ordinary specific heat is compared to the results of a model calculation, namely a lattice dynamical rigid ion model for $(CH_3NH_3)_2MnCl_4$ treating the $(CH_3NH_3)^+$-ions as rigid bodies with rotational and torsional degrees of freedom [79G4, 79S4]. The model parameters were determined from phonon frequencies obtained by infrared [75L2, 75L3, 78A1] and Raman spectroscopy [74S2, 77C4] and by inelastic neutron scattering from a deuterated sample $(CD_3ND_3)_2MnCl_4$ [78L1, 79G4]. The values of the parameters are listed as model no. 5 in [79G4]. By means of this model, the phonon frequencies of all the branches are calculated for N points in the Brillouin zone and from these the specific heat according to

$$C_{\text{phonon}} = \frac{L}{\text{N}}\frac{\partial}{\partial T}\sum_{\text{q}}\ \sum_{\mu}(\hbar\omega_{\text{q},\mu})\ \left[\exp\left(\hbar\omega_{\text{q},\mu}/k_{\text{B}}T\right)-1\right]^{-1} \tag{2.17}$$

where the sum "q" extents over the N points in the Brillouin zone and the sum "μ" over all phonon branches. In this model calculation, the phonon frequencies $\omega_{\text{q},\mu}$ (wavevector $\boldsymbol{q}$ and branch μ) are assumed temperature-independent. The internal modes of $(CH_3NH_3)^+$ and $^+[NH_3(CH_2)_2NH_3]^+$ were studied by Oxton and Knop [77O, 78O2]. For the calculation of C_{phonon} of $(CH_3NH_3)_2MnCl_4$ (Eq. 2.17), these are included as additional Einstein-terms. The calculated data (full line in Fig. 2.19) agree satisfactorily with the experimental data in view of the fact that the parameters are determined independently with no one fitted to the specific heat. The data calculated without the internal modes of $(CH_3NH_3)^+$ (broken line in Fig. 2.19) approach above 200 K their Dulong-Petit value while the internal modes cause a further increase of C_{phonon} in the range 200–400 K because of their high frequencies.

With respect to the structural phase transitions, the specific heat anomalies are presented on an enlarged scale in Fig. 2.20 for the transitions at 94 K [78S2, 79S4], 257 K [77T1] and 394 K [75B1]. Especially the $C_p(T)$ curve for the transition near 94 K shows a narrow λ-like anomaly with an extremely high peak. The other two anomalies near 257 K and 394 K are much broader and the peaks by far not so high. These specific heat anomalies reveal characteristic data of the underlying phase transition. The temperature at which the peak occurs is the phase transition temperature T_C. The extra specific heat due to the phase transition $C_p(T)_{trans}$ is given by the difference of the measured $C_p(T)$ and the lattice part of the specific heat indicated by the broken lines in Fig. 2.20. This $C_p(T)_{trans}$ contributes to the change in enthalpy ΔH connected with the phase transition, see for example [84W1, 84W2]:

$$\Delta H = \int C_p(T)_{trans}\,dT \tag{2.18a}$$

Also the entropy change ΔS can be calculated from $C_p(T)_{trans}$:

$$\Delta S = \int \frac{C_p(T)_{trans}}{T}\,dT \tag{2.18b}$$

The values of T_{Cn}, ΔH_n and ΔS_n for the three phase transitions of $(CH_3NH_3)_2MnCl_4$ as obtained from $C_p(T)_{trans}$ are listed in Table 4 and will not be repeated here. But the values show as well as the $C_p(T)_{trans}$ curve in Fig. 2.20 that the phase transition at 94 K is the one with the most drastic changes in the structure of the lattice (TLT-phase ↔ MLT-phase, cf. Table 4) and therefore with the largest values of ΔH and ΔS. The entropy change ΔS is characteristic for the mechanism of a phase transition and below, in context with these mechanisms, ΔS will be compared to theoretical predictions.

Using neutron or x-ray diffraction, the structure has been determined for many compounds in their various structural phases. Besides the thermal parameters the structures are a very important information about the phase transitions because we can discuss the symmetry changes and the changes of the bonding scheme in the lattice only with the knowledge of the structure including the atomic positions. Without such information, no diagram of the sequence of phase transitions can be presented in Table 4 as is the case for many compounds listed there. It is further very instructive when the lattice parameters are determined as a function of temperature by a diffraction technique. An example of this kind is shown in Fig. 2.21, namely a, b, c, and the monoclinic angle α of $(C_3H_7NH_3)_2CuCl_4$ for the temperature range 20 K–300 K [94J1] including the structural phases δ, ε, ζ, and η (cf. Table 4). $(C_3H_7NH_3)_2CuCl_4$ belongs to the $(C_3H_7NH_3)_2MCl_4$-family (M = Mn, Cu, Cd) which is unique in the series $(C_nH_{2n+1}NH_3)_2MCl_4$ as pointed out by Depmeier [79D1]. These compounds show an exceptionally large number of structural phase transitions and their structural phases exhibit also incommensurate structures [83K3, 86D2]. For $(C_3H_7NH_3)_2CuCl_4$, the γ-phase (outside the temperature range of Fig. 2.21) and the ζ-phase (in Fig. 2.2.1) are incommensurate ones. In Table 4, these structures are denoted as

$$P^{Pbca}_{ss1} \quad \text{and} \quad P^{P2_1/n}_{\bar{1}\;\;1}$$

following the notation of Wolff, Janssen and Janner [81W1] where Pbca and $P2_1/n$ are the basic structures of the incommensurately modulated phases. The preceding letter "P" means that the rational part of the modulation wavevector $\boldsymbol{q}_r = 0$ (cf. Eq. 4.4 of [81W1]). The subscripts "s", "1" and "$\bar{1}$" indicate the symmetry behaviour in the fourth dimension (modulation wavevector) with respect to the generators of the basic space group (cf. Eq. 4.3 of [81W1]). For further information about incommensurate structures, the reader is referred to the review by Janssen and Janner [87J1]. On these grounds, the data for the ζ-phase in Fig. 2.21 are those of the basic structure $P2_1/n11$. A special feature of the sequence of phase transitions in $(C_3H_7NH_3)_2CuCl_4$ is that the transition at 180 K means a jump from the δ-phase (Pbca) to the incommensurate ζ-phase when the sample is cooled down. The commensurate ε-phase ($P2_1/n11$) is reached only by heating from the ζ-phase. Further heating leads then back to the δ-phase. With the transitions δ → ζ and ζ → ε → δ, there is not much change in the lattice parameters a, b, and c, except for the monoclinic angle α which becomes exactly 90° in the orthorhombic δ-phase (see Fig. 2.21). The transition ζ ↔ η, on the other hand, is strongly discontinuous as exhibited by the discontinuous changes of the lattice parameters at 132 K in Fig. 2.21. Jahn et al. [94J1] investigated very carefully and confirmed the interchange of a and b at this transition, so that there is really $a > b$ for $T > 132$ K and $a < b$ for $T < 132$ K (cf. also Table 2).

For monoclinic structures, there is some arbitrariness in the choice of the basic lattice vectors. Therefore, alternative descriptions are often added in Table 2 for the monoclinic low-temperature phases of some compounds like $(CD_3ND_3)_2MnCl_4$, $(C_3H_7NH_3)MnCl_4$ and similar Cu- and Cd-compounds. These different descriptions are presented in Table 2 because part of the published data are based on them, and it seems therefore advisable to discuss this problem in detail here. The description fitting best to our system adopted for the data in Table 2 is the setting $A2_1/b11$ (or $B12_1/a1$) for the structures under consideration. The a-axis (or b-axis) is parallel to the monoclinic twofold axis and the b- and c-axes (or a- and c-axes) are in the mirror plane. The monoclinic angle α (or β) is very near to 90° and thus the c-axis almost perpendicular to the plane of the perovskite-type layer. The corresponding lattice parameters can easily be compared to those of the other structural phases of the compounds under consideration. However, this is not so easy for a different set of lattice vectors as used in some of the references. A good example for the discussion of these problems is the ζ-phase of $(C_3H_7NH_3)_2MnCl_4$ below the lock-in transition at 113 K where the modulation wavevector $\boldsymbol{q}_0 = \sigma \cdot \boldsymbol{b}^*$ ($\sigma = 0.363$ at 130 K in the incommensurate ε-phase $P^{\mathrm{Abma}}_{\mathrm{s}\bar{1}1}$) flips to $\boldsymbol{q}_0 = \frac{1}{2}(\boldsymbol{b}^* \pm \boldsymbol{c}^*)$ so that the resulting ζ-phase is a commensurately modulated one which can also be described as new commensurate phase. This is illustrated in Fig. 2.22 for the structure of the ζ-phase where $\boldsymbol{q}_0 = \frac{1}{2}(\boldsymbol{b}^* + \boldsymbol{c}^*)$ was chosen as the modulation wavevector. The modulation itself is sketched in an exaggerated way as a transverse wave with displacement parallel to the c-axis. Note that only the Mn^{2+}-ions are shown in Fig. 2.22 in order not to overload the figure. The basic structure of the ζ-phase was reported as $A2_1/b11$ by Achiwa et al. [90A1] (cf. Table 2) with the lattice vectors $\boldsymbol{a} = (a, 0, 0)$, $\boldsymbol{b} = (0, b, 0)$, and $\boldsymbol{c} = (0,\ c\cos\alpha, c\sin\alpha)$ which have already been discussed (cf. Eq. 2.11 in Sect. 2.1.4) in context with the two structural domains. For this centered unit cell (with $\alpha \approx 90°$), the lattice parameters are comparable to those of Abma (space group of the commensurate δ-phase and basic structure of the ε-phase). The primitive unit cell of $A2_1/b11$ can as usual be written as

$$\boldsymbol{t}_1 = \boldsymbol{a} \qquad \boldsymbol{t}_2 = \tfrac{1}{2}(\boldsymbol{b} + \boldsymbol{c}) \qquad \boldsymbol{t}_3 = \tfrac{1}{2}(-\boldsymbol{b} + \boldsymbol{c}) \tag{2.19}$$

and in tetragonal and orthorhombic structures $(\boldsymbol{t}_1, \boldsymbol{t}_2, \boldsymbol{t}_3)$, they would only be the set of primitive non-orthogonal lattice vectors. They could not be considered as the lattice vectors of a different structure. But in the monoclinic system, one of these vectors has to be chosen parallel to the twofold axis (a-axis in our case) while the other two can be chosen rather arbitrarily in the mirror plane (with the b- and c-axis in Fig. 2.22). Therefore, the set $(\boldsymbol{t}_1, \boldsymbol{t}_2, \boldsymbol{t}_3)$ can be considered as the lattice vectors of a non-centered monoclinic structure, namely $P2_1/n11$ with $\alpha = \angle(\boldsymbol{t}_2, \boldsymbol{t}_3), = 31.35°$ (cf. Fig. 2.22). In a similar way, we can describe the modulated ζ-phase also as a new not modulated structure with triplication of the unit cell. Muralt et al. [88M1] have proposed the set

$$\boldsymbol{s}_1 = \boldsymbol{t}_1 = \boldsymbol{a} \qquad \boldsymbol{s}_2 = 3\,\boldsymbol{t}_2 = \tfrac{3}{2}(\boldsymbol{b} + \boldsymbol{c}) \qquad \boldsymbol{s}_3 = \boldsymbol{t}_3 = \tfrac{1}{2}(-\boldsymbol{b} + \boldsymbol{c}) \tag{2.20}$$

as the lattice vectors, also space group $P2_1/n11$. Another choice of the lattice vectors was used by Depmeier et al. [83D1]

$$\boldsymbol{g}_1 = \boldsymbol{a} \qquad \boldsymbol{g}_2 = 3\,\boldsymbol{b} \qquad \boldsymbol{g}_3 = \tfrac{1}{2}(-\boldsymbol{b} + \boldsymbol{c}) \tag{2.21}$$

which give the space group $P2_1/b11$. All these systems of lattice vectors are shown in Fig. 2.22. It is obvious that they represent a non-orthogonal set with angles α far away from 90° and violate the rule that one lattice vector should be perpendicular or almost perpendicular to the plane of the layers. It is also obvious that this cannot be avoided by a different nonstandard setting of the space groups. The corresponding lattice parameters are listed in Table 2. They are derived from the sets of vectors in Eqs. 2.20 and 2.21 in the usual way. Following the references, they are denoted also as (a, b, c, α) and not in a different way like, for example, (s_1, s_2, s_3, σ) which would be rather unusual and possibly confusing. Thus, Fig. 2.22 illustrates the modulated ζ-phase, on the one hand, and the arbitrariness in the choice of lattice vectors in monoclinic structures, on the other hand.

Optical methods are a very useful tool for the direct visual observation of domains and structural phase transitions. This is mostly done by means of a microscope equipped with polarizers. The samples are usually thin platelets with the *c*-axis perpendicular to their major faces, and thus this method is appropriate to study the optical anisotropy in the plane of the layer, i.e. the (a, b)-plane. As an example, Fig. 2.23 shows photographs of two samples of $(CH_3NH_3)_2CdCl_4$ which were taken at room temperature through a microscope with a magnification of about 100 [80G1, 82W4]. No polarizers were used in this case because this is not appropriate for a black-and-white photograph. We recall that $(CH_3NH_3)_2CdCl_4$ is at 294 K in the ORT-phase (cf. Table 2) with two domains Abma and Bmab corresponding to *x*- and *y*-orientation of the particles. The sample in Fig. 2.23a is about 2 mm thick. It was freshly grown from an aqueous solution and, fortunately, turned out to be nearly single-domain with only a few wide stripes of the other domain. The domain boundaries extend through the whole sample perpendicular to its faces. They are made visible by light of grazing incidence. The other sample in Fig. 2.23b is about 1 mm thick. It shows a narrow multidomain structure with a great number of much narrower domains. It is worth noting that the domain boundaries do not intersect each other at right angles in the same layer but only in different layers of the sample as can be clearly seen in Fig. 2.23b. Moreover, the number of domains increases by each temperature cycle from 500 K (THT-phase) down to 100 K (MLT-phase) and back to 500 K. When polarizers are used in the study of these domains it is found that the domain boundaries are parallel to the x_0- or y_0-axis of the (x_0, y_0, z_0)-system for the tetragonal parent structure I4/mmm (cf. Figs. 2.1 in Sect. 2.1.2 and 2.11 in Sect. 2.1.4) while the optical index ellipsoid is oriented parallel to the axes of the (x, y, z)-system used for the description of the ORT-phase [74K1]. That means that the light passing the sample is blocked by crossed polarizers when these are oriented at 45° to the domain boundaries. When they are oriented parallel or perpendicular to them the lineary polarized light passing the sample becomes elliptically polarized which is seen as green light through one domain and red light through the other one [82W4]. Such twin domains (Abma and Bmab) have also been observed under the microscope for $(C_3H_7NH_3)_2MnCl_4$ [89Y1] in the β-, γ-, and δ-phases.

A more quantitative method are birefringence investigations, i.e. the measurement of the difference of the refractive indices for directions parallel to two optical axes. For such measurements, also a microscope with polarizers is mostly used and the light sent through a single-domain part of the sample. The linear birefringence can then be determined by means of Babinet-Soleil compensator and a photoelastic modulator [79K3]. In this context, let us discuss the compounds $(CH_3NH_3)_2MnCl_4$, $(CH_3NH_3)_2FeCl_4$ and $(CH_3NH_3)_2CdCl_4$ which have all the same sequence of structural phase transitions THT ↔ ORT ↔ TLT ↔ MLT (cf. Table 4), apart from the MLT-phase which has not been found for the Fe-compound. In the two tetragonal phases THT and TLT, the refractive indices n_a and n_b for the directions parallel to the *a*-, and *b*-axis (*x*- and *y*-axis, cf. Fig. 2.11 in Sect. 2.1.4) are equal for reasons of symmetry. In the orthorhombic ORT-phase, however, they are different and their difference $\Delta n = n_b - n_a$ is the quantity determined by birefringence studies. Fig. 2.24 shows Δn as a function of temperature (200–400 K) for $(CH_3NH_3)_2MnCl_4$ and $(CH_3NH_3)_2FeCl_4$. As expected, Δn is zero above T_{C1} (THT-phase) and below T_{C2} (TLT-phase) for both compounds [74K1]. In the ORT-phase, Δn starts to increase continuously with decreasing temperature at T_{C1}, i.e. at the continuous phase transition, and it drops to zero at T_{C2} indicating the discontinuous character of this phase transition. Thus, Δn behaves like the order parameter at the phase transition THT ↔ ORT or, more precisely, like the square of the order parameter. It can therefore be used to determine the order parameter critical exponent β [74K1, 81K1, 84K1] which is universal for a certain type of phase transitions independent of the particular compound under investigation. A special section will be devoted to critical phenomena and critical exponents where we also return to the results on these compounds and to the numerical values of β and other critical exponents. With the socalled "HAUP"-method [83K1], birefringence and optical activity can be measured simultaneously. By means of such studies on $(C_3H_7NH_3)_2MnCl_4$ [92S2] in its incommensurate γ-phase, it was found that the optical gyration-component g_{33} directly reflects the order parameter of the modulation as determined by other experiments [86M1].

The vibrational spectra depend on the forces between the lattice particles and are therefore sensitive to changes in these forces due to structural changes in the course of a phase transition. Thus, the structural phase transitions can also be studied by measuring the frequencies of the infrared active or Raman active phonons as a function of temperature. In the infrared, usually the reflectivity R is measured by means of a Fourier transform infrared spectrometer [75G1]. The so obtained reflection spectra are often analyzed by applying a Kramers-Kronig integral transform [75L2, 76B2]. For normal incidence, the amplitude reflection coefficient is

$$r = \sqrt{R}\mathrm{e}^{\mathrm{i}\psi} = \frac{1-(n+\mathrm{i}k)}{1+(n+\mathrm{i}k)} \tag{2.22}$$

where ψ is the phase shift of the reflected wave and n and k are the refractive index and the extinction coefficient, respectively. These are related to the complex dielectric constant by $(\varepsilon' + \mathrm{i}\varepsilon'') = (n + \mathrm{i}k)^2$. Provided, R is known for a sufficiently large frequency range, the phase angle ψ can be calculated as a function of frequency by using the Kramers-Kronig integral formula [62G, 72W1]. From R and ψ, n and k and finally ε' and ε'' can be obtained by means of Eq. 2.22. Thus, this method allows to derive the spectra of the imaginary part ε'' from the reflectivity spectra and to determine the frequencies of the infrared active lattice modes from the maxima of ε''. Such measurements have been performed for $(CH_3NH_3)_2MnCl_4$ and related compounds [75L2, 78A1]. For the study of these optically anisotropic compounds linearly polarized light has been used, mostly with $\boldsymbol{E} \parallel \boldsymbol{c}$ or $\boldsymbol{E} \perp \boldsymbol{c}$, although the samples are not isotropic within the (a, b)-plane in the ORT- and MLT-phases and more effort would be required to determine completely the infrared-optical properties in these phases. As an example for such measurements, Fig. 2.25 shows the infrared spectra of $(CH_3NH_3)_2MnCl_4$ for $\boldsymbol{E} \perp \boldsymbol{c}$ [75L2, 75L3] at $T = 180$ K (TLT-phase), namely the reflectivity R, the phase angle ψ, the real and imaginary parts ε' and ε'' of the dielectric constant as a function of frequency expressed in wave numbers ($\tilde{\nu} = 1/\lambda$) as usual in infrared or Raman spectroscopy. Arrows indicate in Fig. 2.25 the 5 frequencies of the infrared active phonons determined in this experiment (cf. Table 2 of [75L2]), e.g. at the maxima of ε''. The influence of phase transitions on the lattice frequencies is illustrated in Fig. 2.26. The temperature dependence of the frequencies of the infrared active modes of $(CH_3NH_3)_2MnCl_4$ for $\boldsymbol{E} \parallel \boldsymbol{c}$ was studied especially in the range 90–100 K [77V1], where the compound undergoes the discontinuous phase transition TLT ↔ MLT. The frequencies $\tilde{\nu}$ in cm^{-1} have been derived for various temperatures by a Kramers-Kronig analysis as described above. On cooling, the vibrational frequencies of the TLT-phase extend to 94.2 K (full lines in Fig. 2.26) and change then within less 0.2 K to their values in the MLT-phase (broken lines in Fig. 2.26). On heating, this rapid change at the discontinuous transition happens at 97.5 K. It is easy to relate the frequencies in the two phases to each other above 170 cm^{-1}, but more difficult below 170 cm^{-1} because the number of infrared active modes is larger in the MLT-phase for reasons of the reduced symmetry, namely 8 for the TLT-phase and 13 for the MLT-phase according to a group theoretical analysis [77C4, 77G3]. We gather from Fig. 2.26 that all 8 modes were observed in the TLT-phase but only 11 in the MLT-phase which means that some of the modes only active in the monoclinic phase have such a small oscillator strength that they show not up in the reflectivity spectra. Further, the transition temperatures for heating and cooling and also the width of the hysteresis range have been found here a little larger than in the birefringence experiments (cf. Table 4 and [74K1]). Direct studies of the dielectric constant $\varepsilon = \varepsilon' + \mathrm{i}\varepsilon''$ provide also useful information about structural phase transitions. For example, such measurements have been performed for $(CH_3NH_3)_2CdCl_4$ at various frequencies, in the technical range at 1 kHz [76L1] and in the microwave (8.1 GHz) and millimeter wave (81 GHz, 600 GHz) ranges [82W4]. The results show for all frequencies drastic changes and hysteresis effects for most of the phase transitions of this compound.

Raman spectroscopy or inelastic scattering of photons is usually performed with an argon ion laser as the exciting light source and with a double or triple monochromator in order to separate and measure the extremely small intensity of the scattered and frequency-shifted light. Many studies of the temperature evolution of the Raman spectra have been performed, especially for the compounds $(CH_3NH_3)_2MnCl_4$ and $(CH_3NH_3)_2CdCl_4$ [74S2, 77C4, 78C2, 81M2, 83M1, 83M2], in order to investigate the influence of the structural phase transitions on the vibrational spectra. Of special interest are the low frequency spectra (cf. Fig. 2.27) because of the possibility to observe a soft mode with a frequency tending to zero when the temperature approaches the transition temperature. The role of soft modes in phase transitions will be discussed below. For the THT ↔ ORT transition of the compounds under consideration, a soft mode would be in the THT-phase a phonon with its wavevector at the X-point of the Brillouin zone which cannot be observed with optical methods [75P1, 77K1, 77G3]. But in the low-temperature phases, this mode would be at the center of the Brillouin zone and would be fully symmetric and therefore Raman active. In a Raman spectroscopic investigation of $(CH_3NH_3)_2CdCl_4$ [83M1, 83M2], the laser beam has been focussed onto a small surface portion of the crystal perpendicular to the *c*-axis. So it became possible to observe single-domain Raman spectra where the α_{xx}- and α_{yy}-spectra and the α_{xz}- and α_{yz}-spectra are different in the orthorhombic ORT-phase but equal in the tetragonal TLT-phase. In multi-domain samples, on the other hand, these spectra are equal in both phases due to superposition of the spectra from the two domains [77C4]. Here, α_{xx} and α_{xy} are the components of the Raman tensor where *x*, *y* and *z* mean that all these specifications of the Raman spectra refer to the (x, y, z) coordinate system for the low temperature phases (cf. Figs. 2.1 in Sect. 2.1.2 and 2.11 in Sect. 2.1.4). The low-frequency spectra of $(CH_3NH_3)_2CdCl_4$ [83M2] with Raman shifts $\Delta\tilde{\nu}$ up to 50 cm^{-1} are presented in Fig. 2.27 for various temperatures between 155 K and 295 K, in Fig. 2.27a the α_{xx}-spectra [scattering geometry: $z(xx)y$] and in Fig. 2.27b the α_{xy}-spectra [scattering geometry: $z(yx)y$]. For the scattering geometry, the usual notation is used as in the references [77C4, 83M1]. With the scattering geometry of Fig. 2.27a, lattice modes of Γ_1^+ (A_g or A_{1g}) symmetry can be observed and thus the expected soft mode. The sequence of phase transitions and the transition temperatures (cf. Table 4) are indicated in the center part of Fig. 2.27. At 295 K (ORT-phase) both spectra, α_{xx} and α_{xy}, show rather broad Rayleigh wings which become very broad for α_{xx} and disappear for α_{xy} at lower temperatures in the TLT-phase. In the α_{xx}-spectrum (Fig. 2.27a), this broad wing develops a maximum near 30 cm^{-1} which was interpreted as the expected soft mode [74S2, 77C4, 78C2]. But from its width, this mode would then be heavily overdamped. Later, detailed considerations [83M1, 83M2] have lead to the conclusion that this is not a soft mode connected with the motions of the (CH_3NH_3)-ions in the ordering process with different hydrogen bonding in the various structural phases but that there are low-lying order parameter fluctuation modes connected with the associated rotational motions of the rigid $CdCl_6$ octahedra. More details of these modes will be discussed below in context with models about the phase transition mechanisms [79K5]. Here it remains to be mentioned that the expected soft mode was not observed either in the THT-phase by means of inelastic neutron scattering [78L1, 79G4]. For these coherent neutron scattering experiments, it was necessary to use a fully deuterated sample of $(CD_3ND_3)_2MnCl_4$.

Not only the vibrational frequencies but also the elastic properties of perovskite-type layer compounds are affected by the structural phase transitions. The elastic constants of a crystal can be determined by measurement of the sound velocity υ_s from which the elastic stiffness constants *C* can be calculated

$$C = \rho \upsilon_s^2 \tag{2.23}$$

where ρ is the mass density of the compound under investigation. Fig. 2.28 shows the temperature dependence of the various elastic stiffness functions in $(CH_3NH_3)_2MnCl_4$ [79G3, 80G2]. The sound velocities for various directions of propagation ***k*** and polarizations ***R*** (cf. Fig. 2.28) have been measured by a highly sensitive phase compensation method [69M1] which allows to resolve relative velocity changes of one part in 10^5. The absolute velocity was determined from sound pulse transit times and sample lengths. Thermal expansion corrections can be applied using the known temperature dependence of the lattice parameters [74K1]. The accuracy of the absolute velocity is about 2%. For the calculation of the elastic constants by means of Eq. 2.23, the measured value $\rho = 1.70$ g/cm^3 has been used for the mass density. Except for C_{66}, the elastic constants exhibit only little influence of the phase transition as can be seen in Fig. 2.28 for the $C_L = \frac{1}{2}(C_{11} + C_{12} + 2\,C_{66})$, C_{11}, and C_{33} longitudinal modes and for the $\frac{1}{2}(C_{11} - C_{12})$ and C_{44} transverse modes. The transition temperatures are shown at the bottom of Fig. 2.28. The elastic constants are denoted here and in Fig. 2.28 with respect to the (x_0, y_0, z_0) coordinate system

(THT-phase, cf. Figs. 2.1 in Sect. 2.1.2 and 2.11 in Sect. 2.1.4) uniquely for all temperatures, i.e. for all phases. In Fig. 2.28, the (x, y, z) system for the low temperature phases is employed solely for the specification of $\boldsymbol{k}$ and $\boldsymbol{R}$ along the x-, y- or z-axis. Of all the modes in Fig. 2.28, as already mentioned, only the C_{66}-mode shows a drastic temperature dependence, namely a softening for decreasing temperature towards the THT ↔ ORT phase transition and for increasing temperature towards TLT ↔ ORT transition. Because of twinning (two crystallographic domains Abma and Bmab) and domain wall effects, it was impossible to obtain results for the C_{66}-mode in the ORT- and MLT-phases.

A similar softening of this elastic mode was also found in $(CH_3NH_3)_2CdCl_4$ [80G2] and $(CH_3NH_3)_2FeCl_4$ [82G1], and we note from Table 4 that all three compounds have the same sequence of phase transitions. For the Fe-compound, values of C_{66} were also reported for the ORT-phase [84Y2], not measured directly because of the above mentioned twinning but derived from other data. In the ORT-phase, C_{66} shows a strong restabilizing effect, i.e. rapidly increasing to higher values, when passing the phase boundary into the ORT-phase after the drastic softening in the TLT-phase and the softening in the THT-phase. The measurements for these results have been performed with a second technique for studying the elastic stiffness constants, namely Brillouin scattering which is the inelastic scattering of photons at the acoustic modes. Experimentally this can be performed with a spectrometer in which a scanning Fabry-Perot interferometer is used in the three- or five-pass configuration in order to analyze the scattered light [81K1]. When the light source, e.g. a krypton ion laser, is used with the full power of 30–50 mW, damage of the sample may occur. Therefore, the power for illumination of the sample is usually reduced to 5–10 mW. The light can be detected by a cooled photomultiplier followed by an electronics for counting single photons. The results obtained by Brillouin scattering for $(CH_3NH_3)_2MnCl_4$ [81K1] and $(CH_3NH_3)_2FeCl_4$ [84K1, 84Y2] agree quite well with those of the sound velocity measurements and show the same drastic temperature dependence of the C_{66}-mode. Moreover, this temperature dependence is nearly the same as that observed for elastic soft modes in a number of compounds with different types of phase transitions [73R1, 81L]. The origin of the softening of the elastic mode is usually a linear coupling of this mode to the order parameter in the phase transition.

9.12.2.2.2 Group-Theoretical Considerations

After these examples for experimental data strongly related to the structural phase transitions, we turn now our attention to symmetry considerations with respect to these transitions. The aim of such group theoretical considerations is twofold. At first, group theory will provide information about the group-subgroup relations between different structural phases which are relevant with respect to the application of Landau's theory of phase transitions and to the question whether a continuous transition can be expected. At second, a group-theoretical analysis provides information about the symmetry of the elementary excitations in the structural phases, including the symmetry of the order parameter in a phase transition and of a soft mode. The relevance of group-subgroup relations between different structural phases becomes obvious when we recall the first two of Landau's criteria for continuous or nearly continuous phase transitions [62L2, 74B3, 75L4, 77G3]:

1) The space group G_1 of the phase of lower symmetry is a subgroup of the space group G_0 of the high symmetry phase.

2) There is one and only one irreducible representation $(n, \boldsymbol{q})$ of G_0 (n - th multiplier representation at wavevector $\boldsymbol{q}$) which contains the unity representation of G_1 (fully symmetric representation Γ_1^+ or A_{1g}) and which specifies the symmetry of the order parameter of the phase transition between G_0 and G_1.

These criteria are the most important in our context for a better understanding of the phase transitions listed in Table 4 and for building a basis for a short introduction to the Landau theory (for a general review see [80C2, 81B3]) and to the models of the phase transitions in halide perovskite layer structures based on this theory (see for example: [78B2, 79B5, 79K5, 81K3, 91C2]).

Whether or not a phase transition fulfills criterion 1) can easily be gathered from the socalled "family-tree" [75B2, 80B3]. There, the crystal structures involved in a sequence of phase transitions are arranged according to their group-subgroup relations. In Fig. 2.29, the family-tree is presented for $(C_nH_{2n+1}NH_3)_2MCl_4$ with n = 1, 2 and M = Mn, Fe, Cd [76H2, 77G3, 78H2], i.e. for those members of the monoammonium family with n-alkylammonium chains where the phase transitions have been studied most extensively by a variety of methods and where the sequence of transitions is well known (cf. Table 4). Fig. 2.29 applies also to the structural phase transitions in perovskite-type layered compounds without hydrocarbon chain like $(NH_4)_2MgF_4$, Rb_2CdCl_4, $Rb_4Cd_3Cl_{10}$ and oxides, e.g. La_2CuO_4, Pr_2NiO_4 and La_2CoO_4. The phase transitions in these compounds will be discussed in more detail below. With respect to the diammonium family with alkylenediammonium chains, the family-tree [78K1, 88C2] is shown in Fig. 2.30 for the compounds $[NH_3(CH_2)_nNH_3]MCl_4$ with M = Mn, Cd and n = 3, 4, 5. The sequence of phase transitions of these compounds has also been established in numerous studies. In both figures, the space groups are listed in the international notation, e.g. I4/mmm, and also in the Schoenflies notation, e.g. D_{4h}^{17}. Before discussing the details of the phase transitions with respect to the group-subgroup relations, some general features should be mentioned about the family-trees. At the top of these "trees", there is the high symmetry "parent" structure G_0, i.e. I4/mmm in Fig. 2.29 and P4/mmm in Fig. 2.30, from which the other space groups G_n ($n \geq 1$) are derived by symmetry reduction. Along the "branches" of the trees, the symmetry reductions are performed in minimal steps such that a space group is always followed by one of its maximal subgroups according to the tables listing the subgroups of crystallographic space groups [66N, 70N, 77N1, 88S2] which are not all easily accessible. There have been defined two kinds of symmetry reducing steps (of order 2 in these examples):

t2: reduction of rotational symmetry, i.e. of point group symmetry operations (abbreviation t $\hat{=}$ translationengleich = equal in translational symmetry)

k2: reduction of translational symmetry, i.e. doubling of the unit cell for order 2 (abbreviation k $\hat{=}$ klassengleich = equal in the class of point group operations)

Changes of the coordinate system and of the lattice parameters are also indicated in Figs. 2.29 and 2.30, e.g. the change from the (x_0, y_0, z_0) system to the (x, y, z) system by $\boldsymbol{a} + \boldsymbol{b}, -\boldsymbol{a} + \boldsymbol{b}, \boldsymbol{c}$ and a doubling of the lattice parameter c by $\boldsymbol{a}, \boldsymbol{b}, 2\,\boldsymbol{c}$. Further, there are shown the numbers Z of formula units in the primitive unit cell (Wigner-Seitz cell) of the corresponding structures and the symmetry (point group) at the site of the transition metal ion. For some structures, e.g. centered ones, the primitive unit cell is smaller than the crystallographic unit cell as defined in the International Tables [69I]. For reasons of a compact presentation with more clarity, it is not advisable to compile all examples for a particular structure at a certain temperature in Figs. 2.29 and 2.30. Family-trees with this additional information are found in the references, e.g. for the monoammonium family in [77G3] and [78H2]. In this paper, the family-trees consist merely of the principal group theoretical data and will be used as a tool together with Tables 2 and 4 for discussing the sequence of structural phase transitions of some perovskite-type layer compounds.

Let us recall the data in Table 2 for this purpose. They demonstrate that the "parent"-structure I4/mmm of the monoammonium family has actually been found experimentally for a number of compounds, namely for $(CH_3NH_3)_2MCl_4$ with M = Mn, Fe, Cd, for $(C_2H_5NH_3)_2MnCl_4$ and for $(C_3H_7NH_3)_2MnCl_4$. On decreasing the temperature, these compounds undergo the transition to the ORT-phase (cf. Tables 2 and 4) with the two domains Abma and Bmab. The family-tree in Fig. 2.29 confirms that this transition is expected to be continuous in agreement with the experimental results. The family-tree shows further that Abma or Bmab are not maximal subgroups of I4/mmm and that the space group Fmmm is the link between them. But Fmmm is only the link in the group theoretical considerations. It is not a real structure of the above listed compounds, as we see from the sequences of phase transitions in Table 4 where we also find that the compounds $(CH_3NH_3)_2MCl_4$ (M = Mn, Fe, Cd) undergo a discontinuous transition to the TLT-phase ($P4_2/ncm$) on further lowering the temperature. Fig. 2.29 shows that this transition means a jump from one branch of the tree to another one. Although Abma or Bmab and $P4_2/ncm$ have a maximal subgroup (Pccn) in common, there is no direct group-subgroup relation between them and, consequently, the phase transition has to be discontinuous. The same arguments apply to the transition from the TLT-phase to the MLT-phase ($A2_1/b11$ or $B12_1/a1$) which is also discontinuous. The space groups of the MLT-phase are subgroups of those of the ORT-phase but such a relation does not exist to the TLT-phase. If a phase transition is along one of the branches of the family-tree, it may be but has not to be continuous. For example, the transition of $(C_2H_5NH_3)_2MCl_4$ (M = Mn, Fe) from the ORT-phase (Abma or Bmab) to the OLT-phase (Pbca or Pcab) is along such a branch and is continuous for the Fe-compound but discontinuous for the Mn-compound.

A comparison of the family-tree for the diammonium compounds (Fig. 2.30) with the structures listed in Tables 2 and 4 reveals that the high symmetry structures P4/mmm, Pmmm, and Cmmm are only hypothetical for these compounds and are not observed experimentally. Probably due to the stronger bonding of the hydrocarbon chains at both ends, the transition from complete order of the chains to dynamical disorder would occur in diammonium compounds at higher temperatures than in monoammonium compounds. And this temperature would be so high that the decomposition temperature is reached before such a transition to one of the high symmetry structures can take place. Moreover, the search for structural phase transitions was in vain in the Mn- and Cd-compounds of the type $[NH_3(CH_2)_2NH_3]MCl_4$ [75K1, 76A1, 76L1, 77B1, 77T1, 92B1]. For the whole temperature range of investigations, these compounds stay in the ordered low-temperature structures $P12_1/a1$ or $P2_1/b11$. Compounds $[NH_3(CH_2)_nNH_3]MCl_4$ with $n > 2$, on the other hand, undergo structural phase transitions, and the character of these transitions (cf. Table 4) agrees with the predictions of the family-tree in Fig. 2.30. For $[NH_3(CH_2)_nNH_3]MCl_4$ with an even or odd number n of carbon atoms, the structures are on different branches of the tree (Fig. 2.30). The reason is that the chains with odd n have a central C-atom and those with even n not. That causes different symmetries of the chains and for odd n, the chains may even have an electric dipole moment [81K3]. The example of the compounds with even and odd n demonstrates that the family-tree can be used not only for discussing and understanding the group-subgroup relations between the structural phases of one compound but also those between the structures of a family of related compounds. The family-trees in Figs. 2.29 and 2.30 and the relations discussed above are by no means comprehensive and complete for all perovskite-type layer compounds in this contribution. For the exceptional sequence of phase transitions of $(C_3H_7NH_3)_2PbCl_4$, a special family-tree was derived [89Z1, 91C1]. The structural phase transitions of long-chain compounds like $(C_{10}H_{21}NH_3)_2CdCl_4$ require also a family-tree different from those in Figs. 2.29 and 2.30 [79K1]. For details, the reader is referred to the references in these cases.

The above considerations about the family-tree and the group-subgroup relations are mostly connected with Landau's criterion 1). We shall turn now to criterion 2), i.e. to the symmetry of the order parameter and of a soft mode, condensating at the transition. For this purpose, we will use the results for the symmetry of the lattice modes obtained with group theoretical methods and the compatibility relations between them. One group theoretical method employed in this context [77G3] is that outlined by Maradudin and Vosko [68M1]. They consider the reducible multiplier representation of the atomic displacements at a certain wavevector in the Brillouin zone which can be block-diagonalized to irreducible (multiplier) representations. By means of a projection technique, symmetry coordinates can be derived for the modes under consideration. If applied to various crystal structures of the same compound, this method yields compatibility relations between the modes in various structures even if there is no group-subgroup relation between the structures since this procedure can be based on the comparison of the symmetry coordinates. If only the compatibility relations are of interest with respect to modes of a particular symmetry for group-theoretically related structures, a simpler method can be used which was described by Lavrencic and Shigenari [73L1]. The results of such group theoretical treatments will be presented here only for the monoammonium family (Fig. 2.29). In these considerations, we will concentrate on some special points of high symmetry in the Brillouin zone of the "parent" structure I4/mmm (see Fig. 2.31). With respect to the (x_0, y_0, z_0) coordinate system, these points are

$$\Gamma : \boldsymbol{q} = (0,0,0), \qquad \mathrm{X} : \boldsymbol{q} = (\tfrac{\pi}{a}, \tfrac{\pi}{a}, 0), \qquad \widetilde{\mathrm{X}} : \boldsymbol{q} = (-\tfrac{\pi}{a}, \tfrac{\pi}{a}, 0) \qquad \mathrm{Z} : \boldsymbol{q} = (0, 0, \tfrac{2\pi}{c})$$

and with respect to the (x, y, z) coordinate system

$$\Gamma : \boldsymbol{q} = (0,0,0), \qquad \mathrm{X} : \boldsymbol{q} = (\tfrac{2\pi}{a}, 0, 0), \qquad \widetilde{\mathrm{X}} : \boldsymbol{q} = (0, \tfrac{2\pi}{a}, 0) \qquad \mathrm{Z} : \boldsymbol{q} = (0, 0, \tfrac{2\pi}{c})$$

The notation Γ, X, Z, etc. is chosen in accordance with the Tables of Zak et al. [69Z]. The points X and $\tilde{\mathrm{X}}$ are symmetry-related and equivalent in tetragonal symmetry (I4/mmm, $\mathrm{P4_2/ncm}$) but not in orthorhombic and lower symmetry (Abma or Bmab, Pcab or Pbca etc.). Fig. 2.31 displays also the two reciprocal space coordinate systems (q_{x0}, q_{y0}, q_{z0}) and (q_x, q_y, q_z) which are used for the description of the structural phases (cf. Figs. 2.5 in Sect. 2.1.2 and 2.11 in Sect. 2.1.4). It is obvious from the number Z of formula units in the primitive unit cell of the various structures in Fig. 2.29 that, in some of the phase transitions, the unit cell is doubled and the Brillouin zone reduced correspondingly. And the above listed points have been chosen because they become reciprocal lattice points or centers Γ of the reduced Brillouin zone. In the transitions from I4/mmm to Abma or Bmab and from Abma to $\mathrm{P4_2/ncm}$ [77G3], these points with the coordinates listed above have to be relabelled according to their position in the new reduced Brillouin zones as follows:

I4/mmm	→	Abma/Bmab	→	$\mathrm{P4_2/ncm}$
Γ	→	Γ / Γ	→	Γ
X	→	Γ / Z	→	Γ
$\tilde{\mathrm{X}}$	→	Z / Γ	→	Γ
Z	→	Z / Z	→	Γ

This is illustrated in Fig. 2.32 where a section through the (q_x, q_z)-plane is shown with the reduction of the Brillouin zones in the phase transitions and with their new boundaries in this plane. After this introduction, we can now proceed to the compatibility relations for selected irreducible representations. These relations show us what the symmetry of a lattice mode will be before and after the phase transition. For the monoammonium family (cf. Fig. 2.29), such an excerpt of the compatibility relations is presented in Fig. 2.33 for the space groups listed in the family-tree. We concentrate there on those irreducible representations which become in one of the transitions the fully symmetric or unity representation (Γ_1^+ or $\mathrm{A_{1g}}$), indicated by heavy lines in Fig. 2.33, and which therefore reflect the symmetry of the order parameter. We find further that there is in all cases an irreducible representation becoming Γ_1^+ in one of its maximal subgroups. All irreducible representations are denoted according to the Tables of Koster et al. [63K1], e.g. Γ_n^+, Γ_n^- for the Γ-point, X_n^+, X_n^- for the X-point, except for the M-point of $\mathrm{P4_2/mmc}$ where the irreducible representations are multiplier representations and not ordinary representations as in all other cases. These multiplier representations are listed in a special character table in [69Z], not for the space group $\mathrm{P4_2/mmc}$, but in the tables for P4/mbm because we use $\mathrm{P4_2/mmc}$ with shifted origin in a nonstandard setting.

The compatibility relations in Fig. 2.33 demonstrate with respect to the phase transitions that

a) in the continuous phase transition I4/mmm → Fmmm → Abma/Bmab the symmetry of the order parameter and, consequently, that of a possible soft mode is X_2^+ for the transition to Abma [75P1, 77G3, 77K1, 83M1, 83M2] and $\tilde{\mathrm{X}}_4^+$ for the transition to the other domain Bmab [77K1, 83M1, 83M2]. That means that this transition is governed by a two-component order parameter. A soft mode would be one with a q-vector at X, at the Brillouin zone boundary, and would be observable only by inelastic neutron scattering. If, on the other hand, the transition would lead to the intermediate space group Fmmm (cf. Fig. 2.29) we would have an order parameter of symmetry Γ_4^+ in I4/mmm. After changing the coordinate system from (x_0, y_0, z_0) to (x, y, z), the order parameter symmetry is Γ_3^+

b) in a hypothetical continuous phase transition I4/mmm → $\mathrm{P4_2/mmc}$ → $\mathrm{P4_2/ncm}$ the symmetry of the order parameter would again be X_2^+ and $\tilde{\mathrm{X}}_4^+$, the same two-component order parameter as in the actually existing transition. Thus, such a following the branches of the family-tree is helpful for model considerations even though the actual transition is a discontinuous one from Abma/Bmab to $\mathrm{P4_2/ncm}$.

In this case, linear combinations of X_2^+ and $\widetilde{X}_4^+$ (I4/mmm) have to be formed for obtaining irreducible representations of $P4_2/mmc$ with symmetry M_3^+ and M_4^+ and of $P4_2/ncm$ with symmetry Γ_1^+ and Γ_3^+. It was already mentioned in context with the discussion of the structural phases of $(CH_3NH_3)_2MnCl_4$ in Sect. 2.1.4 (cf. Fig. 2.11) that there are not two crystallographic domains in case of $P4_2/ncm$ but two antiphase domains [77K1, 83M2]. There is no difference in Fig. 2.33 for the (+)- and the (–)-domain of $P4_2/ncm$ and, thus, no extra listing for these two domains. Only the linear combinations of X_2^+ and $\widetilde{X}_4^+$ to obtain the symmetry Γ_1^+ or Γ_3^+ are different for the two antiphase domains.

c) in a hypothetical phase transition Abma → $A2_1/b11$ the symmetry of the order parameter would be Γ_4^+ of Abma and Γ_2^+ of Bmab in the corresponding transition of the other domain (Bmab → $B12_1/a1$). Both, Γ_2^+ and Γ_4^+ originate from the doubly degenerate irreducible representation Γ_5^+ of I4/mmm. Lattice modes of this symmetry are Raman active.

d) in the phase transition Abma → Pbca the symmetry of the order parameter is Z_4^+ of Abma and Z_2^+ of Bmab in the transition of the other domain (Bmab → Pcab). Z_2^+ originates from X_3^+ and Z_5^+ of I4/mmm while Z_4^+ originates from $\widetilde{X}_3^+$ and Z_5^+.

9.12.2.2.3 Structural Phase Transitions in Monoammonium Compounds

After these group theoretical considerations, let us turn now to the mechanism of the structural phase transitions. It was already mentioned that the NH_3-groups of the hydrocarbon chains are attached to the MCl_6 octahedral layers by hydrogen bonds and that this will be the key to an understanding of the phase transitions. For the low temperature structures with not so much disorder as the high temperature structure I4/mmm, the structure determinations have revealed especially for the $(CH_3NH_3)_2MCl_4$ with M = Mn, Cd [75C1, 76C2, 76H1, 76H2] that the distance between the three H-atoms of the NH_3-group and the nearest neighbouring Cl^--ion is with about 0.24 nm in the range typical for hydrogen bonds. For the structural phases of these compounds, different H-bonding schemes have been found in the analysis of the structural data [76A2, 76B1, 83M2]. In particular, there are two basic H-bonding schemes, namely the orthorhombic configuration as observed in the ORT-phase (Abma or Bmab, cf. Table 4) and the monoclinic configuration in the MLT-phase ($A2_1/b11$ or $B12_1/a1$). These configurations are shown in Fig. 2.34 for the structures Bmab (Fig. 2.34a) and $B12_1/a1$ (Fig. 2.34b). Since the two other domains Abma and $A2_1/b11$ result from an exchange of the *x*- and *y*-axes, the corresponding H-bonding schemes are obtained by rotating the schemes in Fig. 2.34 by 90° about an axis perpendicular to the plane of the drawing (*c*-axis in the orthorhombic case). Characteristic for the orthorhombic configuration are one H-bond to a terminal or axial Cl^--ion and two H-bonds to bridging or equatorial Cl^--ions (cf. Fig. 2.34) while the monocline configuration consists of two H-bonds to axial Cl^--ions and one H-bond to a bridging Cl^--ion. In this context, we recall that there are two types of Cl^--ions in the perovskite-type layers, the bridging or in-plane Cl^--ions between two M^{2+}-neighbours (also called equatorial) and the terminal or out-of-plane Cl^--ions with one M^{2+}-neighbour (also called axial). In the TLT-phase ($P4_2/ncm$) intermediate between the ORT- and the MLT-phase (cf. Table 4), the H-bonding is usually considered to be a superposition of the configurations from the two orthorhombic domains Abma and Bmab [76C2, 84R1], but also a H-bonding scheme similar to the monoclinic configuration has been reported for the TLT-phase of $(CH_3NH_3)_2MnCl_4$ [76H1, 78H2]. Because the $(CH_3NH_3)^+$-ions are distributed over four positions with equal probability of 25% in the high temperature structure I4/mmm for matching the threefold molecular symmetry with the fourfold crystal symmetry, the resulting H-bonding is a superposition of four orthorhombic configurations with all possible orientations. For $(C_2H_5NH_3)_2CdCl_4$ and $(C_3H_7NH_3)_2CdCl_4$ and other monoammonium compounds, similar H-bonding schemes have been found in the structure determinations [77C2, 78C1]. Especially for the OLT-phases (Pbca and Pcab, cf. Table 4), the H-bonding scheme is that of the monoclinic configuration (cf. Fig. 2.34).

The structure determinations by x-ray or neutron diffraction can take into account disorder of the hydrocarbon chains by using split positions with a certain occupation probability in the structure refinement. But dynamic disorder will only increase the thermal ellipsoids. Thus, dynamic effects are more appropriately investigated by magnetic resonance methods, for example ^{35}Cl-NQR [76K1] probing the environment of the Cl^--ions and ^{1}H-NMR or ^{2}D-NMR [76B1, 77B1] and ^{1}H–^{14}N nuclear magnetic double resonance [76S2] probing the behaviour of the NH_3-group. The results of such studies have demonstrated that in $(CH_3NH_3)_2MCl_4$ and similar compounds the $(CH_3NH_3)^+$-ions are not statically distributed among the four positions but that the disorder is highly dynamic with jump rates higher than 10^5 s^{-1} from one position to another one [76K1]. The dynamics is still perceptable in the ORT-phase, only partially frozen in the TLT-phase and finally completely frozen in the MLT-phase [76S2]. Similar conclusions have been drawn from the temperature evolution of Raman spectra [77C4]. A further method to study the dynamics of a system is inelastic neutron scattering. The energy and the wavevector transfer in the scattering process are

$$\hbar\omega = E_\mathrm{i} - E_\mathrm{f} \qquad \boldsymbol{K} = \boldsymbol{k}_\mathrm{i} - \boldsymbol{k}_\mathrm{f} \tag{2.24}$$

where E_i, $\hbar\,\boldsymbol{k}_\mathrm{i}$ and E_f, $\hbar\,\boldsymbol{k}_\mathrm{f}$ are the energy and the momentum of the incident and the scattered neutron, respectively. For compounds with hydrocarbon chains, the incoherent scattering length of the protons is by far the largest compared to all the scattering lengths of the other particles. Thus the studies, performed with time-of-flight neutron spectrometers [78L1, 80K1, 83M1], will yield incoherent inelastic neutron scattering results which predominantly reflect the dynamical properties of the protons. In this method, an average is formed over a range of scattering angles by means of a sufficiently large number of detectors, i.e. averaging over all directions of $\boldsymbol{K}$ as this is the case for powder samples. The result of such a measurement is a frequency distribution $G(\omega)$ similar to the phonon density of states. In fact, the result would be proportional to this density of states in a system with an incoherent scatterer and with one particle per unit cell. Therefore, $G(\omega)$ as defined in Eqs. 4, 13 and 14 of [80K1] is called the generalized phonon density of states, reflecting the dynamics of the H-atoms. In Fig. 2.35, $G(\omega)$ is presented for various temperatures where ω is given in spectroscopic units cm^{-1} in order to allow an easy comparison with infrared and Raman spectra. In addition to broad features representing in fact a kind of density of states, there is a rather narrow and strong peak near 330 cm^{-1} in the spectra for 4 K and 77 K (MLT-phase). With increasing temperature, i.e. for 195 K (TLT-phase) and for 300 K (ORT-phase), this peak decreases and finally disappears and a new broad peak builds up near 95 cm^{-1} which is strongest for 405 K (THT-phase). A lattice dynamical model calculation has been performed in order to explain and understand these spectra [80K1] where for $G(\omega)$ only the vibrational motions of the H-atoms have been taken into account. Even though a damping of the modes was included, this attempt was not very successful. At low temperatures, the model reproduces a strong peak which is shifted a little to lower frequencies and which also decreases with increasing temperature. However, the model does not reproduce the low-frequency peak at high temperatures. In the model, the $(CH_3NH_3)^+$-ions are treated as rigid bodies with translational and rotational degrees of freedom. And as usual in lattice dynamics, the model assumes that the modes represent small vibrations of the particles about their equilibrium position. Probably this condition is not fulfilled in the dynamics of the CH_3NH_3 molecule at higher temperatures. In order to solve some of these problems, a further incoherent inelastic neutron scattering study, also with a time-of-flight spectrometer, has been performed, combined with a complementary Raman scattering investigation [83M1]. In addition to $(CH_3NH_3)_2MnCl_4$, partly deuterated samples $(CD_3NH_3)_2MnCl_4$ and $(CH_3ND_3)_2MnCl_4$ have been studied this time. The range of averaging over the scattering angles is not so large in this experiment so that an average value for the wavevector transfer $\boldsymbol{K}$ can be defined (cf. Fig. 2 of [83M1]). The corresponding amplitude-weighted frequency distributions are $P_{\|}(K^2, \omega)$ and $P_{\perp}(K^2, \omega)$ (see Eq. 4 of [83M1]) where the sample is oriented at 45° or 135° to the incident beam, resp., with the average of $\boldsymbol{K}$ nearly parallel or perpendicular to the octahedral layers. Fig. 2.36 presents these neutron scattering results at $T = 6$ K (MLT-phase). Only in the spectra for $(CH_3NH_3)_2MnCl_4$ and $(CD_3NH_3)_2MnCl_4$, the peak at 325 cm^{-1} is observed. It is stronger for $P_{\|}(K^2, \omega)$ than for $P_{\perp}(K^2, \omega)$. In the spectra for $(CH_3ND_3)_2MnCl_4$, a less strong peak is found at 254 cm^{-1} which is also stronger for $P_{||}(K^2, \omega)$. Thus the peak at 325 cm^{-1} can be assigned to librational or rotational motions of the NH_3-group. The other broader features of the spectra in Fig. 2.36 are mainly due to rotational motion of the CH_3-group since they are much weaker in the spectra for $(CD_3NH_3)_2MnCl_4$. Together with the temperature dependent data in Fig. 2.35, these results indicate that the NH_3-group is fixed by H-bonds to the lattice in the MLT-phase and that the binding becomes much weaker at higher temperatures where the dynamical disorder increases as discussed above.

The results about the dynamics of the system indicate that the structural phase transitions are of the order-disorder type which would explain also why the search was in vain for a soft lattice mode as it is typical for a displacive phase transition [74B3]. The results further indicate that the phase transitions are mainly triggered by changes in the dynamics and by the ordering of the hydrocarbon chains. But also the layers with the MCl_6 octahedra take part in the phase transitions as has been concluded from Raman spectra [83M1, 83M2]. This is more directly observed by a diffuse x-ray scattering investigation on $(CH_3NH_3)_2CdCl_4$ [84M3], namely a disorder also of the octahedra in the ORT- and TLT-phases, since mainly the $CdCl_6$-octahedra are involved in the x-ray scattering process because the scattering factors are much larger for Cd and Cl than for C, N and H. A simple model for disorder in the octahedral layers accounts for the observed scattering pattern. A further aspect in this context is that that only the octahedra are involved in the structural phase transitions observed for compounds without hydrocarbon chains like the fluorides $(NH_4)_2MgF_4$ [96S2], K_2CdF_4 [88A8], the chlorides Rb_2CdCl_4 [85A2, 89K], $Rb_3Cd_2Cl_7$ [88A1, 89F1], $Rb_4Cd_3Cl_{10}$ [90A5, 90B2] and the oxides $La_{2-x}Ba_xCuO_4$ [89A1], $La_{2-x}Sr_xCuO_4$ [89T5], La_2NiO_4 [91R, 93H], Pr_2NiO_4 [91F2, 91M1], La_2CoO_4 [89Y2]. The sequence of phase transitions for these compounds is as for $(CH_3NH_3)_2MCl_4$ [M = Cd, Fe, Mn] (cf. Table 4)

$$I4/mmm \leftrightarrow Bmab\ (Abma) \leftrightarrow P4_2/ncm \leftrightarrow B12_1/a1\ (A2_1/b11)$$

or at least part of it, i.e. not all structures of this sequence are found for all of them experimentally. For doped oxides like $La_{2-x}Ba_xCuO_4$, the sequence of phase transitions depends strongly on the concentration x. The TLT-phase $P4_2/ncm$ is found only for the concentration range $0.05 \le x \le 0.2$ [89A1, 90A6], and the MLT-phase is completely missing. On the other hand, a transition to an orthorhombic low-temperature phase (OLT) with structure Pccn is reported for some oxides [91C3, 93H]. This OLT-phase will be discussed in the next section in the course of model considerations for the phase transitions of $(CH_3NH_3)_2MCl_4$ (M = Cd, Fe, Mn) but has never been observed for these compounds. Among the chlorides, the triple-layer compound $Rb_4Cd_3Cl_{10}$ undergoes the same phase transitions as $(CH_3NH_3)_2MCl_4$, but for the double-layer compound $Rb_3Cd_2Cl_7$, the sequence of phase transitions is different (cf. Table 4).

Because of its importance for the structural phase transitions, it is advisable to consider the tilting and canting of the octahedra in the various phases in more detail. In the high temperature tetragonal phase I4/mmm, the octahedra are perfectly ordered as shown at the top of Fig. 2.37 where layer A refers to the plane $z = 0$ and layer B to the plane $z = 0.5$. On reducing the symmetry to orthorhombic, there will be a washboard-like puckering of the layers due to rotations of the octahedra about the y-axis in the domain Abma and about the x-axis in the domain Bmab (cf. Fig. 2.37, second row). And in the TLT-phase ($P4_2$/ncm), we have diagonal rotations of the octahedra, i.e. rotations about the x_0-axis in layer A and the y_0-axis in layer B for the (+)-domain and with the axes exchanged for the (–)-domain. Finally, the MLT-phase results from rotations of the octahedra about the x_0- and y_0-axis and from an additional rotation about the z-axis (= z_0-axis). As already mentioned, this puckering of the layers and tilting of the octahedra is the only mechanism for the phase transitions in Rb_2CdCl_4, $Rb_3Cd_2Cl_7$ and $Rb_4Cd_3Cl_{10}$ (cf. Table 4) while it is combined with the ordering of the hydrocarbon chains in compounds like $(CH_3NH_3)_2MCl_4$. The interplay of ordering of the NH_4^+-ions and of the octahedra tilting leads in $(NH_4)_2MgF_4$ to the transition I4/mmm ↔ $P12_1/c1$ (cf. Table 4 and [96S2]). That means, in the picture of the family tree Fig. 2.29, the systems jumps from the highest branch to the lowest one in a naturally discontinuous transition. This seems to be a special property of the NH_4^+-ion since the perovskites NH_4MnF_3 and NH_4CdF_3 undergo also a transition in one jump from cubic to orthorhombic symmetry [90B4, 95R2] while the perovskites with alkali-ions $KMnF_3$ and $KCdF_3$ perform the reduction of symmetry step-by-step in several phase transitions [77H4, 84D1, 86H3]. The analogy between perovskites and perovskite-type layer structures has also been used to derive a classification for octrahedral tilt phases for the layered structures [87A1, 87A2, 87H2, 89H1] based on an earlier classification of octahedra tilts in the perovskites [72G1, 75G2]. Also group theoretical considerations are necessary for such a classification which describes the canting and tilting of the octahedra as small rotations about the axes of the octahedra in the way discussed in context with Fig. 2.37, i.e. neighbouring octahedra are rotated in the opposite sense so that the layer of corner-sharing octahedra becomes puckered. Here, we will not enter into the formal description and with respect to these details, the reader is referred to the references, namely for the different structural phases of $(C_nH_{2n+1}NH_3)_2MCl_4$ with M = Mn (n = 1, 2, 3), M = Fe (n = 1), and M = Cd (n = 1, 2, 3) to [87A1, 87A2, 89H1] and for those of Rb_2CdCl_4, $Rb_3Cd_2Cl_7$ and $Rb_4Cd_3Cl_{10}$ to [89H1, 94A, 95A1].

9.12.2.2.4 Model for the Phase Transitions in Monoammonium Compounds

Models for the structural phase transitions of perovskite-type layer structures start usually with the high temperature "parent" phase I4/mmm and with the distribution of the hydrocarbon chains over four positions symmetrical to the fourfold *c*-axis. In the THT- and ORT-structures, the molecular C–N axis of the $(CH_3NH_3)^+$-group is inclined by about 20° with respect to the *c*-axis [75C1, 75H1]. And the dynamic disorder in this phase has been explained by a flipping motion of the $(CH_3NH_3)^+$-group about the *c*-axis from one position to another one [77B1]. This situation is sketched schematically in Fig. 2.38 where the four possible orientations of the C–N axis are shown and where these molecular orientations are numbered by 1, 2, 3, 4. Each of them represents not only the whole $(CH_3NH_3)^+$-group but also the H-bonding scheme belonging to it, i.e. the four possible orientations of the orthorhombic configuration. Let us now denote the occupation probability for these orientations by n_1, n_2, n_3 and n_4. The high temperature structure can then be characterized by [76S2, 77K1, 78B2]

$$\text{I4/mmm} \qquad n_1 = n_2 = n_3 = n_4 = \tfrac{1}{4} \tag{2.25}$$

In the ORT-phase, these probabilities are no longer equal but especially one will be larger than the other three

$$\begin{array}{llll} \text{Abma:} & n_1 > n_2 = n_4 > n_3 & \text{or} & n_3 > n_2 = n_4 > n_1 \\ \text{Bmab:} & n_2 > n_1 = n_3 > n_4 & \text{or} & n_4 > n_1 = n_3 > n_2 \end{array} \tag{2.26}$$

The preferred orientation of the $(CH_3NH_3)^+$-groups in the TLT-phase can be described as

$$\text{P4}_2\text{/ncm:} \quad n_1 = n_2 > n_3 = n_4 \quad \text{or} \quad n_3 = n_4 > n_1 = n_2 \tag{2.27}$$

A description of the MLT-phase with its monoclinic H-bonding configuration and with a monoclinic distortion of the lattice needs an extension of the model and an inclusion of a coupling to the lattice. This is discussed in detail in the literature [78B29] and will not be described here. Values for the occupation probabilities n_m (m = 1, 2, 3, 4) have been obtained by a quasi-elastic incoherent neutron scattering study [84R1]. The sample was $(CD_3NH_3)_2MnCl_4$ and the experimental conditions similar to the inelastic scattering investigation of partly deuterated samples [83M1] discussed above. The experimentally determined elastic incoherent scattering factor EISF was compared to a calculated EISF which takes the reorientational motion (jumps) of the $(CD_3NH_3)^+$-groups into account, namely

type I:	± 90° rotations about the *c*-axis
types II and III:	1 H-bond to a bridging Cl^--ion fixed, the other 2 H-atoms, 1 to a bridging and 1 to a terminal one, exchanged
type IV:	± 120° rotations about the molecular C–N axis

where type I represents a much faster motion than the other types. But all types are needed for a good fit to the experimental data. The occupation probabilities of the best fit (cf. Eqs. 2.26 and 2.27) are [84R1]:

$$\begin{array}{llll} T = 294\ \text{K (ORT-phase):} & n_1 = 0.39\ (1) & n_2 = n_4 = 0.22\ (1) & n_3 = 0.17\ (1) \\ T = 245\ \text{K (TLT-phase):} & n_1 = n_2 = 0.43\ (1) & n_3 = n_4 = 0.07\ (1) & \end{array} \tag{2.28}$$

For the TLT-phase, the fit was better with the orthorhombic H-bonding configuration than with the monoclinic configuration, and it was concluded from these results that the H-bonding in the TLT-phase is in fact a superposition of two orthorhombic configurations.

A model for the structural phase transitions of the perovskite-type layer compounds [75P1, 77K1, 78B2, 79B5] uses generally a Landau-type free energy [74B3, 75L4], i.e. a molecular field approach, with the n_m defined above as the essential parameters. In this way, the internal energy U of the system can be written as [78B2]

$$\begin{aligned} U = \tfrac{A}{2}(n_1^2 + n_2^2 + n_3^2 + n_4^2) + B\,(n_1 n_2 + n_2 n_3 + n_3 n_4 + n_4 n_1) + C\,(n_1 n_3 + n_2 n_4) \\ + \text{higher order terms} \end{aligned} \tag{2.29}$$

This internal energy is appropriate only for the sequence of phase transitions THT ↔ ORT ↔ TLT, and an extended expression with more terms is needed for including the MLT-phase (see [78B2]). The free energy of the system is defined as usual in thermodynamics

$$F = U - T\,S \tag{2.30}$$

where $S \sim [n_1 \ln n_1 + n_2 \ln n_2 + n_3 \ln n_3 + n_4 \ln n_4]$ in this order-disorder model. In these considerations including elastic contributions to the energy, it is more appropriate to express U, F etc. in J/m^3 rather than in J/mol. Instead of continuing the discussion with the occupation probabilities n_1, n_2, n_3, n_4, we will introduce the order parameters η_1, η_2, and η_3 which govern the phase transitions and which are the parameters in the Landau theory [74B3, 75L4]. These order parameters are defined as [77K1, 78B2]

$$\eta_1 = 2\,n_1 - 2\,n_3 \qquad \eta_2 = 2\,n_2 - 2\,n_4 \qquad \eta_3 = 2\,n_1 + 2\,n_3 - 1 = 1 - 2\,n_2 - 2\,n_4 \tag{2.31}$$

A comparison with Eqs. 2.25–2.27 shows that these parameters are in fact very useful for describing the ordering of the hydrocarbon chains in compounds like $(CH_3NH_3)_2MCl_4$. For the THT-, ORT- and TLT-phases the results are

$$\begin{array}{lll} \text{I4/mmm:} & \eta_1 = \eta_2 = \eta_3 = 0 & \\ \text{Abma:} & \eta_1 \neq 0,\ \eta_3 \neq 0 & \text{Bmab: } \eta_2 \neq 0,\ \eta_3 \neq 0 \\ \text{P4}_2\text{/ncm:} & \eta_1 = \eta_2 \neq 0,\ \eta_3 = 0 & \\ \text{Pccn:} & \eta_1 \neq 0,\ \eta_2 \neq 0\ (\eta_1 \neq \eta_2),\ \eta_3 \neq 0 & \end{array} \tag{2.32}$$

That means η_1 is the order parameter for the transition to the ORT-domain Abma with the symmetry X_2^+ in I4/mmm and η_2 the order parameter for that to the ORT-domain Bmab with the symmetry $\tilde{X}_4^+$ in I4/mmm (cf. Fig. 2.33). Both have the symmetry Γ_1^+ in Abma or Bmab, respectively. The third order parameter η_3 has the symmetry Γ_4^+ in I4/mmm [80G2] and Γ_1^+ in both ORT-domains. In Eq. 2.32, the hypothetical orthorhombic low temperature phase (OLT) Pccn (cf. Figs. 2.29 and 2.33) has been included. Although a transition to this structure has not been observed in the compounds under consideration, this OLT-phase is discussed in many model considerations [79K5, 80G2, 83M2, 91C2]. With the three order parameters, the internal energy U can be written as [80G2]

$$U = a\ (\eta_1^2 + \eta_2^2) + \tfrac{1}{2} b\ (\eta_1^4 + \eta_2^4) + c\ \eta_1^2 \eta_2^2 + d\ \eta_3^2 + \tfrac{1}{2} f\ \eta_3^4 - g\ \eta_3 (\eta_1^2 - \eta_2^2) + \ldots \tag{2.33}$$

The entropy can also be converted to the order parameters by inserting

$$n_1 = \tfrac{1}{4}\,(1 + \eta_1 + \eta_3) \qquad n_2 = \tfrac{1}{4}\,(1 + \eta_2 - \eta_3) \qquad n_3 = \tfrac{1}{4}\,(1 - \eta_1 + \eta_3) \qquad n_4 = \tfrac{1}{4}\,(1 - \eta_2 - \eta_3)$$

which is straightforward but the result will not be reproduced here.

In the usual way, the model calculation proceeds by looking for a minimum of the free energy F

$$\frac{\partial F}{\partial \eta_m} = 0 \qquad \frac{\partial^2 F}{\partial \eta_m\, \partial \eta_n} = \left\{ \begin{array}{l} \text{matrix with only} \\ \text{positive eigenvalues} \end{array} \right. \qquad \mathrm{m, n} = 1, 2, 3 \tag{2.34}$$

This is the basic concept of the model, by means of which Blinc et al. [78B2] were able to describe the sequence of phase transitions THT ↔ ORT ↔ TLT in compounds of the type $(CH_3NH_3)_2MCl_4$ (M = Mn, Fe, Cd). In this form, the model cannot describe the transition to the monoclinic MLT-phase but yields a second transition to the orthorhombic phase with domains Abma and Bmab. For obtaining the transition to the MLT-phase within the model, Blinc et al. [78B2] have introduced the above mentioned extension of their model. Then, the correct sequence of phase transitions is obtained when the order parameters η_3 exceeds a critical value. This model has further been extended to order parameter fluctuation relaxational modes by Kind et al. [79K5]. They separated the order parameters into a mean value $\langle p_m \rangle$ and a fluctuation part δp_m (m = 1, 2, ..., 5) where the p_m are the three order parameters η_1, η_2, η_3 and two further order parameters describing the tilting of the octahedra needed for the description of the MLT-phase. The mean values $\langle p_m \rangle$ are solutions of Eq. 2.34, and the fluctuations δp_m give rise to order parameter fluctuation relaxational modes

$$\frac{\delta p_m}{\tau} = \Gamma_m \sum_{n=1}^{5} \frac{\partial^2 F}{\partial p_m \partial p_n}\, \delta p_n \qquad (m = 1, 2, ..., 5) \tag{2.35}$$

where the Γ_m represent the kinetic coefficients. The above system of coupled equations has five eigenvalues $1/\tau$ which, together with the corresponding eigenvectors, determine the order parameter fluctuation modes. The results of Kind et al. [79K5] for $(CH_3NH_3)_2CdCl_4$ have been compared with low-frequency Raman spectra. As already mentioned in context with the discussion of Fig. 2.27, the broad Rayleigh wings in the Raman spectra can only partly be explained with reorientational motions of the hydrocarbon chains and it is necessary to consider also the tilting motions of the octahedra. It was further concluded from the Raman spectra [83M1, 83M2] that the low-lying relaxational modes are less numerous than expected from the model.

With the discovery of the softening of the elastic C_{66}-mode in $(CH_3NH_3)_2MCl_4$ with M = Mn, Cd [79G3, 80G2], the model considerations were extended to include the elastic properties. Comprehensive reviews on the study of structural phase transitions by ultrasonic measurements are found in [73R1] and [81L]. For reasons of simplicity, we consider for $(CH_3NH_3)_2MCl_4$ [M = Mn, Cd] only the elastic strain e_6 corresponding to C_{66} [$6 \,\hat{=}\, x_0\, y_0$ in the (x_0, y_0, z_0) coordinate system]. This is the only one involved in the phase transitions and coupling to the order parameters η_1, η_2, η_3. The corresponding additional term ΔF of the free energy is [80G2]

$$\Delta F = \tfrac{1}{2}\, C_{66}^0\, e_6^2 - \mathrm{h}\, e_6\, \eta_3 - \mathrm{k}\, e_6\, (\eta_1^2 - \eta_2^2) \tag{2.36}$$

where C_{66}^0 is the background elastic stiffness constant of the compound, i.e. without interaction with the system of $(CH_3NH_3)^+$ reorientational motions. With $F + \Delta F$, Eq. 2.34 has been used to establish the stability conditions for the system and to calculate the renormalized elastic constant C_{66} along the lines given by Slonczewski and Thomas [70S3]. For a successful application of this model to the phase transitions of the compounds under consideration and to obtain a good fit the experimental data, especially to the softening of C_{66} in the TLT-phase (cf. Fig. 2.28), it is assumed a temperature dependence

$a = a_0\,(T - T_1)$ near the THT ↔ ORT transition and $d = d_0\,(T_3 - T)$ near the ORT ↔ TLT transition. In order to keep the model stable, especially in the THT-phase, these temperature dependencies are assumed to be valid only in a sufficiently small temperature range near the corresponding phase transition and to have a different temperature dependence at other temperatures [85G1]. The temperature dependence of d suggests further that the corresponding order parameter η_3 would trigger a transition to the OLT-phase Pccn, but the coupling to the elastic strain prevents this transition and induces the first order transition to the ORT-phase.

For $(CH_3NH_3)_2FeCl_4$ with essentially the same softening of the C_{66}-mode [82G1, 84Y2], this mode has further been studied under hydrostatic pressure up to $6 \cdot 10^8$ Pa [82G1] searching for an experimental evidence for an intermediate OLT-phase, but without success. In $(CH_3NH_3)_2MnCl_4$ and $(CH_3NH_3)_2CdCl_4$, on the other hand, a high pressure phase (HP) was found (cf. Table 4). For the Cd-compound, the (T, p)-phase diagram [78H1, 83M3] was determined from Raman scattering results (see Fig. 2.39). For the Mn-compound, the structure of the HP-phase is found to be triclinic ($P\bar{1}$) [89C1, 93C1] and not orthorhombic (Pccn). Detailed considerations show that the mechanism leading to this HP-phase is a different one [83M3], and that the order parameter is different from η_3. Moreover, the results of quasi-elastic incoherent neutron scattering on $(CD_3NH_3)_2MnCl_4$ [84R1] indicate that η_3 is not so important for the ORT ↔ TLT phase transition. Therefore, the assumption of the unusual temperature dependence of d and the use of η_3 as primary order parameter in the ORT ↔ TLT phase transition have been criticised [84I1, 85I, 91C2]. Ishibashi and Suzuki [84I1] have recommended to use a Landau-type free energy with only η_1 and η_2 as order parameters, i.e. without η_3. The model contains only the usual temperature dependence $a = a_0\,(T - T_1)$. Since the softening of C_{66} in the TLT-phase cannot be described in an adequate way with terms up to fourth order (cf. Eq. 2.33), terms up to sixth order have been included. The corresponding internal energy U is obtained by keeping the terms with η_1 and η_2 in Eqs. 2.33 and 2.36, by omitting the terms with η_3 and by adding $\mu\,(\eta_1^2 - \eta_2^2)^2 \cdot (\eta_1^2 + \eta_2^2)$ as possible sixth order term. It is characteristic for this model that it contains no unusual temperature dependence and that it is sufficiently flexible to describe the observed sequence of phase transitions in the methylammonium compounds. In a thorough analysis, Couzi [91C2] has shown that a model with terms up to fourth order in η_1 and η_2 without η_3 can describe properly only the THT ↔ ORT transition and not the ORT ↔ TLT transition. With terms up to sixth order, the model can already account for the behaviour of C_{66}. However, an expansion up to 8th order is required for an adequate description of all experimental data. Couzi's analysis starts with the model of Blinc et al. [78B2] and presents a fair discussion of all the model considerations. His analysis reaches with respect to an intermediate OLT-phase Pccn the conclusion that this is a possible structure within the model. He considers it a major difficulty for the interpretation of the experimental data that the OLT-phase is not observed experimentally in the methylammonium compounds. But very probably, the ORT ↔ TLT transition takes place close to a multicritical ORT–TLT–OLT triple point. And we recall from Sect. 2.2.3 that the OLT-Phase has actually been observed in some perovskite-type layered oxides. For these materials, Ishibashi and Dvorak [94I3] performed model calculations including the OLT-phase Pccn using a Landau-type free energy with terms up to eigth order in η_1 and η_2.

For other compounds $(C_nH_{2n+1}NH_3)_2MCl_4$ with $n > 1$ and M = Mn, Fe, Cd, similar model calculations have been performed, e.g. for $(C_2H_5NH_3)_2FeCl_4$ [85Y2] where, in addition to η_1 and η_2, two further pairs of order parameters have been introduced for modelling the somewhat different sequence of phase transitions (cf. Table 4). For the propylammonium compounds like $(C_3H_7NH_3)_2MnCl_4$, the situation is more complicated for reasons of the incommensurate phases (cf. Table 4) which require an adequate extension of the model. That means the order parameters become space-dependent describing the modulation in the incommensurate phase. Moreover, the Landau free energy is now a functional, i.e. a function to be integrated over the space variables, and its minimum is to be determined by the Euler-Lagrange theory [87J1]. This free energy contains not only the usual terms up to fourth or sixth order in the order parameters but also derivatives of the order parameters with respect to a space variable. In this context, we recall the third criterion of the Landau theory [62L2, 74B3, 75L4, 77G3]:

3) the antisymmetric square $\{(n,\boldsymbol{q})\}^2$ of the irreducible representation $(n,\boldsymbol{q})$ corresponding to the order parameter [cf. criterion 2) above] must not contain the vector representation of G_0 if G_1 is to be a commensurate phase.

If however the transition leads to an incommensurate phase this antisymmetric square may but will not necessarily contain the vector representation, and only if this is the case a socalled Lifshitz invariant will be a new term in the free energy. In $(C_3H_7NH_3)_2MnCl_4$ (cf. Table 4), the first incommensurate is the γ-phase and the transition to the δ-phase is a reentrant one. The β- and the δ-phase have the same structure Abma and reentrant transition means that the modulation amplitude vanishes at the transition and not the incommensurate part of the modulation wavevector [82M1]. The ε-phase is again incommensurate, and finally the transition to the ζ-phase is of the lock-in type where the modulation wavevector changes abruptly and discontinuously from an incommensurate to a rational commensurate value [88M1, 90A1]. Infrared vibrational spectra have given evidence that also in $(C_3H_7NH_3)_2MCl_4$ (M = Mn, Cd) there is a dynamic disorder of the hydrocarbon chains that freezes more and more as the temperature decreases until it is completely frozen finally, e.g. in the ζ-phase of the Mn-compound with ordered chains [81D3]. For an adequate description of the $\alpha \leftrightarrow \beta \leftrightarrow \gamma \leftrightarrow \delta$ phase sequence of the Mn-compound, several models have been derived [82M1, 86I, 86M3]. One of these [86I] uses two order parameters η_1 and η_2. The free energy functional with terms up to sixth order is very similar to the Landau free energy discussed above for the methylammonium compounds. New are the terms with space derivatives

$$\delta\left(\eta_1\frac{\partial\eta_2}{\partial x}-\eta_2\frac{\partial\eta_1}{\partial x}\right)+\frac{\kappa}{2}\left[\left(\frac{\partial\eta_1}{\partial x}\right)^2+\left(\frac{\partial\eta_2}{\partial x}\right)^2\right] \tag{2.37}$$

where the first term is the above mentioned Lifshitz invariant. In view of this term, η_1 and η_2 are put as

$$\eta_1=\eta_0+\tau_0\cos q_0x \qquad \eta_2=-\eta_0+\tau_0\sin q_0x \tag{2.38}$$

Eq. 2.38 describes a sinusoidal modulation in the incommensurate phase and the modulation wavevector should be chosen in such a way that the total free energy becomes a minimum in $\boldsymbol{q}$-space. The modulation is not necessarily sinusoidal and also a new type of soliton solution has been reported for a Landau free energy describing the $\beta \leftrightarrow \gamma \leftrightarrow \delta$ transitions of $(C_3H_7NH_3)_2MnCl_4$ [83M4]. The models have further been extended to four order parameters [88M1, 89I2], and one of them has been used to describe the $\delta \leftrightarrow \varepsilon \leftrightarrow \zeta$ phase sequence of the Mn-compound [88M1]. This model includes a coupling between lattice waves and fluctuations of the rotational disorder of the propylammonium chains. In Cu-compounds [89J] with the cooperative Jahn-Teller effect and orbital ordering (cf. Fig. 2.7 in Sect. 2.1.3), the ordering of the orientation of the long axis of the elongated octahedra is an additional source of order-disorder phenomena. The phase sequence of the propylammonium Cu-compound (cf. Table 4) shows also two incommensurate phases, but a peculiarity is that on cooling the system jumps from the δ-phase over the ε-phase directly to the ζ-phase and the ε-phase can be reached only on heating. In an analysis of their results of optical and x-ray studies [94J1], Jahn et al. have shown that the reconstructive phase transition $\delta \rightarrow \zeta$ is mainly due to octahedron axis switching (OAS) and the other reconstructive $\zeta \rightarrow \eta$ transition due to hydrogen-bond switching (HBS). The latter, i.e. the spontaneous reorientation of the H-bonding, is the mechanism found in all compounds which have been discussed so far (cf. the discussion on context with Fig. 2.34 and Eq. 2.28). The former, a spontaneous 90° switching of the long Jahn-Teller axis of the octahedra within every second layer, occurs only in Cu-compounds. A demonstration of this effect is obtained by comparing the two crystal structures observed for K_2CuF_4 (cf. the discussion in context with Fig. 2.8 in Sect. 2.1.3).

All considerations above have shown that the structural phase transitions in perovskite-type layer compounds are of the order-disorder type. And as measure for the disorder in the most disordered high temperature phases as compared to the mostly ordered low temperature phases, we consider the total change in entropy

$$\Delta S_{\text{tot}} = \sum_{\text{n}} \Delta S_{\text{n}} \tag{2.39}$$

where the summation n is over the transition entropies ΔS_{n} (cf. Eq. 2.18b) of all structural phase transitions of a particular compound. In many compounds, there is a major and one or more minor phase transitions with large and smaller values of ΔS_{n} and ΔH_{n} (cf. Table 4). For some long-chain compounds $(C_nH_{2n+1}NH_3)_2MCl_4$ with $n > 6$ (again abbreviated C_nMCl), this is illustrated in Fig. 2.40 where the change in enthalpy ΔH due to the phase transitions (cf. Eq. 2.18a) is presented for C_nMnCl, C_nCuCl, and C_nCdCl (n = 12 and 14). All these compounds undergo two phase transitions and most of them a major and a minor one, except for $C_{14}CdCl$ which shows two transitions of nearly equal strength. For the Mn- and the Cu-compounds, the major transition occurs at a lower temperature than the minor one while this is reversed for $C_{12}CdCl$. For compounds with more than two phase transitions, the situation is even more complicated. Since we do not want to enter into detailed discussions for each compound separately when comparing the phase transitions of a number of different compounds, it is reasonable to consider ΔS_{tot} as defined in Eq. 2.39 for such a comparison. We recall further that the disorder of a system is usually described not by the enthalpy but by the entropy where the experimental data may be compared to theoretical models. Let us now start with Rb_2CdCl_4 and $Rb_3Cd_2Cl_7$ where ΔS_{tot} results only from the tilting of the octahedra [89F1]. Correspondingly, the values of ΔS_{tot} derived from the data in Table 4 are relatively small: 2.33 J K^{-1} mol^{-1} for Rb_2CdCl_4 and 3.99 J K^{-1} mol^{-1} for $Rb_3Cd_2Cl_7$. For C_1CdCl, C_2CdCl and C_3CdCl, the values of ΔS_{tot} are larger (cf. Table 4), namely 11.21, 9.92, and 23.97 J K^{-1} mol^{-1}, respectively. This is because the dominant origin of ΔS_{tot} is the hydrogen bonding and the dynamical disorder connected with it. The model considerations for C_1MCl compounds (M = Mn, Fe, Cd; cf. Eqs. 2.29–2.35) are based on a distribution of the $(CH_3NH_3)^+$ groups over four equivalent positions in the disordered high temperature phase I4/mmm (cf. Eq. 2.25). The theoretical value of ΔS_{tot} for the disorder as corresponding to this model with four possibilities is for two chains per molecule [81R2]

$$\Delta S_{\text{tot}} = 2\,R \ln 4 = 23.05 \text{ J K}^{-1} \text{ mol}^{-1} \tag{2.40}$$

where R is the universal gas constant. This ΔS_{tot} is larger by a factor of two than the experimental value for C_1CdCl. Obviously the difference in disorder between the THT- and MLT-phases (cf. Table 4) is not so large as expected from the model.

9.12.2.2.5 Long-Chain Compounds

For C_nMCl compounds (M = Mn, Cu, Cd) with longer hydrocarbon chains ($n > 5$), a linear increase of ΔS_{tot} up to values of more than 240 J K^{-1} mol^{-1} for n = 17, 18 is observed. This is illustrated for the Mn-, Cu-, and Cd-compounds in Fig. 2.41. For $n > 5$, the conformational disorder in the chains becomes more and more the dominant process and the possibilities of disorder increase with the number n of carbon atoms. The data in Fig. 2.41 show further that the values of ΔS_{tot} are, on the average, somewhat higher for odd than for even values of n. The gradual change in the dominant mechanism of the phase transitions is also reflected by the transition temperatures [83W3]. They depend strongly on the M^{2+}-ion for short chains with hydrogen bonding as the dominant effect. As an example, two corresponding transition temperatures (cf. Table 4) are $T_{C2} = 257$ K and $T_{C3} = 94.4$ K for C_1MnCl [82W2] and $T_{C2} = 282$ K and $T_{C3} = 164.2$ K for C_1CdCl [81R2]. For longer chains ($n > 5$) with conformational disorder as the dominant effect, the transition temperatures are practically independent of M^{2+}. For C_7MnCl and C_7CdCl [83W3], the nearly identical transition temperatures are $T_{C1} = 314$ K, $T_{C2} = 248$ K and $T_{C1} = 317$ K, $T_{C2} = 250$ K, respectively. Several theoretical estimates for ΔS_{tot} of the long-chain compounds have been considered [78A2, 80H2, 85C1, 85O, 89C2] but only one concept was really successful. This is the idea that the transition to the high-temperature (HT) phase with still solid octahedral layers and a liquid-like disorder of the chains can be considered as a melting of the hydrocarbon chains [79B3, 79K1, 80B2, 89C2]. More precisely, it is the major transition (cf. Fig. 2.40) which corresponds to the melting of the chains [81N]. The minor transitions usually correspond to a two-fold orientational or torsional disorder of the chains.

The entropy change due to the chain melting is expected to be equal to that observed for the melting of n-paraffins [79K1]

$$\Delta S = 0.9\,(\mathrm{n} - 2)\,R \quad \text{per mole chain} \tag{2.41}$$

The melting of the chains means a rapid diffusion of one or more gauche bonds up and down the chains [85O] which are nearly all-trans in the ordered state. The factor (n – 2) in Eq. 2.41 arises from the number of possibilities for gauch configurations, i.e. the number of R′–C–C–R″ configurations in the chain where R′ and R″ are smaller hydrocarbon groups. For the monoammonium compounds under consideration with two chains per molecule, we obtain $\Delta S = 1.8\,(\mathrm{n} - 2)\,R$ per mole for the melting of the chains. This ΔS will be the largest contribution to ΔS_{tot} and the other contributions will be considerably smaller, cf. the minor transitions in Fig. 2.40. Therefore, the ΔS for chain melting is shown as a solid line in Fig. 2.41 and compared there to the experimental values of ΔS_{tot} and is seen to agree quite well with the experimental data. The experimental points are scattered over a width of approximately 20 J K^{-1} mol^{-1} which is larger than the contributions to ΔS_{tot} from most of the minor phase transitions. The "chain melting" model is further supported by x-ray diffraction data [89C2] which show a discontinuous abrupt change of the interlayer distance d at the structural phase transitions due to the increase of d when the chains become disordered. In the HT-phase, there are narrow diffraction lines corresponding to the inorganic matrix and a diffuse scattering zone (0.44–0.53 nm) indicating the high degree of disorder in the chains. The results of incoherent neutron scattering [89G1] have been interpreted with a gradient of disorder of the $-\mathrm{CH}_2-$ units starting at the NH_3 heads fixed to the octahedral layers and increasing towards the CH_3 end group.

The dynamical properties of the hydrocarbon chains can also be studied as a function of temperature by means of infrared and Raman spectroscopy. Such an investigation has been performed for $\mathrm{C}_{10}\mathrm{CdCl}$ [84R2] with two inequivalent chains A and B [79K1]. By comparing the infrared and Raman spectra of $\mathrm{C}_{10}\mathrm{CdCl}$ to the spectra of $\mathrm{C}_{10}\mathrm{MnCl}$ with only chains of the B-type [76C1] and to the results of normal-coordinate calculations, it is possible to discriminate between the vibrational bands of the A- and B-chains in the ordered LT-phase. And a complete understanding of these spectra has proved a sound basis for the discussion of the IM- and HT-phases (cf. Table 4) where the infrared and Raman spectra reflect the conformational disorder of the chains, i.e. the number of additional gauche bonds. The study of partly deuterated derivatives of $(\mathrm{C}_{10}\mathrm{H}_{21}\mathrm{NH}_3)_2\mathrm{CdCl}_4$, namely $(\mathrm{C}_9\mathrm{H}_{19}\mathrm{CD}_2\mathrm{NH}_3)_2\mathrm{CdCl}_4$, $(\mathrm{C}_8\mathrm{H}_{17}\mathrm{CD}_2\mathrm{CH}_2\mathrm{NH}_3)_2\mathrm{CdCl}_4$ and $(\mathrm{C}_6\mathrm{H}_{13}\mathrm{CD}_2\mathrm{C}_3\mathrm{H}_6\mathrm{NH}_3)_2\mathrm{CdCl}_4$, has allowed to obtain rather precise information about the position of the additional gauche bonds on the chains. Further spectroscopic studies of long-chain compounds include a comparison of the vibrational frequencies of the chains in $\mathrm{C}_8\mathrm{CdCl}$, $\mathrm{C}_{12}\mathrm{CdCl}$, and $\mathrm{C}_{16}\mathrm{CdCl}$ with different lengths [85R1] and of the data on $\mathrm{C}_{10}\mathrm{CdCl}$ with those of $\mathrm{C}_{10}\mathrm{H}_{21}\mathrm{NH}_3\mathrm{Cl}$ [85C3] where similar phenomena have been observed in four structural phases including a liquid-crystalline phase. With respect to models and to a Landau free energy, the long-chain compounds have mostly been treated analogously to liquid crystals using existing theories for these systems [79K1, 79B3, 80B2, 81K2, 83K3]. The smectic order parameter ϑ measures the average tilt angle of the molecules with respect to the layer normal, the order parameter S gives the nematic order of the chains averaged over the segments of each chain and over all hydrocarbon chains and, finally, a third order parameter describes the order or disorder of the MCl_6 octahedra and the hydrogen-bonding of the NH_3 groups. The results of the corresponding model calculations are not presented here. With respect to them, the reader is referred to the references, e.g. [79B3, 79K1, 80B2]. In many papers, the analogy of the long-chain monoammonium layer compounds with lipid bilayers has been emphasized and it has been pointed out that the layer compounds are crystalline models of lipid bilayers [79B3, 79K1, 80B2, 81K2, 81N, 83K3, 84N, 85C1].

9.12.2.2.6 Diammonium Compounds

For the discussion of the structural phase transitions in diammonium compounds $[\mathrm{NH}_3(\mathrm{CH}_2)_\mathrm{n}\mathrm{NH}_3]\mathrm{MCl}_4$, it is convenient to introduce the abbreviation $2\text{–}\mathrm{C}_\mathrm{n}\mathrm{MCl}$ for these compounds. Within the diammonium family, $2\text{–}\mathrm{C}_2\mathrm{MnCl}$ and $2\text{–}\mathrm{C}_2\mathrm{CdCl}$ have a stable structure without phase transitions (cf. Table 4) while the compounds with $\mathrm{n} > 2$ undergo several structural phase transitions. The mechanism of these transitions is similar to that of the monoammonium compounds. In the high temperature phases, there is a dynamic disorder of the diammoniumalkylene chains which are at both ends fixed to the octahedral layers by hydrogen bonds, in contrast to the monoammonium compounds with only one end fixed. The H-bonding schemes are illustrated for 2–C_3MnCl as an example in Figs. 2.42 and 2.43. In the α-phase (Imam) and the γ-phase (Pnam), the results of NMR- and NQR-studies [78K1] and of x-ray diffraction [82C] revealed two H-bonds to terminal or axial Cl^- and one H-bond to a bridging or equatorial Cl^-. In the β-phase, on the other hand, there are one H-bond to a terminal Cl^- and two H-bonds to bridging Cl^- as shown in Fig. 2.42. But the bonding scheme of the β-phase could also be intermediate between those two [82C]. The disorder of the chains is the cause why in the structure refinement split positions are introduced with equal occupation probability of 50% and that two chains are shown symmetrical to the mirror plane in Fig. 2.42 for the α- and β-phases. In the low-temperature γ-phase (cf. Table 4), no split positions have been used. The chains are nearly completely ordered in one of two possible positions. But there is still some dynamic disorder. The structural phase transitions are governed by rotational motions of rigid chains about their long axis or, in other words, by jumping of the chains from one position to the other one.

These dynamics, i.e. essentially the dynamics of the protons, have been studied in detail for the Mn-compounds by inelastic and quasi-elastic incoherent neutron scattering. The inelastic scattering monitors mainly the dynamics of the NH_3-group, often in combination with Raman scattering and infrared spectroscopic studies [86S1, 87G1, 89G2, 90G2]. In addition to $[NH_3(CH_2)_nNH_3]MnCl_4$ with n = 3, 4, 5, also partly deuterated samples of $[NH_3(CD_2)_nNH_3]MnCl_4$ and $[ND_3(CH_2)_nND_3]MnCl_4$ have been studied by quasi-elastic incoherent neutron scattering. Such investigations allow the separation of the influences of the C–H and of the N–H protons on the results. As in the case of the monoammonium compounds, the experimentally determined elastic incoherent structure factor EISF has been compared to data calculated by means of a model which takes the following motions within the $[NH_3(CH_2)_nNH_3]^{2+}$ molecular groups into account [89G2, 90G2]:

type 1: the rigid chains in their all-trans configuration perform jumps over two equivalent positions about their main molecular axis.

type 2: the chains are no longer rigid but become distorted and then the rotational motion consists of jumps among four positions corresponding to two equiprobable all-trans conformations and two equiprobable twisted conformations.

type 3: the NH_3-groups perform independently rotations about their C–N axis.

For 2–C_3MCl, the chains occur only in the all-trans conformation as shown for the Mn-compound in Fig. 2.42. For $n > 3$, also twisted chains are observed which can be thought as originating from uncorrelated and independent jumps of the NH_3-groups among their two positions symmetric to the mirror plane. Then, the chain can no longer be considered to be rigid but becomes twisted as presented for the example 2–C_5CdCl in Fig. 2.44. These data have been obtained from x-ray diffraction [87N1, 87N2]. It is assumed in this illustration that the NH_3-group with N(1) = N(11) is fixed with its H-bonds while the other NH_3-group with N(2) → N(12) has jumped to its other position. With equal probability, a second possibility for the twisted chain would be that N(1) → N(11) jumps to its other H-bonding position and N(2) = N(12) remains in its place. Thus there are two orientations not only for the all-trans chains but also for the twisted chains.

The fit of the calculated EISF = $f(Q)$ to the experimental data has contributed considerably to the understanding of the dynamics of the diammoniumalkylene chains [89G2, 90G2]. In 2–C_3MnCl with only all-trans and no twisted chains, motions of type 1 and 3 contribute to the EISF in the high temperature α- and β-phases, while only type 3 contributes to it in the γ-phase where the chains are ordered (cf. Fig. 2.43) and no longer jumps over two positions (type 1) occur. But 2–C_4MnCl and 2–C_5MnCl have also twisted chains in their high temperature phase (OHT for both, cf. Table 4). Thus, the rotational motions of type 2 and 3 have to be taken into account for calculating the EISF. In their low temperature phase (cf. Table 4; 2–C_4MnCl: MRT; 2–C_5MnCl: ORT) where the chains occur only in the all-trans conformation, again types 1 and 3 contribute to the EISF. From the fit of the calculated EISF in both phases, also the characteristic times for these types of motions are obtained. Especially for type 3, the times are considerably smaller in the high temperature phase (1.34 ps for 2–C_4MnCl at 440 K) than in the low temperature one (7.00 ps for 2–C_4MnCl at 333 K) [90G2]. In 2–C_3MnCl, these characteristic times are of the same order of magnitude but slightly different for C–H and N–H protons [87G1] indicating that the chains are not quite rigid and that the jumps of N–H and C–H protons are somewhat uncorrelated even though no twisted chains occur in this compound. One would expect that these results hold also for Cd-compounds where no neutron scattering results can be obtained. But some caution is necessary for such a conclusion since two frozen-in twisted states have been found in the room temperature structure of 2–C_4CdCl [76W1, 81K3] while 2–C_4MnCl exhibits only all-trans states at 295 K (γ-phase, cf. Figs. 2.42 and 2.43).

For the high-temperature phases of 2–C_5MnCl and 2–C_5CdCl, we define p as the probability for twisted chains or the average portion of chains in this state, and $1 - p$ as the corresponding probabilty for all-trans chains. Several methods have been employed to determine p and $1 - p$. From incoherent neutron scattering results [87G1, 88C1], values of p have been derived for

2–C_5MnCl: $p = 0.25$ at 310 K and $p = 0.50$ at 470 K (both in the OHT-phase)

X-ray diffraction and a structure refinement with two orientations for trans chains and two orientations for twisted chains [87N1, 87N2] yielded the value for

2–C_5CdCl: $p = 0.45$ at 353 K (OHT-phase)

For the same compound, the temperature dependence of p has been determined over a wide temperature range from the intensity ratio of two Raman lines at 420 cm^{-1} and 440 cm^{-1} [88C2] where the first line is assigned to a vibrational mode of the twisted chains and the other to the corresponding mode in all-trans chains. The ratio of the reduced intensities, i.e. thermal factors removed, is [88C2, 89N1]

$$I_{420}^{*} / I_{440}^{*} \sim p/(1-p) = A \exp(-\Delta H / RT) \tag{2.42}$$

where R is again the universal gas constant. The temperature dependence of the experimental data of $I_{420}^{*} / I_{440}^{*}$ has yielded $\Delta H = 17.2\ (20)$ kJ mol^{-1} for 2–C_5CdCl [87N2, 88C2]. A similar value of $\Delta H =$ 19.0 kJ mol^{-1} has been reported for 2–C_5MnCl [88C1]. ΔH can be considered the energy necessary to excite the twisted state from the trans state, and the twisted states will be less populated than the trans states. Since both types of chains are distributed between two mirror-related positions, the excess entropy S_{ex} due to the disorder of twisted and all-trans chains is [88C1, 89N1]

$$S_{ex} = -R\ \{(1-p) \ln[(1-p)/2] + p \ln[p/2]\} \tag{2.43}$$

S_{ex} will be at maximum for $p = 0.5$ which means that the number of twisted chains is equal to the number of trans chains. For $p > 0.5$, S_{ex} will not further increase but decrease. Eq. 2.42 allows us to calculate p as a function of temperature. From the experimental data $\Delta H = 17.2$ kJ mol^{-1} and $p = 0.45$ at 353 K, we obtain for 2–C_5CdCl $p \approx 0.4$ at 337 K (transition ORT ↔ OHT, cf. Table 4) and $p \approx 0.7$ at 400 K (just below the transition OHT ↔ MHT). The values of S_{ex} calculated with these values of p by means of Eq. 2.43 do not well agree with the experimental value of ΔS for the ORT → OHT phase transition (cf. Table 4) with only trans chains below the transition and both types of chains above it. Therefore, the value of p deduced for 2–C_5CdCl from x-ray diffraction [87N1, 87N2] is probably overestimated since an ideal "twisted chain" model has been assumed in the structure refinement. Although the disorder of the chains is the dominant effect for the phase transitions of diammonium compounds, also the MCl_6 octahedral layers take part in the dynamical disorder. This was observed for 2–C_5CdCl by diffuse x-ray scattering [89N1] and it is illustrated for 2–C_3MnCl in Figs. 2.42 and 2.43 where the structure exhibits a tilting of the octahedra and a washboard-like puckering of the layers.

Model considerations for the diammonium compounds usually take into account two equivalent positions of the trans chains and two of the twisted chains. In one approach for modelling the phase transitions of 2–C_3CdCl, 2–C_4MnCl, and 2–C_5CdCl, the occupation numbers for the two positions of the trans chains are denoted by n_1 and n_2 and those for the twisted ones by n_3 and n_4. Along the lines sketched in context with Eqs. 2.29–2.35, an internal energy $U = f(n_1, n_2, n_3, n_4)$ is set up and the minimum of the free energy $F - TS$ is determined and the stability conditions are examined [81K3]. For describing within the model not only the low temperature phases but, for example, also the monoclinic high temperature (MHT) phase of 2–C_5CdCl, other model approaches consider not only the phases with the structures Imam (Ibmm), Pnam (Pbnm), Pman (Pbmn) and $P12_1/a1$ ($P2_1/b11$) but the whole family tree of these compounds (cf. Fig. 2.30) including the "parent" structure P4/mmm, i.e. a fictitious THT-phase. A model with the usual Landau free energy [89N1] needs for the following three second order transitions THT → OHT (fictitious), THT → MHT (fictitious) and OHT → ORT (real, cf. Table 4) three different sets of order parameters. The reason is that the phenomena connected with these phase transitions are very complex due to the superposition of orientational and conformational disorder of the diammoniumalkylene chains. More successful is a multidimensional pseudo-spin model [88C2, 89N1]. If we had an order-disorder transition between two phases where a molecule has two possible orientations with equal probability in the high-temperature phase and with one orientation more probable in the low temperature phase, we can map this problem onto an Ising model with pseudo-spins $S = \pm 1$. For our actual problem, we need multidimensional pseudo-spins corresponding to the possible orientations of the chains in the tetragonal symmetry of the fictitious THT-"parent"-phase. Symmetry considerations lead to four orientations of the trans chains and eight orientations of the twisted ones. This multidimensional pseudo-spin model attached to the chain orientation can well describe the two fictitious transitions and the real one of the compound under consideration and is thus able to account for the unusual sequence of phase transitions MHT ↔ OHT ↔ ORT observed in 2–C_5CdCl [88C2, 89N1].

A final remark on the proton dynamics in these compounds with hydrogen bonding deals with the influence of an external electrical field on the protons. An ionic electrical conductivity is established by these protons at the terminal N-atoms. Experimentally, the dielectric properties or directly the conductivity have been studied in a number of perovskite-type layer strucutes, namely in diammonium compounds $[NH_3(CH_2)_nNH_3]MX_4$

with M = Cu and X = Cl for n = 2 [83A1],
with M = Fe and X = Cl for n = 2, 3, 7, 8, 9, 10 [86A2, 88A4, 88A5, 95A2]
with M = Fe and X = $Cl_{1-x}Br_x$ for n = 8, 9 [88A4]
with M = Cd and X = Cl for n = 2, 3 [92B1]

The measured values of the conductivity σ are with 10^{-14}–10^{-5} $(\Omega\ \mathrm{cm})^{-1}$ of the order of magnitude expected for an ionic conductivity. It is strongly temperature dependent and follows usually an Arrhenius law [83A1, 88A4, 88A5, 92B1]

$$\sigma = \sigma_0 \exp\left(-E_{\mathrm{ex}} / k_{\mathrm{B}} T\right) \tag{2.44}$$

at least in temperature ranges without structural changes. In Eq. 2.44, E_{ex} is an excitation energy and σ_0 a factor. It is further worth mentioning that also some monoammonium compounds have been investigated with respect to their dielectric properties and their ionic conductivity, for example $(CH_3NH_3)_2CuCl_4$, $(C_2H_5NH_3)_2CuCl_4$ [83A1] and $(4\text{-}ClC_6H_4NH_3)_2MnCl_4$ [93M1].

9.12.2.3 Figures for 9.12.2 and Tables 2, 3 and 4

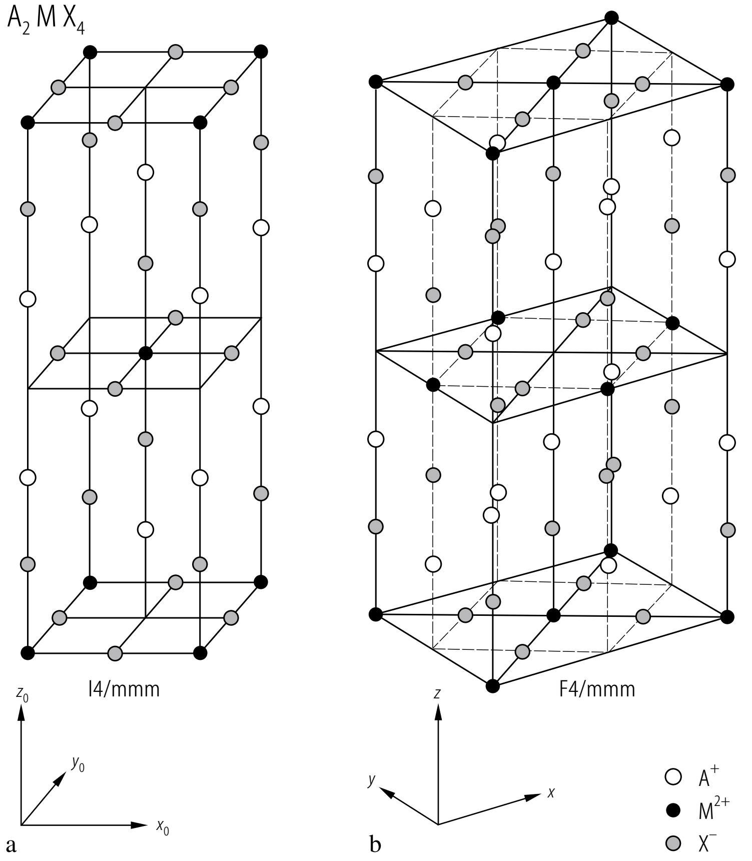

Fig. 2.1. A_2MX_4. **(a)** K_2NiF_4-structure I4/mmm in the coordinate system (x_0, y_0, z_0) and **(b)** description as F4/mmm in the coordinate system (x, y, z) rotated by 45° about the $z = z_0$-axis.

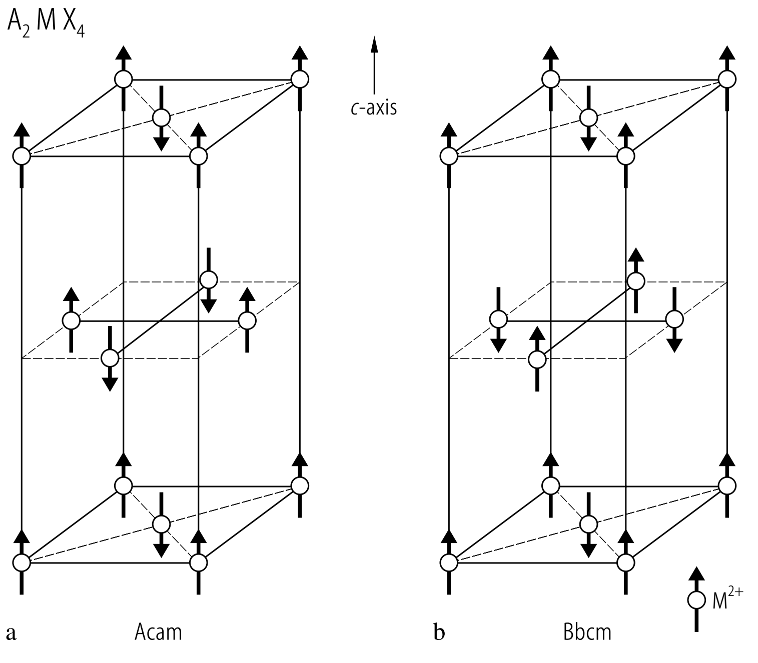

Fig. 2.2. A_2MX_4. Antiferromagnetic compounds of the easy-axis type, structures of the two antiferromagnetic domains: **(a)** Acam and **(b)** Bbcm. Only the M^{2+}-ions are shown. The orientation of the spins parallel or antiparallel to the c-axis is indicated by arrows (taken from [92G1]).

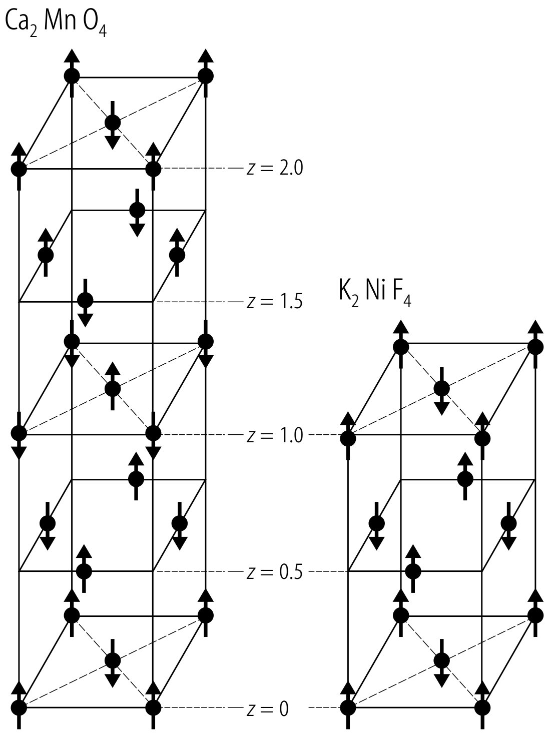

a b

Fig. 2.3. Ca_2MnO_4 and K_2NiF_4. Magnetic structure with antiferromagnetic **(a)** and ferromagnetic **(b)** interlayer interaction in Ca_2MnO_4 and K_2NiF_4, respectively. Only magnetic ions are shown and only one of the two domains for K_2NiF_4 (Bbcm). The units for z are the lattice parameters c of the chemical unit cell. The orientation of the spins is indicated by arrows (after [69C1]).

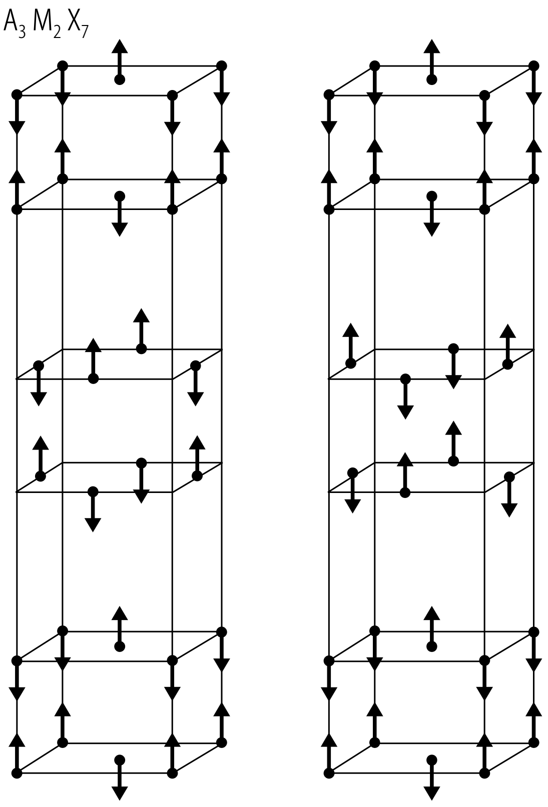

a Acaa b Bbcb

Fig. 2.4. $A_3M_2X_7$. Antiferromagnetic double-layer compounds of the easy-axis type, structures of the two antiferromagnetic domains: **(a)** Acaa and **(b)** Bbcb. Only the M^{2+}-ions are shown. The orientation of the spins parallel and anti-parallel to the c-axis is indicated by arrows (after [76G1]).

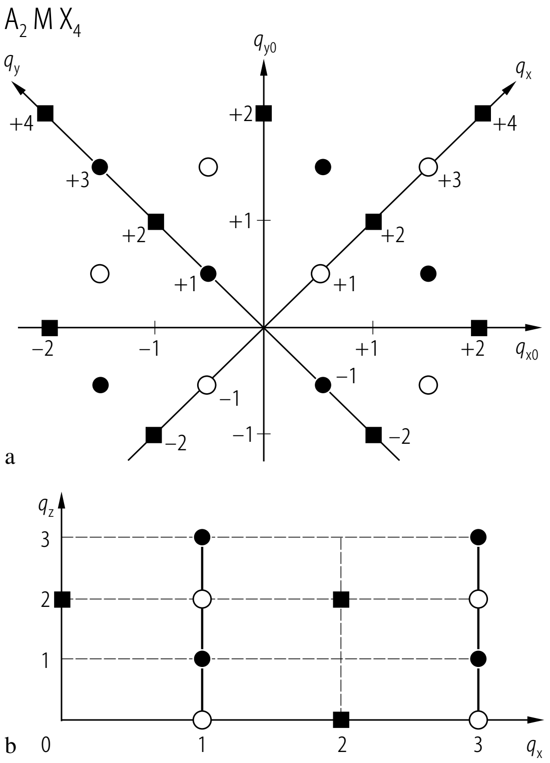

Fig. 2.5. A$_2$MX$_4$. The reciprocal lattice: **(a)** (q_{x0}, q_{y0})- or (q_x, q_y)-plane with the two coordinate systems (details see text) and **(b)** (q_x, q_z)-plane, reciprocal lattice points for nuclear Bragg reflections (full squares), for antiferromagnetic superreflections domain 1 (open circles) and domain 2 (full circles) and the antiferromagnetic Bragg rods (thick lines). The units are $2\pi/a$ and $2\pi/c$ for both systems where $2\pi/a_{(x,y,z)} = \sqrt{2}\pi/a_{(x0,y0,z0)}$.

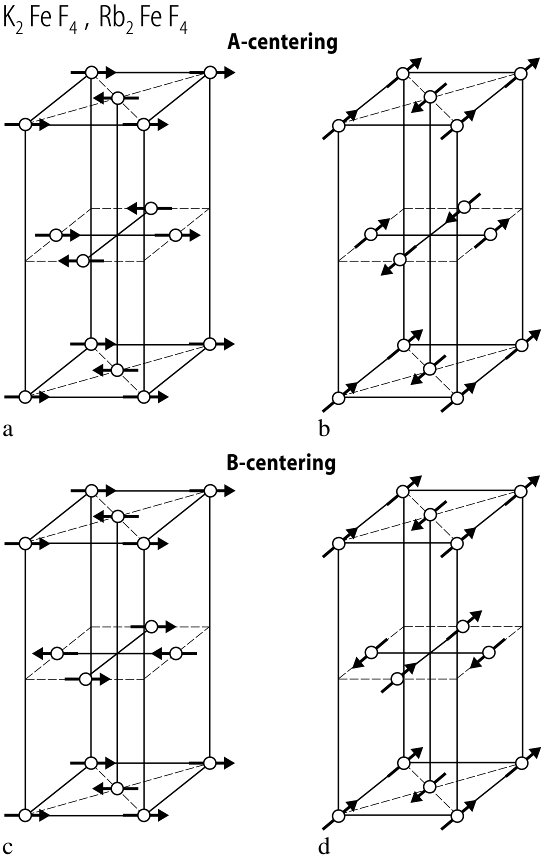

Fig. 2.6. K$_2$FeF$_4$ and Rb$_2$FeF$_4$ with easy-plane antiferromagnetic order. Only the Fe^{2+}-ions are shown with the preferred spin-directions indicated by arrows (parallel to the *x*- or *y*-axis) and with A- or B-centering of the lattice (domains a–d). From these imaginable four domains [79B2], only two were found by neutron diffraction in K$_2$FeF$_4$ [82T1], namely domains b) and c) with ferromagnetic order in the sheets spanned by the spin direction and the *c*-axis (after [82T1]).

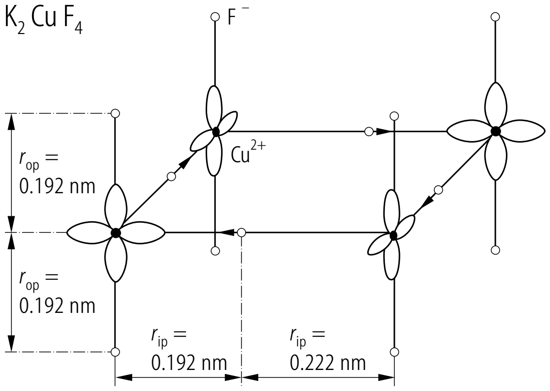

Fig. 2.7. K$_2$CuF$_4$. Orbital ordering and collective Jahn-Teller effect in K$_2$CuF$_4$ (after [73K1]). Arrows indicate the elongation of the Cu-F$_6$ octahedra. The values of the in-plane Cu-F bond lengths r_{ip} and the out-of-plane one r_{op} are taken from results of x-ray diffraction studies [74H1].

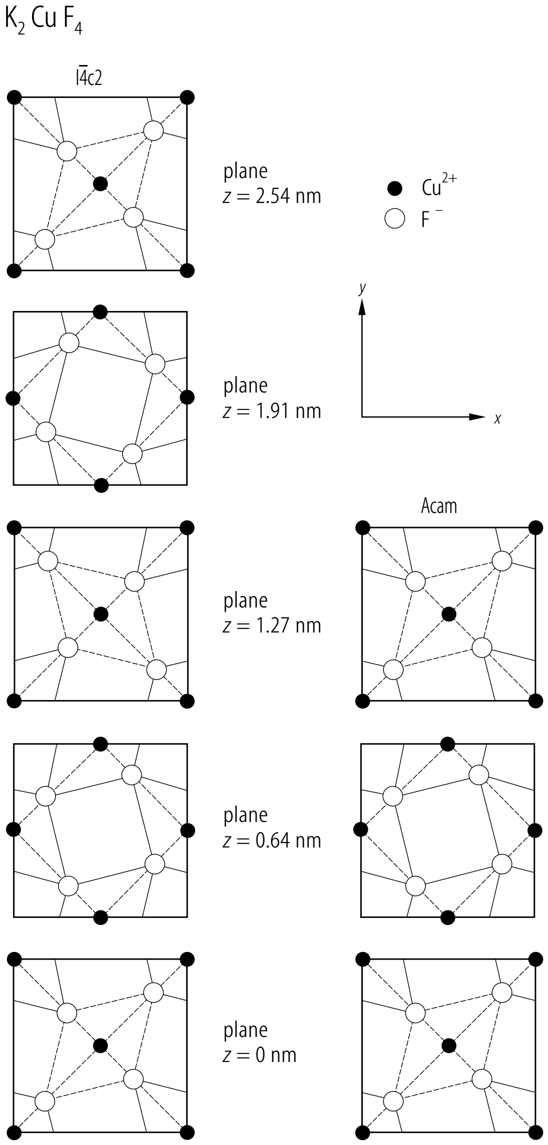

Fig. 2.8. K_2CuF_4. Illustration of the Jahn-Teller ordering in the layers within a unit cell for the two possible structures $I\bar{4}c2$ and Acam. The planes are labelled by their z-coordinate in nm and not in the usual reduced units since the lattice parameters are different for the two structures, c = 1.27 nm for Acam [83H1] and c = 2.54 nm for $I\bar{4}c2$ [74H1].

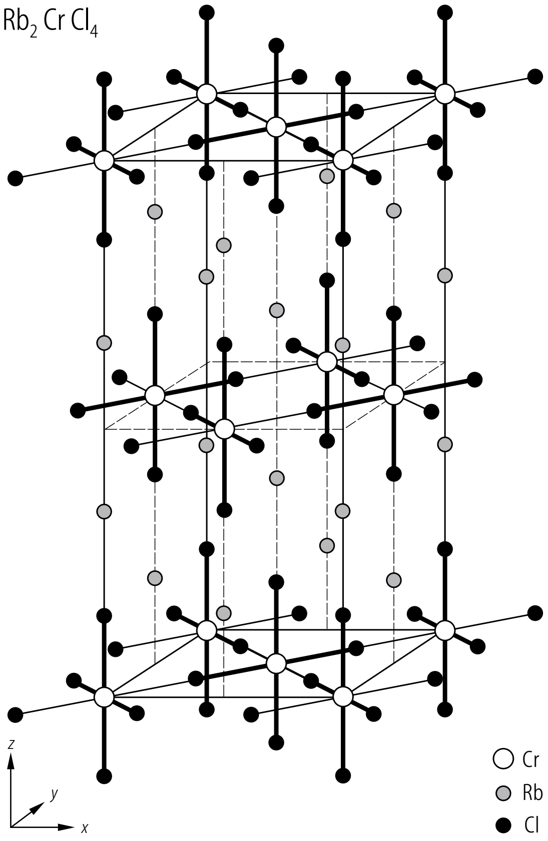

Fig. 2.9. Rb_2CrCl_4. Room temperature structure Bbcm with deformation of the $CrCl_6$ octahedra resulting from orbital ordering and collective Jahn-Teller effect (after [83J1]).

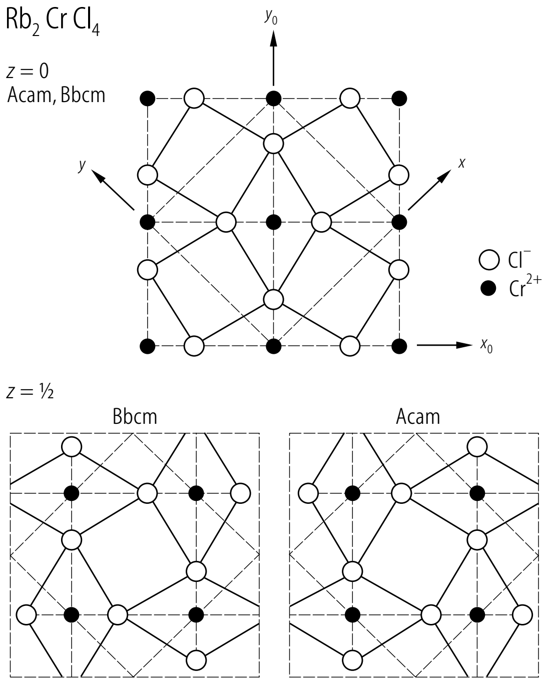

Fig. 2.10. Rb_2CrCl_4. The antiferrodistortive order of the elongated $CrCl_6$ octahedra (elongation exaggerated) in the plane $z = 0$ with no difference for the two crystallographic domains Acam and Bbcm, but with differences in the plane $z = \frac{1}{2}$, as shown in the lower part (after [86D1]).

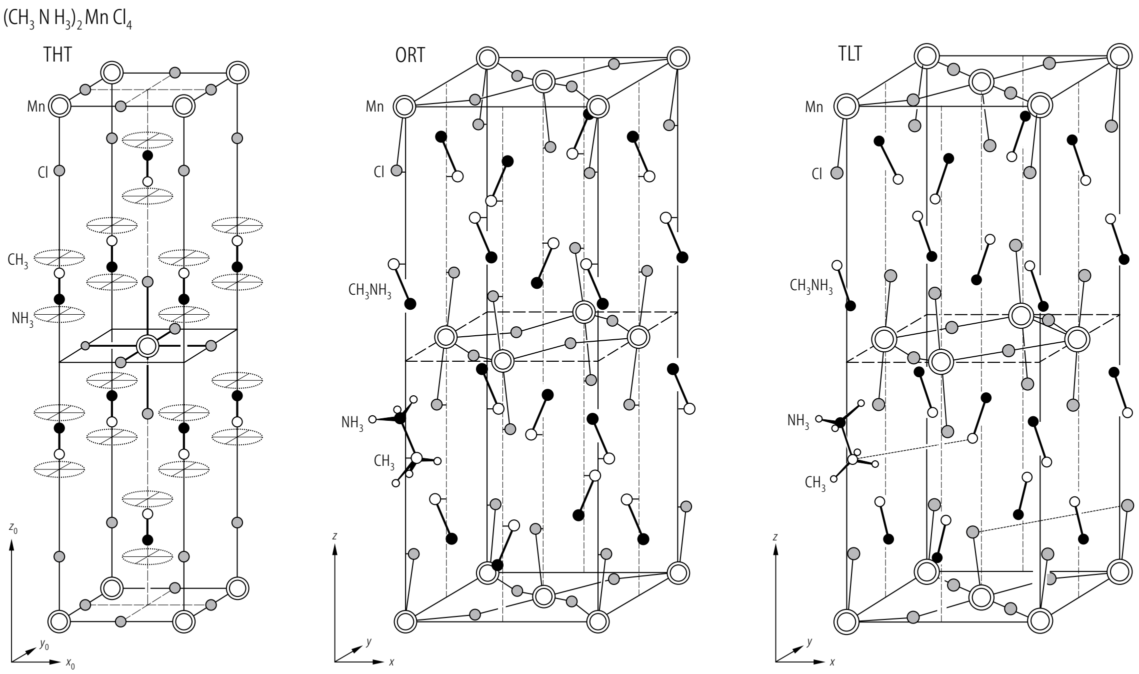

Fig. 2.11. $(CH_3NH_3)_2MnCl_4$. The structures of three phases: I4/mmm (THT-phase), Abma (ORT-phase) and $P4_2$/ncm (TLT-phase) (taken from [75H1] and [76H1]).

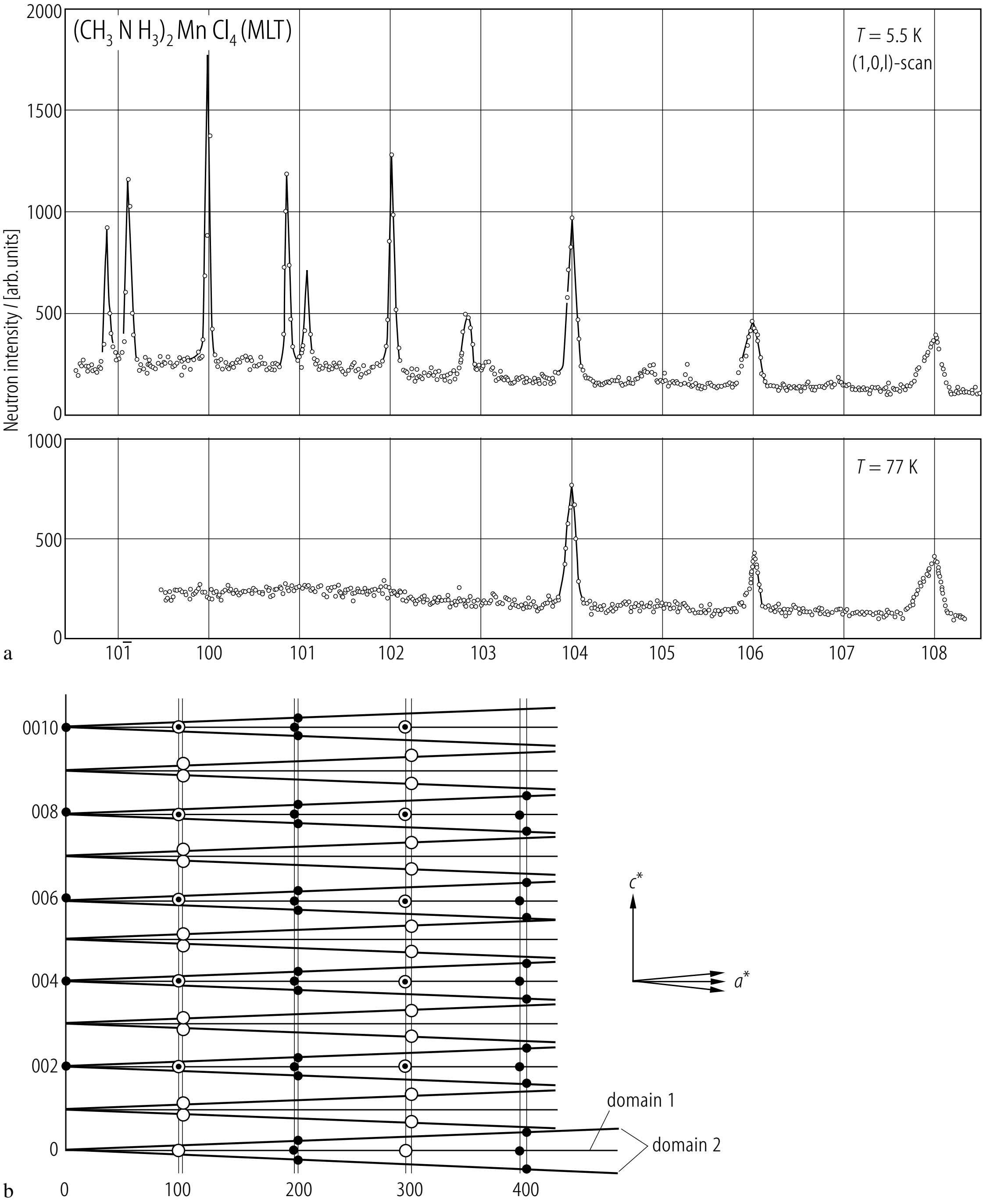

Fig. 2.12. (CH$_3$NH$_3$)$_2$MnCl$_4$ (MLT-phase). **(a)** Neutron diffraction data of a (1, 0, 1)-scan at 5.5 and 77 K, and **(b)** (a^*, c^*) reciprocal lattice plane with $\boldsymbol{a^*} \perp \boldsymbol{c^*}$ for domain 1 and with doubling of a^* for domain 2 due to monoclinic splitting. Open and filled circles refer to magnetic and nuclear reflections, resp., taken from [90A1].

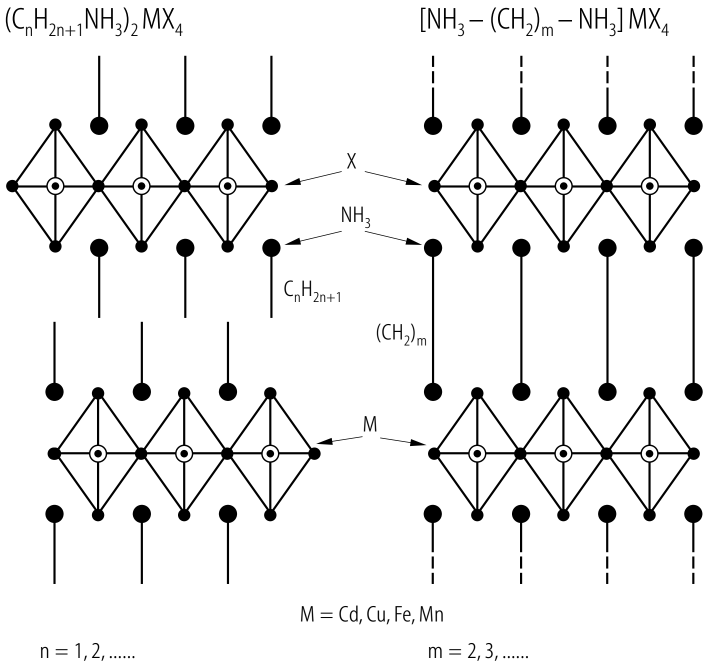

Fig. 2.13. $(C_nH_{2n+1}NH_3)_2MX_4$ and $[NH_3(CH_2)_mNH_3]MX_4$. Schematic representation of the staggered structure of the bis-alkyl-ammonium compounds and the eclipsed structure of the alkylene-diammonium compounds, after [76A2, 77K3, 77K4].

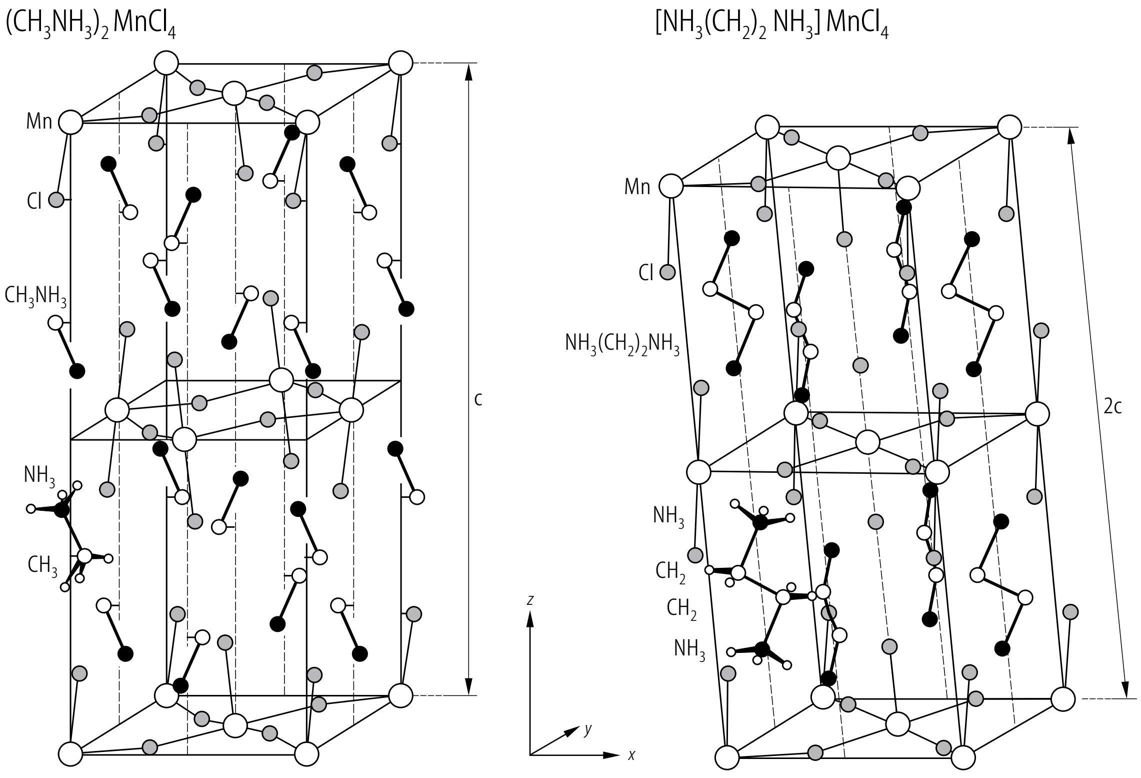

Fig. 2.14. $(CH_3NH_3)_2MnCl_4$ and $[NH_3(CH_2)_2NH_3]MnCl_4$. Comparison of the room temperature structures Abma (ORT-phase) and $P12_1/a1$, after [75H1] and [78T1], respectively. For a better comparison, two unit cells are shown of the diammonium compound.

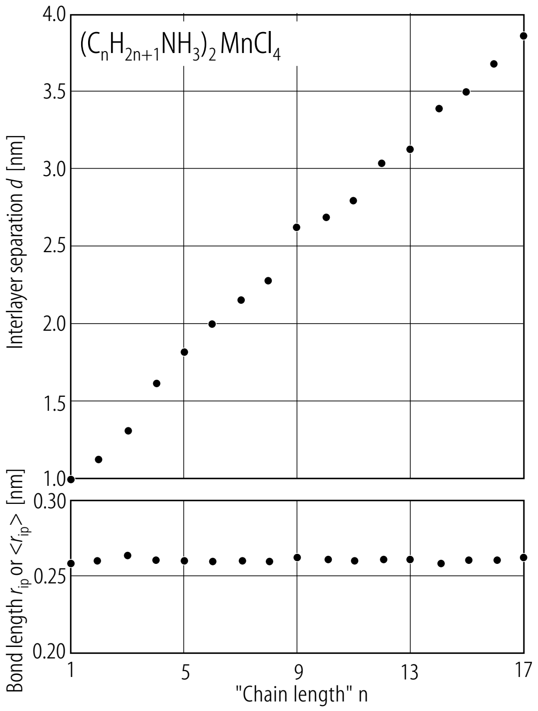

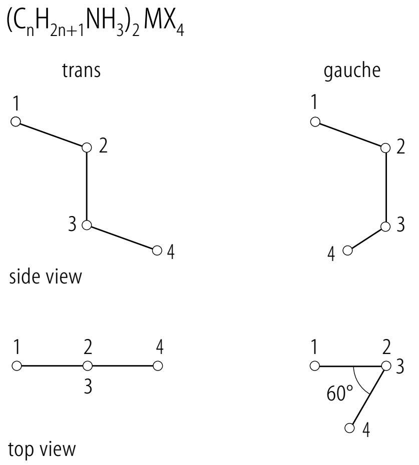

Fig. 2.16. $(C_nH_{2n+1}NH_3)_2MX_4$. Schematic representation of the *trans* and *gauche* configurations found in alkyl chains (taken from [79K1]).

←

Fig. 2.15. $(C_nH_{2n+1}NH_3)_2MnCl_4$ (n = 1 – 17). M-X bond length r_{ip} or $\langle r_{ip}\rangle$ and interlayer separation d as a function of chain length n. The data are taken from Table 3 where also the corresponding references are compiled.

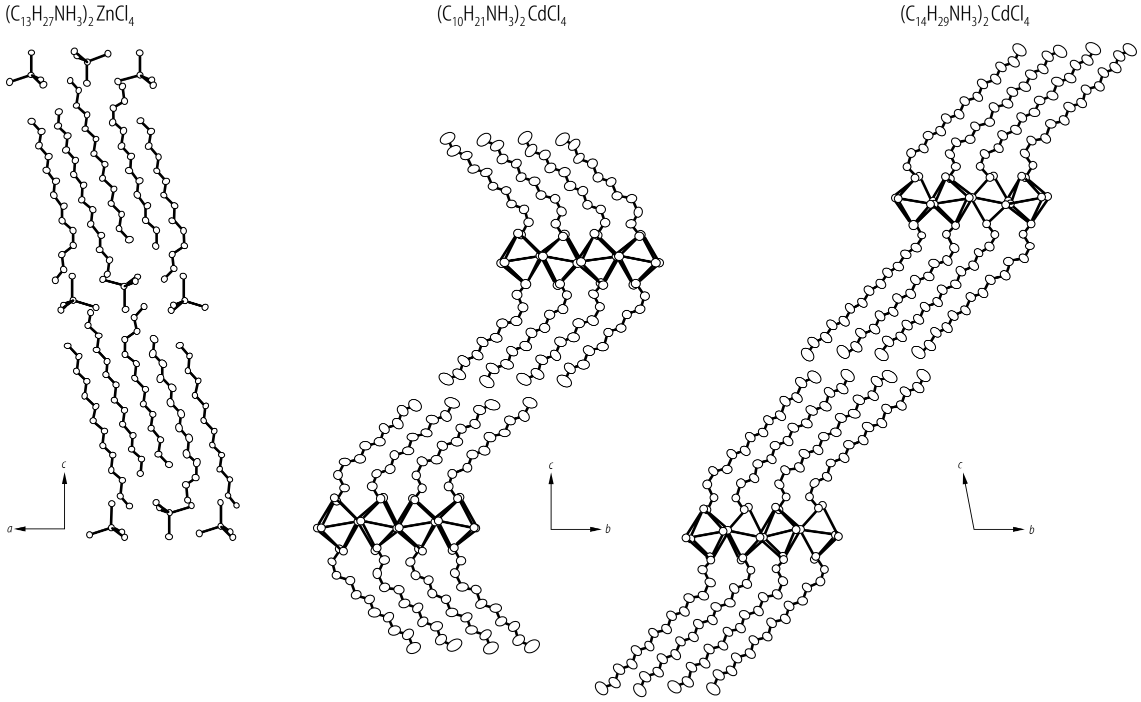
$(C_{13}H_{27}NH_3)_2ZnCl_4$
$(C_{10}H_{21}NH_3)_2CdCl_4$
$(C_{14}H_{29}NH_3)_2CdCl_4$
c
a
c
b
c
b

Fig. 2.17. $(C_{14}H_{29}NH_3)_2CdCl_4$, $(C_{10}H_{21}NH_3)_2CdCl_4$ and $(C_{13}H_{27}NH_3)_2ZnCl_4$. (*b*, *c*) and (*a*, *c*)-projections, resp., of the room temperature structures with the ordered arrangement of long alkyl chains (taken from [88S1], [79K1] and [85Z1], resp.).

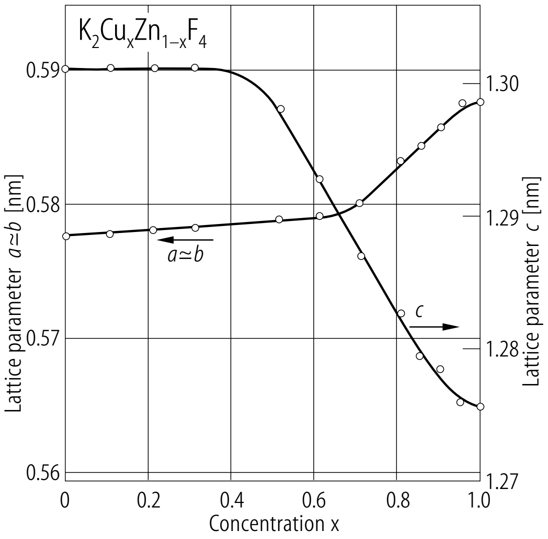

Fig. 2.18. $K_2Cu_xZn_{1-x}F_4$. Variation of the lattice parameters $a \approx b$ and c with the Cu^{2+}-concentration x. The drastic changes on the Cu-rich side are ascribed to the collective Jahn-Teller effect and the orbital ordering of the Cu^{2+}-ions which persist down to x ≈ 0.4 according to these and other experimental results (after [87J2], experimental data from [86H1]).

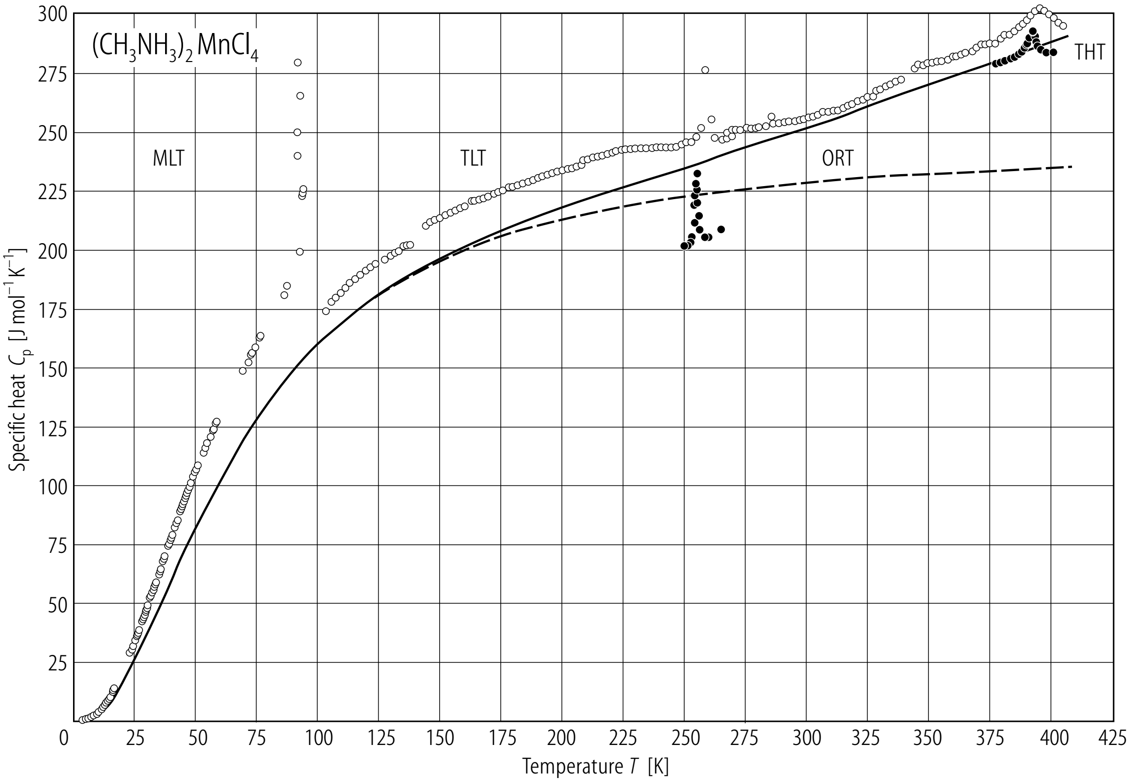

Fig. 2.19. $(CH_3NH_3)_2MnCl_4$. Specific heat C_p versus T for the range $4\ K \le T \le 400\ K$, experimental points (open circles) [78S2, 79S4] and curves (— and – – –) calculated by means of a lattice dynamical model [79G4, 79S4]. The extra points (full circles) represent the experimental data at the structural phase transitions, taken from [75B1] and [77T1]. For further explanations, see text.

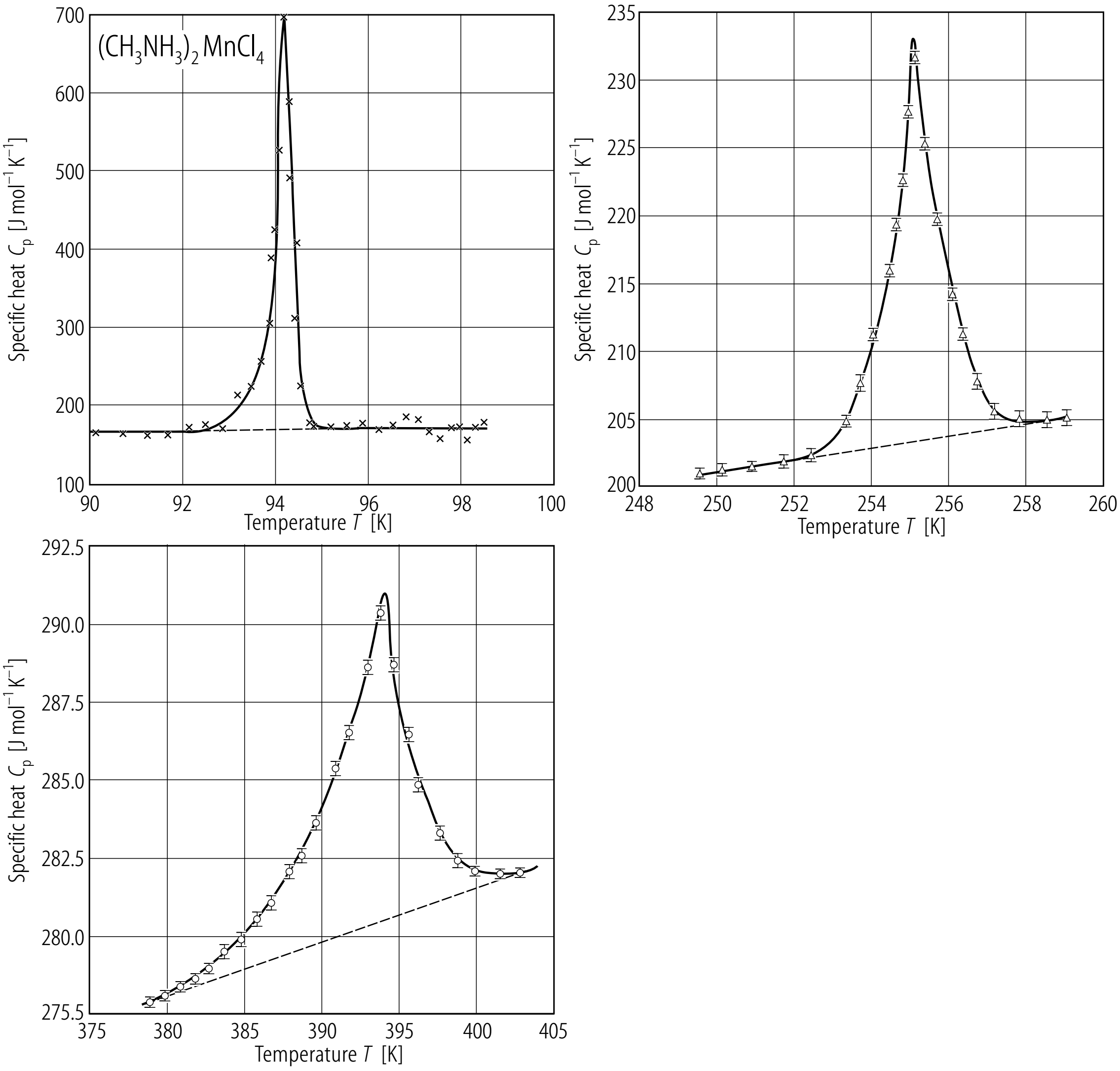

Fig. 2.20. $(CH_3NH_3)_2MnCl_4$. On an expanded scale: the anomalies of the specific heat C_p at the structural phase transitions versus T, the data taken from [78S2], [77T1], and [75B1] for the transitions at about 94 K, 257 K and 394 K, respectively. For details of the phase transitions, see text and Table 4.

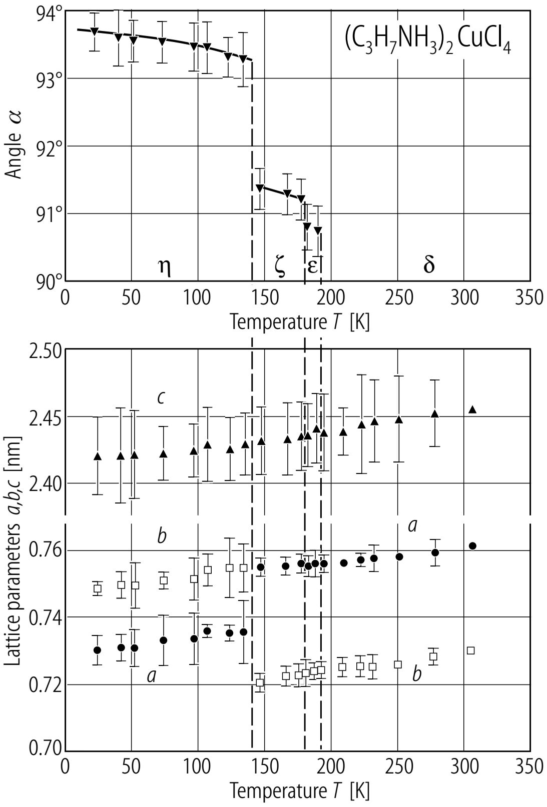

Fig. 2.21. $(C_3H_7NH_3)_2CuCl_4$. The lattice parameters *a*, *b*, *c* and the monoclinic angle *α* as a function of temperature *T* in the structural phases δ, ε, ζ and η (cf. Table 4), obtained by x-ray diffraction. The δ-phase has an orthorhombic structure ($\alpha = 90°$) and the ζ-phase an incommensurate one. The data reveal well the discontinuous transition ζ → η near 135 K (taken from [94J1]).

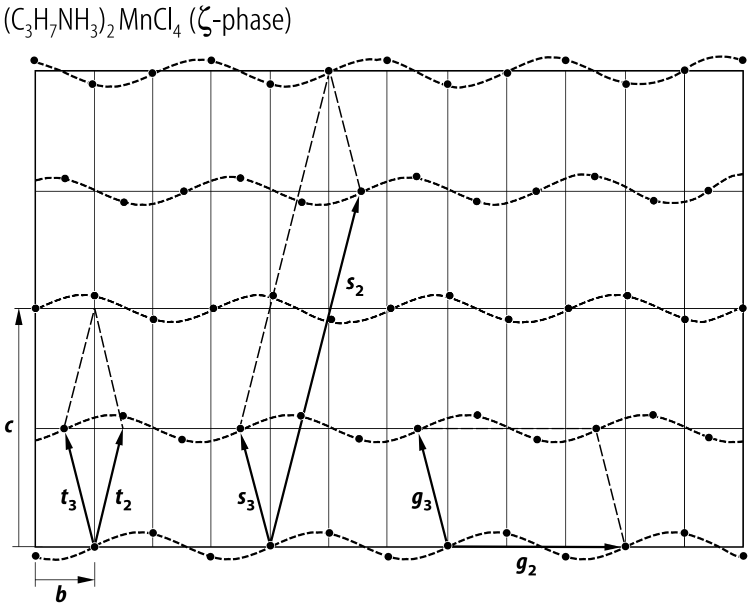

Fig. 2.22. $(C_3H_7NH_3)_2MnCl_4$. Schematic view of the structure of the modulated ζ-phase ((*b*, *c*)-plane ⊥ *a*-axis). Only the Mn^{2+}-ions are shown, the modulation in an exaggerated way as a transverse wave running along $\mathbf{g}_2$ (after [88M1]). Four sets of lattice vectors illustrate the various possibilities for their choice in the monoclinic mirror plane, two for the basic structure and two for a new unmodulated one with triplicated unit cell.

$(CH_3NH_3)_2CdCl_4$

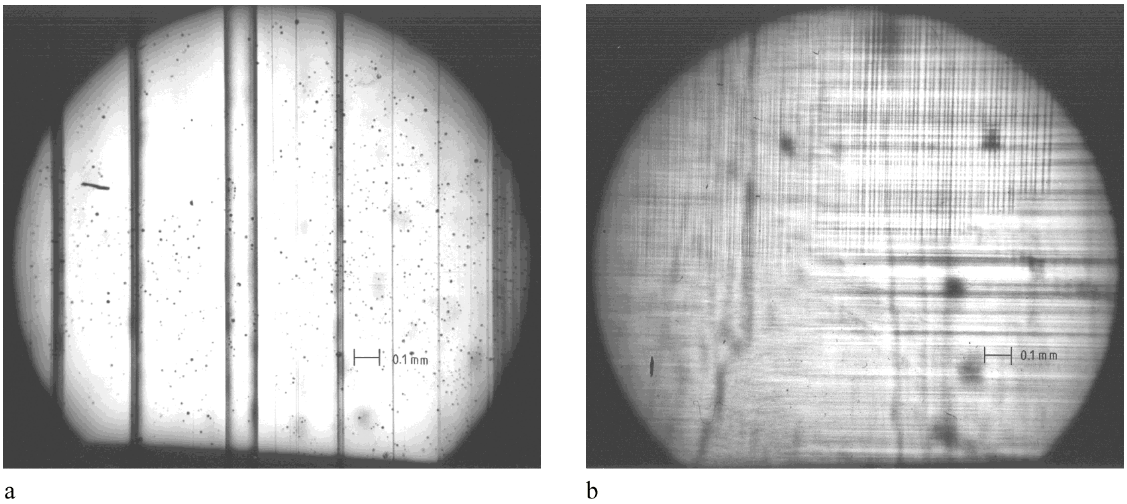

Fig. 2.23. $(CH_3NH_3)_2CdCl_4$. Photographs of the domain structure of a nearly single domain sample **(a)** and of a typical multi-domain sample **(b)**. The photographs were taken through microscope with a magnification of about 100 without using a polarizer and analyser (taken from [80G1, 82W4]).

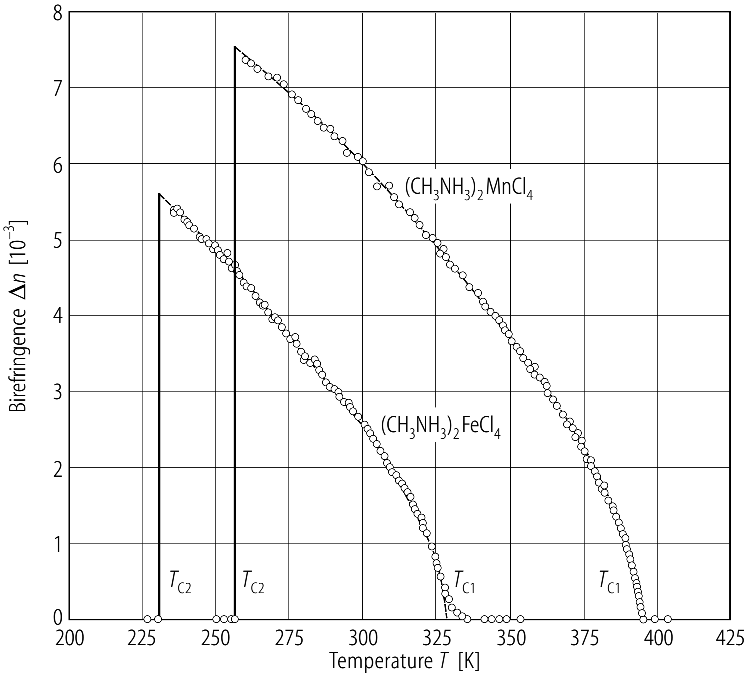

Fig. 2.24. $(CH_3NH_3)_2MnCl_4$ and $(CH_3NH_3)_2FeCl_4$. $\Delta n = n_b - n_a$ versus temperature T, determined by birefringence studies at $\lambda = 550$ nm. Δn is zero in the tetragonal THT- and TLT-phases and $\neq 0$ only in the orthorhombic ORT-phase between T_{C1} (cont. pt.) and T_{C2} (disc. pt.), taken from [74K1].

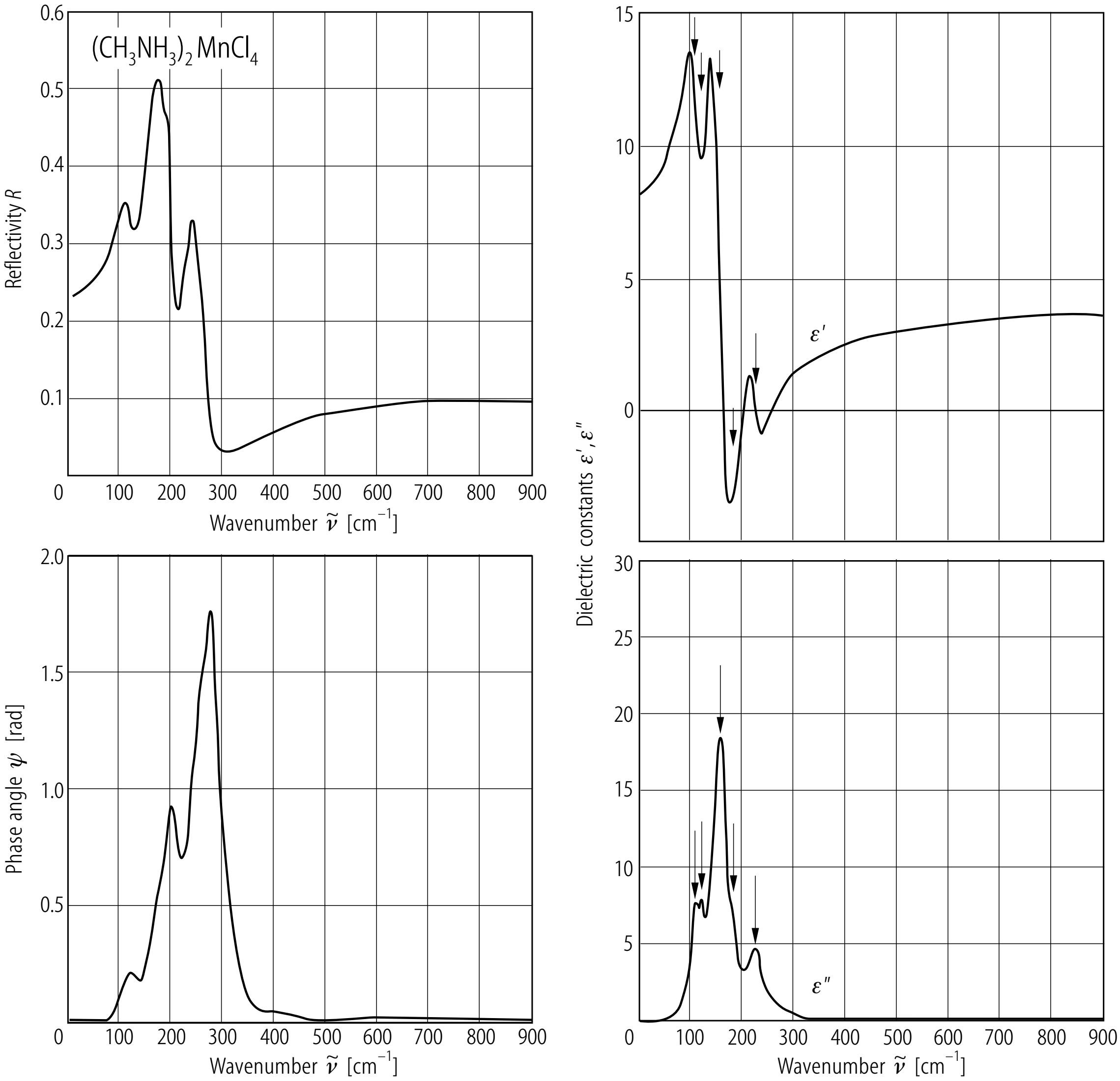

Fig. 2.25. $(CH_3NH_3)_2MnCl_4$. Infrared spectra versus wavenumber $\tilde{\nu}$ for $\boldsymbol{E} \perp \boldsymbol{c}$ at $T = 180$ K: the experimentally determined reflectivity R, the phase angle ψ obtained by a Kramers-Kronig transform, finally real part ε', and imaginary part ε'' of the dielectric constant calculated by means of Eq. 2.20 and by using $(n + \mathrm{i}k)^2 = \varepsilon' + \mathrm{i}\varepsilon''$ (after [75L2, 75L3]). Arrows: see text.

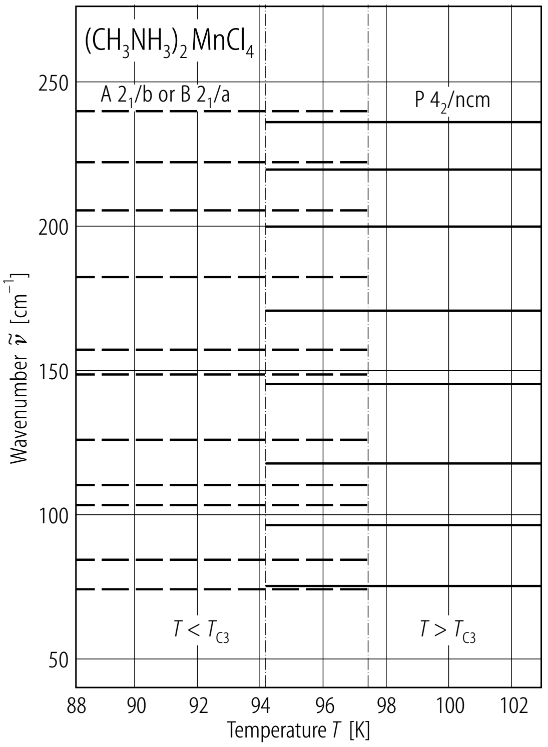

Fig. 2.26. $(CH_3NH_3)_2MnCl_4$. Wavenumbers $\tilde{\nu}$ of the infrared active lattice modes for $\boldsymbol{E} \parallel \boldsymbol{c}$ versus temperature in the range 87–103 K where a discontinuous phase transition occurs. Broken lines denote the modes in the MLT-phase below the transition and full lines the modes in the TLT-phase above it. The range of overlap near 95–97 K marks the thermal hysteresis of the phase transition (taken from [77V1]).

For Fig. 2.27 see next page.

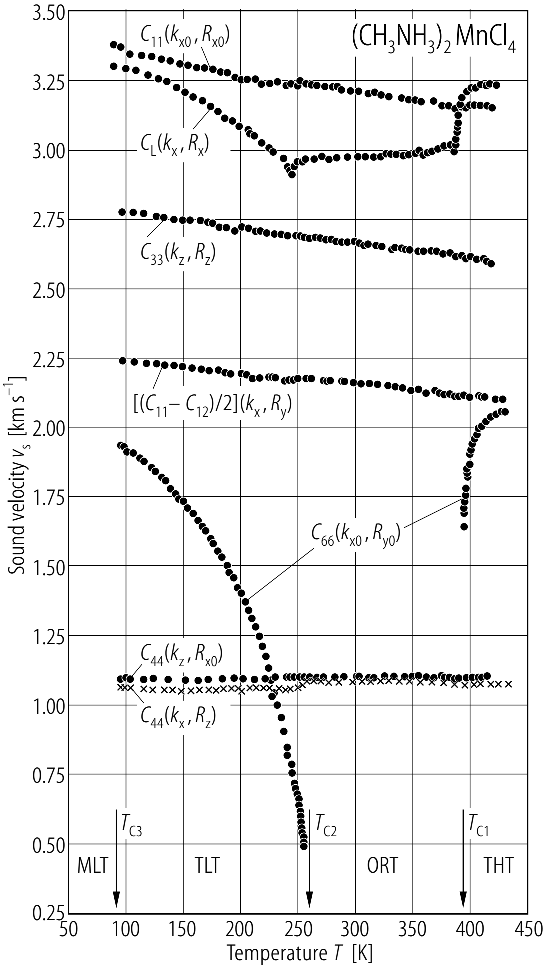

Fig. 2.28. $(CH_3NH_3)_2MnCl_4$. Sound velocities v_s as a function of temperature T, indicating the temperature dependence of the different elastic stiffness constants which are defined with respect to the (x_0, y_0, z_0) coordinate system. k denotes the propagation direction and R the polarization of the ultrasonic wave where some of the directions are more conveniently denoted with respect to the (x, y, z) system (taken from [79G3, 80G2]).

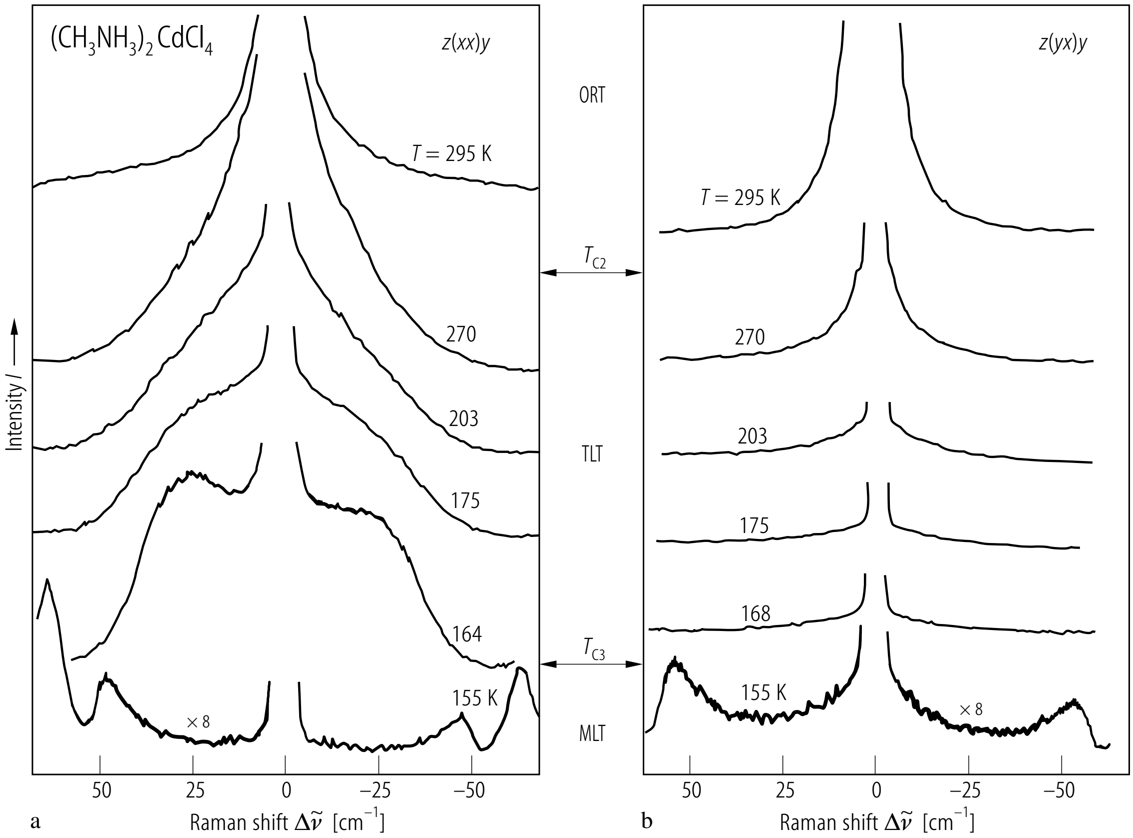

Fig. 2.27. $(CH_3NH_3)_2CdCl_4$. Intensity I versus Raman shift $\Delta\tilde{\nu}$, demonstrating the temperature evolution of the Rayleigh wing and low-lying Raman modes: in the α_{xx}-spectra **(a)** and α_{xy}-spectra **(b)**, scattering geometries: $z(xx)y$ and $z(yx)y$. The temperatures are indicated at the experimental curves $I(\Delta\tilde{\nu})$ and the sequence of phase transitions in the center (after [83M2]).

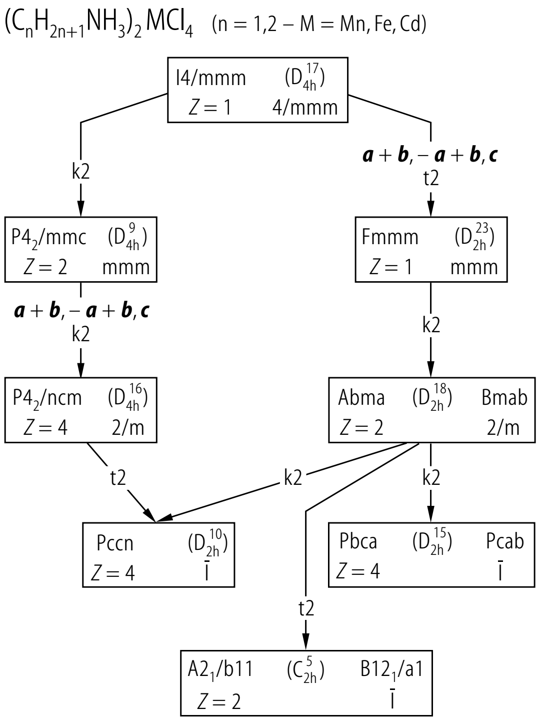
$(C_nH_{2n+1}NH_3)_2MCl_4$ (n = 1,2 – M = Mn, Fe, Cd)
I4/mmm (D_{4h}^{17}) Z = 1 4/mmm
k2
$\mathbf{a}+\mathbf{b}, -\mathbf{a}+\mathbf{b}, \mathbf{c}$ t2
$P4_2/mmc$ (D_{4h}^{9}) Z = 2 mmm
Fmmm (D_{2h}^{23}) Z = 1 mmm
$\mathbf{a}+\mathbf{b}, -\mathbf{a}+\mathbf{b}, \mathbf{c}$ k2
k2
$P4_2/ncm$ (D_{4h}^{16}) Z = 4 2/m
Abma (D_{2h}^{18}) Bmab Z = 2 2/m
t2
k2
k2
Pccn (D_{2h}^{10}) Z = 4 $\bar{1}$
Pbca (D_{2h}^{15}) Pcab Z = 4 $\bar{1}$
t2
$A2_1/b11$ (C_{2h}^{5}) $B12_1/a1$ Z = 2 $\bar{1}$

←

Fig. 2.29. $(C_nH_{2n+1}NH_3)_2MCl_4$ (n = 1, 2; M = Mn, Fe, Cd). Family-tree demonstrating the group-subgroup relations between the space groups of the different structural phases. Two international symbols for a space group indicate different crystallographic domains. k2 and t2 denote the character of the symmetry reducing steps. For further explanations, the reader is referred to the text (after [76H2, 77G3, 78H2]).

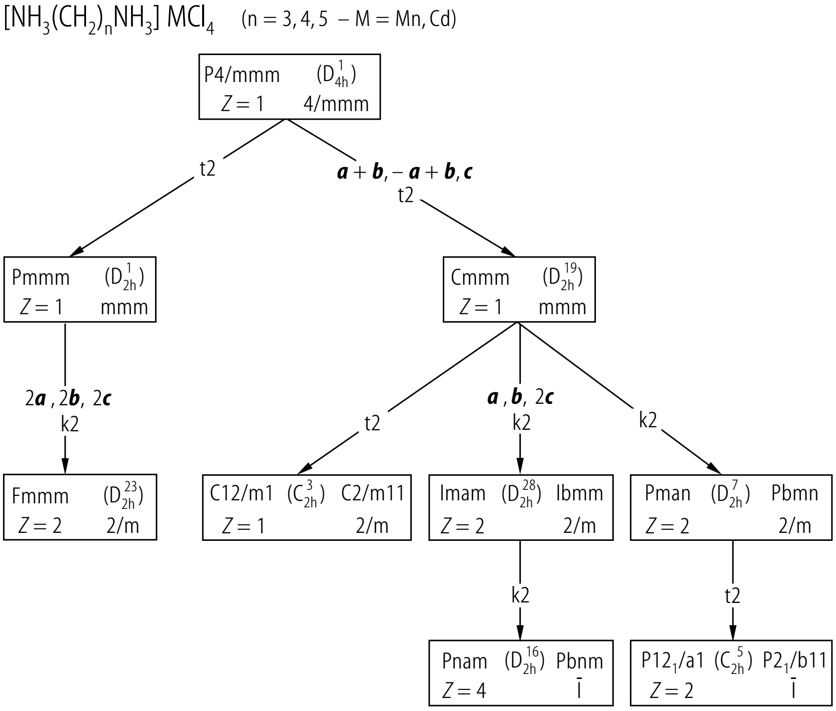
$[NH_3(CH_2)_nNH_3]\,MCl_4$ (n = 3, 4, 5 – M = Mn, Cd)
P4/mmm (D_{4h}^{1}) Z = 1 4/mmm
t2
$\mathbf{a}+\mathbf{b}, -\mathbf{a}+\mathbf{b}, \mathbf{c}$ t2
Pmmm (D_{2h}^{1}) Z = 1 mmm
Cmmm (D_{2h}^{19}) Z = 1 mmm
$2\mathbf{a}, 2\mathbf{b}, 2\mathbf{c}$ k2
t2
$\mathbf{a}, \mathbf{b}, 2\mathbf{c}$ k2
k2
Fmmm (D_{2h}^{23}) Z = 2 2/m
C12/m1 (C_{2h}^{3}) C2/m11 Z = 1 2/m
Imam (D_{2h}^{28}) Ibmm Z = 2 2/m
Pman (D_{2h}^{7}) Pbmn Z = 2 2/m
k2
t2
Pnam (D_{2h}^{16}) Pbnm Z = 4 $\bar{1}$
$P12_1/a1$ (C_{2h}^{5}) $P2_1/b11$ Z = 2 $\bar{1}$

Fig. 2.30. $[NH_3(CH_2)_nNH_3]MCl_4$ (n = 3, 4, 5; M = Mn, Cd). Family-tree demonstrating the group-subgroup relations between the space groups of the different structural phases. Two international symbols for a space group indicate different crystallographic domains. k2 and t2 denote the character of the symmetry reducing steps. For further explanations, the reader is referred to the text (after [78K1, 88C2]).

$(C_nH_{2n+1}NH_3)_2MCl_4$ (n = 1,2 – M = Mn, Fe, Cd)

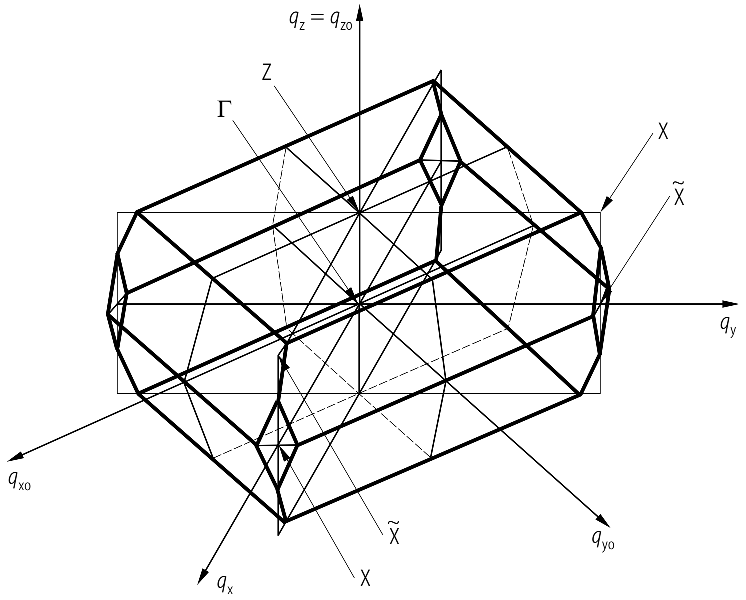

Fig. 2.31. $(C_nH_{2n+1}NH_3)_2MCl_4$ (n = 1, 2; M = Mn, Fe, Cd). Brillouin zone of the high temperature "parent" structure I4/mmm with the high symmetry points $\Gamma, X, \tilde{X}, Z$ and some of its equivalents in neighbouring zones. In addition to the appropriate (q_{x0}, q_{y0}, q_{z0}) coordinate system, also the (q_x, q_y, q_z) system is shown which is suitable for the low temperature phases (after [77G3]).

$(C_nH_{2n+1}NH_3)_2MCl_4$ (n = 1, 2 – M = Mn, Fe, Cd)

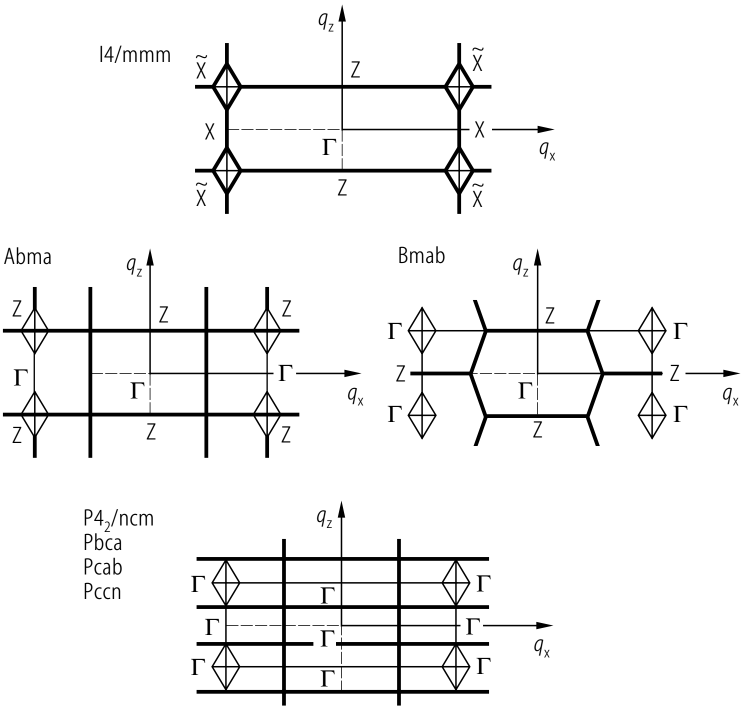

Fig. 2.32. $(C_nH_{2n+1}NH_3)_2MCl_4$ (n = 1, 2; M = Mn, Fe, Cd). (q_x, q_z)-plane in reciprocal space showing the boundaries of the Brillouin zones of the different structural phases (heavy lines) and indicating how the high symmetry points X and $\tilde{X}$ of I4/mmm become Γ and Z points in the reduced Brillouin zones of Abma or Bmab and finally all Z points Γ points in the even smaller Brillouin zone of $P4_2/ncm$. Light lines show the relation of these Brillouin zones to that of the "parent" phase I4/mmm (after [83M2]).

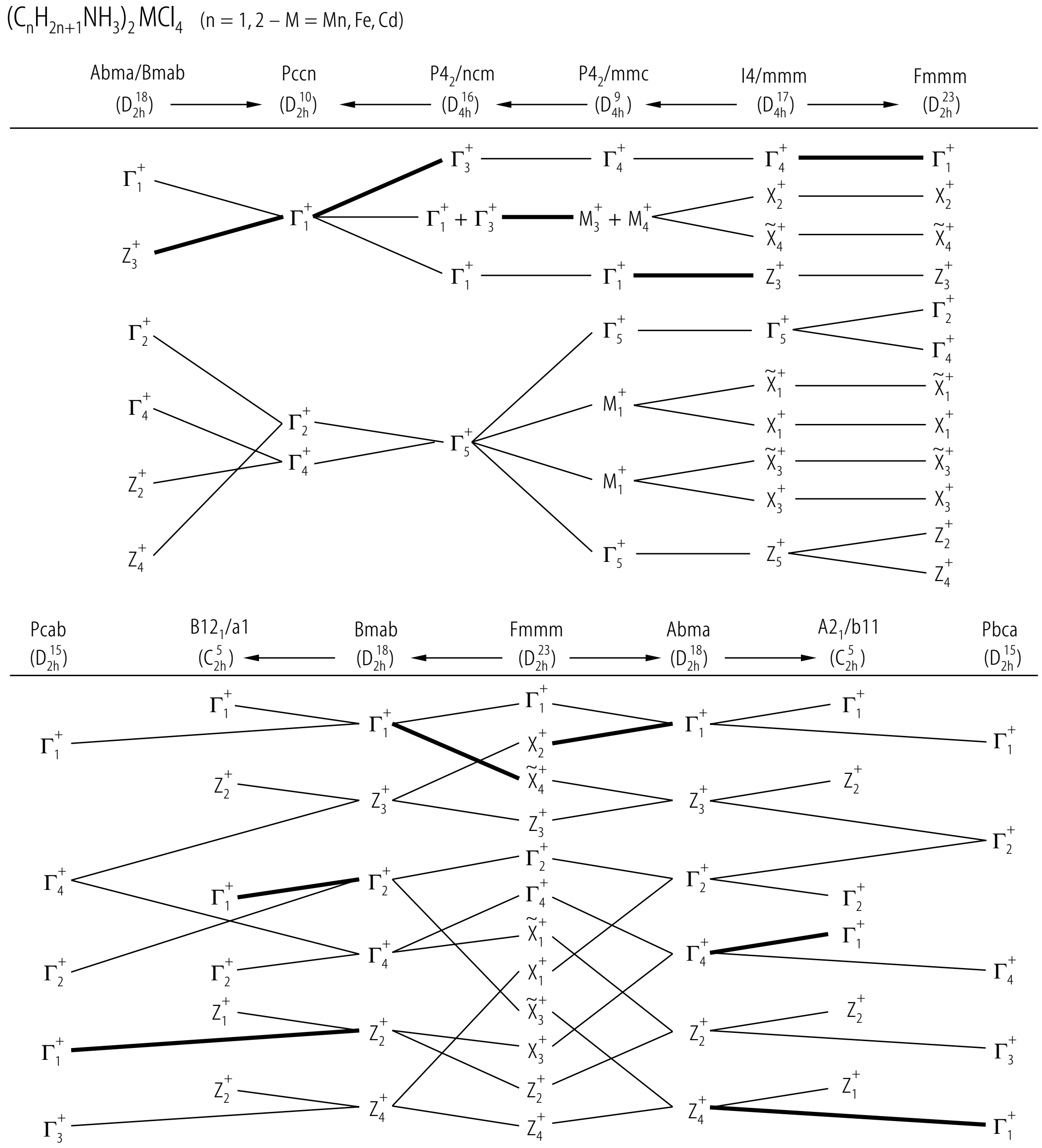
$(C_nH_{2n+1}NH_3)_2MCl_4$ (n = 1, 2 – M = Mn, Fe, Cd)
Abma/Bmab (D_{2h}^{18})
Pccn (D_{2h}^{10})
$P4_2/ncm$ (D_{4h}^{16})
$P4_2/mmc$ (D_{4h}^{9})
I4/mmm (D_{4h}^{17})
Fmmm (D_{2h}^{23})
Γ_1^+ Z_3^+ Γ_2^+ Γ_4^+ Z_2^+ Z_4^+
Γ_1^+ Γ_2^+ Γ_4^+
Γ_3^+ $\Gamma_1^+ + \Gamma_3^+$ Γ_1^+ Γ_5^+
Γ_4^+ $M_3^+ + M_4^+$ Γ_1^+ Γ_5^+ M_1^+ M_1^+ Γ_5^+
Γ_4^+ X_2^+ $\tilde{X}_4^+$ Z_3^+ Γ_5^+ $\tilde{X}_1^+$ X_1^+ $\tilde{X}_3^+$ X_3^+ Z_5^+
Γ_1^+ X_2^+ $\tilde{X}_4^+$ Z_3^+ Γ_2^+ Γ_4^+ $\tilde{X}_1^+$ X_1^+ $\tilde{X}_3^+$ X_3^+ Z_2^+ Z_4^+
Pcab (D_{2h}^{15})
$B12_1/a1$ (C_{2h}^{5})
Bmab (D_{2h}^{18})
Fmmm (D_{2h}^{23})
Abma (D_{2h}^{18})
$A2_1/b11$ (C_{2h}^{5})
Pbca (D_{2h}^{15})
Γ_1^+ Γ_4^+ Γ_2^+ Γ_1^+ Γ_3^+
Γ_1^+ Z_2^+ Γ_1^+ Γ_2^+ Z_1^+ Z_2^+
Γ_1^+ Z_3^+ Γ_2^+ Γ_4^+ Z_2^+ Z_4^+
Γ_1^+ X_2^+ $\tilde{X}_4^+$ Z_3^+ Γ_2^+ Γ_4^+ $\tilde{X}_1^+$ X_1^+ $\tilde{X}_3^+$ X_3^+ Z_2^+ Z_4^+
Γ_1^+ Z_3^+ Γ_2^+ Γ_4^+ Z_2^+ Z_4^+
Γ_1^+ Z_2^+ Γ_2^+ Γ_1^+ Z_2^+ Z_1^+
Γ_1^+ Γ_2^+ Γ_4^+ Γ_3^+ Γ_1^+

Fig. 2.33. $(C_nH_{2n+1}NH_3)_2MCl_4$ (n = 1, 2; M = Mn, Fe, Cd). Except from the compatibility relations between the irreducible representations of the space groups involved in the structural phase transitions of these compounds. The irreducible representations have been selected in order to show that in all cases one irreducible representation of a space group becomes the unity representation Γ_1^+ in one of its maximal subgroups, thus reflecting the symmetry of the order parameter (after [77G3]).

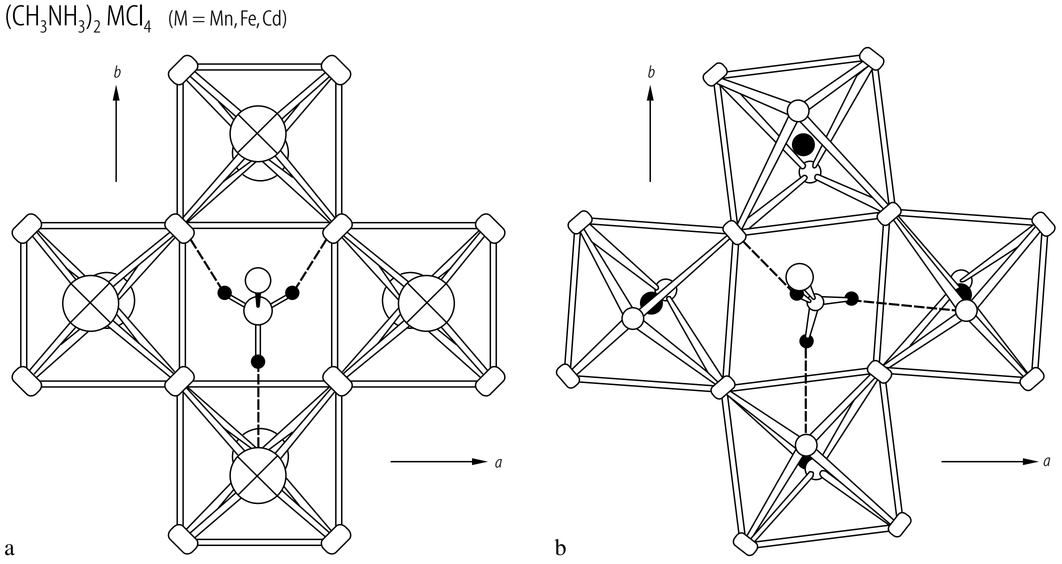

Fig. 2.34. $(CH_3NH_3)_2MCl_4$ (M = Mn, Fe, Cd). Schematic view of the $(CH_3NH_3)^+$-ion in its cavity of the MCl_6-octahedral layer (ORTEP drawing): **(a)** the "orthorhombic" configuration (structure: Bmab) and **(b)** the "monoclinic" configuration (structure: $B12_1/a1$). Broken lines indicate the hydrogen bonds. Only the H-atoms of the NH_3 group are shown, those of the CH_3 group omitted for more clarity (after [75C1, 76C2, 83M2]).

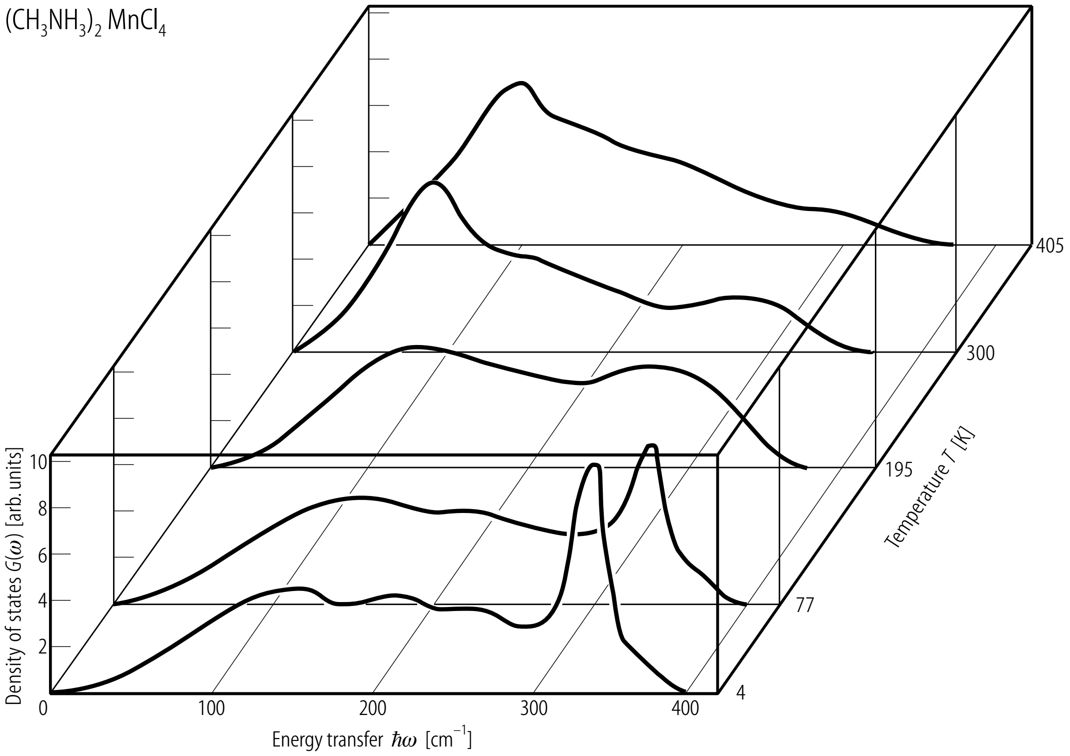

Fig. 2.35. $(CH_3NH_3)_2MnCl_4$. Generalized phonon density of states $G(\omega)$ as obtained from incoherent inelastic neutron scattering, i.e. only the motions of the protons contribute to $G(\omega)$ (after [78L1, 80K1]). The measurements have been performed at various temperatures in the different structural phases: 4 K and 77 K (MLT-phase), 195 K (TLT-phase), 300 K (ORT-phase) and 405 K (THT-phase).

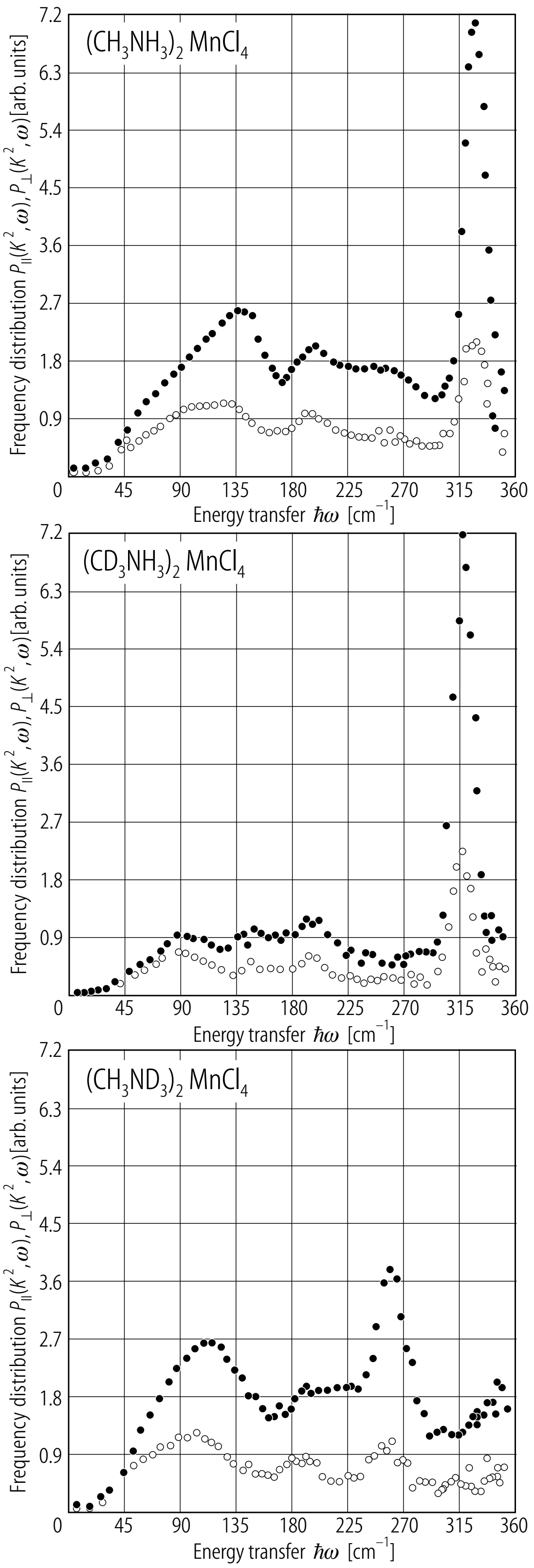

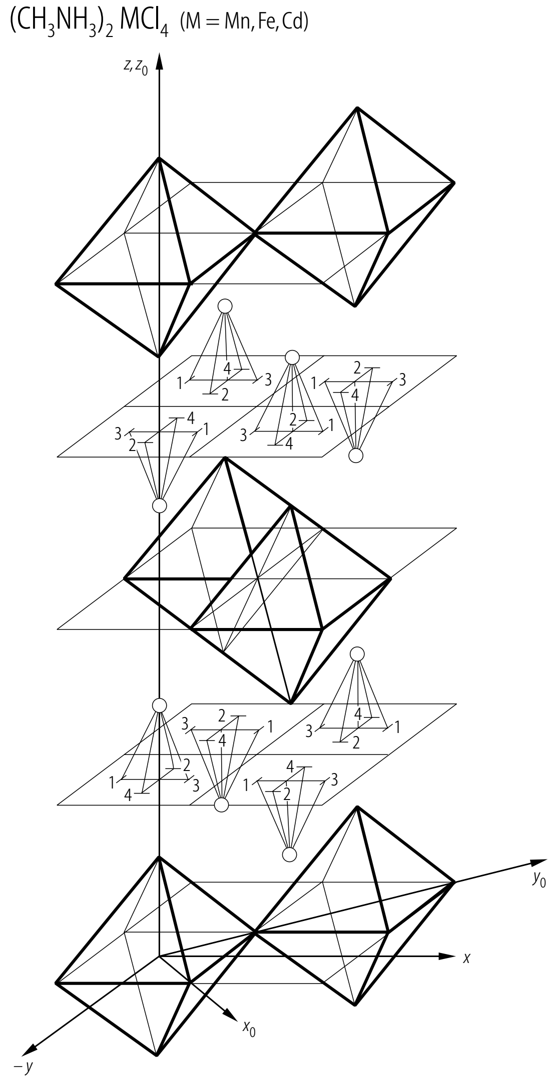

Fig. 2.38. $(CH_3NH_3)_2MCl_4$ with M = Mn, Fe, Cd. Schematic representation of the disordered THT-structure I4/mmm. The Cl^--ions are located at the corners of the octahedra, the M^{2+}-ions in their center are not shown. The $(CH_3NH_3)^+$ molecular groups are represented schematically by their C–N axis which is inclined by about 20° with respect to the $z = z_0$-axis. There are four possible orientations of the molecular groups numbered 1, 2, 3, 4 (taken from [77K1, 79K5]).

For Fig. 2.37 see next page.

←

Fig. 2.36. $(CH_3NH_3)_2MnCl_4$, $(CD_3NH_3)_2MnCl_4$ and $(CH_3ND_3)_2MnCl_4$. Frequency distributions $P_\parallel(K^2, \omega)$ (full circles) and $P_\perp(K^2, \omega)$ (open circles) for the average $\boldsymbol{K}$ essentially parallel and perpendicular to the layers, respectively, obtained from incoherent inelastic neutron scattering with the sample oriented at 45° and 135° to the incident beam, respectively. The data reflecting mainly the motions of the protons have been collected at 6 K (taken from [83M1]).

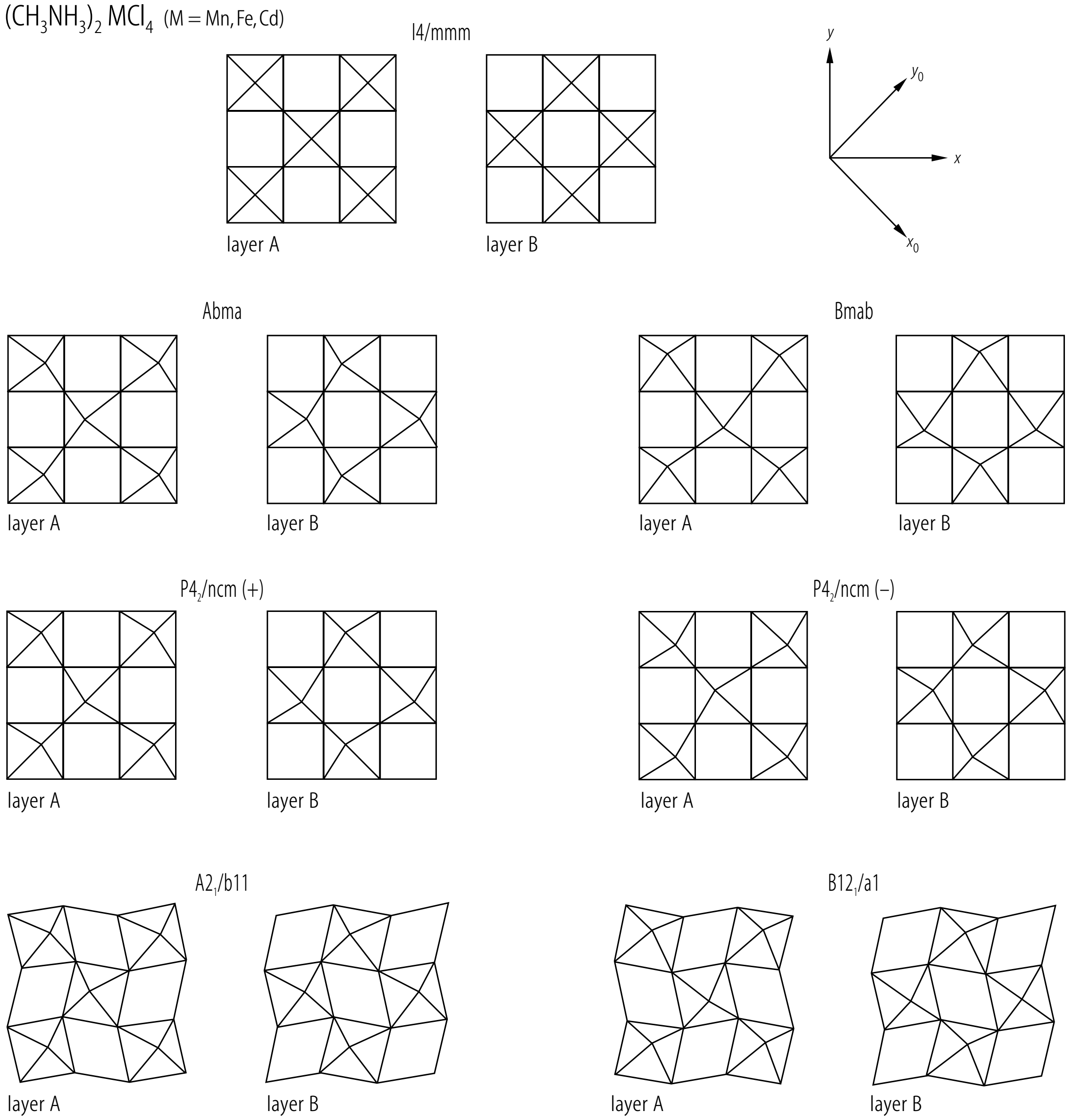

Fig. 2.37. $(CH_3NH_3)_2MCl_4$ with M = Mn, Fe, Cd. Schematic illustration of the tilting of the MCl_6 octahedra and the puckering of the octahedral layers in the THT-, ORT-, TLT- and MLT-phases. Layers A and B correspond to the planes $z = 0$ and $z = 1/2$, respectively. The (x_0, y_0, z_0) and (x, y, z) coordinate systems are also indicated (taken from [83M2]).

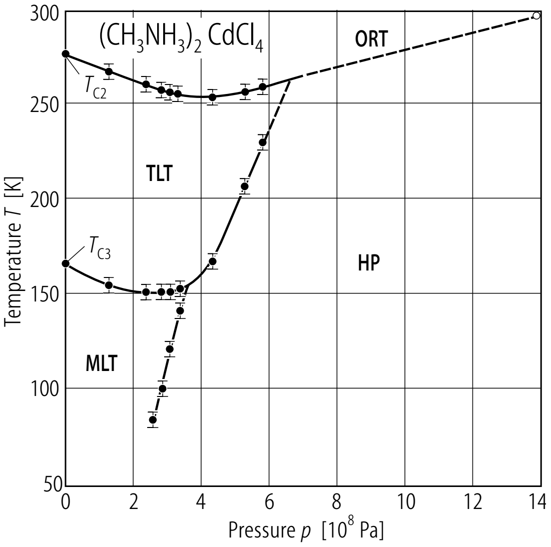

Fig. 2.39. $(CH_3NH_3)_2CdCl_4$. (T, p)-phase diagram, showing the critical temperatures for the structural phase transitions as a function of hydrostatic pressure and also the critical pressure for the transition to the high pressure phase (HP), taken from [83M3]. The data points have been obtained from Raman spectra (full circles) [83M3] and from other experimental data (open circle) [78H1].

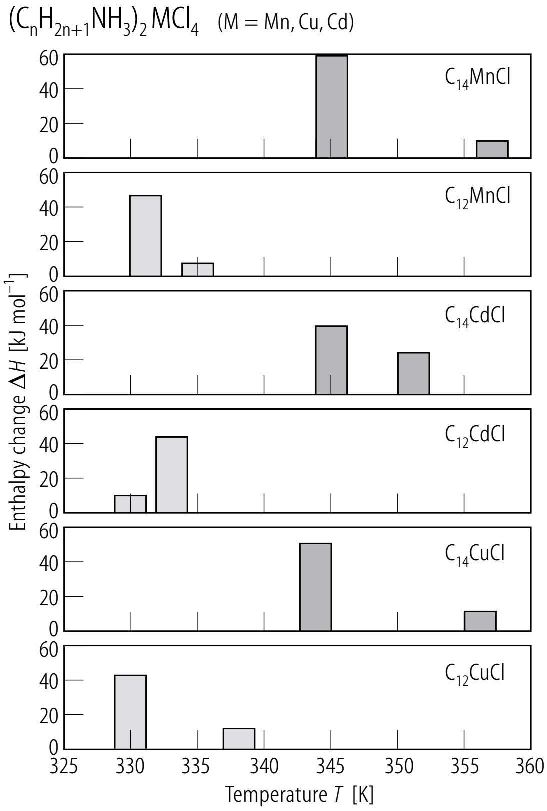

Fig. 2.40. $(C_nH_{2n+1}NH_3)_2MCl_4$ with M = Mn, Cu, Cd and n = 12, 14, abbreviated C_nMCl. Graphic representation of the enthalpy changes ΔH connected with the structural phase transitions. The data have been obtained by d.s.c. (taken from [81N]).

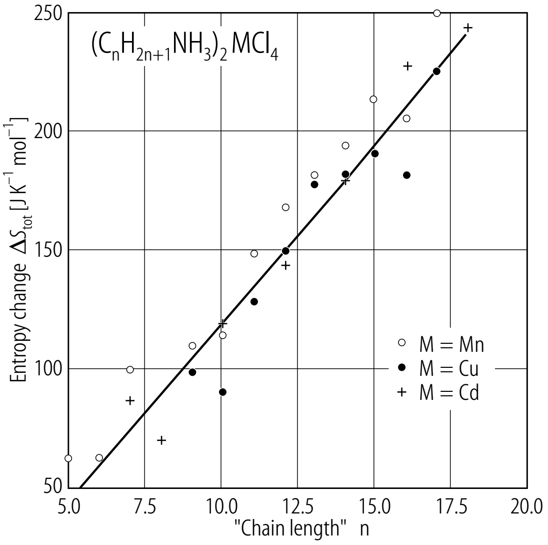

Fig. 2.41. $(C_nH_{2n+1}NH_3)_2MCl_4$ with M = Mn, Cu, Cd. Total change in entropy ΔS_{tot} (cf. Eq. 2.39) versus number n of C-atoms in the hydrocarbon chains. The values of ΔS_{tot} have been derived from the data in Table 4. The line corresponds to the value of ΔS for the melting of the hydrocarbon chains, as obtained for n-paraffines (cf. Eq. 2.41 and [79K1]).

$[NH_3(CH_2)_3NH_3]$ $MnCl_4$

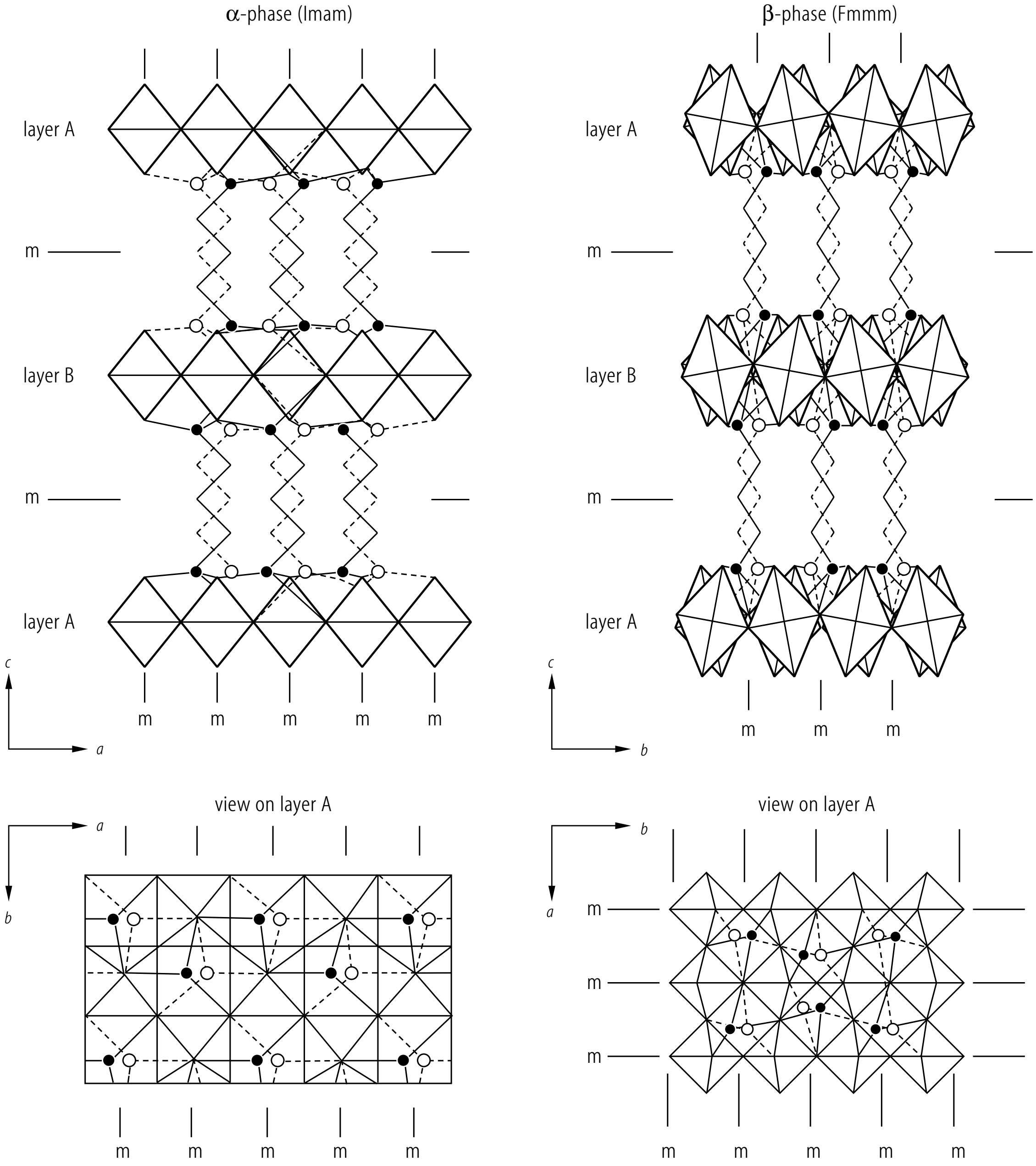

Fig. 2.42. $[NH_3(CH_2)_3NH_3]MnCl_4$. Schematic pictures of the crystal structures in the α- (Imam) and β-phases (Fmmm). The two possible orientations of the chains are shown by full and dashed lines. Layers A and B correspond to the planes $z = 0$ and $z = 1/2$, respectively. For better clarity, only the NH_3 groups above the layer are shown in the view on layer A, together with the H-bonding scheme. The mirror planes denoted by "m" are important symmetry elements of these structures (taken from [78K1]).

$[NH_3(CH_2)_3NH_3]$ $MnCl_4$

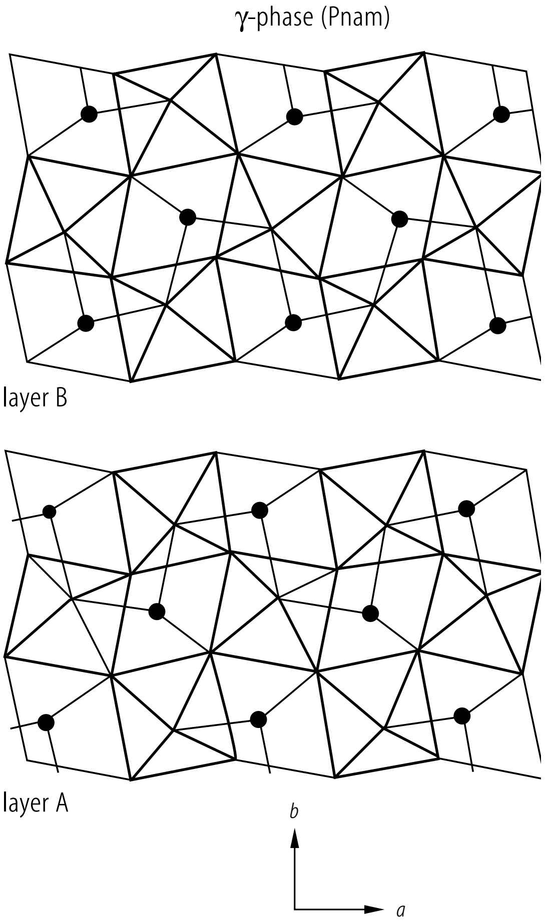

Fig. 2.43. $[NH_3(CH_2)_3NH_3]MnCl_4$. Crystal structure of the γ-phase (Pnam), view on layers A and B corresponding to the planes $z = 0$ and $z = 1/2$, respectively. For more clarity, only the NH_3 groups above the layers A and B are shown, together with their H-bonding scheme (taken from [78K1]).

$[NH_3(CH_2)_5NH_3]$ $CdCl_4$

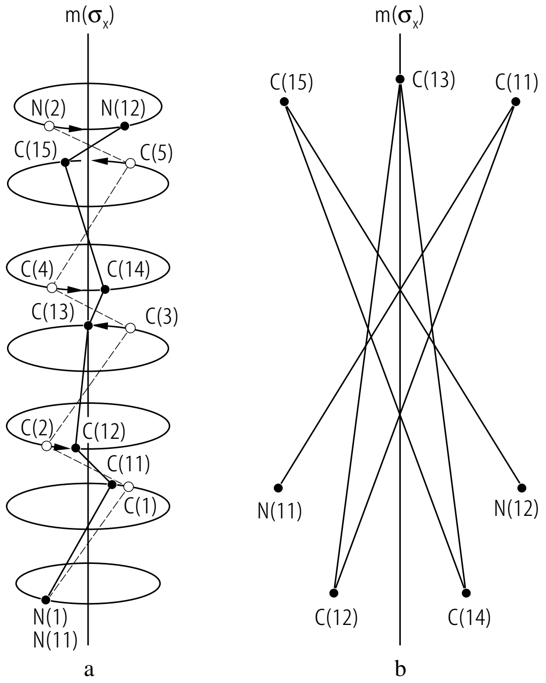

Fig. 2.44. $[NH_3(CH_2)_5NH_3]CdCl_4$. Schematic representation of a "twisted" chain which occurs in the OHT-phase (Imam/Ibmm) as it has been introduced into the structure refinement. The twisted chain N(11)–C(1n)–N(12) is shown by full lines, the corresponding trans chain N(1)–C(n)–N(2) by dashed lines, for both n = 1, 2, ..., 5; **(a)** perspective view of the chains, **(b)** projection onto the (*a*, *b*)-plane (taken from [87N1, 87N2]).

Table 2. Crystallographic Data

Compound	T [K]	Lattice parameters [nm] and angles [deg]	Ref.	Remarks
a) Fluorides				
K_2MgF_4	295	$a = b = 0.3980$ $c = 1.3179$	82B2	[III/12a], s.g.: I4/mmm (No. 139), c.s.d.
Rb_2MgF_4	295	$a = b = 0.40584(5)$ $c = 1.37991(7)$	73S1	[III/12a] rep. – s.g.: I4/mmm (No. 139)
	4.2	$a = b = 0.40447(19)$ $c = 1.3743(5)$	73S1	[III/12a], s.g.: I4/mmm (No. 139)
Tl_2MgF_4		$a = b = 0.4007$ $c = 1.443$	66V	[III/4a] rep. – c. sym.: tetragonal
$(NH_4)_2MgF_4$				
THT-phase	295	$a = b = 0.40567(1)$ $c = 1.38354(6)$	96S2	[III/4a], s.g.: I4/mmm (No. 139), c.s.d.
MLT-phase	20	$a = 0.57039(7)$ $b = 0.57298(8)$ $c = 1.3821(2)$ $\beta = 86.995(7)°$	96S2	s.g.: P12$_1$/c1 (No. 14), c.s.d.
K_2MnF_4	295	$a = b = 0.41664(8)$ $c = 1.3217(6)$*)	74B1	[III/12a] rep. – s.g.: I4/mmm (No. 139)
	295	$a = b = 0.4171(3)$ $c = 1.3259(16)$*)	68L1	[III/12a], s.g.: I4/mmm (No. 139), c.s.d.
	4.2	$a \approx b = 0.5871(4)$ $c = 1.3242(10)$	68L1	[III/12a], s.g.: Acam or Bbcm (No. 64), c.s.d., (m.u.c.)
*) *The first data are more precise and the second ones provide the complete structure at 295 and 4.2 K*				
$K_3Mn_2F_7$	295	$a = b = 0.4187$ $c = 2.1586$	82B2	s.g.: I4/mmm (No. 139), c.s.d.
	4.2	$a = b = 0.4181(3)$ $c = 2.155(2)$	79U	s.g.: I4/mmm (No. 139), (c.u.c.)
$(Rb_xK_{1-x})_2MnF_4$				
x = 0 (K_2MnF_4)	295	$a = b = 0.4188$ $c = 1.330$	64C1	s.g.: I4/mmm (No. 139)
x = 0.25	295	$a = b = 0.4202$ $c = 1.348$	64C1	s.g.: I4/mmm (No. 139)
x = 0.5	295	$a = b = 0.4219$ $c = 1.366$	64C1	s.g.: I4/mmm (No. 139)
x = 0.75	295	$a = b = 0.4232$ $c = 1.378$	64C1	s.g.: I4/mmm (No. 139)
x = 1 (Rb_2MnF_4)	295	$a = b = 0.4249$ $c = 1.392$	64C1	s.g.: I4/mmm (No. 139)
Rb_2MnF_4	295	$a = b = 0.42295(18)$ $c = 1.38883(14)$	73S1	[III/4a], s.g.: I4/mmm (No. 139)
	4.2	$a = b = 0.42124(14)$ $c = 1.3834(8)$	73S1	[III/4a], s.g.: I4/mmm (No. 139), (c.u.c.)
	12	$a = b$, c under hydrostatic pressure	94I1	$0 \le p \le 1.5$ GPa, s.g.: I4/mmm, (c.u.c.)
$Rb_3Mn_2F_7$	295	$a = b = 0.4222(4)$ $c = 2.226(2)$	76N1	s.g.: I4/mmm (No. 139)
Cs_2MnF_4	12	$a = b = 0.4313$ $c = 1.460$*)	94I1	s.g.: I4/mmm (No. 139), (c.u.c.)
	12	$a = b$, c under hydrostatic pressure	94I1	$0 \le p \le 0.7$ GPa, s.g.: I4/mmm, c.u.c.)
*) *For* Cs_2MnF_4, *two modifications have been reported*: β-Cs_2MnF_4 *(I4/mmm, see above) and* α-Cs_2MnF_4 *with as yet unknown structure* [64C1]				

Table 2. Crystallographic Data *(continued)*

Compound	T [K]	Lattice parameters [nm] and angles [deg]	Ref.	Remarks
K_2FeF_4	295	$a = b = 0.414(1)$ $c = 1.300(1)$	82T1	[III/4a], s.g. I4/mmm (No. 139)
	46	$a = 0.5855(3)$ $b = 0.5865(3)$ $c = 1.2894(1)$	81O	c. sym.: orthorh. (m.u.c.)
	4.2	$a = b = 0.412(1)$ $c = 1.286(3)$	82T1	s.g.: I4/mmm (No. 139), (c.u.c.)
$K_3Fe_2F_7$		$a = b = 0.4130(4)$ $c = 2.115(2)$	65P	[III/4a] rep. – s.g.: I4/mmm (No. 139)
Rb_2FeF_4	55	$a = b = 0.4214(8)$ $c = 1.353(2)$	70B1	[III/12a] rep. – s.g.: I4/mmm (No. 139)
Tl_2FeF_4		$a = b = 0.4194$ $c = 1.391$	66V	[III/12a] rep. – c. sym.: tetragonal
K_2CoF_4	295	$a = b = 0.4073$ $c = 1.3087$	82B2	[III/12a], s.g.: I4/mmm (No. 139), c.s.d.
	105	$a \approx b = 0.5737$ $c = 1.3019$	84C1	s.g.: Acam or Bbcm (No. 64), (m.u.c.)
$K_3Co_2F_7$	295	$a = b = 0.4074$ $c = 2.1163$	82B2	s.g.: I4/mmm (No. 139), c.s.d.
Rb_2CoF_4	295	$a = b = 0.4150(1)$ $c = 1.3717(3)$	69B1	[III/12a] rep. – s.g.: I4/mmm (No. 139)
	78	$a \approx b = 0.5817$ $c = 1.3615$	83I1	s.g.: Acam or Bbcm (No. 64), (m.u.c.)
Tl_2CoF_4		$a = b = 0.411$ $c = 1.405$	63R	[III/4a] rep. – c. sym.: tetragonal
K_2NiF_4	295	$a = b = 0.4012$ $c = 1.3076$	82B2	[III/4a], s.g.: I4/mmm (No. 139), c.s.d.
	80	$a = b = 0.3994(4)$ $c = 1.304(1)$	70B1	[III/12a] rep. – s.g.: I4/mmm (No. 139), (c.u.c.)
$K_3Ni_2F_7$	295	$a = b = 0.4015$ $c = 2.1073$	82B2	s.g.: I4/mmm (No. 139), c.s.d.
Rb_2NiF_4		$a = b = 0.4087$ $c = 1.371$	62R	[III/4a] rep. – s.g.: I4/mmm (No. 139)
	78	$a \approx b = 0.5733$ $c = 1.3550$	83I1	s.g.: Acam or Bbcm (No.64), (m.u.c.)
Tl_2NiF_4		$a = b = 0.4051$ $c = 1.422$	62R	[III/4a] rep. – s.g.: I4/mmm (No. 139)
$(NH_4)_2NiF_4$		$a = b = 0.4084$ $c = 1.379$	62R	[III/4a] rep. – s.g.: I4/mmm (No. 139)
K_2CuF_4	295	$a = b = 0.5858(5)$ $c = 2.542(2)$*)	74H1	[III/12a], s.g.: $I\bar{4}c2$ (No. 120), c.s.d.
	295	$a \approx b = 0.58655(7)$ $c = 1.2734(2)$*)	83H1	s.g.: Bbcm (No. 64), c.s.d., (2nd d.: Acam)
	2	$a = b = 0.4119(5)$ $c = 1.2678(5)$	78W1	ref. in I4/mmm (No. 139), (m.u.c., not c.u.c.)

*) *Both structures reported for* K_2CuF_4 ($I\bar{4}c2$ and Bbcm) *describe well the deformation of the* CuF_6 *octahedra due to the orbital ordering and the collective Jahn-Teller effect. They differ only by the stacking of the layers (cf.* Fig. 2.8*). Theoretical considerations show that both are equally possible with nearly the same lattice energy* [95N2]

Compound	T [K]	Lattice parameters [nm] and angles [deg]	Ref.	Remarks
K_2CuF_4: *high pressure modification,* $p > p_C = 9.5$ GPa			96I1	
$p = 14$ GPa	295	$a = 0.6672$ $b = 0.4189$ $c = 1.1165$	98I	s.g.: Ammm (No. 65)
$K_3Cu_2F_7$	295	$a = b = 0.4156(3)$ $c = 2.052(3)$	81H1	ref. in I4/mmm (No. 139), orthorh. deformat.
Rb_2CuF_4	295	$a = b = 0.4238$ $c = 1.329$	88D1	[III/4a], ref. in I4/mmm (No. 139)

Table 2. Crystallographic Data *(continued)*

Compound	T [K]	Lattice parameters [nm] and angles [deg]	Ref.	Remarks
Cs_2CuF_4		$a = b = 0.6234(8)$ $c = 2.806(1)$	76D4	s.g.: $I\bar{4}c2$ (No. 120)
Tl_2CuF_4		$a = b = 0.4199$ $c = 1.366$	63R	[III/4a] rep. – ref. in I4/mmm (No. 139)
K_2ZnF_4	295	$a = b = 0.4058(2)$ $c = 1.3109(3)$	80H1	[III/12a], s.g.: I4/mmm (No. 139), c.s.d.
$K_3Zn_2F_7$	295	$a = b = 0.4060(3)$ $c = 2.1171(9)$	80H1	[III/4a], s.g.: I4/mmm (No. 139), c.s.d.
Rb_2ZnF_4	295	$a = b = 0.41364(20)$ $c = 1.3706(2)$	73S1	[III/12a] rep. – s.g.: I4/mmm (No. 139)
	4.2	$a = b = 0.41125(10)$ $c = 1.3639(3)$	73S1	[III/12a], s.g.: I4/mmm (No. 139)
Tl_2ZnF_4		$a = b = 0.4105$ $c = 1.410$	66V	[III/4a] rep. – s.g.: I4/mmm (No. 139)
$(NH_4)_2ZnF_4$		$a = b = 0.414$ $c = 1.397$	64C2	[III/4a] rep. – s.g.: I4/mmm (No. 139)
K_2CdF_4	295	$a = b = 0.43612(8)$ $c = 1.3266(2)$	73S1	[III/12a] rep. – s.g.: I4/mmm (No. 139)
Rb_2CdF_4	295	$a = b = 0.44017(8)$ $c = 1.39376(12)$	73S1	[III/12a] rep. – s.g.: I4/mmm (No. 139)
	125	$a = b = 0.43874(10)$ $c = 1.3873(2)$	73S1	[III/12a], s.g.: I4/mmm (No. 139)
$Rb_3Cd_2F_7$		$a = b = 0.4403$ $c = 2.271$	68C2	[III/4a] rep. – s.g.: I4/mmm (No. 139)
Cs_2CdF_4	295	no structural data; s.g.: I4/mmm (No. 139) predicted from a crystal-chemical analysis [85B2]. The structure I4/mmm also in accordance with EPR results: $Cs_2CdF_4 : Cr^{3+}$ [86A4], $Cs_2CdF_4 : Gd^{3}$ [87T]		
b) Chlorides, Bromides and Iodides with inorganic A^+-ions				
Rb_2MgCl_4		$a = b = 0.4986(2)$ $c = 1.6172(6)$	73W1	[III/12a] rep. – s.g.: I4/mmm (No. 139)
Rb_2MgCl_3Br		$a = b = 0.5004(5)$ $c = 1.661(1)$	73W1	[III/12a] rep. – s.g.: I4/mmm (No. 139)
$Rb_2MgCl_2Br_2$		$a = b = 0.5028(4)$ $c = 1.697(1)$	73W1	[III/12a] rep. – s.g.: I4/mmm (No. 139)
K_2CrCl_4		$a = 0.731$ $b = 0.734$ $c = 1.497$	73D1	[III/4a], orthorhombic unit cell
Rb_2CrCl_4 [1])	293	$a \approx b = 0.7272(18)$ $c = 1.577(4)$	83J1	[III/4a], s.g.: Acam or Bbcm (No. 64) c.s.d.
	77	$a \approx b = 0.7183(18)$ $c = 1.567(4)$	83J1	s.g.: Bbcm (No. 64), c.s.d., (2nd d.: Acam)
	5.5	$a \approx b = 0.7193(18)$ $c = 1.572(4)$	83J1	s.g.: Bbcm (No. 64), (c.s.g.), c.s.d.
[1]) *In this structure refinement, only the deformation of the octahedra was varied in an otherwise tetragonal crystal. Therefore $a \approx b$ etc.*				
Rb_2CrCl_4 [2])	78	$a = 0.7211(2)$ $b = 0.7185(2)$ $c = 1.5698(2)$	86F1	s.g.: Bbcm (No. 64), c.s.d., (2nd d.: Acam)
	4.2	$a = 0.7197(2)$ $b = 0.7173(2)$ $c = 1.5701(2)$	86F1	s.g.: Bbcm (No. 64), (c.s.g.), c.s.d.
[2]) *In this refinement, not only the deformation of the octahedra but also the lattice parameters have been varied according to the orthorhombic symmetry ($a \neq b$). Comparison of the results of the two refinements shows that the differences are small.*				

Table 2. Crystallographic Data *(continued)*

Compound	*T* [K]	Lattice parameters [nm] and angles [deg]	Ref.	Remarks
Rb_2CrCl_3Br	295	$a = b = 0.5140$ $c = 1.603$	83W1	ref. in I4/mmm (No. 139)
	90	$a = 0.7201(5)$ $b = 0.7201(5)$ $c = 1.6073(2)$	85F1	s.g.: Bbcm (No. 64), c.s.d., (2nd d.: Acam)
	4.2	$a = 0.7189(5)$ $b = 0.7193(5)$ $c = 1.6062(2)$	85F1	s.g.: Bbcm (No. 64) (c.s.g.), c.s.d.
Rb_2CrCl_3I	295	$a = b = 0.5158$ $c = 1.582$	83W1	ref. in I4/mmm (No. 139)
$Rb_2CrCl_2Br_2$	295	$a = b = 0.5179$ $c = 1.642$	83W1	ref. in I4/mmm (No. 139)
	90	$a = 0.7231(5)$ $b = 0.7248(5)$ $c = 1.6385(5)$	85F1	s.g.: Bbcm (No. 64), c.s.d., (2nd d.: Acam)
	4.2	$a = 0.7116(14)$ $b = 0.7234(14)$ $c = 1.6373(5)$	85F1	s.g.: Bbcm (No. 64), (c.s.g.), c.s.d.
$Rb_2CrCl_2I_2$	295	$a = b = 0.5228$ $c = 1.742$	83W1	ref. in I4/mmm (No. 139)
	110	$a = 0.7332(5)$ $b = 0.7340(5)$ $c = 1.7345(3)$	85F1	s.g.: Bbcm (No. 64), c.s.d., (2nd d.: Acam)
	4.2	$a = 0.7313(5)$ $b = 0.7321(5)$ $c = 1.7316(3)$	85F1	s.g.: Bbcm (No. 64), (c.s.g.), c.s.d
$Rb_2CrClBr_3$	295	$a = b = 0.5256$ $c = 1.651$	83W1	ref. in I4/mmm (No. 139)
Cs_2CrCl_4	294	$a = b = 0.5218(1)$ $c = 1.6435(3)$	74H2	ref. in I4/mmm (No. 139)
	78	$a = b = 0.5170(1)$ $c = 1.6377(3)$	74H2	ref. in I4/mmm (No. 139)
	4.2	$a = b = 0.5163(1)$ $c = 1.6379(3)$	74H2	ref. in I4/mmm (No. 139)
$(NH_4)_2CrCl_4$		$a = b = 0.516$ $c = 1.563$	70H	ref. in I4/mmm (No. 139)
$K_3Mn_2Cl_7$	300	$a = b = 0.5027(5)$ $c = 2.5325(10)$	65S	s.g.: I4/mmm (No. 139), c.s.d.
Rb_2MnCl_4		$a = b = 0.505(2)$ $c = 1.614(5)$ *)	77G1	[III/12a], s.g.: I4/mmm (No. 139), c.s.d.
	293	$a = b = 0.5056$ $c = 1.6161$ *)	89S1	s.g.: I4/mmm (No. 139)
	4.2	$a = b = 0.5024$ $c = 1.6093$	89S1	s.g.: I4/mmm (No. 139), (c.u.c.)
*) *The first data provide the complete structure, probably at room temperature, while the second ones are more precise*				
$Rb_3Mn_2Cl_7$	295	$a = b = 0.505(1)$ $c = 2.614(5)$	78G	s.g.: I4/mmm (No. 139), c.s.d.
Rb_2MnCl_3Br		$a = b = 0.5060(3)$ $c = 1.6588(8)$	74W1	s.g.: I4/mmm (No. 139)
$Rb_2MnCl_2Br_2$		$a = b = 0.5073(2)$ $c = 1.6924(3)$	74W1	s.g.: I4/mmm (No. 139)
$Rb_2MnCl_2I_2$		$a = b = 0.5162(2)$ $c = 1.784(1)$	74W1	s.g.: I4/mmm (No. 139)
Rb_2MnBr_4	295	$a = b = 0.537(2)$ $c = 1.732(5)$	79G2	s.g.: I4/mmm (No. 139), c.s.d.
Cs_2MnCl_4	295	$a = b = 0.5135(3)$ $c = 1.688(1)$	74W1	[III/12a], s.g.: I4/mmm (No. 139)
Besides the structure at 295 K (I4/mmm) with corner-sharing $MnCl_6$ *octahedra, there is a high temperature modification of* Cs_2MnCl_4 *with isolated* $MnCl_6$ *tetrahedra* [66S1]				
Cs_2MnCl_3Br		$a = b = 0.5169(3)$ $c = 1.725(1)$	74W1	s.g.: I4/mmm (No. 139)

Table 2. Crystallographic Data *(continued)*

Compound	T [K]	Lattice parameters [nm] and angles [deg]	Ref.	Remarks
$(NH_4)_2MnCl_4$		$a = b = 0.5049(2)$ $c = 1.6148(7)$	74W1	s.g.: I4/mmm (No. 139)
$(NH_4)_2MnCl_2Br_2$		$a = b = 0.5055(5)$ $c = 1.683(1)$	74W1	s.g.: I4/mmm (No. 139)
$(NH_4)_2MnCl_2I_2$		$a = b = 0.5102(4)$ $c = 1.771(1)$	74W1	s.g.: I4/mmm (No. 139)
Rb_2CuCl_4*)	295	$a = 0.7197(2)$ $b = 0.7187(2)$ $c = 1.5534(1)$	74W2	[III/12a], s.g.: Bbcm (No. 64), c.s.d.
$(NH_4)_2CuCl_4$*)	295	$a = 0.720(1)$ $b = 0.720(1)$ $c = 1.546(2)$	64W	[III/4a], s.g.: Bbcm (No. 64), c.s.d.
*) *For* Rb_2CuCl_4 *and* $(NH_4)_2CuCl_4$, *X-ray diffraction data have also been indexed and analysed in the space group* Pnma [71J1] *which is the structure of* Cs_2CuCl_4 *with isolated* $CuCl_4$ *tetrahedra. But in view of the results on* $(C_nH_{2n+1}NH_3)_2CuCl_4$ *the above data seem to be more reliable*				
Rb_2CuCl_3Br	295	$a = 0.7206(4)$ $b = 0.7224(4)$ $c = 1.5920(4)$	74W2	[III/12a], s.g.: Bbcm (No. 64), c.s.d.
$Rb_2CuCl_2Br_2$	295	$a = 0.7242(2)$ $b = 0.7260(2)$ $c = 1.6252(2)$	74W2	[III/12a], s.g.: Bbcm (No. 64), c.s.d.
Rb_2CdCl_4				
α-phase (G_0)	295	$a = b = 0.5207(1)$ $c = 1.6169(2)$	89K	s.g.: I4/mmm (No. 139), c.s.d.
	160	$a = b = 0.5190(1)$ $c = 1.6109(2)$	89K	s.g.: I4/mmm (No. 139), c.s.d.
β-phase (G_1)	105	$a = 0.7307(3)$ $b = 0.7362(3)$ $c = 1.6045(4)$	89K	s.g.: Pccn*) (No. 56), c.s.d.
*) ^{87}Rb-NMR *results* [90A4] *are in favour of the space groups* Abma *or* Bmab *for the* β*-phase* (G_1) *as proposed earlier* [85C1, 85C2] *for this phase*				
$Rb_3Cd_2Cl_7$				
α-phase (G_0)	293	$a = b = 0.5197$ $c = 2.6366$	88A1	s.g.: I4/mmm (No. 139)
β-phase (G_1)	190	$a = 0.7341$ $b = 0.7341$ $c = 2.6235$	88A1	s.g.: Bbmm (No. 63), 2nd d.: Amam
γ-phase (G_2)	150	$a = b = 0.7339$ $c = 2.6157$	88A1	s.g.: $P4_2/mnm$ (No. 136)
$Rb_4Cd_3Cl_{10}$				
α-phase (G_0)	293	$a = b = 0.5182$ $c = 3.6693$	90B2	s.g.: I4/mmm (No. 139)
β-phase (G_1)	210	$a = 0.7318$ $b = 0.7318$ $c = 3.6572$	90B2	s.g.: Bmcb = Bmab (No. 64), 2nd d.: Abma
γ-phase (G_2)	150	$a = b = 0.7317$ $c = 3.6430$	90B2	s.g.: $P4_2/ncm$ (No. 138)
δ-phase (G_3)	100	$a = 0.7476$ $b = 0.7166$ $c = 3.6256$ $\beta = 90.64°$	90B2	s.g.: $B12_1/c1 = B12_1/a1$ (No. 14), 2nd d.: $A2_1/b11$
Cs_2CdCl_4		$a = b = 0.526$ $c = 1.688$	64S1	[III/4a] rep. – s.g.: I4/mmm (No. 139)
$Cs_3Cd_2Cl_7$		$a = b = 0.5241(5)$ $c = 2.724(1)$	68S1	s.g.: I4/mmm (No. 139)

Table 2. Crystallographic Data *(continued)*

Compound	T [K]	Lattice parameters [nm] and angles [deg]			Ref.	Remarks
c) Chlorides and Bromides with organic A^+-ions						
$(CH_3NH_3)_2CrCl_4$	295	$a = 0.727$	$b = 0.743$	$c = 1.889$	78B1	ind. in Cmca (No. 64), [85B1]: s.g.: Aba2 (No. 41)
	87	$a = 0.719$	$b = 0.743$ $\beta = 90.8°$	$c = 1.880$	78B1	ind. in P12$_1$/c1 (No. 14)
	4.2	$a = 0.716$	$b = 0.742$ $\beta = 90.9°$	$c = 1.882$	78B1	ind. in P12$_1$/c1 (No. 14)
$(C_2H_5NH_3)_2CrCl_4$	295	$a = 0.759$	$b = 0.735$	$c = 2.141$	78B1	ind. in Cmca (No. 64)
$(C_3H_7NH_3)_2CrCl_4$	295	$a = 0.761$	$b = 0.736$	$c = 2.471$	82S1	ind. in Cmca (No. 64)
$(C_5H_{11}NH_3)_2CrCl_4$	295	$a = 0.747$	$b = 0.737$	$c = 3.562$	82S1	ind. in Cmca (No. 64)
$(C_{12}H_{25}NH_3)_2CrCl_4$	295	$a = 0.745$	$b = 0.720$	$c = 6.21$	82S1	ind. in Cmca (No. 64)
$(C_6H_5CH_2NH_3)_2CrCl_4$	295	$a = 0.760$	$b = 0.744$	$c = 3.145$	86B1	ind. in Cmca (No. 64)
$(C_6H_5CH_2NH_3)_2CrBr_4$	295	$a = 0.786$	$b = 0.767$	$c = 3.247$	87B1	ind. in Cmca (No. 64)
$(CH_3NH_3)_2MnCl_4$						
THT-phase	404	$a = b = 0.5133(4)$		$c = 1.951(1)$	75H1	[III/12a], s.g.: I4/mmm (No. 139), c.s.d.
ORT-phase	293	$a = 0.7276(3)$	$b = 0.7215(3)$	$c = 1.941$ (1)	75H1	[III/12a], s.g.: Abma (No. 64), c.s.d. (2nd d.: Bmab)
TLT-phase	188	$a = b = 0.723(1)$		$c = 1.932(2)$	76H1	[III/12a]. s.g.: P4$_2$/ncm (No. 138), c.s.d.
MLT-phase	90	$a = 0.713$	$b = 0.725$ $\beta = 92.17°$	$c = 1.930$	74K1	[III/12a] rep. – c. sym.: monoclinic, [77K1]: s.g.: B12$_1$/a1 (No. 14), (2nd d.: A2$_1$/b11)
	4.2	$a = 0.707$	$b = 0.725$ $\beta = 92.5°$	$c = 1.900$	90A1	s.g.: B12$_1$/a1 (No. 14)
$(CD_3ND_3)_2MnCl_4$	High pressure experiments:					
$p = 2 \cdot 10^8$ Pa (ORT)	293	$a = 0.7196(7)$	$b = 0.7230(7)$	$c = 1.9316(17)$	89C1	s.g.: Bmab (No. 64), (2nd d.: Abma)
$p = 2 \cdot 10^8$ Pa (MLT)	60.4	$a = 0.7126(4)$	$b = 0.7249(4)$ $\beta = 92.51(6)°$	$c = 1.9455(19)$	93C1	s.g.: B12$_1$/a1 (No. 14), (2nd d.: A2$_1$/b11)
Alternative description for 60.4 K:		$a = 0.7126(4)$	$b = 0.72149(4)$ $\beta = 112.32°$	$c = 1.0505$	93C1	s.g.: P12$_1$/a1 (No. 14)
$p = 2 \cdot 10^8$ Pa (MLT)	1.4	$a = 0.7124(6)$	$b = 0.7245(8)$ $\beta = 92.66(11)°$	$c = 1.937(4)$	93C1	s.g.: B12$_1$/a1 (No. 14), (c.s.g.)

Table 2. Crystallographic Data *(continued)*

Compound	T [K]	Lattice parameters [nm] and angles [deg]			Ref.	Remarks
$(CD_3ND_3)_2MnCl_4$ (cont.)						
$p = 19 \cdot 10^8$ Pa (ORT)	293	$a = 0.6987(9)$	$b = 0.7050(7)$	$c = 1.8924(19)$	89C1	s.g.: Bmab (No. 64), (2nd d.: Abma)
$p = 21 \cdot 10^8$ Pa (HP)	293	$a = 0.6871(10)$	$b = 0.7419(20)$ $\beta = 83.02(20)°$	$c = 1.7186(21)$	89C1	approximately monoclinic unit cell
$p = 25 \cdot 10^8$ Pa (HP)	293	$a = 0.6919(8)$ $\alpha = 88.70(9)°$	$b = 0.7244(10)$ $\beta = 83.51(9)°$	$c = 1.7189(9)$ $\gamma = 89.53(16)°$	93C1	s.g. P1 (No. 1) or P$\bar{1}$ (No. 2)
	1.4	$a = 0.6881(8)$ $\alpha = 88.44(7)°$	$b = 0.6919(12)$ $\beta = 83.52(12)°$	$c = 1.7121(27)$ $\gamma = 87.62°$	93C1	s.g.: P1 (No. 1) or P$\bar{1}$ (No. 2), (c.s.g.)
$(C_2H_5NH_3)_2MnCl_4$						
THT-phase	>424	$a = b = 0.520(1)$		$c = 2.233(5)$	77D1	s.g.: I4/mmm (No. 139)
ORT-phase	294	$a = 0.7355(3)$	$b = 0.7260(3)$	$c = 2.210(1)$	78D1	[III/12a], s.g.: Abma (No. 64), c.s.d.
OLT-phase	126	$a = 0.7325(8)$	$b = 0.7151(1)$	$c = 2.2035(19)$	77D2	s.g.: Pbca (No. 61), c.s.d., (2nd d.: Pcab)
$(C_3H_7NH_3)_2MnCl_4$						
α-phase	>450	$a = b = 0.520(1)$		$c = 2.789(5)$	77D1	s.g.: I4/mmm (No. 139)
β-phase	400	$a = 0.740(1)$	$b = 0.734(1)$	$c = 2.745(10)$	77D1	s.g.: Abma (No. 64), (2nd d.: Bmab)
γ-phase	360	$a = 0.739(1)$ $\boldsymbol{q}_0 = \delta \cdot \boldsymbol{a}^* + \boldsymbol{c}^*$ with $\delta = 0.178$	$b = 0.725(2)$	$c = 2.672(5)$	81D2	inc. str.: $N^{\mathrm{Abma}}_{\bar{1}11}$ (δ, 0, 1), c.s.d., (2nd d.: $N^{\mathrm{Bmab}}_{1\bar{1}1}$
δ-phase	295	$a = 0.7468(2)$	$b = 0.7247(2)$	$c = 2.5798(20)$	79D1	[III/12a], s.g.: Abma (No. 64), (2nd d.: Bmab)
	182	$a = 0.7458(9)$	$b = 0.7169(9)$	$c = 2.561(5)$	78D2	s.g.: Abma (No. 64), c.s.d.
ε-phase	130	$a = 0.7436(4)$ $\boldsymbol{q}_0 = \sigma \cdot \boldsymbol{b}^*$ with $\sigma = 1/3 + \delta = 0.363(2)$	$b = 0.7310(6)$	$c = 2.5438(12)$	89S2	inc. str.: $P^{\mathrm{Abma}}_{\mathrm{s}\bar{1}1}$ (0, σ, 0)
$\boldsymbol{q}_0 = \sigma \cdot \boldsymbol{b}^* \rightarrow \boldsymbol{q}_0 = \frac{1}{3}(\boldsymbol{b}^* \pm \boldsymbol{c}^*)$ *at the phase transition* $\varepsilon \rightarrow \zeta$ *(lock-in transition)*						
ζ-phase	4.2	$a = 0.744$ $\alpha = 90.2°$	$b = 0.710$	$c = 2.530$	90A1	basic structure A2_1/b11 (No. 14) of ζ*-phase modulated with* $\boldsymbol{q}_0 = \frac{1}{3}(\boldsymbol{b}^* \pm \boldsymbol{c}^*)$

Table 2. Crystallographic Data *(continued)*

Compound	*T* [K]	Lattice parameters [nm] and angles [deg]	Ref.	Remarks
$(C_3H_7NH_3)_2MnCl_4$ (cont.)				
Alternative description of commensurately modulated ζ-phase as a new structure (triplication of the unit cell), cf. Fig. 2.22				
A)	79.5	a = 0.7453 b = 2.1306 c = 1.3121 α = 105.37°	83D1	s.g.: $P2_1/b11$ (No. 14)
	4.2	a = 0.744 b = 2.130 c = 1.315 α = 105.86°		s.g.: $P2_1/b11$ (No. 14), *calculated from the data in* [90A1], *see above*
B)	4.2	a = 0.744 b = 3.938 c = 1.315 α = 31.35°		s.g.: $P2_1/n11$ (No. 14), *calculated from the data in* [90A1], *see above*
$(C_4H_9NH_3)MnCl_4$	294	a = 0.73356(6) b = 0.72512(8) c = 3.1880(6)	79D2	s.g.: Abma (No. 64), c.s.d., (2nd d.: Bmab)
$(C_5H_{11}NH_3)_2MnCl_4$	293	a = 0.7284(2) b = 0.7352(2) c = 3.6134(5)	95F1	s.g.: Bmab (No. 64), (2nd d.: Abma)
$(C_6H_{13}NH_3)_2MnCl_4$	295	a = 0.734(1) b = 0.725(1) c = 3.980(15)	79D1	assumed s.g.: Abma (No. 64)
$(C_7H_{15}NH_3)_2MnCl_4$	293	a = 0.7282(3) b = 0.7319(4) c = 4.2904(9)	95F1	s.g.: Bmab (No. 64), (2nd d.: Abma)
$(C_8H_{17}NH_3)_2MnCl_4$	295	a = 0.7345(6) b = 0.7270(6) c = 4.508(8)	79D1	assumed s.g.: Abma (No. 64)
$(C_9H_{19}NH_3)_2MnCl_4$	293	a = 0.7289(9) b = 0.7338(9) c = 5.288(1)	95F1	s.g.: Bmab (No. 64), (2nd d.: Abma)
$(C_{10}H_{21}NH_3)_2MnCl_4$	295	a = 0.7213(8) b = 0.7337(2) c = 2.6747(21) β = 94.64(5)°	76C1	s.g.: $P12_1/a1$ (No. 14), c.s.d., (2nd d.: $P2_1/b11$)
$(4\text{-}ClC_6H_4NH_3)_2MnCl_4$		a = 0.721 b = 0.728 c = 3.322	79B4	c. sym.: orthorhombic
$(CH_3NH_3)_2FeCl_4$				
THT-phase	>333	a = b = 0.51 c = 1.92	71M1	[III/12a], s.g.: I4/mmm (No. 139), cf. [78H2]
ORT-phase	295	a = 0.727 b = 0.7235 c = 1.940	82M2	c. sym.: orthorh., [78H2]: s.g.: Abma or Bmab
$(C_2H_5NH_3)_2FeCl_4$	295	a = 0.7314 b = 0.7238 c = 2.190	83S1	s.g.: D_{2h}^{18} (No. 64), *not specified*: Abma or Bmab
$(CH_3NH_3)_2CuCl_4$	297	a = 0.7268(4) b = 0.7367(4) c = 0.9971(3) β = 110.89(1)°	87P	[III/12a], s.g.: $P12_1/a1$ (No. 14), c.s.d.
Alternative description for 297 K:		a = 0.7279(4) b = 0.7370(7) c = 1.8648(5) β = 90.46(4)°	87P	s.g.: $B12_1/a1$ (No. 14), (2nd d.: $A2_1/b11$)
	100	a = 0.7155(4) b = 0.7424(4) c = 0.9814(3) β = 109.18(7)°	87P	s.g.: $P12_1/a1$ (No. 14), c.s.d., (2nd d.: $P2_1/b11$)

Table 2. Crystallographic Data *(continued)*

Compound	T [K]	Lattice parameters [nm] and angles [deg]	Ref.	Remarks
$(CD_3ND_3)_2CuCl_4$	400	$a = b = 0.5203(1)$ $c = 1.8767(6)$	84S1	ind. in I4/mmm, [89J]: s.g.: Bbcm (No. 64)
	<8.84	$a = 0.7432$ $b = 0.7035$ $c = 1.859$ $\alpha = 92.5°$	83S2	c. sym.: monoclinic, (s.g.: probably A2_1/b11)
$(C_2H_5NH_3)_2CuCl_4$				
α-phase	367	$a = 0.7474$ $b = 0.7466$ $c = 2.1355$	89J	[III/12a], s.g.: Bbcm (No. 64)
β-phase	361	$a = 0.7456$ $b = 0.7482$ $c = 2.1340$ $\beta \approx 90°$	89J	s.g.: B12$_1$/a1 (No. 14)
γ-phase	295	$a = 0.747(1)$ $b = 0.735(1)$ $c = 2.118(2)$	70S1	s.g.: Pbca (No. 61), c.s.d.
$(C_3H_7NH_3)_2CuCl_4$				
α-phase	450	$a \approx b = 0.7506(6)$ $c = 2.645(2)$	90D1	s.g.: Bbcm (No. 64), c.s.d.
β-phase	433	$a = 0.7530(5)$ $b = 0.7474(4)$ $c = 2.614(2)$	90D1	s.g.: Pbca (No. 61), c.s.d.
γ-phase	400	$a = 0.7592(3)$ $b = 0.7427(2)$ $c = 2.566(1)$ $\boldsymbol{q}_0 = \delta \cdot \boldsymbol{a}^*$ with $\delta = 0.175(5)$	90D2	inc. str.: P^{Pbca}_{ss1} (δ, 0, 0)
δ-phase	360	$a = 0.7653(3)$ $b = 0.7394(3)$ $c = 2.486(2)$	90D1	s.g.: Pbca (No. 61), c.s.d.
	295	$a = 0.765$ $b = 0.733$ $c = 2.466$	70B2	[III/12a] rep. – s.g.: Pbca (No. 61), c.s.d.
	215	$a = 0.7581(6)$ $b = 0.7252(3)$ $c = 2.458(1)$	89D1	s.g.: Pbca (No. 61)
ε-phase	185	$a = 0.756$ $b = 1.268$ $c = 1.278$ $\alpha = 33.04°$	94J1	s.g.: P2$_1$/n11 (No. 14)
Alternative description at 185 K		$a = 0.756$ $b = 0.724$ $c = 2.441$ $\alpha = 90.79°$	94J1	s.g.: A2$_1$/b11 (No. 14)
ζ-phase	165	$a = 0.755$ $b = 0.723$ $c = 2.431$ $\alpha = 91.31°$	94J1	inc. str. – basic structure: A2$_1$/b11 (No. 14)
Alternative description at 165 K		$a = 0.755$ $b = 1.260$ $c = 1.276$ $\alpha = 33.12°$ $\boldsymbol{q}_0 = \delta \cdot \boldsymbol{b}^* + \sigma \cdot \boldsymbol{c}^*$ with $\delta = 0.575(3)$ and $\sigma = 0.079(2)$	94J1	inc. str.: $P^{P2_1/n}_{\bar{1}\;1}$ (0, δ, σ) – basic structure: P2$_1$/n11 or, equivalently, A2$_1$/b11 (No. 14)
Interchange a ↔ b at the phase transition ζ ↔ η				
η-phase	94	$a = 0.733$ $b = 0.752$ $c = 2.425$ $\alpha = 93.48°$	94J1	s.g.: P2$_1$/c11 (No. 14)
	22	$a = 0.730$ $b = 0.748$ $c = 2.419$ $\alpha = 93.72°$	94J1	s.g.: P2$_1$/c11 (No. 14)

Table 2. Crystallographic Data *(continued)*

Compound	T [K]	Lattice parameters [nm] and angles [deg]			Ref.	Remarks
$(C_4H_9NH_3)_2CuCl_4$		$a = 0.730$	$b = 0.743$	$c = 3.081$	72C1	c.sym.: orthorhombic
$(C_5H_{11}NH_3)_2CuCl_4$		$a = 0.7381$	$b = 0.7506$	$c = 3.481$	72C1	[III/12a], c. sym.: orthorhombic
$(C_{10}H_{21}NH_3)_2CuCl_4$		$a = 0.7246$	$b = 0.7568$	$c = 5.105$	72C1	c. sym.: orthorhombic
$(CH_2OH\text{-}CH_2\text{-}NH_3)_2CuCl_4$	295	$a = 0.7431$	$b = 0.7511$ $\beta = 89.56°$	$c = 2.1624$	87L1	s.g.: C 12/c1 (No. 15)
$[C_6H_5NH_3]_2CuCl_4$	295	$a = 0.7180(1)$	$b = 0.7443(1)$ $\beta = 100.71(1)°$	$c = 1.5050(2)$	74L1	s.g.: $P12_1/a1$ (No. 14), c.s.d.
$[C_6H_5CH_2NH_3]_2CuCl_4$	295	$a = 0.759$	$b = 0.728$	$c = 3.130$	76D2	ind. in Pbca (No. 61)
$[C_6H_5(CH_2)_2NH_3]_2CuCl_4$	295	$a = 0.7328(1)$	$b = 0.7295(1)$	$c = 3.8618(5)$	90W1	s.g.: Pcab (No. 61), c.s.d.
$[C_6H_5(CH_2)_3NH_3]_2CuCl_4$	295	$a = 0.739$	$b = 0.730$	$c = 4.023$	76D2	ind. in Pbca (No. 61)
$[C_6H_5(CH_2)_4NH_3]_2CuCl_4$	295	$a = 0.766$	$b = 0.742$	$c = 4.344$	76D2	ind. in Pbca (No. 61)
$[COOH(CH_2)_2NH_3]_2CuCl_4$	295	$a = 0.7402(2)$	$b = 0.7734(1)$ $\beta = 91.82(1)°$	$c = 2.4236$	81W2	s.g.: I12/c1 (No. 15)
$(CH_3NH_3)_2CuCl_2Br_2$	295	$a = 0.7358(1)$	$b = 0.7354(1)$	$c = 1.9209(4)$	91W1	s.g.: Acam (No. 64), c.s.d., disorder (cf. Table 3)
$(CH_3NH_3)_2CuBr_4$		$a = 0.7644$	$b = 0.7815$	$c = 1.918$	72C1	c. sym.: orthorhombic
$(C_2H_5NH_3)_2CuBr_4$		$a = 0.772$	$b = 0.795$	$c = 2.150$	72C1	[III/12a], c. sym.: orthorhombic
$(C_3H_7NH_3)_2CuBr_4$		$a = 0.769$	$b = 0.807$	$c = 2.434$	72C1	[III/12a], c. sym.: orthorh., [77K2]: s.g.: Pbca
$(C_4H_9NH_3)_2CuBr_4$		$a = 0.7708$	$b = 0.7931$	$c = 2.865$	72C1	c. sym.: orthorhombic
$[C_6H_5CH_2NH_3]_2CuBr_4$		$a = 1.0558$	$b = 1.0486$ $\beta = 98.08°$	$c = 6.3473$	92Z2	s.g.: probably A12/a1 (No. 15)
$[C_6H_5(CH_2)_2NH_3]_2CuBr_4$	295	$a = 0.7654(4)$	$b = 0.7756(4)$	$c = 3.8042(18)$	90W1	s.g.: Pcab (No. 61), c.s.d.
$[C_6H_5(CH_2)_3NH_3]_2CuBr_4$		$a = 0.7774$ $\alpha = 90.89°$	$b = 0.7804$ $\beta = 100.77°$	$c = 3.9350$ $\gamma = 88.54°$	92Z2	s.g.: probably $P\bar{1}$ (No. 2)
$[COOH(CH_2)_2NH_3]_2CuBr_4$		$a = 0.7661(1)$	$b = 0.8021(1)$ $\beta = 92.49(2)°$	$c = 2.4295(7)$	83W2	s.g.: I12/c1 (No. 15), c.s.d.
$(C_2H_5NH_3)_2PdCl_4$		$a = 0.744$	$b = 0.802$	$c = 2.051$	77W2	s. sym.: orthorhombic
$(C_3H_7NH_3)_2PdCl_4$	295	$a = 0.7404(3)$	$b = 0.8038(4)$ $\beta = 109.20(2)°$	$c = 1.242(1)$	77W2	s.g.: $P12_1/a1$ (No. 14), c.s.d., (2nd d.: $P2_1/b11$)

Table 2. Crystallographic Data *(continued)*

Compound	*T* [K]	Lattice parameters [nm] and angles [deg]	Ref.	Remarks
$(CH_3NH_3)_2CdCl_4$				
THT-phase	493	$a = b = 0.5302(3)$ $c = 1.934(1)$	76C2	s.g.: I4/mmm (No. 139), c.s.d.
ORT-phase	294	$a = 0.7483(1)$ $b = 0.7384(2)$ $c = 1.922(3)$	75C1	s.g.: Abma (No. 64), c.s.d., (2nd d.: Bmab)
TLT-phase	234	$a = b = 0.7430(4)$ $c = 1.920(2)$	75C1	s.g.: $P4_2/ncm$ (No. 138), c.s.d.
MLT-phase	147	$a = 0.7313(5)$ $b = 0.7467(3)$ $c = 1.937(1)$ $\beta = 91.05(4)°$	76C2	s.g.: $B12_1/a1$ (No. 14), c.s.d., (2nd d.: $A2_1/b11$)
Alternative description at 147 K:		$a = 0.7313(5)$ $b = 0.7467(3)$ $c = 1.0415(6)$ $\beta = 111.60(4)°$	76C2	s.g.: $P12_1/a1$ (No. 14), c.s.d.
$(C_2H_5NH_3)_2CdCl_4$				
ORT-phase	295	$a = 0.7464(1)$ $b = 0.7565(1)$ $c = 2.1879(7)$	77C2	s.g.: Bmab (No. 64), c.s.d., (2nd d.: Abma)
OLT-phase	178	$a = 0.7354(4)$ $b = 0.7478(5)$ $c = 2.211(3)$	77C2	s.g.: Pcab (No. 61), c.s.d., (2nd d.: Pbca)
$(C_3H_7NH_3)_2CdCl_4$				
ORT-phase	210.0	$a = 0.7607(3)$ $b = 0.7370(3)$ $c = 2.5184(6)$	88D2	s.g.: Abma (No. 64), (2nd d.: Bmab)
INC-phase	153.0	$a = 0.7585(5)$ $b = 0.7359(1)$ $c = 2.5053(6)$ $\boldsymbol{q}_0 = \sigma \cdot \boldsymbol{b}^*$ with $\sigma = 0.418(5)$	88D2	inc. str.: $P^{\text{Abma}}_{\text{s}\bar{1}1}(0, \sigma, 0)$
$\boldsymbol{q}_0 = \sigma \cdot \boldsymbol{b}^* \rightarrow \boldsymbol{q}_0 = \boldsymbol{b}^*$ *at the phase transition* INC → OLT *(lock-in transition)*				
OLT-phase	130.5	$a = 0.7568(5)$ $b = 0.7359(1)$ $c = 2.5515(8)$	88D2	s.g.: Pbca (No. 61), *description of modulated phase as commensurate structure*
$(C_8H_{17}NH_3)_2CdCl_4$				
HT-phase	353	$a = 0.749(1)$ $b = 0.758(1)$ $c = 4.788(9)$	83C1	ind. in Amaa (No. 66)
LT-phase	243	$a = 0.741(2)$ $b = 0.753(2)$ $c = 4.534(20)$ $\beta = 96.55(28)°$	83C1	ind. in $P12_1/n1$ (No. 14)
$(C_9H_{19}NH_3)_2CdCl_4$				
LT-phase	295	$a = 0.7819$ $b = 0.7990$ $c = 4.6410$ $\beta = 95.88°$	95K	c. sym.: monoclinic, ind. in $P12_1/n1$ (No. 14)
$(C_{10}H_{21}NH_3)_2CdCl_4$				
HT-phase	318	$a = 0.7460(2)$ $b = 0.7546(2)$ $c = 5.464(2)$	79K1	s.g.: Amaa (No. 66)
IM-phase	308	$a = 0.740(2)$ $b = 0.754(2)$ $c = 5.162(6)$	83C1	c. sym.: orthorh., [79K1]: s.g.: Pmnn (No. 58)
LT-phase	294	$a = 0.7354(1)$ $b = 0.7545(1)$ $c = 5.1620(3)$ $\beta = 91.74(1)°$	79K1	s.g.: $P12_1/n1$ (No. 14)

Table 2. Crystallographic Data *(continued)*

Compound	T [K]	Lattice parameters [nm] and angles [deg]			Ref.	Remarks
$(C_{12}H_{25}NH_3)_2CdCl_4$						
HT-phase	360	$a = b = 0.5310(1)$		$c = 6.431(4)$	85C1	c. sym.: tetragonal
IM-phase 1	334	$a = 0.7470(7)$	$b = 0.7553(7)$	$c = 6.350(4)$	85C1	ind. in Amaa (No. 66)
LT-phase	293	$a = 0.7463(1)$	$b = 0.7523(1)$ $\beta = 96.54(2)°$	$c = 5.9152(8)$	85C1	ind. in $P12_1/n1$ (No. 14)
$(C_{14}H_{29}NH_3)_2CdCl_4$						
α-phase	>352	$a = 0.746(1)$	$b = 0.754(1)$	$c = 3.577$	88S1	c. sym.: orthorhombic
γ-phase	348	$a = 0.732(3)$	$b = 0.745(2)$	$c = 3.360$ $\gamma = 92.2(2)°$	88S1	c. sym.: monoclinic
ε-phase	298	$a = 0.7329(2)$ $\alpha = 98.19(1)°$	$b = 0.7482(1)$ $\beta = 91.70(1)°$	$c = 3.3188(5)$ $\gamma = 90.04(2)°$	88S1	s.g.: $P\bar{1}$ (No. 2), c.s.d.
$(C_{16}H_{33}NH_3)_2CdCl_4$						
HT-phase	360	$a = b = 0.5298(2)$		$c = 8.003(7)$	89C2	c. sym.: tetragonal
IM-phase 1	354	$a = 0.7383(18)$	$b = 0.7641(15)$	$c = 7.645(11)$	89C2	c. sym.: orthorhombic
IM-phase 2	348	$a = 0.7437(10)$	$b = 0.7590(10)$	$c = 7.524(8)$	89C2	c. sym.: orthorhombic
LT-phase	293	$a = 0.7384(5)$	$b = 0.7546(11)$ $\beta = 96.27(6)°$	$c = 7.358(3)$	89C2	c. sym.: monoclinic, s.g.: probably $P12_1/n1$ (No. 14) analogous to $(C_{12}H_{25}NH_3)_2CdCl_4$
$(C_2H_5NH_3)_2HgCl_4$	243	$a = 0.7826(3)$	$b = 0.7828(3)$	$c = 2.0378(3)$	83B1	s.g.: Pccn (No. 56), c.s.d.
$(C_3H_7NH_3)_2HgCl_4$	295	$a = 0.7991(2)$	$b = 0.7779(2)$	$c = 2.3519(2)$	86B2	s.g.: Abma (No. 64), c.s.d., (2nd d.: Bmab)
$(C_3H_7NH_3)_2PbCl_4$						
α-phase (MHT)	360	$a = 0.781(2)$	$b = 0.786(5)$ $\beta = 71.9(2)°$	$c = 1.351(3)$	91C21	s.g.: $P12_1/a1$ (No. 14), (2nd d.: $P2_1/b11$)
β-phase (ORT)	295	$a = 0.7815(1)$	$b = 0.7954(1)$	$c = 2.5034(3)$	89M1	s.g.: Pnam (No. 62), c.s.d., (2nd d.: Pbnm)
$(C_9H_{19}NH_3)_2PbCl_4$	295	$a = 0.7393$	$b = 0.7481$ $\beta = 91.95°$	$c = 4.7464$	95K	c. sym.: monoclinic, ind. in $P12_1/n1$ (No. 14)
$(C_{10}H_{21}NH_3)_2PbI_4$	295	$a = 0.8968$	$b = 0.8667$	$c = 4.251$	89I3	sg.: Pbca (No. 61)

Table 2. Crystallographic Data *(continued)*

Compound	T [K]	Lattice parameters [nm] and angles [deg]			Ref.	Remarks
d) Diammonium Compounds with X = Cl$^-$, Br$^-$						
$[NH_3(CH_2)_3NH_3]CrCl_4$	295	a = 0.7517	b = 0.7235	c = 1.8535	81B1	s.g.: Pbnm (No. 62), (2nd d.: Pnam)
$[NH_3(CH_2)_2NH_3]MnCl_4$	296	a = 0.71303(16)	b = 0.71921(18) β = 92.685(24)°	c = 0.86089(18)	78T1	s.g.: P12$_1$/a1 (No. 14), c.s.d., (2nd d.: P2$_1$/b11)
$[NH_3(CH_2)_3NH_3]MnCl_4$						
α-phase	343	a = 0.7198(2)	b = 0.7398(2)	c = 1.8891(3)	82C	s.g.: Imam (No. 74), c.s.d., (2nd d.: Ibmm)
β-phase	313	a = 1.0254(2)	b = 1.0382(2)	c = 1.8867(3)	82C	s.g.: Fmmm (No. 69), c.s.d.
γ-phase	296	a = 0.7174(1)	b = 0.7361(1)	c = 1.9020(3)	82C	s.g.: Pnam (No. 62), c.s.d. (2nd d.: Pbnm)
$[NH_3(CH_2)_4NH_3]MnCl_4$						
OHT-phase	404	a = 0.7337(3)	b = 0.7218(4)	c = 1.0690(5)	80T1	s.g.: Pbmn (No. 53), c.s.d., (2nd d.: Pman)
MRT-phase	295	a = 0.7307(3) α = 92.67(5)°	b = 0.7177(3)	c = 1.0770(5)	80T1	s.g.: P2$_1$/b11 (No. 14), c.s.d., (2nd d.: P12$_1$/a1)
$[NH_3(CH_2)_5NH_3]MnCl_4$	296	a = 0.7153(2)	b = 0.7360(2)	c = 2.3987(7)	76A1	ref. in Imam (No. 74)
$[NH_3(CH_2)_3NH_3]FeCl_4$	295	a = 0.7108(11)	b = 0.7378(10)	c = 1.857(3)	75W1	s.g.: probably Imam (No. 74), c.s.d.
$[NH_3(CH_2)_2NH_3]NiCl_4$	295	a = 0.6943(1)	b = 0.6995(1) β = 92.925(2)°	c = 0.8441(1)	78S3	s.g.: P12$_1$/a1 (No. 14), (2nd d.: P2$_1$/b11)
$[NH_3(CH_2)_2NH_3]CuCl_4$	296	a = 0.7158(3)	b = 0.7363(3) β = 92.37(3)°	c = 0.8109(3)	78T1	s.g.: P12$_1$/a1 (No. 14), c.s.d., (2nd d.: P2$_1$/b11)
$[NH_3(CH_2)_3NH_3]CuCl_4$	295	a = 0.7200(2)	b = 0.7451(2)	c = 1.8246(6)	76P1	s.g.: Pnam (No. 62), c.s.d., (2nd d.: Pbnm)
$[NH_3(CH_2)_4NH_3]CuCl_4$	293	a = 0.7588(1)	b = 0.7599(1) β = 103.14(1)°	c = 0.9268(1)	90G1	s.g.: P12$_1$/a1 (No. 14), c.s.d., (2nd d.: P2$_1$/b11)
$[NH_3(CH_2)_5NH_3]CuCl_4$	293	a = 0.7747(3)	b = 0.7203(2) β = 102.12(2)°	c = 2.1761(6)	90G1	s.g.: P12$_1$/n1 (No. 14), c.s.d.
$(C_5N_2H_8)CuCl_4$ *)	295	a = 0.6941(2)	b = 0.8348(2) β = 94.63(3)°	c = 1.6848(7)	88W1	s.g.: P12$_1$/c1 (No. 14), c.s.d.
*) $(C_5N_2H_8)CuCl_4$ = *3-ammoniumpyridinium tetrachlorocuprate*						
$[NH_3(CH_2)_2NH_3]CuBr_4$	293	a = 0.7511(19)	b = 0.7803(1) β = 92.12(2)°	c = 0.8334(2)	88H1	s.g.: P12$_1$/a1 (No. 14), c.s.d., (2nd d.: P2$_1$/b11)

Table 2. Crystallographic Data *(continued)*

Compound	T [K]	Lattice parameters [nm] and angles [deg]			Ref.	Remarks
$[NH_3(CH_2)_3NH_3]CuBr_4$	293	a = 0.8086(2)	b = 0.7556(2) β = 96.75(2)°	c = 1.7622(5)	88H1	s.g.: P12$_1$/n1 (No. 14), c.s.d.
$[NH_3(CH_2)_4NH_3]CuBr_4$	293	a = 0.7914(2)	b = 0.7887(4) β = 102.83(2)°	c = 0.9432(2)	90G1	s.g.: P12$_1$/a1 (No. 14), c.s.d.
$[NH_3(CH_2)_5NH_3]CuBr_4$	293	a = 0.8142(3)	b = 0.7560(2) β = 101.49(3)°	c = 2.1736(10)	90G1	s.g.: P12$_1$/n1 (No. 14), c.s.d.
$(C_5N_2H_8)CuBr_4$ *)	295	a = 0.7179(1)	b = 0.8766(2) β = 95.29(1)°	c = 1.7218(3)	88W1	s.g.: P12$_1$/c1 (No. 14), c.s.d.
*) $(C_5N_2H_8)CuBr_4$ = *3-ammoniumpyridinium tetrabromocuprate*						
$[NH_3(CH_2)_2NH_3]PdCl_4$	295	a = 0.734(2)	b = 0.766(2) β = 91.90(1)°	c = 0.791(2)	76B3	s.g.: P12$_1$/a1 (No. 14), c.s.d., (2nd d.: P2$_1$/b11)
$[NH_3(CH_2)_2NH_3]CdCl_4$	295	a = 0.7292(3)	b = 0.7344(3) β = 92.74(3)°	c = 0.8609(5)	92B1	s.g.: P12$_1$/a1 (No. 14), (2nd d.: P2$_1$/b11)
$[NH_3(CH_2)_3NH_3]CdCl_4$						
OHT-phase	400	a = 0.7351(5)	b = 0.7622(5)	c = 1.857(1)	92B1	c. sym.: orthorhombic
ORT-phase	295	a = 0.7352(2)	b = 0.7503(2)	c = 1.9051(5)	92B1	s.g.: Pnam (No. 62), c.s.d., (2^{2nd} d.: Pbnm)
$[NH_3(CH_2)_4NH_3]CdCl_4$		a = 0.721	b = 0.733 β = 92.5°	c = 1.090	76A2	c. sym.: monoclinic
$[NH_3(CH_2)_5NH_3]CdCl_4$						
MHT-phase	433	a = 0.7516	b = 0.7563 β = 98.15°	c = 1.1220	89N1	s.g.: C12/m1 (No. 12)
OHT-phase	353	a = 0.7376(4)	b = 0.7561(1)	c = 2.3555(6)	87N1	s.g.: Imam (No. 74), c.s.d., (2nd d.: Ibmm)
ORT-phase	293	a = 0.7330(2)	b = 0.7504(1)	c = 2.3862(4)	87N1	s.g.: Pnam (No. 62), c.s.d., (2nd d.: Pbnm)
$[NH_3(CH_2)_6NH_3]CdCl_4$	295	a = 0.7306(1)	b = 0.7587(1) β = 91.24(3)°	c = 2.3935(6)	76W1	c. sym.: monoclinic
$[NH_3(CH_2)_7NH_3]CdCl_4$	295	a = 0.7602(1)	b = 0.7307(1) β = 92.10(2)°	c = 2.5716(4)	76W1	c. sym.: monoclinic
$[NH_3(CH_2)_8NH_3]CdCl_4$	295	a = 0.732(1)	b = 0.756(1) β = 92.97(17)°	c = 2.755(3)	76W1	c. sym.: monoclinic

Table 2. Crystallographic Data *(continued)*

Compound	*T* [K]	Lattice parameters [nm] and angles [deg]	Ref.	Remarks
e) Diluted Magnets				
$Rb_2Cr_xMg_{1-x}Cl_4$				
x = 0 (Rb_2MgCl_4)	295	$a = b = 0.4981$ $c = 1.615$	82W1	ref. in I4/mmm (No. 139)
x = 0.2	295	$a = b = 0.5020$ $c = 1.603$	82W1	ref. in I4/mmm (No. 139)
x = 0.6	295	$a = b = 0.5103$ $c = 1.581$	82W1	ref. in I4/mmm (No. 139)
x = 0.7	295	$a = b = 0.5115$ $c = 1.577$	82W1	ref. in I4/mmm (No. 139)
x = 0.9	295	$a = b = 0.5128$ $c = 1.575$	82W1	ref. in I4/mmm (No. 139)
x = 1 (Rb_2CrCl_4)	295	$a = b = 0.5142$ $c = 1.574$	82W1	ref. in I4/mmm (No. 139)
x = 0.73	4.2	$a = 0.7141(6)$ $b = 0.7114(6)$ $c = 1.5761$	86F1	s.g.: Bbcm (No. 64), c.s.d. (2nd d.: Acam)
$Rb_2Mn_xMg_{1-x}F_4$				
x = 0.54	5	$a = b = 0.41457(4)$ $c = 1.3801(15)$	77C3	ref. in I4/mmm (No. 139), (c.s.g.)
x = 0.57	5	$a = b = 0.41500(4)$ $c = 1.3801(15)$	77C3	ref. in I4/mmm (No. 139), (c.s.g.)
x = 0.60(2)	5	$a = b = 0.41542$ $c = 1.3806$	80B1	ref. in I4/mmm (No. 139), (c.s.g.)
$Rb_2Mn_xCd_{1-x}Cl_4$				
x = 0.4	295	$a = b = 0.5137(4)$ $c = 1.617(1)$	82P1	s.g.: I4/mmm (No. 139)
x = 0.5	295	$a = b = 0.5123(5)$ $c = 1.617(1)$	82P1	s.g.: I4/mmm (No. 139)
x = 0.62	295	$a = b = 0.5102(5)$ $c = 1.518(1)$	82P1	s.g.: I4/mmm (No. 139)
x = 0.7	295	$a = b = 0.5095(5)$ $c = 1.620(2)$	82P1	s.g.: I4/mmm (No. 139)
x = 0.8	295	$a = b = 0.5080(4)$ $c = 1.618(1)$	83P	s.g.: I4/mmm (No. 139)
x = 0.9	295	$a = b = 0.5066(4)$ $c = 1.617(1)$	82P1	s.g.: I4/mmm (No. 139)
x = 1 (Rb_2MnCl_4)	295	$a = b = 0.5054(4)$ $c = 1.617(1)$	83P	s.g.: I4/mmm (No. 139)
$K_2Fe_{0.74}Zn_{0.26}F_4$	4.2	$a = b = 0.410(1)$ $c = 1.293(2)$	85D1	ref. in I4/mmm (No. 139), (c.s.g.)
$Rb_2Co_xMg_{1-x}F_4$				
x = 0.550(5)		$a = b = 0.41060(3)$ $c = 1.3732(1)$	80C1	s.g.: I4/mmm (No. 139)
x = 0.575(5)		$a = b = 0.41088(3)$ $c = 1.3733(1)$	80C1	s.g.: I4/mmm (No. 139)
x = 0.583(5)		$a = b = 0.41102(3)$ $c = 1.3734(1)$	80C1	s.g.: I4/mmm (No. 139)
x = 1.0 (Rb_2CoF_4)		$a = b = 0.41440(3)$ $c = 1.3670(1)$	80C1	s.g.: I4/mmm (No. 139)
x = 0.7	5	$a \approx b = 0.57915$ $c = 1.371$	87H1	s.g.: Acam or Bbcm (No. 64), (m.u.c.)
$K_2Ni_xZn_{1-x}F_4$				
x = 0.05	295	$a = b = 0.4056(2)$ $c = 1.3102(7)$	79K2	s.g.: I4/mmm (No. 139)
x = 0.10	295	$a = b = 0.4058(2)$ $c = 1.3101(7)$	79K2	s.g.: I4/mmm (No. 139)
x = 0.25	295	$a = b = 0.4044(2)$ $c = 1.3089(7)$	79K2	s.g.: I4/mmm (No. 139)
x = 0.50	295	$a = b = 0.4038(2)$ $c = 1.3099(7)$	79K2	s.g.: I4/mmm (No. 139)

Table 2. Crystallographic Data *(continued)*

Compound	T [K]	Lattice parameters [nm] and angles [deg]		Ref.	Remarks
$K_2Ni_xZn_{1-x}F_4$ (cont.)					
x = 0.75	295	$a = b = 0.4022(2)$	$c = 1.3089(7)$	79K2	s.g.: I4/mmm (No.139)
x = 1.0 (K_2NiF_4)	295	$a = b = 0.4013(2)$	$c = 1.3083(7)$	79K2	s.g.: I4/mmm (No.139)
$K_2Cu_xZn_{1-x}F_4$					
x = 0.0 (K_2ZnF_4)	295	$a = b = 0.4056(2)$	$c = 1.3107(7)$	79K2	ref. in I4/mmm (No. 139)
x = 0.08	295	$a = b = 0.4064(2)$	$c = 1.3074(7)$	79K2	ref. in I4/mmm (No. 139)
x = 0.16	295	$a = b = 0.4067(2)$	$c = 1.3039(7)$	79K2	ref. in I4/mmm (No. 139)
x = 0.20	295	$a = b = 0.4070(2)$	$c = 1.3026(7)$	79K2	ref. in I4/mmm (No. 139)
x = 0.26	295	$a = b = 0.4077(2)$	$c = 1.3011(7)$	79K2	ref. in I4/mmm (No. 139)
x = 0.31	295	$a = b = 0.4080(2)$	$c = 1.2983(7)$	79K2	ref. in I4/mmm (No. 139)
x = 0.35	295	$a = b = 0.4083(2)$	$c = 1.2979(7)$	79K2	ref. in I4/mmm (No. 139)
x = 0.40	295	$a = b = 0.4086(2)$	$c = 1.2966(7)$	79K2	ref. in I4/mmm (No. 139)
x = 0.46	295	$a = b = 0.4091(2)$	$c = 1.2939(7)$	79K2	ref. in I4/mmm (No. 139)
x = 0.49	295	$a = b = 0.4095(2)$	$c = 1.2915(7)$	79K2	ref. in I4/mmm (No. 139)
x = 0.73	295	$a = b = 0.4120(2)$	$c = 1.2827(7)$	79K2	ref. in I4/mmm (No. 139)
x = 1.0 (K_2CuF_4)	295	$a = b = 0.4149(2)$	$c = 1.2726(7)$	79K2	ref. in I4/mmm (No. 139)
x = 0.92	2	$a = b = 0.4107(5)$	$c = 1.2680(5)$	78W1	ref. in I4/mmm (No. 139)
x = 0.78	2	$a = b = 0.4095(5)$	$c = 1.2765(5)$	78W1	ref. in I4/mmm (No. 139)
$Rb_2Cu_xZn_{1-x}F_4$					
x = 0.0 (Rb_2ZnF_4)	295	$a = b = 0.4134(2)$	$c = 1.3702(7)$	79K2	ref. in I4/mmm (No. 139)
x = 0.01	295	$a = b = 0.4136(2)$	$c = 1.3700(7)$	79K2	ref. in I4/mmm (No. 139)
x = 0.10	295	$a = b = 0.4142(2)$	$c = 1.3681(7)$	79K2	ref. in I4/mmm (No. 139)
x = 0.25	295	$a = b = 0.4147(2)$	$c = 1.3650(7)$	79K2	ref. in I4/mmm (No. 139)
x = 0.50	295	$a = b = 0.4177(2)$	$c = 1.3533(7)$	79K2	ref. in I4/mmm (No. 139)
x = 1.0 (Rb_2CuF_4)	295	$a = b = 0.4247(2)$	$c = 1.3320(7)$	79K2	ref. in I4/mmm (No. 139)
f) Mixed Magnets					
$Rb_2Cr_{1-x}Mn_xCl_4$					
x = 0.011(19)	293	$a = b = 0.5135(3)$	$c = 1.5773(8)$	80M2	ref. in I4/mmm (No. 139)
x = 0.083(13)	293	$a = b = 0.5127(3)$	$c = 1.5806(8)$	80M2	ref. in I4/mmm (No. 139)
x = 0.131(19)	293	$a = b = 0.5121(3)$	$c = 1.5812(8)$	80M3	ref. in I4/mmm (No. 139)
x = 0.306(13)	293	$a = b = 0.5107(3)$	$c = 1.5888(8)$	80M3	ref. in I4/mmm (No. 139)
x = 0.533(11)	293	$a = b = 0.5084(3)$	$c = 1.5968(8)$	80M2	ref. in I4/mmm (No. 139)
x = 0.634(12)	293	$a = b = 0.5083(3)$	$c = 1.6035(8)$	80M2	ref. in I4/mmm (No. 139)
x = 0.827(16)	293	$a = b = 0.5065(3)$	$c = 1.6110(8)$	80M2	ref. in I4/mmm (No. 139)
x = 0.910(14)	293	$a = b = 0.5056(3)$	$c = 1.6152(8)$	80M2	ref. in I4/mmm (No. 139)
x = 0.968(21)	293	$a = b = 0.5056(3)$	$c = 1.6161(8)$	80M2	ref. in I4/mmm (No. 139)

Table 2. Crystallographic Data *(continued)*

Compound	*T* [K]	Lattice parameters [nm] and angles [deg]	Ref.	Remarks
$Rb_2Cr_{1-x}Mn_xCl_4$ (cont.)				
x = 0.011(19)	15	$a = b = 0.5083(3)$ $c = 1.5730(8)$	84M1	ref. in I4/mmm (No. 139)
x = 0.131(19)	15	$a = b = 0.5071(3)$ $c = 1.5756(8)$	84M1	ref. in I4/mmm (No. 139)
x = 0.306(19)	15	$a = b = 0.5062(3)$ $c = 1.5835(8)$	84M1	ref. in I4/mmm (No. 139)
x = 0.533(11)	15	$a = b = 0.5041(3)$ $c = 1.5901(8)$	84M1	ref. in I4/mmm (No. 139)
x = 0.634(12)	15	$a = b = 0.5042(3)$ $c = 1.5977(8)$	84M1	ref. in I4/mmm (No. 139)
x = 0.910(14)	15	$a = b = 0.5023(3)$ $c = 1.6062(8)$	84M1	ref. in I4/mmm (No. 139)
x = 0.968(21)	15	$a = b = 0.5024(3)$ $c = 1.6091(8)$	84M1	ref. in I4/mmm (No. 139)
x = 0.25	4.2	$a = b = 0.5065$ $c = 1.7524$	89S1	ref. in I4/mmm (No. 139)
x = 0.59	4.2	$a = b = 0.5040$ $c = 1.5876$	89S1	ref. in I4/mmm (No. 139)
x = 0.70	4.2	$a = b = 0.5030$ $c = 1.5915$	89S1	ref. in I4/mmm (No. 139)
x = 0.011(19)	293	$a \approx b = 0.7262(4)$ $c = 1.5773(8)$	80M2	s.g.: Bbcm (No. 64), c.s.d., (2nd d.: Acam)
x = 0.011(19)	15	$a \approx b = 0.7188(4)$ $c = 1.5730(8)$	80M3	s.g.: Bbcm (No. 64), c.s.d., (2nd d.: Acam)
$Rb_2Mn_{0.5}Co_{0.5}F_4$	5	$a = b = 0.4177$ $c = 1.372$	80I1	ref. in I4/mmm (No. 139), (c.s.g.)
$Rb_2Mn_{0.5}Ni_{0.5}F_4$	4.2	$a = b = 0.4121$ $c = 1.372$	75A1	ref. in I4/mmm (No. 139), (c.s.g.)
$K_2Mn_xCu_{1-x}F_4$				
x = 0 (K_2CuF_4)		$a = b = 0.4155$ $c = 1.274$	78D3	ref. in I4/mmm (No. 139)
x = 0.09		$a = b = 0.4157$ $c = 1.283$	78D3	ref. in I4/mmm (No. 139)
x = 0.20		$a = b = 0.4163$ $c = 1.290$	78D3	ref. in I4/mmm (No. 139)
$(CH_3NH_3)_2Mn_{0.97}Cu_{0.03}Cl_4$	295	$a = 0.7209(2)$ $b = 0.7272(2)$ $c = 1.9402(7)$	83C2	s.g.: Bmab (No. 64), c.s.d., ORT-phase
$K_2Fe_{1-x}Co_xF_4$				
x = 0 (K_2FeF_4)	4.2	$a \approx b = 0.583(1)$ $c = 1.286(3)$	82T1	s.g.: Acam or Bbcm (No. 64), (m.u.c.)
x = 0.12	4.2	$a \approx b = 0.584$ $c = 1.288$	86V1	s.g.: Acam or Bbcm (No. 64), (m.u.c.)
x = 0.55	4.2	$a \approx b = 0.579$ $c = 1.294$	86V1	s.g.: Acam or Bbcm (No. 64), (m.u.c.)
$Rb_2Co_{1-x}Ni_xF_4$				
x = 0 (Rb_2CoF_4)	78	$a \approx b = 0.5817$ $c = 1.3615$	83I1	s.g.: Acam or Bbcm (No. 64), (m.u.c.)
x = 0.5	78	$a \approx b = 0.5770$ $c = 1.3734$	83I1	s.g.: Acam or Bbcm (No. 64), (m.u.c.)
x = 1 (Rb_2NiF_4)	78	$a \approx b = 0.5733$ $c = 1.3550$	83I1	s.g.: Acam or Bbcm (No. 64), (m.u.c.)
$Rb_2Co_xCu_{1-x}F_4$				
x = 0.037	4.2	$a = b = 0.421$ $c = 1.330$	92S1	ref. in I4/mmm (No. 139)
x = 0.083	4.2	$a = b = 0.421$ $c = 1.330$	92S1	ref. in I4/mmm (No. 139)
x = 0.88	4.2	$a = b = 0.416$ $c = 1.372$	92S1	ref. in I4/mmm (No. 139)

Table 3. M-X Bond Lengths and Interlayer Distances

Compound	T[K]	M-X bond lengths r_{ip} and r_{op} [nm] Interlayer distance d [nm]			Ref.	Remarks
a) Fluorides						
K_2MgF_4	295	$r_{ip} = 0.1990$	$r_{op} = 0.2004$	$d = 0.6590$	82B2	r_{ip}, r_{op}, d: Eqs. 2.1 – 2.3
$(NH_4)_2MgF_4$	295	$r_{ip} = 0.2028(1)$	$r_{op} = 0.1997(3)$	$d = 0.69177(3)$	96S2	r_{ip}, r_{op}, d: Eqs. 2.1 – 2.3
K_2MnF_4	295	$r_{ip} = 0.2086(2)$	$r_{op} = 0.211(2)$	$d = 0.6630(8)$	68L1	r_{ip}, r_{op}, d: Eqs. 2.1 – 2.3
	4.2	$r_{ip} = 0.2076(2)$	$r_{op} = 0.2102(14)$	$d = 0.6621(5)$	68L1	$r_{ip} = a/\sqrt{8}$, r_{op}, d: Eqs. 2.2, 2.3
$K_3Mn_2F_7$	295	$r_{ip} = 0.2094$	$r_{op} = 0.2110$ $r_{op} = 0.2085$	$d = 0.6573$	82B2	r_{ip}, d, 1st r_{op}: Eqs. 2.1, 2.6, 2.7; 2nd r_{op}: c.f.a.p.
	4.2	$r_{ip} = 0.2091(2)$	$r_{op} = 0.209(4)$ $r_{op} = ??$	$d = 0.660(7)$	79U	$r_{ip} = a/\sqrt{8}$; d, 1st r_{op}: Eqs. 2.6, 2.7; 2nd r_{op} not determined
$Rb_3Mn_2F_7$	295	$r_{ip} = 0.2111(2)$	$r_{op} = 0.223(10)$ $r_{op} = ??$	$d = 0.668$	76N1	r_{ip}, d, 1st r_{op}: Eqs. 2.1, 2.6, 2.7; 2nd r_{op} not determined
K_2CoF_4	295	$r_{ip} = 0.2037$	$r_{op} = 0.2025$	$d = 0.6544$	82B2	r_{ip}, r_{op}, d: Eqs. 2.1 – 2.3
$K_3Co_2F_7$	295	$r_{ip} = 0.2037$	$r_{op} = 0.2044$ $r_{op} = 0.2012$	$d = 0.6494$	82B2	r_{ip}, d, 1st r_{op}: Eqs. 2.1, 2.6, 2.7; 2nd r_{op}: c.f.a.p.
K_2NiF_4	295	$r_{ip} = 0.2006$	$r_{op} = 0.2001$	$d = 0.6538$	82B2	r_{ip}, r_{op}, d: Eqs. 2.1 – 2.3
$K_3Ni_2F_7$	295	$r_{ip} = 0.2008$	$r_{op} = 0.2021$ $r_{op} = 0.1990$	$d = 0.6495$	82B2	r_{ip}, d, 1st r_{op}: Eqs. 2.1, 2.6, 2.7; 2nd r_{op}: c.f.a.p.
K_2CuF_4	295	$r_{ip} = 0.192(4)$ $r_{ip} = 0.222(4)$	$r_{op} = 0.1923(16)$	$d = 0.6355(5)$	74H1	2 v. $r_{ip} \hat{=}$ def. oct.; r_{ip}, r_{op}: c.f.a.p.; $d = c/4$
	295	$r_{ip} = 0.1939$ $r_{ip} = 0.2222$	$r_{op} = 0.1932$	$d = 0.6367(1)$	83H1	2 v. $r_{ip} \hat{=}$ def. oct.; r_{ip}, r_{op}: c.f.a.p.; d = Eq. 2.3
$K_3Cu_2F_7$	205	$r_{ip} = 0.1900(7)$ $r_{ip} = 0.2256(7)$	$r_{op} = 0.1968(1)$ $r_{op} = 0.1927(4)$	$d = 0.632(3)$	81H1	2 v. $r_{ip} \hat{=}$ def. oct.; 1st r_{op}: Eq. 2.6; r_{ip}, 2nd r_{op}, d: c.f.a.p.;
K_2ZnF_4	295	$r_{ip} = 0.2029(1)$	$r_{op} = 0.2026(2)$	$d = 0.6555(2)$	80H1	r_{ip}, r_{op}, d: Eqs. 2.1 – 2.3
$K_3Zn_2F_7$	295	$r_{ip} = 0.2029(1)$	$r_{op} = 0.2041(1)$ $r_{op} = 0.2007(4)$	$d = 0.6504(5)$	80H1	r_{ip}, d, 1st r_{op}: Eqs. 2.1, 2.6, 2.7; 2nd r_{op}: c.f.a.p.

Table 3. M-X Bond Lengths and Interlayer Distances *(continued)*

Compound	T[K]	M-X bond lengths r_{ip} and r_{op} [nm] Interlayer distance d [nm]	Ref.	Remarks
b) Chlorides, Bromides and Iodides with inorganic A^+-ions				
$Rb_2MgCl_{4-x}Br_x$		doped with Mn^{2+}, EPR results indicate	73W1	
x = 0		symmetry of Mn^{2+} environment: O_h		$MnCl_6$-octahedra
x = 1		symmetry of Mn^{2+} environment: D_{4h}		$MnCl_4Br_2$-octahedra, Br^- in out-of-plane sites
x = 2		symmetry of Mn^{2+} environment: O_h and D_{4h}		$MnCl_6$- and $MnCl_4Br_2$-octahedra
Rb_2CrCl_4	293	r_{ip} = 0.2387(6) r_{op} = 0.2413(13) d = 0.7885(20) r_{ip} = 0.2755(7)	83J1	2 v. r_{ip} ≙ def. oct.; r_{ip}, r_{op}: c.f.a.p.; d: Eq. 2.3
	77	r_{ip} = 0.2379(6) r_{op} = 0.2366(22) d = 0.7835(20) r_{ip} = 0.2700(7)	83J1	2 v. r_{ip} ≙ def. oct.; r_{ip}, r_{op}: c.f.a.p.; d: Eq. 2.3
	5.5	r_{ip} = 0.2387(6) r_{op} = 0.2371(22) d = 0.786(2) r_{ip} = 0.2700(7)	83J1	2 v. r_{ip} ≙ def. oct.; r_{ip}, r_{op}: c.f.a.p.; d: Eq. 2.3
Rb_2CrCl_3Br	90	r_{ip} = 0.242(1) r_{op} = 0.252(1) d = 0.8037(1) r_{ip} = 0.267(1)	85F1	2 v. r_{ip} ≙ def. oct.; r_{ip}, r_{op}: c.f.a.p.; d: Eq. 2.3
	4.2	r_{ip} = 0.240(1) r_{op} = 0.255(1) d = 0.8031(1) r_{ip} = 0.269(1)	85F1	2 v. r_{ip} ≙ def. oct.; r_{ip}, r_{op}: c.f.a.p.; d: Eq. 2.3
$Rb_2CrCl_2Br_2$	90	r_{ip} = 0.241(1) r_{op} = 0.257(1) d = 0.8193(3) r_{ip} = 0.270(1)	85F1	2 v. r_{ip} ≙ def. oct.; r_{ip}, r_{op}: c.f.a.p.; d: Eq. 2.3
	4.2	r_{ip} = 0.241(1) r_{op} = 0.258(1) d = 0.8187(3) r_{ip} = 0.270(1)	85F1	2 v. r_{ip} ≙ def. oct.; r_{ip}, r_{op}: c.f.a.p.; d: Eq. 2.3
$Rb_2CrCl_2I_2$	110	r_{ip} = 0.239(2) r_{op} = 0.277(2) d = 0.8673(2) r_{ip} = 0.279(2)	85F1	2 v. r_{ip} ≙ def. oct.; r_{ip}, r_{op}: c.f.a.p.; d: Eq. 2.3
	4.2	r_{ip} = 0.240(2) r_{op} = 0.277(2) d = 0.8658(2) r_{ip} = 0.277(2)	85F1	2 v. r_{ip} ≙ def. oct.; r_{ip}, r_{op}: c.f.a.p.; d: Eq. 2.3
$K_3Mn_2Cl_7$	295	r_{ip} = 0.2514 r_{op} = 0.2533 d = 0.7598 r_{op} = 0.2279	65S	r_{ip}, d, 1st r_{op}: Eqs. 2.1, 2.6, 2.7; 2nd r_{op}: c.f.a.p.
Rb_2MnCl_4	295	r_{ip} = 0.253(1) r_{op} = 0.250(5) d = 0.807(3)	77G1	r_{ip}, r_{op}, d: Eqs. 2.1 – 2.3
$Rb_3Mn_2Cl_7$	295	r_{ip} = 0.2526(5) r_{op} = 0.2577(21) d = 0.792(6) r_{op} = 0.2452(38)	78G	r_{ip}, d, 1st r_{op}: Eqs. 2.1, 2.6, 2.7; 2nd r_{op}: c.f.a.p.

Table 3. M-X Bond Lengths and Interlayer Distances *(continued)*

Compound	*T*[K]	M-X bond lengths r_{ip} and r_{op} [nm] Interlayer distance *d* [nm]			Ref.	Remarks
Rb_2MnBr_4	295	$r_{ip} = 0.2685(10)$	$r_{op} = 0.2589(20)$	$d = 0.866(3)$	79G2	r_{ip}, r_{op}, d: Eqs. 2.1 – 2.3
Rb_2CuCl_4	295	$r_{ip} = 0.2370$ $r_{ip} = 0.2716$	$r_{op} = 0.2324$	$d = 0.7767(1)$	74W2	2 v. $r_{ip} \widehat{=}$ def. oct.; r_{ip}, r_{op}: c.f.a.p.; d: Eq. 2.3
Rb_2CuCl_3Br *)	295	$r_{ip} = 0.2291$ $r_{ip} = 0.2811$	$r_{op} = 0.2399$	$d = 0.7960(2)$	74W2	2 v. $r_{ip} \widehat{=}$ def. oct.; r_{ip}, r_{op}: c.f.a.p.; d: Eq. 2.3
$Rb_2CuCl_2Br_2$ *)	295	$r_{ip} = 0.2266$ $r_{ip} = 0.2861$	$r_{op} = 0.2527$	$d = 0.8126(1)$	74W2	2 v. $r_{ip} \widehat{=}$ def. oct.; r_{ip}, r_{op}: c.f.a.p.; d: Eq. 2.3
*) EPR *measurements:* Br^- *only on out-of-plane sites, only* $CuCl_6$ *and* $CuCl_4Br_2$ *octahedra (randomly mixed), but no* $CuCl_5Br$ *octahedra found* [74W2]						
$(NH_4)_2CuCl_4$		$r_{ip} = 0.2300(5)$ $r_{ip} = 0.2793(5)$	$r_{op} = 0.2332(4)$	$d = 0.773(1)$	76P1	2 v. $r_{ip} \widehat{=}$ def. oct.; r_{ip}, r_{op}: c.f.a.p.; d: Eq. 2.3
Rb_2CdCl_4						
α-phase (G_0)	295	$r_{ip} = 0.2603(1)$	$r_{op} = 0.2597(5)$	$d = 0.8085(1)$	89K	r_{ip}, r_{op}, d: Eqs. 2.1 – 2.3
	160	$r_{ip} = 0.2595(1)$	$r_{op} = 0.2587(5)$	$d = 0.8055(1)$	89K	r_{ip}, r_{op}, d: Eqs. 2.1 – 2.3
β-phase (G_1)	105	$r_{ip} = 0.2593(13)$ $r_{ip} = 0.2604(16)$	$r_{op} = 0.2578(16)$	$d = 0.8023(2)$	89K	2 v. r_{ip} r.c. sym.; r_{ip}, r_{op}: c.f.a.p.; d: Eq. 2.3
Cs_2CdCl_4		$r_{ip} = 0.263$	$r_{op} = 0.252$	$d = 0.844$	64S1	r_{ip}, r_{op}, d: Eqs. 2.1 – 2.3
c) Chlorides and Bromides with organic A^+-ions						
$(CH_3NH_3)_2CrCl_4$	295	$r_{ip} = 0.241$ $r_{ip} = 0.282$	$r_{op} = 0.241$	$d = 0.941$	85B1	2 v. $r_{ip} \widehat{=}$ def. oct.; r_{ip}, r_{op}: c.f.a.p.; d: Eq. 2.3
$(C_2H_5NH_3)_2CrCl_4$	295	$\langle r_{ip} \rangle = 0.264$		$d = 1.071$	78B1	$\langle r_{ip} \rangle$: Eq. 2.4; d: Eq. 2.3
$(C_3H_7NH_3)_2CrCl_4$	295	$\langle r_{ip} \rangle = 0.266$		$d = 1.235$	82S1	$\langle r_{ip} \rangle$: Eq. 2.4; d: Eq. 2.3
$(C_5H_{11}NH_3)_2CrCl_4$	295	$\langle r_{ip} \rangle = 0.262$		$d = 1.781$	82S1	$\langle r_{ip} \rangle$: Eq. 2.4; d: Eq. 2.3
$(C_{12}H_{25}NH_3)_2CrCl_4$	295	$\langle r_{ip} \rangle = 0.259$		$d = 3.10$	82S1	$\langle r_{ip} \rangle$: Eq. 2.4; d: Eq. 2.3
$(C_6H_5CH_2NH_3)_2CrCl_4$	295	$\langle r_{ip} \rangle = 0.266$		$d = 1.571$	86B1	$\langle r_{ip} \rangle$: Eq. 2.4; d: Eq. 2.3
$(C_6H_5CH_2NH_3)_2CrBr_4$	295	$\langle r_{ip} \rangle = 0.275$		$d = 1.624$	87B1	$\langle r_{ip} \rangle$: Eq. 2.4; d: Eq. 2.3

Table 3. M-X Bond Lengths and Interlayer Distances *(continued)*

Compound	T[K]	M-X bond lengths r_{ip} and r_{op} [nm] Interlayer distance d [nm]			Ref.	Remarks
$(CH_3NH_3)_2MnCl_4$						
THT-phase	404	$r_{ip} = 0.257(1)$	$r_{op} = 0.250(2)$	$d = 0.976(1)$	75H1	r_{ip}, r_{op}, d: Eqs. 2.1 – 2.3
ORT-phase	293	$r_{ip} = 0.257(2)$	$r_{op} = 0.251(4)$	$d = 0.971(1)$	75H1	r_{ip}, r_{op}: c.f.a.p.; d: Eq. 2.3
TLT-phase	188	$r_{ip} = 0.2556(3)$ $r_{ip} = 0.2578(3)$	$r_{op} = 0.2499$	$d = 0.966(1)$	76H1	2 v. r_{ip} r. c. sym.; r_{ip}, r_{op}: c.f.a.p.; d: Eq. 2.3
$(C_2H_5NH_3)_2MnCl_4$						
ORT-phase	294	$r_{ip} = 0.2593(3)$	$r_{op} = 0.2482(3)$	$d = 1.105(1)$	78D1	r_{ip}, r_{op}: c.f.a.p.; d: Eq. 2.3
OLT-phase	126	$r_{ip} = 0.2572(1)$ $r_{ip} = 0.2585(1)$	$r_{op} = 0.2481(1)$	$d = 1.102(1)$	77D2	2 v. r_{ip} r. c. sym.; r_{ip}, r_{op}: c.f.a.p.; d: Eq. 2.3
$(C_3H_7NH_3)_2MnCl_4$ (δ-ph.)	295	$r_{ip} = 0.2629(5)$	$r_{op} = 0.2475(10)$	$d = 1.290(1)$	72P	r_{ip}, r_{op}: c.f.a.p.; d: Eq. 2.3
	182	$r_{ip} = 0.2601(1)$	$r_{op} = 0.2478(1)$	$d = 1.281(2)$	78D2	r_{ip}, r_{op}: c.f.a.p.; d: Eq. 2.3
$(C_4H_9NH_3)_2MnCl_4$	294	$r_{ip} = 0.2588(0)$	$r_{op} = 0.2468(2)$	$d = 1.5940(3)$	79D2	r_{ip}, r_{op}: c.f.a.p.; d: Eq. 2.3
$(C_5H_{11}NH_3)_2MnCl_4$	293	$\langle r_{ip} \rangle = 0.2587(1)$		$d = 1.8067(3)$	95F1	$\langle r_{ip} \rangle$: Eq. 2.4; d: Eq. 2.3
$(C_6H_{13}NH_3)_2MnCl_4$	295	$\langle r_{ip} \rangle = 0.2579(7)$		$d = 1.990(8)$	79D1	$\langle r_{ip} \rangle$: Eq. 2.4; d: Eq. 2.3
$(C_7H_{15}NH_3)_2MnCl_4$	293	$\langle r_{ip} \rangle = 0.2581(3)$		$d = 2.1452(5)$	95F1	$\langle r_{ip} \rangle$: Eq. 2.4; d: Eq. 2.3
$(C_8H_{17}NH_3)_2MnCl_4$	295	$\langle r_{ip} \rangle = 0.2584(5)$		$d = 2.254(4)$	79D1	$\langle r_{ip} \rangle$: Eq. 2.4; d: Eq. 2.3
$(C_9H_{19}NH_3)_2MnCl_4$	293	$\langle r_{ip} \rangle = 0.2586(6)$		$d = 2.610$	95F1	$\langle r_{ip} \rangle$: Eq. 2.4; d: Eq. 2.3
$(C_{10}H_{21}NH_3)_2MnCl_4$	298	$r_{ip} = 0.2595(2)$ $r_{ip} = 0.2584(2)$	$r_{op} = 0.2485(2)$	$d = 2.6659(21)$	76C1	2 v. r_{ip} r. c. sym.; r_{ip}, r_{op}: c.f.a.p.; $d = c \sin\beta$
$(C_{11}H_{23}NH_3)_2MnCl_4$						
HT-phase	373	$\langle r_{ip} \rangle = 0.254$		$d = 3.100$	74V1	$\langle r_{ip} \rangle$: Eq. 2.5; d det. dir.
LT-phase	298	$\langle r_{ip} \rangle = 0.257$		$d = 2.783$	74V1	$\langle r_{ip} \rangle$: Eq. 2.5; d det. dir.
$(C_{12}H_{25}NH_3)_2MnCl_4$						
HT-phase	373	$\langle r_{ip} \rangle = 0.255$		$d = 3.340$	73V	$\langle r_{ip} \rangle$: Eq. 2.5; d det. dir.
LT-phase	298	$\langle r_{ip} \rangle = 0.257$		$d = 3.028$	73V	$\langle r_{ip} \rangle$: Eq. 2.5; d det. dir.
$(C_{13}H_{27}NH_3)_2MnCl_4$						
HT-phase	373	$\langle r_{ip} \rangle = 0.253$		$d = 3.529$	74V1	$\langle r_{ip} \rangle$: Eq. 2.5; d det. dir.
LT-phase	298	$\langle r_{ip} \rangle = 0.259$		$d = 3.128$	74V1	$\langle r_{ip} \rangle$: Eq. 2.5; d det. dir.

Table 3. M-X Bond Lengths and Interlayer Distances *(continued)*

Compound	T[K]	M-X bond lengths r_{ip} and r_{op} [nm] Interlayer distance d [nm]	Ref.	Remarks
$(C_{14}H_{29}NH_3)_2MnCl_4$				
HT-phase	373	$\langle r_{ip}\rangle = 0.256$ $d = 3.746$	73V	$\langle r_{ip}\rangle$: Eq. 2.5; d det. dir.
LT-phase	298	$\langle r_{ip}\rangle = 0.255$ $d = 3.375$	73V	$\langle r_{ip}\rangle$: Eq. 2.5; d det. dir.
$(C_{15}H_{31}NH_3)_2MnCl_4$				
HT-phase	373	$\langle r_{ip}\rangle = 0.253$ $d = 3.946$	74V1	$\langle r_{ip}\rangle$: Eq. 2.5; d det. dir.
LT-phase	298	$\langle r_{ip}\rangle = 0.259$ $d = 3.486$	74V1	$\langle r_{ip}\rangle$: Eq. 2.5; d det. dir.
$(C_{16}H_{33}NH_3)_2MnCl_4$				
HT-phase	373	$\langle r_{ip}\rangle = 0.256$ $d = 4.178$	73V	$\langle r_{ip}\rangle$: Eq. 2.5; d det. dir.
LT-phase	298	$\langle r_{ip}\rangle = 0.258$ $d = 3.671$	73V	$\langle r_{ip}\rangle$: Eq. 2.5; d det. dir.
$(C_{17}H_{35}NH_3)_2MnCl_4$				
HT-phase	373	$\langle r_{ip}\rangle = 0.252$ $d = 4.366$	74V1	$\langle r_{ip}\rangle$: Eq. 2.5; d det. dir.
LT-phase	298	$\langle r_{ip}\rangle = 0.259$ $d = 3.836$	74V1	$\langle r_{ip}\rangle$: Eq. 2.5; d det. dir.
$(4\text{-}ClC_6H_4NH_3)_2MnCl_4$		$\langle r_{ip}\rangle = 0.256$ $d = 1.66$	79B4	$\langle r_{ip}\rangle$: Eq. 2.4; d: Eq. 2.3
$(C_{11}H_{23}NH_3)_2MnBr_4$	295	$\langle r_{ip}\rangle = 0.274$ $d = 2.659$	81V	$\langle r_{ip}\rangle$: Eq. 2.5; d det. dir.
$(C_{12}H_{25}NH_3)_2MnBr_4$	295	$\langle r_{ip}\rangle = 0.272$ $d = 2.835$	81V	$\langle r_{ip}\rangle$: Eq. 2.5; d det. dir.
$(C_{13}H_{27}NH_3)_2MnBr_4$	295	$\langle r_{ip}\rangle = 0.273$ $d = 2.990$	81V	$\langle r_{ip}\rangle$: Eq. 2.5; d det. dir.
$(C_{14}H_{29}NH_3)_2MnBr_4$	295	$\langle r_{ip}\rangle = 0.272$ $d = 3.175$	81V	$\langle r_{ip}\rangle$: Eq. 2.5; d det. dir.
$(C_{15}H_{31}NH_3)_2MnBr_4$	295	$\langle r_{ip}\rangle = 0.272$ $d = 3.339$	81V	$\langle r_{ip}\rangle$: Eq. 2.5; d det. dir.
$(C_{16}H_{33}NH_3)_2MnBr_4$	295	$\langle r_{ip}\rangle = 0.272$ $d = 3.511$	81V	$\langle r_{ip}\rangle$: Eq. 2.5; d det. dir.
$(CH_3NH_3)_2FeCl_4$	295	$\langle r_{ip}\rangle = 0.2564$ $d = 0.970$	82M2	$\langle r_{ip}\rangle$: Eq. 2.4; d: Eq. 2.3
$(C_{12}H_{25}NH_3)_2FeCl_4$				
HT-phase	393	$\langle r_{ip}\rangle = 0.253$ $d = 3.42(3)$	77L1	$\langle r_{ip}\rangle$: Eq. 2.5; d det. dir.
LT-phase	298	$\langle r_{ip}\rangle = 0.257$ $d = 3.023(6)$	77L1	$\langle r_{ip}\rangle$: Eq. 2.5; d det. dir.
$(CH_3NH_3)_2CuCl_4$	297	$r_{ip} = 0.2283(1)$ $r_{op} = 0.2297(1)$ $d = 0.9316(2)$ $r_{ip} = 0.2907(1)$	87P	2 v. $r_{ip} \hat{=}$ def. oct.; r_{ip}, r_{op}: c.f.a.p.; $d = c \sin\beta$
	100	$r_{ip} = 0.2287(1)$ $r_{op} = 0.2311(1)$ $d = 0.9269(2)$ $r_{ip} = 0.2902(1)$	87P	2 v. $r_{ip} \hat{=}$ def. oct.; r_{ip}, r_{op}: c.f.a.p.; $d = c \sin\beta$
$(C_2H_5NH_3)_2CuCl_4$ (γ-ph.)	295	$r_{ip} = 0.2285(4)$ $r_{op} = 0.2277(6)$ $d = 1.059(1)$ $r_{ip} = 0.2975(50)$	70S1	2 v. $r_{ip} \hat{=}$ def. oct.; r_{ip}, r_{op}: c.f.a.p.; d: Eq. 2.3

Table 3. M-X Bond Lengths and Interlayer Distances *(continued)*

Compound	T[K]	M-X bond lengths r_{ip} and r_{op} [nm] Interlayer distance d [nm]	Ref.	Remarks
$(C_3H_7NH_3)_2CuCl_4$				
α-phase	450	$r_{ip} = 0.2282(3)$ $r_{op} = 0.2267(7)$ $d = 1.323(1)$ $r_{ip} = 0.3026(3)$	90D1	2 v. $r_{ip} \hat{=}$ def. oct.; r_{ip}, r_{op}: c.f.a.p.; d: Eq. 2.3
β-phase	433	$r_{ip} = 0.2284(2)$ $r_{op} = 0.2284(2)$ $d = 1.307(1)$ $r_{ip} = 0.3033(2)$	90D1	2 v. $r_{ip} \hat{=}$ def. oct.; r_{ip}, r_{op}: c.f.a.p.; d: Eq. 2.3
δ-phase	360	$r_{ip} = 0.2298(2)$ $r_{op} = 0.2288(2)$ $d = 1.243(1)$ $r_{ip} = 0.3053(2)$	90D1	2 v. $r_{ip} \hat{=}$ def. oct.; r_{ip}, r_{op}: c.f.a.p.; d: Eq. 2.3
$(C_4H_9NH_3)_2CuCl_4$		$\langle r_{ip}\rangle = 0.260$ $d = 1.514$	72C1	$\langle r_{ip}\rangle$: Eq. 2.4; d: Eq. 2.3
$(C_5H_{11}NH_3)_2CuCl_4$		$\langle r_{ip}\rangle = 0.263$ $d = 1.741$	72C1	$\langle r_{ip}\rangle$: Eq. 2.4; d: Eq. 2.3
$(C_9H_{19}NH_3)_2CuCl_4$				
HT-phase	393	$\langle r_{ip}\rangle = 0.262$ $d = 2.586$	74V2	$\langle r_{ip}\rangle$: Eq. 2.5; d: det. dir.
LT-phase	298	$\langle r_{ip}\rangle = 0.265$ $d = 2.480$	74V2	$\langle r_{ip}\rangle$: Eq. 2.5; d: det. dir.
$(C_{10}H_{21}NH_3)_2CuCl_4$				
HT-phase	393	$\langle r_{ip}\rangle = 0.258$ $d = 2.807$	74V2	$\langle r_{ip}\rangle$: Eq. 2.5; d det. dir.
LT-phase	298	$\langle r_{ip}\rangle = 0.263$ $d = 2.547$	74V2	$\langle r_{ip}\rangle$: Eq. 2.5; d: det. dir.
$(C_{11}H_{23}NH_3)_2CuCl_4$				
HT-phase	393	$\langle r_{ip}\rangle = 0.259$ $d = 3.006$	74V2	$\langle r_{ip}\rangle$: Eq. 2.5; d det. dir.
LT-phase	298	$\langle r_{ip}\rangle = 0.263$ $d = 2.726$	74V2	$\langle r_{ip}\rangle$: Eq. 2.5; d: det. dir.
$(C_{12}H_{25}NH_3)_2CuCl_4$				
HT-phase	393	$\langle r_{ip}\rangle = 0.258$ $d = 3.199$	74V2	$\langle r_{ip}\rangle$: Eq. 2.5; d det. dir.
LT-phase	298	$\langle r_{ip}\rangle = 0.263$ $d = 2.909$	74V2	$\langle r_{ip}\rangle$: Eq. 2.5; d: det. dir.
$(C_{13}H_{27}NH_3)_2CuCl_4$				
HT-phase	393	$\langle r_{ip}\rangle = 0.256$ $d = 3.400$	74V2	$\langle r_{ip}\rangle$: Eq. 2.5; d det. dir.
LT-phase	298	$\langle r_{ip}\rangle = 0.262$ $d = 3.080$	74V2	$\langle r_{ip}\rangle$: Eq. 2.5; d: det. dir.
$(C_{14}H_{29}NH_3)_2CuCl_4$				
HT-phase	393	$\langle r_{ip}\rangle = 0.256$ $d = 3.596$	74V2	$\langle r_{ip}\rangle$: Eq. 2.5; d det. dir.
LT-phase	298	$\langle r_{ip}\rangle = 0.262$ $d = 3.248$	74V2	$\langle r_{ip}\rangle$: Eq. 2.5; d: det. dir.
$(C_{15}H_{31}NH_3)_2CuCl_4$				
HT-phase	393	$\langle r_{ip}\rangle = 0.256$ $d = 3.831$	74V2	$\langle r_{ip}\rangle$: Eq. 2.5; d det. dir.
LT-phase	298	$\langle r_{ip}\rangle = 0.262$ $d = 3.420$	74V2	$\langle r_{ip}\rangle$: Eq. 2.5; d: det. dir.

Table 3. M-X Bond Lengths and Interlayer Distances *(continued)*

Compound	T[K]	M-X bond lengths r_{ip} and r_{op} [nm] Interlayer distance d [nm]	Ref.	Remarks
$(C_{16}H_{33}NH_3)_2CuCl_4$				
HT-phase	393	$\langle r_{ip}\rangle = 0.256$ $d = 4.035$	74V2	$\langle r_{ip}\rangle$: Eq. 2.5; d det. dir.
LT-phase	298	$\langle r_{ip}\rangle = 0.260$ $d = 3.612$	74V2	$\langle r_{ip}\rangle$: Eq. 2.5; d: det. dir.
$(C_{17}H_{35}NH_3)_2CuCl_4$				
HT-phase	393	$\langle r_{ip}\rangle = 0.260$ $d = 4.215$	74V2	$\langle r_{ip}\rangle$: Eq. 2.5; d det. dir.
LT-phase	298	$\langle r_{ip}\rangle = 0.261$ $d = 3.778$	74V2	$\langle r_{ip}\rangle$: Eq. 2.5; d: det. dir.
$(CH_2OH\text{-}CH_2\text{-}NH_3)_2CuCl_4$	295	$r_{ip} = 0.2288$ $r_{op} = 0.2274$ $d = 1.0812$ $r_{ip} = 0.3010$	88W1	2 v. $r_{ip} \hat{=}$ def. oct.; r_{ip}, r_{op}: c.f.a.p.; $d = c \sin\beta$
$(C_6H_5NH_3)_2CuCl_4$	295	$r_{ip} = 0.22804(6)$ $r_{op} = 0.23007(5)$ $d = 1.4788(2)$ $r_{ip} = 0.29718(5)$	76P1	2 v. $r_{ip} \hat{=}$ def. oct.; r_{ip}, r_{op}: c.f.a.p.; $d = c \sin\beta$
$[C_6H_5(CH_2)_2NH_3]_2CuCl_4$	295	$r_{ip} = 0.2286(1)$ $r_{op} = 0.2296(1)$ $d = 1.9309(3)$ $r_{ip} = 0.2899(1)$	90W1	2 v. $r_{ip} \hat{=}$ def. oct.; r_{ip}, r_{op}: c.f.a.p.; $d = c \sin\beta$
$[COOH(CH_2)_2NH_3]_2CuCl_4$	295	$r_{ip} = 0.2307(1)$ $r_{op} = 0.2274(1)$ $d = 1.2112$ $r_{ip} = 0.3077(1)$	81W2	2 v. $r_{ip} \hat{=}$ def. oct.; r_{ip}, r_{op}: c.f.a.p.; $d = c/2 \sin\beta$
$(CH_3NH_3)_2CuCl_2Br_2$				
	295	$d = 0.9605(2)$	91W1	d: Eq. 2.3
in-plane site: Cl (p = 0.88)		$r_{ip} = 0.2387(6)$ $r_{ip} = 0.2755(7)$		2 v. $r_{ip} \hat{=}$ def. oct.; r_{ip}, r_{op}: c.f.a.p.
Br (p = 0.12)		$r_{ip} = 0.2387(6)$ $r_{ip} = 0.2755(7)$		
out-of-plane: Br (p = 0.76)		$r_{op} = 0.2413(13)$		
Cl (p = 0.24)		$r_{op} = 0.2387(6)$		
$(CH_3NH_3)_2CuBr_4$		$\langle r_{ip}\rangle = 0.2733$ $d = 0.959$	72C1	$\langle r_{ip}\rangle$: Eq. 2.4; d: Eq. 2.3
$(C_2H_5NH_3)_2CuBr_4$		$\langle r_{ip}\rangle = 0.277$ $d = 1.075$	72C1	$\langle r_{ip}\rangle$: Eq. 2.4; d: Eq. 2.3
$(C_3H_7NH_3)_2CuBr_4$		$\langle r_{ip}\rangle = 0.279$ $d = 1.216$	72C1	$\langle r_{ip}\rangle$: Eq. 2.4; d: Eq. 2.3
$(C_4H_9NH_3)_2CuBr_4$		$\langle r_{ip}\rangle = 0.2764$ $d = 1.432$	72C1	$\langle r_{ip}\rangle$: Eq. 2.4; d: Eq. 2.3
$(C_{11}H_{23}NH_3)_2CuBr_4$	295	$\langle r_{ip}\rangle = 0.2765$ $d = 2.599$	81V	$\langle r_{ip}\rangle$: Eq. 2.5; d det. dir.
$(C_{12}H_{25}NH_3)_2CuBr_4$	295	$\langle r_{ip}\rangle = 0.276$ $d = 2.771$	81V	$\langle r_{ip}\rangle$: Eq. 2.5; d det. dir.
$(C_{13}H_{27}NH_3)_2CuBr_4$	295	$\langle r_{ip}\rangle = 0.276$ $d = 2.922$	81V	$\langle r_{ip}\rangle$: Eq. 2.5; d det. dir.
$(C_{14}H_{29}NH_3)_2CuBr_4$	295	$\langle r_{ip}\rangle = 0.275$ $d = 3.102$	81V	$\langle r_{ip}\rangle$: Eq. 2.5; d det. dir.

Table 3. M-X Bond Lengths and Interlayer Distances *(continued)*

Compound	T[K]	M-X bond lengths r_{ip} and r_{op} [nm] Interlayer distance d [nm]	Ref.	Remarks
$(C_{15}H_{31}NH_3)_2CuBr_4$	295	$\langle r_{ip} \rangle = 0.278$ $d = 3.163$	81V	$\langle r_{ip} \rangle$: Eq. 2.5; d det. dir.
$(C_{16}H_{33}NH_3)_2CuBr_4$	295	$\langle r_{ip} \rangle = 0.274$ $d = 3.431$	81V	$\langle r_{ip} \rangle$: Eq. 2.5; d det. dir.
$[C_6H_5(CH_2)_2NH_3]_2CuBr_4$	295	$r_{ip} = 0.2418(1)$ $r_{op} = 0.2449(1)$ $d = 1.9021(9)$ $r_{ip} = 0.3057(1)$	90W1	2 v. $r_{ip} \hat{=}$ def. oct.; r_{ip}, r_{op}: c.f.a.p.; d: Eq. 2.3
$[COOH(CH_2)_2NH_3]_2CuBr_4$		$r_{ip} = 0.2444(1)$ $r_{op} = 0.2429(1)$ $d = 1.2136(4)$ $r_{ip} = 0.3172(1)$	83W2	2 v. $r_{ip} \hat{=}$ def. oct.; r_{ip}, r_{op}: c.f.a.p.; $d = c/2 \sin\beta$
$(C_3H_7NH_3)_2PdCl_4$	295	$r_{ip} = 0.2317(7)$ $r_{op} = 0.2308(8)$ $d = 1.173(1)$ $r_{ip} = 0.3190(8)$	77W2	2 v. $r_{ip} \hat{=}$ def. oct.; r_{ip}, r_{op}: c.f.a.p.; $d = c \sin\beta$
$(CH_3NH_3)_2CdCl_4$				
THT-phase	493	$r_{ip} = 0.2651(1)$ $r_{op} = 0.2523(4)$ $d = 0.9670(5)$	76C2	r_{ip}, r_{op}, d: Eqs. 2.1 – 2.3
ORT-phase	294	$r_{ip} = 0.2644(2)$ $r_{op} = 0.2537(5)$ $d = 0.961(1)$	75C1	r_{ip}, r_{op}: c.f.a.p.; d: Eq. 2.3
TLT-phase	234	$r_{ip} = 0.2627(1)$ $r_{op} = 0.2550(3)$ $d = 0960(1)$ $r_{ip} = 0.2665(2)$	75C1	2 v. r_{ip} r. c. sym.; r_{ip}, r_{op}: c.f.a.p.; d: Eq. 2.3
MLT-phase	147	$r_{ip} = 0.2636(1)$ $r_{op} = 0.2572(3)$ $d = 0.9683(5)$ $r_{ip} = 0.2647(2)$	76C2	2 v. r_{ip} r. c. sym.; r_{ip}, r_{op}: c.f.a.p.; $d = c/2 \sin\beta$, *alternative description:* $d = c \sin\beta$
$(C_2H_5NH_3)_2CdCl_4$				
ORT-phase	295	$r_{ip} = 0.2673(1)$ $r_{op} = 0.2522(2)$ $d = 1.0940(4)$	77C2	r_{ip}, r_{op}: c.f.a.p.; d: Eqs. 2.3
OLT-phase	178	$r_{ip} = 0.2649(2)$ $r_{op} = 0.2555(1)$ $d = 1.106(2)$ $r_{ip} = 0.2661(2)$	77C2	2 v. r_{ip} r. c. sym.; r_{ip}, r_{op}: c.f.a.p.; d: Eq. 2.3
$(C_3H_7NH_3)_2CdCl_4$				
ORT-phase	220	$r_{ip} = 0.2667(1)$ $r_{op} = 0.2535(2)$ $d = 1.2592(3)$	78C1	r_{ip}, r_{op}: c.f.a.p.; d: Eqs. 2.3
OLT-phase	≈ 130	$r_{ip} = 0.2651(2)$ $r_{op} = 0.2561(2)$ $d = 1.2758(4)$ $r_{ip} = 0.2561(2)$	78C1	2 v. r_{ip} r. c. sym.; r_{ip}, r_{op}: c.f.a.p.; d: Eq. 2.3
$(C_8H_{17}NH_3)_2CdCl_4$				
HT-phase	353	$\langle r_{ip} \rangle = 0.266(1)$ $d = 2.394(5)$	83C1	$\langle r_{ip} \rangle$: Eq. 2.4; d: Eq. 2.3
LT-phase	243	$\langle r_{ip} \rangle = 0.264(1)$ $d = 2.252(10)$	83C1	$\langle r_{ip} \rangle$: Eq. 2.4; d: Eq. 2.3
$(C_9H_{19}NH_3)_2CdCl_4$				
LT-phase	295	$\langle r_{ip} \rangle = 0.2794$ $d = 2.3083$	95K	$\langle r_{ip} \rangle$: Eq. 2.4; $d = c/2 \sin\beta$

Table 3. M-X Bond Lengths and Interlayer Distances *(continued)*

Compound	T[K]	M-X bond lengths r_{ip} and r_{op} [nm] Interlayer distance d [nm]	Ref.	Remarks
$(C_{10}H_{21}NH_3)_2CdCl_4$				
HT-phase	318	$\langle r_{ip}\rangle = 0.2653(2)$ $d = 2.732(1)$	79K1	$\langle r_{ip}\rangle$: Eq. 2.4; d: Eq. 2.3
IM-phase	308	$\langle r_{ip}\rangle = 0.264(2)$ $d = 2.581(3)$	83C1	$\langle r_{ip}\rangle$: Eq. 2.4; d: Eq. 2.3
LT-phase	294	$\langle r_{ip}\rangle = 0.2634(1)$ $d = 2.580(2)$	79K1	$\langle r_{ip}\rangle$: Eq. 2.4; $d = c/2 \sin\beta$
$(C_{12}H_{25}NH_3)_2CdCl_4$				
HT-phase	360	$r_{ip} = 0.2655(1)$ $d = 3.216(2)$	85C1	r_{ip}, d: Eqs. 2.1, 2.3
IM-phase 1	334	$\langle r_{ip}\rangle = 0.2656(5)$ $d = 3.175(2)$	85C1	$\langle r_{ip}\rangle$: Eq. 2.4; d: Eq. 2.3
LT-phase	293	$\langle r_{ip}\rangle = 0.2649(1)$ $d = 2.938(1)$	85C1	$\langle r_{ip}\rangle$: Eq. 2.4; $d = c/2 \sin\beta$
$(C_{14}H_{29}NH_3)_2CdCl_4$				
α-phase	> 352	$\langle r_{ip}\rangle = 0.265(1)$ $d = 3.577(6)$	88S1	$\langle r_{ip}\rangle$: Eq. 2.4; $d = c$
γ-phase	348	$\langle r_{ip}\rangle = 0.261(2)$ $d = 3.360(7)$	88S1	$\langle r_{ip}\rangle$: Eq. 2.4; $d = c$
ε-phase	298	$d = 3.284$	88S1	$d \approx c \cdot \sin\alpha \cdot \sin\beta$
Cd 1		$r_{ip} = 0.2631(4)$ $r_{ip} = 0.2656(4)$ $r_{op} = 0.2582(4)$		2 v. r_{ip} r. c. sym.; r_{ip}, r_{op}: c.f.a.p.;
Cd 2		$r_{ip} = 0.2670(2)$ $r_{ip} = 0.2650(2)$ $r_{op} = 0.2544(2)$		for each of the two inequivalent Cd-sites
$(C_{16}H_{33}NH_3)_2CdCl_4$				
HT-phase	360	$r_{ip} = 0.2649(1)$ $d = 4.002(4)$	89C2	r_{ip}, d: Eqs. 2.1, 2.3
IM-phase 1	354	$\langle r_{ip}\rangle = 0.2656(12)$ $d = 3.823(6)$	89C2	$\langle r_{ip}\rangle$: Eq. 2.4; d: Eq. 2.3
IM-phase 2	348	$\langle r_{ip}\rangle = 0.2656(7)$ $d = 3.762(4)$	89C2	$\langle r_{ip}\rangle$: Eq. 2.4; d: Eq. 2.3
LT-phase	293	$\langle r_{ip}\rangle = 0.2639(6)$ $d = 3.657(2)$	89C2	$\langle r_{ip}\rangle$: Eq. 2.4; $d = c/2 \sin\beta$
$(C_2H_5NH_3)_2HgCl_4$	243	$r_{ip} = 0.2767(1)$ $r_{op} = 0.2437(1)$ $d = 1.0189(2)$ $r_{ip} = 0.2843(1)$	83B1	2 v. r_{ip} r. c. sym.; r_{ip}, r_{op}: c.f.a.p.; d: Eq. 2.3
$(C_3H_7NH_3)_2HgCl_4$	300	$r_{ip} = 0.2813(1)$ $r_{op} = 0.2426(1)$ $d = 1.176(1)$	86B2	r_{ip}, r_{op}: c.f.a.p.; d: Eq. 2.3
$(C_8H_{17}NH_3)_2HgCl_4$				
HT-phase	365	$d = 2.25$	79B1	d det. dir.
LT-phase	298	$\langle r_{ip}\rangle = 0.278$ $d = 2.10$	79B1	$\langle r_{ip}\rangle$: Eq. 2.5; d det. dir.
$(C_{12}H_{25}NH_3)_2HgCl_4$				
HT-phase	393	$\langle r_{ip}\rangle = 0.274$ $d = 2.97(2)$	75L1	$\langle r_{ip}\rangle$: Eq. 2.5; d det. dir.
LT-phase	298	$\langle r_{ip}\rangle = 0.278$ $d = 2.700(6)$	75L1	$\langle r_{ip}\rangle$: Eq. 2.5; d det. dir.
$(C_{16}H_{33}NH_3)_2HgCl_4$				
HT-phase	365	$d = 3.77$	79B1	d det. dir.
LT-phase	298	$\langle r_{ip}\rangle = 0.278$ $d = 3.28$	79B1	$\langle r_{ip}\rangle$: Eq. 2.5; d det. dir.

Table 3. M-X Bond Lengths and Interlayer Distances *(continued)*

Compound	T[K]	M-X bond lengths r_{ip} and r_{op} [nm] Interlayer distance d [nm]	Ref.	Remarks
$(C_3H_7NH_3)_2PbCl_4$				
ORT-phase	295	$r_{ip} = 0.2830(7)$ $r_{op} = 0.2879(7)$ $d = 1.2517(2)$ $r_{ip} = 0.2878(7)$ $r_{ip} = 0.2899(7)$ $r_{ip} = 0.2911(7)$	89M1	4 values for r_{ip} required by symmetry in this structure; r_{ip}, r_{op}: c.f.a.p.; d: Eq. 2.3
$(C_9H_{19}NH_3)_2PbCl_4$		$\langle r_{ip} \rangle = 0.2630$ $d = 2.3718$	95K	$\langle r_{ip} \rangle$: Eq. 2.4; $d = c/2 \sin\beta$
d) Diammonium Compounds with X = Cl^-, Br^-				
$[NH_3(CH_2)_2NH_3]MnCl_4$	296	$r_{ip} = 0.2556(3)$ $r_{op} = 0.2488(3)$ $d = 0.8599(2)$ $r_{ip} = 0.2578(3)$	78T1	2 v. r_{ip} r. c. sym.; r_{ip}, r_{op}: c.f.a.p.; $d = c \sin\beta$
$[NH_3(CH_2)_3NH_3]MnCl_4$				
α-phase	343	$r_{ip} = 0.25933(5)$ $r_{op} = 0.2483(2)$ $d = 0.9446(2)$	82C	r_{ip}, r_{op}: c.f.a.p.; d: Eq. 2.3
β-phase	313	$r_{ip} = 0.25635(5)$ $r_{op} = 0.24877(8)$ $d = 0.9434(2)$ $r_{ip} = 0.26210(6)$	82C	2 v. r_{ip} r. c. sym.; r_{ip}, r_{op}: c.f.a.p.; d: Eq. 2.3
γ-phase	296	$r_{ip} = 0.25830(6)$ $r_{op} = 0.24932(8)$ $d = 0.9510(2)$ $r_{ip} = 0.25982(6)$	82C	2 v. r_{ip} r. c. sym.; r_{ip}, r_{op}: c.f.a.p.; d: Eq. 2.3
$[NH_3(CH_2)_4NH_3]MnCl_4$				
OHT-phase	404	$r_{ip} = 0.2582(1)$ $r_{op} = 0.2476(4)$ $d = 1.0690(5)$	80T1	r_{ip}, r_{op}: c.f.a.p.; $d = c$
MRT-phase	295	$r_{ip} = 0.2557(4)$ $r_{op} = 0.2486(4)$ $d = 1.0758(6)$ $r_{ip} = 0.2595(4)$	80T1	2 v. r_{ip} r. c. sym.; r_{ip}, r_{op}: c.f.a.p.; $d = c \sin\alpha$
$[NH_3(CH_2)_3NH_3]FeCl_4$	295	$r_{ip} = 0.2573(4)$ $r_{op} = 0.2404(4)$ $d = 0.9285(15)$	75W1	r_{ip}, r_{op}: c.f.a.p.; d: Eq. 2.3
$[NH_3(CH_2)_2NH_3]CuCl_4$	296	$r_{ip} = 0.2288(2)$ $r_{op} = 0.2294(2)$ $d = 0.8102(3)$ $r_{ip} = 0.2882(2)$	78T1	2 v. $r_{ip} \hat{=}$ def. oct.; r_{ip}, r_{op}: c.f.a.p.; $d = c \sin\beta$
$[NH_3(CH_2)_3NH_3]CuCl_4$	295	$r_{ip} = 0.2275(1)$ $r_{op} = 0.2314(1)$ $d = 0.9123(3)$ $r_{ip} = 0.2946(1)$	76P1	2 v. $r_{ip} \hat{=}$ def. oct.; r_{ip}, r_{op}: c.f.a.p.; d: Eq. 2.3
$[NH_3(CH_2)_4NH_3]CuCl_4$	293	$r_{ip} = 0.2308(2)$ $r_{op} = 0.2280(2)$ $d = 0.9025(1)$ $r_{ip} = 0.3100(2)$	90G1	2 v. $r_{ip} \hat{=}$ def. oct.; r_{ip}, r_{op}: c.f.a.p.; $d = c \sin \beta$
$[NH_3(CH_2)_5NH_3]CuCl_4$	293	$d = 1.0638(4)$	90G1	$d = c/2 \sin\beta$
Cu 1		$r_{ip} = 0.2279(1)$ $r_{ip} = 0.3020(10)$ $r_{op} = 0.2299(7)$		2 v. $r_{ip} \hat{=}$ def. oct.; r_{ip}, r_{op}: c.f.a.p.;
Cu 2		$r_{ip} = 0.2307(10)$ $r_{ip} = 0.3058(7)$ $r_{op} = 0.2307(6)$		for each of the two inequivalent Cu-sites
$[NH_3(CH_2)_2NH_3]CuBr_4$	293	$r_{ip} = 0.2431(1)$ $r_{op} = 0.2444(1)$ $d = 0.8328(3)$ $r_{ip} = 0.3034(1)$	88H1	2 v. $r_{ip} \hat{=}$ def. oct.; r_{ip}, r_{op}: c.f.a.p.; $d = c \sin \beta$

Table 3. M-X Bond Lengths and Interlayer Distances *(continued)*

Compound	T[K]	M-X bond lengths r_{ip} and r_{op} [nm] Interlayer distance d [nm]			Ref.	Remarks
$[NH_3(CH_2)_3NH_3]CuBr_4$	293	$d = 0.8750(3)$			88H1	$d = c/2 \sin\beta$
Cu 1		$r_{\mathrm{ip}} = 0.2442(3)$	$r_{\mathrm{ip}} = 0.3148(3)$	$r_{\mathrm{op}} = 0.2440(3)$		2 v. $r_{\mathrm{ip}} \mathrel{\hat{=}}$ def. oct.; r_{ip}, r_{op}: c.f.a.p.;
Cu 2		$r_{\mathrm{ip}} = 0.2432(3)$	$r_{\mathrm{ip}} = 0.3148(3)$	$r_{\mathrm{op}} = 0.2450(3)$		for each of the two inequivalent Cu-sites
$[NH_3(CH_2)_4NH_3]CuBr_4$	293	$r_{\mathrm{ip}} = 0.2442(1)$	$r_{\mathrm{op}} = 0.2431(1)$	$d = 0.9197(2)$	90G1	2 v. $r_{\mathrm{ip}} \mathrel{\hat{=}}$ def. oct.; r_{ip}, r_{op}: c.f.a.p.; $d = c \sin\beta$
		$r_{\mathrm{ip}} = 0.3185(1)$				
$[NH_3(CH_2)_5NH_3]CuBr_4$	293	$d = 1.0650(5)$			90G1	$d = c/2 \sin\beta$
Cu 1		$r_{\mathrm{ip}} = 0.2429(3)$	$r_{\mathrm{ip}} = 0.3164(3)$	$r_{\mathrm{op}} = 0.2450(3)$		2 v. $r_{\mathrm{ip}} \mathrel{\hat{=}}$ def. oct.; r_{ip}, r_{op}: c.f.a.p.;
Cu 2		$r_{\mathrm{ip}} = 0.2430(2)$	$r_{\mathrm{ip}} = 0.3179(3)$	$r_{\mathrm{op}} = 0.2442(3)$		for each of the two inequivalent Cu-sites
$[NH_3(CH_2)_2NH_3]PdCl_4$	295	$r_{\mathrm{ip}} = 0.2300(5)$	$r_{\mathrm{op}} = 0.2323(6)$	$d = 0.791(2)$	76B3	2 v. $r_{\mathrm{ip}} \mathrel{\hat{=}}$ def. oct.; r_{ip}, r_{op}: c.f.a.p.; $d = c \sin\beta$
		$r_{\mathrm{ip}} = 0.3062(5)$				
$[NH_3(CH_2)_2NH_3]CdCl_4$	295	$r_{\mathrm{ip}} = 0.2643(1)$	$r_{\mathrm{op}} = 0.2556(1)$	$d = 0.8599(5)$	92B1	2 v. r_{ip} r. c. sym.; r_{ip}, r_{op}: c.f.a.p.; $d = c \sin\beta$
		$r_{\mathrm{ip}} = 0.2648(1)$				
$[NH_3(CH_2)_3NH_3]CdCl_4$	295	$r_{\mathrm{ip}} = 0.2661(2)$	$r_{\mathrm{op}} = 0.2581(2)$	$d = 0.9556(4)$	77W1	2 v. r_{ip} r. c. sym.; r_{ip}, r_{op}: c.f.a.p.; d: Eq. 2.3
		$r_{\mathrm{ip}} = 0.2680(2)$				
$[NH_3(CH_2)_5NH_3]CdCl_4$						
OHT-phase	353	$r_{\mathrm{ip}} = 0.2658(4)$	$r_{\mathrm{op}} = 0.2547(3)$	$d = 1.1778(3)$	87N1	r_{ip}, r_{op}: c.f.a.p.; d: Eq. 2.3
ORT-phase	293	$r_{\mathrm{ip}} = 0.2645(2)$	$r_{\mathrm{op}} = 0.2562(2)$	$d = 1.1931(2)$	87N1	2 v. r_{ip} r. c. sym.; r_{ip}, r_{op}: c.f.a.p.; d: Eq. 2.3
		$r_{\mathrm{ip}} = 0.2658(2)$				
e) Diluted Magnets						
$RbCr_{0.73}Mg_{0.27}Cl_4$	4.2	$r_{\mathrm{ip}} = 0.2399(30)$	$r_{\mathrm{op}} = 0.2413(11)$	$d = 0.7881(6)$	86F1	2 v. $r_{\mathrm{ip}} \mathrel{\hat{=}}$ def. oct.; r_{ip}, r_{op}: c.f.a.p.; d: Eq. 2.3
		$r_{\mathrm{ip}} = 0.2642(30)$				
f) Mixed Magnets						
$Rb_2Cr_{0.989}Mn_{0.011}Cl_4$	293	$r_{\mathrm{ip}} = 0.2399(15)$	$r_{\mathrm{op}} = 0.2431(2)$	$d = 0.7887(4)$	80M2	2 v. $r_{\mathrm{ip}} \mathrel{\hat{=}}$ def. oct.; r_{ip}, r_{op}: c.f.a.p.; d: Eq. 2.3
		$r_{\mathrm{ip}} = 0.2736(15)$				
	15	$r_{\mathrm{ip}} = 0.2389(8)$	$r_{\mathrm{op}} = 0.2444(2)$	$d = 0.7865(4)$	80M3	2 v. $r_{\mathrm{ip}} \mathrel{\hat{=}}$ def. oct.; r_{ip}, r_{op}: c.f.a.p.; d: Eq. 2.3
		$r_{\mathrm{ip}} = 0.2694(8)$				
$(CH_3NH_3)_2Mn_{0.97}Cu_{0.03}Cl_4$	295	$r_{\mathrm{ip}} = 0.25677(5)$	$r_{\mathrm{op}} = 0.2487(1)$	$d = 0.9701(4)$	82C2	r_{ip}, r_{op}: c.f.a.p.; d: Eq. 2.3

Table 4. Data about Structural Phase Transitions

Compound	Phase sequence, transition temperature T_{Cn} [K], enthalpy ΔH_n [J · mol^{-1}] and entropy ΔS_n [J · mol^{-1} · K^{-1}] of the n - th structural phase transition	References, remarks
a) Fluorides		
$(NH_4)_2MgF_4$	$\mathrm{I4/mmm} \xleftrightarrow[T_C]{disc.} \mathrm{P12_1/c1}$	**struct. pt. studied by:** therm. m. [96S2], diffr. [96S2], see also [68C1]
	THT MLT	
	$T_C = 163(1)$ $\Delta H = 4.9(7) \cdot 10^3$ $\Delta S = 43(7)$	T_C, ΔH, ΔS: d.s.c. [96S2]
b) Chlorides and Bromides with inorganic A$^+$-ions		
Rb_2CdCl_4	$\mathrm{I4/mmm} \xleftrightarrow[T_C]{} \mathrm{Pccn}\begin{pmatrix}\mathrm{Abma}\\ \mathrm{Bmab}\end{pmatrix}$ *)	**struct. pt. studied by:** therm. m. [85A2, 87G2, 90F1]; EPR (Mn-doped samples) [85A1]; birefr. [85A2, 87G2]; opt. m. [87G2, 90A5]; Raman sp. [85A2, 86S2, 92S5]; NMR [90A4]; diffr. [68S1, 85A1, 85A2, 89K, 90A5]
	(α, G_0) (β, G_1)	
	*) *The space group* Pccn *combines the order in* Abma *with that in* Bmab; ^{87}Rb-NMR *studies yielded a high probability for* Abma *or* Bmab [90A4]	
	$T_C = 142.8$ $\Delta S = 2.33$	T_C, ΔS: $C_p(T)$ by ad. cal. [85A2, 87G2]
	$dT_C/dp = -1.4(7) \cdot 10^{-8}$ K/Pa	dT_C/dp: high press. exp. [87G2, 90F1]
$Rb_3Cd_2Cl_7$	$\mathrm{I4/mmm} \xleftrightarrow[T_{C1}]{cont.} \begin{matrix}\mathrm{Amam}\\ \mathrm{Bbmm}\end{matrix} \xleftrightarrow[T_{C2}]{disc.} \mathrm{P4_2/mnm}$	**struct. pt.'s studied by:** therm. m. [88A1, 89F1]; opt. m. [88A1, 90A5]; birefr. [89F1]; diffr. [68S1, 88A1, 90A5]
	(α, G_0) (β, G_1) (γ, G_3)	
	$T_{C1} = 213.6$ $\Delta S_1 = 2.99$	T_{C1}, T_{C2}: opt. m. [88A1]
	$T_{C2} = 172.1$ $\Delta S_2 = 1.00$	ΔS_1, ΔS_2: $C_p(T)$ by ad. cal. [88A1, 89F1]
$Rb_4Cd_3Cl_{10}$	$\mathrm{I4/mmm} \xleftrightarrow[T_{C1}]{cont.} \begin{matrix}\mathrm{Abma}\\ \mathrm{Bmab}\end{matrix} \xleftrightarrow[T_{C2}]{disc.} \mathrm{P4_2/ncm} \xleftrightarrow[T_{C3}]{disc.} \begin{matrix}\mathrm{A2_1/b11}\\ \mathrm{B12_1/a1}\end{matrix}$	**struct. pt.'s studied by:** opt. m. [90A5, 90B2]; diffr. [68S1, 90A5, 90B2]
	(α, G_0) (β, G_1) (γ, G_2) (δ, G_3)	
	$T_{C1} = 237$ $T_{C2} = 194$ $T_{C3} = 136$	T_{C1}, T_{C2}, T_{C3}: opt. m. [90A5, 90B2]

Table 4. Data about Structural Phase Transitions *(continued)*

Compound	Phase sequence, transition temperature T_{Cn} [K], enthalpy ΔH_n [J · mol^{-1}] and entropy ΔS_n [J · mol^{-1} · K^{-1}] of the n - th structural phase transition	References, remarks
c) Chlorides and Bromides with organic A$^+$-ions		
$(CH_3NH_3)_2CrCl_4$	Aba2 (295 K) $\xleftrightarrow[T_C=?]{}$ $P12_1/cl$ (87 K)	different structures at 295 and 87 K [78B1, 85B1], struct. pt. expected, in $C_p(T)$ no sharp anomaly but only broad features observed in the range 100–210 K [82R1]
$(CH_3NH_3)_2MnCl_4$	$\begin{array}{c}\mathrm{I4/mmm}\\(\mathrm{THT})\end{array} \xleftrightarrow[T_{C1}]{cont.} \begin{array}{c}\mathrm{Abma}\\\mathrm{Bmab}\\(\mathrm{ORT})\end{array} \xleftrightarrow[T_{C2}]{disc.} \begin{array}{c}\mathrm{P4_2/ncm}\\(\mathrm{TLT})\end{array} \xleftrightarrow[T_{C3}]{disc.} \begin{array}{c}\mathrm{A2_1/b11}\\\mathrm{B12_1/a1}\\(\mathrm{MLT})\end{array} \xleftrightarrow[T_{C4}]{} ???^{*)}$ *) *a further structural phase transition was concluded from an anomaly in the magn. susceptibility, structure of the new phase not yet determined* [91P]	**struct. pt.'s studied by:** therm. m. [73A1, 75B1, 77D1, 77T1, 78S2, 82W2]; opt. m. [73A1, 74A1]; birefr. [73A1, 74K1, 81K1]; diel. c. [78S1], NMR, NQR [76B1, 76K1]; Raman sp. [74S2, 77C4, 78A1, 78C2, 83M1]; ir spectr. [75L2, 77V1, 78A1, 78L1, 78L2, 81R3]; elast. c. [79G3, 80G2, 81K1]; diffr. [68F1, 72A, 73H1, 74K1, 75H1, 76H1, 77D1, 78L1, 79D1, 83C2, 90A1]; incoh. n.s. [80K1, 83M1, 84R1]
	$T_{C1} = 393.7$ $\Delta H_1 = 63(13)$ $\Delta S_1 = 0.13(4)$	T_{C1}: ^{35}Cl-NQR [76K1]; ΔH_1, ΔS_1: $C_p(T)$ by d.s.c. [75B1]
	$T_{C2} = 257.02(7)$ $\Delta H_2 = 116(1)$ $\Delta S_2 = 0.451(4)$	T_{C2}, ΔH_2, ΔS_2: $C_p(T)$ by ad. cal. [82W2]
	$T_{C3} = 94.37(5)$ $\Delta H_3 = 727(5)$ $\Delta S_3 = 7.76(5)$	T_{C3}, ΔH_3, ΔS_3: $C_p(T)$ by ad. cal. [82W2]
	$T_{C4} = 46$	T_{C4}: meas. χ_{magn} [91P]
	heating: $T_{C2} = 256.9$ $T_{C3} = 95.1$ cooling: $T_{C2} = 256.5$ $T_{C3} = 93.7$	$\}$ T_{C2}, T_{C3} for heating, cooling: [74K1]
$(CD_3ND_3)_2MnCl_4$	same phase sequence as above, slightly different T_{Cn}	
	$T_{C1} = 389.6$	T_{C1}: diffr. [78L1]
	Transition to a new phase at high pressure:	
	$T = 293$ $\begin{array}{c}\mathrm{Abma}\\\mathrm{Bmab}\\(\mathrm{ORT})\end{array} \xleftrightarrow[p_C]{} \begin{array}{c}\mathrm{P1\ \ or\ \ P\bar{1}}\\(\mathrm{HP})\end{array}$	
	$p_C = 2.05(2)$ GPa at 295 K	p_C: high press. exp. [78H1, 89C1, 93C1]

Table 4. Data about Structural Phase Transitions *(continued)*

Compound	Phase sequence, transition temperature T_{Cn} [K], enthalpy ΔH_n [J · mol^{-1}] and entropy ΔS_n [J · mol^{-1} · K^{-1}] of the n - th structural phase transition	References, remarks
$(C_2H_5NH_3)_2MnCl_4$	$I4/mmm \underset{T_{C1}}{\overset{cont.}{\longleftrightarrow}} \begin{matrix}Abma\\Bmab\end{matrix} \underset{T_{C2}}{\overset{disc.}{\longleftrightarrow}} \begin{matrix}Pbca\\Pcab\end{matrix} \longleftrightarrow\ ???*)$ (THT) (ORT) (OLT)	**struct. pt.'s studied by:** therm. m. [73A1, 75B1, 77D1, 77D2, 77T1]; opt. m. [73A1, 74A1]; birefr. [73A1, 81K1, 82B1]; diel. c. [80F1]; elast. c. [81K1, 89Z2]; Raman sp. [76R1, 85H1, 89G6]; ir spectr. [78L1, 78L2, 81R3]; diffr. [74A1, 76D3, 77D1, 77D2, 79D1, 86A1, 90A1]
*)	*a further structural phase transition concluded from anormalies in elastic properties, thermal expansion and magnetic susceptibility, structure of the new phase not determined* [89G6, 89Z2, 91P]	
	$T_{C1} = 424$ $\Delta H_1 = 71(13)$ $\Delta S_1 = 0.17(4)$ $T_{C2} = 225$ $\Delta H_2 = 762$ $\Delta S_2 = 3.5$ $T_{C3} = 47.0(5)$	T_{C1}, ΔH_1, ΔS_1: $C_p(T)$ by d.s.c. [75B1] T_{C2}: birefr. [82B1]; ΔH_2, ΔS_2: $C_p(T)$ by d.s.c. [77T1] T_{C3}: meas. υ_s and thermal expansion: [89Z2]
$(C_3H_7NH_3)_2MnCl_4$	$I4/mmm \underset{T_{C1}}{\overset{cont.}{\longleftrightarrow}} Abma \underset{T_{C2}}{\overset{inc.}{\longleftrightarrow}} N^{Abma}_{\bar{1}11} \underset{T_{C3}}{\overset{reentr.}{\longleftrightarrow}} Abma \underset{T_{C4}}{\overset{inc.}{\longleftrightarrow}} P^{Abma}_{s\bar{1}1} \underset{T_{C5}}{\overset{disc.}{\longleftrightarrow}} P2_1/b11$ (α) (β)* (γ)* (δ)* (ε) (ζ) * *Twin domains* (Abma – Bmab) *observed with microscope for the* β-, γ-, *and* δ-*phases* [89Y1]	**struct. pt.'s studied by:** therm. m. [73A1, 75B1, 77D1, 81W3, 86M1]; therm. e. [84M2, 86M1]; opt. m. [73A1, 74A1, 89Y1]; birefr. [73A1, 82B1, 84M2, 84S2]; HAUP [92S2]; NMR, NQR [82M1, 86M2, 88M1]; ir spectr. [78A1, 81D3]; diffr. [72P, 74A1, 77D1, 78D2, 79D1, 81D2, 82D1, 83D1, 83D2, 86M2, 86M3, 88M1, 89S2, 90A1]
	$T_{C1} = 446$ $\Delta H_1 = 92(13)$ $\Delta S_1 = 0.21(3)$ $T_{C2} = 396$ $\Delta H_2 = 251(21)$ $\Delta S_2 = 0.63(5)$ $T_{C3} = 344$ $\Delta H_3 = 795(21)$ $\Delta S_3 = 2.34(5)$ $T_{C4} = 164.3$ $\Delta H_4 = 496(7)$ $\Delta S_4 = 3.29(5)$ $T_{C5} = 112.8$ $\Delta H_5 = 586(2)$ $\Delta S_5 = 5.47(2)$	T_{C1}: birefr. [73A1]; ΔH_1, ΔS_1: $C_p(T)$ by d.s.c. [75B1] T_{C2}, ΔH_2, ΔS_2: d.s.c. [77D1] T_{C3}, ΔH_3, ΔS_3: d.s.c. [77D1] T_{C4}, ΔH_4, ΔS_4: $C_p(T)$ by ad. cal. [81W3] T_{C5}, ΔH_5, ΔS_5: $C_p(T)$ by ad. cal. [81W3]
$(C_3H_7ND_3)_2MnCl_4$	same phase sequence as above, slightly different T_{Cn} $T_{C1} = 440$ $T_{C2} = 393$ $T_{C3} = 343$ $T_{C4} = 162.5$ $T_{C3} = 114.5$	T_{C1}, T_{C2}, T_{C3}: [86M1]; T_{C4}, T_{C5}: [88M1]
$(C_5H_{11}NH_3)_2MnCl_4$	2 struct. pt.'s observed by d.s.c.	str. diff. ph. not st. in det., only *d* by diffr. [95F1] – further studies: opt. m. and birefr. [73A1]; diffr. [79D1]
	a) heating $T_{C1} = 256$ $\Delta H_1 = 0.17 \cdot 10^4$ $\Delta S_1 = 6.6$ $T_{C2} = 204$ $\Delta H_2 = 1.15 \cdot 10^4$ $\Delta S_2 = 56.4$	$\left.\begin{matrix}T_{C1}, \Delta H_1, \Delta S_1:\\T_{C2}, \Delta H_2, \Delta S_2:\end{matrix}\right\}$ d.s.c. [95F1]
	b) cooling $T_{C1} = 235$ $T_{C2} = 203$	T_{C1}, T_{C2}: d.s.c. [95F1]

Table 4. Data about Structural Phase Transitions *(continued)*

Compound	Phase sequence, transition temperature T_{Cn} [K], enthalpy ΔH_n [$J \cdot mol^{-1}$] and entropy ΔS_n [$J \cdot mol^{-1} \cdot K^{-1}$] of the n - th structural phase transition	References, remarks
$(C_6H_{13}NH_3)_2MnCl_4$	2 struct. pt.'s observed as anomalies in $C_p(T)$	str. diff. ph. not st. in det., only u.c.p. at 295 K [79D1]
	$T_{C1} = 290.9$ $\Delta H_1 = 10035(24)$ $\Delta S_1 = 37.17(8)$ $T_{C2} = 206.3$ $\Delta H_2 = 5311(38)$ $\Delta S_2 = 25.73(18)$	T_{C1}, ΔH_1, ΔS_1: T_{C2}, ΔH_2, ΔS_2: } $C_p(T)$ ad. cal. [85O]
$(C_7H_{15}NH_3)_2MnCl_4$	2 struct. pt.'s observed as anomalies in $C_p(T)$	str. diff. ph. not st. in det., only *d* by diffr. [95F1] – further studies: diffr. [79D1]
	$T_{C1} = 313.8(1)$ $\Delta H_1 = 10197(9)$ $\Delta S_1 = 32.5$ $T_{C2} = 247.95(5)$ $\Delta H_2 = 16930(30)$ $\Delta S_2 = 68.2$	T_{C1}, ΔH_1, ΔS_1: T_{C2}, ΔH_2, ΔS_2: } $C_p(T)$ by ad. cal. [83W3]
$(C_9H_{19}NH_3)_2MnCl_4$	1 struct. pt. observed by d.s.c.	str. diff. ph. not st. in det., only *d* by diffr. [95F1] – further studies: d.s.c. [74V1]; diffr. [74V1, 79D1]
	a) heating $T_C = 293$ $\Delta H = 3.22 \cdot 10^4$ $\Delta S = 109.9$	T_C, ΔH, ΔS: d.s.c. [95F1]
	b) cooling $T_C = 290$	T_C: d.s.c. [95F1]
$(C_{10}H_{21}NH_3)_2MnCl_4$	$??? \xleftrightarrow[T_C]{disc.}$ $P2_1/b11$ $P12_1/a1$ (HT) (LT)	**struct. pt.'s studied by:** therm. m. [73A1, 73V, 75B1]; opt. m. [73A1]; birefr. [73A1]; diffr. [73V, 76C1]; incoh. n.s. [89G1]
	a) heating $T_C = 308$ $\Delta H = 3.49 \cdot 10^4$ $\Delta S = 113$ b) cooling $T_C = 303$ $\Delta H = 3.55 \cdot 10^4$ $\Delta S = 117$	T_C, ΔH, ΔS: T_C, ΔH, ΔS: } d.s.c. [73V]
$(C_{11}H_{23}NH_3)_2MnCl_4$	2 or 3 struct. pt.'s observed by d.s.c., not clearly resolved because of overlap, data presented for one major pt.:	str. diff. ph. not st. in det., only *d* by diffr. [74V1]
	a) heating $T_C = 316$ $\Delta H = 4.63 \cdot 10^4$ $\Delta S = 147$ b) cooling $T_C = 309$ $\Delta H = 4.63 \cdot 10^4$ $\Delta S = 150$	T_C, ΔH, ΔS: T_C, ΔH, ΔS: } d.s.c. [74V1]

Table 4. Data about Structural Phase Transitions *(continued)*

Compound	Phase sequence, transition temperature T_{Cn} [K], enthalpy ΔH_n [J · mol^{-1}] and entropy ΔS_n [J · mol^{-1} · K^{-1}] of the n - th structural phase transition			References, remarks
$(C_{12}H_{25}NH_3)_2MnCl_4$	2 struct. pt.'s observed by d.s.c.			str. diff. ph. not st. in det., only *d* by diffr. [73V, 81N, 84N] – further studies: d.s.c. [75L1], Raman sp. [81N]
	$T_{C1} = 336$ $T_{C2} = 332$	$\Delta H_1 = 0.63 \cdot 10^4$ $\Delta H_2 = 4.98 \cdot 10^4$	$\Delta S_1 = 18.7$ $\Delta S_2 = 150$	$T_{C1}, \Delta H_1, \Delta S_1$: $T_{C2}, \Delta H_2, \Delta S_2$: d.s.c. [81N, 84N]
$(C_{13}H_{27}NH_3)_2MnCl_4$	2 struct. pt.'s observed by d.s.c.			str. diff. ph. not st. in det., only *d* by diffr. [74V1]
	a) heating			
	$T_{C1} = 343$ $T_{C2} = 331$	$\Delta H_1 = 0.75 \cdot 10^4$ $\Delta H_2 = 5.22 \cdot 10^4$	$\Delta S_1 = 22$ $\Delta S_2 = 158$	$T_{C1}, \Delta H_1, \Delta S_1$: $T_{C2}, \Delta H_2, \Delta S_2$: d.s.c. [74V1]
	b) cooling			
	$T_{C1} = 339$ $T_{C2} = 323$	$\Delta H_1 = 0.78 \cdot 10^4$ $\Delta H_2 = 5.12 \cdot 10^4$	$\Delta S_1 = 23$ $\Delta S_2 = 159$	$T_{C1}, \Delta H_1, \Delta S_1$: $T_{C2}, \Delta H_2, \Delta S_2$: d.s.c. [74V1]
$(C_{14}H_{29}NH_3)_2MnCl_4$	2 struct. pt.'s observed by d.s.c.			str. diff. ph. not st. in det., only *d* by diffr. [73V, 81N, 84N]
	$T_{C1} = 357$ $T_{C2} = 345$	$\Delta H_1 = 0.92 \cdot 10^4$ $\Delta H_2 = 5.78 \cdot 10^4$	$\Delta S_1 = 26.4$ $\Delta S_2 = 167.4$	$T_{C1}, \Delta H_1, \Delta S_1$: $T_{C2}, \Delta H_2, \Delta S_2$: d.s.c. [81N, 84N]
$(C_{15}H_{31}NH_3)_2MnCl_4$	3 struct. pt.'s observed by d.s.c. (2nd pt. not well resolved)			str. diff. ph. not st. in det., only *d* by diffr. [74V1]
	a) heating			
	$T_{C1} = 362$ $T_{C2} = 342$ $T_{C3} = 340$	$\Delta H_1 = 1.03 \cdot 10^4$ $\Delta H_3 = 6.26 \cdot 10^4$	$\Delta S_1 = 28.5$ $\Delta S_3 = 184$	$T_{C1}, \Delta H_1, \Delta S_1$: T_{C2}: $T_{C3}, \Delta H_3, \Delta S_3$: d.s.c. [74V1]
	b) cooling			
	$T_{C1} = 357$ $T_{C2} = ?$ $T_{C3} = 334$	$\Delta H_1 = 1.05 \cdot 10^4$ $\Delta H_3 = 6.00 \cdot 10^4$	$\Delta S_1 = 29.4$ $\Delta S_3 = 180$	$T_{C1}, \Delta H_1, \Delta S_1$: T_{C2}: $T_{C3}, \Delta H_3, \Delta S_3$: d.s.c. [74V1]

Table 4. Data about Structural Phase Transitions *(continued)*

Compound	Phase sequence, transition temperature T_{Cn} [K], enthalpy ΔH_n [J · mol^{-1}] and entropy ΔS_n [J · mol^{-1} · K^{-1}] of the n - th structural phase transition	References, remarks
$(C_{16}H_{32}NH_3)_2MnCl_4$	2 struct. pt.'s observed by d.s.c.	str. diff. ph. not st. in det., only *d* by diffr. [73V] – further studies: d.s.c. [75L1]
	a) heating	
	$T_{C1} = 364$ $\Delta H_1 = 1.13 \cdot 10^4$ $\Delta S_1 = 31$	$T_{C1}, \Delta H_1, \Delta S_1$: $T_{C2}, \Delta H_2, \Delta S_2$: } d.s.c. [73V]
	$T_{C2} = 345$ $\Delta H_2 = 5.98 \cdot 10^4$ $\Delta S_2 = 174$	
	b) cooling	
	$T_{C1} = 361$ $\Delta H_1 = 1.16 \cdot 10^4$ $\Delta S_1 = 32$	$T_{C1}, \Delta H_1, \Delta S_1$: $T_{C2}, \Delta H_2, \Delta S_2$: } d.s.c. [73V1]
	$T_{C2} = 338$ $\Delta H_2 = 5.61 \cdot 10^4$ $\Delta S_2 = 167$	
$(C_{17}H_{35}NH_3)_2MnCl_4$	3 struct. pt.'s observed by d.s.c. (2nd pt. not well resolved)	
	a) heating	
	$T_{C1} = 373$ $\Delta H_1 = 1.44 \cdot 10^4$ $\Delta S_1 = 38.6$	$T_{C1}, \Delta H_1, \Delta S_1$: $T_{C2}, \Delta H_2, \Delta S_2$: $T_{C3}, \Delta H_3, \Delta S_3$: } d.s.c. [74V1]
	$T_{C2} = 353$ $\Delta H_2 = 1.00 \cdot 10^4$ $\Delta S_2 = 28.3$	
	$T_{C3} = 349$ $\Delta H_3 = 6.39 \cdot 10^4$ $\Delta S_3 = 183$	
	b) cooling (T_{C2} missing)	
	$T_{C1} = 370$ $\Delta H_1 = 1.42 \cdot 10^4$ $\Delta S_1 = 38.4$	$T_{C1}, \Delta H_1, \Delta S_1$: $T_{C3}, \Delta H_3, \Delta S_3$: } d.s.c. [74V1]
	$T_{C3} = 342$ $\Delta H_3 = 7.06 \cdot 10^4$ $\Delta S_3 = 206$	
$(4\text{-}ClC_6H_4NH_3)_2MnCl_4$	1 struct. pt. observed by d.s.c.	str. diff. ph. not st. in det., only u.c.p. by diffr. [79B4]
	$T_C = 345(3)$ $\Delta H = 2.06(10) \cdot 10^3$	$T_C, \Delta H$: d.s.c. [93M1]; further study: diel. c. [93M1]
$(C_{11}H_{23}NH_3)_2MnBr_4$	2 struct. pt.'s observed by d.s.c. on heating, on cooling the 2nd pt. only, a 3rd pt. observed on reheating after annealing at 270 K for several hours	values of $T_{Cn}, \Delta H_n, \Delta S_n$ by d.s.c. (n = 1 – 3): see [81V], str. diff. ph. not st. in det., only *d* by diffr. [81V]
$(C_{12}H_{25}NH_3)_2MnBr_4$	2 struct. pt.'s observed by d.s.c. on heating, on cooling the 2nd pt. only, a 3rd pt. observed on reheating after annealing at 270 K for several hours	values of $T_{Cn}, \Delta H_n, \Delta S_n$ by d.s.c. (n = 1 – 3): see [81V], str. diff. ph. not st. in det., only *d* by diffr. [81V]
$(C_{13}H_{27}NH_3)_2MnBr_4$	3 struct. pt.'s observed by d.s.c. on heating, on cooling the 3rd pt. only, a 4th pt. observed on reheating after annealing at 270 K for several hours	values of $T_{Cn}, \Delta H_n, \Delta S_n$ by d.s.c. (n = 1 – 4): see [81V], str. diff. ph. not st. in det., only *d* by diffr. [81V]
$(C_{14}H_{29}NH_3)_2MnBr_4$	3 struct. pt.'s observed by d.s.c. on heating and on cooling, a 4th pt. and a 5th pt. observed on reheating after annealing at 270 K for several hours	values of $T_{Cn}, \Delta H_n, \Delta S_n$ by d.s.c. (n = 1 – 5): see [81V], str. diff. ph. not st. in det., only *d* by diffr. [81V]

Table 4. Data about Structural Phase Transitions *(continued)*

Compound	Phase sequence, transition temperature T_{Cn} [K], enthalpy ΔH_n [J · mol^{-1}] and entropy ΔS_n [J · mol^{-1} · K^{-1}] of the n - th structural phase transition	References, remarks
$(C_{15}H_{31}NH_3)_2MnBr_4$	3 struct. pt.'s observed by d.s.c. on heating and on cooling, a 4th pt. observed on reheating after annealing at 270 K for several hours	values of T_{Cn}, ΔH_n, ΔS_n by d.s.c. (n = 1 – 4): see [81V], str. diff. ph. not st. in det., only *d* by diffr. [81V]
$(C_{16}H_{33}NH_3)_2MnBr_4$	3 struct. pt.'s observed by d.s.c. on heating and on cooling, a 4th pt. observed on reheating after annealing at 270 K for several hours	values of T_{Cn}, ΔH_n, ΔS_n by d.s.c. (n = 1 – 4): see [81V], str. diff. ph. not st. in det., only *d* by diffr. [81V]
$(CH_3NH_3)_2FeCl_4$	I4/mmm*) $\xleftrightarrow[T_{C1}]{\textit{cont.}}$ $\begin{array}{l}\text{Abma*)}\\\text{Bmab*)}\end{array}$ $\xleftrightarrow[T_{C2}]{\textit{disc.}}$ $P4_2$/ncm*) (THT) (ORT) (TLT) *) *space group not verified by structure determination but concluded from various experimental data* [71M1, 74K1, 82G1, 84K1, 84Y1, 91C2], *in analogy to* $(CH_3NH_3)_2MnCl_4$ *and* $(CH_3NH_3)_2CdCl_4$	**struct. pt.'s studied by:** therm. m. [82G1, 84Y1]; opt. m. [82G1]; birefr. [74K1, 84K1]; ir spectr. [75L2]; elast. c. [82G1, 84K1, 84Y2]; diffr. [71M1, 74K1, 78H2, 82M2]
	$T_{C1} = 333.03$ $T_{C2} = 231.2$ (heating) $T_{C2} = 231.7$ (cooling)	T_{C1}: birefr. [84K1], T_{C2}: birefr., diffr. [74K1]
	$dT_{C1}/dp = -2.2 \cdot 10^{-8}$ K/Pa $dT_{C2}/dp = -3.6 \cdot 10^{-8}$ K/Pa	$\left.\begin{array}{l}dT_{C1}/dp:\\dT_{C2}/dp:\end{array}\right\}$ high press. exp. [82G1]
$(C_2H_5NH_3)_2FeCl_4$	I4/mmm*) $\xleftrightarrow[T_{C1}]{\textit{cont.}}$ $\begin{array}{l}\text{Abma*)}\\\text{Bmab*)}\end{array}$ $\xleftrightarrow[T_{C2}]{\textit{cont.}}$ $\begin{array}{l}\text{Pbca*)}\\\text{Pcab*)}\end{array}$ $\xleftrightarrow[T_{C3}]{}$?? (THT) (ORT) (OLT) (?) *) *space group not verified by structure determination but concluded from various experimental data* [83S1, 84K1, 84Y1, 85Y1] *in analogy to* $(C_2H_5NH_3)_2MnCl_4$ *and* $(C_2H_5NH_3)_2CdCl_4$	**struct. pt.'s studied by:** therm. m. [84Y1]; opt. m. [83S1]; birefr. [84K1]; diel. c. [83S1]; elast. c. [83S1, 85Y1]
	$T_{C1} = 378.8$ $T_{C2} = 203.5$ $T_{C3} = 133.7$	T_{C1}, T_{C2}, T_{C3}: opt. m., diel. c., elast. c [83S1]
$(C_{12}H_{25}NH_3)_2FeCl_4$	1 struct. pt. observed by d.s.c.	str. diff. ph. not st. in det., only *d* by diffr. [77L1]
	a) heating $T_C = 319$ $\Delta H = 4.4 \cdot 10^4$ $\Delta S = 138$ b) cooling $T_C = 306$ $\Delta H = 4.3 \cdot 10^4$ $\Delta S = 141$	$\left.\begin{array}{l}T_C, \Delta H, \Delta S:\\T_C, \Delta H, \Delta S:\end{array}\right\}$ d.s.c. [75L1]

Table 4. Data about Structural Phase Transitions *(continued)*

Compound	Phase sequence, transition temperature T_{Cn} [K], enthalpy ΔH_n [J · mol^{-1}] and entropy ΔS_n [J · mol^{-1} · K^{-1}] of the n - th structural phase transition	References, remarks
$(C_{16}H_{33}NH_3)_2FeCl_4$	2 struct. pt.'s observed by d.s.c.	str. diff. ph. not st. in det., only *d* by diffr. [74V1]
	a) heating $T_{C1} = 367$ $\quad \Delta H_1 = 1.2 \cdot 10^4$ $\quad \Delta S_1 = 33$ $T_{C2} = 344$ $\quad \Delta H_2 = 5.4 \cdot 10^4$ $\quad \Delta S_2 = 157$	$\left.\begin{array}{l} T_{C1}, \Delta H_1, \Delta S_1: \\ T_{C2}, \Delta H_2, \Delta S_2: \end{array}\right\}$ d.s.c. [75L1]
	b) cooling $T_{C1} = 353$ $\quad \Delta H_1 = 1.2 \cdot 10^4$ $\quad \Delta S_1 = 34$ $T_{C2} = 329$ $\quad \Delta H_2 = 5.4 \cdot 10^4$ $\quad \Delta S_2 = 164$	$\left.\begin{array}{l} T_{C1}, \Delta H_1, \Delta S_1: \\ T_{C2}, \Delta H_2, \Delta S_2: \end{array}\right\}$ d.s.c. [75L1]
$(CH_3NH_3)_2CuCl_4$	$\mathrm{Bbcm} \xleftrightarrow[T_C]{\mathit{cont.}} \mathrm{B12_1/cl}\ (\mathrm{P12_1/cl})$	**struct. pt.'s studied by:** therm. m. [82W3]; opt. m. [89J]; birefr. [77H1, 79K3, 89J]; ir spectr. [76S3, 79S4, 81R3]; diffr. [64W, 79S2, 83S2, 83C2, 84S1, 86J1, 87P, 89J]; opt. spectr. [67W2]
	In diffration studies [87P], *the monoclinic structure was found over temperature range* 100 K – 297 K, *in contrast to earlier results* [84S1] *and in contrast to* $C_p(T)$ *measurements* [82W3] *which revealed an anomaly near* 229 K	
	$T_C = 348$	T_C: birefr. [79K3, 89J]
	$T_C = 229.33$ $\quad \Delta H = 115(4)$ $\quad \Delta S = 0.50(2)$	T_C: $C_p(T)$ by ad. cal. [82W3]
	$T \approx 230$ K: change of colour (thermochromism)	T (colour change): opt. spectr. [67W2], see also [79S2]
$(C_2H_5NH_3)_2CuCl_4$	$\underset{(\alpha)}{\mathrm{Bbcm}} \xleftrightarrow[T_{C1}]{\mathit{cont.}} \underset{(\beta)}{\mathrm{P12_1/c1}} \xleftrightarrow[T_{C2}]{\mathit{disc.}} \underset{(\gamma)}{\mathrm{Pbca}} \xleftrightarrow[T_{C3}]{} \underset{(\delta)}{\text{triclinic*)}}$	**struct. pt.'s studied by:** therm. m. [81T1, 85F2]; therm. e. [81T1, 85F2]; opt. m. [89J]; elast. c. [83K]; ir spectr. [79S4]; birefr. [77H1, 79K3, 81T1, 83K2, 85F2, 89J]; diffr. [70S1, 83T1, 83T2, 86J1, 89J, 91J1]; opt. spectr. [67W2]
	*) *Preliminary diffraction data indicate triclinic symmetry below* T_{C3} [89J]	
	$T_{C1} = 364$	T_{C1}: birefr. [79K3, 83K2], diffr. [89J]
	$T_{C2} = 356$ (heating) $\quad T_{C2} = 338$ (cooling)	T_{C2}: birefr., diffr. [89J]
	$T_{C3} = 233$	T_{C3}: birefr. [83K2, 89J], diffr. [89J]
	$T \approx 230$ K: change of colour (thermochromism)	T (colour change): opt. spectr. [67W2]

Table 4. Data about Structural Phase Transitions *(continued)*

Compound	Phase sequence, transition temperature T_{Cn} [K], enthalpy ΔH_n [J · mol^{-1}] and entropy ΔS_n [J · mol^{-1} · K^{-1}] of the n - th structural phase transition	References, remarks
$(C_3H_7NH_3)_2CuCl_4$	$\begin{tikzcd} \mathrm{Bbcm} \arrow[r, leftrightarrow, "\mathit{cont.}", "T_{C1}"'] & \mathrm{Pbca} \arrow[r, leftrightarrow, "\mathit{inc.}", "T_{C2}"'] & \mathrm{P}^{\mathrm{Pbca}}_{\mathrm{ss1}} \arrow[r, leftrightarrow, "\mathit{reentr.}", "T_{C3}"'] & \mathrm{Pbca} \arrow[rr, "T_{C45}"] & & \mathrm{P}^{\mathrm{P2_1/n}}_{\bar{1}\ \ 1} \arrow[r, leftrightarrow, "\mathit{disc.}", "T_{C6}"'] & \mathrm{P2_1/c11} \\ & & & & \mathrm{P2_1/n11} \arrow[ul, "T_{C4}"'] \arrow[ur, leftrightarrow, "T_{C5}"'] & & \end{tikzcd}$ (α) (β) (γ) (δ) (ε) (ζ) (η)	**struct. pt.'s studied by:** therm. m. [88E]; therm. e. [88E]; opt. m [94J1]; birefr. [88E, 88K2, 89J]; diffr. [70B2, 86J1, 89D1, 89J, 90D1, 90D2, 92S3, 94J1]
	$T_{C1} = 436$ $T_{C2} = 413$ $T_{C3} = 383$ $T_{C4} = 192$ (heating) $T_{C45} = 180$ (cooling) $T_{C5} = 180$ (heat. + cool.) $\Delta H_5 = 1.72(20) \cdot 10^3$ $\Delta S_5 = 13.3(8)$ $T_{C6} = 141$ (heating) $\Delta H_6 = 1.68(17) \cdot 10^3$ $\Delta S_6 = 11.8(8)$ $T_{C6} = 132$ (cooling)	T_{C1}: birefr., therm. e. [88E] T_{C2}, T_{C3}: birefr., diffr. [89J] T_{C4} (heating), T_{C45} (cooling): birefr. diffr. [89J] T_{C5} (heat. + cool.), ΔH_5, ΔS_5: $C_p(T)$ by ad. cal. [88E] T_{C6} (heating), ΔH_6, ΔS_6: $C_p(T)$ by ad. cal. [88E] T_{C6} (cooling): birefr., diffr. [94J1]
$(C_9H_{19}NH_3)_2CuCl_4$	2 struct. pt.'s observed by d.s.c. and ir spectr.	str. diff. ph. not st. in det., only *d* by diffr. [74V2] – further studies: d.s.c. [74V3]
	$T_{C1} = 308$ $\Delta H_1 = 0.46 \cdot 10^4$ $\Delta S_1 = 14.9$ $T_{C2} = 295$ $\Delta H_2 = 2.53 \cdot 10^4$ $\Delta S_2 = 84.9$	$\left.\begin{array}{l} T_{C1}, \Delta H_1, \Delta S_1: \\ T_{C2}, \Delta H_2, \Delta S_2: \end{array}\right\}$ d.s.c. and ir spectr. [95N1]
$(C_{10}H_{21}NH_3)_2CuCl_4$	2 struct. pt.'s observed by NMR	str. diff. ph. not st. in det., only *d* by diffr. [74V2, 81K2] – further studies: d.s.c. [74V3, 78A2]
	$T_{C1} = 315$ (minor pt.) $T_{C2} = 309$ (major pt.) only 2nd pt. observed by d.s.c.	T_{C1}, T_{C2}: NMR [80B2, 81K2]
	a) heating $T_{C2} = 306$ $\Delta H_2 = 2.8 \cdot 10^4$ $\Delta S_2 = 91$ b) cooling $T_{C2} = 301$ $\Delta H_2 = 2.7 \cdot 10^4$ $\Delta S_2 = 91$	$\left.\begin{array}{l} T_{C2}, \Delta H_2, \Delta S_2: \\ \\ T_{C2}, \Delta H_2, \Delta S_2: \end{array}\right\}$ d.s.c. [74V3]

Table 4. Data about Structural Phase Transitions *(continued)*

Compound	Phase sequence, transition temperature T_{Cn} [K], enthalpy ΔH_n [J · mol^{-1}] and entropy ΔS_n [J · mol^{-1} · K^{-1}] of the n - th structural phase transition	References, remarks
$(C_{11}H_{23}NH_3)_2CuCl_4$	1 struct. pt. observed by d.s.c.	str. diff. ph. not st. in det., only *d* by diffr. [74V2]
	a) heating	
	$T_C = 313$ $\Delta H = 3.8 \cdot 10^4$ $\Delta S = 125$	$T_C, \Delta H, \Delta S$: d.s.c. [74V3]
	b) cooling	
	$T_C = 305$ $\Delta H = 4.0 \cdot 10^4$ $\Delta S = 133$	$T_C, \Delta H, \Delta S$:
$(C_{12}H_{25}NH_3)_2CuCl_4$	2 struct. pt.'s observed by d.s.c.	str. diff. ph. not st. in det., only *d* by diffr. [74V2, 77L1, 84N] – further studies: d.s.c. [74V3, 75L1, 78A2, 81N]
	$T_{C1} = 338$ $\Delta H_1 = 0.795 \cdot 10^4$ $\Delta S_1 = 23.7$	$T_{C1}, \Delta H_1, \Delta S_1$: d.s.c. [84N]
	$T_{C2} = 330$ $\Delta H_2 = 4.165 \cdot 10^4$ $\Delta S_2 = 126.8$	$T_{C2}, \Delta H_2, \Delta S_2$:
$(C_{13}H_{27}NH_3)_2CuCl_4$	2 struct. pt.'s observed by d.s.c.	str. diff. ph. not st. in det., only *d* by diffr. [74V2]
	a) heating	
	$T_{C1} = 344$ $\Delta H_1 = 1.0 \cdot 10^4$ $\Delta S_1 = 33$	$T_{C1}, \Delta H_1, \Delta S_1$: d.s.c. [74V3]
	$T_{C2} = 333$ $\Delta H_2 = 4.8 \cdot 10^4$ $\Delta S_2 = 141$	$T_{C2}, \Delta H_2, \Delta S_2$:
	b) cooling	
	$T_{C1} = 340$ $\Delta H_1 = 1.0 \cdot 10^4$ $\Delta S_1 = 33$	$T_{C1}, \Delta H_1, \Delta S_1$: d.s.c. [74V3]
	$T_{C2} = 323$ $\Delta H_2 = 4.7 \cdot 10^4$ $\Delta S_2 = 150$	$T_{C2}, \Delta H_2, \Delta S_2$:
$(C_{14}H_{29}NH_3)_2CuCl_4$	2 struct. pt.'s observed by d.s.c.	str. diff. ph. not st. in det., only *d* by diffr. [74V2, 84N] – further studies: d.s.c. [74V3, 78A2, 81N]
	$T_{C1} = 356$ $\Delta H_1 = 1.09 \cdot 10^4$ $\Delta S_1 = 30.6$	$T_{C1}, \Delta H_1, \Delta S_1$: d.s.c. [84N]
	$T_{C2} = 334$ $\Delta H_2 = 5.02 \cdot 10^4$ $\Delta S_2 = 150.3$	$T_{C2}, \Delta H_2, \Delta S_2$:
$(C_{15}H_{31}NH_3)_2CuCl_4$	2 struct. pt.'s observed by d.s.c.	str. diff. ph. not st. in det., only *d* by diffr. [74V2]
	a) heating	
	$T_{C1} = 358$ $\Delta H_1 = 1.2 \cdot 10^4$ $\Delta S_1 = 33$	$T_{C1}, \Delta H_1, \Delta S_1$: d.s.c. [74V3]
	$T_{C2} = 343$ $\Delta H_2 = 5.4 \cdot 10^4$ $\Delta S_2 = 158$	$T_{C2}, \Delta H_2, \Delta S_2$:
	b) cooling	
	$T_{C1} = 355$ $\Delta H_1 = 1.3 \cdot 10^4$ $\Delta S_1 = 33$	$T_{C1}, \Delta H_1, \Delta S_1$: d.s.c. [74V3]
	$T_{C2} = 337$ $\Delta H_2 = 5.4 \cdot 10^4$ $\Delta S_2 = 158$	$T_{C2}, \Delta H_2, \Delta S_2$:

Table 4. Data about Structural Phase Transitions *(continued)*

Compound	Phase sequence, transition temperature T_{Cn} [K], enthalpy ΔH_{n} [J · mol^{-1}] and entropy ΔS_{n} [J · mol^{-1} · K^{-1}] of the n - th structural phase transition	References, remarks
$(C_{16}H_{33}NH_3)_2CuCl_4$	3 struct. pt.'s observed by d.s.c.	str. diff. ph. not st. in det., only *d* by diffr. [74V2, 77L1] – further studies: d.s.c. [74V3, 78A2]
	a) heating $T_{C1} = 360$ $\Delta H_1 = 1.4 \cdot 10^4$ $\Delta S_1 = 39$ $T_{C2} = 354$ $\Delta H_2 = 0.75 \cdot 10^4$ $\Delta S_2 = 21$ $T_{C3} = 345$ $\Delta H_3 = 3.6 \cdot 10^4$ $\Delta S_3 = 104$	$T_{C1}, \Delta H_1, \Delta S_1$: $T_{C2}, \Delta H_2, \Delta S_2$: } d.s.c. [75L1] $T_{C3}, \Delta H_3, \Delta S_3$:
	b) cooling $T_{C1} = 356$ $\Delta H_1 = 1.4 \cdot 10^4$ $\Delta S_1 = 39$ $T_{C2} = 346$ $\Delta H_2 = 0.97 \cdot 10^4$ $\Delta S_2 = 28$ $T_{C3} = 339$ $\Delta H_3 = 3.9 \cdot 10^4$ $\Delta S_3 = 115$	$T_{C1}, \Delta H_1, \Delta S_1$: $T_{C2}, \Delta H_2, \Delta S_2$: } d.s.c. [75L1] $T_{C3}, \Delta H_3, \Delta S_3$:
$(C_{17}H_{35}NH_3)_2CuCl_4$	3 struct. pt.'s observed by d.s.c.	str. diff. ph. not st. in det., only *d* by diffr. [74V2]
	a) heating $T_{C1} = 368$ $\Delta H_1 = 1.5 \cdot 10^4$ $\Delta S_1 = 42$ $T_{C2} = 361$ $\Delta H_2 = 0.9 \cdot 10^4$ $\Delta S_2 = 25$ $T_{C3} = 352$ $\Delta H_3 = 5.4 \cdot 10^4$ $\Delta S_3 = 158$	$T_{C1}, \Delta H_1, \Delta S_1$: $T_{C2}, \Delta H_2, \Delta S_2$: } d.s.c. [74V3] $T_{C3}, \Delta H_3, \Delta S_3$:
	b) cooling $T_{C1} = 365$ $\Delta H_1 = 1.7 \cdot 10^4$ $\Delta S_1 = 42$ $T_{C2} = 351$ $\Delta H_2 = 1.0 \cdot 10^4$ $\Delta S_2 = 25$ $T_{C3} = 344$ $\Delta H_3 = 5.3 \cdot 10^4$ $\Delta S_3 = 158$	$T_{C1}, \Delta H_1, \Delta S_1$: $T_{C2}, \Delta H_2, \Delta S_2$: } d.s.c. [74V3] $T_{C3}, \Delta H_3, \Delta S_3$:
$(C_3H_7NH_3)_2CuBr_4$		sequence of structural phases and structures studied by diffr. [77K2, 92S3, 94J2] in the temperature range 100 – 300 K (only low temperature phases)

$$\begin{tikzcd}
\mathrm{Bbcm}\ ? \arrow[r, leftrightarrow, "T_{C1}"'] & ?? \arrow[r, leftrightarrow, "T_{C2}"'] & ?? \arrow[r, leftrightarrow, "T_{C3}"'] & \mathrm{Pbca} \arrow[rr, "T_{C45}"] & & \mathrm{P}^{\mathrm{P}2_1/\mathrm{n}}_{\bar{1}\ 1} \arrow[r, leftrightarrow, "disc.", "T_{C6}"'] & \mathrm{P}\bar{1} \arrow[r, leftrightarrow, "T_{C7}"'] & ?? \\
& & & & \mathrm{P}2_1/\mathrm{n}11 \arrow[ul, "T_{C4}"] \arrow[ur, leftrightarrow, "T_{C5}"'] & & & \\
(\alpha) & (\beta) & (\gamma) & (\delta) & (\varepsilon) & (\zeta) & (\eta) & (\vartheta)
\end{tikzcd}$$

$\boldsymbol{q}_0 = \delta \cdot \boldsymbol{b}^* + \sigma \cdot \boldsymbol{c}^* \rightarrow \boldsymbol{q}_0 = 0.5\,(\boldsymbol{b}^* + \boldsymbol{c}^*)$ *at the phase transition* $\zeta \rightarrow \eta$ *(lock-in transition)* [94J2]

Table 4. Data about Structural Phase Transitions *(continued)*

Compound	Phase sequence, transition temperature T_{Cn} [K], enthalpy ΔH_n [$J \cdot mol^{-1}$] and entropy ΔS_n [$J \cdot mol^{-1} \cdot K^{-1}$] of the n - th structural phase transition	References, remarks
$(C_3H_7NH_3)_2CuBr_4$ (cont.)	T_{C1}, T_{C2}, T_{C3}: not determined T_{C4} = 203 (heating) T_{C45} = 183 (cooling) T_{C5} = 187 (heating + cooling) T_{C6} = 146 (heating) T_{C6} = 139 (cooling) T_{C7} = 114 (heating) T_{C7} = 102 (cooling)	$\}$ T_{C4}, T_{C45}, T_{C5}, T_{C6}, T_{C7}: diffr. [92S3, 94J2]
$(C_{11}H_{23}NH_3)_2CuBr_4$	2 struct. pt.'s observed by d.s.c. on heating and on cooling, a 3rd pt. observed on reheating after annealing at 270 K for several hours	values of T_{Cn}, ΔH_n, ΔS_n by d.s.c. (n = 1 – 3): see [81V], str. diff. ph. not st. in det., only *d* by diffr. [81V]
$(C_{12}H_{25}NH_3)_2CuBr_4$	1 struct. pt. observed by d.s.c. on heating and on cooling	values of T_C, ΔH, ΔS by d.s.c.: see [81V], str. diff. ph. not st. in det., only *d* by diffr. [81V]
$(C_{13}H_{27}NH_3)_2CuBr_4$	1 struct. pt. observed by d.s.c. on heating and on cooling	values of T_C, ΔH, ΔS by d.s.c.: see [81V], str. diff. ph. not st. in det., only *d* by diffr. [81V]
$(C_{14}H_{29}NH_3)_2CuBr_4$	1 struct. pt. observed by d.s.c. on heating and on cooling, a 2nd pt. observed on reheating after annealing at 270 K for several hours	values of T_{Cn}, ΔH_n, ΔS_n by d.s.c. (n = 1, 2): see [81V], str. diff. ph. not st. in det., only *d* by diffr. [81V]
$(C_{15}H_{31}NH_3)_2CuBr_4$	1 struct. pt. observed by d.s.c. on heating and on cooling, a 2nd pt. observed on reheating after annealing at 270 K for several hours	values of T_{Cn}, ΔH_n, ΔS_n by d.s.c. (n = 1, 2): see [81V], str. diff. ph. not st. in det., only *d* by diffr. [81V]
$(C_{16}H_{33}NH_3)_2CuBr_4$	2 struct. pt.'s observed by d.s.c. on heating and on cooling, a 3rd pt. observed on reheating after annealing at 270 K for several hours	values of T_{Cn}, ΔH_n, ΔS_n by d.s.c. (n = 1 – 3): see [81V], str. diff. ph. not st. in det., only *d* by diffr. [81V]
$(CH_3NH_3)_2CdCl_4$	$I4/mmm \xleftrightarrow[T_{C1}]{cont.} \begin{matrix} Abma \\ Bmab \end{matrix} \xleftrightarrow[T_{C2}]{disc.} P4_2/ncm \xleftrightarrow[T_{C3}]{disc.} \begin{matrix} A2_1/b11 \\ B12_1/a1 \end{matrix}$ (THT) (ORT) (TLT) (MLT)	**struct. pt.'s studied by:** therm. m. [74B2, 75C1, 76C2, 77T1, 78S2, 81R2]; opt. m. [76C2, 80G1, 82W4]; diel. c. [76L1, 80G1, 80H3, 82W4]; NMR, NQR [76S2, 77B1]; elast. c. [80G2]; Raman sp. [77C4, 78C2, 81M2, 83M1, 83M2, 83M3]; ir spectr. [76S3, 77O, 79S4, 81R3]; diffr. [75C1, 76C2]; diff. x-ray sc. [84M3]
	T_{C1} = 484 ΔH_1 = 79 ΔS_1 = 0.17	T_{C1}, ΔH_1, ΔS_1: $C_p(T)$ by d.s.c. [77T1]
	T_{C2} = 282 ΔH_2 = 66.5 ΔS_2 = 0.24 T_{C3} = 164.2 ΔH_3 = 1750 ΔS_3 = 10.80	T_{C2}, ΔH_2, ΔS_2: T_{C3}, ΔH_3, ΔS_3: $\}$ $C_p(T)$ by ad. cal. [81R2]
	heating: T_{C2} = 279.3 T_{C3} = 164.2 cooling: T_{C2} = 278.5 T_{C3} = 163.5	$\}$ T_{C2}, T_{C3} on heating, cooling: diel. c. [76L1]
	p_C = 1.4 GPa at 295 K	p_C: high press. exp. [78H1, 83M3]

Table 4. Data about Structural Phase Transitions *(continued)*

Compound	Phase sequence, transition temperature T_{Cn} [K], enthalpy ΔH_n [J · mol^{-1}] and entropy ΔS_n [J · mol^{-1} · K^{-1}] of the n - th structural phase transition	References, remarks
$(C_2H_5NH_3)_2CdCl_4$	$\begin{array}{ccccccc} \mathrm{I4/mmm} & \xleftrightarrow[T_{C1}]{\textit{cont.}} & \mathrm{Abma} & \xleftrightarrow[T_{C2}]{\textit{disc.}} & \mathrm{Pbca} & \xleftrightarrow[T_{C3}]{\textit{disc.}} & \mathrm{P2_1/b11^{*})} \\ & & \mathrm{Bmab} & & \mathrm{Pcab} & & \mathrm{P12_1/a1^{*})} \\ \mathrm{(THT)} & & \mathrm{(ORT)} & & \mathrm{(OLT)} & & \mathrm{(MLT)} \end{array}$ *) *space group not verified by structure determination but concluded from the temperature dependence of Raman spectra* [85H1]	**struct. pt.'s studied by:** therm. m. [74B2, 77C2, 77T1]; opt. m. [77C2,]; diel. c. [76L1, 80L1]; NMR [77B1]; Raman sp. [77C4, 81M2, 82H1, 82H2, 82M3, 84H2, 85H1]; ir spectr. [79O1, 79P1, 79P2, 81R3, 82H2], diffr. [77C2]
	$T_{C1} = 485$ $\quad \Delta H_1 = 108$ $\quad \Delta S_1 = 0.22$ $T_{C2} = 216.2(5)$ $\quad \Delta H_2 = 2163$ $\quad \Delta S_2 = 9.7$ $T_{C3} = 114.2(9)$	$T_{C1}, \Delta H_1, \Delta S_1$: $C_p(T)$ by d.s.c. [77T1] T_{C2}: opt. m. [77C2] $\Delta H_2, \Delta S_2$: $C_p(T)$ by d.s.c. [77T1] T_{C3}: opt. m. [77C2]
$(C_3H_7NH_3)_2CdCl_4$	$\begin{array}{ccccccc} \mathrm{Abma} & \xleftrightarrow[T_{C1}]{\textit{inc.}} & \mathrm{P}^{\mathrm{Abma}}_{\mathrm{s}\bar{1}1} & \xleftrightarrow[T_{C2}]{} & \mathrm{Pbca} & \xleftrightarrow[T_{C3}]{} & ?? \\ \mathrm{(ORT)} & & \mathrm{(INC)} & & \mathrm{(OLT)} & & \end{array}$	**struct. pt.'s studied by:** therm. m. [74B2, 78C1, 81W3, 85M]; diel. c. [76L1]; NMR [77B1]; Raman sp. [81M2, 85M]; ir spectr. [81D3]; diffr. [78C1, 85M, 88D2]
	$T_{C1} = 178.7(3)$ $\quad \Delta H_1 = 982(4)$ $\quad \Delta S_1 = 6.16(2)$ $T_{C2} = 156.8(2)$ $\quad \Delta H_2 = 598(5)$ $\quad \Delta S_2 = 3.85(3)$ $T_{C3} = 105.5(1)$ $\quad \Delta H_3 = 1472.3(1)$ $\quad \Delta S_3 = 13.956(1)$	$\left.\begin{array}{l} T_{C1}, \Delta H_1, \Delta S_1: \\ T_{C2}, \Delta H_2, \Delta S_2: \\ T_{C3}, \Delta H_3, \Delta S_3: \end{array}\right\}$ $C_p(T)$ by ad. cal. [81W3]
$(CH_2{=}CHCH_2NH_3)_2-$ $-CdCl_4$	2 struct. pt.'s observed as anomalies in $C_p(T)$	Comparison of this compound with $(C_3H_7NH_3)_2CdCl_4$: 2 instead of 3 struct. pt.'s; higher T_{Cn}, larger ΔH_n and larger $\Delta S_n \rightarrow$ influence of the double bond [82W5]
	$T_{C1} = 266.7(1)$ $\quad \Delta H_1 = 2000(5)$ $\quad \Delta S_1 = 7.87(2)$ $T_{C2} = 206.9(2)$ $\quad \Delta H_2 = 2140(80)$ $\quad \Delta S_2 = 10.5(4)$	$\left.\begin{array}{l} T_{C1}, \Delta H_1, \Delta S_1: \\ T_{C2}, \Delta H_2, \Delta S_2: \end{array}\right\}$ $C_p(T)$ by ad. cal. [82W5]
$(C_7H_{15}NH_3)_2CdCl_4$	2 struct. pt.'s observed as anomalies in $C_p(T)$	str. diff. ph. not st. in det.
	$T_{C1} = 316.74(5)$ $\quad \Delta H_1 = 0.506(8) \cdot 10^4$ $\quad \Delta S_1 = 16.0(2)$ $T_{C2} = 250.00(5)$ $\quad \Delta H_2 = 1.763(1) \cdot 10^4$ $\quad \Delta S_2 = 71.38(4)$	$\left.\begin{array}{l} T_{C1}, \Delta H_1, \Delta S_1: \\ T_{C2}, \Delta H_2, \Delta S_2: \end{array}\right\}$ $C_p(T)$ by ad. cal. [83W3]
$(C_8H_{17}NH_3)_2CdCl_4$	$\begin{array}{ccccc} \mathrm{Amaa^{*})} & \xleftrightarrow[T_{C1}]{} & ?? & \xleftrightarrow[T_{C2}]{} & \mathrm{P12_1/n1^{*})} \\ \mathrm{(HT)} & & \mathrm{(IM)} & & \mathrm{(LT)} \end{array}$	**struct. pt.'s studied by:** therm. m. [83C1, 85R1]; Raman sp. [82R2, 83C1, 85R1]; ir spectr. [85R1]; diffr. [83C1, 85R1]
	*) *space group not verified by a structure determination but concluded from diffraction data* [83C1, 85R1], *in analogy to* $(C_{10}H_{21}NH_3)_2CdCl_4$	
	$T_{C1} = 308.1(4)$ $\quad \Delta H_1 = 0.51(3) \cdot 10^4$ $\quad \Delta S_1 = 16.7(9)$ $T_{C2} = 268.8(5)$ $\quad \Delta H_2 = 1.45(5) \cdot 10^4$ $\quad \Delta S_2 = 54.2(18)$	$\left.\begin{array}{l} T_{C1}, \Delta H_1, \Delta S_1: \\ T_{C2}, \Delta H_2, \Delta S_2: \end{array}\right\}$ d.s.c. [83C1, 85R1]

Table 4. Data about Structural Phase Transitions *(continued)*

Compound	Phase sequence, transition temperature T_{Cn} [K], enthalpy ΔH_n [J · mol^{-1}] and entropy ΔS_n [J · mol^{-1} · K^{-1}] of the n - th structural phase transition	References, remarks
$(C_9H_{19}NH_3)_2CdCl_4$	2 struct. pt.'s observed by d.s.c.	str. diff. ph. not st. in det., only u.c.p. at 295 K [95K] – further studies: Raman sp. and ir spectr. [95K]
	$T_{C1} = 303$ $\quad T_{C2} = 296$	T_{C1}, T_{C2}: d.s.c. [95K]
$(C_{10}H_{21}NH_3)_2CdCl_4$	$\text{Amaa} \xleftrightarrow[T_{C1}]{disc.} \text{Pmnn*)} \xleftrightarrow[T_{C2}]{disc.} \text{P}12_1/\text{n}1$ (HT) (IM) (LT)	**struct. pt.'s studied by:** therm. m. [79K1, 81N, 85R1]; diel. c. [79K1]; NMR, NQR [79B3, 79K1, 80B2, 81K2]; Raman sp. [81N, 84R2, 85C3]; ir spectr. [84R2, 85C3]; diffr. [79B3, 79K1, 81K2, 81N, 83C1]
	*) *space group not verified by a structure determination but concluded from various experimental data and group theory* [79K1, 83C1, 85R1]	
	$T_{C1} = 312$ $\quad \Delta H_1 = 3.276 \cdot 10^4$ $\quad \Delta S_1 = 105(5)$ $T_{C2} = 308$ $\quad \Delta H_2 = 0.462 \cdot 10^4$ $\quad \Delta S_2 = 15(5)$	T_{C1}, ΔH_1, ΔS_1: T_{C2}, ΔH_2, ΔS_2: } d.s.c. [79K1]
$(C_{12}H_{25}NH_3)_2CdCl_4$	$\text{tetragonal}^{+)} \xleftrightarrow[T_{C1}]{cont.} \text{Amaa*)} \xleftrightarrow[T_{C2}]{disc.} ?? \xleftrightarrow[T_{C3}]{disc.} \text{P}12_1/\text{n}1\text{*)}$ (HT) (IM1) (IM2) (LT)	**struct. pt.'s studied by**: therm. m. [81N, 84N, 85C1, 85R1]; Raman sp. [81N, 85C1, 85R1]; ir spectr. [85C1, 85R1,]; diffr. [81N, 84N, 85C1]
	$^{+}$) *space group not determined* *) *indexing of diffraction data* [85C1] *compatible with this space group*	
	$T_{C1} = 345$ $\quad \Delta H_1 \approx 0$ $\quad \Delta S_1 \approx 0$ $T_{C2} \approx 331$ $\quad \Delta H_2 = 0.65(30) \cdot 10^4$ $\quad \Delta S_2 = 21(0)$ $T_{C3} = 327$ $\quad \Delta H_3 = 4.0(3) \cdot 10^4$ $\quad \Delta S_3 = 123(10)$	T_{C1}, ΔH_1, ΔS_1: T_{C2}, ΔH_2, ΔS_2: } d.s.c. [85C1, 85R1] T_{C3}, ΔH_3, ΔS_3:
$(C_{14}H_{29}NH_3)_2CdCl_4$	$\alpha \xleftrightarrow[T_{C1}]{} \beta \xleftrightarrow[T_{C2}]{} \gamma \xleftrightarrow[T_{C3}]{} \delta \xleftrightarrow[T_{C4}]{} \varepsilon\ (\text{P}\bar{1})$	except for the ε-phase, str. diff. ph. not st. in det., only u.c.p. for the α- and γ-phases by diffr. [88S1] – further studies: d.s.c. [81N]; diffr. [84N]
1st set of d.s.c. data	1st heating $\quad T_{C1} = 351$ $\quad T_{C2} = 350$ $\quad T_{C3} = 347$ $\quad T_{C4} = 345$ 1st cooling $\quad \leftarrow T_{C1,2} = 348 \rightarrow$ $\quad T_{C3} = 343$ $\quad T_{C4} = 341$ 2nd heating $\quad T_{C1} = 351$ $\quad T_{C2} = 350$ $\quad T_{C3} = 346$ $\quad T_{C4} = 344$ 2nd cooling $\quad \leftarrow T_{C1,2} = 348 \rightarrow$ $\quad T_{C3} = 343$ $\quad T_{C4} = 341$	T_{C1}, T_{C2}, T_{C3}, T_{C4}: d.s.c. [88S1], *no values for ΔH and ΔS are given in this study because of overlap of the curves corresponding to the pt.'s*
2nd set of d.s.c. data (for comparison)	a) initial heating $T_{C1} = 351$ $\quad \Delta H_1 = 2.30 \cdot 10^4$ $\quad \Delta S_1 = 65.7$ *struct. pt.'s at T_{C2} and T_{C3} missing* $T_{C4} = 345$ $\quad \Delta H_4 = 3.81 \cdot 10^4$ $\quad \Delta S_4 = 109.7$	T_{C1}, ΔH_1, ΔS_1: } d.s.c. [84N] T_{C4}, ΔH_4, ΔS_4:

Table 4. Data about Structural Phase Transitions *(continued)*

Compound	Phase sequence, transition temperature T_{Cn} [K], enthalpy ΔH_n [J · mol^{-1}] and entropy ΔS_n [J · mol^{-1} · K^{-1}] of the n - th structural phase transition	References, remarks
$(C_{14}H_{29}NH_3)_2CdCl_4$ (cont.)	b) reheating	
	$T_{C1} = 351$ $\Delta H_1 = 2.47 \cdot 10^4$ $\Delta S_1 = 69.9$	T_{C1}, ΔH_1, ΔS_1: } d.s.c. [84N]
	struct. pt. at T_{C2} missing	
	$T_{C3} = 347$ $\Delta H_3 = 1.59 \cdot 10^4$ $\Delta S_3 = 46.5$	T_{C3}, ΔH_3, ΔS_3:
	$T_{C4} = 345$ $\Delta H_4 = 2.39 \cdot 10^4$ $\Delta S_4 = 69.1$	T_{C4}, ΔH_4, ΔS_4:
$(C_{16}H_{33}NH_3)_2CdCl_4$	$\text{HT} \xleftrightarrow[T_{C1}]{} \text{IM1} \xleftrightarrow[T_{C2}]{} \text{IM2} \xleftrightarrow[T_{C3}]{} \text{LT}$	str. diff. ph. not st. in det., only u.c.p. by diffr. [89C2]; struct. pt.'s studied by therm. m. and diffr. [85R1, 89C2]
	$T_{C1} = 356$ $\Delta H_1 = 3.15(18) \cdot 10^4$ $\Delta S_1 = 88(5)$	T_{C1}, ΔH_1, ΔS_1: } d.s.c.[89C2]
	$T_{C2} = 352$ $\Delta H_2 = 0.77(3) \cdot 10^4$ $\Delta S_2 = 21.9(17)$	T_{C2}, ΔH_2, ΔS_2:
	$T_{C3} = 345$ $\Delta H_3 = 4.04(22) \cdot 10^4$ $\Delta S_3 = 117(7)$	T_{C3}, ΔH_3, ΔS_3:
$(C_{18}H_{37}NH_3)_2CdCl_4$	4 struct. pt.'s observed as anomalies in $C_p(T)$	str. diff. ph. not st. in det.
	$T_{C1} = 365.6(3)$ $\Delta H_1 = 3.43(3) \cdot 10^4$ $\Delta S_1 = 95(1)$	T_{C1}, ΔH_1, ΔS_1: } $C_p(T)$ by ad. cal. [84W1, 84W2]
	$T_{C2} = 359.5(3)$ $\Delta H_2 = 0.35(1) \cdot 10^4$ $\Delta S_2 = 9.6(3)$	T_{C2}, ΔH_2, ΔS_2:
	$T_{C3} = 356.0(1)$ $\Delta H_3 = 0.23(1) \cdot 10^4$ $\Delta S_3 = 6.5(3)$	T_{C3}, ΔH_3, ΔS_3:
	$T_{C4} = 349.6(1)$ $\Delta H_4 = 4.95(5) \cdot 10^4$ $\Delta S_4 = 132(1)$	T_{C4}, ΔH_4, ΔS_4:
$(C_{10}H_{21}NH_3)_2CdCl_2Br_2$	2 struct. pt.'s observed by d.s.c., only one set T_C, ΔH and ΔS determined since the two not resolved due to overlap	values of T_C, ΔH, ΔS by d.s.c.: see [80H2], str. diff. ph. not st. in det.
$(C_{11}H_{23}NH_3)_2CdCl_2Br_2$	2 struct. pt.'s observed by d.s.c.	values of T_{Cn}, ΔH_n, ΔS_n by d.s.c. (n = 1, 2): see [80H2], str. diff. ph. not st. in det.
$(C_{12}H_{25}NH_3)_2CdCl_2Br_2$	2 struct. pt.'s observed by d.s.c., only one set T_C, ΔH and ΔS determined since the two not resolved due to overlap	values of T_C, ΔH, ΔS by d.s.c.: see [80H2], str. diff. ph. not st. in det.
$(C_{13}H_{27}NH_3)_2CdCl_2Br_2$	3 struct. pt.'s observed by d.s.c.	values of T_{Cn}, ΔH_n, ΔS_n by d.s.c. (n = 1 – 3): see [80H2], str. diff. ph. not st. in det.
$(C_{14}H_{29}NH_3)_2CdCl_2Br_2$	2 struct. pt.'s observed by d.s.c., only one set T_C, ΔH and ΔS determined since the two not resolved due to overlap	values of T_C, ΔH, ΔS by d.s.c.: see [80H2], str. diff. ph. not st. in det
$(C_{15}H_{31}NH_3)_2CdCl_2Br_2$	3 struct. pt.'s observed by d.s.c.	values of T_{Cn}, ΔH_n, ΔS_n by d.s.c. (n = 1 – 3): see [80H2], str. diff. ph. not st. in det.
$(C_{18}H_{37}NH_3)_2CdCl_2Br_2$	2 struct. pt.'s observed by d.s.c.	values of T_{Cn}, ΔH_n, ΔS_n by d.s.c. (n = 1, 2): see [80H2], str. diff. ph. not st. in det.

Table 4. Data about Structural Phase Transitions *(continued)*

Compound	Phase sequence, transition temperature T_{Cn} [K], enthalpy ΔH_n [J · mol^{-1}] and entropy ΔS_n [J · mol^{-1} · K^{-1}] of the n - th structural phase transition	References, remarks
$(C_2H_5NH_3)_2HgCl_4$	2 struct. pt.'s observed as anomalies in $C_p(T)$	str. diff. ph. not st. in det., only struct. at 243 K [83B1] – further studies: opt. m. [84B1]; diel. c. [84B1]
	$T_{C1} = 220(5)$ $\Delta H_1 = 1.66 \cdot 10^3$ $T_{C2} = 190(5)$ $\Delta H_2 = 0.42 \cdot 10^3$	$\left.\begin{array}{l} T_{C1}, \Delta H_1: \\ T_{C2}, \Delta H_2: \end{array}\right\} C_p(T)$ by d.s.c. [84B1]
$(C_3H_7NH_3)_2HgCl_4$	2 struct. pt.'s observed as anomalies in $C_p(T)$	str. diff. ph. not st. in det., only struct. at 295 K [86B2] – further studies: opt. m. [84B1]; diel. c. [84B1]
	$T_{C1} = 205(5)$ $\Delta H_1 = 5.73 \cdot 10^3$ $T_{C2} = 195(5)$ $\Delta H_2 = < 0.05 \cdot 10^3$	$\left.\begin{array}{l} T_{C1}, \Delta H_1: \\ T_{C2}, \Delta H_2: \end{array}\right\} C_p(T)$ by d.s.c. [84B1]
$(C_8H_{17}NH_3)_2HgCl_4$	2 struct. pt.'s observed by d.s.c.	values of T_{Cn}, ΔH_n, ΔS_n by d.s.c. (n = 1, 2): see [79B1], str. diff. ph. not st. in det., only *d* by diffr. [79B1]
$(C_9H_{19}NH_3)_2HgCl_4$	2 struct. pt.'s observed by d.s.c.	values of T_{Cn}, ΔH_n, ΔS_n by d.s.c. (n = 1, 2): see [79B1], str. diff. ph. not st. in det., only *d* by diffr. [79B1]
$(C_{10}H_{21}NH_3)_2HgCl_4$	2 struct. pt.'s observed by x-ray diffr.	str. diff. ph. not st. in det., only d by diffr. [79B1] – further studies: d.s.c. [79B1]
	$T_{C1} = 358$ $T_{C2} = 338$	T_{C1}, T_{C2}: x-ray diffr. [95E]
$(C_{11}H_{23}NH_3)_2HgCl_4$	2 struct. pt.'s observed by d.s.c.	values of T_{Cn}, ΔH_n, ΔS_n by d.s.c. (n = 1, 2): see [79B1], str. diff. ph. not st. in det., only *d* by diffr. [79B1]
$(C_{12}H_{25}NH_3)_2HgCl_4$	1 struct. pt. observed by d.s.c.	values of T_C, ΔH, ΔS by d.s.c.: see [75L1, 79B1], str. diff. ph. not st. in det., only *d* by diffr. [77L1, 79B1]
$(C_{13}H_{27}NH_3)_2HgCl_4$	1 struct. pt. observed by d.s.c.	values of T_C, ΔH, ΔS by d.s.c.: see [79B1], str. diff. ph. not st. in det., only *d* by diffr. [79B1]
$(C_{14}H_{29}NH_3)_2HgCl_4$	1 struct. pt. observed by d.s.c.	values of T_C, ΔH, ΔS by d.s.c.: see [79B1], str. diff. ph. not st. in det., only *d* by diffr. [79B1]
$(C_{15}H_{31}NH_3)_2HgCl_4$	1 struct. pt. observed by d.s.c.	values of T_C, ΔH, ΔS by d.s.c.: see [79B1], str. diff. ph. not st. in det., only *d* by diffr. [79B1]
$(C_{16}H_{33}NH_3)_2HgCl_4$	1 struct. pt. observed by d.s.c.	values of T_C, ΔH, ΔS by d.s.c.: see [75L1, 79B1], str. diff. ph. not st. in det., only *d* by diffr. [77L1, 79B1]

Table 4. Data about Structural Phase Transitions *(continued)*

Compound	Phase sequence, transition temperature T_{Cn} [K], enthalpy ΔH_n [J · mol^{-1}] and entropy ΔS_n [J · mol^{-1} · K^{-1}] of the n - th structural phase transition	References, remarks
$(C_3H_7NH_3)_2PbCl_4$	$\underset{(\alpha)}{P12_1/a1} \xleftrightarrow[T_{C1}]{} \underset{(\beta)}{Pnam} \xleftrightarrow[T_{C2}]{} \underset{(\gamma)}{P12_1/c1^{1)}} \xleftrightarrow[T_{C3}]{} \underset{(\delta)}{??^{2)}} \xleftrightarrow[T_{C4}\,3)]{} \underset{(\varepsilon)}{??}$	**struct. pt.'s studied by:** therm. m. [89Z1]; diel. c. [89Z1]; Raman sp. and ir spectr. [90A2, 92A1]; diffr. [89M1, 91C2]
	$^{1)}$ *preliminary x-ray data* [92A1] $^{2)}$ *possibly an incommensurate phase* [92A1] $^{3)}$ *a first order reentrant phase transition* [92A1]	
	$T_{C1} = 399.5$ $\Delta H_1 = 3.25(20) \cdot 10^3$ $\Delta S_1 = 8.14$ $T_{C2} = 170(6)$ $T_{C3} = 91(4)$ $T_{C4} = 35(5)$	T_{C1}, ΔH_1, ΔS_1: d.s.c. [89Z1] T_{C2}, T_{C3}, T_{C4}: Raman sp. [92A1]
$(C_9H_{19}NH_3)_2PbCl_4$	3 struct. pt.'s observed by d.s.c.	values of T_{Cn}, ΔH_n, ΔS_n by d.s.c. (n = 1 – 3): see [95K], str. diff. ph. not st. in det., only u.c.p. at 295 K [95K]
d) Diammonium Compounds with $X = Cl^-, Br^-$		
$[NH_3(CH_2)_2NH_3]MnCl_4$	no struct. pt. observed in the temperature range from the decomposition temperature down to the onset of magnetic order	**studied by:** d.s.c., NMR, NQR [75K1, 76A1]; ir spectr. [78S3]; Raman sp. [78S3, 89G7]; diffr. [75T1, 76A1, 78T1]
$[NH_3(CH_2)_3NH_3]MnCl_4$	$\underset{(\alpha)}{\begin{matrix}\text{Imam}\\ \text{Ibmm}\end{matrix}} \xleftrightarrow[T_{C1}]{\textit{disc.}} \underset{(\beta)}{\text{Fmmm}} \xleftrightarrow[T_{C2}]{\textit{disc.}} \underset{(\gamma)}{\begin{matrix}\text{Pnam}\\ \text{Pbnm}\end{matrix}} \xleftrightarrow[T_{C3}*)]{} \underset{(\delta)}{??}$	**struct. pt.'s studied by:** therm. m. [76A1, 78K1, 79S3, 82C, 85C2]; opt. m. [76A1]; NMR, NQR [75W1, 76A1, 78K1, 82C]; Raman sp. and ir spectr. [79S3, 87G1]; diffr. [75W1, 76A1, 78K1, 82C]; incoh. n.s. [83S4, 86S1, 87G1, 89G2, 90G2]
	*) *This transition was observed once by d.s.c.* [79S3], *but was not confirmed in later investigations* [87G1]	
	$T_{C1} = 336(1)$ $\Delta H_1 = 640(30)$ $\Delta S_1 = 1.90$ $T_{C2} = 307(1)$ $\Delta H_2 = 725(30)$ $\Delta S_2 = 2.38$ heating: $T_{C2} = 306$ cooling: $T_{C2} = 292$ $T_{C3} = 110$	T_{C1}, ΔH_1, ΔS_1: d.s.c. [85C2] T_{C2}, ΔH_2, ΔS_2: $C_p(T)$ by ad. cal. [85C2] T_{C2} on heating and on cooling: [86S1, 87G1] T_{C3}: d.s.c. [79S3]
$[NH_3(CH_2)_4NH_3]MnCl_4$	$\underset{(OHT)}{\begin{matrix}\text{Pman}\\ \text{Pbnm}\end{matrix}} \xleftrightarrow[T_C]{\textit{cont.}} \underset{(MRT)}{\begin{matrix}P12_1/a1\\ P2_1/b11\end{matrix}}$ $T_C = 381.9(3)$	**struct. pt.'s studied by:** therm. m. [76A1]; opt. m. [76A1; birefr. [81K3]; NMR, NQR [76A1, 81K3]; diffr. [76A1, 80T1, 81K3]; incoh. n.s. [89G2, 90G2] T_C: birefr. [81K3]
$[ND_3(CH_2)_4ND_3]MnCl_4$	same phase sequence as above, slightly different T_C $T_C = 378.2(3)$	T_C: birefr. [81K3]

Table 4. Data about Structural Phase Transitions *(continued)*

Compound	Phase sequence, transition temperature T_{Cn} [K], enthalpy ΔH_n [J · mol^{-1}] and entropy ΔS_n [J · mol^{-1} · K^{-1}] of the n - th structural phase transition	References, remarks
$[NH_3(CH_2)_5NH_3]MnCl_4$	Imam*) / Ibmm*) (OHT) $\xleftrightarrow[T_C]{}$ Pnam*) / Pbnm*) (ORT)	**struct. pt.'s studied by:** therm. m. [76A1, 88C1]; opt. m. [76A1]; Raman sp. [87G1, 87N2]; ir spectr. [87G1]; incoh. n.s. [87G1, 89G2, 90G2]
	*) *structures assumed in analogy to* $[NH_3(CH_2)_5NH_3]CdCl_4$, *cf.* [87N1], *also consistent with the group theoretical analysis of Raman spectra* [87G1]	
	$T_C = 299.6(2)$ $\Delta H = 2.24 \cdot 10^3$ $\Delta S = 8.3$	T_C, ΔH, ΔS: $C_p(T)$ by ad. cal. [88C1]
$[NH_3(CH_2)_2NH_3]CdCl_4$	no struct. pt. observed in the temperature range from 90 K up to 420 K	**studied by:** therm. m. [77T1, 92B1]; diel. c. [76L1, 92B1]; Raman sp. [78S3, 81I1]; NMR [77B1]; ir spectr. [78S3, 79S4]; diffr. [76A2, 81I1, 92B1]
$[NH_3(CH_2)_3NH_3]CdCl_4$	???*) (OHT) $\xleftrightarrow[T_C]{cont.}$ Pnam / Pbnm (ORT)	**struct. pt.'s studied by:** therm. m. [77T1, 80F2, 92B1]; diel. c. [76L1, 92B1]; NMR, NQR [77B1, 81K3]; birefr. [81K3]; ir spectr. [79O1]; diffr. [76A2, 76W1, 77W1, 92B1]
	*) *From group theoretical considerations* [81K3], *space group* Imam *(or* Ibmm), *but diffraction data* [92B1] *state only orthorh. symmetry*	
	$T_C = 375$ $\Delta S = 9.7(8)$	T_C: birefr. [81K3] ΔS: $C_p(T)$ by d.s.c. [80F2]
$[NH_3(CH_2)_4NH_3]CdCl_4$	3 struct. pt.'s observed by d.s.c.	str. diff. ph. not st. in det., only u.c.p. at 295 K [76W1] – further studies: diel. c. [76L1]; NMR [77B1]; diffr. [76A2]
	$T_{C1} = 366$ $\Delta H_1 = 0.212 \cdot 10^3$ $\Delta S_1 = 0.57$ $T_{C2} = 360$ $\Delta H_2 = 0.955 \cdot 10^3$ $\Delta S_2 = 2.65$ $T_{C3} = 335$ $\Delta H_3 = 2.583 \cdot 10^3$ $\Delta S_3 = 7.69$	T_{C1}, ΔH_1, ΔS_1: T_{C2}, ΔH_2, ΔS_2: T_{C3}, ΔH_3, ΔS_3: } d.s.c. [77T1]
$[NH_3(CH_2)_5NH_3]CdCl_4$	C12/m1 / C2/m11 (MHT) $\xleftrightarrow[T_{C1}]{disc.}$ Imam / Ibmm (OHT) $\xleftrightarrow[T_{C2}]{cont.}$ Pnam / Pbnm (ORT)	**struct. pt.'s studied by:** therm. m. [77T1, 80F2, 89N1]; diel. c. [76L1]; birefr. [81K3]; NMR, NQR [77B1, 81K3]; Raman sp. [81M2, 87N2, 88C2, 89N1]; diff. x-ray sc. [89N1]; diffr. [76A2, 76W1, 87N1, 87N2, 89N1]
	$T_{C1} = 417$ (heating) $\Delta S = 1.80$ $T_{C1} = 407$ (cooling) $T_{C2} = 337$ $\Delta S_2 = 9.38$	T_{C1} (heating, cooling): d.s.c. [89N1] ΔS_1: $C_p(T)$ by d.s.c. [80F2] T_{C2}: d.s.c. [89N1], ΔS_2: $C_p(T)$ by d.s.c. [80F2]

9.12.2.4 References for 9.12.2

58R2 Roth, W.L.: Phys. Rev. 110 (1958) 1333.
62G Geick, R.: Z. Phys. 166 (1962) 122.
62L1 Legrand, L., Plumier, R.: Phys. Status Solidi 2 (1962) 317.
62L2 Ljubarski, G.J.: Anwendungen der Gruppentheorie in der Physik, Berlin: Deutscher Verlag der Wissenschaften, 1962.
62R Rüdorff, W., Kändler, J., Babel, D.: Z. Anorg. Allg. Chemie 317 (1962) 261.
63K1 Koster, G.F., Dimmock, J.O., Wheeler, R.G., Statz, H.: Properties of the Thirty-Two Point Groups, Cambridge/Massachusetts: M.I.T. Press, 1963.
63R Rüdorff, W., Lincke, G., Babel, D.: Z. Anorg. Allg. Chemie 320 (1963) 150.
64C1 Cousseins, J.C.: Rev. Chim. Miner. 1 (1964) 573.
64C2 Crocket, D.S., Grossman, R.A.: Inorg. Chem. 3 (1964) 644.
64P Plumier, R.: J. Appl. Phys. 35 (1964) 950.
64S1 Siegel, S., Gebert, E.: Acta Crystallogr. 17 (1964) 790.
64S2 Sykes, M.F., Essam, J.W.: Phys. Rev. 133 (1964) A310.
64W Willett, R.D.: J. Chem. Phys. 41 (1964) 2243.
65P de Pape, R.: Bull. Soc. Chim. France (1965) 3489.
65S Seifert, H.J., Koknat, F.W.: Z. Anorg. Allg. Chemie 341 (1965) 269.
66D1 Domb, C., Dalton, N.W.: Proc. Phys. Soc. 89 (1966) 859.
66N Neubüser, J., Wondratschek, H.: Kristall und Technik 1 (1966) 529.
66S1 Seifert, H.J., Klatyk, K.: Z. Anorg. Allg. Chemie 342 (1966) 1.
66V Vollmer, Ph.D. Thesis, University of Tübingen (Germany), 1966.
67S1 Stucky, G.D., Folkers, J.B., Kistenmacher, T.J.: Acta Crystallogr. 23 (1967) 1064.
67W1 Wiesner, J.R., Srivastava, R.C., Kennard, C.H.L., DiVaira, M., Lingafelter, E.C.: Acta Crystallogr. 23 (1967) 565.
67W2 Willett, R.D., Liles, O.L., Michelson, C.: Inorg. Chem. 6 (1967) 1885.
68C1 Charpin, P., Roux, N., Ehretsmann, J.: C.R. Acad. Sci. Paris, Ser. C, 267 (1968) 484.
68C2 Cousseins, J.C., Perez, C.P.: Rev. Chim. Miner. 5 (1968) 147.
68F1 Foster, J.J., Gill, N.S.: J. Chem. Soc. A (1968) 2625.
68L1 Loopstra, B.O., van Laar, B., Breed, D.J.: Phys. Lett. 26A (1968) 527. Erratum: Phys. Lett. 27A (1968) 188.
68M1 Maradudin, A.A., Vosko, S.H.: Rev. Mod. Phys. 40 (1968) 1.
68S1 Seifert, H.J., Koknat, F.W.: Z. Anorg. Allg. Chemie 357 (1968) 314.
68W1 Wertheim, G.K., Guggenheim, H.J., Levinstein, H.J., Buchanan, D.N.E., Sherwood, R.C.: Phys. Rev. 173 (1968) 614.
69B1 Breed, D.J., Gilijamse, K., Miedema, A.R.: Physica 45 (1969) 205.
69C1 Cox, D.E., Shirane, G., Birgeneau, R.J., MacChesney, J.B.: Phys. Rev. 188 (1969) 930.
69C2 Cracknell, A.P.: Rep. Prog. Phys. 32 (1969) 633.
69I International Tables for X-Ray Crystallography, Vol. 1, Henry, N.F.M., Lonsdale, K. (eds.), Birmingham: The Kynoch Press, 1969.
69L1 Legrand, E., van den Bosch, A.: Solid State Commun. 7 (1969) 1191.
69M1 Moran, T.J., Lüthi, B.: Phys. Rev. 187 (1969) 710:
69S1 Shannon, R.D., Prewitt, C.T.: Acta Crystallogr. B 25 (1969) 925.
69Z Zak, J. (ed.), Casher, A., Glück, M., Gur, Y.: The Irreducible Representations of Space Groups, New York: W.A. Benjamin, 1969.
70B1 Birgeneau, R.J., Guggenheim, H.J., Shirane, G.: Phys. Rev. B 1 (1970) 2211.
70B2 Barendregt, F., Schenk, H.: Physica 49 (1970) 465.
70E Epstein, A., Gurewitz, E., Makovsky, J., Shaked, H.: Phys. Rev. B 2 (1970) 3703.
70G2 Gurewitz, E., Epstein, A., Makovsky, J., Shaked, H.: Phys. Rev. Lett. 25 (1970) 1713.
70H Hardt, H.-D., Streit, G.: Z. Anorg. Allg. Chemie 373 (1970) 97.

70N Neubüser, J., Wondratschek, H.: Minimal Supergroups of the Space Groups, private communication, 1970.
70S1 Steadman, J.P., Willett, R.D.: Inorg. Chim. Acta 4 (1970) 367.
70S2 Shannon, R.D., Prewitt, C.T.: Acta Crystallogr. B 26 (1970) 1046.
70S3 Slonczewski, J.C., Thomas, H.: Phys. Rev. B 1 (1970) 3599.
71J1 Joly, E.: C.R. Acad. Sci. Paris, Ser. C, 272 (1971) 1302.
71M1 Mostafa, M.F., Willett, R.D.: Phys. Rev. B 4 (1971) 2213.
72A van Amstel, W.D., de Jongh, L.J.: Solid State Commun. 11 (1972) 1423.
72C1 Colpa, J.H.P.: Physica 57 (1972) 347.
72G1 Glazer, A.M.: Acta Crystallogr. B 28 (1972) 3384.
72I Ikeda, H., Hirakawa, K.: J. Phys. Soc. Jpn. 33 (1972) 393.
72P Petersen, E.R., Willett, R.D.: J. Chem. Phys. 56 (1972) 1879.
72T1 Tsukuda, N., Okazaki, A.: J. Phys. Soc. Jpn. 33 (1972) 1088.
72W1 Wooten, F.: Optical Properties of Solids, New York, London: Academic Press, 1972.
73A1 Arend, H., Hofmann, R., Waldner, F.: Solid State Commun. 13 (1973) 1629.
73B1 Birgeneau, R.J., Guggenheim, H.J., Shirane, G.: Phys. Rev. B 8 (1973) 304.
73D1 Day, P., Gregson, A.K., Leech, D.H.: Phys. Rev. Lett. 30 (1973) 19.
73H1 Heger, G., Henrich, E., Kanellakopulos, B.: Solid State Commun. 12 (1973) 1157.
73J1 Jahn, I.R., Bittermann, K.: Solid State Commun. 13 (1973) 1897.
73K1 Khomskii, D.I., Kugel, K.I.: Solid State Commun. 13 (1973) 763.
73L1 Lavrencic, B.B., Shigenari, T.: Solid State Commun. 13 (1973) 1329.
73R1 Rehwald, W.: Adv. Phys. 22 (1973) 721.
73S1 Schrama, A.H.M.: Physica 68 (1973) 279.
73V Vacatello, M., Corradini, P.: Gazz. Chim. Ital. 103 (1973) 1027.
73W1 Witteveen, H.T., Reedijk, J.: Solid State Commun. 12 (1973) 397.
74A1 Arend, H., Hofmann, R., Felsche, J.: Ferroelectrics 8 (1974) 413.
74B1 Bittermann, K., Heger, G.: J. Crystal Growth 21 (1974) 82.
74B2 Bloembergen, P., Miedema, A.R.: Physica 75 (1974) 205.
74B3 Blinc, R., Zeks, B.: Soft Modes in Ferroelectrics and Antiferroelectrics, Vol. XIII of Selected Topics in Solid State Physics, Wohlfarth, E.P. (ed.), Amsterdam: North-Holland, 1974.
74H1 Haegele, R., Babel, D.: Z. Anorg. Allg. Chemie 409 (1974) 11.
74H2 Hutchings, M.T., Gregson, A.K., Day, P., Leech, D.H.: Solid State Commun. 15 (1974) 313.
74K1 Knorr, K., Jahn, I.R., Heger, G.: Solid State Commun. 15 (1974) 231.
74L1 Larsen, K.P.: Acta Chem. Scand., Ser. A, 28 (1974) 194
74S1 Samuelsen, E.J.: J. Phys. Chem. Solids 35 (1974) 785.
74S2 Scott, J.F., Dultz, W.: unpublished results 1974, private communication.
74V1 Vacatello, M., Corradini, P.: Gazz. Chim. Ital. 104 (1974) 773.
74V2 Vacatello, M.: Ann. Chim. (Rome) 64 (1974) 19.
74V3 Vacatello, M.: Ann. Chim. (Rome) 64 (1974) 13.
74W1 Witteveen, H.T.: J. Solid State Chem. 11 (1974) 245.
74W2 Witteveen, H.T., Jongejan, D.L., Brandwijk, V.: Mater. Res. Bull. 9 (1974) 345.
75A1 Als-Nielsen, J., Birgeneau, R.J., Guggenheim, H.J., Shirane, G.: Phys. Rev. B 12 (1975) 4963.
75B1 Bocanegra, E.H., Tello, M.J., Arriandiaga, M.A., Arend, H.: Solid State Commun. 17 (1975) 1221.
75B2 Bärnighausen, H.: Acta Crystallogr. A 31 (1975) S3.
75C1 Chapuis, G., Arend, H., Kind, R.: Phys. Status Solidi (a) 31 (1975) 449.
75G1 Geick, R.: Topics in Current Chemistry 58 (1975) 73.
75G2 Glazer, A.M.: Acta Crystallogr. A 31 (1975) 756.
75H1 Heger, G., Mullen, D., Knorr, K.: Phys. Status Solidi (a) 31 (1975) 455.
75K1 Kammer, H.: Helv. Phys. Acta 47 (1975) 442.
75L1 Landi, E., Vacatello, M.: Thermochim. Acta 13 (1975) 441.
75L2 Lehner, N., Strobel, K., Geick, R., Heger, G.: J. Phys. C: Solid State Phys. 8 (1975) 4096.

75L3 Lehner, N.: Diploma Thesis, University of Würzburg (Germany) 1975.
75L4 Landau, L.D., Lifschitz, E.M.: Lehrbuch der theoretischen Physik. Band V: Statistische Physik, 4. Auflage, Berlin: Akademie-Verlag, 1975.
75P1 Petzelt, J.: J. Phys. Chem. Solids 36 (1975) 1005.
75T1 Tichy, K., Benes, J., Arend, H.: Acta Crystallogr. A 31 (1975) S84.
75W1 Willett, R.D., Riedel, E.F.: Chem. Phys. 8 (1975) 112.
76A1 Arend, H., Tichy, K., Baberschke, K., Rys, F.: Solid State Commun. 18 (1976) 999.
76A2 Arend, H., Gränicher, H.: Ferroelectrics 13 (1976) 537.
76B1 Brinkmann, D., Walther, U., Arend, H.: Solid State Commun. 18 (1976) 1307.
76B2 Bürger, H., Strobel, K., Geick, R., Müller-Lierheim, W.: J. Phys. C: Solid State Phys. 9 (1976) 4213.
76B3 Berg, R.W., Søtofte, I.: Acta Chem. Scand. A 30 (1976) 843.
76C1 Ciajolo, M.R., Corradini, P., Pavone, V.: Gazz. Chim. Ital. 106 (1976) 807.
76C2 Chapuis, G., Kind, R., Arend, H.: Phys. Status Solidi (a) 36 (1976) 285.
76D1 Deonarine, S., Joshua, S.J.: Phys. Status Solidi (b) 74 (1976) 659.
76D2 Dupas, A., Le Dang, K., Renard, J.P., Veillet, P., Daoud, A., Perret, R.: J. Chem. Phys. 65 (1976) 4099.
76D3 Depmeier, W.: Acta Crystallogr. B 32 (1976) 303.
76D4 Dance, J.M., Grannec, J., Tressaud, A.: C.R. Acad. Sci. Paris, Ser. C, 283 (1976) 115.
76G1 Gurewitz, E., Makovsky, J., Shaked, H.: Phys. Rev. B 14 (1976) 2071.
76H1 Heger, G., Mullen, D., Knorr, K.: Phys. Status Solidi (a) 35 (1976) 627.
76H2 Heger, G., Mullen, D.: Proc. Conf. Neutron Scattering, Gatlinburg/Tennessee, 1976, p. 439.
76I1 Ito, Y., Akimitsu, J.: J. Phys. Soc. Jpn. 40 (1976) 1333.
76K1 Kind, R., Roos, J.: Phys. Rev. B 13 (1976) 45.
76L1 Levstik, A., Filipic, C., Blinc, R., Arend, H., Kind, R.: Solid State Commun. 20 (1976) 127.
76N1 Navarro, R., Smit, J.J., de Jongh, L.J., Crama, W.J., Ijdo, D.J.W.: Physica 83B (1976) 97.
76P1 Phelps, D.W., Losee, D.B., Hatfield, W.E., Hodgson, D.J.: Inorg. Chem. 15 (1976) 3147.
76R1 Rehaber, E.: Diploma Thesis, University of Regensburg (Germany) 1976.
76S1 Shannon, R.D.: Acta Crystallogr. A 32 (1976) 751.
76S2 Seliger, J., Blinc, R., Arend, H., Kind, R.: Z. Physik B 25 (1976) 189.
76S3 Stoelinga, J.H.M., Wyder, P.: J. Chem. Phys. 64 (1976) 4612.
76W1 Walpen, P.: Diploma Thesis, ETH Zürich (Switzerland) 1976.
76W2 Wondratschek, W., Jeitschko, W.: Acta Crystallogr. A 32 (1976) 664.
77B1 Blinc, R., Burgar, M., Lozar, B., Seliger, J., Slak, J., Rutar, V., Arend, H., Kind, R.: J. Chem. Phys. 66 (1977) 278.
77C2 Chapuis, G.: Phys. Status Solidi (a) 43 (1977) 203.
77C3 Cowley, R.A., Shirane, G., Birgeneau, R.J., Guggenheim, H.J.: Phys. Rev. B 15 (1977) 4292.
77C4 Couzi, M., Daoud, A., Perret, R.: Phys. Status Solidi (a) 41 (1977) 271.
77D1 Depmeier, W., Felsche, J., Wildermuth, G.: J. Solid State Chem. 21 (1977) 57.
77D2 Depmeier, W.: Acta Crystallogr. B 33 (1977) 3713.
77G1 Goodyear, J., Ali, E.M., Steigmann, G.A.: Acta Crystallogr. B 33 (1977) 2932.
77G3 Geick, R., Strobel, K.: J. Phys. C: Solid State Phys. 10 (1977) 4221.
77H1 Heygster, G., Kleemann, W.: Physica 89B (1977) 165.
77H4 Hidaka, M., Hosogi, S., Ono, M., Horai, K.: Solid State Commun. 23 (1977) 503.
77K1 Kind, R.: Phys. Status Solidi (a) 44 (1977) 661.
77K2 van Kempen, H., Mischgofsky, F.H., Wyder, P.: Phys. Rev. B 15 (1977) 4386.
77K3 v. Känel, H., Wachter, P.: Physica 89B (1977) 189.
77K4 Kammer, J.W.: Ph.D. Thesis, ETH Zürich (Switzerland) 1977.
77L1 Landi, E., Salerno, V., Vacatello, M.: Gazz. Chim. Ital. 107 (1977) 27.
77N1 Neubüser, J., Wondratschek, H.: Maximal Subgroups of the Space Groups, 2nd typing 1966, corrected 1977, private communication.
77O Oxton, I.A., Knop, O.: J. Mol. Struct. 37 (1977) 59.
77T1 Tello, M.J., Arriandiaga, M.A., Fernandez, J.: Solid State Commun. 24 (1977) 299.

77V1 Vogtmann, K.: Diploma Thesis, University of Würzburg (Germany) 1977.
77W1 Willett, R.D.: Acta Crystallogr. B 33 (1977) 1641.
77W2 Willett, R.D., Willett, J.J.: Acta Crystallogr. B 33 (1977) 1639.
78A1 Adams, D.M., Stevens, D.C.: J. Phys. C: Solide State Phys. 11 (1978) 617.
78A2 Arriandiaga, M.A., Tello, M.J., Fernandez, J., Arend, H., Roos, J.: Phys. Status Solidi (a) 48 (1978) 53.
78B1 Bellitto, C., Day, P.: J. Chem. Soc. Dalton Trans. (1978) 1207.
78B2 Blinc, R., Zeks, B., Kind, R.: Phys. Rev. B 17 (1978) 3409.
78C1 Chapuis, G.: Acta Crystallogr. B 34 (1978) 1506.
78C2 Couzi, M., Daoud, A., Perret, R.: Proc. Int. Conf. Lattice Dynamics Paris 1977, Balkanski, M., (ed.), Paris: Flammarion Sciences, 1978, p. 714.
78D1 Depmeier, W., Heger, G.: Acta Crystallogr. B 34 (1978) 1698.
78D2 Depmeier, W., Mason, S.A.: Acta Crystallogr. B 34 (1978) 920.
78D3 Dance, J.M., Yoshizawa, Y., Hirakawa, K.: Mater. Res. Bull. 13 (1978) 1111.
78G Goodyear, J., Ali, E.M., Sutherland, H.H.: Acta Crystallogr. B 34 (1978) 2617.
78H1 Hamann, S.D.: High Temp.-High Pressures 10 (1978) 497.
78H2 Heger, G.: Progr. Rep. KfK 2574, Karlsruhe 1978.
78K1 Kind, R., Plesko, S., Roos, J.: Phys. Status Solidi (a) 47 (1978) 233.
78L1 Lehner, N.: Progr. Rep. KfK 2720, Karlsruhe 1978.
78L2 Lehner, N., Heger, G., Geick, R.: Proc. Int. Conf. Lattice Dynamics Paris 1977, Balkanski, M. (ed.), Paris: Flammarion Sciences, 1978, p. 717.
78O2 Oxton, I.A., Knop, O.: J. Mol. Struct. 43 (1978) 17.
78S1 Schröder, B., Strobel, K., Wagner, G., Geick, R.: Infrared Phys. 18 (1978) 893.
78S2 Strobel, K., Gmelin, E., Geick, R.: unpublished results 1978.
78S3 Skaarup, S., Berg, R.W.: J. Solid State Chem. 26 (1978) 59.
78T1 Tichy, K., Benes, J., Hälg, W., Arend, H.: Acta Crystallogr. B 34 (1978) 2970.
78W1 Wagner, V., Krey, U.: Z. Phys. B 30 (1978) 367.
79B1 Busico, V., Salerno, V., Vacatello, M.: Gazz. Chim. Ital. 109 (1979) 581.
79B2 Bevaart, L., Frikkee, E., de Jongh, L.J.: Phys. Rev. B 19 (1979) 4741.
79B3 Blinc, R., Burgar, M.I., Rutar V., Zeks, B., Kind, R. Arend, H., Chapuis, G.: Phys. Rev. Lett. 43 (1979) 1679.
79B4 Blake, A.B., Hatfield, W.E.: J. Chem. Soc. Dalton Trans. (1979) 1725.
79B5 Bhat, D.Kh., Zinenko, V.I.: Sov. Phys. Solid State 21 (1979) 588.
79D1 Depmeier, W.: J. Solid State Chem. 25 (1979) 15.
79D2 Depmeier, W., Chapuis, G.: Acta Crystallogr. B 35 (1979) 1081.
79G1 Gmelin, E.: Thermochim. Acta 29 (1979) 1.
79G2 Goodyear, J., Ali, E.M., Sutherland, H.H.: Acta Crystallogr. B 35 (1979) 456.
79G3 Goto, T., Lüthi, B., Geick, R., Strobel, K.: J. Phys. C: Solid State Phys. 12 (1979) L303.
79G4 Geick, R., Strobel, K.: J. Phys. C: Solid State Phys. 12 (1979) 27.
79G7 Ganguli, D.: J. Solid State Chem. 30 (1979) 353.
79H1 Hidaka, M., Walker, P.: Solid State Commun. 31 (1979) 383.
79K1 Kind, R., Plesko, S., Arend, H., Blinc, R., Zeks, B., Seliger, J., Lozar, B., Slak, J., Levstik, A., Filipic, C., Zagar, V., Lahajnar, G., Milia, F., Chapuis, G.: J. Chem. Phys. 71 (1979) 2118.
79K2 Krause, S.: Ph.D. Thesis, University of Marburg (Germany) 1979.
79K3 Kleemann, W., Schäfer, F.J., Nouet, J.: Physica 97B (1979) 145.
79K4 Kubo, H., Suzuki, Y., Akitomi, T.: J. Phys. Soc. Jpn. 47 (1979) 2029.
79K5 Kind, R., Blinc, R., Zeks, B.: Phys. Rev. B 19 (1979) 3743.
79O1 Oxton, I.A.: J. Mol. Struct. 54 (1979) 11.
79P1 Peyrard, M., Perret, R.: Phys. Status Solidi (a) 52 (1979) 521.
79P2 Peyrard, M., Remoissenet, M.: J. Chem. Phys. 71 (1979) 2732.
79S2 Steijger, J.J.M., Frikkee, E., de Jongh, L.J.: J. Magn. Magn. Mater. 14 (1979) 152.
79S3 Sourisseau, C., Lucazeau, G.: J. Raman Spectrosc. 8 (1979) 311.
79S4 Strobel, K.: Ph.D. Thesis, University of Würzburg (Germany) 1979.

79U van Uijen, C.M.J., Frikkee, E., de Wijn, H.J.: Phys. Rev. B 19 (1979) 509.
80B1 Birgeneau, R.J., Cowley, R.A., Shirane, G., Tarvin, J.A., Guggenheim, H.J.: Phys. Rev. B 21 (1980) 317.
80B2 Blinc, R., Kozelj, M., Rutar, V., Zupanicic, I., Zecs, B., Arend, H., Kind, R., Chapuis, G.: Faraday Discuss. Chem. Soc. 69 (1980) 58.
80B3 Bärnighausen, H.: Commun. Math. Chem. (MATCH) (9) (1980) 139.
80C1 Cowley, R.A., Birgeneau, R.J., Shirane, G., Guggenheim, H.J., Ikeda, H.: Phys. Rev. B 21 (1980) 4038.
80C2 Cowley, R.A.: Adv. Phys. 29 (1980) 1.
80F1 Filipic, C., Levstik, A.: Phys. Status Solidi (a) 57 (1980) K55.
80F2 Fouskova, A.: Ferroelectrics 25 (1980) 451.
80G1 Geick, R., Hofmann, O., Wagner, G.: Int. J. Infrared Millim. Waves 1 (1980) 285.
80G2 Goto, T., Lüthi, B., Geick, R., Strobel, K.: Phys. Rev. B 22 (1980) 3452.
80H1 Herdtweck, E., Babel, D.: Z. Kristallogr. 153 (1980) 189.
80H2 Herreros, J., Tello, M.J., Bocanegra, E.H.: Solid State Commun. 34 (1980) 515.
80H3 Herbst, H.J.: Diploma Thesis, University of Würzburg (Germany) 1980.
80I1 Ikeda, H., Riste, T., Shirane, G.: J. Phys. Soc. Jpn. 49 (1980) 504.
80J Joshua, S.J., Deonarine, S.: Phys. Status Solidi (b) 101 (1980) 135.
80K1 Kesharwani, K.M., Lehner, N., Strobel, K., Geick, R.: J. Phys. C: Solid State Phys. 13 (1980) 1391.
80L1 Levstik, A., Filipic, C.: Phys. Status Solidi (a) 58 (1980) K165.
80M2 Münninghoff, G., Treutmann, W., Hellner, E., Heger, G., Reinen, D.: J. Solid State Chem. 34 (1980) 289.
80M3 Münninghoff, G.: Ph.D. Thesis, University of Marburg (Germany) 1980.
80T1 Tichy, K., Benes, J., Kind, R., Arend, H.: Acta Crystallogr. B 36 (1980) 1355.
81B1 Babar, M.A., Ladd, M.F.C., Larkworthy, L.F., Povey, D.C., Proctor, K.J., Summers, L.J.: J. Chem. Soc., Chem. Commun. 1981, 1046.
81B2 Bloomquist, D.R., Willett, R.D., Dodgen, H.W.: J. Am. Chem. Soc. 103 (1981) 2610.
81B3 Bruce, A.D., Cowley, R.A.: Structural Phase Transitions, London: Taylor & Francis, 1981.
81D2 Depmeier, W.: Acta Crystallogr. B 37 (1981) 330.
81D3 Depmeier, W., Oxton, I.A.: J. Mol. Struct. 77 (1981) 91.
81H1 Herdtweck, E., Babel, D.: Z. Anorg. Allg. Chemie 474 (1981) 113.
81I1 Iqbal, Z., Arend, H., Wachter, P.: J. Phys. C: Solid State Phys. 14 (1981) 1497.
81K1 Käräjämäki, E., Laiho, R., Levola, T., Kleemann, W., Schäfer, F.J.: Physica 111B (1981) 24.
81K2 Kozelj, M., Rutar, V., Zupancic, I., Blinc, R., Arend, H., Kind, R., Chapuis, G.: J. Chem. Phys. 74 (1981) 4123.
81K3 Kind, R., Plesko, S., Günter, P., Roos, J., Fousek, J.: Phys. Rev. B 23 (1981) 5301. Erratum: Phys. Rev. B 24 (1981) 4910.
81L Lüthi, B., Rehwald, W.: Ultrasonic studies near structural phase transitions, in: Structural Phase Transitions I, Topics in Current Physics, Müller, K.A., Thomas, H. (eds.), Vol. 23, Berlin: Springer-Verlag, 1981, p. 131.
81M1 Münninghoff, G., Kurtz, W., Treutmann, W., Hellner, E., Heger, G., Lehner, N., Reinen, D.: Solid State Commun. 40 (1981) 571.
81M2 Mokhlisse, R.: Thèse 3me Cycle, Université de Bordeaux I/France 1981.
81N Needham, G.F., Willett, R.D.: J. Phys. Chem. 85 (1981) 3385.
81O Oswald, M., Ihringer, J., Jahn, I.R.: Z. Kristallogr. 154 (1981) 312.
81R1 Reinen, D., Krause, S.: Inorg. Chem. 20 (1981) 2750.
81R2 Rahman, A., Clayton, P.R., Staveley, L.A.K.: J. Chem. Thermodyn. 13 (1981) 735.
81R3 Rao, C.N.R., Ganguly, S., Ramachandra Swamy, H., Oxton, I.A.: J. Chem. Soc. Faraday Trans. II 77 (1981) 1825.
81T1 Tello. M.J., Mañes, J.L., Fernandez, J., Arriandiaga, M.A., Perez-Mato, J.M.: J.Phys. C: Solid State Phys. 14 (1981) 805.
81V Vacatello, M., de Girolamo, M., Busico, V.: J. Chem. Soc. Faraday Trans. I 77 (1981) 2367.

81W1 de Wolff, P.M., Janssen, T., Janner, A.: Acta Crystallogr. A 37 (1981) 625

81W2 Willett, R.D., Jardine, F.H., Wong, R.J., Landee, C.P., Numata, M.: Phys. Rev. B 24 (1981) 5372.

81W3 White, M.A., Granville, N.W., Davies, N.J., Staveley, L.A.K.: J. Phys. Chem. Solids 42 (1981) 953.

82B1 Brunskill, I.H., Depmeier, W.: Acta Crystallogr. A 38 (1982) 132.

82B2 Babel, D., Herdtweck, E.: Z. Anorg. Allg. Chemie 487 (1982) 75.

82C Crowley, J.C., Dodgen, H.W., Willett, R.D.: J. Phys. Chem. 86 (1982) 4046.

82D1 Depmeier, W., Mason, S.A.: Solid State Commun. 44 (1982) 719.

82G1 Goto, T., Yoshizawa, M., Tamaki, A., Fujimura, T.: J. Phys. C: Solid State Phys. 15 (1982) 3041.

82H1 Hagemann, H., Bill, H.: Chem. Phys. Lett. 87 (1982) 45.

82H2 Hagemann, H., Bill, H.: Chem. Phys. Lett. 90 (1982) 282.

82H3 Hagemann, H., Bill, H.: Chem. Phys. Lett. 93 (1982) 582.

82M1 Muralt, P., Kind, R., Blinc, R., Zeks, B.: Phys. Rev. Lett. 49 (1982) 1019.

82M2 Mostafa, M.F., Semary, M.A., Abdel-Kader, M.M.: Physica 112B (1982) 197.

82M3 Mokhlisse, R., Couzi, M., Wang, C.H.: J. Chem. Phys. 77 (1982) 1138.

82P1 Petrakovskii, G.A., Emel'yanova, L.S., Kokov, I.T., Bondarenko, G.V., Baranov, A.V.: Sov. Phys. JETP 56 (1982) 1260.

82R1 Rahman, A., Staveley, L.A.K., Bellitto, C., Day, P.: J. Chem. Soc., Faraday Trans. II 78 (1982) 1895.

82R2 Ricard, L., Rey-Lafon, M., Haget, Y., Meresse, A., Housty, J., Chanh, N.B.: Raman Spectrosc., Proc. 8th Int. Conf. 1982, p. 437.

82S1 Stead, M.J., Day, P.: J. Chem. Soc. Dalton Trans. (1982) 1081.

82T1 Thurlings, M.P.H., Frikkee, E., de Wijn, H.J.: Phys. Rev. B 25 (1982) 4750.

82W1 Walker, P.J., Wondre, F., Fyne, P.J.: J. Crystal Growth 60 (1982) 155.

82W2 White, M.A., Granville, N.W., Staveley, L.A.K.: J. Phys. Chem. Solids 43 (1982) 341.

82W3 White, M.A., Staveley, L.A.K.: J. Phys. Chem. Solids 43 (1982) 1019.

82W4 Wagner, G.: Ph.D. Thesis, University of Würzburg (Germany) 1982.

82W5 White, M.A., Staveley, L.A.K.: J. Chem. Thermodyn. 14 (1982) 859.

83A1 Ahmed, M.A., Abd El-Kaffar, M.A.: Thermochim. Acta 70 (1983) 217.

83B1 Ben Salah, A., Daoud, A., Constant, G., Jaud, J., Galy, J.: Acta Crystallogr. C 39 (1983) 63.

83C1 Chanh, N.B., Haget, Y., Hauw, C., Meresse, A., Ricard, L., Rey-Lafon, M.: J. Phys. Chem. Solids 44 (1983) 589.

83C2 Chapuis, G., Brunisholz, G., Javet, C., Roulet, R.: Inorg. Chem. 22 (1983) 455.

83D1 Depmeier, W., Mason, S.A.: Solid State Commun. 46 (1983) 409.

83D2 Depmeier, W.: Solid State Commun. 45 (1983) 1089.

83H1 Hidaka, M., Inoue, K., Yamada, I., Walker, P.J.: Physica 121B (1983) 343.

83I1 Ikeda, H., Someya, Y., Endoh, Y., Noda, Y., Shibata, F.: Physica 120B (1983) 193.

83J1 Janke, E., Hutchings, M.T., Day, P., Walker, P.J.: J. Phys. C: Solid State Phys. 16 (1983) 5959.

83K1 Kobayashi, J., Uesu, Y.: J. Appl. Crystallogr. 16 (1983) 204.

83K2 Kleemann, W., Schäfer, F.J., Käräjämäki, E., Laiho, R., Levola, T.: Physica 119B (1983) 269.

83K3 Kind, R.: Ber. Bunsenges. Phys. Chem. 87 (1983) 248.

83M1 Mokhlisse, R., Couzi, M., Lassegues, J.C.: J. Phys. C: Solid State Phys. 16 (1983) 1353.

83M2 Mokhlisse, R., Couzi, M., Loyzance, P.L.: J. Phys. C: Solid State Phys. 16 (1983) 1367.

83M3 Mokhlisse, R., Couzi, M.: Mol. Cryst. Liq. Cryst. 96 (1983) 387.

83M4 Muralt, P., Kind, R.: Helv. Phys. Acta 56 (1983) 689.

83N1 Natsume, Y., Yamada, I.: Solid State Commun. 47 (1983) 839.

83P Petrakovskii, G.A., Yemelyanova, L.S., Velichko, V.V.: Solid State Commun. 48 (1983) 647.

83S1 Suzuki, T., Yoshizawa, M., Goto, T., Yamakami, T., Takahashi, M., Fujimura, T.: J. Phys. Soc. Jpn. 52 (1983) 1669.

83S2 Steijger, J.J.M., Frikkee, E., de Jongh, L.J., Huiskamp, W.J.: Physica 120B (1983) 202.

83S3 Suzuki, Y., Kubo, H.: J. Phys. Soc. Jpn. 52 (1983) 1420.

83S4 Sourisseau, C., Lucazeau, G., Dianoux, A.: J. Phys. (France) 44 (1983) 967.
83T1 Tichy, K., Fischer, P., Depmeier, W.: Würenlingen Report AF-SSP-127 (1983) 29.
83T2 Tichy, K. Depmeier, W.: Würenlingen Report AF-SSP-127 (1983) 31.
83W1 Walker, P.J., Wondre, F., Fyne, P.J.: Mater. Res. Bull. 18 (1983) 1499.
83W2 Willett, R.D., Wong, R.J., Numata, M.: Inorg. Chem. 22 (1983) 3189.
83W3 White, M.A., Davies, N.J., Staveley, L.A.K.: J. Chem. Soc. Faraday Trans. II 79 (1983) 1653.
83Y1 Yamada, I., Shimoda, S., Nagano, S.: J. Magn. Magn. Mater. 31-34 (1983) 645.
83Y2 Yamada, I., Shimoda, S., Nagano, S.: Physica 121B (1983) 127.
84B1 Ben Salah, A., Daoud, A., Miane, J.L., Ravez, J., Hagenmuller, P.: Rev. Chim. Miner. 21 (1984) 795.
84C1 Cowley, R.A., Hagen, M., Belanger, D.P.: J. Phys. C: Solid State Phys. 17 (1984) 3763.
84D1 Darlington, C.N.W.: J. Phys. C: Solid State Phys. 17 (1984) 2859.
84H2 Hagemann, H.R.: Ph.D. Thesis, University of Geneva (Switzerland) 1984.
84I1 Ishibashi, Y., Suzuki, I.: J. Phys. Soc. Jpn. 53 (1984) 903.
84K1 Kleemann, W., Schäfer, F.J., Levola, T., Laiho, R.: Ferroelectrics 55 (1984) 139.
84M1 Münninghoff, G., Hellner, E., Treutmann, W., Lehner, N., Heger, G.: J. Phys. C: Solid State Physics 17 (1984) 1281.
84M2 Minteguia, R.C., Tello, M.J., Perez-Mato, J.M., Gomez-Cuevas, A., Fernandez, J.: Solid State Commun. 50 (1984) 501.
84M3 Mokhlisse, R., Chanh, N.B., Couzi, M., Haget, Y., Hauw, C., Meresse, A.: J. Phys. C: Solid State Physics 17 (1984) 233.
84N Needham, G.F., Willett, R.D., Franzen, H.F.: J. Phys. Chem. 88 (1984) 674.
84R1 Ricard, L., Lassegues, J.C.: J. Phys. C: Solid State Physics 17 (1984) 217.
84R2 Ricard, L., Rey-Lafon, M., Biran, C.: J. Chem. Phys. 88 (1984) 5614.
84S1 Steijger, J.J.M., Frikkee, E., de Jongh, L.J., Huiskamp, W.J.: Physica 123B (1984) 284.
84S2 Schäfer, F.J., Kleemann, W.: Ferroelectrics 55 (1984) 163.
84W1 White, M.A.: Thermochim. Acta 74 (1984) 55.
84W2 White, M.A.: J. Chem. Phys. 81 (1984) 6100.
84Y1 Yoshizawa, M., Suzuki, T., Goto, T., Yamakami, T., Fujimura, T., Nakajima, T., Yamauchi, H.: J. Phys. Soc. Jpn. 53 (1984) 261.
84Y2 Yoshihara, A., Burr, J.C., Mudare, S.M., Bernstein, E.R., Raich, J.C.: J. Chem. Phys. 80 (1984) 3816.
85A1 Aleksandrov, K.S., Emelyanova, L.S., Misyul, S.V., Kokov, I.T.: Solid State Commun. 53 (1985) 835.
85A2 Aleksandrov, K.S., Emelyanova, L.S., Misyul, S.V., Melnikova, S.V., Gorev, M.L., Kokov, I.T., Schäfer, A.D.: Jpn. J. Appl. Phys. Suppl. 24-2 (1985) 399.
85B1 Bellitto, C., Wood, T.E., Day, P.: Inorg. Chem. 24 (1985) 558.
85B2 Beznosikov, B.V., Aleksandrov, K.S.: Sov. Phys. Crystallogr. 30 (1985) 295.
85C1 Chanh, N.B., Hauw, C., Meresse, A., Rey-Lafon, M., Ricard, L.: J. Phys. Chem. Solids 46 (1985) 1413.
85C2 Chhor, K., Bocquet, J.F., Pommier, C.: J. Chem. Thermodyn. 17 (1985) 379.
85C3 Casal, H.L., Cameron, D.G., Mantsch, H.H.: J. Chem. Phys. 89 (1985) 5557.
85D1 Dikken, B.J., Arts, A.F.M., de Wijn, H.J., Vlak, W.A.H.M., Frikkee, E.: Phys. Rev. B 32 (1985) 5600.
85F1 Fyne, P.J., Day, P.: Mater. Res. Bull. 20 (1985) 197.
85F2 Fernandez, J., Gomez Cuevas, A., Arriandiaga, M.A., Socias, C., Tello, M.J.: Phys. Rev B 31 (1985) 4562.
85G1 Geick, R., Lüthi, B.: J. Phys. Soc. Jpn. 54 (1985) 3199.
85H1 Hagemann, H., Bill, H.: J. Phys. C: Solid State Physics 18 (1985) 6441.
85I Ishibashi, Y., Suzuki, I.: J. Phys. Soc. Jpn. 54 (1985) 3201.
85M Mokhlisse, M., Couzi, M., Chanh, N.B., Haget, Y., Hauw, C., Meresse, A.: J. Phys. Chem. Solids 46 (1985) 187.
85N Natsume, Y., Yamada, I.: J. Phys. Soc. Jpn. 54 (1985) 4410.

85O van Oort, J.M., White, M.A.: J. Chem. Soc. Faraday Trans. I 81 (1985) 3059.
85R1 Ricard, L., Cavagnat, R., Rey-Lafon, M.: J. Phys. Chem. 89 (1985) 4887.
85Y1 Yoshihara, A., Suzuki, T., Yamakami, T., Fujimura, T.: J. Phys. Soc. Jpn. 54 (1985) 3376.
85Y2 Yoshihara, A., Suzuki, T., Fujimura, T.: J. Phys. Soc. Jpn. 54 (1985) 4607.
85Z1 Zuñiga, F.J., Chapuis, G.: Mol. Cryst. Liq. Cryst. 128 (1985) 349.
86A1 Achiwa, N., Yoshinari, T., Matsuyama, T., Kawano, S., Aoyagi, K.: Annu. Rep. Res. React. Inst. Kyoto Univ. 19 (1986) 31.
86A2 Ahmed, M.A., El-Desoky, M.M., Radwan, F.A.: Thermochim. Acta 105 (1986) 295.
86A4 Arakawa, M., Ebisu, H., Takeuchi, H.: J. Phys. Soc. Jpn. 55 (1986) 2853.
86B1 Bellitto, C., Day, P., Wood, T.E.: J. Chem. Soc. Dalton Trans. (1986) 847.
86B2 Ben Salah, A., Daoud, A., Bats, J.W., Fuess, H.: J. Solid State Chem. 65 (1986) 151.
86D1 Day, P., Fyne, P.J., Hellner, E., Hutchings, M.T., Münninghoff, G., Tasset, F.: Proc. R. Soc. London A 406 (1986) 39.
86D2 Depmeier, W.: Ferroelectrics 66 (1986) 109.
86F1 Fyne, P.J., Hutchings, M.T., Day, P.: unpublished results 1986, private communication.
86H1 Hidaka, M., et al.: unpublished results 1986, presented by J.P. Jamet, J. Ferre, I. Yamada; J. Phys. C: Solid State Phys. 20 (1987) 3571.
86H3 Hidaka, M., Fujii, H., Maeda, S.: Phase Transitions 6 (1986) 101.
86I Ishibashi, Y.: J. Phys. Soc. Jpn. 55 (1986) 4309.
86J1 Jahn, I.R., Holocher, K., Knorr, K., Ihringer, J.: Z. Kristallogr. 174 (1986) 102.
86M1 Muralt, P.: J. Phys. C: Solid State Phys. 19 (1986) 1689.
86M2 Muralt, P. Caravatti, P., Kind, R., Roos, J.: J. Phys. C: Solid State Phys. 19 (1986) 1705.
86M3 Moudden, A.H., Megtert, S., Garel, T., Grier, B.H.: Phys. Rev. B 34 (1986) 4726.
86S1 Sourisseau, C., Guillaume, F., Lucazeau, G., Dianoux, A.J.: Mol. Phys. 58 (1986) 413.
86S2 Shefer, A.D., Shabanov, V.F., Aleksandrov, K.S.: JETP Lett. 43 (1986) 634.
86V1 Vlak, W.A.H.M., Frikkee, E., Arts, A.F.M., de Wijn, H.W.: Phys. Rev. B 33 (1986) 6470.
87A1 Aleksandrov, K.S., Beznosikov, B.V., Misyul, S.V.: Phys. Status Solidi (a) 104 (1987) 529.
87A2 Aleksandrov, K.S.: Sov. Phys. Crystallogr. 32 (1987) 551.
87A3 Abdalian, A.T., Briat, B., Dugautier, C., Moch, P.: J.Phys. C: Solid State Phys. 20 (1987) 2465.
87B1 Bellitto, C., Filaci, P., Patrizio, S.: Inorg. Chem. 26 (1987) 191.
87G1 Guillaume, F., Sourisseau, C., Lucazeau, G., Dianoux, A.J.: Dynamics of Molecular Crystals, Proc. 41st Int. Meeting on Physical Chemistry Grenoble 1986, Lascombe, J. (ed.), Amsterdam: Elsevier, 1987, p. 173.
87G2 Gorev, M.V., Melnikova, S.V., Flerov, I.N.: Sov. Phys. Solid State 29 (1987) 1199.
87H1 Hagen, M., Cowley, R.A., Nicklow, R.M., Ikeda, H.: Phys. Rev. B 36 (1987) 401.
87H2 Hatch, D.M., Stokes, H.T.: Phys. Rev. B 35 (1987) 8509.
87I Ikeda, H., Tamura, T., Nakashima, S.: J. Phys. C: Solid State Phys. 20 (1987) L461.
87J1 Janssen, T., Janner, A.: Adv. Phys. 36 (1987) 519.
87J2 Jamet, J.P., Ferré, J., Yamada, I.: J. Phys. C: Solid State Phys. 20 (1987) 3571.
87L1 Landee, C.P., Halvorson, K.E., Willett, R.D.: J. Appl. Phys. 61 (1987) 3295.
87N1 Negrier, P., Chanh, N.B., Courseille, C., Hauw, C., Meresse, A., Couzi, M.: Phys. Status Solidi (a) 100 (1987) 473.
87N2 Negrier, P., Couzi, M., Chanh, N.B., Hauw, C., Meresse, A.: Dynamics of Molecular Crystals, Proc. 41st Int. Meeting on Physical Chemistry Grenoble 1986, Lascombe, J. (ed.), Amsterdam: Elsevier, 1987, p. 231.
87P Pabst, I., Fuess, H., Bats, J.W.: Acta Crystallogr. C 43 (1987) 413.
87T Takeuchi, H., Arakawa, M., Ebisu, H.: J. Phys. Soc. Jpn. 56 (1987) 4571. Erratum: J. Phys. Soc. Jpn. 59 (1990) 2297.
88A1 Aleksandrov, K.S., Kokov, I.T., Melnikova, S.V., Misyul, S.V., Flerov, I.N.: Sov. Phys. Solid State 30 (1988) 2098.
88A4 Ahmed, M.A., Radwan, F.A.: J. Phys. Chem. Solids 49 (1988) 1385.
88A5 Ahmed, M.A., Mousa, M.A., Radwan, F.A.: J. Mater. Sci. 23 (1988) 4345.
88A8 Arakawa, M., Ebisu, H., Takeuchi, H.: J. Phys. Soc. Jpn. 57 (1988) 3573.

88C1 Chhor, K., Abello, L., Pommier, C., Sourisseau, C.: J. Phys. Chem. Solids 49 (1988) 1079.

88C2 Couzi, M., Negrier, Ph., Poulet, H., Pick, R.M.: Croatica Chemica Acta 61 (1988) 649.

88D1 Dekker, D., Arts, A.F.M., de Wijn, H.W.: Phys. Rev. B 38 (1988) 11512.

88D2 Doudin, B., Chapuis, G.: Acta Crystallogr. B 44 (1988) 495.

88E Etxebarria, J., Ruiz-Larrea, I., Tello, M.J., Lopez-Echarri, A.: J. Phys. C: Solid State Phys. 21 (1988) 1717.

88H1 Halvorson, K., Willett, R.D.: Acta Crystallogr. C 44 (1988) 2071.

88K2 Kusto, W.J.: Ferroelectrics 80 (1988) 285.

88M1 Muralt, P., Kind, R., Bührer, W.: Phys. Rev. B 38 (1988) 666.

88S1 Schenk, K.J., Chapuis, G.: J. Phys. Chem. 92 (1988) 7141.

88S2 Stokes, H., Hatch, D.: Isotropy Subgroups of the 230 Crystallographic Space Groups, Singapore: World Scientific, 1988.

88W1 Willett, R.D., Place, H., Middleton, M.: J. Am. Chem. Soc. 110 (1988) 8639.

89A1 Axe, J., Mouden, A., Hohlwein, D., Cox, D.E., Mohanty, K.M., Moodenbaugh, A.R.: Phys. Rev. Lett. 62 (1989) 2751.

89C1 Couzi, M., Chanh, N.B., Meresse, A., Negrier, P., Papoular, R.J., Millet, R.: Phase Transitions 14 (1989) 69.

89C2 Chanh, N.B., Housty, J.R., Meresse, A., Ricard, L., Rey-lafon, M.: J. Phys. Chem. Solids 50 (1989) 829.

89D1 Doudin, B., Chapuis, G.: Phase Transitions 16/17 (1989) 185.

89F1 Flerov, I.N., Aleksandrov, K.S., Melnikova, S.V., Kruglik, A.I., Misyul, S.V., Beznosikov, B.V.: Ferroelectrics 96 (1989) 175.

89G1 Guillaume, F., Coddens, G., Dianoux, A.J., Petry, W., Rey-Lafon, M., Sourisseau, C.: Mol. Phys. 67 (1989) 665.

89G2 Guillaume, F., Sourisseau, C., Dianoux, A.J.: Physica B 156&157 (1989) 359.

89G6 Gnezdilov, V.P., Eremenko, V.V., Kurnosov, V.S., Fomin, V.I.: Sov. J. Low Temp. Phys. 15 (1989) 667.

89G7 Gnezdilov, V.P., Eremenko, V.V., Kurnosov, V.S., Fomin, V.I.: Sov. Phys. Solid State 31 (1989) 803.

89H1 Hatch, D.M., Stokes, H.T., Aleksandrov, K.S., Misyul, S.V.: Phys. Rev. B 39 (1989) 9282.

89I1 Ikeda, H., Tamura, T.: Physica B 156&157 (1989) 318.

89I2 Ishibashi, Y., Dvorak, V.: J. Phys. Soc. Jpn. 58 (1989) 914.

89I3 Ishihara, T., Takahashi, J., Goto, T.: Solid State Commun. 69 (1989) 933.

89J Jahn, I.R., Knorr, K., Ihringer, J.: J. Phys.: Condens. Matter 1 (1989) 6005.

89K Kruglik, A.I., Vasilyev, A.D., Aleksandrov, K.S.: Phase Transitions 15 (1989) 69.

89M1 Meresse, A., Daoud, A.: Acta Crystallogr. C 45 (1989) 194.

89N1 Negrier, P., Couzi, M., Chanh, N.B., Hauw, C., Meresse, A.: J. Phys. (France) 50 (1989) 405.

89S1 Sieger, D.: Ph.D. Thesis, University of Würzburg (Germany) 1989.

89S2 Steurer, W., Depmeier, W.: Acta Crystallogr. B 45 (1989) 555.

89T4 Totani, M., Fukada, Y., Yamada, I.: Phys. Rev. B 40 (1989) 10577.

89T5 Thurston, T.R., Birgeneau, R.J., Gabbe, D.R., Jenssen, H.P., Kastner, M.A., Picone, P.J., Preyer, N.W., Axe, J.D., Böni, P., Shirane, G., Sato, M:, Fukuda, K., Shamoto, S.: Phys. Rev. B 39 (1989) 4327.

89Y1 Yamada, K., Orihara, H., Ishibashi, Y.: J. Phys. Soc. Jpn. 58 (1989) 1866.

89Y2 Yamada, K., Matsuda, M., Endoh, Y., Keimer, B., Birgeneau, R.J., Onodera, S., Mizusaki, J., Matsuura, T., Shirane, G.: Phys. Rev. B 39 (1989) 2336.

89Z1 Zangar, H., Miane, J.L., Courseille, C., Chanh, N.B., Couzi, M., Mlik, Y.: Phys. Status Solidi (a) 115 (1989) 107.

89Z2 Zherlitsyn, S.V., Stepanov, A.A., Fil', V.D., Popov, V.P.: Sov. J. Low Temp. Phys. 15 (1989) 712.

90A1 Achiwa, N., Matsuyama, T., Yoshinari, T.: Phase Transitions 28 (1990) 79.

90A2 Abid, Y., Kamoun, M., Daoud, A., Romain, F.: J. Raman Spectrosc. 21 (1990) 709.

90A4 Aleksandrov, K.S., Ageev, O.A.: Sov. Phys. Solid State 32 (1990) 1234.

90A5 Aleksandrov, K.S., Flerov, I.N., Melnikova, S.V., Kruglik, A.I., Misyul, S.V., Ageev, O.A.: Ferroelectrics 104 (1990) 285.

90A6 Aleksandrov, K.S., Misyul, S.V., Ivanova, T.I., Sakhnenko, V.P., Chechin, G.M.: Phase Transitions 22 (1990) 245.

90B2 Bovina, A.F., Kokov, I.T., Melnikova, S.V., Misyul, S.V.: Sov. Phys. Solid State 32 (1990) 1552.

90B4 le Bail, A., Fourquet, J.L., Rubin, J., Palacios, E., Bartolomé, J.: Physica B 162 (1990) 231.

90D1 Doudin, B., Chapuis, G.: Acta Crystallogr. B 46 (1990) 175.

90D2 Doudin, B., Chapuis, G.: Acta Crystallogr. B 46 (1990) 180.

90F1 Flerov, I.N., Gorev, M.V., Aleksandrov, K.S.: Ferroelectrics 106 (1990) 207.

90G1 Garland, J.K., Emerson, K., Pressprich, M.R.: Acta Crystallogr. C 46 (1990) 1603.

90G2 Guillaume, F., Sourisseau, C., Dianoux, A.J.: J. Phys. Chem. 94 (1990) 3438.

90W1 Willett, R.D.: Acta Crystallogr. C 46 (1990) 565.

91C1 Chanh, N.B., Courseille, C., Hauw, C., Meresse, A., Couzi, M., Miane, J.L., Daoud, A., Mlik, Y., Zangar, H.: Phase Transitions 33 (1991) 105.

91C2 Couzi, M.: J. Phys. I 1 (1991) 743.

91C3 Crawford, M.K., Harlow, R.L., McCarron, E.M., Farenth, W.E., Axe, J.D., Chou, H., Huang, Q.: Phys. Rev. B 44 (1991) 7749.

91F1 Fukada, Y., Totani, M., Yamada, I.: J. Phys.: Condens. Matter 3 (1991) 6925.

91F2 Fernández-Diaz, M.T., Rodrĭguez-Carvajal, J., Fillion, G., Fernández, F., Saez-Puche, R.: Z. Phys. B 82 (1991) 275.

91J1 Jahn, I.R., Hagdorn, K.: Z. Kristallogr. Suppl. No. 3 (1991) 133.

91M1 Martinez, J.L., Fernández-Diaz, M.T., Rodrĭguez-Carvajal, J., Odier, P.: Phys. Rev. B 43 (1991) 13766.

91P Pawlowska, M., Wojciechowski, W.: Phys. Status Solidi (a) 127 (1991) K125.

91R Rodrĭguez-Carvajal, J., Fernández-Diaz, M.T., Martinez, J.L.: J. Phys.: Condens. Matter 3 (1991) 3215.

91W1 Willett, R.D.: Acta Crystallogr. C 47 (1991) 1081.

92A1 Abid, Y., Kamoun, M., Daoud, A., Romain, F., Lantie, A.: Phase Transitions 40 (1992) 239.

92B1 Battaglia, L.P., Bonamartini Corradi, A., Pelosi, G., Cramarossa, M.R., Manfredini, T., Pellacani, G.C., Motori, A., Saccani, A., Sandrolini, F., Brigatti, M.F.: Chem. Mater. 4 (1992) 813.

92G1 Greb, H., Pabst, T., Rothaler, M., Mukhin, A.A., Pronin, A.Yu., Strobel, K., Geick, R.: J. Phys.: Condens. Matter 4 (1992) 2281.

92S1 Schins, A.G., Nielsen, M., Arts, A.F.M., de Wijn, H.J.: Physica B 180&181 (1992) 161.

92S2 Saito, K., Kobayashi, J.: Phys. Rev. B 45 (1992) 10264.

92S3 Schwab, K., Jahn, I.R., Knorr, K.: Z. Kristallogr. Suppl. No. 5 (1992) 231.

92S5 Shefer, A.D., Shapiro, I.V., Vtorin, A.N.: Sov. Phys. Solid State 34 (1992) 387.

92Z2 Zhou, P., Drumheller, J.E., Patyal, B., Willett, R.D.: Phys. Rev. B 45 (1992) 12365.

93C1 Chanh, N.B., Duplessix, R., Négrier, P., Papoular, R.J., Durand, D., Millet, R., André, G., Couzi, M.: Phys. Status Solidi (a) 138 (1993) 75.

93H Hayashi, A., Tamura, H., Ueda, Y.: Physica C 216 (1993) 77.

93M1 Mostafa, M.F., Abdel-Kader, M.M., Atallah, A.S., El-Nimer, M.: Phys. Status Solidi (a) 135 (1993) 549.

94A Aleksandrov, K.S., Bartolomé, J.: J. Phys.: Condens. Matter 6 (1994) 8219.

94I1 Iwasa, K., Nishi, M., Ikeda, H., Suzuki, J.: J. Phys. Soc. Jpn. 63 (1994) 1900.

94I3 Ishibashi, Y., Dvorak, V.: J. Phys. Soc. Jpn. 63 (1994) 2202.

94J1 Jahn, I.R., Schwab, K., Knorr, K., Holocher, K.: J. Phys.: Condens. Matter 6 (1994) 10839.

94J2 Jahn, I.R., Schwab, K., Knorr, K.: Z. Kristallogr. Suppl. No. 8 (1994) 710.

95A1 Aleksandrov, K.S.: Crystallogr. Rep. 40 (1995) 251.

95A2 Ahmed, M.A., Darwish, K.A., Mounir, M., Zaki, G.H.: Phys. Status Solidi (a) 148 (1995) 321.

95E Elleuch, H., Bouachir, H., Salah, A.B., Kammoun, M.: Phys. Essays 8 (1995) 82.

95F1 Flandrois, S., Chanh, N.B., Duplessix, R., Maris, Th., Négrier, P.: Phys. Status Solidi (a) 149 (1995) 697.
95K Kammoun, S., Kammoun, M., Daoud, A.: Phys. Essays 8 (1995) 91.
95N1 Ning, G.: J. Solid State Chem. 117 (1995) 97.
95N2 Nikiforov, A.E., Shashkin, S.Yu.: Phys. Solid State 37 (1995) 719.
95R2 Rubĭn, J., Palacios, E., Bartolomé, J., Rodrĭguez-Carvajal, J.: J. Phys.: Condens. Matter 7 (1995) 563.
96I1 Ishizuka, M., Yamada, I., Amaya, K., Endo, S.: J. Phys. Soc. Jpn. 65 (1996) 1927.
96S2 Subĭas, G., Palacios, E., Blasco, J., Garcĭa-Ruiz, J.: J. Phys.: Condens. Matter 8 (1996) 8971.
97T1 Tietze-Jaensch, H., Kockelmann, W., Ibberson, R.M.: ISIS Experimental Report RB8122 (1997).
97T2 Tietze-Jaensch, H., Kockelmann, W.: ISIS Experimental Report RB9091 (1997).
98I Ishizuka, M., Terai, M., Endo, S., Hidaka, M., Yamada, I., Shimomura, O.: J. Magn. Magn. Mater. 177-181 (1998) 725.
98T Tietze-Jaensch, H., van de Kamp, R., Schmidt, W.: Physica B 241-243 (1998) 566.

9.12.3 Magnetic Properties

(For figures and tables of this section see p. 243 ff.)

9.12.3.1 Antiferromagnets

9.12.3.1.1 Exchange Interaction

Magnetic ordering and magnetic phenomena are observed in perovskite-type layer compounds A_2MX_4 (single-layer) or $A_3M_2X_7$ (double-layer) with paramagnetic M^{2+}-ions. Their antiferromagnetic or ferromagnetic order has already been discussed in Sects. 2.1.2 and 2.1.3. Magnetic properties in general are outlined in many excellent reviews [55N, 66K, 74J1, 90A3, 90H, 90J1, 90P] where also an introduction is found to the basic models [55N, 66K], in particular to the Weiss model for ferromagnets and to the Néel molecular field theory for antiferromagnets. Monographs like [70W3] and [79W4] provide an even more basic introduction to magnetism, to its quantum mechanical foundation and to long-range order. Therefore, only some basic aspects will be summarized in this section mainly in order to introduce the notation used in this contribution. In these perovskite-type layer structures, the dominant magnetic interaction is the nearest-neighbour Heisenberg exchange within the layers which causes their two-dimensional (2D) character. In these quasi-2D magnets, the magnetic properties depend predominantly on the intralayer exchange and not so much on the layer separation. Gerstein et al. [74G2, 74G3] have deduced from susceptibility measurements on compounds of the type $(C_nH_{2n+1}NH_3)_2MnCl_4$ with n = 1, 3, 15 that the Néel temperatures T_N of these antiferromagnets do not vary with n although the interlayer separation d varies from $d = 0.97$ nm for n = 1 to $d = 3.49$ nm for n = 15. As is well known from basic quantum mechanics, the exchange interaction results from the electronic properties of the compound under consideration and it is a superexchange in the compounds A_2MX_4 mediated by a X^--ion between two M^{2+}-ions. Attempts to calculate this interaction by means of a theory or theoretical model have to start with the electronic configuration and the corresponding energy levels of the ions involved in this process or with the electronic band structure of the magnetic compound. Unfortunately, detailed information about the electronic structure is not available for most of the perovskite-type layer structure materials. As a step towards a better understanding of the exchange interaction, de Jongh and Block [75J] have collected 1975 all available experimental data on fluoride perovskites AMF_3 and fluoride perovskite-type layer compounds A_2MF_4 (A = K, Rb; M = Mn, Co, Ni) and have derived from these data a relation for the dependence of J on the distance $a_{nn} = 2\,r_{ip} = a$ between two M^{2+}-ions in the octahedral layer (cf. Eq. 2.1, Sect. 2.1.1), of the structure I4/mmm with the lattice constant a. Thus we have to consider the 180° superexchange path M^{2+}–F^-–M^{2+}. The formula deduced from the experimental data is a power law where J is the parameter for the dominant intralayer exchange (cf. Eq. 3.2 below)

$$J(a_{nn}) = J(a_{nn,0}) \cdot (a_{nn} / a_{nn,0})^{-\alpha} \tag{3.1}$$

with $a_{nn,0} = 0.4074$ nm as a reference distance and $|J(a_{nn,0})| = 5.20$ K (Mn^{2+}), = 18.5 K (Co^{2+}), = 40 K (Ni^{2+}). The ratio is $J(Mn^{2+}) : J(Co^{2+}) : J\,(Ni^{2+}) = 1 : 3.6 : 7.7$. For the exponent, they obtained $\alpha = 12$ (cf. [75J]). In this contribution, energies like J are given in K (equivalent temperature) or cm^{-1} (equivalent wave number) omitting in a type of shorthand notation the corresponding factors k_B and hc. Although theory predicts an exponential dependence of J on $a_{nn} = a$, the power law Eq. 3.1 works quite well for the limited range of distances a in the compounds under consideration. As a second step, de Jongh and Block [75J] and Jansen and Block [77J1] have calculated J for these compounds employing a Raleigh-Schröder type exchange perturbation theory which was derived by Jansen [67J, 79K10]. Not only for the above mentioned fluorides but also for some chlorides like Rb_2MnCl_4 and $(CH_3NH_3)_2MnCl_4$, the data calculated by means of this model agree very well with the experimental data. For example, the calculated ratio is $J(Mn^{2+}) : J(Co^{2+}) : J(Ni^{2+}) = 1 : 3.3 : 7.6$. With synchrotron radiation as a powerful light source, spectroscopic studies provided information about the electronic properties and the band structure at least for some of the perovskite-type layer structures. Absorption and reflectance measurements were performed on K_2CoF_4, Rb_2CoF_4 and K_2NiF_4 [85S1], further on the diamagnetic compounds $(C_nH_{2n+1}NH_3)_2CdCl_4$ with n = 1, 2, 3 [89Y3]. K_2NiF_4 was also studied by photoelectron spectroscopy [94S1]. Alternative information can be gathered from theoretical calculations of the electronic structure, i.e. the electronic band structure, which were performed by various methods for K_2NiF_4 [92H2, 93E] and for K_2CuF_4 [93E]. Sangaletti et al. [94S1] have compared the experimental data obtained with synchrotron radiation with density-functional band structure calculations. Dovesi et al. [95D] have calculated the ground state electronic structure of K_2NiF_4 using an ab initio periodic Hartree-Fock approach with the aim to explore the electronic and magnetic properties of this material, in addition to a similar study on $KNiF_3$ [95R3]. Here we are mainly interested in their results for the intralayer exchange interaction. For K_2NiF_4, the calculated value is $J_{\text{calc}} = -31.3$ K in satisfactory agreement with the experimental value $J_{\text{exp}} = -55.1(4)$ K (cf. Table 5). For $KNiF_3$, the corresponding values are $J_{\text{calc}} = -29.8$ K and $J_{\text{exp}} = -50.7(6)$ K [71C2], respectively. In their theory, the dependence of J on the distance $a_{\text{nn}} = a$ between two Ni^{2+} can also be expressed by a power law $J \sim (a_{\text{nn}})^{-\alpha}$ with $\alpha = 11.5$ and $\alpha = 12.3$ for K_2NiF_4 and $KNiF_3$, resp., in good agreement with $\alpha = 12$ derived by de Jongh and Block [75J]. This dependence was further the subject of an experimental study by Struzhkin et al. [93S1]. They have measured under hydrostatic pressures up to 9.5 GPa the pressure dependence of the two-magnon Raman line of K_2NiF_4 at 10 K in the antiferromagnetic state and the pressure dependence of the lattice constant a at 295 K by means of powder x-ray diffraction. Since the frequency of the two-magnon Raman line is proportional to J, they can extract from their experimental data for $J(p)$ and $a(p)$ the relation $J \sim (a_{\text{nn}})^{-\alpha}$ and obtain in this way $\alpha = 9.5(5)$ which agrees better with an earlier theoretical prediction $\alpha = 10$ [66B2] than with the result of de Jongh and Block. All this work on K_2NiF_4 allows us to gain some understanding of the intralayer superexchange mechanism in perovskite-type layer structures. Similar results are available only on K_2CuF_4 and not on other compounds of this kind. The exchange mechanism in K_2CuF_4 will be discussed in detail later in Sect. 3.2.1.

9.12.3.1.2 Mn-Compounds, Spin-Wave Theory

In addition to the dominant intralayer exchange interaction, there are further and usually minor contributions to the energy of the system. These originate from the exchange between next nearest neighbours within the layers, from the interlayer exchange and from the anisotropy energy. For the Mn-compounds to be discussed in this section, the anisotropy is usually small. Our considerations start with an appropriate spin Hamiltonian for single-layer compounds (cf. Fig. 2.1) which specifies the magnetic interactions and energies

$$\mathcal{H} = -2\sum_{\langle i,j\rangle} J_{ij}\boldsymbol{S}_i\boldsymbol{S}_j - g\mu_B\left[\sum_i (H_{0z}+H_A)\,S_{i,z} + \sum_j (H_{0z}-H_A)\,S_{j,z}\right] \tag{3.2}$$

where the exchange interactions are

$J_{ij} = J$ for pairs (i, j) of nearest neighbours within the octahedral layers
$J_{ij} = J_2$ for pairs (i, j) of next nearest neighbours in the layers
$J_{ij} = J'$ for pairs (i, j) of nearest neighbours in adjacent layers.

Positive J_{ij} means ferromagnetic and negative J_{ij} antiferromagnetic interaction. The summation ⟨ij⟩ is extended over the whole lattice where each pair of corresponding neighbours is counted only once. $\boldsymbol{S}_i = (S_{i,x}, S_{i,y}, S_{i,z})$ and $\boldsymbol{S}_j = (S_{j,x}, S_{j,y}, S_{j,z})$ are the spins (operators) at lattice sites i and j. For the discussion of magnetic properties, the magnetic unit cell is relevant and we have to use the (x, y, z) coordinate system defined in Sect. 2.1.1 and not the (x_0, y_0, z_0) system which is only appropriate for the I4/mmm unit cell. Thus, the coordinate directions are specified in Eq. 3.2 with respect to the former system. For the Mn-compounds under consideration, e.g. K_2MnF_4, Rb_2MnF_4, and Rb_2MnCl_4, the anisotropy energy is presented in Eq. 3.2 as a staggered anisotropy field H_A because the ground state of Mn^{2+} is a ^6S spin –

only state and, therefore, the anisotropy is mainly due to magnetic dipolar interactions. Finally, in Eq. 3.2 is included a Zeeman-term where H_{0z} is the external magnetic field applied parallel to the *z*- or *c*-axis, μ_B the Bohr magneton and *g* the isotropic *g*-factor.

An as yet unsolved problem in magnetism is that no exact results are known for the Hamiltonian Eq. 3.2 and even, in its simplest form, for the nearest neighbour Heisenberg model. Only for the 2D Ising model, exact results are available which will be discussed below. Unfortunately, even the ground state is a problem for Heisenberg antiferromagnets since the socalled Néel state with perfect alignment of the spins within the sublattices is not the true ground state. Only in ferromagnets, the ground state at $T = 0$ is given by the total alignment of all spins parallel to the preferred direction. For these reasons, we have to look for approximate solutions of Eq. 3.2. For low temperatures $T < T_C$ or $T < T_N$ sufficiently below the critical regions ($T \approx T_C$ or $T \approx T_N$), such solutions are based on the collective elementary excitations of the system described by Eq. 3.2. These are the spin waves which, in a classical picture, are wavelike precession of the transverse spin components in a perfect crystal with translational invariance. Quantum-mechanically, these excitations are called magnons with the character of Bose quasi-particles. It will be shown below that the spin-wave theory describes as an approximate solution quite satisfactorily the magnetic properties, e.g. the spin-wave dispersion relation $\hbar\omega(\boldsymbol{q})$ at low temperature, the sublattice magnetization M_{subl} and the perpendicular and parallel susceptibilities $\chi_\perp$ and $\chi_\parallel$ of an antiferromagnet as a function of temperature up to temperatures outside the critical regime where fluctuations become important.

Let us now consider as a first example an antiferromagnet with $J = -|J|$ and $J_2 = J' = 0$ where we recall from Sect. 2.1.2 that most of the perovskite-type layer structures with transition metal paramagnetic ions order antiferromagnetically at low temperatures, many of them with the easy axis parallel to the *c*-axis. The first step for an approximate solution of $\mathcal{H}$ (see [66K] and [90A3] for details) is the introduction of local Bose creation and annihilation operators of spin deviations by means of the Holstein-Primakoff transform [40H] which reads for an antiferromagnet with two sublattices (sites i and j)

$$\begin{array}{llll} S_{i,z} = S - a_i^+ a_i & S_i^+ = \sqrt{2S}\, f_i\, a_i & S_i^- = \sqrt{2S}\, a_i^+ f_i & f_i = \sqrt{1 - a_i^+ a_i / 2S} \\ S_{j,z} = -S + b_j^+ b_j & S_j^+ = \sqrt{2S}\, b_j^+ f_j & S_j^- = \sqrt{2S}\, f_j\, b_j & f_j = \sqrt{1 - b_j^+ b_j / 2S} \end{array} \qquad (3.3)$$

The factors f_i and f_j in the Holstein-Primakoff approach provide that solutions are omitted with spin devations greater than $2S$. However, these factors have to be expanded and yield an expansion in $1/2S$. Inserting Eq. 3.3 with the simplest approximation $f_i \approx 1$ and $f_j \approx 1$ into Eq. 3.2, we obtain a bilinear form in the Bose operators which leads to a linear spin-wave theory in which interactions between the spin waves or magnons are neglected and which can be considered an acceptable approximation only at rather low temperatures when only a few magnons are thermally excited. In the next higher approximation with $f_i \approx (1 - a_i^+ a_i/4S)$ and $f_j \approx (1 - b_j^+ b_j/4S)$, the Hamiltonian $\mathcal{H}$ contains terms up to fourth order in the Bose operators the diagonalization of which leads then to the renormalized spin-wave results with the socalled Oguchi corrections [60O1]. These take interactions of the spin waves into account in lowest order. Below, these two approaches will be referred to simply as "linear" and "renormalized" spin-wave theory.

In the next step, the local spin deviation operators are converted to wavevector dependent spin-wave operators on the two sublattices by means of a spatial Fourier transform:

$$\begin{array}{ll} a_q = \sqrt{\frac{2}{N}} \sum\limits_i a_i\, e^{i\boldsymbol{q}\boldsymbol{r}_i} & a_q^+ = \sqrt{\frac{2}{N}} \sum\limits_i a_i^+\, e^{-i\boldsymbol{q}\boldsymbol{r}} \\ b_q = \sqrt{\frac{2}{N}} \sum\limits_i b_i\, e^{-i\boldsymbol{q}\boldsymbol{r}_i} & b_q^+ = \sqrt{\frac{2}{N}} \sum\limits_i b_i^+\, e^{i\boldsymbol{q}\boldsymbol{r}} \end{array} \qquad (3.4a)$$

where *N* is the total number of spins (= magnetic ions) and *N*/2 this number for one of the two sublattices. In this brief introduction, only the steps leading to the final result will be sketched here and we will omit the intermediate results after inserting successively Eqs. 3.3 and 3.4a into $\mathcal{H}$ (Eq. 3.2). For these details, the reader is referred to the reviews mentioned above [66K, 90A3] and to one of the other references about spin-wave theory [74R3, 75R1, 83T4, 83T5]. There, also alternate ways in solving the spin-wave problem are presented, for example employing the Dyson-Maleev expansion [56D, 58M] instead of the Holstein-Primakoff approach.

In the last step, the bilinear part of the Hamiltonian $\mathcal{H}$ (linear spin-wave theory) is diagonalized by means of a Bogoliubov transform:

$$\alpha_q = u_q a_q + \upsilon_q b_q^+ \qquad \alpha_q^+ = u_q a_q^+ + \upsilon_q b_q \tag{3.4b}$$

$$\beta_q = \upsilon_q a_q^+ + u_q b_q \qquad \beta_q^+ = \upsilon_q a_q + u_q b_q^+$$

where α_q^+, β_q^+, α_q, β_q are the creation and annihilation operators for the spin-wave modes of the antiferromagnet under consideration. The coefficients u_q and υ_q can be chosen real in this problem with $u_q^2 - \upsilon_q^2 = 1$. From the terms in $\mathcal{H}$ of fourth order in the Bose operators, only the diagonal terms are kept after the Bogoliubov transform and the nondiagonal terms are rejected. Thus, the final result for the Hamiltonian $\mathcal{H}$ (Eq. 3.2) becomes:

$$\mathcal{H} = -NzS^2|J| - Ng\mu_B H_A S + \sum_q (\hbar\omega_q^+ \alpha_q^+\alpha_q + \hbar\omega_q^- \beta_q^+\beta_q) \tag{3.5}$$

where the first two terms are the spin-wave result for the magnetic energy at $T = 0$, $\hbar\omega_q^+$ and $\hbar\omega_q^-$ are the energies of the two spin-wave branches as a function of wavevector $\boldsymbol{q}$, i.e. $\hbar\omega_q^+$ and $\hbar\omega_q^-$ are abbreviations for $\hbar\omega^+(\boldsymbol{q})$ and $\hbar\omega^-(\boldsymbol{q})$. In Eq. 3.5, z is the number of nearest neighbours. To lowest order in ($1/2S$), i.e. by linear spinwave theory, the magnon energies are

$$\hbar\omega_q^\pm = 2zS|J|\{[(1+h_A)^2 - \gamma_q^2]^{1/2} \mp h_{0z}\} = g\mu_B\{[(H_E + H_A)^2 - (H_E\gamma_q)^2]^{1/2} \mp H_{0z}\} \tag{3.6}$$

with $h_A = H_A/H_E$, $h_{0z} = H_{0z}/H_E$, $g\mu_B H_E = 2zS|J|$, $g = 2.00$, $S = \frac{5}{2}$ (Mn^{2+})

and
$$\gamma_q = \frac{1}{z}\sum_j e^{i\boldsymbol{q}\boldsymbol{r}_j} = \cos\left(\frac{q_x a}{2}\right)\cdot\cos\left(\frac{q_y a}{2}\right)$$

where γ_q is also an abbreviation for $\gamma(\boldsymbol{q})$. In γ_q, the summation j extends over the $z = 4$ nearest neighbours in the quadratic layer and the lattice parameter a refers to the magnetic unit cell with $a \approx b$. There is a lowest magnon energy which occurs for $\boldsymbol{q} = 0$ and which will be discussed below. The largest magnon energy $h\nu_{max}$ is obtained at the boundary of the Brillouin zone for $\boldsymbol{q} = \boldsymbol{q}_{max}$, i.e. $q_x = \pi/a$ or $q_y = \pi/a$. For $\boldsymbol{q}_{max}$, we obtain $\gamma_q = 0$ and Eq. 3.6 yields for zero magnetic field ($H_{0z} = 0$)

$$\hbar\omega^+(\boldsymbol{q}_{max}) = \hbar\omega^-(\boldsymbol{q}_{max}) = h\nu_{max} = g\mu_B(H_E + H_A) \approx g\mu_B H_E \tag{3.7}$$

because of $H_A << H_E$ in most of the Mn^{2+}-compounds. The statement that the anisotropy in Mn-compounds is mainly due to dipolar interaction can be demonstrated by performing a spin-wave calculation not with the simple approach of a staggered anisotropy field H_A but by taking the dipolar interactions explicitly into account. Including the exchange part from Eq. 3.2 but leaving out the anisotropy field and the Zeeman term, the Hamiltonian with the dipolar interactions reads [66H2, 93P1, 94P1, 95P1]

$$\mathcal{H}_{\mathrm{dipolar}} = -2J\sum_{\langle \mathrm{i,j}\rangle} \boldsymbol{S}_{\mathrm{i}}\boldsymbol{S}_{\mathrm{j}} + \tfrac{(g\mu_{\mathrm{B}})^2}{8\pi\mu_{\mathrm{o}}}\sum \left[\boldsymbol{S}_{\mathrm{i}}\boldsymbol{S}_{\mathrm{j}} r_{\mathrm{ij}}^{-3} - 3\,(\boldsymbol{S}_{\mathrm{i}}\boldsymbol{r}_{\mathrm{ij}})\,(\boldsymbol{S}_{\mathrm{j}}\boldsymbol{r}_{\mathrm{ij}})\,r_{\mathrm{ij}}^{-5}\right] \tag{3.8}$$

with $\boldsymbol{r}_{\mathrm{ij}} = \boldsymbol{r}_{\mathrm{i}} - \boldsymbol{r}_{\mathrm{j}}$ where $\boldsymbol{r}_{\mathrm{i}}$ and $\boldsymbol{r}_{\mathrm{j}}$ are the lattice sites of the spins $\boldsymbol{S}_{\mathrm{i}}$ and $\boldsymbol{S}_{\mathrm{j}}$. The remaining notation is equal to that of Eq. 3.2. For calculating the spin-wave energies, the same procedure as for Eq. 3.2 is applied to Eq. 3.8, i.e. the Holstein-Primakoff, the Fourier and the Bogoliubov transforms Eqs. 3.3, 3.4a and 3.4b, respectively. The results obtained for the constant energy term and for $\hbar\omega_{\mathrm{q}}^{\pm}$ show [66H2, 73W2, 93P1, 94P1, 95P1]:

1) that the dipolar interaction energy is a minimum when the spins are aligned parallel or antiparallel to the *c*-axis and that this energy thus determines the easy axis since the Heisenberg model exchange interaction is isotroptic.

2) that there is a difference between $\hbar\omega_{\mathrm{q}}^{+}$ and $\hbar\omega_{\mathrm{q}}^{-}$ even in the absence of an external field which is rather small for realistic values of H_{E} (cf. Eq. 3.6) and H_{AD} (cf. Eq. 3.12 below), which however becomes perceptable when H_{AD} is assumed to be of the same order of magnitude as H_{E} [93P1, 94P1, 95P1]. For the Mn-compounds under consideration in this section, this assumption is not realistic.

3) a wavevector dependence in addition to γ_{q} (cf. Eq. 3.6) originating from the spatial Fourier transform of the lattice sums in the dipolar interactions [73W2].

For a comparison of $\hbar\omega_{\mathrm{q}}^{\pm}$ obtained from Eq. 3.8 to the results from Eq. 3.6, i.e. the results including dipolar interactions to those with the staggered anisotropy field H_{A}, it is convenient to consider the magnon energy at $\boldsymbol{q} = 0$ which is derived from Eq. 3.6 as

$$\nu_{\mathrm{AFMR}}^{\pm} = (\gamma/2\pi)\left[(2H_{\mathrm{E}}H_{\mathrm{A}} + H_{\mathrm{A}}^2)^{1/2} \mp H_{0z}\right] \tag{3.9}$$

where $\gamma = g\mu_{\mathrm{B}}/\hbar$ is the gyromagnetic ratio. Since the magnon frequency at $\boldsymbol{q} = 0$ is mostly determined by antiferromagnetic resonance (AFMR) [55N], $\hbar\omega^{\pm}(\boldsymbol{q} = 0)$ is denoted ν_{AFMR}. The expression of ν_{AFMR} for $H_{0z} = 0$ may be considered as a quantity characteristic for an antiferromagnet

$$\nu_{\mathrm{AFMR}}\,(H_0 = 0) = (\gamma/2\pi)\,(2H_{\mathrm{E}}H_{\mathrm{A}} + H_{\mathrm{A}}^2)^{1/2} \approx (\gamma/2\pi)\,(2H_{\mathrm{E}}H_{\mathrm{A}})^{1/2} \tag{3.10}$$

where in the second form H_{A}^2 has been neglected because of $H_{\mathrm{A}} \ll H_{\mathrm{E}}$. Now let us compare Eq. 3.9 to the results obtained from $\mathcal{H}$ with the dipolar interactions (Eq. 3.8) instead of H_{A}. The corresponding result for $\boldsymbol{q} = 0$ is

$$\nu_{\mathrm{AFMR}}(H_0 = 0)_{\mathrm{dipolar}} \approx (\gamma/2\pi)\,(2H_{\mathrm{E}}H_{\mathrm{AD}})^{1/2} \tag{3.11}$$

where H_{A} (cf. 2nd form of Eq. 3.10) is replaced by the anisotropy field H_{AD} resulting from the dipolar interactions at $\boldsymbol{q} = 0$

$$H_{\mathrm{AD}} = \frac{g\mu_{\mathrm{B}}\,S}{8\pi}\left[\sum_{\mathrm{n}}{}' \frac{r_{\mathrm{n}}^2 - 3z_{\mathrm{n}}^2}{r_{\mathrm{n}}^5} - \sum_{\mathrm{n}} \frac{r_{\mathrm{n}}^2 - 3z_{\mathrm{n}}^2}{r_{\mathrm{n}}^5}\right] \tag{3.12}$$

In Eq. 3.12, the summation n extends over all lattice sites with magnetic ions, i.e. where magnetic moments are located. The vector $\boldsymbol{r}_{\mathrm{n}} = (x_{\mathrm{n}}, y_{\mathrm{n}}, z_{\mathrm{n}})$ is the distance of such a lattice site n to a reference lattice site. Σ_{n} and Σ_{n}' mean summation over the sites on the same sublattice and on the opposite sublattice, respectively. In Eq. 3.11, products of lattice sums (see Eq. 3.12) have been neglected since also $H_{AD} << H_E$. For comparison with experimental data, the dipolar anisotropy field H_{AD} has been calculated for a number of Mn-compounds by means of Eq. 3.12, see for example [73W2, 80S2]. The results are listed in Table 5. They demonstrate that these calculated data are close to the experimentally determined values of H_A in Table 5. The conclusion is therefore that the magnetic anisotropy of Mn-compounds is indeed dominated by the magnetic dipolar interactions.

Not only for Mn-compounds but also for many other compounds, experimental values of ν_{AFMR} for $H_0 = 0$ are compiled in Table 5 as characteristic parameters of these compounds. Usually, antiferromagnetic resonance measurements are performed by sweeping the magnetic field H_{0z} (cf. Eq. 3.9) at a fixed frequency ν and, at resonance, an absorption line is observed. From these data, ν_{AFMR} for $H_0 = 0$ is extracted. The antiferromagnetic linewidth, i.e. full width at half maximum, has frequently also been studied as a function of temperature. When sweeping the field, the linewidth is observed as ΔH_{AFMR} which has been found to increase as T^4 with temperature [83U]:

$$\Delta H_{AFMR} = \Delta H^0_{AFMR} + C_{AFMR} \cdot T^4 \tag{3.13}$$

where ΔH^0_{AFMR} is the linewidth observed for $T \rightarrow 0$ which is mostly the instrumental linewidth. The T^4-dependence of ΔH_{AFMR} indicates relaxation by six-magnon processes [75R2, 76R2, 83U]. In nuclear magnetic resonance (NMR), the corresponding quantity is the spin-lattice relaxation time T_1. NMR experiments have been performed on the $^{19}F_I$ nuclei in K_2MnF_4 and K_2NiF_4 [79W1, 80W1]. F_I are the out-of-plane or axial (terminal) F^--ions while F_{II} are the in-plane or bridging (equatorial) ones as discussed in context with Fig. 2.34 in Sect. 2.2.3 for Cl^--ions (see also Fig. 3.7 below). For $^{19}F_I$-NMR and $H_0 = 0$, three-magnon processes enhanced by four-magnon exchange scattering were found to be dominating the relaxation rate T_1^{-1} in excellent agreement with rigorous spin-wave results [79W1, 80W1]. For $\boldsymbol{H_0}$ applied perpendicular to the c-axis, field-induced two-magnon processes become allowed due to symmetry breaking [78W2, 79W1]. At $H_0 = 3.5$ T, they dominante over the three-magnon processes. For $^{19}F_{II}$-NMR in K_2MnF_4 and $\boldsymbol{H_0}$ applied parallel to the c-axis, the relaxation is again governed by three-magnon processes. When $\boldsymbol{H_0} \parallel \boldsymbol{c}$ approaches the spin-flop field H_{SF} the relaxation time T_1 approaches zero. If H_0 is applied at an angle $\psi \neq 0$ with respect to the c-axis, field, induced two-magnon processes determine the relaxation rate [81W4].

The spin-wave energies $\hbar\omega(\boldsymbol{q})$ calculated with the linear theory (Eq. 3.6) can at low temperatures well be used for describing and analysing the spin-wave dispersion relations as determined by means of inelastic neutron scattering. As an example, the spin-wave dispersion of K_2MnF_4 at 4.5 K is shown in Fig. 3.1, experimental data as points and data calculated by means of Eq. 3.6 as curves. Not only the Bragg rods found in elastic neutron scattering (cf. Fig. 2.5b in Sect. 2.1.2) demonstrate the two-dimensional behaviour of these layer compounds but also the results of the inelastic neutron scattering. The magnon energies $\hbar\omega(\boldsymbol{q})$ in Fig. 3.1 depend only on q_x and q_y as expected from the theoretical results in Eq. 3.6 and not on q_z since the dominating exchange interaction couples only neighbouring spins in the layer in these quasi 2D antiferromagnets. It is well known however [30B, 66M1, 66S2], that an isotropic intralayer exchange alone, i.e. a 2D Heisenberg model, cannot lead to a phase transition with long-range magnetic order at a finite temperature as it is observed at $T_N = 42.15$ K. Thus either the Ising-like anisotropy (cf. Eq. 3.2) or the weak interactions between the layers (interlayer exchange or magnetic dipolar interactions) cause the transition to a 3D antiferromagnetic order in K_2MnF_4 and similar compounds. The values of the characteristic magnetic parameters J and H_A have been obtained for K_2MnF_4 by employing Eq. 3.6 in a fit to the experimental data where J is usually determined from inelastic neutron scattering results [73B1] while H_A is generally obtained with better accuracy from AFMR experiments [73W3].

For Rb_2MnF_4, another quasi 2D antiferomagnet, the spin-wave dispersion relations have been measured for three directions in reciprocal space, namely for $(\zeta, 0, 0)$, $(0.5, \zeta, 0)$ and $(\zeta, \zeta, 0)$, by inelastic scattering of neutrons (cf. Fig. 3.2). This study [77C3] allows to determine the value of the next nearest exchange constant J_2, in addition to J and H_A. With linear spin-wave theory, the magnon energies are obtained for $J_2 \neq 0$ and $H_{0z} = 0$ as

$$\hbar\omega_q = 2zS\,|J|\,\{[1 + h_A + h_{E2}(\gamma_{q2} - 1)]^2 - [\gamma_q]^2\}^{1/2} \tag{3.14}$$

with $h_{E2} = |J_2/J|$ and $\gamma_{q2} = \frac{1}{z_2}\sum_k e^{i\boldsymbol{q}\boldsymbol{r}_k} = \frac{1}{2}[\cos(q_x a) + \cos(q_y a)]$

and with h_A and γ_q as defined in Eq. 3.6. The summation k is extended over the $z_2 = 4$ next nearest neighbours in the quadratic layer. The lattice parameter a in the expression for γ_{q2} refers to the magnetic unit cell with $a \approx b$. The calculated curves in Fig. 3.2 have been obtained by means of Eq. 3.14. The value of J_2 can be extracted from the difference of the magnon energies at reduced wavevectors (0.5, 0, 0) and (0.5, 0.5, 0). However, it is not easy to measure these energies with such an accuracy that the difference yields a reliable result. Finally, it turned out that the exchange constant $J_2 = -0.048\ \mathrm{cm}^{-1}$ for next nearest neighbours is smaller by about two orders of magnitude than the exchange constant $J = -2.639\ \mathrm{cm}^{-1}$ for nearest neighbours and even smaller by about one order of magnitude than $g\mu_B H_A = 0.26\ \mathrm{cm}^{-1}$. Thus it is justified to neglect J_2 in most of the studies of perovskite-type layer compounds. A further consequence of the smallness of J_2/J is that the collinear antiferromagnetic order is not affected by the frustration introduced by an also antiferromagnetic next nearest neighbour exchange interaction. But in case of a much larger ratio $J_2/J \approx 0.4$ and, consequently, a much stronger frustration, the long-range magnetic order may be destroyed [89H2, 92S4, 92R1, 93R1, 95R1].

The values of these and related parameters are compiled for perovskite-type layered compounds like K_2MnF_4 in Table 5, together with other experimental data on magnetic properties. Some of the references including [73B1] have defined the Heisenberg isotropic exchange interaction in a slightly different way. For the convenience of the reader and to allow an easy comparison of the date of different compounds, all parameter values listed in Table 5 have been converted to the notation adopted in Eq. 3.2 which is used throughout this contribution. As already outlined in Sect. 1, it is not advisable to present the data for the exchange constants J etc. and for $g\mu_B H_A$ in Table 5 in the various units found in the references like K, THz, meV and cm^{-1}. All the available data have been unified and are presented in Table 5 in two units, namely in cm^{-1} for an easy comparison with spectroscopic data and in K for an easy comparison with transition temperatures etc. In order to save space in Table 5, an exchange constant J, for example, is not listed in the most correct way as

$$J/hc = \mathrm{xxx\ cm^{-1}} \quad \text{and} \quad J/k_B = \mathrm{yyy\ K} \quad \text{but as} \quad J = \mathrm{xxx\ cm^{-1}} \mathrel{\hat{=}} \mathrm{yyy\ K}$$

in a kind of shorthand notation. It was also laid down in Sect. 9.12.1 that magnetic fields are not given here in the SI-unit A/m but in T as magnetic flux density in vacuum. And the magnetic susceptibility $\chi = \partial M/\partial H$ is dimensionless in these units. In Table 5, experimental data for χ in emu/g or emu/mol have been converted to the dimensionless χ. It should further be noted that often more than one value is presented for parameters like J in Table 5 together with the method by which it has been obtained, especially for widely investigated materials like K_2MnF_4. The methods are briefly discussed below and the different values in Table 5 will provide an impression about the advantages and disadvantages of the methods. The above remarks about units refer mainly to Table 5, and in the figures presented below, sometimes also other units like THz or GHz for $\hbar\omega$ and cm^3/mol for χ are used in accordance with the references.

For including temperature-dependent effects, the renormalized spin-wave theory is needed which utilizes also the diagonal part of the fourth order terms in $\mathcal{H}$ up to order $(1/2S)^1$. In the spin-wave energies in Eq. 3.6, the operator pairs $\alpha_q^+\alpha_q$ and $\beta_q^+\beta_q$ have now been replaced by their thermal averages $n_q^+ = [\exp(\hbar\omega_q^+/k_BT) - 1]^{-1}$ and $n_q^- = [\exp(\hbar\omega_q^-/k_BT) - 1]^{-1}$:

$$\hbar\omega_q^{\pm} = 2zS\,|J|\,\{[(1 + h_A)^2 - \gamma_q^2]^{1/2} \mp h_{0z} \pm (p^+ - p^-) - g_q(R_0 + R_1)\} \tag{3.15}$$

with $$g_q = \frac{1 + h_A - \gamma_q^2}{[(1+h_A)^2 - \gamma_q^2]^{1/2}} \qquad p^{\pm} = \frac{1}{NS}\sum_q n_q^{\pm}$$

and $$R_0 = \frac{1}{NS}\sum_q (g_q - 1) \qquad R_1 = \frac{1}{NS}\sum_q g_q(n_q^+ + n_q^-)$$

where h_A, h_{0z}, H_E and γ_q have the same meaning as defined in Eq. 3.6. The terms with R_0 and R_1 represent the temperature-independent and temperature-dependent renormalizations for $\hbar\omega_q$ in the absence of an external magnetic field while the term $(p^+ - p^-)$ is the magnetic-field induced renormalization. It is due to an unbalance of the two sublattices and is proportional to the magnetization $M \sim H_{0z}$ (cf. Eq. 3.21 below). The values obtained for J and h_A from a fit to the experimental data with the renormalized spin-wave theory will be different from those by linear spin-wave theory. For $T \to 0$, the relation between them is:

$$J_{\text{linear}} = J_{\text{renormalized}} \cdot (1 - R_0) \qquad h_{\text{A, linear}} = h_{\text{A, renormalized}} / (1 - R_0)$$

Only $g\mu_B H_A$ is the same in both approaches. However, we will not use the subscripts "linear" and "renormalized" or any other special notation for the parameters in linear or renormalized theory here and for the entries in Table 5 since the remarks in Table 5 indicate, especially for a spin-wave analysis, whether a set of parameters refers to linear or normalized spin-wave theory. And here in the text, it is clear from the equations what type of theory has been used.

One example of the application of the renormalized spin-wave theory is the calculation ν_{AFMR} for $H_{0z} = 0$, i.e. the result of Eq. 3.15 for $\boldsymbol{q} = 0$, as a function of temperature and to compare it with experimental data. This is shown for K_2NiF_4 in Fig. 3.3. The experimental data have been obtained by far-infrared spectroscopy [71N, 74N1]. The calculation of the theoretical data has been performed with a method somewhat different from that outlined here [74N1], starting from the Hamiltonian

$$\mathcal{H} = -2J \sum_{\langle i,j \rangle} \boldsymbol{S}_i \boldsymbol{S}_j + D \sum_i S_{i,z}^2 - g\mu_B H_{0z} \sum_i S_{i,z} \tag{3.16}$$

where the staggered anisotropy field H_A (cf. Eq. 3.2) is replaced by a single-ion anisotropy term $D \cdot S_{i,z}^2$ (cf. Eq. 3.35 below) with $D < 0$ for an easy-axis antiferromagnet like K_2NiF_4. The agreement between experimental and calculated data in Fig. 3.3 is convincingly good for $T \le 0.5\,T_N$ although the experimental error bars increase with increasing temperature due to the broadening of the AFMR absorption line with a width proportional to T^4 (cf. Eq. 3.13). The temperature dependence of ν_{AFMR} is nearly the same as that of the sublattice magnetization

$$\nu_{\text{AFMR}}(T) / \nu_{\text{AFMR}}(0) \approx M_{\text{subl}}(T) / M_{\text{subl}}(0) \tag{3.17}$$

which has been demonstrated in various investigations [73W3, 74J2, 74N1]. Another object studied experimentally for many compounds is the two-magnon spectrum observed by Raman scattering. This two-magnon Raman line is a broad band arising from the simultaneous excitations of two magnons with $+\boldsymbol{q}$ and $-\boldsymbol{q}$ out of the whole Brillouin zone. Fig. 3.4 shows the two-magnon Raman line for K_2MnF_4, the experimental data and a theoretical Green function calculation of the lineshape [69P2] originally performed for Rb_2MnF_4 and scaled to K_2MnF_4 [73L2]. The two-magnon Raman line has also been studied as a function of temperature. The T-dependence of the peak position E_p and of the width W_p are shown in Fig. 3.5 together with the results of theoretical calculations which are usually obtained with a Green function technique combined with renormalized spin-wave theory [71C2, 71C3, 71K1, 73B2, 76P2, 77L2].

9.12.3.1.3 Temperature-dependent Properties, High Temperature Series

However, not only the magnon energies but also other magnetic quantities can be evaluated by means of renormalized spin-wave theory, including their temperature dependence. Thus, also some thermodynamic functions can be calculated in this way, e.g. the sublattice magnetization $M_{\mathrm{subl}}(T)$, the parallel and the perpendicular susceptibilities $\chi_{\|}(H_0, T)$ and $\chi_{\perp}(H_0, T)$. Let us first consider the case $H_{0z} = 0$ ($\hbar\omega_{\mathrm{q}}^{+} = \hbar\omega_{\mathrm{q}}^{-} = \hbar\omega_{\mathrm{q}}$, $n_{\mathrm{q}}^{+} = n_{\mathrm{q}}^{-} = n_{\mathrm{q}}$). Then the sublattice magnetization is obtained as

$$M_{\mathrm{subl}}(T) = M_0 \left[1 - \frac{1}{NS} \sum_{\mathrm{q}} (f_{\mathrm{q}} - 1) - \frac{2}{NS} \sum_{\mathrm{q}} f_{\mathrm{q}}\, n_{\mathrm{q}} \right] \tag{3.18}$$

with

$$f_{\mathrm{q}} = \frac{1 + h_{\mathrm{A}}}{[(1 + h_{\mathrm{A}})^2 - \gamma^2]^{1/2}} \quad \text{and} \quad M_0 = \frac{N}{2V} g\mu_{\mathrm{B}} S$$

M_0 is the ideal sublattice magnetization with complete alignment of the $N/2$ spins in the volume V, namely parallel or antiparallel to the preferred spin direction in the Néel state. The second temperature-independent term in Eq. 3.18 describes a deviation from this state, expressed by the zero-point spin deviation

$$\Delta_0 S = \frac{1}{N} \sum_{\mathrm{q}} (f_{\mathrm{q}} - 1) \tag{3.19}$$

while the third temperature-dependent term in Eq. 3.18 accounts for the reduction of the sublattice magnetization due to the thermal excitation of magnons. The sublatice magnetization can be determined experimentally either by neutron diffraction or by ^{19}F-NMR. The intensity of an antiferromagnetic superreflection is proportional to M_{subl}^2 while the internal magnetic field encountered by nuclei of the terminal (axial) $\mathrm{F}_{\mathrm{I}}^{-}$-ions ($\mathrm{F}_{\mathrm{I}}$) is directly proportional to M_{subl} [77A1, 77A2]. For K_2MnF_4 and Rb_2MnF_4, Fig. 3.6 presents the temperature dependence of M_{subl} as reflected by the resonance frequency f_{NMR} in $^{19}\mathrm{F}_{\mathrm{I}}$-NMR together with the theoretical temperature dependence according to Eq. 3.18. Up to $T \approx 0.5\, T_{\mathrm{N}}$, M_{subl} can well be described by the renormalized spin-wave theory. But for higher temperatures, the data in Fig. 3.6 indicate that this theory is no longer applicable. The reasons for this breakdown, e.g. begin of the critical fluctuations increasing towards T_{N}, have been discussed in detail by Arts and de Wijn [90A3].

For $H_{0z} = H_0 \neq 0$, the sublattice magnetizations are different for the spin-up (↑) and the spin-down (↓) sublattices

$$\begin{aligned} &\text{spin-up:} && M_{\mathrm{subl}}(\uparrow) = M_0 \left[1 - \Delta_0 S / S - \frac{1}{NS} \sum_{\mathrm{q}} f_{\mathrm{q}} (n_{\mathrm{q}}^{+} + n_{\mathrm{q}}^{-}) + \frac{1}{NS} \sum_{\mathrm{q}} (n_{\mathrm{q}}^{+} - n_{\mathrm{q}}^{-}) \right] \\ &\text{spin-down:} && M_{\mathrm{subl}}(\downarrow) = M_0 \left[-1 + \Delta_0 S / S + \frac{1}{NS} \sum_{\mathrm{q}} f_{\mathrm{q}} (n_{\mathrm{q}}^{+} + n_{\mathrm{q}}^{-}) + \frac{1}{NS} \sum_{\mathrm{q}} (n_{\mathrm{q}}^{+} - n_{\mathrm{q}}^{-}) \right] \end{aligned} \tag{3.20}$$

where the last term in both equations accounts for the unbalance of the two sublattices and for the resulting net magnetization parallel to the applied field.

$$M_{\parallel}(H_{0z}, T) = M_{\mathrm{subl}}(\uparrow) + M_{\mathrm{subl}}(\downarrow) = 2\,M_0 \left[\frac{1}{NS} \sum_{\mathrm{q}} (n_{\mathrm{q}}^{+} - n_{\mathrm{q}}^{-}) \right] \tag{3.21}$$

This net magnetization is sensed by the nuclei of the bridging (equatorial) $\mathrm{F}_{\mathrm{II}}^{-}$ -ions. Fig. 3.7 illustrates that the F_{I}-ions sense the sublattice magnetization and the F_{II}-ions the net magnetization. Thus the shift of f_{NMR} in $^{19}\mathrm{F}_{\mathrm{II}}$-NMR as a function of T and H_{0z} corrected for the Zeeman shift is a measure for $M_{\parallel}(H_{0z}, T)$ [77A1, 77A2] as shown in Fig. 3.8 versus T for various H_{0z} up to 5.003 T. The data calculated by means of Eq. 3.21 agree quite well with the experimental data again up to $T \approx 0.5\ T_{\mathrm{N}}$. For lower magnetic fields, the agreement extends to higher temperatures while the deviations start at lower T for higher fields. From the inflection point of $M_{\parallel}(H_{0z}, T)$ near T_{N}, the variation of T_{N} can be deduced as a function of magnetic field [(H_{0z}, T) phase diagram]. The shift of f_{NMR} in $^{19}\mathrm{F}_{\mathrm{II}}$-NMR also corrected for the Zeeman shift can alternatively be studied versus H_{0z} for a fixed temperature. Such a study yields for $T = 1.2$ K the magnetic field at the spin-flop transition $H_{\mathrm{SF}} = 5.45(5)$ T [77A2]. By differentiating Eq. 3.21 with respect to H_{0z}, the parallel susceptibility $\chi_{\parallel}$ is obtained.

$$\chi_{\parallel}(H_{0z} \to 0) = \frac{2g\mu_{\mathrm{B}}M_0}{2zS\,|J|} \left[\frac{2}{NS} \sum_{\mathrm{q}} n_{\mathrm{q}}^2 \exp\,(\hbar\omega_{\mathrm{q}} / k_{\mathrm{B}}T) \right] \Bigg/ \left[1 + \frac{2zS\,|J|}{k_{\mathrm{B}}T} \frac{2}{NS} \sum_{\mathrm{q}} n_{\mathrm{q}}^2 \exp\,(\hbar\omega_{\mathrm{q}} / k_{\mathrm{B}}T) \right] \tag{3.22}$$

This result of the renormalized spin-wave theory may be compared to experimental data of susceptibility measurements. Before entering into such a discussion, it is favourable to introduce also the analogous result for the perpendicular susceptibility $\chi_{\perp}$, i.e. the susceptibility for a magnetic field perpendicular to the preferred spin direction, the *c*-axis for the easy-axis antiferromagnets. For the spin-wave treatment of $\chi_{\perp}$, the necessary modification of Eq. 3.2 is to replace the Zeeman term for $\boldsymbol{H_0}$ parallel to the *c*-axis by one with $\boldsymbol{H_0}$ perpendicular to the *c*-axis, e.g. parallel to the *x*-direction. The procedure is essentially the same as for $\boldsymbol{H_0} \parallel \boldsymbol{c}$ outlined above (Eqs. 3.2–3.5). After the Holstein-Primakoff and the Fourier transform, the terms linear in the Bose operators are removed by a shift of the origin for these operators. The final result after the Bogoliubov transform (cf. Eq. 3.4b) is

$$\chi_{\perp}(H_{0x} \to 0) = \frac{2g\mu_{\mathrm{B}}M_0}{4zS\,|J| + g\mu_{\mathrm{B}}H_{\mathrm{A}}} \left[1 - \frac{1}{NS} \sum_{\mathrm{q}} (f_{\mathrm{q}} - g_{\mathrm{q}}) \cdot (2n_{\mathrm{q}} + 1) \right] \tag{3.23}$$

The factor in front of the square bracket represents for $H_{\mathrm{A}} = 0$ the well-known meanfield result for $\chi_{\perp}$ (see for example Eq. 36.6 in [66K]). For $T = 0$, Eq. 3.23 reduces to

$$\chi_{\perp}(H_{0x} \to 0,\ T = 0) = \frac{2M_0}{2H_{\mathrm{E}} + H_{\mathrm{A}}} \left[1 - \frac{1}{NS} \sum_{\mathrm{q}} (f_{\mathrm{q}} - g_{\mathrm{q}}) \right] = \frac{2M_0}{2H_{\mathrm{E}} + H_{\mathrm{A}}} \left[1 - \frac{\Delta_0 S}{S} + R_0 \right] \tag{3.24}$$

or in a different notation (cf. Eq. 46.21 in [66K]) for the temperature-independent renormalization factor R_0 (cf. Eq. 3.15)

$$\chi_{\perp}\,(H_{0x} \to 0,\ T = 0) = \frac{2M_0}{2H_{\mathrm{E}} + H_{\mathrm{A}}} \left[1 - \frac{\Delta_0 S}{S} - \frac{e(h_{\mathrm{A}})}{(2 + h_{\mathrm{A}})zS} \right] \tag{3.24a}$$

This second expression for $\chi_{\perp}(T = 0)$ in Eq. 3.24a has frequently been used for the determination of J from experimental data of $\chi_{\perp}(T = 0)$. The relation between spin-wave theory, zero-point spin reduction and $\chi_{\perp}(T = 0)$ has been discussed in detail by de Jongh [73J3] and by Okabe and Fukuchi [78O1].

For small anisotropies as in Mn^{2+}-compounds, the third term in the square brackets can be approximated by $e(0)/2zS = 0.632/2zS$ while for $\Delta_0 S$ the anisotropy has to be taken into account [71C1] and influences perceptibly $\chi_\perp(T = 0)$ [72J1].

The spin-wave results for $\chi_\parallel$ and $\chi_\perp$ are compared in Fig. 3.9 with the experimental results for K_2MnF_4 [82M4] which have been obtained as differential susceptibility with an oscillating field ($H_0 \approx 0.25$ T, $f \approx 117$ Hz). Again, the renormalized spin-wave theory [82M5] proves to be reliable up to $T \approx 0.5\,T_N$. Improvements of the spin-wave theory for $\chi_\parallel$ and $\chi_\perp$ have been reported by Tsuru and Uryu [83T4, 83T5] and compared to the experimental data for K_2MnF_4 [83T3]. However, spin-wave theory alone is not sufficient for the discussion and analysis of the susceptibility because χ has been measured over a wide temperature range from 4.2 K up to 200 K far above $T_N = 43.9$ K. For temperatures $T \approx T_N$ and $T > T_N$, spin-wave theory cannot act as an effective approximation to the experimental results. In the temperature range above T_N, the experimental data of χ show a maximum near 70 K (cf. Fig. 3.9) which is typical for the quasi-two-dimensional compounds under consideration. For the highest temperatures near 200 K, we expect χ to follow the Curie-Weiss Law

$$\chi = \frac{C}{T - \Theta_C} \tag{3.25}$$

with the Curie constant $C = (N/V)\,[(g\mu_B)^2\, S(S+1)\,/\,(3\,\mu_0 k_B)]$ and the Curie-Weiss temperature $k_B\Theta_C = (2/3)\,z\,S\,(S+1)\,J$. For antiferromagnets with $J < 0$, we have $\Theta_C < 0$ and the denominator becomes $T + |\,\Theta_C\,|$. Starting from Eq. 3.24, an approximate solution for χ is the following high-temperature series expansion (h.t.s.):

$$\chi = \frac{C}{T}[1 - \Theta_C\,/\,T]^{-1} \quad \rightarrow \quad \frac{C}{T}[1 + \sum_{n=1}^{\infty} a_n\, K^n] \tag{3.26}$$

where $K = J\,/\,k_B T$ is the variable and a_n are the coefficients of the series. The methods for the derivation of susceptibility high-temperature series expansions for the two- and three-dimensional (2D and 3D) Heisenberg model is explained in detail in the work of Rushbrooke and Wood [58R3] and in the reviews by Rushbrooke et al. [74R2] and by Navarro [90N]. The expansion coefficients a_n have been evaluated and tabulated for n = 1 – 8 for the 2D Heisenberg model with general S on several two-dimensional lattices, including the square lattice (cf. the tables in [90N]). The series expansion in Eq. 3.26 is originally derived for ferromagnets. But it can also be used for antiferromagnets with $K = |\,J\,|\,/\,k_B T$ and $a_n \rightarrow (-1)^n \cdot a_n$ because of $J < 0$ in antiferromagnets. Unfortunately, this series for antiferromagnets has a poor convergence at temperatures not far above T_N [77A3]. Therefore it is advantageous to use the reciprocal series as introduced by Rushbrooke and Woods [58R3] and by Lines [70L1]:

$$\chi^{-1} = \frac{T}{C}[1 + |\,\Theta_C\,|\,/\,T] \quad \rightarrow \quad \frac{T}{C}\left[1 + \sum_{n=1}^{\infty} b_n\, K^n\right] \tag{3.27}$$

where now $K = |\,J\,|\,/\,k_B T$ and where the coefficients b_n are usually derived from $(-1)^n \cdot a_n$ by inversion of the (finite) series Eq. 3.26 with a computer:

$$b_1 = -\,(-1)\cdot a_1 \qquad b_2 = (-1)^2 \cdot (\,a_1^2 - a_2) \qquad b_3 = -\,(-1)^3 \cdot (\,a_1^3 - 2\,a_1\,a_2 + a_3) \qquad \text{etc.}$$

These first examples of b_n show that most coefficients of the reciprocal series are positive and it turns out that the convergence is improved. In his pioneering work when only few experimental results were known, Lines [69L2, 70L1] has performed theoretical considerations and calculations on quasi-two-dimensional magnetic systems and obtained results for $\Delta_0 S$ and its dependence on the anisotropy, for M_{subl} and χ as a function of temperature. From his results, the h.t.s. data for χ^{-1} are reproduced in

Fig. 3.10. They are presented as $\tilde{\chi}/\chi$ versus $k_BT/|J|S(S+1)$ for various values of S where $\tilde{\chi}$ is defined in Eq. 3.28a below. Since Lines has used the series only with 6 coefficients, the error bars increase considerably towards T_N. This can be improved by extending the series with now known coefficients up to n = 8 for general S and up to n = 10 for $S = \frac{1}{2}$ and $S = \infty$ [90N]. For comparison, also the mean field result (Curie-Weiss law) is included in Fig. 3.10 which is asymptotically approached at high temperatures.

Let us now return to Fig. 3.9 with the experimental and calculated data for χ of K_2MnF_4. The fitted h.t.s.-curve agrees quite well with the experimental data for temperatures from slightly above T_N to 200 K. The maximum of χ is reproduced in Fig. 3.9 by the h.t.s.-curve. Generally, calculations of $\chi(T)$ for a 2D Heisenberg antiferromagnet with various values of S [76N4] yield this maximum as a property of quasi 2D antiferromagnets. From all these results, relations have been derived between the exchange constant J and the susceptibility maximum χ_{max} and the temperature T_{max} at which it occurs. With the dimensionless factors τ_m and χ'_m, these relations read [76N2, 76N4, 90N]:

$$k_BT_{max} = \tau_m \cdot S(S+1)\,|J| \qquad\qquad \chi_{max} = \chi'_m \cdot \tilde{\chi} \tag{3.28}$$

with

$$\tilde{\chi} = (N/V)\,(g\mu_B)^2/(\mu_0\,|J|) \tag{3.28a}$$

The factors τ_m and χ'_m depend on the lattice type and weakly on S (see below). For single-layer compounds on a square lattice, some examples of numerical values are (see [90N, 70L1, 78J3]):

$S =$	1/2	1	3/2	2	5/2
$\tau_m =$	2.495(5)	2.18(2)	2.10(2)	2.07(3)	2.06(3)
$\chi'_m =$	0.0469(1)	0.0521(1)	0.0539(1)	0.0547(1)	0.0551(1)

For further values, e.g. for other lattices, see Table IX in [90N]. Stanley and Kaplan [66S2] concluded from their analysis of the high-temperature series expansion that there could be a new type of phase transition in the 2D Heisenberg model at a finite temperature

$$k_BT_C^{(2)} = \tfrac{1}{5}(z-1)\,|J|\,[2S(S+1)-1] \tag{3.29}$$

This transition would be characterized by χ diverging at $T_C^{(2)}$ but $M = 0$ for all $T > 0$. Long-range order would only exist at $T = 0$. However, a small but finite Ising-like anisotropy and/or a small but finite interlayer coupling will change the character of the phase transition and a transition will occur to a magnetic long-range order [73M]. Therefore, the problem of a Stanley-Kaplan transition was considered not relevant to K_2MnF_4 and similar compounds which show long-range order below T_N because of their Ising-like anisotropy [73B1]. But the Stanley-Kaplan formula Eq. 3.29 became in the meantime a tool for estimating $|J|$ from T_N or vice versa. Examples of such use of Eq. 3.29 are listed in Table 5. The dependence of the transition temperatures on the anisotropy was considered for various perovskite-type layer compounds [72J2] with a comparison of experimental values for H_A/H_E, $k_BT_N/|J|$, T_N/Θ_C (cf. Eq. 3.25) and $T_N/T_C^{(2)}$ (cf. Eq. 3.29). The conclusion from this analysis was that the long-range order in these compounds results not only from the Ising-like anisotropy and a weak interlayer coupling but possibly also from finite-size effects [72J2]. In context with Eq. 4.2 in Sect. 4.1.1, recent results will be discussed about long-range magnetic order for the ground state ($T \to 0$) of the 2D Heisenberg model and the 2D XY-model for several spin values S.

The considerations about h.t.s. may be summarised as follows: For $T < T_N$, the susceptibility can well be analysed with the renormalized spin-wave theory, and for $T > T_N$, the high-temperature series expansion is the more appropriate method, not only for K_2MnF_4 but also for other quasi-two-dimensional antiferromagnets [73J3]. These two methods have widely been used by fitting the theory (cf. Eqs. 3.22–

3.24, 3.26, 3.27) to the experimental data for determining the values of J and H_A as they are listed in Table 5. Especially susceptibility data at low and high temperatures have been used to derive values for J. For some compounds, the reader may compare the values for J derived from χ with those determined more directly by inelastic scattering of neutrons. The application of renormalized spin-wave theory to various experimental data, e.g. $\nu_{\text{AFMR}}(T)$, $M_{\text{subl}}(T)$ and $\hbar\omega(\boldsymbol{q})$, has been called a spin-wave analysis of the compound [73W2].

9.12.3.1.4 Double-Layer Compounds

For double-layer compounds like $K_3Mn_2F_7$ and $Rb_3Mn_2F_7$, the above equations have to be modified for a similar analysis of the experimental data and for a determination of the characteristic parameters J and H_A. The main difference to K_2MnF_4 is that there are four sublattices in $K_3Mn_2F_7$. The dominating exchange interaction couples an up-spin not only to the four nearest neighbour down-spins in its layer but also to one neighbouring down-spin in the other layer of the double-layer pair (cf. Fig. 2.4 in Sect. 2.1.2) and a down-spin also to five nearest neighbours. The treatment is usually simplified by assuming the interlayer distance a' (cf. Eqs. 2.6 and 2.7 in Sect. 2.1.1) to be equal to the lattice parameter a so that the same exchange constant J applies to the interaction with all five neighbours. Neglecting again exchange interactions between more distant neighbours and expressing the anisotropy by a staggered field H_A, the Hamiltonian reads for $K_3Mn_2F_7$ and $Rb_3Mn_2F_7$ [77A4]

$$\begin{aligned}\mathcal{H} = -2J&\left[\sum_{\langle \mathrm{i},\mathrm{j}\rangle} \boldsymbol{S}_\mathrm{i}\boldsymbol{S}_\mathrm{j} + \sum_{\langle \mathrm{i},\mathrm{j}'\rangle} \boldsymbol{S}_\mathrm{i}\boldsymbol{S}_{\mathrm{j}'} + \sum_{\langle \mathrm{i}',\mathrm{j}\rangle} \boldsymbol{S}_{\mathrm{i}'}\boldsymbol{S}_\mathrm{j} + \sum_{\langle \mathrm{i}',\mathrm{j}'\rangle} \boldsymbol{S}_{\mathrm{i}'}\boldsymbol{S}_{\mathrm{j}'}\right]\\ &- g\mu_\mathrm{B} H_\mathrm{A}\left[\sum_\mathrm{i} \mathrm{S}_{\mathrm{i,z}} - \sum_\mathrm{j} \mathrm{S}_{\mathrm{j,z}} + \sum_{\mathrm{i}'} \mathrm{S}_{\mathrm{i}',\mathrm{z}} - \sum_{\mathrm{j}'} \mathrm{S}_{\mathrm{j}',\mathrm{z}}\right]\end{aligned} \tag{3.30}$$

where i, j, i′, and j′ refer to the spin-up and spin-down sublattices in layers 1 and 2, respectively. Again, ⟨...⟩ means that each pair of neighbours within the layers or in adjacent layers is counted only once and the subscripts z refer to the magnetic unit cell with the (x, y, z) coordinate system (cf. Fig. 2.1 in Sect. 2.1.2). The four sublattices give rise to four spin-wave branches, i.e. two pairs of doubly degenerate branches if no external field H_0 is applied. Application of linear spin-wave theory to Eq. 3.30 yields for the magnon energies (four branches: l = 1, 2, 3, 4):

$$\begin{aligned}\hbar\omega_\mathrm{q}^{1,2} &= 2zS\,|J|\,[(1+h_\mathrm{A})^2 - (\gamma_\mathrm{q}^{1,2})^2]^{1/2}\\ \hbar\omega_\mathrm{q}^{3,4} &= 2zS\,|J|\,[(1+h_\mathrm{A})^2 - (\gamma_\mathrm{q}^{3,4})^2]^{1/2}\end{aligned} \tag{3.31}$$

with $z = 5, \quad S = \tfrac{1}{2}, \quad h_\mathrm{A} = H_\mathrm{A}/H_\mathrm{E}, \quad H_\mathrm{E} = 2zS\,|J|/g\mu_\mathrm{B},$

$$\gamma_\mathrm{q}^{1,2} = \tfrac{1}{5}\,[4\cos(\tfrac{q_x a}{2})\cdot\cos(\tfrac{q_y a}{2}) + 1] \quad \text{and} \quad \gamma_\mathrm{q}^{3,4} = \tfrac{1}{5}\,[4\cos(\tfrac{q_x a}{2})\cdot\cos(\tfrac{q_y a}{2}) - 1]$$

For both, $K_3Mn_2F_7$ and $Rb_3Mn_2F_7$, no experimental data are available for $\hbar\omega_\mathrm{q}$ from inelastic neutron scattering. For $K_3Mn_2F_7$, only calculated magnon dispersion curves are available (see Fig. 3.11) which have been obtained by means of Eq. 3.31 using the parameter values from a spin-wave analysis of $M_{\text{subl}}(T)$ [77A4, 77A5]. For the lower two branches (l = 1, 2), the spin precessions are in-phase for the two layers of the double-layer system, and for the upper two branches (l = 3, 4), the precessions are out-of-phase as indicated in Fig. 3.11. The energy of the lower branch (l = 1, 2) at $\boldsymbol{q} = 0$ corresponds to the AFMR frequency

$$\hbar\omega^{1,2}(\boldsymbol{q}=0) = h\nu_{\mathrm{AFMR}} = g\mu_{\mathrm{B}}\,[2H_{\mathrm{E}}H_{\mathrm{A}} + H_{\mathrm{A}}^2\,]^{1/2} \tag{3.32a}$$

which has been observed by AFMR in $K_3Mn_2F_7$ and $Rb_3Mn_2Cl_7$ (cf. Table 5). At the Brillouin zone boundary, the two doubly degenerate branches merge into one quadruply degenerate zone edge magnon energy

$$\hbar\omega^{1,2}(\boldsymbol{q}_{\mathbf{max}}) = \hbar\omega^{3,4}(\boldsymbol{q}_{\mathbf{max}}) = h\nu_{\mathrm{BZB}} = g\mu_{\mathrm{B}}[\tfrac{24}{25}H_{\mathrm{E}}^2 + 2H_{\mathrm{E}}H_{\mathrm{A}} + H_{\mathrm{A}}^2]^{1/2} \tag{3.32b}$$

The renormalized spin-wave theory for the double-layer compounds follows the same lines as sketched above for the single-layer compounds. The extension to four sublattices will not be outlined here. For the details, the reader is referred to reference [77A4]. This theory with Oguchi corrections has been employed to $K_3Mn_2F_7$ for calculating the temperature-dependence of $\chi_{\parallel}$ and $\chi_{\perp}$ for $T < T_N$ [77A3]. The results are compared to the experimental data in Fig. 3.12. As for the single-layer compounds, the agreement between experiment and theoretical prediction is good up to $T \approx 0.5\ T_N$.

Some of the equations derived for single-layer compounds in Sect. 3.1.3 can also be used for double-layer compounds, for example the expression for $\chi_{\perp}(T = 0)$ in Eq. 3.24a. However, the numerical values $\Delta_0 S = 0.124$ and $e(0)/z = 0.1221$ are different for double-layer compounds (cf. Table A1 in [76N1]). For $T > T_N$, the susceptibility of $K_3Mn_2F_7$ was also calculated by means of a high-temperature series expansion (cf. Fig. 3.12) which is as well defined by Eqs. 3.26 and 3.27. The coefficients for m square-layer systems (up to m = 7) have been derived and tabulated by Ritchie and Fischer [78R3] under the assumption of free surface conditions and of periodic boundary conditions up to seventh order. Free surface and m = 1 correspond to single-layer compounds. The h.t.s. for m = 2 (double-layer) and free surface has been used to fit the experimental data of $K_3Mn_2F_7$ (cf. Fig. 3.12). The h.t.s. results have also been analysed with respect to Eq. 3.28. The values obtained for a $S = \frac{5}{2}$ double-layer compound are: $\tau_m = 2.70(5)$ and $\chi'_m = 0.0453(2)$ [76N1]. For various numbers m of layers Navarro et al. [76N1, 90N] have compared the susceptibility calculated by means of h.t.s. for $S = \frac{5}{2}$. These data are presented as $\chi(\mathrm{m})/\tilde{\chi}$ versus $k_B T/|J|S(S+1)$ in Fig. 3.13 with $\tilde{\chi}$ given in Eq. 3.28a. The curve for $\mathrm{m} \to \infty$ corresponds to three-dimensional magnets with the cubic perovskite structure (cf. Fig. 1.1 in Sect. 1), e.g. to $KMnF_3$. The susceptibility data in Fig. 3.13 demonstrate that the single-layer compounds A_2MnX_4 (m = 1) and the infinite-layer compounds $AMnX_3$ ($\mathrm{m} \to \infty$) are the extreme cases, namely two-dimensional and three-dimensional magnets, resp., and that the double-layer and triple-layer compounds $A_3Mn_2X_7$ and $A_4Mn_3X_{10}$ (m = 2 and m = 3) are intermediate between those two.

9.12.3.1.5 Ni- and Fe-Compounds

In contrast to Mn^{2+} with its ^6S spin-only ground state ($L = 0$, $S = \frac{5}{2}$), Hund's rules yield as the free-ion ground state ^3F ($L = 3$, $S = 1$) for Ni^{2+} and ^5D ($L = 2$, $S = 2$) for Fe^{2+}. In these cases, the crystalline field in conjunction with spin-orbit coupling is the origin for a single-ion anisotropy. For Ni^{2+}, the splitting of this ground state by the cubic and the tetragonal crystal field and by the spin-orbit coupling leads to a singlet ground state Γ_4^+ (D_{4h}) [73D2]. In the Ni-compounds (K_2NiF_4, $K_3Ni_2F_7$, Rb_2NiF_4), the *c*-axis is still the preferred spin direction. For Fe^{2+}, the effect of the single-ion anisotropy is more drastic since it is responsable that the preferred spin direction is perpendicular to the *c*-axis. Therefore, the Fe-compounds are easy-plane antiferromagnets as discussed in Sect. 2.1.3 in context with Fig. 2.6. Let us now consider the single-ion anisotropy for Fe^{2+} in more detail. The Hamiltonian for a free ion without coupling to other ions may be written as [80T3]

$$\mathcal{H}_{\mathrm{CF+LS}} = \tfrac{1}{5}B_4^4(O_4^0 + 5O_4^4) + \lambda\,\boldsymbol{L}\,\boldsymbol{S} + B_2^0\,O_2^0 \tag{3.33}$$

In Eq. 3.33, the notation is the usual one, see for example [64H]. The first term represents the cubic field which splits the ^{5}D free ion ground state into a $^5\Gamma_5^+$ triplet and a $^5\Gamma_3^+$ doublet at about 8400 cm^{-1} above the triplet. The second term and the third term, i.e. the spin-orbit coupling and the tetragonal crystal field are of nearly equal importance, and the latter splits the triplet into ground singlet and a doublet approximately 500 cm^{-1} above it. As outlined in detail in the paper of Thurlings et al. [82T1], a spin Hamiltonian is derived for the orbital ground state:

$$\mathcal{H} = -2J \sum_{\langle \mathrm{i,j} \rangle} \boldsymbol{S}_\mathrm{i} \boldsymbol{S}_\mathrm{j} + \sum_\mathrm{i} [D\,\mathrm{S}_{\mathrm{i,z}}^2 + a\,\mathrm{S}_{\mathrm{i,z}}^4 + e\,(\mathrm{S}_{\mathrm{i,x}}^4 + \mathrm{S}_{\mathrm{i,y}}^4) + 6\,e\,(\mathrm{S}_{\mathrm{i,x}}\,\mathrm{S}_{\mathrm{i,y}})^2] \qquad (3.34)$$

where the first term is the exchange interaction between nearest neighbours of Fe^{2+}-ions in the layers and the second term is the single-ion anisotropy energy. In this term is some redundance. The effects of the axial terms $D\mathrm{S}_{\mathrm{i,z}}^2$ and $a\mathrm{S}_{\mathrm{i,z}}^4$ cannot be distinguished in spin-wave theory, so the term with "a" will be omitted since it is much smaller than that with "D". Also, the effect of the two in-plane anisotropy terms is practically the same in spin-wave theory, and only the last term $6e(\mathrm{S}_{\mathrm{i,x}}\,\mathrm{S}_{\mathrm{i,y}})^2$ will be kept. Further, the quartic in-plane anisotropy is decoupled within the random phase approximation to a quadratic term, see [82T1]. Thus, the final Hamiltonian for the spin-wave calculations for K_2FeF_4 and Rb_2FeF_4 reads

$$\mathcal{H} = -2J \sum_{\langle \mathrm{i,j} \rangle} \boldsymbol{S}_\mathrm{i} \boldsymbol{S}_\mathrm{j} + \sum_\mathrm{i} [D\mathrm{S}_{\mathrm{i,z}}^2 + E(\mathrm{S}_{\mathrm{i,x}}^2 - \mathrm{S}_{\mathrm{i,y}}^2)] - g_\mathrm{a}\mu_\mathrm{B} H_{0\mathrm{x}} \sum_\mathrm{i} \mathrm{S}_{\mathrm{i,x}} - g_\mathrm{c}\mu_\mathrm{B} H_{0z} \sum_\mathrm{i} \mathrm{S}_{\mathrm{i,z}} \qquad (3.35)$$

In Eqs. 3.34 and 3.35, ⟨i, j⟩ means again that each pair of nearest neighbours is counted once. The summation over i in the anisotropy and Zeeman terms extends over all magnetic ions in both sublattices and g_a and g_c are the g-factors for $\boldsymbol{H}_0 \perp \boldsymbol{c}$ and $\boldsymbol{H}_0 \parallel \boldsymbol{c}$, respectively. The out-plane anisotropy ($D > 0$) forces the spins to a direction perpendicular to the c-axis. The in-plane anisotropy ($E < 0$) makes the x-axis the easy axis. We note that in Eq. 3.34 all terms have the tetragonal symmetry required for the paramagnetic phase. The in-plane term in Eq. 3.35 has still the tetragonal symmetry within the decoupling scheme [82T1]. If E however is treated as an independent fit parameter, this in-plane anisotropy has only the orthorhombic symmetry of the antiferromagnetic phase (cf. Sect. 2.1.2). In this case, E has to be temperature-dependent and must vanish for $T > T_\mathrm{N}$. In addition to the orthorhombic distortion found in the antiferromagnetic phase of Rb_2MnCl_4 by neutron diffraction [97T1, 98T] as mentioned in Sect. 2.1.2, orthorhombic symmetry has also been observed for $T < T_\mathrm{N}$ in Mössbauer spectroscopy on K_2FeF_4 [78T2, 80T3, 82T1] as a nonzero asymmetry $V_\mathrm{xx} - V_\mathrm{yy}$ of the electric field gradient. It was found to decrease with increasing temperature and to vanish near T_N as expected from the symmetry considerations. A similar asymmetry $V_\mathrm{xx} - V_\mathrm{yy}$ was observed in Mössbauer studies on Rb_2FeF_4 [68W1]. Further, optical rotation measurements suggest that there is a slight orthorhombic distortion of the crystal below 50 K of magnetostrictive origin. There have also been model calculations which couple the crystal field Hamiltonian and the spin-wave theory with the magnetoelastic energy. In this framework, an orthorhombic distortion is obtained which produces an in-plane anisotropy of orthorhombic symmetry, in addition to the in-plane anisotropy of tetragonal symmetry [81G1, 82G2]. And both types are required for obtaining a good fit to the experimental data.

In the spin-wave calculations for K_2FeF_4 [82T1], the temperature dependence of E was modeled by scaling it to that of $V_\mathrm{xx} - V_\mathrm{yy}$. Other approaches to the spin-wave theory of easy-plane antiferromagnets have introduced a staggered in-plane anisotropy field [78L3, 80B4, 80B5] which cannot be established from dipolar interactions in this case. For the renormalized spin-wave calculations based on Eq. 3.35, the reader will find the details in [82T1]. Let us consider here only some of the results. The first example are the magnon dispersion curves determined by inelastic neutron scattering (Fig. 3.14). The theory has been applied in a fit to the experimental data (see solid curves in Fig. 3.14). There are two nondegenerate spin-wave branches in this orthorhombic symmetry which join to a degenerate mode at the zone boundary. From the two modes at $\boldsymbol{q} = 0$, the upper is the out-of-plane and the lower the in-plane mode as will be shown in more detail below. The bottom part of Fig. 3.14 demonstrates again the two-dimensionality, namely the independence of $\hbar\omega_\mathrm{q}$ from q_z. Other spin-wave results are the zero-point spin deviation $\Delta_0 S$

and the sublattice magnetization M_{subl} and its variation with temperature (Fig. 3.15). The experimental data for M_{subl} have been determined from the intensities of the (1, 0, 0) and 1, 0, 3) antiferromagnetic Bragg reflections. Good agreement is obtained with the calculated data up to 45 K (≈ 3/4 T_N) if the temperature dependence of $E \sim (V_{xx} - V_{yy})$ is included in the calculation. The susceptibility of K_2FeF_4 has been studied by NMR [82T3] and compared to spin-wave results at temperatures below T_N. For our further discussion, it is sufficient to consider in detail the simpler expressions for the magnon energy obtained with linear spin-wave theory, for $H_{0z} = 0$ and $H_{0x} \neq 0$:

$$\hbar\omega_q = 2zS\,|J|\,\{[(1+A)^2 + h_{0x}^2 - \gamma_q^2 - B^2] \mp 2([(1+A)^2 - \gamma_q^2]\,h_{0x}^2 + \gamma_q^2 B^2)^{1/2}\}^{1/2} \qquad (3.36)$$

where $A = (D - 3E)/2z\,|J|, \quad B = (D + E)/2z\,|J|, \quad h_{0x} = g_a \mu_B H_{0x}/2zS\,|J|, \quad z = 4, \quad S = 2$

and γ_q as defined in Eq. 3.6. For reasons of the more complicated form of the first order corrections in case of the Hamiltonian Eq. 3.35, not only the fit values for J, A and B are different for linear and renormalized theory but also the anisotropy parameters D and E (cf. Table 5 and [82T1]). Considering now $\hbar\omega_q$ for $\boldsymbol{q} = 0$ and introducing the exchange field H_E, the out-of-plane anisotropy field H_A and the in-plane anisotropy field $\tilde{H}_A$, the two AFMR frequencies are for $H_0 = 0$ where in this calculation an isotropic $g = 2.00$ is used:

$$\begin{aligned} &\text{out-of-plane mode:} \quad \nu_{\text{AFMR, out-of-pl.}} = (\gamma/2\pi)\,[H_E\,(2H_A + \tilde{H}_A) + \tfrac{1}{2}\tilde{H}_A(H_A + \tilde{H}_A)]^{1/2} \\ &\text{in-plane mode:} \quad \nu_{\text{AFMR, in-plane}} = (\gamma/2\pi)\,[2H_E\tilde{H}_A + \tfrac{1}{2}\tilde{H}_A(H_A + \tilde{H}_A)]^{1/2} \end{aligned} \qquad (3.37)$$

with $\quad g\mu_B H_E = 2zS\,|J|, \quad g\mu_B H_A = 2DS, \quad g\mu_B \tilde{H}_A = -4ES$

and where γ is again the gyromagnetic ratio. Our notation for H_E, H_A and $\tilde{H}_A$ follows closely that of Thurlings et al. [82T1] because our considerations started with their Hamiltonian and because their values for J, D and E are listed in Table 5. The expressions for ν_{AFMR} in Eq. 3.37 show that the out-of-plane mode depends essentially on the stronger out-of-plane H_A and corresponds to ν_{AFMR} in the easy-axis antiferromagnets discussed above. The in-plane mode, on the other hand, depends critically on the in-plane $\tilde{H}_A$. In other words, if we had only $H_A \neq 0$ or $D \neq 0$ as in the case of the easy-axis antiferromagnets, the frequency of the lower mode would be zero as a consequence of $E = 0$ and $\tilde{H}_A = 0$. In this case, K_2FeF_4 would be a true easyplane antiferromagnet with no preferred spin direction in the basal plane. On these grounds, one would expect E and $\tilde{H}_A$ to be smaller as it turns out from the frequency of the in-plane mode as determined by neutron scattering and by infrared spectroscopy [82T1]. For the out-of-plane mode, the magnetic field dependence ($\boldsymbol{H_0} \parallel \boldsymbol{c}$ and $\boldsymbol{H_0} \perp \boldsymbol{c}$) has been studied also by infrared spectroscopy [78M1, 80D].

But as already mentioned, some authors [78L3, 78M1, 79M2, 80B4, 80B5, 80D] have used a slightly different Hamiltonian describing the in-plane anisotropy by a staggered field $\tilde{H}_A$ (in our notation) while the Heisenberg-type exchange term and the out-of-plane anisotropy, i.e. a single-ion term $D\,S_{i,z}^2$, are the same as in Eq. 3.35. For the latter term, a more correct ordering of the operators in the renormalized spin-wave theory leads to

$$g\mu_B H_A = 2D(S - \tfrac{1}{2}), \text{ in addition to } g\mu_B H_E = 2zS\,|J| \text{ and } g\mu_B \tilde{H}_A \qquad (3.37a)$$

In this model [78L3, 79M2, 80B4, 80B5, 80D], the factor $(S-\frac{1}{2})$ ensures that the single-ion anisotropy (crystal field) does not influence the spin dynamics in $S=\frac{1}{2}$ systems where such an influence is impossible. The Hamiltonian corresponding to Eq. 3.37a has, for example, been applied to $(CH_3NH_3)_2FeCl_4$ [78L3] and the values of the magnetic parameters for this compound in Table 5 refer to Eq. 3.37a.

9.12.3.1.6 Spin-Flop Transition – AFMR under Various Conditions

Now, the question arises whether there is also a single-ion anisotropy in the easy-axis compounds like K_2MnF_4, Rb_2MnF_4, $K_3Mn_2F_7$. Analogous to Sects. 3.1.2 and 3.1.3, a renormalized spin-wave calculation has been performed for K_2MnF_4 and $K_3Mn_2F_7$ where the anisotropy in a Hamiltonian similar to Eq. 3.2 consists of the dipolar interactions of the spins (Eq. 3.8) and a residual single-ion term $DS_{i,z}^2$. The calculated data reproduce well the temperature dependence of the sublattice magnetization for both compounds [84U] and confirm that the out-of-plane anisotropy is dominated by the dipolar interaction in these Mn-compounds but that there is also a small single-ion contribution. The next question is whether there is an in-plane single-ion anisotropy in these compounds. This can certainly not be observed in the antiferromagnetic phase (AF-phase) with the spins aligned parallel or antiparallel to the *c*-axis but it would be observable in the spin-flop phase (SF-phase) with the spins oriented perpendicular to the *c*-axis similar to the magnetic order in K_2FeF_4. These field-dependent phenomena and the (H_0, T) phase diagram for easy-axis antiferromagnets have been outlined in many reviews and, for details, the reader is referred to them [66K, 74J1, 90G3]. Antiferromagnetic resonance (AFMR) with high magnetic fields offers the possibility to answer these questions. The relation between the AFMR frequency and the (H_0, T) phase diagram is shown schematically in Fig. 3.16. H_0 $(= H_{0z})$ is the magnetic field applied parallel to the *c*-axis. The phase diagram H_0 versus temperature T shows at low temperatures for $H_0 < H_{SF}$ the AF-phase (spins $\parallel \boldsymbol{c}$) and for $H_0 > H_{SF}$ the SF-phase (spins $\perp \boldsymbol{c}$) and for high temperatures the paramagnetic phase (PM-phase). As a function of T, ν_{AFMR} decreases gradually and approaches zero for $T \to T_N$. Experimental data with this dependence have been presented for K_2NiF_4 in Fig. 3.3. The dependence of ν_{AFMR} on H_0 shows for $H_0 < H_{SF}$ two Zeeman branches with linearly increasing and decreasing frequencies according to Eq. 3.9. For $H_0 = H_{SF}$, the frequency of the lower branch goes to zero signalling an instability of the system which is then restabilized by the transition to the SF-phase. Then, we have again two AFMR modes. The upper one will turn out to be the out-of-plane mode and the lower nearly field-independent one the in-plane mode. Corresponding experimental data are shown in Fig. 3.17 for Rb_2MnCl_4 which is another easy-axis antiferromagnet [80S2] like K_2MnF_4 and Rb_2MnF_4.

AFMR measurements with frequencies 8–250 GHz and magnetic fields up to 7 T have been performed on Rb_2MnCl_4 not only by the usual method, namely sweeping the magnetic field at fixed frequency, but also by sweeping the frequency at fixed magnetic field employing tunable backwave oscillators [91G1, 92G1]. A remarkable feature in Fig. 3.17 is that at $H_0 = 0$ a splitting is observed into two AFMR modes (cf. insert in Fig. 3.17). This is in contradiction to Eq. 3.9 and the spin-wave considerations below will have to take this into account. The AFMR data in Fig. 3.17 clearly reflect the transition from the antiferromagnetic to the spin-flop phase as shown schematically in Fig. 3.16. The mechanism of this transition is easily understood by considering the static energy density of the AF-phase with a term $\chi_\parallel H_0^2$ describing the magnetization in the AF-phase

$$u(\mathrm{AF}) = -H_E M_{subl} + H_A M_{subl} - \tfrac{1}{2}\chi_\parallel H_0^2$$

and that of the SF-phase

$$u(\mathrm{SF}) = -H_E M_{subl} - \tfrac{1}{2}\chi_\perp H_0^2 \qquad \text{with} \qquad \chi_\perp = 2M_{subl}/(2H_E - H_A)$$

For H_0 smaller than the spin-flop critical field H_{SF}, u(AF) is lower than u(SF). For $H_0 > H_{SF}$, on the other hand, the SF-phase is energetically more favourable because of $\chi_\perp > \chi_\parallel$. Since $\chi_\parallel$ is rather small at low temperatures ($T << T_N$), it is often neglected in the analysis of AFMR experiments. But it is usually included for discussing the spin-flop transition which is characterized by u(AF) = u(SF) [67B1]:

$$(\chi_\perp - \chi_\parallel)\, H_{SF}^2 = 2M_{subl}\, H_A \qquad (3.38)$$

where M_{subl}, $\chi_\perp$ and $\chi_\parallel$ depend on the temperature. Eq. 3.38 can alternatively be written as

$$(1 - \chi_\parallel / \chi_\perp)\, H_{SF}^2 = 2H_E H_A - H_A^2 \qquad (3.38a)$$

In many treatments of AFMR, $M(H_{0z}, T) = \chi_\parallel H_0$ is also included in the spin-wave calculation for ν_{AFMR} (see for example [63F1, 94H]). The result is similar to Eq. 3.9. Neglecting terms with $(\chi_\parallel H_0)^2$, $\nu_{AFMR}^\pm$ is slightly modified as compared to Eq. 3.9

$$\nu_{AFMR}^\pm = (\gamma / 2\pi)\, [2H_E H_A + H_A^2)^{1/2} \mp (1 - \chi_\parallel / \chi_\perp)^{1/2} H_{0z}]$$

Both, Eq. 3.9 and this modified form, show that the lower Zeeman branch (cf. Fig. 3.17) tends to zero near $H_{0z} = H_{SF}$. For $T << T_N$, we may neglect $\chi_\parallel$ not only for ν_{AFMR} but also for H_{SF}

$$H_{SF} = (2H_E\, H_A) - H_A^2)^{1/2} \qquad (3.39)$$

Eq. 3.39 is more compatible to Eq. 3.9 and many similar equations than Eq. 3.38. It means that ν_{AFMR}^+ of the lower branch vanishes for $H_{0z} = H_{SF}$ if H_A^2 can be neglected in comparison to $2H_E H_A$. With $H_E = 87.09$ T and $H_A = 0.175$ T for Rb_2MnCl_4 (cf. Table 5), we can calculate this not quite vanishing ν_{AFMR}^+ by means of Eqs. 3.9 and 3.39 and obtain $\nu_{AFMR} = 155$ MHz. In Fig. 3.17, the frequency of this branch is reduced considerably but is definitely not as small as 155 MHz at the spin-flop transition. This is possibly due to relaxational modes which have been considered the reason for similar effects in the AFMR of $YFeO_3$ and $DyFeO_3$ [87B2, 88B1]. But experimental shortcomings could also be responsible for this behaviour.

For the magnetic (H_0, T) phase diagram (schematically in Fig. 3.16), theory employing renormalization-group methods [74F3, 74N3, 75F1, 76K2, 76P3, 77N5] predicts for a 3D uniaxial Heisenberg antiferromagnet a discontinuous transition from the AF- to the SF-phase if $\boldsymbol{H_0}$ is accurately aligned parallel to the c-axis. Further, a bicritical point (BCP) is predicted where the first order spin-flop line meets the lines of second order phase transitions to the PM-phase. The AF-phase shows a one spin-component ordering with Ising-like critical behaviour (cf. Sects. 4.1.2–4.1.5). In the SF-phase, the ordering is due to two spin-components with XY-like behaviour (cf. Sect. 4.1.8). For a 2D uniaxial Heisenberg antiferromagnet, theory predicts the BCP to be at $T = 0$. But the Ising-like anisotropy and/or a small interplanar coupling (cf. Sect. 3.1.2) which cause a 3D long-range order may move the BCP to finite temperatures [93C2]. Experimentally, the phase diagram of Rb_2MnCl_4 [86R1, 86R2] was studied by neutron diffraction and the results are depicted in Fig. 3.18. The critical point ($H_{C.P.} = 5.55$ T, $T_{C.P.} = 50.5$ K) is a bifurcation point and not, as expected, a BCP. The same kind of bifurcation point has been found for K_2MnF_4 [82J1, 82M4]. As mentioned above, the spin-flop transition is expected to be discontinuous for a correct alignment $\boldsymbol{H_0} \parallel \boldsymbol{c}$. But all experimental results, from AFMR and neutron scattering, on Rb_2MnCl_4, on K_2MnF_4 and also on Rb_2MnF_4 (cf. Fig. 3.17 and [82J1, 82M4, 86R1, 86R2, 91G1, 92G1, 93C2] show a considerable width of the spin-flop transition. This has led to the conclusion that the spin-flop transition is continuous in these 2D compounds, and de Jongh and de Groot assumed this to be principally the case on the basis of a 2D Heisenberg model with a weak uniaxial anisotropy [85G2, 85J1, 86G1, 86J2, 90G3]. But it should also be noted that the transition will be continuous if there is a misorientation of the external $\boldsymbol{H_0}$ with respect to the c-axis larger than $\psi \approx H_A / 2H_E$ [69R]. For a clarification of these problems, Cowley et al. have determined also the phase diagram of Rb_2MnF_4 by neutron diffraction [88C3, 93C2]. It exhibits the expected BCP (see Fig. 3.19) as it was found in a number of 3D uniaxial antiferromagnets, for example, in MnF_2 [76S4, 79K6]. The theoretical curves in the phase diagram for Rb_2MnF_4 (Fig. 3.19) are calculated by means of Eq. 3 in [93C2] with the optimum fit value $2\pi\rho_s = 434.7$ K. The actual value $2\pi\rho_s = 273$ K is only reasonably consistent with the experimental data. In this theory [75F2, 78K3, 93C2], the BCP is located at $T = 0$, but along the spin-flop transition, the two theoretical lines are so close together that they cannot be distinguished in Fig. 3.19. As a further activity in this field, new studies on Rb_2MnCl_4 [96K, 98K1] were recently performed by Monte Carlo simulation and by neutron diffraction. The calculated data clearly exhibit a BCP. The experimental data indicate bicritical behaviour but more data are needed for a definitive answer to this question.

Turning now to the detailed explanation of the AFMR data of Rb_2MnCl_4 in Fig. 3.17, a Hamiltonian is introduced which contains not only the exchange interaction and the out-plane anisotropy as in Eq. 3.2 but also in-plane anisotropy terms of tetragonal symmetry and of orthorhombic symmetry:

$$\mathcal{H} = -2J \sum_{\langle i,j\rangle} \boldsymbol{S}_i \boldsymbol{S}_j - \sum_i \left[D S_{i,z}^2 - 6e\, S_{i,x}^2\, S_{i,y}^2 \mp E\,(S_{i,x}^2 - S_{i,y}^2)\right] - g\mu_B \boldsymbol{H_0} \sum_i \boldsymbol{S}_i \tag{3.40}$$

where D, E and e have the same meaning as in Eqs. 3.34 and 3.35. Analogous to K_2FeF_4 with $+D\,S_{i,z}^2$ [82T1], the out-of-plane anisotropy of Rb_2MnCl_4 is written here in the form $-D\,S_{i,z}^2$ which has also been used for K_2NiF_4 [74N1] and for K_2MnF_4 [76R2, 90G3] although in the latter the dominant contribution originates not from a single-ion anisotropy but from magnetic dipolar interactions. The term with orthorhombic symmetry is again assumed to originate from the orthorhombic symmetry of the AF-phase (cf. Fig. 2.2) because of an orthorhombic distortion resulting probably from magnetostrictive effects (cf. Sect. 2.1.2). As in K_2FeF_4, E will decrease with increasing temperature and vanish at T_N. For the term with E, the upper sign refers to one of the two domains and the lower sign to the other one. It has been shown in Sect. 2.1.2 that two domains (Acam and Bbcm) exist in the antiferromagnetic state (cf. Fig. 2.2). For magnetic resonance, i.e. for the treatment of spin waves near $\boldsymbol{q} = 0$, it is advantageous to convert Eq. 3.40 to an energy density u with macroscopic magnetizations $\boldsymbol{M_a}$ and $\boldsymbol{M_b}$ of the two sublattices [66K, 83G1]:

$$\begin{aligned} u = {} & \frac{H_E}{M_S} \boldsymbol{M_a} \boldsymbol{M_b} - \frac{H_A}{2M_S}(M_{a,z}^2 + M_{b,z}^2) + \frac{\hat{H}_A}{2M_S^3}(M_{a,x}^2\, M_{a,y}^2 + M_{b,x}^2\, M_{b,y}^2) \\ & \pm \frac{\tilde{H}_A}{2M_S}(M_{a,x}^2 - M_{a,y}^2 + M_{b,x}^2 - M_{b,y}^2) - (\boldsymbol{H_0} + \boldsymbol{h})\,(\boldsymbol{M_a} + \boldsymbol{M_b}) \end{aligned} \tag{3.41}$$

The relations between Eqs. 3.40 and 3.41 are as follows:

$$g\mu_B H_E = 2zS|J| \quad g\mu_B H_A = 2DS \quad g\mu_B \hat{H}_A = 12eS \quad g\mu_B \tilde{H}_A = -4\,ES$$

In the Zeeman term, $\boldsymbol{H_0}$ is again the applied static magnetic field and $\boldsymbol{h} \sim \exp[-i(\omega t - \boldsymbol{q}\,\boldsymbol{r})]$ the oscillating magnetic field of the microwave or millimeter wave where the wavevector $\boldsymbol{q}$ of the electromagnetic wave is very small and practically at the center of the Brillouin zone, see Fig. 3.14, where also optical data are shown in the center of the Brillouin zone, in addition to neutron data. In Eq. 3.41, M_S is the (static) sublattice magnetization at low temperatures $M_{subl}(0) = M_0(1 - \Delta_0 S/S)$. The above considerations for K_2MnF_4 etc. have shown that linear spin-wave theory is sufficient for the treatment of magnetic excitations at low temperatures.

The calculations for magnetic resonance under various conditions are now performed using classical torque equations instead of the procedure outlined in Eqs. 3.3–3.6 and 3.9. The equation of motion employed in this context is the socalled Bloch-Bloembergen equation (Eq. 59.18 in [66K]) which is an adaption of the Bloch equations for nuclear magnetic resonance (see for example: [78S5, 81G2]) to ferromagnetic and antiferromagnetic resonance by Bloembergen [50B]:

$$\mathrm{d}\boldsymbol{M}_\mu / \mathrm{d}t = \gamma\,(\boldsymbol{M}_\mu \times \boldsymbol{H}_{\mu,\mathrm{eff}}) - \Lambda\,(\boldsymbol{M}_\mu - \boldsymbol{M}_{\mu,0}) \qquad \mu = \mathrm{a, b} \tag{3.42}$$

with the gyromagnetic ratio γ, the effective magnetic fields

$$\boldsymbol{H}_{\mu,\mathrm{eff}} = -\,[\partial u/\partial M_{\mu,\mathrm{x}},\ \partial u/\partial M_{\mu,\mathrm{y}},\ \partial u/\partial M_{\mu,\mathrm{z}}]$$

and a phenomenological damping constant Λ. The sublattice magnetizations are divided into a static and an oscillating (precessing) part

$$\boldsymbol{M}_\mathbf{a} = \boldsymbol{M}_\mathbf{a,0} + \boldsymbol{m}_\mathbf{a} \qquad \boldsymbol{M}_\mathbf{b} = \boldsymbol{M}_\mathbf{b,0} + \boldsymbol{m}_\mathbf{b}$$

and, in the sense of a linear response theory, products of m_a and m_b and h are neglected for the calculations based on Eq. 3.42. For performing magnetic resonance under various conditions, the static magnetic field may be applied in arbitrary directions with respect to the crystalline axes [(x, y, z) system], described by a polar angle ψ and an azimuthal angle β:

$$\boldsymbol{H}_\mathbf{0} = H_0(\sin\psi\cos\beta,\ \sin\psi\sin\beta,\ \cos\psi) \tag{3.43}$$

For $\boldsymbol{M}_\mathbf{a}$ and $\boldsymbol{M}_\mathbf{b}$, similar angles of rotation are introduced where $m_\mathrm{a}^{(1)}$, $m_\mathrm{a}^{(2)}$, $m_\mathrm{b}^{(1)}$, and $m_\mathrm{b}^{(2)}$ are the two precessing components perpendicular to $\boldsymbol{M}_\mathbf{a,0}$ and $\boldsymbol{M}_\mathbf{b,0}$, resp.:

$$\begin{aligned} M_{\mu,\mathrm{x}} &= [M_{\mu,0}\sin\theta_\mu\,\cos\delta_\mu + m_\mu^{(1)}\cos\theta_\mu\,\cos\delta_\mu - m_\mu^{(2)}\sin\delta_\mu\,] \\ M_{\mu,\mathrm{y}} &= [M_{\mu,0}\sin\theta_\mu\,\sin\delta_\mu + m_\mu^{(1)}\cos\theta_\mu\,\sin\delta_\mu + m_\mu^{(2)}\cos\delta_\mu\,] \\ M_{\mu,\mathrm{z}} &= [M_{\mu,0}\cos\theta_\mu - m_\mu^{(1)}\sin\theta_\mu\,] \end{aligned} \tag{3.44}$$

where again $\mu = \mathrm{a, b}$ and where $M_{\mathrm{a},0} = +M_\mathrm{S}$ and $M_{\mathrm{b},0} = -M_\mathrm{S}$ neglecting $\chi_\parallel$ and the resulting magnetization at low temperatures where $\chi_\parallel \approx 0$. Setting the oscillating components $\boldsymbol{m}_\mathbf{a} = \boldsymbol{m}_\mathbf{b} = \boldsymbol{h} = 0$ and inserting Eqs. 3.43 and 3.44 into Eq. 3.42, the angles θ_a, θ_b, δ_a, and δ_b are determined from the equilibrium conditions, i.e. vanishing torque for the static components of $\boldsymbol{M}_\mathbf{a}$ and $\boldsymbol{M}_\mathbf{b}$. Using these equilibrium directions, Eq. 3.42 yields an inhomogeneous system of linear equations for $m_\mathrm{a}^{(1)}$, $m_\mathrm{a}^{(2)}$, $m_\mathrm{b}^{(1)}$, and $m_\mathrm{b}^{(2)}$ which can be solved to obtain the dynamic magnetic susceptibility χ_dyn of the system:

$$\boldsymbol{m} = \boldsymbol{m}_\mathbf{a} + \boldsymbol{m}_\mathbf{b} = \boldsymbol{\chi}_\mathbf{dyn}\,\boldsymbol{h} \tag{3.45}$$

where $\boldsymbol{m}_\mathbf{a}$ and $\boldsymbol{m}_\mathbf{b}$ are only the oscillating components from Eq. 3.44 and where $\boldsymbol{\chi}_\mathbf{dyn}$ is a tensor. Since $\boldsymbol{h}$ is the magnetic field of an electromagnetic wave, there also exist the other fields of such a wave

$$\boldsymbol{e}, \boldsymbol{d}, \boldsymbol{b} \sim \exp\,[-\,\mathrm{i}(\omega\,t - \boldsymbol{q}\,\boldsymbol{r})]$$

which are related to each other by Maxwell's equations. Using $\boldsymbol{b} = \mu_0(1 + \boldsymbol{\chi}_\mathbf{dyn})\,\boldsymbol{h}$ and $\boldsymbol{d} = (\boldsymbol{\varepsilon})\ \boldsymbol{e}$, elimination of $\boldsymbol{e}$ yields the following equation for $\boldsymbol{h}$ [83G1]:

$$\frac{c^2}{\omega^2}\,\boldsymbol{q} \times [(\boldsymbol{\varepsilon})^{-1}\,(\boldsymbol{q} \times \boldsymbol{h})] = -\,(\mathbf{1} + \boldsymbol{\chi}_\mathbf{dyn})\,\boldsymbol{h} \tag{3.46}$$

This is a homogeneous set of linear equations for the components of $\boldsymbol{h}$ which has nontrivial solutions only if the determinant of the coefficients vanishes. After inserting $\boldsymbol{q}$ which is mostly $\boldsymbol{q} = (0, 0, q)$ for the layered structures, the corresponding secular equation is used to determine the propagation constants of the electromagnetic wave in the magnetic material, i.e. the refractive index n and the extinction coefficient k (cf. Sect. 2.2.1)

$$\frac{c^2 q^2}{\omega^2} = (n + \mathrm{i}\, k)^2 \tag{3.47}$$

In these solutions are also included purely electromagnetic waves, the interaction of electromagnetic waves and AFMR modes (magnetic polaritons, see Sect. 3.2.4 below) and other propagation effects [83G1].

Let us now consider for the discussion of the AFMR data of $\mathrm{Rb_2MnCl_4}$ at first the simplest case: $\boldsymbol{H_0} \parallel \boldsymbol{c}$ ($\psi = 0$) and $H_0 < H_{\mathrm{SF}}$. Then the equilibrium conditions yield $\theta_{\mathrm{a}} = \theta_{\mathrm{b}} = 0$ and $\delta_{\mathrm{a}} = \delta_{\mathrm{b}} = 0$. Let us further assume $\widetilde{H}_{\mathrm{A}} = 0$ and also $\Lambda = 0$ although $\Lambda \neq 0$ is needed in practical calculations for simulating the linewidth. The solution of Eq. 3.42 is then for a microwave or millimeter wave source with frequency ν ($\omega \rightarrow 2\pi\nu$)

$$\boldsymbol{\chi}_{\mathbf{dyn}} = \begin{pmatrix} \chi^{\mathrm{xx}} & \chi^{\mathrm{xy}} & 0 \\ -\chi^{\mathrm{xy}} & \chi^{\mathrm{xx}} & 0 \\ 0 & 0 & 0 \end{pmatrix} \tag{3.48}$$

As the final result according to Eq. 3.46, two circularly polarized modes are obtained with the propagation constants

$$(n + \mathrm{i}\, k)^2 = \varepsilon_\perp\, (\chi^{\mathrm{xx}} \pm \mathrm{i}\, \chi^{\mathrm{xy}}) \tag{3.49}$$

where
$$(\chi^{\mathrm{xx}} \pm \mathrm{i}\, \chi^{\mathrm{xy}}) = \frac{2\gamma^2 M_{\mathrm{S}} H_{\mathrm{A}}}{\gamma^2 [2 H_{\mathrm{E}} H_{\mathrm{A}} + H_{\mathrm{A}}^2] - [2\pi\nu \pm \gamma H_0]^2}$$

and $\varepsilon_\perp$ is the dielectric constant for $\boldsymbol{e} \perp \boldsymbol{c}$. The resonance frequency ν_{AFMR} in Eq. 3.49 for which the denominator vanishes is the same as that obtained from linear spin-wave theory in Eq. 3.9 and in Eq. 3.38 for $\chi_{\parallel} = 0$. Thus, this classical treatment of the spin waves at low temperatures is completely equivalent to the linear spin-wave theory sketched above (Eqs. 3.2–3.6, 3.9). Of course, our first simple approach with $\widetilde{H}_{\mathrm{A}} = 0$ cannot explain the splitting for $H_0 = 0$. Moreover, a comparison with the experimentally obtained AFMR absorption curves for $H_0 = 0$ (cf. Fig. 3.20) shows that these transmission curves cannot be due to circularly polarized modes since the transmission cannot be lower than 50% ($T = 0.5 = 10^{-0.301}$) when circularly polarized modes are excited by linearly polarized light. In Fig. 3.20, the transmission decreases to $T \approx 10^{-0.9}$ at 4.5 K. Thus we have to include $\widetilde{H}_{\mathrm{A}} \neq 0$ into our considerations. Then we obtain for $H_0 = 0$ from Eq. 3.42

$$\boldsymbol{\chi}_{\mathbf{dyn}} = \begin{pmatrix} \chi^{\mathrm{xx}} & 0 & 0 \\ 0 & \chi^{\mathrm{yy}} & 0 \\ 0 & 0 & 0 \end{pmatrix} \tag{3.50}$$

with

$$\chi^{\mathrm{xx}} = \frac{2\gamma^2 M_{\mathrm{S}} (H_{\mathrm{A}} - \widetilde{H}_{\mathrm{A}})}{\gamma^2\, [2 H_{\mathrm{E}} (H_{\mathrm{A}} + \widetilde{H}_{\mathrm{A}}) + H_{\mathrm{A}}^2 - \widetilde{H}_{\mathrm{A}}^2] - (2\pi\nu)^2} \qquad \chi^{\mathrm{yy}} = \frac{2\gamma^2 M_{\mathrm{S}} (H_{\mathrm{A}} + \widetilde{H}_{\mathrm{A}})}{\gamma^2\, [2 H_{\mathrm{E}} (H_{\mathrm{A}} - \widetilde{H}_{\mathrm{A}}) + H_{\mathrm{A}}^2 - \widetilde{H}_{\mathrm{A}}^2] - (2\pi\nu)^2}$$

Eq. 3.50 indicates that the modes for $H_0 = 0$ can be excited with linearly polarized light, the first with h_x and the second with h_y. The ν^2_{AFMR} resulting from χ^{xx} and χ^{yy} (denominator → 0) differ by $\pm 2H_{\mathrm{E}}\tilde{H}_{\mathrm{A}}$ and can thus account for the observed splitting. That both modes are measured with one linear polarization (h_x or h_y) originates from the existence of the two domains with an interchange of the x- and y-directions between them (cf. Fig. 2.2 in Sect. 2.1.2). The different intensities of the two absorption lines in Fig. 3.20 reflect the different occurrence of the two domains. This occurrence and thus the intensities can be changed by performing a spin-flop cycle, i.e. increasing H_0 at 4.2 K above H_{SF} and lower it again to zero [92G1]. We note finally that the exchange field H_{E} is known from inelastic neutron scattering experiments [80S2] and that the anisotropy fields H_{A} and $\tilde{H}_{\mathrm{A}}$ can be determined from the frequencies of the two AFMR modes for $H_0 = 0$ which have been measured by sweeping the frequency. And the solid curves in Fig. 3.17 (ν_{AFMR} versus $\boldsymbol{H_0} \parallel \boldsymbol{c}$) have in principle been calculated with these values (cf. Table 5) by means of Eq. 3.50. But in order to obtain the continuous character of the spin-flop transition by this simple spin-wave theory, the curves in Fig. 3.17 have actually been calculated for H_0 rotated away from the c-axis by an angle $\psi = 0.3°$. For $H_0 \neq 0$, $\boldsymbol{\chi_{\mathrm{dyn}}}$ has also off-diagonal elements and the modes are elliptically polarized. And for magnetic fields $H_0^2 > (2H_{\mathrm{E}}\tilde{H}_{\mathrm{A}})^2/(2H_{\mathrm{E}}H_{\mathrm{A}})$, the influence of $\tilde{H}_{\mathrm{A}}$ is greatly diminished and the modes approach more and more the circularly polarized type.

Next let us discuss the SF-phase with $H_0 > H_{\mathrm{SF}}$ and still $\boldsymbol{H_0} \parallel \boldsymbol{c}$ ($\psi = 0$) with the spins flopped to the basal plane ($\theta_a \approx \pi/2$ and $\theta_b \approx \pi/2$). Then the classical spin-wave theory outlined above (Eqs. 3.42–3.46) yields for the upper mode, the out-of-plane mode, a frequency

$$\nu_{\mathrm{AFMR,\ out\text{-}of\text{-}pl.}} = (\gamma/2\pi)\,[\,H_0^2 - 2\,H_{\mathrm{E}}\,(H_{\mathrm{A}} + \tilde{H}_{\mathrm{A}})\,]^{1/2} \tag{3.51a}$$

where products of the anisotropy fields like $H_{\mathrm{A}}^2, H_{\mathrm{A}}\hat{H}_{\mathrm{A}}, H_{\mathrm{A}}\tilde{H}_{\mathrm{A}}$ have been neglected. This mode is elliptically polarized and can be excited with h_x or h_y. The second mode, the in-plane mode, is nearly independent of H_0 with a frequency (also products of H_{A}, $\hat{H}_{\mathrm{A}}$ and $\tilde{H}_{\mathrm{A}}$ neglected)

$$\nu_{\mathrm{AFMR,\ in\text{-}plane}} = (\gamma/2\pi)\,[2H_{\mathrm{E}}\,(\hat{H}_{\mathrm{A}} - 2\tilde{H}_{\mathrm{A}})]^{1/2} \tag{3.51b}$$

which can only be excited in an unusual longitudinal configuration with h_z, i.e. with $\boldsymbol{h} \parallel \boldsymbol{H_0}$ [63F2], and only by sweeping the frequency. According to Eq. 3.51b, this mode is independent of H_0. But it can only be called nearly field-independent since it exhibits a dependence on H_0 on a much larger scale. In addition to the spin-flop transition, there is another field-induced transition in antiferromagnets, namely the transition to the PM-phase for $H_0 \approx 2H_{\mathrm{E}}$ [64A, 66K, 68F2, 85G2, 85J1, 86G1] where as the typical instability at a phase transition $\nu_{\mathrm{AFMR,\ in\ plane}} \to 0$. With $H_0 \approx 2H_{\mathrm{E}}$, the external magnetic field is strong enough to overcome the antiferromagnetic exchange interaction and to align all spins parallel to the field. In the antiferromagnets like K_2MnF_4, K_2FeF_4, Rb_2MnCl_4 etc., the exchange fields H_{E} are so large that this transition from the SF-phase to the PM-phase is experimentally inaccessable. In case of Rb_2MnCl_4 as an example, we would need $H_0 = 2H_{\mathrm{E}} = 174$ T to observe the transition to the PM-phase. However, in Cu-compounds with a weak interlayer antiferromagnetic exchange coupling (cf. Sect. 3.2.1), both the spin-flop transition and the transition to the PM-phase can be observed at moderate magnetic fields (see Sect. 3.1.8 below) but not in Rb_2MnCl_4. For this compound, we return to our aim to determine the anisotropy fields from AFMR data. Eqs. 3.50 and 3.51b illustrate that both in-plane anisotropy terms in Eq. 3.40 are needed for explaining and analysing the experimental data in Fig. 3.17. The values for the anisotropy fields determined in the way sketched above are (cf. Table 5 and [91G2])

$$g\mu_{\mathrm{B}}H_{\mathrm{A}} = 0.1634\ \mathrm{cm}^{-1} \qquad g\mu_{\mathrm{B}}\hat{H}_{\mathrm{A}} = 0.014\ \mathrm{cm}^{-1} \qquad g\mu_{\mathrm{B}}\tilde{H}_{\mathrm{A}} = 0.0034\ \mathrm{cm}^{-1}$$

The out-of-plane anisotropy field is the largest one and the in-plane ones are smaller by at least one order of magnitude as expected for a Mn-compound. The corresponding data for K_2FeF_4 with dominating single-ion anisotropy

$$g\mu_B H_A = 11.96\ \mathrm{cm}^{-1} \qquad g\mu_B \widetilde{H}_A = 2.72\ \mathrm{cm}^{-1}$$

are considerably larger than the values for Rb_2MnCl_4.

Finally, Rb_2MnCl_4 has also been studied by AFMR for $\boldsymbol{H_0} \perp \boldsymbol{c}$ ($\psi = \pi/2$). The data are presented in Fig. 3.21 for $\beta = 0°$, 24° and 45° (cf. Eq. 3.43). In the simple approximation of Eq. 3.9 with $\widetilde{H}_A = 0$, the results should be independent of β. But such a dependence is observed in Fig. 3.21 and shown in more detail in Fig. 3.22 as field H_{res} at resonance versus β for $\nu = 161$ GHz. These experimental data in Fig. 3.22a look like a splitting of the AFMR mode although there cannot be such a splitting in a two-sublattice antiferromagnet. The model calculation in Fig. 3.22b using the method introduced above (Eqs. 3.40–3.46) presents the solution of this problem. For each domain, the orthorhombic anisotropy field $\widetilde{H}_A$ causes H_{res} to vary with β forming extrema at $\beta = 0°$, 90°, 180°, 270° etc. As explained in context with Eqs. 3.40, 3.41 and 3.50, the interchange of the x- and y-axes for the two domains has the effect that $\widetilde{H}_A$ acts positive for domain 1 and negative for domain 2 (cf. Fig. 3.22b) and the experimental data in Fig. 3.22a result from the simultaneous observation of the two domains and not from a splitting of the AFMR mode. The curves in Fig. 3.21 calculated by means of the classical spin-wave theory include also both domains to achieve a good agreement with the experimental data. This β-dependence of H_{res} for $\boldsymbol{H_0} \perp \boldsymbol{c}$ has not only been observed for Rb_2MnCl_4 but also for K_2MnF_4 [83R3], for $(CH_3NH_3)MnCl_4$ [92G1] and for the mixed crystals $(CH_3NH_3)Mn_{0.91}Cd_{0.09}Cl_4$ [83R3]. In the AFMR studies of Rb_2MnCl_4 with $\boldsymbol{H_0} \perp \boldsymbol{c}$, the upper mode depends strongly on H_0 and can be excited in the usual way by $\boldsymbol{h} \perp \boldsymbol{H_0}$ while the nearly field-independent mode is observed only with $\boldsymbol{h} \parallel \boldsymbol{H_0}$. This was also reported by Zvyagin et al. [85Z2] for AFMR experiments on $[NH_3(CH_2)_3NH_3]MnCl_4$ with $\boldsymbol{H_0}$ parallel to the hard axis. Thus, antiferromagnetic resonance under various conditions is a powerful tool for determining all the different anisotropy constants of a magnetic system while the exchange parameter can better be determined by measuring $\omega(\boldsymbol{q})$ with neutron inelastic scattering. For obtaining all possible information from AFMR, it is essential to perform spin-wave calculations along the lines sketched above and to evaluate the selection rules for the different AFMR modes. Otherwise the results will be incomplete as in a recent AFMR study of Rb_2MnCl_4 [94H]. For example, the nearly field-independent modes are missing in the SF-phase and for $\boldsymbol{H_0} \perp \boldsymbol{c}$. Consequently, only the largest anisotropy constant ($\mathrel{\hat{=}} H_A$) has been determined in this study.

9.12.3.1.7 Canted Antiferromagnets, Weak Ferromagnetism

Some easy-axis antiferromagnets like $(CH_3NH_3)_2MnCl_4$ and $(C_3H_7NH_3)_2MnCl_4$ and also easy-plane antiferromagnets like $(CH_3NH_3)_2FeCl_4$ exhibit a canting of the spins away from the preferred spin direction and a weak ferromagnetism. This behaviour can either be caused by single-ion anisotropy in combination with tilting of the $MnCl_6$ octahedra in the low temperature phases of the above mentioned compounds or by Dzyaloshinskii-Moriya interaction (DMI) or antisymmetric exchange [57D, 58D, 60M, 63M]. A numerical analysis for these Mn-compounds [79G6, 90A1] led to the conclusion that the single-ion anisotropy mechanism is about an order of magnitude too small and that the DMI is actually the origin of the spin canting and the small ferromagnetic moment. In the canted ferromagnet Rb_2CrCl_4 on the other hand, the canting is due to the single-ion anisotropy in connection with the collective Jahn-Teller effect (cf. Sects. 2.1.3 and 3.2.2). For our further considerations, we will start from a Hamiltonian with isotropic intralayer exchange of the Heisenberg-type and with antisymmetric exchange (DMI) between nearest neighbours within the layers [79G6, 90A1]. In addition, the Hamiltonian $\mathcal{H}$ contains a Zeeman term and, for more clarity, only the out-of-plane anisotropy, analogous to the Hamiltonians with DMI used for other materials [67C2, 72Y4]

$$\mathcal{H} = -2J \sum_{\langle i,j \rangle} \boldsymbol{S}_i \boldsymbol{S}_j + 2\boldsymbol{D}_{DM} \sum_{\langle i,j \rangle} (\boldsymbol{S}_i \times \boldsymbol{S}_j) - D \sum_i S_{i,z}^2 - g\mu_B \boldsymbol{H}_0 \sum_i \boldsymbol{S}_i \tag{3.52}$$

where $\boldsymbol{D}_{\mathbf{DM}} = (D_{DM,x}, D_{DM,y}, D_{DM,z})$ is a constant vector and where all other terms have the same meaning as in Eq. 3.40. The antisymmetric exchange constant $|\boldsymbol{D}_{\mathbf{DM}}|$ is usually much smaller than the constant J of the isotropic symmetric exchange. Moriya [60M, 63M] has pointed out that $|\boldsymbol{D}_{\mathbf{DM}}|$ may be estimated from the following relation

$$|\boldsymbol{D}_{\mathbf{DM}}| \approx \left(\frac{g-2}{g}\right) J \tag{3.52a}$$

With respect to the symmetry of the system, the isotropic exchange and the Zeeman terms are invariant under all symmetry operations. The out-of-plane anisotropy term reflects a uniaxial crystal symmetry. And finally, the term for the antisymmetric exchange is subject to severe symmetry restrictions [57D, 58D]. It cannot occur in a compound A_2MX_4 if between two magnetic M^{2+}-ions is a center of inversion symmetry in the chemical unit cell disregarding the spins and their orientation [60M, 63M]. That means the site symmetry of the X^--ion must not contain the inversion. Then, the vector $\boldsymbol{D}_{\mathbf{DM}}$ is perpendicular to the plane through the two M^{2+}-ions and the X^--ion [83N4, 86C2]. Some results of these and of more detailed group theoretical considerations are compiled below for space groups relevant for perovskite-type layer structures. These are confined to simple two-sublattice antiferromagnets

1) tetragonal symmetry (I4/mmm): $D_{DM,x} = D_{DM,y} = D_{DM,z} = 0$

2) orthorhombic symmetry (Acam, Bbcm): $D_{DM,x} = D_{DM,y} = 0$, $D_{DM,z} \neq 0$

3) monoclinic symmetry a) $A2_1/b11$: $D_{DM,x} = 0$, $D_{DM,y} \neq 0$, $D_{DM,z} \neq 0$
b) $B12_1/a1$: $D_{DM,x} \neq 0$, $D_{DM,y} = 0$, $D_{DM,z} \neq 0$

For easy-axis antiferromagnets with $\boldsymbol{M}_{\mathbf{subl}}$ parallel or antiparallel to the c-axis, only $D_{DM,x}$ or $D_{DM,y}$ will effect a canting of the spins away from the c-axis and a weak ferromagnetic magnetization M_y or M_x respectively. In the SF-phase of easy-axis antiferromagnets, however, $D_{DM,z}$ may possibly cause a spin canting. But in the structures Acam and Bbcm of Rb_2MnCl_4, for example, $D_{DM,z}$ will be rather small according to the extremely small orthorhombic distortion. For easy-plane antiferromagnets like K_2FeF_4, $D_{DM,x}$ or $D_{DM,y}$ with $\boldsymbol{D}_{\mathbf{DM}} \perp \boldsymbol{M}_{\mathbf{subl}}$ can effect a spin canting away from the easy plane resulting in a weak ferromagnetic M_z [83N4]. From the rules above, DMI and spin canting will not occur in compounds with the tetragonal structure I4/mmm in their PM-phase and also for easy-axis antiferromagnets like K_2MnF_4, Rb_2MnF_4, K_2CoF_4 and Rb_2MnCl_4 in their AF-phase with the structure Acam and Bbcm. The same is true for easy-plane antiferromagnets like K_2FeF_4 and Rb_2FeF_4 with the structure Abma or Bmab. As discussed in detail in Sects. 2.1 and 2.2, the perovskite-type layer compounds with organic A^+-ions undergo several structural phase transitions between room temperature and their Néel-temperature connected with an ordering of the $(C_nH_{2n+1}NH_3)^+$-ions and a tilting of the MX_6 octahedra. Therefore, the symmetry is lowered at temperatures near T_N so that the above symmetry conditions are met. For example, the Mn-compounds $(C_nH_{2n+1}NH_3)_2MnCl_4$ with n = 1 and n = 3 have a monoclinic structure so that spin canting and weak ferromagnetism are allowed [90A1]. In a nonstandard setting, the structures are $A2_1/b11$ or $B12_1/a1$ with monoclinic angles α or β of 92.5° and 90.2° for n = 1 and n = 3, resp., (cf. Table 2). This allows to use an orthogonal pseudo-orthorhombic coordinate system. It is further evident from structural considerations that the canting of the spins is closely related to the tilting of the $MnCl_6$ octahedra [83N4, 90A1]. Spin canting has also been reported for the compounds $(C_nH_{2n+1}NH_3)_2FeCl_4$ with n = 1 – 4 [80M4, 83N4].

As in the last section (see Eqs. 3.40 and 3.41), it is useful to convert the Hamiltonian Eq. 3.52 to a classical energy density u with the macroscopic sublattice magnetizations $\boldsymbol{M}_{\mathbf{a}}$ and $\boldsymbol{M}_{\mathbf{b}}$ of an easy-axis two-sublattice antiferromagnet with monoclinic symmetry

$$u = \frac{H_E}{M_S} \boldsymbol{M_a M_b} + \frac{H_D}{M_S} (M_{a,z}\, M_{b,x} - M_{a,x}\, M_{b,z}) - \frac{H_A}{2M_S} (M_{a,z}^2 + M_{b,z}^2) - (\boldsymbol{H_0} + \boldsymbol{h})\ (\boldsymbol{M_a} + \boldsymbol{M_b}) \qquad (3.53)$$

with the Dzyaloshinskii-Moriya field H_D which is defined as $g\mu_B H_D = 2zSD_{DM,y}$ without specifying the direction of $\boldsymbol{D_{DM}}$ in H_D. For the rest, the notation is the same as in Eq. 3.41. It follows from the group theoretical analysis above that $D_{DM,y}$ and $(\boldsymbol{M_a} \times \boldsymbol{M_b})_y$ are appropriate for A2$_1$/b11 and that for B12$_1$/a1 with $D_{DM,x} \neq 0$ alternatively $(\boldsymbol{M_a} \times \boldsymbol{M_b})_x$ has to be used in the term with H_D in Eq. 3.53. Similar rules apply to other structures. As a first step, Eq. 3.53 is used to determine the canting angle φ from the equilibrium conditions using the Bloch-Bloembergen equation Eq. 3.42 and Eq. 3.44 with $H_0 = 0$ and $\boldsymbol{m_a} = \boldsymbol{m_b} = \boldsymbol{h} = 0$. In this way, we obtain $\delta_a = \delta_b = 90°$ and $\theta_a = +\varphi$ and $\theta_b = -\varphi$ with

$$\text{tg}\ 2\ \varphi = 2H_D/(2H_E + H_A) \quad \text{or} \quad \varphi \approx H_D/2H_E \qquad (3.54)$$

The angle φ measures the canting of the spins away from the c-axis. Essentially, it depends on the ratio of the Dzyaloshinskii-Moriya field H_D and the exchange field H_E. The static components of the sublattice magnetizations are

$$\boldsymbol{M_a} = (+M_S \sin\varphi, 0, +M_S \cos\varphi) \quad \boldsymbol{M_b} = (+M_S \sin\varphi, 0, -M_S \cos\varphi) \qquad (3.55)$$

That means that the DMI or antisymmetric exchange $(\boldsymbol{M_a} \times \boldsymbol{M_b})_y$ for $D_{DM,y} \neq 0$ induces a weak ferromagnetic moment $M_x = 2M_S \sin\varphi$ parallel to the x-axis while the antiferromagnetic moment is $M_z = \pm M_S \cos\varphi$ parallel to the z- or c-axis. For $D_{DM,x} \neq 0$, on the other hand, the weak ferromagnetic moment due to $(\boldsymbol{M_a} \times \boldsymbol{M_b})_x$ would be parallel to the y-axis. Spin canting is observed experimentally either as a sharp peak at T_N in the magnetic susceptibility χ [60M, 63M] or by direct measurement of the weak ferromagnetic moment. The latter was done for $(C_3H_7NH_3)_2MnCl_4$ [79G6, 80G7, 90A1] and the experimental results were used to determine the canting angle

$$\text{tg}\ \varphi = 8.4 \cdot 10^{-4} \quad \text{or} \quad \varphi = 0.05°$$

With $H_E = 66.3$ T for $(C_3H_7NH_3)_2MnCl_4$ [79G6, 80G7], we obtain $H_D = 111$ mT according to Eq. 3.54. Also for $(CH_3NH_3)_2MnCl_4$ and $(C_nH_{2n+1}NH_3)_2FeCl_4$ with n = 1 and n = 2, the ferromagnet moment was determined [83N4, 96K]. A further aspect of the spin canting and the weak ferromagnetism is that the antisymmetric exchange interaction leads also to a splitting of the zero-field AFMR frequency. A classical spin-wave calculation by means of Eq. 3.42 using the energy density Eq. 3.53 yields for $H_0 = 0$ and for low temperatures ($\chi_{\|} \approx 0$) the following two AFMR frequencies

$$\nu_{AFMR,1} = (\gamma/2\pi)\ \sqrt{(2H_E + H_A)\, H_A} \qquad (3.56a)$$

$$\nu_{AFMR,2} = (\gamma/2\pi)\ \sqrt{(2H_E + H_A)\, H_A + (H_D)^2} \qquad (3.56b)$$

The difference between $\nu_{AFMR,1}$ and $\nu_{AFMR,2}$ and thus the splitting of the zero-field AFMR is extremely small, with $H_A = 29$ mT [81S4, 83G1] and the above values of H_E and H_D for $(C_3H_7NH_3)_2MnCl_4$, we obtain $\nu_{AFMR,1} - \nu_{AFMR,2} = 0.1$ GHz. This difference has not been resolved in the experimental study. Due to the line-broadening, only one AFMR line was observed at 55.5 GHz ($\hat{=}$ 1.85 cm^{-1}, cf. Table 5). For $\boldsymbol{H_0} \parallel \boldsymbol{c}$ and $H_0 < H_{SF}$, the linear spin-wave calculation based on Eq. 3.53 yields two AFMR modes depending linearly on H_0 evolving from the zero-field AFMR as shown for Rb_2MnCl_4 in Fig. 3.17.

So far, only simple two-sublattice antiferromagnets were discussed. But there are a number of compounds with more than two magnetic ions per unit cell, e.g. four ions in the structures Pbca, Pnam and P4$_2$/ncm. These systems can be subdivided into four magnetic sublattices $\boldsymbol{M}_\mathbf{a}$, $\boldsymbol{M}_\mathbf{b}$, $\boldsymbol{M}_\mathbf{c}$, and $\boldsymbol{M}_\mathbf{d}$. Then more complicated terms like that in Eqs. 3.52 and 3.53 may become symmetry-allowed. That means there are a number of combinations of antisymmetric exchange terms which may give rise to spin canting with a weak ferromagnet $\boldsymbol{M}$ or to a hidden spin canting with opposite sign in adjacent layers. Examples of compounds of the latter kind are $(CH_3NH_3)_2CuBr_4$ [80K6, 81S5] and $[NH_3(CH_2)_2NH_3]CuBr_4$ [85R2]. In this context, it is worth noting that the four magnetic ions in four-sublattice antiferromagnets will be located in two neighbouring layers of the perovskite-type layer structures. Accordingly, there are four AFMR modes instead of the two modes in two-sublattice antiferromagnets. Two of the four are ordinary AFMR modes where the spins of the second layer precess in-phase with those in the first layer. The other two modes are usually called exchange modes with an out-of-phase precession of the spins. In case of four or more magnetic ions per unit cell it is advisable to make use of the symmetry properties of the system before deriving the frequencies of the modes by means of a classical spin-wave calculation [79B10, 85Z2, 86K6]. This will not be done in detail here. The interested reader will find derivations in the references, e.g. in [85Z2] for $[NH_3(CH_2)_3NH_3]MnCl_4$, together with the corresponding experimental data.

In Cu-compounds with strong ferromagnetic intralayer coupling and weak antiferromagnetic interlayer coupling, the origin of spin canting is usually not so much the antisymmetric exchange (cf. Eqs. 3.52, 3.53) but a special type of intralayer anisotropic exchange (cf. Eq. 3.99 in Sect. 3.2.3).

$$(H_\mathrm{D}/M_0)\,(M_{\mathrm{a,y}}\,M_{\mathrm{a,z}} - M_{\mathrm{b,y}}\,M_{\mathrm{b,z}})$$

where the parameter is usually also denoted H_D as the Dzyaloshinskii-Moriya field since the effect of this term is very similar to antisymmetric exchange (DMI) although it is in principle a different type of interaction. Moreover, the canting angle φ is usually small in Mn-compounds because of the strong antiferromagnetic intralayer coupling while it is much larger in Cu-compounds where H_D may be of the same order of magnitude as the weak interlayer antiferromagnetic coupling, and the antiferromagnetic moment and the ferromagnetic one are nearly equal for angles φ near 45°. Nevertheless it is common use in the literature to call antiferromagnetic Cu-compounds like $(C_2H_5NH_3)_2CuCl_4$ [73B5] and $(C_2H_5NH_3)_2CuBr_4$ [81S5] with spin canting due to H_D also weak ferromagnets.

9.12.3.1.8 Antiferromagnetic Cu-Compounds

In Sect. 3.1.6, it was already mentioned that more field-induced magnetic phase transitions [64A, 68F3] can be observed in antiferromagnetic Cu-compounds which will be discussed in more detail in this section. In contrast to the Mn-compounds like K_2MnF_4 and Rb_2MnCl_4 with antiferromagnetic intralayer exchange ($J < 0$ in Eq. 3.2), the isotropic intralayer interaction is ferromagnetic ($J > 0$ in Eq. 3.2) in the Cu-compounds due to the collective Jahn-Teller effect and orbital ordering as discussed in Sects. 2.1.3 and 3.2.1. But the weak isotropic interlayer exchange is antiferromagnetic ($J' < 0$ in Eq. 3.2) in some Cu-compounds. They are actually a system of ferromagnetic layers with a weak antiferromagnetic coupling [72B5, 72J3, 72J4, 73B5] and order antiferromagnetically below T_N. $(C_2H_5NH_3)_2CuCl_4$ ($T_\mathrm{N} = 10.3$ K) is an example of such compounds. Its magnetic (H_0, T) phase diagram as obtained by magnetic measurements [72J3, 72J4] is presented in Fig. 3.23. In principle, the phase diagram is similar to that of Rb_2MnCl_4 in Fig. 3.18. The great difference between Figs. 3.18 and 3.23 is that the latter for the Cu-compound shows not only the spin-flop transition but also the transition to the PM-phase at critical fields depending on the direction of H_0 with respect to the crystalline axes. $(C_2H_5NH_3)_2CuCl_4$ has the orthorhombic structure Pbca below room temperature (cf. Table 2). The easy axis is the a-axis and both, the transitions to the SF-phase and to the PM-phase, are observed with $\boldsymbol{H}_\mathbf{0}$ parallel to it. The corresponding critical fields are

for $\boldsymbol{H}_\mathbf{0} \parallel \boldsymbol{a}$
$$H_\mathrm{SF} = (2H'_\mathrm{E}\widetilde{H}_\mathrm{A} - \widetilde{H}_\mathrm{A}^2)^{1/2} \qquad H_\mathrm{PM}^\mathrm{a} = 2H'_\mathrm{E} - \widetilde{H}_\mathrm{A} \tag{3.57}$$

where H_{SF} is completely analogous to Eq. 3.39. The b-axis is the medium axis, i.e. the next preferred axis, and the critical field for the transition to the PM-phase is

for $\boldsymbol{H_0} \parallel \boldsymbol{b}$
$$H_{\mathrm{PM}}^{\mathrm{b}} = 2H'_{\mathrm{E}} + \tilde{H}_{\mathrm{A}} \tag{3.58}$$

Finally, the c-axis is the hard axis and the critical field for the transition to the PM-phase is in this case

for $\boldsymbol{H_0} \parallel \boldsymbol{c}$
$$H_{\mathrm{PM}}^{\mathrm{c}} = (g_{\mathrm{a}}/g_{\mathrm{c}})\,(2H'_{\mathrm{E}} + H_{\mathrm{A}}) \tag{3.59}$$

where the factor $(g_{\mathrm{a}}/g_{\mathrm{c}})$ accounts for the anisotropy of the g-factor. In Eqs. 3.57–3.59, H'_{E}, H_{A} and $\tilde{H}_{\mathrm{A}}$ are the interlayer exchange, the out-of-plane and the in-plane anisotropy fields, resp., which are defined in Eq. 3.96 in Sect. 3.2.3 on the basis of the Hamiltonian for the Cu-compounds (Eq. 3.69 in Sect. 3.2.1) including the anisotropic exchange terms with J_{A} and $\tilde{J}_{\mathrm{A}}$. The above critical fields are derived from the energy density u for antiferromagnetic Cu-compounds (Eq. 3.99 in Sect. 3.2.3 with $+H'_{\mathrm{E}}$ and $H_{\mathrm{D}} = 0$) by classical spin-wave theory where the anisotropy of the g-factor is removed by using an isotropic $g = g_{\mathrm{a}}$ which is advantageous for compounds like $(\mathrm{C_2H_5NH_3})_2\mathrm{CuCl_4}$ with $g_{\mathrm{a}} = g_{\mathrm{b}} \neq g_{\mathrm{c}}$ (cf. Sect. 3.2.3 in context with Eq. 3.96). If not $\boldsymbol{a}$ is the easy axis but $\boldsymbol{b}$ and $\boldsymbol{c}$ still the hard axis, $\boldsymbol{a}$ and $\boldsymbol{b}$ have to be interchanged, i.e. Eq. 3.57 for $\boldsymbol{H_0} \parallel \boldsymbol{b}$ (H_{SF}, $H_{\mathrm{PM}}^{\mathrm{b}}$) and Eq. 3.58 for $\boldsymbol{H_0} \parallel \boldsymbol{a}$ ($H_{\mathrm{PM}}^{\mathrm{a}}$). For any other configuration of easy, medium and hard axis, the crystallographic directions have to be interchanged correspondingly in Eqs. 3.57–3.59.

The numerical values of H'_{E}, H_{A} and $\tilde{H}_{\mathrm{A}}$ are compiled for $(\mathrm{C_2H_5NH_3})_2\mathrm{CuCl_4}$ in Table 5 among those of other compounds. In contrast to antiferromagnets like $\mathrm{K_2MnF_4}$ and $\mathrm{Rb_2MnCl_4}$ with $H_{\mathrm{E}} >> H_{\mathrm{A}}$, $\tilde{H}_{\mathrm{A}}$, the values of H'_{E} and H_{A} are of the same order or magnitude for Cu-compounds like $\mathrm{Rb_2CuCl_4}$ and $(\mathrm{C_2H_5NH_3})_2\mathrm{CuCl_4}$ while $\tilde{H}_{\mathrm{A}}$ is somewhat smaller. This is also evident from Fig. 3.23 where the lines of the transition to the PM-phase are relatively close to each other for $\boldsymbol{H_0} \parallel \boldsymbol{a}$ and $\boldsymbol{H_0} \parallel \boldsymbol{b}$ but that for $\boldsymbol{H_0} \parallel \boldsymbol{c}$ occurs at higher fields due to the larger value of H_{A}. The critical fields Eqs. 3.57–3.59 have successfully been applied to the analysis of the experimental data of $\mathrm{Rb_2CuCl_4}$, $\mathrm{Rb_2CuCl_3Br}$ and $\mathrm{Rb_2CuCl_2Br_2}$ [74W3]. This approach is however not quite correct for $(\mathrm{C_2H_5NH_3})_2\mathrm{CuCl_4}$ which is a covert weak ferromagnet [73B5]. That means this compound is for $H_0 = 0$ a collinear antiferromagnet but shows spin canting for $H_0 \neq 0$. This canting is caused by the special intralayer anisotropic exchange term in Eq. 3.99 with $H_{\mathrm{D}} \neq 0$ (cf. also Sect. 3.1.6). For $\boldsymbol{H_0} \parallel \boldsymbol{a}$ and $\boldsymbol{H_0} \parallel \boldsymbol{b}$, the canting is rather small and has often been neglected. But for $\boldsymbol{H_0} \parallel \boldsymbol{c}$, the influence of H_{D} is more important. For both, $\boldsymbol{H_0} \parallel \boldsymbol{b}$ and $\boldsymbol{H_0} \parallel \boldsymbol{c}$, the spins are rotated from the easy axis (a-axis) to the bc-plane with increasing H_0. The field at which this rotation is finished characterizes the transition to a canted phase. These critical fields are denoted $H_{\mathrm{CF}}^{\mathrm{b}}$ and $H_{\mathrm{CF}}^{\mathrm{c}}$. The expression for $\boldsymbol{H_0} \parallel \boldsymbol{c}$ is [73B5]

$$H_{\mathrm{CF}}^{\mathrm{c}} = (g_{\mathrm{a}}/g_{\mathrm{c}})\,[(2H'_{\mathrm{E}} + H_{\mathrm{A}})\,\tilde{H}_{\mathrm{A}} - H_{\mathrm{D}}^2] / \sqrt{\tilde{H}_{\mathrm{A}}^2 + H_{\mathrm{D}}^2} \tag{3.60}$$

which reduces to $H_{\mathrm{PM}}^{\mathrm{c}}$ in Eq. 3.59 for $H_{\mathrm{D}} = 0$. In the canted phase $(H_0 \geq H_{\mathrm{CF}}^{\mathrm{c}})$, the spins are canted, i.e. there are considerable components along the b-axis, in addition to the partial alignment parallel to $\boldsymbol{H_0} \parallel \boldsymbol{c}$. For $H_0 >> H_{\mathrm{CF}}^{\mathrm{c}}$, the canting is considerably reduced but there is no transition to a PM-phase without canting at finite fields H_0 which is discussed in more detail in Sect. 3.2.3 below.

$(\mathrm{C_2H_5NH_3})_2\mathrm{CuCl_4}$ has further been studied by magnetic resonance in its various phases including the PM-phase [76T2, 78R1, 80Y2, 81C2, 84V1, 88J1]. The corresponding expressions for ν_{AFMR} are compiled for $\boldsymbol{H_0} \parallel \boldsymbol{a}$ and $\boldsymbol{H_0} \parallel \boldsymbol{b}$ in [76T2] with $H_{\mathrm{D}} \approx 0$ neglecting the influence of spin canting which is small in these cases. Vasyukov et al. [84V1] have studied also the effect of the spin canting on ν_{AFMR}, e.g. in the SF-phase. In the PM-phase, there are two magnetic resonance modes in these antiferromagnets, the one with the smaller resonance field $H_{\mathrm{res,\,fm}}$ is the FMR-mode and the other with the larger resonance field $H_{\mathrm{res,afm}}$ and the smaller intensity is the AFMR-mode. The difference in the resonance fields is $H_{\mathrm{res,fm}} - H_{\mathrm{res,afm}} = 2H'_{\mathrm{E}}$. Both modes have been observed in magnetic resonance experiments [78R1, 80Y2]. Especially in the PM-phase, the alignment of the spins parallel to the external field causes a macroscopic magnetization in $(C_2H_5NH_3)_2CuCl_4$ and other antiferromagnetic Cu-compounds. Therefore demagnetization corrections have to be applied (cf. Eq. 3.92 and [78R1]) and the internal field H_{int} to be considered instead of the applied field H_0. These procedures will be discussed in more detail in Sect. 3.2 in context with ferromagnets and ferromagnetic resonance.

9.12.3.1.9 Co-Compounds (2D Ising Model)

Among the quasi-two-dimensional antiferromagnets with perovskite-type layer structure, the Co-compounds K_2CoF_4 and Rb_2CoF_4 are of particular interest because they are the best known realizations of the 2D Ising model for which exact solutions are available [44O, 52Y, 67F1, 90H, 90N] in contrast to the Heisenberg model. The ground state of the free Co^{2+}-ions is ^4F ($L = 3$, $S = \frac{3}{2}$) and the first excited state ^4P ($L = 1$, $S = \frac{3}{2}$). The cubic crystalline field (cf. Eq. 3.33) splits the ^4F-state into a $^4\Gamma_2^+$, a $^4\Gamma_4^+$ and a $^4\Gamma_5^+$ state where $^4\Gamma_4^+(O_h)$ is lowest [79G5, 81C1]. The ^4P-state becomes in O_h symmetry another $^4\Gamma_4^+(O_h)$ state which interacts with the $^4\Gamma_4^+$ ground state which is split by the tetragonal crystal field into $^4\Gamma_2^+(D_{4h})$ and $^4\Gamma_5^+(D_{4h})$, a singlet and a doublet (group theoretical compatibility tables: see [63K1]). With inclusion of the spin-orbit coupling the $^4\Gamma_4^+(O_h)$ ground state is finally split into 6 Kramers doublets, three of symmetry $\Gamma_6^+(D_{4h})$ and three $\Gamma_7^+(D_{4h})$. The energetically lowest is a Γ_6^+ state. These Kramers doublets cannot be split by an electric crystalline field but only by magnetic fields. And in the antiferromagnetically ordered state, such a splitting is effected by the molecular or exchange field. The energy levels of the Co^{2+}-ion resulting from the splitting of the $^4\Gamma_4^+(O_h)$ ground state are shown in Fig. 3.24. They have been determined by Raman spectroscopy on K_2CoF_4 in the range 200–1400 cm^{-1} [79G5]. The observed optical transitions from the ground state to the 11 excited states, i.e. the exciton lines, are the basis for deriving the energy level scheme. By the magnetic field, the symmetry is reduced from D_{4h} to C_{4h}, and the symmetry types of the split components are $\Gamma_5^+(C_{4h})$ and $\Gamma_6^+(C_{4h})$ from a $\Gamma_6^+(D_{4h})$ Kramers doublet, while they are $\Gamma_7^+(C_{4h})$ and $\Gamma_8^+(C_{4h})$ from a $\Gamma_7^+(D_{4h})$ Kramers doublet. The model calculations yielding the level scheme in Fig. 3.24 include not only the tetragonal crystal field and the spin-orbit coupling but also a molecular field H_{MF} which can be written for the ground state as [79G5, 82S2]

$$g_c\mu_B H_{\mathrm{MF}} = 2z\,\langle S_z\rangle_0\,|J| \tag{3.61}$$

In Eq. 3.61, z is again the number of nearest neighbours, $\langle S_z\rangle_0$ is the mean value or expectation value of S_z in the ground state and J the exchange constant in the isotropic Heisenberg model (cf. first term in Eqs. 3.2, 3.30, 3.34, and 3.40). The splitting of the doublets by H_{MF} is also presented in Fig. 3.24 together with the corresponding group theoretical labels for the energy levels. The model includes further propagating excitons with $\hbar\omega = f(\boldsymbol{q})$. As noted before, the observed optical transitions refer to $\boldsymbol{q} = 0$. The model does not explain all details of the experimental results but it allows a good insight to the energy levels of Co^{2+} in compounds like K_2CoF_4 and Rb_2CoF_4 which are responsible for the special magnetic properties of these compounds [81C1]. The lowest exciton in Fig. 3.24 corresponding to the $\Gamma_6^+(D_{4h})$ ground Kramers doublet are the usual magnons. The dispersion is relatively small compared to Mn-compounds (cf. Figs. 3.1, 3.2, and 3.11) indicating a large anisotropy in K_2CoF_4. Since the Kramers doublets behave as spin $\frac{1}{2}$ states, a single-ion anisotropy cannot exist for Co^{2+} as discussed in Sect. 3.1.5 for Fe^{2+} (Eqs. 3.34, 3.35) and in Sect. 3.1.6 for Mn^{2+} (Eq. 3.40). The anisotropy can only be expressed as anisotropic exchange for spin $\frac{1}{2}$ systems. Therefore, the magnons are described for the Co-compounds in terms of an effective spin $\frac{1}{2}$ Hamiltonian as follows [69B1, 78I2, 79G5, 79M1, 90H]

$$\mathcal{H} = -2 \sum_{\langle i,j \rangle} [J_{\parallel} \mathrm{S}_{i,z} \mathrm{S}_{j,z} + J_{\perp} (\mathrm{S}_{i,x} \mathrm{S}_{j,x} + \mathrm{S}_{i,y} \mathrm{S}_{j,y})] \tag{3.62}$$

with $\mathrm{S}_{i,z}$, $\mathrm{S}_{j,z} = \pm\frac{1}{2}$. The subscripts x, y, and z refer again to the magnetic unit cell (cf. Figs. 2.1 and 2.2 in Sect. 2.1.2). The ratio of the exchange constants in Eq. 3.62 is always $J_{\perp}/J_{\parallel} < 1$ (cf. Table 5). The Hamiltonian Eq. 3.62 belongs to a strongly anisotropic $S = \frac{1}{2}$ Heisenberg model, in the literature also called XXZ-model [88K3, 89N2]. In the extreme cases $J_{\perp} = 0$ and $J_{\parallel} = 0$, it includes the Ising model and the XY-model, respectively. The application of linear spin-wave theory to Eq. 3.62 in the way outlined in Eqs. 3.2–3.6 results in the magnons or spin waves with an energy

$$\hbar\omega_q = z\sqrt{(J_{\parallel})^2 - (J_{\perp}\,\gamma_q)^2} \tag{3.63}$$

where z and γ_q have the same meaning as in Eq. 3.6. The usual factor $2S$ (cf. Eqs. 3.6, 3.14, 3.31, and 3.36) has been omitted here because of $S = \frac{1}{2}$. The magnon dispersion $\hbar\omega_q$ has been measured for Rb_2CoF_4 by neutron inelastic scattering (see Fig. 3.25) which exhibits a relatively small difference between $\hbar\omega$ at $\boldsymbol{q} = 0$ and $\hbar\omega$ at the zone boundary. Fig. 3.25 shows further that the magnons are still observed at temperatures close to T_N with an extremely small temperature renormalization. The AFMR frequency for $\boldsymbol{q} = 0$ is

$$h\nu_{AFMR} = z\sqrt{(J_{\parallel})^2 - (J_{\perp})^2} \tag{3.64}$$

For K_2CoF_4 and Rb_2CoF_4, ν_{AFMR} is near 200 cm^{-1} and can be observed only by 1-magnon Raman scattering and not by infrared spectroscopy because of the strong absorption due to infrared-active phonons in this range [76B2, 82S3, 83R1]. For comparison of the exchange interaction and the anisotropy in Co-compounds (Eq. 3.62) with the more weakly anisotropic Mn-, Fe- and Ni-compounds (Eqs. 3.2, 3.35 and 3.40), a conversion may be used [69B1, 72J2] from $J_{\parallel}$ to J of the isotropic Heisenberg model according to

$$-2J \sum_{\langle i,j \rangle} \boldsymbol{S}_i \boldsymbol{S}_j$$

(cf. Eqs. 3.2, 3.8, 3.30, 3.35 and 3.40) by means of

$$J = J_{\parallel} / (2\langle S_z \rangle_0)^2 \tag{3.65a}$$

with $\langle S_z \rangle_0$ defined in Eq. 3.61. For the anisotropy, a similar conversion is from $J_{\perp}/J_{\parallel}$ to $h_A = H_A/H_E$ by means of

$$h_A = (1 - J_{\perp}/J_{\parallel}) \tag{3.65b}$$

These relations (Eqs. 3.65a and 3.65b) are referred to and used in some reviews and in Table 5. If in Eq. 3.62 $J_{\perp}$ were equal to zero, $\hbar\omega_q$ would be independent of $\boldsymbol{q}$. Then $\mathcal{H}$ (Eq. 3.62) would be that of a pure 2D Ising model and $\hbar\omega$ would be the Ising excitation energy. But Fig. 3.25 clearly shows that we cannot omit the transverse spin components for the excitations of this system since the dispersion due to $J_{\perp}$ is small but not negligible. However, as already mentioned, K_2CoF_4 and Rb_2CoF_4 are the best realizations of the 2D Ising model found among magnetic systems. A better proof for this statement is the sublattice magnetization as determined by neutron diffraction [74I2] and by $^{19}F_I$-NMR [85D2]. The results for $M_{\mathrm{subl}}(T) \sim (I_{\mathrm{Bragg}})^{1/2}$ obtained by neutron scattering [74I2] are compared in Fig. 3.26 to the exact results for the 2D Ising model [52Y, 67F1, 90H, 90N]

$$M_{\mathrm{subl}}(T)/M_{\mathrm{subl}}(0) = [1 - \sinh^{-4}(J_{\parallel}/k_B T)]^{1/8} \tag{3.66}$$

and the agreement between experiment and theory is perfect over the whole temperature range from $T = 0$ to $T = T_N$. Since there is no such exact solution for the Heisenberg model, approximations have to be used for the Mn-, Ni-, Fe-compounds etc. by means of which an agreement can be achieved only over a limited temperature range. For example, the reduced sublattice magnetization of K_2FeF_4 presented in Fig. 3.15 agrees with the results of normalized spin-wave theory only up to $T \approx 0.75\,T_N$ and a power law dependence is used for temperatures nearer to T_N. In the exact solution for the Co-compounds (Eq. 3.66), $M_{\mathrm{subl}}(T)/M_{\mathrm{subl}}(0)$ vanishes for $\sinh(J_{\parallel}/k_B T) = 1$. This relation defines the critical temperature in the 2D Ising model [44O, 67F1, 90N]. Thus the ratio of $J_{\parallel}$ and $k_B T_N$ is

$$J_{\parallel}/k_B T_N = \mathrm{Arsinh}\ 1 = \ln(\sqrt{2}+1) = 0.8814 \tag{3.67}$$

For Rb_2CoF_4, $J_{\parallel}$ and T_N have been determined independently [78I2]. If the value of T_N is inserted to Eq. 3.67, the resulting value for $J_{\parallel}$ agrees with the experimental one within a few percent. A difference show the susceptibilities $\chi_{\parallel}$ and $\chi_{\perp}$ of the Co-compounds in comparison to the other compounds, $\chi_{\parallel}$ and $\chi_{\perp}$ are different not only for temperatures below T_N but also for temperatures above T_N (cf. Table 5). Further, the experimental data [69B1] may also be compared with the results for the 2D Ising model using the following ratios

$$\begin{aligned} &\chi_{\parallel,\max}/\chi_{\parallel}(T_N) = 1.552 && T_{\parallel,\max}/T_N = 1.5371 \\ &\chi_{\perp,\max}/\chi_{\perp}(T_N) = 1.040629 && T_{\perp,\max}/T_N = 1.08872 \\ &\chi_{\perp,\max}(T_N)/\chi_{\perp}(0) = 1.136951 && \end{aligned} \tag{3.68}$$

In Eq. 3.68, $\chi_{\parallel,\max}$ and $\chi_{\perp,\max}$ are the maximum values of $\chi_{\parallel}$ and $\chi_{\perp}$ and $T_{\parallel,\max}$ and $T_{\perp,\max}$ are the temperatures at which the maxima occur. The ratios in Eq. 3.68 have been calculated by means of the exact solutions for the 2D Ising model [63F3, 67F1]. The values of the corresponding experimental data are close to the theoretical ones [69B1]. In addition to the exact results presented above, low- and high-temperature series expansions have also been developed for the 2D Ising model which have also contributed to our understanding and to our confidence in such series expansions. Details in this respect are found in the reviews of Temperley [72T2], Domb [74D1] and Navarro [90N]. For example, the agreement of the results of h.t.s. with the exact data has proved the reliability of the h.t.s. method. More about the Co-compounds and their relation to the 2D Ising model will be discussed in context with the critical properties in Sect. 4.1.2.

9.12.3.2 Ferromagnets

9.12.3.2.1 Cu-Compounds

Most perovskite-type layer structures exhibit antiferromagnetic ordering within the layers below the critical temperature, and only a few compounds show ferromagnetic order. Such intralayer ferromagnetism occurs in Cu- and Cr-compounds as a consequence of a collective Jahn-Teller effect and orbital ordering as discussed in Sect. 2.1.3. Although all Cu-compounds of the halide perovskite layer type show this ferromagnetic order in the layer, their overall magnetic order depends on the interlayer interaction which may be ferro- or antiferromagnetic (see Fig. 3.27) so that some compounds, e.g. K_2CuF_4 and $(CH_3NH_3)_2CuCl_4$, are ferromagnets and some others like Rb_2CuCl_4 and $(C_2H_5NH_3)_2CuCl_4$

of the 2D Ising model found among magnetic systems. A better proof for this statement is the sublattice magnetization as determined by neutron diffraction [74I2] and by $^{19}F_I$-NMR [85D2]. The results for $M_{\text{subl}}(T) \sim (I_{\text{Bragg}})^{1/2}$ obtained by neutron scattering [74I2] are compared in Fig. 3.26 to the exact results for the 2D Ising model [52Y, 67F1, 90H, 90N]

$$M_{\text{subl}}(T)/M_{\text{subl}}(0) = [1 - \sinh^{-4}(J_{\|}/k_BT)]^{1/8} \tag{3.66}$$

and the agreement between experiment and theory is perfect over the whole temperature range from $T = 0$ to $T = T_N$. Since there is no such exact solution for the Heisenberg model, approximations have to be used for the Mn-, Ni-, Fe-compounds etc. by means of which an agreement can be achieved only over a limited temperature range. For example, the reduced sublattice magnetization of K_2FeF_4 presented in Fig. 3.15 agrees with the results of normalized spin-wave theory only up to $T \approx 0.75\,T_N$ and a power law dependence is used for temperatures nearer to T_N. In the exact solution for the Co-compounds (Eq. 3.66), $M_{\text{subl}}(T)/M_{\text{subl}}(0)$ vanishes for $\sinh(J_{\|}/k_BT) = 1$. This relation defines the critical temperature in the 2D Ising model [44O, 67F1, 90N]. Thus the ratio of $J_{\|}$ and k_BT_N is

$$J_{\|}/k_BT_N = \text{Arsinh}\ 1 = \ln(\sqrt{2}+1) = 0.8814 \tag{3.67}$$

For Rb_2CoF_4, $J_{\|}$ and T_N have been determined independently [78I2]. If the value of T_N is inserted to Eq. 3.67, the resulting value for $J_{\|}$ agrees with the experimental one within a few percent. A difference show the susceptibilities $\chi_{\|}$ and $\chi_{\perp}$ of the Co-compounds in comparison to the other compounds, $\chi_{\|}$ and $\chi_{\perp}$ are different not only for temperatures below T_N but also for temperatures above T_N (cf. Table 5). Further, the experimental data [69B1] may also be compared with the results for the 2D Ising model using the following ratios

$$\begin{array}{ll} \chi_{\|,\max}/\chi_{\|}(T_N) = 1.552 & T_{\|,\max}/T_N = 1.5371 \\ \chi_{\perp,\max}/\chi_{\perp}(T_N) = 1.040629 & T_{\perp,\max}/T_N = 1.08872 \\ \chi_{\perp,\max}(T_N)/\chi_{\perp}(0) = 1.136951 & \end{array} \tag{3.68}$$

In Eq. 3.68, $\chi_{\|,\max}$ and $\chi_{\perp,\max}$ are the maximum values of $\chi_{\|}$ and $\chi_{\perp}$ and $T_{\|,\max}$ and $T_{\perp,\max}$ are the temperatures at which the maxima occur. The ratios in Eq. 3.68 have been calculated by means of the exact solutions for the 2D Ising model [63F3, 67F1]. The values of the corresponding experimental data are close to the theoretical ones [69B1]. In addition to the exact results presented above, low- and high-temperature series expansions have also been developed for the 2D Ising model which have also contributed to our understanding and to our confidence in such series expansions. Details in this respect are found in the reviews of Temperley [72T2], Domb [74D1] and Navarro [90N]. For example, the agreement of the results of h.t.s. with the exact data has proved the reliability of the h.t.s. method. More about the Co-compounds and their relation to the 2D Ising model will be discussed in context with the critical properties in Sect. 4.1.2.

9.12.3.2 Ferromagnets

9.12.3.2.1 Cu-Compounds

Most perovskite-type layer structures exhibit antiferromagnetic ordering within the layers below the critical temperature, and only a few compounds show ferromagnetic order. Such intralayer ferromagnetism occurs in Cu- and Cr-compounds as a consequence of a collective Jahn-Teller effect and orbital ordering as discussed in Sect. 2.1.3. Although all Cu-compounds of the halide perovskite layer type show this ferromagnetic order in the layer, their overall magnetic order depends on the interlayer interaction which may be ferro- or antiferromagnetic (see Fig. 3.27) so that some compounds, e.g. K_2CuF_4 and $(CH_3NH_3)_2CuCl_4$, are ferromagnets and some others like Rb_2CuCl_4 and $(C_2H_5NH_3)_2CuCl_4$

are antiferromagnets. Because of the strong ferromagnetic intralayer exchange, the weaker interlayer interaction determines the magnetic porperties of these compounds. And the interaction with adjacent layers is stronger in this case since it does not cancel as it does in compounds with antiferromagnetic intralayer coupling, e.g. in Mn-compounds (cf. Fig. 2.2 and discussion in Sect. 2.1.2) where the spins of four nearest neighbours in adjacent layers are oriented antiparallel to those of the other four neighbours so that this interaction cancels in ideal tetragonal symmetry. For ferromagnetic intralayer exchange, on the other hand, the spins of all 8 nearest neighbours in adjacent planes are oriented parallel to each other (cf. Fig. 3.27) and their influence adds up to a perceptible interlayer interaction for both, ferro- and antiferromagnetic interlayer coupling (Fig. 3.27 a and b) which determines the type of magnetic order in these compounds.

Let us first concentrate on the details of Cu-compounds and later turn to Cr-compounds. One of the most investigated and therefore best known Cu-compounds is K_2CuF_4. Its collective Jahn-Teller effect and orbital ordering has not only been verified by means of various structure determinations [74H1, 79H1, 81H1, 81R1, 83H1] but also been observed by diffraction with polarized neutrons [76I1]. The tetragonal deformation of the octahedra has further been confirmed by EPR measurements and ligand field spectroscopy [74F1] and by NMR studies [71Y2, 75D1, 75G4, 81F1], particularly that the octahedra are elongated and not compressed along the x_0- or y_0-axis. Moreover, the spin densities on antibonding orbitals obtained by neutron scattering investigations are definitely not consistent with the K_2NiF_4 structure I4/mmm [73H2, 74H4]. As already mentioned in Sect. 3.1.1. for Mn^{2+} etc., the superexchange in K_2CuF_4 and other Cu-compounds results from the electronic structure of these compounds and theoretical studies yield, as expected, ferromagnetic coupling for the intralayer exchange of Jahn-Teller distorted K_2CuF_4 which is due to the exchange coupling of ground- and excited-state orbitals of Cu^{2+} [58G, 59A, 59K, 63A]. In addition, also the Jahn-Teller effect has been dealt with in a number of theoretical papers [83N3, 83R2, 83S6] and in reviews by Reinen and Friebel [79R1] and by Kugel and Khomski [82K1]. Especially emphasized is its relation to properties like the optical spectra [86S3] and the effect of fibronic coupling on EPR spectra [86R3]. One result of these theoretical considerations is that the antiferrodistortive orbital order with doubling of the unit cell in the basal plane as it is realized in K_2CuF_4 (see upper part of Fig. 3.28) and other Cu-compounds will lead to the ferromagnetic interaction within the layers [73K1, 79K2, 96I1]. However, if the orbital order is ferrodistortive (see lower part of Fig. 3.28) as this is the case for La_2CuO_4 [77G5] the resulting intralayer exchange interaction is antiferromagnetic. Quite recently, the magnetic susceptibility of K_2CuF_4 has been studied under high pressures up to 13 GPa [96I1, 98I]. The interesting result is that at pressures larger than $p_C \approx 9.5$ GPa K_2CuF_4 becomes antiferromagnetic instead of ferromagnetic [96I1]. This pressure-induced magnetic phase transition is accompanied by a transition to a high pressure phase with the structure Ammm [98I]. The change in the magnetic properties is explained as resulting from a ferrodistortive orbital order similar to that shown for La_2CuO_4 in Fig. 3.28. Thus these results of high pressure experiments on K_2CuF_4 are a contribution to a better understanding of the exchange interaction in Cu-compounds.

The monoammonium Cu-compounds $(C_nH_{2n+1}NH_3)_2CuX_4$ with $X = Cl$, Br have attracted much attention in the early days of research on perovskite-type layer structures. And the values of parameters like J, J' (H'_E), H_A and $\widetilde{H}_A$ have been compiled in a number of reviews with tables [74M2, 75Y, 76B5, 76J1, 77B3]. Some of these data are not identical with the entries to Table 5 which are the most recent ones. The ferro- or antiferromagnetic interlayer interaction in these compounds has also been the subject of theoretical studies. And it has been shown for K_2CuF_4 that the ferromagnetic interlayer coupling is caused by interference effects between inequivalent hopping paths [95F2]. The diammonium Cu-compounds $[NH_3(CH_2)_nNH_3]CuX_4$ especially with respect to the interlayer coupling have different properties as documented in a number of papers with tables for comparison of the numerical values [79K8, 81S6, 84R6, 88H1, 94S3]. For our further discussion, we will reproduce here a survey of the intralayer and interlayer exchange constants of mono- and diammonium Cu-compounds from Table 5:

$(C_2H_5NH_3)_2CuCl_4$	$J = 18.6$ K	$J' = -14.3$ mK
$(C_5H_{11}NH_3)_2CuCl_4$	$J = 15.9$ K	$J' = -0.27$ mK
$(C_2H_5NH_3)_2CuBr_4$	$J = 19.0$ K	$J' = -33$ mK
$[NH_3(CH_2)_2NH_3]CuCl_4$	$J = 23.0$ K	$J' = -13.7$ K
$[NH_3(CH_2)_5NH_3]CuCl_4$	$J = 14.1$ K	$J' = -0.04$ K
$[NH_3(CH_2)_2NH_3]CuBr_4$	$J = 38.2$ K	$J' = -68.4$ K

All these compounds are antiferromagnets. The intralayer exchange constant J is very similar for mono- and diammonium compounds. It does further not vary much with chain length or with replacing Cl^- by Br^-. The interlayer exchange constant J' is considerably smaller than J (3–4 orders of magnitude) for the monoammonium compounds as experienced also for K_2CuF_4 and many other perovskite-type layer structures. But for the diammonium compounds with n = 2, J' is of the same order of magnitude as J. And we note that the compounds with $J' \approx J$ are no longer quasi-2D magnets but ordinary 3D magnets with a tendency towards 1D magnetic behaviour for $J' > J$. For mono- and diammonium compounds, J' decreases with increasing chain length. For understanding this difference between mono- and diammonium compounds, it is necessary to recall from Sect. 2.1.4, especially from Figs. 2.13 and 2.14, the eclipsed structures of the diammonium compounds in contrast to the staggered structures of the monoammonium compounds. In the eclipsed structures, the interlayer exchange turns out to be a strong superexchange interaction through a two-halide bridge ($Cu^{2+} - X^- - X^- - Cu^{2+}$). Naively, one would expect this to lead to a smaller exchange coupling than a one-halide bridge ($Cu^{2+} - X^- - Cu^{2+}$). By means of a Rayleigh-Schrödinger type of exchange perturbation theory (method of Jansen et al. [67J, 79K10], cf. Sect. 3.1.1) with two cations and two anions [78K9] the interlayer exchange constant J' has been calculated for a number of diammonium Cu-compounds [82B4, 84S5]. These theoretical results show rather large values for J' in agreement with the experimental data (see above). Further, an empirical relation shows that J' depends strongly on the distance d_{X-X} between the two halides as [94S3]

$$J' \sim (d_{X-X})^{-\alpha} \quad \text{with } \alpha = 10.9(2) \text{ for X = Cl and } \alpha = 6.8(2) \text{ for X = Br}$$

while J depends on the Cu-X distance r_{ip} in the layer (see Sect. 2.1.1 and Table 3)

Ferro- and antiferromagnetic Cu-compounds have many properties in common and it is useful to discuss both types together in this section, e.g. the dominant ferromagnetic intralayer exchange due to the collective orbital ordering. One advantage of this proceeding is that the spin-wave calculations are very similar for both types of Cu-compounds. Some particular properties of antiferromagnetic Cu-compounds like $(C_2H_5NH_3)_2CuCl_4$ were already presented in Sect. 3.1.8 in context with field-induced phase transitions in antiferromagnets. At least in the monoammonium compounds, the paramagnetic phase is easily accessable with moderate fields because of the small antiferromagnetic exchange field H'_E. For the ferromagnet K_2CuF_4 with H'_E smaller than the in-plane anisotropy field $\widetilde{H}_A$, we expect easy-plane or XY-like behaviour. For compounds with longer hydrocarbon chains, H'_E may become even smaller than $\widetilde{H}_A$ so that easy-axis or Ising-like behaviour may be expected. These critical properties will be discussed in detail in Sects. 4.1.7–4.1.9.

After these more general remarks, we will now enter into the spin-wave calculations for Cu-compounds. The electronic ground state of a free Cu^{2+}-ion is ${}^2D$ ($L = 2$, $S = \frac{1}{2}$) according to Hund's rules. This is split by the cubic crystalline field of the ligands into a lower ${}^2\Gamma_3^+$ doublet and a higher ${}^2\Gamma_5^+$ triplet state. The doubly degenerate ${}^2\Gamma_3^+$ state gives rise to the Jahn-Teller effect which lowers the symmetry and lifts the degeneracy. Finally, we end up with the Cu^{2+}-ion in a $S = \frac{1}{2}$ state so that no single-ion anisotropy is possible in the same way as for Co^{2+} (cf. Sect. 3.1.9) and all anisotropy will originate only from anisotropic exchange and from magnetic dipolar interactions. In the spin-Hamiltonian for the Cu-compounds, only the anisotropic exchange is therefore included as the source of anisotropy:

$$\mathcal{H} = -2J \sum_{\langle i,j \rangle} \boldsymbol{S}_i \boldsymbol{S}_j + 2J_A \sum_{\langle i,j \rangle} S_{i,z} S_{j,z} + 2\widetilde{J}_A \sum_{\langle i,j \rangle} S_{i,y} S_{j,y} - 2J' \sum_{\langle i,k \rangle} \boldsymbol{S}_i \boldsymbol{S}_k - g_a \mu_B H_{0x} \sum_i S_{i,x} \tag{3.69}$$

where $J > 0$ describes the ferromagnetic intralayer exchange, J_A and $\widetilde{J}_A$ denote the out-of-plane and the in-plane anisotropic exchange and J' as before (cf. Eq. 3.2 in Sect. 3.1.2) the interlayer exchange. The last term in Eq. 3.69 is the Zeeman term with the external magnetic field H_{0x} and corresponding g-factor g_a. Here, the x-direction is assumed to be the direction of the spontaneous magnetization M. The anisotropic exchange interaction can be estimated from the anisotropy of the g-factor [72Y2, 89D2]

$$J_A \approx [(g_a - g_c)/g_c]^2 \, J \tag{3.70}$$

where g_c is the g-factor for $\boldsymbol{H_0} \parallel \boldsymbol{c}$. The anisotropic magnetic dipolar interaction is not treated separately in Eq. 3.69 but the anisotropic exchange terms may comprise it [76T1]. For K_2CuF_4, mostly the example for demonstrating the properties of Cu-compounds, the in-plane anisotropy field is extremely small. It was found in NMR experiments that it is smaller than 10^{-5} T even at $T = 30$ mK [83F1, 83F2]. On the other hand, FMR experiments on K_2CuF_4 and $K_2Cu_{0.95}Zn_{0.05}F_4$ [89A2] revealed a small but definitely perceptable angular dependence of H_{res} and ΔH_{FMR} in the basal plane [$\beta = \angle(H_0, a\text{-axis})$, cf. Eq. 3.43 in Sect. 3.1.6]. In particular, $H_{res}(\beta)$ and $\Delta H_{FMR}(\beta)$ clearly reflect the four-fold crystal symmetry indicating an in-plane anisotropy field $\hat{H}_A$ of tetragonal symmetry as introduced in Eq. 3.41 (Sect. 3.1.6) for Rb_2MnCl_4 and not an anisotropy field $\widetilde{H}_A \sim \widetilde{J}_A$ of orthorhombic symmetry. Moreover, the spin-wave linewidths obtained in parallel pumping experiments [78Y1, 81Y] show also this four-fold symmetry, and from these results, a value $\hat{H}_A = 5 \cdot 10^{-4}$ T has been deduced for $T \to 0$ and $\hat{H}_A \to 0$ for $T \approx 4$ K [81Y]. A spin-wave gap observed in FMR experiments [89D2] seems also to support $\hat{H}_A \neq 0$. But this problem is still somewhat controversial for K_2CuF_4. For other Cu-compounds, an orthorhombic in-plane anisotropy $\widetilde{J}_A$ ($\widetilde{H}_A$) has been determined in accordance with the crystal structures. Its value is mostly larger than the interplane exchange constant J'. This in-plane anisotropy then determines a preferred spin direction in the basal plane. For our further considerations about K_2CuF_4, we will assume $\widetilde{H}_A = 0$ and $\hat{H}_A \approx 0$ and thus no preferred direction for this compound in the basal plane.

For K_2CuF_4 and other Cu-compounds, Tsuru and Uryu [76T1, 77U, 77T3] have developed a renormalized spin-wave theory as it was outlined already in Sect. 3.1.2 (cf. Eqs. 3.2–3.5). This requires that the direction of spin orientation is made the z-axis, the axis of quantization. In Eq. 3.69, we have used our usual coordinate system with the unique z-axis perpendicular to the layers. But before applying the Holstein-Primakoff transform (Eq. 3.3) it is necessary to introduce a new coordinate system (ζ, η, ζ) which is related to the (x, y, z) system by $x \leftrightarrow \zeta$, $y \leftrightarrow \xi$ and $z \leftrightarrow \eta$ which will be used only for the spin-wave theory and the results will be transferred back to the (x, y, z) system. In the linear spin-wave approximation, the magnon energy can be calculated as function of q and be compared with the results of inelastic neutron scattering obtained at low temperatures where the temperature renormalization of the magnon energies can be neglected. The complete spin-wave dispersion relation is [76T1, 77T3]

$$\hbar\omega_q = 2zSJ \, \{[(1-\gamma_q) + h'_E \, (1-\gamma'_q) + h_A\gamma_q + h_{0x}] \; [(1-\gamma_q) + h'_E \, (1-\gamma'_q) + \widetilde{h}_A\gamma_q + h_{0x}]\}^{1/2} \tag{3.71}$$

where the reduced parameters are defined as

$$h'_E = z'J'/zJ, \qquad h_A = J_A/J, \qquad \widetilde{h}_A = \widetilde{J}_A/J, \qquad h_{0x} = g_a\mu_B H_{0x}/(2zSJ)$$

with $z = 4$, $z' = 8$ and $S = \frac{1}{2}$. The values of the exchange constants are listed for various compounds in Table 5. Eq. 3.71 follows closely the notation of Tsuru and Uryu but it should be noted that, for practical applications, the demagnetization effects in a ferromagnet with $M \neq 0$ have to be taken care of and H_{0x} to be replaced by the internal field $H_{\text{int,x}} = H_{0x} - N^{x}M$ acting on the spins [76Y3], in reduced form $h_{\text{int,x}} = g_{a}\mu_{B}H_{\text{int,x}}/(2zSJ)$. The q-dependent parameters γ_q and γ'_q are defined in the usual way. The expressions for γ_q and γ'_q depend on the coordinate system in reciprocal space and for the ferromagnetic Cu-compounds it is advisable to use an I4/mmm pseudo cell with one magnetic ion in the primitive unit cell disregarding the actual crystal structure since γ_q and γ'_q depend only on the positions of the Cu^{2+}-ions and not on the deformations of the halide octahedra due to the collective Jahn-Teller effect. Fig. 3.29 shows a section through the Brillouin zone and the neighbouring zones for I4/mmm in the plane $q_z = 0$ (broken lines in Fig. 3.29). As long as the spin waves do not depend on q_z, we can use as a 2D approximation the Brillouin zone of the corresponding square lattice (full lines in Fig. 3.29). For comparison, also a section is shown through the Brillouin zone of Acam with two magnetic ions per unit cell and that of the corresponding square lattice (dotted and dash-dot lines in Fig. 3.29, resp.). The latter is appropriate for antiferromagnets discussed in Sect. 2.1.2. The differences between the contours of the Brillouin zones of the 3D structures and of those of the square lattices arise from the centering of the 3D structures, see for example Fig. 2.31 with the Brillouin zone for I4/mmm. While the (q_x, q_y, q_z) system is employed for the antiferromagnets with two magnetic ions per primitive unit, we will use for ferromagnets like K_2CuF_4 the (q_{x0}, q_{y0}, q_{z0}) coordinate system (cf. Fig. 3.29). Thus, the parameters γ_q and γ'_q can be written as

$$\gamma_q = \tfrac{1}{2}\left[\cos(q_{x0}a) + \cos(q_{y0}a)\right] \qquad \gamma'_q = \cos\left(\frac{q_{x0}a}{2}\right)\cdot\cos\left(\frac{q_{y0}a}{2}\right)\cdot\cos\left(\frac{q_{z0}c}{2}\right) \tag{3.71a}$$

where the lattice parameters a and c are those of the I4/mmm pseudo cell. The expression for γ'_q indicates that the two-dimensional approximation for the Brillouin zone is only applicable if the magnon energies do not depend on q_z as it has been confirmed experimentally for antiferromagnetic compounds (cf. Figs. 3.1 in Sect. 3.1.2 and 3.14 in Sect. 3.1.5). The discussion of the experimental data for K_2CuF_4 will show that γ'_q with q_{z0} gains influence on $\hbar\omega_q$ only for rather small q_{x0} and q_{y0} where the actual contour of the Brillouin zone in the plane $q_{z0} = 0$ is unimportant. Tsuru and Uryu [77T4] have extended their renormalized spin-wave theory to antiferromagnetic Cu-compounds like $(C_2H_5NH_3)_2CuCl_4$ where the intraplane coupling of the spins is still ferromagnetic but the smaller interplane coupling antiferromagnetic. This theory is more complicated because of the two sublattices in an antiferromagnet and because of several phases to be treated, e.g. antiferromagnetic and spin-flop phases.

The magnon dispersion has been determined for K_2CuF_4 in the (1, 0, 0) and (1, 1, 0) directions [76F, 83H4]. The results for the (1, 0, 0) direction are reproduced in Fig. 3.30. In addition to $\tilde{h}_A = 0$ ($\tilde{J}_A = 0$), we have $h_{0x} = 0$ since the experiment has been performed without external field ($H_{0x} = 0$). In the range $0.1 \leq \zeta_{x0} \leq 0.5$ ($\zeta_{x0} = q_{x0}/a^*$) the experimental data in Fig. 3.30 can be described by the following approximative form of Eq. 3.71

$$\hbar\omega_q = zSJ\left[1 - \cos(q_{x0}a)\right] = zSJ\left[1 - \cos(2\pi\zeta_{x0})\right] \tag{3.72}$$

Similar to the situation in antiferromagnets, these experimental results are primarily used to determine a reliable value for J. The values for J_A and J' are better determined in FMR experiments [74Y1, 76Y2], the latter especially by parallel pumping studies. Eq. 3.72 resembles the magnon dispersion of an ideal 2D Heisenberg ferromagnet. The approximation used in Eq. 3.72 works so well because J_A and J' are small enough that they become perceptible in $\hbar\omega_q$ only for smaller values of ζ_{x0}. This will occur in the ranges $2zSJ\sin^2(\pi\zeta_{x0}) \approx 2z'SJ'$ and $2zSJ\sin^2(\pi\zeta_{x0}) \approx 2zSJ_A\cos^2(\pi\zeta_{x0})$ where the identity $\gamma_q = \cos^2(\pi\zeta_{x0})$ has been used. This has been verified experimentally by inelastic neutron scattering for small ζ_{x0} using a cold neutron source [78M2, 83H4]. The results show a shift to higher energy in the range $0 \leq \zeta_{x0} \leq 0.06$ with respect to the curve given by Eq. 3.72 (see Fig. 3.31). The upshifted curve is obtained when J_A and J' are included in the calculation, i.e. using Eq. 3.71 (for K_2CuF_4) with $h_{0x} = 0$ and $\tilde{h}_A = 0$ but with $h_A \neq 0$ and $h'_E \neq 0$

$$\hbar\omega_q = 2zSJ\{[\sin^2(\pi\zeta_{x0}) + h_A\cos^2(\pi\zeta_{x0}) + h'_E(1-\gamma'_q)][\sin^2(\pi\zeta_{x0}) + h'_E(1-\gamma'_q)]\}^{1/2} \qquad (3.73)$$

where γ'_q may be approximated by $\cos(q_{z0}c/2) = \cos(\pi\zeta_{z0})$ for such small values of ζ_{x0} (or ζ_{y0}). With $h'_E \approx 0$ which is justified for $h'_E << \sin^2(\pi\zeta_{x0})$, Eq. 3.73 represents the magnon dispersion of a 2D XY-ferromagnet. But if h'_E cannot be neglected $\hbar\omega_q$ depends via γ'_q also on q_z. That means that we are dealing with a 3D XY-ferromagnet. Eq. 3.73 is further the basis for defining ζ_1 and ζ_2 which are indicated in Fig. 3.31 which are the solutions of $\sin^2(\pi\zeta_{x0}) = h'_E$ and of $\sin^2(\pi\zeta_{x0}) = h_A \cos^2(\pi\zeta_{x0})$ yielding $\zeta_1 = \pi^{-1}(h'_E)^{1/2} = 0.006$ and $\zeta_2 = \pi^{-1}(h_A)^{1/2} = 0.03$, respectively. Thus ζ_1 is a rough estimate for the crossover from the 3D XY- to the 2D XY-regime. In the 3D XY-range, neither J' nor J_A can be neglected in Eq. 3.73 while in the 2D XY-range J' is negligible but not J_A. Finally, ζ_2 marks the crossover to the 2D Heisenberg range. With somewhat different definitions of ζ_1 and ζ_2 the resulting values would be different but of the same order of magnitude. The upper curve in Fig. 3.31 has been calculated by means of Eq. 3.73 with $\gamma'_q \approx 0$, i.e. an intermediate value has been inserted for q_{z0}. The results demonstrate that the shift of the magnon energy to higher values can be explained for $\zeta_{x0} > 0.015$ with $J_A \neq 0$ alone since the effect of J' is perceptable only for $\zeta_{x0} < 0.015$ where a shaded area indicates in Fig. 3.31 the influence of J' on $\hbar\omega_q$ for the whole range $0 \leq q_{z0} \leq c^*$. It should further be noted that a spin-wave gap occurs at $\zeta_{x0} = 0$ only if $q_{z0} \neq 0$, i.e. $h'_E(1-\gamma'_q) \neq 0$.

By means of renormalized spin-wave theory, Tsuru and Uryu [77U] have derived a formula for the dependence of the (spontaneous) magnetization M of a two-dimensional Heisenberg ferromagnet on temperature T and external field H_{0x} applied parallel to $\boldsymbol{M}$:

$$M(H_{0x}, T) = (N/V)g_a\mu_B\left[S - \Theta\ln\left(\frac{2\pi\Theta}{h_\kappa}\right) - \frac{\pi^2}{12}\Theta^2 - \frac{h_{0x}}{2\pi}\right] \qquad (3.74)$$

where $$\Theta = k_B T/(2\pi zSJ)$$

and $$h_\kappa = \tfrac{1}{2}\left(\sqrt{h_{0x} + \tilde{h}_A} + \sqrt{h_{0x} + \tilde{h}_A + 2h'_E}\right)\left(\sqrt{h_{0x} + h_A} + \sqrt{h_{0x} + h_A + 2h'_E}\right)$$

In the derivation of Eq. 3.74, the usual summation of q over the whole (2D) Brillouin zone (cf. Eq. 3.18 in Sect. 3.1.3) has been replaced here by an integration. The temperature and magnetic field dependence of the reduced magnetization [74K4] $M(H_0, T)/M_0$ has been studied by means of ^{63}Cu- and ^{19}F-NMR where $f_{NMR} \sim M$. The results are shown as a function of temperature for various magnetic fields $\boldsymbol{H_0} \parallel \boldsymbol{a}$, i.e. $\boldsymbol{H_0} \parallel \boldsymbol{M}$, in Fig. 3.32. The calculated curves have been obtained with a somewhat different approach of spin-wave theory [74K4]. If we were using Eq. 3.74 for this purpose we had to insert the reduced internal field $h_{int,x}$ instead of h_{0x} (cf. the discussion in context with Eq. 3.71). The data in Fig. 3.32 illustrate that the external field $\boldsymbol{H_0}$ parallel to the magnetization counteracts the decrease of M with increasing temperature and that the phase transition to the paramagnetic state with $M \equiv 0$ above T_C is suppressed by such a field in a ferromagnet. If, on the other hand, an external field is applied perpendicular to the easy plane in K_2CuF_4, i.e. $\boldsymbol{H_0} \parallel \boldsymbol{c}$, this field is not the conjugate variable to the order parameter and does not destroy the phase transition. The magnetization $\boldsymbol{M_z} \parallel \boldsymbol{c}$ of K_2CuF_4 has been measured for various magnetic fields $\boldsymbol{H_{int}} \parallel \boldsymbol{c}$ as a function of temperature and the results (see Fig. 3.33) demonstrate that a phase transition ferromagnetic to paramagnetic is observed [81H2, 89D2] and $T_C(H)$ can be determined by means of the condition $\partial M/\partial T = \max$. Turning now to the case $H_0 = 0$, it is worth noting that Eq. 3.74 is only meaningful for $h_\kappa \neq 0$, i.e. for $h_A \neq 0$ and $h'_E \neq 0$ or $\tilde{h}_A \neq 0$. Let us consider two special cases, at first a 2D ferromagnet with in-plane ($\tilde{J}_A$) and out-of-plane (J_A) anisotropic exchange like $(CH_3NH_3)_2CuCl_4$ where h'_E can be neglected and secondly a 2D Heisenberg ferromagnet with $h_A = 0$ and $\tilde{h}_A = 0$. For the former, the zero-field magnetization becomes in the lowest order approximation from Eq. 3.74 [77U] for $H_0 = 0$ and $H'_E \approx 0$

$$M(T) = (N/V)\, g_a\mu_B \left[S - \Theta \ln\left(\frac{\pi\Theta}{\sqrt{h_A \tilde{h}_A}} \right) \right] \tag{3.75}$$

or

$$M(T) = M_0 \left[1 - \frac{k_B T}{2\pi\, zS^2 J} \ln\left(\frac{k_B T}{2zS\sqrt{J_A \tilde{J}_A}} \right) \right] \tag{3.75a}$$

where $M_0 = (N/V) g_a \mu_B S$ is the ideal value of the magnetization. For a 2D Heisenberg ferromagnet where only $h'_E \neq 0$ on the other hand, the magnetization for $H_0 = 0$ is obtained from Eq. 3.74 as follows [76T1, 90F2]

$$M(T) = M_0 = \left[1 - \frac{k_B T}{2\pi\, zS^2 J} \ln\left(\frac{k_B T}{z'SJ'} \right) \right] \tag{3.76}$$

For the integration process in deriving Eq. 3.76, the temperature has been assumed to be high enough that $k_B T >> J'$. This condition is not fulfilled for experiments at extremely low temperatures. For example, $k_B T = z'J'$ at $T = 0.018$ K for K_2CuF_4. Then the integration is performed in a different way and yields

$$M(T) = M_0 \left[1 - \frac{1}{S}\sqrt{\frac{zJ}{2z'J'}}\, \zeta\left(\frac{3}{2}\right) \left(\frac{k_B T}{2\pi\, zSJ} \right)^{3/2} \right] \tag{3.77}$$

where $\zeta(u)$ is the Riemann's ζ-function. Since for $k_B T << J'$ all three directions in reciprocal space are treated the same way, the result Eq. 3.77 is identical to the usual form with a $T^{3/2}$ temperature dependence of the magnetization of a three-dimensional ferromagnet [30B]

$$M(T)/M(0) = 1 - C_M T^{3/2} \tag{3.78}$$

In many applications of Eq. 3.78, the factor C_M is used as an adjustable parameter which is determined in a fit to the experimental data. The thermal excitation of magnons can be considered the origin of the decrease of the magnetization with temperature. But the magnons take not only part on this process but also in the relaxation processes in nuclear magnetic resonance. Similar to the situation in antiferromagnets, the results of ^{19}F-NMR in K_2CuF_4 show that the relaxation rate $1/T_1$ is dominated in K_2CuF_4 by three-magnon processes in combination with an anisotropic hyperfine interaction [76D6]. The transverse relaxation $1/T_2$ has been measured in K_2CuF_4 with ^{19}F-, ^{63}Cu- and ^{35}-Cl-NMR by a spin-echo method [77K5]. It is considerably decreased by the XY-like anisotropy as can be concluded from the good agreement of theoretical calculations with the experimental observations.

A further application of spin-wave theory for a better description of the magnetic properties of ferromagnetic Cu-compounds is the calculation of the contribution of the spin waves to the magnetic specific heat C_{magn} at low temperatures. Here again, the system is considered a 2D Heisenberg ferromagnet, i.e. only $J \neq 0$ and $J_A = \tilde{J}_A = J' = 0$. Then, the magnon energy is given in the linear approximation by Eq. 3.72. The contribution of each magnon to the magnetic energy U_{magn} is $\hbar\omega_q \cdot n_q$

and to C_{magn} $\partial(\hbar\omega_{\text{q}} \cdot n_{\text{q}})/\partial T$ where $n_{\text{q}} = [\exp(\hbar\omega_{\text{q}}/k_{\text{B}}T) - 1]^{-1}$ (cf. Sect. 3.1.2). Thus the magnetic contribution to the specific heat becomes in the low temperature limit [72C1, 77B3]

$$C_{\text{magn}} = \sum_{\text{q}} \frac{\partial(\hbar\omega_{\text{q}} \cdot n_{\text{q}})}{\partial T} \quad \to \quad C_{\text{magn}}/R = \frac{\pi k_{\text{B}}T}{24SJ} \tag{3.79}$$

In Eq. 3.79, the final result is again obtained by converting the sum over q into an integration. This theoretically predicted linear dependence of C_{magn} on T agrees in principle with the experimental findings at low temperatures [72C1, 77B3] where linear spin-wave theory and non-interacting magnons are appropriate. For temperatures somewhat higher, a further term has been added representing a nonlinear spin-wave contribution [81T2] so that C_{magn} becomes

$$C_{\text{magn}}/R = \frac{\pi k_{\text{B}}T}{24SJ} + 0.123\left(\frac{k_{\text{B}}T}{J}\right)^2 \tag{3.80}$$

The significance of the second term has been illustrated for K_2CuF_4 ($T_C = 6.25$ K) where the first term alone reproduces the experimentally determined magnetic specific heat up to about 1.75 K ($k_BT/J = 0.15$) and both terms up to about 3.5 K ($k_BT/J = 0.31$) [81T2]. A linear temperature dependence of C_{magn} has also been obtained with Green's function techniques [73Y1] for the $S = \frac{1}{2}$ 2D Heisenberg ferromagnet on a square lattice with a slightly larger prefactor

$$C_{\text{magn}}/R = \frac{7\pi k_{\text{B}}T}{72J} \tag{3.79a}$$

Colpa [72C1] has measured the slope of C_{magn} at low temperatures for a number of compounds $(C_nH_{2n+1}NH_3)_2CuX_4$ with X = Cl and X = Br and $n \le 6$. When the exchange constant J is known from other experiments, we can compare the experimental results to the theoretical predictions in Eq. 3.79 or 3.79a. It turns out that the experimental results agree generally better with the values resulting from Eq. 3.79a than with those obtained from Eq. 3.79 which are mostly smaller by about 10% while Eq. 3.79a yields only slightly larger values by about 3–4%, on the average. Finally, the Green's function result (Eq. 3.79a) agrees better with extrapolated experimental data (cf. Sect. 4.1.7) than Eq. 3.79 [77B3].

9.12.3.2.2 Cr-Compounds

In this section the second class of materials will be presented with collective Jahn-Teller effect, orbital ordering and intralayer ferromagnetic exchange coupling, namely Cr-compounds. Most of them have ferromagnetic interlayer exchange and are therefore ferromagnets. Many of their properties have been described by P. Day and coworkers [86B1, 86D3, 86D4]. Some have been reported to be antiferromagnets, e.g. Rb_2CrBr_4, $(NH_4)_2CrBr_4$ [81B5], $(C_5H_5NH)_2CrCl_4$ [75L8] and also $CsCrCl_3$ [70L2] which does not belong to the perovskite-type layer structures. Among the latter with M = Cr is Rb_2CrCl_4 a widely studied and therefore well understood prototype. Its cooperative Jahn-Teller effect and the antiferrodistortive order of the elongated $CrCl_6$ octahedra have already been discussed in Sect. 2.1.3 in context with Figs. 2.9 and 2.10. It has been verified by various structure investigations [79D5, 80M2, 80M3, 83J1, 86B3, 86D1, 86F1] and by ^{53}Cr-NMR [77D3]. The structure is orthorhombic, and there are two crystallographic domains Acam and Bbcm which differ by the arrangement of the elongated octahedra in the plane $z = \frac{1}{2}$ (cf. Fig. 2.10). In contrast to K_2CuF_4 [74H1, 79H1], the structural studies of Rb_2CrCl_4 have not revealed any indication for an equivalent structure like $I\bar{4}c2$ [95N2] with a different stacking of the layers (cf. Fig. 2.8 in Sect. 2.1.3). The orbital ordering has also been observed in Rb_2CrCl_4 by diffraction with polarized neutrons [82M6, 86D1]. The theoretical considerations about the ferromagnetic intralayer exchange interaction by Khomski and Kugel [73K1, 82K1] have been extended from Cu^{2+} to Cr^{2+} by Eremin and Kalinenkov [78E]. The cooperative Jahn-Teller effect in Cr^{2+}-compounds is treated in detail in the review by Reinen and Friebel [79R1].

The electronic configuration of Cr^{2+} is $3d^4$ with a free ion ground state ^5D ($L = 2$, $S = 2$). It is split into a lower $^5\Gamma_3^+$ doublet and a $^5\Gamma_5^+$ triplet excited state by the cubic crystalline field of the ligands. These states are further split and their degeneracy is lifted by the reduced symmetry due to the elongation of the octahedra by the Jahn-Teller effect, so that the actual ground state is a singlet one with $S = 2$ [79D3, 86D3], presumably a $^5\Gamma_1^+$ state [77F2]. Therefore, we expect for Cr^{2+} a single-ion anisotropy which is not possible for K_2CuF_4 with $S = \frac{1}{2}$ as discussed in the last section. Neutron diffraction experiments have revealed that the magnetic structure of Rb_2CrCl_4 below T_C is a canted ferromagnetic order. This is illustrated in Fig. 3.34. The single-ion anisotropy tends to align the spins along the long axis of the distorted octahedra in the basal plane. Without the exchange interaction, we would have two sublattices denoted a and b in Fig. 3.34 with the spins aligned alternately along the x_0- and the y_0-axis. The ferromagnetic exchange interaction, on the other hand, tends to align the spins parallel to each other. The resulting easy direction of the spins is almost along the x- or y-direction, nearly at 45° to the anisotropy easy axes, the x_0- and y_0-direction [81H4, 86D3]. In Fig. 3.34, there are also indicated the two coordinate systems (x_0, y_0, z_0) and (x, y, z) which refer to the parent structure I4/mmm and the orthorhombic structures Acam or Bbcm, resp. (cf. Fig. 2.1 in Sect. 2.1.1). The competition between the ferromagnetic exchange and the single-ion anisotropy causes a canting of the spins in the two sublattices. The canting angle is $\pm\delta$ with respect to the x- or y-axis (shown for the x-axis in Fig. 3.34). It is small ($\delta \approx 1°$–$2°$) since the exchange field $H_E \sim 2zS\tilde{J}$ acting on the spins is much larger than the anisotropy field $H_{A1} \sim (S - \frac{1}{2})\,\tilde{P}$ (values of H_E and H_{A1}: see Table 5). The spin canting has been confirmed experimentally by neutron diffraction [83J1, 84M1]. Structure factor calculations show that the intensity is [83J1]

$I \sim (\mu_{Cr} \cdot \cos\delta)^2$ for the magnetic contribution to a nuclear Bragg reflection
$I \sim (\mu_{Cr} \cdot \sin\delta)^2$ for an “antiferromagnetic” superlattice Bragg reflection

where μ_{Cr} is the magnetic moment of the Cr^{2+}-ion. By measuring and analysing not only the strong ordinary reflections but also the much weaker superlattice reflections, the experimental data yield a value of $\delta = \pm 2.1°$ for the canting of the spins alternately away from the x- or y-axis [84M1] as sketched in Fig. 3.34.

A spin Hamiltonian for Rb_2CrCl_4 and related Cr-compounds has to take into account the two sublattices a and b similar to the spin wave calculations for antiferromagnets (cf. Sect. 3.1.2). This means that we have to start our considerations based on the Acam or Bbcm structure with two magnetic ions per unit cell, employing the (x, y, z) coordinate system instead of the (x_0, y_0, z_0) system used for K_2CuF_4. Thus the in-plane anisotropy term will not be written with $S_{a,x0}$ and $S_{b,y0}$ but with the equivalent expressions $(S_{ax} - S_{ay})/\sqrt{2}$ and $(S_{bx} + S_{by})/\sqrt{2}$. In this way, the spin Hamiltonian denoted $\mathcal{H}(1)$ [81H4, 93A] becomes

$$\mathcal{H}(1) = -2\tilde{J}\sum_{\langle i,j\rangle} \boldsymbol{S}_{i,a}\,\boldsymbol{S}_{j,b} - 2J'\sum_{\langle i',j'\rangle} \boldsymbol{S}_{i'}\,\boldsymbol{S}_{j'} - \tfrac{1}{2}\tilde{P}\sum_{i}\,[(S_{i,ax} - S_{i,ay})^2 + (S_{i,bx} + S_{i,by})^2] + \tilde{D}\sum_{i}\,[S^2_{i,az} + S^2_{i,bz}] \tag{3.81}$$

where $\tilde{J}$ and J' are the constants of the intralayer and the interlayer exchange, respectively. The term with $\tilde{P}$ is the above mentioned in-plane anisotropy term with the tendency to align the spins along the x_0- and y_0-axes. The term with $\tilde{D}$ is the out-of-plane anisotropy term with the tendency to force the spins into the easy plane. The symbols $\langle i, j\rangle$ and $\langle i', j'\rangle$ mean again that the summation is taken over all pairs of nearest neighbours counting each pair only once, firstly the four neighbours in the layer, belonging to the other sublattice, and secondly the eight neighbours in the adjacent layers. Since J' is much smaller than

$\tilde{J}$ no difference is made here for the two sublattices. Finally, the summation "i" extends over all ions of one sublattice since the contributions from sublattices a and b are written separately in Eq. 3.81.

The Hamiltonian $\mathcal{H}(1)$ is the basis for a renormalized spin-wave calculation which has been performed by Lindgard et al. [80L2] and Hutchings et al. [81H4]. Such a procedure (cf. Sect. 3.1.2) requires the ζ- or spin-quantization axis to be parallel to the direction of spin orientation in the magnetic structure. Thus a rotation of the coordinate system is necessary, from that with the unique *z*-axis parallel to the crystalline *c*-axis to that with the ζ-axis parallel to the spin-orientation axis. These rotations can be expressed by the following matrix equations for sublattices a and b

$$(\mathrm{S}_{\mathrm{i,a}\xi}, \mathrm{S}_{\mathrm{i,a}\eta}, \mathrm{S}_{\mathrm{i,a}\zeta}) = \begin{pmatrix} 0 & 0 & +1 \\ -\sin\delta & -\cos\delta & 0 \\ +\cos\delta & -\sin\delta & 0 \end{pmatrix} \cdot \begin{pmatrix} \mathrm{S}_{\mathrm{i,ax}} \\ \mathrm{S}_{\mathrm{i,ay}} \\ \mathrm{S}_{\mathrm{i,az}} \end{pmatrix}$$

$$(\mathrm{S}_{\mathrm{i,b}\xi}, \mathrm{S}_{\mathrm{i,b}\eta}, \mathrm{S}_{\mathrm{i,b}\zeta}) = \begin{pmatrix} 0 & 0 & +1 \\ +\sin\delta & -\cos\delta & 0 \\ +\cos\delta & +\sin\delta & 0 \end{pmatrix} \cdot \begin{pmatrix} \mathrm{S}_{\mathrm{i,bx}} \\ \mathrm{S}_{\mathrm{i,by}} \\ \mathrm{S}_{\mathrm{i,bz}} \end{pmatrix} \tag{3.82}$$

The ζ-axes rotated away from the *x*-axis by $\pm\delta$ for sublattice a and b are marked as ζ_a and ζ_b in Fig. 3.34. The renormalized spin-wave calculation for $\mathrm{Rb_2CrCl_4}$ by Hutchings et al. [81H4] does not quite follow the lines discussed in Sect. 3.1.2 (cf. Eqs. 3.2–3.15). The transformation of the spin operators $\mathrm{S}_{\mathrm{i,a}\xi}$, $\mathrm{S}_{\mathrm{i,a}\eta}$ and $\mathrm{S}_{\mathrm{i,a}\zeta}$ to magnon Bose operators a_i^+ and a_i for sublattice a and analogously for sublattice b is not performed by the method of Holstein-Primakoff [40H] but by the approach of matching the matrix elements (MME) [74L2, 76L3]. The application of the rotation Eq. 3.82 to $\mathcal{H}(1)$ (Eq. 3.81) creates terms linear in the Bose operators which are removed by applying a linear transformation to these operators. The resulting condition that the linear terms vanish is the equilibrium condition expressing the balance between exchange and the in-plane anisotropy field

$$\mathrm{tg}\, 2\delta = [\tilde{P}\,(S - \tfrac{1}{2})] / [2zS\tilde{J}] \tag{3.83}$$

where S is the spin value ($S = 2$ for Cr^{2+}) and $z = 4$ the number of nearest neighbours. An alternative form of Eq. 3.83 is very useful to determine δ from experimental data

$$[\mathrm{tg}\, 2\delta]^2 = [P\,(S - \tfrac{1}{2})] / [2zSJ] \tag{3.84}$$

where $P = \tilde{P} \sin 2\delta$ and $J = \tilde{J} \cos 2\delta$ are abbreviations which will frequently be used in our further considerations. The factor $(S - \frac{1}{2})$ in Eq. 3.83 and in the following equations below ensures that the single-ion anisotropy has no influence on the spinwave spectrum of spin $S = \frac{1}{2}$ systems like $\mathrm{K_2CuF_4}$. And we recall from Sects. 3.1.5 and 3.1.9 that the same is true for the single-ion anisotropy in antiferromagnets like $\mathrm{K_2FeF_4}$ ($S = 2$) and $\mathrm{K_2CoF_4}$ ($S = \frac{1}{2}$). It should further be noted in this context that a classical spin-wave calculation (cf. Sect. 3.1.6) instead of the MME method or a similar transformation would yield $\tilde{P}S$ and not $\tilde{P}\,(S - \frac{1}{2})$ as in Eq. 3.83. For low temperatures, we may apply linear spin-wave theory to Eq. 3.81 and neglect the renormalization terms. Since the anisotropy terms are much larger than the interlayer exchange, we will neglect the latter and put $J' = 0$. Then, we obtain for the spin-wave energies (see Eq. A 1.3 of [81H4])

$$(\hbar\omega_{\mathrm{q}})^2 = \{2zS\widetilde{J}\,(\cos 2\delta \pm \gamma_{\mathrm{q}}) + [D\,(1+\gamma_{\mathrm{q}}) + 2P]\,(S-\tfrac{1}{2})\}\times$$
$$\times\{2zSJ\,(1\pm\gamma_{\mathrm{q}}) + [D\,(1-\gamma_{\mathrm{q}}) + 2P]\,(S-\tfrac{1}{2})\} \qquad 3.85)$$

with the abbreviations P, J as in Eq. 3.84 and a new one $D = \widetilde{D} + \frac{1}{2}\widetilde{P}\,(1 - \sin 2\delta)$. For reasons of the spin canting and the two sublattices in Rb_2CrCl_4, the (x, y, z) coordinate system is used as for the antiferromagnets in Sect. 3.1.2. Consequently, the appropriate unit cell in reciprocal space is the small Brillouin zone for antiferromagnets with $0 \le qa \le \pi/2$ in q_x-direction (cf. Fig. 3.29) and we obtain two magnon branches. The upper and the lower sign in Eq. 3.85 refers to the upper and lower branch, respectively. In the literature however, very often the two branches are unfolded into the larger ferromagnetic Brillouin zone (cf. Fig. 3.29) and to consider Rb_2CrCl_4 as a ferromagnet with one magnetic ion per unit cell (I4/mmm) using the (q_{x0}, q_{y0}, q_{z0}) coordinate system in reciprocal space with $0 \le qa \le \pi$ for $\boldsymbol{q} = (q, q, 0)$ corresponding to $\boldsymbol{q} = (q_{x0}, 0, 0)$ in the other system. Then, Eq. 3.85 has to be modified as follows

$$(\hbar\omega_{\mathrm{q}})^2 = \{2zS\widetilde{J}\,(\cos 2\delta - \gamma_{\mathrm{q}}) + [D\,(1+|\gamma_{\mathrm{q}}|) + 2P]\,(S-\tfrac{1}{2})\}\times$$
$$\times\{2zS\widetilde{J}\,\cos 2\delta\;\;(1-\gamma_{\mathrm{q}}) + [D\,(1-|\gamma_{\mathrm{q}}|) + 2P]\,(S-\tfrac{1}{2})\} \qquad (3.85a)$$

where $\gamma_{\mathrm{q}} = \frac{1}{2}(\cos q_{x0}a + \cos q_{y0}a)$ is now identical with the expression for the ferromagnet K_2CuF_4 in Eq. 3.71a. As already mentioned, the canting angle δ turns out to be small, experimental value $\delta = 2.1°$ and fit value from spin-wave theory (Eqs. 3.84 and 3.85) $\delta = 1.1°$. On the other hand, the Hamiltonian $\mathcal{H}(1)$ is relatively complicated and the handling of the terms of fourth order in the Bose operators becomes rather lengthy. Therefore, an approximate Hamiltonian $\mathcal{H}(2)$ has also been used for calculating the spin-wave energies of Rb_2CrCl_4 [81H4]

$$\mathcal{H}(2) = -2J\sum_{\langle \mathrm{i,j}\rangle} \boldsymbol{S}_{\mathrm{i}}\boldsymbol{S}_{\mathrm{j}} - 2J'\sum_{\langle \mathrm{i}',\mathrm{j}'\rangle} \boldsymbol{S}_{\mathrm{i}'}\boldsymbol{S}_{\mathrm{j}'} - P\sum_{\mathrm{i}} \mathrm{S}^2_{\mathrm{i,x}} + D\sum_{\mathrm{i}} \mathrm{S}^2_{\mathrm{i,z}} \qquad (3.86)$$

where J, P and D have the same meaning as defined in context with Eqs. 3.83 and Eq. 3.85. $\mathcal{H}(2)$ is the standard Hamiltonian for an easy-plane ferromagnet ($D > 0$) with an in-plane anisotropy. In Eq. 3.86, the x-axis will be the easy axis for $P > 0$, i.e. the direction of the spontaneous magnetization. This again is a simplification because the y-axis can as well be the easy axis and the results of FMR experiments will show a fourfold symmetry in the basal plane. The spin canting is no longer shown explicitly in $\mathcal{H}(2)$ but its consequences on the parameters J, P, and D are taken implicitly into account (cf. also Eq. 3.84). For a renormalized spin-wave calculation with $\mathcal{H}(2)$, it is also necessary to make the x-axis the ζ- or quantization axis. Eq. 3.82 yields with $\delta = 0$ $x \leftrightarrow \zeta$, $y \leftrightarrow -\eta$ and $z \leftrightarrow \xi$. Finally, the spin-wave spectrum obtained from $\mathcal{H}(2)$ (Eq. 3.86) will consist of one nondegenerate magnon branch in the larger I4/mmm Brillouin zone which has been discussed above as an unfolding of the two branches from $\mathcal{H}(1)$. It is therefore not surprising that the magnon energies derived from $\mathcal{H}(2)$ for low temperatures by linear spin-wave theory differ only little from those in Eq. 3.85a neglecting again the interlayer exchange ($J' = 0$)

$$(\hbar\omega_{\mathrm{q}})^2 = \left\{2zSJ\,(1-\gamma_{\mathrm{q}}) + [D\,(1+|\gamma_{\mathrm{q}}|) + 2P]\left(S-\tfrac{1}{2}\right)\right\}\times$$
$$\times\left\{2zSJ\,(1-\gamma_{\mathrm{q}}) + [D\,(1-|\gamma_{\mathrm{q}}|) + 2P]\left(S-\tfrac{1}{2}\right)\right\} \qquad (3.87)$$

The difference between $(\hbar\omega_{\mathrm{q}})^2$ in Eqs. 3.85a and 3.87 is that a term $-4zS\widetilde{J}\gamma_{\mathrm{q}}\sin^2\delta$ has been neglected in Eq. 3.87 which is indeed rather small. A further consequence of the spin canting in Rb_2CrCl_4 and of the in-plane anisotropy field is that there is a spin-wave gap at $\boldsymbol{q} = 0$ with a width for $T \to 0$ calculated by means of Eq. 3.85 from Hamiltonian $\mathcal{H}(1)$

$$(h\nu_{\text{gap}})^2 = \left[(S-\tfrac{1}{2})(2\tilde{D}+\tilde{P}+\tilde{P}\sin 2\delta) - 4zS\tilde{J}\sin^2\delta\right] \cdot \left[(S-\tfrac{1}{2})2\tilde{P}\sin 2\delta\right] \tag{3.88}$$

When starting from $\mathcal{H}(2)$ (Eq. 3.86) instead of $\mathcal{H}(1)$, the small term $4zS\tilde{J}\sin^2\delta$ is again neglected and we obtain for $T \to 0$ the simpler and more often used expression for $h\nu_{\text{gap}}$ [81H4]

$$h\nu_{\text{gap}} = (S-\tfrac{1}{2})\; 2\sqrt{(D+P)\,P} \tag{3.89}$$

where sometimes $P = \tilde{P}\sin 2\delta$ is neglected as small compared to $D \approx \tilde{D} + \frac{1}{2}\tilde{P}$ (neglecting also here $\tilde{P}\sin 2\delta$) [87A3, 88B3]. Thus ν_{gap}^2 is essentially proportional to the product of the out-of-plane and in-plane anisotropy fields which are related to D and P as will be discussed below in context with ferromagnetic resonance (FMR, see Eq. 3.100). This is different from the AFMR frequency in antiferromagnets where, in the simplest case (Eq. 3.10 in Sect. 3.1.2), the leading term of ν_{AFMR}^2 is the product of the exchange field H_{E} and the out-of-plane anisotropy field H_{A}. From Eqs. 3.88 and 3.89 it is obvious, on the other hand, that ν_{gap}^2 is proportional to $\sin 2\delta$ and vanishes for $\delta = 0$.

The magnon dispersion curves have been determined for Rb_2CrCl_4 by neutron inelastic scattering for $\boldsymbol{q} \mathrel{\hat{=}} (\zeta, \zeta, 0)$ with $\zeta = q_{x0}/a^* = q_{y0}/a^*$ ($a^* \approx b^*$) [80L2, 81H4]. The complete magnon branch for $0 \le \zeta \le 0.5$ has been measured at 20 K. Additional data have been acquired at 5 K, 40 K and 50 K for small ζ ($0 \le \zeta \le 0.05$). All these experimental results are reproduced in Fig. 3.35. The complete set of data for 20 K has been the basis for two independent fits to $\mathcal{H}(1)$ (Eq. 3.81) and $\mathcal{H}(2)$ (Eq. 3.86). The obtained parameter values are listed in Table 5. At the elevated temperature $T = 20\ \text{K} = 0.38\ T_{\text{C}}$, linear spin-wave theory is not sufficient for these fits and temperature renormalization terms are taken into account. For large wavevectors ($\zeta > 0.15$), the magnon dispersion curve can be analysed in terms of the ideal 2D Heisenberg model ([80L2, 81H4], see also [76H4]) with $\delta = 0$ and $\tilde{D} = \tilde{P} = D = P = 0$ in Eqs. 3.86 and 3.87, similar to K_2CuF_4 [83H4]. The corresponding expression for $\hbar\omega_{\text{q}}$ (see Eq. 3.72) can well be fitted to the experimental points for $\zeta > 0.15$ [76H4]. But at smaller wavevectors ($\zeta < 0.15$) the anisotropy terms, especially the out-of-plane anisotropy, have a considerable influence on the results of spin-wave calculations and have to be included for a realistic fit to the experimental data. Thus there will be a crossover for Rb_2CrCl_4 from 2D Heisenberg to 2D XY-model behaviour as discussed for K_2CuF_4 in the preceding section. The data for $0 \le \zeta \le 0.05$ show that the magnon gap exhibits a strong temperature normalization. Additional high resolution neutron inelastic scattering [86H2] and ferromagnetic resonance (FMR) experiments [84S3] have revealed that the decrease of the gap energy with increasing temperature is so drastic that ν_{gap} is already practically zero at 50 K well below T_{C}. This means that the temperature dependence of ν_{gap} is very different from that of the order parameter while in antiferromagnets the temperature dependence of ν_{AFMR} is almost equal to that of the sublattice magnetization M_{subl} (Eq. 3.17 in Sect. 3.1.2).

In the magnetic structure of Rb_2CrCl_4 (Fig. 3.34), we have to distinguish two magnetic sublattices with a canting of the spins away from the x- or y-axis alternately by a small angle $\pm\delta$. And it has been mentioned in context with $\mathcal{H}(1)$ (Eq. 3.81) that the appropriate description is with two magnetic ions per unit cell and that the corresponding Brillouin zone is the small antiferromagnetic one (cf. Fig. 3.29). The two magnon branches are usually called the "acoustic" and the "optic" branch. At $\boldsymbol{q} = 0$, the lower mode (acoustic) is the spin-wave gap discussed above and the upper mode (optic) ist the maximum spin-wave energy with $h\nu_{\max} \approx 4zS\tilde{J}$. In order to make easier a comparison to other ferromagnets and to use the approximate Hamiltonian $\mathcal{H}(2)$, the spin waves of Rb_2CrCl_4 have been described as one branch in an extended Brillouin zone and also the experimental data are presented in Fig. 3.35 in this way. We recall further from Fig. 3.29 that the ferromagnetic zone boundary is $(\frac{1}{2}, \frac{1}{2}, 0)$ in the system (q_{x0}, q_{y0}, q_{z0}) or $(1, 0, 0)$ in the system (q_x, q_y, q_z). For antiferromagnets, this is a superlattice reciprocal lattice point. In contrast to ordinary ferromagnets without spin canting, $\nu_{\max}$ is really at $\boldsymbol{q} = 0$ in Rb_2CrCl_4 and has been observed by Raman scattering [87A3]. Also from these results, values were derived for the parameters of Rb_2CrCl_4 by means of a spin-wave calculation. We obtain for $\mathcal{H}(1)$ from Eq. 3.85 for low temperatures neglecting terms like $\tilde{P}\sin 2\delta$ or $4zS\tilde{J}\sin^2\delta$ which are here really negligible in comparison to the leading term $4zSJ$ (cf. the values in Table 5)

$$h\nu_{\max} = \left([4zS\tilde{J}] \cdot \left[4zS\tilde{J} + \left(S - \tfrac{1}{2}\right)(2\tilde{D} + \tilde{P})\right] \right)^{1/2} \tag{3.90}$$

which can further be simplified by the approximation [87A3, 88B3]

$$h\nu_{\max} \approx 4zSJ + D\left(S - \tfrac{1}{2}\right) \tag{3.90a}$$

where $J \approx \tilde{J}$ and $D \approx \tilde{D} + \frac{1}{2}\tilde{P}$. For the analysis of the Raman data, the (linear) spin-wave theory has not employed the MME method [81H4] mentioned above but Briat et al. [88B3] have used a different method and extended the spin-wave theory for Rb_2CrCl_4 by including a Zeeman term and by calculating not only the magnon energies but also the eigenvectors for external field $\boldsymbol{H}_0 \parallel (1, 1, 0)$, $\boldsymbol{H}_0 \parallel (1, 0, 0)$ and $\boldsymbol{H}_0 \parallel (0, 0, 1)$. The problem of the renormalized spin-wave theory for an easy-plane ferromagnet with single-ion anisotropy has attracted much attention from a more theoretical point of view [79B6, 79R2, 80B8, 84R3, 86T2]. The basic Hamiltonian for an ideal easy-plane ferromagnet is

$$\mathcal{H} = -2J \sum_{\langle i, j \rangle} \boldsymbol{S}_i \boldsymbol{S}_j + D \sum_{i} S_{i,z}^2 \tag{3.91}$$

with $J > 0$, $D > 0$ and without in-plane anisotropy. This ideal system will have no magnon gap ($\omega_q \to 0$ for $q \to 0$). Using the Hamiltonian Eq. 3.91 several theoretical papers have dealt with the problem to derive spin-wave energies that meet the conditions already introduced here which can be summarized as follows [86T2]

1) Kinematic consistency: The single-ion anisotropy or the crystal field must not influence the spin-wave energies in spin $S = \frac{1}{2}$ systems (factor $S - \frac{1}{2}$).
2) Goldstone mode: A mode with $\omega = 0$ must exist in view of the continuous symmetry in the easy plane.

In this respect, the various methods like Holstein-Primakoff [40H] or Dyson-Maleev transform [56D, 58M] or the method of matching the matrix elements [74L2, 76L3] have critically been compared [86T2]. And also a proof has been published that all these three procedures are equivalent [79R2] if the transformations are not applied naively but with sufficient care. Finally, all these efforts have not only been made for a better understanding of the spin waves in Rb_2CrCl_4 since there are a number of other materials which are also good realizations of an easy-plane ferromagnet but which belong to classes of materials outside the scope of this contribution.

9.12.3.2.3 Spin-Reorientation Transitions – FMR under Various Conditions

Completely analogous to antiferromagnetic resonance (AFMR) in antiferromagnets, ferromagnetic resonance (FMR) is a powerful tool for studying ferromagnets, especially for determining their anisotropies [66K, 83G1]. Also FMR experiments are performed with a microwave or millimeter wave source and usually by sweeping the external magnetic field H_0. A major difference between FMR and AFMR is that the macroscopic magnetization M of a ferromagnet and the resulting demagnetization effects have to be taken into account while effects of this kind can usually be neglected in antiferromagnets. Thus, the magnetic field H_{int} acting in the ferromagnetic sample is not equal to the applied field H_0 due to these demagnetization effects

$$H_{\mathrm{int},\alpha} = H_{0\alpha} - N^{\alpha} M_{\alpha} \qquad \alpha = x, y, z \tag{3.92}$$

where M_{α} is the α-component of the magnetization and N^{α} the corresponding demagnetization coefficient. According to our choice of the units for H and M, no factor 4π or $1/\mu_0$ is required in Eq. 3.92 (cf. Sect. 1). The coefficients N^{α} can be calculated exactly for ellipsoid-shaped samples [45O, 45S] and only approximately for real samples of perovskite-type layer structures which are mostly thin slabs of circular or rectangular shape. For quasi-optical arrangements in FMR experiments with millimeter waves, a usual approximation is to assume the sample to be a thin sheet with the *c*-axis perpendicular to the sheet and with rather extended lateral dimensions. Then we have approximately $N^{z} = N^{c} = 1$, $N^{x} = N^{a} = 0$ and $N^{y} = N^{b} = 0$. This means $H_{\mathrm{int,x}} = H_{0x}$, $H_{\mathrm{int,y}} = H_{0y}$ and $H_{\mathrm{int,z}} = H_{0z} - M_z$, i.e. H_x, H_y and B_z are continuous at the interface sample-air. In our context, ferromagnetic resonance means the socalled uniform mode and not the magnetostatic modes which also can be observed under favourable conditions [66K, 80B6, 84G2]. Demagnetization corrections are also necessary when studying the susceptibility χ in ferromagnets by magnetic measurements. With respect to the applied field H_0, the apparent susceptibility χ_{app} is obtained as

$$M_{\alpha} = \chi_{\mathrm{app}}^{\alpha\alpha}\, H_{0\alpha} \tag{3.93a}$$

while the true susceptibility χ is

$$M_{\alpha} = \chi^{\alpha\alpha}\, H_{\mathrm{int},\,\alpha} = \chi^{\alpha\alpha}\,(H_{0\alpha} - N^{\alpha} M_{\alpha}) \tag{3.93b}$$

where α is one of the coordinate directions *x*, *y* or *z* assuming a susceptibility tensor with only diagonal elements. By means of Eqs. 3.93a and 3.93b, the measured χ_{app} can be corrected for the demagnetization effects and the true susceptibility χ be calculated [86K2]

$$(\chi^{\alpha\alpha})^{-1} = (\chi_{\mathrm{app}}^{\alpha\alpha})^{-1} - N^{\alpha} \tag{3.94a}$$

Eqs. 3.92–3.94 apply not only to static or dc measurements but also to magnetic measurements in an ac field of frequency *f* which yield the ac susceptibility

$$\chi_{\mathrm{ac}}^{\alpha\alpha}(\omega) = \chi'_{\mathrm{ac}}(\omega) + \mathrm{i}\,\chi''_{\mathrm{ac}}(\omega) \tag{3.95}$$

with the real part χ'_{ac}, the imaginary part χ''_{ac} and $\omega = 2\pi f$. Also here, the indices α mean that m_{α} is observed as response to h_{α} $(\alpha = x, y, z)$. In χ' and χ'', the indices α are omitted for more lucidity if they are not essential for the discussion of the particular problem. Eqs. 3.92–3.94 apply further in ferromagnets to the elements of the dynamic susceptibility χ_{dyn} with its real part χ' and imaginary part χ'' (see Eqs. 3.46, 3.48–3.50 in Sect. 3.1.6). The demagnetization corrections for χ can be separated into real and imaginary part which was derived by Dekker et al. [89D3]

$$\chi' = \frac{\chi'_{\mathrm{app}} - N\,[(\chi'_{\mathrm{app}})^2 + (\chi''_{\mathrm{app}})^2]}{[1 - N\,\chi'_{\mathrm{app}}]^2 + [N\,\chi''_{\mathrm{app}}]^2}$$
$$\chi'' = \frac{\chi''_{\mathrm{app}} - N\,[(\chi'_{\mathrm{app}})^2 + (\chi''_{\mathrm{app}})^2]}{[1 - N\,\chi'_{\mathrm{app}}]^2 + [N\,\chi''_{\mathrm{app}}]^2} \qquad (3.94b)$$

For most of the susceptibility measurements listed in Tables 5 and 6, see for example [75D2, 76D5, 81S1, 81H2, 86C1, 86K2, 88D1, 95S1], the experimental data have been corrected for the demagnetization effects by means of Eqs. 3.94a or b. Such electromagnetic corrections are not required for the susceptibility determined from quasi-elastic neutron scattering experiments. If such investigations are performed in an applied magnetic field, H_{int} according to Eq. 3.92 and not H_0 is the relevant magnetic field.

For FMR studies, also the internal field H_{int} has to be calculated from H_0 since H_0 is swept in the resonance experiment but H_{int} is the quantity that can be compared with the anisotropy fields in the sample. And following this concept, it is useful to introduce as for AFMR (cf. Eqs. 3.42–3.44 in Sect. 3.1.6) the macroscopic magnetization $\boldsymbol{M}$ which can be separated into a static part $\boldsymbol{M_0}$ and an oscillating (precessing) part $\boldsymbol{m}$. The spin Hamiltonians, e.g. Eq. 3.69 for K_2CuF_4 and Eqs. 3.81 and 3.86 for Rb_2CrCl_4, are then converted to a macroscopic energy density u (see Eq. 3.41 in Sect. 3.1.6). There, the parameters in the Hamiltonians are expressed as magnetic fields. In order to remove the anisotropy of the g-factor from the spin-wave calculations, an isotropic g is used in these procedures which is taken equal to g_a. With $g = g_a$, the fields in the energy density u are for K_2CuF_4 and other Cu-compounds

$$H_{\mathrm{E}} = 2zSJ/g_a\mu_{\mathrm{B}} \qquad H'_{\mathrm{E}} = 2z'S\,|\,J'\,|\,/\,g_a\mu_{\mathrm{B}} \qquad H_{\mathrm{A}} = 2zSJ_{\mathrm{A}}/g_a\mu_{\mathrm{B}} \qquad \widetilde{H}_{\mathrm{A}} = 2zS\widetilde{J}_{\mathrm{A}}/g_a\mu_{\mathrm{B}} \qquad (3.96)$$

With these definitions, h'_{E}, h_{A}, and $\widetilde{h}_{\mathrm{A}}$ (cf. Eq. 3.71) can be rewritten as

$$h'_{\mathrm{E}} = H'_{\mathrm{E}}\,/\,H_{\mathrm{E}} \qquad h_{\mathrm{A}} = H_{\mathrm{A}}/H_{\mathrm{E}} \qquad \widetilde{h}_{\mathrm{A}} = \widetilde{H}_{\mathrm{A}}\,/\,H_{\mathrm{E}} \qquad (3.96a)$$

For most Cu-compounds, we have $g_a = g_b \neq g_c$. Only for $[COOH(CH_2)_2NH_3]_2CuCl_4$, a small difference between g_a and g_b has been reported [81W2]. Therefore it is useful to use for the spin-wave calculation an isotropic g-factor $g = g_a$ and to take the anisotropy of the g-factor into account by applying for $\boldsymbol{H_0} \parallel \boldsymbol{c}$ a modified magnetic field

$$H_0^* = (g_c/g_a)H_0 \qquad (3.97)$$

in the final results instead of H_0. Such use of an isotropic g-factor in spin-wave calculations is quite common [74Y1, 76Y2, 76Y3, 77T4, 88D3], but very frequently with an isotropic $g = 2$. Then, modified fields are necessary for both, $\boldsymbol{H_0} \perp \boldsymbol{c}$ and $\boldsymbol{H_0} \parallel \boldsymbol{c}$. It is to be pointed out again that in the following spin-wave calculations the magnetic dipolar interactions are always assumed to be included in the anisotropy fields in order to keep the results more lucid and clear. In some of the references, on the other hand, the dipolar interactions have been treated separately and the corresponding lattice sums (cf. Eq. 3.8 in Sect. 3.1.2) calculated. So the interested reader is referred to them [74Y1, 74Y3, 76Y2, 76Y3, 81C2, 87Y2, 88J1, 88Y1]. Finally, the energy density u is derived for ferromagnetic interlayer exchange and thus for ferromagnetic Cu-compounds resulting from the Hamiltonian Eq. 3.69 by means of Eq. 3.96

$$u = -\frac{H_\mathrm{E}}{2M_0}\boldsymbol{M}\,\boldsymbol{M} - \frac{H'_\mathrm{E}}{2M_0}\boldsymbol{M}\,\boldsymbol{M} + \frac{H_\mathrm{A}}{2M_0}M_\mathrm{z}^2 + \frac{\widetilde{H}_\mathrm{A}}{2M_0}M_\mathrm{y}^2$$
$$-\,(\boldsymbol{H_0} + \boldsymbol{h})\,\boldsymbol{M} + \tfrac{1}{2}\boldsymbol{M}\,\mathrm{N}\,\boldsymbol{M} \qquad (3.98)$$

where the Zeeman term in the second line of Eq. 3.98 contains the applied static field $\boldsymbol{H_0}$, the ac or microwave field $\boldsymbol{h}$ and, in addition, a demagnetization term [88D3]. M_0 (cf. Eq. 3.75a) is the value of the magnetization for $T \rightarrow 0$ which is listed for $\mathrm{K_2CuF_4}$ and other compounds in Table 5. Eq. 3.98 is the basis for classical spin-wave calculations in context with ferromagnetic resonance experiments on Cu-compounds without spin-canting. But some of these compounds show spin canting and, as ferromagnets, weak antiferromagnetism. For example, $\mathrm{(CH_3NH_3)_2CuCl_4}$ is a covert weak antiferromagnet which exhibits spin canting only for $H_0 \neq 0$ [88D3] and is a normal collinear ferromagnet for $H_0 = 0$. For description of such a system by spin-wave theory, it has to be divided into two sublattices a and b where every second layer belongs to sublattice a and the other layers between them to sublattice b. With an additional term of special intralayer anisotropic exchange which describes the spin canting effects, the energy density u becomes

$$u = -\frac{H_\mathrm{E}}{2M_\mathrm{S}}(\boldsymbol{M_\mathrm{a}}\boldsymbol{M_\mathrm{a}} + \boldsymbol{M_\mathrm{b}}\boldsymbol{M_\mathrm{b}}) \mp \frac{H'_\mathrm{E}}{M_\mathrm{S}}\boldsymbol{M_\mathrm{a}}\boldsymbol{M_\mathrm{b}} + \frac{H_\mathrm{A}}{2M_\mathrm{S}}(M_\mathrm{a,z}^2 + M_\mathrm{b,z}^2) + \frac{\widetilde{H}_\mathrm{A}}{2M_\mathrm{S}}(M_\mathrm{a,y}^2 + M_\mathrm{b,y}^2)$$
$$+\frac{H_\mathrm{D}}{M_\mathrm{S}}(M_\mathrm{a,y}M_\mathrm{a,z} - M_\mathrm{b,y}\,M_\mathrm{b,z}) - (\boldsymbol{H_0} + \boldsymbol{h})\,(\boldsymbol{M_\mathrm{a}} + \boldsymbol{M_\mathrm{b}}) + \tfrac{1}{2}(\boldsymbol{M_\mathrm{a}} + \boldsymbol{M_\mathrm{b}})\,\mathrm{N}\,(\boldsymbol{M_\mathrm{a}} + \boldsymbol{M_\mathrm{b}}) \qquad (3.99)$$

where the upper sign for the interlayer exchange $(-H'_\mathrm{E})$ refers to a ferromagnet with hidden or open spin canting, e.g. $\mathrm{(CH_3NH_3)_2CuCl_4}$. $M_\mathrm{S} = \frac{1}{2}M_0$ is the static value of the sublattice magnetization ($M_\mathrm{a,0} = M_\mathrm{b,0} = M_\mathrm{S}$) where M_0 is the magnetization of the ferromagnet in this case (cf. Eq. 3.75a). Eq. 3.99 can also be used as the starting point for spin-wave calculations on antiferromagnetic Cu-compounds (lower sign: $+H'_\mathrm{E}$) with and without spin canting. In the latter case, Eq. 3.99 is with $H_\mathrm{D} = 0$ the basis for calculating the AFMR frequencies [76T2] and the critical fields (Eqs. 3.57–3.59 in Sect. 3.1.8). And with $H_\mathrm{D} \neq 0$, Eq. 3.99 is the basis for treating systems with spin canting. Examples are $\mathrm{(C_2H_5NH_3)_2CuBr_4}$, a canted antiferromagnet and weak ferromagnet [81S5], and $\mathrm{(C_2H_5NH_3)_2CuCl_4}$, a covert weak ferromagnet, i.e. the spins are canted only for $H_0 \neq 0$ [73B5]. The terms in Eq. 3.99 with H_A for the out-of-plane anisotropy and with $\widetilde{H}_\mathrm{A}$ for the in-plane anisotropy are taylored for compounds like $\mathrm{(CH_3NH_3)_2CuCl_4}$, $\mathrm{(C_2H_5NH_3)_2CuCl_4}$ and $\mathrm{[COOH(CH_2)_2NH_3]_2CuCl_4}$ with

$$\boldsymbol{a}\text{: easy axis,}\quad \boldsymbol{b}\text{: medium axis,}\quad \boldsymbol{c}\text{ or }\boldsymbol{c}'\text{: hard axis}\quad (H_\mathrm{A} > 0,\ \widetilde{H}_\mathrm{A} > 0) \qquad (3.99\mathrm{a})$$

where the crystallographic directions $\boldsymbol{a}$, $\boldsymbol{b}$, and $\boldsymbol{c}$ are identical with the coordinate directions of the (x, y, z) system (cf. Fig. 2.1 in Sect. 2.1.2). The anisotropies are different for other Cu-compounds like $\mathrm{(C_2H_5NH_3)_2CuBr_4}$ with

$$\boldsymbol{b}\text{: easy axis,}\quad \boldsymbol{a}\text{: medium axis,}\quad \boldsymbol{c}\text{ or }\boldsymbol{c}'\text{: hard axis}\quad (H_\mathrm{A} > 0,\ \widetilde{H}_\mathrm{A} < 0) \qquad (3.99\mathrm{b})$$

which requires in our model to change the sign of $\widetilde{H}_\mathrm{A}$ Some Cu-compounds like $\mathrm{[COOH(CH_2)_2NH_3]_2CuBr_4}$ are not of the easy-plane type with $H_\mathrm{A} > 0$ but more of the easy-axis type so that also a change of sign is necessary for H_A:

$$\boldsymbol{c} \text{ or } \boldsymbol{c}'\text{: easy axis,} \quad \boldsymbol{b}\text{: medium axis,} \quad \boldsymbol{a}\text{: hard axis} \quad (H_\mathrm{A} < 0, \widetilde{H}_\mathrm{A} < 0) \tag{3.99c}$$

Eqs. 3.99a–3.99c refer to the Hamiltonian in Eq. 3.69, to H_A and $\widetilde{H}_\mathrm{A}$ in Eq. 3.96 and to the resulting energy density in Eq. 3.99 and not to other definitions of H_A and $\widetilde{H}_\mathrm{A}$ e.g. for easy-axis Mn-compounds (see, for example, Eq. 3.41). That means that $H_\mathrm{A} < 0$ or $\widetilde{H}_\mathrm{A} < 0$ implies also $J_\mathrm{A} < 0$ or $\widetilde{J}_\mathrm{A} < 0$ in Eq. 3.69. Further, $\boldsymbol{c}'$ is a direction perpendicular to $\boldsymbol{a}$ and $\boldsymbol{b}$ introduced in some Cu-compounds with monoclinic symmetry like $[\mathrm{COOH(CH_2)_2NH_3}]_2\mathrm{CuX_4}$ with X = Cl, Br [81W2, 83W2]. It should also be noted that Eq. 3.99 cannot be used without introduction of additional anisotropy terms for systems like $(\mathrm{C_6H_5CH_2NH_3})_2\mathrm{CuCl_4}$ where the easy axis is the (1, 1, 0)-direction. Finally, the data on magnetic properties including the spin anisotropies are compiled in Table 5 also for a number of Cu-compounds with reference to Eqs. 3.99a–3.99c.

Bloembergen et al. [73B5] have studied the field-induced phase transitions of the antiferromagnet $(\mathrm{C_2H_5NH_3})_2\mathrm{CuCl_4}$ from the AF-phase to the SF- and PM-phases which are easily accessable in this case because of the small value of H'_E, as mentioned already in Sects. 3.1.6 and 3.1.8 (cf. Fig. 3.23). Their analysis is based on an energy density similar to Eq. 3.99. Moreover, $(\mathrm{C_2H_5NH_3})_2\mathrm{CuCl_4}$ is a system with covert spin canting ($H_\mathrm{D} \neq 0$) where the spins rotate for $\boldsymbol{H_0} \parallel \boldsymbol{b}$ and $\boldsymbol{H_0} \parallel \boldsymbol{c}$ with increasing H_0 from the easy axis (a-axis) to the bc-plane, and critical fields H^α_CF ($\alpha = b, c$) mark the transition of the system to a canted phase in which the sublattice magnetizations parallel to the a-axis vanish (cf. H^c_CF in Eq. 3.60 of Sect. 3.1.8). Especially for $\boldsymbol{H_0} \parallel \boldsymbol{c}$, there is at $H_0 = H^\mathrm{c}_\mathrm{CF}$ a considerable canting of the spins by an angle φ_c away from the c-axis in the bc-plane which results from [73B5]

$$\mathrm{tg}\, \varphi_\mathrm{c} = H_\mathrm{D} / \widetilde{H}_\mathrm{A} \tag{3.100a}$$

With the values for $(\mathrm{C_2H_5NH_3})\mathrm{CuCl_4}$, Eq. 3.100a yields $\varphi_\mathrm{c} \approx 60°$ and Eqs. 3.59, 3.60 yield $H^\mathrm{c}_\mathrm{CF} \approx 0.5\, H^\mathrm{c}_\mathrm{PM}$. If the external field H_0 is further increased above H^c_CF, the canting angle φ_c is reduced according to the equation (cf. [88D3])

$$(2\,H'_\mathrm{E} + H_\mathrm{A} - \widetilde{H}_\mathrm{A})\sin\varphi_\mathrm{c}\cos\varphi_\mathrm{c} + H_\mathrm{D}\cos 2\varphi_\mathrm{c} = H^*_0 \sin\varphi_\mathrm{c} \tag{3.100b}$$

which shows that an exact solution $\varphi_\mathrm{c} = 0$ cannot be obtained for finite H^*_0 (cf. Eq. 3.97) and that the system therefore does not undergo a transition to a PM-phase with $\varphi_\mathrm{c} = 0$. But the system approaches this state asymptotically. And at a field of $H_0 \approx 2.6\, H^\mathrm{c}_\mathrm{CF}$, the magnetization M_z has already reached 99.5% of its maximum value $2M_\mathrm{S}$ (cf. Fig. 6 in [73B5]). But there is still a component $M_\mathrm{y} \approx \pm 0.1\, M_\mathrm{S}$ due to the spin canting ($\varphi_\mathrm{c} \approx 5.7°$ in this case). Another example for spin canting is $(\mathrm{C_2H_5NH_3})_2\mathrm{CuBr_4}$ where $\boldsymbol{b}$ is the easy axis and $\boldsymbol{c}$ the hard axis. That means, the spins are for $H_0 = 0$ already in the bc-plane and subject to the action of H_D. For $H_0 = 0$ and for $\boldsymbol{H_0} \parallel \boldsymbol{c}$, Eq. 3.100b can be used also in this case to calculate the canting angle φ_c. For $H_0 = 0$, the result is $\varphi_\mathrm{c} = 49.5°$ (see Table 5 and [81S5]). In this context, it is worth to be noted that in the canted system and in the PM-phase of systems without canting, a considerable magnetization is build up, especially at low temperature because of the ferromagnetic correlations due to the strong intralayer exchange field H_E. Therefore, the demagnetization term has been included in Eq. 3.99 not only for ferromagnetic but also for antiferromagnetic compounds. It should further be noted that the ferromagnetic exchange terms in Eqs. 3.98 and 3.99 will not contribute to the spin-wave energies in the usual treatment of the energy density u by means of the Bloch-Bloembergen equation (Eq. 3.42 in Sect. 3.1.6) but only to the static energy density of the system.

In a way similar to that for the Cu-compounds, magnetic fields are introduced for the ferromagnet Rb_2CrCl_4 and other Cr-compounds. The fields corresponding to the parameters in $\mathcal{H}(1)$ (Eq. 3.81) are

$$H_E = 2zS\tilde{J}\,/\,g\mu_B \qquad H_{A1} = 2\tilde{P}\left(S-\tfrac{1}{2}\right)/\,g\mu_B \qquad H_{A2} = 2\tilde{D}\left(S-\tfrac{1}{2}\right)/g\mu_B \tag{3.101}$$

where the small interlayer exchange $H'_E \sim J'$ has been neglected and an isotropic g-factor $g = 2.00$ has been used since the values of g_a and g_c are nearly 2.00 in Rb_2CrCl_4 (cf. Table 5). Thus we obtain from $\mathcal{H}(1)$ with two sublattices $\boldsymbol{M}_\mathbf{a}$ and $\boldsymbol{M}_\mathbf{b}$ for canted ferromagnets like Rb_2CrCl_4 the energy density

$$\begin{aligned} u(1) = &-\frac{H_E}{M_S}\boldsymbol{M}_\mathbf{a}\boldsymbol{M}_\mathbf{b} + \frac{H_{A2}}{2M_S}(M_{a,z}^2 + M_{b,z}^2) + \frac{H_{A1}}{4M_S}\,[(M_{a,x} - M_{a,y})^2 + (M_{b,x} + M_{b,y})^2] \\ &-(\boldsymbol{H}_\mathbf{0} + \boldsymbol{h})\,(\boldsymbol{M}_\mathbf{a} + \boldsymbol{M}_\mathbf{b}) + \tfrac{1}{2}\,(\boldsymbol{M}_\mathbf{a} + \boldsymbol{M}_\mathbf{b})\,\mathbf{N}\,\;(\boldsymbol{M}_\mathbf{a} + \boldsymbol{M}_\mathbf{b}) \end{aligned} \tag{3.102}$$

where again the sublattice magnetization M_S is approximately equal to half of the total magnetization $M_0/2$ neglecting the small antiferromagnetic component due to the spin canting ($\delta = 1.1°$, cf. Table 5). In Eq. 3.102, the exchange term is needed also in the Bloch-Bloembergen equation for establishing the equilibrium condition yielding the canting angle. We recall from Sect. 3.2.2 that for the analysis of the data from inelastic neutron scattering on Rb_2CrCl_4 an approximate Hamiltonian $\mathcal{H}(2)$ has been used in which the spin canting is neglected and the system treated like a simple ferromagnet. The corresponding magnetic fields are (omitting again $H'_E \sim J'$)

$$H_E = 2zSJ/g\mu_B \qquad H_A = 2D\left(S-\tfrac{1}{2}\right)/\,g\mu_B \qquad \tilde{H}_A = 2P\left(S-\tfrac{1}{2}\right)/\,g\mu_B \tag{3.103}$$

where the magnetic fields have again been calculated with $g = 2.00$ as a convenient approximation. The relation between D, P in Eq. 3.103 and $\tilde{D}, \tilde{P}$ in Eq. 3.101 is given in Eq. 3.85. The energy density u resulting from $\mathcal{H}(2)$ is equal to that in Eq. 3.98 and will therefore not be repeated here. A disadvantage of this energy density is that it contains an orthorhombic in-plane symmetry which is appropriate for Cu-compounds like $(CH_3NH_3)_2CuCl_4$ but not for Rb_2CrCl_4. It will be shown below that the FMR data for Rb_2CrCl_4 exhibit the fourfold crystal symmetry when the external field $\boldsymbol{H}_\mathbf{0}$ is applied at various angles with respect to the a-axis in the basal plane. It is therefore more suitable to use for the interpretation of the FMR data on Rb_2CrCl_4 the following energy density

$$u = -\frac{H_E}{2M_0}\boldsymbol{M}\,\boldsymbol{M} + \frac{H_A}{2M_0}M_z^2 + \frac{\hat{H}_A}{2M_0^3}(M_xM_y)^2 - (\boldsymbol{H}_\mathbf{0} + \boldsymbol{h})\,\boldsymbol{M} + \tfrac{1}{2}\boldsymbol{M}\,\mathbf{N}\,\boldsymbol{M} \tag{3.104}$$

where the term with $\tilde{H}_A$ reflects the fourfold crystal symmetry as in Eq. 3.41 (3.1.6) for the analysis of the AFMR data of Rb_2MnCl_4.

In the magnetic order of the easy-plane ferromagnet Rb_2CrCl_4 (cf. Fig. 3.34), the easy axis is the $(1,0,0)$ or $(0,1,0)$ direction of the (x,y,z) coordinate system (cf. Fig. 2.1 in Sect. 2.1.2) and, according to the strengths of the anisotropy fields which are listed in Table 5, the medium axis is the $(1,1,0)$ or $(1,\bar{1},0)$ direction and the hard axis the $(0,0,1)$ direction. This can be confirmed by FMR experiments under various conditions where the magnetic field $\boldsymbol{H}_\mathbf{0} = H_0(\sin\psi\,\cos\beta,\ \sin\psi\,\sin\beta,\ \cos\psi)$ (cf. Eq. 3.43 in Sect. 3.1.6) is applied in various directions with respect to the crystalline axes. For example, $\boldsymbol{H}_\mathbf{0} \parallel (1,0,0)$ corresponds to $\psi = 90°$ and $\beta = 0$ and $\boldsymbol{H}_\mathbf{0} \parallel (0,0,1)$ to $\psi = 0$ (β irrelevant). Fig. 3.36 shows the experimental results for Rb_2CrCl_4 at 4.2 K presented as ν_{FMR} versus applied field H_0 [84G3, 91G2]. With the field parallel to the easy axis ($\psi = 90°$, $\beta = 0$) ν_{FMR} increase with increasing field H_0. For $\boldsymbol{H}_\mathbf{0}$ parallel to the medium axis ($\psi = 90°$, $\beta = 45°$), ν_{FMR} decreases first with increasing field and goes to zero when the internal field H_{int} equals the in-plane anisotropy field $\hat{H}_A$, i.e. $H_0 = \hat{H}_A = 0.231$ T. This instability is removed in a spin reorientation transition. When $H_0 > \hat{H}_A$, the system restabilizes by rotating the spins away from the easy direction until they are aligned parallel to the field, i.e. parallel to the medium axis in this case. This phenomenon has further been studied by more detailed FMR experiments and also as a function of temperature [84F2, 84S3]. A similar behaviour is observed for $\boldsymbol{H_0} \parallel (0, 0, 1)$ ($\psi = 0°$). The frequency ν_{FMR} approaches zero for $H_{\text{int}} = H_0 - M_0 = H_A = 3.181$ T. The corresponding value of H_0 in Fig. 3.36 is 3.411 T, where for M_0 the value for $T \to 0$ has been used (0.230 T). In this spin reorientation transition, the external field overcomes the out-of-plane anisotropy field H_A and the spins are rotated into a direction parallel to the field, i.e. parallel to the (0, 0, 1) direction. The solid curves in Fig. 3.36 are the result of a classical spin-wave calculation by means of the Bloch-Bloembergen equation, starting from the energy density u in Eq. 3.104. That the term with $\hat{H}_A$ is needed in Eq. 3.104 for the calculation of ν_{FMR} is illustrated in Fig. 3.37 which shows the FMR results for Rb_2CrCl_4 for various directions of H_0 in the basal plane ($\boldsymbol{H_0} \perp \boldsymbol{c}$). The measurements were performed with $\nu = 61.1$ GHz. The data are presented as field at resonance H_{res} versus the azimuthal angle β. The experimental points in Fig. 3.37 are a clear evidence for the fourfold crystal symmetry and the calculated curves can only be obtained with Eq. 3.104 and by no means with Eq. 3.98. Finally, FMR data have also been taken for Rb_2CrCl_4 with $\nu = 61.1$ GHz bei rotating the external field H_0 from the easy axis ($\beta = 0°$) and from the medium axis ($\beta = 45°$) to the hard direction. The results are shown in Fig. 3.38 as H_{res} versus polar angle ψ where $\psi = 0°$ corresponds to $\boldsymbol{H_0} \parallel \boldsymbol{c}$ and $\psi = \pm 90°$ to $\boldsymbol{H_0} \perp \boldsymbol{c}$. These experimental data provide the information for determining the out-of-plane anisotropy field H_A as well as the in-plane anisotropy field $\hat{H}_A$. The results in Fig. 3.38 for $\psi = 0°$ and $\psi = 90°$ can also be found in Fig. 3.36 by drawing a horizontal line at $\nu_{\text{FMR}} = 61.1$ GHz. But Fig. 3.36 contains more data taken at other frequencies between 30 GHz and 170 GHz.

Similar results of FMR investigations are available for K_2CuF_4 and for other ferromagnetic Cu-compounds like $(CH_3NH_3)_2CuCl_4$ [87D1, 88D3, 89D2, 90D3]. The structure of $(CH_3NH_3)_2CuCl_4$ is monoclinic which can be described as $B12_1/a1$ with $\beta \approx 90°$ (cf. Table 2) so that it may be considered approximately as orthorhombic. Thus the magnetic properties are well reproduced by Eq. 3.98 which is also used for calculating the FMR frequencies of K_2CuF_4 usually neglecting the small quantities $\tilde{H}_A \approx 0$ and $H'_E \approx 0$. In $(CH_3NH_3)_2CuCl_4$, the configuration of easy and hard axes is given by Eq. 3.99a. Since the mathematical handling of the equilibrium conditions is easier for orthorhombic symmetry it is opportune to reproduce some standard expressions for ν_{FMR} [76Y3, 87D1, 88D3, 89D2, 90D3] as derived from Eq. 3.98 or an equivalent energy density. He results are for $(CH_3NH_3)_2CuCl_4$ where the demagnetization factors (Eq. 3.92) are assumed to be $N^c \approx 1$, $N^a \approx 0$ and $N^b \approx 0$. Thus, we obtain

for $\boldsymbol{H_0}$ parallel to the easy axis, i.e. $\boldsymbol{H_0} \parallel \boldsymbol{a}$

$$\nu_{\text{FMR}}^2 = (\gamma_a/2\pi)^2\,(H_0 + \tilde{H}_A)\,(H_0 + H_A + M_0) \tag{3.105}$$

and for $\boldsymbol{H_0}$ parallel to the medium (next preferred) axis, i.e. $\boldsymbol{H_0} \parallel \boldsymbol{b}$

$$\begin{aligned} &H_0 \le \tilde{H}_A \qquad && \nu_{\text{FMR}}^2 = (\gamma_a/2\pi)^2\,[\tilde{H}_A\,(H_A + M_0)]\,[1 - (H_0/\tilde{H}_A)^2] \\ &H_0 > \tilde{H}_A \qquad && \nu_{\text{FMR}}^2 = (\gamma_a/2\pi)^2\,(H_0 - \tilde{H}_A)\,(H_0 + H_A + M_0 - \tilde{H}_A) \end{aligned} \tag{3.106}$$

with the gyromagnetic ratio $\gamma_a = g_a \mu_B/\hbar$. Eqs. 3.105 and 3.106 apply in general to FMR with $\boldsymbol{H_0}$ parallel to the easy axis and to the medium axis, resp., also for other configurations of easy and hard axes, e.g. those in Eq. 3.99b and 3.99c. But usually, the demagnetization corrections have to be adapted to these other configurations. The interested reader will find the expressions for ν_{FMR} with general demagnetization corrections in [76Y3]. The magnetic field at resonance H_{res} for a fixed frequency ν can easily be obtained by inverting Eq. 3.105 or Eq. 3.106. It is further worth noting that both, Eqs. 3.105 and 3.106, yield for $H_0 = 0$ a ferromagnetic spin-wave gap for nonzero H_{A} and $\widetilde{H}_{\text{A}}$. Analogous to Eq. 3.89 for Rb_2CrCl_4 the gap frequency is for $(\text{CH}_3\text{NH}_3)_2\text{CuCl}_4$ and similar compounds

$$\nu_{\text{gap}} = (\gamma_{\text{a}}/2\pi)\,[\,\widetilde{H}_{\text{A}}\,(H_{\text{A}} + M_0)]^{1/2} \tag{3.107}$$

Experimental results on $(\text{CH}_3\text{NH}_3)_2\text{CuCl}_4$ for $\boldsymbol{H_0} \parallel \boldsymbol{a}$ and $\boldsymbol{H_0} \parallel \boldsymbol{b}$ at $T = 1.2$ K, 4.2 K, and 10 K are presented in Fig. 3.39 as ν_{FMR} versus $H_0 = H_{\text{int}}$. As in Fig. 3.36 for Rb_2CrCl_4, the data for $\boldsymbol{H_0}$ parallel to the easy axis (a-axis) exhibit an increasing ν_{FMR} with increasing H_0 as predicted by Eq. 3.105. The data for $\boldsymbol{H_0}$ parallel to the medium axis (b-axis) reflect the spin reorientation transition at $H_0 = \widetilde{H}_{\text{A}}$, especially clear for the lowest temperature $T = 1.2$ K. At 10 K ($T_{\text{C}} = 8.9$ K), the in-plane anisotropy field $\widetilde{H}_{\text{A}}$ is reduced to zero and no spin reorientation transition is observed with $\nu_{\text{FMR}} \to 0$. At these temperatures, the out-of-plane anisotropy H_{A} is still $\neq 0$ as derived from the results for $\boldsymbol{H_0} \parallel \boldsymbol{c}$ below. The measurements for $\boldsymbol{H_0} \parallel \boldsymbol{b}$ offer the possibility to study the spin reorientation transition at various temperatures and to determine the temperature dependence of $\widetilde{H}_{\text{A}}$. Finally, the FMR frequencies become [76Y3, 87D1, 88D3, 89D2, 90D3]

for $\boldsymbol{H_0}$ parallel to the hard axis, i.e. $\boldsymbol{H_0} \parallel \boldsymbol{c}$

a) for $H_{\text{int}} \leq H_{\text{A}}^{\Delta}$:

$$\nu_{\text{FMR}}^2 = (\gamma_{\text{a}}/2\pi)^2\,[\widetilde{H}_{\text{A}}\,(H_{\text{A}} + M_0^{\theta})]\;[1 - \{H_0^*/(H_{\text{A}} + M_0^{\theta})\}^2] \tag{3.108}$$

b) for $H_{\text{int}} > H_{\text{A}}^{\Delta}$:

$$\nu_{\text{FMR}}^2 = (\gamma_{\text{a}}/2\pi)^2\,(H_0^* - H_{\text{A}} - M_0^*)\;(H_0^* - H_{\text{A}} - M_0^* + \widetilde{H}_{\text{A}}) \tag{3.109}$$

or

$$\nu_{\text{FMR}} \approx (\gamma_{\text{c}}/2\pi)\;(H_0 - H_{\text{A}}^{\Delta} - M_0) \tag{3.109a}$$

with $H_{\text{A}}^{\Delta} = (g_{\text{a}}/g_{\text{c}})\,H_{\text{A}}$, $M_0^{\theta} = [\sin^2\theta + (g_{\text{c}}/g_{\text{a}})^2\cos^2\theta\,]^{1/2} M_0$, $M_0^* = (g_{\text{c}}/g_{\text{a}})\,M_0$

where θ is the angle between the magnetization and the c-axis and where H_0^* has been defined in Eq. 3.97. These are the necessary modifications since all spin-wave calculations are performed with an isotropic g-factor $g = g_{\text{a}}$ (cf. discussion in context with Eqs. 3.96 and 3.97). FMR studies for $\boldsymbol{H_0} \parallel \boldsymbol{c}$ with the application of Eqs. 3.108 and 3.109 were performed also for $(\text{CH}_3\text{NH}_3)_2\text{CuCl}_4$ [89D2, 90D3]. The results obtained at 1.2 K, 4.2 K, and 9 K are shown in Fig. 3.40 as FMR frequency ν_{FMR} versus internal field $H_{\text{int}} = H_0 - M_0$. Especially the data for 1.2 K show at $H_{\text{int}} = H_{\text{A}}^{\Delta}$ a softening of ν_{FMR} thus indicating a reorientation transition of the spins which are parallel to $\boldsymbol{H_0}$ above the transition. At higher temperatures like 4.2 K, H_{A}^{Δ} is found from a linear extrapolation of the experimental data $\nu_{\text{FMR}}(H_{\text{int}})$ to the H_{int}-axis while a minimum of ν_{FMR} occurs for a field lower than H_{A}^{Δ}. In their analysis, Demokritov et al. [89D2, 90D3] have identified the magnetic field of this minimum as the critical field H_{C} at which the phase transition ferromagnetic to paramagnetic occurs for a temperature $T < T_{\text{C}}$. Measurements of the type shown in Fig. 3.40 were made at various temperatures in order to obtain $H_{\text{A}}(T)$ and $H_{\text{C}}(T)$. Inversion of the data $H_{\text{C}}(T)$ yields the transition temperature $T_{\text{C}}(H)$. As mentioned before, Eqs. 3.105–3.109 can also be applied to FMR results on K_2CuF_4 setting $\widetilde{H}_A = 0$ [84G1, 84K3, 89D2]. For the latter compound, the FMR results for $T_C(H)$ [89D2] may be compared to those obtained from magnetization measurements [81H2] by means of the condition $\partial M/\partial T = \max$. It turns out that the FMR data yield a somewhat higher temperature closer to the maximum of the $M_z(T)$ curves in Fig. 3.33 (cf. Fig. 4 of [89D2]).

9.12.3.2.4 Magnetic Polaritons

For the discussion of antiferromagnetic resonance (AFMR) under various conditions in Sect. 3.1.6, it was advantageous, e.g. with respect to selection rules, to consider the oscillating magnetic field $\boldsymbol{h}$ as part of an electromagnetic wave, and to use Maxwell's equations in addition to the Bloch-Bloembergen equation (Eq. 3.38). This offered the opportunity to determine the optical constants $cq/\omega = (n + \mathrm{i}k)$ (cf. Eq. 3.47) by means of the wave equation (Eq. 3.46) resulting from Maxwell's equations which is repeated here for convenience

$$\frac{c^2}{\omega^2}\boldsymbol{q}\times[(\boldsymbol{\varepsilon})^{-1}(\boldsymbol{q}\times\boldsymbol{h})] = -(\mathbf{1}+\boldsymbol{\chi}_{\mathbf{dyn}})\,\boldsymbol{h}$$

The inclusion of Maxwell's equations and the use of the wave equation (Eq. 3.46) are also appropriate for FMR as shown for K_2CuF_4 by Kullmann et al. [84K2, 84K3]. It is outlined there that Eqs. 3.46 and 3.47 yield two solutions for $\boldsymbol{H_0} \parallel (1, 0, 0)$ and $\boldsymbol{q} \parallel (0, 0, 1)$

1) $\boldsymbol{h} \parallel (0, 1, 0)$ $$(n+\mathrm{i}k)_1^2 = \varepsilon_{xx}\left[1+\frac{(2\pi\nu_{FMR})^2\,M/H_0}{(2\pi\nu_{FMR})^2-(\omega+\mathrm{i}\Lambda)^2}\right] \qquad (3.110)$$

2) $\boldsymbol{h} \parallel (1, 0, 0)$ $$(n+\mathrm{i}k)_2^2 = \varepsilon_{yy} \qquad (3.111)$$

where M is the magnetization at the temperature of the measurement as is also H_A in ν_{FMR}. The first solution is the FMR mode with ν_{FMR} as given in Eq. 3.105 with $\widetilde{H}_A = 0$ for K_2CuF_4 and the second one a nonmagnetic mode. That means that the solutions of the wave equation Eq. 3.46 consist not only of the FMR modes (magnons) but also of purely electromagnetic waves (photons) and modes resulting from the coupling of magnons and photons, namely magnetic polaritons. In contrast to the treatment of antiferromagnets in Sect. 3.1.6, we have to use for ferromagnets the internal fields and to apply the demagnetizing corrections as discussed in the beginning of this section. Magnetic polaritons and the coupling of magnons and photons have been described theoretically for ferromagnets some decades ago [60A, 60G, 62P, 68A] while such theories for antiferromagnets appeared somewhat more recently [72M2, 75B4, 77S3, 77S4]. Let us here at first evaluate the optical constants from Eq. 3.110 by means of the solution of Eq. 3.46. Then, the transmission and the reflectivity of the sample can be calculated by employing standard formulae, see e.g. Eqs. 8 and 10 in [84K2]. The calculated data may then be compared to the experimental ones. A transmission spectrum of a K_2CuF_4 sample with a thickness of $d = 1.835$ mm is presented in Fig. 3.41a. The data have been obtained for $\boldsymbol{H_0} \parallel (1, 0, 0)$ at $T = 4.2$ K with $\nu = 87.95$ GHz by varying the magnetic field. Therefore, the frequency of 87.95 GHz has to be inserted in Eq. 3.110 and then n and k can be calculated as a function of the applied field H_0. The transmission of K_2CuF_4 is plotted as reduced transmitted intensity $I(H_0)/I(H_0 = 0)$ so that values larger than 1 may occur in contrast to conventional transmission data. Figs. 3.41b and 3.41c show the calculated optical constants n and k also as a function of H_0. The input data for this calculation include not the only magnetic data (Table 5) but also the complex dielectric constant ε_{xx}. They are listed in Tables 1 and 2 of [84K2].

By means of the values of n and k, $I(H_0)/I(H_0 = 0)$ is obtained (solid line in Fig. 3.41a) which agrees quite well with the experimental data (open circles). The damping constant Λ is the only disposable parameter in this procedure. It was determined by an optimum fit to the experimental data ($\Lambda = 0.01$ GHz). The outstanding feature in Fig. 3.41 is that the transmission of the sample is practically zero between $H_0 = H_{\text{ar}} = 2.54$ T and $H_0 = H_{\text{res}} = 2.60$ T where n is also nearly zero and k has large values up to 35. Please note that n is presented on a linear scale in Fig. 3.41b and k on a logarithmic one (Fig. 3.41c). Obviously, electromagnetic waves cannot propagate through the sample in this range which can be identified with the socalled "polariton gap" as outlined in more detail below. The other structures in the transmission spectrum in Fig. 3.41 are due to interferences from multiple reflections in the sample. For a more detailed discussion of the magnetic polaritons, let us return to Eq. 3.110 and let us assume $\Lambda \approx 0$ and $\varepsilon'' \approx 0$. Instead of solving Eq. 3.110 for (n + ik) we leave the wavevector q in the form cq/ω in this equation

$$\frac{c^2 q^2}{\omega^2} = \varepsilon_{\text{xx}} \left[1 + \frac{(2\pi \nu_{\text{FMR}})^2 M/H_0}{(2\pi \nu_{\text{FMR}})^2 - (\omega + \mathrm{i}\Lambda)^2} \right] \tag{3.112}$$

and consider the resulting Eq. 3.112 as a dispersion relation $\omega(q)$. Solving it for ω, we obtain two branches which are separated by a gap where no real solutions exist for Eq. 3.112. The boundaries of this gap are

1) the FMR frequency: $$\nu_{\text{FMR}} = (\gamma_{\text{a}}/2\pi) \sqrt{H_0 \, (H_0 + H_{\text{A}} + M)} \tag{3.113}$$

and

2) the antiresonance frequency $$\nu_{\text{AR}} = \nu_{\text{FMR}} \sqrt{1 + M/H_0} \tag{3.114}$$

where the FMR frequency corresponds to $\mu_{\text{dyn}} = (1 + \chi_{\text{dyn}}) \to \infty$ and the antiresonance frequency to $\mu_{\text{dyn}} = (1 + \chi_{\text{dyn}}) \to 0$. In insulating ferromagnets like K_2CuF_4, the FMR is observed at ν_{FMR} while a resonance pattern is found at ν_{AR} for thin films of metals. For frequencies far away from ν_{FMR} and ν_{AR}, the solutions of Eq. 3.112 are electromagnetic waves (photons) and closer to these frequencies mixtures of photons and magnons, the magnetic polaritons. The experiments on K_2CuF_4 were performed with a fixed frequency by varying the magnetic field. Consequently, the resonance field H_{res} and the antiresonance field H_{ar} have been evaluated for this frequency by means of Eqs. 3.113 and 3.114. They are indicated in Fig. 3.41 marking the polariton gap in which n and k assume extreme values while the transmission is practically zero. Electromagnetic waves with frequencies in this gap do not penetrate the sample but are mostly reflected giving rise to a “reststrahlenband” as the high reflectivity of alkali halides due to phonon polaritons has been called by Rubens. For normal incidence, the reflectivity R of K_2CuF_4 with the magnetic reststrahlenband has been measured with $\nu = 66.82$ GHz for a sample of thickness $d = 0.77$ mm at $T = 4.2$ K, see Fig. 3.42 (open circles). By means of Eq. 3.110, the optical constants n and k were calculated also for this case and finally the reflectivity of the sample (solid curve). The agreement between experimental and calculated data is good in Fig. 3.42 which exhibit the expected high reflectivity between H_{ar} and H_{res} and outside this range some further structures again due to interferences from multiple reflections in the sample. The broken line in Fig. 3.42 shows the "ideal" reststrahlenband which would be obtained from a thick sample that only light reflected from the front surface is observed as usually in case of phonon-polaritons [74M1]. This case was simulated for K_2CuF_4 by calculating R for normal incidence and $d \to \infty$. This reststrahlenband extends actually from H_{ar} to H_{res} and shows no other structures due to interferences. While magnetic polaritons have been studied in a number of antiferromagnets like FeF_2, CoF_2 and La_2CuO_4 [78S7, 81S3, 82H8, 83B2, 83H5, 92K1], K_2CuF_4 seems to be the only ferromagnet where the magnetic polaritons have been studied in such detail [84K2, 84K3].

9.12.3.2.5 Parallel Pumping Experiments

A special form of investigating magnetic systems with microwaves is the parallel pumping technique [60K1, 60K2, 60S]. Yamazaki has applied it to layered ferromagnets [73Y2, 74Y1, 76Y2, 76Y3]. This method is particularly suited for the experimental determination of the interlayer exchange constant J'. In contrast to the ordinary FMR configuration with the oscillating microwave field $\boldsymbol{h}$ perpendicular to the static field $\boldsymbol{H_0}$, $\boldsymbol{h}$ is parallel to $\boldsymbol{H_0}$ for parallel pumping. With this technique, two magnons with $+\boldsymbol{q}$ and $-\boldsymbol{q}$ are created in the process of absorption of microwave photons. In principle, this technique is similar to the two-magnon Raman line observed for many antiferromagnets like K_2MnF_4, K_2NiF_4, K_2FeF_4 and K_2CoF_4 by Raman scattering (cf. Figs. 3.4 and 3.5 in Sect. 3.1.2). But with microwave photon energies, only the magnons for $\boldsymbol{q} \parallel (0, 0, 1)$ can be excited in the quasi-2D ferromagnets. Assuming the magnetization $\boldsymbol{M}$ to be parallel to the x-axis and $\boldsymbol{h}$ and $\boldsymbol{H_0}$ to be parallel to $\boldsymbol{M}$, the interaction of the microwave field $\boldsymbol{h}$ with the spin system in a parallel pumping experiment can be described by [74Y1, 76Y2]

$$\mathcal{H}' = g_a \mu_B h_0 \cdot \cos \omega t \sum_i \mathrm{S}_{i,x} \tag{3.115}$$

where h_0 is the amplitude of the microwave field with frequency ω. The theoretical treatment of parallel pumping proceeds with a rotation of the coordinate system from (x, y, z) to (ξ, η, ζ) with $x \leftrightarrow \zeta$, $y \leftrightarrow \xi$ and $z \leftrightarrow \eta$ as in Sect. 3.2.1. Then, the spin operators $\mathrm{S}_{i,x}$ are converted to magnon creation and annihilation operators a_i^+ and a_i or, after the Fourier transform, to a_q^+ and a_q. Finally, the net absorption of energy per second becomes in the stationary state

$$\frac{\mathrm{d}W}{\mathrm{d}t} = (\gamma_a h_0)^2 \sum_q \frac{|B_q|^2}{\hbar\omega_q} n_q \frac{\gamma_a \Delta H_q}{(\gamma_a \Delta H_q)^2 + (\omega - 2\omega_q)^2} \tag{3.116}$$

where $\hbar\omega_q$ is the magnon energy for the spin wave with wavevector $\boldsymbol{q}$, n_q the thermal occupation number ($n_q = [\exp(\hbar\omega_q / k_B T) - 1]^{-1}$), $\gamma_a \Delta H_q$ the spinwave linewidth and its reciprocal $(\gamma_a \Delta H_q)^{-1}$ the spin-wave relaxation time. The gyromagnetic ratio γ_a is again $g_a \mu_B / \hbar$ as in Eqs. 3.105 and 3.106. The factor B_q in Eq. 3.116 becomes in case of $\boldsymbol{H_0} \parallel (1, 0, 0)$

$$\begin{aligned} 2B_q &= g_a \mu_B H_A && \text{for } \boldsymbol{q} \parallel (1,0,0) \\ 2B_q &= g_a \mu_B (H_A - M) && \text{for } \boldsymbol{q} \parallel (0,1,0) \\ 2B_q &= g_a \mu_B (H_A + M) && \text{for } \boldsymbol{q} \parallel (0,0,1) \end{aligned} \tag{3.117}$$

With increasing microwave power, more and more magnons are created by parallel pumping. When the growth rate exceeds the decay rate due to relaxation of the system, the particular spin wave becomes instable and the corresponding instability threshold is usually expressed [74Y1] as the minimum threshold amplitude $h_{0,C}$ of the microwave field

$$h_{0,C} = \frac{\hbar\omega_q}{|B_q|} \Delta H_q \tag{3.118}$$

An example of the microwave absorption with h_0 above and below the threshold is shown in Fig. 3.43. The sample is K_2CuF_4 at $T = 1.31$ K. The absorption is significantly larger for the incident microwave power P_i above the threshold ($P_i/P_C = 16$ dB) than for P_i below the threshold ($P_i/P_C = -4$ dB) where P_C is the threshold power at $H_0 = H_1$. The fields marked H_1, H_2 and H_3 in Fig. 3.43 will be explained below.

The parallel pumping experiments are performed with a fixed pumping frequency ω_p by varying the applied magnetic field H_0. The frequency of the parallel pumped magnon is $\omega_\mathrm{q} = \omega_\mathrm{p}/2$. Its wavevector can be calculated from the spin-wave dispersion relation using ω_q and H_0. For this purpose, we have to use the complete dispersion relation $\hbar\omega(\boldsymbol{q})$ as derived in Eq. 3.71 (Sect. 3.2.1). Since $\hbar\omega_\mathrm{p}/2$ means a photon energy in the microwave range and the interlayer exchange field H'_E is extremely small, the magnons for $\boldsymbol{q} \parallel (0, 0, 1)$ should be included for the whole range $0 \le q_\mathrm{z} \le c^*$ with the approximation (cf. Eq. 3.71a)

$$H'_\mathrm{E}\,(1-\gamma'_\mathrm{q}) \approx H'_\mathrm{E}\left[1-\cos\left(\frac{cq_\mathrm{z}}{2}\right)\right] = 2H'_\mathrm{E}\sin^2\left(\frac{cq_\mathrm{z}}{4}\right) \tag{3.119}$$

while the terms with the large intralayer exchange field H_E may be approximated as assuming orthorhombic crystal symmetry

$$H_\mathrm{E}\,(1-\gamma_\mathrm{q}) \approx H_\mathrm{E}\left(\frac{a^2q_\mathrm{x}^2+b^2q_\mathrm{y}^2}{4}\right) \tag{3.120}$$

With these approximations and including the demagnetization corrections for $\boldsymbol{H_0} \parallel (1, 0, 0)$, i.e. $H_{0\mathrm{x}} = H_0$, we obtain for the magnon dispersion relation for $\mathrm{K_2CuF_4}$ and related Cu-compounds

$$\begin{aligned}\omega_\mathrm{q}^2 = \gamma_\mathrm{a}^2 &\left[H_\mathrm{E}\left(\frac{a^2q_\mathrm{x}^2+b^2q_\mathrm{y}^2}{4}\right)+2H'_\mathrm{E}\sin^2\left(\frac{cq_\mathrm{z}}{4}\right)+H_\mathrm{A}+H_0-N^\mathrm{x}M\right]\times\\ \times&\left[H_\mathrm{E}\left(\frac{a^2q_\mathrm{x}^2+b^2q_\mathrm{y}^2}{4}\right)+2H'_\mathrm{E}\sin^2\left(\frac{cq_\mathrm{z}}{4}\right)+\widetilde{H}_\mathrm{A}+H_0-N^\mathrm{x}M\right]\end{aligned} \tag{3.121}$$

where all fields are defined in Eq. 3.96, the demagnetization term with the magnetization M (= M_x at the temperature T) in Eq. 3.92 and the gyromagnetic ratio in Eqs. 3.105 and 3.106. In his theoretical considerations for explaining the results of the parallel pumping experiments, Yamazaki has added to the usual Hamiltonian Eq. 3.69 for $\mathrm{K_2CuF_4}$ and other Cu-compounds the magnetic dipolar interaction Hamiltonian (see Eq. 3.8 in Sect. 3.1.2) and treated them separately. In order to obtain more lucid and not so complicated expressions for the magnon frequencies, we assume here as before in Eqs. 3.69 and 3.71 (Sect. 3.2.1) the dipolar interactions to be included approximately in the anisotropy fields H_A and $\widetilde{H}_\mathrm{A}$. The next step is to include the other fields $\boldsymbol{e}$, $\boldsymbol{d}$, and $\boldsymbol{b}$ of the microwave wave, in addition to the pumping field $\boldsymbol{h}$ and to make use of the wave equation Eq. 3.46 as in the case of magnetic polaritons (see above). And finally, the pumping frequency ω_p or, more precisely, the magnon frequency $\omega_\mathrm{q} = \omega_\mathrm{p}/2$ is inserted to Eq. 3.121 and the other resulting equations. Then the magnon dispersion relations can be calculated in an unusual way as wavevector $\boldsymbol{q}$ versus applied magnetic field H_0. The result of such a calculation for $K_2\mathrm{CuF_4}$ is shown in Fig. 3.44a. There are three dispersion curves, namely one for $\boldsymbol{q} \parallel (1, 0, 0)$, one for $\boldsymbol{q} \parallel (0, 0, 1)$ and one for $\boldsymbol{q} \parallel (0, 1, 0)$. The electromagnetic propagation effects are the origin of the different values H_0 of the three dispersion curves for $\boldsymbol{q} \to 0$. Three characteristic values of $H_{0\mathrm{x}}$ are marked in Fig. 3.44 by H_1, H_2 and H_3. Comparison with the dispersion curves yields the following consequences for the parallel pumping process [74Y1, 76Y2]

a) $H_1 \le H_0 \le H_2$: preferably magnons with $\boldsymbol{q} \parallel (0,0,1)$ are excited

b) $\left.\begin{array}{l} H_2 \le H_0 \le H_3 \\ H_0 < H_1 \end{array}\right\} \left\{\begin{array}{l}\text{magnons are excited with } \boldsymbol{q} \approx 0 \text{ and with } \boldsymbol{q} \\ \text{between the } c\text{-axis and the } c\text{-plane}\end{array}\right.$

c) $H_0 > H_3$: no magnons can be excited outside the range of dispersion curves

The limiting values H_1, H_2, and H_3 of H_0 can be calculated from the corresponding dispersion relations.

They are solutions of the following equations [76Y3]

a) for $\boldsymbol{H_0} \parallel (1,0,0)$ and $\boldsymbol{q} \parallel (0,0,1)$

$$\begin{aligned}(\omega_\mathrm{p}/2)^2 &= [\omega(q=c^*)]^2 = \gamma_\mathrm{a}^2\,[2H'_\mathrm{E} + H_1 - N^\mathrm{x}M + \widetilde{H}_\mathrm{A}]\cdot[2H'_\mathrm{E} + H_1 - N^\mathrm{x}M + H_\mathrm{A} + M]\\ (\omega_\mathrm{p}/2)^2 &= [\omega(q\to 0)]^2 = \gamma_\mathrm{a}^2\,[H_2 - N^\mathrm{x}M + \widetilde{H}_\mathrm{A}]\cdot[H_2 - N^\mathrm{x}M + H_\mathrm{A} + M]\end{aligned} \tag{3.122}$$

b) for $\boldsymbol{H_0} \parallel (1,0,0)$ and $\boldsymbol{q} \parallel (1,0,0)$

$$(\omega_\mathrm{p}/2)^2 = [\omega(q\to 0)]^2 = \gamma_\mathrm{a}^2\,[H_3 - N^\mathrm{x}M + \widetilde{H}_\mathrm{A}]\cdot[H_3 - N^\mathrm{x}M + H_\mathrm{A}] \tag{3.123}$$

The limiting field for $\boldsymbol{H_0} \parallel (1,0,0)$ and $\boldsymbol{q} \parallel (0,1,0)$ with $\boldsymbol{q} \to 0$ is not of importance for the parallel pumping experiment but has been observed in FMR studies with optical detection [80B6]. It is the solution H_0 of the following equation

$$[\omega(q\to 0)]^2 = \gamma_\mathrm{a}^2\,[H_0 - N^\mathrm{x}M + \widetilde{H}_\mathrm{A} + M]\cdot[H_0 - N^\mathrm{x}M + H_\mathrm{A}] \tag{3.124}$$

The absorption of microwave energy in K_2CuF_4 due to subthreshold parallel pumping is reproduced in Fig. 3.44b. The experimental points (∘) agree very well with the theoretical curve (solid line). For comparison, also the magnon density of states (broken line) is shown in Fig. 3.44b. Also indicated are the fields H_1, H_2 and H_3 which have been calculated by means of Eqs. 3.122 and 3.123 with the values of H'_E, H_A, M for K_2CuF_4 and with $\widetilde{H}_\mathrm{A} = 0$. The good agreement between calculated and experimental data in Fig. 3.44 demonstrates in a convincing way that the interpretation of the data is correct and that by subthreshold parallel pumping mostly magnons with $\boldsymbol{q} \parallel (0,0,1)$ are excited because B_q has largest value for $\boldsymbol{q} \parallel (0,0,1)$ [cf. Eq. 3.117]. The magnon dispersion along $\boldsymbol{q} \parallel (0,0,1)$ with $H_1 < H_2$ as shown for K_2CuF_4 in Fig. 3.44a refers to $H'_\mathrm{E} > 0$ (ferromagnetic interlayer coupling). For $(C_2H_5NH_3)_2CuCl_4$ with $H'_\mathrm{E} < 0$, i.e. antiferromagnetic interlayer coupling, this magnon branch is bended in the opposite direction resulting in $H_1 > H_2$ (cf. [74Y3, 76Y3]). Therefore, this method is very well suited for an experimental determination of the interlayer exchange field H'_E, positive or negative. By increasing the microwave power above the threshold level, the absorption is increased and also absorption is observed in the range $H_2 \le H_0 \le H_3$ as the experimental data show in Fig. 3.43.

Such parallel pumping experiments for determining H'_E have been performed for K_2CuF_4 and for a number of other Cu-compounds, e.g. $(C_nH_{2n+1}NH_3)_2CuCl_4$ with n = 1 – 6 (see Table 5), and that for various temperatures below T_C to determine H'_E as a function of temperature [74Y1, 74Y3, 76Y2, 76Y3]. Many other investigations by parallel pumping have been performed on K_2CuF_4 and $(CH_3NH_3)_2CuCl_4$. In studies at temperatures near and above T_C [82Y1], it was found that the shape of the absorption curve changes from that determined by the density of states (Fig. 3.44b) to a more symmetric shape at $T > T_\mathrm{C}$. Since the threshold amplitude $h_{0,\mathrm{C}}$ is proportional to the spin-wave linewidth ΔH_q (Eq. 3.118), ΔH_q can be determined from the results of parallel pumping experiments [78Y1, 80Y2, 81Y, 88Y1]. For $(C_2H_5NH_3)_2CuCl_4$ with a strong intralayer ferromagnetic exchange coupling and a weak antiferromagnetic interlayer coupling, parallel pumping has been used to create antiferromagnetic spin waves at the Brillouin zone-boundary [83Y4, 87Y2]. Parallel pumping combined with FMR studies have revealed the complicated magnetic structure of $(C_4H_9NH_3)_2CuCl_4$ [77Y2, 77Y3], namely a canting of the spins by ±17° away from the *a*-axis towards the *b*-axis in adjacent layers so that a weak ferromagnet moment results along the *b*-axis. With microwave powers above the threshold, the saturation of the pumped magnons has been studied [80Y1].

9.12.3.3 Doped and Mixed Systems

9.12.3.3.1 Paramagnetic Centres in Diamagnetic Host Crystals

This Section 3.3 is devoted to the special magnetic properties of doped and mixed crystals within the family of perovskite-type layer structures A_2MX_4. We recall from the introduction (Sect. 1.3) that we are considering here doped and mixed systems of the type $A_2M_x\widetilde{M}_{1-x}X_4$ with two different divalent ions M^{2+} and $\widetilde{M}^{2+}$. And these solid solutions are called diluted systems when, for example, M^{2+} is a paramagnetic ion and $\widetilde{M}^{2+}$ is a diamagnetic one. At first, we will focus our attention to extreme dilutions, namely diamagnetic host crystals $A_2\widetilde{M}X_4$ doped with a small amount of paramagnetic ions M^{2+}, i.e. concentrations $x \ll 1$. That means we are dealing with magnetic systems far beyond the percolation limit x_p (see next section) above which 3D long-range magnetic order (LRO) is observed. For such small values of the concentration x, single paramagnetic ions M^{2+} in a diamagnetic environment are the most probable case with a probability of $x \cdot (1-x)^4$ on a square lattice while the probability for a pair of paramagnetic ions on nearest neighbour sites is $4 \cdot x^2 \cdot (1-x)^6$ [58B, 65K]. It follows from these relations that for concentrations $x \approx 0.01$ most of the paramagnetic ions M^{2+} form isolated impurity centres which can be called paramagnetic centres in the diamagnetic host crystals $A_2\widetilde{M}X_4$. In these mixed crystals, the M^{2+}-ions like Mn^{2+}, Fe^{2+}, Co^{2+} etc. replace the $\widetilde{M}^{2+}$-ions like Mg^{2+}, Zn^{2+}, Cd^{2+} etc. substitutionally. Sometimes, the host crystals $A_2\widetilde{M}X_4$ are doped with trivalent ions M^{3+} like Cr^{3+}, Fe^{3+}, Gd^{3+} etc. which form also paramagnetic centres on regular $\widetilde{M}^{2+}$-sites which have mostly associated defects for compensation of the extra electrical charge (see below). The following paramagnetic centres have been studied by various experimental and theoretical methods

K_2MgF_4 : Cr^{3+} [82T4, 88A9], Mn^{2+} [60O2, 70S5, 73S1, 74N2, 95Z2], Co^{2+} [92M6],
Ni^{2+} [69Y, 70Y2, 95Z2]

Rb_2MgF_4: Cr^{3+} [88A9], Mn^{2+} [73S1, 74N2]

K_2ZnF_4 : Cr^{3+} [82T4, 83T6, 88A9], Mn^{2+} [68R, 72F2, 73F2, 73S1, 95Z2], Fe^{2+} [88V1], Co^{2+} [68F2],
Ni^{2+} [72Y5, 84L1, 95Z2], Cu^{2+} [79K2, 86R3]

Rb_2ZnF_4 : Cr^{3+} [86A4, 88A9], Mn^{2+} [73S1], Fe^{3+} [91T1], Cu^{2+} [79K2], Gd^{3+} [96A]

K_2CdF_4 : Cr^{3+} [88A8], Mn^{2+} [73S1]

Rb_2CdF_4 : Cr^{3+} [86A4, 88A9], Mn^{2+} [73S1], Fe^{3+} [91T2], Gd^{3+} [87T, 96A]

Cs_2CdF_4 : Cr^{3+} [86A4, 88A9], Gd^{3+} [87T, 96A] antiferromagnetic interlayer coupling, parallel pumping has been used to create antiferromagnetic spin waves at the Brillouin zone-boundary [83Y4, 87Y2]. Parallel pumping combined with FMR studies have revealed the complicated magnetic structure of $(C_4H_9NH_3)_2CuCl_4$ [77Y2, 77Y3], namely a canting of the spins by ±17° away from the *a*-axis towards the *b*-axis in adjacent layers so that a weak ferromagnet moment results along the *b*-axis. With microwave powers above the threshold, the saturation of the pumped magnons has been studied [80Y1].

9.12.3.3 Doped and Mixed Systems

9.12.3.3.1 Paramagnetic Centres in Diamagnetic Host Crystals

This Section 3.3 is devoted to the special magnetic properties of doped and mixed crystals within the family of perovskite-type layer structures A_2MX_4. We recall from the introduction (Sect. 1.3) that we are considering here doped and mixed systems of the type $A_2M_x\tilde{M}_{1-x}X_4$ with two different divalent ions M^{2+} and $\tilde{M}^{2+}$. And these solid solutions are called diluted systems when, for example, M^{2+} is a paramagnetic ion and $\tilde{M}^{2+}$ is a diamagnetic one. At first, we will focus our attention to extreme dilutions, namely diamagnetic host crystals $A_2\tilde{M}X_4$ doped with a small amount of paramagnetic ions M^{2+}, i.e. concentrations $x \ll 1$. That means we are dealing with magnetic systems far beyond the percolation limit x_p (see next section) above which 3D long-range magnetic order (LRO) is observed. For such small values of the concentration x, single paramagnetic ions M^{2+} in a diamagnetic environment are the most probable case with a probability of $x \cdot (1-x)^4$ on a square lattice while the probability for a pair of paramagnetic ions on nearest neighbour sites is $4 \cdot x^2 \cdot (1-x)^6$ [58B, 65K]. It follows from these relations that for concentrations $x \approx 0.01$ most of the paramagnetic ions M^{2+} form isolated impurity centres which can be called paramagnetic centres in the diamagnetic host crystals $A_2\tilde{M}X_4$. In these mixed crystals, the M^{2+}-ions like Mn^{2+}, Fe^{2+}, Co^{2+} etc. replace the $\tilde{M}^{2+}$-ions like Mg^{2+}, Zn^{2+}, Cd^{2+} etc. substitutionally. Sometimes, the host crystals $A_2\tilde{M}X_4$ are doped with trivalent ions M^{3+} like Cr^{3+}, Fe^{3+}, Gd^{3+} etc. which form also paramagnetic centres on regular $\tilde{M}^{2+}$-sites which have mostly associated defects for compensation of the extra electrical charge (see below). The following paramagnetic centres have been studied by various experimental and theoretical methods

K_2MgF_4 : Cr^{3+} [82T4, 88A9], Mn^{2+} [60O2, 70S5, 73S1, 74N2, 95Z2], Co^{2+} [92M6],
Ni^{2+} [69Y, 70Y2, 95Z2]

Rb_2MgF_4: Cr^{3+} [88A9], Mn^{2+} [73S1, 74N2]

K_2ZnF_4 : Cr^{3+} [82T4, 83T6, 88A9], Mn^{2+} [68R, 72F2, 73F2, 73S1, 95Z2], Fe^{2+} [88V1], Co^{2+} [68F2],
Ni^{2+} [72Y5, 84L1, 95Z2], Cu^{2+} [79K2, 86R3]

Rb_2ZnF_4 : Cr^{3+} [86A4, 88A9], Mn^{2+} [73S1], Fe^{3+} [91T1], Cu^{2+} [79K2], Gd^{3+} [96A]

K_2CdF_4 : Cr^{3+} [88A8], Mn^{2+} [73S1]

Rb_2CdF_4 : Cr^{3+} [86A4, 88A9], Mn^{2+} [73S1], Fe^{3+} [91T2], Gd^{3+} [87T, 96A]

Cs_2CdF_4 : Cr^{3+} [86A4, 88A9], Gd^{3+} [87T, 96A]

Rb_2MgCl_4, Rb_2MgCl_3Br, $Rb_2MgCl_2Br_2$: Mn^{2+} [73W1]

Rb_2CdCl_4 : Mn^{2+} [82P1, 85A1]

Cs_2CdCl_4 : Cr^{3+} [81K12]

Let us first discuss the centres with divalent paramagnetic ions. They have mostly been studied by electron paramagnetic resonance (EPR), some also by electron-nuclear double resonance (ENDOR) and by magnetic measurements. The experimental data usually analyzed on the basis of a spin Hamiltonian which is similar to the Hamiltonians for ferro- or antiferromagnets introduced in the previous sections, cf. Eqs. 3.33–3.35 (Sect. 3.1.5), Eq. 3.40 (Sect. 3.1.6) and Eqs. 3.81, 3.86 (Sect. 3.2.2)

$$\begin{aligned}\mathcal{H} = {} & g_{\|}\mu_B H_z S_z + g_{\perp}\mu_B\,(H_x S_x + H_y S_y) + D\left[S_z^2 - \tfrac{1}{3}S\,(S+1)\right] + E\,(S_x^2 - S_y^2) \\ & + A_{hf} S_z I_z + B_{hf}\,(S_x I_x + S_y I_y) - g_I \mu_N \boldsymbol{H}\,\boldsymbol{I} + \text{higher order terms}\end{aligned} \qquad (3.125)$$

Of course, the Heisenberg-type exchange interaction is missing in Eq. 3.125 for an isolated paramagnetic impurity, also a magnetic field arising from dipolar interactions. The crystal field or anisotropy terms with D and E have the same meaning as in Eq. 3.40. That with D is completed here to the form of the Stevens operator equivalent [64H]. That with E is only needed for centres with orthorhombic symmetry but not for those with tetragonal one. The terms with A_{hf} and B_{hf} describe the hyperfine coupling between electronic spin $\boldsymbol{S}$ and nuclear spin $\boldsymbol{I}$. In addition to the Zeeman term for the electronic spin, there is an analogous term for the nuclear spin in Eq. 3.125. The coupling between $\boldsymbol{S}$ and $\boldsymbol{H}$ is appropriate for the description of EPR experiments while that between $\boldsymbol{I}$ and $\boldsymbol{H}$ is needed for describing NMR or ENDOR studies [73S1]. For reasons of more lucidity, the higher order terms are not reproduced here. The interested reader will find them in [72F2, 73S1, 74N2].

As an example of an EPR investigation [82P1], the EPR spectrum of isolated Mn^{2+} in $Rb_2Mn_{0.01}Cd_{0.99}Cl_4$ for $\boldsymbol{H_0} \parallel \boldsymbol{c}$ at room temperature is presented in Fig. 3.45. The spin values of Mn^{2+} are $S = 5/2$ and $I = 5/2$. Instead of one EPR line expected if $\mathcal{H}$ would consist only of the first two terms, a fine structure of five groups of lines is caused by the axial crystal field (parameter D), and each group is split into six lines by the hyperfine interaction (parameter A_{hf} in this case). And such investigations are the appropriate tool for the determination of the values of the parameters in the spin Hamiltonian Eq. 3.125. The values of D derived for a variety of host crystals span a relatively wide range. Schrama has obtained from ENDOR experiments at 4.2 K for Mn^{2+} [73S1] the following values for D (host crystals in parentheses):

D [cm^{-1}] = +0.0108(5) [K_2MgF_4], +0.00626(5) [K_2ZnF_4], +0.00212(10) [K_2CdF_4],
–0.00532(5) [Rb_2MgF_4], –0.00814(8) [Rb_2ZnF_4], +0.00602(7) [Rb_2CdF_4]

Larger values of D have been determined by EPR for isolated Ni^{2+} [70Y2, 72Y5]

D [cm^{-1}] = –0.352(1) [K_2MgF_4], –1.25(1) [K_2ZnF_4]

The tetragonal anisotropy proportional to D is related to a deformation of the ideally regular octahedron of F^- ligands at the paramagnetic centre [95Z2]. This is a local distortion different from the tetragonal distortion of the host crystals which can be calculated from the data for r_{ip} and r_{op} (cf. Eqs. 2.1 and 2.2 in Sect. 2.1.1) in Table 3. If we define tg $\alpha = r_{ip}/r_{op}$ the distortion is $\alpha - \alpha_0$ where $\alpha_0 = 45°$ is the value of the regular octahedron ($r_{ip} = r_{op}$). Thus $\alpha - \alpha_0 > 0$ means that the octahedra are compressed and $\alpha - \alpha_0 < 0$ that they are elongated. The data in Table 1 of [95Z2] show that the local distortion in the immediate environment of the paramagnetic impurity is strongly influenced by the behaviour of the same M^{2+}-ion in the pure crystal A_2MX_4 but there is also some influence of host crystal with its tendency for compressing or elongating the octahedra. The results for D of Mn^{2+} paramagnetic centres have further initiated some theoretical calculations of D taking into account the overlap contributions to the axial field [73F2, 74N2]. For this purpose, the hyperfine interaction with the ligand nuclei is added to the spin Hamiltonian. For more details of the interpretation of EPR spectra from ions with an S-state, the reader is referred to the review of Newman and Urban [75N]. In systems with a somewhat higher impurity concentration x, also EPR signals are found which can be attributed to pairs of paramagnetic ions. So Ni^{2+}-pairs were identified in K_2MgF_4 and K_2ZnF_4 [70Y2, 72Y5]. The theoretical description needs then a spin Hamiltonian like Eq. 3.125 for each paramagnetic ion and an exchange coupling term

$$2J\boldsymbol{S}_1\boldsymbol{S}_2 \quad \text{or} \quad 2J_2\boldsymbol{S}_1\boldsymbol{S}_2 \tag{3.126}$$

where J is, as defined in Sect. 3.1.2 (Eq. 3.2), the exchange constant for nearest neighbours in the layers and J_2 that for next nearest neighbours in the layers. Since J corresponds to 1148 GHz in K_2NiF_4 (cf. Table 5), the quantum energy of the source for the EPR study (ν = 9.25 GHz) is not sufficient to observe the signal of nearest neighbour pairs but only that of next-nearest neighbour pairs with the much smaller J_2. The analysis of the EPR signal from these Ni^{2+}-pairs in K_2MgF_4 yields $J_2 = 0.22\ \mathrm{cm^{-1}}$ corresponding to 6.16 GHz. But measurements of the magnetic susceptibility χ of $K_2Ni_xMg_{1-x}F_4$ with x = 0.042, 0.087, 0.120 [69Y] have provided also an information about J of isolated nearest neighbour pairs, namely $J = 44.66\ \mathrm{cm^{-1}}$ corresponding to 1250 GHz. If however EPR experiments, e.g. $Rb_2Co_{0.3}Mg_{0.7}F_4$ [92M6], are performed with much higher frequencies at much higher pulsed magnetic fields [$220\ \mathrm{GHz} \le \nu \le 762\ \mathrm{GHz}$] and [$0 \le H_0 \le 11\ \mathrm{T}$], absorption lines are found which are ascribed to single Co^{2+}-ions, to Co^{2+} nearest-neighbours pairs, and for x = 0.3 also to trimers of Co^{2+}-ions.

Let us turn now to the centres with trivalent paramagnetic ions which replace substitutionally diamagnetic $\tilde{M}^{2+}$-ions so that a charge imbalance results. This leads to centres mostly with a charge compensation that involves also some neighbouring sites. For M^{3+}-ions like Cr^{3+}, Fe^{3+} and Gd^{3+} in an $A_2\tilde{M}X_4$ host crystal, the following centres can be distinguished

centre I: isolated M^{3+}-ion, no charge compensation

centre II: vacancy V_A at an A^+-site nearest to the M^{3+}-impurity

centre III: vacancy V_M at a $\tilde{M}^{2+}$-site nearest to the M^{3+}-impurity

centre IV: in samples co-doped with Li^+ or Na^+ at a $\tilde{M}^{2+}$-site nearest to the M^{3+}-impurity

centre V: O^{2-}-ion at a X^--site nearest to the M^{3+}-impurity

Some of these centres are illustrated in Fig. 3.46, namely centres I, III and V. The drawings in Fig. 3.46 show that the symmetry of these centres is lowered for reasons of the associated defects. While centre I has usually tetragonal symmetry with some deformation of the octahedron along the z-axis, centres III, IV and V have at most orthorhombic symmetry. For a centre II system, Fe^{3+} in Rb_2ZnF_4, monoclinic symmetry has been reported [91T1]. The principal z-axis of the centre is canted away by 7° from the crystalline c-axis. The analysis of the experimental results for the trivalent centres is also based on a spin Hamiltonian similar to that in Eq. 3.125. Often, a socalled spin Hamiltonian separation analysis is performed, see for example Takeuchi et al. and Arakawa et al. [86A4, 87T, 88A9, 91T1, 96A]. Rudowicz [88R1, 88R2] has shown this method to be a particular case of a more general model, namely his net charge compensation model (NCC). For the details of the analysis and the interpretation of the experimental data, the reader is referred to the references. Centres with trivalent ions like Cr^{3+}- Li^+ (centre IV) and Gd^{3+}- O^{2-} (centre V) occur also in fluoride perovskites, see for example [80B11, 84T1], and the results may be compared to those for fluoride perovskite-type layer structures. A comparison of the data of Cr^{3+}- V_M and Cr^{3+}- Li^+, centres III and IV, resp., in a large variety of $A\tilde{M}X_3$ and $A_2\tilde{M}X_4$ host crystals allows the determination of host lattice effects [88A9].

At the end of this section, it is perhaps worth to mention that EPR studies on paramagnetic centres are not only performed in order to determine *g*-factors and anisotropy or crystal field parameters but that they are also a useful tool for investigations involving lattice vibrations and arrangement or canting of the octahedra. For example, Witteveen and Reedijk [73W1] were able to show by means of EPR experiments on Mn-doped mixed crystals $Rb_2MgCl_{4-x}Br_x$ with x = 0, 1, 2 that the Br^--ions are located preferably at out-of-plane X^-sites and that only $MnCl_6$ and $MnCl_4Br_2$ octahedra are found in the mixed crystals. Further, Riley et al. [86R3] have studied the effect of vibronic coupling on the EPR spectra of isolated Cu^{2+}-ions in K_2ZnF_4. That means a coupling of the electronic states of the Cu^{2+}-ion to the typical Jahn-Teller modes. Thus, the results provide information about the Jahn-Teller effect [79R1] which becomes a collective one in concentrated Cu-compounds like K_2CuF_4. Similarly, the vibrational effects on the magnetic properties of Fe^{2+} in K_2ZnF_4 were studied by ^{57}Fe Mössbauer and magnetic measurements [88V1]. The coupling of a paramagnetic centre to the static and dynamical properties of the host lattice makes the centre a sensitive probe for structural phase transitions. Therefore, these can be studied by EPR on appropriate paramagnetic centres, for a review see [91M2]. A famous example are Fe^{3+}-V_O centres in $SrTiO_3$, i.e. Fe^{3+} on Ti^{4+} sites and a vacancy at a nearest O^{2-}-site, where EPR provides a probe [71M3] to determine the temperature dependence of the order parameter, i.e. the canting angle of the octahedra, below the continuous phase transition at 105.5 K. Results of studying structural phase transitions by EPR on paramagnetic centres are also available for perovskite-type layer structures, namely on Mn^{2+} in Rb_2CdCl_4 [85A1] with information about the structural phase transition at $T_C = 142.8$ K (cf. Table 4) and on Cr^{3+}-V_M centres in K_2CdF_4 [88A8] with the indication of a structural phase transition at $T_C \approx 376$ K.

9.12.3.3.2 Magnetic Ordering in Diluted Systems

Let us now consider dilutions $A_2M_x\widetilde{M}_{1-x}X_4$ over a wide range of concentrations $0 \leq x \leq 1$. The properties of dilute magnets have been reviewed by Stinchcombe [83S10]. Where samples can be grown over a wide concentration range, such mixed crystals were studied comprehensively by various methods as the following examples will show

$Rb_2Mn_xMg_{1-x}F_4$ [76K6, 77C3, 77C7, 80B1, 84B4]

$K_2Fe_xZn_{1-x}F_4$ [85D1, 86D5]

$Rb_2Co_xMg_{1-x}F_4$ [78I3, 78S4, 79I1, 79I2, 79I3, 80C1, 81I2, 84B4]

$K_2Cu_xZn_{1-x}F_4$ [78W1, 79W3, 80H10, 80O2, 80O3, 81T2, 87J2, 89A2]

In these compounds, three-dimensional (3D) long-range magnetic order (LRO) occurs only if the concentration x is above the critical percolation concentration x_p, i.e. the minimum concentration for which the magnetic ions can form an infinite cluster via their exchange interactions. For $x < x_p$, the magnetic ions form only finite clusters and no longer an infinite one. A number of reviews deal with the percolation problem and with percolation theory, summarizing the earlier work [71S3, 72E, 73K5], and presenting more recent results [79S7, 80E3, 85S2, 92S6, 94N]. The value of x_p depends only on the topology of the lattice and not on the type of interactions [60E]. Therefore, the value is the same for Ising- and Heisenberg-type interactions, for ferro- and antiferromagnets. But there are two types of dilution, bond-dilution where single bonds are removed and site-dilution where lattice particles are removed. This is illustrated for the square lattice in Fig. 3.47 which shows that only the site-dilution applies to the diluted magnets where a magnetic ion is removed with all four bonds (exchange interactions) while the removal of one exchange interaction (bond) is not appropriate for our problem. Estimates and theoretical values for x_p have been obtained by various methods, e.g. Monte Carlo simulations [61F, 86K7, 89Y4, 92Z3], series expansions [64S2, 76S8, 76S10], renormalization group [78R3] and an experimental study [74W4]. The most recent and most accurate value of x_p is for site-dilution on the square lattice limiting the interactions to nearest neighbours [92Z3]

$$x_p = 0.5927460(5) \tag{3.127a}$$

and if also interactions between next nearest neighbours are included [66D1]

$$x_p(1,2) = 0.410 \tag{3.127b}$$

We recall from Sect. 3.1.1 that the intralayer nearest neighbour exchange interaction is the dominant one in perovskite-type layer structures. Therefore, the percolation limit is given by Eq. 3.127a for these compounds. But for the collective Jahn-Teller effect and orbital ordering, e.g. in Cu-compounds, also next nearest neighbours have to be taken into account, and thus Eq. 3.127b is appropriate for this case (cf. [83H1, 86H1, 87J2, 87M1] and discussion in Sect. 2.1.5). For comparison, the value for site-dilution on a simple cubic lattice (only nearest neigbour interaction) is [88Z2, 90C2]

$$x_p = 0.311605(10) \tag{3.127c}$$

In cubic perovskites, the magnetic ions form a simple cubic lattice and Eq. 3.127c applies to them. For other lattices (3–6 dimensions), values of x_p are found in original papers [64S2, 73K4, 76K7, 76S9, 81H5, 83G2] and in tables of reviews [77M3, 79S7, 83S10, 92I1, 94N].

In diluted magnets with $x > x_p$, the onset of LRO is below a critical temperature $T_C(x)$ which depends on the concentration x. $T_C(1)$ is the critical temperature of the pure system and, for $x \to x_p$, $T_C(x)$ approaches zero. For the diluted antiferromagnets $K_2Mn_xMg_{1-x}F_4$, $KMn_xMg_{1-x}F_3$ and $K_2Co_xMg_{1-x}F_4$, the Néel temperatures were determined from magnetic measurements [70B5, 73B6]. The results are shown in Fig. 3.48 as $T_N(x)/T_N(1)$ versus concentration x. For high concentrations x, the decrease of $T_N(x)/T_N(1)$ is almost linear but with a slope different for all three compounds. As expected, the experimental data are consistent with $T_N(x)/T_N(1) \to 0$ at the corresponding percolation limit marked $x_p(2D)$ and $x_p(3D)$ for the square lattice and the simple cubic lattice (cf. Eqs. 3.127 a, c), respectively. The slope of the initial linear part of $T_N(x)/T_N(1)$ is called the initial gradient I_g and is defined by

$$I_g = \frac{1}{T_C(1)} \left(\frac{\partial T_C(x)}{\partial x} \right)_{x=1} \tag{3.128}$$

where the more general critical temperature T_C is used instead of the Néel temperature T_N for an antiferromagnet. With I_g, the initial linear part of $T_C(x)$ can be written as [75F3]

$$T_C(x) = T_C(1)\,[1 - I_g\,(1 - x)] \tag{3.129}$$

The experimental data in Fig. 3.48 [70B5] yield the following values for I_g (cf. Table 5):

$K_2Mn_xMg_{1-x}F_4$	$I_g = 3.0(7)$	(2D Heisenberg)
$KMn_xMg_{1-x}F_3$	$I_g = 1.33(10)$	(3D Heisenberg)
$K_2Co_xMg_{1-x}F_4$	$I_g = 1.6(1)$	(2D Ising)

These data show that I_g depends not only on the lattice as x_p but also on the type of interactions where we recall from Sects. 3.1.2 and 3.1.9 that Mn-compounds behave Heisenberg-like and Co-compounds Ising-like. Similar experimental data were obtained by a variety of experimental methods like neutron diffraction, magnetization measurements, magnetic resonance studies, Mössbauer investigations for the following diluted systems (see Table 5)

$Rb_2Cr_{0.73}Mg_{0.27}Cl_4$, $T_C = 42$ K [86F1], $Rb_2Cr_xCd_{1-x}Cl_4$ [82K6],

$Rb_2Mn_xCd_{1-x}Cl_4$ [84E, 84P, 87G3, 89B4], $K_2Fe_xZn_{1-x}F_4$, $I_g = 2.4(2)$ [85D1],

$Rb_2Co_xMg_{1-x}F_4$, $I_g = 1.95(5)$ [78S4], $Rb_2Ni_xZn_{1-x}F_4$ [84D2, 85D2],

$K_2Cu_xZn_{1-x}F_4$, $I_g \approx 2.0$ [80H10], $I_g = 3.0$ [80O2]

The initial gradient I_g was also object of a number of theoretical treatments with the aim of obtaining theoretical values for I_g. Among other methods, the concentration expansion method was applied to 2D Ising-model diluted ferromagnets [77I3, 78I4]. This technique is based on a series expansion of the susceptibility of diluted ferromagnets with respect to the concentration x of magnetic ions for both, Ising and Heisenberg spin $\frac{1}{2}$ systems [62E, 63H]

$$\chi(T) = \sum_{n,\alpha} N\, A_{n\alpha}\, x^n\, (1-x)^m\, \chi_{n\alpha}(T) \tag{3.130}$$

where $\chi_{n\alpha}(T)$ is the susceptibility per atom of a particular n-ion cluster. It is defined here as n magnetic ions so arranged that each one is connected by a nearest neighbour exchange interaction to at least one other ion of the cluster but has no connection to any of the other $(Nx - n)$ magnetic ions. The subscript α is used to distinguish between different types of n-ion clusters. In Eq. 3.130, N is the total number of magnetic ions, $A_{n\alpha}$ is the number of ways in which the n-ion cluster (type α) can be implemented. Further, x^n is the probability for an n-ion cluster and $(1-x)^m$ the probability for the appropriate number m of diamagnetic ions for isolating the cluster from the other magnetic ions. These probabilities are listed for some lattices, including the square lattice, in [63H, 65K]. For example, the probability for a pair of magnetic ions surrounded by diamagnetic ions on the square lattice is $4 \cdot x^2 \cdot (1-x)^6$ as already mentioned in the last section. By rearranging $(1-x)^m$ in powers of x, we obtain finally for the susceptibility $\chi(T)$ a power series in x [62E, 63H]

$$\chi(T) = \chi_0\, x \sum_{n=0}^{\infty} a_n(T)\, x^n \tag{3.131}$$

where $\chi_0 = C/T$ is the susceptibility of a noninteracting system (Curie law, cf. Eq. 3.25 in Sect. 3.1.3). By means of an expansion like Eq. 3.131, Idogaki and Uryu [77I3, 78I4] calculated $T_N(x)/T_N(1)$ for an Ising system and achieved good agreement with the experimental data for $K_2Co_xMg_{1-x}F_4$ [70B5] and $Rb_2Co_xMg_{1-x}F_4$ [78S4], see Fig. 2 in [78I4] and Fig. 2 in [78S4]. The expansion Eq. 3.131 has been extended to include not only the dominant exchange interaction but also anisotropy and contributions from further neighbour interactions [77I3, 78I4]. For calculating the initial gradient I_g, also high temperature series expansions (h.t.s., cf. Eqs. 3.26 and 3.27 in Sect. 3.1.3) have been used [72R]. By means of a random-phase-approximation theory, McGurn [79G8] has calculated I_g for diluted antiferromagnets on various lattices varying the anisotropy from the Heisenberg to the Ising model. In the limiting cases, he obtained

for the 2D Heisenberg model (square lattice)	$I_g = \pi = 3.142$
for the 2D Ising model (square lattice)	$I_g = 1.33$
for the 3D Heisenberg model (simple cubic lattice)	$I_g = 1.68$

Comparing these results with the experimental data in Fig. 3.48, we find good agreement for $K_2Mn_xMg_{1-x}F_4$ (2D Heisenberg) but a not so good one for $KMn_xMg_{1-x}F_3$ (3D Heisenberg) and $K_2Co_xMg_{1-x}F_4$ (2D Ising). Many other calculations [74H5, 78D4, 78Y4] also yield values $I_g \approx 1.33$ which are too small in comparison to the experimental data 1.6 and 1.95. One reason for this discrepancy may be that the transverse spin components cannot be neglected completely as in the ideal Ising model but that a strongly anisotropic Heisenberg model (cf. Eq. 3.62 in Sect. 3.1.9) would be more appropriate. For example, the theory of McGurn [79G8] yields the larger value $I_g = 1.43$ for $J_\perp \neq 0$ and the ratio $J_\perp/J_\parallel \approx 0.55$ corresponding to K_2CoF_4 and Rb_2CoF_4. In case of the easy-plane system $K_2Fe_xZn_{1-x}F_4$, the theory yields with the anisotropy corresponding to pure K_2FeF_4 $I_g = 2.2$ which is in good agreement with the experimental data. Based on the exact results for the 2D Ising model of the pure system which are outlined in Sect. 3.1.9 and in more detail in Sect. 4.1.2, Thorpe and McGurn [79T3, 80T6] have derived a model for the diluted 2D Ising model by means of an effective medium theory where the boundary between paramagnetic and antiferromagnetically ordered phase in the (T, x)-plane, i.e. $T_N(\mathrm{x})$, is obtained in analytic form [80T6]

$$\frac{T_N(\mathrm{x})}{T_N(1)} = K_C\left\{\mathrm{Ar\,tanh}\left[\frac{\tanh K_C}{1-(1-\mathrm{x})/q_0}\right]\right\}^{-1} \tag{3.132}$$

where $$K_C = \frac{1}{2}\,J_\parallel/[k_B T_N(1)] = \frac{1}{2}\ln(\sqrt{2}+1) \qquad \text{[cf. Eq. 3.67 in Sect. 3.1.9]}$$

and $$q_0 = \frac{1}{2}(1+\sqrt{2}/\pi) = 0.725079\ldots$$

The data calculated by means of this model are, on the whole, somewhat larger than the experimental results for $Rb_2Co_xMg_{1-x}F_4$ (see Fig. 1 of [80T6]). And the decrease of the experimental data is for decreasing x with $I_g = 1.95$ larger than the theoretical ones with initial gradient $I_g = \sinh 2K_C/(2q_0K_C) = 1.565$. This may again be due to neglecting the transverse spin components and/or due to the approximations made in the model. The larger $T_N(\mathrm{x})$ and the correspondingly smaller I_g lead to $\mathrm{x}_p = 0.575$, setting $T_N(\mathrm{x}) = 0$ in Eq. 3.132, instead of 0.593 of Eq. 3.127a.

For a 2D Ising dilute ferromagnet, Monte Carlo simulations [76C4, 76S11] have been performed for $\mathrm{x} = 0.7$, 0.8, and 0.9 with calculation of the magnetic energy U_{magn}, the magnetic contribution to the specific heat C_{magn}, the magnetization M (order parameter) and the magnetic susceptibility χ. For the pure system, i.e. for the 2D Ising model, C_{magn} and χ will be discussed in detail in Sect. 4.1.2 (cf. Eqs. 4.4, 4.6, 4.1 and 4.8, resp.). Here it is only mentioned that these two response functions exhibit for the pure system ($\mathrm{x} = 1$) a singularity at $T_C(1)$. At first, all results of the Monte Carlo study reflect the decrease of $T_C(\mathrm{x})$ for decreasing x with initial slope $I_g = 1.47(5)$. Further, C_{magn} and χ show for $\mathrm{x} = 0.7$ a broad maximum near $T_C(0.7)$ and no singularity as for the pure system and for small dilutions. Experimental results are available for C_{magn} of the diluted Ising-like antiferromagnetic system $Rb_2Co_xMg_{1-x}F_4$ ($0.5 \leq \mathrm{x} \leq 1.0$) and of the diluted ferromagnetic system $K_2Cu_xZn_{1-x}F_4$ ($0.26 \leq \mathrm{x} \leq 1.0$). The results on $Rb_2Co_xMg_{1-x}F_4$ [78S4] show for $0.9 < \mathrm{x} \leq 1.0$ a sharp peak at $T_N(\mathrm{x})$ indicating a symmetric logarithmic singularity as expected for the 2D Ising model (cf. Eq. 4.6 in Sect. 4.1.2). For $0.8 < \mathrm{x} \leq 0.9$, a cusp is resolved in the experimental data with a maximum which broadens and shifts to lower T with decreasing concentration x. For $\mathrm{x} = 0.5$, 0.6, 0.7 near the percolation limit, no apparent peaks of C_{magn} could be observed in the experimental data. Thus, the experimental data show the same trend as the Monte Carlo results [76C4], but the decay of the sharp peak at T_N with decreasing x seems to be steeper in the experimental than in the Monte Carlo data.

The magnetic contribution C_{magn} to the specific heat of $K_2Cu_xZn_{1-x}F_4$ has been studied by specific heat measurements [81T2] for concentrations x above and below the percolation critical concentration x_p. Some of the results for low temperatures ($0.3\,\mathrm{K} \leq T \leq 4.7\,\mathrm{K}$) are reproduced in Fig. 3.49. The experimental data for $\mathrm{x} = 1.0$ (pure K_2CuF_4) show an increase of C_{magn} up to 2 K linear in T (see line in Fig. 3.49) in accordance with the theory for a 2D Heisenberg ferromagnet (cf. Eq. 3.79 in Sect. 3.2.1).

Above 2 K, there is an enhanced increase due to the influence of a term quadratic in T as discussed already at the end of Sect. 3.2.1 (cf. Eq. 3.80). Outside the temperature range of Fig. 3.49, C_{magn} of K_2CuF_4 shows a sharp peak at $T_C = 6.25$ K and reaches a broad maximum at 9 K [81T2]. Completely different are the data for $x = 0.59 \approx x_p$ and the solid curve for $x = 0.59$ agreeing quite well with the experimental data is the result of a calculation of C_{magn} for a one-dimensional (1D) $S = \frac{1}{2}$ Heisenberg ferromagnet by Blöte [75B9], adapting it to Fig. 3.49 by using $J = 11.36\text{ K} \approx 11.4\text{ K}$ (pure K_2CuF_4, cf. Table 5). For small temperatures ($0 \le T \le 0.4$ K), his tabulated data are complemented by the standard result of spin-wave theory for a 1D Heisenberg ferromagnet (cf. Eq. 3.79 in Sect. 3.2.1)

$$C_{\text{magn}} / R = 0.5527\,(k_B T / J)^{1/2} \tag{3.133}$$

where Blöte found the prefactor too large and reduced it to 0.3908 for a better agreement. Other calculations of C_{magn} [64B] yield a similar prefactor 0.42. In Fig. 3.49, the increase ~ $T^{1/2}$ is followed by a broad plateau at temperatures above 0.4 K. For a better understanding of the agreement between the calculated 1D data and the experimental ones of a 2D system near the percolation threshold, Fig. 3.50 presents a computer simulation for a diluted system $A_2M_x\widetilde{M}_{1-4}X_4$ with $x = 0.50$ just below x_p. The simulation is performed for site-dilution on a square lattice. Only the paramagnetic M^{2+}-ions and their connections via exchange interactions are shown in Fig. 3.50 providing an impression of the shape and the number of finite clusters near x_p. As confirmed by many experimental data and theoretical considerations [75D3, 75S3, 75S4, 76B7, 76S7, 80B1, 80C1], the average coordination number of the M^{2+}-ions in these clusters in Fig. 3.50 is close to two, i.e. that of a linear chain. Correlations and magnetic ordering via the exchange interactions depend strongly on a large number of 1D links because the clusters are highly ramified. It is therefore justified to compare the experimental data of diluted systems with $x \approx x_p$ to the theoretical predictions for a linear chain [72G3]. Finally, the remaining C_{magn} data for $x = 0.68$ and $x = 0.80$ show an increase with temperature similar to that of pure K_2CuF_4 and exhibit a strongly broadened peak at $T_C(0.68) = 1.4(2)$ K and $T_C(0.80) = 3.1(1)$ K, respectively. The data for $x = 0.36$ below the percolation threshold show a broad plateau with an increase at lower temperatures similar to that for $x = 0.59$. These features are ascribed to the contributions of finite clusters to C_{magn} [81T2]. Further information about C_{magn} of the diluted system $K_2Cu_xZn_{1-4}F_4$ originate from linear magnetic birefringence (LMB) studies [87J2] where the birefringence results from magnetic phenomena. Jahn [73J2] has demonstrated convincingly in his pioneering work that C_{magn} cannot be obtained only by specific heat measurements but also by LMB studies and that the result Δn of a LMB measurement is proportional to the magnetic energy U_{magn}, possibly with an additive constant. And its derivative with respect to T is proportional C_{magn}:

$$\text{LMB:} \qquad \mathrm{d}(\Delta n)/\mathrm{d}T \sim C_{\text{magn}} \tag{3.134}$$

The results of the LMB study confirm those of the specific heat measurements. Especially for $x = 1$ and $x = 0.60$, they also represent the magnetic specific heat of a 2D and a 1D Heisenberg ferromagnet, resp., as shown in Eqs. 3.79 and 3.80 (Sect. 3.2.1) and in Eq. 3.133, see also [64B, 72G3, 75B9].

The magnetic contribution to the specific heat C_{magn} is one of the response functions which show a singularity at T_C in the pure system, and the magnetic susceptibility χ of a ferromagnet another one as already discussed in context with the Monte Carlo simulation for diluted systems [76C4]. Also susceptibility data are available for the diluted system $K_2Cu_xZn_{1-x}F_4$. Okuda et al. [80O2, 80O3] have determined $\chi(T)$ for $\boldsymbol{H_0} \perp \boldsymbol{c}$, i.e. $\boldsymbol{H_0}$ parallel to the easy plane. Their results may be summarized as follows

$x = 0.68 > x_p$: $\chi(T)$ diverges at $T_C \approx 1.1$ K

$x = 0.60 \approx x_p$: $\chi(T)$ shows the behaviour of $\chi_{1D}(T)$, the susceptibility of a 1D system

$x = 0.50 < x_p$: $\chi(T)$ deviates from both, $\chi = C/T$ (Curie law) and χ_{1D}

$x = 0.40 \ll x_p$: $\chi(T) = \chi_0 = C/T$ (Curie law)

That means, there is a transition to LRO for x = 0.68 as expected. Near the percolation threshold, also the susceptibility can be described in terms of χ_{1D} of a one-dimensional system. And the dilutions with concentrations below x_p exhibit more and more with decreasing x the susceptibility of a paramagnet (Curie law), i.e. that of a noninteracting system, where the Curie constant *C* is defined in Eq. 3.25 (Sect. 3.1.3). The magnetic susceptibility χ_{1D} of a linear Heisenberg ferromagnet was derived by several authors [64B, 64F2, 68S4, 72G3]. Okuda et al. [80O3] find that their experimental data for x = 0.60 agree excellently very well with the exact theoretical result of Bonner and Fisher [64B] using for the *g*-factor and the exchange parameter *J* the values of pure K_2CuF_4 ($g_a = g_b = 2.284 \approx 2.30$, $J = 11.36$ K ≈ 11.4 K, cf. the data for K_2CuF_4 in Table 5)

$$\chi_{1D} = \chi_0 \cdot [1 + (k_B T/J)^{-\vartheta}] \tag{3.135}$$

where the value of ϑ may range from 0.8 to 1.0. For the temperature range of the study of χ ($0 < T \le 25$ K), there is little effect of varying ϑ and no information can be gained about the value of ϑ from a comparison of calculated and experimental data.

Next, let us turn to nuclear magnetic resonance (NMR) and Mössbauer investigations of diluted magnets. In Sect. 3.1.3, the sublattice magnetization $M_{subl}(T)$, the order parameter of an antiferromagnet, has been introduced (cf. Eq. 3.18) and its determination for pure antiferromagnets by neutron diffraction and by NMR. It was shown there that M_{subl} is proportional to the square root of the intensity of an antiferromagnetic superreflection as shown in Fig. 3.15 (Sect. 3.1.5) for K_2FeF_4. On the other hand, $M_{subl}(T)/M_{subl}(0)$ can equally well be derived from the temperature dependence of the NMR frequency $f_{NMR}(T)$ which is for F_I^--ions directly proportional to $M_{subl}(T)$ while $f_{NMR}(T)$ from $^{19}F_{II}$-NMR reflects the net magnetization (cf. Figs. 3.6–3.8 in Sect. 3.1.3 with experimental data for K_2MnF_4 and Rb_2MnF_4). The results of such studies on diluted systems will evidence that neutron diffraction is a method to obtain averages while NMR and Mössbauer studies are a probe for local properties. For $K_2Mn_xMg_{1-x}F_4$ and $K_2Mn_xZn_{1-x}F_4$ [80L4, 80L5], there are impurity-associated satellites of the NMR signals from $^{19}F_I$- and $^{19}F_{II}$-ions adjacent to the nonmagnetic impurities. The analysis of these data yields that the local M_{subl} is severely modified in the first shell of Mn^{2+}-ions neighbouring the Mg^{2+}- or Zn^{2+}-ion and that the further shells are only weakly affected. This statement is in good agreement with a calculation for a 13-site cluster (impurity and the first three shells of Mn^{2+} neighbours) employing a Green's function method combined with renormalized spin-wave theory (cf. Sect. 3.1.2). Another example of NMR studies as a probe for the local magnetic fields is the result of $^{19}F_I$-NMR on $K_2Co_{0.83}Zn_{0.17}F_4$ (cf. Fig. 3.51) where three resonances with different f_{NMR} are observed which are attributed to the local fields of Co^{2+}-ions having in their nearest neighbour shell n = 2, 3 or 4 other Co^{2+}-ions [85D2]. The solid lines in Fig. 3.51 are the result of a cluster Ising model calculation where the 2D Ising model is solved for the cluster of the central ion and its n magnetic neighbours representing the further environment by a virtual crystal magnetization $M_{VC}(T) = 0.5\,[1 - \sinh^{-4}(J_{VC}/k_B T)]^{1/8}$ (cf. Eq. 3.66 in Sect 3.1.9). Then, the local magnetization $M_{0,n}(T)$ of the central ion is obtained as

$$M_{0,\mathrm{n}}(T) = \frac{1}{2}\,\frac{\cosh^{\mathrm{n}}(u) - \cosh^{\mathrm{n}}(\upsilon)}{\cosh^{\mathrm{n}}(u) + \cosh^{\mathrm{n}}(\upsilon)} \tag{3.136}$$

with $u = [6\,M_{VC}(T) + 1] \cdot [J/(2k_B T)]$ and $\upsilon = [6\,M_{VC}(T) - 1] \cdot [J/(2k_B T)]$

Excellent fits to the experimental data are obtained with $J_{VC} = -72.3$ K and $J = -90(3)$ K (n = 4), $J = -91(3)$ K (n = 3) and $J = -95(5)$ K (n = 2). These values for J are all close to the value for pure K_2CoF_4 (cf. Table 5). The integrated intensities of the three NMR lines are expected to have the statistical weight

$$W_n(x) = \frac{4!}{n!\,(4-n)!}\,x^n\,(1-x)^{4-n} \tag{3.137}$$

which is the probability that a Co^{2+}-ion has among its 4 nearest neighbours n paramagnetic Co^{2+}-ions and (4 – n) diamagnetic Zn^{2+}-ions. The experimentally observed intensity ratios agree with $W_n(0.83)$ calculated by means of Eq. 3.137. Also three $^{19}F_I$-NMR resonance lines have been obtained in $K_2Ni_{0.96}Zn_{0.04}F_4$ and $K_2Ni_{0.85}Zn_{0.15}F_4$ which reflect again the local field at a Ni^{2+}-ion surrounded by n = 2, 3, 4 nearest Ni^{2+}-neighbours. In case of this Heisenberg-like system, the theoretical procedure outlined above for the Ising System $K_2Co_xZn_{1-x}F_4$ (Eq. 3.136) cannot be applied but a method similar to that for the diluted Mn-compounds [80L4] is used instead. The diluted easy-plane antiferromagnet $K_2Fe_{0.74}Zn_{0.26}F_4$ was studied by neutron diffraction and by Mössbauer spectroscopy [85D1, 86D5]. The Mössbauer results exhibit at high T (> 23 K) a paramagnetic Fe^{2+} quadrupole doublet and at low T (< 11 K) a six-line hyperfine-split absorption spectrum. Between 11 and 23 K, both types are observed. The six-line spectrum is consistent with a planar spin-ordering. It is analyzed by a least-square fitting with hyperfine field H_{hf}, the quadrupole coupling constant eQV_{zz} and the asymmetry of the electric field gradient $V_{xx} - V_{yy}$ which reflects the orthorhombic symmetry of the antiferromagnetic order (see the discussion in Sect. 3.1.5 and Fig. 2.6 in Sect. 2.1.3). Analogous to NMR where $f_{NMR}(T)$ is proportional to the local magnetization $M_{subl}(T)$, the hyperfine field $H_{hf}(T)$ in Mössbauer spectroscopy is also proportional to the local $M_{subl}(T)$. Thus, we can derive from $H_{hf}(T)$ also the local $M_{subl}(T)/M_{subl}(0)$ which is presented for $K_2Fe_{0.74}Zn_{0.26}F_4$ in Fig. 3.52. It is compared there to $M_{subl}(T)/M_{subl}(0)$ obtained from neutron diffraction, i.e. from the square root of the intensity of the (1, 0, 0) antiferromagnetic Bragg reflection. The latter represents the order parameter for 3D LRO which decreases faster with increasing temperature than the local magnetization. The arrow in Fig. 3.52 indicates the temperature (11 K) above which Mössbauer spectra due to paramagnetic Fe^{2+}-ions are observed. Above this temperature, the neutron ridge intensity at (1, 0, 0.4) shows an increase indicating a partial 2D ordering. A detailed analysis leads to the conclusion that below $T_N = 22.6(1)$ K both, neutron ridge intensity and paramagnetic Mössbauer spectra, originate from the same parts of the crystal with 2D regions of typically 10 lattice units in size [85D1, 86D5]. They appear to fluctuate on a timescale faster than that typical for Mössbauer experiments (10^{-8} s) but show correlations in neutron diffraction (10^{-11} s).

9.12.3.3.3 Spin Waves in Diluted Magnets

The dilution, i.e. the doping of a magnetic compound with diamagnetic ions, has primarily the effect that the paramagnetic ions are surrounded by a number n < 4 paramagnetic neighbours as illustrated in Fig. 3.51 in the last section. On the average, this will lead to a decrease of spin-wave frequencies similar to the decrease of $T_C(x)$ towards the percolation threshold (cf. Fig. 3.48 in the last section). But we may also expect that the magnon spectra reflect the smaller number of paramagnetic neighbours. The spin waves of diluted systems are studied by the same methods as pure antiferro- and ferromagnets, e.g. by magnetic resonance, neutron inelastic scattering, Mössbauer studies etc. as outlined in two reviews [72C2, 74E] which present also the theoretical treatment of such systems but which deal mainly with 3D antiferromagnets, among them also some perovskites like $KMn_xZn_{1-x}F_3$. With respect to 2D diluted magnets, more experimental data are available for diluted antiferromagnets than for diluted ferromagnets:

$Rb_2Mn_xMg_{1-x}F_4$ [75H6, 76C3, 76K6, 77C3, 78H3]
$K_2Fe_xZn_{1-x}F_4$ [85D1, 86D5]
$K_2Cu_xZn_{1-x}F_4$ [78W1]
$Rb_2Co_xMg_{1-x}F_4$ [79I3, 80C1]
$Rb_2Mn_xCd_{1-x}Cl_4$ [84E, 84P, 87G3, 89B4]

The above mentioned average behaviour is probably best to observe by studying the magnetic excitations at $q = 0$ in the centre of the Brillouin zone, e.g. in antiferromagnets by antiferromagnetic resonance (AFMR). Such studies [84E, 84P] were performed on the uniaxial antiferromagnets $Rb_2Mn_xCd_{1-x}Cl_4$ ($0.7 \leq x \leq 1.0$). The main effect of dilution is a drastic decrease of the AFMR frequency ν_{AFMR} for $H_0 = 0$ and, correspondingly, of H_{SF}. In addition, susceptibility measurements were performed in order to determine the exchange field H_E for the diluted system. For these weakly anisotropic Mn-compounds, ν_{AFMR} and H_{SF} are proportional to $(2H_EH_A)^{1/2}$ (cf. Eqs. 3.38 and 3.49 in Sect. 3.1.6) neglecting H_A^2 and also the other smaller anisotropy fields like $\hat{H}_A$ and $\tilde{H}_A$ (cf. Eqs. 3.50 and 3.51). Thus, H_A can be determined from ν_{AFMR} or H_{SF} with H_E known from the χ measurement. The values of T_N, ν_{AFMR}, H_{SF}, H_E and H_A are listed in Table 5. In subsequent AFMR experiments [87G3, 89B4], a splitting of ν_{AFMR} for $H_0 = 0$ was resolved for the diluted samples with $x = 0.91$ and 0.80 as it was also observed in pure Rb_2MnCl_4 (cf. Table 5 and Fig. 3.17 in Sect. 3.1.6). This splitting is ascribed to an orthorhombic distortion below T_N. Fig. 3.53 presents the results for $x = 0.91$ and 0.80 as ν_{AFMR} versus external field $\boldsymbol{H_0}$ applied parallel to the *c*-axis. The data show the above mentioned splitting for $H_0 = 0$ and reflect the spin-flop transition at the critical field $H_0 = H_{SF}$ (cf. Table 5).

In these magnetic resonance experiments, no random-field effects due to the applied field H_0 were observed as they are discussed in Sect 4.1.12. It is outlined there that a uniform magnetic field applied parallel to the anisotropy axis (*c*-axis) will cause a random magnetic field in diluted uniaxial antiferromagnets which destroy the transition to the antiferromagnetic phase and lead to frozen-in domain states. For $\boldsymbol{H_0} \parallel \boldsymbol{c}$, the spin-flop phase is not affected by random fields. This was shown in detail in the investigation [93C2] of the magnetic phase diagram of $Rb_2Mn_{0.70}Mg_{0.30}F_4$, see also Sect. 4.1.12. All the experiments on $Rb_2Mn_xCd_{1-x}Cl_4$ were performed under zero-field-cooling (ZFC) conditions. Mostly, the metastable domain states are observed under field-cooling (FC) conditions. All results on this system were reproducible and did not show any dependence on prior sample history, and FC experiments were not performed. One point to mention about disorder in the samples is that all magnetic resonance spectra show a line $\nu = (\gamma/2\pi)\, H_0$ not shown in Fig. 3.53. This paramagnetic resonance line far below T_N is ascribed to uncoupled Mn^{2+}-ions which are not subject to an exchange field.

We return now to the discussion of the decrease of ν_{AFMR} and H_{SF} with dilution in $Rb_2Mn_xCd_{1-x}Cl_4$. In Fig. 3.53, H_{SF}, $\nu_{AFMR,1}$ and $\nu_{AFMR,2}$ at $H_0 = 0$ of pure Rb_2MnCl_4 (cf. Table 5) are indicated by arrows for comparison with the results for $x = 0.91$ and 0.80. It is astonishing that the splitting $\nu_{AFMR,2} - \nu_{AFMR,1}$ for $H_0 = 0$ does not decrease in spite of the overall decrease of ν_{AFMR}. Also in the diluted system, it will be due to an orthorhombic distortion. The main effect of the dilution, the decrease of ν_{AFMR} and H_{SF}, may be compared with the results of model considerations. This decrease cannot be accounted for by a simple virtual crystal or average model which will be discussed below in context with magnetic mixtures and which yields for dilutions a linear scaling of ν_{AFMR} and H_{SF} with x for weakly anisotropic Mn-compounds [77B7]. A coherent-potential-approximation model [76T4] predicts a much steeper decrease for 3D diluted antiferromagnets. For the 2D system $Rb_2Mn_xCd_{1-x}Cl_4$, the decrease may be expressed quantitatively by an approximate initial slope analogous to that defined for $T_N(x)$ in Eq. 3.128, namely as

$$\frac{1}{\nu_{AFMR}(1)}\left(\frac{\partial \nu_{AFMR}(x)}{\partial x}\right)_{x=1} = \frac{1}{H_{SF}(1)}\left(\frac{\partial H_{SF}(x)}{\partial x}\right)_{x=1} \approx 3.0 \qquad (3.138)$$

The value of this initial slope for ν_{AFMR} and H_{SF} is very similar to that calculated for $H_E(x)$ by Harris and Kirkpatrick [77H5]. Starting from a hydrodynamic description [69H2], they have calculated low-frequency long-wavelength response functions for diluted magnets on various lattices. Among them is $C(x)$ which results from the expansion for small q of the magnon dispersion relation $\omega(\boldsymbol{q})$ for a Heisenberg antiferromagnet (cf. Eq. 3.6 in Sect 3.1.2 with $H_0 = 0$ and neglecting H_A for $\omega >> \omega_{AFMR}$) yielding a linear dispersion [69H2]

$$\omega = \gamma H_{\mathrm{E}} \sqrt{1-\gamma_{\mathrm{q}}^{2}} \approx \left(\frac{1}{2}\gamma H_{\mathrm{E}} a\right) q = Cq \tag{3.139}$$

where $\gamma = g\mu_{\mathrm{B}}/\hbar$ is the gyromagnetic ratio. In their Fig. 10, Harris and Kirkpatrick [77H5] present the calculated data $C(\mathrm{x})/C(1)$ for a diluted antiferromagnet on a square lattice. For the initial slope of $C(\mathrm{x})/C(1)$, they obtain 2.94, using $H_{\mathrm{A}}/H_{\mathrm{E}} = 0.005$ which is appropriate for $\mathrm{Rb_2MnF_4}$ [75A1, 77C3]. For $\mathrm{Rb_2MnCl_4}$, this value is $H_{\mathrm{A}}/H_{\mathrm{E}} = 0.002$ [80S2] which would lead to a somewhat larger initial slope. Below x ≈ 0.9, the curve of $C(\mathrm{x})/C(1)$ is less steep and finally approaches zero at the percolation threshold (cf. Fig. 10 in [77H5]). From their data, we can calculate $H_{\mathrm{E}}(\mathrm{x})/H_{\mathrm{E}}(1)$ after correcting $C(\mathrm{x})$ for the x-dependence of the lattice constant a (see Table 2 and [82P1]). The exchange constant J depends on a as $J \sim a^{-12}$ (cf. the discussion in Sect. 3.1.1 and [75J]) and thus $C \sim H_{\mathrm{E}}\, a \sim a^{-11}$. The calculated data $H_{\mathrm{E}}(\mathrm{x})$ may be compared to the experimental data in Table 5. Mostly, the values for H_{E} determined from the susceptibility [84E, 84P] are larger than the calculated ones, e.g. $H_{\mathrm{E,exp}} = 68.3$ T and $H_{\mathrm{E,calc}} = 39.5$ T for x = 0.80. In both cases, Eq. 3.138 leads to a significant decrease of H_{A} with decreasing x which is even larger for the experimental values of H_{E}.

By neutron inelastic scattering, also the magnetic excitations were studied in diluted antiferromagnets $\mathrm{Rb_2Mn_xMg_{1-x}F_4}$ with x = 0.54, 0.57 [76K6, 77C3] and $\mathrm{Rb_2Co_xMg_{1-x}F_4}$ with x = 0.575 [79I3, 80C1]. These concentrations are slightly below the critical percolation concentration $\mathrm{x_p}$, (cf. Eq. 3.127a) and there are only finite clusters of the magnetic ions and no transition to an antiferromagnetic LRO. Thus, the neutron scattering results will not necessarily show well-defined magnons and magnon branches as they are observed in pure systems. This is illustrated in Fig. 3.54 where experimental data for $\mathrm{Rb_2MnF_4}$ are presented as neutron counting rate versus energy transfer $\hbar\omega$ at constant wavevector transfer of $\boldsymbol{K} \,\hat{=}\, (0.5, -0.5, 0)$ and $\boldsymbol{K} \,\hat{=}\, (1, 0.5, 0)$. These vectors $\boldsymbol{K}$ are equivalent to $\boldsymbol{q} \,\hat{=}\, (0.5, 0.5, 0)$ and $\boldsymbol{q} \,\hat{=}\, (0.5, 0, 0)$, which are both located at the zone boundary (cf. Fig. 3.2 in Sect. 3.1.2). The data in Fig. 3.54, the socalled neutron groups show in both cases a single maximum corresponding to the magnon frequency at these wavevectors $\boldsymbol{q}$. For the diluted systems, an interesting result is that the neutron groups are much broader than in pure systems and that they exhibit a structure with several maxima, especially at low temperatures. This structure is in $\mathrm{Rb_2Mn_xMg_{1-x}F_4}$ most clearly observed at the zone boundary [$\boldsymbol{q} \,\hat{=}\, (0.5, 0, 0)$], it persists at all wavevectors but is much less pronounced at the zone centre [$\boldsymbol{q} \,\hat{=}\, (0, 0, 0)$]. For $\mathrm{Rb_2Mn_{0.57}Mg_{0.43}F_4}$, the neutron scattering data in Fig. 3.55 show for a wavevector transfer $\boldsymbol{K} \,\hat{=}\, (0.5, 0, 2.9)$ such a structure with four maxima from which four excitation frequencies may be determined instead of one as usual for the magnon branch in uniaxial antiferromagnets. Cowley and Buyers [72C2, 76C3] have pointed out that this structure is a consequence of the different possible environments of the paramagnetic ions in mixed or diluted systems and that the magnetic excitations reflect these different environments. They have introduced the "Ising cluster approximation" where the energies of these excitations are calculated for diluted systems as Ising cluster energies

$$E_{\mathrm{n}} = 2nS\,|J| \tag{3.140}$$

In Eq. 3.140, n is the number of paramagnetic nearest neighbours by which a paramagnetic ion ($\mathrm{Mn^{2+}}$ or $\mathrm{Co^{2+}}$) is surrounded. Disregarding the first somewhat distorted maximum in Fig. 3.55, the other three are marked in the figure by arrows and by numbers n corresponding to E_{n} in Eq. 3.140. For the two samples of $\mathrm{Rb_2Mn_xMg_{1-x}F_4}$ with x = 0.54 and x = 0.57, the experimentally determined excitation energies corresponding to the maxima in the neutron scattering data of Cowley et al. [77C3] are at the zone boundary

$n =$	1	2	3	4	
for x = 0.54	------	0.76(4)	1.17(4)	1.55(4)	THz
for x = 0.57	------	0.74(5)	1.20(4)	1.57(4)	THz
calculated:	0.396	0.792	1.188	1.584	THz

where the values in the last line are calculated by means of Eq. 3.140 with $J = –79.19$ GHz which is nearly the value of pure Rb_2MnF_4 ($J = –79.12$ GHz, see Table 5 and [77C3]). The value of J for the diluted samples accounts for the variation of the lattice constant a with concentration x (see Table 2 and [73S1, 77C3]). The solid curve in Fig. 3.55 is the result of a computer simulation along the lines of a theory by Thorpe and Alben [76T3] using $g\mu_B H_A = 7.6$ GHz (pure Rb_2MnF_4) and $J = –87.05$ GHz obtained from a fit to the experimental data. In this context, it should be mentioned that there are many theoretical calculations which predict such structures in the neutron scattering function $S(\boldsymbol{K}, \omega)$ corresponding to the Ising cluster energies [74H6, 75C3, 75H6, 76A9, 76K6, 76T3]. Cowley et al. [77C3] pointed further out that their experimental data agree better with the results of computer simulations [75H6, 76T3, 76K6] than with calculated data [73B7, 74H7, 74H8, 75C3] based on the coherent potential approximation [67S2]. Simpler theoretical models like that of Dzyub [74D2] and of Matsubara [80M6, 80M7] allow an easy qualitative overview of the behaviour of diluted systems but are less successful with respect to quantitative results. The model of Matsubara accounts especially for the environment of a magnetic ion in diluted and mixed magnetic systems. Thus it yields four solutions for all systems but his results for AFMR exhibit one dominant peak for weakly anisotropic systems like Mn-compounds and four distinct peaks for strongly anisotropic ones like Co-compounds (cf. Figs. 2–4 in [80M6]). His results for the neutron scattering $S(\boldsymbol{K}, \omega)$ agree also qualitatively well with the experimental data (cf. Figs. 3.55 and 3.56 below). Finally, we recall from Sect. 3.1.3 that in antiferromagnets the ground state deviates from the ideal Néel state and that $\langle S_z \rangle \neq S$ or, as shown in Eqs. 3.18 and 3.19, $\langle S_z \rangle = S - \Delta_0 S$ with the zero-point spin deviation $\Delta_0 S$. For pure Mn-compounds, typical values are $\Delta_0 S = 0.17–0.18$. Also based on the theory of Thorpe and Alben [76T3], Halley and Holcomb [78H3] have calculated $\Delta_0 S$ for a diluted antiferromagnetic Mn-system like $Rb_2Mn_xMg_{1-x}F_4$ and obtained a distribution for $\Delta_0 S$ which widens considerably with decreasing x and the average value of which increases to about $\Delta_0 S \approx 0.38$ for $x = x_p$. Similar results were obtained by Dikken et al. [85D1] for $K_2Fe_xZn_{1-x}F_4$ from Mössbauer studies.

Another example of a diluted antiferromagnet studied by neutron inelastic scattering for concentrations x below x_p is $Rb_2Co_xMg_{1-x}F_4$ [79I3, 80C1]. The experimental data for $x = 0.575$ are reproduced in Fig. 3.56, as intensity (neutron counting rate) versus energy transfer $\hbar\omega$ at constant wavevector transfer $\boldsymbol{K} \triangleq (1 - \zeta_x, 0, 4.23)$. In this case, a structure with four maxima is observed over the whole Brillouin zone. There is only little dispersion very similar to that of pure Rb_2CoF_4 (cf. Fig. 3.25 and Eq. 3.63 in Sect. 3.1.9). For all three values of ζ_x in Fig. 3.56, i.e. for $\zeta_x = 0$, 0.25, and 0.5, the four maxima in the experimental data for $Rb_2Co_{0.575}Mg_{0.425}F_4$ reflect the Ising energies of Co^{2+}-ions in different environments, i.e. with $n = 1$, $n = 2$, $n = 3$, and $n = 4$ Co^{2+}-neighbours. The wavevector dependence of the excitations in Fig. 3.56 is well reproduced by the magnon dispersion relation Eq. 3.63 for the Ising systems K_2CoF_4 and Rb_2CoF_4 if this is modified by replacing the number of nearest neighbours $z = 4$ in the square lattice by the number n of actual Co^{2+} nearest neighbours

$$E_n(\boldsymbol{q}) = E_{n,q} = n \sqrt{(J_{\parallel})^2 - (J_{\perp}\gamma_q)^2} \tag{3.141}$$

where $J_{\parallel}$ and $J_{\perp}$ are explained in Sect. 3.1.9 and γ_q defined in context with Eq. 3.6 in Sect. 3.1.2. Satisfactory agreement is obtained by applying Eq. 3.141 to the data in Fig. 3.56 with the values for $J_{\parallel}$ and $J_{\perp}$ of pure Rb_2CoF_4 (cf. Table 5 and [78I2]). At the zone boundary ($\zeta_x = 0.5$ and $\gamma_q = 0$), we obtain analogous to Eq. 3.140 with $2S = 1$ for $S = \frac{1}{2}$ of Co-compounds

$$E_n = n\,|J_{\parallel}| \tag{3.141a}$$

However, the solid curves in Fig. 3.56 are not calculated by means of Eq. 3.141a but the result of a computer simulation by Cowley et al. [80C1] adapting the theory of Thorpe and Alben [76T3] to Co-compounds. A detailed analysis of the experimental data yields that the frequencies of the excitations are not in the expected ratios 4 : 3 : 2 : 1 but in the ratios 3.68 : 2.80 : 1.91 : 1. This discrepancy is ascribed to the inadequacy of the effective $S = \frac{1}{2}$ model for the Co^{2+}-ion. The energy levels of Co^{2+} (cf. Fig. 3.24 in

Sect. 3.1.9) resulting from the splitting of the $^4\Gamma_4^+(\mathrm{O_h})$ ground state in cubic symmetry are the effect of the tetragonal crystal field, of the spin-orbit coupling and of the molecular field due to the exchange interaction. Because of the interplay of these three mechanisms, the final splitting of the Kramers doublets by the molecular field is not linear in H_{MF} (cf. Eq. 3.61 in Sect. 3.1.9) and thus not proportional to $J_{\parallel}$ as assumed in Eq. 3.141a. Therefore, $\widetilde{E}_{\mathrm{n}} = E_{\mathrm{n}} - \alpha\, E_{\mathrm{n}}^3$ has been used as a model for the nonlinearity of the splitting. Then, excellent agreement is obtained between experimental data and the results of the computer simulation (cf. Fig. 3.56). Optimum parameter values are $J_{\parallel} = -1.813$ THz and $\alpha = 0.00137\ \mathrm{THz^{-2}}$ (cf. Table 5). The identification of the lines in Fig. 3.56 can further be founded on the relative intensities of the observed excitation lines [79I3] with their expected statistical weight $W_{\mathrm{n}}(\mathrm{x})$ (cf. Eq. 3.137) for n $\mathrm{Co^{2+}}$ nearest neighbours and $(4 - n)$ diamagnetic ones

$n =$	1	2	3	4
$W_{\mathrm{n}}(\mathrm{x}) =$	$4\mathrm{x}(1-\mathrm{x})^3$	$6\mathrm{x}^2(1-\mathrm{x})^2$	$4\mathrm{x}^3(1-\mathrm{x})$	x^4
calc. x = 0.89	0.005	0.058	0.310	0.627
exp. x = 0.89	------	------	0.31(3)	(0.63)
calc. x = 0.70	0.076	0.265	0.412	0.240
exp. x = 0.70	0.07(3)	0.24(3)	0.38(5)	(0.24)

where the experimental data are those at 6 K which are normalized to the theoretical values at $n = 4$ (therefore in bracketts). For concentrations $0.10 \le \mathrm{x} \le 0.58$, another neutron inelastic scattering study on $\mathrm{Rb_2Co_xMg_{1-x}F_4}$ [92I2, 94I4] has revealed also intracluster excitations, in addition to the Ising cluster excitations discussed above. The intracluster excitations are treated as the excitations of isolated clusters by diagonalizing the corresponding Hamiltonian as shown for dimers and trimers, for example, by Svensson et al. [78S12]. A further neutron inelastic scattering study was performed on $\mathrm{Rb_2Co_xMg_{1-x}F_4}$ with x = 0.60, 0.70 with the spectrometer HET at the pulsed spallation neutron source ISIS [95I2, 96I2]. The surprising result was that the Ising cluster excitations were observed up to temperatures far above the Néel temperature. They can clearly be seen at 5 T_{N} and 2 T_{N} for x = 0.60 (T_{N} = 20 K) and x = 0.70 (T_{N} = 45 K), respectively. This phenomenon is most probably due to the extremely slow dynamics of the spins in diluted magnets near the percolation threshold with fractal properties (cf. Sect. 4.1.12). If the time scale of the spin fluctuations is very large in comparison to the neutron travelling time through the sample, the system appears to be ordered, even far above T_{N} due to the short-range correlations.

As already mentioned at the beginning of this section, only one diluted ferromagnetic system, namely $\mathrm{K_2Cu_xZn_{1-x}F_4}$ (x = 0.78, 0.92), was studied [78W1] by neutron inelastic scattering with special attention to the effect of the dilution on the magnon frequencies and the magnon linewidth. A main result of this investigation is that the neutron groups for $\mathrm{K_2Cu_xZn_{1-x}F_4}$ show no structure with three or four maxima resulting from Ising cluster energies, in contrast to diluted antiferromagnets like $\mathrm{Rb_2Mn_xMg_{1-x}F_4}$ and $\mathrm{Rb_2Co_xMg_{1-x}F_4}$. This is in agreement with theoretical predictions by Krey and Schlichting [75K3] for diluted ferro- and antiferromagnets. A final remark concluding this section is that further data on diluted systems are compiled in Table 5, either as indicated in the text above or additional to the examples presented here.

9.12.3.3.4 Excitations in Mixed Antiferromagnets

In this section, mixed crystals $A_2M_x\tilde{M}_{1-x}X_4$ will be considered where both end members, A_2MX_4 and $A_2\tilde{M}X_4$ are antiferromagnets, for example of the easy-axis type with the preferred spin direction parallel or antiparallel to the crystalline *c*-axis. In such a system, there will be antiferromagnetic long range order (LRO) below the critical temperature T_N over the whole concentration range $0 \le x \le 1$. In addition to the super-exchange interaction between nearest neighbours pairs of M^{2+}- and of $\tilde{M}^{2+}$-ions as in pure A_2MX_4 and $A_2\tilde{M}X_4$, resp., there will also be an exchange interaction between neighbouring M^{2+}- and $\tilde{M}^{2+}$-ions. And for $x = 0.5$, i.e. the system $A_2M_{0.5}\tilde{M}_{0.5}X_4$, the concentration of each constituent is below the critical percolation limit $x_p = 0.593$ (cf. Eq. 3.127a) and the infinite cluster associated with the LRO cannot be formed by the exchange interaction between pairs of M^{2+}- and between pairs of $\tilde{M}^{2+}$-ions since both species occur only in finite clusters. Thus, the randomness of the system will not be a small perturbation but will have a dominating influence [76A3]. And the LRO can only be established by including the exchange interaction between M^{2+}- and $\tilde{M}^{2+}$-ions as emphasized by Kirkpatrick and Harris [75K4]. A sharp phase transition is observed in these systems as indicated by a sharp anomaly in the magnetic specific heat C_{magn} when macroscopic fluctations of the concentration x are sufficiently reduced [81I3]. The experimental data in Table 6 show that the critical behaviour of mixed easy-axis antiferromagnets is in general the same as that observed in pure easy-axis antiferromagnets (see Sects. 4.1.2–4.1.6 and Table 6) although there is a randomness in the mixed systems as discussed in some theoretical papers which deal with the critical behaviour of random systems [74H5, 74H9, 75A5, 75E1, 75L11, 76G5] mainly employing renormalization-group techniques. Some of them are also mentioned in Sect. 4.1.12 in context with the random exchange Ising model (REIM) which applies not only to diluted systems but may also be applicable to mixed antiferromagnets. However, the Harris criterion [74H5] states that randomness is irrelevant if the specific heat exponent $\alpha < 0$ and will cause important effects if $\alpha > 0$. Thus, it does not provide a definitive prediction for the Ising model with $\alpha = 0$. As in the pure materials, the magnetic LRO can be studied in mixed antiferromagnets by neutron scattering and also by ^{19}F-NMR which probes the local sublattice magnetization as outlined in Sect. 3.3.2 for diluted systems. In the mixed system $K_2Mn_xNi_{1-x}F_4$ [77L5, 80L4, 80L5, 83V2, 84V6], the local magnetization was studied by $^{19}F_I$-NMR, i.e. the impurity-associated satellites in NMR, for x = 0.975, 0.98, 0.995 near isolated Ni^{2+}-impurities and for $x \approx 0.01$ near isolated Mn^{2+}-impurities. The results are similar to those obtained for diamagnetic Zn^{2+} and Mg^{2+} impurities in K_2MnF_4 [80L4, 80L5]. Also the 13-site cluster model calculation is the same as for the diluted crystals and as discussed in detail in Sect. 3.3.2. Further, the spin-lattice relaxation time T_1 was determined by $^{19}F_I$-NMR [83V1] for isolated Ni^{2+} in K_2MnF_4 and for isolated Mn^{2+} in K_2NiF_4 and compared to those for Mn^{2+} in K_2MnF_4 and for Ni^{2+} in K_2NiF_4, appropriately scaled with the squared ratio of the hyperfine constants. The essential results are that the autocorrelation function is reduced at Ni^{2+} impurities in K_2MnF_4 and enhanced for Mn^{2+} impurities in K_2NiF_4.

After these introductory remarks, our attention will be focussed on the magnetic excitations which were studied by means of neutron inelastic scattering for the following mixtures of two easy-axis antiferromagnets (cf. Table 5)

$Rb_2Mn_{0.5}Co_{0.5}F_4$ [80I1], $Rb_2Mn_{0.5}Ni_{0.5}F_4$ [75A1, 75B10, 77S1], $Rb_2Co_{0.5}Ni_{0.5}F_4$ [83I1]

All three systems show two magnon branches. That means they exhibit a two-mode behaviour [74E]. In $Rb_2Mn_{0.5}Ni_{0.5}F_4$, a transition to antiferromagnetic LRO occurs at $T_N = 68.72$ K, intermediate between Rb_2MnF_4 ($T_N = 38.4$ K) and Rb_2NiF_4 ($T_N = 91$ K). The magnon dispersion of $Rb_2Mn_{0.5}Ni_{0.5}F_4$ for $T = 7$ K is shown in Fig. 3.57, the experimental points and, for comparison, the dispersion curves of the two end members Rb_2MnF_4 and Rb_2NiF_4 as dashed lines. Obviously, the lower branch of the mixed crystal is close to that of pure Rb_2MnF_4 and may be called the Rb_2MnF_4-like one. The upper branch of the mixed crystal falls into the spin-wave band of pure Rb_2NiF_4 and may be called the Rb_2NiF_4-like one although it shows much less dispersion than pure Rb_2NiF_4. Some measurements at 66 K show that the excitations broaden somewhat with increasing temperature in both branches but remain well-defined magnetic excitations. The solid curves in Fig. 3.57 are calculated by means of a relatively simple model, the mean crystal model which is often also called virtual crystal or average model. In this model, it is assumed that x M^{2+}-ions and (1 – x) $\tilde{M}^{2+}$-ions are located on each site of the two sublattices. This is fictitious and cannot account for the true distribution of the ions over the lattice sites and for their true environment. But this model with four sublattices is a very helpful tool for the discussion of the excitations of magnetic mixed crystals. The corresponding Hamiltonian can be written as follows

$$\begin{aligned}\mathcal{H} = {} & -2x^2 J_{AA} \sum_{\langle i,j\rangle} \boldsymbol{S}_{a,i}\boldsymbol{S}_{b,j} - 2\,(1-x)\,x\,J_{AB} \sum_{\langle i,j\rangle} [\boldsymbol{S}_{a,i}\boldsymbol{S}_{d,j} + \boldsymbol{S}_{c,i}\boldsymbol{S}_{b,j}] - 2\,(1-x)^2\, J_{BB} \sum_{\langle i,j\rangle} \boldsymbol{S}_{c,i}\boldsymbol{S}_{d,j} \\ & - x\,D_A \left[\sum_i (S^z_{a,i})^2 + \sum_j (S^z_{b,j})^2\right] - (1-x)\,D_B \left[\sum_i (S^z_{c,i})^2 + \sum_j (S^z_{d,j})^2\right]\end{aligned} \tag{3.142}$$

where

$\boldsymbol{S}_{a,i}$ and $\boldsymbol{S}_{b,j}$ denote M^{2+}-spins on sites i and j in sublattices 1 and 2, respectively.
$\boldsymbol{S}_{c,i}$ and $\boldsymbol{S}_{d,j}$ denote $\tilde{M}^{2+}$-ions on sites i and j in sublattices 1 and 2, respectively.

J_{AA}, J_{AB}, and J_{BB} are the parameters for the exchange interaction between $M^{2+} - M^{2+}$, $M^{2+} - \tilde{M}^{2+}$, and $\tilde{M}^{2+} - \tilde{M}^{2+}$ nearest neighbours ions.

D_A and D_B are the constants of the out-of-plane anisotropy while S_A and S_B are the spin values of the M^{2+}- and $\tilde{M}^{2+}$-ions, respectively.

As usual in this contribution, the exchange parameters are positive for ferromagnetic and negative for antiferromagnetic exchange interaction and ⟨i, j⟩ mean in the summation that each pair of ions is counted only once. The out-of-plane anisotropy energy is presented here in the single-ion form (cf. Eq. 3.16 in Sect. 3.1.2 and Eq. 3.35 in Sect. 3.1.5). In Eq. 3.142 D_A and D_B are positive for easy-axis systems and negative for easy-plane ones. In order to keep the above expressions for the mean crystal model as transparent as possible, no terms for an in-plane anisotropy and for the interaction with an external magnetic field H_0 have been included which can easily be added but cause all following expressions to become also more lengthy. A classical spin-wave treatment of Eq. 3.142 including a spatial Fourier transform yield the following quartic equation for the q-dependent magnon frequencies

$$\begin{aligned}&(\hbar\omega)^4 - (\hbar\omega)^2\,(E^2_{AA} - E^2_{AA,q} + E^2_{BB} - E^2_{BB,q} - 2\,E_{AB,q}E_{BA,q}) \\ &+ (E^2_{AA} - E^2_{AA,q})\,(E^2_{BB} - E^2_{BB,q}) - 2\,E_{AA}E_{BB}E_{AB,q}E_{BA,q} \\ &- 2\,E_{AA,q}E_{BB,q}E_{AB,q}E_{BA,q} + E^2_{AB,q}E^2_{BA,q} = 0\end{aligned} \tag{3.143}$$

with

$$E_{AA} = 2\,x\,z\,S_A\,|J_{AA}| + 2\,(1-x)\,z\,S_B\,|J_{AB}| + 2\,S_A D_A$$

$$E_{BB} = 2\,x\,z\,S_A\,|J_{AB}| + 2\,(1-x)\,z\,S_B\,|J_{BB}| + 2\,S_B D_B$$

$$E_{AA,q} = 2\,x\,z\,S_A\,|\,J_{AA}\,|\,\gamma_q \qquad E_{BB,q} = 2\,(1-x)\,z\,S_B\,|\,J_{BB}\,|\,\gamma_q$$

$$E_{AB,q}\,E_{BA,q} = 4\,x\,(1-x)\,z^2\,S_A\,S_B\,J_{AB}^2\gamma_q^2$$

where $\gamma_q = \frac{1}{z}\sum_j e^{i\boldsymbol{q}\,\boldsymbol{r}_j} = \cos\left(\frac{q_x a}{2}\right)\cdot\cos\left(\frac{q_y a}{2}\right)$ (cf. Eq. 3.6 in Sect. 3.1.2) and where z is again the number of nearest of neigbours, i.e. $z = 4$ on the square lattice. For $Rb_2Mn_{0.5}Ni_{0.5}F_4$, we have to identify M^{2+} with Mn^{2+} and $\widetilde{M}^{2+}$ with Ni^{2+} further

$$J_{AA} = J_{Mn\text{–}Mn},\; J_{AB} = J_{Mn\text{–}Ni},\; J_{BB} = J_{Ni\text{–}Ni},\; 2\,S_A\,D_A = g_{Mn}\mu_B H_{A,Mn},\; 2\,S_B\,D_B = g_{Ni}\mu_B H_{A,Ni}.$$

If then x = 0.5 is inserted to Eqs. 3.142 and 3.143, the latter is completely equivalent to Eq. 19 of Als-Nielsen et al. [75A1, 75B10] by means of which they have calculated the magnon dispersion curves of $Rb_2Mn_{0.5}Ni_{0.5}F_4$ (solid curves in Fig. 3.57) using the values of the parameters for pure Rb_2MnF_4

$$J_{Mn\text{–}Mn} = -2.64\ \mathrm{cm}^{-1}, \qquad g_{Mn}\mu_B H_{A,Mn} = 0.24\ \mathrm{cm}^{-1} \approx 0\ \text{(neglected)}$$

(details see Table 5 and [70B1, 73B1, 73W2, 73W3]) and those for pure Rb_2NiF_4

$$J_{Ni\text{–}Ni} = -33.5\ \mathrm{cm}^{-1}, \qquad g_{Ni}\mu_B H_{A,Ni} = 2.26\ \mathrm{cm}^{-1}$$

(details see Table 5 and [75A1]. For the exchange between Mn- and Ni-ions, an estimate is used which worked well in a number of 3D magnetic mixed crystals [72C2]

$$J_{Mn-Ni} = \sqrt{J_{Mn-Mn}J_{Ni-Ni}} = -9.40\ \mathrm{cm}^{-1}$$

so that there is no adjustable parameter in this model calculation. Nevertheless, the agreement between experiment and calculated data is remarkably good for this simple model, especially for the lower branch with perfect agreement within the error limits, while there are deviations up to 10 % in the upper branch, except for the zone boundary. And there have been other calculations employing more sophisticated theories like models based on the coherent-potential approximation [75C3, 76C3] following the lines of previous calculations for 3D mixed antiferromagnets [72B7, 74D3]. Further calculations were performed with Green's function and equation of motion techniques [75A4, 75K4, 76T3, 76K6]. All these theoretical approaches yield a better agreement with the experimental data, including magnon dispersion curves and the temperature dependence of the sublattice magnetization. Also numerical simulations were performed on $K_2Mn_xNi_{1-x}F_4$ [74H10, 75S2] the results of which can as well be used for the discussion of the properties of $Rb_2Mn_{0.5}Ni_{0.5}F_4$.

We can expect the mean crystal or virtual crystal model to reproduce well only the peak positions of the neutron groups and not their structure, and we recall from the last section that the neutron inelastic scattering data of the diluted systems $Rb_2Mn_{0.57}Mg_{0.43}F_4$ (cf. Fig. 3.55) and $Rb_2Co_{0.575}Mg_{0.425}F_4$ (cf. Fig. 3.56) show a structure with four maxima corresponding to the Ising cluster energies for the possible environments of the Mn^{2+}- and Co^{2+}-ions in these compounds. The mixture of two antiferromagnets $Rb_2Mn_{0.5}Ni_{0.5}F_4$ has for both constituents a concentration below x_p similar to the diluted systems in the last section. And the neutron inelastic scattering intensity with the background subtracted shows at (0.5, 0, 0) two broad bands (cf. Fig. 3.58) which may be considered as the not quite resolved Mn^{2+} and Ni^{2+} Ising cluster modes indicated as vertical lines in Fig. 3.58. The "Ising cluster approximation" of Cowley and Buyers [72C2, 76C3] was introduced for dilute systems in Eq. 3.140 in the last section. For mixed magnets, Eq. 3.140 is to be extended to the original form of Cowley and Buyers, namely to

$$E_{n,A} = 2\,n\,S_A\,|J_{AA}| + 2\,(z-n)\,S_B\,|J_{AB}|$$
$$E_{n,B} = 2\,n\,S_A\,|J_{AB}| + 2\,(z-n)\,S_B\,|J_{BB}| \qquad (3.144)$$

where the notation is the same as in Eqs. 3.142 and 3.143. In Eq. 3.144, $E_{n,A}$ and $E_{n,B}$ are the Ising cluster energies of the M^{2+}- and $\widetilde{M}^{2+}$-ions (subscripts A and B), resp., having as nearest neighbours n M^{2+}-ions and $(z-n)$ $\widetilde{M}^{2+}$-ions $(0 \le n \le 4)$. The energies $E_{n,A}$ and $E_{n,B}$ (vertical lines in Fig. 3.58) have been calculated for Mn^{2+} (subscript A) and Ni^{2+} (subscript B) in $Rb_2Mn_{0.5}Ni_{0.5}F_4$ using the same parameter values given above for the mean crystal model calculation. The intensities of these cluster modes are proportional to the probability for the occurrence of such clusters $W_n(x)$ (see Eq. 3.137). The length of the vertical lines in Fig. 3.58 is proportional to $W_n(0.5)$ scaled separately for Mn and Ni modes so as to obtain agreement with the observed peak intensities. We note finally that the mean crystal model Eq. 3.142 yields for $q = q_{max}$ $(\gamma_q = 0)$ at the zone boundary

$$\hbar\omega_{1,2} = E_{AA} = 2\,x\,z\,S_A\,|J_{AA}| + 2\,(1-x)\,z\,S_B\,|J_{AB}| + 2\,S_A\,D_A$$
$$\hbar\omega_{3,4} = E_{BB} = 2\,x\,z\,S_A\,|J_{AB}| + 2\,(1-x)\,z\,S_B\,|J_{BB}| + 2\,S_B\,D_B$$

If the small anisotropy terms are neglected, $\hbar\omega_{1,2}$ and $\hbar\omega_{3,4}$ agree with the average of $E_{n,A}$, $E_{n,B}$, i.e. for the average value $\bar{n} = xz = 2$ with $E_{2,A}$ and $E_{2,B}$ (cf. Eq. 3.144) and with the position of the peaks in Fig. 3.58, but do not reproduce the width of these peaks. But as already mentioned, these simple models are useful approximations for an overview and good agreement with all experimental data is obtained by more elaborate theoretical calculations, as for example in [76C3, 76T3].

Similar neutron inelastic scattering results as for $Rb_2Mn_{0.5}Ni_{0.5}F_4$ were reported for $Rb_2Mn_{0.5}Co_{0.5}F_4$ ($T_N = 65$ K, see [80I1]) and $Rb_2Co_{0.5}Ni_{0.5}F_4$ ($T_N = 115$ K, see [83I1]). The results for these easy-axis systems will not be discussed in detail here. It was already mentioned that for both two magnon branches were observed. Also for $Rb_2Co_{0.5}Ni_{0.5}F_4$, calculations with the mean crystal or average model were performed. For $S = \frac{1}{2}$ Co^{2+}-ions, Ikeda et al. [83I1] have adapted the model to anisotropic exchange (see their Eq. 1) as already used in Sect. 3.1.9 for pure Co-compounds (cf. Eq. 3.62). The results of their model calculations were not satisfactory when they used as input parameters the exchange constants of pure Rb_2CoF_4 and Rb_2NiF_4 and for the Co-Ni-exchange the geometric mean of the constants of the pure constituents. Therefore they used parameter values (see Table 5) obtained from a fit to the experimental data which are smaller than those found for the pure crystals. With the fit values, the agreement with the experimental data is improved. The fine structure in the neutron scattering intensity at the zone boundary fits well to the Ising cluster energies (cf. Eq. 3.144) also calculated with the fit parameters.

The magnetic mixed system $Rb_2Mn_{0.5}Ni_{0.5}F_4$ was also studied with Raman spectroscopy by Fleury and Guggenheim [75F4]. They have not single magnon modes observed but magnon pair modes: a Ni-Ni-mode at 372 cm^{-1} and a Mn-Ni-mode at 248 cm^{-1}. The corresponding Mn-Mn-mode was not observed. These experimental data were also analysed by means of the Ising cluster model. The idea is that the pair modes arise from the excitation of the spins on two neighbouring sites, i.e. the Ni-Ni-mode from a nearest neighbour pair of Ni-ions (again subscript B) which may be surrounded by n_1 and n_2 Mn-ions (subscript A) and by $(z-1-n_1)$ and $(z-1-n_2)$ Ni-ions, respectively. Under these conditions, the energy of the Ni-Ni-mode becomes (see Eq. 1 of [75F4])

$$\hbar\omega_{BB}\,(n_1, n_2) = 2\,(n_1 + n_2)\,S_A\,|J_{AB}| + 2\,(2z-2-n_1-n_2)\,S_B\,|J_{BB}| - 2\,|J_{BB}| \qquad (3.145)$$

where the first two terms are the Ising cluster energies of the two Ni-ions and the last term takes approximately into account the magnon-magnon interaction in such a pair mode [66M2, 69E, 69T]. A similar expression was derived by Fleury and Guggenheim for the Mn-Ni-mode (Eq. 1 of [75F4]). Also in the Raman data, the Ising cluster modes are not resolved and only the pair-mode centre frequences calculated with $\bar{n}_1 = \bar{n}_2 = x\,(z-1)$ can be compared with the peak positions in the experimental data.

With the above values for $J_{\mathrm{AA}} = J_{\mathrm{Mn–Mn}}$, $J_{\mathrm{AB}} = J_{\mathrm{Mn–Ni}}$, and $J_{\mathrm{BB}} = J_{\mathrm{Ni–Ni}}$ which gave a satisfactory agreement with the neutron scattering data, Fleury and Guggenheim obtained by means of Eq. 3.144 and their Eq. 1 too large values for the peak positions outside the error limits. A fit to their experimental data yielded the drastically reduced values (cf. Table 5)

$$J_{\mathrm{Mn–Mn}} = -2.90\ \mathrm{cm}^{-1} \qquad J_{\mathrm{Mn–Ni}} = -9.17\ \mathrm{cm}^{-1} \qquad J_{\mathrm{Ni–Ni}} = -29.0\ \mathrm{cm}^{-1}$$

They also investigated the temperature dependence of the magnon pair spectra which turned out to be similar to that of the two-magnon spectra in pure antiferromagnets.

Next let us consider the situation that the concentration x is either small or close to one, so that the mixed crystal does not contain nearly equal portions of both end members but that one constituent is the host crystal with a small doping of the other one. When the mean crystal or average model (Eq. 3.142) is solved for small x ≈ 0, i.e. x << 1, the quartic secular equation Eq. 3.143 yields four solutions

$$\hbar\omega_{1,2} = \sqrt{(2zS_{\mathrm{B}}\,|J_{\mathrm{BB}}| + 2S_{\mathrm{B}}D_{\mathrm{B}})^2 - (2zS_{\mathrm{B}}\,|J_{\mathrm{BB}}|\,\gamma_{\mathrm{q}})^2} \tag{3.146a}$$

$$\hbar\omega_{3,4} = 2zS_{\mathrm{B}}\,|J_{\mathrm{AB}}| + 2S_{\mathrm{A}}D_{\mathrm{A}} \tag{3.146b}$$

where $\hbar\omega_{1,2}$ represents the usual magnon dispersion relation of the host crystal (subscript B) and $\hbar\omega_{3,4}$ an excitation localized on isolated ions of the dopant (subscript A). For x ≈ 1, i.e. (1 – x) << 1, the other end member (subscript A) becomes the host and the first one (subscript A) the dopant. The solutions of Eq. 3.143 are obtained by interchanging the subscripts A and B so that $\hbar\omega_{1,2}$ is again the magnon dispersion relation of the host crystal (now subscript A) and

$$\hbar\omega_{3,4} = 2zS_{\mathrm{A}}\,|J_{\mathrm{AB}}| + 2S_{\mathrm{B}}D_{\mathrm{B}} \tag{3.146c}$$

again a localized mode residing on isolated impurities. It can be seen on Fig. 3.57 that reducing drastically the Ni-concentration in the mixed system will finally lead to the magnon dispersion relation of $\mathrm{Rb_2MnF_4}$ and to a local mode in $\mathrm{Rb_2MnF_4 : Ni^{2+}}$ above the spin-wave band of $\mathrm{Rb_2MnF_4}$. Reducing, on the other hand, the Mn-concentration, the expected result is the magnon dispersion relation of $\mathrm{Rb_2NiF_4}$ and a local mode in $\mathrm{Rb_2NiF_4 : Mn^{2+}}$ below the spin-wave band of $\mathrm{Rb_2NiF_4}$, i.e. a localized mode in its antiferromagnetic gap or, simply, a gap mode. If the frequency of the local mode falls into the spin-wave band of the host, it becomes a resonant band mode. The terms "local mode", "gap mode", and "resonant band mode" have first been used for lattice dynamics in crystals with impurities (see for instance [66M3, 66M4] or [69G3]) and later been adapted to magnetic problems [69W1]. For the discussion of these phenomena connected with isolated impurities in otherwise pure host crystals, we will no longer use the notation $\mathrm{Rb_2Mn_xNi_{1-x}F_4}$ but the more appropriate ones $\mathrm{Rb_2MnF_4 : Ni^{2+}}$ and $\mathrm{Rb_2NiF_4 : Mn^{2+}}$ which more clearly marks the host and the dopant the concentration of which is typically a few per cent.

The expressions Eqs. 3.146b and 3.146c are only first approximations for the frequency of the local modes. In the late sixties, more accurate results were derived in a number of theoretical treatments employing Green's function and other techniques, mostly for 3D doped antiferromagnets [68L2, 68L3, 68T2, 69P1, 69W1, 70T], see also the review by Cowley and Buyers [72C2]. In these theories, not only the isolated impurity but also its z nearest neighbours were taken into account. The magnetic modes residing on these neighbours were classified according to their symmetry with respect to the paramagnetic point group of the impurity and its neighbours. Such a group theoretical analysis was performed by Lovesey [68L2] for the rutile structure ($\mathrm{MnF_2}$ etc.) and by Parkinson [69P1] for the cubic perovskite structure. Later, all these results were also applied to the quasi 2D magnets with perovskite-type layer structure. For the latter, the group theoretical analysis for the impurity and its four nearest neighbours yields for the impurity: a Γ_1^+-mode (A_{1g}, s_0-mode)

and for the four nearest neighbours: a Γ_1^+-mode (A_{1g}, s_1-mode), a Γ_3^+-mode (B_{1g}, d-mode), and a doubly degenerate Γ_5^--mode (E_u, 2 p-modes).

The notation of these magnetic modes is according to the corresponding symmetry of electronic eigenfunctions [68L2, 68T2, 69P1, 72C2]. Thus the local mode residing primarily on the isolated impurity is called s_0-mode and an excitation of the s_0-mode and of the d-mode primarily residing on the nearest neighbours is called the (s_0 + d) pair mode.

These defect modes have been studied in the 2D perovskite-type layer structures by various spectroscopic methods, mostly by FIR and Raman spectroscopy, but also by IR emission spectroscopy [81B8], by fluorescence spectroscopy [75L5, 75L6, 77L2] and by neutron inelastic scattering [95I4]. While the local mode above the spin-wave band of the host was observed in the 3D antiferromagnet MnF_2 for a number of defects, eg. $MnF_2 : Co^{2+}$ [68H, 69S3, 69W2), $MnF_2 : Ni^{2+}$ [68M4], $MnF_2 : Fe^{2+}$ [68W2, 69W2], only few results were reported for such local modes in the 2D systems under consideration. Only for (see Table 5)

$K_2MnF_4 : Ni^{2+}$ [75L5, 75L6, 77L2],

$\omega(s_0)$ was determined from fluorescence spectra. The search for this mode in $K_2MnF_4 : Co^{2+}$ was in vain [76L6]. However, the frequencies $\omega(s_0)$ were determined for localized gap modes in a number of systems, namely in

$K_2FeF_4 : Mn^{2+}$ [78M1],

$K_2CoF_4 : Mn^{2+}$ [80B13, 81B8], $K_2CoF_4 : Fe^{2+}$ [81B8, 82F],

$Rb_2CoF_4 : Mn^{2+}$ [81B8, 95I4], $Rb_2CoF_4 : Ni^{2+}$ [81B8]

Further, the (s_0 + d) pair mode was observed in some systems, in general by Raman scattering

$K_2MnF_4 : Ni^{2+}$ [75L5, 75L6, 77L2], $K_2MnF_4 : Co^{2+}$ [76L6, 79M2],

$K_2FeF_4 : Co^{2+}$ [84F4], $K_2CoF_4 : Fe^{2+}$ [82F]

The excitation energies determined in these experiments offer the possibility to determine the constant J_{AB} of the impurity-host exchange interaction. For all these localized modes and pair modes, the energies and the exchange constants deduced from them are compiled in Table 5. The geometric mean of the exchange parameters of the two end members as the parameter for the exchange between the host ions and the impurities

$$\hat{J}_{AB} = -\sqrt{|J_{AA}| \cdot |J_{BB}|} \tag{3.147}$$

worked well for J_{Mn-Ni} in $Rb_2Mn_{0.5}Ni_{0.5}F_4$ but is not a general solution for this problem. Within the frame of a molecular field approximation [69W3], the Néel temperatures of the mixed system form a straight line connecting the Néel temperatures of the end members if $J_{AB} = \hat{J}_{AB}$ where J_{AB} is the actual value and $\hat{J}_{AB}$ that calculated by means of Eq. 3.147. For $Rb_2Co_xNi_{1-x}F_4$ however, the experimentally determined Néel temperatures lie above that line [81I3] and a value $J_{Co-Ni} = 1.29\ \hat{J}_{Co-Ni}$ is obtained by means of a fit to the molecular field approximation. Therefore, useful information can be gained from a careful analysis of the excitation frequencies. For an experimental determination of J_{AB}, the energy $\hbar\omega(s_0)$ of the local gap mode [77L2, 78M1] was not only compared to the mean field approximation (Eqs. 3.146b and 3.146c) but also to theoretical results obtained by Green's function methods and cluster approximations [70T] and by other methods [69W1]. If the impurity is Co^{2+} or if the host is a Co-compound, the analysis is to be performed with an anisotropic exchange interaction, not only for the Co-compound (cf. Eq. 3.62 in Sect. 3.1.9) but also for the impurity-host exchange. In these cases [79M2, 80B13, 81B8, 82F], the longitudinal part $J_{\parallel,\mathrm{AB}}$ is usually determined from $\hbar\omega(\mathrm{s}_0)$ by means of a mean field or Ising approximation. The transverse part $J_{\perp,\mathrm{AB}}$ is then determined by a perturbation calculation with the transverse part of the Hamiltonian [66M2, 72C2]. The values of the constants J_{AB}, $J_{\parallel,\mathrm{AB}}$, and $J_{\perp,\mathrm{AB}}$ for the impurity-host exchange determined from the excitation energies are collected for the systems under consideration in Table 5 and compared to the geometric means calculated by Eq. 3.147 which are denoted $\hat{J}_{\mathrm{AB}}$, $\hat{J}_{\parallel,\mathrm{AB}}$, and $\hat{J}_{\perp,\mathrm{AB}}$ in order to distinguish them more easily from the experimental values J_{AB} etc. The theory of Thorpe [70T] was further employed to calculate the lineshape of the $(\mathrm{s}_0 + \mathrm{d})$ pair mode for $K_2MnF_4 : Co^{2+}$ [76L6] in good agreement with the experimental data.

9.12.3.3.5 Mixed Antiferromagnets with Competing Anisotropies

The virtual crystal or average model Eq. 3.142 cannot only be used to calculate, at least approximately, the excitation frequencies of the system as outlined in context with Eq. 3.143. It can also be employed for obtaining some information about the groundstate of the system, i.e. its magnetic ordering. This is performed by calculating the orientation angles for the four sublattices from the equilibrium conditions, i.e. vanishing torque for the static components of the sublattices (cf. Eqs. 3.42–3.44 in Sect. 3.1.6). In this section, we assume that all exchange interactions are antiferromagnetic, i.e. $J_{\mathrm{AA}} < 0$, $J_{\mathrm{AB}} < 0$, and $J_{\mathrm{BB}} < 0$ in Eq. 3.142. If then the anisotropy constants are both positive, i.e. $D_{\mathrm{A}} > 0$ and $D_{\mathrm{B}} > 0$ in Eq. 3.142, the preferred spin direction will be parallel or antiparallel to the *c*-axis for the mixed system over the whole concentration range $0 \le \mathrm{x} \le 1$. But if one end member is an easy-axis antiferromagnet ($D_{\mathrm{A}} > 0$), e.g. K_2CoF_4, and the other one an easy-plane antiferromagnet ($D_{\mathrm{B}} < 0$), e.g. K_2FeF_4, there is a competition of the anisotropies in the corresponding mixed system, e.g. $K_2Fe_{1-x}Co_xF_4$, between ordering parallel or perpendicular to the *c*-axis. For small concentrations $\mathrm{x} \ll 1$, the easy-plane ordering of the host (subscript B) is dominating, and for concentrations close to one $(1 - \mathrm{x}) \ll 1$, the easy-axis ordering of the other end member (subscript A) will dominate. But in the intermediate concentration range, the competition between the two types of anisotropy will lead to a reorientation of the system, to a transition from the easy-plane to the easy-axis type. A simple estimate of the critical concentration at which this could happen is to look for the cancellation of the reduced anisotropy fields $h_{\mathrm{A}} = H_{\mathrm{A}}/H_{\mathrm{E}}$ (cf. Eq. 3.6 in Sect. 3.1.2) weighted with the appropriate concentration factor i.e. for $K_2Fe_{1-x}Co_xF_4$

$$\mathrm{x} \cdot h_{\mathrm{A,Co}} = (1 - \mathrm{x}) \cdot h_{\mathrm{A,Fe}} \tag{3.148}$$

The solution of Eq. 3.148 is x = 0.21 for $K_2Fe_{1-x}Co_xF_4$ with the values from Table 5:

$$h_{\mathrm{A,Co}} = (1 - J_{\perp}/J_{\parallel}) = 0.488 \qquad h_{\mathrm{A,Fe}} = |D/zJ| = 0.132$$

A calculation with a mean field or virtual crystal model will yield a better estimate. For this purpose, the definition of orientation angles in Eq. 3.44 of Sect. 3.1.6 is extended to four sublattices (μ = a, b, c, d). As long as in-plane anisotropy terms are neglected we may set $\delta_{\mathrm{a}} = \delta_{\mathrm{b}} = \delta_{\mathrm{c}} = \delta_{\mathrm{d}} = 0$, i.e. the static components of the four sublattices are restricted to the (x, z)-plane. For the system $K_2Fe_{1-x}Co_xF_4$, the static components of the sublattice magnetizations are the polar angles can be written as

$$M_{\mathrm{a},0} = -M_{\mathrm{b},0} = M_{\mathrm{Co}} \quad \text{and} \quad M_{\mathrm{c},0} = -M_{\mathrm{d},0} = M_{\mathrm{Fe}} \tag{3.149a}$$

$$\theta_{\mathrm{a}} = \theta_{\mathrm{b}} = \theta_{\mathrm{Co}} \quad \text{and} \quad \theta_{\mathrm{c}} = \theta_{\mathrm{d}} = \theta_{\mathrm{Fe}} \tag{3.149b}$$

where M_{Co} and M_{Fe} are the sublattice magnetizations due to the Co^{2+}- and the Fe^{2+}-ions, respectively. Along the lines of the Matsubara's model (see Sect. 3.3.3 and [80M6, 80M7]) extended to mixed antiferromagnets with competing anisotropies [77M5, 78O3, 81M6], Hagen and Higgins [88H3] have calculated within such an average crystal approximation the ground state configuration of $K_2Fe_{1-x}Co_xF_4$ and found for $0 \leq x \leq 0.2$ $\theta_{Fe} = \theta_{Co} = 90°$ (easy-plane or planar antiferromagnetic phase), for $0.2 \leq x \leq 0.24$ an oblique antiferromagnetic phase (OAF) with $0° \leq \theta_{Fe}, \theta_{Co} \leq 90°$ and $\theta_{Fe} \neq \theta_{Co}$, and finally for $0.24 \leq x \leq 1$ $\theta_{Fe} = \theta_{Co} = 0°$ (easy-axis or axial antiferromagnetic phase). A corresponding (T_N, x) phase diagram with three antiferromagnetic phases, the paramagnetic phase and a tertracritical point was theoretically predicted for randomly mixed magnets by Aharony and Fishman [76A12, 78F4] and was also dealt with in another theoretical study [81M7].

The question is now how far these theoretical estimates and predictions are confirmed by experimental data. The magnetic ordering of $K_2Fe_{1-x}Co_xF_4$ was studied by neutron scattering [83V3, 84H3, 86V1], by Mössbauer studies [84F3, 85V3], by susceptibility measurements [84F3] and by a ^{19}F-NMR investigation [86V2]. The results are depicted in Fig. 3.59 and the numerical values are listed in Table 6. At low temperatures, there is the planar antiferromagnetic phase (AF, planar) for concentrations $0 \leq x \leq 0.18$, the oblique antiferromagnetic phase (OAF) for $0.18 \leq x \leq 0.32$, and the axial antiferromagnetic phase (AF, axial) for concentrations $0.32 \leq x \leq 1.0$. The paramagnetic phase (PM) at high temperatures is separated from the antiferromagnetic phases by the line of critical temperatures T_N. The boundaries between the OAF-phase and the other AF-phases mark a transition temperature T_R, a reorientation temperature at which a change occurs in the magnetic order of the system. These four phase-transition lines meet in a tetracritical point as predicted by Aharony and Fishman [76A12, 78F4]. In Fig. 3.59, this multicritical point is at $x_{C.P.} = 0.22$ and $T_{C.P.} = 57$ K [86V1]. For a better understanding of the magnetic ordering in $K_2Fe_{1-x}Co_xF_4$, it is advisable to look in more detail at the experimental data, first at those obtained by neutron scattering. The intensity of antiferromagnetic superreflections is proportional to the square of the sublattice magnetization M_{subl} [71B1, 71M2, 73B1, 77B2] as already mentioned in context with Eq. 3.18 in Sect. 3.1.3 and with Eq. 3.66 in Sect. 3.1.9. And since M_{subl} is a measure for the 3D LRO in antiferromagnets, information about this order is gained from the intensities of antiferromagnetic Bragg reflections studied as a function of temperature by neutron scattering. In these quasi-2D materials, antiferromagnetic Bragg rods are observed as mentioned in Sect. 2.1.2 and shown in Fig. 2.5b. The temperature dependence of such a Bragg rod intensity will analogously provide information about 2D ordering, which is usually a finite and not a long-range order. Only in the Ising-compounds K_2CoF_4 and Rb_2CoF_4, a 2D LRO is possible because of the existence of a phase transition at $T_C > 0$ in the 2D Ising model (cf. Sect. 3.1.9). The intensity of the antiferromagnetic Bragg rod at $\boldsymbol{K} \mathrel{\hat{=}} (1, 0, 0.4)$ is shown in Fig. 3.60 as a function of temperature in the range $(0 \leq T \leq 100$ K) for several concentrations x of the system $K_2Fe_{1-x}Co_xF_4$. In all cases, there is an increase of the intensity with decreasing temperature, reaching a maximum at the Néel temperature T_N and decreasing then for temperatures below T_N due to the onset of 3D LRO and due to the transfer of scattering intensity from the Bragg rod to the Bragg reflections. Therefore, T_N can be determined from the maximum of the rod intensity or from the temperature where the intensity of a Bragg reflection or $M_{subl}(T)$ vanishes (see Fig. 3.26 in Sect. 3.1.9). The experimental points in Fig. 3.59 at the boundary to the PM-phase $(\hat{=} T_N)$ correspond to the maxima of the rod intensities in Fig. 3.60. In addition to the maximum at $T_N = 64.4$ K, the experimental data for $x = 0.27$ show a second broader maximum at the reorientation temperature $T_R = 27$ K. As expected from Fig. 3.59, only the spin components parallel to the *c*-axis undergo at T_N a transition to LRO (axial AF-phase) while below T_R a canted antiferromagnetic order is established with spin components parallel and perpendicular to the *c*-axis (OAF-phase). This was deduced from a detailed analysis of the neutron scattering data [86V1]. The samples with $x = 0.12$ and $x = 0.18$ show below T_N the planar antiferromagnetic order and that with $x = 0.55$ the axial one, as expected from Fig. 3.59. We note further that for $x = 0.12$ and $x = 0.18$, the rod intensity goes to zero at low temperature while it does not for $x = 0.27$ and $x = 0.55$ indicating that the spins fail to achieve a complete 3D LRO but only a finite 2D order in the layers with less correlation between them. The intensities of several antiferromagnetic Bragg reflections (cf. Fig. 1 of [86V1]) increase for $x = 0.12$, 0.18, and 0.55 steadily with decreasing temperature while that for $x = 0.27$ shows a first rise for $T < T_N$ and a second distinct one for $T < T_R$ which can also be seen in the results of a Mössbauer study for $x = 0.27$ [85V3] while it is absent there also for x = 0.55 and x = 0.70. These results are presented in Fig. 3.61 as the temperature dependence of the hyperfine field H_{hf} which is directly proportional to the sublattice magnetization. They are in accordance with the (T_N, x) phase diagram (cf. Fig. 3.59).

Neutron scattering, Mössbauer, and NMR data provide also information about the cant angles θ_{Fe} and θ_{Co} (Eq. 3.149b) in the OAF-phase [84H3, 85V3, 86V2]. Mössbauer studies allow a measurement of θ_{Fe} while the NMR data yield values for θ_{Fe} and θ_{Co}. The temperature dependence of various antiferromagnetic Bragg reflections was further used to determine the order parameter critical exponent β (for definition and details see Sect. 4.1.4, especially Eq. 4.20). It turns out that β reaches a maximum for concentrations near the tetracritical point (cf. the detailed data in Table 6). Further, the local magnetizations of $K_2Fe_{1-x}Co_xF_4$ were investigated with ^{19}F-NMR [86V2, 88V2]. A number of signals are observed for x = 0.12, 0.18, 0.27, and 0.55 which are assigned to the resonance NMR frequency for ^{19}F-ions near Fe^{2+}- and Co^{2+}-ions surrounded by a certain number ($0 \le n \le 4$) of Fe^{2+}- and Co^{2+}-neighbours. In addition, neutron inelastic scattering experiments were performed on $K_2Fe_{1-x}Co_xF_4$ for x = 0.2, x = 0.27, and x = 0.6 [84H3, 87H4]. The resulting magnon dispersion relations for x = 0.6 (axial AF-phase) consist of two branches and are very similar to those of $Rb_2Mn_{0.5}Ni_{0.5}F_4$ (cf. Fig. 3.57) and other easy-axis mixed antiferromagnets discussed in the last section. For x = 0.27 (OAF-phase), two low-frequency branches ($\hbar\omega < 100$ cm^{-1}) were determined (cf. Fig 3.62) which join to a degenerate magnon state at the zone boundary as observed in pure K_2FeF_4 (see Fig. 3.14 in Sect. 3.1.5). Finally, Hagen and Higgins [88H3] performed a model calculations with an average crystal approximation [81M6] and a computer simulation for the ground state properties and the magnon dispersion of $K_2Fe_{0.73}Co_{0.27}F_4$ where the computer simulation accounts also for fluctuations in the concentration and the spin cant angles θ_{Fe} and θ_{Co}. As input parameters, they have used the values of $J_{\|,Co-Co}$, $J_{\perp,Co-Co}$, J_{Fe-Fe}, D_{Fe}, and E_{Fe} reported for the pure end members K_2CoF_4 and K_2FeF_4 (see Table 5 and [79M1, 82T1]). As constants for the exchange between Fe^{2+} and Co^{2+}, the values

$$\hat{J}_{\|,\,Fe-Co} = -18.55 \text{ cm}^{-1} \text{ (cf. Table 5)} \quad \text{and} \quad \hat{J}_{\perp,\,Fe-Co} = -13.3 \text{ cm}^{-1}$$

calculated by means of Eq. 3.147 were used. In contrast to the average-crystal model, the computer simulation yields for the ground state properties that θ_{Fe} and θ_{Co} start to deviate from 90° near x = 0.12 which is still in the planar AF-phase and reach the final value 0° near x = 0.50. For x = 0.27 in the OAF-phase, a broad distribution of cant angles results from the computer simulation which is absent in the average model calculation. In Fig. 3.62, the experimental data for the magnon dispersion relation of $K_2Fe_{0.73}Co_{0.27}F_4$ are compared to the results of the simple model calculation and of the computer simulation based on the above mentioned results for the ground state of the system. The computer simulation data (solid lines in Fig. 3.62) agree much better with the experimental points than the average-crystal model (broken lines), except for the gap of the lower branch at $q = 0$. Here, the agreement for the computer simulation can be improved by using an in-plane anisotropy constant $E_{Fe} = -0.12$ cm^{-1} smaller than that for pure K_2FeF_4 ($E_{Fe} = -0.20$ cm^{-1}) without affecting perceptibly the results at higher energies. Thus, it seems that E_{Fe} which depends on the orthorhombic symmetry in the ordered state is indeed smaller for the mixed crystal.

A similar mixed system with competing anisotropies is $Rb_2Fe_{1-x}Co_xF_4$. It was investigated by Mössbauer spectroscopy [84H4] the results of which indicate a (T_N, x) phase diagram with OAF-phase and a tetracritical point very similar to $K_2Fe_{1-x}Co_xF_4$ (cf. Fig. 3.59). Another mixture of an easy-axis with an easy-plane antiferromagnet is $K_2Mn_{1-x}Fe_xF_4$. Its magnetic ordering and structure was studied by neutron scattering [77B8, 78B4, 78B10, 78B11] and by susceptibility measurements [78B4, 78B10]. Also renormalized spin-wave calculations were performed [78L3]. The (T_N, x) phase diagram resulting from all these data (see Table 6 and Fig. 1 of [79B2]) shows also an axial AF-phase (for $x \le 0.02$), a planar AF-phase for $x \ge 0.03$, an OAF-phase and a tetracritical point at $x_{C.P.} = 0.026$, $T_{C.P.} = 36$ K [86F5]. Because of the small anisotropy of Mn^{2+}, all this happens for Fe^{2+}-concentrations smaller than 5% ($x < 0.05$). An estimate for the critical concentration analogous to Eq. 3.148 yields for $K_2Mn_{1-x}Fe_xF_4$

$$x \cdot h_{A,Fe} = (1 - x) \cdot h_{A,\,Mn} \tag{3.150}$$

As solution of Eq. 3.150, we obtain x = 0.027 with the values from Table 5:

$$h_{A,Fe} = |D/zJ| = 0.132 \qquad h_{A,Mn} = 0.0036$$

This simple estimate is again close to the critical concentration in the (x, T) phase diagram. For the system $K_2Mn_{1-x}Fe_xF_4$, samples were investigated with $x = 0.023 < x_{C.P.}$ and $x = 0.028 > x_{C.P.}$ so that, before entering into the OAF-phase below T_R, one of them (x = 0.023) exhibits in the range ($T_R \le T \le T_N$) ordering of the axial spin components and the other one (x = 0.028) ordering of the planar spin components. Theoretically, the results of a mean-field model calculation were compared to the experimentally determined (T_N, x) phase diagram [81S8, 82S6]. Further, n-diffraction experiments were performed on a sample with x = 0.022 in external fields $\boldsymbol{H_0} \parallel \boldsymbol{c}$ up to 5 T in order to obtain the (H_0, T) phase diagram of this sample (see Fig. 3.63). We recall from Sect. 3.1.6 the usual (H_0, T) phase diagram of an easy-axis antiferromagnet with (axial) antiferromagnetic (AF), spin-flop (SF), paramagnetic (PM) phases and a bicritical point (see Figs. 3.18 and 3.19) which is different from that in Fig. 3.63 for the x = 0.022 sample. For low fields ($H_0 < 1$ T), this sample is for $T \le T_R = 16$ K in the OAF-phase, for $T_R \le T \le T_N = 40.5$ K in the axial AF-phase and for $T > T_N$ paramagnetic. For fields of 3–4 T, it undergoes a transition to a field-induced planar antiferromagnetic phase which is equivalent to the SF-phase of an easy-axis antiferromagnet. The experimental points in Fig. 3.63 result from scanning the intensity of the (1, 0, 0) or (0, 1, 0) antiferromagnetic Bragg peak either as function of T at fixed H_0 or as function of H_0 at fixed T (solid and open circles, resp., in Fig. 3.63). In the phase diagram, all four phase boundaries seem to meet in one point which would then be a tetracritical point. Similar magnetic phase diagrams with an OAF-phase and a tetracritical point but not quite the same as Fig. 3.63 were predicted theoretically [73L3, 75B7, 76A13].

9.12.3.3.6 Mixed Magnets with Competing Exchange Interactions

Competing exchange interactions arise in a mixed crystal when one end member is a ferromagnet and the other one an antiferromagnet. Examples of such systems are $Rb_2Cr_{1-x}Mn_xCl_4$ and $Rb_2Co_xCu_{1-x}F_4$ where we recall from Sects. 3.1.6 and 3.19 that Rb_2MnCl_4 and Rb_2CoF_4 are easy-axis antiferromagnets and from Sects. 3.2.1 and 3.2.2 that Rb_2CrCl_4 and Rb_2CuF_4 are easy-plane ferromagnets. The combination of ferro- and antiferromagnetic exchange leads to competing exchange interactions and to frustration when a spin cannot satisfy simultaneously the ferro- or antiferromagnetic bonds to its nearest neighbours. For Ising spins on a square lattice, there is a theoretical study of the frustration effect [77V3]. In addition to competing exchange, these model systems exhibit also competing anisotropies as discussed in the last section. Further, the orbital ordering of the Cr^{2+}- and Cu^{2+}-ions in Rb_2CrCl_4 and Rb_2CuF_4, resp., occurs also in the mixed crystals for sufficiently large (1 – x). It leads to two distinct exchange interactions between Mn^{2+}- and Cr^{2+}-ions and between Co^{2+}- and Cu^{2+}-ions which is shown for $Rb_2Co_{0.22}Cu_{0.78}F_4$ as an example in Fig. 3.64. The exchange depends on the orientation of the Cu^{2+}-orbital relative to the Cu-Co bond [88D7, 88D10, 88D11]. If the d-orbital points toward the Co^{2+}-ion, the exchange is antiferromagnetic, and it is ferromagnetic otherwise. Thus, there are two antiferromagnetic (Cu-Co and Co-Co) and two ferromagnetic bonds (Cu-Co and Cu-Cu) in $Rb_2Co_xCu_{1-x}F_4$ where only the average of the two Cu-Co exchange parameters is accessible in experiments. The same scheme of exchange bonds as in Fig. 3.64 holds also for $Rb_2Cr_{1-x}Mn_xCl_4$ [84M7].

Some basic information about the magnetic ordering in these systems is obtained by spectroscopic methods. By Raman scattering [88M4], one-magnon spectra are observed for $Rb_2Cr_{1-x}Mn_xCl_4$ on the Cr-rich side for x = 0.01, 0.13, 0.20 at the maximum magnon energy $h\nu_{max} \approx 165$ cm^{-1} which are broader in comparison to pure Rb_2CrCl_4 where also this mode is not at the zone boundary but Raman-active at $q = 0$ because of the spin-canting and the doubling of the unit cell (cf. Eq. 3.90a in Sect. 3.2.2 and [87A3, 88B3]). On the Mn-rich side for x > 0.5, the Raman spectra show the two-magnon bands as usual in antiferrromagnets (cf. Figs. 3.4 and 3.5 in Sect. 3.1.2). Further, magnetic resonance experiments were performed on $Rb_2Cr_{1-x}Mn_xCl_4$ for various concentrations x. In some cases, not only AFMR or FMR were studied but also the EPR linewidth and its increase towards the critical temperatures [83T7, 84K6, 84T2]. Other AFMR or FMR measurements [84G3, 91G2] were carried out under various conditions, i.e. for $\boldsymbol{H_0} \parallel \boldsymbol{c}$ and for $\boldsymbol{H_0} \perp \boldsymbol{c}$ with $\beta = 0$ and $\beta = 45°$ where β is the angle between $\boldsymbol{H_0}$ and the x-axis (cf. Eq. 3.43). Thus it was possible to identify on the Mn-rich side for $0.96 \leq x \leq 1.0$ the AFMR spectra typical for an easy-axis antiferromagnet. The results for x = 0.972 are shown in Fig. 3.65 which look similar to those of pure Rb_2MnCl_4 (Fig. 3.17) but with a smaller zero-field ν_{AFMR} and a smaller spin-flop field H_{SF} as was already observed in diluted $Rb_2Mn_xCd_{1-x}Cl_4$ (x = 0.91, 0.80). If in $Rb_2Cr_{1-x}Mn_xCl_4$ the Co^{2+} concentration is further increased, the single-ion anisotropy of Cr^{2+} overcomes the axial anisotropy of Mn^{2+} analogous to the examples shown in the last section (cf. Eqs. 3.148 and 3.150), and the axial antiferromagnetic order changes into an oblique order and finally into a planar antiferromagnetic order. And already for x = 0.934, the AFMR spectra (see Fig. 3.66) show the pattern of an easy-plane antiferromagnet like those observed for K_2FeF_4 (see Sect. 3.1.5 and [80D]) with the larger $\nu_{AFMR,out\text{-}of\text{-}pl.}$ and the smaller $\nu_{AFMR,in\text{-}plane}$ for $H_0 = 0$ (cf. Eq. 3.37 in Sect. 3.1.5). On the Cr-rich side, the magnetic resonance spectra for x = 0.37 in Fig. 3.67 look similar to those of pure Rb_2CrCl_4 (cf. Fig. 3.36), i.e. of an easy-plane ferromagnet. In comparison to Rb_2CrCl_4, the in-plane anisotropy, i.e. the difference between the data for $\beta = 0$ and $\beta = 45°$, is quite diminished. The solid lines in Figs. 3.65–3.67 are generated by model calculations [85G3, 86G2, 91G2] employing an average or virtual crystal model which was introduced in context with Eqs. 3.142 and 3.143. For the discussion of the magnetic resonance experiments, the Hamiltonian Eq. 3.142 is converted to a classical energy density u, supplemented by in-plane anisotropy and Zeeman terms:

$$\begin{aligned} u = {} & x^2 \frac{H_{E,MM}}{M_M} \boldsymbol{M_a M_b} + x(1-x) \frac{H_{E,MC}}{(M_M M_C)^{1/2}} [\boldsymbol{M_a M_d} + \boldsymbol{M_c M_b}] - (1-x)^2 \frac{H_{E,CC}}{M_C} \boldsymbol{M_c M_d} \\ & - x \frac{H_{A,M}}{2M_M} [M_{a,z}^2 + M_{b,z}^2] + x \frac{\hat{H}_{A,M}}{2M_M^3} [M_{a,x}^2\, M_{a,y}^2 + M_{b,x}^2\, M_{b,y}^2] \\ & + (1-x) \frac{H_{A,C}}{2M_C} [M_{c,z}^2 + M_{d,z}^2] + (1-x) \frac{\hat{H}_{A,C}}{2M_C^3} [M_{c,x}^2\, M_{c,y}^2 + M_{d,x}^2\, M_{d,y}^2] \\ & - (\boldsymbol{H_0} + \boldsymbol{h}) \cdot [x\, \boldsymbol{M_a} + x\, \boldsymbol{M_b} + (1-x)\, \boldsymbol{M_c} + (1-x)\, \boldsymbol{M_d}] \end{aligned} \quad (3.151)$$

where the notation is similar to Eq. 3.142. $\boldsymbol{M_a}$, $\boldsymbol{M_b}$, $\boldsymbol{M_c}$, and $\boldsymbol{M_d}$ denote the magnetizations of the four sublattices (a ≙ Mn ↑, b ≙ Mn ↓, c ≙ Cr ↑, d ≙ Cr ↓). The subscripts M and C refer to Mn and Cr, respectively. Thus, $H_{E,MM}$ and $H_{E,CC}$ are the exchange fields for the Mn-Mn and Cr-Cr interactions with the values of pure Rb_2MnCl_4 and pure Rb_2CrCl_4 (cf. Table 5). No corrections were made for the change of the lattice parameters in the mixed crystal system. Within the model, the Cr-Cr exchange term is counted negative because of the ferromagnetic exchange between Cr^{2+}-ions while the antiferromagnetic interactions are set positive, including the Mn-Cr exchange the average of which was determined to be antiferromagnetic by optical studies (see Table 5 and [82W8, 86D4]). The out-of-plane anisotropy terms in Eq. 3.151 are negative for Mn ($H_{A,M}$) and positive for Cr ($H_{A,C}$) reflecting the easy-axis character of Rb_2MnCl_4 and the easy-plane one of Rb_2CrCl_4. The in-plane anisotropy terms are of the type with tetragonal symmetry as in the energy densities for the magnetic resonance experiments on Rb_2MnCl_4 (cf. Eq. 3.41 in Sect. 3.1.6) and on Rb_2CrCl_4 (cf. Eq. 3.104 in Sect. 3.2.3). In the model for the mixed crystals, for Rb_2MnCl_4 the small orthorhombic in-plane anisotropy field $\tilde{H}_A$ and for Rb_2CrCl_4 the small spin canting have been neglected. The demagnetization corrections are not written explicitly in Eq. 3.151 but have been applied for samples with ferromagnetic order. The model calculations were performed along the lines described for the analysis of the AFMR experiments on pure Rb_2MnCl_4 in Sect. 3.1.6. They started with the values of the pure end members also for the anisotropy fields $H_{A,M}$, $H_{A,C}$, $\hat{H}_{A,M}$, and $\hat{H}_{A,C}$ (see Table 5 and Table 1 of [91G2]). But in the course of this procedure, it turned out that an optimum agreement between experimental and calculated was obtained by assuming the anisotropy fields to be dependent on the concentration x (see Table 2 of [91G2]). For the samples in the intermediate concentration range with x = 0.59, 0.70, and 0.75 however, the fit procedure leads to unreasonable values for the anisotropy fields so that the model was abandoned for these samples. Thus, the model is appropriate to give some insight into the magnetic structures of the system $Rb_2Cr_{1-x}Mn_xCl_4$ with competing exchange and competing anisotropies on the Mn-rich side (Figs. 3.65 and 3.66) and on the Cr-rich side (Fig. 3.67). In addition to the magnetic resonance experiments, also magnetization measurements were performed on $Rb_2Cr_{1-x}Mn_xCl_4$ samples for concentrations x = 0.980, 0.972 on the Mn-rich side and x = 0, 0.083, 0.131, 0.306 on the Cr-rich side [86G2, 86G3]. And the average model describes also quite well the magnetization data on the Cr-rich side as demonstrated in Fig. 3.68 with magnetization M at 4.2 K for $\boldsymbol{H_0} \perp \boldsymbol{c}$. The strong decrease of the saturation magnetization with increasing Mn^{2+}-concentration results from the antiferromagnetic coupling between Mn^{2+}- and Cr^{2+}-ions in this mixed system. Since this virtual crystal model averages over all local environments of the ions, it cannot take into account the randomness of this system and cannot deal explicitly with different neighbour configurations. Therefore, we cannot expect it to be an adequate description in the intermediate concentration range where it failed to describe reasonably well the magnetic resonance data.

So we are left with the question what happens for intermediate concentrations x where ferro- and antiferromagnetic exchange interactions cancel each other. Some theoretical studies have derived (T_C, x) phase diagrams for competing exchange interactions. Some of them [75A6, 79F3, 79O3, 84H5] show a ferromagnetic, an antiferromagnetic and a mixed phase, in addition to the paramagnetic phase where the four lines separating the phases meet in a tetracritical point. Others [78M4, 80F3] predict a spin-glass phase at low temperatures between the ferro- and the antiferromagnetic phase as shown schematically in Fig. 3.69. In particular, a model calculation was performed for mixtures with competing exchange and a Jahn-Teller effect in one end member like $Rb_2Cr_{1-x}Mn_xCl_4$ and $Rb_2Co_xCu_{1-x}F_4$ [84M7] where also a spin-glass phase is obtained for intermediate concentrations. Much attention was focussed on spin glasses in the last 25 years and the important results are compiled in a number of review papers [85H4, 86B7, 86M5, 86Y3, 96M]. For an excellent introduction into this subject and into the properties of spin glasses, the reader is referred to the monograph by Mydosh [93M3]. A spin glass is a magnetic phase like those with LRO, namely the ferromagnetic and the antiferromagnetic one. It is characterized by competing exchange interactions which exhibits a "freezing transition" at a freezing temperature T_f or T_C to a new kind of order where the spins are aligned in random directions in a frozen state. The question whether the system undergoes a new type of phase transition [87S3] or fails merely to establish complete thermal equilibrium during the observation time has been answered meanwhile in favour of the phase transition. In model considerations, the competing exchange interactions are treated as random positive or negative bonds, e.g. in the famous model of Edwards and Anderson [75E2] and its solution by Sherrington and Kirkpatrick [75S5]. But also site-random models have been discussed [79O4]. While for diluted artiferromagnets it was advantageous to consider them as site-diluted and not as bond-diluted, it is more appropriate to discuss the spin glasses under consideration in terms of bond-randomness and not in terms of site-randomness. For our further discussion, it is not necessary to present here a comprehensive introduction to spin glasses. Only some experimental characteristics are compiled here:

1) The ac suceptibility shows a cusp at a frequency-dependent freezing temperature T_f.

2) There is no anomaly of the magnetic specific heat C_{magn} at T_f

3) There is a hysteresis in the FC-ZFC dc-susceptibility and a thermo-remanent magnetization in FC experiments.

4) There is no magnetic LRO and, thus, no magnetic Bragg intensity observed below T_f in neutron scattering experiments.

Along the lines of these characteristics, spin-glass behaviour has been observed in $Rb_2Cr_{1-x}Mn_xCl_4$ for x = 0.42, 0.6, 0.62 [82K7, 82K8, 83K10] and in $Rb_2Co_xCu_{1-x}F_4$ for x = 0.218, 0.326 [88D1, 88D11]. As an example of evidence for spin-glass behaviour, Fig. 3.70 presents the ac susceptibility χ_{ac} of $Rb_2Cr_{0.4}Mn_{0.6}Cl_4$ for $\boldsymbol{h} \perp \boldsymbol{c}$ and as a function of temperature with the cusp at the frequency-dependent freezing temperature T_f. Another example illustrates the temperature variation of the low-field (H_0 = 1 mT) dc susceptibility of $Rb_2Co_{0.218}Cu_{0.782}F_4$ in Fig. 3.71. In the field-cooling experiment (FC), $\chi_{\|c}$ for $\boldsymbol{H_0} \| \boldsymbol{c}$ (see Fig. 3.71a) increases monotonically upon a typical slow cooling rate of 5 mK/s. The susceptibility $\chi_{\|c}$ obtained by zero-field cooling (ZFC) exhibits a maximum near 3 K which is phenomenologically identified with T_f. There are strong dynamic effects, as the maximum and thus T_f depends on the waiting time t_W between switching on the field and taking the data. For t_W = 10 s and t_W = 90 s, the maxima are at T_f = 3.10(2) K and T_f = 2.97(2) K (see Table 5). The data in Fig. 3.71b demonstrate that the FC and ZFC data of $\chi_{\perp c}$ for $\boldsymbol{H_0} \perp \boldsymbol{c}$ are indistinguishable proving that only the spin components parallel to the *c*-axis are involved in the spin-glass freezing. This is expected from the strong axial anisotropy of Co^{2+} and, since $S_{Co} = \frac{1}{2}$ and $S_{Cu} = \frac{1}{2}$, $Rb_2Co_xCu_{1-x}F_4$ with $0.18 \le x \le 0.40$ can be called an experimental realization of a 2D Ising spin glass on a square lattice. Samples with spin glass behaviour of the mixed system $Rb_2Cr_{1-x}Mn_xCl_4$ (x = 0.42, 0.50, 0.53, 0.62) have further been studied by magnetic resonance [82K8, 82K9]. The results for 20–35 GHz at $\boldsymbol{H_0} \perp \boldsymbol{c}$ [82K8] were interpreted in terms of results on metallic spin glasses [80S6, 85G4] although only one mode was observed in $Rb_2Cr_{1-x}Mn_xCl_4$ out of three modes observed in the metallic spin glass. The results for 50–170 GHz at $\boldsymbol{H_0} \| \boldsymbol{c}$ give evidence for a strong planar anisotropy resulting from the single-ion anisotropy of Cr^{2+} due to the crystal field effects which were studied for the mixed system by Rudowicz et al. [92R2, 93R3]. Thus, $Rb_2Cr_{1-x}Mn_xCl_4$ may be considered an approximation to a 2D XY-spin-glass with nearly classical spins (S_{Cr} = 2 and S_{Mn} = 2.5).

For the whole concentration range $0 \le x \le 1$ of $Rb_2Co_xCu_{1-x}F_4$, the critical temperatures T_C for transitions to ordered ferro- and antiferromagnetic phases as well as the freezing temperatures for spin glasses were determined by susceptibility measurements [88D1, 88D11] and by neutron scattering [92S1, 92S8]. The results are compiled in Table 5 and in the (T_C, x) phase diagram Fig. 3.72. In the range $0 \le x \le 0.18$, ferromagnetic order is observed with competing anisotropy, starting with a planar ferromagnetic phase, followed by an oblique ferromagnetic phase and finally an axial ferromagnetic phase where the four phase lines meet in a tetracritical point (see insert to Fig. 3.72). This is analogous to Fig. 3.59 in the last section, namely the phase diagram of $K_2Fe_{1-x}Co_xF_4$. The only difference is that $Rb_2Co_xCu_{1-x}F_4$ with $0 \le x \le 0.18$ is a ferromagnetic system with competing anisotropies while $K_2Fe_{1-x}Co_xF_4$ is an antiferromagnetic one. In the range $0.18 \le x \le 0.40$, $Rb_2Co_xCu_{1-x}F_4$ exhibits spin glass freezing. While the transition temperatures T_C to an ordered phase are marked by circles in Fig. 3.72, the freezing temperatures T_f are shown as crosses with a dashed line. The solid phase boundary lines in Fig. 3.72 are continued in the spin-glass range as T_C = 0 since a 2D random-bond Ising spin glass is predicted to have no proper spin glass transition for $T_C > 0$ but to have one for $T_C = 0$ [79M3, 80M8, 84B7], i.e. the lower critical dimension is for these systems larger than two. However, there is some evidence for a spin glass transition in a 2D site-random Ising model [95S3]. For the remaining range $0.40 \le x \le 1.0$, Fig. 3.72 shows axial antiferromagnetic order of $Rb_2Co_xCu_{1-x}F_4$ because the antiferromagnetic exchange and the easy-axis anisotropy of the Co^{2+}-ions is dominating for these concentrations. Similar susceptibility and neutron scattering investigations were performed also for $Rb_2Cr_{1-x}Mn_xCl_4$ [81M1, 82K6, 84K8, 84M1, 86K12, 86N3, 88H4, 88K8, 88S7, 88T2, 89S1, 91S1, 92S7]. The resulting phase diagram is not so clear as that for $Rb_2Co_xCu_{1-x}F_4$ in Fig. 3.72 and will therefore be discussed later in Sect. 4.1.13 in context with critical properties. A peculiarity of this system is that on the Cr-rich side ($0 \le x \le 0.5$) first a transition to ferromagnetic order is observed around 30–40 K and then a re-entrant spin-glass freezing near 10 K [84K8, 86K10, 86K12, 88K8, 91S1]. The ac susceptibility for these samples (see Fig. 3.73) shows upon lowering the temperature a steep increase of χ_{ac} for $\boldsymbol{h} \perp \boldsymbol{c}$ at T_C and reaches then a plateau which is probably due to demagnetization effects. We recall from Eq. 3.94a in Sect. 3.2.3 that the observed susceptibility $\chi^{\alpha\alpha}_{app}$ approaches the demagnetization coefficient N^{α} when the true susceptibility $\chi^{\alpha\alpha}$ diverges at the transition to the ferromagnetic phase. This transition is sharp for x = 0.17 and 0.36 while it becomes broad for x = 0.50. The experimental data in Fig. 3.73 show further a rather steep decrease of χ_{ac} which indicates the re-entrant spin-glass freezing and which is absent in pure Rb_2CrCl_4 [86K10]. This decrease and the freezing temperature T_f derived from it are frequency-dependent (see e.g. Fig. 11 of [88K8]). Such re-entrant spin-glass behaviour was found in a number of spin-glass systems [93M3]. In a physical picture, it may be explained as the melting or freezing of frustrated spins [86S7] which influence little the ferromagnetic properties when they are molten but strongly when they are frozen in the spin-glass state. It has further been shown that in such systems ferromagnetic and spin-glass orderings may coexist [81G5, 82S7]. Finally, re-entrance phenomena like those observed in $Rb_2Cr_{1-x}Mn_xCl_4$ were predicted in Monte Carlo simulations for the 2D random-bond XY-spin-glass [85K2, 86K11].

Also the magnetic excitations reveal unusual and peculiar properties in these systems with competing exchange interactions and competing anisotropies. For concentrations close to the end member Rb_2CuF_4 however, neutron inelastic scattering data taken at 6.7 K [92S8] yield for $Rb_2Co_{0.037}Cu_{0.963}F_4$ a spin-wave branch which is well described by the approximation for a 2D Heisenberg ferromagnet (see Eq. 3.72 in Sect. 3.2.1) with an effective $J = 10.3(3)$ K although the sample with x = 0.037 undergoes at $T_C = 5.4$ K a transition to an axial and at $T_R = 3.3$ K to the oblique ferromagnetic phase (cf. Fig. 3.72 and Table 5). But there is obviously no influence of the anisotropy fields on the Heisenberg approximation. For the system $Rb_2Cr_{1-x}Mn_xCl_4$ on the other hand, samples with concentrations x = 0.25, 0.59, and 0.70 were studied by neutron inelastic scattering [86S5, 87S2, 88S7, 88S8]. These concentrations are sufficiently away from x = 0 and x = 1 so that the randomness will influence the results. One sample (x = 0.25) is on the Cr-rich side with ferromagnetic order, one (x = 0.70) on the Mn-rich side with antiferromagnetic and the last one (x = 0.59) with spin-glass behaviour. For a comparing discussion of the magnetic excitations in these three samples representing the essential three possibilities of magnetic ordering in $Rb_2Cr_{1-x}Mn_xCl_4$ with different Brillouin zones, it is advisable to use a common system of wavevectors for their description, namely the coordinate system (q_{x0}, q_{y0}, q_{z0}) in reciprocal space corresponding to the (x_0, y_0, z_0) coordinate system in real space based on the I4/mmm unit cell (cf. discussion and Fig. 2.5 in Sect. 2.1.2). The (q_{x0}, q_{y0})-plane in reciprocal space is shown in Fig. 3.74. The point (1, 1, 0) represents a nuclear Bragg reflection of I4/mmm and is thus in our considerations the centre of the "ferromagnetic" Brillouin zone (dashed line in Fig. 3.74) without doubling of the unit cell. The point (0.5, 0.5, 0) corresponds to an antiferromagnetic superreflection and is therefore taken as the centre of the "antiferromagnetic" Brillouin zone (solid line in Fig. 3.74) with doubling of the unit cell. For a common description of the magnetic excitations in all three samples, the reduced wavevector ζ is chosen in relation to the wavevector $\boldsymbol{Q}$

$$\boldsymbol{Q} = (1-\zeta)\,a^* + (1-\zeta)\,b^* \quad \text{or} \quad \boldsymbol{Q} \mathrel{\hat{=}} (1-\zeta,\,1-\zeta,\,0) \tag{3.152}$$

That means ζ runs from 0 to 0.5 for the ferromagnetic sample (x = 0.25) and from 0.5 to 0.25 for the antiferromagnetic sample (x = 0.70). For the spin-glass sample (x = 0.5), the range will be also $0 \le \zeta \le 0.5$. The experimental results are reproduced in Figs. 3.75 and 3.76 for $Rb_2Cr_{0.3}Mn_{0.70}Cl_4$ and $Rb_2Cr_{0.75}Mn_{0.25}C1_4$, respectively. The widths of the neutron groups are larger in the mixed crystals than in pure materials. This width of the excitations is indicated by bars in the figures, namely by vertical bars for constant-Q scans and by horizontal bars for constant-energy scans. Most of the data were taken at 5 K, and some of the data for x = 0.25 at 13 K. But there is no significant temperature shift in the experimental data (circles and triangles in Fig. 3.76). Surprisingly, there is a coexistence of a usual spin-wave branch and of dispersionless modes in the excitation spectra. And it is even more surprising that the magnon branches in Figs. 3.75 and 3.76 are identical to those of pure Rb_2MnCl_4 (see Fig. 4 of [80S2]) and Rb_2CrCl_4 (see Fig. 3.35 and [80E1, 81H4]), resp., except for a small range for the zone boundary (see dashed lines in Figs. 3.75 and 3.76). From the results in mixed antiferromagnets like $Rb_2Mn_{0.5}Ni_{0.5}F_4$ (cf. Fig. 3.57), one would expect that also in the $Rb_2Cr_{1-x}Mn_xCl_4$ the magnons would be shifted to higher or lower energies with respect to those of the pure end members. The dispersionless part of the excitations was identified as cluster modes and the horizontal solid lines were calculated by means of the Ising cluster approximation [72C2, 76C3] introduced in Eq. 3.140 for diluted magnets and in Eq. 3.144 for mixed antiferromagnets, which has to be extended here to non-collinear magnetic systems

$$\begin{aligned} E_{n,M} &= 2\,n\,S_M J_{MM} \cos\delta_{MM} + 2\,(z-n)\,S_C J_{MC} \cos\delta_{MC} \\ E_{n,C} &= 2\,n\,S_M J_{MC} \cos\delta_{MC} + 2\,(z-n)\,S_C J_{CC} \cos\delta_{CC} \end{aligned} \tag{3.153}$$

where the subscripts M and C refer to Mn and Cr, resp., i.e. $S_M = 2.5$ and $S_C = 2.0$. The angles δ_{MM}, δ_{MC}, and δ_{CC} measure the differences between the equilibrium spin directions in the *c*-plane for a pair of $Mn^{2+} - Mn^{2+}$, $Mn^{2+} - Cr^{2+}$ and $Cr^{2+} - Cr^{2+}$ nearest neighbours, resp., which were calculated by means of the virtual crystal or average model (Eq. 3.151). Note that in Eq. 3.153 no longer the absolute value of the exchange parameters is used and that they enter the equation with the appropriate sign

$$J_{MM} = -121.9 \text{ GHz} \qquad J_{MC} = -45.0 \text{ GHz} \qquad J_{CC} = +157.5 \text{ GHz}$$

These are, converted to GHz, the values of pure Rb_2MnCl_4 (J_{MM}), of pure Rb_2CrCl_4 (J_{CC}) and of the mixed system from optical studies (J_{MC}), all listed in Table 5. For antiferromagnetic order, the value of δ will be close to 180° and with $\cos\delta \approx -1$ the negative sign of J will be compensated and thus E_n becomes positive. For ferromagnetic order, δ will be close to 0° with $\cos\delta \approx +1$ and again a positive E_n results. For our mixed system, the angles depend strongly on the concentration x

x = 0.25	$\delta_{MM} = 129°$	$\delta_{MC} = 242°$	$\delta_{CC} = 6°$
x = 0.59	$\delta_{MM} = 168°$	$\delta_{MC} = 250°$	$\delta_{CC} = 28°$
x = 0.70	$\delta_{MM} = 174°$	$\delta_{MC} = 243°$	$\delta_{CC} = 48°$

and with these values, $E_{n,M}$ and $E_{n,C}$ were calculated for the clusters indicated to the right of the Fig. 3.75 and 3.76. The agreement with the dispersionsless experimental data is remarkably good. It should further be mentioned that in the antiferromagnetic sample (x = 0.70, Fig. 3.75) the cluster modes were observed beyond $\zeta = 0.25$ but not the magnons. The results for the spin-glass sample $Rb_2Cr_{0.41}Mn_{0.59}Cl_4$ in Fig. 3.77 (full circles for data obtained with the IN8 in Grenoble and open triangles for data obtained with the triple-axis spectrometer in Saclay) are not very different from those of the other two samples, except that the widths of the excitations have become larger. There are again dispersionless cluster modes in rather good agreement with the data calculated by means of Eq. 3.153. And quasi as an intermediate link between the other two samples, ferro- as well as antiferromagnetic *q*-dependent spin waves have been found. However, the excitations were only observed for values of *q* counted from the corresponding zone centre which are larger than the inverse correlation length κ or with a wavelength smaller than the correlation length. By means of neutron scattering [86N3, 88S7] with scans across the Bragg rod at (0.5, 0.5, 0.25), the inverse correlation length κ and the energy width or relaxation rate Γ (cf. Eq. 4.131) were determined as a function of temperature for this sample (see Fig. 3.78). For decreasing the temperature, κ decreases and reaches a constant value for $0 \le T \le 20$ K while Γ decreases also and approaches zero at about 11 K. That means the spatial disorder remains at a certain level at low temperatures while the temporal disorder and the temporal fluctuations disappear at the freezing temperature T_f. The low-temperature value of κ is indicated in Fig. 3.77 by arrows. In conclusion, the excitation spectra of the three $Rb_2Cr_{1-x}Mn_xCl_4$ samples (x = 0.25, 0.59, 0.70) are of a novel type and unusually rich. Therefore, the question arose whether these findings can be interpreted within the framework of harmonic magnon theory or whether some of the features are due to anharmonic effects. Therefore, a theoretical calculation [88C6, 88S9] was performed for the neutron scattering function $S(\boldsymbol{Q}, \omega)$ (cf. [68M2, 71M2] and Eq. 4.21 in Sect. 4.1.5) where $\boldsymbol{Q}$ is the reciprocal lattice vector defined in Eq. 3.152. For the calculation, a method was employed which was derived for disordered systems like spin glasses [80W3, 81C4]. In this equation-of-motion technique, the classical equilibrium spin configuration, i.e. the ground state, is first obtained in this numerical simulation. Then, for each spin separately, a Holstein-Primakoff expansion (cf. [40H] and Eq. 3.3 in Sect. 3.1.2) is carried out and only the lowest order terms are kept for calculating $S(\boldsymbol{Q}, \omega)$ for harmonic spin dynamics. The theoretical results confirm completely the experimental findings and their interpretation given above, namely the coexistence of propagating spin waves and dispersionless cluster modes with a high degree of localization. The similarity of the spectra of the three samples is an indication that they all originate from nearly the same degree of disorder. No excitation spectra of this type have been observed in other spin-glass systems, there are similar spectra only in the quasi-one-dimensional system $CsMn_{0.89}Fe_{0.11}Br_3$ also with competing exchange interactions [86G4]. The experimental results for the 3D Ising spin glass $Fe_{0.4}Mg_{0.6}Cl_2$ look different from those presented above [87W1, 87W2]. For another 3D system $Eu_xSr_{1-x}S$, the search for magnetic excitations by neutron inelastic scattering was not very successful [81M8] although such excitations were predicted theoretically [80K8, 81K15].

Some other mixed magnets with competing exchange interactions and competing anisotropy are $K_2Mn_xCu_{1-x}F_4$, $K_2Co_xCu_{1-x}F_4$ and $(CH_3NH_3)_2Mn_xCu_{1-x}Cl_4$ which were also investigated with various methods. Magnetic resonance experiments were performed in order to obtain information about the magnetic ordering, about the preferred spin direction and the magnetic anisotropies in the mixed crystals [80B12, 83Y1, 83Y5, 88Y2]. Susceptibility measurements and neutron scattering experiments served to establish for both, $K_2Mn_xCu_{1-x}F_4$ [78D3, 86K13] and $K_2Co_xCu_{1-x}F_4$ [90I2, 90I3, 90K3], the (T_C, x) phase diagrams which look very similar to that for $Rb_2Co_xCu_{1-x}F_4$ (cf. Fig. 3.72) and show again concentration ranges with spin-glass behaviour. In $K_2Mn_xCu_{1-x}F_4$, there are also two exchange interactions between Mn^{2+}- and Cu^{2+}-ions as discussed above for $Rb_2Co_xCu_{1-x}F_4$ and $Rb_2Cr_{1-x}Mn_xCl_4$. The average exchange parameter was determined by optical studies [78F3] from an analysis of impurity-induced magnon sidebands and found to be negative (antiferromagnetic). In magnetization measurements on $K_2Mn_xCu_{1-x}F_4$ [89I5], the results show in the range $0 \le x \le 0.18$ (ferromagnetic order!) for low external fields H_0 the same dependence on x as $Rb_2Cr_{1-x}Mn_xCl_4$ (see Fig. 3.68) with an evidence for the antiferromagnetic coupling between the two kinds of magnetic ions. In addition to these results, the experiments on $K_2Mn_xCu_{1-x}F_4$ yield for high magnetic fields ($H_0 > 10$ T) a reorientation of the Mn^{2+}-ions. Under the influence of the field, their spins are reversed and directed parallel to the field. With these complements on systems with competing exchange interactions, we may conclude that the most interesting result is the spin-glass behaviour in the intermediate concentration range of these quasi-two-dimensional mixed systems with the problem that for a 2D random bond Ising spin-glass a proper transition to a spin-glass phase is not possible because of $T_C = 0$.

9.12.3.4 Figures for 9.12.3 and Table 5

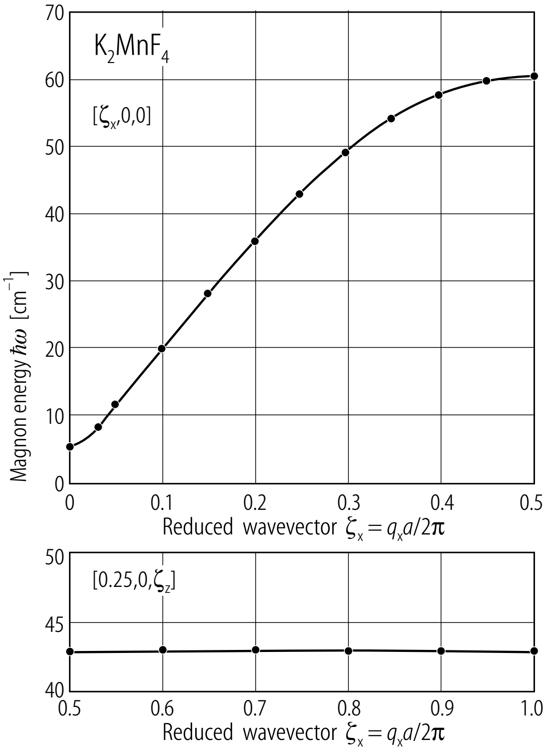

Fig. 3.1. K_2MnF_4. Spin-wave dispersion at 4.5 K, i.e. magnon energy $\hbar\omega$ versus $\boldsymbol{q} \mathrel{\hat{=}} (\zeta_x, 0, 0)$ and $\boldsymbol{q} \mathrel{\hat{=}} (0.25, 0, \zeta_z)$, the latter demonstrating the 2D character of this compound. The solid line represents a best fit with linear spin-wave theory (Eq. 3.6), taken from [73B1].

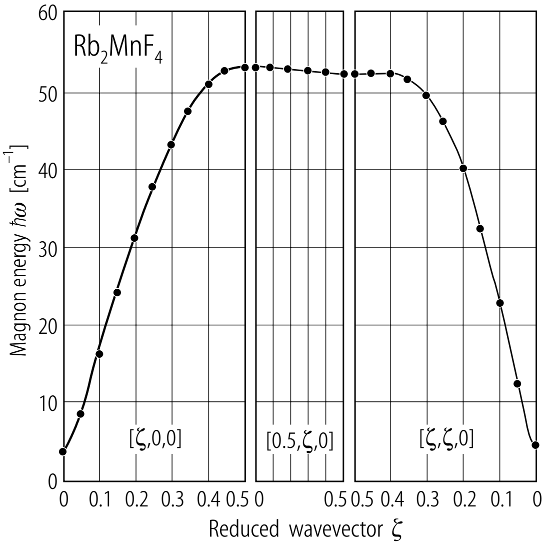

Fig. 3.2. Rb_2MnF_4. Spin-wave dispersion at 4.2 K, i.e. magnon energy $\hbar\omega$ versus $\boldsymbol{q} \mathrel{\hat{=}} (\zeta, 0, 0)$, $\boldsymbol{q} \mathrel{\hat{=}} (0.5, \zeta, 0)$ and $\boldsymbol{q} \mathrel{\hat{=}} (\zeta, \zeta, 0)$. The solid curve results from a fit with linear spin-wave theory (Eq. 3.14), including J_2 for next nearest neighbour exchange interaction (taken from [77C3]).

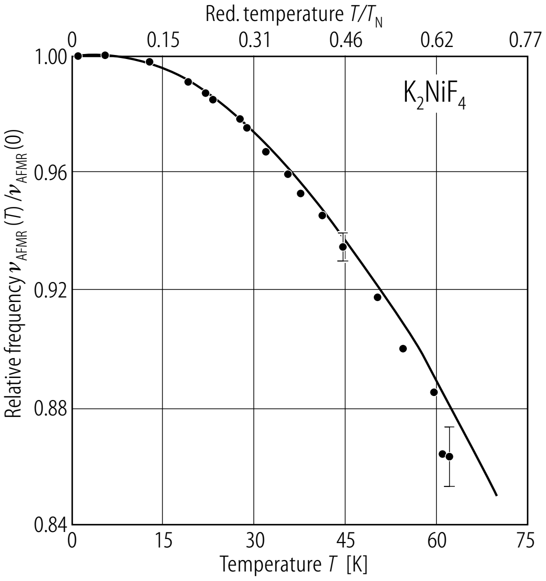

Fig. 3.3. K_2NiF_4. Temperature dependence of the AFMR frequency, presented as relative frequency $\nu_{AFMR}(T)/\nu_{AFMR}(0)$, experimental points and theoretical curve calculated by renormalized spin-wave theory (after [74N1]).

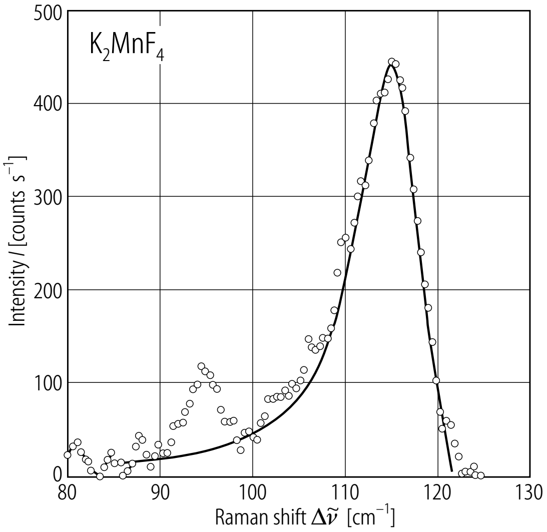

Fig. 3.4. K_2MnF_4. Two-magnon Raman scattering line observed in xx-polarization, experimental points with the background subtracted and solid curve, a theoretical Green function calculation [69P2], scaled from Rb_2MnF_4 to K_2MnF_4 (taken from [73L2, 77L2]). The peak at 93 cm^{-1} is due to residual scattering from a strong Γ_5^+ optical phonon.

For Fig. 3.6. see next page.

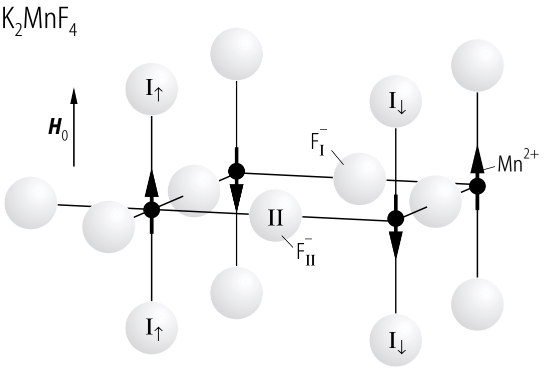

Fig. 3.7. K_2MnF_4. Sites of the Mn^{2+}-ions with magnetic moments according to the antiferromagnetic order, and of the adjacent F_I^- and F_{II}^- -ions. The NMR frequencies of the F_I nuclei reflect the magnetizations of the spin-up and the spin-down sublattices, resp., while the NMR frequency of the F_{II} nuclei scales with of the net magnetization (taken from [77A2]).

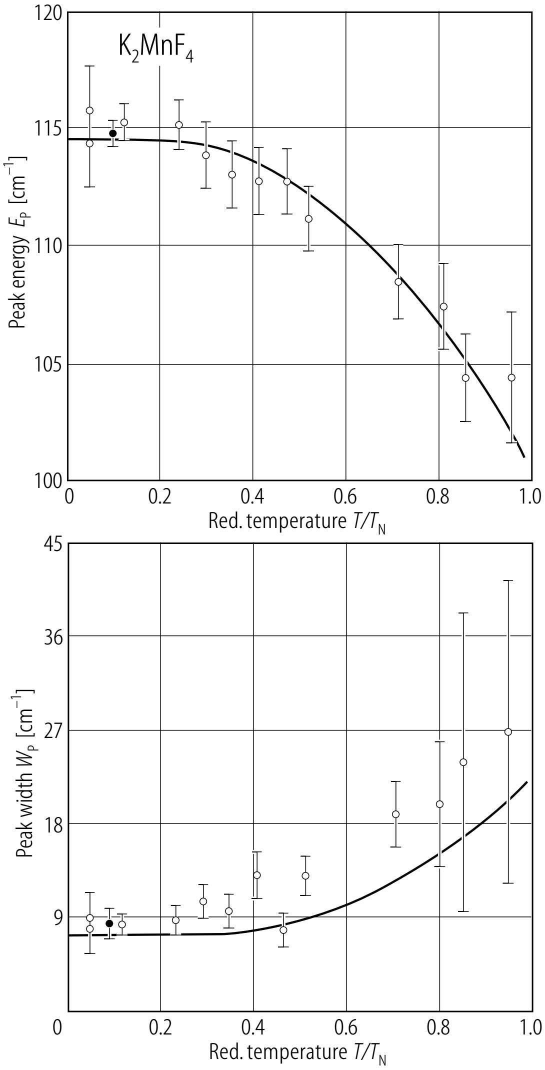

Fig. 3.5. K_2MnF_4. Temperature dependence of the peak energy E_p and the peak width W_p of the two-magnon Raman line; theoretical calculation combining renormalized spin-wave theory with Green function technique (solid lines) and experimental points with error bars (open circles from [76P2] and closed circle from [73L2], taken from [76P2]).

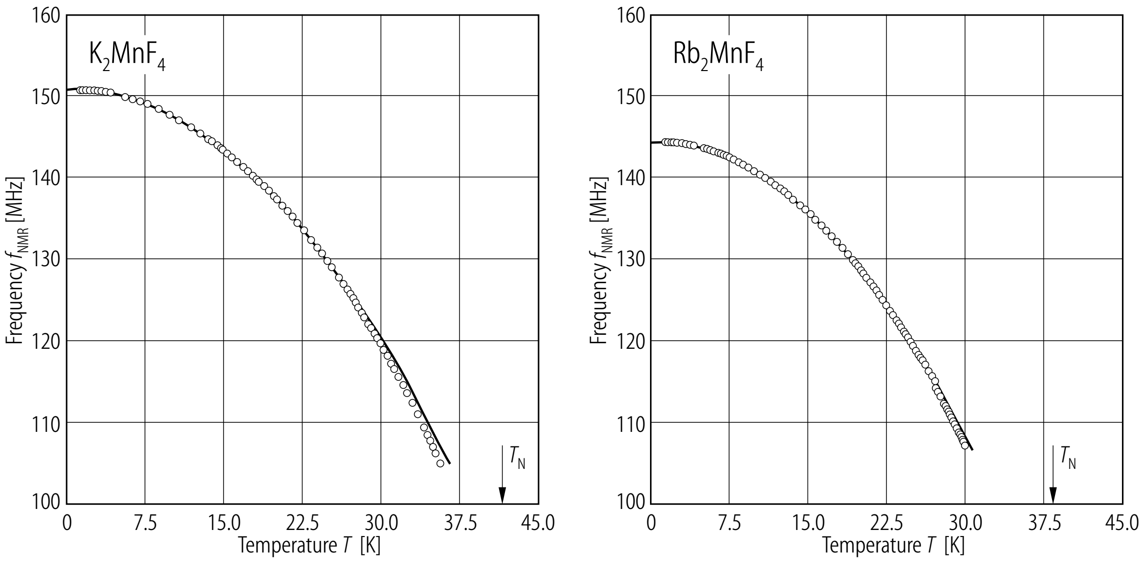

Fig. 3.6. K_2MnF_4, Rb_2MnF_4. Temperature dependence of the NMR frequency f_{NMR} of the out-of-plane $^{19}F_I$ nuclei which is proportional to the sublattice magnetization M_{subl}, experimental points and solid curves representing a fit with renormalized spin-wave theory (cf. Eq. 3.18) up to 18 K and 17 K, respectively. The two Néel temperatures T_N are also indicated (taken from [73W2]).

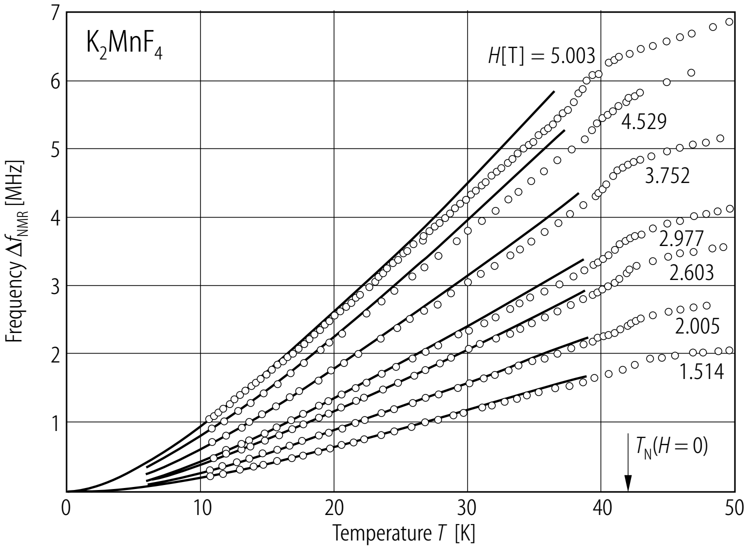

Fig. 3.8. K_2MnF_4. Temperature dependence of the net magnetization for various external magnetic fields H applied parallel to the c-axis, as reflected by the NMR frequency Δf_{NMR} of the in-layer $^{19}F_{II}$ nuclei, corrected for the Zeeman shift. The solid lines have been calculated with renormalized spin-wave theory using Eq. 3.21 (after [77A2]).

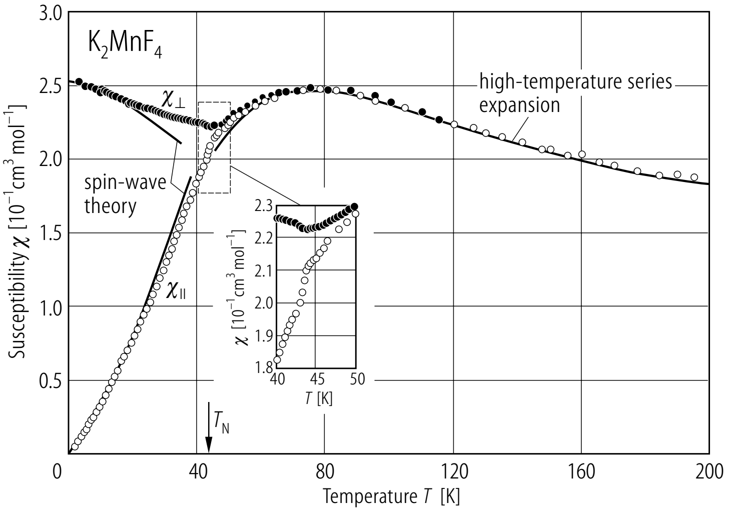

Fig. 3.9. K_2MnF_4. Temperature dependence of the molar magnetic susceptibilities χ above T_N, $\chi_{\parallel}$ (open circles) and $\chi_{\perp}$ (full circles) below T_N for $H_0 \to 0$, obtained as differential χ with an oscillating field (117 Hz). Below 40 K, the solid curves are calculated with renormalized spin-wave theory similar to Eqs. 3.22 and 3.23. Above T_N, the solid curve results from a fit to a high-temperature series expansion (cf. Eqs. 3.26 and 3.27), taken from [82M4].

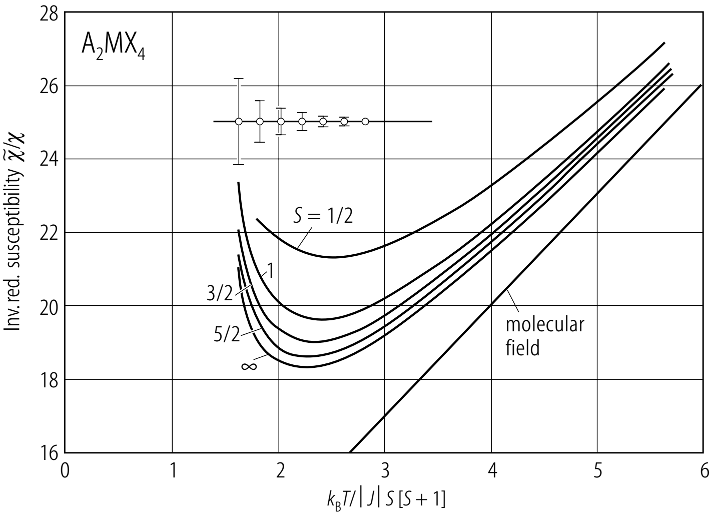

Fig. 3.10. A_2MX_4. Temperature dependence of χ^{-1} for the spin-S quadratic-layer Heisenberg antiferromagnet for various S, presented as $\tilde{\chi}/\chi$ ($\tilde{\chi}$: Eq. 3.28a) versus $k_BT/|J|S(S+1)$, calculated by extrapolating the high-temperature series expansion. Indicated are typical errors resulting from the extrapolation and increasing with decreasing temperature. The results are acceptable except for $S=\frac{1}{2}$ where the extrapolation is less accurate. Also plotted is the molecular field result (Curie-Weiss law Eq. 3.25), after [70L1].

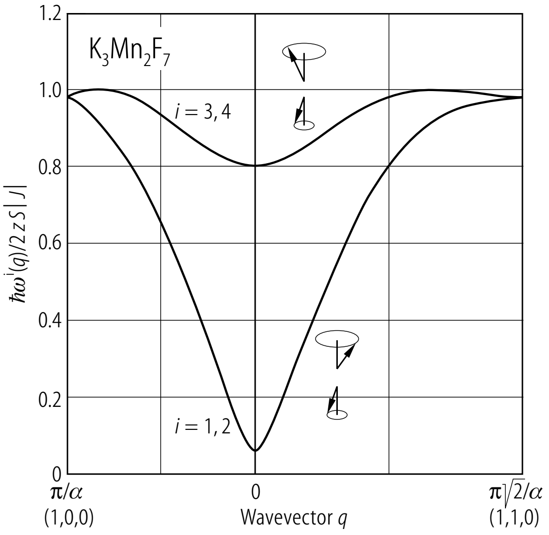

Fig. 3.11. $K_3Mn_2F_7$. Spin-wave dispersion, i.e. reduced magnon energies $\hbar\omega^{i}(q)/2zS|J|$ versus wavevector q for $\boldsymbol{q} \parallel (1,0,0)$ and $\boldsymbol{q} \parallel (1,1,0)$, i.e. the lower branch (i = 1, 2) and the upper branch (i = 3, 4), which correspond to in-phase and out-of-phase precessions of the spins in a pair of layers as indicated schematically. Both branches are doubly degenerate since $H_0 = 0$. The curves are the result of a linear spin-wave calculation using Eq. 3.31 (taken from [77A4]).

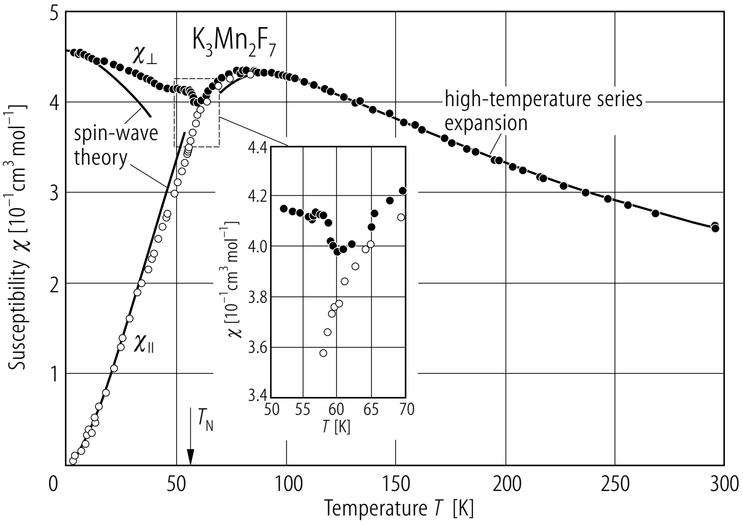

Fig. 3.12. $K_3Mn_2F_7$. Temperature dependence of the molar magnetic susceptibilities χ above T_N, $\chi_\parallel$ (open circles) and $\chi_\perp$ (full circles) below T_N for $H_0 \to 0$, corrected for diamagnetic contributions. Below 40 K, the solid curves are calculated by means of renormalized spin-wave theory [77A4]. Above T_N, the solid curve results from a fit to a high-temperature series expansion (cf. Eqs. 3.26 and 3.27), taken from [77A3].

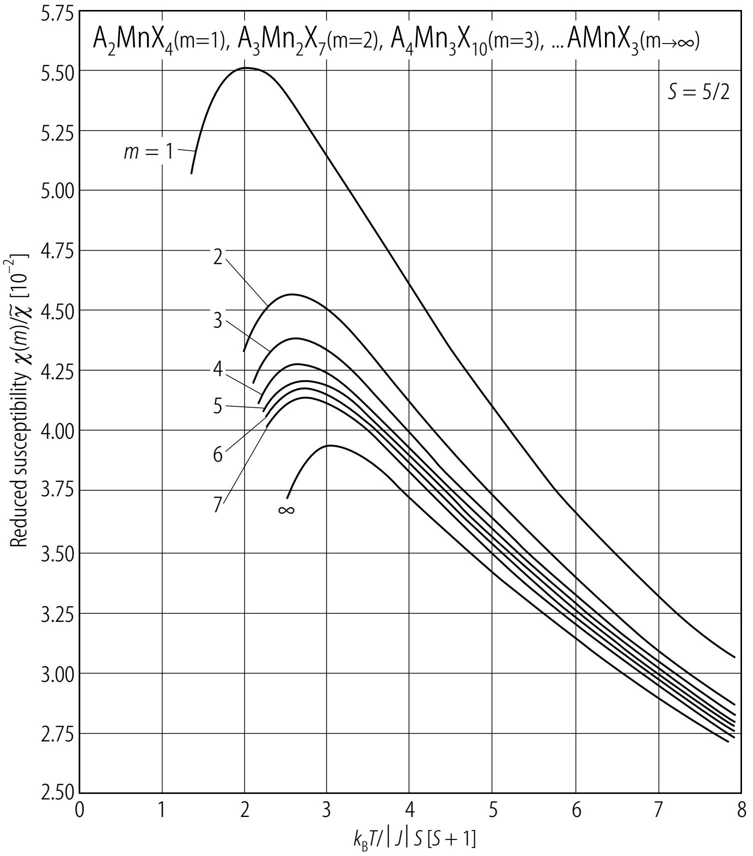

Fig. 3.13. A_2MnX_4 (m = 1), $A_3Mn_2X_7$ (m = 2), $A_4Mn_3X_{10}$ (m = 3), ..., $AMnX_3$ (m → ∞). Predictions for the antiferromagnetic susceptibility $\chi(m)/\tilde{\chi}$ ($\tilde{\chi}$: Eq. 3.28a) vs $k_BT/|J|S(S+1)$ for the $S = \frac{5}{2}$ Heisenberg model from a high-temperature series with the coefficients for a system of m coupled square layers with free boundary conditions (taken from [76N1, 90N]).

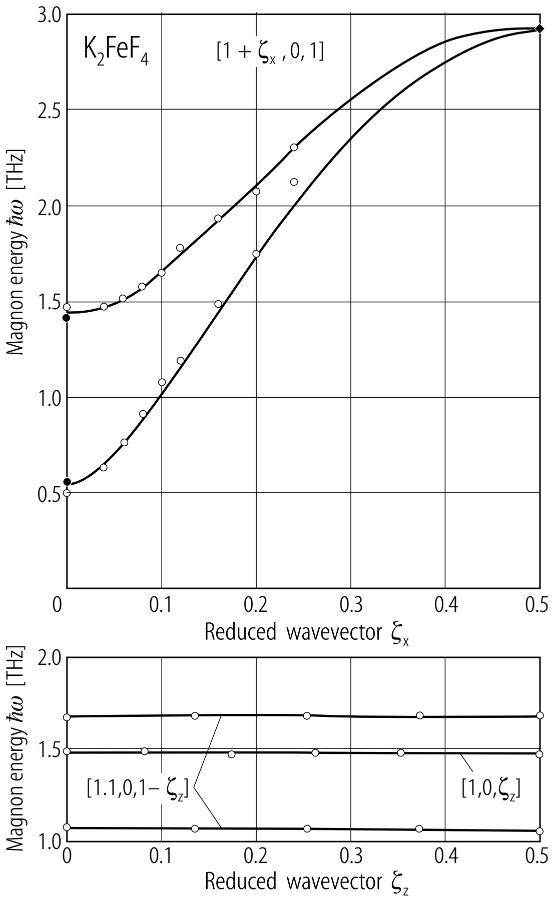

Fig. 3.14. K$_2$FeF$_4$. Spin-wave dispersion (two nondegenerate branches) at $T = 4.2$ K, i.e. magnon energy $\hbar\omega$ vs. $\boldsymbol{q} \hat{=} (1 + \zeta_x, 0, 1)$, $\boldsymbol{q} \hat{=} (1.1, 0, 1 - \zeta_z)$ and $\boldsymbol{q} \hat{=} (1, 0, \zeta_z)$, the latter two demonstrating the 2D character. Experimental points measured with inelastic neutron scattering (open circles), far-infrared absorption (full circles) and Raman scattering (full diamond). The solid curves in the upper part represent a fit to the renormalized spin-wave dispersion relation (taken from [82T1]).

→

Fig. 3.16. Easy-axis antiferromagnet A$_2$MnX$_4$. Schematic illustration of the relation between the AFMR frequency ν_{AFMR} and the (H_0, T) phase diagram for $H_0 = H_{0z} \parallel c$-axis. The (H_0, T) diagram shows for $H_0 < H_{SF}$ the afm. phase (AF), for $H_0 > H_{SF}$ the spin-flop phase (SF) and for higher T the paramagnetic phase (PM). For $H_0 = 0$, $\nu_{AFMR}(T)$ is shown with $\nu_{AFMR} \to 0$ for $T \to T_N$. For $T \approx 0$, $\nu_{AFMR}(H_0)$ exhibits two Zeeman branches, reflects the spin-flop transition at $H_0 = H_{SF}$ and shows again two modes for $H_0 > H_{SF}$.

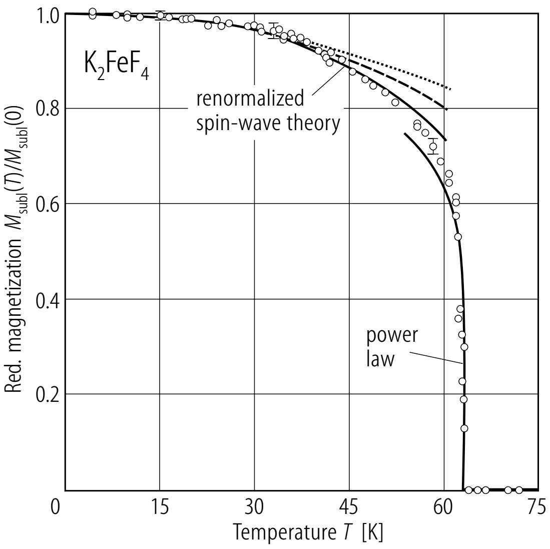

Fig. 3.15. K$_2$FeF$_4$. Reduced sublattice magnetization $M_{subl}(T)/M_{subl}(0)$, the experimental points determined from the intensities of the (1, 0, 0) and (1, 0, 3) superreflections. The curves are the results of spin-wave calculations: renormalized theory with $E(T) \sim V_{xx} - V_{yy}$ (solid curve) and with E = const. (dashed curve); further linear, unrenormalized theory (dotted curve). Near T_N, the experimental data are well described by a power law (taken from [82T1]).

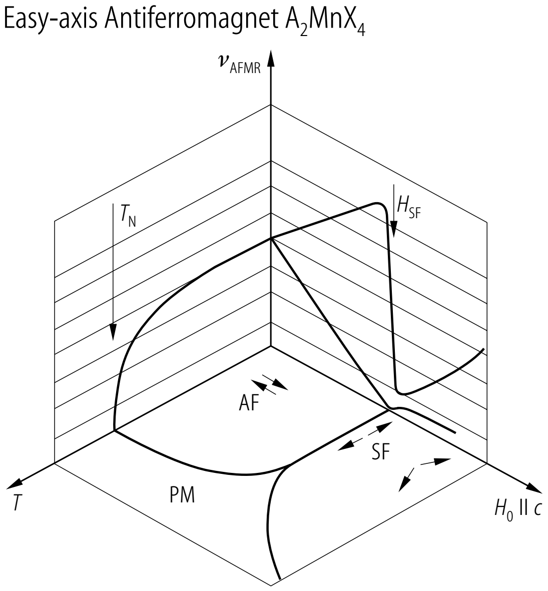

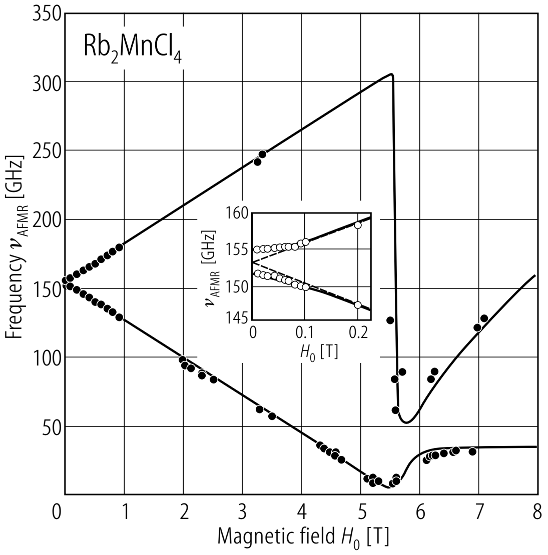

Fig. 3.17. Rb$_2$MnCl$_4$. AFMR frequency ν_{AFMR} at 4.2 K versus magnetic field H_0 applied parallel to the *c*-axis, experimental points and curves calculated by classical spin-wave theory, see Eqs. 3.41–3.51. The insert shows in detail the zero-field splitting of ν_{AFMR} due to an orthorhombic deformation below T_N (after [91G2, 92G1]).

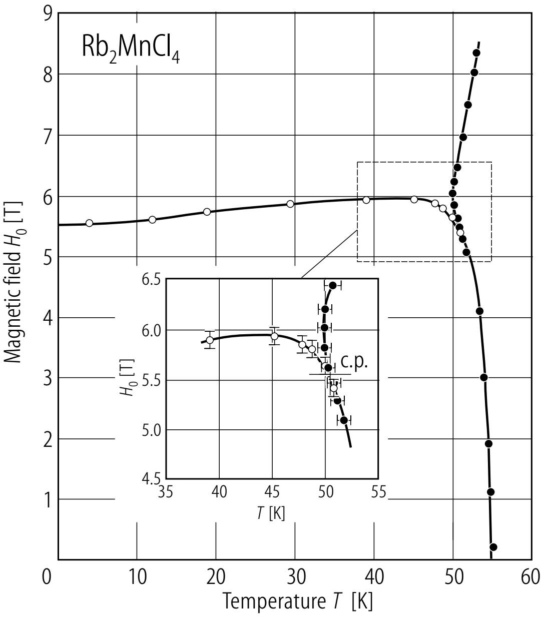

Fig. 3.18. Rb$_2$MnCl$_4$. Magnetic (H_0, T) phase diagram with the boundaries between the antiferromagnetic, the spin-flop and the paramagnetic phases as determined by neutron diffraction. The solid lines are guides to the eye. The insert shows in detail the critical point (c.p.), a bifurcation point. For further details, see text (after [86R2]).

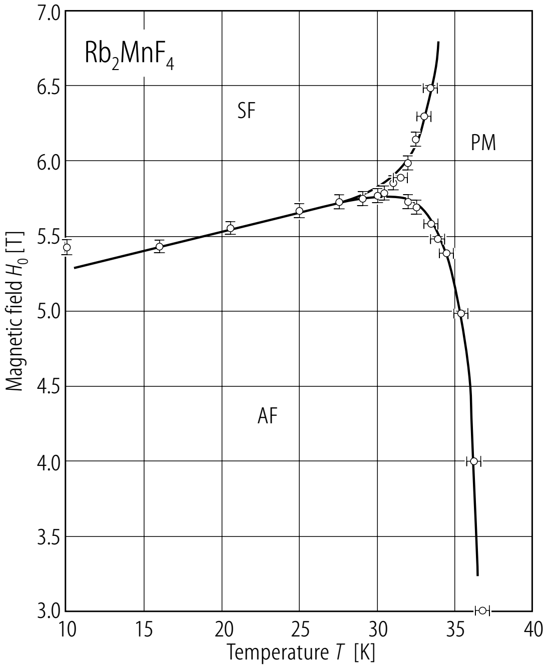

Fig. 3.19. Rb$_2$MnF$_4$. Magnetic (H_0, T) phase diagram with the boundaries between the antiferromagnetic (AF), the spin-flop (SF) and the paramagnetic (PM) phases as determined by neutron diffraction, experimental points and calculated curves. The critical point is a bicritical one. For further explanations, especially with respect to the theoretical curves, see text (after [88C3, 93C2]).

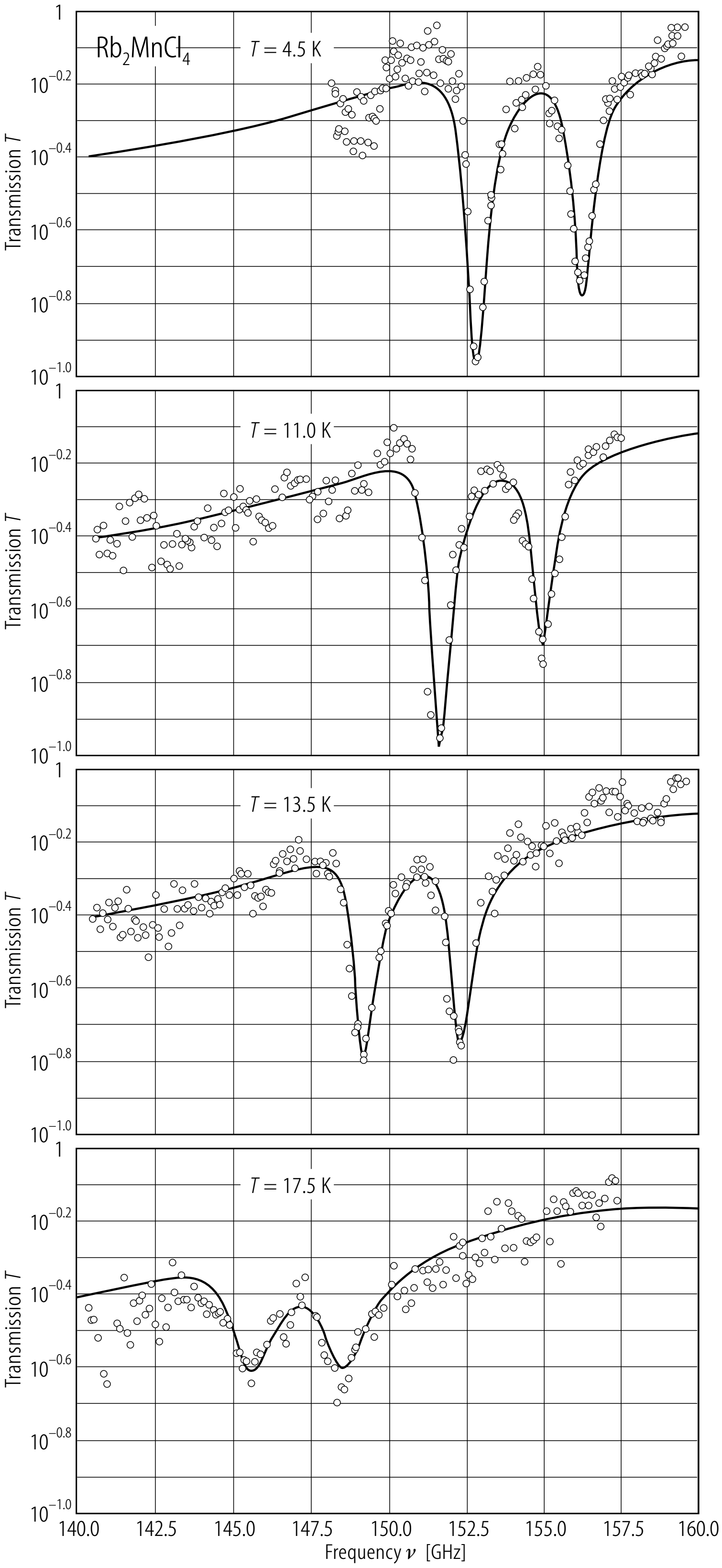

Fig. 3.20. Rb_2MnCl_4. Zero-field splitting of the antiferromagnetic resonance, transmission T versus frequency ν at various temperatures. The experimental points (open circles) have been obtained with a tunable backwave oscillator by sweeping the frequency. The $T(\nu)$-curves are calculated by an oscillator model (Eq. 1 in [92G1]), taken from [92G1].

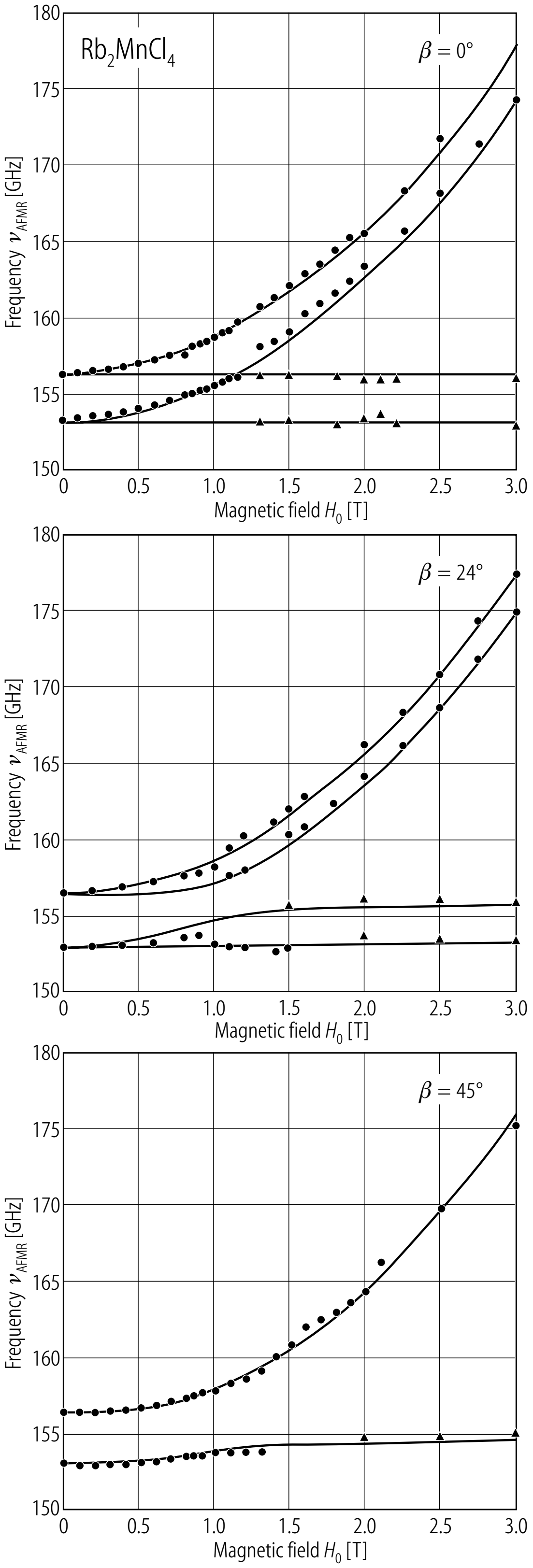

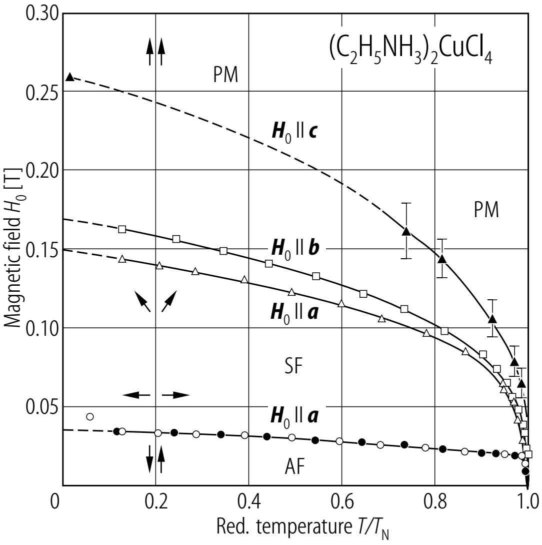

Fig. 3.23. (C$_2$H$_5$NH$_3$)$_2$CuCl$_4$. Magnetic (H_0, T/T_N) phase diagram with the boundaries between the antiferromagnetic (AF), the spin-flop (SF) and the paramagnetic (PM) phases as derived from susceptibility measurements. Experimental data: transition to the SF-phase (open circles, full circles) for $\boldsymbol{H_0} \parallel \boldsymbol{a}$ (easy axis), transition to the PM-phase (open triangles) for $\boldsymbol{H_0} \parallel \boldsymbol{a}$, (open squares) for $\boldsymbol{H_0} \parallel \boldsymbol{b}$ (medium axis) and (full triangles) (σ) for $\boldsymbol{H_0} \parallel \boldsymbol{c}$ (hard axis), after [72J3, 72J4].

For Fig. 3.22 see next page.

←

Fig. 3.21. Rb$_2$MnCl$_4$. AFMR frequency ν_{AFMR} at 4.2 K versus magnetic field H_0 applied perpendicular to the c-axis for $\beta = 0°$, 24° and 45° ($\beta = \angle(\boldsymbol{H_0}, \boldsymbol{a})$ where $\boldsymbol{a} \parallel x$-axis), experimental points observed for $\boldsymbol{h} \perp \boldsymbol{H_0}$ (full circles) and $\boldsymbol{h} \parallel \boldsymbol{H_0}$ (full triangles). The solid curves result from a classical spin-wave calculation based on the method outlined in Eqs. 3.41–3.47 (taken from [91G1, 92G1]).

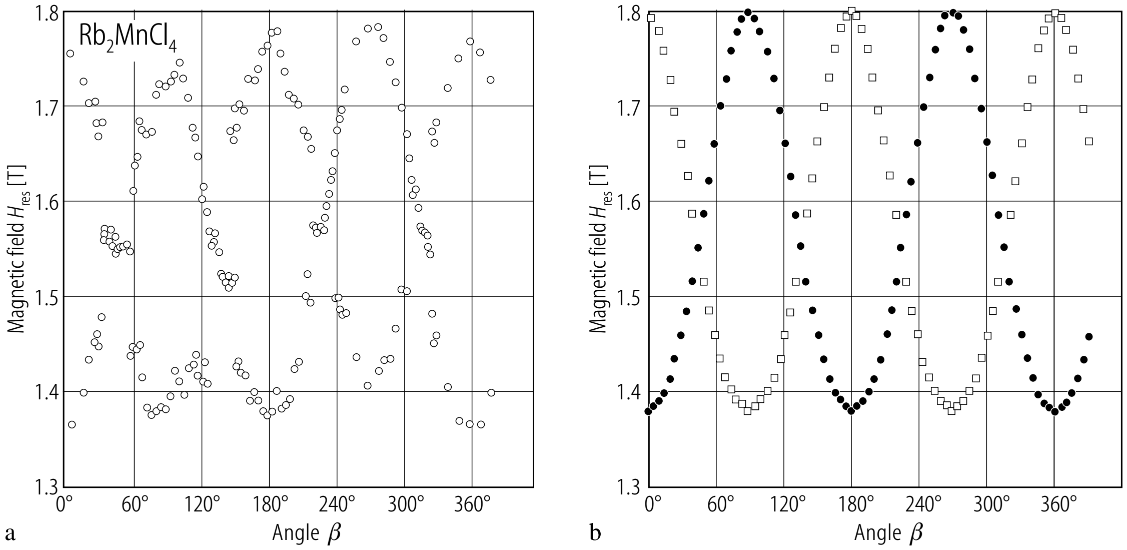

Fig. 3.22. Rb_2MnCl_4. AFMR (ν = 161 GHz), magnetic field at resonance H_{res} in the configuration $\boldsymbol{H_0} \perp \boldsymbol{c}$ as a function of the angle β between H_0 and the a-axis (x-axis), **(a)** experimental data (open circles) and **(b)** results of classical spin-wave calculation based on Eqs. 3.41–3.47 for domain 1 (full circles) and domain 2 (open squares), taken from [92G1].

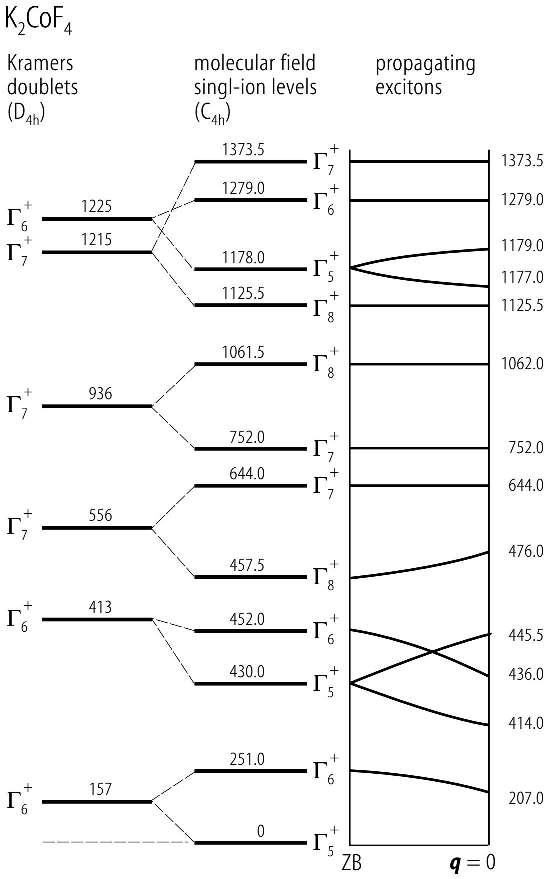

Fig. 3.24. K_2CoF_4. Splitting of the $^4\Gamma_4^+$ (O_h) ground state into 6 Kramers doublets (symmetry D_{4h}) by the crystal field and spin-orbit coupling, into 12 molecular-field single-ion levels (symmetry C_{4h}) which become $\boldsymbol{q}$-dependent excitons (ZB = zone boundary of the Brillouin zone). The level energies in cm^{-1} have been determined by Raman spectroscopy, after [79G5].

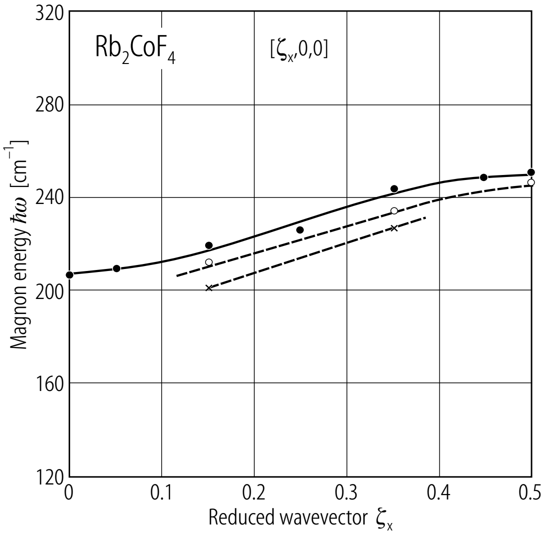

Fig. 3.25. Rb_2CoF_4. Spin-wave dispersion, i.e. magnon energy $\hbar\omega$ versus $\boldsymbol{q} \triangleq (\zeta_x, 0, 0)$ at $T = 6$K (full circles), at $T = T_N - 1.24$ K (open circles) and at $T = T_N - 0.56$ K (crosses). The solid line respresents the best fit of Eq. 3.63 to the data at 6 K. The broken lines are guide to the eye (taken from [78I2]).

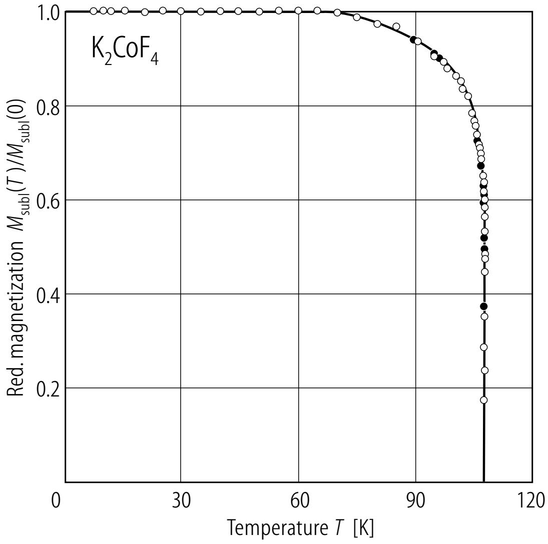

Fig. 3.26. K_2CoF_4. Reduced sublattice magnetization $M_{subl}(T)/M_{subl}(0)$, the experimental points determined from the intensities of the superreflections (1, 0, 0) (open circles) and (3, 0, 0) (full circles). The curve represents the exact result for the 2D Ising model (Eq. 3.66), taken from [74I2].

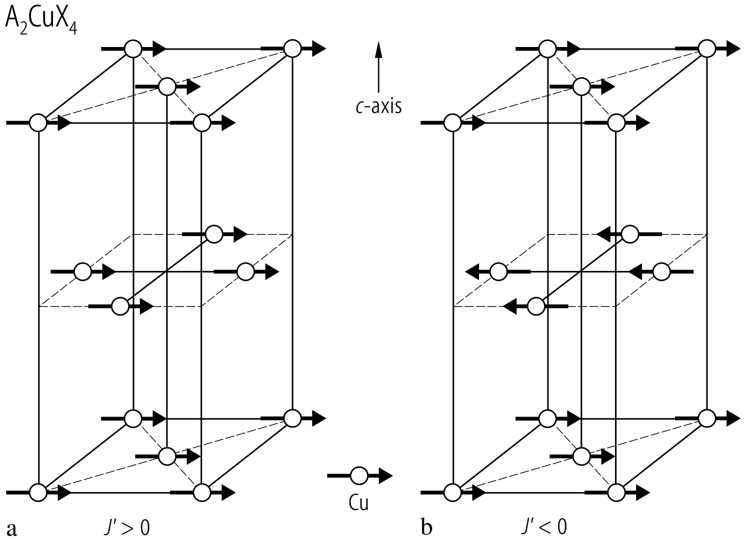

Fig. 3.27. A_2CuX_4. Ferromagnetic ordering within the layers ($J > 0$) and **(a)** ferromagnetic ordering of the layers ($J' > 0$) and **(b)** antiferromagnetic ordering of the layers ($J' < 0$) where J and J' are the intralayer and the interlayer exchange constants, respectively.

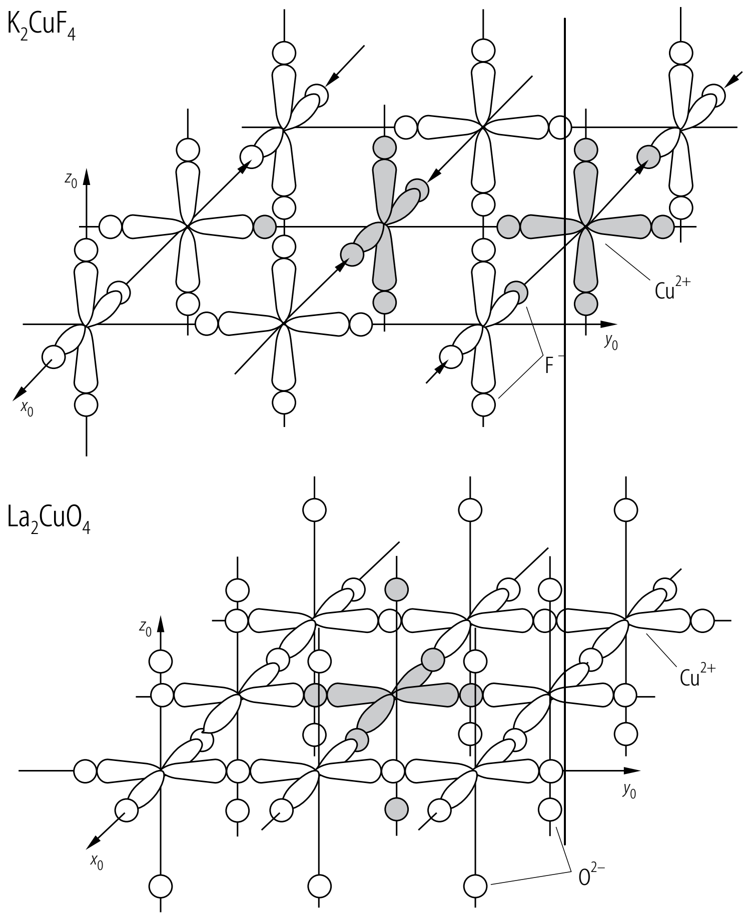

Fig. 3.28. K_2CuF_4 and La_2CuO_4. Orbital ordering different in these two compounds, antiferrodistortive in K_2CuF_4 and ferrodistortive in La_2CuO_4 which leads to ferromagnetic order in K_2CuF_4 and antiferromagnetic order in La_2CuO_4. The basic (x_0, y_0, z_0) coordinate system is indicated (taken from [96I1]).

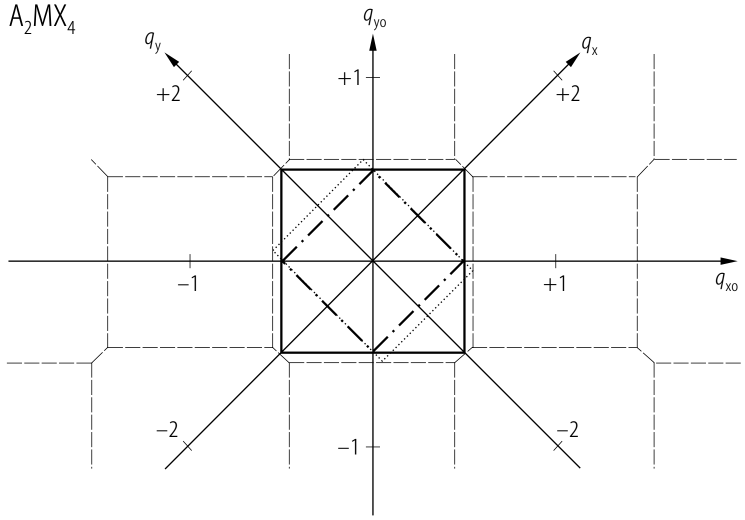

Fig. 3.29. A_2MX_4. 2D-approximation, i.e. a square lattice: ferromagnetic Brillouin zone [(q_{x0}, q_{y0})-system, heavy solid line] and antiferromagnetic Brillouin zone [(q_x, q_y)-system, heavy dash-dot line]. The sections through the (q_x, q_y)-plane of the Brillouin zones of the 3D lattices are not quite equal to the 2D approximations, fm. (I4/mmm, dashed lines) and afm. (Acam, dotted line).

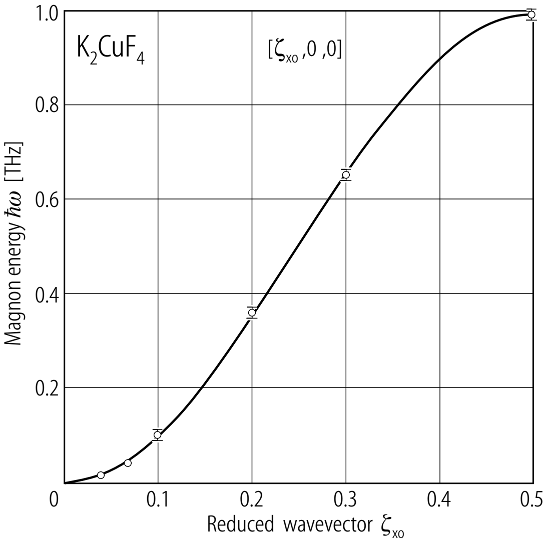

Fig. 3.30. K_2CuF_4. Spin-wave dispersion at $T = 1.1$ K, i.e. magnon energy $\hbar\omega$ versus $\boldsymbol{q} \mathrel{\hat{=}} (\zeta_{x0}, 0, 0)$ for the full range $0 \leq \zeta_{x0} \leq 0.5$ (high-q mode). The solid line represents a best fit to Eq. 3.72, the dispersion relation of a 2D Heisenberg model (taken from [83H4]).

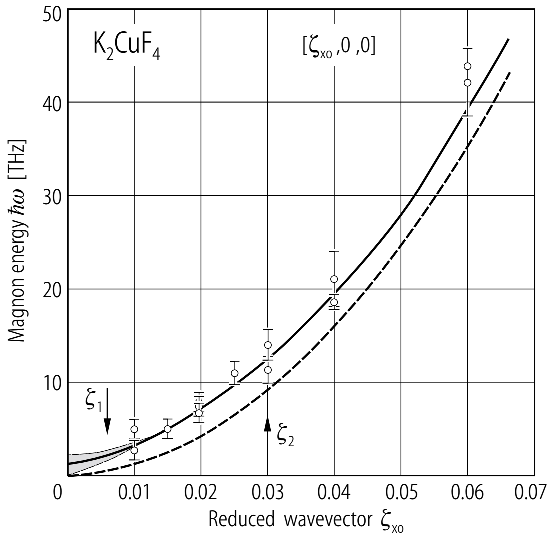

Fig. 3.31. K_2CuF_4. Spin-wave dispersion at $T = 1.1$ K, i.e. magnon energy $\hbar\omega$ versus $\boldsymbol{q} \mathrel{\hat{=}} (\zeta_{x0}, 0, 0)$ for the range $0 \leq \zeta_{x0} \leq 0.06$ (low-q mode). The solid curve results from a fit to Eqs. 3.71 and 3.73. The dashed line is obtained for $h_A = 0$, ζ_1 and ζ_2 mark the boundaries of the 2D XY-regime as explained in the text. The shaded area indicates the influence of q_{z0} in the 3D XY-regime (taken from [83H4]).

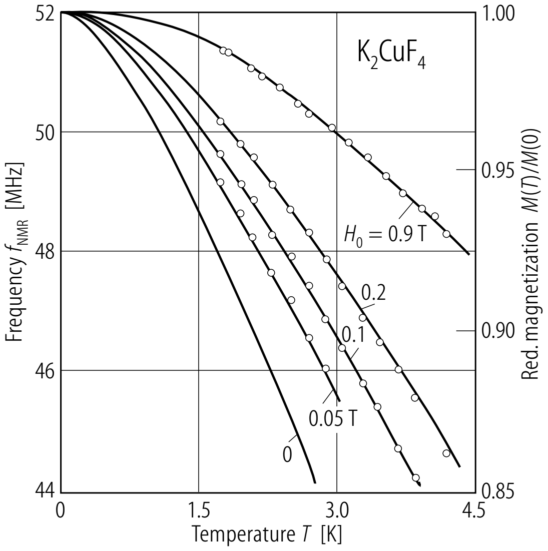

Fig. 3.32. K_2CuF_4. Reduced magnetization $M(H_0, T) / M(0)$ for $\boldsymbol{H_0} \perp \boldsymbol{c}$ as reflected by the NMR frequency f_{NMR} of the $^{19}F_I$ nuclei for various values of H_0 (experimental points). Also shown is f_{NMR} of the ^{63}Cu nuclei for $H_0 = 0$ scaled to f_{NMR} of $^{19}F_I$. The solid curves for $H_0 \neq 0$ are calculated with renormalized spin-wave theory as described in [74K4] (taken from [74K4]).

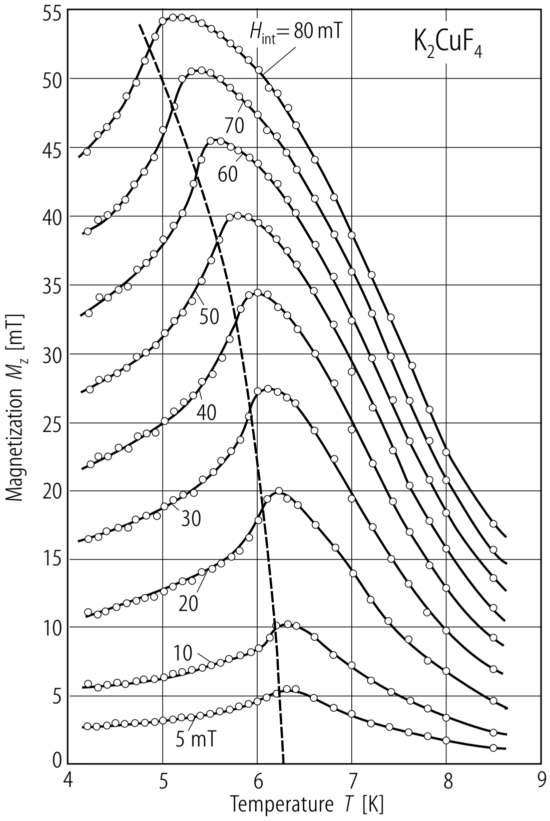

Fig. 3.33. K$_2$CuF$_4$. Magnetization $M_z(T)$ induced by a magnetic field applied parallel to the c-axis, experimental points for various values of H_{int}, i.e. H_0 corrected for demagnetization effects (cf. Eq. 3.92). The broken line is a critical line marking $T_C(H_{int})$ as derived from $\partial M/\partial T$ = max. The solid lines are guides to the eye (taken from [81H2]).

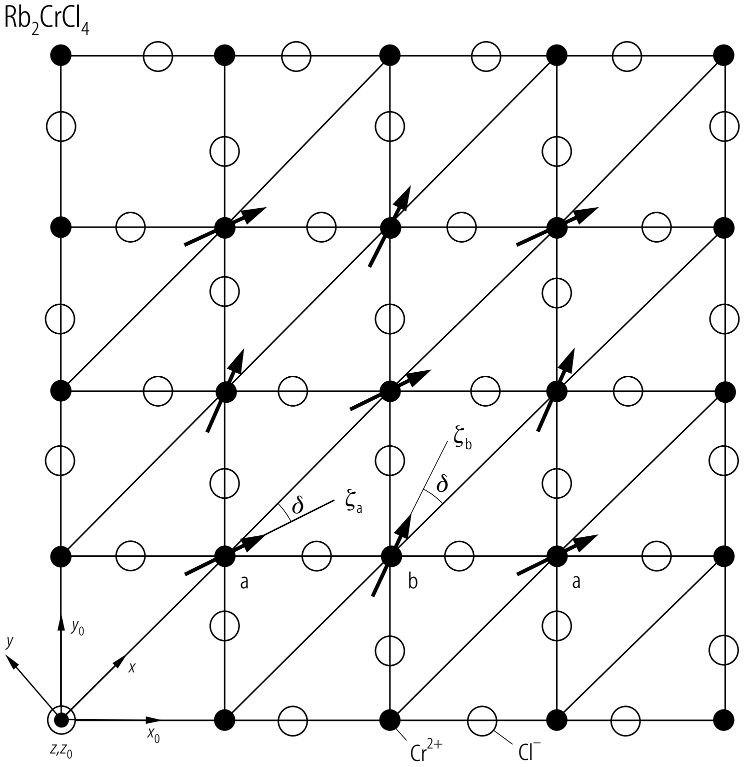

Fig. 3.34. Rb$_2$CrCl$_4$. Magnetic and crystal structure in the (0, 0, 1)-plane. The displacements of the Cl$^-$-ions due to the collective Jahn-Teller effect give rise to alternating uniaxial crystal fields on the Cr^{2+}-ions, resulting in a canted spin structure with two sublattices denoted a and b. The canting angle δ is exaggerated in the figure ($\delta \approx 0°$). Indicated are also the (x_0, y_0, z_0) and (x, y, z) coordinate systems (after [81H4, 86D3]).

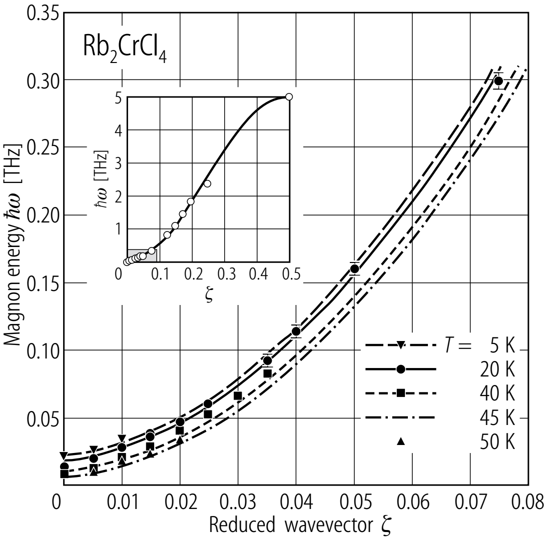

Fig. 3.35. Rb_2CrCl_4. Spin-wave dispersion at several temperatures, i.e. magnon energy $\hbar\omega$ versus $\boldsymbol{q} \hat{=} (\zeta, \zeta, 2.9)$ for $0 \le \zeta \le 0.08$ and in the insert for $0 \le \zeta \le 0.5$, experimental points and calculated curves giving a best fit with renormalized spin-wave theory to Hamiltonian $\mathcal{H}(1)$ [Eq. 3.81] (taken from [81H4]).

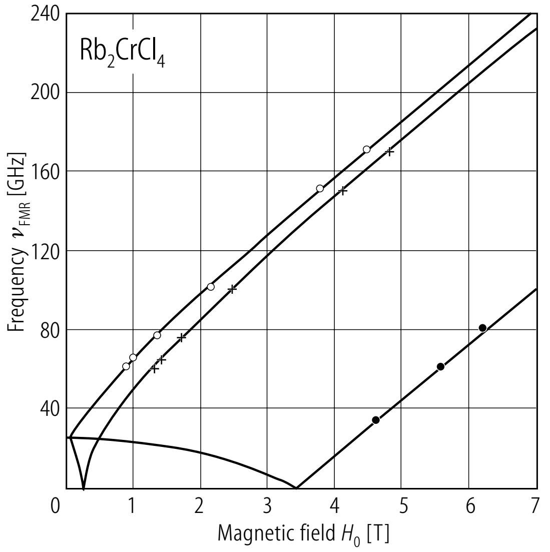

Fig. 3.36. Rb_2CrCl_4. FMR frequency ν_{FMR} at 4.2 K versus magnetic field H_0 applied perpendicular to the c-axis [$\psi = 90°$, $\beta = 0°$ (open circles) and $\beta = 45°$ (plusses)] and parallel to the c-axis [$\psi = 0°$ (full circles)]. The curves are calculated by classical spin-wave theory starting from Eq. 3.104 (see text), after [84G3, 91G2].

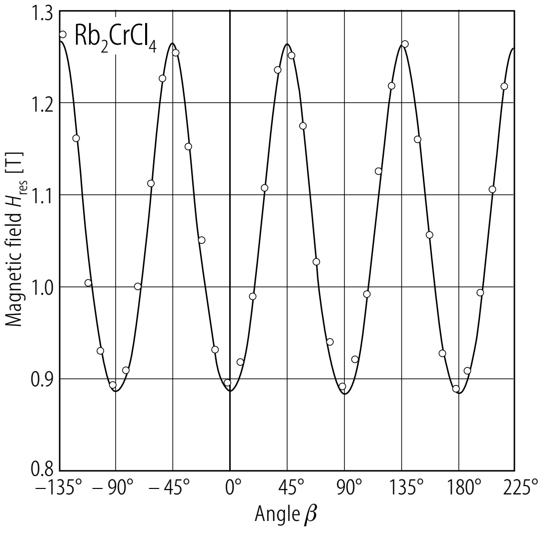

Fig. 3.37. Rb_2CrCl_4. Angular dependence of the FMR at 61.1 GHz in the basal plane, magnetic field H_{res} at resonance versus $\beta = \angle(\boldsymbol{H_0}, \boldsymbol{a})$ where $\boldsymbol{a} \parallel x$-axis, experimental points and curves calculated by classical spin-wave theory starting from Eq. 3.104. The β-dependence of H_{res} clearly reflects the fourfold crystal symmetry (after [82L1].

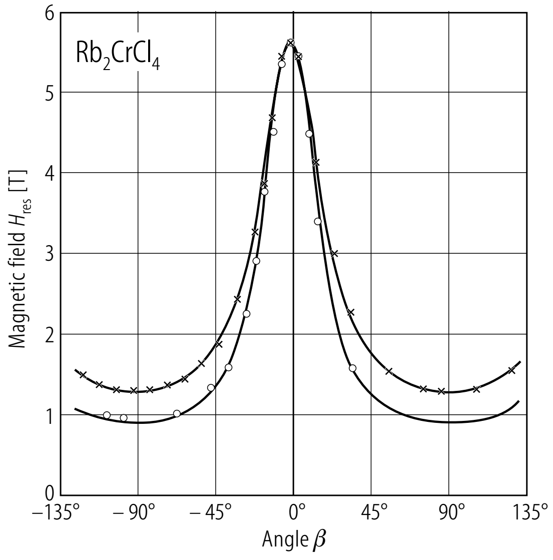

Fig. 3.38. Rb_2CrCl_4. FMR at 61.1 GHz, dependence of the magnetic field H_{res} at resonance on the polar angle ψ when the external field H_0 is applied at various angles ψ from $\psi = 0°$ (c-axis) to $\psi = 90°$ (basal plane), experimental points for $\beta = 0°$ (open circles) and for $\beta = 45°$ (crosses) and curves calculated by classical spin-wave theory starting from Eq. 3.104 (taken from [82L1]).

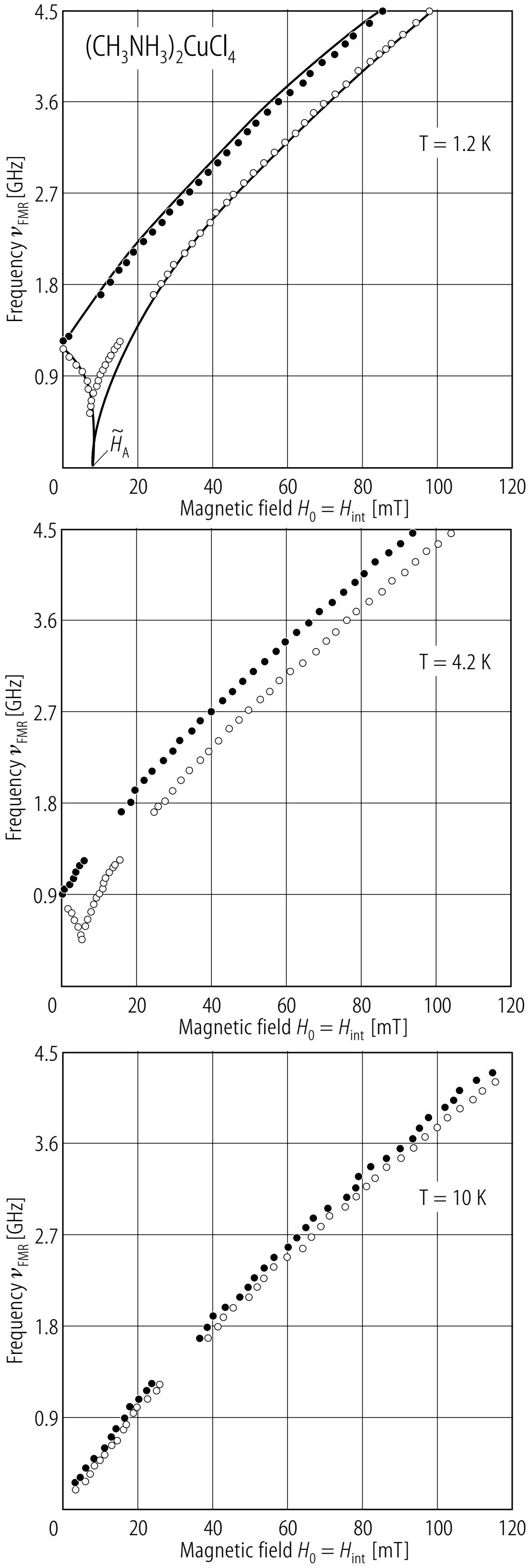

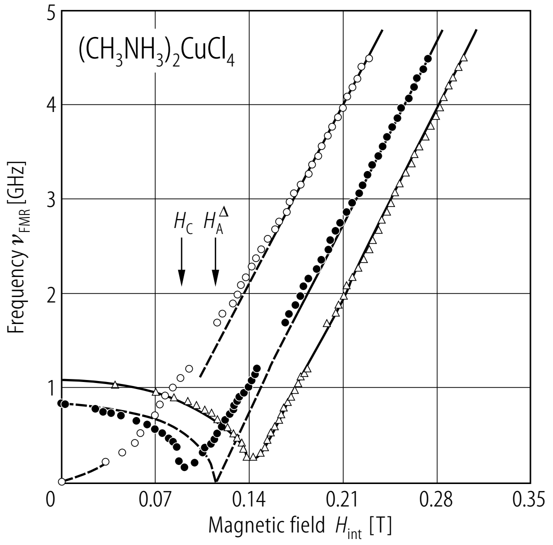

Fig. 3.40. (CH$_3$NH$_3$)$_2$CuCl$_4$. FMR frequency ν_{FMR} versus internal field H_{int}, applied parallel to the *c*-axis (hard axis), at $T = 1.2$ K (open triangles), at $T = 4.2$ K (full circles) and at $T = 9$ K (open circles). The solid curves (1.2 K) were calculated using Eqs. 3.108 and 3.109 or 3.109a. For $T < T_C$, the data reflect the spin reorientation transition. H_A^Δ and H_C are the modified anisotropy field and the phase transition field, resp. (after [89D2, 90D3]).

←

Fig. 3.39. (CH$_3$NH$_3$)$_2$CuCl$_4$. FMR frequency ν_{FMR} versus magnetic field H_0 for $\boldsymbol{H_0} \parallel \boldsymbol{a}$ (full circles) and $\boldsymbol{H_0} \parallel \boldsymbol{b}$ (open circles), i.e. parallel to the easy and medium axis, resp., at $T = 1.2$ K, $T = 4.2$ K and $T = 10$ K as indicated. The solid curves (1.2 K) were calculated using Eqs. 3.105, 3.106. For $\boldsymbol{H_0} \parallel \boldsymbol{b}$ and $T < T_N$, experimental and calculated data reflect the spin reorientation transition (after [89D2]).

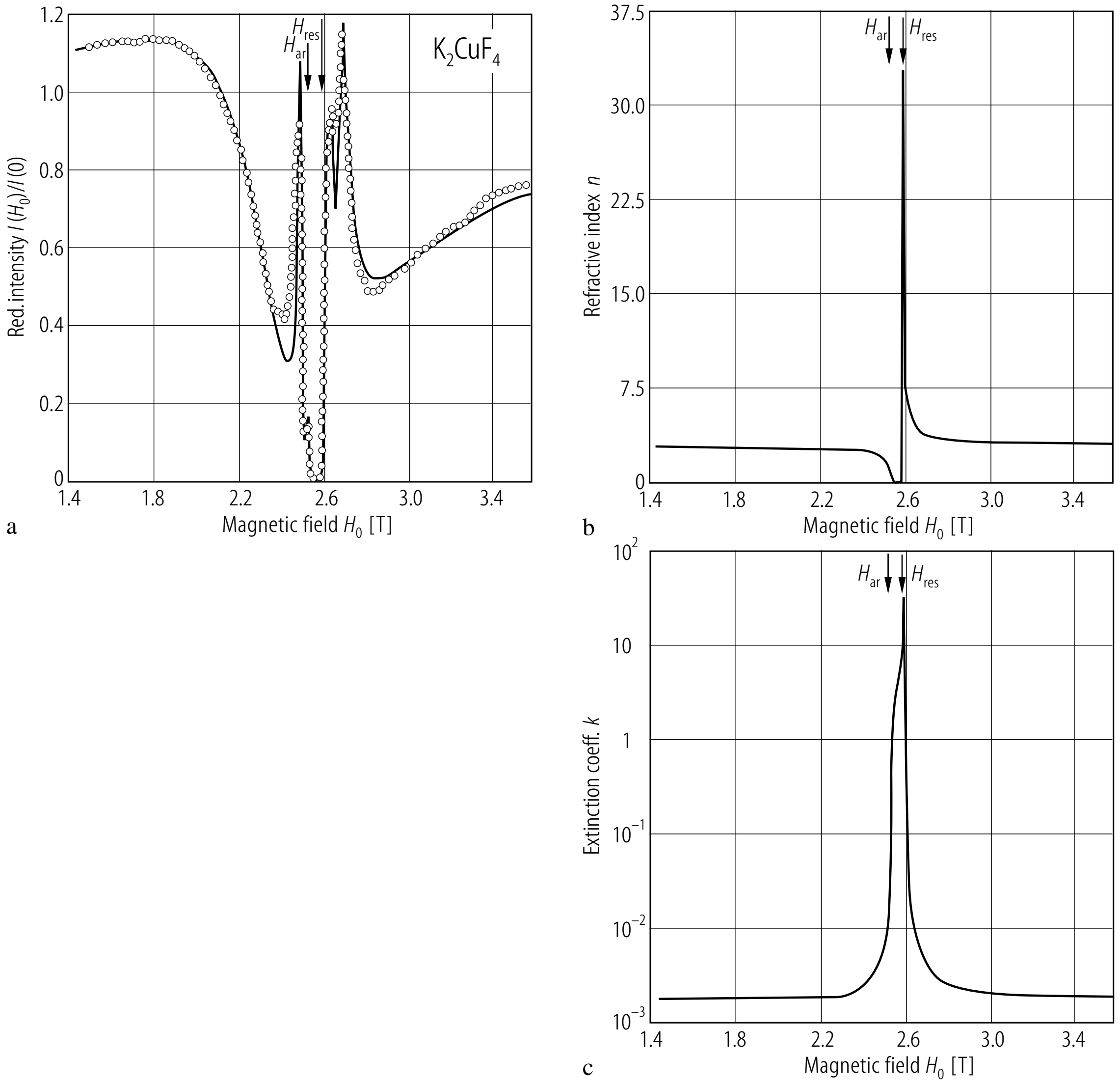

Fig. 3.41. K$_2$CuF$_4$. **(a)** Reduced transmitted intensity $I(H_0)/I(0)$ through a $d = 1.835$ mm thick sample for $\boldsymbol{H_0} \perp \boldsymbol{c}$ and $\nu = 87.95$ GHz at $T = 4.2$ K, experimental points and curve calculated as explained in the text; **(b)**, **(c)**: calculated optical constants n and k. The polariton gap with $I(H_0) \approx 0$ is bounded by the fields H_{ar} and H_{res} (see text and Eqs. 3.113, 3.114), taken from [84K2].

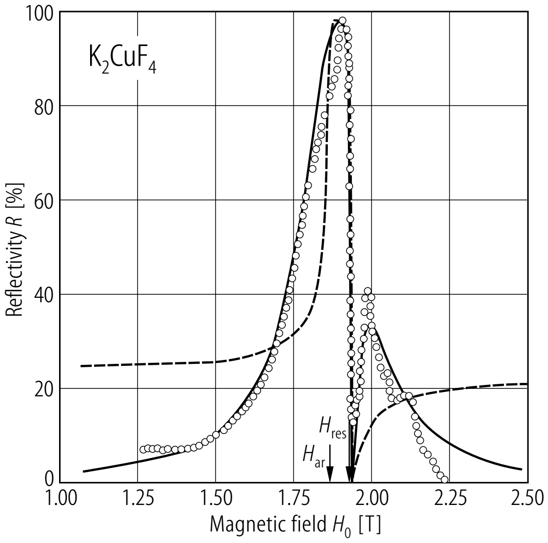

Fig. 3.42. K$_2$CuF$_4$. Reflectivity $R(H_0)$ of a $d = 0.77$ mm thick sample for $\boldsymbol{H_0} \perp \boldsymbol{c}$ and $\nu = 66.82$ GHz at $T = 4.2$ K, experimental points and curve calculated as explained in the text. The high reflectivity near $H_0 = 1.9$ T represents a reststrahlenband. The broken curve, calculated for $d \to \infty$, is an "ideal" reststrahlenband between the fields H_{ar} and H_{res} (see text and Eqs. 3.113, 3.114), taken from [84K2].

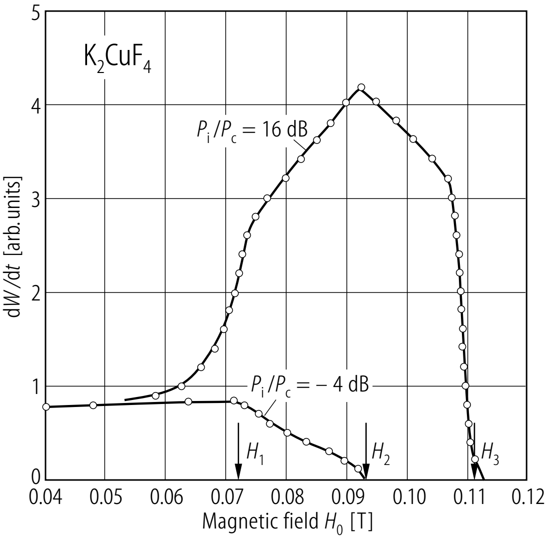

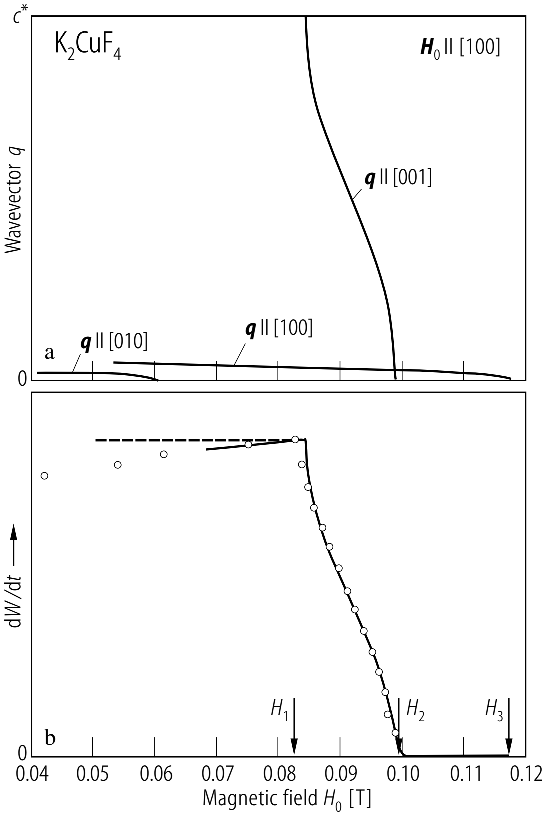

Fig. 3.44. K$_2$CuF$_4$. Parallel pumping: **(a)** spin-wave dispersion, i.e. wavevector q versus magnetic field H_0 for $\boldsymbol{H_0} \parallel (1,0,0)$ at fixed frequency $\omega_p/2\pi = 8.949$ GHz; and **(b)** subthreshold absorption at 4.2 K, i.e. absorbed microwave power dW/dt versus H_0, experiment (open circles), theory (cf. Eq. 3.112) (full line) and magnon density of states (broken line). H_1, H_2, H_3 are explained in the text (after [76Y2]).

←
Fig. 3.43. K$_2$CuF$_4$. Parallel pumping: absorbed microwave power dW/dt ($\omega_p/2\pi = 8.912$ GHz) versus applied magnetic field H_0 for $\boldsymbol{H_0} \parallel (1,0,0)$ at $T = 1.31$ K, below and above threshold. P_i and P_c are the incident and the threshold power at H_2, respectively. H_1, H_2, H_3 are explained in the text (taken from [74Y1]).

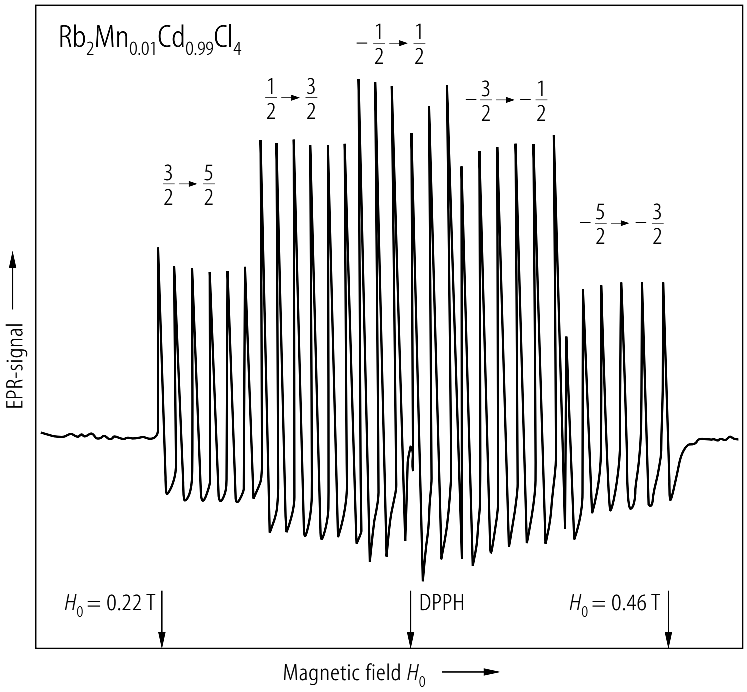

Fig. 3.45. $Rb_2Mn_{0.01}Cd_{0.99}Cl_4$. Electron paramagnetic resonance (EPR) spectrum of isolated Mn^{2+}-ions for $\boldsymbol{H_0} \parallel \boldsymbol{c}$ showing five groups of lines due to the anisotropy (fine structure) with the transitions $S_z \rightarrow S_z + 1$, each split into six lines by hyperfine interaction (taken from [82P1]).

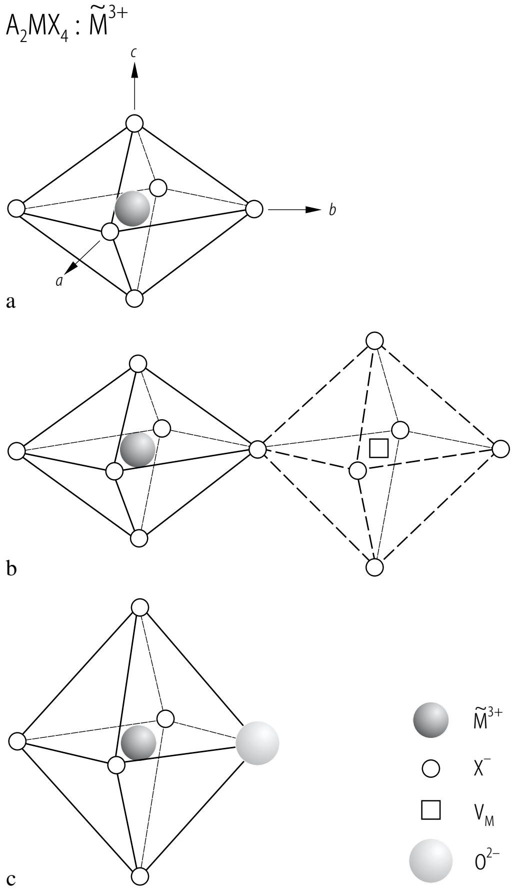

Fig. 3.46. A_2MX_4 doped with a small amount of $\tilde{M}^{3+}$. Schematic model of the octahedron around the impurity for **(a)** centre I, **(b)** centre III and **(c)** centre V. Centre I without, centres III and V with charge compensation. For further details, see text (after [96A]).

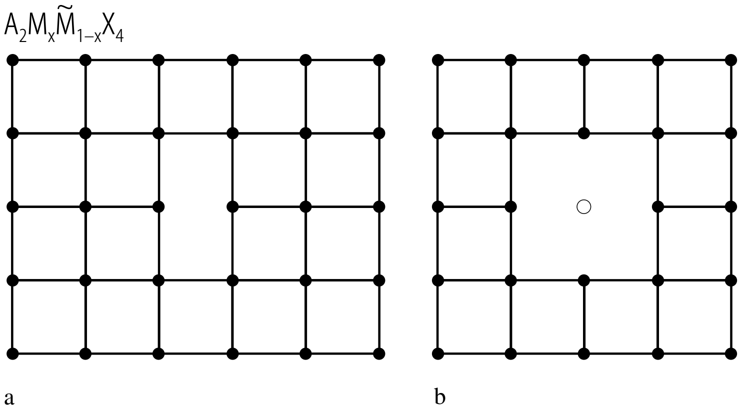

Fig. 3.47. $A_2M_x\tilde{M}_{1-x}X_4$. Demonstration of bond- and site-dilution on a square lattice, **(a)** one bond (exchange interaction) removed and **(b)** one site removed, i.e. one paramagnetic M^{2+}-ion replaced by a diamagnetic $\tilde{M}^{2+}$-ion. From the lattice, only the M^{2+}-sites are shown (taken from [83S10]).

For Fig. 3.48 see next page.

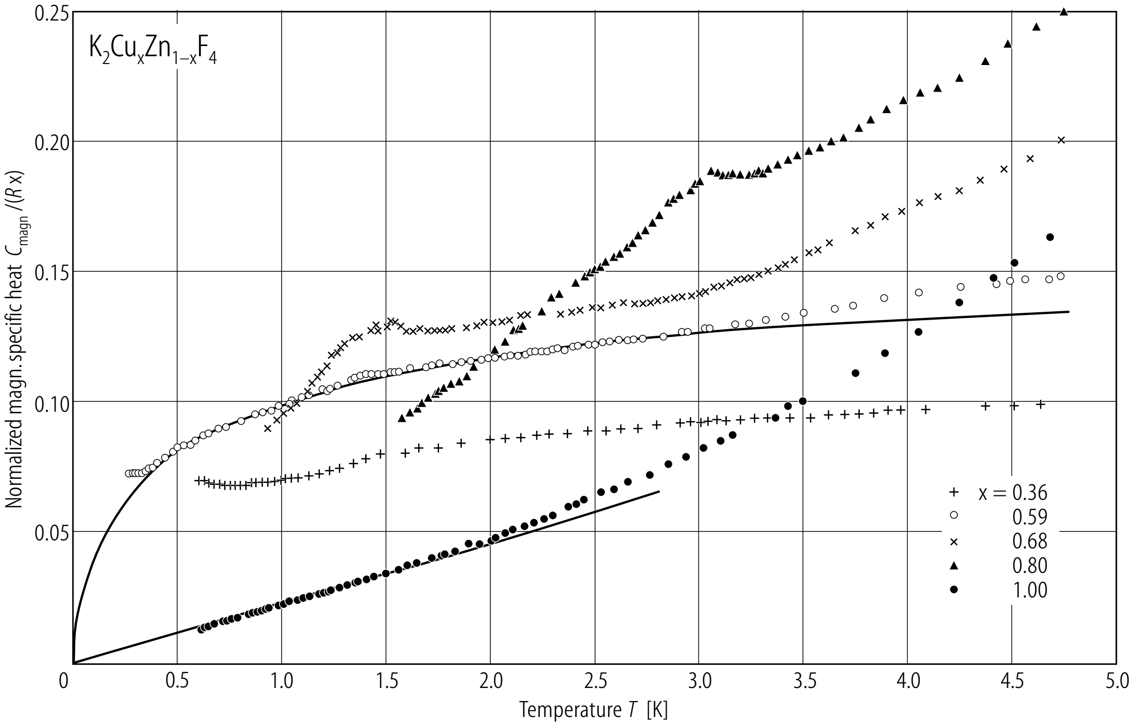

Fig. 3.49. $K_2Cu_xZn_{1-x}F_4$. Magnetic contribution C_{magn}/R to the specific heat normalized to the concentration x as a function of temperature T. The solid lines are theoretical curves for $x = x_p$ and $x = 1$ which are explained in the text (after [81T2]).

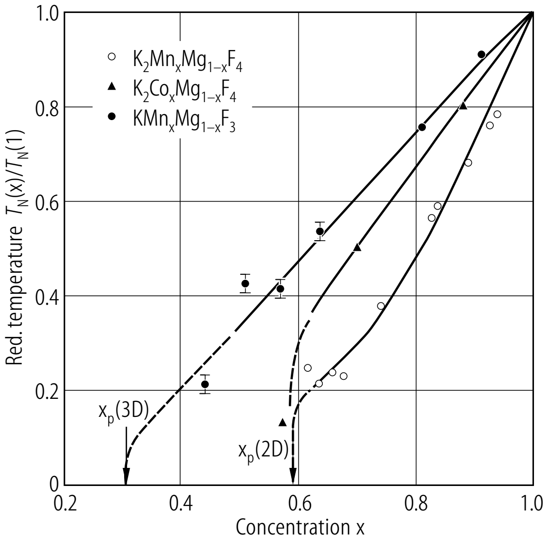

Fig. 3.48. $K_2Mn_xMg_{1-x}F_4$, $K_2Co_xMg_{1-x}F_4$, $KMn_xMg_{1-x}F_3$. Reduced Néel temperatures $T_N(x)/T_N(1)$ versus concentration x. The theoretical values of the critical percolation concentrations for the square and the simple cubic lattices are marked by $x_p(2D)$ and $x_p(3D)$, respectively. The lines are guide to the eye. For further details, see text (taken from [70B5]).

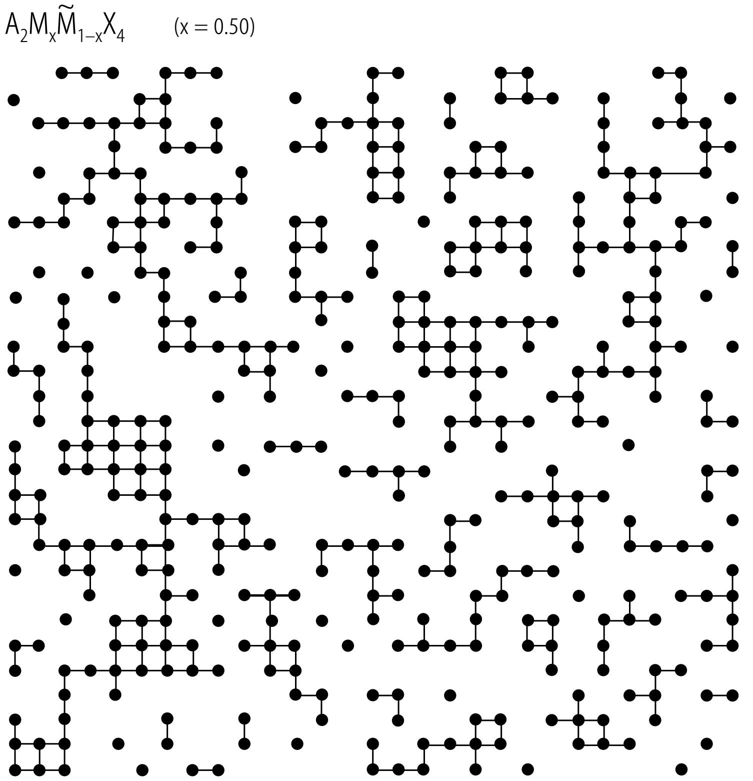

Fig. 3.50. $A_2M_x\tilde{M}_{1-x}X_4$. Diluted system with paramagnetic M^{2+}- and diamagnetic $\tilde{M}^{2+}$-ions, computer simulation of the shape of the M^{2+}-cluster on a square lattice with site-dilution for a concentration x = 0.50 (taken from [80B1]).

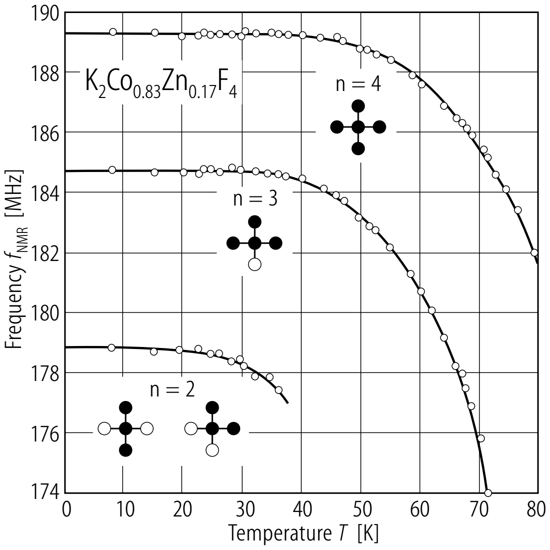

Fig. 3.51. K$_2$Co$_{0.83}$Zn$_{0.17}$F$_4$. Temperature dependence of the ^{19}F$_I$-NMR frequencies f_{NMR}, extrapolated to zero external field, for clusters with n Co^{2+} nearest neighbours as indicated. The solid curves are calculated by means of Eq. 3.136 as explained in the text (taken from [85D2]).

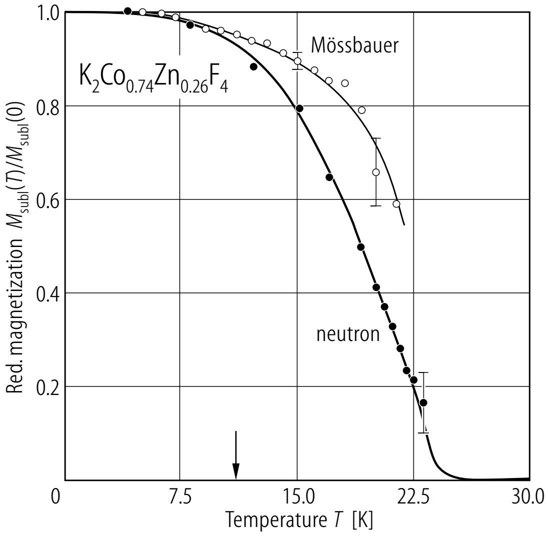

Fig. 3.52. K$_2$Fe$_{0.74}$Zn$_{0.26}$F$_4$. Reduced sublattice magnetization $M_{subl}(T)/M_{subl}(0)$ as derived from square root of the intensity of the (1, 0, 0) antiferromagnetic Bragg peak representing the 3D order parameter and as deduced from Mössbauer spectra representing the local sublattice magnetization. The arrow marks the temperature above which paramagnetic Mössbauer absorptions are observed (taken from [85D1]).

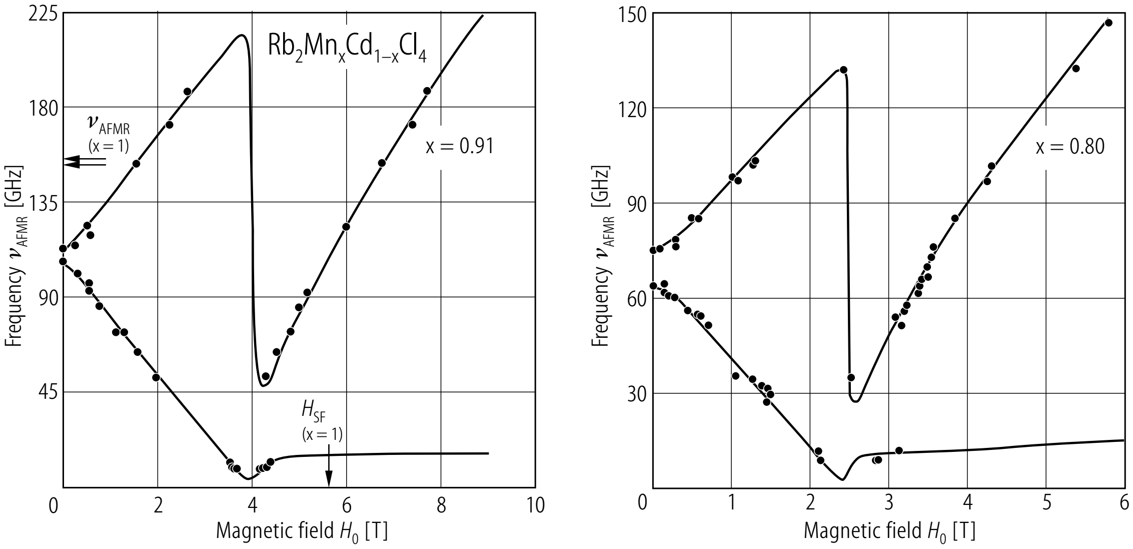

Fig. 3.53. Rb$_2$Mn$_x$Cd$_{1-x}$Cl$_4$ with x = 0.91, 0.80. AFMR frequency ν_{AFMR} at $T = 4.2$ K versus magnetic field H_0 applied parallel to the c-axis, experimental points and curves calculated by classical spin-wave theory. In the left part, indicated by arrows are the two zero-field AFMR frequencies and the spin-flop field of pure Rb$_2$MnCl$_4$ (after [89B4]).

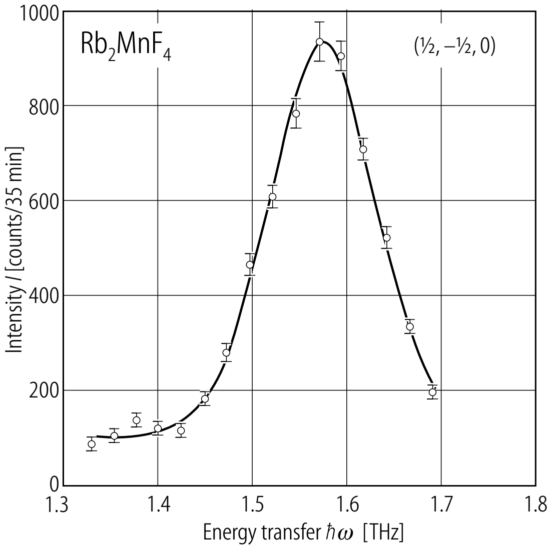

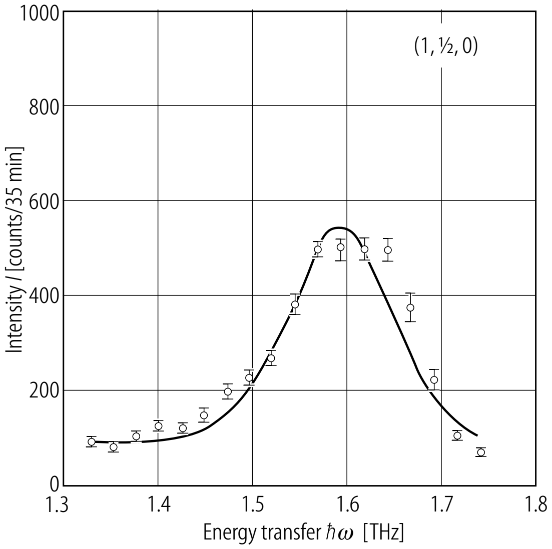

Fig. 3.54. Rb_2MnF_4. Neutron inelastic scattering intensity versus energy transfer at constant wavevector transfer (0.5, –0.5, 0) and (1, 0.5, 0) at 4.2 K. The curves are Gaussians fitted to the experimental data, the width corresponding to the spectrometer resolution (taken from [77C3]).

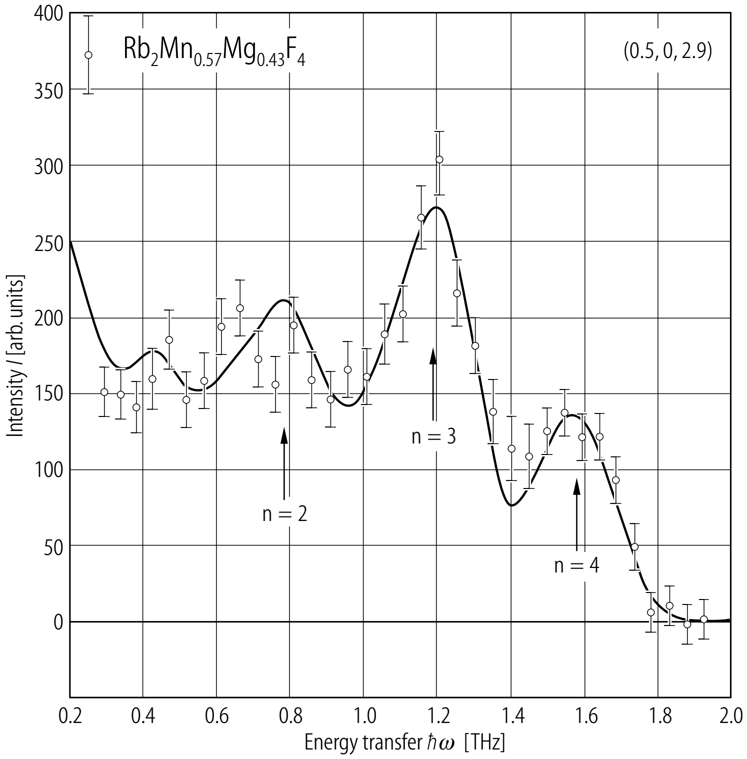

Fig. 3.55. $Rb_2Mn_{0.57}Mg_{0.43}F_4$. Neutron inelastic scattering intensity versus energy transfer at constant wavevector transfer (0.5, 0, 2.9) at 1.22 K, experimental points and theoretical curve. Arrows indicate the maxima corresponding to the Ising cluster energies for n = 2, 3, 4 (after [77C3]).

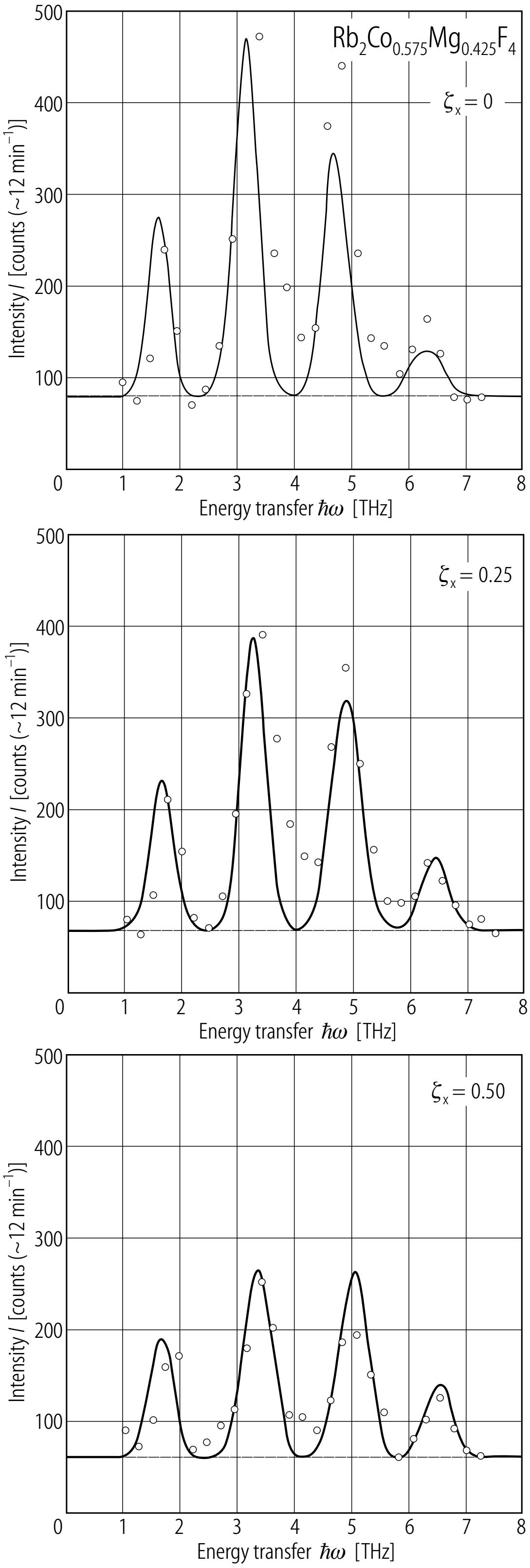

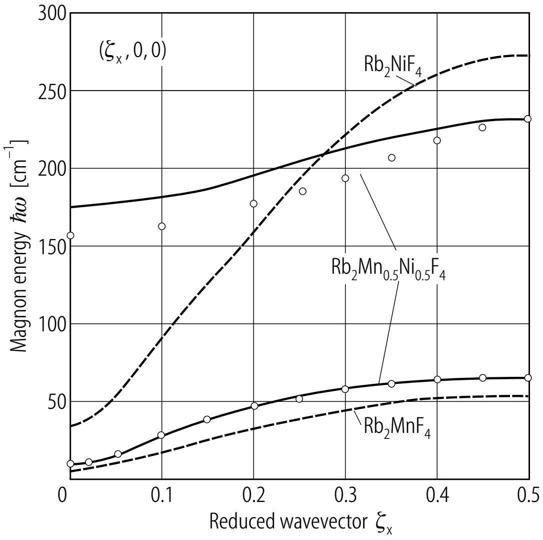

Fig. 3.57. $Rb_2Mn_{0.5}Ni_{0.5}F_4$. Spin-wave dispersion relation $\hbar\omega(\boldsymbol{q})$ for $\boldsymbol{q} \mathrel{\hat{=}} (\zeta_x, 0, 0)$, experimental points (open circles) and results (solid lines) of a mean-crystal model calculation (cf. Eqs. 3.142, 3.143). For comparison, the dispersion curves for the pure crystals Rb_2MnF_4 and Rb_2NiF_4 are presented (dashed lines) which are calculated by linear spin-wave theory using Eq. 3.6. All parameter values are given and explained in the text (taken from [75A1]).

←

Fig. 3.56. $Rb_2Co_{0.575}Mg_{0.425}F_4$. Neutron inelastic scattering intensity versus magnon energy transfer for constant wavevector $\boldsymbol{K} \mathrel{\hat{=}} (1-\zeta_x, 0, 4.23)$ at 6.5 K, experimental points and solid lines resulting from computer simulations convoluted with the spectrometer resolution (after [80C1]).

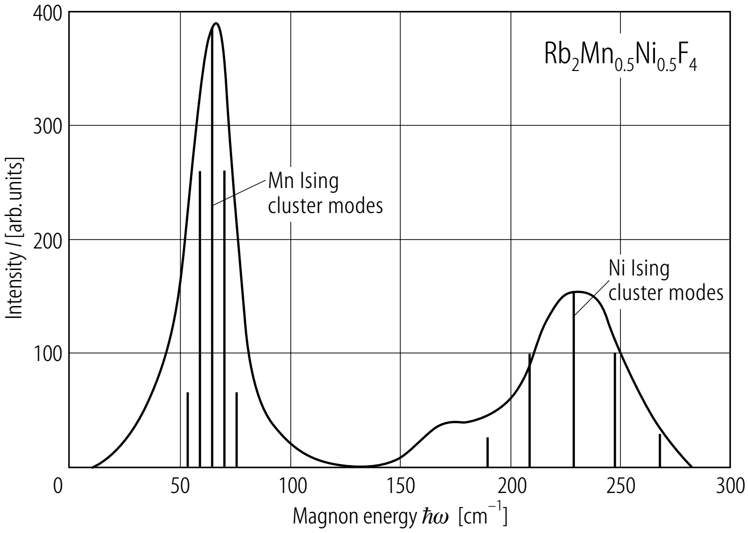

Fig. 3.58. $Rb_2Mn_{0.5}Ni_{0.5}F_4$. Smoothed neutron scattering intensity I (solid line) versus magnon energy $\hbar\omega$ at the zone boundary $\boldsymbol{q} \mathrel{\hat{=}} (0.5, 0, 0)$ with the background subtracted. The vertical lines mark the Mn^{2+} and Ni^{2+} Ising cluster modes (cf. Eq. 3.144) the relative intensities of which are chosen to give agreement with the observed peak hights (taken from [75B10]).

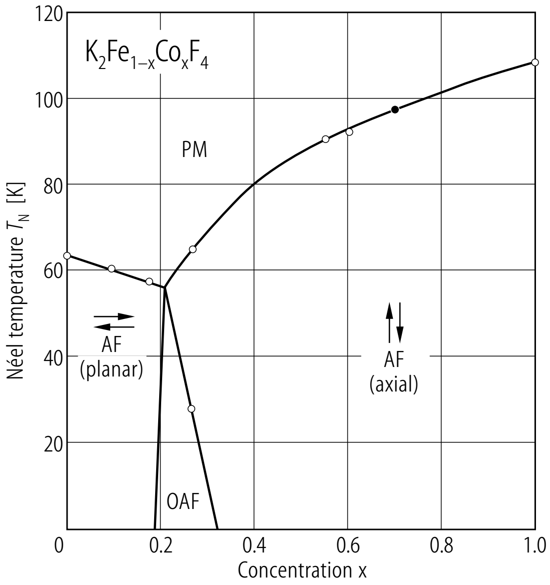

Fig. 3.59. $K_2Fe_{1-x}Co_xF_4$. (T_N, x) phase diagram (after [83V3, 85V3]), derived from neutron scattering data (open circles) [83V3, 84H3, 86V1] and from Mössbauer experiments (full circle) [84F3, 85V3]. Solid lines separate the paramagnetic (PM), the planar antiferromagnetic (AF, planar), the oblique antiferromagnetic (OAF) and the axial antiferromagnetic (AF, axial) phases. The data for x = 0 and x = 1 are taken from [74I1, 74I2, 78T2, 82T1].

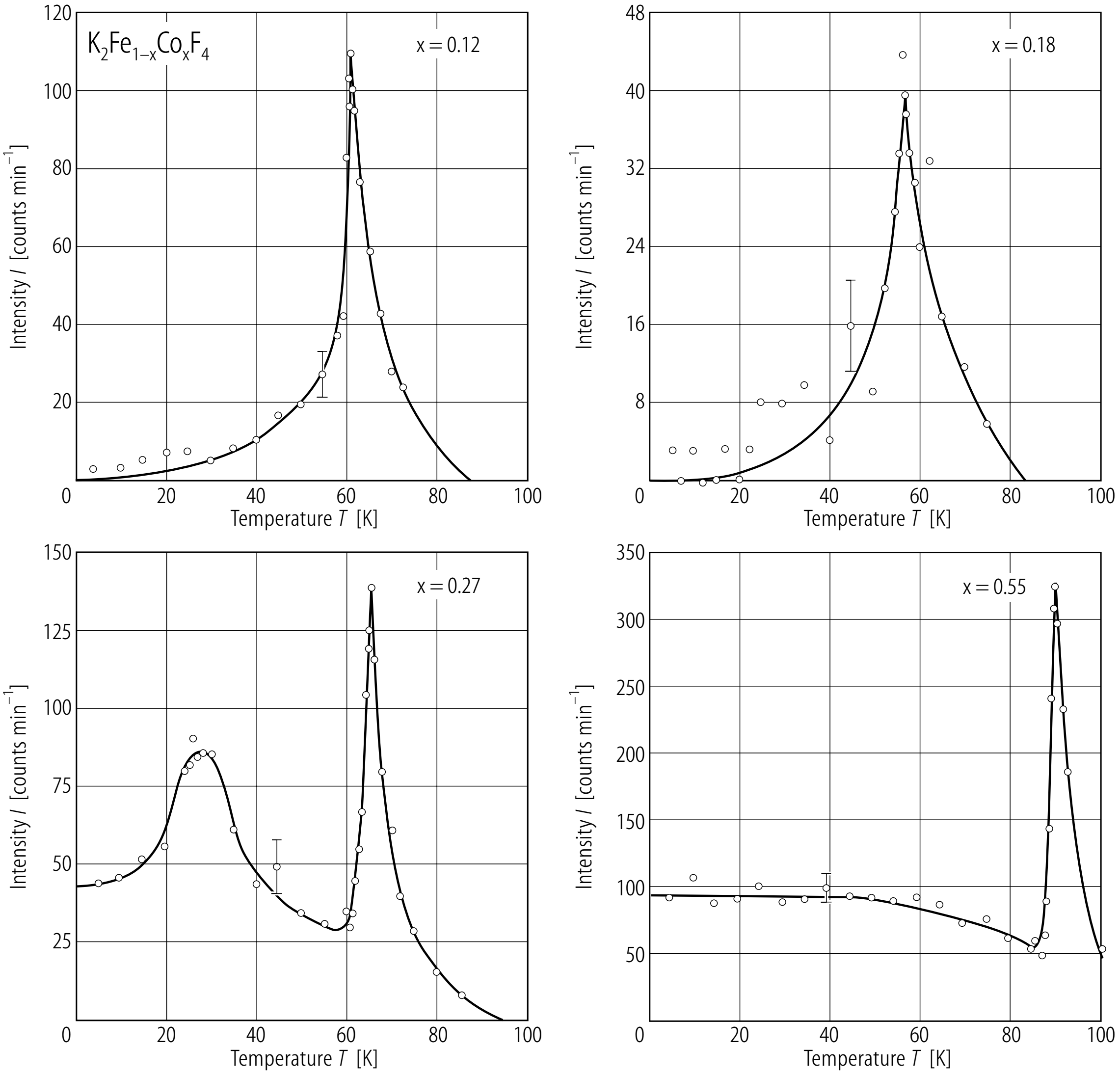

Fig. 3.60. $K_2Fe_{1-x}Co_xF_4$ with x = 0.12, 0.18, 0.27, 0.55. Temperature dependence of the rod scattering intensity I at $\boldsymbol{Q} \mathrel{\hat{=}} (1, 0, 0.4)$. Note the different scales of the intensity I. For interpretation of the data, see text (taken from [86V1]).

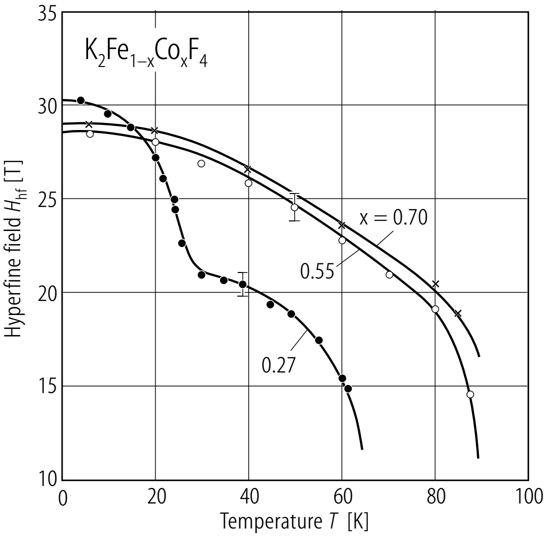

Fig. 3.61. $K_2Fe_{1-x}Co_xF_4$ with x = 0.27, 0.55, 0.70. Mössbauer study: hyperfine field H_{hf} versus temperature T. The (T_N, x) phase diagram (see Fig. 3.59) shows that two transitions are expected for x = 0.27. For further explanations, see text (taken from [85V3]).

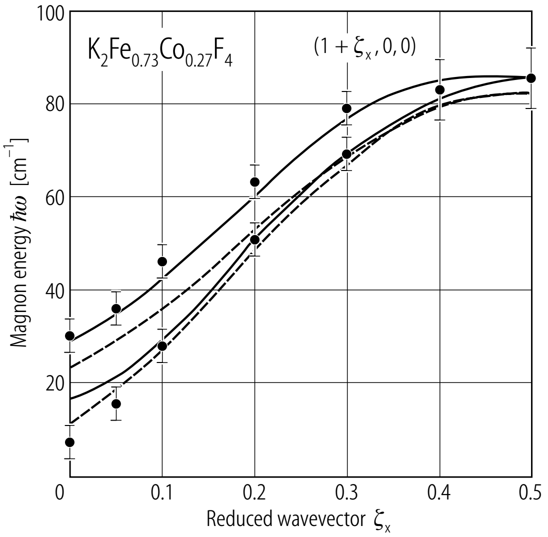

Fig. 3.62. $K_2Fe_{0.73}Co_{0.27}F_4$. Spin-wave dispersion $\hbar\omega(\boldsymbol{q})$ for $\boldsymbol{q} \hat{=} (1 + \zeta_x, 0, 0)$, experimental points from [87H4] and results of a computer simulation (solid lines) and of an average-crystal approximation (broken lines), after [88H3]. The model parameters are given and discussed in the text.

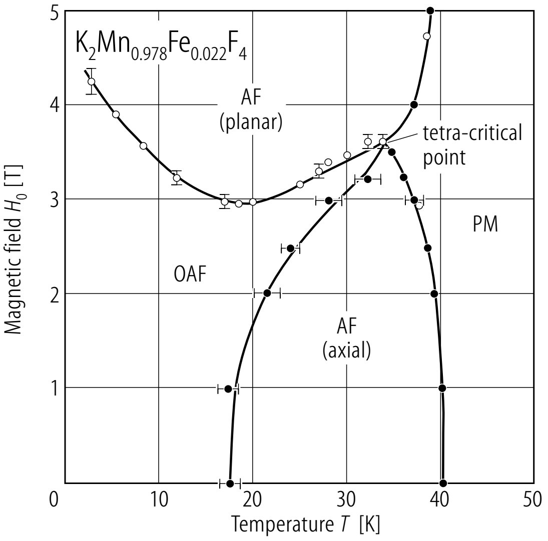

Fig. 3.63. $K_2Mn_{0.978}Fe_{0.022}F_4$. ($H_0$, T) phase diagram for $\boldsymbol{H_0} \parallel \boldsymbol{c}$ with the boundaries between the planar antiferromagnetic (AF, planar), the oblique antiferromagnetic (OAF), the axial antiferromagnetic (AF, axial) and the paramagnetic (PM) phases as determined by neutron diffraction with temperature scans at constant field H_0 (open circles) and field scans at constant T (full circles), taken from [79B2].

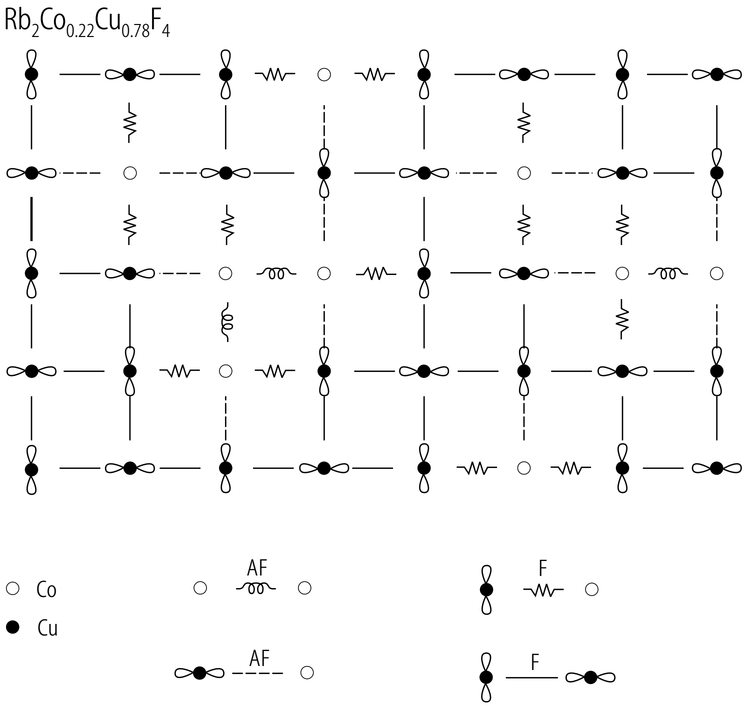

Fig. 3.64. Rb$_2$Co$_{0.22}$Cu$_{0.78}$F$_4$. Example for the distribution of ferromagnetic (F) Cu-Cu and Co-Cu as well as antiferromagnetic (AF) Co-Co and Co-Cu exchange interactions, after [88D10, 88D11]. For further explanations see text.

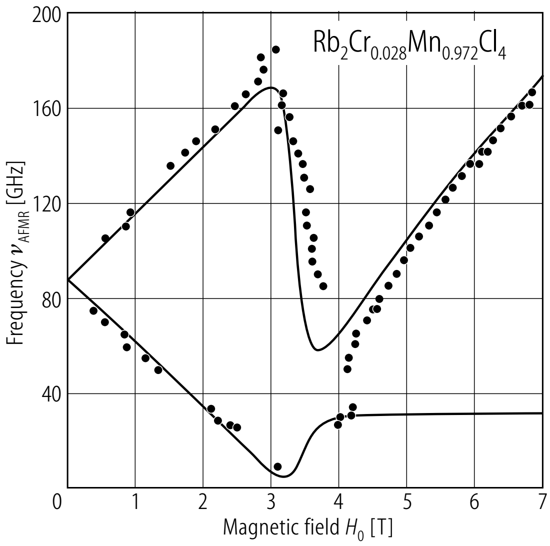

Fig. 3.65. Rb$_2$Cr$_{0.028}$Mn$_{0.972}$Cl$_4$. AFMR frequency ν_{AFMR} at 4.2 K versus magnetic field H_0, applied parallel to the *c*-axis, experimental points and curves calculated by the virtual crystal or average model (cf. Eq. 3.151). These AFMR spectra are typical for an easy-axis antiferromagnet, very similar to those of pure RbMnCl$_4$ (Fig. 3.17), taken from [91G2].

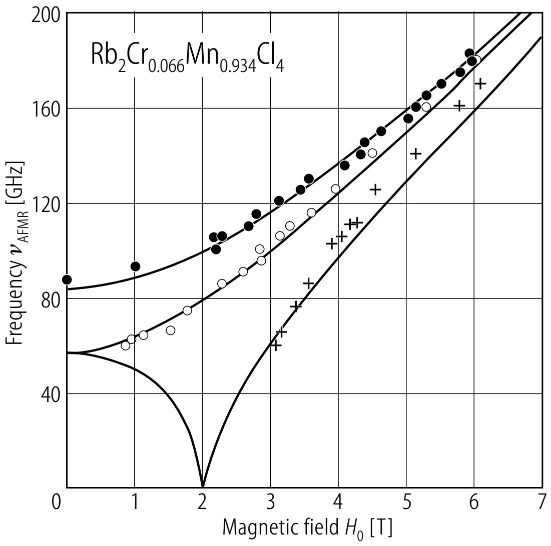

Fig. 3.66. Rb$_2$Cr$_{0.066}$Mn$_{0.934}$Cl$_4$. AFMR frequency ν_{AFMR} at 4.2 K versus magnetic field H_0, experimental points for $\boldsymbol{H_0} \parallel \boldsymbol{c}$ (full circles), for $\boldsymbol{H_0} \perp \boldsymbol{c}$, $\beta = 0°$ (open circles) and $\boldsymbol{H_0} \perp \boldsymbol{c}$, $\beta = 45°$ (plusses). The curves are calculated by the virtual crystal or average model (cf. Eq. 3.151). These AFMR spectra are typical for an easy-plane antiferromagnet like K$_2$FeF$_4$, taken from [91G2].

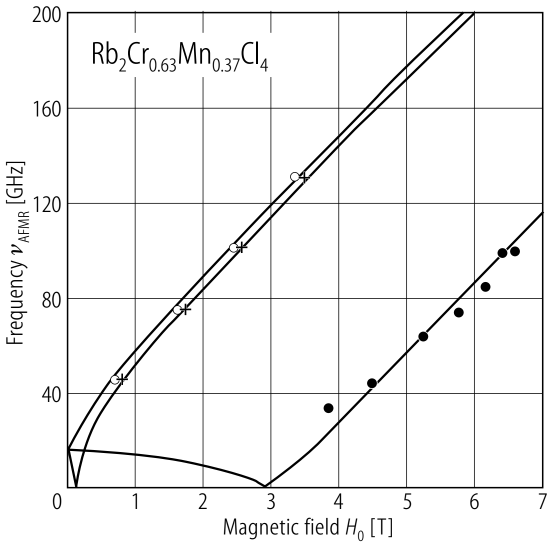

Fig. 3.67. $Rb_2Cr_{0.63}Mn_{0.37}Cl_4$. FMR frequency ν_{FMR} at 4.2 K versus magnetic field H_0, experimental points for $\boldsymbol{H_0} \parallel \boldsymbol{c}$ (full circles), for $\boldsymbol{H_0} \perp \boldsymbol{c}$, $\beta = 0°$ (open circles), and $\boldsymbol{H_0} \perp \boldsymbol{c}$, $\beta = 45°$ (plusses). The curves are calculated by the virtual crystal or average model (cf. Eq. 3.151). These FMR spectra are typical for an easy-plane ferromagnet very similar to those of pure Rb_2CrCl_4 (Fig. 3.36), taken from [91G2].

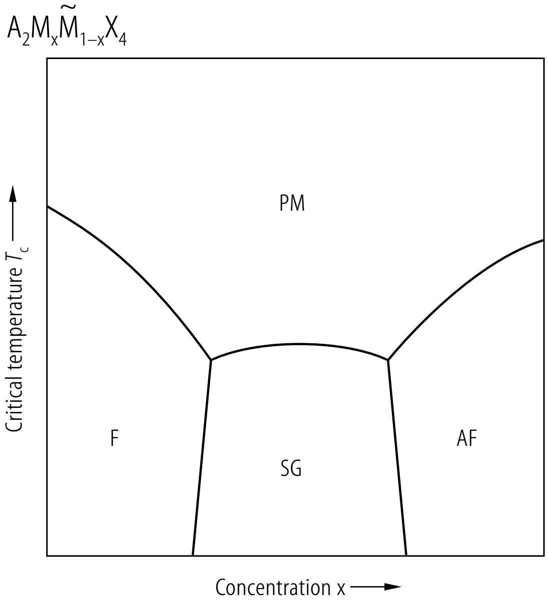

Fig. 3.69. $A_2M_x\tilde{M}_{1-x}X_4$. Schematic (T_C, x) phase diagram of a random mixture of the ferromagnet $A_2\tilde{M}X_4$ and antiferromagnet A_2MX_4. The competing exchange interactions lead to a ferromagnetic phase (F) for $x < 0.3$, an antiferromagnetic one for $x > 0.7$ and a spin-glass phase for intermediate concentrations x. At higher temperatures, the system is paramagnetic (PM), after [80F3].

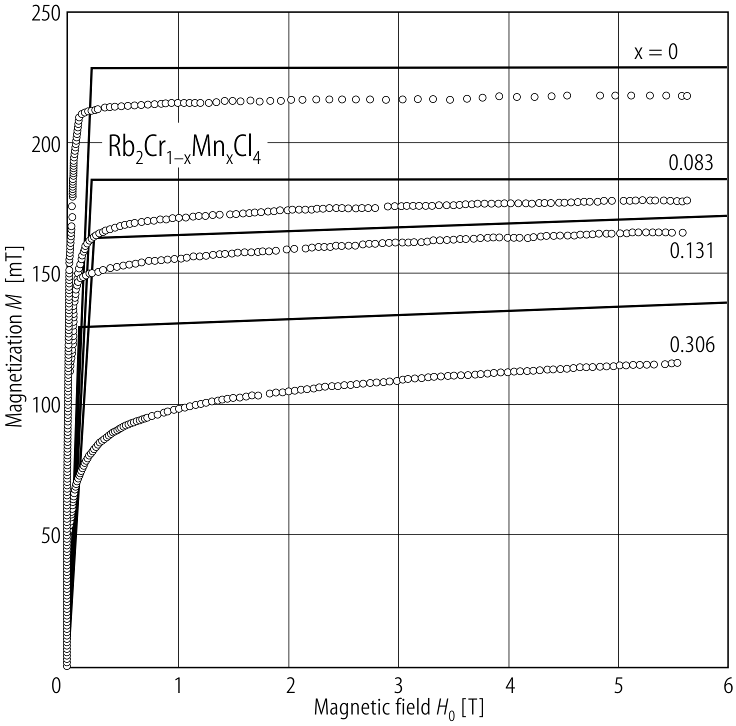

Fig. 3.68. $Rb_2Cr_{1-x}Mn_xCl_4$ with x = 0, 0.083, 0.131, 0.306. Magnetization M at 4.2 K versus magnetic H_0, applied perpendicular to the *c*-axis, experimental points and solid lines calculated by means of the virtual crystal or average model (see Eq. 3.151), taken from [86G3].

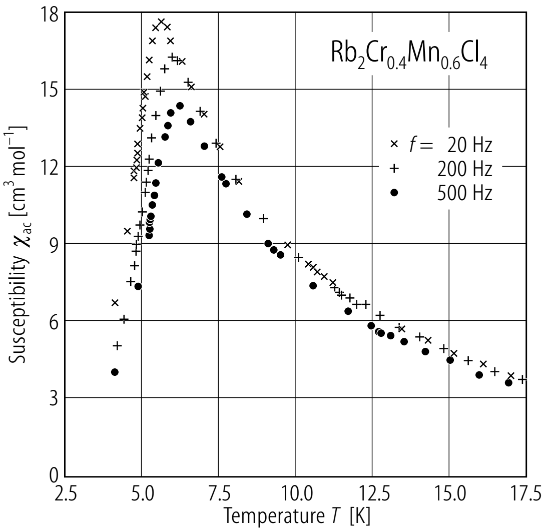

Fig. 3.70. Rb$_2$Cr$_{0.4}$Mn$_{0.6}$Cl$_4$. Temperature dependence of the ac susceptibility χ_{ac} obtained for $\boldsymbol{h} \perp \boldsymbol{c}$ at the frequencies $f = 20$, 200, 500 Hz. The maximum indicates the frequency-dependent freezing temperature T_f, after [83K10].

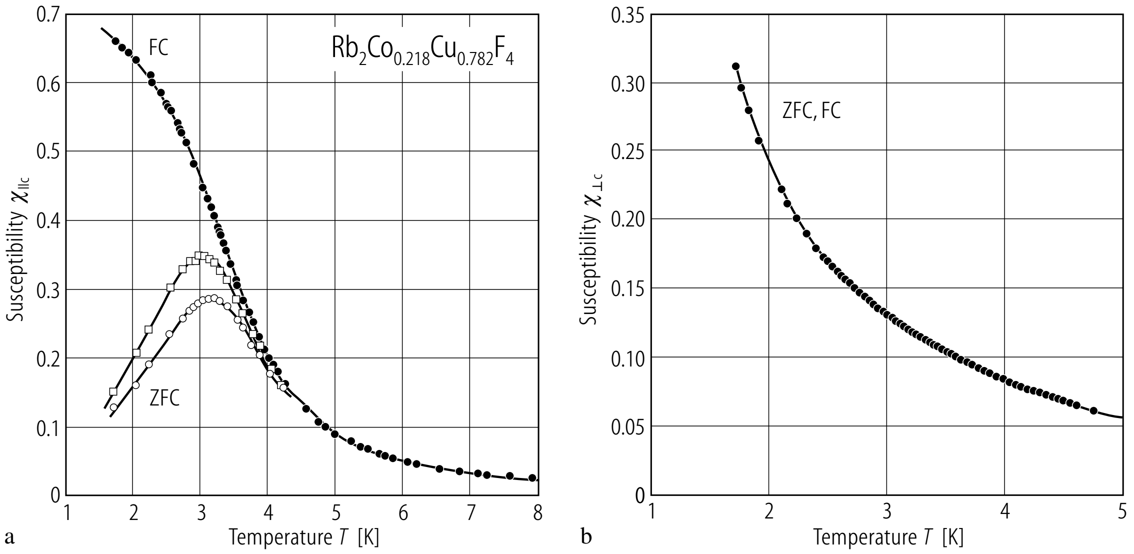

Fig. 3.71. Rb$_2$Co$_{0.218}$Cu$_{0.782}$F$_4$. **(a)** Temperature dependence of the static susceptibility $\chi_{||c}$ for $\boldsymbol{H}_0 \parallel \boldsymbol{c}$, obtained with $H_0 = 1$ mT in a field-cooling procedure (FC, full circles) and in a zero-field-cooling procedure (ZFC), switching on the field after waiting times of 10 s (open circles) and 90 s (open squares) and **(b)** the T-dependence of the coincident FC and ZFC susceptibilities $\chi_{\perp c}$ for $\boldsymbol{H}_0 \perp \boldsymbol{c}$ (taken from [88D1, 88D11]).

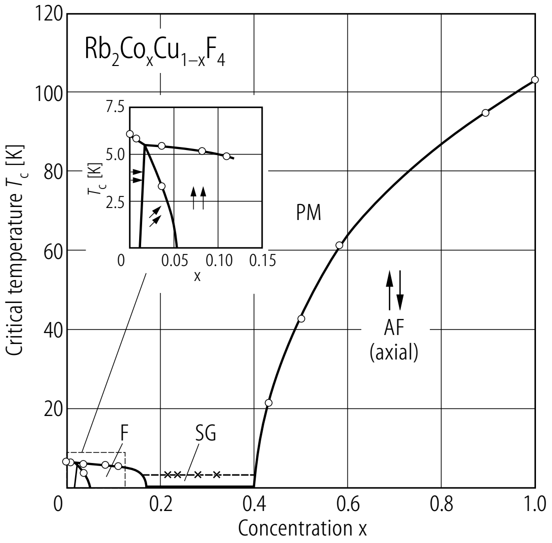

Fig. 3.72. $Rb_2Co_xCu_{1-x}F_4$. (T_C, x) phase diagram with the critical temperatures (open circles) at the boundary to the paramagnetic phase (PM), i.e. the Curie temperature T_C for the planar, oblique and axial ferromagnetic phases (F, see also inset), the Néel temperature T_N for the axial antiferromagnetic phase (AF) and the spin-glass range (SG) with T_f (crosses) and $T_C = 0$, after [88D1, 88D11].

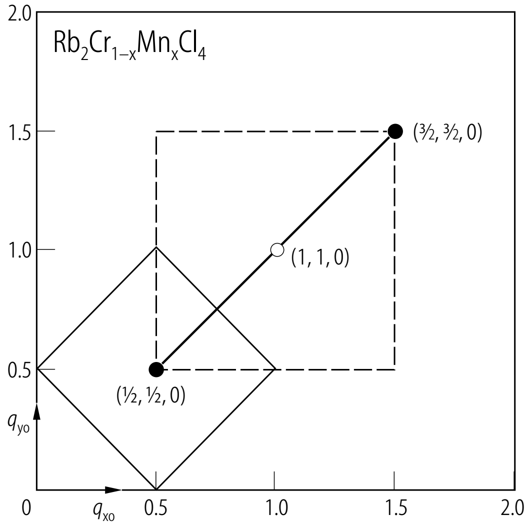

Fig. 3.74. $Rb_2Cr_{1-x}Mn_xCl_4$. Geometry of reciprocal space, (q_{x0}, q_{y0}) plane, for neutron inelastic scattering experiments. The point (1, 1, 0) corresponds to a nuclear Bragg peak and the broken line to the ferromagnetic Brillouin zone boundaries around it in 2D approximation. Around the antiferromagnetic superlattice reflection $(\frac{1}{2}, \frac{1}{2}, 0)$, the solid line represents the antiferromagnetic Brillouin zone, also in 2D approximation (taken from [88S8]).

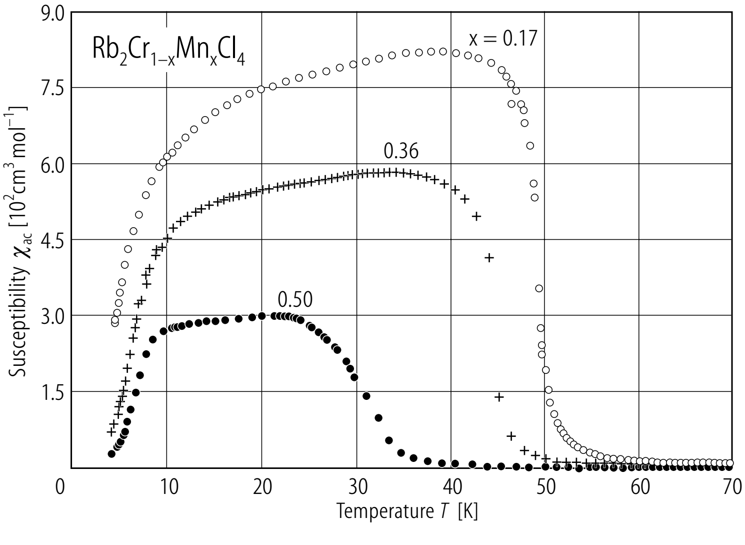

Fig. 3.73. $Rb_2Cr_{1-x}Mn_xCl_4$ with x = 0.17, 0.36, 0.50. ac susceptibility χ_{ac} versus temperature T, obtained with $f = 20$ Hz. The maxima of the slope $|d\chi_{ac}/dT|$ represent the temperatures T_f of spin-glass freezing (reentrant) and T_C of ferromagnetic ordering (taken from [84K8]).

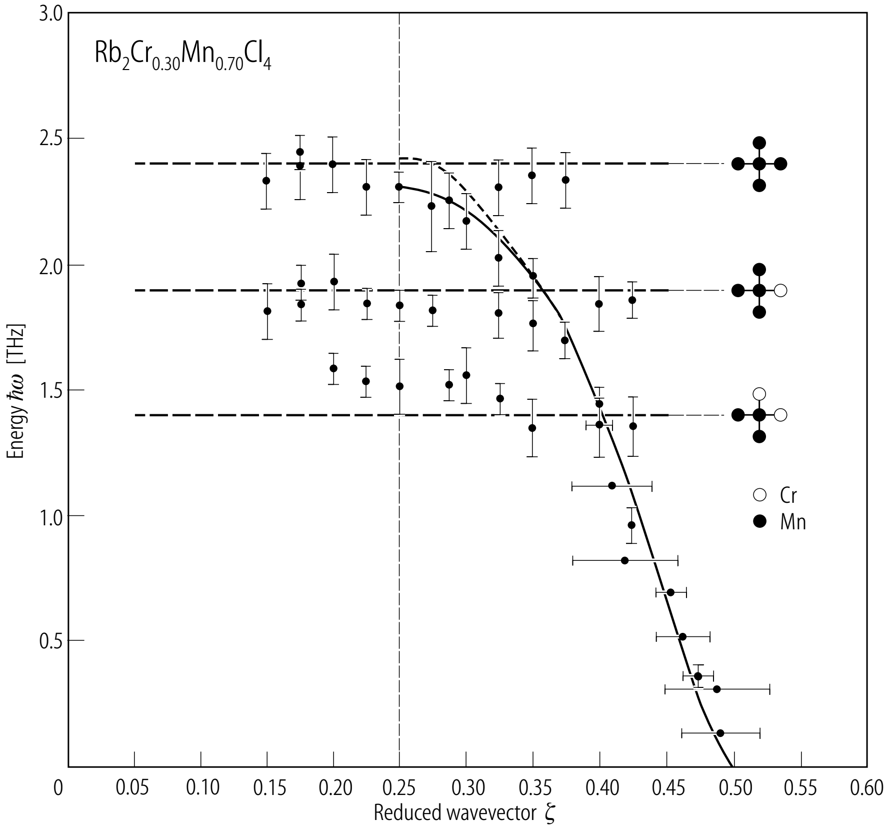

Fig. 3.75. $Rb_2Cr_{0.30}Mn_{0.70}Cl_4$. Magnetic excitations $\hbar\omega$ at 5 K versus reduced wavevector ζ (see Eq. 3.152). The excitations consist of a spin-wave branch (antiferromagnetic: $0.25 \le \zeta \le 0.5$, solid line: guide to the eye; broken line: spin waves of pure Rb_2MnCl_4) and of dispersionless cluster modes (horizontal lines calculated by Eq. 3.153, corresponding nearest neighbour configurations to the right), after [88S7, 88S8]. For further explanations see text.

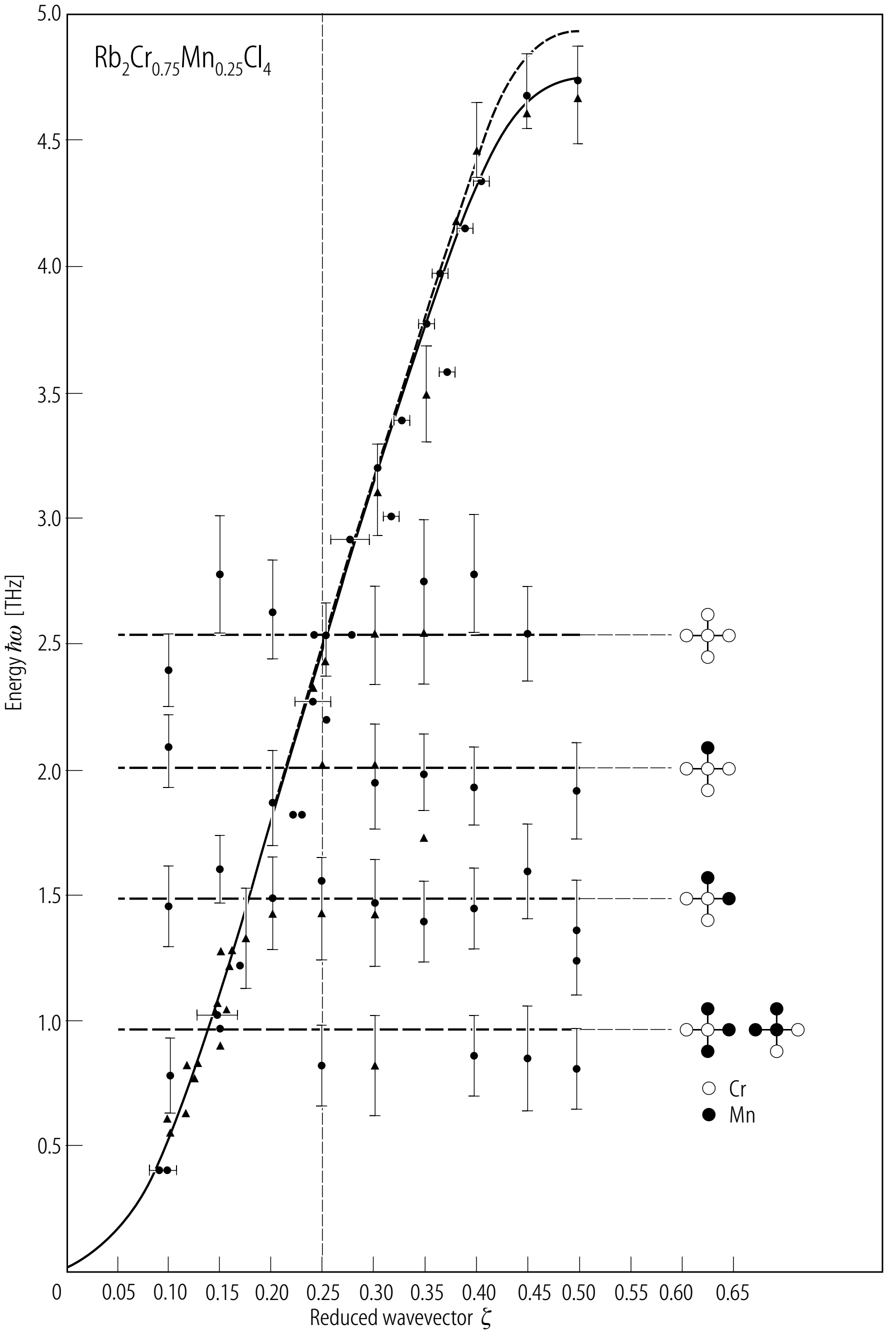

Fig. 3.76. $Rb_2Cr_{0.75}Mn_{0.25}Cl_4$. Magnetic excitations $\hbar\omega$ at 5 K (full circles) and 13 K (full triangles) versus reduced wavevector ζ (see Eq. 3.152). The excitations consist of a spin-wave branch (ferromagnetic: $0 \le \zeta \le 0.5$, solid line: guide to the eye; broken line: spin waves of pure Rb_2CrCl_4) and of dispersionless cluster modes (horizontal lines calculated by Eq. 3.153, corresponding nearest neighbour configurations to the right), after [88S7, 88S8]. For further explanations see text.

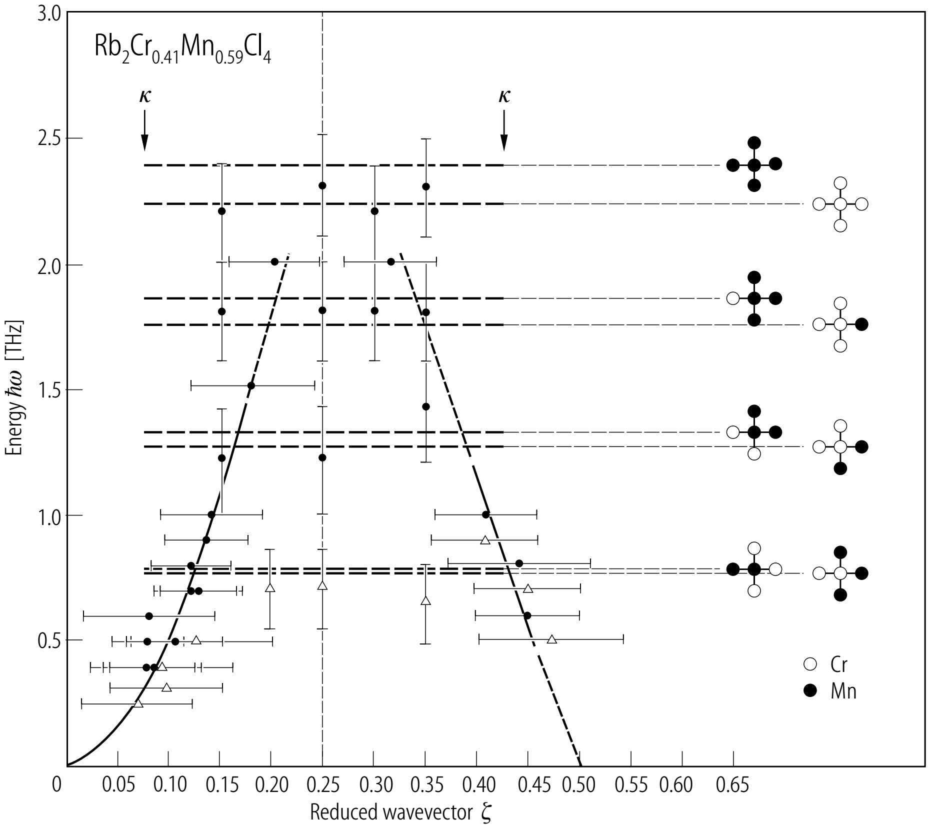

Fig. 3.77. $Rb_2Cr_{0.41}Mn_{0.59}Cl_4$. Magnetic excitations $\hbar\omega$ at 5 K versus reduced wavevector ζ (see Eq. 3.152) experimental points (full circles and open triangles). The excitations consist of "ferromagnetic" and "antiferromagnetic" spin waves (solid lines: guide to the eye) and of dispersionless cluster modes (horizontal lines calculated by Eq. 3.153, corresponding nearest neighbour configurations to the right), taken from [88S7, 88S8]. For further explanations see text.

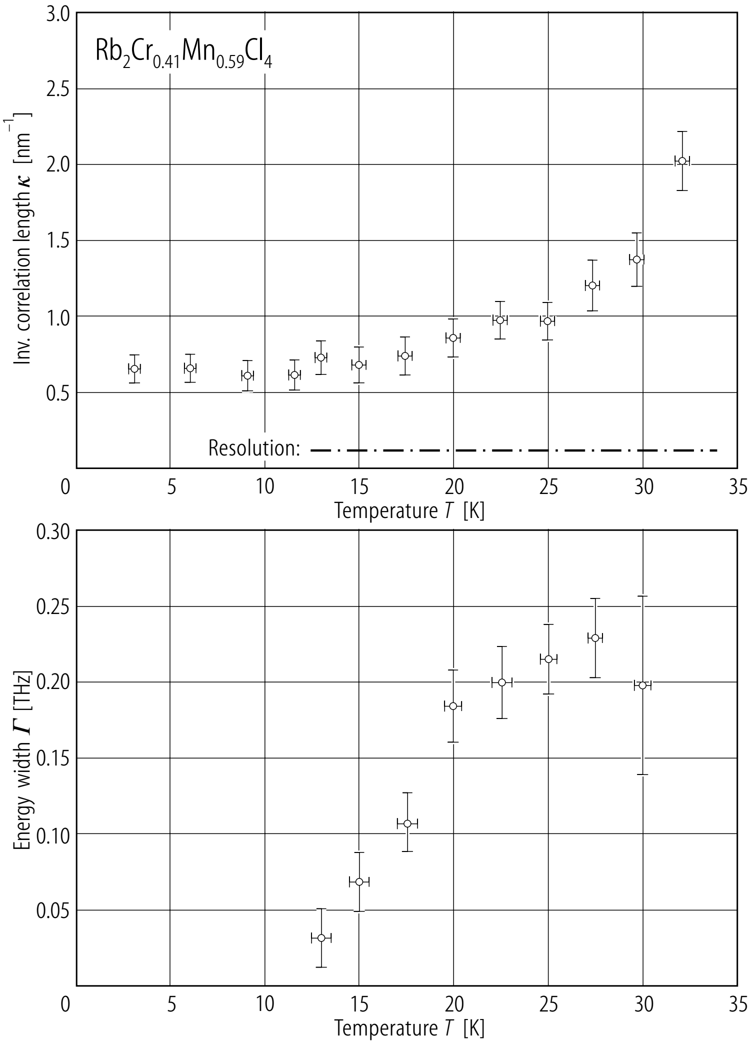

Fig. 3.78. $Rb_2Cr_{0.41}Mn_{0.59}Cl_4$. Inverse correlation length κ and energy width Γ versus temperature T, as obtained from scans across the magnetic rod $(\frac{1}{2}, \frac{1}{2}, \frac{1}{4})$ with a triple axis spectrometer (taken from [88S7]).

Table 5. Data concerning Magnetic Properties

Compound	Characteristic magnetic parameters: J, H_E, H_A, H_0, M, χ, g, T_C, T_N etc. [definitions see Table 1, units are given below]	References, remarks
a) Fluorides		
K_2MnF_4	Antiferromagnet, $\boldsymbol{M}_{\mathbf{subl}} \parallel \boldsymbol{c}$ (magn. order see Fig. 2.2)	
1) meas. and anal. of χ	$\chi_{\parallel}(T)$, $\chi_{\perp}(T)$ [4 K $\leq T \leq$ 300 K]	[66B1, 67B1, 68V, 69B1], see also [73J3, 78B4, 82M4]
	min. $\chi_{\perp}$: $T_N = 45.0(10)$ K $\rightarrow J = -3.10(7)\ \text{cm}^{-1} \mathrel{\hat{=}} -4.46(10)$ K	$T_N \approx T_C^{(2)} \rightarrow J$: Eq. 3.29, see also [66S2]
	$\chi(T > T_N)$ = h.t.s. $\rightarrow J = -2.92\ \text{cm}^{-1} \mathrel{\hat{=}} -4.20$ K	h.t.s.: Eqs. 3.26, 3.27; coeff. see [70L1, 90N]
	$\chi_{\perp}(T = 0) \rightarrow J = -2.92(10)\ \text{cm}^{-1} \mathrel{\hat{=}} -4.20(15)$ K $\chi_{\parallel}(T < T_N) \rightarrow J = -3.13(14)\ \text{cm}^{-1} \mathrel{\hat{=}} -4.50(20)$ K	$\chi_{\perp}(T = 0)$: Eq. 3.24a; $\chi_{\perp}(T)$: Eq. 3.23 $\chi_{\parallel}(T)$: Eq. 3.22; fit to the exp. data
	$H_{SF} = 5.51(10)\ T \rightarrow H_A = 0.231$ T $[(\chi_{\perp} - \chi_{\parallel}) = 3.53 \cdot 10^{-3}]$	h.m.f. exp. at $T = 4.2$ K [67B1]; $H_{SF} \rightarrow H_A$: Eq. 3.38
2) el. + quasi-el. n-scatt.	afm. Bragg refl. (1, 0, 0): $I(T) \sim M^2_{\text{subl}}(T) \rightarrow T_N = 42.15(2)$ K	[68L1, 72I, 73B1, 73I, 74I1]
3) EPR, NMR	$g_c = 2.0026$ $\Delta_0 S = 0.17(3)$	EPR [71Y1] AFMR/EPR + NMR [68R, 70W1, 71W, 72B1, 73W3]
4) AFMR	$H_0 = 0$, $T \rightarrow 0$: $h\nu_{AFMR} = 5.14(4)\ \text{cm}^{-1} \mathrel{\hat{=}} 7.40(5)$ K T-dependence of ν_{AFMR} [1.5 K $\leq T \leq$ 38 K]	AFMR at 24 GHz [73W3] ν_{AFMR}: Eqs. 3.9 and 3.10
	$H_0 = 0$, $T = 4.2$ K: $h\nu_{AFMR} = 5.1(1)\ \text{cm}^{-1} \mathrel{\hat{=}} 7.34(14)$ K	ir spectr. [75L6, 77L2]
	AFMR LW: $\Delta H^0_{AFMR} = 84$ mT, $C_{AFMR} = 5.9 \cdot 10^{-7}$ T/K^4	[83U]: reanalysis of $\Delta H_{AFMR}(T)$ of [73W3] using Eq. 3.13
5) inel. n-scatt	$\omega(\boldsymbol{q})$ for $(\zeta_x, 0, 0)$ at 4.5 K $J_2 \approx 0$, $g\mu_B H_A = 0.220(3)\ \text{cm}^{-1} \mathrel{\hat{=}} 0.317(4)$ K, $h_A = 0.0036$	[73B1], $\zeta_x = q_x/a^*$; fit to the exp. data with linear spin-w. th. (cf. Eqs. 3.2–3.5, 3.6); parameters: see below
6) spin-wave analysis	exp. data included: $\nu_{AFMR}(T)$, $M_{\text{subl}}(T)$ and $\omega(\boldsymbol{q})$ $(z = 4, S = 5/2, g = 2.00, J_2 \approx 0, \lvert J'/J \rvert \leq 5 \cdot 10^{-4})$	[73B1, 73W2, 73W3]
	$J = -3.01(2)\ \text{cm}^{-1} \mathrel{\hat{=}} -4.34(3)$ K, $H_E = 64.5$ T $T = 0$: $h_A = 0.0036$, $g\mu_B H_A = 0.219\ \text{cm}^{-1}$, $H_A = 0.235$ T	parameter values according to linear spin-w. th. (cf. Eqs. 3.2–3.5, 3.6)
	$J = -2.92(2)\ \text{cm}^{-1} \mathrel{\hat{=}} -4.21(3)$ K, $H_E = 62.6$ T $T = 0$: $h_A = 0.0038$, $g\mu_B H_A = 0.219\ \text{cm}^{-1}$, $H_A = 0.235$ T	parameter values according to renorm. spin-w. th. (cf. Eqs. 3.2–3.5, 3.15)
	calc.: $\Delta_0 S = 0.171$, $H_{AD} = 0.257$ T	[73W2]; $\Delta_0 S$: Eq. 3.19; H_{AD}: Eq. 3.12
	calc.: $\lvert J \rvert = 4.21$ K $\rightarrow T_C^{(2)} = 41.6$ K ($T_N = 42.15$ K)	[73W2]; $\lvert J \rvert \rightarrow T_C^{(2)}$: Eq. 3.29; see also [72J2]

Table 5. Data concerning Magnetic Properties *(continued)*

Compound	Characteristic magnetic parameters: J, H_E, H_A, H_0, M, χ, g, T_C, T_N etc. [definitions see Table 1, units are given below]	References, remarks
K_2MnF_4 (cont.)		
7) 2-magn. Raman L.	$T \approx 2$ K: peak pos. at 114.0(5) cm^{-1}	Raman sp. [73L2, 74L3, 75L5, 75L6, 77L2]
	T-dependence of peak pos. and width	Raman sp. [76P2, 77L2, 77P1]
	anal. of 2-magn. Raman L. together with AFMR data:	[77L2]
	$J = -3.015(15)$ $cm^{-1} \hat{=} -4.34(2)$ K, $H_E = 64.4$ T $h_A = 0.00363$, $g\mu_B H_A = 0.219(2)$ cm^{-1}, $H_A = 0.234$ T	parameters in theoretical calculations based on linear spin-w. th. (cf. Eqs. 3.2–3.5, 3.6)
	$J = -2.925(15)$ $cm^{-1} \hat{=} -4.21(2)$ K, $H_E = 62.7$ T $h_A = 0.00386$, $g\mu_B H_A = 0.226(2)$ cm^{-1}, $H_A = 0.242$ T	parameters in theoretical calculations based on renorm. spin-w. th. (cf. Eqs. 3.2–3.5, 3.15)
8) mixed anisotropy	resid. single-ion anis.: $D = -0.006(1)$ $cm^{-1} \hat{=} -0.009(2)$ K	spin-w. th.: dipolar interact. + resid. single-ion anis. [84U]
9) (H_0, T) phase diagram	observed critical point: bifurcation point, not bicritical one	n-diffr. [82J1]; χ-meas. [82M4]; theor. details: Sect. 3.1.5
10) ^{19}F-NMR	F_I; $f_{NMR}(T) \sim M_{subl}(T)$	$^{19}F_I$-NMR [70W2, 73W2]
	$\boldsymbol{H_0} \parallel \boldsymbol{c}$, $[0 \leq T \leq T_N]$: $F_I \rightarrow f_{NMR}(H_0, T) \sim M_{subl}(H_0, T)$, $F_{II} \rightarrow \Delta f_{NMR}(H_0, T) \sim M(H_0, T) \rightarrow H_{SF} = 5.45(5)$ T (1.2 K)	[77A1, 77A2]; $M_{subl}(T)$ and $M(T)$ also calc. with renorm. spin-w. th. (Eqs. 3.2–3.5, 3.15, 3.18, 3.21)
	F_I, F_{II}: determination of T_1 for $H_0 = 0$ [1.5 K $\leq T \leq$ 12 K], for $\boldsymbol{H_0} \perp \boldsymbol{c}$ [1.5 K $\leq T \leq$ 8 K] and for $\boldsymbol{H_0} \parallel \boldsymbol{c}$ [$T = 4.2$ K]	[78W2, 79W1, 80W1, 81W4]; discussion of the mechanism for T_1: see Sect. 3.1.2
11) optical studies	MCD 24900–25500 cm^{-1}	[74S4]
	intrinsic emission $^4T_{1g}(G) \rightarrow {}^6A_{1g}(S)$ at $T = 1.7$ K	exciton line, magnon sideband [77S2]
$K_3Mn_2F_7$	Antiferromagnet, $\boldsymbol{M_{subl}} \parallel \boldsymbol{c}$ (magn. order see Fig. 2.4)	
1) meas. and anal. of χ	$\chi_\parallel(T)$, $\chi_\perp(T)$ [4 K $\leq T \leq$ 300 K] $\rightarrow T_N = 58(1)$ K	[77A3], see also [76N1]
	$\chi(T > T_N)$ = h.t.s. $\rightarrow J = -2.79$ (8) $cm^{-1} \hat{=} -4.02(12)$ K	h.t.s.: Eqs. 3.26, 3.27; coeff. see [73R3]
	$\chi_\perp(T = 0) \rightarrow J = -2.65(6)$ $cm^{-1} \hat{=} -3.81(8)$ K, $h_A = 1.9 \cdot 10^{-3}$	$\chi_\perp(T = 0)$: Eq. 3.24a; h_A: Eq. 3.31
	$\chi_\parallel(T < T_N) \rightarrow J = -2.68(7)$ $cm^{-1} \hat{=} -3.85(10)$ K	$\chi_\parallel(T)$: fit to the exp. data, details see [77A3]
	$T \approx 1.3$ K: $H_{SF} = 4.1(1)$ T $\rightarrow H_A = 0.112(20)$ T	[76N1], measurement of H_{SF} $H_{SF} \rightarrow H_A$: Eq. 3.39 ($H_E = 75.2$ T; $z = 5$, $S = 5/2$)

Table 5. Data concerning Magnetic Properties *(continued)*

Compound	Characteristic magnetic parameters: J, H_E, H_A, H_0, M, χ, g, T_C, T_N etc. [definitions see Table 1, units are given below]	References, remarks
$K_3Mn_2F_7$ (cont.)		
2) el. + quasi-el. n-scatt	afm. Bragg refl. (1, 0, 2): $I(T) \sim M^2_{\rm subl}(T) \rightarrow T_N = 58.3(2)$ K magn. Bragg rod ($\bar{1}$, 0, 1.46): sinusoidal modulation of I because of magn. double-layer period 0.418(7) nm	[78U, 79U]; double-layer period corresponds to a' (cf. Eqs. 2.6 and 2.7)
3) EPR, NMR	$\Delta_0 S = 0.12(3)$	AFMR + ^{55}Mn-NMR [82U]
4) AFMR	$H_0 = 0$, $T \rightarrow 0$: $h\nu_{\rm AFMR} = 4.02(3)$ cm^{-1} $\widehat{=}$ 5.78(5) K AFMR LW: $\Delta H^0_{\rm AFMR} = 72$ mT, $C_{\rm AFMR} = 1.1 \cdot 10^{-7}$ T/K^4	[83U]: AFMR at 24 GHz; $\nu_{\rm AFMR}$: Eqs. 3.10, 3.32; anal. of $\Delta H_{\rm AFMR}(T)$ using Eq. 3.13
5) ^{19}F-NMR	F adjacent to magn. double layer: $f_{\rm NMR}(T) \sim M_{\rm subl}(T)$	^{19}F-NMR [77A4]
6) mixed anisotropy	resid. single-ion anis.: $D = -0.004(1)$ cm^{-1} $\widehat{=}$ $-0.006(2)$ K	spin-w. th.: combination of magn. dipolar interact. and resid. single-ion anis. [84U]
7) spin-wave analysis	exp. data included: $M_{\rm subl}(T)$; ($z = 5$, $S = 5/2$, $g = 2.00$)	[77A4, 77A5]; ($J_2 \approx 0$, $\lvert J'/J \rvert \approx 10^{-4}$)
	$J = -2.70(1)$ cm^{-1} $\widehat{=}$ $-3.89(2)$ K, $H_E = 72.4$ T $T = 0$: $h_A = 0.00193(6)$, $g\mu_B H_A = 0.131$ cm^{-1}, $H_A = 0.140$ T	parameter values according to linear spin-w. th., Eqs. 3.30, 3.31; further details see [77A4]
	$J = -2.638(10)$ cm^{-1} $\widehat{=}$ $-3.795(15)$ K, $H_E = 70.62$ T $T = 0$: $h_A = 0.00198(6)$, $g\mu_B H_A = 0.131$ cm^{-1}, $H_A = 0.140$ T	parameter values according to renorm. spin-w. th., details see [77A4]
	calc.: $\Delta_0 S = 0.124$, $H_{AD} = 0.120$ T	[77A4]; formulae for $\Delta_0 S$ and H_{AD}: see also [77A4]
8) 2-magn. Raman L.	T-dependence of peak pos. and width	Raman sp. [77P2, 80P1, 80P2]
	anal. of 2-magn. Raman L.:	[80P2]: theor. calc. of 2-magn. Raman L.
	$J = -2.67(3)$ cm^{-1} $\widehat{=}$ $-3.84(4)$ K, $H_E = 71.5$ T $h_A = 0.00199$, $g\mu_B H_A = 0.133$ cm^{-1}, $H_A = 0.143$ T	parameters in theoretical calculations based on renorm. spin-w. th., details see [77A4, 80P2]
Rb_2MnF_4	Antiferromagnet, $\boldsymbol{M}_{\rm subl} \parallel \boldsymbol{c}$ (magn. order see Fig. 2.3)	
1) AFMR	$H_0 = 0$, $T \rightarrow 0$: $h\nu_{\rm AFMR} = 5.06(4)$ cm^{-1} $\widehat{=}$ 7.28(5) K T-dependence of $\nu_{\rm AFMR}$ [1.5 K $\le T \le$ 34 K]	AFMR at 24 GHz [73W3] $\nu_{\rm AFMR}$: Eqs. 3.9 and 3.10
	AFMR LW: $\Delta H^0_{\rm AFMR} = 84$ mT, $C_{\rm AFMR} = 5.9 \cdot 10^{-7}$ T/K^4	[83U]: reanalysis of $\Delta H_{\rm AFMR}(T)$ of [73W3] using Eq. 3.13

Table 5. Data concerning Magnetic Properties *(continued)*

Compound	Characteristic magnetic parameters: J, H_E, H_A, H_0, M, χ, g, T_C, T_N etc. [definitions see Table 1, units are given below]	References, remarks
Rb_2MnF_4 (cont.)		
2) meas. and anal. of χ	$\chi_{\parallel}(T)$, $\chi_{\perp}(T)$ [$4\ K \leq T \leq 300\ K$] min. $\chi_{\perp}$: $T_N = 38.5(10)\ K \rightarrow J = -2.65(7)\ cm^{-1} \mathrel{\hat{=}} -3.82(10)\ K$	[67B1, 68V, 69B1], see also [73J3] $T_N \approx T_C^{(2)} \rightarrow J$: Eq. 3.29, see also [66S2]
	$\chi(T > T_N)$: h.t.s. $\rightarrow J = -2.57\ cm^{-1} \mathrel{\hat{=}} -3.70\ K$	h.t.s.: Eqs. 3.26, 3.27; coeff. see [70L1, 90N]
	$\chi_{\perp}(T = 0) \rightarrow J = -2.32(12)\ cm^{-1} \mathrel{\hat{=}} -3.34(17)\ K$	$\chi_{\perp}(T = 0)$: Eq. 3.24a; $\chi_{\perp}(T)$: Eq. 3.23
	$\chi_{\parallel}(T < T_N) \rightarrow J = -2.67(7)\ cm^{-1} \mathrel{\hat{=}} -3.84(10)\ K$	$\chi_{\parallel}(T)$: Eq. 3.22; fit to the exp. data
	$H_{SF} = 5.08(13)\ T \rightarrow H_A = 0.232\ T\ [(\chi_{\perp} - \chi_{\parallel}) = 3.87(7) \cdot 10^{-3}]$	h.m.f. exp. at $T = 4.2\ K$ [67B1]; $H_{SF} \rightarrow H_A$: Eq. 3.38
3) el. + quasi-el. n-scatt	several afm. Bragg reflections: $I(T) \sim M_{subl}^2(T)$	[70B1]
	(1, 0, 1): K_2NiF_4-type order $\rightarrow T_N = 38.41(7)\ K$ (1, 0, 1/2), 1 = odd: Ca_2MnO_4-type order $\rightarrow T_N = 38.37(7)\ K$	$\left.\right\}\left\{\right.$ see also text in Sect. 2.1 for the two types of magnetic ordering with further references
	$T_N(p)$ [$0 \leq p \leq 1.5\ GPa$]: see Fig. 1 of [94I1]	$p \mathrel{\hat{=}}$ hydrostatic pressure
4) EPR, NMR	$\Delta_0 S = 0.17(3)$	AFMR + ^{55}Mn-NMR [70W1, 71W, 73S1]
5) ^{19}F-NMR	F_I: $f_{NMR}(T) \sim M_{subl}(T)$	$^{19}F_I$-NMR [73W2]
6) inel. n-scatt.	$\boldsymbol{\omega}(\boldsymbol{q})$ for (ζ, 0, 0), (0.5, ζ, 0), (ζ, ζ, 0) at 4.5 K ($z = 4$, $S = 5/2$, $g = 2.00$)	[75A1, 77C3], $\zeta = q_x/a^* = q_y/a^*$ ($b^* \approx a^*$) $J_2 \mathrel{\hat{=}}$ next-nearest-neighbours exchange interaction
	$J = -2.761(11)\ cm^{-1} \mathrel{\hat{=}} -3.907(16)\ K$, $H_E = 58.17(24)\ T$ $J_2 = -0.048(7)\ cm^{-1} \mathrel{\hat{=}} -0.069(10)\ K$, $H_{E2} = 1.02(15)\ T$ $h_A = 0.0048$, $g\mu_B H_A = 0.26(4)\ cm^{-1}$, $H_A = 0.28(4)\ T$	$\left.\right\}\left\{\right.$ fit to the exp. data with linear spin-w. th., extended to include the nnn exchange interaction (cf. Eqs. 3.2, 3.14)
7) spin-wave analysis	exp. data included: $\nu_{AFMR}(T)$ and $M_{subl}(T)$	[73W2, 73W3]; ($\lvert J'/J \rvert \leq 8 \cdot 10^{-4}$)
	$J = -2.65(3)\ cm^{-1} \mathrel{\hat{=}} -3.81(5)\ K$, $H_E = 56.7\ T$, $J_2 \approx 0$ $T = 0$: $h_A = 0.0045$, $g\mu_B H_A = 0.241(4)\ cm^{-1}$, $H_A = 0.259\ T$	$\left.\right\}\left\{\right.$ parameter values according to linear spin-w. th. (cf. Eqs. 3.2–3.5, 3.6)
	$J = -2.57(3)\ cm^{-1} \mathrel{\hat{=}} -3.69(5)\ K$, $H_E = 55.0\ T$, $J_2 \approx 0$ $T = 0$: $h_A = 0.0047$, $g\mu_B H_A = 0.241(4)\ cm^{-1}$, $H_A = 0.259\ T$	$\left.\right\}\left\{\right.$ parameter values according to renorm. spin-w. th. (cf. Eqs. 3.2–3.5, 3.15)
	calc.: $\Delta_0 S = 0.171$, $H_{AD} = 0.248\ T$	[73W2]; $\Delta_0 S$: Eq. 3.19; H_{AD}: Eq. 3.12
	calc.: $\lvert J \rvert = 3.69\ K \rightarrow T_C^{(2)} = 36.5\ K$ ($T_N = 38.4\ K$)	[73W2]; $\lvert J \rvert \rightarrow T_C^{(2)}$: Eq. 3.29; see also [72J2]

Table 5. Data concerning Magnetic Properties *(continued)*

Compound	Characteristic magnetic parameters: J, H_E, H_A, H_0, M, χ, g, T_C, T_N etc. [definitions see Table 1, units are given below]	References, remarks
Rb$_2$MnF$_4$ (cont.)		
8) (H_0, T) phase diagram	observed critical point identified as bicritical point	n-scatt. [88C3, 93C2]; detailed discussion: Sect. 3.1.6
9) optical studies	optical transition $^6\mathrm{A}_1(\mathrm{S}) \rightarrow {}^4\mathrm{T}_{1g}(\mathrm{G})$ studied at 2 K	(17545–17700 cm^{-1}), magnon sideband [68I]
Rb$_3$Mn$_2$F$_7$	Antiferromagnet, $\boldsymbol{M}_{\mathbf{subl}} \parallel \boldsymbol{c}$ (magn. order see Fig. 2.4)	
meas. and anal. χ	$\chi_{\mathrm{powder}}(T)$ [4 K $\le T \le$ 270 K]	[76N1]
	$\chi(T > T_N)$: h.t.s. $\rightarrow J = -2.47(14)$ cm$^{-1} \mathrel{\hat{=}} -3.56(20)$ K	h.t.s.: Eqs. 3.26, 3.27; coeff. see [73R3]
	$H_A = 0.137(26)$ T	exp. value [76N1]
β-Cs$_2$MnF$_4$	Antiferromagnet, $\boldsymbol{M}_{\mathbf{subl}} \parallel \boldsymbol{c}$ (magn. order see Fig. 2.2)	
el. + inel. n-scatt.	$T_N(p)$ [$0 \le p \le 0.67$ GPa]: see Fig. 3 of [94I1]	$p \mathrel{\hat{=}}$ hydrostatic pressure
	$J = -4.30$ cm$^{-1} \mathrel{\hat{=}} -6.19$ K	estimated, preliminary inel. n-scatt. exp. at 7.5 K [94I1]
K$_2$FeF$_4$	Antiferromagnet, $\boldsymbol{M}_{\mathbf{subl}} \perp \boldsymbol{c}$ (magn. order see Fig. 2.6)	
1) meas. and anal. of χ	$\chi_\parallel(T)$, $\chi_\perp(T)$ [4.2 K $\le T \le$ 300 K]	χ: ^{19}F-NMR and magnetometer [82T3]; see also [69L1]
	$\chi(T > T_N)$: h.t.s.$\rightarrow J = -5.73(10)$ cm$^{-1} \mathrel{\hat{=}} -8.25(15)$ K, $g_a = 2.26(7)$	h.t.s.: Eqs. 3.26, 3.27; coeff. see [70L1, 90N]
	$T < T_N$: $\chi_\perp(T)$, $\chi_\parallel(T)$ calc. by renorm. spin-w. th.	parameter values: see spin-wave analysis
2) el. + quasi-el. n-scatt.	afm. Bragg reflections (1, 0, 0), (1, 0, 3): $I(T) \sim M^2_{\mathrm{subl}}(T)$ $\rightarrow T_N = 63.0(3)$ K	[80T2, 82T1]; see also Mössbauer study [78T2]
3) ^{19}F-NMR	F$_\mathrm{I}$: $f_{\mathrm{NMR}}(T) \sim M_{\mathrm{subl}}(T)$, $g_a = 2.25(7)$, $g_c = 2.12(10)$	^{19}F$_\mathrm{I}$-NMR [82T3]
4) Mössbauer study	asymmetry of the EFG $V_{xx} - V_{yy} = f(T) \ne 0$ for $T < T_N$ $\rightarrow E \ne 0 \rightarrow \widetilde{H}_A \ne 0 \rightarrow \nu_{\mathrm{AFMR,\,in\text{-}plane}} \ne 0$	[78T2, 80T3]; see also [81G1]
5) meas. ν_{AFMR}	$\left.\begin{matrix} T = 1.7\ \mathrm{K} \\ H_0 = 0 \end{matrix}\right\\} \left\\{\begin{matrix} h\nu_{\mathrm{AFMR,out\text{-}of\text{-}pl.}} = 47.7(8)\ \mathrm{cm}^{-1} \mathrel{\hat{=}} 68.6(12)\ \mathrm{K} \\ h\nu_{\mathrm{AFMR,in\text{-}plane}} = 18.7(8)\ \mathrm{cm}^{-1} \mathrel{\hat{=}} 26.9(12)\ \mathrm{K} \end{matrix}\right.$	$\left.\right\\}\left\\{\begin{matrix}\text{ir spectr. [82T1] and 1-magn. Raman sp. [78M1, 79M2]} \\ \nu_{\mathrm{AFMR}}\text{: Eq. 3.37; see also [80D]}\end{matrix}\right.$
	T-dependence of $\nu_{\mathrm{AFMR,out\text{-}of\text{-}pl.}}$ and AFMR LW	ir spectr., Raman sp. [78M1, 79M2], theory T-dep. [82G2]
	H_0-dependence of $\nu_{\mathrm{AFMR,out\text{-}of\text{-}pl.}}$ for $\boldsymbol{H_0} \parallel \boldsymbol{c}$, $\boldsymbol{H_0} \perp \boldsymbol{c}$	ir spectr. [80D]; see also [78M1, 79M2]

Table 5. Data concerning Magnetic Properties *(continued)*

Compound	Characteristic magnetic parameters: J, H_E, H_A, H_0, M, χ, g, T_C, T_N etc. [definitions see Table 1, units are given below]	References, remarks
K_2FeF_4 (cont.)		
6) inel. n-scatt.	$\omega(\boldsymbol{q})$ for (ζ_x, 0, 0) at 4.2 K (2 branches)	[82T1], $\zeta_x = q_x/a^*$; fit to the exp. data with renorm. spin-w. th.: parameter values see spin-wave analysis
	values of J, D, E: see spin-wave analysis, $J_2 \approx 0$	
7) spin-wave analysis	exp. data included: ν_{AFMR}, $\omega(\boldsymbol{q})$ and $M_{subl}(T)$	[80T2, 82T1, 82T2]
	($z = 4$, $S = 2$; g_c, g_a: see ^{19}F-NMR),	
	$J = -5.70(10)\ \mathrm{cm}^{-1} \mathrel{\hat{=}} -8.20(15)$ K	parameter values according to linear spin-w. th., cf. Eqs. 3.35, 3.36; $g\mu_B H_A = +2DS$, $g\mu_B \tilde{H}_A = -4ES$, cf. Eq. 3.37; further details see [80T2, 82T1]
	out-of-pl. anis.: $D = +2.99(7)\ \mathrm{cm}^{-1} \mathrel{\hat{=}} +4.30(10)$K	
	in-plane anis.: $E = -0.20(2)\ \mathrm{cm}^{-1} \mathrel{\hat{=}} -0.29(3)$ K	
	$J = -5.46(10)\ \mathrm{cm}^{-1} \mathrel{\hat{=}} -7.85(15)$ K, $\Delta_0 S = 0.171$	parameter values according to renorm. spin-wave th., definitions and details of the theory see [82T1]
	out-of-pl. anis.: $D = +3.96(7)\ \mathrm{cm}^{-1} \mathrel{\hat{=}} +5.70(10)$ K	
	in-plane anis.: $E = -0.34(2)\ \mathrm{cm}^{-1} \mathrel{\hat{=}} -0.49(3)$ K	
	calc.: $\Delta_0 S = 0.101$	[82T1]; $\Delta_0 S$ calc. by spin-w. theory, see also [82T1]
8) 2-magn. Raman L.	$T = 2.1$ K: peak pos. at 182.4(10) cm^{-1}	Raman sp. [77T2, 78M1, 79M2, 82T2]
	T-dependence of peak pos. and width	
	anal. of 2-magn. Raman L. using renorm. spin-w. th.	[77T2, 82T1, 82T2], parameter values: see spin-wave analysis
$K_3Fe_2F_7$	Antiferromagnet, $\boldsymbol{M}_{subl} \perp \boldsymbol{c}$	
Mössbauer study	$T_N = 93$ K, $J = -3.6(4)\ \mathrm{cm}^{-1} \mathrel{\hat{=}} 5.2(6)$ K	[80T3], J calc. from $g\mu_B H_{MF} = 2z \lvert J \rvert \langle S_x \rangle_T$ (cf. Eq. 3.61)
	asymmetry of the EFG $V_{xx} - V_{yy} = f(T) \neq 0$ for $T < T_N$	[80T3]; see also [81G1]
	$\rightarrow E \neq 0 \rightarrow \tilde{H}_A \neq 0 \rightarrow \nu_{AFMR,in\text{-}plane} \neq 0$	
Rb_2FeF_4	Antiferromagnet, $\boldsymbol{M}_{subl} \perp \boldsymbol{c}$ (magn. order see Fig. 2.6)	
1) meas. and anal. of χ	$\chi(T)$ for $\boldsymbol{H_0} \parallel (1, 0, 0)$, $\parallel (1, 1, 0)$, $\parallel (0, 0, 1)$ [4 K $\leq T \leq$ 300 K]	[68W1]
	max. χ at $T_{max} = 90$ K $\rightarrow J = -5.06\ \mathrm{cm}^{-1} \mathrel{\hat{=}} -7.25$ K	$T_{max} \rightarrow J$: Eq. 3.28; see also Table IX in [90N]
2) Mössbauer study	asymmetry of the EFG $V_{xx} - V_{yy} = f(T) \neq 0$ for $T < T_N$	[78T2, 80T3]; see also [81G1]
	$\rightarrow E \neq 0 \rightarrow \tilde{H}_A \neq 0 \rightarrow \nu_{AFMR,in\text{-}plane} \neq 0$	

Table 5. Data concerning Magnetic Properties *(continued)*

Compound	Characteristic magnetic parameters: J, H_E, H_A, H_0, M, χ, g, T_C, T_N etc. [definitions see Table 1, units are given below]	References, remarks
Rb_2FeF_4 (cont.)		
3) el. + quasi-el. n-scatt	afm. Bragg reflections (1, 0, 0), (1, 0, 4): $I(T) \sim M^2_{\text{subl}}(T)$ magn. Bragg rod (1, 0, 0.25) $\rightarrow T_N = 56.3(2)$ K	[70B1]
	calc.: $\lvert J \rvert = 7.27$ K $\rightarrow T_C^{(2)} = 48.0$ K ($T_N = 56.3$ K)	[72J2]; $\lvert J \rvert \rightarrow T_C^{(2)}$: Eq. 3.29
4) meas. ν_{AFMR}	$T = 2$ K $h\nu_{\text{AFMR,out-of-pl.}} = 37.6(5)\ \text{cm}^{-1} \mathrel{\hat{=}} 54.1(7)$ K $H_0 = 0$ $h\nu_{\text{AFMR,in-plane}}$: not determined	ir spectr. and 1-magn. Raman sp. [78M1, 79M2] ν_{AFMR}: Eq. 3.37
	T-dependence of $\nu_{\text{AFMR,out-of-pl.}}$ and LW H_0-dependence of $\nu_{\text{AFMR,out-of-pl.}}$	ir spectr. [78M1, 79M2], theory T-dependence [82G2]
5) 2-magn. Raman L.	$T = 2$ K: peak pos. at 160.5 cm^{-1} T-dependence of peak pos. and width	Raman sp. [78M1, 79M2]
	anal. of 2-magn. Raman L. together with ν_{AFMR} data: ($z = 4$, $S = 2$, $g_c = 2.5$)	[78M1, 79M2]
	$J = -5.05\ \text{cm}^{-1} \mathrel{\hat{=}} -7.27$ K out-of-pl. anis.: $D = +2.2\ \text{cm}^{-1} \mathrel{\hat{=}} +3.2$ K in-plane anis.: $\tilde{H}_A \ll H_A$ (not determined)	parameters in theoretical calculation using linear spin-w. th. (cf. Eqs. 3.35–3.37a), $g\mu_B H_A = 2\,DS$, in-plane anisotropy defined as staggered field $\tilde{H}_A$
K_2CoF_4	Antiferromagnet, $\boldsymbol{M}_{\textbf{subl}} \parallel \boldsymbol{c}$ (magn. order see Fig. 2.2)	
1) meas. and anal. of χ	$\chi_{\parallel}(T)$, $\chi_{\perp}(T)$ [4 K $\le T \le$ 300 K], $\chi_{\parallel} > \chi_{\perp}$ at all $T > T_N$	[69B1], see also [63S, 69L1]
	$\chi_{\parallel,\max}/\chi_{\parallel}(T_N)$, $\chi_{\perp,\max}/\chi_{\perp}(T_N)$, $\chi_{\perp}(T_N)/\chi_{\perp}(0)$ etc.	exp. values close to exact results (cf. Eq. 3.68) [69B1]
	$J_{\parallel} = -67.4(3)\ \text{cm}^{-1} \mathrel{\hat{=}} -97.0(5)$ K, $g_c = 6.40(5)$ $J_{\perp} = -20.6(13)\ \text{cm}^{-1} \mathrel{\hat{=}} -29.6(19)$ K, $g_a = 3.21$ $J_{\perp}/J_{\parallel} = 0.305(20)$	[69B1]: model calc. with eff. spin 1/2 Ham. (Eq. 3.62) for strongly anisotropic uniaxial afm. (Co-compounds = good realization of the 2D-Ising model)
	$J = -13.4\ \text{cm}^{-1} \mathrel{\hat{=}} -19.3$ K, calc. with $\langle S_z \rangle_0 = 1.12(7)$	J: Eq. 365a (for comp. with other compounds)
	calc.: $\lvert J_{\parallel} \rvert = 97$ K, $S = \frac{1}{2} \rightarrow T_C^{(2)} = 29.1$ K ($T_N = 107$ K)	[72J2], $\lvert J \rvert \rightarrow T_C^{(2)}$: Eq. 3.29

Table 5. Data concerning Magnetic Properties *(continued)*

Compound	Characteristic magnetic parameters: J, H_E, H_A, H_0, M, χ, g, T_C, T_N etc. [definitions see Table 1, units are given below]	References, remarks
K_2CoF_4 (cont.)		
2) el. + quasi-el. n-scatt.	magn. Bragg reflections: $\sqrt{I} \sim M_{subl} \sim [1 - \sinh^{-4}(J_{\parallel}/k_B T)]^{1/8}$ magn. Bragg rod: $I(T) \to T_N = 107.85(5)$ K; $\lvert J'/J_{\parallel} \rvert < 10^{-3}$	[74I1, 74I2]; $M_{subl}(T)/M_{subl}(0)$: Eq. 3.66 (exact solution for 2D Ising model)
3) meas. ν_{AFMR}	$H_0 = 0$, $T = 4$ K: $h\nu_{AFMR} = 206.5\ \mathrm{cm}^{-1} \mathrel{\hat{=}} 297.1$ K T-dependence of ν_{AFMR} and AFMR LW	1-magn. Raman sp. [79M1, 79M2]; see also [76G2]; ν_{AFMR}; Eq. 3.64
4) excitons	excitations within the 12 levels from $^4\Gamma_4^+(O_h)$ of Co^{2+}	Raman sp. [79G5, 80G3]
	fit to the exp. data: $B_2^0 = -425\ \mathrm{cm}^{-1}$, $\lambda = -228\ \mathrm{cm}^{-1}$ $J = -11.55\ \mathrm{cm}^{-1} \mathrel{\hat{=}} -16.62$ K, $\langle S_z \rangle_0 = 1.17$	exciton model including crystal field, spin-orbit coupling (B_2^0, λ: Eq. 3.33) and molecular field (Eq. 3.61)
	$J_{\parallel} = -62.8\ \mathrm{cm}^{-1} \mathrel{\hat{=}} -90.4$ K, $g_c = 3.7$ $J_{\perp} = -35.5\ \mathrm{cm}^{-1} \mathrel{\hat{=}} -51.1$ K, $J_{\perp}/J_{\parallel} = 0.57$	derivation of the parameters of the eff. spin 1/2 Hamiltonian (Eq. 3.62) from the exiton data
5) ^{19}F-NMR	$f_{NMR}(T) \sim M_{subl}(T) \sim [1 - \sinh^{-4}(J_{eff}/k_B T)]^{1/8}$ with $J_{eff} = -66.5\ \mathrm{cm}^{-1} \mathrel{\hat{=}} -95.7$ K	$^{19}F_I$-NMR, $J_{eff} \approx 0.94\ J_{\parallel}$ [85D2]; see also [68F2, 72B2]; $M_{subl}(T)/M_{subl}(0)$: Eq. 3.66 (2D Ising model)
6) 2-magn. Raman L.	$T = 4$ K: peak pos. at 468 cm^{-1} T-dependence of peak pos. and width	Raman sp. [79M1, 79M2]
	anal. of 2-magn. Raman L. together with ν_{AFMR} data ($z = 4$, $S = \frac{1}{2}$)	[79M1, 79M2]
	$J_{\parallel} = -60.1\ \mathrm{cm}^{-1} \mathrel{\hat{=}} -86.5$ K, $J_{\perp} = -30.8\ \mathrm{cm}^{-1} \mathrel{\hat{=}} -44.3$ K, $J_{\perp}/J_{\parallel} = 0.512$	parameters in theoretical calculations based on linear spin-w. th. with eff. spin1/2 Hamiltonian (Eq. 3.62)
7) optical studies	absorption spectrum 6700–25500 cm^{-1} ($T \approx 295$ K), transitions within the d^7-configuration	[68T1]
	absorption spectrum 5000–50000 cm^{-1} ($T \approx 4.2$ K)	[69M2]
	absorption edge near 5.7 eV ($T \approx 295$ K) reflectance spectra 10–35 eV ($T \approx 295$ K)	optical study with synchrotron radiation [85S1]
Rb_2CoF_4	Antiferromagnet, $\boldsymbol{M}_{\mathbf{subl}} \parallel \boldsymbol{c}$ (magn. order see Fig. 2.2)	
1) el. + quasi-el. n-scatt.	several afm. Bragg refl.: $I \sim M_{subl}^2 \to T_N = 103.025(10)$ K	[73S4, 74S1, 74S3]

Table 5. Data concerning Magnetic Properties *(continued)*

Compound	Characteristic magnetic parameters: J, H_E, H_A, H_0, M, χ, g, T_C, T_N etc. [definitions see Table 1, units are given below]	References, remarks
Rb_2CoF_4 (cont.)		
2) meas. ν_{AFMR}	$H_0 = 0$, $T = 4.2$ K: $h\nu_{AFMR} = 211$ cm^{-1} $\hat{=}$ 304 K T-dependence of ν_{AFMR}	} 1-magn. Raman sp. [82S2]; ν_{AFMR}: Eq. 3.64
3) meas. and anal. of χ	$\chi_\parallel(T)$, $\chi_\perp(T)$ [4 K $\le T \le$ 300 K], $\chi_\parallel > \chi_\perp$ at all $T > T_N$	[69B1]
	$\chi_{\parallel,max}/\chi_\parallel(T_N)$, $\chi_{\perp,max}/\chi_\perp(T_N)$, $\chi_\perp(T_N)/\chi_\perp(0)$ etc.	exp. values close to exact results (cf. Eq. 3.68) [69B1]
	$J_\parallel = -63.3(3)$ cm^{-1} $\hat{=}$ $-91.0(5)$ K, $g_c = 7.02(5)$ $J_\perp = -14.6(9)$ cm^{-1} $\hat{=}$ $-20.9(14)$ K, $g_a = 3.07$ $J_\perp/J_\parallel = 0.230(15)$	[69B1]: model calc. with eff. spin 1/2 Ham. (Eq. 3.62) for strongly anisotropic uniaxial afm. (Co-compounds = good realization of the 2D-Ising model)
	$J = -10.5$ cm^{-1} $\hat{=}$ -15.1 K, calc. with $\langle S_z\rangle_0 = 1.23(7)$	J: Eq. 3.65a (for comp. with other compounds)
	calc.: $\lvert J_\parallel\rvert = 91$ K, $S = \frac{1}{2} \to T_C^{(2)} = 27.3$ K ($T_N = 101$ K)	[72J2]; $\lvert J\rvert \to T_C^{(2)}$: Eq. 3.29
4) excitons	excitations within the 12 levels from $^4\Gamma_4^+$ (O_h) of Co^{2+}	Raman sp. [76G2, 79G5, 80G3]
	fit to the exp. data: $B_2^0 = -635$ cm^{-1}, $\lambda = -228$ cm^{-1} $J = -9.65$ cm^{-1} $\hat{=}$ -13.88 K, $\langle S_z\rangle_0 = 1.24$	exciton model including crystal field, spin-orbit coupling (B_2^0, λ: Eq. 3.33) and molecular field (Eq. 3.61)
	$J_\parallel = -59.6$ cm^{-1} $\hat{=}$ -85.8 K, $g_c = 4.45$ $J_\perp = -26.6$ cm^{-1} $\hat{=}$ -38.3 K, $J_\perp/J_\parallel = 0.45$	values of the parameters of the eff. spin 1/2 Ham. (Eq. 3.62) as derived from the exciton data
5) ^{19}F-NMR	$^{19}F_I$-NMR $\to T_N = 99.8$ K	[72B2]
6) inel. n-scatt	$\omega(\boldsymbol{q})$ for (ζ_x, 0, 0) at 6.0(1) K ($z = 4$, $S = \frac{1}{2}$; g_c, g_a: see meas. and anal. of χ)	[78I2]; $\zeta_x = q_x/a^*$
	$J_\parallel = -62.3(5)$ cm^{-1} $\hat{=}$ $-89.7(7)$ K $J_\perp = -34.5(14)$ cm^{-1} $\hat{=}$ $-49.6(20)$ K, $J_\perp/J_\parallel = 0.553$	fit to the exp. data using linear spin-w. th. and the eff. spin 1/2 Hamiltonian (Eq. 3.62); $\hbar\omega_q$: Eq. 3.63
	calc.: $T_N = 100.9$ K $\to \lvert J_\parallel\rvert = 88.9(2)$ K $\hat{=}$ 61.8(2) cm^{-1}	$\lvert J_\parallel\rvert$ calc. using Eq. 3.67 (2D-Ising model)
7) 2-magn. Raman L.	$T = 4$ K: peak pos. at 452 cm^{-1}	Raman sp. [82S2]
	anal. of 2-magn. Raman L. together with ν_{AFMR} data: $g_c\mu_B H_{MF} = 140$ cm^{-1}, $\langle S_z\rangle_0 = 1.27 \to J = -13.8$ cm^{-1}	} [82S2]: parameters in theoretical calculation using a mean field approach H_{MF}: Eq. 3.61

Table 5. Data concerning Magnetic Properties *(continued)*

Compound	Characteristic magnetic parameters: J, H_E, H_A, H_0, M, χ, g, T_C, T_N etc. [definitions see Table 1, units are given below]	References, remarks
Rb_2CoF_4 (cont.)		
8) optical studies	2 electr. dipole lines (magnon sidebands) in π-polarization at 22763 cm^{-1} and 22950 cm^{-1}, corresponding 0-magnon in σ-polarization, Zeeman splitting in fields up to 30 T	[83H3]
	absorption edge near 5.7 eV ($T \approx 295$ K) reflectance spectra 12–27 eV ($T \approx 295$ K)	optical study with synchrotron radiation [85S1]
K_2NiF_4	Antiferromagnet, $\boldsymbol{M}_{\mathbf{subl}} \parallel \boldsymbol{c}$ (magn. order see Fig. 2.2)	
1) el. + quasi-el. n-scatt.	afm. Bragg refl. (1, 0, 0): $I(T) \sim M^2_{\text{subl}}(T) \rightarrow T_N = 97.1$ K	[69B2, 70B1]
2) EPR, NMR	$\Delta_0 S = 0.20(3)$	AFMR/EPR + ^{55}Mn-NMR [71W]
3) meas. and anal. of χ	$\chi_{\parallel}(T)$, $\chi_{\perp}(T)$ [4 K $\le T \le$ 300 K], $T_N = 100.5$ K	[63S, 67L, 69L1, 69M3, 70M], see also [62R, 63G]
	$\chi(T > T_N)$: h.t.s. $\rightarrow J = -35.1\ cm^{-1} \mathrel{\hat{=}} -50.5$ K	[67L, 73J3]; h.t.s.: Eqs. 3.26, 3.27; coeff. see [70L1, 90N]
	$\chi_{\perp}(T = 0) \rightarrow J = -34.8\ cm^{-1} \mathrel{\hat{=}} -50.1$ K	[70M]; $\chi_{\perp}(T = 0)$: Eq. 3.24, $\chi_{\perp}(T)$: Eq. 3.23
	$\chi_{\parallel}(T < T_N) \rightarrow J = -38.2\ cm^{-1} \mathrel{\hat{=}} -55.0$ K	[69M3]; $\chi_{\parallel}(T)$: Eq. 3.22, fit to the exp. data
	$H_{SF} = 19.0\ T \rightarrow H_A = 0.61$ T	h.m.f. exp. at $T = 4.2$ K [70M], $H_{SF} \rightarrow H_A$: Eq. 3.38
4) meas. ν_{AFMR}	$H_0 = 0$, $T = 4.2$ K: $h\nu_{\text{AFMR}} = 19.6(2)\ cm^{-1} \mathrel{\hat{=}} 28.2(3)$ K	ir spectr. [71N, 74N1], see also [70B4]; ν_{AFMR}: Eq. 3.10
	$T = 4.2$ K: $\nu_{\text{AFMR}} = 19.7\ cm^{-1}$, $H_{SF} = 18.3$ T, $g_c = 2.31(4)$	AFMR 70–120 GHz, pulsed fields up to 19 T [72Y1]
	T-dependence of ν_{AFMR} [4 K $\le T \le$ 75 K]	ir spectr. [70B4, 74N1]
	calc.: T-dependence of ν_{AFMR} and of M_{subl}	using renorm. spin-w. th., details see [74N1]
5) inel. n-scatt.	$\omega(\boldsymbol{q})$ for (ζ_x, 0, 0) at 5.0 K: $J = -38.8(2)\ cm^{-1} \mathrel{\hat{=}} -55.9(3)$ K	[69S2, 70B3] $\zeta_x = q_x/a^*$
	$J_2 \approx -0.2\ cm^{-1} \mathrel{\hat{=}} -0.3$ K, $g_c = 2.22(6)$, ($z = 4$, $S = 1$) $h_A = 0.0019$, $g\mu_B H_A = 0.59\ cm^{-1}$, $H_A = 0.57$ T	parameters from the fit to the exp. data using linear spin-w. th. (cf. Eqs. 3.2–3.5, 3.6)

Table 5. Data concerning Magnetic Properties *(continued)*

Compound	Characteristic magnetic parameters: J, H_E, H_A, H_0, M, χ, g, T_C, T_N etc. [definitions see Table 1, units are given below]	References, remarks
K_2NiF_4 (cont.)		
6) spin-wave analysis	exp. data included: $\nu_{AFMR}(T)$, $M_{subl}(T)$ and $\omega(\boldsymbol{q})$	[69S2, 73W2], see also renorm. spin-w. th. [74R3, 75R1]
	$J = -38.3(3)\ \mathrm{cm^{-1}} \hat{=} 55.1(4)\ \mathrm{K}$, $J_2 \approx 0$, $\lvert J'/J \rvert \le 3 \cdot 10^{-4}$ $T = 0$: $h_A = 0.00194$, $g\mu_B H_A = 0.59\ \mathrm{cm^{-1}}$, $H_A = 0.573\ \mathrm{T}$	parameter values according to linear spin-w. th. (cf. Eqs. 3.2–3.5, 3.6)
	$J = -35.5(3)\ \mathrm{cm^{-1}} \hat{=} 51.1(4)\ \mathrm{K}$, $J_2 \approx 0$, $\lvert J'/J \rvert \le 3 \cdot 10^{-4}$ $T = 0$: $h_A = 0.00209$, $g\mu_B H_A = 0.59\ \mathrm{cm^{-1}}$, $H_A = 0.573\ \mathrm{T}$	parameter values according to linear spin-w. th. (cf. Eqs. 3.2–3.5, 3.15)
	calc.: $\Delta_0 S = 0.177$, $H_{AD} = 0.128\ \mathrm{T}$	[73W2]; $\Delta_0 S$: Eq. 3.19; H_{AD}: Eq. 3.12
	calc.: $\lvert J \rvert = 51.1\ \mathrm{K} \rightarrow T_C^{(2)} = 92\ \mathrm{K}$ ($T_N = 97.1$ K)	[73W2]; $\lvert J \rvert \rightarrow T_C^{(2)}$: Eq. 3.29, see also [72J2]
7) 2-magn. Raman L.	$T \approx 4$ K: peak pos. at 525 cm^{-1}	Raman sp. [74T]; see also [70F, 71C3]
	theory: shape of 2-magn. Raman line	[71C2, 71C3]
	T-dependence of peak pos. and width	Raman sp. [70F, 74T, 76P2, 77P1], see also [70S4]
8) ^{19}F-NMR	F_I: $f_{NMR}(T) \sim M_{subl}(T)$	$^{19}F_I$ -NMR [70W2, 71W, 73W2]
	F_I, F_{II}: determination of T_1 for $H_0 = 0$ [$1.5\ \mathrm{K} \le T \le 55\ \mathrm{K}$], for $\boldsymbol{H_0} \perp \boldsymbol{c}$ [$1.5\ \mathrm{K} \le T \le 20\ \mathrm{K}$] and for $\boldsymbol{H_0} \parallel \boldsymbol{c}$ [$T = 4.2$ K]	[78W2, 79W1, 80W1, 81W4]; discussion of the mechanism for T_1: see Sect. 3.1.2
9) high press. exp.	measurement of the pressure dependence of the 2-magn. Raman L. ($\nu \sim J$) at 10 K and of the lattice parameter a at 295 K $\rightarrow J \sim (a_{nn})^{-\alpha}$ with $\alpha = 9.5(5)$	[93S1]: Raman sp. and x-ray diffr. under hydrostatic pressures up to $p = 9.5$ GPa; results yield $J(p)$ and $a_{nn} = a(p) \rightarrow J(a_{nn}) \sim (a_{nn})^{-\alpha}$, see: Eq. 3.1; cf. Sect. 3.1.1
10) excitons	various exciton lines 6000–18000 cm^{-1}	Raman sp. [78A3, 88A2]
11) ultrason. study	elast. const. C_{11}, C_{33}, C_{44}, C_{66} for $0 \le T \le 300$ K, small anomaly in C_{11} near $T_N = 92.2$ K	[76G3]: sound velocity measured with a phase compensation method; $\rho = 3.37\ \mathrm{g/cm^3}$
12) optical studies	absorption spectrum and MCD at 295 K	(20000–28000 cm^{-1}) [73F1]
	absorption spectra 5000–40000 cm^{-1} (77 K, 295 K)	[73P1]
	NIR absorption spectrum 6500–9500 cm^{-1} at 1.8 K T-dependence of exciton line at 6898 cm^{-1}	[74K2], $g_c = 2.27(4)$
	absorption spectrum at 90 K and 300 K ($\boldsymbol{E} \perp \boldsymbol{c}$)	(5000–28000 cm^{-1}) [76I3]
	absorption edge near 6.4 eV ($T \approx 295$ K) reflectance spectra 10–35 eV ($T \approx 295$ K)	optical study with synchroton radiation [85S1]

Table 5. Data concerning Magnetic Properties *(continued)*

Compound	Characteristic magnetic parameters: J, H_E, H_A, H_0, M, χ, g, T_C, T_N etc. [definitions see Table 1, units are given below]	References, remarks
$K_3Ni_2F_7$	Antiferromagnet, $\boldsymbol{M}_{\mathbf{subl}} \parallel \boldsymbol{c}$ (magn. order see Fig. 2.4)	
1) 2-magn. Raman L.	$T = 35$ K: peak pos. at 610 cm^{-1}	Raman sp. [72F1]
	anal. of 2-magn. Raman L.:	[80P2]: exp. data for $T = 35$ K, theory for $T \to 0$
	$J\left(1+\frac{25\,H_A}{24\,H_E}\right) = -33.2(2)\ cm^{-1} \mathrel{\hat{=}} -47.7(3)$ K; $T_N \approx 130$ K	parameters in theoretical calculations, details see [80P2]
2) optical studies	absorption spectrum and MCD at 6 K	(15000–16500 cm^{-1}) [72F1]
	absorption spectrum (295 K) and MCD (6 K, 295 K)	(14500–17500 cm^{-1}) [74P1]
Rb_2NiF_4	Antiferromagnet, $\boldsymbol{M}_{\mathbf{subl}} \parallel \boldsymbol{c}$ (magn. order see Fig. 2.2)	
1) meas. ν_{AFMR}	$H_0 = 0$, $T = 4.2$ K: $h\nu_{AFMR} = 34.5(2)\ cm^{-1} \mathrel{\hat{=}} 49.6(3)$ K exp.: T-dependence of ν_{AFMR} and AFMR LW	ir spectr. [74N1]; ν_{AFMR}: Eqs. 3.9 and 3.10
	calc. T-dependence of ν_{AFMR} and M_{subl}	using renorm. spin-w. th., details see [74N1]
2) meas. and anal. of χ	$\chi_\parallel$, $\chi_\perp$ [4 K $\le T \le$ 300 K]	[70M], see also [62R, 73F1]
	$\chi_\perp(T=0) \to J = -29.1\ cm^{-1} \mathrel{\hat{=}} -41.8$ K, $\Delta_0 S = 0.19$	[70M]; $\chi_\perp(T=0)$: Eq. 3.24; calc. $\Delta_0 S$: [73J3]
	$H_{SF} = 35.0$ T $\to H_A = 2.5$ T	h.m.f. exp. at $T = 4.2$ K [70M], $H_{SF} \to H_A$: Eq. 3.38
3) ^{19}F-NMR	T-dependence of NMR LW $\to T_N = 90.4$ K	NMR on powder samples [69M3]
4) $\omega(\boldsymbol{q})$ model calculation	$T_N = 91$ K, $J = -33(2)\ cm^{-1} \mathrel{\hat{=}} -48(3)$ K $g\mu_B H_A = 2.26(14)\ cm^{-1} \mathrel{\hat{=}} 3.2(2)$ K	[75A1]: value of J estimated from existing data, incl. scaling from K_2NiF_4; H_A from $h\nu_{AFMR}$ using $H_E = 2z\,S\,J$
	calc.: $\lvert J \rvert = 48.2$ K $\to T_C^{(2)} = 86.7$ K ($T_N = 97.03$ K)	[72J2]; $\lvert J \rvert \to T_C^{(2)}$: Eq. 3.29; T_N: see [80H4, 81I3]
5) optical studies	absoprtion spectra and MCD at 50 K, 102 K, 295 K	(20000–28000 cm^{-1}) [73F1], see also [74P1]
	absorption spectra 5000–40000 cm^{-1} (77 K, 295 K)	[73P1]
	absorption spectra at 90 K and 300 K ($\boldsymbol{E} \perp \boldsymbol{c}$)	(5000–28000 cm^{-1}) [76I3]
Tl_2NiF_4	only few and incomplete data on magnetic properties	[69M3]

Table 5. Data concerning Magnetic Properties *(continued)*

Compound	Characteristic magnetic parameters: J, H_E, H_A, H_0, M, χ, g, T_C, T_N etc. [definitions see Table 1, units are given below]	References, remarks
K_2CuF_4	Ferromagnet, $\mathbf{M} \perp \mathbf{c}$ (magn. order see Fig. 3.27)	
1) meas. and anal. of χ	$\chi(T)$ for $\mathbf{H_0} \parallel \mathbf{a}, \parallel \mathbf{c}$ [$20\ \mathrm{K} \le T \le 300\ \mathrm{K}$], $T_C = 6.25$ K	[72Y2], see also [69L1, 70Y1]
	$\chi(T > T_C)$: h.t.s. $\rightarrow J = 7.8\ \mathrm{cm}^{-1} \mathrel{\hat{=}} 11.2$ K ($S = 1/2$)	h.t.s.: Eqs. 3.26, 3.27; coeff. see [67B2, 90N]
	calc.: $H_{AD} = 0.090$ T	[72Y2]; formulae for H_{AD}: see also [72Y2]
2) EPR	$g_a = g_b = 2.284$, $g_c = 2.088$	[84G1, 84G2], see also [72Y2, 74Y1, 81R1, 83Y3, 95S1]
3) n-diffraction	magn. contribution to (0, 0, l) Bragg refl. [l = 4, 10] $I_{magn}(T) \sim M^2(T) \rightarrow T_C = 6.25$ K	[72H2, 73H3], see also [79H2, 81H3]
4) NMR	^{63}Cu-, ^{19}F$_I$-NMR: $f_{NMR}(H_0, T) \sim M(H_0, T)$ a) $M(H_0, T)$ for $\boldsymbol{H_0} \perp \boldsymbol{c}$; b) $M(T)$ for $H_0 = 0$: $C_M = 0.02972\ \mathrm{K}^{-3/2}$	[73K2, 74K4], see also [73D3]; theory: a) renorm. spin-w. th., b) data fitted to Eq. 3.78
	^{63}Cu-, ^{65}Cu-NMR: $f_{NMR}(T) \sim M(T)$ [$0.03\ \mathrm{K} \le T \le 1.9\ \mathrm{K}$] $T > 1$ K: $C_M = 0.0294\ \mathrm{K}^{-3/2}$ (^{63}Cu), $C_M = 0.0313\ \mathrm{K}^{-3/2}$ (^{65}Cu)	[90F2], exp. data fitted to Eq. 3.78 ($T \ge 1$ K), to Eq. 3.76 ($0.1\ \mathrm{K} \le T \le 1$ K) and to Eq. 3.77 ($T \le 0.1$ K)
	^{19}F$_I$-, ^{19}F$_{II}$-NMR: determination of T_1, T_2 [$1.65\ \mathrm{K} \le T \le 4.3\ \mathrm{K}$]	[76D6], see also [77K5]; discussion of T_1: Sect. 3.1.2
5) FMR	8.9 GHz, $\boldsymbol{H_0} \perp \boldsymbol{c} \rightarrow H_A(T)$ [$1.2\ \mathrm{K} \le T \le 4.2\ \mathrm{K}$], $T = 0$: $H_A^{\Delta} = 0.230$ T, $H_A = 0.210$ T, $g_a\mu_B H_A = 0.322$ K	[74Y1]; H_A: Eq. 3.96; H_A^{Δ}: Eq. 3.109a $\nu_{FMR} \rightarrow H_A(T)$: Eqs. 3.105 ($\boldsymbol{H_0} \parallel \boldsymbol{a}$), 3.106 ($\boldsymbol{H_0} \parallel \boldsymbol{b}$)
	9 GHz, $T = 1.2$ K: $H_{res}(\beta)$ and $\Delta H_{FMR}(\beta)$	[89A2], see also [81Y]; $\boldsymbol{H_0} \perp \boldsymbol{c}$, $\beta = \angle(\boldsymbol{H_0}, \boldsymbol{a})$, $\boldsymbol{a} \parallel x$-axis
	$100\ \mathrm{MHz} \le \nu \le 4.5$ GHz, for $\boldsymbol{H_0} \parallel \boldsymbol{c}$, $\boldsymbol{H_0} \perp \boldsymbol{c}$ [$1.2\ \mathrm{K} \le T \le 20\ \mathrm{K}$]	[89D2, 90D3], see also [84G1, 84G2]
	determination of $H_C(T)$ [$\boldsymbol{H_0} \parallel \boldsymbol{c}$], $H_A(T)$, $M(T)$ $T = 0$: $H_A^{\Delta} = H_C = 0.243(3)$ T, $H_A = 0.122$ T, $M = M_0 = 0.1234$ T	ν_{FMR}: Eqs. 3.105, 3.106, 3.108 and 3.109; H_A: Eq. 3.96; H_A^{Δ}: Eq. 3.109a; M_0: Eqs. 3.75a–3.76
	FMR by Brillouin scatt.: uniform and magnetostatic modes	[80B6], $\omega(\boldsymbol{q})$: Eqs. 3.122–3.124
	magnetostatic modes: $\nu = 9.27$ GHz, $T = 1.45$, 2.5 K	[84G1, 84G2]; theory see: [65D, 65J, 74Y2]
	magnetic polaritons: $\nu = 66.82$, 87.95 GHz, $T = 4.2$ K	[84K2, 84K3]
6) parallel pumping	subthr. p. p. (8.9, 35, 73 GHz) $\rightarrow H'_E(T)$ [$1.2\ \mathrm{K} \le T \le 4.2\ \mathrm{K}$] $T = 0$: $H'_E = 11.5$ mT, $g_a\mu_B H'_E = 0.0177$ K, $J' = 0.0022$ K	[73Y2, 74Y1, 76Y2]; p. p.: Eqs. 3.116–3.121; $\omega(\boldsymbol{q})$: Eqs. 3.122–3.124
	subthr. p. p.: observation of magnon density of states	[76Y2]; exp. data comp. to calc. magnon density of states
	subthr. p. p. ($\omega_p/2\pi = 9.45$ GHz) at 4.2, 8.1, 15.8, 31.2 K	[82Y1]; exp. data different for $T < T_C$ and for $T > T_C$

Table 5. Data concerning Magnetic Properties *(continued)*

Compound	Characteristic magnetic parameters: J, H_E, H_A, H_0, M, χ, g, T_C, T_N etc. [definitions see Table 1, units are given below]	References, remarks
K_2CuF_4 (cont.)		
6) parallel pumping (cont.)	saturation of parallel pumped magnons	[80Y1]
	spin-wave linewidth: $\Delta H_q(T)$ reflects the 4-fold crystal symmetry $\to \hat{H}_A = 0.5$ mT ($T = 0$), $\hat{H}_A \to 0$ ($T \approx 4$ K)	[81Y], see also [78Y1]; p. p. study for various directions of H_0 in the basal plane [1.4 K $\le T \le$ 4.2 K]
	chaos: spin-wave instability by perpendicular pumping	[87Y1]
7) inel. n-scatt.	$\omega(\boldsymbol{q})$ for (ζ, ζ, 0) at $T = 2$ K: $J = 7.90$ cm^{-1} $\hat{=}$ 11.36 K	[76F, 78M2], see also [76M3], $\zeta = q_{x0}/a^* = q_{y0}/a^*$
	$\omega(\boldsymbol{q})$ for (ζ_{x0}, 0, 0) at $T = 1.05$ K: $J = 8.29$ cm^{-1} $\hat{=}$ 11.93 K	[83H4]; $\zeta_{x0} = q_{x0}/a^*$, $S = 1/2$, $z = 4$, $z' = 8$
	$J_A = 0.062$ cm^{-1} $\hat{=}$ 0.089 K, $h_A = 0.0075$, $H_A = 0.232$ T $J' = 0.0015$ cm^{-1} $\hat{=}$ 0.0022 K, $h'_E = 3.7 \cdot 10^{-4}$, $H'_E = 11.5$ mT	fit of the exp. data to $\mathcal{H}$ (Eq. 3.69) with linear spin-w. th. (cf. Eqs. 3.71–3.73); H_E, H_A, H'_E : Eq. 3.96
8) el. + quasi-el. n-scatt.	determination of J' from $\chi(\boldsymbol{q})$ near T_C $J'/J = 1.65 \cdot 10^{-4}$, $J' = 0.0014$ cm^{-1} $\hat{=}$ 0.0020 K	$\chi(q_{x0}, q_{y0}, q_{z0})$: Eqs. 4.55–4.51 [73H3]
	polarized neutrons $\to$ magn. form factor $f(\boldsymbol{K})$ for Cu^{2+}	[76A6]
9) thermal conductivity	exp. study of $\lambda(T, H_0)$ [2 K $\le T \le$ 70 K, $H_0 = 0.09$ T]	[76M2], heat transport due to 2D magnons
10) optical studies	absorption bands near 7900, 9500, 12300 cm^{-1}	[75L7], crystal field transitions
	Faraday rotation 20000–40000 cm^{-1}	[76L2]
	absorption spectrum 5000–16000 cm^{-1}; MCD, MLD; determination of J in excited state (8766 cm^{-1})	[77F1, 79F1], see also [74K3, 75K2]
	LMB and Faraday rotation: study of fm. stripe domains	[80K2, 82N1, 87M1]; diffr. theory: [81K5, 82N1, 82N2]
	absorption 5000–17000 cm^{-1}, MCD, Zeeman spectra	[90R2], 2 zero-phonon lines (magnetic dipole origin)
Rb_2CuF_4	Ferromagnet, $\boldsymbol{M} \perp \boldsymbol{c}$ (magn. order see Fig. 3.27)	
1) meas. and anal. of χ	$\chi(T)$ for $\boldsymbol{H_0} \parallel \boldsymbol{c}$, $\boldsymbol{H_0} \perp \boldsymbol{c}$ [1.5 K $\le T \le$ 8 K] $\to T_C = 6.05(9)$ K	[88D1], see also [95S1]
	$T > T_C$: $\chi(T)$ for $\boldsymbol{H_0} \perp \boldsymbol{c}$ [25 K $\le T \le$ 250 K] h.t.s. $\to J = 8.55$ cm^{-1} $\hat{=}$ 12.3 K ($S = 1/2$)	[95S1] h.t.s.: Eqs. 3.26, 3.27; coeff. see [67B2, 90N]
2) EPR	$g_a = g_b = 2.285$, $g_c = 2.086$	EPR at about 10 GHz [95S1]

Table 5. Data concerning Magnetic Properties *(continued)*

Compound	Characteristic magnetic parameters: J, H_E, H_A, H_0, M, χ, g, T_C, T_N etc. [definitions see Table 1, units are given below]	References, remarks
Cs_2CuF_4	Ferromagnet, $\boldsymbol{M} \perp \boldsymbol{c}$ (magn. order see Fig. 3.27)	
1) meas. and anal. of χ	$\chi(T)$ for $\boldsymbol{H_0} \parallel \boldsymbol{c}$, $\boldsymbol{H_0} \perp \boldsymbol{c}$ [$2\ \mathrm{K} \le T \le 10\ \mathrm{K}$] $\rightarrow T_C = 6.05$ K	[95S1]
	$T > T_C$: $\chi(T)$ for $\boldsymbol{H_0} \perp \boldsymbol{c}$ [$25\ \mathrm{K} \le T \le 250\ \mathrm{K}$] h.t.s. $\rightarrow J = 8.76\ \mathrm{cm}^{-1} \mathrel{\hat{=}} 12.6$ K ($S = 1/2$)	[95S1] h.t.s.: Eqs. 3.26, 3.27; coeff. see [67B2, 90N]
2) EPR	$g_a = g_b = 2.274$, $g_c = 2.081$	EPR at about 10 GHz [95S1]
b) Chlorides, Bromides and Iodides with inorganic A^+-ions		
K_2CrCl_4	Ferromagnet, $\boldsymbol{M} \perp \boldsymbol{c}$ (magn. order see Fig. 3.34)	
1) meas. and anal. of χ	$\chi(T)$ [$80\ \mathrm{K} \le T \le 300\ \mathrm{K}$] $\chi(T > T_C)$: h.t.s. $\rightarrow J = 3.30\ \mathrm{cm}^{-1} \mathrel{\hat{=}} 4.75$ K ($S = 2$, $g = 2.00$)	[75L9], see also [75G5, 79D3] h.t.s.: Eqs. 3.26, 3.27; coeff. see [70L1, 90N]
2) optical studies	absorption spectra 8000–28000 cm^{-1} [$4.2\ \mathrm{K} \le T \le 300\ \mathrm{K}$]	[73D1]
	reflectance spectra 7000–23000 cm^{-1}, $T = 90, 295$ K	[75L8]
	T-dependence of the intensity of the exciton magnon band at 15900 cm^{-1} [$4\ \mathrm{K} \le T \le 15\ \mathrm{K}$], $T_C \approx 65$ K	[76G4], see also [78B1, 79D3]; theoretical calc. using linear spin-w. th. ($J = 3.5\ \mathrm{cm}^{-1}$, $D = 1\ \mathrm{cm}^{-1}$, cf. Eq. 3.16)
Rb_2CrCl_4	Ferromagnet, $\boldsymbol{M} \perp \boldsymbol{c}$ (magn. order see Fig. 3.34)	
1) meas. and anal. of χ	$\chi(H_0, T)$ for $\boldsymbol{H_0} \parallel (1, 1, 0)$ [$0 \le H_0 \le 70$ mT, $5\ \mathrm{K} \le T \le 52\ \mathrm{K}$]	[86K2]
	$\chi(H_0, T)$ for $\boldsymbol{H_0} \parallel (1, 0, 0)$ [$0 \le H_0 \le 180$ mT, $5\ \mathrm{K} \le T \le 41\ \mathrm{K}$] $\rightarrow H_C(T)$ for spin reorientation transition	[86K2]; spin reorientation transition = transition from canted to collinear ferromagnet
2) EPR	$g_a = g_b = 1.995(15)$, $g_c = 1.98(2)$	[86G2]: EPR ($\nu \approx 10$ GHz) at 300 K; see also [89S1]
3) FMR	$H_A = 3.181$ T, $\hat{H}_A = 0.231$ T [$M_0 = 0.230$ T]	[85G3, 91G2]: ($\nu \approx 100$ GHz); H_A, $\hat{H}_A$: Eqs. 3.103, 3.104
	$\boldsymbol{H_0} \parallel (1, 0, 0)$: study of spin reorientation transition	[84F2, 84S3]: optically detected and ordinary FMR

Table 5. Data concerning Magnetic Properties *(continued)*

Compound	Characteristic magnetic parameters: J, H_E, H_A, H_0, M, χ, g, T_C, T_N etc. [definitions see Table 1, units are given below]	References, remarks
Rb_2CrCl_4 (cont.)		
4) inel. n-scatt.	$\omega(\boldsymbol{q})$ for $(\zeta, \zeta, 0)$ at 5, 40, 45, 50 K [small q: $0 \le \zeta \le 0.08$] and at 20 K full q-range [$0 \le \zeta \le 0.5$]; $T_C = 52.40(5)$ K	[81H4], see also [76H4, 80E1, 80L2]; $\zeta = q_{x0}/a^* = q_{y0}/a^*$; $S = 2$, $z = 4$; calculation of H_E, H_A etc. with $g = 2.00$
	$\widetilde{J} = 5.25(13)\ \mathrm{cm}^{-1} \mathrel{\hat{=}} 7.56(19)$ K, $H_E = 90.03$ T, $\delta = 1.1°$ $\widetilde{P} = 2.18(13)\ \mathrm{cm}^{-1} \mathrel{\hat{=}} 3.14(18)$ K, $H_{A1} = 7.01$ T $\widetilde{D} = -0.28(12)\ \mathrm{cm}^{-1} \mathrel{\hat{=}} -0.41(17)$ K, $H_{A2} = -0.92$T	exp. data fitted to $\mathcal{H}(1)$, cf. Eq. 3.81 with $J' \approx 0$; parameter values according to renorm. spin-w. th. [80E1, 81H4]; H_E, H_{A1}, H_{A2}: Eq. 3.101
	$J = 5.25(13)\ \mathrm{cm}^{-1} \mathrel{\hat{=}} 7.56(19)$ K, $H_E = 90.03$ T $D = 0.74(10)\ \mathrm{cm}^{-1} \mathrel{\hat{=}} 1.06(15)$ K, $H_A = 2.37$ T $P = 0.085(10)\ \mathrm{cm}^{-1} \mathrel{\hat{=}} 0.123(14)$ K, $\widetilde{H}_A = 0.275$ T	exp. data fitted to $\mathcal{H}(2)$, cf. Eq. 3.86 with $J' \approx 0$; parameter values according to renorm. spin-w. th. [80E1, 81H4]; H_E, H_A, $\widetilde{H}_A$: Eq. 3.103
	T-dependence of $\omega(\boldsymbol{q})$ for $(\zeta, \zeta, 0)$ with $\zeta = 0.1, 0.25, 0.4$ and for $(\zeta_{x0}, 0, 0)$ with $\zeta_{x0} = 015$ [$5.3\ \mathrm{K} \le T \le 62.7$ K]	[78F1]; $T_C = 52.8(4)$ K $\zeta = q_{x0}/a^* = q_{y0}/a^*$ $(b^* \approx a^*)$, $\zeta_{x0} = q_{x0}/a^*$
5) el. + quasi-el. n-scatt.	determination of J' from $\chi(\boldsymbol{q})$	$\chi(q_{x0}, q_{y0}, q_{z0})$: Eqs. 4.55–4.57
	a) $J'/J = 6.5 \cdot 10^{-5}$, $J' = 0.3 \cdot 10^{-3}\ \mathrm{cm}^{-1} \mathrel{\hat{=}} 0.5 \cdot 10^{-3}$ K	[93A], TAS6-data (Risø)
	b) $J'/J = 1.5 \cdot 10^{-4}$, $J' = 0.8 \cdot 10^{-3}\ \mathrm{cm}^{-1} \mathrel{\hat{=}} 1.1 \cdot 10^{-3}$ K	[93A], D10-data (ILL, Grenoble)
	c) $J'/J = 2.3 \cdot 10^{-4}$, $J' = 1.2 \cdot 10^{-3}\ \mathrm{cm}^{-1} \mathrel{\hat{=}} 1.7 \cdot 10^{-3}$ K	[93V]
	polarized neutrons → magn. form factor $f(\boldsymbol{K})$ for Cr^{2+}	[79D3]
6) NMR	^{53}Cr-NMR a) $f_{NMR}(T) \sim M(T)$	[85T]; a) exp. data compared to spin-wave calculations
	b) determination of T_1 and T_2	[85T, 86T1]; discussion of mechanism for T_1: Sect. 3.1.2
	^{35}Cl-, ^{37}Cl-NMR → covalency between Cr^{2+}- and Cl^- -ions	[88K6]
	^{35}Cl: asymmetry of the EFG $V_{xx} - V_{yy}$ due to the deformation of the $CrCl_6$ octahedra	[90Z1]
7) 1-magnon Raman sp.	$h\nu_{max} = 168.0(2)\ \mathrm{cm}^{-1}$ (optic branch, $\boldsymbol{q} = 0$, cf. Eq. 3.90)	[87A3; exp. data analysed by linear spin-w. th. [88B3]

Table 5. Data concerning Magnetic Properties *(continued)*

Compound	Characteristic magnetic parameters: J, H_E, H_A, H_0, M, χ, g, T_C, T_N etc. [definitions see Table 1, units are given below]	References, remarks
Rb_2CrCl_4 (cont.)		
8) optical studies	reflectance spectra 7000–23000 cm^{-1}, $T = 90, 295$ K	[75L8]
	T-and H_0-dependence of absorption spectra in the visible: $\boldsymbol{H_0} \parallel (1, 0, 0), \parallel (1, 1, 0), \parallel (0, 0, 1)$ [$0.85\ K \le T \le 50$ K, $0 \le H_0 \le 3$ T]	[79D4, 82J3]
	$T > 3$ K: $I(T)$ of band at 631 nm $\rightarrow \nu_{gap} = 25.0$ GHz ($H_0 = 0$)	intensity: $I(T) \sim T^2 \cdot \exp[-(h\nu_{gap} + g\mu_B H_0)/(k_B T)]$
	intensity $I(T)$ of the 530 nm absorption band, related more to short-range than to long-range correlations	[80B7], exp. data comp. to estimates from n-scatt. data (long-range) and to theory [74V4] (short-range)
	T- and H_0-dependence of absorption profiles in the visible: $\boldsymbol{H_0} \parallel (1, 0, 0), \parallel (1, 1, 0), \parallel (0, 0, 1)$ [$0.35\ K \le T \le 1.3$ K, $0 \le H_0 \le 3$ T]	[88B3]; exp. data comp. to calculated absorption profiles, the magnons described by spin-w. theory
Rb_2CrCl_3Br	Ferromagnet, $\boldsymbol{M} \perp \boldsymbol{c}$ (magn. order see Fig. 3.34)	
1) el. + quasi-el. n-scatt.	$T_C = 55$ K (details see Table 6)	[86B3, 86D3, 86D4]
Rb_2CrCl_3Br (cont.)		
2) optical studies	T-dependence of absorption spectra in the visible: [$0.35\ K \le T \le 20$ K], $I(T)$ of absorption bands at 530 nm and at 630 nm $\rightarrow h\nu_{gap} = 2.5(3)\ K \triangleq 52(6)$ GHz	[86B3] intensity $I(T) \sim T^2 \cdot \exp[-(h\nu_{gap})/(k_B T)]$
	intensity I(T) of the 530 nm aborption band, related more to short-range than to long-range correlations	[86B3], exp. data comp. to estimates from n-scatt. data (long-range) and to theory [74V4] (short-range)
$Rb_2CrCl_2Br_2$	Ferromagnet, $\boldsymbol{M} \perp \boldsymbol{c}$ (magn. order see Fig. 3.34)	
1) el. + quasi-el. n-scatt.	scans along rod $(0, 0, 1 + \zeta_z) \rightarrow T_C = 57.0$ K, $J'/J = 1.02 \cdot 10^{-3}$	[93V]
2) optical studies	T-dependence of absorption spectra in the visible: [$0.35\ K \le T \le 20$ K], $I(T)$ of absorption bands at 530 nm and at 630 nm $\rightarrow h\nu_{gap} = 2.7(5)\ K \triangleq 56(10)$ GHz	[86B3] intensity $I(T) \sim T^2 \cdot \exp[-(h\nu_{gap})/(k_B T)]$
	intensity $I(T)$ of the 530 nm absorption band, related more to short-range than to long-range correlations	[86B3], exp. data comp. to estimates from n-scatt. data (long-range) and to theory [74V4] (short-range)

Table 5. Data concerning Magnetic Properties *(continued)*

Compound	Characteristic magnetic parameters: J, H_E, H_A, H_0, M, χ, g, T_C, T_N etc. [definitions see Table 1, units are given below]	References, remarks
$Rb_2CrCl_2I_2$	Ferromagnet, $\boldsymbol{M} \perp \boldsymbol{c}$ (magn. order see Fig. 3.34)	
meas. M and χ	exp. data M, $\chi \rightarrow T_C = 56.9(2)$ K, $J = 4.0$ cm$^{-1} \triangleq 5.8$ K	[91V2], vibrating sample magnetometer, Faraday balance, SQUID;
	at $T = 4.2$ K: $H_A = 4.5(2)$ T, $\hat{H}_A = 0.16(2)$ T	H_A, $\hat{H}_A$: Eqs. 3.103, 3.104
Rb_2CrBr_4	only few and incomplete data on magnetic properties	[81B5]
Cs_2CrCl_4	only few and incomplete data on magnetic properties	[74H2, 75G5, 78L8, 75L9]
Cs_2CrBr_4	only few and incomplete data on magnetic properties	[81B5]
$(NH_4)_2CrCl_4$	only few and incomplete data on magnetic properties	[75L8]
$(NH_4)_2CrBr_4$	only few and incomplete data on magnetic properties	[81B5]
Rb_2MnCl_4	Antiferromagnet, $\boldsymbol{M}_{\mathbf{subl}} \parallel \boldsymbol{c}$ (magn. order see Fig. 2.2)	
1) meas. and anal. of χ	$\chi_{\parallel}(T)$, $\chi_{\perp}(T)$ [1.5 K $\leq T \leq$ 300 K]	[94H], see also [74W1]
	$T > T_N$: exp. data comp. to h.t.s. calculation	h.t.s.: special series, details see [77K7, 78K4, 94H]
2) meas. M induced by H_0	H_0- and ψ-dependence of M at $T = 4.2$ K [0 $\leq H \leq$ 6 T]	[78F2], see also [86G3]
	$\psi = \angle(\boldsymbol{H}_\mathbf{0}, c\text{-axis}) \rightarrow H_{SF} = 5.6$ T	
3) EPR	$g_a = g_b = 2.004(2)$, $g_c = 1.999(2)$	[86G2]: EPR ($\nu \approx 10$ GHz) at 300 K; see also [89S1]
4) AFMR	AFMR (9–250 GHz), $\boldsymbol{H}_\mathbf{0} \parallel \boldsymbol{c}$, $\boldsymbol{H}_\mathbf{0} \perp \boldsymbol{c}$, various conditions	[81S4, 84G3, 91G1, 91G2], see also [84K6, 94H]
	$H_0 = 0$, $T = 4.2$ K: $\nu_{AFMR,1} = 153.0$ GHz, $\nu_{AFMR,2} = 156.2$ GHz	orthorh. distortion $\rightarrow$ splitting of ν_{AFMR} [89G5, 92G1]
	$\rightarrow H_A = 0.175$ T, $\hat{H}_A = 0.015$ T, $\tilde{H}_A = 3.6$ mT	H_A, $\hat{H}_A$, $\tilde{H}_A$: see Eqs. 3.41, 3.50–3.51b
	T-dependence: $\nu_{AFMR}(T)$, $H_A(T)$ [4.2 K $\leq T \leq$ 50 K]	[80S2, 88G3, 90G4]
	AFMR LW: $C_{AFMR} = 2.5 \cdot 10^{-7}$ T/K^4 ($\nu = 62, 95, 126$ GHz)	anal. of ΔH_{AFMR} using Eq. 3.13, note: $\Delta H^0_{AFMR} = f(\nu)$
5) el. + quasi-el. n-scatt.	afm. Bragg refl. (1, 0, 0): $I(T) \sim M^2_{subl}(T) \rightarrow T_N = 56.0$ K	[80S2]

Table 5. Data concerning Magnetic Properties *(continued)*

Compound	Characteristic magnetic parameters: J, H_E, H_A, H_0, M, χ, g, T_C, T_N etc. [definitions see Table 1, units are given below]	References, remarks
Rb_2MnCl_4 (cont.)		
6) inel. n-scatt.	$\omega(\boldsymbol{q})$ for $(\zeta_x, 0, 0)$ and $(0.3, 0, 0.5)$ at $T = 8$ K fit to exp. data with renorm. spin-wave theory	[80S2], $\zeta_x = q_x/a^*$ fit: Eq. 3.15; parameter values: see spin-wave analysis
	high resolution study splitting of $\hbar\omega_q$ into 2 modes typically 20 GHz apart and a new additonal mode in the spin-flop phase	[92T1, 97T3, 98T]; magn. field $\boldsymbol{H_0} \parallel \boldsymbol{c}$ [$0 \le H_0 \le 6.5$ T]; splitting of ≈ 20 GHz expl. as finite-size effect [98T; add. mode possibly a vortex-like excitation, see [97T3]
7) spin-wave analysis	exp. data included: $\nu_{AFMR}(T)$, $M_{subl}(T)$ and $\omega(\boldsymbol{q})$	[78S8, 80S2]
	$(z = 4,\ S = 5/2,\ g = 2.000,\ J_2 \approx 0,\ J' \approx 0,\ \tilde{H}_A \approx 0,\ \hat{H}_A \approx 0)$	J_2, J': Eq. 3.2; $\hat{H}_A$, $\tilde{H}_A$: Eq. 3.41
	$J = -4.07\ \mathrm{cm^{-1}} \mathrel{\widehat{=}} -5.85\ \mathrm{K}$, $H_E = 87.09$ T $T = 0$: $h_A = 2.02 \cdot 10^{-3}$, $g\mu_B H_A = 0.165\ \mathrm{cm^{-1}}$, $H_A = 0.176$ T 4.2 K: $h_A = 2.01 \cdot 10^{-3}$, $g\mu_B H_A = 0.163\ \mathrm{cm^{-1}}$, $H_A = 0.175$ T	parameter values obtained with a fit to the exp. data using linear spin-wave theory (cf. Eqs. 3.2–3.5, and 3.6)
	$J = -3.94\ \mathrm{cm^{-1}} \mathrel{\widehat{=}} -5.67\ \mathrm{K}$, $H_E = 84.42$ T $T = 0$: $h_A = 2.09 \cdot 10^{-3}$, $g\mu_B H_A = 0.165\ \mathrm{cm^{-1}}$, $H_A = 0.176$ T	parameter values according to renorm. spin-w. th. (cf. Eqs. 3.2–3.5, 3.15)
	calc.: $\Delta_0 S = 0.177$, $H_{AD} = 0.135$ T	[80S2]; $\Delta_0 S$: Eq. 3.19, H_{AD}: Eq. 3.12
8) (H_0, T) phase diagram	observed critical point: bifurcation point, not bicritical one, but results of new studies: indications of a bicritical point	n-diffr. [86R1, 86R2]; n-diffr. and Monte-Carlo simulation [96K, 98K1]; see also [80P4]
9) optical studies	fluorescence (5700–8000 $\mathrm{cm^{-1}}$) at $T = 25$, 76, 100 K	[71K2]
	intrinsic emission ${}^4T_{1g}(G) \rightarrow {}^6A_{1g}(S)$ at $T = 1.7$ K	exciton line, magnon sideband [77S2]
	optical absorption, MCD (15000–45000 $\mathrm{cm^{-1}}$) $T = 15$ K: study of magnon sideband near 26500 $\mathrm{cm^{-1}}$	electronic transitions [84B3, 84V2], s. also [79P4, 81G3] comp. of exp. data with calc. lineshape [95T2]
	high resolution absorption, excitation spectroscopy, and luminescence, also time-resolved	study of the ${}^6A_{1g} \rightarrow {}^4T_{1g}(G)$ transition, also on Er^{3+}-, Nd^{3+}-doped samples; [84K4, 84K5], s. also [82P2]
$Rb_3Mn_2Cl_7$	Antiferromagnet, $\boldsymbol{M_{subl}} \parallel \boldsymbol{c}$ (magn. order see Fig. 2.4)	
1) meas. M induced by H_0	H_0-dependence of M at $T = 4.2$ K for $\boldsymbol{H_0} \parallel \boldsymbol{c}$, $\boldsymbol{H_0} \perp \boldsymbol{c}$ [$0 \le H_0 \le 6$ T] $\rightarrow H_{SF} = 3.84(5)$ T	[87K1]; H_{SF}: Eq. 3.39

Table 5. Data concerning Magnetic Properties *(continued)*

Compound	Characteristic magnetic parameters: J, H_E, H_A, H_0, M, χ, g, T_C, T_N etc. [definitions see Table 1, units are given below]	References, remarks
$Rb_3Mn_2Cl_7$ (cont.)		
2) el. + quasi-el. n-scatt.	afm. Bragg refl. (1, 0, 2): $I(T) \sim M^2_{subl}(T) \rightarrow T_N \approx 64.5$ K	[76G1]
3) AFMR	$\nu_{AFMR}(H_0)$ for $\boldsymbol{H_0} \parallel \boldsymbol{c}$ at $T = 4.2$ K [$0 \le H_0 \le 6$ T] $H_0 = 0$, $T = 4.2$ K: $\nu_{AFMR} = 107(1)$ GHz, $g = 1.97$	AFMR at $\nu = 50$–130 GHz [87K1]
4) optical studies	optical absorption, MCD (15000–45000 cm^{-1})	electronic transitions [84B3]
	$q = q_{max}$: $h\nu_{BZB} = 90\ cm^{-1} \rightarrow g\mu_B H_E = 2.70$ THz, $H_E = 98$ T $h\nu_{BZB}$, $h\nu_{AFMR} \rightarrow g\mu_B H_A = 2.11$ GHz, $H_A = 0.077$ T	$h\nu_{BZB}$ from exciton-magnon spacing in the optical spectra; $h\nu_{AFMR}$: Eq. 3.32a, $h\nu_{BZB}$: Eq. 3.32b
	high resolution absorption, excitation spectroscopy, luminescence, also time-resolved	study of the ${}^6A_1 \rightarrow {}^4T_1(G)$ transition [84K5]
Cs_2MnCl_4	Antiferromagnet, $\boldsymbol{M_{subl}} \parallel \boldsymbol{c}$ (magn. order see Fig. 2.2)	
1) meas. and anal. of χ	$\chi_{powder}(T)$ [$4.2\ K \le T \le 240$ K], corr. for $MnCl_2$ impurities $\chi(T > T_N)$: h.t.s. $\rightarrow J = -3.5\ cm^{-1} \mathrel{\hat{=}} -5.0$ K	[74W1] h.t.s.: Eqs. 3.26, 3.27; coeff. see [70L1, 90N]
2) el. + quasi-el. n-scatt.	several afm. Bragg reflections: $I(T) \sim M^2_{subl}(T)$, afm.	[70E]
	Bragg rods observed $\rightarrow T_N = 52$ K	
Rb_2CuCl_4	Antiferromagnet, $\boldsymbol{M_{subl}} \perp \boldsymbol{c}$ (magn. order see Fig. 3.27)	
1) EPR	$g_a = g_b = 2.16(1)$, $g_c = 2.06(1)$	[74W3]
2) meas. and anal. of χ	$\chi(T)$ [$4.2\ K \le T \le 150$ K] $\chi(T > T_N)$: h.t.s. $\rightarrow J = 13.1(2)\ cm^{-1} \mathrel{\hat{=}} 18.8(3)$ K	[74W3], vibrating sample magnetometer h.t.s.: Eqs. 3.26, 3.27; coeff. see [67B2, 70L1, 90N]
3) meas. $\chi(H_0)$, $M(H_0)$	$\chi(H_0, T)$ [$0 \le H_0 \le 1.5$ T, $4.2\ K \le T \le 25$ K], χ_{ac} at $f = 250$ kHz, field-induced M [$0 \le H_0 \le 5.5$ T] at various T	[74W3], vibrating sample magnetometer, twin T-bridge for meas. χ at 250 kHz
	exp. data $\rightarrow T_N = 13.7(1)$ K, $H_{SF} = 70(3)$ mT, $H^c_{PM} = 1.70(4)$ T	[74W3], see also [74M2, 75Y, 76B5, 76J1, 77B3];
	$H_E = 51.8(8)$ T, $H'_E = 0.77(3)$ T, $J' = -0.097\ cm^{-1} \mathrel{\hat{=}} -0.140$ K,	determination of T_N, H'_E, H_A and $\tilde{H}_A$: see [74W3];
	$H_A = 0.076(30)$ T, $\tilde{H}_A = 3.2(10)$ mT	H_{SF}, H^c_{PM}: Eqs. 3.57, 3.59; H_E, H'_E, H_A, $\tilde{H}_A$: Eq. 3.96

Table 5. Data concerning Magnetic Properties *(continued)*

Compound	Characteristic magnetic parameters: J, H_E, H_A, H_0, M, χ, g, T_C, T_N etc. [definitions see Table 1, units are given below]	References, remarks
Rb_2CuCl_3Br	Antiferromagnet, $\boldsymbol{M}_{\mathbf{subl}} \perp \boldsymbol{c}$ (magn. order see Fig. 3.27)	
1) EPR	$g_a = g_b = 2.14(1)$, $g_c = 2.06(1)$	[74W3]
2) meas. and anal. of χ	$\chi(T)$ [$4.2\ K \le T \le 150\ K$] $\chi(T > T_N)$: h.t.s. $\rightarrow J = 12.2(2)\ cm^{-1} \triangleq\ 17.6(3)\ K$	[74W3], vibrating sample magnetometer h.t.s.: Eqs. 3.26, 3.27; coeff. see [67B2, 70L1, 90N]
3) meas. $\chi(H_0)$, $M(H_0)$	$\chi(H_0, T)$ [$0 \le H_0 \le 3\ T$, $4.2\ K \le T \le 28\ K$], χ_{ac} at $f = 250$ kHz, field-induced M [$0 \le H_0 \le 5.5\ T$] at various T	[74W3], vibrating sample magnetometer, twin T-bridge for meas. χ at 250 kHz
	exp. data $\rightarrow T_N = 15.2(1)\ K$, $H_{SF} = 90(5)\ mT$, $H^c_{PM} = 3.5(1)\ T$ $H_E = 49.0(8)\ T$, $H'_E = 1.55(7)\ T$, $J' = -0.19\ cm^{-1} \triangleq -0.28\ K$, $H_A = 0.27(4)\ T$, $\widetilde{H}_A = 2.6(10)\ mT$	[74W3], see also [72M2, 75Y, 76B5, 76J1] determination of T_N, H'_E, H_A and $\widetilde{H}_A$: see [74W3]; H_{SF}, H^c_{PM} : Eqs. 3.57, 3.59; H_E, H'_E , H_A , $\widetilde{H}_A$: Eq. 3.96
$Rb_2CuCl_2Br_2$	Antiferromagnet, $\boldsymbol{M}_{\mathbf{subl}} \perp \boldsymbol{c}$ (magn. order see Fig. 3.27)	
1) EPR	$g_a = g_b = 2.13(1)$, $g_c = 2.08(1)$	[74W3]
2) meas. and anal. of χ	$\chi(T)$ [$4.2\ K \le T \le 150\ K$] $\chi(T > T_N)$: h.t.s. $\rightarrow J = 11.3(2)\ cm^{-1} \triangleq\ 16.3(3)\ K$	[74W3], vibrating sample magnetometer h.t.s.: Eqs. 3.26, 3.27; coeff. see [67B2, 70L1, 90N]
3) meas. $\chi(H_0)$, $M(H_0)$	$\chi(H_0, T)$ [$0 \le H_0 \le 5\ T$, $4.2\ K \le T \le 26\ K$], χ_{ac} at $f = 250$ kHz, field-induced M [$0 \le H_0 \le 5.5\ T$] at various T	[74W3], vibrating sample magnetometer, twin T-bridge for meas. χ at 250 kHz
	exp. data $\rightarrow T_N = 17.2(1)\ K$, $H_{SF} = 118(4)\ mT$, $H^c_{PM} = 5.65(9)\ T$ $H_E = 45.6(8)\ T$, $H'_E = 2.34(10)\ T$, $J' = -0.29\ cm^{-1} \triangleq -0.42\ K$, $H_A = 0.83(4)\ T$, $\widetilde{H}_A = 3(1)\ mT$	[74W3], see also [72M2, 75Y, 76B5, 76J1] determination of T_N, H'_E, H_A and $\widetilde{H}_A$: see [74W3]; H_{SF}, H^c_{PM} : Eqs. 3.57, 3.59; H_E, H'_E , H_A , $\widetilde{H}_A$: Eq. 3.96
$(NH_4)_2CuCl_4$	Antiferromagnet, $\boldsymbol{M}_{\mathbf{subl}} \perp \boldsymbol{c}$ (magn. order see Fig. 3.27)	
meas. and anal. of χ	$\chi_{powder}(T)$ [$1\ K \le T \le 200\ K$] $\chi(T > T_N)$: h.t.s. $\rightarrow J = 11.8\ cm^{-1} \triangleq 17.0\ K$ ($H_E = 48.2\ T$)	[72L3] h.t.s. Eqs. 3.26, 3.27; coeff. see [67B2, 70L1, 90N]
	peak of $\chi \rightarrow T_N = 11.2\ K$; $\chi(T \rightarrow 0)$: $H'_E = 0.307\ T$, $J' = -0.038\ cm^{-1} \triangleq -54\ mK$, $g_a = 2.10$	[72L3], see also [74M2, 76B5] H_E, H'_E : Eq. 3.96

Table 5. Data concerning Magnetic Properties *(continued)*

Compound	Characteristic magnetic parameters: J, H_E, H_A, H_0, M, χ, g, T_C, T_N etc. [definitions see Table 1, units are given below]	References, remarks
c) Chlorides and Bromides with organic A$^+$-ions		
$(CH_3NH_3)_2CrCl_4$	Ferromagnet, $\boldsymbol{M} \perp \boldsymbol{c}$ (magn. order see Fig. 3.34)	
1) meas. and anal. χ	$\chi(T)$ [$60\ K \le T \le 200\ K$]	[78B1], see also [78L4]
	$\chi(T > T_C)$: h.t.s. $\rightarrow J = 4.5\ cm^{-1} \hat{=} 6.5\ K$, $g = 2.00$	h.t.s.: Eqs. 3.26, 3.27; coeff. see [70L1, 78B1, 90N]
2) meas. M	$M(T)/M(0) \rightarrow T_C = 42\ K$	SQUID magnetometer [80G6], quoted in [78B1, 86B1]
3) specific heat	$C_p(T)$ [$4.2\ K \le T \le 300\ K$], magn. and lattice contributions	[82R1]
4) optical studies	absorption spectra 15000–27000 cm^{-1}	[78B1], see also [78B6]
	reflectance spectra 8000–260000 cm^{-1} at 90 K, 295 K	[78L4]
	intensity $I(T)$ of the 530 nm absorption band, related more to short-range than to long-range correlations	[80B7]; exp. data comp. to estimates from magn. meas. (long-range) and to theory [74V4] (short-range)
	$I(H_0, T)$ of 530 and 630 nm absorption bands for $\boldsymbol{H_0} \parallel \boldsymbol{b}$ [$0 \le H_0 \le 5\ T$, $3\ K \le T \le 10\ K$] $\rightarrow h\nu_{gap} = 1.9\ K$, $g = 1.93(1)$ $\rightarrow P = 0.296\ K$, $\delta = 1.9°$, assuming $D = 1.06\ K$ (Rb_2CrCl_4)	[85B1]; intensity $I(T) \sim T^2 \cdot \exp[-(h\nu_{gap})/(k_BT)]$; $h\nu_{gap}$, $D \rightarrow P$: Eq. 3.89; P, $J \rightarrow \delta$: Eq. 3.84; note: there are minor errors in the calc. of [85B1]
$(C_2H_5NH_3)_2CrCl_4$	Ferromagnet, $\boldsymbol{M} \perp \boldsymbol{c}$ (magn. order see Fig. 3.34)	
1) meas. and anal. χ	$\chi(T)$ [$55\ K \le T \le 150\ K$]	[78B1], see also [78L4]
	$\chi(T > T_C)$: h.t.s. $\rightarrow J = 3.5\ cm^{-1} \hat{=} 5.0\ K$, $g = 1.95$	h.t.s.: Eqs. 3.26, 3.27; coeff. see [70L1, 78B1, 90N]
2) meas. M	$M(T)/M(0) \rightarrow T_C = 41\ K$	SQUID magnetometer [80G6], quoted in [78B1, 86B1]
3) optical studies	absorption spectra 15000–21000 cm^{-1} at 7 K, 298 K results discussed with respect to coll. JTE and orb. order	[87B4], see also [78B1]
	intensity $I(T)$ of the 530 nm absorption band, related more to short-range than to long-range correlations	[80B7]; exp. data comp. to estimates from magn. meas. (long-range) and to theory [74V4] (short-range)
$(C_3H_7NH_3)_2CrCl_4$	Ferromagnet, $\boldsymbol{M} \perp \boldsymbol{c}$ (magn. order see Fig. 3.34)	
1) meas. and anal. χ	$\chi(T)$ [$60\ K \le T \le 120\ K$]	[82S1]
	$\chi(T > T_C)$: h.t.s. $\rightarrow J = 3.25\ cm^{-1} \hat{=} 4.7\ K$, $g = 1.95$	h.t.s.: Eqs. 3.26, 3.27; coeff. see [70L1, 82S1, 90N]
2) meas. M	$M(T)/M(0) \rightarrow T_C = 39.5\ K$	SQUID magnetometer [80G6], quoted in [86B1]

Table 5. Data concerning Magnetic Properties *(continued)*

Compound	Characteristic magnetic parameters: J, H_E, H_A, H_0, M, χ, g, T_C, T_N etc. [definitions see Table 1, units are given below]	References, remarks
$(C_5H_{11}NH_3)_2CrCl_4$	only few and incomplete data on magnetic properties	[82S1, 86B1]
$(C_{12}H_{25}NH_3)_2CrCl_4$	only few and incomplete data on magnetic properties	[82S1, 86D3, 86D4]
$(C_6H_5NH_3)_2CrCl_4$	only few and incomplete data on magnetic properties	[83B3]
$(C_5H_5NH)_2CrCl_4$	only few and incomplete data on magnetic properties	[75L8]
$(C_6H_5CH_2NH_3)_2CrCl_4$	Ferromagnet, $\boldsymbol{M} \perp \boldsymbol{c}$	
1) meas. and anal. χ	$\chi(T)$ [40 K $\le T \le$ 150 K]	[86B1]
	$\chi(T > T_C)$: h.t.s. $\rightarrow J = 3.7\ \mathrm{cm}^{-1} \mathrel{\hat{=}} 5.3$ K, $g = 2.10$	h.t.s.: Eqs. 3.26, 3.27; coeff. see [70L1, 86B1, 90N]
	χ'_{ac} at $f = 198$ Hz [5 K $\le T \le$ 60 K] $\rightarrow T_C = 37$ K	[86B1]
2) optical studies	intensity $I(T)$ of the 630 nm absorption band	[86B1]; [1.5 K $\le T \le$ 14 K]: $I(T) \sim T^2$
$(CH_3NH_3)_2CrBr_4$	only few and incomplete data on magnetic properties	[81B5]
$(C_2H_5NH_3)_2CrBr_4$	only few and incomplete data on magnetic properties	[81B5, 87B4]
$(C_3H_7NH_3)_2CrBr_4$	only few and incomplete data on magnetic properties	[81B5]
$(C_5H_{11}NH_3)_2CrBr_4$	only few and incomplete data on magnetic properties	[81B5]
$(C_8H_{17}NH_3)_2CrBr_4$	only few and incomplete data on magnetic properties	[81B5]
$(C_{12}H_{25}NH_3)_2CrBr_4$	only few and incomplete data on magnetic properties	[81B5]
$(C_6H_5NH_3)_2CrBr_4$	only few and incomplete data on magnetic properties	[81B5]
$(C_5H_5NH)_2CrBr_4$	only few and incomplete data on magnetic properties	[81B5]
$(C_6H_5CH_2NH_3)_2CrBr_4$	Ferromagnet, $\boldsymbol{M} \perp \boldsymbol{c}$	
meas. and anal. χ	$\chi(T)$ [45 K $\le T \le$ 215 K]	[86B5, 87B1]
	$\chi(T > T_C)$: h.t.s. $\rightarrow J = 4.55\ \mathrm{cm}^{-1} \mathrel{\hat{=}} 6.55$ K, $g = 2.00$	h.t.s.: Eqs. 3.26, 3.27; coeff. see [70L1, 86B5, 90N]
	χ'_{ac} at $f = 198$ Hz [40 K $\le T \le$ 75 K] $\rightarrow T_C = 52.0(1)$ K	[87B1]

Table 5. Data concerning Magnetic Properties *(continued)*

Compound	Characteristic magnetic parameters: J, H_E, H_A, H_0, M, χ, g, T_C, T_N etc. [definitions see Table 1, units are given below]	References, remarks
$(CH_3NH_3)_2MnCl_4$	Antiferromagnet, $\boldsymbol{M}_{\mathbf{subl}} \parallel \boldsymbol{c}$ (spin canting, weak fm.: $\boldsymbol{M} \perp \boldsymbol{c}$)	details see [90A1], weak fm. due to DMI (Eq. 3.52)
1) meas. and anal. of χ	$\chi(T)$ [4.2 K $\le T \le$ 300 K], corr. for $MnCl_2$ impurities; $T > T_N$: $\chi_{max} \rightarrow J = -3.5(1)\ cm^{-1} \hat{=} -5.0(2)$ K, h.t.s.; $T = 4.2$ K: $M(H_0)$ for $\boldsymbol{H_0} \parallel \boldsymbol{c} \rightarrow H_{SF} = 3.6(3)$ T, $h_A = 0.0011$	[72A], see also [73H1] $\chi_{max} \rightarrow J$: Eq. 3.28; h.t.s.: Eqs. 3.26, 3.27 $H_{SF} \rightarrow H_A$: Eq. 3.39; $H_A \rightarrow h_A$: Eq. 3.6
	$\chi(T)$ [78 K $\le T \le$ 300 K], $\chi_{ac}(T)$ ($f = 33$ Hz) [4.2 K $\le T \le$ 140 K] χ''_{ac} sharp peak at $T_N = 45.3(5)$ K resulting from weak fm.	[74G2]; χ: Faraday techn., χ_{ac}: initial susceptibility techn. spin canting, weak fm. $\boldsymbol{M}$ due to DMI (Eqs. 3.52, 3.53)
2) AFMR	$H_0 = 0$, $T = 4.2$ K: $h\nu_{AFMR} = 3.47\ cm^{-1} \hat{=} 4.99$ K T-dependence: $\nu_{AFMR}(T)$, $H_A(T)$ [4.2 K $\le T \le$ 43 K]	[78S1, 78S8, 80S2, 81S4]; $\nu = 64.0, 83.5, 92.8$ GHz; ν_{AFMR}: Eqs. 3.9, 3.10; H_D not observed in AFMR
	AFMR LW: $C_{AFMR} = 3.7 \cdot 10^{-7}\ T/K^4$ ($\nu = 64, 84$ GHz)	[80S4]; anal. of ΔH_{AFMR} using Eq. 3.13, ($\Delta H^0_{AFMR} = f(\nu)$)
3) inel. n-scatt	$\omega(\boldsymbol{q})$ for $(\zeta_x, 0, 0)$, $(0.2, 0, 0.5)$, $(0.3, 0, 0.5)$ at $T = 8.5$ K fit to exp. data with renorm. spin-wave theory	[80S2], $\zeta_x = q_x/a^*$ fit: Eq. 3.15; parameter values: see spin-wave analysis
4) spin-wave analysis	exp. data included: $\nu_{AFMR}(T)$, $M_{subl}(T)$ and $\omega(\boldsymbol{q})$	[78S8, 80S2]
	($z = 4$, $S = 5/2$, $g = 2.000$, $J_2 \approx 0$, $J' \approx 0$, $\widetilde{H}_A \approx 0$, $\hat{H}_A \approx 0$)	J_2, J': Eq. 3.2; $\hat{H}_A$, $\widetilde{H}_A$: Eq. 3.41
	$J = -3.34\ cm^{-1} \hat{=} -4.80$ K, $H_E = 71.45$ T $T = 0$: $h_A = 1.36 \cdot 10^{-3}$, $g\mu_B H_A = 0.091\ cm^{-1}$, $H_A = 0.097$ T	parameter values according to linear spin-w. theory (cf. Eqs. 3.2–3.5, and 3.6)
	$J = -3.23\ cm^{-1} \hat{=} -4.65$ K, $H_E = 69.3$ T $T = 0$: $h_A = 1.40 \cdot 10^{-3}$, $g\mu_B H_A = 0.091\ cm^{-1}$, $H_A = 0.097$ T	parameter values according to renorm. spin-w. th. (cf. Eqs. 3.2–3.5, 3.15)
	calc.: $\Delta_0 S = 0.181$, $H_{AD} = 0.128$ T	[80S2]; $\Delta_0 S$: Eq. 3.19, H_{AD}: Eq. 3.12
5) meas. M	weak fm. $M(T)$ due to spin canting [5 K $\le T \le$ 45 K] $T = 0$: $M \hat{=} 0.028\ \mu_B \rightarrow \varphi = 0.32°$, $H_D = 0.40$ T	SQUID magnetometer [96 K] $M(T = 0) \rightarrow \varphi$: Eq. 3.55 ($M_S \approx M_0 \hat{=} 5\ \mu_B$); H_D: Eq. 3.54
6) optical studies	optical absorption 4000–44000 cm^{-1} [4.2 K $\le T \le$ 300 K]	electronic transitions [76A7]
	$T = 15$ K: study of magnon sideband near 26500 cm^{-1}	comp. of exp. data with calc. lineshape [95T2]

Table 5. Data concerning Magnetic Properties *(continued)*

Compound	Characteristic magnetic parameters: J, H_E, H_A, H_0, M, χ, g, T_C, T_N etc. [definitions see Table 1, units are given below]	References, remarks
$(C_2H_5NH_3)_2MnCl_4$	Antiferromagnet, $\boldsymbol{M}_{\mathbf{subl}} \parallel \boldsymbol{c}$ (spin canting, weak fm.: $\boldsymbol{M} \perp \boldsymbol{c}$)	details see [90A1], weak fm. due to DMI (Eq. 3.52)
1) meas. and anal. χ	$\chi_{\text{powder}}(T)$, $\chi_{\text{ac, powder}}(T)$ [4.2 K $\le T \le$ 300 K]	[79G6], see also [73H1, 89Z2, 91P]
	χ_{ac}: sharp peak at $T_N = 43.1(2)$ K resulting from weak fm.	spin canting, weak fm. $\boldsymbol{M}$ due to DMI (Eqs. 3.52, 3.53)
	$T > T_N$: $\chi(T) \rightarrow J = -3.20(3)\ \text{cm}^{-1} \hat{=} -4.60(5)$ K	theory $\chi(T)/\tilde{\chi}$ for $S = \frac{5}{2}$ afm. [76N4, 90N]; $\tilde{\chi}$: Eq. 3.28a
	$T = 1.2$ K: $M(H_0)$ for $\boldsymbol{H_0} \parallel \boldsymbol{c} \rightarrow H_{SF} = 3.10(3)$ T, $H_A = 68.5$ mT	$H_{SF} \rightarrow H_A$: Eq. 3.39
2) el. + quasi-el. n.scatt.	afm. Bragg refl. (1, 0, 0): $I(T) \sim M^2_{\text{subl}}(T) \rightarrow T_N = 42.1(2)$ K	[86A1, 90A1], see also [89Z2]
3) AFMR	$H_0 = 0$, $T = 4.2$ K: $h\nu_{AFMR} = 2.98\ \text{cm}^{-1} \hat{=} 4.29$ K; under various conditions: $H_E = 70.0$ T, $H_A = 70$ mT, $H_{SF} = 3.2$ T	[88S4, 89Z2], see also [81S4, 83G1, 89S3, 89S4] ν_{AFMR}: Eqs. 3.9, 3.10; H_{SF}: Eq. 3.39
4) (H_0, T) phase diagram	observed critical point identified as bicritical point	magn. meas. [76N3]; spin-flop transition broadened
5) optical studies	optical absorption 4000–40000 cm^{-1}	electronic transitions [76A7]
	T-dependence of the optical absorption near 24000 cm^{-1}	transition $^6A_{1g} \rightarrow {}^4A_{1g}\,(^4G)$, $^4E_g(^4G)$ [78K5]
	$T = 4.2$ K: study of the magnon sideband near 26500 cm^{-1}	[76K3, 78K6], see also [79T2]
	spin-w. calc. with: $J = -3.4\ \text{cm}^{-1}$, $g\mu_B H_A = 0.1\ \text{cm}^{-1}$	comparison of exp. data with calc. lineshape
$(C_3H_7NH_3)_2MnCl_4$	Antiferromagnet, $\boldsymbol{M}_{\mathbf{subl}} \parallel \boldsymbol{c}$ (spin canting, weak fm.: $\boldsymbol{M} \perp \boldsymbol{c}$)	details see [90A1], weak fm. due to DMI (Eq. 3.52)
1) meas. and anal. χ	$\chi_{\text{powder}}(T)$ [78K $\le T \le$ 300 K] $\chi_{ac}(T)$ [1 K $\le T \le$ 200 K]	[79G6, 80G7], effects of domains on χ_{ac} see [80G8]
	χ_{ac}: sharp peak at $T_N = 39.2(3)$ K resulting from weak fm.	spin canting, weak fm. due to DMI (Eqs. 3.52, 3.53)
	$T > T_N$: $\chi(T) \rightarrow J = -3.09(3)\ \text{cm}^{-1} \hat{=} -4.45(5)$ K	theory $\chi(T)/\tilde{\chi}$ for $S = \frac{5}{2}$ afm. [76N4, 90N]; $\tilde{\chi}$: Eq. 3.28a
	$T = 1.2$ K: $M(H_0)$ for $\boldsymbol{H_0} \parallel \boldsymbol{c} \rightarrow H_{SF} = 1.63(2)$ T, $h_A = 3 \cdot 10^{-4}$	$H_{SF} \rightarrow H_A$: Eq. 3.39; h_A: Eq. 3.6
2) meas. M	weak fm. $M(T)$ due to spin canting [5 K $\le T \le$ 39 K]	SQUID magnetometer [90A1]
	$T = 0$: $M \hat{=} 4.2 \cdot 10^{-4}\ \mu_B \rightarrow \varphi = 0.05°$, $H_D = 0.111$ T	$M(T = 0) \rightarrow \varphi$: Eq. 3.55 ($M_S \approx M_0 \hat{=} 5\ \mu_B$); H_D: Eq. 3.54
3) el. + quasi-el. n-scatt.	afm. Bragg refl. (1, 0, 1): $I(T) \sim M^2_{\text{subl}}(T) \rightarrow T_N = 39.3\ (1)$ K	[90A1]
4) AFMR	$H_0 = 0$, $T = 4.2$ K: $h\nu_{AFMR} = 1.85\ \text{cm}^{-1} \hat{=} 2.66$ K	[81S4, 83G1], AFMR (ν = 37.0, 87.4 GHz)
5) optical studies	T-dependence of the optical absorption near 24000 cm^{-1}	transition $^6A_{1g} \rightarrow {}^4A_{1g}\,(^4G)$, $^4E_g(^4G)$ [78K5]
	$T = 15$ K: study of the magnon sideband near 26500 cm^{-1}	comp. of exp. data with calc. lineshape [95T2]

Table 5. Data concerning Magnetic Properties *(continued)*

Compound	Characteristic magnetic parameters: J, H_E, H_A, H_0, M, χ, g, T_C, T_N etc. [definitions see Table 1, units are given below]	References, remarks
$(C_5H_{11}NH_3)_2MnCl_4$	only few and incomplete data on magnetic properties	[95F1]
$(C_7H_{15}NH_3)_2MnCl_4$	only few and incomplete data on magnetic properties	[95F1]
$(C_9H_{19}NH_3)_2MnCl_4$	only few and incomplete data on magnetic properties	[95F1]
$(C_{15}H_{31}NH_3)_2MnCl_4$	only few and incomplete data on magnetic properties	[74G3]
$(4\text{-}FC_6H_4NH_3)_2MnCl_4$	only few and incomplete data on magnetic properties	[79B4], $4\text{-}FC_6H_4NH_3$ = 4-fluoroanilinium
$(4\text{-}ClC_6H_4NH_3)_2MnCl_4$	only few and incomplete data on magnetic properties	[79B4, 93M1], $4\text{-}ClC_6H_4NH_3$ = 4-chloroanilinium
$(4\text{-}BrC_6H_4NH_3)_2MnCl_4$	only few and incomplete data on magnetic properties	[79B4], $4\text{-}BrC_6H_4NH_3$ = 4-bromoanilinium
$(C_2H_5NH_3)_2MnBr_4$	only few and incomplete data on magnetic properties	[73W4, 75R4]
$(C_3H_7NH_3)_2MnBr_4$	only few and incomplete data on magnetic properties	[73W4, 79G6]
$(CH_3NH_3)_2FeCl_4$	Antiferromagnet, $\boldsymbol{M}_{\mathbf{subl}} \perp \boldsymbol{c}$ (spin canting, weak fm.: $\boldsymbol{M} \parallel \boldsymbol{c}$)	details see [83N4]; weak fm. due to DMI (Eq. 3.52)
1) meas. χ	$\chi(T)$ [78 K $\le T \le$ 215 K] sharp peak at $T_N \approx 95$ K resulting from weak fm.	[80M4], see also [77M2, 83N4] spin canting, weak fm. due to DMI (Eqs. 3.52, 3.53)
2) meas. M	weak fm. $M(T)$ due to spin canting [4 K $\le T \le$ 160 K], $\boldsymbol{M} \parallel \boldsymbol{c}$, $M(T=0) \triangleq 0.08\ \mu_B \rightarrow \varphi = 1.1°$	[83N4]: $M(T=0) \rightarrow \varphi$: Eq. 3.55; $M_S \approx M_0$ (cf. Eq. 3.18)
3) Mössbauer study	hyperfine field $H_{hf}(T)/H_{hf}(0) = M_{subl}(T)/M_{subl}(0)$	[77K8] (exp. data)
	spin-w. th. fitted to $M(T)$: $J = -8(1)\ \text{K} \triangleq -5.6(7)\ \text{cm}^{-1}$, $g\mu_B H_A = 14.0\ \text{K} \triangleq 9.7\ \text{cm}^{-1}$, $g\mu_B \widetilde{H}_A = 12.8\ \text{K} \triangleq 8.9\ \text{cm}^{-1}$	[78L3]; renorm. spin-w. th., modfied model with $g\mu_B H_A = D(S - \frac{1}{2})$ and staggered $g\mu_B \widetilde{H}_A$ (Eq. 3.37a)
$(C_2H_5NH_3)_2FeCl_4$	Antiferromagnet, $\boldsymbol{M}_{\mathbf{subl}} \perp \boldsymbol{c}$ (spin canting, weak fm.: $\boldsymbol{M} \parallel \boldsymbol{c}$)	details see [83N4]; weak fm. due to DMI (Eq. 3.52)
1) C_{magn}	$T_N = 98.36$ K (details see Table 6)	[84Y1], C_p by high resolution ac cal.
2) meas. χ	$\chi(T)$ [78 K $\le T \le$ 380 K] $\rightarrow T_N = 90$ K small peak at T_N resulting from weak fm.	[80M4], see also [71M1] [83N4]
3) meas. M	weak fm. $M(T)$ due to spin canting [4 K $\le T \le$ 160 K], $\boldsymbol{M} \parallel \boldsymbol{c}$, $M(T=0) \triangleq 0.04\ \mu_B \rightarrow \varphi = 0.65°$	[83N4]; $M(T=0) \rightarrow \varphi$: Eq. 3.55; $M_S \approx M_0$ (cf. Eq. 3.18)

Table 5. Data concerning Magnetic Properties *(continued)*

Compound	Characteristic magnetic parameters: J, H_E, H_A, H_0, M, χ, g, T_C, T_N etc. [definitions see Table 1, units are given below]	References, remarks
$(C_3H_7NH_3)_2FeCl_4$	only few and incomplete data on magnetic properties	[71M1, 80M4]
$(C_4H_9NH_3)_2FeCl_4$	only few and incomplete data on magnetic properties	[80M4]
$(C_6H_5CH_2NH_3)_2FeCl_4$	only few and incomplete data on magnetic properties	[71M1, 73W5]
$(4\text{-}ClC_6H_4NH_3)_2FeCl_4$	only few and incomplete data on magnetic properties	[79B4], $4\text{-}ClC_6H_4NH_3$ = 4-chloroanilinium
$(CH_3NH_3)_2FeCl_3Br$	only few and incomplete data on magnetic properties	[78S9]
$(CH_3NH_3)_2FeCl_2Br_2$	only few and incomplete data on magnetic properties	[77M2]
$(CH_3NH_3)_2CuCl_4$	Ferromagnet, $\boldsymbol{M} \parallel \boldsymbol{a}$ (covert spin canting, $\boldsymbol{c}$: hard axis)	details see [72J4, 84S4, 88D3, 89D2]; struct.: $P2_1/b11$
1) meas. and anal. χ	$\chi_{\text{powder}}(T)$ [$13\ K \le T \le 150\ K$], $\chi'_{ac}(T)$, $\chi''_{ac}(T)$ at $f = 119$ Hz for $\mathbf{H_0} \parallel \mathbf{a}, \parallel \mathbf{b}, \parallel \mathbf{c}$ [$0.3\ K \le T \le 14\ K$] $\rightarrow T_C = 8.903(2)$ K	[84S4], see also [69J, 71J2, 72D, 87A4]
	$\chi(T > T_C)$: h.t.s. $\rightarrow J = 13.3(2)\ \text{cm}^{-1} \hat{=} 19.2(3)$ K	[84S4]; h.t.s.: Eqs. 3.26, 3.27; coeff. see [67B2, 90N]
	calc.: $J = 19.2$ K, $S = \frac{1}{2} \rightarrow T_C^{(2)} = 5.8$ K ($T_C = 8.9$ K)	[72J2]; $J \rightarrow T_C^{(2)}$: Eq. 3.29
	$\chi(T, p)$ [$6\ K \le T \le 18\ K$, $0 \le p \le 10^9$ Pa] $\rightarrow T_C(p)$	[80M5]
2) EPR	$g_a = g_b = 2.169(3)$, $g_c = 2.054(2)$ ($\nu \approx 35$ GHz)	[69D, 72D, 76Y3, 89D2], see also [67W2]
3) NMR	^{35}Cl-NMR: $f_{NMR}(T) \sim M(T)$ [$1.8\ K \le T \le 4.2\ K$],	[77K9], see also [74K6, 77D4]
	exp. data comp. with $M(T)$ calc. by renorm. spin-w. th.: $J = 18.4$ K, $h_A = 2.54 \cdot 10^{-3}$, $\tilde{h}_A = 1.8 \cdot 10^{-4}$, $h'_E = 7.9 \cdot 10^{-5}$	calculation of $M(T)$ with renorm. spin-w. th. derived in [76T1, 77U] (cf. Eq. 3.74); h_A, $\tilde{h}_A$, h'_E : Eq. 3.71
	determination of T_1 and T_2: T_1 of ^{1}H, T_2 of ^{35}Cl, ^{63}Cu	T_2: [77K5], T_1: [82N3]
4) FMR	$1.2\ \text{GHz} \le \nu \le 4.0$ GHz, $\boldsymbol{H_0} \parallel \boldsymbol{c}$, $T = 1.3$ K; 2 FMR-modes observed for $\boldsymbol{H_0} \parallel \boldsymbol{c}$ due to spin canting in adjacent layers	[88D3]; spin canting and afm. component resulting from anisotropic exchange ~ H_D (cf. Eq. 3.99)
	$100\ \text{MHz} \le \nu \le 4.5$ GHz, for $\boldsymbol{H_0} \parallel \boldsymbol{a}, \parallel \boldsymbol{b}, \parallel \boldsymbol{c}$ [$1.2 \le T \le 20$ K]	[87D1, 88D3, 89D2, 90D3], see also [75R5, 76Y3]
	determ. of $H_C(T)$ [$\boldsymbol{H_0} \parallel \boldsymbol{c}$], $H_A(T)$, $\tilde{H}_A(T)$, $\nu_{gap}(T)$	
	$T = 0$: $H_A^{\Delta} = H_C = 0.148(2)$T, $\tilde{H}_A = 8.6$ mT, $\nu_{gap} = 1.240$ GHz $\rightarrow H_A = 0.140$ T, $J_A = 51$ mK, $\tilde{J}_A = 3.1$ mK, $M_0 = 51.3$ mT	ν_{FMR}: Eqs. 3.105–3.109; H_A^{Δ} : Eq. 3.109a H_A, $\tilde{H}_A$: Eq. 3.96; M_0: Eqs. 3.75–3.76

Table 5. Data concerning Magnetic Properties *(continued)*

Compound	Characteristic magnetic parameters: J, H_E, H_A, H_0, M, χ, g, T_C, T_N etc. [definitions see Table 1, units are given below]	References, remarks
$(CH_3NH_3)_2CuCl_4$ (cont.)		
5) parallel pumping	subthr. p. p. ($\nu = 8.9$ GHz) $\rightarrow H'_E(T)$ [$1.2\ K \le T \le 4.2\ K$] $T = 0$: $H'_E = 4.15$ mT, $g_a \mu_B H'_E = 6.05$ mK, $J' = +0.75$ mK	[74Y3, 76Y3], see also [80Y1, 81W6, 82Y1]; p. p.: Eqs. 3.116–3.121; $\omega(\boldsymbol{q})$: Eqs. 3.122–3.124
	p. p. spectra (8.91 GHz) → spin-wave relaxation	[88Y1]
	chaos: p. p. experiments ($\omega_p/2\pi = 9.39$ GHz, $T = 1.645$ K) produce chaotic oscillations of the magnon amplitude	[86Y1, 87Y3]
6) thermal conductivity	exp. study of $\lambda(t, H_0)$ [$1.5\ K \le T \le 25\ K$, $0 \le H_0 \le 6.5\ T$]	[77C5, 77L3], see also [69G1]; heat transport by magnons
7) optical studies	absorption spectra 8000–25000 cm^{-1} [$4.2\ K \le T \le 300\ K$] and reflectivity 20000–40000 cm^{-1} at $T = 300$ K	[75A3], see also [67W2, 77H1]; electronic transitions
$(CD_3ND_3)_2CuCl_4$	Ferromagnet, weak afm., preferred spin direction in adjacent layers at ± 23° from *b*-axis in *bc*-plane	details see [79S2, 83S2]; struct.: $A2_1/b11$
1) meas. and anal. χ	$\chi'_{ac}(T)$, $\chi''_{ac}(T)$ at $f = 20.7$ Hz [$4\ K \le T \le 20\ K$] $\rightarrow T_C = 8.84$ K $\chi'_{ac}(T)$ for $\boldsymbol{H_0} \parallel \boldsymbol{a}, \parallel \boldsymbol{b}, \parallel \boldsymbol{c} \rightarrow H_A = 90$ mT, $\widetilde{H}_A = 3.3$ mT	[79S2, 84S4]
2) el. and quasi-el. n-scatt.	magn. contribution to (0, 0, 2) Bragg refl.: $I_{magn}(T) \sim M^2(T)$, spin-w. th. fitted to $M(T)$: $J = 13.4(3)\ cm^{-1} \hat{=} 19.3(5)$ K	[83S2, 84S4], see also [87A4]; calc. of $M(T)$ with renorm. spin-w. th. derived in [76T1, 77U], cf. Eq. 3.71
$(C_2H_5NH_3)_2CuCl_4$	Antiferromagnet, $\boldsymbol{M_{subl}} \parallel \boldsymbol{a}$ (covert spin canting, $\boldsymbol{c}$: hard axis)	details see [71J3, 72B5, 72J4, 73B5, 84V1]; struct.: Pbca
1) meas. and anal. χ	$\chi(T)$ [$6.5\ K \le T \le 150$], $\chi(T)$ for $\boldsymbol{H_0} \parallel \boldsymbol{a}, \parallel \boldsymbol{b}, \parallel \boldsymbol{c}$ [$1.2\ K \le T \le 19\ K$] $\rightarrow T_N = 10.20(1)$ K	[71J2, 72J4], see also [69J, 72D] renom. spin-w. th. for $\chi(T)$: see [77T4]
	$\chi(T > T_N)$: h.t.s. $\rightarrow J = 12.9(3)\ cm^{-1} \hat{=} 18.6(5)$ K	[71J2, 72J4]; h.t.s.: Eqs. 3.26, 3.27; coeff. see [67B2, 90N]
	calc.: $J = 18.6$ K, $S = \frac{1}{2} \rightarrow T_C^{(2)} = 5.6$ K ($T_N = 10.2$ K)	[72J2]; $J \rightarrow T_C^{(2)}$: Eq. 3.29
2) EPR	$g_a = g_b = 2.164(3)$, $g_c = 2.053(2)$ ($\nu \approx 35$ GHz)	[69D, 72D], see also [67W2, 75R5, 76Y3]

Table 5. Data concerning Magnetic Properties *(continued)*

Compound	Characteristic magnetic parameters: J, H_E, H_A, H_0, M, χ, g, T_C, T_N etc. [definitions see Table 1, units are given below]	References, remarks
$(C_2H_5NH_3)_2CuCl_4$ (cont.)		
3) (H_0, T) phase diagram	determ. of $H_{SF}(T)$; $H^{a}_{PM}(T)$, $H^{b}_{PM}(T)$, $H^{c}_{PM}(T)$	[72J3, 72J4]; meas. of χ and differential $\chi = \partial M/\partial H$;
	$T = 0$: $H'_E = 80(1)$ mT, $H_A = 91.8$ mT, $\widetilde{H}_A = 9(1)$ mT	linear spin-w. th. with $H_D \approx 0$ (cf. Eqs. 3.57–3.59, 3.99)
	determ. of $H_{SF}(T)$, $H^{a}_{CF}(T)$, $H^{b}_{CF}(T)$, $H^{c}_{CF}(T)$: $T = 1$ K:	[72B5, 73B5]; meas. of χ and torque measurements;
	$H'_E = 83$ mT, $H_A = 158$ mT, $\widetilde{H}_A = 7.5$ mT; $H_D = 11.9$ mT	linear spin-w. th. with $H_D \neq 0$ (cf. Eqs. 3.57–3.60, 3.99)
	high pressure exp.: $\chi_{ac}(p)$ at 37 Hz [$0 \le p \le 7.5 \cdot 10^8$ Pa],	[83C3], see also [81P1]
	AFMR (9 GHz) [$0 \le p \le 4.4 \cdot 10^8$ Pa], both for $\boldsymbol{H_0} \parallel \boldsymbol{a}$, $\parallel \boldsymbol{b}$	
	$\rightarrow H_A(p)$, $\widetilde{H}_A(p)$ [1.4 K], $H_{SF}(p)$, $H^{a}_{PM}(p)$, $H^{b}_{PM}(p)$ [1.8 K]	linear spin-w. th. with $H_D \approx 0$ (cf. Eqs. 3.57–3.59, 3.99)
4) AFMR	[$358\ \text{MHz} \le \nu \le 880\ \text{MHz}$] for $\boldsymbol{H_0} \parallel \boldsymbol{a}$, $\parallel \boldsymbol{b}$ at $T = 1.2$ K	[76T2], see also [76Y3]; linear spin-w. th. with $H_D \approx 0$
	$\rightarrow H'_E = 77.2$ mT, $H_A = 123.2$ mT, $\widetilde{H}_A = 7.4$ mT	(Eq. 3.99); ν_{AFMR}: see [76T2]; H'_E, H_A, $\widetilde{H}_A$: Eq. 3.96
	[$0 < \nu \le 4$ GHz], $\boldsymbol{H_0} \parallel \boldsymbol{a}$, $T = 4.2$ K: influence of spin canting	[84V1]; linear spin-w. th. with $H_D = 11.9$ mT (Eq. 3.99)
	PM-phase, $\nu = 8.9$ GHz [$4.2\ \text{K} \le T \le 20$ K] $\rightarrow H_{res,fm}$, $H_{res,afm}$	[78R1, 80Y2], see also [73A6, 75R5]; cf. Sect. 3.1.8
	[$0.8\ \text{GHz} \le \nu \le 8$ GHz], $T = 1.4$ K, $\boldsymbol{H_0} \parallel \boldsymbol{a}$, $\parallel \boldsymbol{b}$: H_{AD} incl. in	[81C2]; influence of magn. dipolar interactions; linear spin-w.th.
	$H_A \rightarrow$ AF-phase $H_A = 180$ mT, PM-phase $H_A = 139$ mT	with $H_D \neq 0$ (Eq. 3.99) and $\mathcal{H}_{dipolar}$ (Eq. 3.8)
5) parallel pumping	subthr. p. p. ($\nu = 8.9$ GHz) $\rightarrow H'_E(T)$ [$1.2\ \text{K} \le T \le 4.2$ K]	[74Y3, 76Y3], H'_E see also [72J4, 73B5, 76T2, 81W6]
	$T = 0$: $H'_E = 79(2)$ mT, $g_a \mu_B H'_E = 114$ mK, $J' = -14.3$ mK	p. p.: Eqs. 3.116–3.121; $\omega(\boldsymbol{q})$: Eqs. 3.122–3.124
	p. p. at 8.9 GHz: $\Delta H_q(T)$ in PM-phase [$1.2\ \text{K} \le T \le 2.7$ K]	[80Y2]
	p. p. above threshold: $\omega(q = c^*)$ vs. $\boldsymbol{H_0} \parallel \boldsymbol{a}$ [$0 \le H_0 \le 0.15$ T]	[83Y4, 87Y2]; linear spin-w. th. with $H_D \neq 0$
	perpendicular pumping: spin-wave instabilities at H_{SF}	[88J1]
6) NMR	^{35}Cl-, ^{63}Cu-NMR: $f_{NMR}(T) \sim M(T)$ [$1.4\ \text{K} \le T \le 4.2$ K]	[77D4], see also [80K3]; calc. with renorm. spin-w. th.
	^{35}Cl-NMR, $\boldsymbol{H_0} \parallel \boldsymbol{a}$, $T = 1.75$ K: $f_{NMR} \rightarrow M_{subl}(\uparrow)$, $M_{subl}(\downarrow)$	[77K9], see also [80K3]; calc. with renorm. spin-w. th.
7) thermal conductivity	exp. study of $\lambda(T)$ [$1.5\ \text{K} \le T \le 20$ K] at $H_0 = 0$ and 6.5 T	[77C5, 77L3]; heat transport by magnons
8) optical studies	absorption 8000–22000 cm^{-1}, Faraday rotation	[77H1], electronic transitions

Table 5. Data concerning Magnetic Properties *(continued)*

Compound	Characteristic magnetic parameters: J, H_E, H_A, H_0, M, χ, g, T_C, T_N etc. [definitions see Table 1, units are given below]	References, remarks
$(C_3H_7NH_3)_2CuCl_4$	Antiferromagnet	
1) meas. and anal. χ	$\chi(T)$ [$6.5\ K \le T \le 150\ K$] $\rightarrow T_N = 7.65\ K$	[71J2], see also [69J, 72D]
	$\chi(T > T_N)$: h.t.s. $\rightarrow J = 11.1\ cm^{-1} \hat{=} 16.0\ K$	h.t.s.: Eqs. 3.26, 3.27; coeff. see [67B2, 90N]
2) EPR	$g_a = g_b = 2.160(3)$, $g_c = 2.053(2)$ ($\nu \approx 35$ GHz)	[72D], see also [76Y3]
3) parallel pumping	subthr. p. p. ($\nu = 8.9$ GHz) $\rightarrow H'_E\ (T)$ [$1.2\ K \le T \le 4.2\ K$]	[76Y3]; p. p.: Eqs. 3.116–3.121;
	$T = 0$: $H'_E = 1.6(3)$ mT, $g_a \mu_B H'_E = 2.3$ mK, $J' = -0.285$ mK	$\omega(\boldsymbol{q})$: Eqs. 3.122–3.124
4) NMR	^{35}Cl-NMR: $f_{NMR}(T) \sim M(T)$ [$1.8\ K \le T \le 4.2\ K$],	[77K9], see also [77D4]
	exp. data comp. with $M(T)$ calc. by renorm. spin-w. th.	[77T3]
5) various methods	$H_A = 130(7)$ mT, $\tilde{H}_A = 8(1)$ mT	see Tables in [74M2, 75Y, 76B5, 76J1, 77B3]
$(C_4H_9NH_3)_2CuCl_4$	Antiferromagnet; spin canting in field-induced PM-phase by ± 17° from *a*-axis in *ab*-plane for adjacent layers	details see [77Y2, 77Y3]
1) meas. and anal. χ	$\chi(T)$ [$6.5\ K \le T \le 150\ K$] $\rightarrow T_N = 7.33\ K$	[71J2], see also [69J]
	$\chi(T > T_N)$: h.t.s. $\rightarrow J = 10.7\ cm^{-1} \hat{=} 15.4\ K$	h.t.s.: Eqs. 3.26, 3.27; coeff. see [67B2, 90N]
2) EPR	$g_a = g_b = 2.165(3)$, $g_c = 2.050(2)$ ($\nu = 8.9$ GHz)	[76Y3]
3) parallel pumping	subthr. p. p. ($\nu = 8.9$ GHz) $\rightarrow H'_E\ (T)$ [$1.2\ K \le T \le 4.2\ K$]	[76Y3]; p. p.: Eqs. 3.116–3.121;
	$T = 0$: $H'_E = 1.6(3)$ mT, $g_a \mu_B H'_E = 2.3$ mK, $J' = -0.285$ mK	$\omega\ (\boldsymbol{q})$: Eqs. 3.122–3.124
	β-dependence of p. p. above threshold and of FMR reveal spin canting by ± 17° from *a*-axis in field-induced PM-phase	[77Y2, 77Y3]; $\beta = \angle(\boldsymbol{H_0}, \boldsymbol{a})$ in *ab*-plane, $\boldsymbol{a} \parallel x$-axis
4) FMR	$\nu = 8.9$ GHz $\rightarrow H_A(T)$, $\tilde{H}_A\ (T)$ [$1.2\ K \le T \le 4.2\ K$]	[76Y3]; field-induced PM-phase with $\boldsymbol{M_a} \parallel \boldsymbol{M_b} \parallel \boldsymbol{H_0}$:
	$T = 0$: $H_A = 119(4)$ mT, $\tilde{H}_A = 21.6(15)$ mT	ν_{FMR} see Eqs. 3.105–3.109
5) NMR	^{35}Cl-NMR: $f_{NMR}(T) \sim M(T)$ [$1.8\ K \le T \le 4.2\ K$],	[77K9], see also [77D4]
	exp. data comp. with $M(T)$ calc. by renorm. spin-w. th.:	calculation of $M(T)$ with renorm. spin-w. th. derived
	$J = 15.8$ K, $H_A = 121$ mT, $\tilde{H}_A = 22$ mT, $H'_E = 1.6$ mT	in [76T1, 77U] (cf. Eq. 3.74); H_A, $\tilde{H}_A$, H'_E : Eq. 3.96

Table 5. Data concerning Magnetic Properties *(continued)*

Compound	Characteristic magnetic parameters: J, H_E, H_A, H_0, M, χ, g, T_C, T_N etc. [definitions see Table 1, units are given below]	References, remarks
$(C_5H_{11}NH_3)_2CuCl_4$	Antiferromagnet	
1) meas. and anal. χ	$\chi(T)$ [6.5 K $\leq T \leq$ 150 K] $\rightarrow T_N = 7.30$ K $\chi(T > T_N)$: h.t.s. $\rightarrow J = 11.05\ \mathrm{cm}^{-1} \mathrel{\hat{=}} 15.9$ K	[71J2], see also [69J] h.t.s.: Eqs. 3.26, 3.27; coeff. see [67B2, 90N]
2) EPR	$g_a = g_b = 2.160(3)$, $g_c = 2.054(2)$ ($\nu = 8.9$ GHz)	[76Y3]
3) FMR	$\nu = 8.9$ GHz $\rightarrow H_A(T)$, $\tilde{H}_A(T)$ [1.2 K $\leq T \leq$ 4.2 K] $T = 0$: $H_A = 140(4)$ mT, $\tilde{H}_A = 10.0(5)$ mT	[76Y3]; field-induced PM-phase with $\boldsymbol{M}_\mathbf{a} \parallel \boldsymbol{M}_\mathbf{b} \parallel \boldsymbol{H}_\mathbf{0}$: ν_{FMR} see Eqs. 3.105–3.109
4) parallel pumping	subthr. p. p. ($\nu = 8.9$ GHz) $\rightarrow H'_E(T)$ [1.2 K $\leq T \leq$ 4.2 K] $T = 0$: $H'_E = 1.5(3)$ mT, $g_a\mu_B H'_E = 2.15$ mK, $J' = -0.27$ mK	[76Y3]; p. p.: Eqs. 3.116–3.121; $\omega(\boldsymbol{q})$: Eqs. 3.122–3.124
$(C_6H_{13}NH_3)_2CuCl_4$	Antiferromagnet	
1) meas. and anal. χ	$\chi(T)$ [6.5 K $\leq T \leq$ 150 K] $\rightarrow T_N = 7.75$ K $\chi(T > T_N)$: h.t.s. $\rightarrow J = 11.9\ \mathrm{cm}^{-1} \mathrel{\hat{=}} 17.1$ K	[71J2], see also [69J] h.t.s.: Eqs. 3.26, 3.27; coeff. see [67B2, 90N]
2) EPR	$g_a = g_b = 2.164(3)$, $g_c = 2.052(3)$ ($\nu = 8.9$ GHz)	[76Y3]
3) FMR	$\nu = 8.9$ GHz $\rightarrow H_A(T)$, $\tilde{H}_A(T)$ [1.2 K $\leq T \leq$ 4.2 K] $T = 0$: $H_A = 155(5)$ mT, $\tilde{H}_A = 18.5(10)$ mT	[76Y3]; field-induced PM-phase with $\boldsymbol{M}_\mathbf{a} \parallel \boldsymbol{M}_\mathbf{b} \parallel \boldsymbol{H}_\mathbf{0}$: ν_{FMR} see Eqs. 3.105–3.109
4) parallel pumping	subthr. p. p. ($\nu = 8.9$ GHz) $\rightarrow H'_E(T)$ [1.2 K $\leq T \leq$ 4.2 K] $T = 0$: $H'_E = 1.0(3)$ mT, $g_a\mu_B H'_E = 1.5$ mK, $J' = -0.19$ mK	[76Y3]; p. p.: Eqs. 3.116–3.121; $\omega(\boldsymbol{q})$: Eqs. 3.122–3.124
$(C_{10}H_{21}NH_3)_2CuCl_4$	Ferromagnet	$J' > 0$, see [72J4]
1) meas. and anal. χ	$\chi(T)$ [6.5 K $\leq T \leq$ 150 K] $\rightarrow T_C = 7.91$ K $\chi(T > T_C)$: h.t.s. $\rightarrow J = 12.4\ \mathrm{cm}^{-1} \mathrel{\hat{=}} 17.9$ K	[71J2] h.t.s.: Eqs. 3.26, 3.27; coeff. see [67B2, 90N]
2) NMR	^{35}Cl-NMR: $f_{NMR}(T) \sim M(T)$ [1.8 K $\leq T \leq$ 4.2 K], exp. data comp. with $M(T)$ calc. by renorm. spin-w. th.: $J = 16.0$ K, $h_A = 3.7 \cdot 10^{-3}$, $\tilde{h}_A = 6 \cdot 10^{-5}$, $h'_E = 2 \cdot 10^{-6}$	[77D4] renorm. spin-w. th. of [77D4]; h_A, $\tilde{h}_A$, h'_E: Eq. 3.71 alternative values h_A, $\tilde{h}_A$, h'_E: see [74M2, 75Y, 76B5]

Table 5. Data concerning Magnetic Properties *(continued)*

Compound	Characteristic magnetic parameters: J, H_E, H_A, H_0, M, χ, g, T_C, T_N etc. [definitions see Table 1, units are given below]	References, remarks
$(C_2H_4OH\text{-}NH_3)_2CuCl_4$	only few and incomplete data on magnetic properties	[87L1], $C_2H_4OH\text{-}NH_3$ = ethanolammonium
$[C_6H_5NH_3]_2CuCl_4$	only few and incomplete data on magnetic properties	[77Z, 82W6]
$[C_6H_5(CH_2)NH_3]_2CuCl_4$	Ferromagnet $\boldsymbol{M} \parallel (1, 1, 0)$ ($\boldsymbol{c}$: hard axis)	details see [76D2, 80E2, 87K2, 90K2]
1) EPR	$g_a = g_b = 2.163(3)$, $g_c = 2.046(3)$ ($\nu = 8.9$ GHz)	[76Y3], see also [76D2]
2) FMR	$\nu = 8.9$ GHz $\rightarrow H_A(T)$, $\tilde{H}_A(T)$ [1.2 K $\le T \le 4.2$ K] $T = 0$: $H_A = 145(5)$ mT, $\tilde{H}_A = 3.2(2)$ mT	[76Y3], see also [76D2, 77D5, 78R2, 80E2]; ν_{FMR}: Eqs. 3.105–3.109; note. $\boldsymbol{M} \parallel \boldsymbol{H_0}$, (1, 1, 0) = easy axis
3) parallel pumping	subthr. p. p. ($\nu = 8.9$ GHz) $\rightarrow H'_E(T)$ [1.2 K $\le T \le 4.2$ K] $T = 0$: $H'_E = 0.8(3)$ mT, $g_a\mu_B H'_E = 1.2$ mK, $J' = +0.15$ mK	[76Y3]; p. p.: Eqs. 3.116–3.121; $\omega(\boldsymbol{q})$: Eqs. 3.122–3.124
4) NMR	^{35}Cl-, ^{63}Cu-NMR: $f_{NMR}(T) \sim M(T)$ [1.4 K $\le T \le 4.2$ K], exp. data comp. with $M(T)$ calc. by renorm. spin-w. th.: $J = 16.5$ K ($H_E = 45.4$ T), $H_A = 121$ mT, $\tilde{H}_A = 2.5$ mT	[76D2, 77D5, 78R2], see also [80E2] renorm. spin-w. th. for calc. $M(T)$ not specified in detail; theory also fitted to $f_{NMR}(H_0)$ for $\boldsymbol{H_0} \parallel (1, 1, 0)$
5) (H_{int}, T)-phase diagram	$\chi_{ac}(H_{int}, T)$ at 30 Hz [4.2 K $\le T \le 30$ K, $0 \le H_{int} \le 1.5$ mT] for $\boldsymbol{H_0} \parallel (1, 1, 0)$, two magn. pt. observed for $H_{int} < 0.25$ mT; $H_{int} = 0$: $T_{C1} = 7.0$ K, $T_{C2} = 5.0$ K; $H_{int} \ge 0.25$ mT: $T_C = 7.0$ K	[87K2, 90K2], see also [78R2, 84K7] at $H_{int} = 0.25$ mT, T_{C1} and T_{C2} merge into one T_C; origin of the two magn. pt. not yet clarified
$[C_6H_5(CH_2)_2NH_3]_2CuCl_4$	Ferromagnet $\boldsymbol{M} \parallel \boldsymbol{a}$ ($\boldsymbol{c}$: hard axis)	details see [76D2, 76Y3]; struct.: presumably Pbca
1) EPR	$g_a = g_b = 2.158(3)$, $g_c = 2.053(2)$ ($\nu = 8.9$ GHz)	[76Y3]
2) FMR	$\nu = 8.9$ GHz $\rightarrow H_A(T)$, $\tilde{H}_A(T)$ [1.2 K $\le T \le 4.2$ K] $T = 0$: $H_A = 176(5)$ mT, $\tilde{H}_A = 21.8(15)$ mT	[76Y3], see also [76D2, 77D5, 78R2, 80E2]; ν_{FMR}: Eqs. 3.105–3.109; note: $\boldsymbol{M} \parallel \boldsymbol{H_0}$
3) parallel pumping	subthr. p. p. ($\nu = 8.9$ GHz) $\rightarrow H'_E(T)$ [1.2 K $\le T \le 4.2$ K] $T = 0$: $H'_E = 0.6(3)$ mT, $g_a\mu_B H'_E = 0.8$ mK, $J' = +0.1$ mK	[76Y3]; p. p.: Eqs. 3.116–3.121; $\omega(\boldsymbol{q})$: Eqs. 3.122–3.124
4) NMR	^{35}Cl-NMR: $f_{NMR}(T) \sim M(T)$ [1.8 K $\le T \le 4.2$ K], $T_C = 9.2$ K, exp. data comp. with $M(T)$ calc. by renorm. spin-w. th.: $J = 18.4$ K ($H_E = 52.4$ T), $H_A = 142.4$ mT, $\tilde{H}_A = 20$ mT	[76D2, 77D5, 78R2], see also [80E2] renorm. spin-w. th. for calc. $M(T)$ not specified in detail; theory also fitted to $f_{NMR}(H_0)$ for $\boldsymbol{H_0} \parallel \boldsymbol{a}$

Table 5. Data concerning Magnetic Properties *(continued)*

Compound	Characteristic magnetic parameters: J, H_E, H_A, H_0, M, χ, g, T_C, T_N etc. [definitions see Table 1, units are given below]	References, remarks
$[C_6H_5(CH_2)_3NH_3]_2CuCl_4$	only few and incomplete data on magnetic properties	[76D2, 77D5, 80E2]
$[COOH(CH_2)_2NH_3]_2CuCl_4$	Ferromagnet, $\boldsymbol{M} \parallel \boldsymbol{b}$ ($\boldsymbol{c'}$: hard axis, $\boldsymbol{c'} \perp \boldsymbol{a}, \boldsymbol{b}$)	details see [81W2; $\angle(\boldsymbol{c}, \boldsymbol{c'}) = \beta - 90°$; struct.: I12/c1
1) meas. and anal. χ	$\chi_{\mathrm{powder}}(T)$ [4 K $\le T \le$ 105 K]	[81W2]
	$\chi(T > T_C)$: h.t.s. $\rightarrow J = 9.7\ \mathrm{cm}^{-1} \mathrel{\hat{=}} 13.9$ K	h.t.s.: Eqs. 3.26, 3.27; coeff. see [67B2, 90N]
	$\chi(T)$ for $\boldsymbol{H_0} \parallel \boldsymbol{a}, \parallel \boldsymbol{b}, \parallel \boldsymbol{c'}$ [1.5 K $\le T \le$ 11.5 K], $T_C = 6.5(5)$ K	[81W2]; $\boldsymbol{c'} \perp \boldsymbol{a}, \boldsymbol{b}$; $\angle(\boldsymbol{c}, \boldsymbol{c'}) = \beta - 90° = 1.82°$
	$\rightarrow H_A = 95$ mT, $\tilde{H}_A = 20$ mT	H_A, $\tilde{H}_A$: Eq. 3.96
2) EPR	$g_a = 2.171$, $g_b = 2.151$, $g_{c'} = 2.045$ ($\nu = 9.36$ GHz)	[81W2]; $\boldsymbol{c'} \perp \boldsymbol{a}, \boldsymbol{b}$
3) meas. M	$M(H_0)$ for $\boldsymbol{H_0} \parallel \boldsymbol{a}, \parallel \boldsymbol{b}, \parallel \boldsymbol{c'}$ [$0 \le H_0 \le 0.45$ T] $\rightarrow J' > 0$	[81W2]
$(C_5H_9NH_3)_2CuCl_4$	only few and incomplete data on magnetic properties	[92L3]; $C_5H_9NH_3$ = cyclopentylammonium
$(CH_3NH_3)_2Cu(Cl_xBr_{1-x})_4$	mixed crystals $0 \le x \le 1.0$	details see [78K7, 79K7, 80K4, 82K4, 83K5]
	x = 0: $J' < 0$, antiferromagnet, $\boldsymbol{c}$: easy axis, $T_N = 15.8$ K	see [80K6, 81S5]
	x $\approx$ 0.1: cancellation of J'?	see [78K7, 79K7, 83K5]
	x = 1: $J' > 0$, ferromagnet, $\boldsymbol{a}$: easy axis, $T_C = 8.9$ K	see [72J4, 79S2, 84S4, 88D3, 89D2]
1) meas. and anal. χ	$\chi(H_0)$ [$0 \le H_0 \le 1$ T] for $\boldsymbol{H_0} \parallel \boldsymbol{a}, \parallel \boldsymbol{b}, \parallel \boldsymbol{c}$ and various x at $T = 4.2$ K $\rightarrow T_C$(x), min. at x = 0.1: $T_C(0.1) = 9.6$ K	} [80K4, 80K5], see also [78K7]
2) EPR	x = 0.5: $g_a = g_b = 2.122(6)$, $g_c = 2.035$ (6)	[72D]
3) NMR	^{35}Cl-, ^{63}Cu-, ^{65}Cu-, ^{79}Br-, ^{81}Br-NMR at $T = 1.75$ K $\rightarrow$ $0 \le x \le 0.03$: afm. LRO, spins at 31°–27° from c-axis $0.03 \le x \le 0.18$: oblique phase, spins inclined by 0°–59° from (1, 0, 0) towards c-axis $0.18 \le x \le 0.97$: fm. LRO, spins parallel (1, 0, 0)	[81K8, 82K4, 83K5], see also [79K7, 81K7, 83K6, 83K7]
$(C_3H_7NH_3)_2CuCl_2Br_2$	only few and incomplete data on magnetic properties	[72D, 77Z]

Table 5. Data concerning Magnetic Properties *(continued)*

Compound	Characteristic magnetic parameters: J, H_E, H_A, H_0, M, χ, g, T_C, T_N etc. [definitions see Table 1, units are given below]	References, remarks
$(CH_3NH_3)_2CuBr_4$	Four-sublattice antiferromagnet with hidden spin canting	details see [80K6, 81S5]
1) meas. and anal χ	$\chi_{ac,\ powder}(T)$ at 80 Hz [$1.2\ K \le T \le 21\ K$] → $T_N = 15.8$ K	[80K6]
	$\chi_{ac}(H_0)$ at 80 Hz for $\boldsymbol{H_0} \parallel \boldsymbol{a}, \parallel \boldsymbol{b}, \parallel \boldsymbol{c}$ [$0 \le H_0 \le 0.8$ T] → no weak ferromagnetism; ***c***: easy axis, ***a***: hard axis	[80K6]; $T = 4.2$ K, $\boldsymbol{H_0} \parallel \boldsymbol{c}$: $\chi_{ac}(H_0)$ exhibits at 0.52 T an anomaly probably due to a flop-like transition
2) EPR	$g_a = g_b = 2.09(1)$, $g_c = 2.05(1)$	[80K6]
3) various methods	$T_N = 15.78$ K, $J = 14.6\ cm^{-1} \mathrel{\hat{=}} 21.0$ K, $H_E = 44.1$ T $H'_E = 1.15$ T ($J' = 0.20$ K), $H_A = -200$ mT, $\tilde{H}_A = -20$ mT	see Tables in [76B5, 77B3], see also [74M2]; H'_E, H_A, $\tilde{H}_A$: Eq. 3.96; $H_A < 0$ and $\tilde{H}_A < 0$ (cf. Eq. 3.99c)
4) NMR	^{79}Br-, ^{81}Br-NMR → afm. with 4 sublattices in 4 layers: $\boldsymbol{M_a}$, $\boldsymbol{M_b}$, $\boldsymbol{M_c}$, $\boldsymbol{M_d}$ inclined by +27°, –27°, +153°, –153°, resp., from the *c*-axis in the *bc*-plane	[81S5]; 4 sublattices in 4 layers because of strong fm. intralayer coupling; no fm. moment, hidden spin canting; not determined: chemical and magnetic unit cell
$(C_2H_5NH_3)_2CuBr_4$	Antiferromagnet, $\boldsymbol{M_{subl}} \parallel \boldsymbol{b}$ (spin canting, ***c***: hard axis)	details see [80K7, 81S5]; struct.: presumably Pbca
1) meas. and anal. χ	$\chi(T)$ [$6.5\ K \le T \le 150\ K$] → $T_N = 10.85$ K $\chi(T > T_N)$: h.t.s. → $J = 13.2\ cm^{-1} \mathrel{\hat{=}} 19.0$ K	[71J2], see also [69J] h.t.s.: Eqs. 3.26, 3.27; coeff. see [67B2, 90N]
2) EPR	$g_a = g_b = 2.153$, $g_c = 2.047$	[73W6]
3) various methods	$H'_E = 185$ m T ($J' = -33$ mK), $H_A = 183$ mT, $\tilde{H}_A = 40$ mT	see Tables in [76B5, 77B3], see also [74M2, 75Y]
4) NMR	^{79}Br-, ^{81}Br-NMR: $f_{NMR}(H_0) \sim M(H_0)$ for $\boldsymbol{H_0} \parallel \boldsymbol{c}$ at 1.7 K → canted magn. structure Pb′c′a with $\varphi_c = 49.5°$ at $H_0 = 0$, fit values for $\boldsymbol{H_0} \parallel \boldsymbol{c}$: $2\,H'_E + H_A = 80(5)$ mT, $H_D = 0.25(2)$ T	[81S5], see also [77K2, 80K7] exp. data fitted by linear spin-w. th. using Eq. 3.99 with $+H'_E$; $H_A < 0$ (cf. Eq. 3.99b); φ_c: Eq. 3.100b
$(C_3H_7NH_3)_2CuBr_4$	Antiferromagnet (spin canting, weak ferromagnet)	details see [77K2]; struct.: Pbca
1) meas. and anal. χ	$\chi(T)$ [$6.5\ K \le T \le 150\ K$] → $T_N = 10.50$ K $\chi(T > T_N)$: h.t.s. → $J = 14.8\ cm^{-1} \mathrel{\hat{=}} 21.3$ K	[71J2], see also [69J] h.t.s.: Eqs. 3.26, 3.27; coeff. see [67B2, 90N]
2) EPR	$g_a = g_b = 2.153$, $g_c = 2.047$	[73W6]
3) various methods	$H'_E = 230$ m T ($J' = -42$ mK), $H_A = 135$ mT, $\tilde{H}_A = 80$ mT	see Tables in [76B5, 77B3], see also [74M2, 75Y]
4) optical studies	Faraday effect, polarizing microscope → magn. structure: polytypes Pb′c′a and Pb′ca′	[77K2]

Table 5. Data concerning Magnetic Properties *(continued)*

Compound	Characteristic magnetic parameters: J, H_E, H_A, H_0, M, χ, g, T_C, T_N etc. [definitions see Table 1, units are given below]	References, remarks
$(C_4H_9NH_3)_2CuBr_4$	only few and incomplete data on magnetic properties	[71J2, 74M2, 76B5, 77B3]
$(C_5H_{11}NH_3)_2CuBr_4$	only few and incomplete data on magnetic properties	[71J2, 74M2, 76B5, 77B3]
$(C_6H_{13}NH_3)_2CuBr_4$	only few and incomplete data on magnetic properties	[77B3]
$[C_6H_5(CH_2)NH_3]_2CuBr_4$	only few and incomplete data on magnetic properties	[80E2, 92Z1, 92Z2]
$[C_6H_5(CH_2)_2NH_3]_2CuBr_4$	only few and incomplete data on magnetic properties	[92Z2]
$[C_6H_5(CH_2)_3NH_3]_2CuBr_4$	only few and incomplete data on magnetic properties	[92Z2]
$[COOH(CH_2)_2NH_3]_2CuBr_4$	Ferromagnet, $\boldsymbol{M} \parallel \boldsymbol{c}$ ($\boldsymbol{a}$: hard axis, $\boldsymbol{c}' \perp \boldsymbol{a}, \boldsymbol{b}$)	details see [83W2]; $\angle(\boldsymbol{c}, \boldsymbol{c}') = \beta - 90°$; struct.:I12/c1
1) meas. and anal. χ	$\chi_{\text{powder}}(T)$ [4 K $\leq T \leq$ 150 K]	[83W2]
	$\chi(T > T_N)$: h.t.s. $\rightarrow J = 14.7\ \text{cm}^{-1} \mathrel{\hat{=}} 21.2$ K	h.t.s.: Eqs. 3.26, 3.27; coeff. see [67B2, 90N]
	$\chi(T)$ for $\boldsymbol{H_0} \parallel \boldsymbol{a}, \parallel \boldsymbol{b}, \parallel \boldsymbol{c}'$; [1.5 K $\leq T \leq$ 14 K], $T_C = 10.0(5)$ K	[83W2]; $\boldsymbol{c}' \perp \boldsymbol{a}, \boldsymbol{b}$; $\angle(\boldsymbol{c}, \boldsymbol{c}') = \beta - 90° = 2.49°$;
	$\rightarrow H_A = -60$ mT, $\tilde{H}_A = 30$ mT	H_A, $\tilde{H}_A$: Eq. 3.96; $H_A < 0$ and $\tilde{H}_A < 0$ (cf. Eq. 3.99c)
2) EPR	$g_a = g_b = 2.098$, $g_{c'} = 2.044$	[83W2]; $\boldsymbol{c}' \perp \boldsymbol{a}, \boldsymbol{b}$
3) meas. M	$M(H_0)$ at 4.2 K [$\boldsymbol{H_0} \parallel \boldsymbol{a}, \parallel \boldsymbol{b}, \parallel \boldsymbol{c}'$; $0 \leq H_0 \leq 0.5$ T] $\rightarrow J' > 0$	[83W2]
$(C_6H_{11}NH_3)_2CuBr_4$	only few and incomplete data on magnetic properties	[92L3]; $C_6H_{11}NH_3$ = cyclohexylammonium
d) Diammonium Compounds with X = Cl^-, Br^-		
$[NH_3(CH_2)_2NH_3]CrCl_4$	only few and incomplete data on magnetic properties	[78L4]
$[NH_3(CH_2)_3NH_3]CrCl_4$	only few and incomplete data on magnetic properties	[81B1, 83B3, 86D3, 86D4]
$[NH_3(CH_2)_2NH_3]MnCl_4$	Antiferromagnet, $\boldsymbol{M}_{\textbf{subl}} \parallel \boldsymbol{c}$ (spin canting, weak fm.: $\boldsymbol{M} \perp \boldsymbol{c}$)	details see [76A1, 81K9]; weak fm. due to DMI
1) LMB	$\Delta n(T)$ [4 K $\leq T \leq$ 290 K], $\text{d}(\Delta n)/\text{d}T \sim C_{\text{magn}}$, $T_N = 54(2)$ K	[78K8, 79K8]; sample: $[ND_3(CH_2)_2ND_3]MnCl_4$
	$C_{\text{magn}}(T > T_N)$: h.t.s. $\rightarrow J = -3.5\ \text{cm}^{-1} \mathrel{\hat{=}} -5$ K	h.t.s. for C_{magn}: Eq. 4.39; coeff. see [73Y3, 90N]
	$\Delta n(H_0, T)$ for $\boldsymbol{H_0} \parallel \boldsymbol{c}$ [$0 < T \leq 45$ K, $0 \leq H_0 \leq 10$ T]	[78K8, 79K8]; sample: $[ND_3(CH_2)_2ND_3]MnCl_4$
	$T = 0$: $H_{SF} = 3.6(2)$ T $\rightarrow H_A = 87$ mT ($H_E = 74.4$ T)	H_{SF}: Eqs. 3.38, 3.39; behaviour at crit. point [76R3]
2) AFMR	$H_0 = 0$, $T = 4.2$ K: $h\nu_{\text{AFMR}} = 3.37\ \text{cm}^{-1} \mathrel{\hat{=}} 4.85$ K	[81S4, 83G1], see also [81K9]

Table 5. Data concerning Magnetic Properties *(continued)*

Compound	Characteristic magnetic parameters: J, H_E, H_A, H_0, M, χ, g, T_C, T_N etc. [definitions see Table 1, units are given below]	References, remarks
$[NH_3(CH_2)_3NH_3]MnCl_4$	Four-sublattice antiferromagnet, $\boldsymbol{M}_{\mathbf{subl}} \parallel (\pm \sin\theta, 0, \cos\theta)$ with $\theta = 7°$; $\boldsymbol{b}$: hard axis; spin canting, weak fm.: $\boldsymbol{M} \parallel \boldsymbol{b}$	details see [76A1, 76L4, 83S7, 85Z2]; struct.: Pnam
1) meas. and anal. χ	$\chi(T)$ [$50 \le T \le 220$ K] $\chi(T > T_N)$: h.t.s. $\rightarrow J = -3.2\ \text{cm}^{-1} \hat{=} -4.6$ K	[76L4], see also [75W1] h.t.s.: Eqs. 3.26, 3.27; coeff. see [70L1, 90N]
	$\chi(T)$ for $\boldsymbol{H}_0 \parallel \boldsymbol{a}, \parallel \boldsymbol{b}, \parallel \boldsymbol{c}$; [$4\ \text{K} \le T \le 100$ K, $H_0 = 0.1$ T, 1 T] $\rightarrow T_N = 43.6$ K, $\boldsymbol{c}$: easy axis, $\boldsymbol{b}$: hard axis	[76L4], see also [75W1, 88Z1]
2) meas. M induced by H_0	$M(H_0, T)$ for $\boldsymbol{H}_0 \parallel \boldsymbol{c}$ [$4.2\ \text{K} \le T \le 34$ K, $0 \le H_0 \le 1.6$ T] $T = 0$, $H_{SF} = 2.45\ \text{T} \rightarrow H_A = 44$ mT ($H_E = 68.5$ T)	[76L4, 77B6] H_{SF}: Eqs. 3.38, 3.39; behaviour at crit. point [76R3]
3) AFMR	4 sublattices: 2 ordinary AFMR and 2 exchange modes $H_0 = 0$, $T = 4.2$ K: $\nu_{\text{AFMR},1} =$ 74.5 GHz, $\nu_{\text{AFMR},2} =$ 77.5 GHz $\nu_{\text{AFMR},3} = 122.9$ GHz, $\nu_{\text{AFMR},4} = 125.7$ GHz	[83S7, 85Z2]: AFMR under various conditions ($\boldsymbol{H}_0 \parallel \boldsymbol{b}$, $\boldsymbol{H}_0 \parallel \boldsymbol{c}$); spins inclined by $\theta = \pm 7°$ from c-axis in ac-plane and canted by $\varphi = 0.07°$ towards b-axis
	$\rightarrow$ ($H_E = 68.5$ T), $H_{A1} = 54$ m T, $H_{A2} = 9$ mT, $H_{A3} = 34$ mT $H'_E = 46$ mT, $H_{D1} = 0.17$ T, $H_{D2} = 0.13$ T	[85Z2], see also [86K6]; linear spin-w. calc. for a four-sublattice afm. with definitions of the parameters
$[NH_3(CH_2)_4NH_3]MnCl_4$	Four-sublattice antiferromagnet, $\boldsymbol{M}_{\mathbf{subl}} \parallel (\pm \sin\theta, 0, \cos\theta)$ with $\theta = 16°$; spin canting, weak fm.	details see [88S5]; spin canting due to DMI (see Eq. 3.52); struct.: $P2_1/b11$
1) meas. χ and M	$\chi_\parallel(T)$, $\chi_\perp(T)$ [$4\ \text{K} \le T \le 200$ K], $M(H_0)$ induced by $\boldsymbol{H}_0 \parallel \boldsymbol{c}$ [$0 \le H_0 \le 3.5$ T] $\rightarrow H_{SF} = 3.3(2)$ T at 1.6 K	[76A1]
2) meas. sound velocity	anomaly in $\upsilon_s(T)$ [$4\ \text{K} \le T \le 20$ K] $\rightarrow T_N = 42.6(3)$ K	[88Z1]
3) AFMR	4 sublattices: 2 ordinary AFMR and 2 exchange modes $H_0 = 0$, $T = 4.2$ K: $\nu_{\text{AFMR},1\text{–}2} = 92.1$ GHz $\nu_{\text{AFMR},3\text{–}4} = 96.0$ GHz	AFMR under various conditions [81S4, 83G1, 88S5]; observed: one ordinary AFMR mode and one much weaker exchange mode, both doubly degenerate
	$\nu^2_{\text{AFMR},1-2} - \nu^2_{\text{AFMR},3-4} = \gamma^2 4 H_E H'_E \rightarrow H'_E = 3.3$ mT	[88S5]; linear spin-w. th. for 4 sublattices [85Z2, 86K6]
$[NH_3(CH_2)_5NH_3]MnCl_4$	only few and incomplete data on magnetic properties	[81S4, 88Z1]
$[NH_3(CH_2)_2NH_3]FeCl_4$	only few and incomplete data on magnetic properties	[82M2, 83S9]
$[NH_3(CH_2)_3NH_3]FeCl_4$	only few and incomplete data on magnetic properties	[75W1, 82M2, 83S9]

Table 5. Data concerning Magnetic Properties *(continued)*

Compound	Characteristic magnetic parameters: J, H_E, H_A, H_0, M, χ, g, T_C, T_N etc. [definitions see Table 1, units are given below]	References, remarks
$[NH_3(CH_2)_4NH_3]FeCl_4$	only few and incomplete data on magnetic properties	[83S9]
$[NH_3(CH_2)_5NH_3]FeCl_4$	only few and incomplete data on magnetic properties	[83S9]
$[NH_3(CH_2)_6NH_3]FeCl_4$	only few and incomplete data on magnetic properties	[82M2, 83S8, 95M1]
$[NH_3(CH_2)_7NH_3]FeCl_4$	only few and incomplete data on magnetic properties	[83S9]
$[NH_3(CH_2)_3NH_3]FeCl_2Br_2$	only few and incomplete data on magnetic properties	[81M5]
$[NH_3(CH_2)_6NH_3]FeCl_2Br_2$	only few and incomplete data on magnetic properties	[81M5]
$[NH_3(CH_2)_2NH_3]NiCl_4$	only few and incomplete data on magnetic properties	[78S3]
$[NH_3(CH_2)_2NH_3]CuCl_4$	Antiferromagnet, $\boldsymbol{M}_{\mathbf{subl}} \parallel \boldsymbol{b}$ ($\boldsymbol{c}$: hard axis, $\lvert J'/J \rvert = 0.60$)	details see [77K4, 78A4, 79K8, 79S5]; struct.: $P12_1/a1$
1) meas. and anal. χ	$\chi(H_0, T)$ for $\boldsymbol{H_0} \parallel \boldsymbol{a}, \parallel \boldsymbol{b}, \parallel \boldsymbol{c}$; [$4\ K \le T \le 300\ K$, $0 \le H_0 \le 2.2\ T$] $\rightarrow T_N = 31.5(1)\ K$, $\boldsymbol{b}$: easy axis, $H_{SF} = 0.85(5)\ T$	[79S5], see also [77K4, 81S6, 83K8, 84R6]
	$\chi(T > T_N)$: h.t.s. for intralayer and interlayer exchange: $J = 16.0(3)\ cm^{-1} \mathrel{\hat{=}} 23.0(5)\ K$, $J' = -9.5(3)\ cm^{-1} \mathrel{\hat{=}} -13.7(5)\ K$	h.t.s.: see [66D2], a series expansion up to 5th order in (J/k_BT) and (J'/k_BT)
2) meas. M induced by H_0	$M(H_0)$ for $\boldsymbol{H_0} \parallel \boldsymbol{a}, \parallel \boldsymbol{b}, \parallel \boldsymbol{c}$; [$0 \le H_0 \le 2.0\ T$] $M(H_0, T)$ for $\boldsymbol{H_0} \parallel \boldsymbol{b}$ [$1.5\ K \le T \le 35\ K$, $0 \le H_0 \le 2.0\ T$]	[77K4]; sample: $[ND_3(CH_2)_2ND_3]CuCl_4$ $M(H_0, T) \rightarrow H'_E$, H_A, $\tilde{H}_A$: see [77K4, 79K8]
	$\rightarrow H_{SF} = 0.88\ T$ at $1.5\ K$, $H^a_{PM} = 56.8\ T$, $H^c_{PM} = 60.0\ T$: $H'_E = 28.6(6)\ T$ ($J' = -20.8\ K$), $H_A = 0.2(6)\ T$, $\tilde{H}_A = 13.3(3)\ mT$	H'_E, H_A, $\tilde{H}_A$: Eq. 3.96 (note: $z' = 2$); H_{SF}, H^a_{PM}, H^b_{PM}, H^c_{PM} : Eqs. 3.57–3.59 with $\boldsymbol{a} \leftrightarrow \boldsymbol{b}$ ($\boldsymbol{b}$: easy axis!)
3) EPR	$g_a = g_b = 2.164$, $g_c = 2.051$	[83K8], see also [77K4, 79K8, 81S6, 82K5]
4) parallel pumping	chaos: a microwave instability with 1 µW holding power	[82B3]; low threshold level, strong anisotropy
	chaos: delayed transient absorption at the threshold	[86F3]
	chaos: self-oscillations in the absorption above threshold	[88W3, 88W4]; nonlinear AFMR
	hyperchaotic behaviour in nonlinear AFMR	[92M3]
5) optical studies	reflectivity 16000–$97000\ cm^{-1}$ (2.0–$12.0\ eV$) at 300 K, optical absorption 6500–$24000\ cm^{-1}$ at 4.6 K, 300 K	[77K3, 79K8]; electronic transitions, T-dependence of absorption edge ($h\nu \approx 2.4$ e.V)

Table 5. Data concerning Magnetic Properties *(continued)*

Compound	Characteristic magnetic parameters: J, H_E, H_A, H_0, M, χ, g, T_C, T_N etc. [definitions see Table 1, units are given below]	References, remarks
$[NH_3(CH_2)_3NH_3]CuCl_4$	Antiferromagnet, $\boldsymbol{M}_{\mathbf{subl}} \parallel \boldsymbol{b}$ ($\boldsymbol{c}$: hard axis, $\lvert J'/J \rvert = 0.10$)	details see [79K8]; struct.: Pnam
1) meas. and anal χ	$\chi(T)$ [$20\ \mathrm{K} \le T \le 250\ \mathrm{K}$] $T > T_N$: h.t.s. $\rightarrow J = 11.5(10)\ \mathrm{cm}^{-1} \hat{=} 16.5(15)\ \mathrm{K}$, $H_E = 45.3\ \mathrm{T}$	[79K8], see also [76P1, 84R6] h.t.s.: Eqs. 3.26, 3.27; coeff. see [67B2, 90N]
	$\chi(T)$ for $\boldsymbol{H_0} \parallel \boldsymbol{a}, \parallel \boldsymbol{b}, \parallel \boldsymbol{c}$; [$4\ \mathrm{K} \le T \le 100\ \mathrm{K}$] $\rightarrow T_N = 14.9(3)\ \mathrm{K}$, $\boldsymbol{b}$: easy axis, $\boldsymbol{c}$: hard axis	[79K8]; also measured $M(H_0)$ at 4.2 K for $\boldsymbol{H_0} \parallel \boldsymbol{a}, \parallel \boldsymbol{b}, \parallel \boldsymbol{c}$ [$0 \le H_0 \le 5\ \mathrm{T}$]
	$\chi(T > T_N)$: h.t.s. for intralayer and interlayer exchange: $J = 13.9\ \mathrm{cm}^{-1} \hat{=} 20.0\ \mathrm{K}$, $J' = -1.4\ \mathrm{cm}^{-1} \hat{=} -2.0\ \mathrm{K}$	[81S6]; reanalysis of the exp. data of [76P1]; h.t.s.: see [66D2], up to 5th order in (J/k_BT) and (J'/k_BT)
2) EPR	$g_a = g_b = 2.169$, $g_c = 2.055$	[82K5], see also [77S6]
3) (H_0, T) phase diagram	LMB: $\Delta n(H_0, T)$ [$1.8\ \mathrm{K} \le T \le 14.8$, $0 \le H_0 \le 5\ \mathrm{T}$]	[79K8]
	$\mathrm{T} = 0$: $\mathrm{H_{SF}} = 0.28\ \mathrm{T}$, $H^{b}_{PM} \approx H^{a}_{PM} = 4.6\ \mathrm{T}$, $H^{c}_{PM} = 5.0\ \mathrm{T}$, $H'_E = 2.27\ (10)\ \mathrm{T}$ ($\mathrm{J'} = -1.65\ \mathrm{K}$), $\mathrm{H_A} = 0.44(5)\ \mathrm{T}$, $\widetilde{H}_A = 17(2)\ \mathrm{mT}$	H'_E, H_A, $\widetilde{H}_A$: Eq. 3.96 (note: $z' = 2$); H_{SF}, H^{a}_{PM}, H^{b}_{PM}, H^{c}_{PM} : Eqs. 3.57–3.59 with $\boldsymbol{a} \leftrightarrow \boldsymbol{b}$ ($\boldsymbol{c}$: easy axis!)
4) optical studies	T-dependence of absorption edge ($h\nu \approx 2.7\ \mathrm{eV}$)	[79K8]
$[NH_3(CH_2)_4NH_3]CuCl_4$	Antiferromagnet, $\boldsymbol{M}_{\mathbf{subl}} \parallel \boldsymbol{b}$ ($\boldsymbol{c}$: hard axis, $\lvert J'/J \rvert = 0.012$)	details see [81S7]; struct.: $P12_1/a1$
1) meas. and anal χ	$\chi_{\mathrm{powder}}(T)$ [$4.2\ \mathrm{K} \le T \le 130\ \mathrm{K}$] $\rightarrow T_N = 8.85\ \mathrm{K}$ $T > T_N$: h.t.s. $\rightarrow J = 9.0(1)\ \mathrm{cm}^{-1} \hat{=} 13.0(2)\ \mathrm{K}$, $H_E = 35.7\ \mathrm{T}$	[81S7], see also [81S6] h.t.s.: Eqs. 3.26, 3.27; coeff. see [67B2, 90N]
2) EPR	$g_a = g_b = 2.167$, $g_c = 2.047$	[81S7, 82K5]
3) (H_0, T) phase diagram	meas. $M(H_0, T)$ [$4\ \mathrm{K} \le T \le 9\ \mathrm{K}$, $0 \le H_0 \le 0.4\ \mathrm{T}$]	M for $\boldsymbol{H_0} \parallel \boldsymbol{a}, \parallel \boldsymbol{b}, \parallel \boldsymbol{c}$ [81S7], see also [81S6]
	$T = 0$: $H_{SF} = 97(4)\ \mathrm{mT}$, $H^{b}_{PM} = 0.44(1)\ \mathrm{T}$, $H^{a}_{PM} = 0.46(1)\ \mathrm{T}$, $H^{c}_{PM} = 0.64(2)\ \mathrm{T} \rightarrow H'_E = 0.22(1)\ \mathrm{T}$ ($J' = -0.16\ \mathrm{K}$), $H_A = 0.165\ \mathrm{T}$, $\widetilde{H}_A = 10(8)\ \mathrm{mT}$	H'_E, H_A, $\widetilde{H}_A$: Eq. 3.96 (note: $z' = 2$ for diammonium compounds); H_{SF}, H^{a}_{PM}, H^{b}_{PM}, H^{c}_{PM} : Eqs. 3.57–3.59 with $\boldsymbol{a} \leftrightarrow \boldsymbol{b}$ ($\boldsymbol{b}$: easy axis!)

Table 5. Data concerning Magnetic Properties *(continued)*

Compound	Characteristic magnetic parameters: J, H_E, H_A, H_0, M, χ, g, T_C, T_N etc. [definitions see Table 1, units are given below]	References, remarks
$[NH_3(CH_2)_5NH_3]CuCl_4$	Antiferromagnet, $\boldsymbol{M}_{\mathbf{subl}} \parallel \boldsymbol{b}$ ($\boldsymbol{c}$: hard axis, $\lvert J'/J \rvert = 0.003$)	details see [79K8]; struct.: $P12_1/n1$
1) meas. and anal χ	$\chi(T)$ [20 K ≤ T ≤ 250 K] $\chi(T > T_N)$: h.t.s. $\rightarrow J = 9.8(1)\ \mathrm{cm}^{-1} \mathrel{\widehat{=}} 14.1(2)$ K	[79K8], see also [81S6, 84R6] h.t.s.: Eqs. 3.26, 3.27; coeff. see [67B2, 90N]
2) meas. χ and $M(H_0)$	$\chi(T)$ [$1.5 \le T \le 15$ K], $M(H_0)$ at $T = 1.6$ K [$0 \le H_0 \le 0.5$ T], both for $\boldsymbol{H_0} \parallel \boldsymbol{a}, \parallel \boldsymbol{b}, \parallel \boldsymbol{c}$:	[79K8, see also [81S6, 84R6]
	$\rightarrow T_N = 7.6(2)$ K, $H_{SF} = 18(3)$ mT, $H'_E = 54(5)$ mT	H'_E, H_A, $\tilde{H}_A$: Eq. 3.96 (note: $z' = 2$ for diammonium comp.);
	($J' = -0.04$ K), $H_A = 0.14(5)$ T, $\tilde{H}_A = 3.1(10)$ mT	H_{SF}: Eqs. 3.57 with $\boldsymbol{a} \leftrightarrow \boldsymbol{b}$ ($\boldsymbol{b}$: easy axis!)
3) optical studies	T-dependence of absorption edge ($h\nu \approx 2.4$ eV)	[79K8]
$[NH_3(CH_2)_6NH_3]CuCl_4$	only few and incomplete data on magnetic properties	[84R6]
$[NH_3(CH_2)_7NH_3]CuCl_4$	only few and incomplete data on magnetic properties	[84R6]
$[NH_3(CH_2)_8NH_3]CuCl_4$	only few and incomplete data on magnetic properties	[84R6]
$[NH_3(CH_2)_9NH_3]CuCl_4$	only few and incomplete data on magnetic properties	[84R6]
$[NH_3(CH_2)_{10}NH_3]CuCl_4$	only few and incomplete data on magnetic properties	[84R6]
$[NH_3(CH_2)_2NH_3]CuCl_2Br_2$	only few and incomplete data on magnetic properties	[84R6]
$C_5N_2H_8CuCl_4$	Antiferromagnet ($\lvert J'/J \rvert = 0.8$)	$C_5N_2H_8$ = 3-ammoniumpyridinium
1) meas. χ and $M(H_0)$	exp. data analysed by series expansions $\rightarrow J = 10(1)\ \mathrm{cm}^{-1} \mathrel{\widehat{=}} 14(2)$ K, $J' = -8(1)\ \mathrm{cm}^{-1} \mathrel{\widehat{=}} -11(2)$ K	2D series expansion for the Heisenberg model with appropriate mean field corrections [94S3]
2) EPR	$g_a = g_b = 2.160$, $g_c = 2.052$	[88W1]
$[NH_3(CH_2)_2NH_3]CuBr_4$	Four-sublattice afm. with hidden spin canting ($\lvert J'/J \rvert = 1.8$)	details see [85R2]; struct.: $P12_1/a1$
1) EPR	$g_a = g_b = 2.097$, $g_c = 2.049$	[83K8]
2) meas. and anal. χ	$\chi_{\mathrm{powder}}(T)$ [$50\ \mathrm{K} \le T \le 220$ K] $\rightarrow T_N = 58$ K	[84R6]; T_N sample-dependent, probably impurities
	$\chi(T > T_N)$: h.t.s. for intralayer and interlayer exchange: $J = 26.5\ \mathrm{cm}^{-1} \mathrel{\widehat{=}} 38.2$ K, $J' = -47.5\ \mathrm{cm}^{-1} \mathrel{\widehat{=}} -68.4$ K	h.t.s.: see [66D2], a series expansion up to 5th order in (J/k_BT) and (J'/k_BT)

Table 5. Data concerning Magnetic Properties *(continued)*

Compound	Characteristic magnetic parameters: J, H_E, H_A, H_0, M, χ, g, T_C, T_N etc. [definitions see Table 1, units are given below]	References, remarks
$[NH_3(CH_2)_2NH_3]CuBr_4$ (cont.)		
3) AFMR	resonance exp. at 3.8 K under various conditions $\rightarrow H_A = 22$ mT, $\widetilde{H}_A = 1.7$ mT	[85R2]; AFMR results indicate a four-sublattice afm. with hidden spin canting
$[NH_3(CH_2)_3NH_3]CuBr_4$	Antiferromagnet ($\|J'/J\| = 1.0$)	details see [82S5, 84R6]; struct.: $P12_1/a1$
1) EPR	$g_a = g_b = 2.094$, $g_c = 2.046$	[83K8], see also [73W6]
2) meas. and anal. χ	$\chi_{powder}(T)$ [30 K $\le T \le$ 240 K] $\rightarrow T_N = 40(1)$ K	[82S5], see also [83K8, 84R6]
	$\chi(T > T_N)$: h.t.s. for intralayer and interlayer exchange: $J = 18.1(7)$ cm$^{-1} \hat{=} 26(1)$ K, $J' = -18.1(7)$ cm$^{-1} \hat{=} -26(1)$ K	h.t.s.: see [66D2], a series expansion up to 5th order in (J/k_BT) and (J'/k_BT)
$[NH_3(CH_2)_4NH_3]CuBr_4$	Antiferromagnet ($\|J'/J\| = 0.17$)	details see [82S5, 84R6]; struct.: $P12_1/a1$
1) EPR	$g_a = g_b = 2.097$, $g_c = 2.048$	[83K8]
2) meas. and anal. χ	$\chi_{powder}(T)$ [6.5 K $\le T \le$ 150 K] $\rightarrow T_N = 19(1)$ K	[82S5], see also [83K8, 84R6]
	$\chi(T > T_N)$: h.t.s. for intralayer and interlayer exchange: $J = 20.2(7)$ cm$^{-1} \hat{=} 29(1)$ K, $J' = -3.5(7)$ cm$^{-1} \hat{=} -5(1)$ K	h.t.s.: see [66D2], a series expansion up to 5th order in (J/k_BT) and (J'/k_BT)
$[NH_3(CH_2)_5NH_3]CuBr_4$	only few and incomplete data on magnetic properties	[84R6]
$[NH_3(CH_2)_6NH_3]CuBr_4$	only few and incomplete data on magnetic properties	[84R6]
$[NH_3(CH_2)_7NH_3]CuBr_4$	only few and incomplete data on magnetic properties	[84R6]
$[NH_3(CH_2)_8NH_3]CuBr_4$	only few and incomplete data on magnetic properties	[84R6]
$[NH_3(CH_2)_9NH_3]CuBr_4$	only few and incomplete data on magnetic properties	[84R6, 90Z2]
$[NH_3(CH_2)_{10}NH_3]CuBr_4$	only few and incomplete data on magnetic properties	[84R6]
$C_5N_2H_8CuBr_4$	Antiferromagnet ($\|J'/J\| = 2.6$)	$C_5N_2H_8$ = 3-ammoniumpyridinium
meas. χ and $M(H_0)$	exp. data analysed by series expansions $\rightarrow J = 14(2)$ cm$^{-1} \hat{=} 20(3)$ K, $J' = -36(5)$ cm$^{-1} \hat{=} -52(7)$ K	2D series expansion for the Heisenberg model with appropriate mean field corrections [94S3]

Table 5. Data concerning Magnetic Properties *(continued)*

Compound	Characteristic magnetic parameters: J, H_E, H_A, H_0, M, χ, g, T_C, T_N etc. [definitions see Table 1, units are given below]	References, remarks
e) diluted magnets		
$\mathbf{Rb_2Cr_xMg_{1-x}Cl_4}$	$x > x_p$: Ferromagnet, $\boldsymbol{M} \perp \boldsymbol{c}$ (magn. order see Fig. 3.34)	
el. + quasi-el. n-scatt.	$x = 0.89$: magn. contribution to (0,0,4) Bragg refl.: $I(T) \sim M^2(T) \rightarrow T_C = 42$ K	[86D4, 86F1]
$\mathbf{Rb_2Cr_xCd_{1-x}Cl_4}$	$x > x_p$: Ferromagnet, $\boldsymbol{M} \perp \boldsymbol{c}$ (magn. order see Fig. 3.34)	
meas. M	$T_C(x)$ for various x: see Fig. 1 of [82K6]	$T_C \hat{=}$ steepest descent of the curve $M(T)$
$\mathbf{K_2Mn_xMg_{1-x}F_4}$	$x > x_p$: Antiferromagnet, $\boldsymbol{M}_{\mathbf{subl}} \parallel \boldsymbol{c}$ (magn. order see Fig. 2.2)	
1) magn. meas.	$T_N(x)/T_N(1)$ for various x: see Fig. 3.48; $I_g = 3.0(7)$	[70B5]; $T_N(1) = 45.0$ K; I_g: Eqs. 3.128, 3.129
2) meas. M induced by H_0	$x = 0.93$: $H_{SF} = 4.5(2)$ T; $x = 0.74$: $H_{SF} = 1.5(5)$ T	[73B6]
3) ^{19}F-NMR	$x = 0.978$: $J = -2.85(2)$ cm^{-1} $\hat{=}$ $-4.105(25)$ K	[80L4, 80L5]; F_I: $f_{NMR}(T) \sim M_{subl}(T) \rightarrow J$ (Eqs. 3.15, 3.18)
4) AFMR	$x = 0.978$, $T = 0$, $H_0 = 0$: $h\nu_{AFMR} = 4.75(3)$ cm^{-1} $\hat{=}$ $6.83(5)$ K	[80L4, 80L5]
$\mathbf{K_2Mn_xZn_{1-x}F_4}$	$x > x_p$: Antiferromagnet, $\boldsymbol{M}_{\mathbf{subl}} \parallel \boldsymbol{c}$ (magn. order see Fig. 2.2)	
1) ^{19}F-NMR	$x = 0.996$: $J = -2.88(2)$ cm^{-1} $\hat{=}$ $-4.150(25)$ K	[80L4, 80L5]; F_I: $f_{NMR}(T) \sim M_{subl}(T) \rightarrow J$ (Eqs. 3.15, 3.18)
2) AFMR	$x = 0.996$, $T = 0$, $H_0 = 0$: $h\nu_{AFMR} = 5.05(3)$ cm^{-1} $\hat{=}$ $7.27(5)$ K	[80L4, 80L5]
$\mathbf{Rb_2Mn_xMg_{1-x}F_4}$	$x > x_p$: Antiferromagnet, $\boldsymbol{M}_{\mathbf{subl}} \parallel \boldsymbol{c}$ (magn. order see Fig. 2.2)	
1) el. + quasi-el. n-scatt.	$x = 0.70$: $T_N = 14.2(3)$ K (details see Table 6)	[93C2]
2) inel. n-scatt.	$x = 0.54$, 0.57: $\hbar\omega$ for $\boldsymbol{K}$ $\hat{=}$ (0.5, 0, 2.9) at 1.22 K	[77C3]
	structures in $I(q)$ peaking at Ising cluster energies E_n which are absent in pure Rb_2MnF_4 (cf. Figs. 3.54, 3.55)	E_n calculated for n = 2, 3, 4 with Eq. 3.140 , using $J = -2.641$ cm^{-1} $\hat{=}$ -79.19 GHz [77C3]
$\mathbf{(C_3H_7NH_3)_2Mn_{1-x}Zn_xCl_4}$	$(1-x) > x_p$: Antiferromagnet, $\boldsymbol{M}_{\mathbf{subl}} \parallel \boldsymbol{c}$ (spin canting, weak fm.)	
meas. χ_{ac}	$0.001 < x < 0.05$: $T_N = 39.2$ K, independent of these small x	[96S1]; see also Table 6

Table 5. Data concerning Magnetic Properties *(continued)*

Compound	Characteristic magnetic parameters: J, H_E, H_A, H_0, M, χ, g, T_C, T_N etc. [definitions see Table 1, units are given below]	References, remarks
$Rb_2Mn_xCd_{1-x}Cl_4$	x > x_p: Antiferromagnet, $\boldsymbol{M}_{\mathbf{subl}} \parallel \boldsymbol{c}$ (magn. order see Fig. 2.2)	
1) meas. and anal. of χ	x = 0.90: $H_E = 93.15$ T x = 0.80: $H_E = 68.34$ T x = 0.70: $H_E = 31.2$ T	[84E, 84P]; H_E determined from static χ at 6 K
2) AFMR	ν_{AFMR} (H_0) for $\boldsymbol{H}_{\mathbf{0}} \parallel \boldsymbol{c}$ at 4.2 K	(40–140 GHz) [84E, 84P], (10–180 GHz) [87G3, 89B4]
	x = 0.91: $\nu_{AFMR,\,1} = 108$ GHz, $\nu_{AFMR,\,2} = 112$ GHz, $H_{SF} = 4.05(10)$ T, $T_N = 47(3)$ K	[87G3, 89B4]; ν_{AFMR} for $H_0 = 0$ at 4.2 K; $\nu_{AFMR}(T) \to T_N$
	x = 0.90: $\nu_{AFMR} = 102$ GHz, $H_{SF} = 3.64$ T, $H_A = 0.0721$ T, $T_N = 43(2)$ K	[84E, 84P]; ν_{AFMR} for $H_0 = 0$ at 4.2 K; EPR: $H_{res}(T) \to T_N$; $H_{SF} \to H_A$: Eq. 3.39
	x = 0.80: $\nu_{AFMR,\,1} = 62$ GHz, $\nu_{AFMR,\,2} = 74$ GHz, $H_{SF} = 2.40(10)$ T, $T_N = 31(2)$ K	[87G3, 89B4]; ν_{AFMR} for $H_0 = 0$ at 4.2 K; $\nu_{AFMR}(T) \to T_N$
	x = 0.80: $\nu_{AFMR} = 57$ GHz, $H_{SF} = 2.04$ T, $H_A = 0.030$ T, $T_N = 26(1)$ K	[84E, 84P]; ν_{AFMR} for $H_0 = 0$ at 4.2 K; EPR: $H_{res}(T) \to T_N$; $H_{SF} \to H_A$: Eq. 3.39
	x = 0.74: $\nu_{AFMR} = 50.7$ GHz, $H_{SF} = 1.81(20)$ T, $T_N = 26(2)$ K	[87G3, 89B4]; ν_{AFMR} for $H_0 = 0$ at 4.2 K; $\nu_{AFMR}(T) \to T_N$
	x = 0.70: $\nu_{AFMR} = 35.8$ GHz, $H_{SF} = 1.28$ T, $H_A = 0.026$ T, $T_N = 15(1)$ T	[84E, 84P]; ν_{AFMR} for $H_0 = 0$ at 4.2 K; EPR: $H_{res}(T) \to T_N$; $H_{SF} \to H_A$: Eq. 3.39
$(C_3H_7NH_3)_2Mn_{1-x}Cd_xCl_4$	(1–x) > x_p: Antiferromagnet, $\boldsymbol{M}_{\mathbf{subl}} \parallel \boldsymbol{c}$ (spin canting, weak fm.)	
meas. χ_{ac}	$0.001 < x < 0.05$: $T_N = 39.2$ K, independent of these small x	[96S1]; see also Table 6
$K_2Fe_xZn_{1-x}F_4$	x > x_p: Antiferromagnet, $\boldsymbol{M}_{\mathbf{subl}} \perp \boldsymbol{c}$ (magn. order see Fig. 2.6)	
1) Mössbauer study	$T_N(x)/T_N(1)$ for various x: see Fig. 4 of [85D1], $I_g = 2.4(2)$	$T_N(1) = 63.0(3)$ K; I_g: Eqs. 3.128, 3.129
2) Mössbauer study and n-diffraction	x = 0.74: afm. Bragg refl. (1,0,0): $I(T) \sim M^2_{subl}(T)$ (3D order parameter), $H_{hf} \sim$ local staggered magnetization $T \to 0$, $H_0 = 0$: $\nu_{AFMR} = 15(2)\ \mathrm{cm}^{-1} \mathrel{\hat{=}} 22(3)$ K	[85D1, 86D5]; between $T_N = 22$ K (cf. Table 6) and $T \approx 11$ K: local magnetization ($\sim H_{hf}$) larger than 3D order parameter $\sqrt{I(1,0,0)}$, see Fig. 3.52

Table 5. Data concerning Magnetic Properties *(continued)*

Compound	Characteristic magnetic parameters: J, H_E, H_A, H_0, M, χ, g, T_C, T_N etc. [definitions see Table 1, units are given below]	References, remarks
$K_2Co_xMg_{1-x}F_4$	x > x_p: Antiferromagnet, $\boldsymbol{M}_{\mathbf{subl}} \parallel \boldsymbol{c}$ (magn. order see Fig. 2.2)	
magn. meas.	$T_N(x)/T_N(1)$ for various x: see Fig. 3.48, $I_g = 1.6(1)$ $\chi_\perp(T \to 0)$ for various x: see Table II of [73B6]	[70B5]; $T_N(1) = 108$ K; I_g : Eqs. 3.128, 3.129
$Rb_2Co_xMg_{1-x}F_4$	x > x_p: Antiferromagnet, $\boldsymbol{M}_{\mathbf{subl}} \parallel \boldsymbol{c}$ (magn. order see Fig. 2.2)	
1) el. + quasi-el. n-scatt.	$T_N(x)$ for various x: see Table 6, $I_g = 1.95(5)$	[78S4, 79I1, 81I2, 83B4]; I_g: Eqs. 3.128, 3.129
2) inel. n-scatt.	x = 0.575: $\hbar\omega$ for $\boldsymbol{K} \mathrel{\hat{=}} (1 - \zeta_x, 0, 4.23)$ [$\zeta_x = 0, 0.25, 0.5$] at 6.5 K → Ising cluster excitations for n = 1, 2, 3, 4 (cf. Fig. 3.56)	[80C1], see also [79I3]; the Ising cluster modes are almost dispersionless
	Solid curves in Fig. 3.56 not calculated with Eq. 3.141 but are the result of a computer simulation with $J_\parallel = -1.813$ THz $\mathrel{\hat{=}}$ 87.0 K and $\alpha = 0.00137$ THz^{-2}	at $q_x \mathrel{\hat{=}} 0.5$ the frequencies are for n = 1, 2, 3, 4: (exp.) 1.8(1), 3.4(1), 5.0(1), 6.5(1) THz, (theory) 1.62, 3.36, 5.05, 6.50 THz, resp.
	x = 0.70: $\hbar\omega$ in magn. field $H_0 = 0$ and $H_0 = 6.5$ T at 5.0 K, $\boldsymbol{H_0} \parallel \boldsymbol{c}$ and $\boldsymbol{K} \mathrel{\hat{=}} (1, 2, 0)$, $\boldsymbol{H_0} \perp \boldsymbol{c}$ and $\boldsymbol{K} \mathrel{\hat{=}} (0.5, 0, 3.2)$	[83B4]; Ising cluster excitations, Zeeman shift observed only for $\boldsymbol{H_0} \parallel \boldsymbol{c}$, not for $\boldsymbol{H_0} \perp \boldsymbol{c}$
3) pulsed n-scatt.	x = 0.1, 0.2, 0.3, 0.4, 0.5, 0.58: $\hbar\omega$ integrated over several scattering angles, intracluster excitations from pairs and trimers of Co^{2+}-ions and also Ising cluster excitations	[92I2, 94I4]
	x = 0.60, 0.70: $\hbar\omega$, integrated over the range 10° – 30° of scattering angles, Ising cluster excitations observed for 1.56 K ≤ T ≤ 100 K (x = 0.60) and 10 K ≤ T ≤ 100 K (x = 0.70)	[95I2, 96I2]; x = 0.60: $T_N = 20$ K, i.e. $T = 100$ K $\mathrel{\hat{=}}$ 5 T_N x = 0.70: $T_N = 45$ K, i.e. $T = 100$ K $\mathrel{\hat{=}}$ 2.2 T_N
$K_2Co_xZn_{1-x}F_4$	x > x_p: Antiferromagnet, $\boldsymbol{M}_{\mathbf{subl}} \parallel \boldsymbol{c}$ (magn. order see Fig. 2.2)	
NMR	x = 0.83: $^{19}F_I$-NMR → 3 $f_{NMR}(T)$ (cf. Fig. 3.51) corresponding to clusters of Co^{2+}-ions with n = 2, 3, 4 nearest Co^{2+}-neighbours as indicated in Fig. 3.51	[85D2]; $f_{NMR} \sim$ local magnetization; theoretical calc.(Ising cluster model: Eq. 3.136) with $J_{VC} = -72.3$ K and $J = -95(5)$, $-91(3)$, $-90(3)$ K for n = 2, 3, 4, resp.
$K_2Ni_xZn_{1-x}F_4$	x > x_p: Antiferromagnet, $\boldsymbol{M}_{\mathbf{subl}} \parallel \boldsymbol{c}$ (magn. order see Fig. 2.2)	
1) el. + quasi-el. n-scatt.	x = 0.75, 0.85, 0.96: $T_N = 62$, 77, 92 K, resp., details: Table 6	[84D2, 85D2]
2) NMR	x = 0.85, 0.96: $^{19}F_I$-NMR → 3 $f_{NMR}(T)$ corresponding to Ni^{2+}-ions surrounded by n = 2, 3, 4 nearest Ni^{2+}-neighbours	[85D2]; $f_{NMR} \sim$ local magnetization; theoretical calculations (Ising cluster model: Eq. 3.136)

Table 5. Data concerning Magnetic Properties *(continued)*

Compound	Characteristic magnetic parameters: J, H_E, H_A, H_0, M, χ, g, T_C, T_N etc. [definitions see Table 1, units are given below]	References, remarks
$K_2Cu_xZn_{1-x}F_4$	x > x_p: Antiferromagnet, $\boldsymbol{M}_{\mathbf{subl}} \perp \boldsymbol{c}$ (magn. order see Fig. 3.27)	
1) magn. meas.	$T_C(x)/T_C(1)$: see Fig. 2 of [80O2], $I_g = 3.0$	see also [80H10]; $T_C(1) = 6.25$ K; I_g: Eqs. 3.128, 3.129
2) C_{magn}	C_{magn} measured for x = 0.36, x_p = 0.59, 0.68, 0.80, 1.00; presented as $C_{magn}/(R \cdot x)$ in Fig. 3.49	[81T2]; x = x_p: model for 1D Heisenberg fm.; x = 1: model for 2D Heisenberg fm. (cf. Sect. 3.3.2)
3) meas. and anal. χ	x = 0.40, 0.50, 0.60, 0.68: $\chi(T)$ for ($0 < T \le 25$ K), presented as $\chi^{-1}(T)$ and $_{10}\log\chi$ versus $_{10}\log T$	[80O3]; exp. data for x ≈ x_p fit well to the theoretical model for an 1D Heisenberg fm.
4) inel. n-scatt.	x = 0.78: $\omega(\boldsymbol{q})$ for $\boldsymbol{q} \triangleq (\zeta, \zeta, 0)$ at $T = 2$ K, magnon lineshapes without Ising cluster structures	[78W1]; exp. data compared to theoretical calculations; some additional data available for x = 0.92
5) FMR	x = 0.95, 9 GHz, $T = 1.2$ K: $H_{res}(\beta)$ and $\Delta H_{FMR}(\beta)$	[89A2]; $\boldsymbol{H_0} \perp \boldsymbol{c}$, $\beta = \angle(\boldsymbol{H_0}, \boldsymbol{a})$, $\boldsymbol{a} \parallel x$-axis
6) LMB, Faraday rotation	x = 0.94, 0.90: study of ferromagnetic stripe domains	[87M1]; x-dependence of dimensions of stripe domains
f) mixed magnets		
$Rb_2V_xCr_{1-x}Cl_4$	Mixed magnetic system	
1) el. + quasi-el. n-scatt.	x = 0.03: magn. contribution to (0,0,4) Bragg refl.: $I(T) \sim M^2(T) \rightarrow T_C = 49.3$ K	[86D4, 86F1]
2) optical studies	x = 0.03: $J_{V\text{-}Cr} = -4.4\ \mathrm{cm}^{-1} \triangleq -6.3$ K	[86D4, 86F1], impurity-induced magnon sidebands
$Rb_2Cr_{1-x}Mn_xCl_4$	Mixed system with competing exchange interactions	
1) el. + quasi-el. n-scatt. and meas. χ	$T_C(x)$, $T_N(x)$ for various x: see Fig. 4.49 in Sect 4.1.13; more details are presented in Table 6	[84M1, 86N3, 88H4, 88K8, 88S7, 88T2, 89S1, 92S7], see also [81M1, 82K6, 84K8, 86K12, 91S1]
2) el. + inel. n-scatt.	x = 0.59: rod scan → $\kappa(T)$, $\Gamma(T) \rightarrow T_f = 11$ K	[86N3, 88S7]; $\Gamma \rightarrow 0 \triangleq T_f$ (spin glass freezing)
3) meas. and anal. χ	x = 0.60: $\chi_{ac}(T)$ [f = 20, 200, 500 Hz; $4\ \mathrm{K} \le T \le 17$ K]	[83K10, 88K8], see also [82K8]; spin glass behaviour
	x = 0.17, 0.36, 0.39, 0.50: $\chi_{ac}(T)$ [f = 20 Hz; $4\ \mathrm{K} \le T \le 70$ K]	[84K8, 86K10, 88K8]; re-entrant spin glass
4) meas. M	x = 0.58: $\boldsymbol{H_0} \perp \boldsymbol{c}$, $T = 4.2$ K $\rightarrow M(H_0) \rightarrow$ hysteresis	[82K8]; hysteresis ≙ spin glass behaviour, s. also [82K7]
	x = 0.972, 0.98, 1.00: $M(H_0)$ for $\boldsymbol{H_0} \parallel \boldsymbol{c}$ [$0 \le H_0 \le 8$ T] at 4.2 K	[86G3]; x = 0.98, 1.0: steep increase ≙ H_{SF}
	x = 0.083, 0.131, 0.306: $M(H_0)$ for $\boldsymbol{H_0} \parallel \boldsymbol{c}$ and $\boldsymbol{H} \perp \boldsymbol{c}$ [$0 \le H_0 \le 6$ T] at 4.2 K	[86G3], s. also [89S1]; calculation with average model

Table 5. Data concerning Magnetic Properties *(continued)*

Compound	Characteristic magnetic parameters: J, H_E, H_A, H_0, M, χ, g, T_C, T_N etc. [definitions see Table 1, units are given below]	References, remarks
$Rb_2Cr_{1-x}Mn_xCl_4$ (cont.)		
5) magn. resonance	x = 0, 0.13, 0.24, 0.37: ν_{FMR} for $\boldsymbol{H_0} \parallel \boldsymbol{c}$, $\boldsymbol{H_0} \perp \boldsymbol{c}$ ($\beta = 0°, 45°$) at 4.2 K → FMR pattern typical for an easy-plane fm.	[84G3, 86G2, 91G2], s. also [84T2]; calculations with average model Eq. 3.151, parameters: [91G2]
	x = 0.59, 0.70, 0.75: ν for $\boldsymbol{H_0} \parallel \boldsymbol{c}$, $\boldsymbol{H_0} \perp \boldsymbol{c}$ ($\beta = 0°, 45°$) at 4.2 K	[84G3, 86G2, 91G2], see also [82K8, 82K9]
	x = 0.86, 0.90, 0.934: ν_{AFMR} for $\boldsymbol{H_0} \parallel \boldsymbol{c}$, $\boldsymbol{H_0} \perp \boldsymbol{c}$ ($\beta = 0°, 45°$) at 4.2 K → AFMR pattern typical for an easy-plane afm.	[84G3, 86G2, 91G2]; calculations with average model Eq. 3.151, parameters: [91G2]
	x = 0.966, 0.972, 0.980, 1.00: ν_{AFMR} for $\boldsymbol{H_0} \parallel \boldsymbol{c}$ at 4.2 K → AFMR pattern typical for an easy-axis afm.	[84G3, 86G2, 91G2], s.also [84K6]; calculations with average model Eq. 3.151, parameters: [91G2]
6) optical studies	x = 0.018, 0.038: $J_{Cr\text{-}Mn} = -1.5\ \mathrm{cm}^{-1} \mathrel{\hat{=}} -2.15$ K later corrected: $J_{Cr\text{-}Mn} = -2.1\ \mathrm{cm}^{-1} \mathrel{\hat{=}} -3.0$ K	[82W8], impurity-induced magnon sidebands [86D4]
7) inel. n-scatt.	x = 0.25, 0.59, 0.70: $\omega(\boldsymbol{q})$ for (ζ, ζ, 0) at 5 K, 13 K (x = 0.25); coexistence of spin waves and Ising cluster excitations, see Figs. 3.75–3.77 with corresponding neighbour configurations	[86S5, 87S2, 88S7, 88S8]; $\zeta = q_x/a^* = q_y/a^*$ ($a^* \approx b^*$); calc. Ising cluster energies (Eq. 3.153), parameters: [88S8]; computer simulation: [88C6, 88S9]
8) NMR	x = 0, 0.1, 0.2: ^{35}Cl-NMR at 1.7 K → samples x = 0, 0.1 are fm., sample x = 0.2 in a re-entrant spin glass state	[86K12]
9) Raman spectr.	x = 0, 0.01, 0.13, 0.20: 1-magnon line at $T \approx 8$ K	[84M4]; x = 0: $h\nu_{max} = 168.1\ \mathrm{cm}^{-1}$ [87A3], cf. Eq.3.90
$Rb_2Cr_{1-x}Fe_xCl_4$	Mixed magnetic system	
optical studies	x = 0.05: $J_{Cr\text{-}Fe} = -3.6\ \mathrm{cm}^{-1} \mathrel{\hat{=}} -5.2$ K	[86D4, 86F1], impurity-induced magnon sidebands
$K_2Mn_{1-x}Fe_xF_4$	Mixed interferromagnets with competing anisotropies	
1) el. + quasi-el. n-scatt. and meas. χ	T_N(x), T_R(x) for various x: see Table 6, different types of antiferromagnetic ordering: see Fig. 1 of [79B2]	[77B8, 78B4, 78B10, 78B11, 78L3, 79B2, 86F5] $T_R \mathrel{\hat{=}}$ reorientation temperature
2) (H_0, T) phase diagram	x = 0.022: several magn. phases, phase boundaries meet in a tetracritical point: $H_{C.P.} = 3.53(3)$ T, $T_{C.P.} = 35.4(4)$ K	[79B2]: n-diffr. with $\boldsymbol{H_0} \parallel \boldsymbol{c}$; [78B4]: meas. M for $\boldsymbol{H_0} \parallel \boldsymbol{c}$; [86F5]: values for $H_{C.P.}$ and $T_{C.P.}$
3) local gap mode	K_2FeF_4: Mn^{2+} $\hbar\omega(s_0) = 40.5\ \mathrm{cm}^{-1}$ $\rightarrow J_{Mn\text{-}Fe} = -3.68\ \mathrm{cm}^{-1}$ $\hat{J}_{Mn\text{-}Fe} = -4.14\ \mathrm{cm}^{-1}$	[78M1], ir spectr. and 1-magnon Raman spectr. $\hat{J}_{Mn\text{-}Fe}$ calc. like $\hat{J}_{AB}$ by means of Eq. 3.147

Table 5. Data concerning Magnetic Properties *(continued)*

Compound	Characteristic magnetic parameters: J, H_E, H_A, H_0, M, χ, g, T_C, T_N etc. [definitions see Table 1, units are given below]	References, remarks
$K_2Mn_xCo_{1-x}F_4$	Mixed antiferromagnets, $\boldsymbol{M}_{\mathbf{subl}} \parallel \boldsymbol{c}$ (magn. order see Fig. 2.2)	
1) el. + quasi-el. n-scatt.	x = 0.98: $T_N = 44$ K (details in Table 6)	[78B4]
2) magnon pair mode	K_2MnF_4:Co^{2+} $\hbar\omega(s_0 + d) = 256(1)\ cm^{-1}$ at $T = 2$ K	[76L6]; Raman spectroscopy
3) local gap mode	K_2CoF_4: Mn^{2+} $\hbar\omega(s_0) = 54\ cm^{-1}$ at 1.2 K additional line at 56 cm^{-1} for $T > 20$ K, $g_c = 1.80(5)$	[80B13, 81B8], ir spectroscopy
	$\rightarrow J_{\parallel,\ Mn\text{-}Co} = -14.3\ cm^{-1}$ $\quad \hat{J}_{\parallel,\ Mn\text{-}Co} = -13.45\ cm^{-1}$ $J_{\perp,\ Mn\text{-}Co} = -7.84\ cm^{-1}$ $\quad \hat{J}_{\perp,\ Mn\text{-}Co} = -9.63\ cm^{-1}$	$\hat{J}_{\parallel,\ Mn\text{-}Co}$, $\hat{J}_{\perp,\ Mn\text{-}Co}$ calc. like $\hat{J}_{AB}$ by means of Eq. 3.147
$Rb_2Mn_xCo_{1-x}F_4$	Mixed antiferromagnets, $\boldsymbol{M}_{\mathbf{subl}} \parallel \boldsymbol{c}$ (magn. order see Fig. 2.2)	
1) el. + quasi-el. n-scatt.	afm. Bragg refl. (1,0,0): $I(T) \sim M^2_{subl}(T) \rightarrow T_N \approx 65$ K	[80I1]
2) inel. n-scatt.	x = 0.5: $\omega(\boldsymbol{q})$ for $(\zeta_x, 0, 0)$ at 5 K, 50 K and 65 K	[80I1]; $\zeta_x = q_x/a^*$; 2 magnon branches: see Fig. 3 of [80I1]
3) local gap mode	Rb_2CoF_4: Mn^{2+} $\hbar\omega(s_0) = 49.7\ cm^{-1}$ at 4 K additional line 51.5 cm^{-1} for $T > 20$ K, $g_c = 1.75$	ir spectr. [81B8]; neutron inelastic scattering [95I4]
	$J_{\parallel,\ Mn\text{-}Co} = -13\ cm^{-1}$ $\quad \hat{J}_{\parallel,\ Mn\text{-}Co} = -12.85\ cm^{-1}$ $J_{\perp,\ Mn\text{-}Co} = -7.13\ cm^{-1}$ $\quad \hat{J}_{\perp,\ Mn\text{-}Co} = -9.56\ cm^{-1}$	$\hat{J}_{\parallel,\ Mn\text{-}Co}$, $\hat{J}_{\perp,\ Mn\text{-}Co}$ calc. like $\hat{J}_{AB}$ by means of Eq. 3.147
$K_2Mn_xNi_{1-x}F_4$	Mixed antiferromagnets, $\boldsymbol{M}_{\mathbf{subl}} \parallel \boldsymbol{c}$ (magn. order see Fig. 2.2)	
1) local mode, pair modes	K_2MnF_4: Ni^{2+} $\hbar\omega(s_0) = 194.8(6)\ cm^{-1}$ $\hbar\omega(s_0 + d) = 237.0\ cm^{-1}$, $\hbar\omega(s_0 + s_0) = 400.7(10)\ cm^{-1}$	[75L5, 75L6, 77L2], fluorescence and Raman spectr.
2) ^{19}F-NMR	x ≈ 0.005, 0.01: $J_{Ni\text{-}Ni} = -35.5(3)\ cm^{-1}$, $J_{Mn\text{-}Ni} = -11.22(7)\ cm^{-1}$ x = 0.975, 0.995: $J_{Mn\text{-}Mn} = -2.92(2)\ cm^{-1}$, $J_{Mn\text{-}Ni} = -9.0(3)\ cm^{-1}$	[80L4, 80L5, 83V2, 84V6], see also [77L5]; $^{19}F_I$: $f_{NMR}(T) \sim \langle S^z_i(T) \rangle$, details on $0 \leq i < \infty$: see [80L4]
3) AFMR	x = 0.975, $T \rightarrow 0$, $H_0 = 0$: $h\nu_{AFMR} = 5.08(3)\ cm^{-1} \mathrel{\hat{=}} 7.31(5)$ K	[80L4, 80L5]

Table 5. Data concerning Magnetic Properties *(continued)*

Compound	Characteristic magnetic parameters: J, H_E, H_A, H_0, M, χ, g, T_C, T_N etc. [definitions see Table 1, units are given below]	References, remarks
$Rb_2Mn_{0.5}Ni_{0.5}F_4$	Mixed antiferromagnet, $\boldsymbol{M}_{\mathbf{subl}} \parallel \boldsymbol{c}$ (magn. order see Fig. 2.2)	
1) el.+ quasi-el. n-scatt.	T_N = 68.72 K (details see Table 6)	[76A3, 77B2, 77S1]
2) inel. n-scatt.	$\omega(\boldsymbol{q})$ for (ζ_x, 0, 0) at 7 K (2 branches)	[75A1, 75B10, 76C3, 77S1]; $\zeta_x = q_x/a^*$
	$J_{Mn\text{-}Mn} = -2.64$ cm^{-1}, $(g\mu_B H_A)_{Mn} = 0.24$ cm$^{-1} \approx 0$ (neglected) $J_{Ni\text{-}Ni} = -33.5$ cm^{-1}, $(g\mu_B H_A)_{Ni} = 2.26$ cm^{-1} $\hat{J}_{Mn-Ni} = 9.40$ cm^{-1} ($\hat{J}_{AB}$: Eq. 3.147)	parameter values from the fit to the exp. data with linear spin-w. th. using the mean crystal or average model (see Eqs. 3.142 and 3.143)
	$\omega(\boldsymbol{q})$ for $\boldsymbol{q} \mathrel{\hat{=}}$ (0.5, 0, 0): increased width of $I(q)$ due to Ising cluster modes $E_{n,\,Ni}$, $E_{n,\,Mn}$ (cf. Fig. 3.58)	[75B10]: $E_{n,\,Ni}$, $E_{n,\,Mn}$ calculated using Eq. 3.144 and the values of the parameters as given above
3) pair modes	modes Ni-Ni: $\hbar\omega$ = 372 cm^{-1} , Mn-Ni: $\hbar\omega$ = 248 cm^{-1} mode Mn-Mn: not observed in Raman spectr.	[75F4]; calculation with an Ising cluster model using $J_{Mn\text{-}Mn} = -2.90$ cm^{-1}, $J_{Mn\text{-}Ni} = -9.17$ cm^{-1} , $J_{Ni\text{-}Ni} = -29.0$ cm^{-1}
$K_2Mn_xCu_{1-x}F_4$	Mixed system with competing exchange interactions	
1) meas. χ and EPR	$\chi_{dc}(T)$ and $\chi_{ac}(T)$ [f = 80 Hz] for $\boldsymbol{H_0} \parallel \boldsymbol{c}$ and $\boldsymbol{H_0} \perp \boldsymbol{c}$ $\rightarrow T_C$ (x), T_N(x) and magn. order: see Fig. 7 of [86K13]	[83Y5, 86K13], see also [78D3, 83Y1]
2) FMR	x = 0.02, 0.04, 0.07; ν = 9 GHz, T = 1.2 K: $H_{res}(\beta)$, $\Delta H_{FMR}(\beta)$	[89A2]; $\boldsymbol{H_0} \perp \boldsymbol{c}$, $\beta = \angle(\boldsymbol{H_0}, \boldsymbol{a})$, $\boldsymbol{a} \parallel x$-axis
3) LMB, Faraday rotation	d(Δn)/dT ~ C_{magn} for various x $\rightarrow J_{Mn\text{-}Cu} = -42$ cm^{-1}	[88J2]
	x = 0.01, 0.03, 0.05: study of ferromagnetic stripe domains	[87M1]; x-dependence of dimensions of stripe domains
4) meas. M	pulsed high-field $M(H_0)$ [$0 \leq H_0 \leq 37$ T] at T = 1.8 K,	[89I5]
	$\boldsymbol{H_0} \perp \boldsymbol{c}$ for $0 \leq x \leq 0.18$ (fm.), $\boldsymbol{H_0} \parallel \boldsymbol{c}$ for $0.57 \leq x \leq 1.0$ (afm.)	$M(H_0)$ for $\boldsymbol{H_0} \parallel \boldsymbol{c} \rightarrow H_{SF}$(x): see Fig. 7 of [89I5]
5) optical studies	x < 10^{-4}: $J_{Mn\text{-}Cu} = -52(2)$ cm$^{-1} \mathrel{\hat{=}} -75(3)$ K	[78F3], impurity-induced magnon sidebands
$(CH_3NH_3)_2Mn_{1-x}Cu_xCl_4$	Mixed system with competing exchange interactions	
FMR	x = 0.5: nonlinear microwave absorption ($\nu \approx$ 10 GHz)	[93P3]; hysteresis above 30 W of microwave power

Table 5. Data concerning Magnetic Properties *(continued)*

Compound	Characteristic magnetic parameters: J, H_E, H_A, H_0, M, χ, g, T_C, T_N etc. [definitions see Table 1, units are given below]	References, remarks
$K_2Fe_{1-x}Co_xF_4$	Mixed antiferromagnets with competing anisotropies	
1) several methods	$T_N(x)$, $T_R(x)$ for various x: see Table 6 (T_C, x) phase diagram: see Fig. 3.59	[83V3, 84F3, 84H3, 85V3, 86V1, 86V2, 88V2] $T_R \mathrel{\hat{=}}$ reorientation temperature
2) inel. n-scatt.	x = 0.27: $\omega(\boldsymbol{q})$ for $\boldsymbol{K} \mathrel{\hat{=}} (1+\zeta_x, 0, 0)$ at T = 5 K	[87H4], similar results for x = 0.2, 0.6 [84H3]
	$J_{\parallel,\,\text{Co-Co}} = -60.3\ \text{cm}^{-1}$, $J_{\perp,\,\text{Co-Co}} = -31.0\ \text{cm}^{-1}$ $J_{\parallel,\,\text{Fe-Fe}} = J_{\perp,\,\text{Fe-Fe}} = -5.73\ \text{cm}^{-1}$, $D_{\text{Fe}} = 4.0\ \text{cm}^{-1}$, $E_{\text{Fe}} = 0.3\ \text{cm}^{-1}$ $\hat{J}_{\parallel,\,\text{Fe-Co}} = -18.55\ \text{cm}^{-1}$, $\hat{J}_{\perp,\,\text{Fe-Co}} = -13.3\ \text{cm}^{-1}$	[88H3]; values of the parameters for an average model calculation and a computer simulation for $\omega(\boldsymbol{q})$ (Fig. 3.62); D, E: Eq. 3.35; $\hat{J}_{\text{AB}}$: Eq. 3.147
3) local gap mode, pair mode	K_2CoF_4: Fe^{2+} $\hbar\omega(s_0) = 55.4\ \text{cm}^{-1}$, $\hbar\omega(s_0 + d) = 271\ \text{cm}^{-1}$	[81B8, 82F], ir spectr. and Raman spectr.
pair mode	K_2FeF_4: Co^{2+} $\hbar\omega(s_0 + d) = 225\ \text{cm}^{-1}$	[84F4], ir spectr. and Raman spectr.
	$J_{\parallel,\,\text{Fe-Co}} = -17.0\ \text{cm}^{-1}$ $\hat{J}_{\parallel,\,\text{Fe-Co}} = -18.5\ \text{cm}^{-1}$ $J_{\perp,\,\text{Fe-Co}} = -9.95\ \text{cm}^{-1}$ $\hat{J}_{\perp,\,\text{Fe-Co}} = -13.25\ \text{cm}^{-1}$	$\hat{J}_{\parallel,\,\text{Mn-Co}}$, $\hat{J}_{\perp,\,\text{Mn-Co}}$ calc. like $\hat{J}_{\text{AB}}$ by means of Eq. 3.147
$Rb_2Fe_xCo_{1-x}F_4$	Mixed antiferromagnets with competing anisotropies	
1) Mössbauer study	$T_N(x)$, $T_R(x)$, $\theta_{\text{Fe}}(x)$ for various x: see Table 6	[84H4]; $T_R \mathrel{\hat{=}}$ reorientation temperature
2) (T_N , x) phase diagram	model calculation	details of the model: see [77M5, 78O3, 84H4]
	$J_{\parallel,\,\text{Co-Co}} = -51.0\ \text{cm}^{-1}$, $J_{\perp,\,\text{Co-Co}} = -28.0\ \text{cm}^{-1}$ $J_{\parallel,\,\text{Fe-Fe}} = J_{\perp,\,\text{Fe-Fe}} = -3.4\ \text{cm}^{-1}$, $h_{\text{A,Fe}} = D_{\text{Fe}}/zJ_{\text{Fe-Fe}} = 0.22$ $\hat{J}_{\parallel,\,\text{Fe-Co}} = -13.2\ \text{cm}^{-1}$, $\hat{J}_{\perp,\,\text{Fe-Co}} = -9.8\ \text{cm}^{-1}$	values of the parameters for the model calculation; $\hat{J}_{\parallel,\,\text{Fe-Co}}$ and $\hat{J}_{\perp,\,\text{Fe-Co}}$ calc. like $\hat{J}_{\text{AB}}$ (Eq.3.147); model results are presented in Fig. 7 of [84 H4]
$K_2Co_xNi_{1-x}F_4$	Mixed antiferromagnets, $\boldsymbol{M}_{\textbf{subl}} \parallel \boldsymbol{c}$ (magn. order see Fig. 2.2)	
ir emission spectroscopy	K_2CoF_4: Ni^{2+} $\hbar\Delta\omega = 188\ \text{cm}^{-1}$ and $\hbar\Delta\omega = 200\ \text{cm}^{-1}$ $\rightarrow J_{\parallel,\,\text{Co-Ni}} = -47(2)\ \text{cm}^{-1}$ $\hat{J}_{\parallel,\,\text{Co-Ni}} = -48.0\ \text{cm}^{-1}$ $J_{\perp,\text{Co-Ni}} = -31(6)\ \text{cm}^{-1}$ $\hat{J}_{\perp,\,\text{Co-Ni}} = -34.3\ \text{cm}^{-1}$	[81B8]; transitions within the ground state of Ni^{2+} ($\vert -1 > \rightarrow \vert 0 >, \vert 0 > \rightarrow \vert +1 >$) split by H_E of Co^{2+}; $\hat{J}_{\parallel,\,\text{Co-Ni}}$, $\hat{J}_{\perp,\,\text{Co-Ni}}$ calc. like $\hat{J}_{\text{AB}}$ with Eq. 3.147

Table 5. Data concerning Magnetic Properties *(continued)*

Compound	Characteristic magnetic parameters: J, H_E, H_A, H_0, M, χ, g, T_C, T_N etc. [definitions see Table 1, units are given below]	References, remarks
$Rb_2Co_xNi_{1-x}F_4$	Mixed antiferromagnets, $\boldsymbol{M}_{\mathbf{subl}} \parallel \boldsymbol{c}$ (magn. order see Fig. 2.2)	
1) C_{magn}	symmetric logarithmic singularity → T_N(x) x = 0.50, 0.65, 0.80: T_N = 114.8, 112.9, 111.9 K, resp.	[81I3]; more details: see Table 6
2) inel. n-scatt.	x = 0.5: $\omega(\boldsymbol{q})$ for (ζ_x, 0, 0) at low T (two branches)	[83I1], $\zeta_x = q_x/a^*$
	$J_{\parallel,\,\text{Co-Co}} = -59\ \text{cm}^{-1}$, $J_{\perp,\,\text{Co-Co}} = -32\ \text{cm}^{-1}$ $J_{\parallel,\,\text{Ni-Ni}} = J_{\perp,\,\text{Ni-Ni}} = -27\ \text{cm}^{-1}$, $g_{Ni}\mu_B H_{A,\,Ni} = 2.26\ \text{cm}^{-1}$ $J_{\parallel,\,\text{Co-Ni}} = -40\ \text{cm}^{-1}$, $J_{\perp,\,\text{Co-Ni}} = -29\text{cm}^{-1}$ (T_N = 115 K)	parameter values from the fit to the exp. data with linear spin-wave theory using the mean crystal or average model (see Eqs. 3.142 and 3.143)
3) ir emission spectroscopy	Rb_2CoF_4: Ni^{2+} $\hbar\Delta\omega$ = 178 cm^{-1} and $\hbar\Delta\omega$ = 189 cm^{-1} $\rightarrow J_{\parallel,\,\text{Co-Ni}} = -44(2)\ \text{cm}^{-1}$ $\hat{J}_{\parallel,\,\text{Co-Ni}} = -45.7\ \text{cm}^{-1}$ $J_{\perp,\text{Co-Ni}} = -32(6)\ \text{cm}^{-1}$ $\hat{J}_{\perp,\,\text{Co-Ni}} = -34.0\ \text{cm}^{-1}$	[81B8]; transitions within the ground state of Ni^{2+} ($\lvert -1 > \rightarrow \lvert 0 >, \lvert 0 > \rightarrow \lvert +1 >$) split by H_E of Co^{2+}; $\hat{J}_{\parallel,\,\text{Co-Ni}}$, $\hat{J}_{\perp,\,\text{Co-Ni}}$ calc. like $\hat{J}_{AB}$ with Eq. 3.147
$K_2Co_xCu_{1-x}F_4$	Mixed system with competing exchange interactions	
1) el.+ quasi-el. n-scatt. and meas. χ	T_C(x), T_N(x) for various x: see Fig. 10 of [90I3], the different types of magn. order are indicated	[90I2, 90I3, 90K3]
2) meas. M	pulsed high-field $M(H_0)$ [$0 \le H_0 \le 37$ T] at T = 1.8 K, $\boldsymbol{H_0} \perp \boldsymbol{c}$ for $0 \le x \le 0.29$ (fm.), $\boldsymbol{H_0} \parallel \boldsymbol{c}$ for $0.50 \le x \le 0.92$ (afm.)	[89I5]
3) LMB	$d(\Delta n)/dT \sim C_{magn} \rightarrow J_{\text{Co-Cu}} \approx -38(17)\ \text{cm}^{-1} \mathrel{\hat{=}} -55(25)$ K	[96J], estimate of average value for $J_{\text{Co-Cu}}$ (cf. Fig. 3.64)
4) FMR	x = 0.003, 0.007, 0.01; 9 GHz, T = 1.2 K: $H_{res}(\beta)$, $\Delta H_{FMR}(\beta)$	[89A2], see also [88Y2]; $\mathbf{H_0} \perp \mathbf{c}$, $\beta = \angle(\mathbf{H_0}, \mathbf{a})$, $\mathbf{a} \parallel$ x-axis
5) Faraday rotation	x = 0.03: study of ferromagnetic stripe domains	[88W5]; dimensions of stripe domains determined

Table 5. Data concerning Magnetic Properties *(continued)*

Compound	Characteristic magnetic parameters: J, H_E, H_A, H_0, M, χ, g, T_C, T_N etc. [definitions see Table 1, units are given below]	References, remarks
$Rb_2Co_xCu_{1-x}F_4$	Mixed system with competing exchange interactions	
1) el. + quasi-el. n-scatt. and meas. χ	study of several magn. Bragg refl. and Bragg rods and meas. of $\chi_{\|c}$, $\chi_{\perp c}$ (ZFC, FC exp.); χ'_{ac} , χ''_{ac} (various f)	In addition to competing exchange interactions, there are also competing anisotropies in this system
	0 ≤ x ≤ 0.18: ferromagnetic order (cf. Fig. 3.72)	
	x = 0.008: $T_C = 5.78(6)$ K	[88D1, 88D11]: $\chi_{\perp c}$, χ'_{ac} ($f = 350$ Hz)
	tetracritical point: $x_{C.P.} = 0.02(1)$ $T_{C.P.} = 5.5(1)$ K	[88D1, 88D11]
	x = 0.037: $T_C = 5.40(5)$ K, $T_R = 3.32(5)$ K	[88D1, 88D11]: $\chi_{\|c}$, $\chi_{\perp c}$; [92S1, 92S8]: n-scatt.
	x = 0.083: $T_C = 5.15(5)$ K	[88D1, 88D11]: $\chi_{\|c}$; [92S1, 92S8]: n-scatt.
	x = 0.110: $T_C = 4.93(5)$ K	[88D1, 88D11]: $\chi_{\|c}$ (FC, ZFC), χ'_{ac} ($f = 8, 244, 3530$ Hz)
	0.18 ≤ x ≤ 0.40: 2D Ising spin glass (cf. Fig. 3.72)	
	x = 0.218: T_f ($t_w = 10$ s) = 3.10(2) K, T_f ($t_w = 90$ s) = 2.97(2) K,	[88D1, 88D11]: $\chi_{\|c}$ (ZFC with t_w); t_w $\hat{=}$ waiting time, cf. Sect. 3.3.6 and Fig. 3.71
	x = 0.326: T_f ($t_w = 10$ s) = 3.23(4) K, T_f ($t_w = 90$ s) = 3.17(4) K	
	0.40 ≤ x ≤ 1.00: antiferromagnetic order (cf. Fig. 3.72)	
	x = 0.430: $T_N = 21(1)$ K, x = 0.498: $T_N = 42(1)$ K	[88D1, 88D11]: $\chi_{\|c}$ for x = 0.430, 0.498, 0.579, 0.892 and 1.00 [92S1, 92S8, 94S4, 95S2]: n-scatt. for x = 0.88
	x = 0.579: $T_N = 61(1)$ K, x = 0.88: $T_N = 88.1(1)$ K	
	x = 0.892: $T_N = 95(1)$ K, x = 1.00: $T_N = 103(1)$ K	
2) C_{magn}	$C_{magn} \approx C_p(Rb_2Co_xCu_{1-x}F_4) - C_p\,(K_2ZnF_4)$	[95R5]; approx. lattice part C_p (K_2ZnF_4): [76I2]
	x = 0.083: λ-like anomaly (singularity) at $T_C = 5.18$ K	
	x = 0.110: λ-like anomaly (singularity) at $T_C = 5.04$ K	
	x = 0.218: x = 0.281: no anomaly at T_f, only broad maximum near 40 K	
3) magn. measurements	estimated average value: $J_{Co\text{-}Cu} \approx -6\ \mathrm{cm}^{-1} \hat{=} -9$ K	[88D1, 88D7, 88D10]; see also Fig. 3.64
4) inel. n-scatt.	x = 0.037: $\omega(\boldsymbol{q})$ for $\boldsymbol{K}$ $\hat{=}$ $(1 + \zeta_{x0}, 0, 0.7)$ at $T = 6.7$ K	[92S8]; $1 + \zeta_{x0} = q_{x0}/a^*$; single branch like K_2CuF_4
	$J_{Cu\text{-}Cu} = 7.2\ (2)\ \mathrm{cm}^{-1}$ $\hat{=}$ 10.3(3) K; little influence of Co^{2+}	[92S8]: linear spin-w. calculation with Eq. 3.72

9.12.3.5 References for 9.12. 3

30B Bloch, F.: Z. Phys. 61 (1930) 206.
40H Holstein, T., Primakoff, H.: Phys. Rev. 58 (1940) 1098.
44O Onsager, L.: Phys. Rev. 65 (1944) 117.
45O Osborn, J.A.: Phys. Rev. 67 (1945) 351.
45S Stoner, E.C.: Philos. Mag. 36 (1945) 803.
50B Bloembergen, N.: Phys. Rev. 78 (1950) 572.
52Y Yang, C.N.: Phys. Rev. 85 (1952) 808.
55N Nagamiya, T., Yosida, K., Kubo, R.: Adv. Phys. 4 (1955) 1.
56D Dyson, F.J.: Phys. Rev. 102 (1956) 1217.
57D Dzyaloshinskii, I.E.: Sov. Phys. JETP 5 (1957) 1259.
58B Behringer, R.E.: J. Chem. Phys. 29 (1958) 537.
58D Dzyaloshinskii, I.: J. Phys. Chem. Solids 4 (1958) 241.
58G Goodenough, J.B.: J. Phys. Chem. Solids 6 (1958) 287.
58M Maleev, S.V.: Sov. Phys. JETP 6 (1958) 776.
58R3 Rushbrooke, G.S., Wood, P.J.: Mol. Phys. 1 (1958) 257.
59A Anderson, P.W.: Phys. Rev. 115 (1959) 2.
59K Kanamori, J.: J. Phys. Chem. Solids 10 (1959) 87.
60A Auld, B.A.: J. Appl. Phys. 31 (1960) 1642.
60E Elliott, R.J., Heap, B.R., Morgan, D.J., Rushbrooke, G.S.: Phys. Rev. Lett. 5 (1960) 366.
60G Gintzburg, M.A.: Sov. Phys. Solid State 2 (1960) 833.
60K1 Kaganov, M.I., Tsukernik, V.: Sov. Phys. JETP 10 (1960) 587.
60K2 Kaganov, M.I., Tsukernik, V.: Sov. Phys. JETP 11 (1960) 952.
60M Moriya, T.: Phys. Rev. 120 (1960) 91.
60O1 Oguchi, T.: Phys. Rev. 117 (1960) 117.
60O2 Ogawa, S.: J. Phys. Soc. Jpn. 15 (1960) 1475.
60S Schlömann, J., Green, J.J., Milano, U.: J. Appl. Phys. 31 (1960) 396S.
61F Frisch, H.L., Sonnenblick, E., Vyssotsky, V.A., Hammersley, J.M.: Phys. Rev. 124 (1961) 1021.
62E Elliott, R.J., Heap, B.R.: Proc. R. Soc. (London) A265 (1962) 264.
62P Pincus, P.: J. Appl. Phys. 33 (1962) 553.
62R Rüdorff, W., Kändler, J., Babel, D.: Z. Anorg. Allg. Chemie 317 (1962) 261.
63A Anderson, P.W.: Theory of magnetic exchange interactions in insulators and semiconductors, in: Solid State Physics, Seitz, F., Turnbull, D. (eds.), New York: Academic Press, 1963, Vol. 14, p. 99.
63F1 Foner, S.: Phys. Rev. 130 (1963) 183.
63F2 Freiser, M.J., Seiden, P.E., Teaney, D.T.: Phys. Rev. Lett. 10 (1963) 293.
63F3 Fisher, M.E.: J. Math. Phys. 4 (1963) 278.
63G Gorter, E.W.: J. Appl. Phys. 34 (1963) 1253.
63H Heap, B.R.: Proc. Phys. Soc. 82 (1963) 252.
63K1 Koster, G.F., Dimmock, J.O., Wheeler, R.G., Statz, H.: Properties of the Thirty-Two Point Groups, Cambridge/Massachusetts: M.I.T. Press, 1963.
63M Moriya, T.: Weak Ferromagnetism, in: Magnetism, Rado, G.T., Suhl, H. (eds.), New York: Academic Press, 1963, Vol. 1, p. 111.
63S Srivastava, K.G.: Phys. Lett. 4 (1963) 55.
64A Anderson, F.B., Callen, H.B.: Phys. Rev. 136 (1964) A1068.
64B Bonner, J.C., Fisher, M.E.: Phys. Rev. 135 (1964) A640.
64F2 Fisher, M.E.: Am. J. Phys. 32 (1964) 343.
64H Hutchings, M.T.: Point charge calculations of energy levels of magnetic ions in crystalline electric fields, in: Solid State Physics, Seitz, F., Turnbull, H. (eds.), New York: Academic Press, 1964, Vol. 16, p. 227.
64S2 Sykes, M.F., Essam, J.W.: Phys. Rev. 133 (1964) A310.

65D Damon, R.W., van de Waart, H.: J. Appl. Phys. 36 (1965) 3453.
65J Joseph, R.I., Schlömann, E.: J. Appl. Phys. 36 (1965) 1579.
65K Kreitman, M.M., Barnett, D.L.: J. Chem. Phys. 43 (1965) 364.
66B1 Breed, D.J.: Phys. Lett. 23 (1966) 181.
66B2 Bloch, D.: J. Phys. Chem. Solids 27 (1966) 881.
66D1 Domb, C., Dalton, N.W.: Proc. Phys. Soc. 89 (1966) 859.
66D2 Dalton, N.W.: Proc. Phys. Soc. 88 (1966) 659.
66H2 Harris, A.B.: Phys. Rev. 143 (1966) 353.
66K Keffer, F.: Spin waves, in: Encyclopedia of Physics, Flügge, S. (ed.), Berlin: Springer-Verlag, 1966, Vol. XVIII/2, p. 249.
66M1 Mermin, N.D., Wagner, H.: Phys. Rev. Lett. 17 (1966) 1133.
66M2 Misetich, A., Dietz, R.E.: Phys. Rev. Lett. 17 (1966) 392
66M3 Maradudin, A.A.: Theoretical and experimental aspects of the effect of point defects and disorder on the vibrations of crystals – 1, in: Solid State Physics, Seitz, F., Turnbull, D. (eds.), New York/London: Academic Press, 1966, Vol. 18, p. 274.
66M4 Maradudin, A.A.: Theoretical and experimental aspects of the effect of point defects and disorder on the vibrations of crystals – 2, in: Solid State Physics, Seitz, F., Turnbull, D. (eds.), New York/London: Academic Press, 1966, Vol. 19, p. 1.
66S2 Stanley, H.E., Kaplan, T.A.: Phys. Rev. Lett. 17 (1966) 913.
67B1 Breed, D.J.: Physica 37 (1967) 35.
67B2 Baker, G.A., Gilbert, H.E., Eve, J., Rushbrooke, G.S.: Phys. Lett. 25A (1967) 207.
67C2 Cinader, G.: Phys. Rev. 155 (1967) 453.
67F1 Fisher, M.E.: Rep. Prog. Phys. 30 (1967) 615.
67J Jansen, L.: Phys. Rev. 162 (1967) 63.
67L Lines, Phys. Rev. 164 (1967) 736.
67S2 Soven, P.: Phys. Rev. 156 (1967) 809.
67W2 Willett, R.D., Liles, O.L., Michelson, C.: Inorg. Chem. 6 (1967) 1885.
68A Akhiezer, A.I., Bar'yakhtar, V.G., Peletminskii, S.V.: Spin Waves, Amsterdam: North-Holland Publishing Corp., 1968.
68F2 Folen, V.J., Krebs, J.J., Rubenstein, M.: Solid State Commun. 6 (1968) 865.
68F3 Feder, J., Pytte, E.: Phys. Rev. 168 (1968) 640.
68H Holden, T.M., Cowley, R.A., Buyers, W.J.L., Stevenson, R.W.H.: Solid State Commun. 6 (1968) 145.
68I Imbusch, G.F., Guggenheim, H.J.: Phys. Lett. 28A (1968) 160.
68L1 Loopstra, B.O., van Laar, B., Breed, D.J.: Phys. Lett. 26A (1968) 527. Erratum: Phys. Lett. 27A (1968) 188.
68L2 Lovesey, S.W.: J. Phys. C: Solid State Phys. 1 (1968) 102.
68L3 Lovesey, S.W.: J. Phys. C: Solid State Phys. 1 (1968) 118.
68M2 Marshall, W., Lowde, R.D.: Rep. Prog. Phys. 31 (1968) 705.
68M4 Moch, P., Parisot, G., Dietz, R.E., Guggenheim, H.J.: Phys. Rev. Lett. 21 (1968) 1596.
68R Rubinstein, M., Folen, V.J.: Phys. Lett. 28A (1968) 108.
68S4 Smith, T., Friedberg, S.A.: Phys. Rev. 176 (1968) 660.
68T1 Tiwari, J.S., Mehra, A., Srivastava, K.G.: Phys. Status Solidi 28 (1968) 61.
68T2 Tonegawa, T.: Prog. Theor. Phys. 40 (1968) 1195.
68V de Vries, G., Breed, D.J., Maarschall, E.P., Miedema, A.R.: J. Appl. Phys. 39 (1968) 1207.
68W1 Wertheim, G.K., Guggenheim, H.J., Levinstein, H.J., Buchanan, D.N.E., Sherwood, R.C.: Phys. Rev. 173 (1968) 614.
68W2 Weber, R.: Phys. Rev. Lett. 21 (1968) 1260.
69B1 Breed, D.J., Gilijamse, K., Miedema, A.R.: Physica 45 (1969) 205.
69B2 Birgeneau, R.J., Guggenheim, H.J., Shirane, G.: Phys. Rev. Lett. 22 (1969) 720.
69C2 Cracknell, A.P.: Rep. Prog. Phys. 32 (1969) 633.
69D Drumheller, J.E., Amundson, P.H., Emerson, K.: J. Chem. Phys. 51 (1969) 5729.
69E Elliott, R.J., Thorpe, M.F.: J. Phys. C: Solid State Phys. 2 (1969) 1630.

69G1 Gorter, F.W., Noordermeer, L.J., Kop, A.R., Miedema, A.R.: Phys. Lett. 29A (1969) 331.
69G3 Genzel, L.: Impurity-induced lattice absorption, in: Optical Properties of Solids, New York: Plenum Press, 1969, Chapter 15, p.453.
69H2 Halperin, B.I., Hohenberg, P.C.: Phys. Rev. 188 (1969) 898.
69J de Jongh, L.J., Botterman, A.C., de Boer, F.R., Miedema, A.R.: J. Appl. Phys. 40 (1969) 1363.
69L1 Legrand, E., van den Bosch, A.: Solid State Commun. 7 (1969) 1191.
69L2 Lines, M.E.: J Appl. Phys. 40 (1969) 1352.
69M2 Maisch, W.G.: J. Appl. Phys. 40 (1969) 1330.
69M3 Maarschall, E.P., Botterman, A.C., Vega, S., Miedema, A.R.: Physica 41 (1969) 473.
69P1 Parkinson, J.B.: J. Phys. C: Solid State Phys. 2 (1969) 2003.
69P2 Parkinson, J.B.: J. Phys. C: Solid State Phys. 2 (1969) 2012.
69R Rohrer, H., Thomas, H.: J. Appl. Phys. 40 (1969) 1025.
69S2 Skalyo, J., Shirane, G., Birgeneau, R.J., Guggenheim, H.J.: Phys. Rev. Lett. 23 (1969) 1394.
69S3 Svensson, E.C., Buyers, W.J.L., Holden, T.M., Cowley, R.A., Stevenson, R.W.H.: Can. J. Phys. 47 (1969) 1983.
69T Thorpe, M.F.: Phys. Rev. Lett. 23 (1969) 472.
69W1 Weber, R.: Z. Phys. 223 (1969) 299.
69W2 Weber, R.: J. Appl. Phys. 40 (1969) 995.
69W3 Wertheim, G.K., Guggenheim, H.J., Butler, M., Jaccarino, V.: Phys. Rev. 178 (1969) 804.
69Y Yamaguchi, Y., Sakamoto, N.: J. Phys. Soc. Jpn. 27 (1969) 1444.
70B1 Birgeneau, R.J., Guggenheim, H.J., Shirane, G.: Phys. Rev. B 1 (1970) 2211.
70B3 Birgeneau, R.J., Skalyo, J., Shirane, G.: J. Appl. Phys. 41 (1970) 1303.
70B4 Birgeneau, R.J., de Rosa, F., Guggenheim, H.J.: Solid State Commun. 8 (1970) 13.
70B5 Breed, D.J., Gilijamse, K., Sterkenburg, J.W.E., Miedema, A.R.: J. Appl. Phys. 41 (1970) 1267.
70E Epstein, A., Gurewitz, E., Makovsky, J., Shaked, H.: Phys. Rev. B 2 (1970) 3703.
70F Fleury, P.A., Guggenheim, H.J.: Phys. Rev. Lett. 24 (1970) 1346.
70L1 Lines, M.E.: J. Phys. Chem. Solids 31 (1970) 101.
70L2 Larkworthy, L.F., Trigg, J.K.: Chem. Commun. 1970, p.1221.
70M Matsuura, M., Gilijamse, K., Sterkenburg, J.E.W., Breed, D.J.: Phys. Lett. 33A (1970) 363.
70S4 Suzuki, N., Kamimura, H.: Solid State Commun. 8 (1970) 149.
70S5 Schrama, A.H.M., Wouters, P.I.J., de Wijn, H.W.: Phys. Rev. B 2 (1970) 1235.
70T Thorpe, M.F.: Phys. Rev. B 2 (1970) 2690.
70W1 Walstedt, R.E., de Wijn, H.W., Guggenheim, H.J.: Phys. Rev. Lett. 25 (1970) 1119.
70W2 de Wijn, H.W., Walstedt, R.E., Walker, L.R., Guggenheim, H.J.: Phys. Rev. Lett. 24 (1970) 832.
70W3 White, R.M.: Quantum Theory of Magnetism, New York/San Francisco: McGraw-Hill, 1970.
70Y1 Yamada, I.: J. Phys. Soc. Jpn. 28 (1970) 1585.
70Y2 Yamaguchi, Y.: J. Phys. Soc. Jpn. 29 (1970) 1163.
71B1 Birgeneau, R.J., Skalyo, J., Shirane, G.: Phys. Rev. B 3 (1971) 1736.
71C1 Colpa, J.H.P., Sieverts, E.G., van der Linde, R.H.: Physica 51 (1971) 573.
71C2 Chinn, S.R., Zeiger, H.J., O'Connor, J.R.: Phys. Rev. B 3 (1971) 1709.
71C3 Chinn, S.R., Davies, R.W., Zeiger, H.J.: Phys. Rev. B 4 (1971) 4017.
71J2 de Jongh, L.J., van Amstel, W.D.: J. Phys. (France) 32 (1971) C1-880.
71J3 de Jongh, L.J., van Amstel, W.D., Miedema, A.R.: 1st European Conf. On Condensed Matter, Geneva 1971, Summaries p. 44.
71K1 Kamimura, H., Suzuki, N., Watarai, S.: J. Phys. (France) 32 (1971) C1-1055.
71K2 Kestigian, M., Holloway, W.W.: Phys. Status Solidi (a) 6 (1971) K19.
71M1 Mostafa, M.F., Willett, R.D.: Phys. Rev. B 4 (1971) 2213.
71M2 Marshall, W., Lovesey, S.W.: Theory of Thermal Neutron Scattering, Oxford: Clarendon Press, 1971.
71M3 Müller, K.A., Berlinger, W.: Phys. Rev. Lett. 26 (1971) 13.
71N Nagata, K., Tomono, Y., Kajiura, M.: J. Phys. Soc. Jpn. 30 (1971) 1209.
71S3 Shante, V.K.S., Kirkpatrick, S.: Adv. Phys. 20 (1971) 325.

71W de Wijn, H.W., Walstedt, R.E., Walker, L.R., Guggenheim, H.J.: J. Appl. Phys. 42 (1971) 1595.
71Y1 Yokozawa, Y.: J. Phys. Soc. Jpn. 31 (1971) 1590.
71Y2 Yamada, I., Kubo, H., Shimohigashi, K.: J. Phys. Soc. Jpn. 30 (1971) 896.
72A van Amstel, W.D., de Jongh, L.J.: Solid State Commun. 11 (1972) 1423.
72B1 Bucci, C., Guidi, G., Vignali, C., Fano, V., Giordano, M.: Solid State Commun. 33 (1972) 393.
72B2 Bucci, C., Guidi, G.: Nuovo Cimento 8 B (1972) 53.
72B5 Bloembergen, P., Franse, J.J.M.: Solid State Commun. 10 (1972) 325.
72B7 Buyers, W.J.L., Pepper, D.E., Elliott, R.J.: J. Phys. C: Solid State Phys. 5 (1972) 2611.
72C1 Colpa, J.H.P.: Physica 57 (1972) 347.
72C2 Cowley, R.A., Buyers, W.J.L.: Rev. Mod. Phys. 44 (1972) 406.
72D Drumheller, J.E., Dickey, D.H., Reklis, R.P., Zaspel, C.E., Glass, S.J.: Phys. Rev. B 5 (1972) 4631.
72E Essam, J.W.: Percolation and cluster size, in: Phase Transitions and Critical Phenomena, Domb, C., Green, M.S. (eds.), London/New York: Academic Press, 1972, Vol. 2, p. 197.
72F1 Ferguson, J., Krausz, E.R., Robertson, G.B., Guggenheim, H.J.: Chem. Phys. Lett. 17 (1972) 551.
72F2 Folen, V.J.: Phys. Rev. B 6 (1972) 1670.
72G3 Gerstein, B.C., Gehring, F.D., Willett, R.D.: J. Appl. Phys. 43 (1972) 1932.
72H2 Hirakawa, K., Ikeda, H.: J. Phys. Soc. Jpn. 33 (1972) 1483.
72I Ikeda, H., Hirakawa, K.: J. Phys. Soc. Jpn. 33 (1972) 393.
72J1 de Jongh, L.J.: Phys. Lett. 40A (1972) 33.
72J2 de Jongh, L.J., Bloembergen, P., Colpa, J.H.P.: Physica 58 (1972) 305.
72J3 de Jongh, L.J.: Solid State Commun. 10 (1972) 537.
72J4 de Jongh, L.J., van Amstel, W.D., Miedema, A.R.: Physica 58 (1972) 277.
72L3 Lécuyer, B., Renard, J.P. Herpe, A.: C.R. Acad. Sci. Paris, Ser. B, 275 (1972) 73.
72M2 Manohar, C., Venkataraman, G.: Phys. Rev. B 5 (1972) 1993.
72R Rushbrooke, G.S., Muse, R.A., Stephenson, R.L., Pirnie, K.: J. Phys. C: Solid State Phys. 5 (1972) 3371.
72T2 Temperly, H.V.N.: Two-dimensional Ising models, in: Phase Transitions and Critical Phenomena, Domb, C., Green, M.S. (eds.), London/New York: Academic Press, 1972, Vol. 1, p. 227.
72Y1 Yamazaki, Y., Watanabe, K., Abe, H.: J. Phys. Soc. Jpn. 32 (1972) 862.
72Y2 Yamada, I.: J. Phys. Soc. Jpn. 33 (1972) 979.
72Y4 Yoshioka, H., Saiki, K.: J. Phys. Soc. Jpn. 33 (1972) 1566.
72Y5 Yamaguchi, Y.: Solid State Commun. 11 (1972) 1611.
73A6 Ajiro, Y., Miura, M.: J. Phys. Soc. Jpn. 35 (1973) 1787.
73B1 Birgeneau, R.J., Guggenheim, H.J., Shirane, G.: Phys. Rev. B 8 (1973) 304.
73B2 Balucani, U., Tognetti, V.: Phys. Rev. B 8 (1973) 4247.
73B5 Bloembergen, P., Berkhout, P.J., Franse, J.J.M.: Int. J. Magnetism 4 (1973) 219.
73B6 Breed, D.J., Gilijamse, K., Sterkenburg, J.W.E., Miedema, A.R.: Physica 68 (1973) 303.
73B7 Buyers, W.J.L., Pepper, D.E., Elliott, R.J.: J. Phys. C: Solid State Phys. 6 (1973) 1933.
73D1 Day, P., Gregson, A.K., Leech, D.H.: Phys. Rev. Lett. 30 (1973) 19.
73D2 Deonarine, S., Joshua, S J.: Phys. Status Solidi (a) 20 (1973) 595.
73D3 Le Dang, K., Veillet, P., Renard, J.P., Jacoboni, C.: Phys. Lett. 43A (1973) 39.
73F1 Ferré, J., Pisarev, R.V., Harding, M.J., Badoz, J., Kizhaev, S.A.: J. Phys. C: Solid State Phys. 6 (1973) 1623.
73F2 Folen, V.J.: Phys. Rev. B 7 (1973) 2771.
73H1 Heger, G., Henrich, E., Kanellakopulos, B.: Solid State Commun. 12 (1973) 1157.
73H2 Hirakawa, K., Ikeda, H.: J. Phys. Soc. Jpn. 35 (1973) 1608.
73H3 Hirakawa, K., Ikeda, H.: J. Phys. Soc. Jpn. 35 (1973) 1328.
73I Ikeda, H., Hirakawa, K.: J. Phys. Soc. Jpn. 35 (1973) 617.
73J2 Jahn, I.R.: Phys. Status Solidi (b) 57 (1973) 681.
73J3 de Jongh, L.J.: AIP Conf. Proc. 10 (1973) 561.
73K1 Khomskii, D.I., Kugel, K.I.: Solid State Commun. 13 (1973) 763.
73K2 Kubo, H., Shimohigashi, K., Yamada, I.: J. Phys. Soc. Jpn. 34 (1973) 1687.

73K4 Kirkpatrick, S.: Solid State Commun. 12 (1973) 1279.
73K5 Kirkpatrick, S.: Rev. Mod. Phys. 45 (1973) 574.
73L2 Lehmann, W., Weber, R.: Phys. Lett. 45A (1973) 33.
73L3 Liu, K.S., Fisher, M.E.: J. Low Temp. Phys. 10 (1973) 655.
73M Mikeska, H.J.: Z. Phys. 261 (1973) 437.
73P1 Pisarev, R.V., Karamyan, A.A., Nesterova, N.N., Syrnikov, P.P.: Opt. Spectrosc. 35 (1973) 88.
73R3 Ritchie, D.S., Fisher, M.E.: Phys. Rev. B 7 (1973) 480.
73S1 Schrama, A.H.M.: Physica 68 (1973) 279.
73S4 Samuelsen, E.J.: Phys. Rev. Lett. 31 (1973) 936.
73W1 Witteveen, H.T., Reedijk, J.: Solid State Commun. 12 (1973) 397.
73W2 de Wijn, H.W., Walker, L.R., Walstedt, R.E.: Phys. Rev. B 8 (1973) 285. Erratum: Phys. Rev. B 9 (1974) 2419.
73W3 de Wijn, H.W., Walker, L.R., Geschwind, S., Guggenheim, H.J.: Phys. Rev. B 8 (1973) 299.
73W4 Willett, R.D., Extine, M.: Phys. Lett. 44A (1973) 503.
73W5 Willett, R.D., Gerstein, B.G.: Phys. Lett. 44A (1973) 153.
73W6 Willett, R.D., Extine, M.: Chem. Phys. Lett. 23 (1973) 281.
73Y1 Yamaji, K., Kondo, J.: Phys. Lett. 45A (1973) 317.
73Y2 Yamazaki, H.: J. Phys. Soc. Jpn. 34 (1973) 270.
73Y3 Yamaji, K., Kondo, J.: J. Phys. Soc. Jpn. 35 (1973) 25.
74D1 Domb, C.: Ising Model, in: Phase Transitions and Critical Phenomena, Domb, C., Green, M.S. (eds.), London/New York: Academic Press, 1974, Vol. 3, p. 357.
74D2 Dzyub, I.P.: Phys. Status Solidi (b) 61 (1974) 383.
74D3 Dzyub, I.P.: Phys. Status Solidi (b) 66 (1974) 339.
74E Elliot, R.J., Krumhansl, J.A., Leath, P.L.: Rev. Mod. Phys. 46 (1974) 465.
74F1 Friebel, C., Reinen, D.: Z. Anorg. Allg. Chemie 407 (1974) 193.
74F3 Fisher, M.E., Nelson, D.R.: Phys. Rev. Lett. 32 (1974) 1350.
74G2 Gerstein, B.C., Chang, K., Willett, R.D.: J. Chem. Phys. 60 (1974) 3454.
74G3 Gerstein, B.C., Chee Chow, Caputo, R., Willett, R.D.: AIP Conf. Proc. 24 (1974) 361.
74H1 Haegele, R., Babel, D.: Z. Anorg. Allg. Chemie 409 (1974) 11.
74H2 Hutchings, M.T., Gregson, A.K., Day, P., Leech, D.H.: Solid State Commun. 15 (1974) 313.
74H4 Hirakawa, K., Ikeda, H.: Phys. Rev. Lett. 33 (1974) 374.
74H5 Harris, A.B.: J. Phys. C: Solid State Phys. 7 (1974) 1671.
74H6 Huber, D.L.: Phys. Rev. B 10 (1974) 4621.
74H7 Holcomb, W.K.: J. Phys. C: Solid State Phys. 7 (1974) 4299.
74H8 Harris, A.B., Leath, P.L., Nickel, B.G., Elliott, R.J.: J. Phys. C: Solid State Phys. 7 (1974) 1695.
74H9 Harris, A.B., Lubensky, T.C.: Phys. Rev. Lett. 33 (1974) 1540.
74H10 Huber, D.L.: Solid State Commun. 14 (1974) 1153.
74I1 Ikeda, H.: J. Phys. Soc. Jpn. 37 (1974) 660.
74I2 Ikeda, H., Hirakawa, K.: Solid State Commun. 14 (1974) 529.
74J1 de Jongh, L.J., Miedema, A.R.: Adv. Phys. 23 (1974) 1.
74J2 Joshua, S.J., Deonarine, S.: Phys. Status Solidi (a) 25 (1974) K125.
74K2 Kleemann. W., Pommier, J.: Phys. Status Solidi (b) 66 (1974) 747.
74K3 Kleemann, W., Farge, Y.: J. Phys. Lett. (France) 35 (1974) L135.
74K4 Kubo, H.: J. Phys. Soc. Jpn. 36 (1974) 675.
74K6 Karimov, Yu.S.: Sov. Phys. JETP 38 (1974) 129.
74L2 Lindgard, P.A., Danielsen, O.: J. Phys. C.: Solid State Phys. 7 (1974) 1523.
74L3 Lehmann, W., Weber, R.: Proc. Int. Conf. Magnetism Moscow 1973, publ. 1974 by Academy of Sciences of the USSR, Vol. I, p. 194.
74M1 Mills, D.L., Burstein, E.: Rep. Prog. Phys. 37 (1974) 817.
74M2 Miedema, A.R., Bloembergen, P., Colpa, J.H.P., Gorter, F.W., de Jongh, L.J., Noordermeer, L.: AIP Conf. Proc. 18 (1974) part 2, 806.
74N1 Nagata, K., Tomono, Y.: J. Phys. Soc. Jpn. 36 (1974) 78.
74N2 Narayana, P.A.: Phys. Rev. B 10 (1974) 2676.

74N3 Nelson, D.R., Kosterlitz, J.M., Fisher, M.E.: Phys. Rev. Lett. 33 (1974) 813.
74P1 Pisarev, R.V., Ferré, J., Petit, R.H., Krichetsov, B.B., Syrnikov, P.P.: J. Phys. C: Solid State Phys. 7 (1974) 4143.
74R2 Rushbrooke, G.S., Baker jr., G.A., Wood, P.J.: Heisenberg Model, in: Phase Transitions and Critical Phenomena, Domb, C., Green, M.S. (eds), London/New York: Academic Press, 1974, Vol. 3, p. 246.
74R3 Rastelli, E., Tassi, A., Reatto, L.: J. Phys. C: Solid State Phys. 7 (1974) 1735.
74S1 Samuelsen, E.J.: J. Phys. Chem. Solids 35 (1974) 785.
74S3 Samuelsen, E.J.: Proc. Int. Conf. Magnetism Moscow 1973, publ. 1974 by Academy of Sciences of the USSR, Vol. IV, p. 276.
74S4 Schwartz, R.W., Spencer, J.A., Yeakel, W.C., Schatz, P.N., Maisch, W.G.: J. Chem. Phys. 60 (1974) 2598.
74T Toms, D.J., O'Sullivan, W.J., Guggenheim, H.J.: Solid State Commun. 14 (1974) 715.
74V4 Villain, J.: J. Phys. (France) 35 (1974) 27.
74W1 Witteveen, H.T.: J. Solid State Chem. 11 (1974) 245.
74W3 Witteveen, H.T.: Physica 71 (1974) 204.
74W4 Watson, B.P., Leath, P.L.: Phys. Rev. B 9 (1974) 4893.
74Y1 Yamazaki, H.: J. Phys. Soc. Jpn. 37 (1974) 667.
74Y2 Yukawa, T., Abe, K.: J. Appl. Phys. 45 (1974) 3146.
74Y3 Yamazaki, H.: Proc. Int. Conf. Magnetism Moscow 1973, publ. 1974 by Academy of Sciences of the USSR, Vol. I, p. 276.
75A1 Als-Nielsen, J., Birgeneau, R.J., Guggenheim, H.J., Shirane, G.: Phys. Rev. B 12 (1975) 4963.
75A3 Arend, H., Schoenes, J., Wachter, P.: Phys. Status Solidi (b) 69 (1975) 105.
75A4 Alben, R., Thorpe, M.F.: J. Phys. C: Solid State Phys. 8 (1975) L275.
75A5 Aharony, A.: Phys. Rev. B 12 (1975) 1038.
75A6 Aharony, A.: Phys. Rev. Lett. 34 (1975) 590.
75B4 Bose, S.M., E-Ni Foo, Zuniga, M.A.: Phys. Rev. B 12 (1975) 3855.
75B7 Bruce, A., Aharony, A.: Phys. Rev. B 11 (1975) 478.
75B9 Blöte, H.W.J.: Physica 79B (1975) 427.
75B10 Birgeneau, R.J., Walker, L.R., Guggenheim, H.J., Als-Nielsen, J., Shirane, G.: J. Phys. C: Solid State Phys. 8 (1975) L328.
75C3 Coombs, G.J., Cowley, R.A.: J. Phys. C: Solid State Phys. 8 (1975) 1889.
75D1 Le Dang, K., Veillet, P.: Phys. Rev. B 11 (1975) 4128.
75D2 Dupas, A., Renard, J.P.: Phys. Lett. 53A (1975) 141.
75D3 Domb, C., Schneider, T., Stoll, E.: J. Phys. A: Math. Gen. 9 (1975) L90.
75E1 Emery, V.J.: Phys. Rev. B 11 (1975) 239.
75E2 Edwards, S.F., Anderson, P.W.: J. Phys. F: Metal Phys. 5 (1975) 965.
75F1 Fisher, M.E.: AIP Conf. Proc. 24 (1975) 273.
75F2 Fisher, M.E.: Phys. Rev. Lett. 34 (1975) 1634.
75F3 Fisher, M.E., Au-Yang, H.: J. Phys. C: Solid State Phys. 8 (1975) L418.
75F4 Fleury, P.A., Guggenheim, H.J.: Phys. Rev. B 12 (1975) 985.
75G4 Gupta, L.C., Vijayaraghavan, R., Damle, S.D., Rao, U.R.K., Le Dang, K., Veillet, P.: J. Magn. Reson. 17 (1975) 41.
75G5 Gregson, A.K., Day, P., Leech, D.H., Fair, M.J., Gardner, W.E.: J. Chem. Soc. Dalton Trans. (1975) 1306.
75H6 Holcomb, W.K., Harris, A.B.: AIP Conf. Proc. 24 (1975) 102.
75J de Jongh, L.J., Block, R.: Physica 79B (1975) 568.
75K2 Kleemann, W., Farge, Y.: J. Phys. (France) 36 (1975) 1293.
75K3 Krey, U., Schlichting, H.J.: Z. Phys. B 21 (1975) 157.
75K4 Kirkpatrick, S., Harris, A.B.: Phys. Rev. B 12 (1975) 4980.
75L5 Lehmann, W., Weber, R.: Proc. Int. Conf. Light Scattering in Solids, Campinas 1975, p. 279.
75L6 Lehmann, W., Macco, F., Weber, R.: Physica 80B (1975) 27.
75L7 Laiho, R.: Phys. Status Solidi (b) 69 (1975) 579.

75L8 Larkworthy, L.F., Trigg, J.K., Yavari, A.: J. Chem. Soc. Dalton Trans. (1975) 1879.
75L9 Leech, D.H., Machin, D.J.: J. Chem. Soc. Dalton Trans. (1975) 1609.
75L11 Lubensky, T.C.: Phys. Rev. B 11 (1975) 3573.
75N Newman, D.J., Urban, W.: Adv. Phys. 24 (1975) 793.
75R1 Rastelli, E., Tassi, A.: Phys. Rev. B 11 (1975) 4711.
75R2 Rezende, S.M., Zeks, B.: Phys. Lett. 54A (1975) 135.
75R4 Riedel, E.F., Willett, R.D.: Solid State Commun. 16 (1975) 413.
75R5 Reimann, H., Hagen, H., Waldner, F., Berlinger, W., Arend, H.: Solid State Commun. 17 (1975) 1319.
75S2 Schlichting, H.J., Krey, U.: Z. Phys. B 20 (1975) 375.
75S3 Stauffer, D.: Z. Phys. B 22 (1975) 161.
75S4 Skal, A., Shklovskii, B.I.: Sov. Phys. Semicond. 8 (1975) 1029.
75S5 Sherrington, D., Kirkpatrick, S.: Phys. Rev. Lett. 35 (1975) 1792.
75W1 Willett, R.D., Riedel, E.F.: Chem. Phys. 8 (1975) 112.
75Y Yamaji, K., Kondo, J.: J. Phys. Soc. Jpn. 39 (1975) 1239.
76A1 Arend, H., Tichy, K., Baberschke, K., Rys, F.: Solid State Commun. 18 (1976) 999.
76A3 Als-Nielsen, J., Birgeneau, R.J., Guggenheim, H.J., Shirane, G.: J. Phys. C: Solid State Phys. 9 (1976) L121.
76A6 Akimitsu, J., Ito, Y.: J. Phys. Soc. Jpn. 40 (1976) 1621.
76A7 Arend, H., v. Känel, H., Wachter, P.: Phys. Status Solidi (b) 74 (1976) 151.
76A9 Alben, R., Thorpe, M.F.: AIP Conf. Proc. 29 (1976) 250.
76A12 Aharony, A., Fishman, S.: Phys. Rev. Lett. 37 (1976) 1587.
76A13 Aharony, A., Imry, Y.: Solid State Commun. 20 (1976) 899.
76B2 Bürger, H., Strobel, K., Geick, R., Müller-Lierheim, W.: J. Phys. C: Solid State Phys. 9 (1976) 4213.
76B5 Bloembergen, P.: Physica 81B (1976) 205.
76B7 Birgeneau, R.J., Cowley, R.A., Shirane, G., Guggenheim, H.J.: Phys. Rev. Lett. 37 (1976) 940.
76C3 Cowley, A.R.: AIP Conf. Proc. 29 (1976) 243.
76C4 Ching, W.Y., Huber, D.L.: Phys. Rev. B 13 (1976) 2962.
76D2 Dupas, A., Le Dang, K., Renard, J.P., Veillet, P., Daoud, A., Perret, R.: J. Chem. Phys. 65 (1976) 4099.
76D5 Dupas, A., Renard, J.P.: J. Phys. (France) 37 (1976) C1-213.
76D6 Le Dang, K., Veillet, P.: Phys. Rev. B 13 (1976) 1919.
76F Funahashi, S., Moussa, F., Steiner, M.: Solid State Commun. 18 (1976) 433.
76G1 Gurewitz, E., Makovsky, J., Shaked, H.: Phys. Rev. B 14 (1976) 2071.
76G2 Gesland, J.Y., Quilichini, M., Scott, J.F.: Solid State Commun. 18 (1976) 1243.
76G3 Gorodetzky, G., Lüthi, B., Eibschütz, M., Guggenheim, H.J.: Phys. Lett. 56A (1976) 479.
76G4 Gregson, A.K., Day, P., Okiji, A., Elliott, R.J.: J. Phys. C: Solid State Phys. 9 (1976) 4497.
76G5 Grinstein, G., Luther, A.: Phys. Rev. B 13 (1976) 1329.
76H4 Hutchings, M.T., Fair, M.J., Day, P., Walker, P.J.: J. Phys. C: Solid State Phys. 9 (1976) L55.
76I1 Ito, Y., Akimitsu, J.: J. Phys. Soc. Jpn. 40 (1976) 1333.
76I2 Ikeda, H., Hatta, I., Tanaka, M.: J. Phys. Soc. Jpn. 40 (1976) 334.
76I3 Iio, K., Nagata, K.: J. Phys. Soc. Jpn. 41 (1976) 1550.
76J1 de Jongh, L.J.: Physica 82B (1976) 247.
76K2 Kosterlitz, J.M., Nelson, D.R., Fisher, M.E.: Phys. Rev. B 13 (1976) 412.
76K3 Kojima, N., Ban, T., Tsujikava, I.: J. Phys. Soc. Jpn. 41 (1976) 1809.
76K6 Kirkpatrick, S.: AIP Conf. Proc. 29 (1976) 141.
76K7 Kirkpatrick, S.: Phys. Rev. Lett. 36 (1976) 69.
76L2 Laiho, R., Levola, T.: Solid State Commun. 18 (1976) 1619.
76L3 Lindgard, P.A., Kowalska, A.: J. Phys. C.: Solid State Phys. 9 (1976) 2081.
76L4 Losee, D.B., McGregor, K.T., Estes, W.E., Hatfield, W.E.: Phys. Rev. B 14 (1976) 4100.
76L6 Lehmann, W., Macco, F., Weber, R.: Solid State Commun. 20 (1976) 1049.
76M2 Miike, H., Yoshinaga, J., Hirakawa, K.: J. Phys. Soc. Jpn. 41 (1976) 347.

76M3 Moussa, F., Villain, J.: J. Phys. C: Solid State Phys. 9 (1976) 4433.
76N1 Navarro, R., Smit, J.J., de Jongh, L.J., Crama, W.J., Ijdo, D.J.W.: Physica 83B (1976) 97.
76N3 Nösselt, J., Heger, G., Moser, R.: Progr. Rep. Teilinstitut Nukleare Festkörperphysik of the IAK in Karlsruhe, KFK 2357 (1976) 81.
76N4 Navarro, R.: Ph.D. Thesis, University of Zaragoza (Spain) 1976.
76P1 Phelps, D.W., Losee, D.B., Hatfield, W.E., Hodgson, D.J.: Inorg. Chem. 15 (1976) 3147.
76P2 van der Pol, A., de Korte, G., van der Wal, A.J., de Wijn, H.W.: Solid State Commun. 19 (1976) 177.
76P3 Pelcovitz, P.A., Nelson, D.R.: Phys. Lett. 57A (1976) 23.
76R2 Rezende, S.M., White, R.M.: Phys. Rev. B 14 (1976) 2939.
76R3 Rys, F.: AIP Conf. Proc. 29 (1976) 458.
76S4 Shapira, Y., Becerra, C.C.: Phys. Lett. 57A (1976) 483.
76S7 Stanley, H.E., Birgeneau, R.J., Reynolds, P.J., Nicoll, J.F.: J. Phys. C: Solid State Phys. 9 (1976) L553.
76S8 Sykes, M.F., Gaunt, D.S., Glen, M.: J. Phys. A: Math. Gen. 9 (1976) 97.
76S9 Sykes, M.F., Gaunt, D.S., Glen, M.: J. Phys. A: Math. Gen. 9 (1976) 1705.
76S11 Stoll, E., Schneider, T.: J. Phys. A: Math. Gen. 9 (1976) L67.
76T1 Tsuru, K., Uryu, N.: J. Phys. Soc. Jpn. 41 (1976) 804.
76T2 Tanimoto, M., Kato, T., Yokozawa, Y.: Phys. Lett. 58A (1976) 66.
76T3 Thorpe, M.F., Alben. R.: J. Phys. C: Solid State Phys. 9 (1976) 2555.
76T4 Tahir-Kheli, R.A., Rezende, S.M., Brady Moreira, F.G., Fittipaldi, I.P.: J. Phys. C: Solid State Phys. 9 (1976) L403.
76Y2 Yamazaki, H., Tanaka, M.: J. Phys. Soc. Jpn. 41 (1976) 1540.
76Y3 Yamazaki, H.: J. Phys. Soc. Jpn. 41 (1976) 1911.
77A1 Arts, A.F.M., van Uijen, C.M.J., de Wijn, H.W.: Physica 86-88B (1977) 663.
77A2 Arts, A.F.M., van Uijen, C.M.J., de Wijn, H.W.: Phys. Rev. B 15 (1977) 4360.
77A3 Arts, A.F.M., van Uijen, C.M.J., van Luijk, J.A., de Wijn, H.W., Beers, C.J.: Solid State Commun. 21 (1977) 13.
77A4 Arts, A.F.M., de Wijn, H.W.: Phys. Rev. B 15 (1977) 4348.
77A5 Arts, A.F.M., de Wijn, H.W.: Physica 86-88B (1977) 647.
77B2 Birgeneau, R.J., Als-Nielsen, J., Shirane, G.: Phys. Rev. B 16 (1977) 280.
77B3 Bloembergen, P.: Physica 85B (1977) 51.
77B6 Baberschke, K., Rys, F., Arend, H.: Physica 86-88B (1977) 685.
77B7 Brady Moreira, F.G., Fittipaldi, I.P., Rezende, S.M., Tahir-Kheli, R.A., Zeks, B.: Phys. Status Solidi (b) 80 (1977) 385.
77B8 Bevaart, L., Lebesque, J.V., Frikkee, E., de Jongh, L.J.: Physica 86-88B (1977) 729.
77C3 Cowley, R.A., Shirane, G., Birgeneau, R.J., Guggenheim, H.J.: Phys. Rev. B 15 (1977) 4292.
77C5 Coenen, L.H.M., De Lang, H.N., Stoelinga, J.H.M., van Kempen, H., Wyder, P.: Physica 86-88B (1977) 968.
77C7 Cowley, R.A., Shirane, G., Birgeneau, R.J., Guggenheim, H.J.: Physica 86-88B (1977) 727.
77D3 Le Dang, K., Veillet, P., Walker, P.J.: J. Phys. C: Solid State Phys. 10 (1977) 4593.
77D4 Dupas, A., Le Dang, K., Renard, J.P., Veillet, P.: J. Phys. C: Solid State Phys. 10 (1977) 3399.
77D5 Dupas, A., Le Dangh, K., Renard, J.P., Veillet, P.: Physica 86-88B (1977) 687.
77F1 Ferré, J., Regis, M., Farge, Y., Kleemann, W.: Physica 89B (1977) 181.
77F2 Fair, M.J., Gregson, A.K., Day, P., Hutchings, M.T.: Physica 86-88B (1977) 657.
77G5 Grande, B., Müller-Buschbaum, H., Schweizer, M.: Z. Anorg. Allg. Chemie 428 (1977) 120.
77H1 Heygster, G., Kleemann, W.: Physica 89B (1977) 165.
77H5 Harris, A.B., Kirkpatrick, S.: Phys. Rev. B 16 (1977) 542.
77I3 Idogaki, T., Uryu, N.: J. Phys. Soc. Jpn. 43 (1977) 845.
77J1 Jansen, L., Block, R.: Physica 86-88B (1977) 1012.
77K2 van Kempen, H., Mischgofsky, F.H., Wyder, P.: Phys. Rev. B 15 (1977) 4386.
77K3 v. Känel, H., Wachter, P.: Physica 89B (1977) 189.
77K4 Kammer, J.W.: Ph.D. Thesis, ETH Zürich (Switzerland) 1977.

77K5 Kubo, H., Machida, Y., Uryu, N.: J. Phys. Soc. Jpn. 43 (1977) 459.
77K7 Katsumata, K.: Solid State Commun. 23 (1977) 481.
77K8 Keller, H., Kündig, W., Arend, H.: Physica 86-88B (1977) 683.
77K9 Kubo, H., Kaneshima, N., Hashimoto, Y., Tsuru, K., Hirakawa, K.: J. Phys. Soc. Jpn. 42 (1977) 484.
77L2 Lehmann, W., Weber, R.: J. Phys. C: Solid State Phys. 10 (1977) 97.
77L3 De Lang, H.N., van Kempen, H., Wyder, P.: Phys. Rev. Lett. 39 (1977) 467.
77L5 van Luijk, J.A., Twigt, W., Verhaak, M.T.C.M., de Wijn, H.W.: J. Magn. Magn. Mater. 6 (1977) 120.
77M2 Mostafa, M.F., Semary, M.A., Ahmed, M.A.: Phys. Lett. 61A (1977) 183.
77M3 Mano, H.: Progr. Theor. Phys. 57 (1977) 1848.
77M5 Matsubara, F., Inawashiro, S.: J. Phys. Soc. Jpn. 42 (1977) 1529.
77N5 Nelson, D.R., Pelcovits, R.A.: Phys. Rev. B 16 (1977) 2191.
77P1 van der Pol, A., de Korte, G., Bosman, G., van der Wal, A.J.: Physica 86-88B (1977) 665.
77P2 van der Pol, A., Thurlings, M.P.H., de Wijn, H.W.: J. Magn. Magn. Mater. 6 (1977) 122.
77S1 Shirane, G., Birgeneau, R.J.: Physica 86-88B (1977) 639.
77S2 Srivastava, J.P., Gerhardt, V.: J. Phys. C: Solid State Phys. 10 (1977) L13.
77S3 Sarmento, E.F., Tilley, D.R.: J. Phys. C: Solid State Phys. 10 (1977) 795.
77S4 Sarmento, E.F., Tilley, D.R.: J. Phys. C: Solid State Phys. 10 (1977) 4269.
77S6 Soos, Z.G., McGregor, K.T., Cheung, T.T.P., Silverstein, A.J.: Phys. Rev. B 16 (1977) 3037.
77T2 Thurlings, M.P.H., van der Pol, A., de Wijn, H.W.: Solid State Commun. 24 (1977) 829.
77T3 Tsuru, K., Uryu, N.: Physica 92B (1977) 79.
77T4 Tsuru, K., Uryu, N.: Physica 92B (1977) 166.
77U Uryu, N., Tsuru, K.: Physica 86-88B (1977) 689.
77V3 Vannimenus, J., Toulouse, G.: J. Phys. C: Solid State Phys. 10 (1977) L537.
77Y2 Yamazaki, H.: J. Phys. Soc. Jpn. 42 (1977) 57.
77Y3 Yamazaki, H.: Physica 86-88B (1977) 649.
77Z Zaspel, C.E., Drumheller, J.E.: Phys. Rev. B 16 (1977) 1771.
78A3 Abdalian, A.T., Moch, P.: J. Appl. Phys. 49 (1978) 2189.
78A4 Arend, H., v. Känel, H., Wachter, P.: J. Appl. Phys. 49 (1978) 2206.
78B1 Bellitto, C., Day, P.: J. Chem. Soc. Dalton Trans. (1978) 1207.
78B4 Bevaart, L., Frikkee, E., Lebesque, J.V., de Jongh, L.J.: Phys. Rev. B 18 (1978) 3376.
78B6 Bellitto, C., Day, P.: J. Chem. Soc., Chem. Commun. 1978, 511.
78B10 Bevaart, L., Frikkee, E., Lebesque, J.V., de Jongh, L.J.: Solid State Commun. 25 (1978) 539.
78B11 Bevaart, L., Frikkee, E., de Jongh, L.J.: Solid State Commun. 25 (1978) 1031.
78D3 Dance, J.M., Yoshizawa, Y., Hirakawa, K.: Mater. Res. Bull. 13 (1978) 1111.
78D4 Domany, E.: J. Phys. C: Solid State Phys. 11 (1978) L337.
78E Eremin, M.V., Kalinenkov, V.N.: Sov. Phys. Solid State 20 (1978) 2051.
78F1 Fair, M.J., Hutchings, M.T., Day, P., Ghosh, R., Walker, P.J.: J. Phys. C: Solid State Phys. 11 (1978) L813.
78F2 Fedoseeva, N.V., Sperakova, I.P., Bazhan, A.N., Beznosikov, B.V.: Sov. Phys. Solid State 20 (1978) 1600.
78F3 Ferré, J., Régis, M.: Solid State Commun. 26 (1978) 225.
78F4 Fishman, SW., Aharony, A.: Phys. Rev. B 18 (1978) 3507.
78H3 Halley, J.W., Holcomb, W.K.: J. Phys. C: Solid State Phys. 11 (1978) 753.
78I2 Ikeda, H., Hutchings, M.T.: J. Phys. C: Solid State Phys. 11 (1978) L529.
78I3 Ikeda, H., Hutchings, M.T., Suzuki, M.: J. Phys. C: Solid State Phys. 11 (1978) L359.
78I4 Idogaki, T., Uryu, N.: J. Phys. Soc. Jpn. 45 (1978) 1498.
78K3 Kosterlitz, J.M., Santos, M.A.: J. Phys. C: Solid State Phys. 11 (1978) 2835.
78K4 Katsumata, K., Tonegawa, T.: Solid State Commun. 25 (1978) 925.
78K5 Kojima, N., Ban, T., Tsujikawa, I.: J. Phys. Soc. Jpn. 44 (1978) 919.
78K6 Kojima, N., Ban, T., Tsujikawa, I.: J. Phys. Soc. Jpn. 44 (1978) 923.
78K7 Kimishima, Y., Watanabe, T.: J. Phys. Soc. Jpn. 45 (1978) 1415.

78K8 v. Känel, H., Arend, H., Wachter, P.: Phys. Lett. 64A (1978) 480.
78K9 van Kalkeren, G., Block, R., Jansen, L.: Physica 93B (1978) 195.
78L3 Lebesque, J.V., Colpa, J.H.P., Bevaart, L.: Physica 95B (1978) 123.
78L4 Larkworthy, L.F., Yavari, A.: J. Chem. Soc. Dalton Trans. (1978) 1236.
78M1 Macco, F., Lehmann, W., Breitling, W., Slawska-Wanieska, A.E., Weber, R., Dürr, U.: Solid State Commun. 26 (1978) 429.
78M2 Moussa, F., Hennion, B., Mons, J., Pepy, G.: Solid State Commun. 27 (1978) 141.
78M4 Moorjani, K., Ghatak, S.K.: Solid State Commun. 26 (1978) 357.
78O1 Okabe, T., Fukuchi, M.: Solid State Commun. 28 (1978) 559.
78O3 Oguchi, T., Ishikawa, T.: J. Phys. Soc. Jpn. 45 (1978) 1213.
78R1 Reimann, H., Hagen, H., Waldner, F., Arend, H.: Phys. Rev. Lett. 40 (1978) 1344.
78R2 Renard, J.P., Corbel, G., Dupas, A.: unpublished results 1978, private communication.
78R3 Reynolds, P.J., Stanley, H.E., Klein, W.: J. Phys. A: Math. Gen. 11 (1978) L199.
78S1 Schröder, B., Strobel, K., Wagner, G., Geick, R.: Infrared Phys. 18 (1978) 893.
78S3 Skaarup, S., Berg, R.W.: J. Solid State Chem. 26 (1978) 59.
78S4 Suzuki, M., Ikeda, H.: J. Phys. C: Solid State Phys. 11 (1978) 3679.
78S5 Slichter, C.P.: Principles of magnetic resonance (2nd edition), in: Springer Series in Solid-State Sciences, Cardona, M., Fulde, P., Queisser, H.-J. (eds.), Berlin: Springer-Verlag, 1978, Vol. 1.
78S7 Sanders, R.W., Jaccarino, V., Rezende, S.M.: Solid State Commun. 28 (1978) 907.
78S8 Schröder, B., Wagner, V., Lehner, N., Geick, R.: J. Phys. (France) 39 (1978) C6-753.
78S9 Semary, M.A., Mostafa, M.F., Ahmed, M.A.: Solid State Commun. 25 (1978) 443.
78S12 Svensson, E.C., Harvey, M., Buyers, W.J.L., Holden, T.M.: J. Appl. Phys. 49 (1978) 2150.
78T2 Thurlings, M.P.H., Hendriks, E.M., de Wijn, H.W.: Solid State Commun. 27 (1978) 1289.
78U van Uijen, C.M.J., de Wijn, H.W., Frikkee, E.: J. Phys. (France) 39 (1978) C6-755.
78W1 Wagner, V., Krey, U.: Z. Phys. B 30 (1978) 367.
78W2 van der Wal, A.J., de Wijn, H.W.: J. Phys. (France) 39 (1978) C6-757.
78Y1 Yamazaki, H.: J. Phys. Soc. Jpn. 45 (1978) 1419.
78Y4 Yeomans, J.M., Stinchcombe, R.B.: J. Phys. C: Solid State Phys. 11 (1978) L525.
79B2 Bevaart, L., Frikkee, E., de Jongh, L.J.: Phys. Rev. B 19 (1979) 4741.
79B4 Blake, A.B., Hatfield, W.E.: J. Chem. Soc. Dalton Trans. (1979) 1725.
79B6 Balucani, U., Tognetti, V., Pini, M.G.: J. Phys. C: Solid State Phys. 12 (1979), 5513.
79B10 Bar'yakhtar, V.G., Vitebskii, I.M., Yablonskii, D.A.: Sov. Phys. JETP 49 (1979) 703.
79D3 Day, P.: Accounts of Chemical Research 12 (1979) 236.
79D4 Day, P., Janke, E., Wood, T.E., Woodwark, D.: J. Phys. C: Solid State Phys. 12 (1979) L329.
79D5 Day, P., Hutchings, M.T., Janke, E., Walker, P.J.: J. Chem. Soc., Chem. Commun. 1979, 711.
79F1 Ferré, J., Regis, M., Farge, Y., Kleemann, W.: J. Phys. C: Solid State Phys. 12 (1979) 2671.
79F3 Fishman, S., Aharony, A.: Phys. Rev. B 19 (1979) 3776.
79G5 Gosso, J.P., Moch, P., Gesland, J.Y., Nouet, J.: J. Phys. (France) 40 (1979) 1067.
79G6 Groenendijk, H.A., van Duyneveldt, A.J., Willett, R.D.: Physica 98B (1979) 53.
79G8 McGurn, A.R., J. Phys. C: Solid State Phys. 12 (1979) 3523.
79H1 Hidaka, M., Walker, P.: Solid State Commun. 31 (1979) 383.
79H2 Hirakawa, K., Yoshizawa, H.: J. Phys. Soc. Jpn. 47 (1979) 368.
79I1 Ikeda, H., Suzuki, M., Hutchings, M.T.: J. Phys. Soc. Jpn. 46 (1979) 1153.
79I2 Ikeda, H., Suzuki, M., Hutchings, M.T.: J. Magn. Magn. Mater. 14 (1979) 163.
79I3 Ikeda, H., Shirane, G.: J. Phys. Soc. Jpn. 46 (1979) 30.
79K2 Krause, S.: Ph.D. Thesis, University of Marburg (Germany) 1979.
79K6 King, A.R., Rohrer, H.: Phys. Rev. B 19 (1979) 5864.
79K7 Kimishima, Y., Nishihara, H.: Solid State Commun. 32 (1979) 245.
79K8 v. Känel, H.: Physica 96B (1979) 167.
79K10 van Kalkeren, G., Schmidt, W.W., Block, R.: Physica 97B (1979) 315.
79M1 Macco, F., Lehmann, W., Weber, R.: J. Phys. C: Solid State Phys. 12 (1979) L233.
79M2 Macco, F.: Ph.D. Thesis, University of Konstanz (Germany) 1979.
79M3 Morgenstern, I., Binder, K.: Phys. Rev. Lett. 43 (1979) 1615.

79O3 Oguchi, T., Ishikawa, T.: J. Phys. Soc. Jpn. 47 (1979) 1760.
79O4 Oguchi, T., Ueno, Y.: J. Phys. Soc. Jpn. 46 (1979) 729.
79P4 Popov, E.A., Kotlyarski, M.M.: Phys. Status Solidi (b) 96 (1979) 163.
79R1 Reinen, D., Friebel, C.: Structure and Bonding, Vol. 34, Berlin: Springer-Verlag, 1979, p. 1.
79R2 Rastelli, E., Lindgard, P.A.: J. Phys. C: Solid State Phys. 12 (1979) 1899.
79S2 Steijger, J.J.M., Frikkee, E., de Jongh, L.J.: J. Magn. Magn. Mater. 14 (1979) 152.
79S5 Snively, L.O., Seifert, P.L., Emerson, K., Drumheller, J.E.: Phys. Rev. B 20 (1979) 2101.
79S7 Stauffer, D.: Phys. Rep. 54 (1979) 1.
79T3 Thorpe, M.F., McGurn, A.R.: Phys. Rev. B 20 (1979) 2142.
79U van Uijen, C.M.J., Frikkee, E., de Wijn, H.J.: Phys. Rev. B 19 (1979) 509.
79W1 van der Wal, A.J., de Wijn, H.W.: Phys. Rev. B 20 (1979) 3712.
79W3 Wagner, V., Krey, U.: J. Magn. Magn. Mater. 14 (1979) 169.
79W4 White, R.M., Geballe, Th.H.: Long range order in solids, in: Solid Sate Physics, Ehrenreich, H., Seitz, F., Turnbull, D. (eds.), New York: Academic Press, 1979, Supplement 15.
80B1 Birgeneau, R.J., Cowley, R.A., Shirane, G., Tarvin, J.A., Guggenheim, H.J.: Phys. Rev. B 21 (1980) 317.
80B4 Balucani, U., Pini, M.G., Tognetti, V.: J. Magn. Magn. Mater. 15-18 (1980) 371.
80B5 Balucani, U., Pini, M.G., Tognetti, V.: J. Phys. C: Solid State Phys. 13 (1980) 2925.
80B6 Borovik-Romanov, A.S., Kreines, N.M., Laiho, R., Levola, T., Zhotikov, V.G.: J. Phys. C: Solid State Phys. 13 (1980) 879.
80B7 Bellitto, C., Fair, M.J., Wood, T.E., Day, P.: J. Phys. C: Solid State Phys. 13 (1980) L627.
80B8 Balucani, U., Pini, M.G., Rettori, A., Tognetti, V.: J. Phys. C: Solid State Phys. 13 (1980) 3895.
80B11 Buzaré, J.Y., Fayet-Bonnel, M., Fayet, J.C.: J. Phys. C: Solid State Phys. 13 (1980) 857.
80B12 Barberis, D., Hagen, H., Mettler, J., Reimann, H., Waldner, F., Arend, H.: J. Magn. Magn. Mater. 15-18 (1980) 747.
80B13 Betz, E., Dürr, U.: Physica 98B (1980) 197.
80C1 Cowley, R.A., Birgeneau, R.J., Shirane, G., Guggenheim, H.J., Ikeda, H.: Phys. Rev. B 21 (1980) 4038.
80D Dürr, U., Schleehauf, O.: Solid State Commun. 35 (1980) 847.
80E1 Elliott, R.J., Hengeltraub, A., Harrop, M.C., Ziman, T.A.L.: J. Magn. Magn. Mater. 15-18 (1980) 359.
80E2 Estes, W.E., Losee, D.B., Hatfield, W.E.: J. Chem. Phys. 72 (1980) 630.
80E3 Essam, J.W.: Rep. Prog. Phys. 43 (1980) 833.
80F3 Fishman, S., Aharony, A.: Phys. Rev. B 21 (1980) 280.
80G3 Gesland, J.Y., Gosso, J.P., Moch, P., Nouet, J., Quilichini, M.: J. Magn. Magn. Mater. 15-18 (1980) 797.
80G6 Gregson, A.K., Moxon, N.: private communication 1980.
80G7 Groenendijk, H.A., van Duyneveldt, A.J., Willett, R.D.: J. Magn. Magn. Mater. 15-18 (1980) 1035.
80G8 Groenendijk, H.A., Van Duyneveldt, A.J., Willett, R.D.: Physica 101B (1980) 320.
80H4 Hatta, I., Ikeda, H.: J. Phys. Soc. Jpn. 48 (1980) 77.
80H10 Hashimoto, T., Kojima, Y., Ikegami, T., Yamada, I.: J. Magn. Magn. Mater. 15-18 (1980) 227.
80I1 Ikeda, H., Riste, T., Shirane, G.: J. Phys. Soc. Jpn. 49 (1980) 504.
80K2 Kleemann, W., Schäfer, F.J.: J. Magn. Magn. Mater. 21 (1980) 143.
80K3 Kubo, H., Suzuki, Y., Akitomi, T., Tsuru, K., Hirakawa, K.: J. Phys. Soc. Jpn. 48 (1980) 399.
80K4 Kimishima, Y.: J. Phys. Soc. Jpn. 49 (1980) 470.
80K5 Kimishima, Y., Nishihara, H., Watanabe, T.: J. Magn. Magn. Mater. 15-18 (1980) 229.
80K6 Kimishima, Y.: J. Phys. Soc. Jpn. 49 (1980) 62.
80K7 Kubo, H., Suzuki, Y., Akitomi, T., Tsuru, K., Kimishima, Y.: J. Phys. Soc. Jpn. 48 (1980) 1387.
80K8 Krey, U.: Z. Phys. B 38 (1980) 243.
80L2 Lindgard, P.A., Als-Nielsen, J., Hutchings, M.T.: J. Magn. Magn. Mater. 15-18 (1980) 343.
80L4 van Luijk, J.A., Arts, A.F.M., de Wijn, H.W.: Phys. Rev. B 21 (1980) 1963.
80L5 van Luijk, J.A., Arts, A.F.M., de Wijn, H.W.: J. Magn. Magn. Mater. 15-18 (1980) 362.

80M2 Münninghoff, G., Treutmann, W., Hellner, E., Heger, G., Reinen, D.: J. Solid State Chem. 34 (1980) 289.
80M3 Münninghoff, G.: Ph.D. Thesis, University of Marburg (Germany) 1980.
80M4 Mostafa, M.F., Semary, M.A., Ahmed, M.A.: J. Magn. Magn. Mater. 15-18 (1980) 448.
80M5 Missel, F.P., Paduan-Filho, A.: Solid State Commun. 34 (1980) 527.
80M6 Matsubara, F.: J. Phys. Soc. Jpn. 49 (1980) 81.
80M7 Matsubara, F.: J. Phys. Soc. Jpn. 49 (1980) 1731.
80M8 Morgenstern, I., Binder, K.: Phys. Rev. B 22 (1980) 288.
80O2 Okuda, Y., Tohi, Y., Yamada, I., Haseda, T.: J. Phys. Soc. Jpn. 49 (1980) 936.
80O3 Okuda, Y., Yamada, I., Watanabe, J., Haseda, T.: J. Phys. Soc. Jpn. 49 (1980) 2136.
80P1 van der Pol. A., Thurlings, M.P.H., de Wijn, H.W.: J. Magn. Magn. Mater. 15-18 (1980) 801.
80P2 van der Pol, A., Thurlings, M.P.H., de Wijn, H.W.: Phys. Rev. B 21 (1980) 1173.
80P4 Popov, E.A., Kotlyarski, M.M.: Sov. Phys. Solid State 22 (1980) 1763.
80S2 Schröder, B., Wagner, V., Lehner, N., Kesharwani, K.M., Geick, R.: Phys. Status Solidi (b) 97 (1980) 501.
80S4 Strobel, K., Frank, J., Rosshirt, K., Geick, R.: Int. J. Millim. Waves 1 (1980) 295.
80S6 Schultz, S., Gullikson, E.M., Fredkin, D.R., Tovar, M.: Phys. Rev. Lett. 45 (1980) 1508.
80T2 Thurlings, M.P.H., Frikkee, E., de Wijn, H.W.: J. Magn. Magn. Mater. 15-18 (1980) 369.
80T3 Thurlings, M.P.H., van Diepen, A.M., de Wijn, H.W.: J. Magn. Magn. Mater. 15-18 (1980) 637.
80T6 Thorpe, M.F., McGurn, A.R.: Solid State Commun. 33 (1980) 663.
80W1 van der Wal, A.J., de Wijn, H.W.: J. Magn. Magn. Mater. 15-18 (1980) 683.
80W3 Walker, L.R., Walstedt, R.E.: Phys. Rev. B 22 (1980) 3816.
80Y1 Yamazaki, H., Zautkin, V.V., Morishige, Y., Chikamatsu, M.: J. Phys. Soc. Jpn. 49 (1980) 139.
80Y2 Yamazaki, H.: J. Phys. Soc. Jpn. 49 (1980) 923.
81B1 Babar, M.A., Ladd, M.F.C., Larkworthy, L.F., Povey, D.C., Proctor, K.J., Summers, L.J.: J. Chem. Soc., Chem. Commun. 1981, 1046.
81B5 Babar, M.A., Larkworthy, L.F., Yavari, A.: J. Chem. Soc. Dalton Trans. (1981) 27.
81B8 Betz, E., Knierim, W., Dürr, U.: J. Magn. Magn. Mater. 25 (1981) 61.
81C1 Carlin, R.L.: J. Appl. Phys. 52 (1981) 1993.
81C2 Chikamatsu, M., Tanaka, M., Yamazaki, H.: J. Phys. Soc. Jpn. 50 (1981) 2876.
81C4 Ching, W.Y., Huber, D.L., Leung, K.M.: Phys. Rev. B 23 (1981) 6126.
81F1 Fujii, M., Wakai, F., Abe, H., Hirai, A.: J. Phys. Soc. Jpn. 50 (1981) 1109.
81G1 Gaididi, Yu.B., Loktev, V.M.: Solid State Commun. 39 (1981) 1077.
81G2 Geick, R.: Topics in Current Chemistry 95 (1981) 89.
81G3 Ghosh, B., Mukherjee, R.K.: Phys. Status Solidi (b) 106 (1981) 699.
81G5 Gabay, M., Toulouse, G.: Phys. Rev. Lett. 47 (1981) 201.
81H1 Herdtweck, E., Babel, D.: Z. Anorg. Allg. Chemie 474 (1981) 113.
81H2 Hirakawa, K., Ubukoshi, K.: J. Phys. Soc. Jpn. 50 (1981) 1909.
81H3 Hirakawa, K., Shirane, G., Axe, J.D.: J. Phys. Soc. Jpn. 50 (1981) 787.
81H4 Hutchings, M.T., Als-Nielsen, Lindgard, P.A., Walker; P.J.: J. Phys. C: Solid State Phys. 14 (1981) 5327.
81H5 Heermann, D.W., Stauffer, D.: Z. Phys. B 44 (1981) 339.
81I2 Ikeda, H.: J. Phys. Soc. Jpn. 50 (1981) 3215.
81I3 Ikeda, H., Abe, T., Hatta, I.: J. Phys. Soc. Jpn. 50 (1981) 1488.
81K5 Kleemann, W., Ferré, J.: Phys. Rev. B 24 (1981) 1568.
81K7 Kimishima, Y., Akimitsu, J., Watanabe, T.: Physica 107B (1981) 495.
81K8 Kubo, H., Suzuki, Y., Akitomi, T., Tsuru, K.: J. Phys. Soc. Jpn. 50 (1981) 2855.
81K9 Kobets, M.I., Stepanov, A.A., Zvyagin, A.I.: Physica 108B (1981) 843.
81K12 Kay, D., McPherson, G.L.: J. Phys. C: Solid State Phys. 14 (1981) 3247.
81K15 Krey, U.: Z. Phys. B 42 (1981) 231.
81M1 Münninghoff, G., Kurtz, W., Treutmann, W., Hellner, E., Heger, G., Lehner, N., Reinen, D.: Solid State Commun. 40 (1981) 571.
81M5 Mostafa, M.F., Semary, M.A., Abdel-Kader, M.: Phys. Lett. 82A (1981) 350.

81M6 Matsubara, F.: J. Phys. Soc. Jpn. 50 (1981) 1469.

81M7 Mukamel, D.: Phys. Rev. Lett. 46 (1981) 845.

81M8 Maletta, H., Zinn, W., Scheuer, H., Shapiro, S.M.: J. Appl. Phys. 52 (1981) 1735.

81P1 Paduan-Filho, A., Missel, F.P., Carlin, R.L.: Solid State Commun. 37 (1981) 529.

81R1 Reinen, D., Krause, S.: Inorg. Chem. 20 (1981) 2750.

81S1 Suzuki, M., Ikeda, H.: J. Phys. Soc. Jpn. 50 (1981) 1133.

81S3 Sanders, R.W., Belanger, R.M., Motokawa, M., Jaccarino, V., Rezende, S.M.: Phys. Rev. B 23 (1981) 1190.

81S4 Strobel, K., Geick, R.: Physica 108B (1981) 951.

81S5 Suzuki, Y., Tsuru, K., Kimishima, Y., Kubo, H.: J. Phys. Soc. Jpn. 50 (1981) 1479.

81S6 Snively, L.O., Tuthill, G.F., Drumheller, J.E.: Phys. Rev. B 24 (1981) 5349.

81S7 Snively, L.O., Drumheller, J.E., Emerson, K.: Phys. Rev. B 23 (1981) 6013.

81S8 Someya, Y.: J. Phys. Soc. Jpn. 50 (1981) 3897.

81T2 Takeda, K., Okuda, Y., Yamada, I., Haseda T.: J. Phys. Soc. Jpn. 50 (1981) 1917.

81U van Uijen, C.M.J., de Wijn, H.W.: Phys. Rev. B 24 (1981) 5368.

81W2 Willett, R.D., Jardine, F.H., Wong, R.J., Landee, C.P., Numata, M.: Phys. Rev. B 24 (1981) 5372.

81W4 van der Wal, A.J., de Wijn, H.W.: Phys. Rev. B 23 (1981) 5950.

81W6 Wong, R.J.H., Willett, R.D., Drumheller, J.E.: J. Chem. Phys. 74 (1981) 6018.

81Y Yamazaki, H., Morishige, Y., Chikamatsu, M.: J. Phys. Soc. Jpn. 50 (1981) 2872.

82B3 Barberis, D., Waldner, F., Arend, H.: J. Appl. Phys. 53 (1982) 8348.

82B4 Block, R., Jansen, L.: Phys. Rev. B 26 (1982) 148.

82F Fendler, K., Lehmann, W., Weber, R., Dürr, U.: J. Phys. C: Solid State Phys. 15 (1982) L533.

82G2 Gaididi, Yu.B., Loktev, V.M.: Solid State Commun. 44 (1982) 801.

82H8 Häussler, K.M., Lehmeyer, A., Merten, L.: Phys. Status Solidi (b) 111 (1982) 513. Erratum: Phys. Status Solidi (b) 114 (1982) 277.

82J1 de Jongh, L.J., Regnault, L.P., Rossat-Mignod, J., Henry, J.Y.: J. Appl. Phys. 53 (1982) 7963.

82J3 Janke, E., Wood, T.E., Ironside, C., Day, P.: J. Phys. C: Solid State Phys. 15 (1982) 3809.

82K1 Kugel, K.I., Khomskii, D.I.: Sov. Phys. Usp. 25 (1982) 231.

82K4 Kubo, H., Suzuki, Y., Kimishima, Y., Nishihara, H.: J. Phys. Soc. Jpn. 51 (1982) 2699.

82K5 Kite, T.M., Drumheller, J.E., Emerson, K.: J. Magn. Reson. 48 (1982) 20.

82K6 Kurtz, W.: Solid State Commun. 42 (1982) 875.

82K7 Katsumata, K., Nire, T., Tanimoto, M.: Solid State Commun. 43 (1982) 711.

82K8 Katsumata, K., Nire, T., Tanimoto, M., Yoshizawa, H.: Phys. Rev. B 25 (1982) 428.

82K9 Kohles, N., Theuerkaufer, H., Strobel, K., Geick, R., Treutmann, W.: J. Phys. C: Solid State Phys. 15 (1982) L137.

82L1 Lenz, N., Strobel, K., Geick, R.: unpublished results 1982.

82M2 Mostafa, M.F., Semary, M.A., Abdel-Kader, M.M.: Physica 112B (1982) 197.

82M4 Mulder, C.A.M., Stipdonk, H.L., Kes, P.H., van Duyneveldt, A.J., de Jongh, L.J.: Physica 113B (1982) 380.

82M5 Mulder, C.A.M., Capel, H.W., Perk, J.H.H.: Physica 112B (1982) 147.

82M6 Münninghoff, G., Hellner, E., Fyne, P.J., Day, P., Hutchings, M.T., Tasset, F.: J. Phys. (France) 43 (1982) C7-243.

82N1 Nitsche, W., Kleemann, W.: Opt. Commun. 41 (1982) 1.

82N2 Nitsche, W., Kleemann, W.: J. Magn. Magn. Mater. 28 (1982) 163.

82N3 Nishihara, H., Goto, T., Kimishima, Y., Kubo, H.: J. Phys. Soc. Jpn. 51 (1982) 407.

82P1 Petrakovskii, G.A., Emel'yanova, L.S., Kokov, I.T., Bondarenko, G.V., Baranov, A.V.: Sov. Phys. JETP 56 (1982) 1260.

82P2 McPherson, G.L., Talluto, K., Auerbach, R.A.: Solid State Commun. 43 (1982) 817.

82R1 Rahman, A., Staveley, L.A.K., Bellitto, C., Day, P.: J. Chem. Soc., Faraday Trans. II 78 (1982) 1895.

82S1 Stead, M.J., Day, P.: J. Chem. Soc. Dalton Trans. (1982) 1081.

82S2 Sontag, H., Macco, F., Fendler, K., Lehmann, W.P., Weber, R.: J. Phys. C: Solid State Phys. 15 (1982) L409.

82S3 Strobel, K., Geick, R.: J. Phys. C: Solid State Phys. 15 (1982) 2105.

82S5 Snively, L.O., Haines, D.N., Emerson, K., Drumheller, J.E.: Phys. Rev. B 26 (1982) 5245.

82S6 Someya, Y.: Phys. Status Solidi (a) 74 (1982) 167.

82S7 Schlottmann, P., Bennemann, K.H.: Phys. Rev. B 25 (1982) 6771.

82T1 Thurlings, M.P.H., Frikkee, E., de Wijn, H.J.: Phys. Rev. B 25 (1982) 4750.

82T2 Thurlings, M.P.H., van der Pol, A., de Wijn, H.W.: Phys. Rev. B 25 (1982) 4765.

82T3 Thurlings, M.P.H., Dikken, B.J., Arts, A.M.F., de Wijn, H.W.: Phys. Rev. B 25 (1982) 4771.

82T4 Takeuchi, H., Arakawa, M., Aoki, H., Yosida, T., Horai, K.: J. Phys. Soc. Jpn. 51 (1982) 3166.

82U van Uijen, C.M.J., Miltenburg, J.C.M., de Wijn, H.W.: J. Phys. C: Solid State Phys. 15 (1982) 299.

82W6 Willett, R.D., Waldner, F.: J. Appl. Phys. 53 (1982) 2680.

82W8 Wood, T.E., Cox, P.A., Day, P., Walker, P.J.: J. Phys. C: Solid State Phys. 15 (1982) L787.

82Y1 Yamazaki, H., Soares, E.A., Panepucci, H., King, A.R.: Solid State Commun. 43 (1982) 655.

83B2 Belanger, R.M., Jaccarino, V., Geschwind, S.: J. Magn. Magn. Mater. 31-34 (1983) 681.

83B3 Babar, M.A., Larkworthy, L.F., Tandon, S.S.: J. Chem. Soc. Dalton Trans. (1983) 1081.

83B4 Birgeneau, R.J., Yoshizawa, H., Cowley, R.A., Shirane, G., Ikeda, H.: Phys. Rev. B 28 (1983) 1438.

83C3 Chikamatsu, M., Yamazaki, H., Yamagata, K., Abe, H.: J. Magn. Magn. Mater. 31-34 (1983) 1191.

83F1 Fujii, M., Hirai, A.: J. Magn. Magn. Mater. 31-34 (1983) 719.

83F2 Fujii, M., Hirai, A.: J. Phys. Soc. Jpn. 52 (1983) 2898.

83G1 Geick, R., Strobel, K.: Magnetic resonances in perovskite-type layer structures, in: Reviews of Infrared and Millimeter Waves, Button, K.J. (ed.), New York: Plenum Press, 1983, Vol. 1, p. 249.

83G2 Gaunt, D.S., Sykes, M.F.: J. Phys. A: Math. Gen. 16 (1983) 783.

83H1 Hidaka, M., Inoue, K., Yamada, I., Walker, P.J.: Physica 121B (1983) 343.

83H3 Hort, H., Mori, T., Ikeda, H., Date, M.: J. Magn. Magn. Mater. 31-34 (1983) 575.

83H4 Hirakawa, K., Yoshizawa, H., Axe, J.D., Shirane, G.: J. Phys. Soc. Jpn. 52 (1983) 4220.

83H5 Häussler, K.M., Brandmüller, J., Merten, L., Finsterhölzl, H. Lehmeyer, A.: Phys. Status Solidi (b) 117 (1983) 225.

83I1 Ikeda, H., Someya, Y., Endoh, Y., Noda, Y., Shibata, F.: Physica 120B (1983) 193.

83J1 Janke, E., Hutchings, M.T., Day, P., Walker, P.J.: J. Phys. C: Solid State Phys. 16 (1983) 5959.

83K5 Kubo, H., Suzuki, Y., Hirakawa, K.: J. Magn. Magn. Mater. 31-34 (1983) 1461.

83K6 Kubo, H., Suzuki, Y., Tanimoto, M., Uryu, N.: J. Phys. Soc. Jpn. 52 (1983) 1373.

83K7 Kubo, H., Akitomi, T., Suzuki, Y., Tsuru, K., Uryu, N.: J. Magn. Magn. Mater. 31-34 (1983) 711.

83K8 Kite, T.M., Drumheller, J.E.: J. Magn. Reson. 54 (1983) 253.

83K10 Katsumata, K.: J. Magn. Magn. Mater. 31-34 (1983) 1435.

83N3 Nikiforov, A.E., Shashkin, S.Yu., Levitan, M.L., Agamalyan, T.H.: Phys. Status Solidi (b) 118 (1983) 419.

83N4 Nakajima, T., Yamauchi, H., Goto, T., Yoshizawa, M., Suzuki, T., Fujimura, T.: J. Magn. Magn. Mater. 31-34 (1983) 1189.

83R1 Rauh, H., Geick, R., Lehner, N., Bouillot, J., Eckold, G.: Phys. Status Solidi (b) 115 (1983) 463.

83R2 Reinen, D.: Comments Inorg. Chem. 2 (1983) 227.

83R3 Reusch, W., Girwidz, R., Strobel, K., Geick, R.: unpublished results 1983.

83S2 Steijger, J.J.M., Frikkee, E., de Jongh, L.J., Huiskamp, W.J.: Physica 120B (1983) 202.

83S6 Shashkin, S.Yu., Nikiforov, A.E.: Sov. Phys. Solid State 25 (1983) 46.

83S7 Stepanov, A.A., Kobets, M.I., Zvyagin, A.I.: Sov. J. Low Temp. Phys. 9 (1983) 391.

83S8 Semary, M.A., Abdel-Kader, M.M., Mostafa, M.F.: Chem. Phys. Lett. 96 (1983) 641.

83S9 Semary, M.A., Mostafa, M.F., Abdel-Kader, M.M.: Phys. Status Solidi (a) 76 (1983) K131.

83S10 Stinchcombe, R.B.: Dilute magnetism, in: Phase Transitions and Critical Phenomena, Domb, C., Lebowitz, J.L. (eds.), London/New York: Academic Press, 1983, Vol. 7, p. 152.

83T3 Tsuru, K., Uryu, N.: J. Magn. Magn. Mater. 31-34 (1983) 1201.

83T4 Tsuru, K., Uryu, N.: Physica 115B (1983) 205.

83T5 Tsuru, K., Uryu, N.: Physica 119B (1983) 265.

83T6 Takeuchi, H., Arakawa, M.: J. Phys. Soc. Jpn. 52 (1983) 279.

83T7 Tanimoto, M., Katsumata, K.: J. Magn. Magn. Mater. 31-34 (1983) 1389.

83U van Uijen, C.M.J., Arts, A.F.M., de Wijn, H.W.: Solid State Commun. 47 (1983) 455.
83V1 van der Vlist, H., Claassen, W.C.M., Arts, A.F.M., de Wijn, H.W.: J. Magn. Magn. Mater. 31-34 (1983) 1183.
83V2 van der Vlist, Arts, A.F.M., de Wijn, H.W.: J. Magn. Magn. Mater. 31-34 (1983) 1185.
83V3 Vlak, W.A.H.M., Frikkee, E., Arts, A.F.M., de Wijn, H.W.: J. Phys. C: Solid State Phys. 16 (1983) L1015.
83W2 Willett, R.D., Wong, R.J., Numata, M.: Inorg. Chem. 22 (1983) 3189.
83Y1 Yamada, I., Shimoda, S., Nagano, S.: J. Magn. Magn. Mater. 31-34 (1983) 645.
83Y3 Yamada, I., Morishita, I., Tokuyama, T.: Physica 115B (1983) 179.
83Y4 Yamazaki, H., Chikamatsu, M.: J. Magn. Magn. Mater. 31-34 (1983) 685.
83Y5 Yamada, I., Nagano, S., Shimoda, S.: Physica 123B (1983) 47.
84B3 Briat, B., Vervoitte, A., Canit, J.C., Francke, E.: Solid State Commun. 50 (1984) 229.
84B4 Birgeneau, R.J., Cowley, R.A., Shirane, G., Yoshizawa, H.: J. Stat. Phys. 34 (1984) 817.
84B7 Bray, A.J., Moore, M.A.: J. Phys. C: Solid State Phys. 17 (1984) L463.
84D2 Dikken, B.J., Arts, A.F.M., de Wijn, H.W., Kjems, J.K.: Phys. Rev. B 30 (1984) 2970.
84E Emel'yanova, L.S.: Preprint No. 281F, Akademiya Nauk SSSR, Institut Fiziki im. L.V. Kirenskogo, Krasnoyarsk 1984 (in Russian).
84F2 Fyne, P.J., Day, P., Hutchings, M.T., Depinna, S., Cavenett, B.C., Pynn, R.: J. Phys. C: Solid State Phys. 17 (1984) L245.
84F3 Fendler, K., von Eynatten, G.: Z. Phys. B 54 (1984) 313.
84F4 Fendler, K., Lehmann, W.P., Weber, R., Dürr, U.: J. Phys. C: Solid State Phys. 17 (1984) 4019.
84G1 Grieb, T., Kullmann, W., Fehr, P., Strobel, K., Geick, R.: J. Phys. C: Solid State Phys. 17 (1984) 6843.
84G2 Grieb, T., Kullmann, W., Strobel, K., Geick, R.: Int. J. Infrared Millim. Waves 5 (1984) 1235.
84G3 Grieb, T., Strobel, K., Geick, R.: Solid State Commun. 51 (1984) 923.
84H3 Higgins, S.A., Cowley, R.A., Hagen, M., Kjems, J., Dürr, U., Fendler, K.: J. Phys. C: Solid State Phys. 17 (1984) 3235.
84H4 Hiraoka, Y., Ito, A.: J. Phys. Soc. Jpn. 53 (1984) 3957.
84H5 Houard, J., Gomes, A.A.: J. Phys. Soc. Jpn. 53 (1984) 4266.
84K2 Kullmann, W., Strobel, K., Geick, R.: J. Phys. C: Solid State Phys. 17 (1984) 6855.
84K3 Kullmann, W., Strobel, K., Geick, R.: Int. J. Infrared Millim. Waves 5 (1984) 1251.
84K4 Kambli, U., Güdel, H.U.: Inorg. Chem. 23 (1984) 3479.
84K5 Kambli, U., Güdel, H.U., Briat, B.: J. Phys. C: Solid State Phys. 17 (1984) 3113.
84K6 Katsumata, K., Tuchendler, J., Tanimoto, M.: Solid State Commun. 50 (1984) 193.
84K7 Kimishima, Y., Nagano, H.: Solid State Commun. 52 (1984) 275.
84K8 Katsumata, K., Tanimoto, M., Mitsuda, S., Endoh, Y.: J. Phys. Soc. Jpn. 53 (1984) 3315.
84L1 Lukin, S.N.: Sov. Phys. Solid State 26 (1984) 771.
84M1 Münninghoff, G., Hellner, E., Treutmann, W., Lehner, N., Heger, G.: J. Phys. C: Solid State Physics 17 (1984) 1281.
84M4 Motokawa, M., Harada, T., Sakakibara, T., Date, M., Ikeda, H., King, A.R.: J. Phys. Soc. Jpn. 53 (1984) 2710.
84M7 Matsubara, F., Katsumata, K.: Solid State Commun. 49 (1984) 1165.
84M8 McMillan, W.L.: J. Phys. C: Solid State Phys. 17 (1984) 3179.
84P Petrakovskii, G.A., Emel'yanova, L.S., Pozduyakov, V.G., Korolev, V.K.: Sov. Phys. Solid State 26 (1984) 728.
84R3 Rastelli, E., Tassi, A.: J. Phys. C: Solid State Phys. 17 (1984) 727.
84R6 Rubenacker, G.V., Haines, D.N., Drumheller, J.E., Emerson, K.: J. Magn. Magn. Mater. 43 (1984) 238.
84S3 Strobel, K., Geick, R.: Solid State Commun. 52 (1984) 249.
84S4 Steijger, J.J.M., Frikkee, E., de Jongh, L.J., Huiskamp, W.J.: Physica 123B (1984) 271.
84S5 Straatman, P., Block, R., Jansen, L.: Phys. Rev. B 29 (1984) 1415.
84T1 Takeuchi, H., Arakawa, M.: J. Phys. Soc. Jpn. 53 (1984) 376.
84T2 Tanimoto, M., Katsumata, K.: Solid State Commun. 50 (1984) 445.

84U van Uijen, C.M.J., de Wijn, H.W.: Phys. Rev. B 30 (1984) 5265.
84V1 Vasyukov, V.N., Zhuravlev, A.V., Lukin, S.N., Pashkevich, Yu.G.: Sov. Phys. Solid State 26 (1984) 790.
84V2 Vervoitte, A., Canit, J.C., Briat, B., Kambli, U.: Phys. Status Solidi (b) 124 (1984) 87.
84V6 van der Vlist, H., Arts, A.F.M., de Wijn, H.W.: Phys. Rev. B 30 (1984) 5270.
84Y1 Yoshizawa, M., Suzuki, T., Goto, T., Yamakami, T., Fujimura, T., Nakajima, T., Yamauchi, H.: J. Phys. Soc. Jpn. 53 (1984) 261.
85A1 Aleksandrov, K.S., Emelyanova, L.S., Misyul, S.V., Kokov, I.T.: Solid State Commun. 53 (1985) 835.
85B1 Bellitto, C., Wood, T.E., Day, P.: Inorg. Chem. 24 (1985) 558.
85D1 Dikken, B.J., Arts, A.F.M., de Wijn, H.J., Vlak, W.A.H.M., Frikkee, E.: Phys. Rev. B 32 (1985) 5600.
85D2 Dikken, B.J., Dekker, C., Arts, A.F.M., de Wijn, H.W.: Phys. Rev. B 32 (1985) 5785.
85G2 de Groot, H.J.M., de Jongh, L.J.: Solid State Commun. 56 (1985) 7.
85G3 Grieb, T., Geick, R.: Solid State Commun. 53 (1985) 919.
85G4 Gullikson, E.M., Dalichaouch, R., Schultz, S.: Phys. Rev. B 32 (1985) 507.
85H4 Huang, C.Y.: J. Magn. Magn. Mater. 51 (1985) 1.
85J1 de Jongh, L.J., de Groot, H.J.M.: Solid State Commun. 53 (1985) 737.
85K2 Kawamura, H., Tanemura, M.: J. Phys. Soc. Jpn. 54 (1985) 4479.
85R2 Rubenacker, G.V., Waplak, S., Hutton, S.L., Haines, D.N., Drumheller, J.E.: J. Appl. Phys. 57 (1985) 3341.
85S1 Samoggia, G., Parmigiani, F., Leccabue, F.: Solid State Commun. 55 (1985) 157.
85S2 Stauffer, D.: Introduction to Percolation Theory, London/Philadelphia: Taylor & Francis, 1985.
85T Tsuru, K., Uryu, N., Le Dang, K., Veillet, P.: J. Phys. Soc. Jpn. 54 (1985) 3111.
85V3 Vlak, W.A.H.M., Dikken, B.J., Arts, A.F.M., de Wijn, H.W.: Phys. Rev. B 31 (1985) 4496.
85Z2 Zvyagin, A.I., Kobets, M.I., Krivoruchko, V.N., Stepanov, A.A., Yablonskii, D.A.: Sov. Phys. JETP 62 (1985) 1328.
86A1 Achiwa, N., Yoshinari, T., Matsuyama, T., Kawano, S., Aoyagi, K.: Annu. Rep. Res. React. Inst. Kyoto Univ. 19 (1986) 31.
86A4 Arakawa, M., Ebisu, H., Takeuchi, H.: J. Phys. Soc. Jpn. 55 (1986) 2853.
86B1 Bellitto, C., Day, P., Wood, T.E.: J. Chem. Soc. Dalton Trans. (1986) 847.
86B3 Bramwell, S.T., Day, P., Hutchings, M.T., Thorne, J.R.G., Visser, D.: Inorg. Chem. 25 (1986) 417.
86B5 Bellitto, C.: J. Magn. Magn. Mater. 54-57 (1986) 1495.
86B7 Binder, K., Young, A.P.: Rev. Mod. Phys. 58 (1986) 801.
86C1 Cornelius, C.A., Day, P., Fyne, P.J., Hutchings, M.T., Walker, P.J.: J. Phys. C: Solid State Phys. 19 (1986) 909.
86C2 Carlin, R.L.: Magnetochemistry, Berlin/New York: Springer-Verlag, 1986.
86D1 Day, P., Fyne, P.J., Hellner, E., Hutchings, M.T., Münninghoff, G., Tasset, F.: Proc. R. Soc. London A 406 (1986) 39.
86D3 Day, P.: Proc. Indian Nat. Sci. Acad. 52A (1986) 117.
86D4 Day, P.: J. Magn. Magn. Mater. 54-57 (1986) 1442.
86D5 Dikken, B.J., Arts, A.F.M., de Wijn, H.W., Vlak, W.A.H.M., Frikkee, E.: J. Magn. Magn. Mater. 54-57 (1986) 30.
86F1 Fyne, P.J., Hutchings, M.T., Day, P.: unpublished results 1986, private communication.
86F3 Floeder, W., Barberis, D.R., Warden, M., Waldner, F.: J. Magn. Magn. Mater. 54-57 (1986) 1137.
86F5 Frikkee, E., Bevaart, L., de Jongh, L.J.: private communication 1986.
86G1 de Groot, H.J.M., de Jongh, L.J.: Physica 141B (1986) 1.
86G2 Grieb, Th.: Ph.D. Thesis, University of Würzburg (Germany) 1986.
86G3 Grieb, Th. Wacker, K., Naumann, E., Treutmann, W., Heger, G., Geick, R.: Phys. Status Solidi (b) 136 (1986) 585.
86G4 Gaulin, B.D., Collins, M.F., Sasnowska, I.: Physica 136B (1986) 360.
86H1 Hidaka, M., et al.: unpublished results 1986, presented by J.P. Jamet, J. Ferré, I. Yamada: J. Phys. C: Solid State Phys. 20 (1987) 3571.

86H2 Hutchings, M.T., Day, P., Janke, E., Pynn, R.: J. Magn. Magn. Mater. 54-57 (1986) 673.
86J2 de Jongh, L.J., Brom, H.B., de Groot, H.J.M., Hijmans, Th.W., Korring, W.H.: J. Magn. Magn. Mater. 54-57 (1986) 1447.
86K2 Kleemann, W., Otte, D., Usadel, K.D., Brieskorn, G.: J. Phys. C: Solid State Phys. 19 (1986) 395.
86K6 Krivoruchko, V.N., Stepanov, A.A., Yablonskii, D.A.: Sov. J. Low Temp. Phys. 12 (1986) 411.
86K7 Kertész, J.: J. Phys. A: Math. Gen. 19 (1986) 599.
86K10 Katsumata, K.: J. Magn. Magn. Mater. 54-57 (1986) 75.
86K11 Kawamura, H., Tanemura, M.: J. Phys. Soc. Jpn. 55 (1986) 1802.
86K12 Kubo, H., Hamasaki, T., Tanimoto, M., Katsumata, K.: J. Phys. Soc. Jpn. 55 (1986) 3301.
86K13 Kimishima, Y., Ikeda, H., Furukawa, A., Nagano, S.: J. Phys. Soc. Jpn. 55 (1986) 3574.
86M5 Mydosh, J.A.: Hyperfine Interact. 31 (1986) 347.
86N3 Naumann, E.: Ph.D. Thesis, University of Marburg (Germany) 1986.
86R1 Rauh, H., Kullmann, W., Geick, R., Erkelens, W.A.C., Regnault, L.P., Rossat-Mignod, J.: J. Magn. Magn. Mater. 54-57 (1986) 717.
86R2 Rauh, H., Erkelens, W.A.C., Regnault, L.P., Rossat-Mignod, J., Kullmann, W., Geick, R.: J. Phys. C: Solid State Phys. 19 (1986) 4503.
86R3 Riley, M.J., Hitchman, M.A., Reinen, D.: Chem. Phys. 102 (1986) 11.
86S3 Shashkin, S.Yu., Goddard III, W.A.: Phys. Rev. B 33 (1986) 1353.
86S5 Sieger, D., Tietze, H., Geick, R., Bates, S., Cowley, R.A., Treutmann, W., Steigenberger, U.: Solid State Commun. 60 (1986) 847.
86S7 Saslow, W.M., Parker, G.: Phys. Rev. Lett. 56 (1986) 1074.
86T1 Tsuru, K., Uryu, N., Le Dang, K., Veillet, P.: J. Magn. Magn. Mater. 54-57 (1986) 1199.
86T2 Tsuru, K.: J. Phys. C: Solid State Phys. 19 (1986) 2031.
86V1 Vlak, W.A.H.M., Frikkee, E., Arts, A.F.M., de Wijn, H.W.: Phys. Rev. B 33 (1986) 6470.
86V2 Vlak, W.A.H.M., van Dort, M.J., Arts, A.F.M., de Wijn, H.W.: J. Magn. Magn. Mater. 54-57 (1986) 41.
86Y1 Yamazaki, H., Warden, M.: J. Phys. Soc. Jpn. 55 (1986) 4477.
86Y3 Young, A.P., Bhatt, R.N.: J. Magn. Magn. Mater. 54-57 (1986) 6.
87A3 Abdalian, A.T., Briat, B., Dugautier, C., Moch, P.: J. Phys. C: Solid State Phys. 20 (1987) 2465.
87A4 Ain, J. Phys. (France) 48 (1987) 2103.
87B1 Bellitto, C., Filaci, P., Patrizio, S.: Inorg. Chem. 26 (1987) 191.
87B2 Balbashov, A.M., Berezin, A.G., Gufan, Yu.M., Kolyadko, G.S., Marchukov, P.Yu., Rudashevskii, E.G.: Sov. Phys. JETP 66 (1987) 174.
87B4 Bellitto, C., Brunners, H., Güdel, H.: Inorg. Chem. 26 (1987) 2750.
87D1 Demokritov, S.O., Kreines, N.M., Kudinov, V.I., Petrov, S.V.: JETP Lett. 46 (1987) 128.
87G3 Greiner, P.: Diploma Thesis, University of Würzburg (Germany) 1987.
87H4 Higgins, S.A., Vlak, W.A.H.M., Hagen, M., Cowley, R.A., Arts, A.F.M., de Wijn, H.W.: J. Phys. C: Solid State Phys. 20 (1987) 833.
87J2 Jamet, J.P., Ferré, J., Yamada, I.: J. Phys. C: Solid Sate Phys. 20 (1987) 3571.
87K1 Katsumata, K., Tuchendler, J.: J. Phys. C: Solid State Phys. 20 (1987) 4873.
87K2 Kimishima, Y.: Jpn. J. Appl. Phys. Suppl. 26-3 (1987) 867.
87L1 Landee, C.P., Halvorson, K.E., Willett, R.D.: J. Appl. Phys. 61 (1987) 3295.
87M1 Matsuura, M., Nojiri, H., Watanabe, M., Yamada, I.: J. Magn. Soc. Jpn. 11, Supplement S1 (1987) 91.
87S2 Sieger, D., Tietze, H., Geick, R., Schweiss, P., Treutmann, W., Frings, P.: Solid State Commun. 64 (1987) 1413.
87S3 Salamon, M.B.: J. Appl. Phys. 61 (1987) 4228.
87T Takeuchi, H., Arakawa, M., Ebisu, H.: J. Phys. Soc. Jpn. 56 (1987) 4571, Erratum: J. Phys. Soc. Jpn. 59 (1990) 2297.
87W1 Wong, P.-z., Yoshizawa, H., Shapiro, S.M., Mydosh, J.A., Palstra, T.T.M.: Phys. Rev. Lett. 58 (1987) 1276.
87W2 Wong, P.-z., Yoshizawa, H., Shapiro, S.M.: J. Appl. Phys. 61 (1987) 4077.
87Y1 Yamazaki, H.: J. Phys. Soc. Jpn. 56 (1987) 4134.

87Y2 Yamazaki, H., Chikamatsu, M., Tanaka, M.: J. Phys. Soc. Jpn. 56 (1987) 340.
87Y3 Yamazaki, H., Mino, M., Nagashima, H., Warden, M.: J. Phys. Soc. Jpn. 56 (1987) 742.
88A2 Abdalian, A.T., Moch, P.: J. Phys. C: Solid State Phys. 21 (1988) 767.
88A8 Arakawa, M., Ebisu, H., Takeuchi, H.: J. Phys. Soc. Jpn. 57 (1988) 3573.
88A9 Arakawa, M., Ebisu, H., Takeuchi, H.: J. Phys. Soc. Jpn. 57 (1988) 2801.
88B1 Balbashov, A.M., Gufan, Yu.M., Marchukov, P.Yu., Rudashevskii, E.G.: Sov. Phys. JETP 67 (1988) 821.
88B3 Briat, B., Bramwell, S.T., Canit, J.C., Day, P., Thorne, J.R.G.: Proc. R. Soc. London A 415 (1988) 277.
88C3 Cowley, R.A., Birgeneau, R.J., Thurston, T., Shirane, G.: J. Phys. (France) 49 (1988) C8-1221.
88C6 Ching, W.Y., Huber, D.L.: Solid State Commun. 68 (1988) 723.
88D1 Dekker, C., Arts, A.F.M., de Wijn, H.W.: Phys. Rev. B 38 (1988) 11512.
88D3 Demokritov, S.O., Kreines, N.M., Kudinov, V.I., Petrov, S.V., Chubukov, A.V.: Sov. Phys. JETP 67 (1988) 2552.
88D7 Dekker, C., Arts, A.F.M., de Wijn, H.W.: J. Appl. Phys. 63 (1988) 4334.
88D10 Dekker, C., Arts, A.F.M., de Wijn, H.W.: Phys. Rev. B 38 (1988) 8985.
88D11 Dekker, C.: Ph.D. Thesis, University of Utrecht (Netherlands) 1988.
88G3 Greb, H., Greiner, P., Sauer, H., Strobel, K.H., Geick, R.: J. Phys. (France) 49 (1988) C8-1487.
88H1 Halvorson, K., Willett, R.D.: Acta Crystallogr. C 44 (1988) 2071.
88H3 Hagen, M., Higgins, S.A.: J. Phys. C: Solid State Phys. 21 (1988) 2701.
88H4 Higgins, S., Cowley, R.A.: J. Phys. C: Solid State Phys. 21 (1988) 2215.
88J1 Jun Shi, Yamazaki, H., Mino, M.: J. Phys. Soc. Jpn. 57 (1988) 3580.
88J2 Jamet, J.P., Ferré, J., Yamada, I., Itoh, M.: J. Phys. (France) 49 (1988) C8-1501.
88K3 Kubo, T., Kishi, T.: Phys. Rev. Lett. 61 (1988) 2585.
88K6 Kubo, H., Hamasaki, T., Tanimoto, M.: J. Phys. Soc. Jpn. 57 (1988) 4379.
88K8 Katsumata, K., Tuchendler, J., Uemura, Y.J., Yoshizawa, H.: Phys. Rev B 37 (1988) 356.
88M4 Moch, P., Abdalian, A.T., Dugautier, C., Briat, B., Nerozzi, M.: J. Phys. (France) 49 (1988) C8-1503.
88R1 Rudowicz, C.: Solid State Commun. 65 (1988) 631.
88R2 Rudowicz, C.: Phys. Rev. B 37 (1988) 27.
88S4 Stepanov, A.A., Pashchenko, V.A., Kobets, M.I.: Sov. J. Low Temp. Phys. 14 (1988) 669.
88S5 Stepanov, A.A., Pashchenko, V.A., Kobets, M.I.: Sov. J. Low Temp. Phys. 14 (1988) 304.
88S7 Sieger, D., Tietze, H., Geick, R., Schweiss, P., Heger, G., Treutmann, W.: J. Appl. Phys. 63 (1988) 3729.
88S8 Sieger, D., Tietze, H., Schweiss, P., Treutmann, W., Bates, S., Cowley, R.A., Geick, R.: Phys. Script. 38 (1988) 429.
88S9 Sieger, D., Ching, W.Y., Huber, D.L., Geick, R.: J. Phys. (France) 49 (1988) C8-1021.
88T2 Tietze, H., Sieger, D., Schweiss, P., Geick,R., Treutmann, W.: J. Phys. (France) 49 (1988) C8-1253.
88V1 Varret, F., Ducouret-Cereze, A.: J. Phys. (France) 49 (1988) C8-847.
88V2 Vlak, W.A.H.M., van Dort, M.J., Arts, A.F.M., de Wijn, H.W.: Phys. Rev. B 38 (1988) 11659.
88W1 Willett, R.D., Place, H., Middleton, M.: J. Am. Chem. Soc. 110 (1988) 8639.
88W3 Warden, M., Waldner, F.: J. Phys. (France) 49 (1988) C8-1573.
88W4 Warden, M., Waldner, F.: J. Appl. Phys. 64 (1988) 5386.
88W5 Watanabe, M., Yokotani, A., Matsuura, M., Yamada, I.: J. Phys. (France) 49 (1988) C8-1897.
88Y1 Yamazaki, H.: J. Phys. Soc. Jpn. 57 (1988) 267.
88Y2 Yamada, I., Anbe, T., Yamaguchi, Y., Itoh, M.: J. Phys. (France) 49 (1988) C8-1489.
88Z1 Zherlitsyn, S.V., Stepanov, A.A., Fil', V.D., Le Gall, A.: Sov. J. Low Temp. Phys. 14 (1988) 408.
88Z2 Ziff, R.M., Stell, G.: LaSC (Ann Arbor, Michigan), report-no. 88-4 (1988), results presented in the review by J.P. Clerc et al. [90C2].
89A2 Anbe, T., Yamaguchi, Y., Itoh, M., Yamada, I., Fujii, H., Hidaka, M.: J. Phys.: Condens. Matter 1 (1989) 5921.
89B4 Brotzeller, C.: Diploma Thesis, University of Würzburg (Germany) 1989.

89D2 Demokritov, S.O., Kreines, N.M., Kudinov, V.I.; Petrov, S.V.: Sov. Phys. JETP 68 (1989) 1277.

89D3 Dekker, C., Arts, A.F.M., de Wijn, H.W., van Duyneveldt, A.J., Mydosh, J.A.: Phys. Rev. B 40 (1989) 11243.

89G5 Greb, H., Geick, R.: Infrared Phys. 29 (1989) 765.

89H2 Hirsch, J.E., Tang, S.: Phys. Rev. B 39 (1989) 2887.

89I5 Itoh, M., Yamada, I., Sakakibara, T., Goto, T.: J. Phys. Soc. Jpn. 58 (1989) 684.

89N2 Nishimori, H., Ozeki, Y.: J. Phys. Soc. Jpn. 58 (1989) 1027.

89S1 Sieger, D.: Ph.D. Thesis, University of Würzburg (Germany) 1989.

89S3 Stepanov, A.A., Zvyagin, A.I., Volotskii, S.V., Kobets, M.I., Pashchenko, V.A.: Sov. J. Low Temp. Phys. 15 (1989) 57.

89S4 Stepanov, A.A., Yablonskii, D.A.: Sov. J. Low Temp. Phys. 15 (1989) 122.

89Y3 Yoshinari, T., Nanba, T., Shimanuki, S., Fujisawa, M., Matsuyama, T., Ikezawa, M., Aoyagi, K.: J. Phys. Soc. Jpn. 58 (1989) 2276.

89Y4 Yonezawa, F., Sakamoto, S., Hori, M.: Phys. Rev. B 40 (1989) 636.

89Z2 Zherlitsyn, S.V., Stepanov, A.A., Fil', V.D., Popov, V.P.: Sov. J. Low Temp. Phys. 15 (1989) 712.

90A1 Achiwa, N., Matsuyama, T., Yoshinari, T.: Phase Transitions 28 (1990) 79.

90A3 Arts, A.F.M., de Wijn, H.W.: Spin waves in two-dimensional magnetic systems, theory and applications, in: Magnetic Properties of Layered Transition Metal Compounds, de Jongh, L.J. (ed.), Dordrecht: Kluwer Academic, 1990, p. 191.

90C2 Clerc, J.P., Giraud, G., Langier, J.M., Luck, J.M.: Adv. Phys. 39 (1990) 191.

90D3 Demokritov, S.O., Kreines, N.M., Kudinov, V.I., Petrov, S.V.: J. Magn. Magn. Mater. 90&91 (1990) 305.

90F2 Fujii, M.: J. Phys. Soc. Jpn. 59 (1990) 4449.

90G3 de Groot, H.J.M., de Jongh, L.J.: Field-induced phenomena in two-dimensional weakly anisotropic Heisenberg antiferromagnets, in: Magnetic Properties of Layered Transition Metal Compounds, de Jongh, L.J. (ed.), Dordrecht: Kluwer Academic, 1990, p. 379.

90G4 Greb, H.: Ph.D. Thesis, University of Würzburg (Germany) 1990.

90H Hirakawa, K., Ikeda, H.: Neutron scattering experiments on two-dimensional Heisenberg and Ising magnets, in: Magnetic Properties of Layered Transition Metal Compounds, de Jongh, L.J. (ed.), Dordrecht: Kluwer Academic, 1990, p. 231.

90I2 Itoh, M., Yamada, I., Ishizuka, M., Amaya, K., Koboyashi, T., Koga, K., Motoya, K.: J. Magn. Magn. Mater. 90&91 (1990) 353.

90I3 Itoh, M., Yamada, I., Ishizuka, M., Amaya, K., Koboyashi, T., Koga, K., Motoya, K.: J. Phys. Soc. Jpn. 59 (1990) 1792.

90J1 de Jongh, L.J.: Introduction to low-dimensional magnetic systems, in: Magnetic Properties of Layered Transition Metal Compounds, de Jongh, L.J. (ed.), Dordrecht: Kluwer Academic, 1990, p. 1.

90K2 Kimishima, Y.: J. Magn. Magn. Mater. 90&91 (1990) 301.

90K3 Kadowaki, H., Yoshizawa, H., Itoh, M., Yamada, I.: J. Phys. Soc. Jpn. 59 (1990) 713.

90N Navarro, R.: Application of high- and low-temperature series expansions to two-dimensional magnetic systems, in: Magnetic Properties of Layered Transition Metal Compounds, de Jongh, L.J. (ed.), Dordrecht: Kluwer Academic, 1990, p. 105.

90P Pokrovsky, V.L., Uimin, G.V.: Theory of two-dimensional magnets, in: Magnetic Properties of Layered Transition Metal Compounds, de Jongh, L.J. (ed.), Dordrecht: Kluwer Academic, 1990, p. 53.

90R2 Riley, M.J., Dubicki, L., Moran, G., Krausz, E.R., Yamada, I.: Inorg. Chem. 29 (1990) 1614.

90Z1 Zenmyo, K., Tokita, M., Kubo, H.: J. Phys. Soc. Jpn. 59 (1990) 1520.

90Z2 Zhou, P., Drumheller, J.E.: J. Appl. Phys. 67 (1990) 5755.

91G1 Geick, R., Greb, H., Hock, B., Jaitner, H., Maier, D., Pabst, T., Treutmann, W., Hosoya, S.: Infrared Phys. 32 (1991) 91.

91G2 Grieb, T., Pabst, T., Kieslich, A., Lindner, J., Rauschmann, H., Strobel, K., Treutmann, W., Geick, R.: J. Phys.: Condens. Matter 3 (1991) 9757.

91M2 Müller, K.A., Fayet, J.C.: Structural Phase Transitions studied by Electron Paramagnetic Resonance, in: Structural Phase Transitions II, Topics in Current Physics, Müller, K.A., Thomas, H. (eds.) Vol. 45, Berlin: Springer-Verlag, 1991, p. 1.
91P Pawlowska, M., Wojciechowski, W.: Phys. Status Solidi (a) 127 (1991) K125.
91S1 Schmidt, W.: Ph.D. Thesis, University of Würzburg (Germany) 1991.
91T1 Takeuchi, H., Arakawa, M., Ebisu, H.: J. Phys.: Condens. Matter 3 (1991) 4405.
91T2 Takeuchi, H., Ebisu, H., Arakawa, M.: J. Phys. Soc. Jpn. 60 (1991) 304.
91V2 Visser, D., Bramwell, S.T., Kremer, R.K.: J. Appl. Phys. 69 (1991) 6024.
92G1 Greb, H., Pabst, T., Rothaler, M., Mukhin, A.A., Pronin, A.Yu., Strobel, K., Geick, R.: J. Phys.: Condens. Matter 4 (1992) 2281.
92H2 Hatta, S., Kasovski, R.V., Hsu, W.Y.: J. Appl. Phys. 72 (1992) 4480.
92I1 Isichenko, M.B.: Rev. Mod. Phys. 64 (1992) 961.
92I2 Ikeda, H., Ohoyama, K.: Phys. Rev. B 45 (1992) 7484.
92K1 Krivoruchko, V.N., Primak, T.E.: Phys. Lett. A 164 (1992) 310.
92L3 Landee, C.P., Greeney, R.E.: J. Magn. Magn. Mater. 104-107 (1992) 788.
92M3 Moser, H.R., Meier, P.F., Warden, M., Waldner, F.: J. Magn. Magn. Mater. 104-107 (1992) 2129.
92M6 Motokawa, M., Ohta, H., Yoshida, K., Ikeda, H.: J. Magn. Magn. Mater. 104 -107 (1992) 947.
92R1 Richter, J.: J. Magn. Magn. Mater. 104-107 (1992) 505.
92R2 Rudowicz, C., Yi-yang Zhou: J. Magn. Magn. Mater. 111 (1992) 153.
92S1 Schins, A.G., Nielsen, M., Arts, A.F.M., de Wijn, H.J.: Physica B 180&181 (1992) 161.
92S4 Schulz, H.J., Ziman, T.A.L.: Europhys. Lett. 18 (1992) 355.
92S6 Stauffer, D, Aharony, A.: Introduction to Percolation Theory, London/Philadelphia: Taylor & Francis, 1992, 2nd edition.
92S7 Sieger, D., Schmidt, W., Tietze-Jaensch, H., Geick, R., Schweiss, P., Treutmann, W., Godfrin, H.: J. Magn. Magn. Mater. 104-107 (1992) 895.
92S8 Schins, A.G., Arts, A.F.M., de Wijn, H.W., Nielsen, M.: J. Magn. Magn. Mater. 104-107 (1992) 931.
92T1 Tietze-Jaensch, H., Sieger, D., Jaitner, H., Geick, R., Schweiss, P., Treutmann, W., Regnault, L.P., Fak, B.: J. Magn. Magn. Mater. 104-107 (1992) 897.
92Z1 Zhou, P., Tuthill, G.F., Drumheller, J.E.: Phys. Rev. B 45 (1992) 2541.
92Z2 Zhou, P., Drumheller, J.E., Patyal, B., Willett, R.D.: Phys. Rev. B 45 (1992) 12365.
92Z3 Ziff, R.M.: Phys. Rev. Lett. 69 (1992) 2670.
93A Als-Nielsen, J., Bramwell, S.T., Hutchings, M.T., McIntyre, G.J., Visser, D.: J. Phys.: Condens. Matter 5 (1993) 7871
93C2 Cowley, R.A., Aharony, A., Birgeneau, R.J., Pelcovits, R.A., Shirane, G., Thurston, T.: Z. Phys. B 93 (1993) 5.
93E Eyert, V., Höck, K.-H.: J. Phys.: Condens. Matter 5 (1993) 2987.
93M1 Mostafa, M.F., Abdel-Kader, M.M., Atallah, A.S., El-Nimer, M.: Phys. Status Solidi (a) 135 (1993) 549.
93M3 Mydosh, J.A.: Spin Glasses: An Experimental Introduction, London: Taylor & Francis, 1993.
93P1 Pich, C., Schwabl, F.: Phys. Rev. B 47 (1993) 7957.
93P3 Patrin, G.S., Volkov, N.V., Fedoseeva, N.V., Nikolaev, E.M.: JETP Lett. 57 (1993) 189.
93R1 Richter, J.: Phys. Rev. B 47 (1993) 5794.
93R3 Rudowicz, C., Du, M., Zhou, Y., Yeung Yanyuen: Physica B 191 (1993) 323.
93S1 Struzhkin, V.V., Schwarz, U., Wilhelm, H., Syassen, K.: Mater. Sci. Eng. A 168 (1993) 103.
93V Visser, D., Bramwell, S.T.: J. Appl. Phys. 73 (1993) 5345.
94H Hagiwara, M., Katsumata, K., Tuchendler, J.: J. Phys.: Condens. Matter 6 (1994) 545.
94I1 Iwasa, K., Nishi, M., Ikeda, H., Suzuki, J.: J. Phys. Soc. Jpn. 63 (1994) 1900.
94I4 Ikeda, H.: Physica A 204 (1994) 328.
94N Nakayama, T., Yakubo, K., Orbach, R.L.: Rev. Mod. Phys. 66 (1994) 381.
94P1 Pich, C., Schwabl, F.: Phys. Rev. B 49 (1994) 413.

94S1 Sangaletti, L., Parmigiani, F., Ratner, E., Shen, Z.-X., Chemelli, C., Jepsen, O.: Phys. Rev. B 50 (1994) 17854.

94S3 Sivron, N., Grigereit, T.E., Drumheller, J.E., Emerson, K., Willett, R.D.: J. Appl. Phys. 75 (1994) 5952.

94S4 Schins, A.G., Nielsen, M., Arts, A.F.M., de Wijn, H.W.: Phys. Rev. B 49 (1994) 8911.

95D Dovesi, R., Ricart, J.M., Saunders, V.R., Orlando, R.: J. Phys.: Condens. Matter 7 (1995) 7997.

95F1 Flandrois, S., Chanh, N.B., Duplessix, R., Maris, Th., Negrier, P.: Phys. Status Solidi (a) 149 (1995) 697.

95F2 Feldkemper, S., Weber, W., Schulenburg, J., Richter, J.: Phys. Rev. B 52 (1995) 313.

95I2 Ikeda, H., Iwasa, K., Fernandez-Baca, J.A., Nicklow, R.M.: Physica B 213&214 (1995) 146.

95I4 Iwasa, K., Ikeda, H.: Physica B 213&214 (1995) 197.

95M1 Mostafa, M.F., Emrick, R.M.: Physica B 210 (1995) 67.

95N2 Nikiforov, A.E., Shashkin, S.Yu.: Phys. Solid State 37 (1995) 719.

95P1 Pich, C., Schwabl, F.: J. Magn. Magn. Mater. 140-144 (1995) 1709.

95R1 Richter, J., Ivanov, N.B., Retzlaff, K.: J. Magn. Magn. Mater. 140-144 (1995) 1609.

95R3 Ricart, J.M., Dovesi, D., Roetti, C., Saunders, V.: Phys. Rev. B 52 (1995) 2381.

95R5 Ramirez, A.P., Schins, A.G., Arts, A.F.M., de Wijn, H.W.: J. Magn. Magn. Mater. 140-144 (1995) 1713.

95S1 Sasaki, S., Narita, N., Yamada, I.: J. Phys. Soc. Jpn. 64 (1995) 2701.

95S2 Schins, A.G., Nielsen, M., Arts, A.F.M., de Wijn, H.W.: J. Magn. Magn. Mater. 140-144 (1995) 1715.

95S3 Shirakura, T., Matsubara, F.: J. Phys. Soc. Jpn. 64 (1995) 2338.

95T2 Tsuboi, T.: Phys. Rev. B 52 (1995) 3406.

95Z2 Zheng Wen-Chen: Solid State Commun. 94 (1995) 317.

96A Arakawa, M., Ebisu, H., Takeuchi, H.: J. Phys.: Condens. Matter 8 (1996) 11299.

96I1 Ishizuka, M., Yamada, I., Amaya, K., Endo, S.: J. Phys. Soc. Jpn. 65 (1996) 1927.

96I2 Iwasa, K., Ikeda, H., Anderson, K.H., Eccleston, R.S.: J. Phys. Soc. Jpn. 65 (1996) 1038.

96J Jamet, J.P., Landee, C.P., Ferré, J., Ayadi, M., Gaubi, H., Yamada, I.: J. Phys.: Condens. Matter 8 (1996) 5501.

96K van de Kamp, R.: Ph.D. Thesis, Technical University of Berlin (Germany) 1996.

96M Mydosh, J. Magn. Magn. Mater. 157&158 (1996) 606.

96S1 Subbaraman, K., Zaspel, C.E., Drumheller, J.E.: J. Appl. Phys. 79 (1996) 5368.

97T1 Tietze-Jaensch, H., Kockelmann, W., Ibberson, R.M.: ISIS Experimental Report RB8122 (1997).

97T2 Tietze-Jaensch, H., Kockelmann, W.: ISIS Experimental Report RB9091 (1997).

97T3 Tietze-Jaensch, H., van de Kamp, R., Schmidt, W., Geick, R., Treutmann, W., Vorderwisch, P.: Physica B 234-237 (1997) 564.

98I Ishizuka, M., Terai, M., Endo, S., Hidaka, M., Yamada, I., Shimomura, O.: J. Magn. Magn. Mater. 177-181 (1998) 725.

98K1 van de Kamp, R., Steiner, M., Tietze-Jaensch, H.: Physica B 241-243 (1998) 570.

98T Tietze-Jaensch, H., van de Kamp, R., Schmidt, W.: Physica B 241-243 (1998) 566.

9.12.4 Critical Phenomena

(For figures of this section and Table 6 see p. 427)

9.12.4.1 Static Critical Behaviour

9.12.4.1.1 General

In the critical region, close to the critical point (phase transition temperature), the theories discussed so far are inadequate to describe accurately the behaviour, namely the socalled critical behaviour of a system undergoing a phase transition. In context with the structural phase transitions, the Landau theory for second order phase transitions [75L4, 80C2] and model calculations based on it [78B2, 79K5, 81K3] have been discussed in Sects. 2.2.2 and 2.2.4. In context with magnetic properties and magnetic phase transitions, the molecular field theory [55N, 66K] has been mentioned in Sects. 3.1.1–3.1.3 etc. and the spin-wave theories [66K, 90A3] have been discussed in more detail there. All these theories do not take into account the fluctuations, as mentioned in Sect. 3.1.2–3.1.4 several times, and therefore fail to describe accurately the critical behaviour. The Sect. 4.1 is devoted to the static critical phenomena [67F1, 67H2, 67K1], and in Sect. 4.2, the dynamic ones will be discussed. Some of the thermodynamic functions exhibit singularities (divergences) near T_C, e.g. the divergence of the susceptibility χ, due to an enormous increase of the fluctuations. For a magnet, the thermodynamic functions of interest in this context are:

1) the magnetic contribution to the specific heat C_{magn}
2) the magnetization M (ferromagnet) or sublattice magnetization M_{subl} (antiferromagnet)
3) the magnetic susceptibility χ, the staggered susceptibility of an antiferromagnet
4) the correlation length ξ which measures the degree of magnetic order

The magnetization M of a two-dimensional Ising ferromagnet may be a good example for demonstrating the critical behaviour near T_C. For this system, an exact solution exists for M (cf. Eq. 3.66 in Sect. 3.1.9, [44O, 52Y]) and we can derive a series expansion with the reduced temperature $t = (T - T_C)/T_C$ as parameter:

$$M(T)/M(0) = [1 - \sinh^{-4}(J_{\|}/k_B T)]^{1/8} \rightarrow B_0\,|\,t\,|^{1/8} + B_1\,|\,t\,|^{9/8} + B_2\,|\,t\,|^{17/8} + \ldots \tag{4.1}$$

with $J_{\|}/k_B T_C = \ln(\sqrt{2}+1)$ (cf. Eq. 3.67). The first term is the leading one for $t \rightarrow 0$, i.e. $T \rightarrow T_C$. The exponent 1/8 is the critical exponent (β) and $B_0 = 1.222410$ [67F1] the critical amplitude. The further expansion coefficients B_1 and B_2 have been derived by Guttmann [75G3] who used $T_C/T - 1$ instead of t as the expansion parameter.

Such critical exponents characterizing the limiting behaviour for $t \rightarrow 0$ and critical amplitudes have been defined for all thermodynamic functions listed above, for reviews see [67F1, 67F2, 71S1, 74J1, 78L5, 90J1]:

1) magnetic contribution to the specific heat $C_{\mathrm{magn}} \sim (A^{\pm}/\alpha^{\pm})\,|\,t\,|^{\alpha^{\pm}}$
2) order parameter M (ferromagnet), M_{subl} (antiferromagnet) $\sim B_0\,|\,t\,|^{\beta}$
3) magnetic susceptibility $\chi \sim C_0^{\pm}\,|\,t\,|^{-\gamma^{\pm}}$
4) critical isotherm ($T = T_C$): $H \sim |\,M\,|^{\delta} \cdot \mathrm{sign}(M)$
5) inverse correlation length $\kappa = \xi^{-1} \sim \kappa_0^{\pm}\,|\,t\,|^{\nu^{\pm}}$
6) wavevector dependence of χ at T_C: $\chi(q, T_C) \sim q^{-2+\eta}$
   corresponding to pair correlation function $G(\boldsymbol{r}) \sim |\,t\,|^{-(d-2+\eta)}$

where $\alpha^{\pm}$, β, $\gamma^{\pm}$, δ, $\nu^{\pm}$ and η are the critical exponents. $A^{\pm}$, B_0, $C_0^{\pm}$ and $\kappa_0^{\pm}$ are the critical amplitudes, and d is the lattice dimension. The superscripts "+" and "–" refer to the ranges $t > 0$ and $t < 0$, respectively. The definition of the correlation function will be discussed in more detail below. According to the generally accepted and well known concepts about critical phenomena, the critical exponents and amplitudes do not depend on the special properties of a system under consideration and are the same for all systems belonging to the same universality class [76A8, 76K5]. These classes depend on the spatial or lattice dimensionalty d and on the order parameter or spin dimensionalty n of the system. The latter can best be illustrated for a magnetic system with nearest neighbours exchange interaction by the number of effective spin components in the Hamiltonian [90J1]

$$\mathcal{H} = -2 \sum_{\langle \mathrm{i,\,j} \rangle} [J_{\mathrm{x}} \mathrm{S}_{\mathrm{i,\,x}} \mathrm{S}_{\mathrm{j,\,x}} + J_{\mathrm{y}} \mathrm{S}_{\mathrm{i,\,y}} \mathrm{S}_{\mathrm{i,\,y}} + J_{\mathrm{z}} \mathrm{S}_{\mathrm{i,\,z}} \mathrm{S}_{\mathrm{j,\,z}}] \tag{4.2}$$

The summation $\langle \mathrm{i, j} \rangle$ is extended over the whole lattice where each pair of nearest neighbours is counted only once. We recall further from Sects. 2.1.2 and 3.1.2 that the magnetic unit cell of the perovskite-type layer structures is described by means of the (x, y, z) coordinate system. The spin dimension n means the number of components of the order parameter, namely

n = 1: Ising model ($J_{\mathrm{z}} \neq 0, J_{\mathrm{x}} = J_{\mathrm{y}} = 0$)
n = 2: XY-model ($J_{\mathrm{x}} = J_{\mathrm{y}} \neq 0, J_{\mathrm{z}} = 0$)
n = 3: isotropic Heisenberg model ($J_{\mathrm{x}} = J_{\mathrm{y}} = J_{\mathrm{z}} \neq 0$).

An overview over all three models has been given for classical spins by Stanley [74S5]. It should be noted that these models apply not only to magnetic systems but are used for a wide variety of systems undergoing phase transitions.

The lattice dimension d has a considerable influence on the phase transitions. For one-dimensional lattices (d = 1, linear chains), no phase transitions are possible for $T_{\mathrm{C}} > 0$. For two-dimensional lattices (d = 2), a phase transition with $T_{\mathrm{C}} > 0$ exists only for the Ising model with long-range order (LRO) for $T \neq 0$ while in two dimensions the XY-model and the Heisenberg model, both with continuous symmetry, undergo no phase transition to a LRO at nonzero temperatures [66M1, 67H1, 68M3] due to divergent fluctuations of the Goldstein mode with $\omega \to 0$. However, this Hohenberg-Mermin-Wagner theorem does not exclude LRO at $T = 0$. And recently, such order has been proved for the ground state of antiferromagnets in two dimensions with nearest neighbours coupling, in particular for the 2D Heisenberg model with spin $S \geq 1$ [86N1, 88A3, 88K3, 92H1]. Only for the $S = \frac{1}{2}$ Heisenberg model, a rigorous proof for such a LRO has not yet been achieved [88K4, 92H1]. But there are strong arguments for a LRO at $T = 0$ since the experimental data on $\mathrm{La_2CuO_4}$ (2D $S = \frac{1}{2}$ antiferromagnet) cannot be easily analysed in terms of a model without assuming such a LRO [89C3]. For the 2D XY-model, on the other hand, LRO at $T = 0$ has been conjectured and also rigorously proved for all spins, including $S = \frac{1}{2}$ [88K3, 89N2, 89O, 91W2]. Much attention has been focussed on this problem for 2D quantum systems after 1987 because of its relevance to the magnetic properties of $\mathrm{La_2CuO_4}$ and the related high-temperature superconductors. And there was also a discussion whether in 2D quantum systems integer and half-integer spins behave differently [86A3, 88A7, 88D4, 89C3] as it is known from 1D systems where the Haldane conjecture [83H6, 83H7, 85H2] has predicted an energy gap in the excitation spectrum for integer spin and a gapless excitation spectrum for half-integer spins which has been confirmed experimentally for linear chain systems, see for example the review by Halperin [92H1]. Most arguments lead to the conclusion that such a difference is absent in 2D systems [88D5, 88W3] as long as the antiferromagnetic spin configuration (Néel state) is well defined at all points in the (2 + 1) space-time dimensions [88H2].

After these remarks about the magnetic order, let us return to the brief and by far not comprehensive introduction to critical phenomena and critical behaviour the aim of which is to introduce the notation used in this contribution for the presentation of the experimental data in Table 6. For a more basic description and for more details, the reader is referred to the above mentioned reviews [67F1, 71S1, 90J1]. For comparison with the experimental results in Table 6 and for the discussion of these data, the theoretical values of the critical exponents are reproduced in Table 7. According to the static sealing laws [71S1], the critical exponents are equal for $T > T_C$ and $T < T_C$

$$\alpha^+ = \alpha^- = \alpha \quad \gamma^+ = \gamma^- = \gamma \quad \nu^+ = \nu^- = \nu \tag{4.3}$$

so that the superscripts "+" and "–" can be omitted. In the following, the superscripts will be used only for experimental data where it is necessary to specify whether the data have been obtained for $T > T_C$ or for $T < T_C$. Otherwise, the critical exponents will simply be denoted as α, γ, and ν. The critical amplitudes, on the other hand, are in general different for $T > T_C$ and $T < T_C$ so that there the superscripts have usually to be used. The data in the first row of Table 7 are the exact results for the 2D Ising model [67F1] and those in the next three rows for n = 1 – 3 in 3D systems are compiled in [95L] from results obtained by field-theoretical methods [77G4] with the error limits in brackets, see also [80G5, 92K2].

Table 7. Theoretical values of critical exponents

	α	β	γ	ν	η
d = 2, n = 1 (Ising)	0 (log)	1/8	7/4	1	1/4
d = 3, n = 1 (Ising)	0.1100(24)	0.3249(10)	1.2402(09)	0.6300(08)	0.0315(25)
d = 3, n = 2 (XY)	–0.0079(30)	0.3460(10)	1.3160(12)	0.6693(10)	0.0335(25)
d = 3, n = 3 (Heis.)	–0.1162(33)	0.3648(12)	1.3866(12)	0.7054(11)	0.0340(25)

For the 3D Ising model more recent values are available from Monte Carlo simulations [98K2]

$\beta = 0.3269(6)$ [96T], $\gamma = 1.239(3)$ [91F3], $\nu = 0.6289(8)$ [91F3], $\eta = 0.026(3)$ [92B3]

The values of the critical exponent δ have not been listed in Table 7. It can be calculated for all four cases by means of the relation (cf. Eq. 4.13 below)

$$\delta = 1 + \gamma / \beta \tag{4.3a}$$

which yields for the 2D Ising model, for example, $\delta = 15$.

9.12.4.1.2 2D Ising Model

When comparing the experimental values of the critical exponents (cf. Table 6) with the theoretical ones in Table 7, it turns out that most of them agree quite well with those of the 2D Ising model, even in the case of weakly anisotropic easy-axis compounds like K_2MnF_4 and K_2NiF_4. The reason for this critical behaviour is that the continuous symmetry of the Heisenberg model is broken by the Ising-like anisotropy which favors the *c*-axis as the easy axis and which is responsible for the magnetic phase transition in these compounds. And the dipolar interactions dominating the anisotropy in Mn-compounds favor also the *c*-axis and thus a single spin-component order parameter. The influence of the dipolar interactions on the critical behaviour of ferro- and antiferromagnets has been discussed in detail by Aharony [73A2, 73A3, 73A4, 73A5] and by Schwabl and coworkers [88F1, 88S3, 92F1, 92F2, 93P1, 94P1, 95P1]. We note further that the situation is different for easy-plane ferro- and antiferromagnets. If there is not a strong in-plane anisotropy which determines an easy-axis in the basal plane, i.e. the in-plane anisotropy is small or negligible, the system will most probably behave critically according to the 2D XY-model which will be discussed in Sect 4.1.8 below.

In this section, we first will discuss further results for the 2D Ising model [67F1, 67F2, 72T2, 74D1, 78L5, 90H, 90N] and then the experimental data of easy-axis compounds. In addition to the critical exponents, all critical amplitudes and further expansion parameters are known from the exact solution of the 2D Ising model. Some of these results will briefly be described now. The value of B_0 has already been quoted in context with Eq. 4.1. Since all compounds with an easy axis among the perovskite-type layer structures are antiferromagnets (cf. Sect. 2.1.2) let us be specific and consider an antiferromagnet with 4 nearest neighbours on the square lattice. The 2D Ising model Hamiltonian is then given by Eq. 4.2 with $J_z \neq 0$ and $J_x = J_y = 0$ or, more conveniently, in the notation of Eq. 3.62 (Sect. 3.1.9) with $J_{\|} \neq 0$ and $J_{\perp} = 0$. The energy per mole due to the magnetic ordering is [66W]

$$U_{\mathrm{magn}} = -L\,|J_{\|}|\left\{\tanh(u) - \frac{\sinh^2(u)-1}{\sinh(2u)}\left[\frac{2}{\pi}K(\upsilon)-1\right]\right\} \tag{4.4}$$

with $u = |J_{\|}|/k_B T$ and $\upsilon = 2\sinh(u)/\cosh^2(u)$. $K(\upsilon)$ is the complete elliptic integral of the first kind and L Avogadro's number. For $T = 0$, $T = T_N$ and $T \to \infty$, Eq. 4.4 yields $U_0 = -L\,|J_{\|}|$, $U_{\mathrm{magn}} = U_C = -L\,|J_{\|}|/\sqrt{2}$ and $U_{\mathrm{magn}} \to 0$, respectively. The value U_0 for $T = 0$ can also be written $-LzS^2\,|J_{\|}|$ ($z = 4$, $S = \frac{1}{2}$) and agrees in this form with the spin-wave value for 1 mole ($N = L$) in Eq. 3.5 (Sect. 3.1.2). The asymptotic behaviour of the magnetic energy near T_N can be written as [67F1]

$$U_{\mathrm{magn}} = U_C + R\,A\,(T_N - T)\cdot \ln|T/T_N - 1| \tag{4.4a}$$

where $R = L\,k_B$ is the universal gas constant. The critical amplitude A ($A^+ = A^-$) of $(U_{\mathrm{magn}} - U_C)/R$ in Eq. 4.4a is in the 2D Ising model

$$A = (2/\pi)\,[\ln(\sqrt{2}+1)\,]^2 = 0.494\,538\,589\,2\,\ldots \tag{4.5}$$

The temperature derivative of U_{magn} is the magnetic contribution C_{magn} to the specific heat which becomes for $T \approx T_N$ [44O, 67F1, 90J1]

$$C_{\mathrm{magn}} = \partial U_{\mathrm{magn}}/\partial T = -R\,A\cdot \ln|T/T_N - 1| = R\,A\,|\ln|t|\,| \tag{4.6}$$

That means that the specific heat of the 2D Ising model has a logarithmic singularity at T_N (or T_C) which is indicated as $\alpha = 0$ (log) in Table 7. And this value is indeed obtained for $C_{\mathrm{magn}} \sim |\ln|t|\,|$ according to the definition of the critical exponents [71S1, 74J1]

$$\alpha = \lim_{t\to 0} \ln|C_{\mathrm{magn}}|/\ln|t| = 0 \tag{4.7}$$

We note further that the logarithmic singularity of C_{magn} is symmetric for the 2D-Ising model, i.e. $A^+ = A^- = A$ or $A^+/A^- = 1$. In three dimensions, the universal ratio A^+/A^- is in general different from 1 [74B5], for the XY-model it is ≈ 1, for the Ising model < 1 and for the Heisenberg model > 1.

The next function to be discussed is the susceptibility χ. In case of an antiferromagnet, χ is the staggered susceptibility which is obtained from quasi-elastic neutron scattering as explained below. In the critical region ($T \approx T_N$), χ can be written as [90N]

$$\chi(t)/\chi_0 = C_0^{\pm}\,|t|^{-7/4} + C_1^{\pm}\,|t|^{-3/4} + C_2^{\pm}\,|t|^{+1/4} + \ldots \tag{4.8}$$

where $\chi_0 = C/T$ is the susceptibility of a noninteracting system, i.e. the Curie law with the Curie constant C (cf. Eq. 3.25, Sect. 3.1.3). The critical amplitudes C_0^+ and C_0^- are for the 2D Ising model [73B3, 74G1, 76W3]

$$C_0^+ = 0.962\,581\,732\,2\,... \qquad C_0^- = 0.025\,536\,971\,9\,... \\ \text{with } C_0^+ / C_0^- = 37.693\,652\,0\,... \tag{4.9}$$

The values of the further expansion coefficients $C_1^+, C_1^-, C_2^+, C_2^-$ and higher order corrections are found in the literature [73B3, 74G1, 88G1, 88G2]. Closely related to the susceptibility χ is the inverse correlation length $\kappa = \xi^{-1}$. On the basis of Onsager's results [44O], the following expression has been derived [67F2] for κa

$$\kappa a_{\mathrm{nn}} = \ln \coth(|J_{\parallel}| / 2k_{\mathrm{B}}T) - |J_{\parallel}| / k_{\mathrm{B}}T \qquad \text{for } T \geq T_{\mathrm{N}} \tag{4.10}$$

and an analogous expression with an additional factor (–2) for $T < T_{\mathrm{N}}$. In Eq. 4.10, a_{nn} is the distance between nearest neighbour magnetic ions. In the layer structures, a_{nn} is equal to the lattice constant a of the chemical unit cell (cf. Fig. 2.1 in Sect. 2.1.1) and $a_{\mathrm{nn}} = a/\sqrt{2}$ when a is the lattice constant of the magnetic unit cell. The expansion of κa_{nn} near T_{N} yields the critical amplitudes

$$\kappa_0^+ a_{\mathrm{nn}} = 2 \ln(\sqrt{2} + 1) = 1.762\,747\,174\,... \qquad \text{and} \qquad \kappa_0^- = 2\,\kappa_0^+ \tag{4.11}$$

In experiments, the inverse correlation length κ is usually measured in reciprocal lattice units a^*. That means the measured quantity is κ / a^* and the critical amplitude is obtained as $\kappa_0^+ / a^* = \kappa_0^+ a_{\mathrm{nn}} / 2\pi$ = 0.280 549 926... if a^* refers to the chemical unit cell and $\kappa_0^+ / a^* = \kappa_0^+ a_{\mathrm{nn}} / \sqrt{2}\pi$ = 0.396 757 511... [84C1] if a^* is the reciprocal lattice vector of the magnetic unit cell.

Eqs. 4.4–4.11 summarize the critical behaviour of the various thermodynamic functions which can also be considered as response functions of a magnetic system, in this section with critical behaviour close to the predictions of the 2D Ising model. However, many relations are more general and apply also to the XY-model and the Heisenberg model, apart from the numerical values. Now, the critical exponents in Table 7 are not all independent but there are relations between them according to the static scaling laws. For details, the reader is referred to introductions like [71S1] and [80G4]. Two examples of scaling relations are the following for the susceptibility χ [80G4, 81S1, 88D1] and for the magnetization M [83K4]

$$\chi(t, H_{\mathrm{int}}) = |t|^{-\gamma} \cdot \Psi_{\pm}(H_{\mathrm{int}} / |t|^{\Delta}) \tag{4.12a}$$

or

$$\chi(t, H_{\mathrm{int}}) = H_{\mathrm{int}}^{-\gamma/\Delta} \cdot \hat{\Psi}_{\pm}(H_{\mathrm{int}} / |t|^{\Delta}) \tag{4.12b}$$

$$M(t, H_{\mathrm{int}}) = H_{\mathrm{int}}^{1/\delta} \cdot \tilde{\Psi}_{\pm}(|t| / H_{\mathrm{int}}^{1/\Delta}) \tag{4.12c}$$

where t is the reduced temperature, H_{int} the internal field which is not equal to the applied field H_0 due to demagnetization effects, especially in ferromagnets. The exponent Δ is defined below in Eq. 4.13. Further, $\Psi_{\pm}(u)$, $\hat{\Psi}_{\pm}(u)$ and $\tilde{\Psi}_{\pm}(\upsilon)$ are homogeneous functions of the variables u and υ, with the subscript "+" for $T > T_{\mathrm{N}}$ and "–" for $T < T_{\mathrm{N}}$. Of the above mentioned relations among the critical exponents some are useful, in addition to Eqs. 4.3 and 4.3a (theoretical values: see Table 7):

$$d\nu = 2 - \alpha \qquad (2 - \eta)\,\nu = \gamma \\ \alpha + 2\beta + \gamma = 2, \qquad \Delta = \beta + \gamma = \delta\beta \tag{4.13}$$

In a similar way, universal relations between the critical amplitudes have been derived by means of the scaling hypothesis [76A4, 77A6], for example A^+/A^- and C_0^+ / C_0^-. One of these universal relations reads for the 2D Ising model [72S1]

$$X = \left(\frac{t}{\kappa\, a_{\mathrm{nn}}}\right)^2 \cdot \frac{C_{\mathrm{magn}}}{R\,|\ln|t||} = \frac{A^+}{(\kappa_0^+ a_{\mathrm{nn}})^2} = \frac{1}{2\pi} \tag{4.14}$$

It can be used to reduce the number of system-dependent scale factors from three to two (two-scale-factor universality) [72S1, 76H3]. The value of X for the 2D Ising model is obtained by using Eqs. 4.5, 4.6, 4.11 and $\nu = 1$ from Table 7. For three-dimensional systems, the universal ratios A^+/A^- and κ_0^+ / κ_0^- and also an expression analogous to Eq. 4.14 have been calculated by various methods. The values are compiled in [76B6]. For the 2D Ising model, Bruce [81B4] has derived another combination of critical amplitudes

$$R_{\mathrm{S}} = \frac{C_0^+ (\kappa_0^+ a_{\mathrm{nn}})^{\mathrm{d}}}{B_0^2 (2\pi)^{\mathrm{d}}} \tag{4.15}$$

which can be used to test this relation and therefore the hypothesis of two-scale-factor universality by means of a single neutron scattering experiment. It will be shown below that R_{S} is proportional to ratio of the experimental results obtained above and below T_{N} for the same reduced temperature t. In Eq. 4.15, d is as before the lattice dimension. The factor $(2\pi)^{\mathrm{d}}$ has been included for the convenience to express κ in units of a^*. For the 2D Ising model, $R_{\mathrm{S}} = 0.050\,701\,893$ is obtained with the values of B_0, C_0^+ and $\kappa_0^+ a_{\mathrm{nn}}$ from Eqs. 4.1, 4.9 and 4.11.

9.12.4.1.3 Experimental Determination of α

In Table 6, the experimental data are presented together with the method which was used for their measurement. For the understanding of the mostly brief statements in the table, it is necessary to outline in this context some details of the analysis of the experimental raw data and how the critical exponents are derived from them. We note from Tables 6 and 7 that most values of the experimentally determined critical exponents are close to those of the 2D Ising model. Let us now consider, as the first example, the magnetic contribution to the specific heat C_{magn}. The experimental data of C_{p} show usually lattice background, in addition to C_{magn} at temperatures near T_{N}. Fig. 4.1 shows such data for K_2CoF_4. The full line in Fig. 4.1 results from a fit to the molar specific heat C_{p} by means of [75I1, 80H4]

$$C_{\mathrm{p}} = R\,[A^{\pm}/\alpha^{\pm}) \cdot (|t|^{-\alpha^{\pm}} - 1) + D^{\pm} + E\,t] \tag{4.16}$$

with "+" for $T > T_{\mathrm{N}}$ and "–" for $T < T_{\mathrm{N}}$. The prefactor R (universal gas constant) ensures that the expression in the square bracketts is dimensionless. The first term is the singular part chosen here in a form that allows to consider $\alpha \to 0$ but does not assume $\alpha = 0$, the value expected for the 2D Ising model (cf. Table 7). The next two terms represent the background, i.e. the lattice specific heat, a constant term and a term linear in reduced temperature t with the same factor E for $T > T_{\mathrm{N}}$ and $T < T_{\mathrm{N}}$. The fit in Fig. 4.1 has been performed with the constraints $\alpha^+ = \alpha^-$. Another possibility used alternatively for such a fit is [75I1, 80H4]

$$C_{\mathrm{p}} = R\,[A^{\pm}\,|\ln|t|| + D^{\pm} + E\,t] \tag{4.17}$$

with the singular part in a form which assumes a symmetric logarithmic singularity and $\alpha = 0$. In Sect. 3.1.9, it was emphasized that K_2CoF_4 and Rb_2CoF_4 are the best known realizations of the 2D Ising model and the question arises whether Eqs. 4.16 and 4.17 can also be used to fit the specific heat data of weakly anisotropic systems like K_2MnF_4 and K_2NiF_4. Before answering this question, we recall from Sect. 3.3.2 that C_{magn} cannot only be obtained by specific heat measurements but also from linear birefringence studies where the birefringence is induced by magnetic phenomena (LMB = linear magnetic birefringence). As already pointed out there, Jahn [73J2] demonstrated that Δn, the result of the birefringence measurement, is proportional to the magnetic energy U_{magn} and $\text{d}(\Delta n)/\text{d}T$ proportional to the magnetic contribution to the specific heat C_{magn}. The theoretical foundation for these experiments [73J1, 74K2, 75S1, 78I1, 84FI] states that Δn is proportional to the nearest neighbours spin pair correlation function and thus to the magnetic energy U_{magn}. The experimental results of $\text{d}(\Delta n)/\text{d}T$ for K_2MnF_4 [79J, 84F1], K_2FeF_4 [81K4], K_2NiF_4 and Rb_2NiF_4 [78I1] show that the Ising-like sharp peak at T_N corresponding to the singular part of C_{magn} is embedded in a broad maximum between T_N and room temperature. The latter will be discussed below in context with ferromagnets, especially that such a broad maximum looks like C_{magn} for the 2D Heisenberg model [74J1, 90N] where no sharp peak is expected due to the absence of a phase transition for $T > 0$. For the Mn-compounds $(C_nH_{2n+1}NH_3)_2MnCl_4$ with n = 1 and n = 3, the magnetic specific heat has been determined from ordinary specific measurements [81W3, 82W2] as the difference of C_p of the Mn-compound and of C_p of the diamagnetic Cd-compound. In this way, only the broad maximum of C_{magn} was observed and the singular part could not be resolved. But these results have been used to obtain also the entropy change ΔS_{magn} connected with the magnetic phase transition by means of Eq. 2.18b (see Sect. 2.2.1). For the compound $(C_3H_7NH_3)_2MnCl_4$, the result is $\Delta S_{\text{magn}} = 12\ \text{JK}^{-1}\text{mol}^{-1}$ [81W3] close to the theoretically expected value $R\ln 6 = 14.9\ \text{JK}^{-1}\text{mol}^{-1}$. The broad maximum in C_{magn} is an evidence for the short-range magnetic order at these temperatures which is also reflected in the susceptibility measurements (cf. Sect. 3.1.3 and Table 5) and in the neutron scattering discussed below for $T > T_N$. This short-range order is also reflected in the temperature dependence of intensity of double-excitonic optical transitions in K_2NiF_4 [77P3].

From the data of his LMB investigation of K_2MnF_4, Jahn [79J, 84F1] has extracted the singular part Δn_s of Δn in the vicinity of T_N (see Fig. 4.2). The variation of $[\Delta n_s(T) - \Delta n_s(T_N)]$ and $\text{d}(\Delta n_s)/\text{d}T$ with T is exactly that expected for U_{magn} and C_{magn} (Eqs. 4.4a and 4.6). Moreover, the experimental results for $[\Delta n_s(T) - \Delta n_s(T_N)]$ have successfully been fitted to $(U_C - U_{\text{magn}})/R = A \cdot T_N \cdot t \cdot \ln|t|$. The temperature derivative $\text{d}(\Delta n_s)/\text{d}T$, obtained from $\Delta n_s(T)$ by a mathematical procedure, is then proportional to $A\,|\ln|t||$. Similar results have been obtained also with LMB for K_2NiF_4 and Rb_2NiF_4 [77I2]. Another result confirming the exact relations of the 2D Ising model is that $\text{d}(\Delta n)/\text{d}T$ from an LMB study of Rb_2CoF_4 [83N2] has successfully been fitted to

$$\text{d}(\Delta n)/\text{d}T = F\,[(A^{\pm}/\alpha)\cdot(|t|^{-\alpha} - 1) + D^{\pm} + E\,t] \tag{4.18}$$

where $\alpha^{+} = \alpha^{-}$ has been assumed and where F is a factor of the order $10^{-6}\ \text{K}^{-1}$ relating the LMB data to C_{magn} in units of R. The data for K_2MnF_4 in Fig. 4.2 and also specific heat and LMB studies of many other weakly anisotropic layered materials show the symmetric logarithmic singularity of the 2D Ising model. But measurements of the specific heat of K_2MnF_4, K_2NiF_4 and Rb_2NiF_4 revealed that the critical amplitudes A^{+} and A^{-} are much smaller (cf. Table 6) than theoretically predicted for the 2D Ising model (cf. Eq. 4.5). As illustrated for the spin-wave excitations for Co-compounds in Sect. 3.1.9, we cannot completely ignore the transverse spin components and have to consider also here the anisotropic Heisenberg or XXZ-model (Hamiltonian see weakly anisotropic compounds). The anisotropy can be expressed by $h_A = H_A/H_E$ (Eq. 3.6, Sect. 3.1.2) or $h_A = (1 - J_{\perp}/J_{\|})$ (Eq. 3.65, Sect 3.1.9) where $h_A = 1$ means the Ising model and $h_A = 0$ the Heisenberg model. Hatta and Ikeda [80H4] have treated this problem with respect to C_{magn} and obtained the following expression for the specific heat critical amplitude

$$A_{\text{theory}} = A^{+} = A^{-} = (2/\pi)\ [\ln(\sqrt{2} + 1)]^2 \cdot \frac{\ln(2S+1)}{\ln 2} \cdot \sqrt{h_A} \tag{4.19}$$

For $h_A = 1$ and $S = \frac{1}{2}$, Eq. 4.19 reproduces the result for the 2D Ising model in Eq. 4.5. For $h_A = 0$, i.e. for the isotropic Heisenberg model, Eq. 4.19 can no longer be applied since there is is no phase transition at finite temperature in two dimensions since it is a consequence of the fact that the Ising-like anisotropy is responsible for the phase transition in materials like K_2MnF_4. Together with the corresponding experimental data, the values for A_{theory} are listed in Table 6 for a variety of materials which are in fair agreement with the experimental data for A^+ and A^-.

9.12.4.1.4 Experimental Determination of β

The sublattice magnetization $M_{\text{subl}}(T)$ of an antiferromagnet is usually obtained by studying the antiferromagnetic superreflections (cf. Sect. 2.1.2) as a function of temperature using neutron diffraction. It was already mentioned in Sects. 3.1.3, 3.1.9, and 3.3.5 that the intensity of a superreflection at $\boldsymbol{Q}_0 \mathrel{\hat{=}} (\mathrm{h, k, l})$ is proportional to the square of M_{subl} and thus an indicator for 3D long-range order [71B1, 71M2, 73B1, 77B2]

$$I(\boldsymbol{Q}_0, T)/I(\boldsymbol{Q}_0, 0) \sim [M_{\text{subl}}(T)/M_{\text{subl}}(0)]^2 = B_0^2\,|t|^{2\beta} \tag{4.20}$$

Eq. 4.20 is the basis for determining the critical exponent β. It is correct as long as extinction effects are absent, i.e. if the Bragg scattering is sufficiently weak and the neutron beam is not attenuated perceptibly on its path through the sample. As an example, the upper part of Fig. 4.3 shows for K_2NiF_4 the peak intensity of the (1, 0, 0) superreflection over the temperature the range $0 \le T \le T_N$ ($T_N = 97.23$ K). The lower part of Fig. 4.3 presents the peak intensity and the halfwidth of a scan across a magnetic Bragg rod at (1, 0, 0.25) for the temperature range $0 \le T \le 200$ K. These Bragg rods or ridges in quasi-2D magnets were already mentioned in Sect. 2.1.2 (cf. Fig. 2.5). In Sect. 3.3.5, the rod intensity was used as a measure for 2D ordering. Its sharp maximum (cf. Figs. 3.60 and 4.3) allows a determination of the Néel temperature T_N. In this and the next section, these considerations will be extended to an analysis of the neutron scattering results, i.e. scans through a Bragg peak and scans across a Bragg rod, with respect to the magnetic phase transition and to the critical properties. For $T > T_N$, there are only 2D correlations and the ridges are flat without structure in q_z-direction as demonstrated by Birgeneau et al. [70B1]. For $T < T_N$, the intensity is transferred from the rods to sharp Bragg reflections with the onset of 3D LRO. But also the width of such scans is of interest because it is a measure for the correlation length ξ. For the magnetic Bragg reflections, the width is usually given by the spectrometer resolution indicating a 3D long-range order ($\xi \to \infty$). The 2D order deduced from the width of the rod scans is usually a finite one, i.e. a finite ξ. In the lower part of Fig. 4.3, the ridge intensity increases strongly on lowering the temperature from 200 K towards T_N while the halfwidth decreases (cf. lower part of Fig. 4.3). This indicates an increase of the range of the 2D order and an increase of ξ. We will see below that the halfwidth is proportional to the inverse κ of the correlation length ξ.

Qur analysis starts with the intensity of the Bragg reflections (cf. Eq. 4.20). A double-logarithmic plot of $[I(\boldsymbol{Q}_0, T)/I(\boldsymbol{Q}_0, 0)]^{1/2} = M_{\text{subl}}(T)/M_{\text{subl}}(0)$, i.e. of the experimental data, is used to determine the critical exponent β and eventually the critical amplitude B_0. Such a plot, namely log $[M_{\text{subl}}(T)/M_{\text{subl}}(0)]$ versus log $(-t)$, is shown in Fig. 4.4 with the experimental data from three antiferromagnetic superreflections for $K_3Mn_2F_7$. In addition, Fig. 4.4 presents also experimental data (solid lines without experimental points) for K_2MnF_4 and for the 3D antiferromagnet MnF_2 as well as the exact solution for the 2D $S = \frac{1}{2}$ Ising model (cf. Eq. 4.1) where the latter is identical with the experimental data for K_2CoF_4 and Rb_2CoF_4 (cf. Fig. 3.26 in Sect. 3.1.9). The slope to these data gives the 2D Ising value $\beta = 0.125$ (cf. Eq. 4.1 and Table 7). The corresponding slopes for K_2MnF_4 and for $K_3Mn_2F_7$ yield values $\beta = 0.150$ and $\beta = 0.154$, resp., which are close to the 2D Ising value. The curve for MnF_2 is much steeper and yields $\beta = 0.335$ [66H1] close to the 3D Ising value (cf. Table 7). Therefore, the critical behaviour of K_2MnF_4 and of $K_3Mn_2F_7$ can be called Ising-like. That the experimental data for $K_3Mn_2F_7$ follow the curve for MnF_2 in the range $10^{-1} \le (-t) \le 1$ is not relevant in this context because it is outside the critical range.

9.12.4.1.5 Experimental Determination of γ, ν and η

For ferromagnets, the other critical exponents γ^+ (or γ^-), ν^+ (or ν^-) and η can be determined from magnetic measurements, e.g. study of the magnetic susceptibility χ. For antiferromagnets, they are usually determined by neutron scattering from the magnetic rods. Let us consider this case in more detail and discuss the neutron scattering cross section for the diffuse scattering contribution in the intensity measured by a scan across the rod. This scattering cross section can be written as [68M2, 71B1, 71M2, 76A5, 77B2, 78L5]

$$\frac{\mathrm{d}^2\sigma}{\mathrm{d}\Omega\ \mathrm{d}\omega} = A(\boldsymbol{k}_\mathrm{i}, \boldsymbol{k}_\mathrm{f}) \sum_{\alpha\beta} (\delta_{\alpha\beta} - K_\alpha K_\beta / K^2) \cdot S_\mathrm{D}^{\alpha\beta}(\boldsymbol{K}, \omega) \tag{4.21}$$

where $\boldsymbol{k}_\mathrm{i}$, $\boldsymbol{k}_\mathrm{f}$, $\boldsymbol{K}$ and ω have the meaning as defined in Eq. 2.24 (Sect. 2.2.3), α and β are coordinate directions in the (x, y, z) system. The prefactor $A(\boldsymbol{k}_\mathrm{i}, \boldsymbol{k}_\mathrm{f})$ is explained in [68M2] and [71M2]. The scattering function $S_\mathrm{D}^{\alpha\beta}$ $(\boldsymbol{K}, \omega)$ is the most interesting part in Eq. 4.21. It is the Fourier transform in space and time of the spin pair correlation function (see for example [71S1])

$$G^{\alpha\beta}(\boldsymbol{r}, t) \sim \langle\, S_{\mathrm{i},\alpha}(T), S_{\mathrm{j},\beta}(0)\,\rangle - \langle S_{\mathrm{i},\alpha}(t)\rangle\,\langle S_{\mathrm{j},\beta}(0)\rangle \tag{4.22}$$

with $\boldsymbol{r} = \boldsymbol{r}_\mathrm{i} - \boldsymbol{r}_\mathrm{j}$ and where t is the time (exceptionally not the reduced temperature!) and ⟨ ⟩ means the thermal average. The definition shows that $G^{\alpha\beta}(\boldsymbol{r}, t)$ is directly related to the above mentioned fluctuations. The scattering function is usually expressed as [71B1]:

$$S_\mathrm{D}^{\alpha\beta}(\boldsymbol{K}, \omega) = \frac{\mu_0 k_\mathrm{B} T}{(g\mu_\mathrm{B})^2}\, \chi^{\alpha\beta}(\boldsymbol{K})\, \frac{\hbar\omega / k_\mathrm{B} T}{1 - \exp(-\hbar\omega / k_\mathrm{B} T)}\, F^{\alpha\beta}(\boldsymbol{K}, \omega) \tag{4.23}$$

where $\chi^{\alpha\beta}(\boldsymbol{K})$ is the wavevector-dependent susceptibility and $F^{\alpha\beta}(\boldsymbol{K}, \omega)$ the frequency distribution or spectral shape function with the property

$$\int_{-\infty}^{+\infty} F^{\alpha\beta}(\boldsymbol{K}, \omega)\, \mathrm{d}\omega = 1$$

The critical fluctuations near T_N are dominated by low-frequency fluctuations so that the relation $\hbar\omega << k_\mathrm{B} T$ holds. Then, the factor $(\hbar\omega / k_\mathrm{B} T) / [1 - \exp(-\hbar\omega / k_\mathrm{B} T)]$ in Eq. 4.23 can be approximated by 1, then integration over ω yields

$$\int_{-\infty}^{+\infty} S_\mathrm{D}^{\alpha\beta}(\boldsymbol{K}, \omega)\, \mathrm{d}\,\omega = \frac{\mu_0 k_\mathrm{B} T}{(g\mu_\mathrm{B})^2}\, \chi^{\alpha\beta}(\boldsymbol{K}) \tag{4.24}$$

Eq. 4.24 means that we can obtain the wavevector-dependent susceptibility $\chi^{\alpha\beta}(\boldsymbol{K})$ directly when we measure the frequency integral of $S_\mathrm{D}^{\alpha\beta}$ $(\boldsymbol{K}, \omega)$. This can be done in a neutron scattering experiment with a two-axis spectrometer (diffractometer). The integration is performed accurately in the experiment if for our quasi-two-dimensional magnets $\boldsymbol{k}_\mathrm{f}$ is parallel to the c-axis of the sample (quasi-elastic approximation, see [71B1]). For an easy-axis antiferromagnet with uniaxial symmetry, we have

$$\chi^{\alpha\beta}\!: \quad \chi^{xx} = \chi^{yy} = \chi_\perp, \quad \chi^{zz} = \chi_\parallel, \quad \chi^{\alpha\beta} = 0 \quad \text{for } \alpha \neq \beta \tag{4.25}$$

For other systems with a different symmetry, e.g. the easy-plane antiferromagnet K_2FeF_4, Eq. 4.25 does not hold and special considerations are necessary, see [82T1]. Finally, the quasi-elastic neutron scattering cross section is obtained by inserting Eq. 4.25 into Eq. 4.21 and integrating over the frequency ω

$$\left.\frac{\mathrm{d}\sigma}{\mathrm{d}\Omega}\right|_{\mathrm{D}} = A(\boldsymbol{k}_{\mathrm{i}},\boldsymbol{k}_{\mathrm{f}})\frac{\mu_0 k_{\mathrm{B}}T}{(g\mu_{\mathrm{B}})^2}[(1+K_z^2/K^2)\chi_\perp(\boldsymbol{K})+(1-K_z^2/K^2)\chi_\|(\boldsymbol{K})] \tag{4.26}$$

Eq. 4.26 is the basic relation for magnetic critical scattering, i.e. for the results of the scans across the magnetic rods at temperatures near T_N. For the rod scan, the wavevector transfer is $\boldsymbol{K} = \boldsymbol{Q}_0 + \boldsymbol{q}$ where $\boldsymbol{Q}_0$ is a vector in reciprocal space located on the Bragg rod and $\boldsymbol{q}$ a wavevector perpendicular to the rod. For $\boldsymbol{K} = \boldsymbol{Q}_0$, $\chi(\boldsymbol{Q}_0)$ is the staggered susceptibility, the response of the system to a field $H(\boldsymbol{Q}_0)$. This is the spatial Fourier transform of the staggered $H(\boldsymbol{r}) \sim \exp(\mathrm{i}\boldsymbol{Q}_0\boldsymbol{r})$ which is positive at spin-up sites and negative at spin-down sites. These staggered susceptibilities $\chi_\|$ and $\chi_\perp$ depend only on the distance q (absolute value of $\boldsymbol{q}$) to the Bragg rod in reciprocal space. We can drop now $\boldsymbol{Q}_0$ for the further discussion but include explicitly the dependence on the reduced temperature $t = T/T_N - 1$. Then, $\chi_\perp$ and $\chi_\|$ are written in a more convenient notation

$$\chi_\perp(\boldsymbol{K}) \to \chi_\perp(q,t) \qquad \chi_\|(\boldsymbol{K}) \to \chi_\|(q,t) \tag{4.27}$$

The two susceptibilities are related to the transverse and to the longitudinal fluctuations, and only $\chi_\|(q,t)$ is divergent at T_N while $\chi_\perp(q,t)$ is noncritical. It is smaller than $\chi_\|(q,t)$ and can be assumed constant below T_N. Fig. 4.5 shows the values of the subsceptibilities for $q = 0$ on top of the ridge for K_2NiF_4. In the weakly anisotropic compounds like K_2MnF_4 and K_2NiF_4, $\chi_\perp(q,t)$ has nonnegligible values, and the problem is the appropriate separation of $\chi_\perp(q,t)$ and $\chi_\|(q,t)$ in the experimental results. One way to separate the susceptibilities is to use their different temperature dependence. While $\chi_\|(q,t)$ is dominant at $T \approx T_N$, $\chi_\perp(q,t)$ dominates for $T < T_N$ (cf. Fig. 4.5). Details of this procedure have been described by Birgeneau et al. [77B2]. For the strongly anisotropic K_2CoF_4 and Rb_2CoF_4, the transverse fluctuations are almost completely suppressed because of the Ising nature of these compounds and $\chi_\perp(q,t)$ can be neglected [74I2, 74S1].

The further analysis of the rod scan is usually performed by fitting an approximate mathematical form for $\chi_\|(q,t)$ to the experimental data, including the corrections for the finite resolution of the neutron spectrometer by means of a convolution of the approximate form with the resolution function. The simplest approximate form for $\chi(q,t)$ is the Ornstein-Zernike form, a simple Lorentzian [71S1, 76A3, 77B2]

$$\chi_{\mathrm{OZ}}(q,t) = \chi(0,t)\frac{1}{1+(q/\kappa)^2} \tag{4.28}$$

where κ is the inverse correlation length. This approximate form is frequently used. It approximates well the exact form for $\chi(q,t)$ above the phase transition but it has the disadvantage that it implies $\eta = 0$ since $\chi_{\mathrm{OZ}} \sim q^{-2}$ for $\kappa \to 0$ ($T \to T_N$) and not $\sim q^{-2+\eta}$ with $\eta = 0.25$ as expected for the 2D Ising model (cf. Table 7). Therefore, η was taken into account in an improved form known as Fisher approximant [64F1, 74I2, 79U]

$$\chi_{\mathrm{F}}(q,t) = \chi(0,t)\frac{1}{[1+(q/\kappa)^2]^{1-\eta/2}} \tag{4.29}$$

which has the correct asymptotic behaviour $\chi_{\mathrm{F}} \sim q^{-2+\eta}$ for $\kappa \to 0$ ($T \to T_N$) and which also has been employed in the range $t > 0$ ($T > T_N$). An even better form for this range with the correct asymptotic behaviour is the Fisher-Burford approximant [67F2, 84C1]

$$\chi_{\mathrm{FB}}(q,t) = \chi(0,t)\,\frac{[1+\Phi^2(q/\kappa)^2]^{\eta/2}}{1+(q/\kappa)^2} \tag{4.30}$$

which has also the correct leading term for large (q/κ). The factor Φ in the numerator has the rather small value $\Phi = 0.029\,413\,86$ for the 2D Ising model. Thus χ_{FB} reduces to the Ornstein-Zernike form χ_{OZ} (Eq. 4.28) for small (q/κ). For the range $t < 0$ ($T < T_{\mathrm{N}}$), an improved form in comparison to the Ornstein-Zernike one is the Tarko-Fisher approximant [75T2, 84C1]

$$\chi_{\mathrm{TF}}(q,t) = \chi(0,t)\,\frac{[1+\varphi^2(q/\kappa)^2]^{\eta/2}}{[1-\lambda+\lambda\sqrt{1+(q/\kappa)^2}\,]^2} \tag{4.31}$$

In Eq. 4.31, the numerical values for a fit to the experimental data are $\varphi = 0.2$ and $\lambda = 0.45$ [84C1]. Tracy and McCoy [75T3] have calculated the exact form of $\chi(q, t)$ numerically for the 2D Ising model. They have compared their results to the approximate forms listed above (Eqs. 4.28–4.31) and compiled in their Table V the range of (q/κ) for which the error made by using the approximant is smaller than a certain limit (0.01%–10%). Fig. 4.6 shows an example of the data of a rod scan and of the curves obtained by a least-square fit with one of the approximate forms convoluted with the experimental resolution function. The sample is K_2CoF_4 for which $\chi_\perp(q, t)$ is negligible and where only $\chi_\parallel(q, t)$ contributes to the neutron scattering intensity. One scan has been taken above $T_{\mathrm{N}} = 107.7$ K. In this case, the fits have been performed with the Ornstein-Zernike form (Eq. 4.28). For the other scan taken below T_{N}, a better fit result was obtained with the Tarko-Fisher form (Eq. 4.31) than with the Ornstein-Zernike form.

The results of such rod scans and the corresponding fits as shown in Fig. 4.6 are performed at a sufficient number of temperatures. The results of the fits, namely $\chi_\parallel(0, t)$ and $\kappa(t)$, can now be used to determine the critical exponents $\gamma^\pm$ and $\nu^\pm$ by means of Eqs. 4.8 and 4.11

$$\chi_\parallel(0,t) = \chi_0\, C_0^\pm\, |t|^{-\gamma^\pm} \tag{4.32}$$

$$\kappa(t)/a^* = (\kappa_0^\pm/a^*)\cdot|t|^{\nu^\pm} \tag{4.32a}$$

where again "+" is used for $t > 0$ and "–" for $t < 0$. The slopes of log-log plots of $\chi_\parallel(0, t)$ and $\kappa(t)$ versus t yield the critical exponents. Since most of the rod scans are performed for $t > 0$, the superscript "+" is usually omitted for γ and ν in Table 6 but not for C_0^+ and κ_0^+. One of the exceptions is the study of K_2CoF_4 for $t > 0$ and $t < 0$. The corresponding log-log plots in Fig. 4.7 yield straight lines and exhibit the single-power-law behaviour as expected from Eqs. 4.32 and 4.32a. The resulting values for γ^+, γ^-, ν^+, ν^- and η agree also in this case quite well with the 2D Ising values (cf. Table 7). Often $\chi_\parallel(0, t)\cdot T$ is plotted instead of $\chi_\parallel(0, t)$ [77B2] in order to remove the dependence of $\chi_0 \sim T^{-1}$ on t when determining γ. However, this is only a small correction in the range $10^{-4} \le |t| \le 10^{-1}$. The relative error using T_{N} instead of $T = T_{\mathrm{N}}(1 + t)$ is $|t|$. One method to determine η is by using it as an optimum fit parameter [74I2, 79I1]. The fits are performed with the Fisher form $\chi_{\mathrm{F}}(q, t)$ (Eq. 4.29) and that value of η is the final result for which the goodness of the fit is a minimum. Another method is to determine the product $\eta\cdot\nu$ by a log-log plot of [77B2]

$$\chi_\parallel(0,t)\cdot T\cdot\kappa^2(t) \sim t^{-\gamma}\cdot t^{2\nu} + \ldots = t^{\eta\cdot\nu} + \ldots \tag{4.33}$$

where the relation $(2-\eta)\nu = \gamma$ has been used from Eq. 4.13. Such a plot with data for $T > T_{\mathrm{N}}$ is presented in Fig. 4.8 for K_2NiF_4 and the mixed crystal $Rb_2Mn_{0.5}Ni_{0.5}F_4$. The slopes of the resulting straight lines agree also in this case with that for the 2D Ising model. It is now straight forward to obtain the value of η from the product $\eta\cdot\nu$ if ν has been determined by means of Eq. 4.32a. For many compounds, also the critical amplitudes C_0^+ and κ_0^+ have been derived from rod scans, i.e. from $\chi_{\|}(0, t)$ and $\kappa(t)$, using Eqs. 4.32 and 4.32a. The values so obtained for K_2CoF_4 and Rb_2CoF_4 (cf. Table 6) agree fairly well with those of the 2D Ising model (cf. Eqs. 4.9 and 4.11). For the weakly anisotropic compounds K_2MnF_4, K_2NiF_4 etc., however, the Ising-like anisotropy has to be taken into account not only for the critical amplitude A (cf. A_{theory} in Eq. 4.19) but also for κ_0^+. With the help of the universal relation $(\kappa_0^+ a_{\text{nn}})^2 = 2\pi\, A^+$ (cf. Eq. 4.14), Hatta and Ikeda [80H5] have obtained a theoretical value for κ_0^+ / a^* and its dependence on the anisotropy h_A

$$(\kappa_0^+ / a^*)_{\text{theory}} = \frac{\sqrt{2}}{\pi}\,[\ln(\sqrt{2}+1)] \cdot (h_A)^{1/4} \tag{4.34}$$

The values $(\kappa_0^+ / a^*)_{\text{theory}}$ calculated by means of Eq. 4.34 using the linear spin-wave values for h_A agree quite well with the experimental data. For $Rb_2Mn_{0.5}Ni_{0.5}F_4$ ($h_A = 0.0071$ [77B2]), K_2MnF_4 ($h_A = 0.0036$ [73W2]) and K_2NiF_4 ($h_A = 0.0019$ [73W2]), we obtain $(\kappa_0^+ / a^*)_{\text{theory}} =$ 0.115, 0.097 and 0.083, respectively. All these considerations are concerned with the determination of the critical exponents and amplitudes from $\chi_{\|}(q, t)$. But the above mentioned separation of the two susceptibilities for this analysis requires also a fit to $\chi_{\perp}(q, t)$ which is usually performed with the simplest form, i.e. the Ornstein-Zernike form (Eq. 4.28). The constant part in the range $0 \le T \le T_N$ can be written as [77B2]

$$\chi_{\perp}(q, t) = \chi_{\perp}(0, t) \cdot [1 + (q / \kappa_{\perp}^-)^2]^{-1} \tag{4.35}$$

where $\kappa_{\perp}^-$ is obtained from the fit to experimental data. Since mostly spin-wave excitations are involved in the transverse fluctuations described by $\chi_{\perp}(q, t)$ a theoretical value for $\kappa_{\perp}^- / a^*$ can be deduced from spin-wave theory. With the linear, not renormalized theory, $\kappa_{\perp}^- / a^* = \sqrt{2h_A} / \pi$ is obtained where $h_A = H_A / H_E$ is again the anisotropy parameter. For K_2MnF_4 and K_2NiF_4, the calculated values 0.027 and 0.020, resp., agree fairly well with the experimental data for $\kappa_{\perp}^- / a^*$ (cf. Table 6).

9.12.4.1.6 Experimental Test of Two-Scale-Factor Universality

The results for K_2CoF_4 and Rb_2CoF_4 which are good realizations of the 2D Ising model can also be used to test the hypothesis of two-scale-factor universality (cf. Sect. 4.1.2) which has been mentioned already in context with Eqs. 4.14 and 4.15. With neutron scattering data, this test is performed with the ratio R_S of critical amplitudes. The experiments have to be performed for the same value of $|t|$ above and below T_N. One possibility is to determine the involved critical amplitudes separately from the fits to the experimental data and to calculate then R_S [84C1]. The other possibility is to take directly the ratio of the neutron scattering intensities at the position $\boldsymbol{Q}_0$ of an antiferromagnetic superreflection [83H2, 84H1]. Then, the observed intensity $I(\boldsymbol{Q}_0, -t)$ for $T < T_N$ will be dominated by the contribution from the Bragg reflection (cf. Eq. 4.20) and the contribution from diffuse scattering (cf. Eq. 4.26) will be negligible. For $T > T_N$, the observed intensity $I(\boldsymbol{Q}_0, +t)$ consists only of contributions from diffuse scattering (magnetic rod):

$$I(\boldsymbol{Q}_0, -t) \sim B_0^2 \cdot (-t)^{2\beta} \quad \text{and} \quad I(\boldsymbol{Q}_0, +t) \sim \chi_{\|}(0, +t) \sim C_0^+ \cdot (+t)^{-\gamma} \tag{4.36}$$

where ($-t$) and ($+t$) refer to the same absolute value $|t|$ of the reduced temperature for the measurement below and above T_N. The ratio of these two intensities multiplied by $\kappa^2(+t)\cdot a^2/(2\pi)^2$ for $d = 2$ is then proportional to R_S

$$\frac{I(\boldsymbol{Q}_0,+t)\cdot\kappa^2(+t)\cdot a^2}{I(\boldsymbol{Q}_0,-t)\cdot(2\pi)^2} \sim \frac{C_0^+\cdot(\kappa_0^+ a)^2\cdot(+t)^{-\gamma+2\nu}}{B_0^2\cdot(2\pi)^2\cdot(-t)^{2\beta}} \sim R_S \tag{4.37}$$

In Eq. 4.37, the terms with t cancel because of the relations $\alpha + 2\beta + \gamma = 2$ and $d\nu = 2\nu = 2 - \alpha$ between the critical exponents (cf. Eq. 4.13) which yield $-\gamma + 2\nu = 2\beta$. The proportionality factors omitted here like neutron beam intensity, resolution volume in reciprocal space etc. are all known from experimental data, for details the reader is referred to [83H2, 84H1].

The experimental values R_S obtained for K_2CoF_4 and Rb_2CoF_4 (cf. Table 6) agree quite well with the theoretical value for the 2D Ising model quoted in context with Eq. 4.15. Since these compounds are good realizations of the 2D Ising model it is possible that a transition occurs to a 2D long-range order below T_N instead of the usual 3D ordering. Such a 2D order has actually been found in samples which are rapidly cooled through T_N from above which exhibit also 3D long-range order when they are slowly cooled through T_N or when the rapidly cooled samples are annealed at T_N. These effects have been observed by neutron scattering in Rb_2CoF_4 and in $Rb_2Co_xMg_{1-x}F_4$ mixed crystals where Co^{2+} is diluted by Mg^{2+} [73S4, 78I3, 79I2]. In these measurements, $(1, 0, \zeta_z)$ scans are performed along the ridge, e.g. for $-1 \le \zeta_z \le 0$, as shown in Fig. 4.9 for a sample of $Rb_2Co_{0.75}Mg_{0.25}F_4$. We recall from Fig. 2.5 in Sect. 2.1.2 that $\zeta_z = 0$ corresponds to the antiferromagnetic Bragg peak (1, 0, 0) of one domain and $\zeta_z = -1$ to the superreflection (1, 0, –1) of the other domain. The signal between these two is the intensity on top of the ridge due to 2D correlations. Curve A in Fig. 4.9 represents the result after rapid cooling from ≈ 80 K to 4.2 K in a few seconds ($T_N = 60$ K [84M4]). Curve B has been obtained after slow cooling from ≈ 70 K to ≈ 30 K in about 15 min. The difference between the two curves is striking. In curve A, almost all scattering intensity is distributed uniformly over the Bragg rod with small and very broad indications of the Bragg peaks. From their width, the correlation between the layers is small, and the layers are nearly uncorrelated (2D long-range order). For less rapid cooling, sharp Bragg peaks appear and less intensity is found in the Bragg rod indicating the increasing correlation between the layers. The total intensity (Bragg rods + Bragg peaks) is the same for both curves within the error limits. These effects are enhanced in the diluted $Rb_2Co_xMg_{1-x}F_4$ samples but are also observed in pure Rb_2CoF_4. The 2D order is stable at low temperatures for several days. When the temperature is increased to somewhat below T_N, the neutron scattering results become time-dependent. Within hours, the scattering intensity is shifted more and more from the rod to the Bragg peaks indicating that the 2D order is converted to the usual 3D order [79I2].

9.12.4.1.7 2D Heisenberg Model

The experimental data of weakly anisotropic layered structures, antiferromagnets like K_2MnF_4 or ferromagnets like K_2CuF_4, indicate that they can be considered realizations of the 2D Heisenberg model on a square lattice only in an approximative way since all these compounds have some sort of small anisotropy or small interlayer exchange coupling. In K_2CuF_4 for example, the magnon energies are approximately that of a 2D Heisenberg ferromagnet for sufficiently large $\boldsymbol{q}$. In Sect. 3.2.1, it turned out that the spin-wave dispersion curves [83H4] for the (1, 0, 0) direction (cf. Figs. 3.30 and 3.31) can successfully be fitted to a 2D Heisenberg model for reduced wavevector $\zeta_{x0} > 0.1$ (cf. Eq. 3.72) where we can neglect the contributions of the anisotropy or the interlayer coupling ($h_A \approx 0$, $h'_E \approx 0$). And in Fig. 3.31 ζ_2 marks the wavevector where the contributions from J and J_A to $\hbar\omega_q$ are equal and where the influence of the XY-like anisotropy can no longer be neglected. Similar considerations can be made for weakly anisotropic antiferromagnets. We recall further from Sect. 3.1.2 that the 2D Heisenberg model with its continuous symmetry does not have a transition to long-range order for $T_C > 0$ [30B, 66M1] but such a transition may occur at $T_C = 0$ [76M4]. Thus (see also Sect. 3.1.2), the anisotropy or the interlayer coupling are essential for the existence of a transition to ferro- or antiferromagnetic order at a finite temperature. Experimental data with respect to these questions, namely for C_{magn} and χ, have been discussed for a number of compounds by de Jongh [78J]. The actual critical behaviour of the perovskite-type layer compounds is determined by this anisotropy or the interlayer coupling. The discussion in Sect. 4.1.3–4.1.5 and also the data in Table 6 show that most of the weakly anisotropic antiferromagnets show 2D Ising critical behaviour due to their Ising-like easy-axis anisotropy. The critical behaviour of the Cu-compounds, on the other hand, depends on the strength of h'_E and $\tilde{h}_A$ relative to each other. For $h'_E > \tilde{h}_A$ as in K_2CuF_4, the critical behaviour is that according to the 2D XY-model and 3D XY-model. For the compounds $(C_nH_{2n+1}NH_3)_2CuCl_4$ with n ≥ 1 and mostly $\tilde{h}_A > h'_E$, one would expect Ising-like critical behaviour. But the experimental data which are sufficiently available only for the compound with n = 1 show no unique behaviour. The susceptibility data for $T > T_C$ exhibit for both, $(CH_3NH_3)_2CuCl_4$ and $(CD_3ND_3)_2CuCl_4$, the expected Ising behaviour with a crossover from 2D to 3D [76J1, 78J, 79O2, 80O1, 84S4] and for $T < T_C$, the value of β from the deuterated sample is close to theoretical one for the finite-size XY-model [83S2, 84S4], see Eq. 4.66 below. Moreover, Ain [87A4] has concluded from his ac-susceptibility and neutron diffraction data that the magnetic phase transition is of the Kosterlitz-Thouless type in this compound, cf. Sect. 4.1.8 below. And Demokritov et al. [89D2, 90D3] have concluded from their magnetic resonance data a Kosterlitz-Thouless temperature $T_{KT} = 8.4$ K, in addition to $T_C = 8.9$ K, for $(CH_3NH_3)_2CuCl_4$.

Let us first turn to the theoretical predictions for the 2D Heisenberg model on a square lattice. It was already presented in Sect. 3.1.3 that Stanley and Kaplan [66S2] performed an analysis of high temperature series expansions (h.t.s.) for the susceptibility χ (cf. Eq. 3.26) and came to the conclusion that there exists a $T_C^{(2)} > 0$ at which the susceptibility diverges but below which there is no spontaneous magnetization ($M \equiv 0$). With the extension of the series by further terms, new results [73Y3] seem to support more the non-divergence of χ at finite temperatures. Generally, the analysis by means of the h.t.s. is one of the methods with which the magnetic properties of the 2D Heisenberg model have been studied theoretically. In some of the studies, anisotropy has been included for modelling the properties of real layered compounds [67D]. Also double-layer and other multi-layer structures have been treated in this way [73R3]. A re-examination of the h.t.s. for χ [75C2] yielded that the correlation length ξ does not follow a conventional power law for $T > T_C$ (cf. Sect. 4.1.1) but will exhibit a temperature dependence like $\exp(A\ t^{-\mu})$ with an exponent μ and a constant factor A. Many publications consider a Heisenberg model with general spin or treat the spins even as classical vectors while we are mostly interested in the $S = \frac{1}{2}$ Heisenberg ferromagnet in view of the Cu-compounds with $S = \frac{1}{2}$. Employing the Green's function formalism, this case has also been studied [73Y1, 73M, 75Y]. The Green's function treatment of the $S = \frac{1}{2}$ 2D Heisenberg ferromagnet by Yamaji and Kondo [75Y] or by Mikeska [73M] includes anisotropy and interlayer exchange as small perturbations of the ideal Heisenberg model. One of the results is the transition temperature T_C [75Y] for $H_0 = 0$

$$k_B T_C = 2\pi J / \ln\,[16 / h_{\kappa,0}] \tag{4.38}$$

with

$$h_{\kappa,0} = \tfrac{1}{2}\left(\sqrt{\tilde{h}_A} + \sqrt{\tilde{h}_A + 2h'_E}\right) \cdot \left(\sqrt{h_A} + \sqrt{h_A + 2h'_E}\right) \qquad \text{(cf. Eq. 3.74)}$$

where $h_A = J_A / J$, $\tilde{h}_A = \tilde{J}_A / J$ and $h'_E = z'J' / zJ$ are again the reduced parameters of the system (cf. Eq. 3.71). With the values listed in Table 5, Eq. 4.38 yields $T_C = 8.11$ K for K_2CuF_4 instead of the experimental value $T_C = 6.25$ K. If the perturbations in Eq. 4.38 vanish ($h_A \to 0$, $\tilde{h}_A \to 0$, $h'_E \to 0$) we obtain $T_C \to 0$ as expected for the 2D Heisenberg model. Based on the above mentioned theoretical result; and those of many other investigations including renormalization-group analysis [71B3, 72B4, 73B4, 75P2, 80S3], it is now generally accepted that the ideal 2D Heisenberg model does not undergo any phase transition at $T > 0$ (see also [79P3, 90N, 90P, 90R1]). Since a phase transition is absent in the ideal 2D Heisenberg model, the specific heat is expected to exhibit a broad contour with a maximum but without a singularity [74J1, 80S3], a Schottky-type anomaly similar to 1D magnetic systems [76S5]. These properties of the 2D Heisenberg model are not disproved by the results of Monte Carlo simulations.

These were performed for ideal systems on a square lattice without perturbations, namely a 2D classical magnet [78S5] and a $S = \frac{1}{2}$ antiferromagnet [88R5], as well as for systems with anisotropies which break the Heisenberg isotropy. For an Ising-like anisotropy as in K_2NiF_4 etc. [76B4], a conventional phase transition with $T_C > 0$ is expected and found in the Monte Carlo results. For magnets with easy-plane anisotropy like K_2CuF_4, Rb_2CrCl_4 etc. [82K3, 86K4, 89G3], a transition to a topological LRO is observed in the result at a finite T_C (see 2D XY-model, next section). But surprisingly, also the Monte Carlo simulations for the ideal system yield a finite $T_C \neq 0$ and a magnetization or sublattice magnetization $M \neq 0$ at low T. This may be due to finite-size effects [79B8, 86B4] because such calculations require a finite system, e.g. 900 or 2500 spins. Recently, an analytic solution has been obtained for the susceptibility, the magnetic specific heat and the spin-spin correlation function of the 2D classical Heisenberg model [95C1]. The critical exponents obtained in this way ($\alpha = 0$, $\gamma = 3$, $\nu = 1$, $\eta = -1$), however, differ considerably from those obtained by renormalization group analysis [74F2].

In order to learn more about the properties of the 2D Heisenberg model on a square lattice, the experimental data of a number of copper compounds have been analysed. The aim of such an comparative analysis is to remove the influence of the anisotropy and the interlayer coupling and to extract the data for an ideal 2D Heisenberg system by means of an extrapolation [75B5]. Navarro and de Jongh [76N2] have performed such an analysis for the magnetic susceptibility χ and extrapolated the susceptibility χ_H of an ideal 2D Heisenberg ferromagnet from the experimental data of various Cu-compounds. Fig. 4.10 shows χ/χ_0 for K_2CuF_4, for the compounds $(C_nH_{2n+1}NH_3)_2CuCl_4$ with n =1, 3, 10 and the extrapolated curve χ_H/χ_0 versus a reduced scale k_BT/J ($\chi_0 = C/T$, cf. Eq. 4.8). For high temperatures ($k_BT/J > 1.5$), the experimental χ-data exhibit no difference for these compounds and agree quite well with the predictions of the h.t.s. for χ of the 2D Heisenberg model. For lower temperatures ($k_BT/J < 1.5$), the h.t.s. becomes more and more unreliable and other theoretical concepts are needed. Santos and Kosterlitz [78K3] treated this problem with renormalization-group methods and obtained $\chi/\chi_0 \sim (k_BT/J)^2 \exp(4\pi J/k_BT)$. The extrapolated data of Navarro and de Jongh [76N2] exhibit in principle this behaviour in the range $0.5 < k_BT/J < 1.1$ (see Fig. 1 in [78K3]). However, the prefactor in the exponential is 3.6 for the extrapolated data instead of 4π. When the experimental data of χ depart from the common curve χ_H/χ_0, the anisotropic exchange and the interlayer coupling can no longer be neglected and have its influence on χ. Fig. 4.10 shows that χ of K_2CuF_4 is larger than that of the other compounds in this range because K_2CuF_4 exhibits a larger h_A than the other Cu-compounds which all have nearly the same h_A. The data in Fig. 4.10 mean also that, for example, K_2CuF_4 undergoes first a crossover to a 2D XY-system when h_A becomes important and finally a crossover to a 3D XY-system when also h'_E is relevant. Such crossover phenomena will be discussed in Sect. 4.1.9. The estimate χ_H for the 2D Heisenberg model extracted from the experimental data is probably of limited accuracy but certainly more reliable than other approaches to this problem.

Bloembergen [77B3] has performed a similar analysis for the magnetic specific heat of several Cu-compounds. The measurement of the specific heat C_p and the separation of the lattice part from the magnetic part C_{magn} is described in a publication by Bloembergen and Miedema [74B2]. Similar as for weakly anisotropic antiferromagnets like K_2MnF_4, K_2FeF_4, K_2NiF_4 etc., the magnet specific heat of the ferromagnetic Cu-compounds consists of a broad maximum mostly peaked for $T > T_C$ and a narrow sharp spike at $T = T_C$. For K_2CuF_4, Takeda et al. [81T2] determined C_{magn} also with a broad maximum and a sharp spike at T_C as already presented in Sect. 3.3.2 in context with the diluted system $K_2Cu_xZn_{1-x}F_4$ (cf. Fig. 3.49). The experimental results of Bloembergen [77B3] for Rb_2CuCl_4 and $(C_nH_{2n+1}NH_3)_2CuCl_4$ with n = 1 and 2 are presented in Fig. 4.11 versus a reduced scale k_BT/J. The broad contour is almost the same for all three compounds while the spikes at the corresponding critical temperature T_C (T_N for Rb_2CuCl_4 and $(C_2H_5NH_3)_2CuCl_4$, T_C for $(CH_3NH_3)_2CuCl_4$) are different in height and intensity as shown in more detail in Fig. 4.12. And even on the reduced scale, they appear in different positions since T_C depends not only on J but also on J_A and J'. This has been elucidated by Jou and Chen [73J4] for $T_C(h_A)$ in their Table 1 for an Ising-like anisotropy where k_BT_C/J is listed for $0.2 \leq h_A \leq 1.0$. Bloembergen [76B5] has investigated the influence of h'_E on T_C. His results are compiled as k_BT_C/J versus h'_E for $0.0031 \leq h'_E \leq 0.5$ in his Table V. Let us return now to the problem of C_{magn} for the ideal

2D Heisenberg model. The broad maximum is a good basis for deriving it from the experimental data. Theoretically, it is predicted to show a Schottky-type anomaly and not a singularity because of the absence of a phase transition [74J1, 80S3]. Experimental data are only available in the range $0.25 \le k_B T/J \le 1.40$. Outside this range, the curve in Fig. 4.11 is calculated by using reliable approximations. For low temperatures ($0 \le k_B T/J \le 0.25$), the linear T-dependence is modelled with the Green's functions result for the square lattice Eq. 3.79a (Sect. 3.2.1). For high temperatures ($k_B T/J > 1.40$), the curve common for all compounds is obtained by means of the high temperature series expansion for C_{magn}. In Sect. 3.1.3, only the h.t.s. for χ and χ^{-1} were introduced in Eqs. 3.26 and 3.27. In a similar way, a high temperature series can also be established for C_{magn} [58R3, 74R2, 90N]

$$C_{\text{magn}} / R = \frac{2}{3} z\, S^2 (S+1)^2 K^2 \left[1 + \sum_{n=1}^{\infty} c_n K^n \right] \tag{4.39}$$

where $K = J/k_B T$ as in Eq. 3.26. For the $S = \frac{1}{2}$ Heisenberg ferromagnet on a square lattice, the coefficients c_n have been derived by Baker et al. [67B2] and by Yamaji and Kondo [73Y3]. They are also listed in Table B-IV of the review by Navarro [90N]. Eq. 4.39 has been used to calculate the common curve in Fig. 4.11 for $k_B T/J > 1.4$. The h.t.s. for C_{magn} becomes really reliable for $k_B T/J > 2.4$ and interpolation techniques and approximations have been employed to bridge the gap. In addition to the graphic presentation, the estimate for C_{magn} of the 2D Heisenberg model on a square lattice has been listed in Table V of [77B3]. A question still to be answered is whether the sharp spike in the specific heat as shown in Fig. 4.12 is Ising-like due to a crossover from the XY-model to the Ising model or whether such a spike is a specific heat anomaly of the 2D XY-model.

9.12.4.1.8 2D XY-Model

In contrast to the 2D Heisenberg model, the 2D XY-model seems to be a better candidate for the new kind of phase transition at a finite temperature predicted by Stanley and Kaplan [66S2]. This transition would be characterized by a diverging susceptibility without magnetic long-range order (LRO) and spontaneous magnetization. According to Kosterlitz and Thouless [73K3, 78K2], the 2D XY-system cannot have an ordinary symmetry-breaking phase transition but the novel kind of transition would be mediated by the unbinding of vortex-antivortex pairs into a gas of free vortices at the critical temperature $T_{KT} > 0$. T_{KT} is the Kosterlitz-Thouless temperature which is not identical with the actual transition temperature T_C in real systems like K_2CuF_4 and Rb_2CrCl_4. The vortices are new nonlinear excitations of the system [71B3, 72B4] which form a topological long-rarge order which is no magnetic LRO with $M \neq 0$. They are characterized by a vorticity Q which can be defined as [73K3, 74K5, 90P]

$$Q = \frac{1}{2\pi} \oint \nabla \delta(\boldsymbol{r})\, \mathrm{d}\boldsymbol{s} \tag{4.40}$$

where the angle $\delta(\boldsymbol{r})$ denotes the direction of the spin at point $\boldsymbol{r}$ with respect to the x-axis in the basal plane. Fig. 4.13 shows two simple examples of vortices, one with $Q = +1$ and the other with $Q = -1$. The existence of this new type of transition in the 2D XY-model has primarily been verified in Monte Carlo computer simulations [77K6, 77S5, 78M3], which also provide for $T < T_{KT}$ evidence of vortex-antivortex pairs with opposite Q and the corresponding topological long-range order. An equilibrium spin configuration after 2000 Monte Carlo steps is reproduced in Fig. 4.14. It is the typical vortex-antivortex range at a temperature of $k_B T = 0.5(2S^2 J) \approx 0.6\, T_{KT}$. The vortex pairs are enclosed by broken lines in Fig. 4.14. Theoretical calculations have been performed not only for the XY-model but also for the plane rotator model which belongs to the same universality class [74B7, 77B4, 95P2]. The data in Fig. 4.14 are based on this classical planar or plane rotator model [78M3, 79T1]

$$\mathcal{H} = -2J \sum_{\langle \mathrm{i,j} \rangle} (\mathrm{S}_{\mathrm{i,x}}\mathrm{S}_{\mathrm{j,x}} + \mathrm{S}_{\mathrm{i,y}}\mathrm{S}_{\mathrm{j,y}}) = -2S^2 J \sum_{\langle \mathrm{i,j} \rangle} \cos(\delta_\mathrm{i} - \delta_\mathrm{j}) \qquad [\mathrm{S}_{\mathrm{i,z}} \equiv 0,\ \mathrm{S}_{\mathrm{j,z}} \equiv 0] \qquad (4.41)$$

where $\delta_\mathrm{i} = \delta(\boldsymbol{r}_\mathrm{i})$ and $\delta_\mathrm{j} = \delta(\boldsymbol{r}_\mathrm{j})$ are the orientation angles of the spins at $\boldsymbol{r}_\mathrm{i}$ and $\boldsymbol{r}_\mathrm{j}$, resp., (cf. Eq. 4.40). In this model, the spins are classical two-dimensional magnetic vectors in the basal plane. Two other models in this context are the classical and the quantum 2D XY-model which were also employed in Monte Carlo simulations

$$\mathcal{H} = -2J \sum_{\langle \mathrm{i,j} \rangle} (\mathrm{S}_{\mathrm{i,x}}\mathrm{S}_{\mathrm{j,x}} + \mathrm{S}_{\mathrm{i,y}}\mathrm{S}_{\mathrm{j,y}}) \qquad [\mathrm{S}_{\mathrm{i,z}} \not\equiv 0,\ \mathrm{S}_{\mathrm{j,z}} \not\equiv 0] \qquad (4.42)$$

In the classical XY-model [84G4], the spins $\boldsymbol{S}_\mathrm{i}$ and $\boldsymbol{S}_\mathrm{j}$ are classical three-dimensional magnetic vectors so that $\mathrm{S}_{\mathrm{i,z}}$ and $\mathrm{S}_{\mathrm{j,z}}$ can give rise to out-of-plane fluctuations. A classical treatment is only justified for large spin values, strictly for $S \to \infty$. But for small S and especially for $S = \frac{1}{2}$, this procedure is not adequate and the quantum 2D XY-model is more appropriate. Eqs. 4.41 and 4.42 refer to ferromagnetic models in view of our examples (see below). But the ferromagnetic model can easily be converted to an antiferromagnetic one by an unitary transformation [88O, 96B]. Therefore, most of the results, e.g. the transition temperature are the same for both cases. It should further be noted that the models Eq. 4.41 and Eq. 4.42 are often not strictly distinguished in the literature and the plane rotator model also called 2D XY-model, see for example [86F2, 88G4, 88W2, 95O2]. As experimental realisations of these models, we will discuss here magnetic systems like $\mathrm{K_2CuF_4}$ [90H] and $\mathrm{Rb_2CrCl_4}$ [86D3] and not the analogy between the XY-model and superfluidity in ^{4}He or superconducting grains. For additional information, the reader is recommended to consult the reviews on this topic [74B7, 78K2, 79P3, 80B9, 90H, 90P, 90R1].

The critical properties of the 2D XY-model have been derived by Kosterlitz [74K5]. Because the nature of the Kosterlitz-Thouless transition is very different from an ordinary phase transition, the correlation length $\xi(T)$ does not diverge according to a conventional power law $t^{-\gamma}$ for T approaching the critical temperature from above ($T > T_\mathrm{KT}$) but faster than that according to an exponential

$$\xi(T) \sim \exp(b\tilde{t}^{-1/2}) \qquad (4.43)$$

where $\tilde{t} = (T - T_\mathrm{KT})/T_\mathrm{KT}$ is the reduced temperature with respect to T_KT and b a factor. Eq. 4.43 has first been derived by Kosterlitz [74K5] with a renormalization group analysis. It has subsequently been confirmed by Monte Carlo calculations [86F2, 88G4]. The Kosterlitz-Thouless temperature T_KT is a nonuniversal quantity, it depends on the model and its parameters. Following the literature, a dimensionless equivalent of the temperature is introduced

$$\tilde{T} = (k_\mathrm{B}T)/(2S^2J) \qquad (4.43\mathrm{a})$$

That means we measure the energy $k_\mathrm{B}T$ in units of $2S^2J$, in accordance with our notation for the exchange Hamiltonian in Eq. 3.2 (Sect. 3.1.2). For the quantum 2D XY-model, S is often replaced by $\tilde{S} = S + \frac{1}{2}$ instead of using $S(S+1)$ for S^2 [90D5, 92D1, 95C2, 96B]. Monte Carlo simulations and also high temperature series expansions have been used to obtain reliable values for $\tilde{T}_\mathrm{KT}$. Extensively studied was the planar model Eq. 4.41 [86F2, 88G4, 88W2, 93B3]. The most precise value for this model is $\tilde{T}_\mathrm{KT} =$ 0.892 [94S2, 95O2] obtained with special care to overcome the finite-size effects in Monte Carlo calculations. For the classical 2D XY-model Eq. 4.42 with $S_z \neq 0$ there is a reduction of $\tilde{T}_\mathrm{KT}$ due to out-of-plane fluctuations [95P2], namely to $\tilde{T}_\mathrm{KT} = 0.699$ [95C3]. In the quantum 2D XY-model, $\tilde{T}_\mathrm{KT}$ is further reduced because of quantum renormalization [85L, 90D5]. The reduction depends on S and is most drastic for $S = \frac{1}{2}$ $(\tilde{S} = 1)$ with $\tilde{T}_{\mathrm{KT}} = 0.353$ [92D1]. The factor b in Eq. 4.43 is also a nonuniversal constant, and various values mostly in the range between 1.50 and 2.00 have been obtained in fits to Monte Carlo results [88G4, 93B3, 95O2]. In analysing experimental data, Als-Nielsen et al. [93A] have used $b = 2.12$ for $\mathrm{Rb_2CrCl_4}$ and Hirakawa et al. [82H5] $b = 1.5$ for $\mathrm{K_2CuF_4}$. According to the relation $\chi \sim \xi^{2-\eta}$, a similar exponential divergence is obtained for the susceptibility χ

$$\chi(T) \sim \exp\left(B\,\tilde{t}^{-1/2}\right) = \exp\left[b\,(2-\eta)\,\tilde{t}^{-1/2}\right] \tag{4.44}$$

where for $T \approx T_{\mathrm{KT}}$ $\eta = 0.25$ (cf. Eq. 4.48b below), i.e. the same value as in the 2D Ising model (cf. Table 7). The exponential divergence of ξ and χ, first predicted by Kosterlitz [74K5], has been confirmed by Monte Carlo simulations [91J2, 92G2, 93J] the results of which favor the Kosterlitz-Thouless theory over a conventional second order phase transition with the conventional power law divergence of ξ and χ. But there has also been a critical discussion about the validity and the correct interpretation of the Kosterlitz-Thouless theory [88P] with the result that this theory is correct as outlined in this section [88G4].

For $T \le T_{\mathrm{KT}}$, the Kosterlitz-Thouless theory predicts a divergence of the correlation length and the susceptibility at all temperatures

$$\xi, \chi \to \infty \qquad \text{for all } T \le T_{\mathrm{KT}} \tag{4.45}$$

and the magnetization vanishes in this temperature range ($M \equiv 0$) due to the absence of a magnetic LRO. There is only the topological LRO as discussed above. Eq. 4.45 means essentially that all temperatures in the range $0 \le T \le T_{\mathrm{KT}}$ correspond to a critical point. A further consequence of Eq. 4.45 is that the conventional critical exponents diverge for $T \le T_{\mathrm{KT}}$

$$\beta \to \infty, \quad \gamma \to \infty, \quad \nu \to \infty \qquad \text{for all } T \le T_{\mathrm{KT}} \tag{4.45a}$$

But the ratio γ/β will be finite in this temperature range [74K5] and thus also $\delta = 1 + \gamma/\beta$. If a magnetization M is induced by a weak external field H_0, we have

$$M \sim H_{\mathrm{int}}^{1/\delta(T)} \tag{4.46}$$

where H_{int} is the internal field resulting from H_0. Since all temperatures below T_{KT} correspond to a critical point, $\delta(T)$ is a function of temperature. At $T = T_{\mathrm{KT}}$, δ has the value $\delta = 15$. Also the exponent η of the correlation function is finite for $T \le T_{\mathrm{KT}}$. In case of two dimensions (2D) without LRO, the spatial dependence of the correlation function can be written as (cf. Eq. 4.22 and [74K5, 77J2, 78M3])

$$G(\boldsymbol{r}) = \langle \boldsymbol{S}_{\mathrm{i}}\, \boldsymbol{S}_{\mathrm{j}} \rangle \sim \left(\frac{r}{a}\right)^{-\eta(T)} \tag{4.47}$$

where $\boldsymbol{r} = \boldsymbol{r}_{\mathrm{i}} - \boldsymbol{r}_{\mathrm{j}}$, $r = |\boldsymbol{r}|$, $\eta(T)$ also a function of temperature ($0 \le T \le T_{\mathrm{KT}}$) and a the lattice constant. In contrast to Eq. 4.22, no averages $\langle |\boldsymbol{S}_{\mathrm{i}}| \rangle$ and $\langle |\boldsymbol{S}_{\mathrm{j}}| \rangle$ are subtracted in Eq. 4.47 because they vanish due to the lack of LRO in the ideal 2D XY-model. In general, η is related to the ratio of the spin stiffness ρ_{s} and the temperature [92M7]. For $T << T_{\mathrm{KT}}$, the spin-wave approximation for η is given by the unrenormalized spin-stiffness $\rho_{\mathrm{s}} = 2S^2J$ [72B4, 89C3] and the temperature [92M7]

$$T \approx 0: \quad \eta = (2\pi\,\tilde{K})^{-1} \quad \text{with} \quad \tilde{K} = (2S^2J)/(k_{\mathrm{B}}T) \tag{4.48a}$$

With increasing temperatures nearer to but still below $T_{\rm KT}$, the spin stiffness and with it the relative spin stiffness $\widetilde{K}$ will considerably be renormalized due to the presence of vortex-antivortex pairs [72B4]:

$$\widetilde{K} \to \widetilde{K}_{\rm eff}$$

This renormalization is elucidated by recent theoretical studies of 2D easy-plane magnets [92M4, 93P2]. At $T_{\rm KT}$, the renormalized $\widetilde{K}_{\rm eff}$ and η will assume universal values

$$\widetilde{K}_{\rm eff} = \tfrac{2}{\pi} \qquad \eta = (2\pi\,\widetilde{K}_{\rm eff})^{-1} = 0.25 \qquad (T = T_{\rm KT}) \tag{4.48b}$$

The theory for the 2D XY-model predicts further that $\widetilde{K}_{\rm eff}$ will perform a "universal jump" at $T_{\rm KT}$ [74K5, 77N3, 94B1] (see also: [73P2, 74P2])

$$\widetilde{K}_{\rm eff} = \tfrac{2}{\pi} \xrightarrow{\text{"jump"}} \widetilde{K}_{\rm eff} = 0 \tag{4.48c}$$

Another property of 2D XY magnetic systems is that at low temperatures, i.e. for $T << T_{\rm KT}$, there is coexistence of spin-waves (linear excitations) and vortex-antivortex pairs with opposite Q (nonlinear excitations) [73K3, 78S6]. The spin-wave dispersion can be approximated for small $q = (q_{\rm x0}^2 + q_{\rm y0}^2)^{1/2}$ in the 2D XY-regime (approximately $0.01 \le q/a^* \le 0.1$) for K_2CuF_4 [83H4] using Eq. 3.71 (Sect. 3.2.1) with $\widetilde{h}_{\rm A} = 0$, $h_{\rm 0x} = 0$ and neglecting $h'_{\rm E}$

$$\hbar\omega_{\rm q} = \{[2\,z\,S\,J\,(1-\gamma_{\rm q})]\;[2\,z\,S\,J_{\rm A}\,\gamma_{\rm q}]\,\}^{1/2} \approx z\,S\,\sqrt{J\,J_{\rm A}}\,aq \tag{4.49a}$$

and for Rb_2CrCl_4 [80L2, 81H4] employing Eq. 3.87 (Sect. 3.2.2) and neglecting the in-plane anisotropy $P = \widetilde{P}\,\sin 2\delta$

$$\hbar\omega_{\rm q} = \left\{\left[2zSJ\,(1-\gamma_{\rm q})\right]\left[D\,(1+|\gamma_{\rm q}|)\,(S-\tfrac{1}{2})\right]\right\}^{1/2} \approx \sqrt{zSJD(S-\tfrac{1}{2})}\;aq \tag{4.49b}$$

This linear dispersion $\omega_{\rm q} \sim q$ with spin-wave velocity $c = \omega_{\rm q}/q$ is characteristic for XY-model ferromagnets [69H2, 73B4, 74V4, 75V, 86K3] where the out-of-plane anisotropy fields with $J_{\rm A}$ and D force the spins into the easy plane and create the XY-model symmetry. In the 2D Heisenberg regime (approximately $0.1 \le q/a^* \le 0.5$), the ideal Heisenberg model without any anisotropy term is a good approximation for the experimentally observed magnon dispersion curves [76F, 76H4, 79D3, 81H4, 83H4]. In this case, we obtain for K_2CuF_4 from Eq. 3.71 with $h_{\rm A} = h'_{\rm E} = \widetilde{h}_{\rm A} = h_{\rm 0x} = 0$ and for Rb_2CrCl_4 from Eq. 3.87 with $D = P = \widetilde{D} = \widetilde{P} = 0$

$$\hbar\omega_{\rm q} = 2zSJ\,(1-\gamma_{\rm q}) \approx \tfrac{1}{2}\,zSJa^2q^2 \tag{4.50}$$

This quadratic dispersion is typical for Heisenberg ferromagnets [69H2, 86K3]. In Eqs. 4.49a, 4.49b and 4.50, the lattice constant a refers to the I4/mmm pseudo-cell with one magnetic ion per unit cell. Thus, the magnon dispersion relations of the two easy-plane ferromagnets under consideration agree quite well with the predictions for the 2D XY-model and the 2D Heisenberg model in the corresponding wavevector ranges. A similar difference as in the limiting behaviour for small q is also observed in the temperature dependence of the magnon energies. The experimental data for K_2CuF_4 are shown in Fig. 4.15. They correspond to the magnon dispersion curve for the (1, 0, 0) direction in Fig. 3.30 (Sect. 3.2.1) measured at 1.05 K [83H4]. The data in Fig. 4.15 reveal a drastic decrease of the spin-wave energies at $T_{\rm C}$ for

$\zeta_{x0} \leq 0.03$ (2D XY-model) and become overdamped for $T > T_C$. The dashed line marked Γ_q in Fig. 4.15 denotes the boundary between underdamped and overdamped spin waves. The spin waves for $\zeta_{x0} \geq 0.04$ (2D Heisenberg model), on the other hand, are not overdamped above T_C with much less temperature renormalization. In the wavevector range $0.01 \leq \zeta_{x0} \leq 0.03$, the K_2CuF_4 data are in accordance with 2D XY-model. The drastic drop of the magnon energies near T_C is equivalent to a similar drastic decrease of $\widetilde{K}_{\text{eff}}$ (cf. Eqs. 4.48a, 4.48b) since both are proportional to each other as pointed out by Bramwell et al. [95B1], see also [90S]

$$\widetilde{K}_{\text{eff}} = \frac{2S^2J}{k_BT}\,\frac{\omega(T)}{\omega(0)} \tag{4.51}$$

Thus, the experimental data for $\zeta_{x0} \leq 0.03$ in Fig. 4.15 are an indication for the "universal jump" (cf. Eq. 4.48c) in the spin-wave stiffness [83H4, 90H]. A similar temperature variation of the magnon energies has been observed in Rb_2CrCl_4 [86H2]. We note, however, that the experimental data do not exhibit a discontinuous jump. They fall steeply but continuously to zero between T_{KT} and T_C. The results of Monte Carlo simulations exhibit also this continuous decrease [86K3].

Let us finally consider the predictions for the specific heat of the 2D XY-model and the 2D planar modell. Eqs. 4.45 and 4.45a imply that the specific heat exponent will diverge according to $\alpha = 2 - 2\beta - \gamma \to -\infty$ (cf. Eq. 4.13). Thus, the specific heat will be regular for the 2D XY-model and exhibit no singularity at T_{KT} as follows from renormalization group and h.t.s. studies for the XY-model as well as for the planar model [68S2, 74B7, 74K5, 77B4, 79B7, 81S2]. Probably there will be a broad maximum as shown in Fig. 4.11 for the ideal 2D Heisenberg model. The Schottky-type anomaly is explained in this case as corresponding to the gradual dissociation of vortex-antivortex pairs with increasing temperature [79B7]. The results of Monte Carlo simulations brought some surprise with respect to the magnetic specific heat. In contrast to the above predictions, C_{magn} revealed a sharp peak at temperatures somewhat higher than T_{KT} for all three models, namely at $T = 1.15\,T_{KT}$ for the plane rotator model [79T1], at $T = 1.13\,T_{KT}$ for the 2D classical XY-model [84G4] and at $T = 1.02\,T_{KT}$ for the $S = \frac{1}{2}$ 2D XY-model [84R4, 84R5]. Moreover, the experimental data of C_{magn} for Rb_2CuF_4 and $(C_nH_{2n+1}NH_3)_2CuCl_4$ with n = 1, 2 in Fig. 4.11 show also such sharp peaks which could be due to a singularity of the specific heat. But, as already mentioned in the last section, we are not sure whether this is really due to the 2D XY-model or to Ising-like or to 3D behaviour.

A comparison of the predictions for ξ and χ (Eqs. 4.43–4.45) with the experimental data will show that the ferromagnetic compounds under consideration are really realizations of the 2D XY-model, at least in the wavevector or temperature range where they can be expected to show 2D XY-behaviour. The crossover to the 3D XY-range and the 2D Heisenberg range will be discussed in detail in the next section. Here, we will concentrate on the comparison of the experimental data with the theory. As in Sect. 4.1.5 for antiferromagnets, also for the easy-plane ferromagnets K_2CuF_4 and Rb_2CrCl_4 a very effective method for determining κ and χ is quasi-elastic neutron scattering [82H5, 82H6, 93A]. In addition, the susceptibility χ of ferromagnets can also be determined by magnetic measurements which have partly been static or dc ones [76D5, 81H2, 86K2] with $\chi_{\parallel}$ for $\boldsymbol{H_0} \parallel \boldsymbol{a}$ and $\chi_{\perp}$ for $\boldsymbol{H_0} \parallel \boldsymbol{c}$ in case of K_2CuF_4. Partly, these were ac studies where $\boldsymbol{m} \sim e^{-2\pi i f t}$ is the response to an ac field $\boldsymbol{h} \sim e^{-2\pi i f t}$. Then, the ac susceptibility tensor is (cf. Eq. 3.95 in Sect. 3.2.3)

$$\chi_{\text{ac}}^{\alpha\alpha} = \partial m_\alpha / \partial h_\alpha \tag{4.52}$$

with $\alpha = x, y, z$ (coordinate axes) or $\alpha = a, b, c$ (crystalline axes). The frequency f is usually between

500 Hz and 1 kHz. For measuring the frequency dependence of χ_{ac} and for determining the relaxation time τ_c (cf. Sect. 4.2) a wide range of frequencies was employed, e.g. 0.3 Hz–50 kHz [89D3] and 1 MHz–200 MHz [80H6].

The cross section for diffuse neutron scattering has already been derived in Sect. 4.1.5 (cf. Eqs. 4.21–4.26). If the magnetization M is parallel to the x-axis, the susceptibility tensor for neutron scattering becomes (cf. Eq. 4.25)

$$\chi^{\alpha\beta}: \quad \chi^{xx} = \chi_{\parallel} \quad \chi^{yy} = \chi_{\perp} \quad \chi^{zz} = ?$$

Since all measurements have been performed with $\boldsymbol{K} \parallel \boldsymbol{c}$, it follows from Eq. 4.21 that χ^{zz} will not be observed and that the quasi-elastic scattering cross section becomes (cf. Eq. 4.26 and [73H3])

$$\left.\frac{\mathrm{d}\sigma}{\mathrm{d}\Omega}\right|_{\mathrm{D}} \sim \frac{\mu_0 k_{\mathrm{B}} T}{(g\mu_{\mathrm{B}})^2}\left[\chi_{\perp}(q,T) + \chi_{\parallel}(q,T)\right] \tag{4.53}$$

where $\boldsymbol{K} = \boldsymbol{Q}_0 + \boldsymbol{q}$ has been used and $\boldsymbol{Q}_0$ been dropped as in Eq. 4.27. In Eq. 4.53, the ordinary temperature T is given and not the reduced one since there are two of the latter now: t with respect to T_C and $\tilde{t}$ with respect to T_{KT}. The neutron intensity has been scanned across the ferromagnetic Bragg rod for K_2CuF_4 [82H5, 82H6] and for Rb_2CrCl_4 [93A] at various temperatures above and below T_C. Hirakawa and Ikeda [73H3] have concluded from their considerations that in case of K_2CuF_4 $\chi_{\parallel}$ and $\chi_{\perp}$ have to be distinguished only in a very narrow range around T_C: $T_C \pm 0.03$ K. Below T_C, $\chi_{\perp}$ is dominant and $\chi_{\parallel}$ can be neglected. In the paramagnetic region ($T > T_C + 0.03$ K), on the other hand, we have $\chi_{\parallel} = \chi_{\perp} = \chi$.

The neutron scattering results for $T > T_C$ have been analysed mostly by means of the Ornstein-Zernike form χ_{OZ} (Eq. 4.28) and in some cases by the Fisher approximant χ_F (Eq. 4.29). The resulting $\kappa(T)$ and $\chi(T)$ have been fitted with reasonable success to the Kosterlitz-Thouless theory Eqs. 4.43 and 4.44, for K_2CuF_4 in the 2D XY-range $6.6\,\mathrm{K} \le T \le 7.3\,\mathrm{K}$ [81H2, 82H5, 82H6] and for Rb_2CrCl_4 [93A] in the range $55\,\mathrm{K} \le T \le 120$ K. The experimental data and the fit curve are shown for $\kappa(T)$ of K_2CuF_4 in Fig. 4.16 and for $\chi(q = 0, T)$ of Rb_2CrCl_4 in Fig. 4.17. The agreement between experimental data and theoretical curves is obviously good and thus gives evidence for the 2D XY critical behaviour of these two easy-plane ferromagnets. The fit parameters are listed in Table 6.

Closer to T_C, the two compounds exhibit 3D critical behaviour (3D XY-model) with the conventional power laws for $\chi(T)$ and $\kappa(T)$. Therefore, the interlayer exchange coupling (J') and also q_z have to be included in the analysis of $\chi(\boldsymbol{q})$ in this temperature range near T_C ($T < 55$ K for Rb_2CrCl_4). This inclusion is achieved with a mean-field form for $\chi(\boldsymbol{q}, T)$ due to Marshall and Lowde [68M2]

$$\chi(q,T) = \frac{\chi_0}{(T - T_C)/T_C + [J(0) - J(\boldsymbol{q})]/J(0)} \tag{4.54}$$

where $\quad \chi_0 = C/T \quad$ (Eq. 4.8) $\quad$ and $\quad J(\boldsymbol{q}) = \sum\limits_{r_{nn}} J(\boldsymbol{r}_{nn}) \cdot \exp(\mathrm{i}\,\boldsymbol{q}\,\boldsymbol{r}_{nn})$

The summation r_{nn} extends over all nearest neighbours in the layer and in the adjacent layers. For K_2CuF_4 and Rb_2CrCl_4 in the I4/mmm pseudo-cell, we obtain

$$J(\boldsymbol{q}) = zJ\gamma_q + z'J'\gamma'_q \quad \text{and} \quad J(0) = zJ + z'J' \approx zJ$$

where for small q

$$\gamma_q \approx 1 - \frac{a^2}{4}(q_{x0}^2 + q_{y0}^2) \quad \text{and} \quad \gamma'_q \approx 1 - \frac{a^2}{8}(q_{x0}^2 + q_{y0}^2) - \frac{c^2}{8}q_{z0}^2$$

Inserting this with $z = 4$ and $z' = 8$ into Eq. 4.54 and replacing the mean-field expression $4\,(T - T_C)/T_C$ by the conventional form for the inverse correlation length $(\kappa_0^+ a\, t^{\nu^+})^2$, the final expression of $\chi(\boldsymbol{q}, T)$ for the determination of $\kappa(T)$ is

$$\chi(q,t) = \frac{4\chi_0}{(\kappa_0^+ a\, t^{\nu})^2 + a^2(q_{x0}^2 + q_{y0}^2) + (J'/J)c^2 q_{z0}^2} \tag{4.55}$$

where now the reduced temperature $t = T/T_C - 1$ is taken with respect to T_C. Since the scans across the ferromagnetic Bragg rod are along q_{x0} or q_{y0} at a fixed value of q_{z0}, Eq. 4.55 can be converted to the usual Ornstein-Zernike form (Eq. 4.28) for determining $\kappa(t)$

$$\chi_{OZ}(q,t) = \frac{\chi(0,t)}{1 + (q_{x0}^2 + q_{y0}^2)/\kappa^2} \tag{4.56}$$

with $\kappa^2 = (\kappa_0^+ t^{\nu})^2 + \kappa_z^2$ and $\kappa_z^2 = (J'/J)\cdot(c/a)^2 \cdot q_{z0}^2$. Instead of the Ornstein-Zernike form, also other approximate forms from Sect. 4.1.5 (see Eqs. 4.29–4.31) may be used. For the available experimental data, the so obtained values of the critical exponents γ and ν are mostly close to the values for the 3D XY-model ($\gamma = 1.32$ and $\nu = 0.67$, see Table 7), e.g. For Rb_2CrCl_4 $\gamma = 1.35(2)$ from LMB studies [86K2] and $\nu = 0.825(25)$ from quasi-elastic neutron scattering [93A]. Measurements of $\chi(q, t)$ very close to T_C ($\kappa^2 = \kappa_z^2$!) offer the possibility of determining the interlayer exchange constant J'. For $T \approx T_C$, the Lorentzian width κ of $\chi(q, t)$ is given solely by κ_z, and J' can be evaluated from the experimental value of κ_z, from the lattice constants and the intralayer exchange constant J

$$J' = J(\kappa_z a)^2/(q_{z0}\, c)^2 \tag{4.57}$$

The value for K_2CuF_4 is $J' = 0.0020$ K as derived from neutron scattering employing Eq. 4.57 [73H3] in good agreement with $J' = 0.0022$ K from FMR parallel pumping experiments (see Table 5 and [74Y1, 76Y2]). For Rb_2CrCl_4, $J' \approx 0.0011$ K is obtained by means of Eq. 4.57 [93A, 93V].

The intensity I_{rod} of the quasi-elastic neutron scattering from the ferromagnetic Bragg rods of these compounds, especially of K_2CuF_4, is rather high below T_C and increases linearly with temperature ([82H5, 82H6], see also [73H3, 79H2, 80H8]). The corresponding experimental data are reproduced in Fig. 4.18. Surprisingly, this intensity depends also strongly on the position ζ_{z0} at which the scan across the rod has been taken, namely at $\boldsymbol{Q}_0 \mathrel{\hat{=}} (0, 0, 2 - \zeta_{z0})$. We recall from Sect. 4.1.5 that for $T < T_C$ the wavevector dependent susceptibility $\chi_\perp$ depends on the magnon spectra as outlined in the discussion about $\kappa_\perp^-$ in context with Eq. 4.35. For the ferromagnet K_2CuF_4 with no spin-wave gap ($\omega \to 0$ for $\boldsymbol{q} \to 0$), spin waves with much lower energy occur than in antiferromagnets like K_2MnF_4 and Rb_2MnCl_4 since there the lowest magnon energy is the spin-wave gap $h\nu_{AFMR}$. Therefore the low-energy spin waves in the ferromagnet will give rise to larger neutron scattering intensities. Hirakawa and Yoshizawa [79H2] have performed a spin-wave calculation for a quantitative explanation of the experimental data in Fig. 4.18. Starting with an expression equivalent to Eq. 3.71 (Sect. 3.2.1), they have calculated the spin-wave energies $\hbar\omega(\boldsymbol{q})$ and the number of magnons excited in thermal equilibrium $n(\boldsymbol{q}) = [\exp(\hbar\omega_q / k_B T) - 1]^{-1}$ (cf. Eqs. 3.15 and 3.18 in Sects. 3.1.2 and 3.1.3) where $\boldsymbol{q} = \boldsymbol{K} - \boldsymbol{Q}_0 = (0, 0, \zeta_{z0} c^*)$ is the magnon wavevector on top of the ferromagnetic ridge. Then $n(\boldsymbol{q})$ has been convoluted with the resolution function $R(\boldsymbol{q})$ of the neutron spectrometer in order to obtain an expression proportional to the scattering intensity $I(\boldsymbol{q})$

$$I(\boldsymbol{q}) \sim \int_{q'} f^2(\boldsymbol{K})\, n(\boldsymbol{q}+\boldsymbol{q}')\, R(\boldsymbol{q}+\boldsymbol{q}')\, \mathrm{d}^3\boldsymbol{q}' \tag{4.58}$$

In Eq. 4.58, $f(\boldsymbol{K})$ is the magnetic form factor of Cu^{2+} [76A6]. The result of this calculation is shown for $T = 4.21$ K in Fig. 4.19 together with the corresponding experimental data for K_2CuF_4. These are the difference of the neutron scattering data at 4.21 K for zero external field and those at the same temperature but for $H_0 = 0.2$ T where the diffuse scattering intensity below T_C is practically zero (see Fig. 1 of [79H2]). The theoretical data in Fig. 4.19 have been calculated for the XY-model (solid curve) and for the Heisenberg model (broken curve). The difference between these two results from the slower increase of $\hbar\omega_q$ with ζ_{z0} for the Heisenberg model as compared to the XY-model. For K_2CuF_4 $(\widetilde{J}_A = 0)$ in zero magnetic field ($H_0 = 0$), Eq. 3.71 yields for the magnon energies on top of the ridge ($q_{x0} = 0$, $q_{y0} = 0$) in case of the XY-model ($J_A \neq 0$)

$$\hbar\omega(q_{z0}) = 2S\sqrt{2zz'J_A J'}\,\sin\left(\tfrac{\pi}{2}\zeta_{z0}\right)$$

and in case of the Heisenberg model ($J_A = 0$)

$$\hbar\omega(q_{z0}) = 4S\,z'J'\sin^2\left(\tfrac{\pi}{2}\zeta_{z0}\right)$$

in complete analogy to Eqs. 4.49a and 4.49b. The quadratic dependence of $\hbar\omega_q$ on ζ_{z0} for the latter causes smaller values of $\hbar\omega_q$ for small ζ_{z0} and thus higher scattering intensities I_{rod}. The experimental data in Fig. 4.19 agree well with the calculated data for the XY-model but not with those for the Heisenberg model. From Figs. 4.18 and 4.19, it is clear that the diffuse scattering intensity seems to diverge for $\zeta_{z0} \to 0$. Since no LRO exists in the 2D XY-model, this high intensity is not identified as a Bragg point magnetic intensity but is interpreted as the divergence of χ predicted for the 2D XY-model at all $T \leq T_C$ (cf. Eq. 4.45). Thus, the experimental data in Figs. 4.18 and 4.19 are in accordance with this model.

When we now look at the other experimental data for $T < T_C$ we find that they are not all in agreement with the predictions for the ideal 2D XY-model. For example, both compounds, K_2CuF_4 and Rb_2CrCl_4, have a Curie-temperature below which they exhibit a 3D LRO with a magnetization $M \neq 0$ [73H3, 77F2, 79D3]. Fig. 4.20 presents the reduced magnetization $M(T)/M(0)$ for K_2CuF_4 as a function of reduced temperature T/T_C and, for comparison, the sublattice magnetization $M_{subl}(T)/M_{subl}(0)$ for K_2MnF_4 and K_2NiF_4 versus T/T_N. The data for K_2CuF_4 have been measured independently by two methods, by NMR [73K2] and by neutron diffraction [73H3]. In the last section, a finite Curie temperature T_C and a transition to magnetic LRO has been ascribed to the perturbations of the 2D Heisenberg model (cf. Sect. 4.1.7), namely the anisotropy fields and the interlayer exchange interaction (cf. Eq. 4.38). And we have to keep in mind that Eqs. 4.43–4.48 are theoretical results for an ideal XY-model while all materials considered as a realization of this model have usually a finite out-of-plane anisotropy field (J_A in K_2CuF_4, D in Rb_2CrCl_4), an interlayer exchange coupling ($J' \neq 0$) and an in-plane anisotropy field ($P \neq 0$ in Rb_2CrCl_4). It is therefore necessary to extend our consideration to a 2D XY-model with perturbations. As a first step, we will discuss the 2D anisotropic Heisenberg model which provides a continuous change from the ideal 2D XY-model to the ideal 2D Heisenberg model. The Hamiltonian of this XXZ model is usually written as follows

$$\mathcal{H} = -2J\sum_{\langle i,j\rangle}\left[S_{i,x}S_{j,x} + S_{i,y}S_{j,y} + \lambda\, S_{i,z}S_{j,z}\right] \qquad (0 \leq \lambda < 1) \tag{4.59}$$

where the same notation is used as in Eq. 4.2 (Sect. 4.1.1). The parameter λ describes an out-of-plane anisotropic exchange as introduced for K_2CuF_4 (cf. Eq. 3.69 in Sect. 3.2.1). In Eq. 4.59, $\lambda = 0$ corresponds to the 2D XY-model and $\lambda = 1$ to the 2D Heisenberg model. The low-temperature in-plane and out-of-plane static and dynamic behaviour of this model with general λ are discussed in a number of publications [92M5, 93M2, 94P2]. Monte Carlo simulations at higher temperatures [82K3, 86K4, 92M4, 93P2, 95C3, 96B] yield the λ-dependence of T_{KT}. All these results show that T_{KT} decreases only slightly with increasing λ (cf. Fig. 2 of [86K4], Fig. 2 of [92M4] and Fig. 3 of [96B]) and approaches zero logarithmically for $\lambda \to 1$ as predicted theoretically [76K9, 80H7]

$$\widetilde{T}_{KT}(\lambda \to 1) \sim |\ln(1-\lambda)|^{-1} \tag{4.60}$$

The studies for various values of λ outside the range of Eq. 4.60 [92D2, 95C2, 95C3, 96B] confirm that even a slight anisotropy ($1 - \lambda << 1$) leads still to a Kosterlitz-Thouless transition. For the classical XXZ ferromagnet, Cuccoli et al. obtained $\widetilde{T}_{KT} = 0.561$ for $\lambda = 0.99$. For a $S = \frac{1}{2}$ quantum XXZ antiferromagnet, the corresponding result is $\widetilde{T}_{KT} = 0.25$ for $\lambda = 0.98$ [92D2] where we recall that the theoretical result $\widetilde{T}_{KT}$ is the same for ferro- and antiferromagnets. A further result of Monte Carlo simulations [89G4, 94W] is that for λ below a critical value λ_C planar or in-plane vortices are stable while for $\lambda > \lambda_C$ out-of-plane vortices, i.e. vortices with out-of-plane components, become stable. The value of λ_C depends on the lattice type. For the square lattice it is $\lambda_C = 0.7044$ [94W]. From these results, the vortices in K_2CuF_4 ($\lambda = 0.99$) are expected to have out-of-plane components and thus to be different from those in an ideal XY-system [90H].

The out-of-plane anisotropy breaks the Heisenberg isotropy but not the symmetry of the 2D XY-model or the plane rotator model. But the latter symmetry is broken by an in-plane anisotropy field. Thus it is of special interest to undertake theoretical studies of the 2D XY-model with an in-plane anisotropy field h_p as a perturbation [75V, 77J2, 83L, 86K5, 89G3] where p denotes its p-fold symmetry. For h_2, i.e. a two-fold Ising-like symmetry (p = 2), the Kosterlitz-Thouless phase transition and the formation of vortices are suppressed [77J2]. For sufficiently small in-plane anisotropy field and for p ≥ 6, two transitions are expected. With decreasing temperature, the system will undergo at $T = T_{KT}$ a transition to a Kosterlitz-Thouless phase with topological LRO and at $T = T_C < T_{KT}$ a transition to an Ising-like ordered phase [77J2]. For the perovskite-type layer structures under consideration, e.g. in Rb_2CrCl_4 (cf. Eq. 3.81 and Fig. 3.34 in Sect. 3.2.2), the in-plane anisotropy field has 4-fold symmetry which is on the borderline between these two cases p < 4 and p > 4. Monte Carlo simulations have revealed that h_4 will probably not destroy the topological LRO [83L]. The results of a model simulation for Rb_2CrCl_4 [89G3] give evidence for also two transition temperatures in case of h_4, $\widetilde{T}_1 = 0.5$ and $\widetilde{T}_2 = 0.8$ where $\widetilde{T}_2$ corresponds to $\widetilde{T}_{KT}$ while $\widetilde{T}_1$ cannot be observed because of the onset of 3D ordering.

A third type of perturbation of the ideal 2D XY-model is the interlayer exchange coupling. Hikami and Tsuneto [80H7] have treated this problem and found that there will be a spontaneous magnetization for $J' \neq 0$

$$M(T) \sim (J'/J)^{\eta(T)/4} = (J'/J)^{1/(8\pi\widetilde{K}_{\mathrm{eff}})} \tag{4.61}$$

where $\eta(T)$ and $\widetilde{K}_{\mathrm{eff}}(T)$ have been defined in context with Eqs. 4.47 and 4.48. This magnetization results from the fact that close to T_C the compound with interlayer coupling will show 3D behaviour as explained in the analysis of χ above (cf. Eqs. 4.54 and 4.55). For the ideal 2D XY-model with $J' = 0$, this will not be the case and, accordingly, Eq. 4.61 yields $M \equiv 0$. Another argument is based on the discussion of the magnon dispersion curves of K_2CuF_4 in Sect. 3.2.1 that for wavevectors smaller than $\boldsymbol{q} = (\zeta_1 a^*, 0, 0)$ the system behaves not two-dimensionally but three-dimensionally. Therefore we can expect the behaviour according to the 2D XY-model only for lengths smaller than a/ζ_1. This will be more elucidated by introducing finite-size effects as they are encountered in all Monte Carlo simulations [79B8, 86B4]. Miyashita et al. [78M3, 80M9] have studied the plane rotator model (Eq. 4.41) by the Monte Carlo method and focussed their attention on the finite-size effects which become obvious especially for $T < T_C$. They introduce a reduced susceptibility $\hat{\chi}$ and the average of the square of the magnetization $\langle \hat{M}^2 \rangle$, both as dimensionless quantities. When N is the number of rotators or spins, the size dependence of $\hat{\chi}$ and $\langle \hat{M}^2 \rangle$ can be expressed as [78M3]

$$\hat{\chi} = \langle \hat{M}^2 \rangle / N = N^{\mathrm{a}(T)} \tag{4.62}$$

where a(T) is a new temperature-dependent exponent which is related to $\eta(T)$ and $\tilde{K}_{\mathrm{eff}}(T)$ by

$$\mathrm{a}(T) = 1 - \tfrac{1}{2}\,\eta(T) = 1 - [4\pi\,\tilde{K}_{\mathrm{eff}}(T)]^{-1} \tag{4.63}$$

We recall from Eqs. 4.48a and 4.48b that, in general, $\tilde{K}_{\mathrm{eff}}$ is renormalized due to the presence of vortices. Only for low temperatures, it can be replaced by the spin-wave approximation $\tilde{K} = 2S^2 J / k_B T$. At $T = T_{KT}$, the universal values $\eta = 0.25$, $\tilde{K}_{\mathrm{eff}} = 2/\pi$ and $\delta = 15$ imply a(T_{KT}) = 0.875. Kawabata and Bishop [82K3] have used Eq. 4.62 to evaluate a(T) and $\eta(T)$ from their Monte Carlo results. Hirakawa and Ubukoshi [81H2] have measured $M(H_0, T)$ of K$_2$CuF$_4$ for $\boldsymbol{H_0} \parallel \boldsymbol{a}$ and determined a(T) and the exponent $\delta(T)$ (cf. Eq. 4.46) from their experimental results for $\chi = \partial M / \partial H$ by means of Eq. 4.62 and by using the relations

$$\delta(T) = \frac{1 + \mathrm{a}\,(T)}{1 - \mathrm{a}\,(T)} = 8\pi \tilde{K}_{\mathrm{eff}} - 1 \qquad \text{or} \qquad \mathrm{a}(T) = \frac{\delta(T) - 1}{\delta(T) + 1} \tag{4.64}$$

which result from the application of the relations for δ and η in Eq. 4.13 (Sect. 4.1.2) for d = 2. Cornelius et al. [86C1] have derived a(T) and δ(T) in a similar way for Rb$_2$CrC1$_4$. For K$_2$CuF$_4$, the temperature dependence of a(T) derived from the experimental data [81H2] is illustrated in Fig. 4.21 (open circles) compared to the result of a Monte Carlo simulation for a 50 × 50 lattice (filled circles). For $T \to 0$, we have a = 1 as expected and for low T, the data agree quite well with the spin-wave approximation (dashed line in Fig. 4.21). With increasing temperature, a(T) approaches its universal value 0.875 at the Kosterlitz-Thouless temperature T_{KT}. At T_{KT}, it is expected to drop discontinuously to zero [78M3, 81H2, 82H6, 82K3, 86C1]. But the experimental as well as the Monte Carlo data in Fig. 4.21 show a drastic but still continuous decrease above T_{KT} which is probably due to finite-size effects (see below). It is further obvious that $\chi \to \infty$ at all $T \le T_{KT}$ (Eq. 4.45) is valid only for an infinite system and that Eq. 4.62 agrees with that for $N \to \infty$. Also the spontaneous magnetization M which should be zero in an ideal 2D XY-system is a finite-size dependent phenomenon. Bramwell and Holdsworth [93B1, 93B2] derived the following expression (see also [79T1])

$$M(N, T) \sim (2N)^{-\eta(T)/4} = (2N)^{-1/(8\pi \tilde{K}_{\mathrm{eff}})} \tag{4.65}$$

where N again is the number of rotators or spins. Further, Eq. 4.65 yields $M \to 0$ for $N \to \infty$ as required by the theory for an infinite system. For $T < T_C$, the magnetization $M(N, T)$ of a finite-size 2D XY-system follows a conventional power law $M \sim (-t)^{\beta}$ with t as the ordinary reduced temperature $t = T/T_C - 1$ and where the exponent β has a universal value [93A, 93B1, 93B2]

$$\beta = 3\pi^2/128 = 0.23132\ \ldots \tag{4.66}$$

This value of β is quite different from the values in Table 7 of the 2D Ising model ($\beta = 0.125$) and of 3D systems ($\beta = 0.3\ \ldots$). And the meaning of the experimental result was not so clear when $\beta = 0.22$ was determined for K_2CuF_4 in the range $0.07 \le |t| \le 0.3$ from neutron scattering experiments [72H2, 73H3, 90J1] and $\beta = 0.24$ in the same range from LMB studies [80K2]. For Rb_2CrCl_4, $\beta = 0.23$ has been obtained in the range $T < T_C - 0.8$ K from neutron scattering data [93A] and $\beta = 0.28$ from LMB [82K2]. A comparison of the experimental values of β of a great variety of A_2MX_4 compounds shows that most of these values are either close to 0.125 (2D Ising) or to 0.231 (2D XY) [93B2].

Another consequence of the finite size of the system is that there is not only one transition temperature but there are three characteristic temperatures [80H7, 93B1, 94B2]

1) T_{KT}: is to be used in $\tilde{t} = T/T_{KT} - 1$, $\xi(T)$ and $\chi(T)$ for $T > T_C$ (Eqs. 4.43 and 4.44).

2) T^*: at this T, $\eta(T)$, $\tilde{K}_{\text{eff}}(T)$ have their universal values $\eta(T^*) = 0.25$, $\tilde{K}_{\text{eff}}(T^*) = 2/\pi$.

3) T_C: the ordering temperature, to be used in $t = T/T_C - 1$, $M \sim (-t)^\beta$ (Eq. 4.66)

These three temperatures are different because of the finite size of the system [80H7, 93B1, 94B2]

$$\tilde{T}^* = \tilde{T}_{KT} + \frac{\pi^2}{4c(\ln L)^2} \qquad \tilde{T}_C = \tilde{T}_{KT} + \frac{\pi^2}{c(\ln L)^2} \tag{4.67}$$

where $L = \sqrt{N}$ is a characteristic length of the system, in units of the lattice constant a, and where c is a factor to be discussed in more detail in context with Eq. 4.68. $\tilde{T}_{KT}$, $\tilde{T}^*$ and $\tilde{T}_C$ are again the temperatures measured in units of $2S^2J$ or $2\tilde{S}^2J$ (quantum systems) as defined in Eq. 4.43a. For an infinite system, all three merge into one transition temperature T_{KT}. In the temperature range near T_{KT} and T^*, Bramwell and Holdsworth [94B1] have derived values of the relative spin stiffness $\tilde{K}_{\text{eff}}$ for Rb_2CrCl_4 from various experimental data, namely from inelastic neutron scattering [81H4, 86H2] by means of Eq. 4.51, from weak field magnetism [86C1] using Eqs. 4.46 and 4.64 and from neutron diffraction [93A] employing an inverted form of Eq. 4.65

$$\tilde{K}_{\text{eff}} = -\frac{1}{8\pi}[\ln(2N)/\ln M(T)] \tag{4.65a}$$

where M is the magnetization obtained from the magnetic contribution $I_{\text{magn}} \sim M^2$ to the Bragg peak (0, 0, 4) and N is the number of spins for which an effective value N_{eff} has been inserted (see below). The results of this comparison are shown in Fig. 4.22. The data obtained by these different methods agree with each other in a convincing way and also with the theoretically derived slope $\partial\tilde{K}_{\text{eff}}/\partial T$ at $T = T^*$. Please note that the "universal jump" (Eq. 4.48c) is not observed for $\tilde{K}_{\text{eff}}$ in Fig. 4.22, there is only a drastic continuous decrease above T^* which has been explained as a rounding resulting from finite-size effects. Thus, the data in Fig. 4.22 can be considered as a strong evidence that the interpretation of the experimental data in terms of a finite-size 2D XY-model is correct. The analysis of the data for Rb_2CrCl_4 yields with respect to this model for the characteristic temperatures assuming that the spins ($S = 2$ in this case) can be treated classically [81H4, 86C1, 93A, 95B1] and taking values for J etc. from Table 5

Rb_2CrCl_4: $T_{KT} = 43.4$ K $\quad T^* = 45.6$ K $\quad T_C = 52.4$ K

$\tilde{T}_{KT} = 0.718 \quad \tilde{T}^* = 0.754 \quad \tilde{T}_C = 0.866 \quad (2S^2J = 60.48\ \text{K})$

Bramwell et al. [94B1, 94B2, 95B1] have derived this finite-size 2D XY-model especially for Rb_2CrCl_4 on a classical basis. They have used the difference $\tilde{T}_C - \tilde{T}_{KT}$ to calculate a value for $L = L_{eff}$ and $N = N_{eff}$ by means of Eq. 4.67 using for the nonuniversal parameter c the following relation [95B1]

$$c = \frac{\pi^2}{\tilde{T}_{KT} b^2} \tag{4.68}$$

where $b = 2.12$ is the parameter in the exponential temperature dependence of ξ (Eq. 4.43). In this way, they obtained $L_{eff} \approx 100$ and $N_{eff} \approx 10^4$ which are to be compared to experimental data. Neutron scattering data show that the correlation length ξ in Rb_2CrCl_4 [93A, 95B1] is not infinite below T_C (cf. Eq. 4.45) but is nearly constant at a small but finite value $(\xi/a)^{-1} \cong 0.0125$ (see Fig. 4.23). The value $\xi/a = 80$ may then be considered as L_{eff} in agreement with the above value. It has further already been mentioned in context with Eq. 4.61 that 2D XY-model behaviour can only be expected on length scales smaller than about $(J/J')^{1/2}$ which is also an estimate for L_{eff}, and J/J' for N_{eff} where J and J' are the intralayer and interlayer exchange constants. For Rb_2CrCl_4 (cf. Table 5), this ratio is $J/J' \approx N_{eff} \approx 7000$, also in reasonable agreement with the value calculated from $\tilde{T}_C$ and $\tilde{T}_{KT}$. Although such a procedure has not yet been reported in the literature, let us now use the quantum description for the spin in Rb_2CrCl_4 and replace S by $\tilde{S} = S + \frac{1}{2} = \frac{5}{2}$. Then, we obtain

Rb_2CrCl_4: $\tilde{T}_{KT} = 0.459$ $\tilde{T}^* = 0.483$ $\tilde{T}_C = 0.552$ $(2\tilde{S}^2 J = 94.50\ \mathrm{K})$

This value for $\tilde{T}_{KT}$ fits better to the theoretical results for the quantum XXZ model by Biagini et al. [96B] than the classical value although the data for Rb_2CrCl_4 are with $\lambda \approx 0.93$ ($\lambda \approx 1 - D/2J$) somewhat outside the range of their calculation of $\tilde{T}_{KT}$. For the quantum treatment, the values for L_{eff} and N_{eff} obtained with Eq. 4.67 are the same as above if c is calculated using Eq. 4.68. For K_2CuF_4 finally, only this treatment is justified because of $S = \frac{1}{2}$ ($\tilde{S} = 1$). The characteristic temperatures are in this case [72H2, 73H3, 81H2, 82H5, 82H6]:

K_2CuF_4: $T_{KT} = 5.50\ \mathrm{K}$ $T^* = 5.69\ \mathrm{K}$ $T_C = 6.25\ \mathrm{K}$
$\tilde{T}_{KT} = 0.231$ $\tilde{T}^* = 0.238$ $\tilde{T}_C = 0.262$ $(2\tilde{S}^2 J = 23.86\ \mathrm{K})$

The value for $\tilde{T}_{KT}$ of K_2CuF_4 with $\lambda = 1 - J_A/J = 0.99$ (cf. Table 5) agrees very well with the quantum Monte Carlo data of Ding [92D2]. By means of Eqs. 4.67 and 4.68, we obtain $L_{eff} \approx 60$ and $N_{eff} \approx 3600$ for K_2CuF_4 in comparison to $J/J' \approx 5700$.

On the basis of all data discussed in this section, we conclude that the easy-plane compounds K_2CuF_4 and Rb_2CrCl_4 show the critical behaviour of a 2D XY-model according to the Kosterlitz-Thouless theory and its complements for finite-size effects, at least in certain wave-number and temperature ranges. The corresponding temperature ranges are shown for Rb_2CrCl_4 in Fig. 4.23. In a small range around T_C (51 K–55 K), the system exhibits 3D behaviour. At higher temperatures, the experimental data fit well to the 2D XY-model (Eqs. 4.43 and 4.44) while at temperatures below T_C finite-size 2D XY-model behaviour, together with the 3D ordering, is observed (Eqs. 4.62–4.67) with the finite size determined by the interlayer exchange coupling. This finite-size 2D XY-behaviour is also expected for the spin-flop phase of uniaxial antiferromagnets. And for the spin-flop phase of Rb_2MnCl_4, the analysis of neutron diffraction data yields actually $\beta = 0.26$ [96K, 98K1] close to the 2D XY value (Eq. 4.66). A still unanswered question concerns the magnetic contribution to the specific heat (C_{magn}) where experimental data and Monte Carlo simulation data show a sharp spike at a temperature near T_C in contrast to the theoretical prediction. In one study of K_2CuF_4 the spike was reported to be analysed [76Y1] a symmetric logarithmic singularity (2D Ising model). Probably, the magnetic specific heat of the 2D XY-model exhibits a sharp spike but not necessarily a singularity. But this spike cannot be ascribed to finite-size effects since the results of Monte Carlo simulations [89F2, 92G2] show that ξ and χ are sensitive to finite-size effects while C_{magn} is insensitive to them.

9.12.4.1.9 Crossover Phenomena

In the discussion of the magnetic properties of the easy-plane ferromagnets K_2CuF_4, Rb_2CuF_4 and similar compounds, a number of crossovers (abbreviated: ×-overs) have already been discussed. First examples were the magnon dispersion relation $\hbar\omega(\boldsymbol{q})$ of K_2CuF_4 (Figs. 3.30 and 3.31 in Sect. 3.2.1) and Rb_2CrCl_4 (Fig. 3.35 in Sect. 3.2.2). At certain wavevectors (ζ_1 and ζ_2 in Fig. 3.31) ×-overs are observed from 2D Heisenberg to 2D XY-model and from 2D XY- to 3D XY-model behaviour. Such ×-overs are also observable in the temperature variation of M, κ, χ. We recall from Sect. 4.1.7 that the susceptibility data of the compounds $(C_nH_{2n+1}NH_3)_2CuCl_4$ with n = 1, 3, 10 and of K_2CuF_4 in Fig. 4.10 deviate at a ×-over point from the common curve χ_H of the 2D Heisenberg model to higher values [76N2] when the out-of-plane anisotropy $h_A = J_A/J$ becomes important, namely to 2D XY-behaviour (K_2CuF_4) or possibly to 2D Ising behaviour $[(C_nH_{2n+1}NH_3)_2CuCl_4]$. In Fig. 4.10, the deviation from χ_H is proportional to h_A. All compounds undergo a further ×-over to 3D behaviour when h'_E becomes relevant. Based on the experimental data about the critical behaviour of Rb_2CrCl_4, Fig. 4.23 shows the ×-overs 2D XY ↔ 3D XY above and below T_C at the crossover temperatures $T_\times \approx 51$ K and $T_\times \approx 55$ K. Generally, it is an indication for a ×-over when the usual log-log plot does not result in a straight line. This has, for example, been observed for χ of K_2CuF_4 [75D2, 76D5]. One possibility is that the log-log plot yields a completely bended curve which is the case for K_2CuF_4 in the 2D XY-range for $T > T_C$ where not a power law is expected for χ but an exponential dependence (cf. Eq. 4.44). A second possibility is that the log-log plot exhibits two or more straight parts with bended sections between them where a ×-over happens. This is shown for the magnetization M of K_2CuF_4 [73H3, 90J1] in Fig. 4.24 as obtained from the magnetic Bragg intensity I_{magn} of (0, 0, 1) reflections (l = 2, 4, 6, 8, 10, 12). The critical exponent β derived from $I_{\text{magn}} \sim M^2$ shows a ×-over from $\beta = 0.22$ (2D XY, cf. Eq. 4.66) for $|t| > 0.064$ ($T < 5.85$ K) to $\beta = 0.333$ (3D XY, cf. Table 7) for $|t| < 0.064$ ($T > 5.85$ K). For $T > T_C$, ×-over phenomena have been observed for the susceptibility χ and the inverse correlation length κ in K_2CuF_4 [81H2, 82H5, 82H6, 90H] and in Rb_2CrCl_4 [93A]. For K_2CuF_4, Hirakawa et al. have determined from these data the ×-over temperatures:

3D XY ↔ 2D XY: $T_\times = 6.6$ K
2D XY ↔ 2D Heisenberg: $T_\times = 7.3$ K

Using these temperatures and taking also into account the magnetic fields $H_A = 0.231$ T and H'_E = 12.6 mT (cf. Table 5) which are characteristic for the ×-overs, they [81H2, 82H5, 82H6, 90H] proposed a (T, H)-phase diagram (see Fig. 4.25) with the corresponding ×-over lines. It was shown in the preceding section that χ and κ of K_2CuF_4 agree between $T_\times = 6.6$ K and $T_\times = 7.3$ K with the theoretical predictions for the 2D XY-model (Eqs. 4.43 and 4.44). Below about 5.85 K and for $H_0 = 0$, where Fig. 4.25 indicates 3D behaviour the system shows also finite-size 2D XY-behaviour, e.g. with respect to the magnetization as discussed above in context with Fig. 4.24. From the ×-over temperatures, fields and lines in Fig. 4.25, the impression may arise that these are sharp and well-defined boundaries. But it will be shown below that this is not so and that there are broad ×-over ranges where the system changes gradually from one type to another. Thus, ×-over temperatures and fields are not unique quantities but depend on the definition used in the particular case. They should be taken as a good estimate and not as a rigorous value.

After this introduction with examples, let us enter now into a more systematic treatment of the ×-over phenomena. Since the critical properties depend on the lattice dimension d and then spin dimension n (cf. Sect. 4.1.1) two kinds of crossover have to be distinguished [76J1], namely

1) a lattice dimensionality crossover, e.g. a $d = 2$ to $d = 3$ (2D ↔ 3D) ×-over
2) a spin dimensionality crossover, e.g. a $n = 2$ to $n = 3$ (XY ↔ Heisenberg) ×-over

In the example K_2CuF_4, both types of ×-over have been observed, namely at $T_\times = 6.6$ K a lattice dimensionality one and at $T_\times = 7.3$ K a spin dimensionality one. Theoretical considerations [72L1, 73L4, 76I4, 78N2] treat usually the lattice dimensionality 2D ↔ 3D ×-over in the Ising model because the 2D Ising model undergoes a well defined phase transition. Liu and Stanley [72L1, 73L4] have discussed this case (see Fig. 4.26). Fig. 4.26a shows the transition temperature T_C as a function of the relative interlayer coupling $j' = J'/J$ in a (j', T)-phase diagram which separates the magnetically ordered regime from the paramagnetic one. $T_C(0) > 0$ is the transition temperature of the 2D Ising system. For $j' > 0$, the system behaves as a 3D Ising one, at least for temperatures close to the transition, while its behaviour is 2D Ising-like at higher temperatures. The 3D Ising region is separated from the 2D Ising region by the slightly shaded ×-over range in Fig. 4.26a. Its limits are marked as $T_A(j') = T_{0.01}(j')$ and $T_B(j')$. The scaling hypothesis predicts that all curves $T_m(j')$ [m = A, B, C etc.] approach $T_C(0)$ according to a power law

$$T_m(j') - T_C(0) \sim (j')^{1/\phi} \tag{4.69}$$

where ϕ is the crossover critical exponent (Ising model: $\phi = 1.75$). We note that Eq. 4.69 is only meaningful for the considered Ising model. It has already been mentioned in context with Eqs. 4.18 and 4.33, i.e. critical amplitudes $A \sim (h_A)^{1/2}$ and $\kappa_0^+ \sim (h_A)^{1/4}$, that weakly anisotropic antiferromagnets show Ising-like critical behaviour but the limit $h_A \to 0$ does not lead to meaningful results because the 2D Heisenberg model does not undergo any phase transition for $T > 0$ (cf. Sect. 4.1.7). For $h_A \to 0$, the behaviour of the system depends on other perturbations of the ideal 2D Heisenberg model like h'_E or $\tilde{h}_A$ (cf. Eq. 4.38). Returning to the more lucid ×-over phenomena in the Ising model, we introduce the definition for T_p ($p = 0.01$, 0.1 etc.) [72L1] based on the susceptibility data in order to have a quantitative measure for the temperatures in the ×-over range instead of merely qualitative estimates

$$\chi(T_p, j')/\chi(T_p, 0) - 1 = p \tag{4.70}$$

Such a definition of T_p could also apply to other magnetic properties like the magnetization M or the magnon energies $\hbar\omega(\boldsymbol{q})$. In addition to $T_A(j') = T_{0.01}(j')$, in Fig. 4.26a is also presented $T_{0.1}(j')$ which is nearly in the center of the ×-over range and which could be used as a definition of $T_\times$. For a certain fixed value j'_1 of j' as an example (see dotted line in Fig. 4.26a), the reduced susceptibility $\chi(j'_1)/\chi_0$ is drawn schematically together with $\chi(0)/\chi_0$ of the 2D Ising model in the Fig. 4.26b where $\chi_0 = C/T$ is again the susceptibility of a noninteracting system. The susceptibility $\chi(j'_1)$ diverges at the transition temperature $T_C(j'_1)$ while $\chi(0)$ diverges at $T_C(0)$. Fig. 4.26c finally shows the susceptibility log-log plot. The straight lines correspond in the range $[T < T_B(j'_1)]$ to the 3D Ising critical exponent $\gamma = 1.25$ (cf. Table 7) and in the range $[T > T_A(j'_1)]$ to the 2D Ising critical exponent $\gamma = 1.75$. Between $T_A(j'_1)$ and $T_B(j'_1)$ is the ×-over range. Thus, the three parts of Fig. 4.26 illuminate the various aspects of a 3D ↔ 2D lattice dimensionality ×-over of an Ising system. It was already mentioned that the Cu-compounds $(C_nH_{2n+1}NH_3)_2CuCl_4$ show Ising-like critical behaviour for $T > T_C$, as for example the susceptibility experimental data of the compounds with n = 1 and n = 10 [76J1, 78J] with the expected 3D ↔ 2D ×-over (see Fig. 4.27).

Another useful treatment is the description of the lattice dimensionality crossover by means of a Taylor expansion with $j' = J'/J$ as the expansion parameter. For the susceptibility χ, this expansion reads [72L1, 73L4, 76J1, 76J2, 78N2]

$$\chi(j') = \chi^{(0)}(0) + \chi^{(1)}(0) \cdot j' + \tfrac{1}{2!}\chi^{(2)}(0) \cdot (j')^2 + \ldots \tag{4.71}$$

where $\chi^{(n)}(0) = \partial^n \chi / (\partial j')^n \,|_{j'=0}$ is the n = th derivative of χ with respect to j'. Its asymptotic behaviour is [72K, 72L2]

$$(1 - T_C(0)/T)^{-\gamma(n)} \qquad \text{for} \quad T \to T_C(0) \tag{4.72}$$

with $\gamma(n) = \gamma_{2D} + n\phi$ (Ising model: $\gamma_{2D} = 1.75$ and ×-over exponent $\phi = 1.75$). We can now identify from Eq. 4.71 first $\chi(j') = \chi_{3D}$ and $\chi^{(0)}(0) = \chi_{2D}$ as the susceptibilities for the 3D and the 2D regime, respectively. The first derivative $\chi^{(1)}(0)$ has been determined by Liu and Stanley [72L1, 73L4] and reads in the reduced form χ/χ_0

$$\chi^{(1)}(0)/\chi_0 = 2z'(J/k_BT) \cdot [\chi^{(0)}(0)/\chi_0]^2 \tag{4.73}$$

Neglecting the second order term in Eq. 4.71 and combining the results of Eqs. 4.71 and 4.73, we obtain finally

$$\chi_{3D}/\chi_0 = \chi_{2D}/\chi_0 + (2z'J'/k_BT) \cdot (\chi_{2D}/\chi_0)^2 \tag{4.74}$$

As a consequence of Eq. 4.74, the deviation of χ_{3D} from χ_{2D} depends on the sign of J'. We should also note that a ×-over behaviour is better to observe for ferromagnetic intralayer exchange coupling ($J > 0$) as in the Cu- and Cr-compounds. Then, χ will diverge towards T_C and will give rise to pronounced crossover phenomena. For antiferromagnetic intralayer coupling ($J < 0$), on the other hand, χ stays finite through T_N and crossover phenomena will hardly be observable [76J2]. The statement of Eq. 4.74 has quantitavely been confirmed by a theoretical calculation for the susceptibility of an $S = 1/2$ Ising model with a 2D ↔ 3D lattice dimensionality crossover [78N2], from a square to a simple cubic lattice. The results are reproduced in Fig. 4.28 assuming ferromagnetic intralayer exchange coupling ($J > 0$) which is favourable for the observation of ×-over effects. The center curve (heavy line in Fig. 4.28) is the common χ_{2D} curve, an exact result for the 2D Ising model, from which the χ_{3D} curves deviate at the ×-over to 3D-behaviour, i.e. to larger $\chi/\tilde{\chi}$ values for ferromagnetic interlayer coupling (curves 1, 2, and 3 in Fig. 4.28 with $J'/J = +0.05$, +0.1, and +0.2, resp. and $\tilde{\chi}$: see Eq. 3.28a in Sect. 3.1.3). The deviation is negative, on the other hand, for antiferromagnetic interlayer coupling (curves 4, 5, and 6 with $J'/J = -0.05$, –0.1, and –0.2, resp.). For these antiferromagnets, the shown susceptibility is $\chi_{||}$ ($\chi_{||}/\tilde{\chi}$) which displays a maximum above T_N (arrows in Fig. 4.28) which is typical for quasi-2D antiferromagnets (cf. Figs. 3.9 and 3.12 in Sects. 3.1.3 and 3.1.4). In the experimental susceptibility data, these effects are expected to be observed for the Cu-compounds $(C_nH_{2n+1}NH_3)_2CuCl_4$ since they have the required ferromagnetic intralayer coupling. And in accordance with Eq. 4.74 and with the Ising model calculations (cf. Fig. 4.28), the experimental χ-curve of the compound with n = 1 (see Fig. 4.29) deviates from the common 2D curve to higher values because of ferromagnetic interlayer coupling [76J1, 78J] and the deviation is negative for n = 2 and n = 3 because of antiferromagnetic interlayer coupling. For the antiferromagnets (n = 2 and n = 3), the susceptibility $\chi_{||}$ passes through the above mentioned maximum above T_N. It should be noted that $\chi_\perp$ also typical for an antiferromagnet is not shown in Fig. 4.29.

An expansion of the form Eq. 4.71 can be made for any thermodynamic function of the system near a lattice dimensionality ×-over. For the magnetic contribution C_{magn} to the specific heat, such expansion reads, following the literature now with $h'_E = z'J'/zJ = (z'/z)j'$ as the expansion parameter [77B3]:

$$C_{magn}(h'_E) = C^{(0)}_{magn}(0) + C^{(1)}_{magn}(0) \cdot h'_E + \tfrac{1}{2!}C^{(2)}_{magn}(0) \cdot (h'_E)^2 + \ldots \tag{4.75}$$

where $C_{\mathrm{magn}}^{(\mathrm{n})}$ is the n = th derivative of C_{magn} with respect to h'_{E}. In case of the specific heat, the first derivative vanishes [72L1, 73L4, 76J2] and the ×-over behaviour is determined by the second derivative. In a reduced form, we obtain [73L4, 77B3]

$$[C_{\mathrm{magn}}^{3\mathrm{D}} - C_{\mathrm{magn}}^{2\mathrm{D}}]/C_{\mathrm{magn}}^{2\mathrm{D}} = \tfrac{1}{2!}[C_{\mathrm{magn}}^{(2)}(0)/C_{\mathrm{magn}}^{2\mathrm{D}}]\cdot(h'_{\mathrm{E}})^2 \sim (z'J'/k_{\mathrm{B}}T)^2\cdot(\chi_{2\mathrm{D}}/\chi_0)^2 \tag{4.76}$$

where $C_{\mathrm{magn}}^{3\mathrm{D}} = C_{\mathrm{magn}}(h'_{\mathrm{E}})$ and $C_{\mathrm{magn}}^{2\mathrm{D}} = C_{\mathrm{magn}}^{(0)}(0)$. The second derivative of C_{magn} diverges as

$$[T/T_{\mathrm{C}}(0) - 1]^{-\alpha_2} \qquad \text{for} \quad T \to T_{\mathrm{C}}(0) \tag{4.77}$$

with $\alpha_2 = \alpha_{2\mathrm{D}} + 2\phi$ where $\alpha_{2\mathrm{D}}$ and ϕ are the specific heat critical exponent of the 2D system and the ×-over exponent, resp., (Ising model: $\alpha_{2\mathrm{D}} = 0$, $\phi = 1.75$). In contrast to the susceptibility χ (cf. Eq. 4.74 and Fig. 4.28), the specific heat is always increased by the 3D influence of h'_{E}, independent of the sign of J' and h'_{E} (Eq. 4.76). By means of Eqs. 4.75 and 4.76, Bloembergen has determined the 2D ↔ 3D ×-over temperature $T_{\times}$ for a number of Cu-compounds and has also calculated the values of $(z'J'/k_{\mathrm{B}}T_{\times})^2\cdot(\chi_{2\mathrm{D}}/\chi_0)^2$, i.e. the essential factors in Eq. 4.76 with $T = T_{\times}$, using the known experimental data of these compounds from various sources. In context with Fig. 4.10 (Sect. 4.1.7), it was mentioned that the out-of-plane anisotropy has also a considerable influence on the critical properties and the ×-over phenomena. Therefore, Bloembergen [77B3] has further performed an extrapolation of the transition temperature T_{C} and the ×-over temperature $T_{\times}$ to the case $h_{\mathrm{A}} = J_{\mathrm{A}}/J = 0$ for the Cu-compounds. In this ideal case, T_{C} and $T_{\times}$ depend only on h'_{E}. All these data are compiled in Bloembergen's Table II [77B3].

9.12.4.1.10 3D XY-Model – Structural Phase Transitions

The structural phase transitions of perovskite-type layer compounds are dealt with in detail in Sect. 2.2. Also for these phase transitions, the critical properties have been studied and critical exponents and amplitudes determined. These will be discussed in this section separately from the magnetic phase transitions. The general and universal aspects are the same in both cases but the system-dependent parameters, e.g. the order parameter, are different. Since the lattice dynamics of these compounds show 3D behaviour as outlined in the introduction (Sect. 1.2), we expect also for the critical properties of the structural phase transitions 3D behaviour while the magnetic properties exhibit predominantly 2D behaviour. The sequence of structural phase transitions and parameters like the critical temperatures are listed in Table 4. For the compounds $(CH_3NH_3)_2MCl_4$ with M = Mn, Fe, we will concentrate on the continuous transition between the tetragonal high temperature (THT) and the orthorhombic room temperature (ORT) phases. In context with the step-wise ordering of the $(CH_3NH_3)^+$-ions in the course of the phase transitions, three order parameters η_1, η_2 and η_3 have been defined in Sect. 2.2.4. For the transition THT ↔ ORT, η_1 and η_2 are the essential order parameters, and we recall from Sect. 2.2.4 that there has been some controversy about the role of η_3. In this section, we will limit our considerations to η_1 and η_2. The model considerations there lead to a Landau-type free energy (cf. Eqs. 2.33 and 2.37) which will be reproduced here in a somewhat modified form as used especially for discussing the properties of Fe-compounds [82G1, 82Y2, 83S1, 84Y1]

$$U = a(\eta_1^2 + \eta_2^2) + \tfrac{b}{2}(\eta_1^4 + \eta_2^4) + c\,\eta_1^2\eta_2^2 + \tfrac{\kappa}{2}[(\nabla\eta_1)^2 + (\nabla\eta_2)^2] - \tfrac{1}{2}S_{66}^0\,\sigma_6^2 - \xi\,\sigma_6\,(\eta_1^2 - \eta_2^2) \tag{4.78}$$

where also included is the elastic C_{66} mode and its coupling to the order parameter (cf. Eq. 2.36 in Sect. 2.2.4). In Eq. 2.36, this is described by the elastic strain e_6 ($6 \mathrel{\hat{=}} x_0y_0$) and the elastic constant C_{66}. But in Eq. 4.78 completely analogous to Eq. 2.36, the elastic stress σ_6, the field conjugate to the strain e_6 is used and, correspondingly, the elastic compliance S_{66} where for the compounds under consideration

$$\sigma_6 = C_{66}\, e_6 \quad \text{and} \quad e_6 = S_{66}\, \sigma_6 \tag{4.79}$$

In Eq. 4.78, S^0_{66} means the value of the elastic compliance without coupling to η_1 and η_2. With respect to the THT ↔ ORT phase transition, it was shown in detail in Sect. 2.2.1 that the C_{66} elastic mode softens in the THT-phase when the temperature approaches the critical temperature T_{C1} from above. If $C_{66} \to 0$ for $T \to T_{C1}$, its inverse S_{66} will diverge. The two order parameters η_1 and η_2 in Eq. 4.78 correspond to a two-component spin ($n = 2$, cf. the discussion in context with Eq. 4.2 in Sect. 4.1.1). Therefore, this system is expected to exhibit the critical behaviour of the 3D XY-model [78B8, 78C4, 82G1, 82Y2, 84Y1]. The experimentally determined critical exponents (see Table 6) should be compared to the theoretical values which are listed in Table 7 in Sect. 4.1.1 and will not be repeated here. In addition, the universal ratio A^+/A^- of the specific heat critical amplitudes may also be compared to experimental data. Its theoretical value $A^+/A^- = 1.05$ is an average of the values calculated by different methods, see Table II of [76B6].

The determination of critical exponents and amplitudes with respect to the structural phase transitions follows closely the lines presented in Sects. 4.1.3–4.1.5. Since the perovskite-type layer compounds undergo in general more than one structural phase transition with critical temperatures T_{Cn} ($n = 1, 2, 3, \ldots$), the reduced temperature (cf. Eq. 4.1 in Sect. 4.1.1) is defined here correspondingly as

$$t_n = (T - T_{Cn}) / T_{Cn} \quad (n = 1, 2, 3, \ldots) \tag{4.80}$$

where the subscript n will only be omitted in those cases when a compound undergoes only one phase transition. Most transitions are accompanied by an anomaly in the specific heat C_p as shown in some examples in Figs. 2.19 and 2.20 in Sect. 2.2.1 and as listed Table 4. In this section, we will concentrate on such investigations where the critical properties of C_p are determined. Since the specific heat exponent α is practically zero for the 3D XY-model (cf. Table 7), C_p will show a logarithmic singularity also in this case. This is illustrated for the THT ↔ ORT phase transition of $(CH_3NH_3)_2FeCl_4$ at $T_{C1} = 332.5$ K in Fig. 4.30. After subtraction of the background specific heat $C_{p,0}$ due to lattice vibrations, the anomaly of the specific heat has successfully been fitted to [82G1]

$$\Delta C_p = C_p - C_{p,0} = R\,[A^{\pm}\,|\ln|t_1||+D^{\pm}] \tag{4.81}$$

thus confirming the logarithmic singularity at T_{C1}. As in Sect. 4.1.3, the superscripts "+" and "–" mean $T > T_{C1}$ ($t_1 > 0$) and $T < T_{C1}$ ($t_1 < 0$), respectively. The fit parameters A^+, A^-, D^+ and D^- are listed in Table 6. In other cases, the background specific heat was approximated by a function linear in t as assumed also in the magnetic case (cf. Sect. 4.1.3). Therefore, the same expressions can be used for a fit to the experimental data. We have only to replace t by t_n and obtain for a logarithmic singularity ($\alpha = 0$) at T_{Cn} (cf. Eq. 4.17)

$$C_p = R\,[A^{\pm}\,|\ln|t_n||+D^{\pm}+E\,t_n] \tag{4.82a}$$

and for determining also α^+ and α^- (cf. Eq. 4.16)

$$C_p = R\,[(A^{\pm}/\alpha^{\pm})\cdot(|t_n|^{-\alpha^{\pm}}-1)+D^{\pm}+E\,t_n] \tag{4.82b}$$

where again "+" refers to $T > T_{Cn}$ ($t_n > 0$) and "–" to $T < T_{Cn}$ ($t_n < 0$). Eqs. 4.82a and 4.82b have especially been employed for the analysis of the specific heat data of $(C_2H_5NH_3)_2FeCl_4$ [84Y1] where both transitions, THT ↔ ORT and ORT ↔ OLT, are continuous and have been studied with respect to their critical properties. For both Fe-compounds, the specific heat critical data (cf. Table 6) obtained for the THT ↔ ORT phase transition ($T_{C1} = 332.5$ K and 377.5 K, resp.) agree quite well with the theoretical predictions for the 3D XY-model (cf. Table 7 and [76B6]) and could well be analysed with Eq. 4.81 or Eq. 4.82a. A different behaviour has been observed for the ORT ↔ OLT phase transition of $(C_2H_5NH_3)_2FeCl_4$ ($T_{C2} = 203.5$ K). Therefore, the specific heat data are also analysed with Eq. 4.82b and values $\alpha^+ = 0.068$ and $\alpha^- = 0.26$ are obtained. The ratio A^+/A^- is far from the value 1.05 for the 3D XY-model, namely 0.232 for $\alpha = 0$ and 0.343 for $\alpha^+ \neq \alpha^- \neq 0$. Since the ORT ↔ OLT transition is accompanied by a dielectric anomaly [83S1], the critical behaviour of the specific heat at this transition is explained by the influence of electric dipole-dipole interactions. Including these, a critical amplitude ratio $A^+/A^- = 0.25$ is theoretically predicted [78N4, 84Y1] which agrees quite well with the experimental data.

The order parameter critical exponent β can be determined, as in the magnetic case (cf. Sect. 4.1.4), by neutron diffraction from the intensity of a superreflection in the low-symmetry phase (cf. Sect. 2.1.4 and Fig. 2.12). This intensity is proportional to the square of the order parameter (cf. Eq. 4.20 in Sect 4.1.4)

$$\text{superreflection (h, k, l):}\quad I \sim |t_n|^{2\beta} \qquad (t_n < 0) \tag{4.83}$$

A second possibility for determining β is linear birefringence (LB) where Δn is zero in the high symmetry phase, e.g. THT, and nonzero in the phase of lower symmetry, e.g. ORT. As in the case of neutron scattering (Eq. 4.83), the result Δn of the measurement is proportional to the square of the order parameter

$$\Delta n \sim |t_n|^{2\beta} \qquad (t_n < 0) \tag{4.84}$$

Among others, also the Cu-compounds $(CH_3NH_3)_2CuCl_4$ and $(C_2H_5NH_3)_2CuCl_4$ were studied by linear birefringence [79K3]. Their structural phase transitions Bbcm ↔ $P12_1/c1$ are expected to be continuous. However, they are slightly discontinuous due to the coupling of the order parameter to elastic strains [69L3] and a first order jump of Δn at the critical temperature (cf. Figs. 1 and 2 of [79K3])

$$\Delta n(T_{Cn}) \tag{4.84a}$$

is reported for these compounds. Further, the values for the critical exponent β obtained by this LB investigation are considerably lower than expected for the 3D XY-model. This may be due to two reasons. Firstly, the experiments on single-domain samples involve a symmetry-breaking uniaxial stress [74A2] and, consequently, Ising-like critical behaviour. Secondly, the proximity of the tricritical point (TCP) causes a drastic reduction of β [79A], similar to the result $\beta = 0.18$ obtained for $RbCaF_3$ by Buzaré et al. [79B11]. In addition to LB measurements, Kind et al. [81K3] have used a third method for determining directly the order parameter. On partly deuterated diammonium compounds $[ND_3(CH_2)_nND_3]MCl_4$ with M = Mn, Cd and n = 3, 4, 5, they performed ^{2}D-NMR-NQR measurements near the phase transitions and determined the temperature dependence of the order parameter η which is related to the orientations of the $[ND_3(CH_2)_nND_3]$ chains, i.e. $\eta = 0$ if the two orientations are equally populated and $\eta \neq 0$ if one orientation is preferred. Thus, they obtain

$$\eta \sim |t_n|^{\beta} \tag{4.85}$$

In this way, they studied the continuous phase transitions of the Cd-compounds with n = 3 ($T_C = 370$ K) and n = 5 ($T_{C2} = 333$ K) and of the Mn-compound with n = 4 ($T_C = 377$ K). The resulting data for β are compiled in Table 6.

The softening of C_{66} and the divergence of S_{66} at T_{C1} offers also the possibility to study the critical properties of the system as outlined in the reviews by Rehwald and Lüthi [73R1, 81L]. The experimental data S_{66} near T_{C1} for $(CH_3NH_3)_2FeCl_4$ are shown in Fig. 4.31a which exhibit the increase of S_{66} towards T_{C1} in the THT-phase [82G1]. Fig. 4.31b presents the log-log plot of ΔS_{66} versus t_1 which indicates that the critical behaviour of S_{66} can be described by a power law

$$\Delta S_{66} = S_{66} - S_{66}^0 = S_{66}^+ (t_1)^{-\rho} \tag{4.86}$$

for $T > T_{C1}$ ($t_1 > 0$) and where S_{66}^{+} is the critical amplitude. The critical exponent ρ is related to the specific heat exponent α and the crossover exponent ϕ [76M5]. According to the scaling hypothesis, the free energy can be written in a scale-invariant form as [74A2, 82G1]

$$G(t_1, \sigma_6) = (t_1)^{2-\alpha} \cdot F\,[\sigma_6 / (t_1)^{\phi}] \tag{4.87}$$

where F is a scaling function, homogeneous in $\sigma_6/(t_1)^{\phi}$, where ϕ is the crossover exponent. With $\Delta S_{66} = \partial^2 G / \partial\sigma_6^2$, we obtain for the exponent

$$\rho = 2\phi + \alpha - 2 \tag{4.87a}$$

It follows from Eq. 4.78 that σ_6 couples to the order parameter fluctuations $(\eta_1^2 - \eta_2^2)$. An ultrasonic stress σ_6 propagating in the x_0-direction and polarized in the y_0-direction will act as a symmetry breaking field [74A2, 75B7]. And for a sufficiently large σ_6, the two order parameters η_1 and η_2 will no longer be equivalent and the system may show a crossover to an Ising-like behaviour [74A2]. Theoretical values of the crossover exponent are for the 3D XY-model $\phi = 1.20$ [76M5] and $\phi = 1.16$ (ε-expansion, $n = 2$ and $\varepsilon = 4 - d = 1$) [72W3, 82G1]. Thus, we expect values for ρ between 0.32 and 0.40 and we gather from Table 6 that the experimental value is $\rho = 0.42$ in good agreement with the theoretical predictions. The critical behaviour of the sound attenuation at T_{C1} has also been studied for $(CH_3NH_3)_2FeCl_4$ and $(C_2H_5NH_3)_2FeCl_4$ [82Y2, 83S1]. These results will be discussed in context with dynamic critical properties in Sect. 4.2.2 below.

Summarizing this section, we may conclude that the critical behaviour at the structural phase transitions of perovskite-type layer compounds is three-dimensional without any quasi-two-dimensional features as the magnetic phase transitions and it is, except for same special cases, that of the 3D XY-model.

9.12.4.1.11 Critical Behaviour near the Percolation Threshold

In diluted ferro- or antiferromagnets of the type $A_2M_x\widetilde{M}_{1-x}X_4$ with paramagnetic M^{2+}-ions and diamagnetic $\widetilde{M}^{2+}$-ions as discussed in Sect. 3.3.2, we expect some influence of the concentration x on the critical behaviour, especially near and below the percolation concentration x_p. As can be seen in Fig. 3.48 (Sect. 3.3.2) for the systems $K_2Mn_xMg_{1-x}F_4$, $KMn_xMg_{1-x}F_3$ and $K_2Co_xMg_{1-x}F_4$ as examples, the critical temperature $T_N(x)$ decreases from $T_N(1)$ at $x = 1$ to $T_N(x_p) = 0$ at $x = x_p$. That means, we have in a (T, x) phase diagram a line of second order phase transitions which ends at the point $(T = 0,\ x = x_p)$. Below this line, the system is ordered, antiferromagnetically in this case, and disordered above this line. The approach of the line $T_C(x)$ to $(T = 0,\ x = x_p)$ is different for Ising and Heisenberg systems where T_C is the critical temperature in general. Theoretical considerations [75S3, 77L4] yield for $x > x_p$ but close to x_p

$$\begin{aligned} &T_C(x) \sim |\ln(x - x_p)|^{-1} && \text{(Ising model)} \\ &T_C(x) \sim (x - x_p)^{\phi} && \text{(Heisenberg model)} \end{aligned} \tag{4.88}$$

where ϕ is the percolation crossover exponent introduced below in context with the critical properties. The point $(T = 0,\ x = x_p)$ is a multicritical point with a multicritical behaviour in its neighbourhood [77S8]. A more detailed and more rigorous introduction to this field, i.e. percolation theory, critical behaviour at the percolation threshold and examples of experimental data, can be found in a number of reviews which not all can be listed here but only some of them, e.g. about the early approaches to the percolation problem [71S3, 72E], about more recent concepts and results [79S7, 80E3, 83S10, 84B4, 85S2, 92S6], and about the relation between fractals and percolation [86S4, 87H3, 90C2, 92I1, 94N].

Here, only the basic facts will be given for the multicritical behaviour near the point ($T = 0$, $x = x_p$). It may be approached along two essentially different directions [77S8]

a) on the concentration axis $x \longrightarrow x_p$ at $T = 0$ where the system exhibits pure geometrical or percolation critical behaviour with the percolation critical exponents α_p, β_p, γ_p, δ_p, ν_p etc. This behaviour can be expected for very low temperatures.

b) for $T \longrightarrow 0$ and $x = x_p$, the system will exhibit pure thermal critical behaviour with the thermal critical exponents α_T, β_T, γ_T, δ_T, ν_T etc.

Approaching the multicritical point on any path with $x < x_p$, a crossover from thermal to geometric critical behaviour will occur, governed by the percolation crossover exponent ϕ:

$$\nu_p / \nu_T = \phi \qquad \gamma_p / \gamma_T = \phi \qquad \eta_p = \eta_T = \eta \tag{4.89}$$

For Ising systems, the theoretical value of the crossover exponent is $\phi = 1.0$ for all lattice dimensions $1 \le d \le 6$ [75T4, 78W3] while for 2D Heisenberg systems $\phi = 1.7$ was reported [76S7]. That means that for Ising systems the critical behaviour is independent of the path on which the multicritical point is approached.

The thermal exponents in b) are defined in the same way as introduced in Sects. 4.1.1–4.1.5. And all relations between them including the scaling relations (cf. Eqs. 4.3a and 4.13) apply to them, also the relations for their experimental determination (Eqs. 4.16, 4.20, 4.32, and 4.32a). These thermal exponents at the percolation point ($T = 0$, $x = x_p$) are marked with a subscript "T" since they are not necessarily equal to those at ($T_N(1)$, $x = 1$) [78Y4, 79S6] which are presented in Sect. 4.1.1–4.1.5 without a subscript. According to the Harris-criterion [74H5], we will have different situations for positive or negative specific heat exponents α of the pure or random exchange system (see REIM in the next section).

The definitions of the percolation critical exponents in a) are different since their theoretical foundation is entirely based on probabilistic arguments and on geometrical quantities like cluster sizes and cluster distributions. The quantities needed for introducing the percolation critical exponents are (see for example [80E3]

1) the pair connectedness function $C_2(r, x)$:
$C_2(r, x)$ is the conditional probability that at a distance r from an occupied site is another site occupied and in the same cluster. Experiments [80B1] suggest that the spatial Fourier transform of $C_2(r, x)$ has the form $C_2(q, x) \sim (q^2 + \kappa_G^2(x))^{-1}$ (Lorentzian). Thus in two dimensions

$$C_2(r, x) \sim K_0(\kappa_G r) \rightarrow (\kappa_G r)^{-1/2} \exp(-\kappa_G r) \tag{4.90}$$

where K_0 is the zeroth order modified Bessel function or Macdonald function and the expression behind the arrow its asymptotic behaviour for large r.

2) the geometrical correlation length $\xi_G(x)$:
Its inverse $\kappa_G(x) = \xi_G^{-1}(x)$ appeared already above in context with Eq. 4.90, $\xi_G(x)$ is the RMS distance of a particle from the origin which is connected to the origin

$$\xi_G(x) = \kappa_G^{-1}(x) \sim (x_p - x)^{-\nu_p} \qquad x \rightarrow x_p^- \tag{4.91}$$

The critical behaviour, especially of ξ_G, was studied by Stinchcombe [79S6] for bond- and site-diluted $S = \frac{1}{2}$ Heisenberg and Ising magnets.

3) mean size $S(\mathrm{x})$ of finite clusters below the percolation threshold:
$S(\mathrm{x})$ is also related to $C_2(r, \mathrm{x})$ [77R], it is equal to $C_2(q = 0, \mathrm{x})$:

$$S(\mathrm{x}) = \iint C_2(r,\mathrm{x})\,\mathrm{d}\tau \sim (\mathrm{x_p} - \mathrm{x})^{-\gamma_\mathrm{p}} \qquad \mathrm{x} \to \mathrm{x_p^-} \tag{4.92}$$

Cluster sizes in general and the mean size $S(\mathrm{x})$ are elucidated for $\mathrm{x} \approx \mathrm{x_p}$ by the results of Monte Carlo simulations [76L5].

4) percolation probability $P(\mathrm{x})$:
$P(\mathrm{x})$ is the fraction of occupied sites that belong to the infinite cluster above threshold:

$$P(\mathrm{x}) \sim (\mathrm{x} - \mathrm{x_p})^{\beta_\mathrm{p}} \qquad \mathrm{x} \to \mathrm{x_p^+} \tag{4.93}$$

$P(\mathrm{x})$ is proportional to the magnetic moment per site $\mu_0(\mathrm{x}, 0)$ for zero external field (cf. Eq. 4.95 below).

5) Mean number $K(\mathrm{x})$ of finite clusters of any size:
This number is proportional to the free energy of the system and therefore

$$K(\mathrm{x}) \sim (\mathrm{x_p} - \mathrm{x})^{2-\alpha_\mathrm{p}} \tag{4.94}$$

since each cluster contributes $k_\mathrm{B}T \cdot \ln 2$ to the free energy.

6) Field dependence of the magnetic moment at $\mathrm{x} = \mathrm{x_p}$:
The magnetic moment per site in an external field H_0 is $\mu(\mathrm{x}, h)$ where $h = 2\mu_\mathrm{B}H_0/k_\mathrm{B}T$. For $\mathrm{x} = \mathrm{x_p}$ the magnetic moment is

$$\mu_\mathrm{C}(h) \sim h^{1/\delta_\mathrm{p}} \tag{4.95}$$

Eqs. 4.90–4.95 summarize the definitions of the percolation critical exponents as we will need part of them below for the discussion of experimental data because their analysis and interpretation is based on some of these definitions. An alternative form of definitions is due to D. Stauffer [79S7, 85S2, 92S6]. He considers in detail the clusters in the diluted magnet. Their size is s, i.e. the number of occupied sites in the cluster, and $n_\mathrm{s}(\mathrm{x})$ is the size distribution, i.e. the number of clusters with size s at the concentration x. As already mentioned in Sect. 3.3.1 in context with paramagnetic centres, $n_\mathrm{s}(\mathrm{x})$ is the probability for having an s-cluster at the concentration x, i.e. $n_1(\mathrm{x}) = \mathrm{x}(1-\mathrm{x})^4$ for s = 1 and $4\mathrm{x}^2(1-\mathrm{x})^6$ for s = 2. In terms of the cluster size s and the cluster distribution $n_\mathrm{s}(\mathrm{x})$, the percolation critical behaviour can be expressed as

$$\left[\sum_\mathrm{s} n_\mathrm{s}(\mathrm{x})\right]_\mathrm{sing} \sim |\mathrm{x} - \mathrm{x_p}|^{2-\alpha_\mathrm{p}} \tag{4.96a}$$

$$\left[\sum_\mathrm{s} \mathrm{s} \cdot n_\mathrm{s}(\mathrm{x})\right]_\mathrm{sing} \sim |\mathrm{x} - \mathrm{x_p}|^{\beta_\mathrm{p}} \tag{4.96b}$$

$$\left[\sum_\mathrm{s} \mathrm{s}^2 \cdot n_\mathrm{s}(\mathrm{x})\right]_\mathrm{sing} \sim |\mathrm{x} - \mathrm{x_p}|^{-\gamma_\mathrm{p}} \tag{4.96c}$$

$$\left[\sum_{s} s \cdot n_s(x_p) \cdot e^{-hs}\right]_{\text{sing}} \sim h^{1/\delta_p} \qquad (4.96d)$$

To these definitions, Eq. 4.91 ($\xi_G \sim |x - x_p|^{-\nu_p}$) has to be added for completing the set of critical exponents. In Eqs. 4.96a–4.96d, the subscript "sing" denotes the leading nonanalytic part. Stauffer has further introduced two new exponents for describing the scaling behaviour of $n_s(x)$

$$n_s(x) \sim s^{-\tau_p} f[(x - x_p) \cdot s^{\sigma_p}] \qquad (4.97)$$

where $f(z)$ is a scaling function with $f(0) = 1$ so that the cluster distribution at the threshold becomes $n_s(x_p) \sim s^{-\tau_p}$. Combining Eq. 4.97 with Eqs. 4.96a–4.96d, the new exponents σ_p and τ_p can be written in terms of the other percolation exponents

$$\tau_p = 2 + \delta_p^{-1} \qquad \sigma_p = (\beta_p \delta_p)^{-1} = (\beta_p + \gamma_p)^{-1} = \Delta_p^{-1} \qquad (4.98)$$

and, in addition to Eq. 4.98, the exponents α_p, β_p, γ_p etc. also obey the sealing laws [75D4], e.g. $\Delta_p = \beta_p + \gamma_p = \beta_p\, \delta_p$ and $\eta_p = 2 - \gamma_p / \nu_p$, as introduced in Eqs. 4.3a and 4.13 for the thermal exponents α, β, γ etc. of the pure system.

A diluted magnet near the percolation threshold can be considered a fractal. A definition of a fractal was given by Mandelbrot. An introduction to fractals and their application in physics can be found in monographs by Mandelbrot and by Feder and Aharony [77M4, 82M7, 89M5, 90F3]. The application of the concept of fractals to the percolation problem has contributed significantly to the understanding of these phenomena. The aspects of the percolation clusters as fractals are discussed in [84M5, 84M6] and also in a number of reviews [79S7, 87H3, 90B5, 90C2, 92I1, 94N], in some of them in a different context since fractals and percolation theory are not only useful for dilute magnetic system but also for diffusion and conduction or transport in disordered media. With respect to the critical properties near the percolation threshold, two properties of fractals are most important:

1) the self-similarity in fractals

2) a unique non-integer fractal dimension

Fractals are classified as deterministic if the self-similarity is exact and as random if it is considered as the average. And percolating systems are an example of the latter case, a random fractal. Stanley et al. [76S7, 77S7] have studied cluster shapes at the percolation threshold and pointed out the relation to fractals. Kapitulnik et al. [83K9] have shown by Monte Carlo simulations that the infinite cluster for $x > x_p$ is homogeneous on large length scales ($r >> \xi_G$), i.e. the apparent dimension is d (= 2). On shorter length scales ($r << \xi_G$), this cluster is self-similar and has a fractal dimension $D_f < 2$. Stauffer [79S7, 85S2, 92S6] introduces for the description of the clusters their radius R_s and their density profile $D_s(r)$. The latter is the probability that a lattice site at a distance r from the centre of mass of a s-cluster belongs to the cluster. The scaling form of the radius and of the density profile is

$$R_s \sim s^{\sigma_p \nu_p} \tilde{R}[(x - x_p) \cdot s^{\sigma_p}] \qquad (4.99a)$$

$$D_s(r) \sim s^{-1/\delta_p} \tilde{D}[r / s^{\sigma_p \nu_p}, (x - x_p) \cdot s^{\sigma_p}] \qquad (4.99b)$$

where $\tilde{R}$ and $\tilde{D}$ are homogeneous scaling functions and r is measured in units of the lattice constant. For percolation clusters at x_p, the density profiles $D_s(r)$ are all similar (self-similarity) [79H3] and depend mainly on the ratio $r/s^{\sigma_p \nu_p}$, or equivalently on $s/r^{1/\sigma_p \nu_p}$. Because of this similarity, the exponent $1/\sigma_p \nu_p$ can be considered an effective dimensionality and is defined the fractal dimensionality

$$D_f = (\sigma_p \nu_p)^{-1} = d - \beta_p/\nu_p = \Delta_p/\nu_p \tag{4.100}$$

where the various expressions for D_f result from an application of the scaling relations Eqs. 4.3a, 4.13 and 4.98. For $x = x_p$, the cluster radius becomes $R_s \sim s^{\sigma_p \nu_p}$ or $s \sim R_s^{D_f}$ (cf. Eq. 4.99a). It will be shown below in Eq. 4.102, that the theoretically calculated exact value of D_f is 91/48 = 1.896 in 2D systems. Monte Carlo simulations yielded $D_f = 1.900(9)$ [83K9], $D_f = 91/48 \pm 1\%$ [83M5] and $D_f = 1.88(2)$ [86N2], thus confirming the definition Eq. 4.100. Larssen [87L2] derived a possibly exact fractal dimension from conformal invariance $D_f = (100 - n^2)/48$ where n is an integer and which is to be applied not only to our problem (n = 3) but also to other fractal systems. The experimental determination of the fractal dimension of a diluted antiferromagnet near the percolation threshold, e.g. $Rb_2Co_xMg_{1-x}F_4$, is based on the above mentioned fact that the system appears to be homogeneous on length scales larger than geometrical correlation length ξ_G and to show fractal properties for lengths smaller than ξ_G. That means the intensity of elastic neutron scattering at an antiferromagnetic superreflection, e.g. (1, 0, 0), will be different for q smaller or larger than $\kappa_G = \xi_G^{-1}$ [87O1, 93I, 94I4]

$$\begin{aligned} q < \kappa_G \qquad & I(\boldsymbol{q}) \sim \delta(\boldsymbol{K} - \boldsymbol{Q}_0) \\ q > \kappa_G \qquad & I(\boldsymbol{q}) \sim q^{-D_f} \end{aligned} \tag{4.101}$$

where $\boldsymbol{q} = \boldsymbol{K} - \boldsymbol{Q}_0$ and $\boldsymbol{Q}_0$ the reciprocal lattice vector of the antiferromagnetic superreflection. By studying elastic neutron scattering near the antiferromagnetic (1, 0, 0) superreflection from $Rb_2Co_xMg_{1-x}F_4$ with x = 0.60, 0.65, 0.70, Ikeda et al. [93I, 94I4] have determined the fractal dimension of this percolating system (cf. Table 6)

$$D_f = 1.95(7)$$

in good agreement with the theoretical predictions. For calculating κ_G, they have used Eq. 4.91, i.e. the relation $\kappa_G \sim |x - x_p|^{\nu_p}$ with $\nu_p = 1.333$ (see Eq. 4.102 below). An earlier definition of an effective cluster dimensionality by Stanley et al. [76S7, 77S7] $D_p = \gamma_p/\nu_p$ leads to a smaller theoretical value $D_p = 86/48 = 1.792$. But now the definition Eq. 4.100 based on the self-similarity is the generally accepted one for the fractal dimension D_f which also agrees quite well with the experimental value.

Estimates and approximate values for the percolation critical exponents were obtained by series expansions [75D5, 76S8, 76S10, 78B9], by Monte Carlo simulations [80R, 86K7] and by renormalization-group methods [75H5, 78K10, 78R3, 79S6]. Since 1980, exact values are available based on the den Nijs and Nienhuis conjectures [79N, 80N2, 80P6, 81B6, 82N4, 87N3]. These exact values of the percolation critical exponents for d = 2 and of the fractal dimension are

$$\begin{aligned} \alpha_p &= -\tfrac{2}{3} = -0.66667 & \beta_p &= \tfrac{5}{36} = 0.13889 \\ \gamma_p &= \tfrac{43}{18} = 2.38889 & \nu_p &= \tfrac{4}{3} = 1.33333 \\ \delta_p &= \tfrac{91}{5} = 18.20000 & \Delta_p &= \tfrac{91}{36} = 2.52778 \\ \tau_p &= \tfrac{187}{91} = 2.05495 & \sigma_p &= \tfrac{36}{91} = 0.39560 \\ \eta_p &= \tfrac{5}{24} = 0.20833 & D_f &= \tfrac{91}{48} = 1.89583 \end{aligned} \tag{4.102}$$

By now, these values are in common use as theoretical ones [90C2, 92I1, 94N]. One of these reviews [92I1] has collected the available approximate values for comparison with the exact ones. They agree excellently with the results of Monte Carlo simulations [81E, 89Y5] which confirm also the universality of these critical exponents, i.e. they depend only on the lattice dimension d and not on the lattice type and also not on the type of dilution [89Y5]. That means they are the same for a triangular, a square or a honeycomb lattice in two dimensions and also the same for bond and site dilution. For lattice dimensions larger than two, no exact data are available. But one general statement can be made: For d → 6 the critical exponents approach the classical mean field values [76K7].

Experimentally, the spin fluctuations in diluted antiferromagnets were investigated by neutron scattering from the antiferromagnetic Bragg rods. Results of extensive investigations were reported for $Rb_2Mn_xMg_{1-x}F_4$ [76B6, 77C7, 80B1], nearly a Heisenberg system, and for $Rb_2Co_xMg_{1-x}F_4$ [80C1, 84B4], an Ising system. The concentrations x were close to the percolation threshold, $x = 0.54$, 0.57, 0.60 ($Rb_2Mn_xMg_{1-x}F_4$) and $x = 0.55$, 0.575, 0.583, 0.595 ($Rb_2Co_xMg_{1-x}F_4$). The determination of the critical exponents γ, ν and η from neutron scans across the Bragg rod is discussed in detail in Sect. 4.1.5, see Eqs. 4.21–4.27. For adapting the notation to that used by Birgeneau et al. [80B1] and by Cowley et al. [80C1], the total scattering functions $S^{\|}(\boldsymbol{K})$ and $S^{\perp}(\boldsymbol{K})$ are defined in relation to the wavevector dependent susceptibilities (cf. Eqs. 4.24–4.26)

$$S^{\|}(\boldsymbol{K}) = \frac{\mu_0 k_B T}{(g\mu_B)^2}\chi_{\|}(\boldsymbol{K}) \qquad S^{\perp}(\boldsymbol{K}) = \frac{\mu_0 k_B T}{(g\mu_B)^2}\chi_{\perp}(\boldsymbol{K}) \tag{4.103}$$

where "||" corresponds to "zz" and "⊥" to "xx" and "yy" as outlined in Eq. 4.25. The observed intensity of quasi-elastic neutron scattering can then be written as

$$I(\boldsymbol{K}) \sim \left[(1+K_z^2/K^2)\cdot S^{\perp}(\boldsymbol{K}) + (1-K_z^2/K^2)\cdot S^{\|}(\boldsymbol{K})\right] \tag{4.104}$$

For Heisenberg-like Mn- and Ni-compounds, the separation $S^{\|}(\boldsymbol{K})$ and $S^{\perp}(\boldsymbol{K})$ is a problem which has to be dealt with (cf. Fig. 4.5 in Sect. 4.1.5). For the dilute system $Rb_2Mn_xMg_{1-x}F_4$, it will be explained below that $I(\boldsymbol{K})$ can be used for the determination of the critical exponents without such a separation. In strongly anisotropic Ising-like Co-compounds, the transverse fluctuations are negligible and thus $I(\boldsymbol{K})$ proportional to $S^{\|}(\boldsymbol{K})$. For a rod scan, the wavevector transfer is $\boldsymbol{K} = \boldsymbol{Q}_0 + \boldsymbol{q}$ where $\boldsymbol{Q}_0$ is a vector in reciprocal space located on the Bragg rod and $\boldsymbol{q}$ a vector perpendicular to the rod. The experiments on $Rb_2Mn_xMg_{1-x}F_4$ and $Rb_2Co_xMg_{1-x}F_4$, were performed at $\boldsymbol{Q}_0 \,\hat{=}\, (1, 0, 0.4)$ (Mn: $x = 0.54$, 057 and Co: all concentrations) and at $\boldsymbol{Q}_0 \,\hat{=}\, (1, 0, 0.2)$ (Mn: $x = 0.60$). The value of $\boldsymbol{Q}_0$ is only useful for calculating the contributions of $S^{\|}(\boldsymbol{K})$ and $S^{\perp}(\boldsymbol{K})$ and is not needed in the following analysis of the experimental data. As in Sect. 4.1.5, we can therefore drop $\boldsymbol{Q}_0$, and keep only the dependence on $q = |\boldsymbol{q}|$. For the critical behaviour, also $\mu(T)$, a temperature variable and $\Delta x = x_p - x$ are important

$$I(\boldsymbol{K}) \to I(q, \Delta x, \mu) \sim \frac{A_{DS}\cdot\kappa^{\eta}}{q^2+\kappa^2} \tag{4.105}$$

where the expression to the right is the Ornstein-Zernike form (Eq. 4.28) with an additional factor κ^{η} and where $q^2 = q_x^2 + q_y^2$. Eq. 4.105 was successfully employed for the analysis of the experimental data of both, $Rb_2Mn_xMg_{1-x}F_4$ and $Rb_2Co_xMg_{1-x}F_4$. This form is a simple and plausible way [80B1] to generalize the exact results of Thorpe [75T4] for a random 1D Heisenberg antiferromagnet. In Eq. 4.105, the inverse correlation length κ depends on Δx and $\mu(T)$

$$\kappa(\Delta x, \mu) = \kappa(\Delta x, 0) + \kappa(0, \mu) \tag{4.106}$$

where, again based on the results of Thorpe, it is assumed that the geometrical and thermal inverse correlation lengths are simply additive, since the part depending on Δx is identical with the geometrical inverse correlation length κ_G in Eq. 4.91

$$\kappa(\Delta \mathrm{x}, 0) = \kappa_G = \kappa_G^0 (1 - \mathrm{x}/\mathrm{x}_p)^{\nu_p} \tag{4.107}$$

For the thermal part depending on μ (or on T), there is for $\mathrm{x} < \mathrm{x}_p$ no reduced temperature $t = 1 - T/T_C$ because of the absence of a phase transition and a critical temperature T_C. Instead, the correlation length ξ_{1D} of the corresponding 1D system should be used as Lubensky [77L4] pointed out in his scaling theory for diluted magnets, completely analogous to the 1D behaviour of C_{magn} and χ as presented in Sect. 3.3.2 together with some theoretical foundations. For the ideal 1D Ising and the ideal 1D Heisenberg model, the correlation length ξ_{1D} was derived by Fisher [64F2] and its inverse can be written as [76S5, 80B1]

$$\kappa_{1D}\, a_{nn} = -\ln u \tag{4.108}$$

with $u = \tanh\,[2S\,(S+1)\,|J|/k_B T]$ (Ising model)
and $u = \coth\,[2S\,(S+1)\,|J|/k_B T] - [2S\,(S+1)\,|J|/k_B T]^{-1}$ (Heisenberg model)

Fig. 4.32 presents $\kappa_{1D}^{I}\, a_{nn}$ and $\kappa_{1D}^{H}\, a_{nn}$ versus $[k_B T]/[2S(S+1)\,|J|\,]$ for the Ising and the Heisenberg models, resp., as calculated with Eq. 4.107. For a realistic treatment however, the Ising-like anisotropy of the Mn-compounds has to be taken into account. Using the results of Blume et al. [75B8] and inserting the parameter values for pure Rb_2MnF_4, Birgeneau et al. [80B1] calculated the inverse correlation lengths $\kappa_{1D}^{\parallel}$ and $\kappa_{1D}^{\perp}$ for an anisotropic antiferromagnet where "||" and "⊥" refer to the anisotropy axis, i.e. the *c*-axis. The corresponding curves in Fig. 4.32 show that above 0.2 both, $\kappa_{1D}^{\parallel} a_{nn}$ and $\kappa_{1D}^{\perp} a_{nn}$, approach $\kappa_{1D}\, a_{nn}$ of the Heisenberg model, and below 0.1, $\kappa_{1D}^{\parallel}$ exhibits a crossover to the Ising model. If such a crossover is present in the pure system, it should also occur for $\mathrm{x} \approx \mathrm{x}_p$ in the scaling description of the diluted system [80S5]. Therefore, $\kappa_{1D}^{\parallel}$ is used for $Rb_2Mn_xMg_{1-x}F_4$ as the thermal part of κ

$$\kappa(0, \mu) = D_{DS} \cdot [\kappa_{1D}^{\parallel}(T)]^{\nu_T} \tag{4.109a}$$

where D_{DS} is a factor close to one. For $Rb_2Co_xMg_{1-x}F_4$, the result for the Ising linear chain is appropriate

$$\kappa(0, \mu) = D_{DS} \cdot [\kappa_{1D}^{I}(T)]^{\nu_T} \tag{4.109b}$$

The experimental data on $Rb_2Mn_xMg_{1-x}F_4$ and $Rb_2Co_xMg_{1-x}F_4$ were fitted to Eq. 4.105. The calculated data were compared to the experimental ones after convolution with the resolution function of the neutron spectrometer (see Fig. 10 of [80B1] and Fig. 4 of [80C1]). From the width of the Lorentzian, experimental values for κa_{nn} were obtained as shown for $Rb_2Mn_xMg_{1-x}F_4$ in Fig. 4.33. The curves represent the combination of Eqs. 4.106, 4.107 and 4.109a

$$\kappa(\Delta \mathrm{x}, \mu)\, a_{nn} = \kappa_G\, a_{nn} + D_{DS}\, [\kappa_{1D}^{\parallel}(T)\, a_{nn}]^{\nu_T} \tag{4.110a}$$

where the geometrical inverse correlation length κ_G is the value of κ for $T \to 0$ for the $\mathrm{x} = 0.54$ and $\mathrm{x} = 0.57$ samples. For the $\mathrm{x} = 0.60$ sample, the data indicate a smeared phase transition near 8–9 K. The experimental data of all samples were successfully fitted to a single Lorentzian and a separation of $S^{\parallel}(q)$ and $S^{\perp}(q)$ seems not necessary. However, such a separation was performed by means of neutron inelastic scattering (cf. Fig. 12 of [80B1]) which shows that $S^{||}(q) >> S^{\perp}(q)$ for $T < 5$ K, i.e. $I(q, \Delta x, \mu)$ dominated by $S^{||}(q)$. On the other hand, Fig. 4.32 indicates that $S^{||}(q) = S^{\perp}(q)$ for $T > 10$ K so that a separation is impossible. And the data in the range $5 \text{ K} \le T \le 10$ K were excluded in the fit. The curves in Fig. 4.33 are calculated by means of Eq. 4.110a with the theoretical values of $\kappa_{1D}^{||}(T)$ (cf. Fig. 4.32 and [75B8, 80B1]) and with the values of κ_G, ν_T and D_{DS} obtained from the fit. The values of ν_T and D_{DS} are for $Rb_2Mn_xMg_{1-x}F_4$ [80B1]

$$\nu_T = 0.90(5) \qquad D_{DS} = 1.00(5)$$

These data and also all following ones on percolation critical properties are listed in Table 6. For the system $Rb_2Co_xMg_{1-x}F_4$, the inverse correlation length κa_{nn} determined from the width of the Lorentzian fitted to the experimental data can be described

$$\kappa(\Delta x, \mu)\, a_{nn} = \kappa_G\, a_{nn} + D_{DS}\, [\kappa_{1D}^{I}(T)\, a_{nn}]^{\nu_T} \tag{4.110b}$$

where the only difference to Eq. 4.110a is that $\kappa_{1D}^{||}$ is replaced by κ_{1D}^{I} for this Ising system. The fit to Eqs. 4.105 and 4.110b yields values of ν_T and D_{DS} also for $Rb_2Co_xMg_{1-x}F_4$ [80C1]

$$\nu_T = 1.32(4) \qquad D_{DS} = 0.96(6)$$

In order to determine the percolation critical exponent ν_p, the data for κ_G were fitted to Eq. 4.107. The result is illustrated in Fig. 4.34 where the curve is calculated with Eq. 4.107 using the fit values

$$\kappa_G^0 = 3 \qquad \nu_p = 1.354(15)$$

The curve is in good agreement with the experimental points for both systems, $Rb_2Mn_xMg_{1-x}F_4$ and $Rb_2Co_xMg_{1-x}F_4$, thus demonstrating the universality of this percolation critical exponent being the same for Heisenberg and Ising systems and depending only on the lattice dimension.

Not only the width of the Lorentzian fitted to the experimental data but also the amplitude provides information about the critical behaviour of the samples. On top of the ridge ($q = 0$), the observed intensity is (cf. Eq. 4.105)

$$I(q = 0, \Delta x, \mu) = I(q = 0) \sim A_{DS} \cdot \kappa^{-(2-\eta)} \tag{4.111}$$

The experimental data of $I(q = 0)$ are shown for $Rb_2Mn_xMg_{1-x}F_4$ in Fig. 4.35. For the $x = 0.54$ and $x = 0.57$ samples, $I(q = 0)$ approaches a constant finite value below 2 K while $I(q = 0)$ for $x = 0.60$ tends to diverge near 8–9 K because of the magnetic phase transition mentioned above. Using the experimental values for κ (Fig. 4.33), the curves in Fig. 4.35 are obtained as an optimum fit of Eq. 4.111 to the experimental points [80B1] with

$$2 - \eta = 1.66(8) \quad \text{or} \quad \eta = 0.34(8)$$

for $Rb_2Mn_xMg_{1-x}F_4$. For higher temperatures where $\kappa_{1D}^{||}(T)$ dominates κ, $\kappa^{-(2-\eta)}$ will be proportional to $(1 - x/x_p)^{\gamma_T}$ according to $(2 - \eta)\, \nu_T = \gamma_T$, and we obtain

$$\gamma_T = 1.50(15)$$

In an analogous way, the corresponding values were determined for $Rb_2Co_xMg_{1-x}F_4$ [80C1]

$$2 - \eta = 1.68(8) \qquad \eta = 0.32(8) \qquad \gamma_T = 2.4(1)$$

where the latter value results from an extrapolation to x_p since the fit values for $x = 0.55$, 0.575, 0.583 depend on x and increase monotonicaly from 1.53(7) to 2.17(6). For concentrations $x > x_p$, also the samples of the Co-system undergo a magnetic phase transition with thermal critical exponents close to those of the pure 2D Ising model, different from those for $x < x_p$ [80C1]. With the result $\nu_p = 1.354$, finally the crossover exponent ϕ can be evaluated

$$\phi = \nu_p / \nu_T = 1.48(15) \qquad \text{for} \quad Rb_2Mn_xMg_{1-x}F_4$$
$$\phi = \nu_p / \nu_T = 1.03 \qquad \text{for} \quad Rb_2Co_xMg_{1-x}F_4$$

where the value for the Co-system agrees quite well with the theoretical prediction $\phi = 1$. With the theoretical value for $(2 - \eta_p) = 1.7917$ (cf. Eq. 4.102), the percolation critical exponent for S(x) (Eq. 4.92) becomes $\gamma_p = 2.43(3)$ [80B1]. Unfortunately, it was not possible to determine also the exponents β_p and β_T from measurements of the intensity of antiferromagnetic superreflections because of the large uncertainties near ($x = x_p$, $T = 0$).

At the end of this section, the experimental data on the critical behaviour of diluted antiferromagnets near the percolation multicritical point may be summarized by comparing them to theoretical values (Eq. 4.102) and to the results of a theoretical study by Coniglio [81C3]

a) percolation critical exponents

2D experiment: $\nu_p = 1.354(15)$, $\gamma_p = 2.43(3)$
theory (Eq. 4.102): $\nu_p = 1.33333$, $\gamma_p = 2.38889$

b) thermal critical exponents

$Rb_2Mn_xMg_{1-x}F_4$, 2D dilute Heisenberg model
experiment: $\nu_T = 0.90(5)$ $\gamma_T = 1.50(15)$ $\phi = 1.48(15)$
theory [81C3]: $\nu_T = 0.92$ $\gamma_T = 1.65$ $\phi = 1.43$

$Rb_2Co_xMg_{1-x}F_4$, 2D dilute Ising model
experiment: $\nu_T = 1.32(4)$ $\gamma_T = 2.4(1)$ $\phi = 1.03$
theory [81C3]: $\nu_T = 1.33$ $\gamma_T = 2.4$ $\phi = 1$

The agreement between experimental and theoretical data is very good giving some confidence in the analysis and interpretation of the results presented in this section. The differences in the thermal critical exponents for the Heisenberg and the Ising system are believed to be due to the differences in the excitations. For both types, the geometrical "excitations" are local, while the thermal excitations are local for the Ising system and extended for the Heisenberg one. This would explain $\phi = 1$ for the Ising system. In the Heisenberg system, the excitations may propagate primarily along the backbone of the cluster, and one might expect ϕ to be determined by the effective dimensionality of the backbone. In addition to these diluted antiferromagnets, also the diluted ferromagnet $K_2Cu_xZn_{1-x}F_4$ has been studied by neutron scattering [79W3]. Scans were performed across the fm. Bragg rod at $\boldsymbol{Q}_0 \mathrel{\hat{=}} (0, 0, 4.5)$ and the results fitted with a Lorentzian in order to determine the inverse correlation length κa_{nn}.

9.12.4.1.12 Random Field Effects – Random Field Ising Model

Special critical behaviour is expected for magnetic systems, e.g. a ferromagnet, which is subjected to a random field H_{RF} with $\langle H_{RF}\rangle = 0$ and $\langle H_{RF}^2\rangle \neq 0$. If the random field is conjugate to the order parameter, the magnetically ordered state will become unstable against even weak random fields for dimensions $d \leq 4$ if the order parameter has continuous symmetry and for dimensions $d \leq 2$ in Ising systems according to theoretical considerations by Imry and Ma [75I2]. This was a merely academic problem until the realization by Fishman and Aharony [79F2] that random field systems can effectively generated by applying a uniform magnetic field H_0 to diluted easy-axis antiferromagnets parallel to the easy axis. The critical behaviour of the corresponding pure antiferromagnets is usually Ising-like as turned out in the discussion of their critical properties in Sects. 4.1.2–4.1.5 (see also Table 6). Thus, the random-field Ising model (RFIM) can be studied experimentally in such antiferromagnets with the possibility to control the strength of the random field through the easily controllable strength of the applied uniform field. And it was shown that the static critical behaviour is identical for ferromagnets with random fields and dilute antiferromagnets in a uniform field [84C2, 84L2]. In this contribution, only a brief introduction to the RFIM can be given together with the most instructive experimental results. But the reader finds more theoretical and experimental details in a number of reviews, namely an introduction to random fields, frozen-in disorder etc. by Fisher et al. [88F2], reports on early experimental results by Birgeneau et al. [84B4] and on theoretical considerations by Imry [84I2], a survey on more recent theoretical views by Nattermann and Villain [88N] and, finally, a collection of recent results on 2D and 3D RFIM systems by Belanger [88B5], by Jaccarino and King [90J2] and by Belanger and Young [91B1]. Before entering more deeply into the RFIM, it is necessary for a systematic discussion to make up for the socalled random exchange model (REIM) which should have been introduced already in the last section. But, as we will see below, there is little difference for 2D systems between the Ising model (IM) of the pure antiferromagnet and the REIM of the diluted one.

The REIM describes the properties of a diluted Ising system which is subject to random exchange because of the missing exchange interaction due to the nonmagnetic impurities (cf. Fig. 3.50 in Sect. 3.3.2). The critical properties of random-spin systems in general, i.e. also of the REIM, may be different from those of the pure nonrandom systems [74H9, 75L11, 76A10, 76G5, 85P]. There are available estimates and calculations for the critical exponents of the random system, especially for the 3D REIM [77J3, 82N5, 83J2, 83J3, 89M6]. The most reliable ones are found in [82N5, 83J2, 89M6]. For the 2D REIM, the situation is somewhat complicated because there exist two different theories. Dotsenko and Dotsenko (DD) [82D2, 82D3, 83D3] found in their theoretical study that sufficiently close to the phase transition the specific heat C_{magn}, the susceptibility χ and the magnetization M will have the following forms

$$C_{magn} \sim \ln\ln(1/|t|) \qquad \chi \sim t^{-2}\exp\left[-\frac{a}{2}(\ln\ln|1/t|)^2\right] \qquad M \sim \exp\,[-a\,(\ln\ln|1/t|)^2]$$

which imply the values $\alpha = 0$, $\gamma = 2$, and $\beta = 0$ for the 2D REIM critical exponents. The results of DD for χ and M have been questioned by Shalaev, Shankar and Ludwig (SSL) [84S6, 87S1, 88L1, 88S6] who predicted for the 2D REIM also a double-logarithmic form for C_{magn} but the same power laws as in the non-random 2D IM for χ and for M which are according to Shalaev [84S6] modified by logarithmic corrections

$$C \sim \ln\ln(1/|t|) \qquad \chi \sim t^{-7/4}\,|\ln t|^{7/8} \qquad M \sim t^{1/8}\,|\ln t|^{-1/4}$$

These results were confirmed by a calculation of the REIM critical exponents [89M6]

$$\alpha = -0.004, \quad \gamma = 1.753, \quad \nu = 1.002, \quad \eta = 0.251$$

An extensive Monte Carlo investigation was performed for a further clarifying of the controversy between the two conflicting theories [90W2, 90W3]. The results clearly confirm the theoretical predictions of SSL with the above critical exponents of the 2D IM ($\alpha = 0$, $\gamma = 1.75$, $\nu = 1.00$, $\eta = 0.25$; cf. Table 7). Also the logarithmic corrections were observed in the Monte Carlo studies. Thus it seems that the theory of SSL is correct and that the theory of DD leads to questionable results [88C5].

Experimental data about the critical behaviour of the diluted Ising system $Rb_2Co_xMg_{1-x}F_4$ are available from specific heat measurements [78S4], from neutron scattering [79I1, 81I2, 87H1] and from LMB studies [83F3] (cf. Table 6). The values of the critical exponents agree well with those of the 2D IM thus confirming also the theory of SSL and the Monte Carlo results, except for the logarithmic corrections the effect of which is too small to be observed experimentally. For extensive neutron scattering experiments [81I2], very carefully grown samples were extremely slowly cooled in order to establish a 3D LRO. The exponents β, ν, η and the critical amplitude κ_0^+/a^* were determined in the way outlined in Sects. 4.1.4 and 4.1.5, respectively. In order to confirm experimentally one of the two conflicting theories (DD and SSL), Hagen et al. [87H1, 92C2] performed a further neutron scattering study on $Rb_2Co_{0.7}Mg_{0.3}F_4$ with a careful lineshape analysis, employing a Lorentzian (Eq. 4.28) above T_N and a modified Tarko-Fisher approximant (Eq. 4.31) below T_N. Thus, they were able to determine, as compiled in Table 6, not only the critical exponents

$$\beta = 0.13(2) \qquad \gamma = 1.75(7) \qquad \nu = 1.08(6)$$

but also the universal ratios and combination of the critical amplitudes

$$C_0^+/C_0^- = 36(5) \qquad \kappa_0^-/\kappa_0^+ = 1.95(11) \qquad R_S = 0.062(10)$$

All these values for $H_0 = 0$ (REIM) agree well with the exact results for the 2D IM (cf. Eqs. 4.9, 4.11 and 4.15 in Sect. 4.1.2, see also Sect. 4.1.6 and [84C1]). In order to obtain information about the magnetic contribution C_{magn} to the specific heat and about the critical exponent α, Ferreira et al. [83F3] have studied $Rb_2Co_{0.85}Mg_{0.15}F_4$ by LMB and measured Δn as a function of temperature. The experimental data for the temperature derivative $d(\Delta n)/dT \sim C_{magn}$ for $H_0 = 0$ (cf. Fig. 4.36) indicate a symmetric logarithmic singularity with $\alpha = 0$ for the REIM which is typical also for the 2D IM. Thus, these data could be fitted to (see Table 6)

$$d(\Delta n)/dT = F\,[A^{\pm}\,|\ln|t|| + D^{\pm} + E\,t] \tag{4.112}$$

where the notation is the same as in Eq. 4.18 (Sect. 4.1.3), i.e. $t = T/T_N - 1$ is the reduced temperature and F a factor of the order 10^{-6} K^{-1} relating the LMB data to C_{magn} in units of R (cf. Eq. 4.18 in Sect. 4.1.3). Also the ratio $A^+/A^- = 0.95$ obtained in the fit is close to the theoretical value of the 2D IM. Thus, the experimental data show no difference between IM and REIM in two dimensions since the effect of the logarithmic modifications is too small to be observed in the experimental data, as already mentioned. But such a difference between REIM and IM is clearly seen for 3D Ising systems, e.g. for FeF_2 and $Fe_xZn_{1-x}F_2$ mixed crystals. These are well studied with respect to REIM and RFIM. Therefore, some results on $Fe_xZn_{1-x}F_2$ are included in this section although they do not belong to the family of perovskite-type layer structures. FeF_2 is a strongly anisotropic antiferromagnet ($H_A/H_E = 0.33$, $T_N = 78.39$ K). The critical behaviour of pure FeF_2 can be characterized as 3D Ising-like with the following values of the critical exponents [83B6, 87B8, 88R3]

$$C_p\!: \alpha = 0.111(7), \quad A^+/A^- = 0.543(20); \qquad d(\Delta n)/dT\!: \alpha = 0.155(4), \quad A^+/A^- = 0.528\,(10)$$

n-scattering: $\nu = 0.64(1)$, $\gamma = 1.25(2)$, $\kappa_0^+/\kappa_0^- = 0.53(1)$, $C_0^+/C_0^- = 4.6(2)$

magnetostriction: $\beta = 0.33(2)$

These values agree well with the theoretical values for the 3D IM (cf. Table 7) and for the amplitude ratio $A^+/A^- \approx 0.5$ (not included in Table 7). For the diluted system $Fe_xZn_{1-x}F_2$ with $x_p < x < 1$ in zero applied field (REIM), the experimentally determined critical exponents are [83B7, 86B6, 88R3, 88R4, 91F6]

$d(\Delta n)/dT$ $(0.24 \leq x \leq 1.0)$: $\alpha = -0.09(3)$, $A^{\pm}(x) \sim (1-x)^{-1.9(3)}$

n-scatt. (x = 0.46): $\nu = 0.69(1)$, $\gamma = 1.31(3)$, $C_0^+/C_0^- = 2.8(2)$, $\kappa_0^+/\kappa_0^- = 0.69(2)$

magnetostriction (x = 0.46): $\beta = 0.35(1)$; Mössbauer spectra (x = 0.9): $\beta = 0.350(9)$

For this 3D System, the REIM critical exponents are obviously different from the IM values. They agree quite well with the theoretical predictions [82N5, 83J2, 89M6]. The experimental results further indicate a change of sign for α which is of importance with respect to the Harris criterion [74H5]. There are also theoretical predictions for the ratios of the REIM critical amplitudes [83N5].

Turning now back to the random field problem, to the RFIM, it was already mentioned that the lower critical dimension above which a phase transition can occur is larger than in the case without random fields where the lower critical dimension is one for Ising systems and two for Heisenberg systems. That means there will be a dimensional reduction and the critical behaviour in random fields in a system of dimension d will be equivalent to that in a system without random field of dimension $d - \Theta$ so that the hyperscaling law (cf. Eq. 4.13 in Sect 4.1.2) has to be changed to

$$2 - \alpha = d\,\nu \quad \rightarrow \quad 2 - \alpha = (d - \Theta)\,\nu \tag{4.113}$$

with $\Theta > 0$ is a new parameter [76G6]. Some theoretical treatments of this problem find that Θ may depend on the sign of α in the REIM [85S3, 85S4] and some others come to the conclusion that $\Theta = 2$, i.e. the critical behaviour of a d-dimensional system with random field will be the same as that of a (d – 2)-dimensional system without random fields [76A11, 77Y4, 79P5, 81P2]. This may be true for Heisenberg systems, but there are many theoretical arguments that the value is $\Theta = 1$ for Ising systems [81B7, 81K13, 82G3, 83A3, 84G5, 85V2, 87B7]. Further, Imbrie [84I3] has rigorously proved that a phase transition exists for the RFIM in three dimensions. The details of these theoretical studies and the methods used there, e.g. whether the random fields are assumed a continuous Gaussian distribution or a bimodal distribution with $\pm h_{RF}$, are found in the reviews, especially in [91B1], or in the original papers.

The influence of random fields was studied experimentally for the 2D system $Rb_2Co_{0.85}Mg_{0.15}F_4$. With LMB measurements [83F3] for $H_0 = 0$, 0.5, 1.5, 2.0 T, information was gained about $d(\Delta n)/dT \sim C_{magn}$ (see Fig. 4.36). For $H_0 = 0$, in the REIM regime, the data show the already above mentioned symmetric logarithmic singularity. With increasing H_0, an increasingly rounded maximum appears which is shifted to lower temperatures. For passing from the REIM to the RFIM, crossover scaling has to be applied with respect to the critical properties. So the temperature shift of the maximum of $d(\Delta n)/dT$ is described in terms of a reduced temperature

$$t = [T - T_N + b\,H_0^2]/T_N \tag{4.114}$$

where $T_N = T_N(x)$ is the Néel temperature for $H_0 = 0$ and the concentration x and where $T_N - b\,H_0^2 = T_N^{MF}$ is the mean field transition temperature for $H_0 \neq 0$ with the mean field shift [84C2]

$$b\,H_0^2 = \frac{T_N^{MF}[g\mu_B S H_0/k_B T_N]^2}{[1 + \Theta_C/T_N^{MF}]^2} \tag{4.115a}$$

In Eq. 4.115a, $\Theta_C = \Theta_C(x)$ is the Curie-Weiss temperature (cf. Eq. 3.25 in Sect. 3.1.3) for $H_0 = 0$ and the concentration x. The reduced random field h_{RF} is given in its relation to H_0 by [84C2]

$$h_{RF}^2 = \frac{(g\mu_B S)^2 \langle H_{RF}^2 \rangle}{(k_B T)^2} = \frac{x\,(1-x)\,[g\mu_B S H_0 / k_B T]^2\,[T_N(x=1)/T]^2}{[1+\Theta_C / T]^2} \tag{4.115b}$$

That means $h_{RF}^2 \sim \langle H_{RF}^2 \rangle$ is proportional to $x(1-x)\,H_0^2$ which was pointed out already by Wong et al. [82W7, 83W5] in their derivation of $\langle H_{RF}^2 \rangle$ for diluted antiferromagnets. In terms of the reduced temperature (Eq. 4.114), the rounded maxima of $\mathrm{d}(\Delta n)/\mathrm{d}T$ for $Rb_2Co_{0.85}Mg_{0.15}F_4$ in Fig. 4.36 can well be described by

$$t_C(H_0) = -(c\,h_{RF}^2)^{1/\phi} \tag{4.116}$$

where ϕ is the exponent for the crossover from REIM to RFIM critical behaviour and c is a nonuniversal factor the dependence of which on the concentration x was demonstrated by Ferreira et al. [91F4, 91F5] for $Fe_xZn_{1-x}F_2$. The value of ϕ is expected to be equal to the exponent γ of the REIM system or a little larger, $\phi/\gamma = 1.05 - 1.10$ [86A6]. For the diluted Co-system, the experimentally determined values of the parameters in Eq. 4.116 are $\phi = \gamma = 1.74(2)$ [85B3] and $c = 0.9^{+0.5}_{-0.4}$ [83F3]. The rounding of the maxima of $\mathrm{d}(\Delta n)/\mathrm{d}T$ in an applied magnetic field can be characterized in terms of the scaling variable $h_{RF}^2 / |t|^{\phi}$ by the following scaling function [79F2, 83B5, 83F3, 84B5]

$$C_{\text{magn}}/R = g(|t|/h_{RF}^{2/\phi}) - A^* \ln h_{RF} \tag{4.117a}$$

or with a factor F instead of R for LMB results and with $h = (g\mu_B S H_0)/(k_B T) \sim h_{RF}$ for a better comparison with the experimental data [83F3]

$$F \cdot \tilde{g}(|t|/h^{2/\phi}) = \mathrm{d}(\Delta n)/\mathrm{d}T + F \cdot \tilde{A}^* \ln h \tag{4.117b}$$

In Fig. 4.37, the experimental data of $Rb_2Co_{0.85}Mg_{0.15}F_4$ with $\boldsymbol{H_0} \parallel \boldsymbol{c}$ are plotted as $\mathrm{d}(\Delta n)/\mathrm{d}T + F \cdot \tilde{A}^* \ln h$ versus $t \cdot h^{-2/\phi}$ for various applied fields ($0.1\ \mathrm{T} \le H_0 \le 2.0\ \mathrm{T}$) and for reduced temperatures ($10^{-3} \le |t| \le 10^{-2}$). The values used for ϕ and $F \cdot \tilde{A}^*$ are 1.75 and $1.64 \cdot 10^{-6}\ \mathrm{K}^{-1}$, respectively (cf. Table 6). The data are seen to collapse on a single curve which is, apart from the constant factor F, the scaling function $\tilde{g}(|t|/h^{1/\phi})$ of Eq. 4.117b, except for some points at small fields $H_0 \le 0.2$ T which probably results from concentration gradients. All features of the experimental data from LMB experiments are consistent with theoretical predictions and computer simulations for the 2D REIM → RFIM crossover [84B6].

For $Rb_2Co_xMg_{1-x}F_4$, also neutron scattering experiments were performed for samples with x = 0.70 [82Y3, 83B4, 83C4]. For a fit to the lineshape of scans across the antiferromagnetic Bragg rod, a pure Lorentzian turned out to be inadequate and a sum of a Lorentzian and a Lorentzian squared had to be used for the scattering function $S^{\parallel}(\boldsymbol{K})$ (cf. Eq. 4.103) which only contributes perceptibly to $S(\boldsymbol{K})$ in Ising-like Co-compounds

$$S^{\parallel}(\boldsymbol{K}) = S^{\parallel}(q) = S(q) = \frac{A_{RF}}{(\kappa^2 + q^2)} + \frac{B_{RF}}{(\kappa^2 + q^2)^2} \tag{4.118}$$

where $\boldsymbol{K} = \boldsymbol{Q}_0 + \boldsymbol{q}$ is used again and $\boldsymbol{Q}_0$ omitted. The Lorentzian is a mean-field approximation for the staggered susceptibility $\chi(\boldsymbol{K})$, and the Lorentzian squared is related to the disconnected susceptibility

[91B1] in random field systems $\chi_{\text{dis}}(\boldsymbol{K}) \sim [\langle S_q \rangle \langle S_{-q} \rangle]_{\text{av}}$ which is zero for $h_{\text{RF}} = 0$, see also [84L2, 84R7, 85S3, 85V1]. From the width of the scans across the rod, the inverse correlation length κ was determined as a function of temperature for various magnetic fields $\boldsymbol{H_0} \parallel \boldsymbol{c}$ $[0 \leq H_0 \leq 6.0\ \text{T}]$, corrected for the spectrometer resolution. The data are shown as κ / a^* versus T in Fig. 4.38. They were obtained by cooling the sample in the applied field (FC). For $H_0 = 0$, κ approaches zero at $T_N = 42.5$ K thus indicating the usual transition to long range antiferromagnetic order. But for fields $H_0 > 0$, the data in Fig. 4.38 show a finite value of κ for $T \rightarrow 0$ which means that these FC experiments do not lead to the usual magnetic order but to a frozen-in nonequilibrium state. Analogous to the analysis of κ in the percolation problem (Eq. 4.106), also for the data in Fig. 4.38, the assumption was made that κ can be separated into a temperature dependent part and a part depending on H_0 [83B4]

$$\kappa(H_0, T) = \kappa(H_0, 0) + \kappa(0, T) \tag{4.119}$$

where $\kappa(H_0, 0)$ is the constant part for $T \rightarrow 0$ and $\kappa(0, T) \sim \exp(-E / k_B T)$ the thermal part with an activation energy E. In addition, the experiments have revealed that only $\boldsymbol{H_0} \parallel \boldsymbol{c}$ affects the magnetic ordering and not fields $\boldsymbol{H_0} \perp \boldsymbol{c}$ in accordance with theoretical considerations [78A5].

Further neutron scattering experiments [85B3, 85B4] provided more information about the ordering in 2D $\text{Rb}_2\text{Co}_x\text{Mg}_{1-x}\text{F}_4$ below the temperature of the rounded maxima of $\mathrm{d}(\Delta n)/\mathrm{d}T \sim C_{\text{magn}}$ (cf. Fig. 4.36). The intensity I of the (1, 0, 0) antiferromagnetic Bragg peak was studied for $\text{Rb}_2\text{Co}_{0.85}\text{Mg}_{0.15}\text{F}_4$ as a function of temperature under various conditions (see Fig. 4.39) with magnetic fields $\boldsymbol{H_0} \parallel \boldsymbol{c}$. For $H_0 = 0$, the results show the usual increase of $I(1, 0, 0)$ below T_N with decreasing T indicating the antiferromagnetic LRO since $I(1, 0, 0)$ is proportional to the square of the sublattice magnetization, i.e. of the order parameter. For cooling the sample in zero field (ZFC), the LRO is preserved when the field is applied. When then the temperature is raised, the data in Fig. 4.39 show a drastic decrease of $I(1, 0, 0)$ at a temperature dependent on H_0 indicating a decrease of the LRO at temperatures well below the region of the rounded C_{magn}-maximum. By cooling the sample in the applied field (FC), completely different results with much smaller $I(1, 0, 0)$ were obtained indicating again metastability and frozen-in nonequilibrium states but nearly no LRO. Measurements of the magnetic susceptibility and of the magnetization under ZFC and FC conditions [83I3, 83I4] indicate also the existence of non-equilibrium domain states with rather long relaxation times (several hours). The data on random field effects in $\text{Rb}_2\text{Co}_x\text{Mg}_{1-x}\text{F}_4$ are summarized in Table 6.

The general conclusion from all these results [83B4, 83C4, 85B3, 85B4, 85J2, 86K8, 88B5, 90J2] was that the magnetic phase transition is destroyed in this 2D RFIM system. A further conclusion is that the system, i.e. $\text{Rb}_2\text{Co}_{0.85}\text{Mg}_{0.15}\text{F}_4$, will be in equilibrium above the temperature where the ZFC data in Fig. 4.39 join the FC data and where the result of an experiment does no longer depend on the prior history of the sample. Belanger et al. [85B3, 85B4] have defined this metastability boundary $T_M(H_0)$ as the temperature of the maximum of $-\mathrm{d}I(1, 0, 0) / \mathrm{d}T$ in the ZFC data

$$T_M(H_0) = t_M(H_0) \cdot T_N + T_N - b\, H_0^2 \qquad \text{with} \qquad t_M(H_0) = -\,(c_M\ h_{\text{RF}}^2)^{1/\phi} \tag{4.120}$$

and from the experimental data, they have determined $\phi = 1.74(2)$ and $c_M = 29(1)$. These results ensure, on the other hand, that the system is in equilibrium at the rounded maximum of C_{magn} since $T_M(H_0) < T_C(H_0)$. Experiments in pulsed high magnetic fields up to 50 T [84M4, 85K1] yield a metastability boundary $T_M(H_0)$ different from that resulting from the neutron scattering data because of the different time scales (neutron scattering: $t \approx 10^3$ s, high field pulses: $t \approx 10^{-3}$ s), i.e. the system cannot react fast enough in the pulsed high field experiments and shows a magnetic order until a critical field H_{Cr} above which disorder prevails [84M4]. The RFIM in high magnetic fields was also studied by a Monte Carlo simulation [85D3]. The critical dynamics [84A, 86A5, 95I3] and the ordering kinetics [83I4, 85B3, 85B4, 90I1] of the RFIM will be included in a separate section in context with other disorder phenomena.

The 3D RFIM, on the other hand, undergoes a magnetic phase transition [84I3, 87B7] at a transition temperature

$$T_C(H_0) = t_C(H_0) \cdot T_N + T_N - b\,H_0^2 \tag{4.121}$$

with a reduced part $t_C(H_0)$ of the form given by Eq. 4.116. This is demonstrated for $Fe_{0.6}Zn_{0.4}F_2$ in Fig. 4.40 with LMB data $d(\Delta n)/dT$ [83B5] completely analogous to those for $Rb_2Co_{0.85}Mg_{0.15}F_4$ in Fig. 4.36. For $H_0 = 0$, an asymmetric cusp is observed corresponding to the REIM value $\alpha = -0.09$ [83B7] while the data for $H_0 = 1.4$ and 2.0 T exhibit a narrow spike indicating a symmetric logarithmic singularity corresponding to a sharp phase transition. $Fe_xZn_{1-x}F_2$ was also investigated by neutron scattering, by ac susceptibility and optical Faraday rotation studies [83B5, 84B5, 85B6, 86B6, 86K9, 86M4]. The results may be summarized as follows where the critical exponents for the RFIM ($H_0 \neq 0$, $\boldsymbol{H_0} \parallel \boldsymbol{c}$) are marked with a superscript "~":

LMB (x = 0.6, $H_0 = 2$ T): $T_C = 46.13$ K, $\tilde\alpha = 0$ (log), $A^+/A^- = 1.13(1)$

n-scattering (x = 0.6, $H_0 = 2$ T): $\tilde\nu = 1.00(15)$, $\tilde\gamma = 1.75(20)$, $\tilde\eta \approx 0.25$

exponent ϕ for the crossover REIM → RFIM by various methods:
$\phi = 1.40(5)$ [85B6], $\phi = 1.42(3)$ [86B6], $\phi = 1.44(4)$ [86K9], $\phi = 1.42(5)$ [86M4]

Thus, the ratio of ϕ and $\gamma_{REIM} = 1.31$ becomes $\phi/\gamma_{REIM} = 1.08$ in accordance with the theoretical prediction [86A6]. The neutron scattering data were analysed by means of Eq. 4.118, i.e. a sum of a Lorentzian and a Lorentzian squared, and by convolving $S(q)$ with the resolution function of the spectrometer. Analogous to Eq. 4.105, the amplitudes A_{RF} and B_{RF} in Eq. 4.118 are proportional to κ with the appropriate exponents $\tilde\eta$ and $\tilde\eta'$

$$A_{RF} \sim \kappa^{\tilde\eta} \sim |t - t_C|^{\tilde\eta\tilde\nu} \qquad B_{RF} \sim \kappa^{\tilde\eta'} = \kappa^{2\tilde\eta} \sim |t - t_C|^{2\tilde\eta\tilde\nu} \tag{4.122}$$

where $\tilde\eta'$ is the exponent corresponding to the disconnected susceptibility with $\tilde\eta' \leq 2\tilde\eta$ [85S4]. Application of scaling laws [85B7] and also the experimental data suggest $\tilde\eta' = 2\tilde\eta$ as used in Eq. 4.122. The neutron scattering data were analysed with respect to the second form for A_{RF} and B_{RF} because of the larger uncertainties in κ as compared to $|t - t_C|$ [85B6]. The observation of the phase transition in a 3D RFIM system and the determination of the critical behaviour may be obscured by a slowed down dynamics, by nonequilibrium effects and hysteretic behaviour [84Y3, 85B5] and also by concentration gradients [88B6, 88K7]. The values of the critical exponents for $Fe_xZn_{1-x}F_2$ with $H_0 \neq 0$ (RFIM) agree well with the theoretical ones for the 2D Ising model. In the theoretical results for the 3D RFIM is still some discrepancy. Although it is clear that a phase transition will occur at low temperatures and sufficiently small fields [84V5, 87B7], the character of the phase transition is still unclear. The critical behaviour is rather consistently described by scaling theories [85B7, 85V2, 86F4] where the lattice dimension d is replaced $d - \Theta$ (cf. Eq. 4.113). These theories assume the usual second order magnetic phase transition. However, Monte Carlo simulations support only partly this scenario [86O1, 86O2] while others indicate a first order transition [85Y3, 86Y2] with the critical exponents of the 2D Ising model. Recently, Monte Carlo studies were performed with the aim to clarify the situation, with the bimodal distribution [93R2] and the Gaussian distribution [95R4] of the random field. From the latter, a two-exponent scaling ($\tilde\eta' = 2\tilde\eta$!) and a discontinuous transition results, and the values of the critical exponents are

$$\tilde\nu = 1.1(2), \qquad \tilde\eta = 0.50(5), \qquad \tilde\eta' = 1.03(5), \qquad \tilde\beta = 0$$

That means the order parameter, the magnetization, will be discontinuous at T_C, but there is no divergence of C_{magn} and no latent heat at the phase transition. Thus, the transition can be called a discontinuous one, but it may perhaps be better to call it a "hybrid order" transition [95R4]. Also, the experimental situation is not so clear as it seems from the above quoted results. In recent Faraday optical measurements on $Fe_{0.85}Mg_{0.15}Br_2$ [94K], a cusp-like behaviour of C_{magn} ($\tilde{\alpha} \to -1$) was observed instead of a symmetric logarithmic singularity. But there are still open questions since dynamic rounding might be the origin of the observed cusp-like behaviour [94K].

Random-field effects in the 2D RFIM like destruction of the phase transition and frozen-in metastable domain states were also observed in a number of other 2D diluted antiferromagnets (see Table 6). Dikken et al. [84D2] studied $K_2Ni_xZn_{1-x}F_4$ with x = 0.75, 0.85, 0.96 by neutron scattering under FC conditions. They performed scans along the antiferromagnetic Bragg rod (q_z-direction) through the (0, 1, 0) superreflection and found that the system quenches into non-equilibrium domain states. The breakup of ordering along the *c*-axis (3D LRO) was found in the neutron scattering results which were fitted to

$$S^{\parallel}(q_z) \sim \frac{\sinh(\kappa_z c)}{\cosh(\kappa_z c) - \cos(q_z c)} \tag{4.123}$$

which results from a discrete Fourier transform along the *c*-axis and which becomes a Lorentzian for small $\kappa_z c << 1$ [84D2]. They found further that the order in the layers is also affected by the random fields but remains unexpectedly long-ranged (2D LRO). A not so drastic breakup of LRO along the *c*-axis (3D LRO) was observed even for $H_0 = 0$ in $K_2Ni_xZn_{1-x}F_4$ [84D2] and $K_2Mn_xZn_{1-x}F_4$ [87D2] which is ascribed to the site-random fields due to the imbalance of exchange interaction induced by the dilution. An especially interesting problem is the influence of the random fields on the magnetic (H_0, T) phase diagram of a diluted 2D antiferromagnet. Therefore, Cowley, Birgeneau et al. [88C3, 91B2, 93C2] have studied the phase diagram of the diluted system $Rb_2Mn_{0.7}Mg_{0.3}F_4$ by neutron diffraction. For pure 2D uniaxial antiferromagnets like Rb_2MnCl_4, Rb_2MnF_4 etc., the phase diagram with the antiferromagnetic (AF) phase, the spin-flop (SF) phase, the paramagnetic (PM) phase and the multicritical point has been presented in Sect. 3.1.6 (cf. Figs. 3.18 and 3.19). The phase diagram of the diluted uniaxial antiferromagnet $Rb_2Mn_{0.7}Mg_{0.3}F_4$ is reproduced in Fig. 4.41. The external field $\boldsymbol{H_0} \parallel \boldsymbol{c}$ necessary for such an investigation destroys the transition from the PM- to the AF-phase, and the random fields cause metastable domain states. Only for small H_0, near the temperature axis in Fig. 4.41, antiferromagnetic LRO exists in the range $0 \le T \le T_N = 14.2(3)$ K. For the SF-phase, on the other hand, the ordering and the critical behaviour is not affected by the random fields [78A5]. There will be a topological LRO as observed in the pure antiferromagnets and as described for the 2D XY-model in Sect. 4.1.8. Thus, there is a well defined boundary $H_{SF}(T)$ of this phase (cf. Fig. 4.41). Although the usual spin-flop transition is not observed over a wide range in the phase diagram of such diluted antiferromagnets but only under special conditions like AFMR experiments at low temperatures (cf. Fig. 3.53 in Sect. 3.3.3), this transverse phase will also here be called spin-flop phase. At fields below $H_{SF}(T)$ and for $T < T_N$, metastable behaviour and domain states due to the random fields are observed. Similar to the LMB data for $Rb_2Co_{0.85}Mg_{0.15}F_4$ (cf. Fig. 4.39 and Eq. 4.120), a sharp metastability boundary $T_M(H_0)$ (cf. Fig. 4.41) is found below which the neutron scattering results depend on the prior history of the sample and indicate metastable behaviour. When the field H_0 is raised from $H_0 = 0$ towards the metastability boundary, there is a range of H_0 in which the 3D LRO is not much affected but, above a certain field H_0 marked LRO in Fig. 4.41, the LRO is drastically reduced. If H_0, on the other hand, is lowered from high values where no LRO exists, no onset of a 3D LRO is observed. Cowley, Birgeneau et al. [91B2, 93C2] have also derived a theory of the random-field phase diagram. And the curve in Fig. 4.41 for the boundary H_{SF} of the transverse phase is calculated by means of their Eq. (28) in [93C2] with the parameter values $D = 55$ K, $C = 1.67$ and $H_B = 1.25$ T. For calculating the curve for the metastability boundary $T_M(H_0)$, Eq. (30) [93C2] is employed with $T_N(0) = 14.2$ K and with the value $\phi = 1.74(17)$ for the crossover exponent (cf. Eqs. 4.116–4.117b). This value of ϕ agrees well with that obtained for $Rb_2Co_{0.85}Mg_{0.15}F_4$ [85B3] and with theoretical predictions [86A6]. The proportionality factor is 0.19. A further theoretical result is that the bicritical point is moved to $T = 0$ [93C2].

A final remark to this section is that random fields effects are not only found in diluted antiferromagnets to which a uniform external field $\boldsymbol{H_0} \parallel \boldsymbol{c}$ has been applied but that such effects are also observed in mixed antiferromagnets with competing anisotropies where the random fields originate from the competing anisotropy fields and the exchange fields acting on the neighbours. For two such compounds, $K_2Mn_{1-x}Fe_xF_4$ [86F5] and $K_2Fe_{1-x}Co_xF_4$ [84V7] (cf. Sect. 3.3.5), random field effects have been reported which are similar to those discussed above for diluted systems in a uniform field, e.g. the destruction of 3D LRO and the appearance of nonequilibrium domain states in FC experiments. For details see Table 6.

9.12.4.1.13 Critical Properties of Spin Glasses – 2D Ising Spin Glass

It was already mentioned in Sect. 3.3.6 that the mixed system $Rb_2Co_xCu_{1-x}F_4$ shows spin glass behaviour in the concentration range $0.18 \le x \le 0.40$, and the system $Rb_2Cr_{1-x}Mn_xCl_4$ exhibits re-entrant spin glass behaviour for $0.2 \le x \le 0.7$. Both insulating systems are short-range spin glasses since the competing exchange interactions causing the spin-glass behaviour are short-ranged. This is in contrast to metallic spin glasses where the dominating interactions are long-ranged. The first system $Rb_2Co_xCu_{1-x}F_4$ with its Ising-like anisotropy represents a good experimental realization of a 2D random-bond Ising spin glass. We recall further from Sect. 3.3.6 that the 2D Ising spin glass has no transition to a spin glass phase for $T_C > 0$ but that theoretical considerations yield $T_C = 0$ for this system [79M3, 80M8, 84B7, 84M8]. Experimentally, a freezing temperature $T_f > 0$ was observed (cf. Fig. 3.72) different from $T_C = 0$. This is similar to the difference between the critical temperature T_C and the Kosterlitz-Thouless temperature T_{KT} due to finite-size effects in the easy-plane ferromagnets Rb_2CrCl_4 and K_2CuF_4 (cf. Sect. 4.1.8). The reason for this behaviour will be discussed below in context with dynamic effects in spin glasses. Here, we will focus our attention on the static critical properties. And these can be observed also for a system with $T_C = 0$ since the fluctuations and low-lying excitations which are thought to be characteristic for the spin-glass phase are also present at and above T_C as well as in spin glasses with $T_C = 0$ [92N]. The spin glass correlation length ξ will therefore diverge for $T \to 0$ as $T^{-\nu}$ apart from corrections because of $T_C = 0$ [85H6]. These critical properties may be studied on $Rb_2Co_xCu_{1-x}F_4$ with $0.18 \le x \le 0.40$ by measurements of the magnetization M as a function of applied field H_0. Fig. 4.42 shows experimental results $M(H_0)$ for $x = 0.218$ at four different temperatures. Obviously, M does not depend linearly on H_0, and the nonlinear part is essential for the critical behaviour. M can be expanded in a series of odd powers of H_0/T [77S9, 84K9]. Following the analysis of Dekker et al. [88D8, 88D10, 88D11], H_0/T is replaced by $\chi_0 H_0$ where χ_0 is ideally the susceptibility, of a noninteracting system (Curie law) $\chi_0 = C/T$ with C defined in Eq. 3.25 in Sect. 3.1.3. Then the series for M can be written as

$$M = \chi_0 H_0 - a_3 (\chi_0 H_0)^3 + a_5 (\chi_0 H_0)^5 - a_7 (\chi_0 H_0)^7 + \ldots \qquad (4.124)$$

where not only χ_0 but also the coefficients a_3, a_5, a_7, etc. depend on the temperature. For a spin glass with a transition at $T_C > 0$, the first term $\chi_0 H_0$ in Eq. 4.124 is nonsingular at T_C. But the coefficient a_3 of the first nonlinear term is related to the spin glass order parameter susceptibility and is proportional to $(T - T_C)^{-\gamma}$ [76O, 77C8, 77S9]. From an expansion of the free energy in H_0/T [77S9], the critical exponents for the other coefficients are derived as $a_{2n+1} \sim (T - T_C)^{-n(\gamma+\beta)+\beta}$ for $n \ge 1$. Thus, the first coefficients will diverge at T_C as

$$a_3 \sim (T - T_C)^{-\gamma} \quad a_5 \sim (T - T_C)^{-(2\gamma+\beta)} \quad a_7 \sim (T - T_C)^{-(3\gamma+2\beta)} \qquad (4.125)$$

As a next step, the susceptibility $\chi = M/H_0$ is derived from the experimental data of M. For some magnetic fields between 0.1 mT and 1 T, the results for χ are presented as a function of temperature in Fig. 4.43. The nonlinear part of χ can now be expressed as [88D10]

$$\chi_{nl} = 1 - M/(\chi_0 H_0) = a_3(\chi_0 H_0)^2 - a_5(\chi_0 H_0)^4 + \ldots \qquad (4.126)$$

Similar to the scaling relations Eqs. 4.12 a–c in Sect. 4.1.2, the scaling relation for the nonlinear susceptibility reads $\chi_{\mathrm{nl}} = T^{\beta} \cdot g(H_0/T^{\Gamma})$ with $\Gamma = 1 + \frac{1}{2}(\beta + \gamma)$ [77S9, 81B9]. For practical use, Dekker et al. [88D7, 88D10] have replaced also in this relation H_0/T by $\chi_0 H_0$ in order to allow for deviations of χ_0 from strict Curie behaviour $\chi_0 = C/T$. Thus, they have used the scaling relation in the form

$$\chi_{\mathrm{nl}} \cdot T^{-\beta} = \hat{g}(\chi_0 H_0 / T^{\Gamma-1}) \tag{4.127}$$

where g and $\hat{g}$ are scaling functions homogeneous with respect to their arguments. The experimental data of χ_{nl} determined for fields from 0.1 mT to 1.25 T and for temperatures from 3.20 K to 4.25 K were plotted as $\chi_{\mathrm{nl}} \cdot T^{-\beta}$ versus $\chi_0 H_0 / T^{\Gamma-1}$, see Fig. 3 of [88D7] or Fig. 7 of [88D10]. The values for Γ and β were adjusted to gain optimum coincidence of the data on a universal curve. Thus, the critical exponents of the 2D Ising spin glass $\mathrm{Rb_2Co_{0.218}Cu_{0.782}F_4}$ are obtained as

$$\beta = 0.0(1) \qquad \Gamma = 3.2(2) \qquad \text{and} \qquad \gamma = 4.4(4)$$

These results agree with the predictions $\beta = 0$ and $\Gamma = 3.5(5)$ of a Monte Carlo simulation [84K9] for the 2D Edwards-Anderson spin glass model [75E2, 75S5].

A second way to determine the critical exponents β and γ is to analyse the temperature variation of the coefficients a_3 and a_5. For this purpose, a sufficiently large number of $M(H_0)$ isotherms (some of them shown in Fig. 4.42) were fitted to Eq. 4.124 cut off after the third term with χ_0, a_3 and a_5 as adjustable parameters. This procedure was restricted to the range of fields where the next term $a_7(\chi_0 H_0)^7$ is still negligible. The solid lines in Fig. 4.42 indicate the quality of the fit. They are calculated by means of Eq. 4.124 using the parameter values obtained in the fit. The temperature variation of the result for χ_0 equals the curves of M/H_0 in Fig. 4.43 for $H_0 = 0.1$ mT and $H_0 = 1$ mT which are practically indistinguishable. Finally, the temperature dependences of a_3 and a_5 are illustrated in Fig. 4.44 as a log-log plot. Above approximately $T_{\mathrm{f}} \approx 3$ K, $a_3(T)$ and $a_5(T)$ can well be described by a power law with divergence at $T_{\mathrm{C}} = 0$ (solid lines in Fig. 4.44). At lower temperatures, they deviate from the power law to lower values. This is ascribed to the slow but finite cooling rate which prevents the system to attain its equilibrium [88D10]. The exponents resulting from a fit of $a_3(T)$ and $a_5(T)$ to Eq. 4.125 are (see also Table 6)

$$\gamma = 4.5(2) \qquad \text{and} \qquad \gamma + \beta = 9.0(5) \qquad \text{yielding} \qquad \beta = 0.0(7)$$

The correlation length critical exponent ν for the spin-glass $\mathrm{Rb_2Co_{0.218}Cu_{0.782}F_4}$ is determined in combination with dynamical critical properties from the imaginary part $\chi''_{\mathrm{ac}}(\omega, T)$ of the ac susceptibility $\chi_{\mathrm{ac}}(\omega, T)$. The extremely slow relaxation of such disordered systems is better described by activated dynamic scaling than by conventional dynamic scaling. For a 2D spin glass with $T_{\mathrm{C}} = 0$, the dynamics of excitations up to length scales $L \le \xi \sim T^{-\nu}$ is expected to be dominated by thermal activation over energy barriers of height $B \sim L^{\psi}$ where ψ is the barrier exponent with $0 \le \psi \le 1$ [85H5, 87F1, 91G3]. Close to the transition, the divergence of ξ implies the existence of divergent barriers and, concomitantly, an extreme slowing down of the relaxation times. More details of this droplet model [86F6] will be presented in context with the dynamic critical properties of the 2D Ising spin glass in Sect. 4.2.2. In our context, we will use here only the fact that the dynamic quantities can be assumed to be functions of the scaling variable $\ln(\omega\tau_0)/\xi^{\psi}$ where τ_0 is a microscopic time [87F1] and, accordingly, $\chi''_{\mathrm{ac}}(\omega, T)$ can be brought into the activated-dynamic scaling form [88D8, 88D9, 89D3]

$$\chi''_{\mathrm{ac}}(\omega, T) = T^{\mathrm{q}} \cdot \mathcal{F}[-\ln(\omega\tau_0) \cdot T^{\psi\nu}] \tag{4.128}$$

with $$\mathrm{q} = -1 - \nu(2 - \eta - \psi) = -1 - \gamma + \psi\nu$$

where γ, ν, η are the usual critical exponents and $\mathcal{F}$ is a scaling function. Dekker et al. [88D8, 88D9, 89D3] have determined $\chi''_{ac}(\omega, T)$ for various frequencies $f = \omega/2\pi$ from 0.3 to 50000 Hz at temperatures running from 1 K to 7 K (see Fig. 4.45). These data were then reproduced as $\chi''_{ac}(\omega, T)\cdot T^{-q}$ versus $-\ln(\omega\tau_0)\cdot T^{\psi\nu}$ (see Fig. 4.46). For this scaling plot, the values of the parameters q, ψν, and τ_0 were optimized in order to achieve maximal coincidence of the data on a universal curve. The resulting values for which scaling is obeyed quite well are (cf. Table 6)

$$q = -3.0(5) \qquad \psi\nu = 2.2(3) \qquad \tau_0 = 10^{-13(1)}\ \mathrm{s}$$

from which the following values of the critical exponents are derived

$$\gamma = 4.2(6) \qquad \nu = 2.3(4) \qquad \psi = 0.9(2) \qquad \text{with } \eta = 0.2(2)\ \text{(fixed)}$$

where the value for η was adopted as a small positive one as appropriate for a 2D Ising spin glass [89D3]. The value for γ agrees well with the results obtained from the nonlinear susceptibility γ = 4.4(4) and 4.5(2).

These experimental results for the critical exponents of 2D Ising spin glass may now be compared with the values found in theoretical calculations. These are based upon two models which yield different results. One is the 2D random-bond Ising spin glass with a $\pm J$ distribution of the bonds, and the other one with a Gaussian bond distribution like the Edwards-Anderson model [75E2]. The theoretical results were obtained by various methods like model considerations [75S5, 76A13], high-temperature series expansion [86S6], transfer matrix method [83C5, 84B7], finite-size scaling [85H6, 88B7] and Monte Carlo simulations [83M6, 87O2, 96R]. Typical results obtained for the 2D Ising spin glass with $\pm J$ bond distribution are [83C5, 83M6, 86S6, 87O2, 88B7]

$$T_C = 0.02(11)\,J \qquad \beta = 0.10(3) \qquad \gamma = 4.6(5) \qquad \nu = 2.6(4) \qquad \eta = 0.20(5)$$

and for the 2D Ising spin glass with Gaussian distribution [84B7, 84M9, 85H6, 96R1]

$$\beta = 0 \qquad \gamma = 7.0(2) \qquad \nu = 3.6(2) \qquad \eta = 0$$

where $\eta = 0$ results also from an additional scaling law $2 - \eta = d$ for $T_C = 0$ [82B5]. The reader is recommended to consult also a similar compilation of critical exponent values in Table 6.2 on p. 193 of [93M3]. At first, the differences between these two sets evidence that the 2D Ising spin glass with $\pm J$ bond distribution and that with Gaussian bond distribution are not in the same universality class. Secondly, the experimental data for $Rb_2Co_{0.218}Cu_{0.782}F_4$ fit far better to those for the 2D spin glass with $\pm J$ distribution. Therefore, this model seems to be more appropriate to describe the critical properties of this insulating spin glass. Up to now, the magnetic contribution C_{magn} to the specific heat and its critical exponent α has not been mentioned, neither in the experimental data nor in the theoretical results. The reason for this is that C_{magn} of the spin glass sample with x = 0.218 in the system $Rb_2Co_xCu_{1-x}F_4$ shows no singularity near T_f or near $T_C = 0$ but only a broad maximum due to short-range correlations near 40 K [88D1, 95R5], while samples with x = 0.083 and x = 0.11 show broadened λ-shaped peaks at $T_C = 5.18$ K and $T_C = 5.04$ K, resp., below which they order ferromagnetically [95R5].

The other system $Rb_2Cr_{1-x}Mn_xCl_4$ is, on the other hand, a realization of a 2D spin glass with XY-like continuous symmetry. Less is known with respect to its critical properties in comparison to the 2D Ising spin glass. There have been a number of theoretical investigations for the 2D random-bond XY-model. One problem studied theoretically is the ground state of a 2D XY-model with ferromagnetic interactions to which some antiferromagnetic bonds were added [79F4, 89V]. As in the 2D XY-model, discussed in Sect. 4.1.8, the spins are confined to the basal plane and may form vortices. Villain [77V2] has introduced frustration and the chirality κ to the disordered 2D XY-model. He considers four-spin plaquettes with ferro- and antiferromagnetic interactions which may be unfrustrated with $\kappa = 0$ (Fig. 4.47a) and frustrated with $\kappa = +1$ and $\kappa = -1$ (Figs. 4.47b and 4.47c). He showed further that this model can be mapped onto a

2D Ising spin glass with Coulomb interactions where the spins are the chiralities $\kappa = \pm 1$. This model may be compared to the spin configuration (see Fig. 4.48) of an array of 10 × 10 spins obtained within a classical ground state calculation for an array of 40 × 40 spins for a $Rb_2Cr_{0.41}Mn_{0.59}Cl_4$ spin glass sample [88C6, 88S9]. The Cr- and the Mn-spins art represented by arrows. The actual spin values 2.0 and 2.5 are replaced by the average value $\overline{S} = 0.59 \cdot 2.0 + 0.41 \cdot 2.5 = 2.21$ [88C6] which gives the length of the arrows in Fig. 4.48 for those spins confined to the *c*-plane while shorter arrows indicate a significant spin component perpendicular to the plane and parallel to the *c*-axis. The single-ion anisotropy of the Cr^{2+}-ions favours spin directions perpendicular to the *c*-axis. But frustration of some spins may lead in the classical calculation to spin orientations parallel to the *c*-axis. On the whole, the spin configuration in Fig. 4.48 can obviously be thought as composed of such four-spin plaquettes. Villain's chirality concept served as a basis for many other model calculations for the 2D XY spin glass. A basic question is that for the effect of disorder and frustration on the Kosterlitz-Thouless transition [73K3, 78K2] to a topological LRO and a transition to a ferromagnetic state due to finite-size effects in the pure 2D XY-model (cf. Sect. 4.1.8). To answer this question, Monte Carlo simulations were performed on the 2D $\pm J$ XY spin glass [81K14]. In their simulation of this chiral spin glass, Kawamura and Tanemura [85K2, 87K3] find a chiral ordering at $T_C = 0$ and a spin glass susceptibility critical exponent $\gamma = 1.9(1)$. The Monte Carlo results of Jain and Young [86J3] predict also a transition at $T_C = 0$ and yield for 2D systems the following values of the critical exponents

$$\gamma = 1.80(5) \qquad \nu = 1.08(27) \qquad \eta = 0.3(3)$$

In contrast, Teitel and Jayaprakash [83T8] conclude from their Monte Carlo calculation for the fully frustrated XY-model a transition at a finite temperature $T_C > 0$ and as in the 2D XY-model a universal jump of $\tilde{K}_{\text{eff}}$ (cf. Eqs. 4.48 a–c) near T_C from about $2/\pi$ to zero. They emphasize that the nature of the transition is deeply influenced by the existence of the chiral degrees of freedom. So, the theoretical situation seems to be not yet fully clarified.

With respect to the experimental results on $Rb_2Cr_{1-x}Mn_xCl_4$, all transition temperatures from the paramagnetic phase (PM) to the ferromagnetically (F) or antiferromagnetically ordered phase (AF) and finally to the re-entrant spin-glass freezing (RSG) obtained by various groups working in this field [84M1, 86N3, 88H4, 88K8, 88S7, 88T2, 89S1, 92S7] are compiled in the (T_C, x) phase diagram of $Rb_2Cr_{1-x}Mn_xCl_4$ (Fig. 4.49), see also [81M1, 82K6, 84K8, 86K12, 91S1]. The data in Fig. 4.49 are widely scattered and especially the bounderies PM-F and PM-AF seem to be not very well defined. Some average values are indicated by dashed lines. And the question arises whether these transitions are really good phase transitions or whether the transition is destroyed as in 2D random-field systems which we have discussed in the preceding section. Doubts about the transition come up when for x = 0.70 [88T2] and x = 0.75 [88H4] the order parameter critical exponent deduced from the intensity of the (1, 0, 0) antiferromagnetic Bragg reflection is reported $\beta \approx 0.5$ for which no explanation is available. We note further that the magnetic excitations of $Rb_2Cr_{1-x}Mn_xCl_4$ with x = 0.25, 0.59, 0.70 consist of wave-like magnons and dispersionless cluster modes (see Figs. 3.75–3.77 in Sect. 3.3.6). All these results are rather unusual but qualitatively identical for all three samples where one shows antiferromagnetic order, one spin-glass behaviour and one ferromagnetic order. This is possibly due to the high degree of disorder in these samples. Such disorder was, for example, reported for the x = 0.70 sample [88T2] where the inverse correlation length κ and the relaxation rate Γ derived from the width in q and ω of a rod scan at (1, 0, 0.28) remain finite below the transition temperature far above the spectrometer resolution. The value of κ stays at that level down to about 10 K where it increases again at the onset of a freezing process. Thus, the antiferromagnetic order in this sample is not long-ranged but finite. Our conclusion is that the magnetic order is of finite range in time and space for concentrations sufficiently away from the end members with true long-range magnetic order. For the x = 0.20 sample, the critical exponent β was deduced from the magnetic intensity of the (0, 0, 4) Bragg reflection as 0.223 [91S1] by analysing the experimental data by means of a new 4D integration technique in the ($\boldsymbol{q}$, ω) space [92S9]. This value of β is close to $\beta = 0.231$ for a 2D XY-model (cf. Eq. 4.66).

Finally, it is worth mentioning that also in $Rb_2Co_xCu_{1-x}F_4$ disorder phenomena were observed in the ordered phases, e.g. for x = 0.88 with easy-axis antiferromagnetic order below $T_N = 88.1$ K [92S1, 94S4, 95S2]. Upon lowering the temperature towards T_N, the inverse correlation length κ does not vanish at T_N but stays finite at a value κ_1 corresponding to $\xi_1 / a = 14.5$. The system exhibits a crossover from 2D Ising behaviour for $T > T_N$ to a multidomain state in the range 75 K $\le T \le T_N$ and to a 3D LRO with $\kappa \to 0$ below 75 K. The analysis of the data above T_N required an ansatz

$$\kappa = \kappa_1 + \kappa_0^+ t^\nu \tag{4.129}$$

analogous to percolation (cf. Eq. 4.106) and to random field effects (Eq. 4.119) and where t is the reduced temperature. A fit of the experimental values for κ to Eq. 4.129 at temperatures above T_N yielded $\nu = 1.02(4)$, $\kappa_0^+ / a^* = 0.34(3)$ and $\kappa_1 / a^* = 0.011(2)$ (cf. Table 6). The critical exponent γ was then determined by means of the relation

$$\chi^{cc}(q = 0)_{\text{ideal}} = \chi^{cc}(q = 0)\ [(\kappa_1 + \kappa_0^+ t^\nu) / (\kappa_0^+ t^\nu)]^{2-\eta} \sim t^{-\gamma} \tag{4.130}$$

A fit to the experimental data for $\chi^{cc}(q = 0)$ to Eq. 4.130 lead to $\gamma = 1.5(2)$. These values for the critical exponents (see also Table 6) compare well with the theoretical ones for the 2D Ising model (cf. Table 7). Thus, the experimental data are more uniform with respect to the phase transition properties for $Rb_2Co_xCu_{1-x}F_4$ with 2D Ising spin glass behaviour than for $Rb_2Cr_{1-x}Mn_xCl_4$ which is a re-entrant 2D XY spin glass for intermediate concentrations x. Summarizing this section, we have seen from the experimental data and from theoretical considerations that these mixed systems with competing exchange interactions and with competing anisotropies exhibit a number of disorder phenomena.

9.12.4.2 Dynamic Critical Properties and Relaxation

9.12.4.2.1 Characteristic Frequency from Neutron Inelastic Scattering

The fluctuations giving rise to the critical phenomena are not only frozen spatial fluctuations as discussed in context with the static critical behaviour in Sect. 4.1.5 but also temporal fluctuations. The latter will clearly have an effect on the correlation function (Eq. 4.22) and, consequently, on the neutron scattering cross section in Eq. 4.21 and can thus be studied experimentally. Such an investigation has been performed for Rb_2CoF_4 [82H4]. As a first step in Sect. 4.1.5, we have bypassed the frequency dependence in the neutron scattering data by integrating Eq. 4.21 over ω (cf. Eq. 4.24, quasi-elastic approximation [71B1]). Now, we will focus our attention to this frequency dependence reflecting the temporal fluctuations which may be observed by inelastic scattering of neutrons with a triple-axis spectrometer. For the interpretation of such experimental data, the spectral shape function $F^{\alpha\beta}(\boldsymbol{K}, \omega)$ in Eq. 4.23 is to be considered for which also Eq. 4.25 applies in case of an uniaxial easy-axis antiferromagnet. As mentioned already in context with the static critical behaviour in Sect. 4.1.5, the transverse fluctuations will be strongly suppressed in Rb_2CoF_4 due to the large anisotropy and only the longitudinal ones observed. Therefore, only $F^{zz}(\boldsymbol{K}, \omega) = F_{\|}(\boldsymbol{K}, \omega)$ will be kept in $d^2\sigma/d\Omega\, d\omega$ (Eq. 4.21) and all other $F^{\alpha\beta}(\boldsymbol{K}, \omega)$ are neglected. If it is justified to assume a single relaxation rate the spectral shape function will simply have the form of a Lorentzian [67H2, 82H4]

$$F_{\|}(\boldsymbol{K}, \omega) = [\Gamma_{\|}(\boldsymbol{K}) / \pi] \cdot [\Gamma_{\|}^2(\boldsymbol{K}) + \omega^2]^{-1} \tag{4.131}$$

where $\Gamma_{\|}(\boldsymbol{K})$ is the relaxation rate or, in the sense of the dynamic scaling hypothesis [69H1, 77H2], the characteristic frequency of the longitudinal critical spin fluctuations. For the measurement of $F_{\|}(\boldsymbol{K}, \omega)$ by neutron scattering, also rod scans are performed but now as constant-$\boldsymbol{K}$ scans with a triple axis

Finally, it is worth mentioning that also in $Rb_2Co_xCu_{1-x}F_4$ disorder phenomena were observed in the ordered phases, e.g. for $x = 0.88$ with easy-axis antiferromagnetic order below $T_N = 88.1$ K [92S1, 94S4, 95S2]. Upon lowering the temperature towards T_N, the inverse correlation length κ does not vanish at T_N but stays finite at a value κ_1 corresponding to $\xi_1/a = 14.5$. The system exhibits a crossover from 2D Ising behaviour for $T > T_N$ to a multidomain state in the range $75\ \mathrm{K} \le T \le T_N$ and to a 3D LRO with $\kappa \to 0$ below 75 K. The analysis of the data above T_N required an ansatz

$$\kappa = \kappa_1 + \kappa_0^+ t^\nu \tag{4.129}$$

analogous to percolation (cf. Eq. 4.106) and to random field effects (Eq. 4.119) and where t is the reduced temperature. A fit of the experimental values for κ to Eq. 4.129 at temperatures above T_N yielded $\nu = 1.02(4)$, $\kappa_0^+/a^* = 0.34(3)$ and $\kappa_1/a^* = 0.011(2)$ (cf. Table 6). The critical exponent γ was then determined by means of the relation

$$\chi^{cc}(q=0)_{\mathrm{ideal}} = \chi^{cc}(q=0)\ [(\kappa_1 + \kappa_0^+ t^\nu)/(\kappa_0^+ t^\nu)]^{2-\eta} \sim t^{-\gamma} \tag{4.130}$$

A fit to the experimental data for $\chi^{cc}(q=0)$ to Eq. 4.130 lead to $\gamma = 1.5(2)$. These values for the critical exponents (see also Table 6) compare well with the theoretical ones for the 2D Ising model (cf. Table 7). Thus, the experimental data are more uniform with respect to the phase transition properties for $Rb_2Co_xCu_{1-x}F_4$ with 2D Ising spin glass behaviour than for $Rb_2Cr_{1-x}Mn_xCl_4$ which is a re-entrant 2D XY spin glass for intermediate concentrations x. Summarizing this section, we have seen from the experimental data and from theoretical considerations that these mixed systems with competing exchange interactions and with competing anisotropies exhibit a number of disorder phenomena.

9.12.4.2 Dynamic Critical Properties and Relaxation

9.12.4.2.1 Characteristic Frequency from Neutron Inelastic Scattering

The fluctuations giving rise to the critical phenomena are not only frozen spatial fluctuations as discussed in context with the static critical behaviour in Sect. 4.1.5 but also temporal fluctuations. The latter will clearly have an effect on the correlation function (Eq. 4.22) and, consequently, on the neutron scattering cross section in Eq. 4.21 and can thus be studied experimentally. Such an investigation has been performed for Rb_2CoF_4 [82H4]. As a first step in Sect. 4.1.5, we have bypassed the frequency dependence in the neutron scattering data by integrating Eq. 4.21 over ω (cf. Eq. 4.24, quasi-elastic approximation [71B1]). Now, we will focus our attention to this frequency dependence reflecting the temporal fluctuations which may be observed by inelastic scattering of neutrons with a triple-axis spectrometer. For the interpretation of such experimental data, the spectral shape function $F^{\alpha\beta}(\boldsymbol{K}, \omega)$ in Eq. 4.23 is to be considered for which also Eq. 4.25 applies in case of an uniaxial easy-axis antiferromagnet. As mentioned already in context with the static critical behaviour in Sect. 4.1.5, the transverse fluctuations will be strongly suppressed in Rb_2CoF_4 due to the large anisotropy and only the longitudinal ones observed. Therefore, only $F^{zz}(\boldsymbol{K}, \omega) = F_{\|}(\boldsymbol{K}, \omega)$ will be kept in $\mathrm{d}^2\sigma/\mathrm{d}\Omega\ \mathrm{d}\omega$ (Eq. 4.21) and all other $F^{\alpha\beta}(\boldsymbol{K}, \omega)$ are neglected. If it is justified to assume a single relaxation rate the spectral shape function will simply have the form of a Lorentzian [67H2, 82H4]

$$F_{\|}(\boldsymbol{K}, \omega) = [\Gamma_{\|}(\boldsymbol{K})/\pi] \cdot [\Gamma_{\|}^2(\boldsymbol{K}) + \omega^2]^{-1} \tag{4.131}$$

where $\Gamma_{\|}(\boldsymbol{K})$ is the relaxation rate or, in the sense of the dynamic scaling hypothesis [69H1, 77H2], the characteristic frequency of the longitudinal critical spin fluctuations. For the measurement of $F_{\|}(\boldsymbol{K}, \omega)$ by neutron scattering, also rod scans are performed but now as constant-$\boldsymbol{K}$ scans with a triple axis spectrometer. The wavevector transfer ist again $\boldsymbol{K} = \boldsymbol{Q}_0 + \boldsymbol{q}$ with $\boldsymbol{Q}_0$ located on the Bragg rod, e.g. $\boldsymbol{Q}_0 \triangleq (1, 0, \zeta_z)$, and $\boldsymbol{q}$ perpendicular to the rod, e.g. $\boldsymbol{q} \triangleq (\zeta, \zeta, 0)$. Similar to the approach in the investigation of the static critical properties it is advantageous to express $\Gamma_{\|}(\boldsymbol{K})$ as function of $q = |\boldsymbol{q}|$ and of the inverse correlation length $\kappa = \kappa_0^+ t^\nu$ $(T > T_N)$ instead of the reduced temperature t (cf. Eq. 4.27)

$$\Gamma_{\|}(\boldsymbol{K}) \rightarrow \Gamma_{\|}(q, \kappa) \tag{4.132}$$

At $T = T_N$, $\Gamma_{\|}(q, \kappa)$ will go to zero, and according to the dynamic critical scaling laws [69H1, 71S1 ,77H2, 82H4], it may be expressed as

$$\Gamma_{\|}(q, \kappa) = q^z \cdot \Omega^{\pm}(q/\kappa) \quad \text{and} \quad \Gamma_{\|}(q, \kappa) = \kappa^z \cdot \tilde{\Omega}^{\pm}(q/\kappa) \tag{4.133}$$

In Eq. 4.133, z is the dynamic critical exponent, $\Omega^{\pm}(q/\kappa)$ and $\tilde{\Omega}^{\pm}(q/\kappa)$ are universal scaling functions homogeneous in q/κ [71S1] and "+" and "–" refer again to $T > T_N$ and $T < T_N$, respectively. Theoretical values for z are listed below in Table 8 for various systems. For the 2D Ising antiferromagnet, conventional theory yields $z = 2 - \eta = 1.75$. The results of various methods for calculating z have been reviewed by Mazenko and Valls [81M3]. And it was the intention of an inelastic neutron scattering study of Rb_2CoF_4 [82H4] to obtain a direct experimental value for z. In the constant-$\boldsymbol{K}$ scans, the scan variable is the frequency ω. The experimental data are peaked at $\omega = 0$ and $q = 0$. We recall that in case of Co-compounds only $\chi_{\|}(q, t)$ contributes to the signal in addition to $\Gamma_{\|}(q, \kappa)$. The former is taken into account using the Fisher approximant (Eq. 4.29) and inserting there the experimental values $\eta = 0.2$ and, by using Eq. 4.32a for κ, $\nu^+ = 0.99$.and $\kappa_0^+ / a^* = 0.362$ (see Table 6 and [74S1, 79I1]). By means of a fit of the neutron intensity $I(\omega)$ to Eq. 4.131, then the width $\Gamma_{\|}$ in frequency space is obtained. For scans at $T > T_N$ on top of the rod, i.e. with $q = 0$, the analysis of $\Gamma_{\|}$ yields values for z and for the critical amplitude Ω_0^+ (see Table 6 and [82H4]) according to

$$\Gamma_{\|}(0, \kappa) = \tilde{\Omega}_0^+ \cdot \kappa^z + \ldots = \tilde{\Omega}_0^+ \cdot (\kappa_0^+)^z \cdot t^{z\nu} + \ldots \tag{4.134}$$

The critical exponent z is here again determined by means of a log-log plot as shown for the static critical properties of K_2CoF_4 in Fig. 4.7 in Sect. 4.1.5. A second possibility for the determination of z is to perform ω-scans at $T = T_N$ $(t = 0)$ for various values of q and to determine thus z and Ω_0 by means of

$$\Gamma_{\|}(q, 0) = \Omega_0 \cdot q^z + \ldots \tag{4.135}$$

The values of z obtained from the scans on top of the rod or across the rod at $T = T_N$ agree quite well within the limits of experimental error. The average value is $z_{av} = 1.69$ (cf. Table 6), and it agrees also with the theoretical value $2 - \eta = 1.75$ (cf. Table 8 below).

9.12.4.2.2 Relaxation Time – Activated Dynamics – Aging

Dynamic critical phenomena may not only be studied by neutron scattering as in the last section but also by ultrasonic studies near structural phase transitions and by measurements of the ac susceptibility. When the temporal fluctuations and the relaxation processes are the same as those contributing to the neutron scattering results on Rb_2CoF_4, the relaxation time τ would simply be the reciprocal of the relaxation rate or characteristic frequency Γ, i.e. $\Gamma_{\|}(q, \kappa)$ in case of Rb_2CoF_4 (cf. Eq. 4.132)

$$\tau = \Gamma^{-1} \sim \xi^{z} \sim t^{-z\nu} \tag{4.136}$$

The relation between the relaxation time τ and the power law of the reduced temperature t in Eq. 4.136 was, for example, employed for the interpretation of the results of a computer simulation for a 3D short-range Heisenberg spin glass [86O3], and a critical exponent $z\nu = 5.9(2)$ was obtained. The critical divergence of the sound attenuation α near a structural phase transition at T_{C1} [73R1, 81L] follows also a power law

$$\alpha = \alpha_0 + \alpha^{+} t^{-\tilde{\rho}} \qquad \text{with} \qquad \tilde{\rho} = \rho + z\nu \tag{4.137}$$

where the exponent ρ is defined in Eq. 4.87a in Sect. 4.1.10 so that $\tilde{\rho} - \rho$ yields $z\nu$. But this critical exponent is also obtained from an analysis of the frequency dependence of the sound attenuation and a determination of the relaxation time τ

$$\alpha - \alpha_0 \sim \frac{\omega\,\tau^2}{1 + (\omega\,\tau)^2} \qquad \text{with} \qquad \tau = \tau_0^{+} \cdot (t_1)^{-z\nu} \tag{4.138}$$

In Eq. 4.138, τ_0^{+} is the critical amplitude of the relaxation time and $t_1 = T/T_{C1} - 1$ the reduced time. Such ultrasonic studies with the determination of $\tilde{\rho}$, $z\nu$ and τ_0^{+} were performed on $(CH_3NH_3)_2FeCl_4$ [82Y2] and $(C_2H_5NH_3)_2FeCl_4$ [83S1] near the continuous transition from the THT to the ORT phase (cf. Table 4). The results (see Table 6) compare well with theoretical predictions for the 3D XY-model [76M5], namely with the values $\tilde{\rho} = 1.73$ and $z\nu = 1.36$.

The relaxation time τ can also be determined from measurements of the ac susceptibility at various frequencies $\omega = 2\pi f$ and temperatures T

$$\chi_{\mathrm{ac}}^{\alpha\alpha}(\omega, T) = \partial m_{\alpha} / \partial h_{\alpha} = \chi'_{\mathrm{ac}}(\omega, T) + \mathrm{i}\,\chi''_{\mathrm{ac}}(\omega, T) \tag{4.139}$$

Eq. 4.139 combines the statements of Eq. 3.95 in Sect. 3.2.3 and of Eq. 4.52 in Sect. 4.1.8 where $\boldsymbol{h} \sim \mathrm{e}^{-2\pi \mathrm{i} f t}$ is the ac field and $\boldsymbol{m}$ the response of the system to it. The superscripts α denote directions, either crystallographic ones ($\alpha = a, b, c$) or coordinate axes ($\alpha = x, y, z$). In general, the measured data χ_{app}, i.e. the apparent susceptibility, have to be corrected for demagnetization effects in the way shown in Eq. 3.94b in Sect. 3.2.3 (see also [89D3]). This correction procedure requires that both, χ'_{ac} and χ''_{ac} are measured. If only χ'_{ac} is available one should use the procedure for correction and analysis of the data employed by Kötzler et al. in their relaxation investigations [76K8]. If a system is studied with only a single relaxation mechanism and a single relaxation time τ, the internal χ_{ac}, corrected for demagnetization effects, can be expressed as the Debye equation [80H6, 80H10, 89D3]

$$\chi_{\mathrm{ac}}(\omega, T) = \chi_{\mathrm{ad}} + \frac{\chi_{\mathrm{it}} - \chi_{\mathrm{ad}}}{1 - \mathrm{i}\,\omega\,\tau} \tag{4.140a}$$

with

$$\chi'_{\mathrm{ac}} = \chi_{\mathrm{ad}} + \frac{\chi_{\mathrm{it}} - \chi_{\mathrm{ad}}}{1 + (\omega\,\tau)^2} \qquad \chi''_{\mathrm{ac}} = \frac{(\chi_{\mathrm{it}} - \chi_{\mathrm{ad}})\,\omega\,\tau}{1 + (\omega\,\tau)^2} \tag{4.140b}$$

In the Eqs. 4.140, χ_{ad} and χ_{it} are the adiabatic and the isothermal susceptibility, resp., where χ_{it} is obtained for $\omega \to 0$, i.e. for ω so small that $\omega\tau_0 << 1$, and χ_{ad} refers to $\omega \to \infty$. For each frequency and each temperature, τ can be evaluated from Eq. 4.140 by means of [76K8, 80H6]

$$\tau = (\chi_{\mathrm{it}} - \chi_{\mathrm{ad}}) \cdot \mathrm{d}\chi_{\mathrm{ac}}^{-1} / \mathrm{d}(-\mathrm{i}\omega) \quad \text{or} \quad \tau = \chi''_{\mathrm{ac}} / [\omega \cdot (\chi'_{\mathrm{ac}} - \chi_{\mathrm{ad}})] \tag{4.141}$$

On K_2CuF_4 [80H6] and $(CH_3NH_3)_2CuCl_4$ [79O2, 80O1], ac measurements were performed with the determination of τ which is then analysed with respect to its divergence at the critical temperature. The correspondingly long relaxation times are responsible for the critical slowing down at the phase transition to ferromagnetic order in this case. The value for the exponent of τ obtained in this procedure (cf. Table 6), e.g. by means of Eq. 4.141, seems not to be simply related to zν. Therefore, a new exponent Λ was introduced for τ from ac measurements [79O2, 80H6]

$$\tau \sim t^{-\Lambda} \tag{4.142}$$

The difference between the static critical exponent γ and Λ is the exponent of Onsager's kinetic coefficient L [79O2]. The value of Λ reported for $(CH_3NH_3)_2CuCl_4$ is $\Lambda = 1.05$ although γ determined from $\chi_{\mathrm{ac}}(\omega \to 0)$ is 1.73 close to that for the 2D Ising model and thus zν could be expected also to be $z\nu = 1.75$ as in Rb_2CoF_4 from neutron scattering (see last section and [82H4]). This example demonstrates that Λ is not equal to zν. Whether or not more than one relaxation time is involved in the relaxation processes can be decided by means of a Cole-Cole plot which is a semicircle for one relaxation time and which deviates from the semicircle if more than one τ is taken into account. Elimination of $\omega\tau$ from Eq. 4.140b yields the following equation for χ'_{ac} and χ''_{ac}

$$[\chi'_{\mathrm{ac}} - \tfrac{1}{2}(\chi_{\mathrm{it}} + \chi_{\mathrm{ad}})]^2 + [\chi''_{\mathrm{ac}}]^2 = \tfrac{1}{4}[\chi_{\mathrm{it}} - \chi_{\mathrm{ad}}]^2 \tag{4.143}$$

which represents a semicircle because of $\chi''_{\mathrm{ac}} > 0$. For $K_2Cu_{0.75}Zn_{0.25}F_4$ [80H10], the Cole-Cole plot reveals two curves which are nearly semicircles. One is due to spin fluctuations present from high temperatures to slightly below T_C while the second appears slightly above T_C and is observed also in the ferromagnetic region below T_C. The latter is ascribed to ferromagnetically ordered clusters in this random system with a rather long lifetime. For the diluted sample $(CH_3NH_3)_2Cu_{0.92}Cd_{0.08}Cl_4$ [80O1], the curves in the Cole-Cole plot for several temperatures (see Fig. 4.50) are undoubtedly semicircles for reduced temperatures $t = T/T_C - 1 > 0.8$. But they deviate more and more from a semicircle form upon approaching the phase transition, i.e. for smaller t. Thus, the results indicate a single relaxation time far enough away from the transition but a distribution of relaxation times closer to T_C. For $t < 0.02$, the Cole-Cole plot forms an angle of 45° with the χ'_{ac}-axis. The same behaviour is observed for the theoretically derived dynamic susceptibility of a spin glass with Gaussian bond distribution near T_f [77K10]. Therefore, it is believed that these findings for $(CH_3NH_3)_2Cu_{0.92}Cd_{0.08}Cl_4$ are probably due to the randomness in this system.

A really wide-spread distribution of relaxation time was found for the 2D short-range Ising spin glass $Rb_2Co_{0.218}Cu_{0.782}F_4$ the general properties and the static critical behaviour of which were already presented in Sect. 3.3.6 and 4.1.13, respectively. Dekker et al. [88D9, 88D11, 89D3, 90M] have measured the ac susceptibility $\chi_{\mathrm{ac}}(\omega, T)$, i.e. χ'_{ac} and χ''_{ac}, for frequencies $0.3\ \mathrm{Hz} \le f \le 50\ \mathrm{kHz}$ and for temperatures $1\ \mathrm{K} \le T \le 7\ \mathrm{K}$. From their results, the real part χ'_{ac} is presented in Fig. 4.51 where we note that the maximum which is equal to the freezing temperature T_f depends considerably on the frequency, from $T_f = 3.3$ K for $f = 0.2$ Hz to $T_f = 3.75$ K for $f = 50$ KHz. We recall further from Sect. 4.1.13 that theory predicts for 2D Ising systems a transition to a spin glass phase at $T_C = 0$ while the experimental data for χ'_{ac} indicate a finite freezing temperature. The also determined results for the imaginary part χ''_{ac} have already been reproduced in Fig. 4.45 in Sect. 4.1.13 in context with the determination of the static critical exponents γ, ν and η (cf. Table 6) by means of activated dynamic scaling (cf. Eq. 4.128 and Fig. 4.46) the concept of which will be elucidated in more detail in this section. In view of the extremely broad

τ-distribution, the Cole-Cole equation was employed after the experimental data were corrected for demagnetization effects

$$\chi_{\mathrm{ac}}(\omega, T) = \chi_{\mathrm{ad}} + \frac{\chi_{\mathrm{it}} - \chi_{\mathrm{ad}}}{1 - (\mathrm{i}\omega\,\tau_{\mathrm{c}})^{1-\alpha}} \tag{4.144a}$$

$$\chi_{\mathrm{ac}}(\omega, T) = \chi_{\mathrm{ad}} + \frac{1}{2}\,(\chi_{\mathrm{it}} - \chi_{\mathrm{ad}})\left[1 - \frac{\sinh[(1-\alpha)\ln(\omega\,\tau_{\mathrm{c}})] - \mathrm{i}\cos(\alpha\,\pi/2)}{\cosh[(1-\alpha)\ln(\omega\,\tau_{\mathrm{c}})] + \sin(\alpha\,\pi/2)}\right] \tag{4.144b}$$

where τ_{c} is the mean or centre relaxation time and the parameter α determines the width of the distribution. For $\alpha = 1$, the distribution becomes infinitely wide and, for $\alpha = 0$, Eq. 4.144 reduces to Eq. 4.140 with a single τ, i.e. to the Debye equation. In the analysis of the experimental findings for $Rb_2Co_{0.218}Cu_{0.782}F_4$, the next step is to use the Cole-Cole plot for the determination of χ_{it}, χ_{ad} and α. For $\alpha \neq 0$, an additional term is added to Eq. 4.143

$$[\chi'_{\mathrm{ac}} - \tfrac{1}{2}(\chi_{\mathrm{it}} + \chi_{\mathrm{ad}})]^2 + [\chi''_{\mathrm{ac}}]^2 + \chi''_{\mathrm{ac}}\,\frac{\chi_{\mathrm{it}} - \chi_{\mathrm{ad}}}{\mathrm{tg}\,[(1-\alpha)\,\pi/2]} = \tfrac{1}{4}\,[\chi_{\mathrm{it}} - \chi_{\mathrm{ad}}]^2 \tag{4.145}$$

The values for α determined in this way are $\alpha = 0.848(5)$ at 6.00 K and $\alpha = 0.900(2)$ at 3.50 K as listed in Table 6. They are evidence that the distribution is extremely wide. The next step is to extract τ_{c} for each temperature by adjusting the experimental data to χ'_{ac} and χ''_{ac} in Eq. 4.144 simultaneously and inserting the values for χ_{it}, χ_{ad} and α there. The resulting data for τ_{c} in Fig. 4.52 demonstrate the extreme slowing down of the system, τ_{c} increases over 18 decades from 10^{-12} to 10^{6} s in the small temperature range from 7 K to 3.5 K. A fit of these data to a conventional power law (Eqs. 4.136 and 4.138) yields unreasonable values for T_{C} and $z\nu$. Therefore, activated dynamic scaling is more adequate for this disordered system with large randomness. While conventional dynamic scaling means $\tau \sim \xi^{z}$, activated dynamics is based on the droplet model of Fisher and Huse ([86F4, 86F6], see also [85V2]) where a typical droplet energy is $F \sim L^{\theta}$ where θ is the stiffness exponent. Theoretical calculations yield $\theta = -0.25$ for a 2D Ising system [88F4] so that excitations of arbitrary low energy destroy the spin glass order at finite temperatures. The exponent ν of the correlation length ξ is then identified as $\nu = |\theta|^{-1}$ from the condition that F is of order T and thus

$$F \approx T \sim L^{\theta} \approx \xi^{\theta}$$

At shorter length scales, the dynamics of excitations and also the relaxation is governed by thermal activation over energy barriers of height $B \sim L^{\psi}$ where ψ is the barrier exponent [85H5, 87F1, 91G3]. This leads to the relaxation time $\tau = \tau_0 \exp(B/k_{\mathrm{B}}T)$ [87F2] or

$$\ln(\tau/\tau_0) = B/k_{\mathrm{B}}T \sim \xi^{\psi}/T \sim T^{-(1+\psi\nu)} \tag{4.146}$$

The solid line in Fig. 4.52 is the result of a fit of the experimental data in Fig. 4.52 for $Rb_2Co_{0.218}Cu_{0.782}F_4$ to the expression

$$\tau_{\mathrm{c}} = \tau_0 \exp[(b/T)^{1+\psi\nu}] \tag{4.147}$$

The fit extending over the temperature range $3.7\ \mathrm{K} \le T \le 6.8$ K yields $\psi\nu = 2.2(2)$, $\tau_0 = (2 \pm 1) \cdot 10^{-13}$ s and b = 10.8(6) K. With ν = 2.3(4) reported in Sect. 4.1.13, the resulting values are (cf. Table 6)

$$\psi\nu = 2.2(2) \qquad \psi = 0.9(2) \qquad \theta = -1/\nu = -0.43(7)$$

For comparison, theoretical considerations [93M3] yielded $\theta = -0.38(3)$ while ψ is restricted to the range $0 \le \psi \le 1$ [93M3]. Other theoretical studies found

$\theta = -0.25$ and $\psi = 1$ for an Ising spin glass [88F4, 91G3], but

$\theta = 1$ and $\psi = 0.25$ for a random Ising ferromagnet [85H5, 87H5].

Thus, both experimental values of dynamic exponents for activated dynamic scaling in $Rb_2Co_{0.218}Cu_{0.782}F_4$ agree with the theoretical predictions, although the value for θ is a little large compared to the second theoretical value. A last point with respect to these experiments is to elucidate the wide distribution of relaxation times in $Rb_2Co_{0.218}Cu_{0.782}F_4$. The expression for this distribution according to Eq. 4.144 is

$$g(\tau) = \frac{1}{2\pi} \; \frac{\sin(\alpha\,\pi)}{\cosh[(1-\alpha)\ln(\tau/\tau_c)] - \cos(\alpha\,\pi)} \tag{4.148}$$

For some representative temperatures, $g(\tau)$ is reproduced in Fig. 4.53 which shows that $g(\tau)$ is symmetric about τ_c. The widths of the curves extend far beyond the time window of the experiments (shaded area in Fig. 4.53) extending from 10^{-5} s to 1 s, corresponding to the frequency range 0.3 Hz to 50 kHz. The drastic increase of τ_c upon lowering the temperature and the extreme width of the distribution for τ is probably a characteristic of the 2D Ising spin glass a realization of which is $Rb_2Co_{0.218}Cu_{0.782}F_4$, and there are no experimental data available for another compound.

The long relaxation times in $Rb_2Co_{0.218}Cu_{0.782}F_4$ mean that the system will need a corresponding long time (10^6 s $\triangleq$ 3.86 months) until equilibrium is reached. To study such equilibration effects, i.e. aging of the system, measurements as a function of time are necessary. The aging of the sample means probably the growth of domains. For normal growth kinetics, the size R of a domain after a time t (note that t is not the reduced temperature here!) is $R(t) \sim t^{1/2}$ [62L3, 78K11, 80P5]. In case of activated dynamics with barriers of height B between domains we will have analogous to Eq. 4.146

$$\ln(t/\tau_0) = B/k_B T \sim R^{\psi}/T \quad \text{or} \quad R(t) \sim [T\ln(t/\tau_0)]^{1/\psi} \tag{4.149}$$

Different classes for growth kinetics including the two above cases were studied by Lai et al. with Monte Carlo simulations [88L2]. Several time-dependent studies were performed on members of the $Rb_2Co_xCu_{1-x}F_4$ family by Schins et al. [91S2, 93S2, 93S3, 95V, 96M]. Measurements of the dc susceptibility were made with FC or ZFC procedures and introducing some waiting time before taking the data. Also the ac susceptibility was measured, in this case also as a function of time. Let us concentrate on the studies of χ_{ac} and the analysis of the experimental data. Following the lines of Fisher and Huse [88F3, 88F4], Schins et al. [93S2, 93S3] employed for the analysis of their data an expression for the time- and frequency-dependent ac susceptibility based on Eq. 4.149

$$\frac{\chi'_{ac}(\omega,t) - \chi'_{ac}(\omega,\infty)}{\chi'_{ac}(\omega,t)} = c' \left[\frac{|\ln(\omega/\omega_0)|}{\ln(t/\tau_0)}\right]^{(d-\theta)/\psi} \tag{4.150}$$

where $\chi'_{ac}(\omega,\infty)$ is the equilibrium value for $t \to \infty$. An analogous expression exists for $\chi''_{ac}(\omega,t)$. The ac investigations start with a quench of the sample from a temperature well above T_f, i.e. 8 K or 9 K, to a temperature close to T_f, i.e. 3.7 K, 3.9 K, and 4.1 K. The frequency range is chosen to optimize the experimental time window with respect to the relaxation times (Fig. 4.52), e.g. 0.01–10 Hz for a spin glass sample with x = 0.22. The ac susceptibility, χ'_{ac} and χ''_{ac} were then studied for various frequencies as a function of time, typically up to 10^4 s. The experimental data obtained in this way fit well to Eq. 4.150 with the choice $\tau_0 = 1/\omega_0 = 2 \cdot 10^{-13}$ s. The only fit parameter is then the exponent $(\mathrm{d} - \theta)/\psi$, and the values obtained in the fit are (see also Table 6)

x = 0.11 (ferromagnet)	$(\mathrm{d} - \theta)/\psi = 5.0(9)$	→	$\psi = 0.20(5)$	[93S2, 95V]
x = 0.22 (spin glass)	$(\mathrm{d} - \theta)/\psi = 2.4(2)$	→	$\psi = 0.93(10)$	[93S2, 93S3]
x = 0.33 (spin glass)	$(\mathrm{d} - \theta)/\psi = 2.1(2)$	→	$\psi = 1.06(10)$	[91S2, 93S3]

The values of ψ were calculated using the theoretical values for θ, namely $\theta = 1$ for the random ferromagnet and $\theta = -0.25$ for the spin glass. These results indicate that aging and activated dynamic scaling is not only found in the 2D spin glasses but also in samples of $\mathrm{Rb_2Co_xCu_{1-x}F_4}$ with ferromagnetic order confirming the findings about disorder and randomness in the mixed magnets with competing exchange interactions in Sect. 4.1.13. The aging and domain growth in a 2D Ising spin glass with Gaussian bond distribution was also the subject of extensive Monte Carlo simulations [94R] by calculating the autocorrelation function which scales with $t/\tau(t_\mathrm{w})$ where t is the time and τ is equal to the waiting time t_w for t_w smaller than the equilibrium time. The results are compatible with $\xi \sim (\ln t_\mathrm{w})^{1/\psi}$ ($\psi = 0.63$) but can also be fitted to conventional power law.

Also in diluted systems like $\mathrm{Rb_2Co_xMg_{1-x}F_4}$, time evolutions were observed which are not compatible with a domain growth proportional to $t^{1/2}$ but give evidence for logarithmic time dependence, for example in studying the time variation of magnetic order after a rapid quench by measuring the Bragg intensity $I(t)$ of the (1, 0, 0) reflection [83I2] or by observing the equilibration in random field systems [83I4, 85B3, 85B4]. We recall from Sect. 4.12 that a uniform field H_0 creates a random field in diluted systems and destroys the long-range magnetic order in 2D systems. The recovery of LRO after switching off the external field H_0 was investigated as a function of time for $\mathrm{Rb_2Co_{0.6}Mg_{0.4}F_4}$ with a $\mathrm{Co^{2+}}$-concentration close to the percolation threshold $\mathrm{x_p} = 0.593$. The time dependence of the magnetization M turned out to be proportional to $[\ln t]^\mathrm{x}$, apart from a constant term [90I1, 94I4]. This is exactly the form of Eq. 4.150 and thus an indication of aging in the sense discussed above. The value for x was found as $\mathrm{x} = (\mathrm{d} - \theta)/\psi = 3.5$ at 15 K. Another aspect of such diluted system is that they have fractal properties. The scattering function $S(\omega)$ was studied by high-resolution neutron inelastic scattering for $\mathrm{Rb_2Co_{0.6}Mg_{0.4}F_4}$ [95I3]. The experimental data can well be described by the following form of $S(\omega)$

$$S(\omega) = \int_{-\infty}^{+\infty} S(\boldsymbol{K}, \omega)\, \mathrm{d}^3 K = \frac{A_\mathrm{S}}{\omega^2 + \Gamma^2} + B_\mathrm{S}\, \omega^{-0.35(6)} \tag{4.151}$$

where the first term is the usual Lorentzian describing the critical scattering near T_N and the second term is due to anomalous spin diffusion, i.e. the diffusion of random walks on a percolating network. The theoretical description for this term is based on the work of Alexander et al. on fractals [82A, 83G3]. It yields for the exponent

$$\mathrm{D_f}/(2 + \theta) - 1 = -0.340$$

with the fractal dimension $\mathrm{D_f} = 1.896$ and $\theta = 0.871$. Aeppli et al. [84A, 86A5] have determined the dynamic critical exponent $\mathrm{z} = 2.4$ for $\mathrm{Rb_2Co_{0.58}Mg_{0.42}F_4}$ (cf. Table 6) and ascribed this value higher than $\mathrm{z} = 1.69$ for pure $\mathrm{Rb_2CoF_4}$ to anomalous spin diffusion. But according to theoretical studies [85H3, 85R5], the larger value of z for $\mathrm{Rb_2Co_{0.58}Mg_{0.42}F_4}$ may well be due to dynamical critical fluctuations near the percolation threshold in Ising systems.

Weak quasi-static singularities [95B2] were observed for the diluted ferromagnet $K_2Cu_{0.8}Zn_{0.2}F_4$ in the Griffiths regime by measuring the susceptibility χ' in zero magnetic field. Griffiths singularities [69G2] are expected in diluted ferromagnets in the temperature range between the Curie temperature of the pure material $T_C(0)$ and the Curie temperature of the diluted system $T_C(\mathrm{x})$ [85R4, 87B6]. Theoretical studies, including Monte Carlo simulations, mainly focussed on the dynamic aspects of the Griffiths phase, i.e. on the long-time behaviour of the autocorrelation function [88B4, 88D6, 89B5, 89C4, 92A2]. Thus it seems important that some experimental data on a diluted ferromagnet are reported. Significant deviations are found from the expected critical behaviour of $\chi' \sim [T - T_C(\mathrm{x})]^{-\gamma}$ at temperatures slightly below $T_C(0)$ by a linear regression data analysis.

9.12.4.2.3 Spin-Wave Lineshape of a 2D Heisenberg Ferromagnet

The static and dynamical behaviour of the correlation function will also influence strongly the lineshape of the spin waves of a magnetic system, i.e. the lineshape of the observed signal in neutron inelastic scattering. This has been studied in detail experimentally for K_2CuF_4 by Moussa and Villain [76M3, 77M1] and by Hirakawa et al. [83H4] and the experimental data have been compared to the theoretical expressions for a 2D Heisenberg ferromagnet [76M3, 77M1]. The neutron scattering cross section and the scattering function corresponding to inelastic neutron scattering are completely analogous to the cross section for diffuse or quasi-elastic neutron scattering derived in Sect. 4.1.5 (cf. Eq. 4.21) with the scattering function $S_D^{\alpha\beta}(\boldsymbol{K}, \omega)$ (Eq. 4.23) which is the Fourier transform in space and time of the correlation function $G^{\alpha\beta}(\boldsymbol{r}, t)$ (Eq. 4.22). In a similar way, the cross section for inelastic neutron scattering is proportional to the scattering function $S(\boldsymbol{q}, \omega)$ where $\boldsymbol{q}$ is the magnon wavevector in the first Brillouin zone and $\hbar\omega$ the magnon energy and where the superscripts αβ (xx, yy, zz or ξξ, ηη, ζζ) are omitted according to the notation of Moussa and Villain [76M3]. In their theory, $S(\boldsymbol{q}, \omega)$ is the space and time Fourier transform of the following correlation function

$$\langle S_\xi(\boldsymbol{r}, 0)\, S_\xi(\boldsymbol{r}', t) + S_\eta(\boldsymbol{r}, 0)\, S_\eta(\boldsymbol{r}', t)\rangle \tag{4.152}$$

where S_ξ and S_η are the transverse spin components in the (ξ, η, ζ) coordinate system introduced for K_2CuF_4 in context with Eq. 3.71 in Sect. 3.2.1 for the application of the Holstein-Primakoff transform so that the spin components S_ξ and S_η are finally related to the magnon creation and annihilation operators which are required for the inelastic neutron scattering process. The experiments on K_2CuF_4 for the determination of $S(\boldsymbol{q}, \omega)$ have been performed [76M3, 77M1, 83H4] in that wavevector range where K_2CuF_4 is a good approximation to a 2D Heisenberg ferromagnet (cf. Sects. 3.2.1, 4.1.7–4.1.9), i.e. the range $0.1 \le \zeta \le 0.5$ for both, $\boldsymbol{q} \mathrel{\hat{=}} (\zeta, 0, 0)$ [83H4] and $\boldsymbol{q} \mathrel{\hat{=}} (\zeta, \zeta, 0)$ [76F, 76M3]. The experimental data agree rather well with the theoretical predictions for the spin-wave lineshape, i.e. for the scattering function $S(\boldsymbol{q}, \omega)$ of a 2D Heisenberg ferromagnet. Since magnons have been measured in the Heisenberg range ($\zeta_x > 0.1$) also above T_C up to temperatures near 2 T_C, the comparison between experiment and theory is performed not only for temperatures below the Curie temperature T_C but also for temperatures above T_C. Since the 2D Heisenberg model does not develop a spontaneous magnetization, the theory cannot be based on an order parameter M but the spin-spin correlation function (cf. Eq. 4.22 in Sect. 4.1.5 and Eq. 4.47 in Sect. 4.1.8) may be used. Its spatial dependence is for low temperatures [76M3]

$$\langle S_\zeta(r)\, S_\zeta(0)\rangle \sim \left(\frac{r}{a}\right)^{-1/2\pi\widetilde{K}} \tag{4.153}$$

where r is the distance $|\boldsymbol{r} - \boldsymbol{r}'|$, a the lattice constant and $\widetilde{K} = (2S^2 J)/(k_B T)$ here again the ratio of the spin-wave stiffness and the temperature. As in Eq. 4.47, no averages $\langle S_\zeta(r)\rangle$ and $\langle S_\zeta(0)\rangle$ are subtracted in Eq. 4.153 because they vanish at all temperatures due to the lack of LRO in the 2D Heisenberg model.

Analogous to $L_{\mathrm{eff}} = (\xi/a) \sim (J/J')^{1/2}$ (cf. Fig. 4.23 for Rb_2CrCl_4 in Sect. 4.1.8, Moussa and Villain define a characteristic length of the system

$$r_1 / a = \sqrt{k_B T / J'} \tag{4.154}$$

which separates 3D from 2D behaviour due to the interlayer exchange coupling J' (cf. Eq. 3.69 in Sect. 3.2.1). For all lengths smaller than r_1, the system can be expected to behave as a 2D Heisenberg model. The difference with the considerations about the 2D XY-model is that in Eq. 4.154 $k_B T$ is used instead of the Heisenberg exchange constant J so that r_1 temperature-dependent while L_{eff} is not. For a real system like K_2CuF_4, a second crossover is expected from 2D Heisenberg to 2D XY behaviour. In the theory of Moussa and Villain, this crossover should occur near

$$r_2 / a = \sqrt{k_B T / J_A} \tag{4.155}$$

where J_A is the constant of the out-of-plane anisotropic exchange (cf. Eq. 3.69 in Sect. 3.2.1). It follows from Eqs. 4.154 and 4.155 that K_2CuF_4 will behave according to the 2D XY-model in the range $r_2 < r < r_1$. But fortunately, the effects of the 2D XY-model instead of the 2D Heisenberg model on the spin-wave linewidth compensate each other [76M3] and thus these results are not changed by the 2D XY-range. Next, Moussa and Villain have derived a mean value $\langle \hat{M} \rangle$ of the magnetization for the 2D Heisenberg model resulting from the interlayer coupling. In their theory, $\langle \hat{M} \rangle$ is obtained as a dimensionless magnetization per spin

$$\langle \hat{M} \rangle = S(a / r_1)^{1/4\pi\tilde{K}} = S(J' / k_B T)^{1/8\pi\tilde{K}} \tag{4.156}$$

with $\tilde{K}$ as already defined in Eq. 4.153. $\langle \hat{M} \rangle$ in Eq. 4.156 agrees with the results of Berezinskii and Blank [73B4]. It is, on the other hand, very similar to the result of Hikami and Tsuneto [80H7] for the 2D XY-model with interlayer coupling. Not all details of the theory of Moussa and Villain [76M3] can be reproduced here but only the essential results. They have considered for temperatures below T_C the Fourier transform $S(\boldsymbol{q}, \omega)$ of the correlation function Eq. 4.152. There are two contributions to $S(\boldsymbol{q}, \omega)$, a δ-function-like and a smooth part. At low temperatures, e.g. $T = 2$ K for K_2CuF_4, the δ-function part is dominating and the smooth part can be neglected

$$S(\boldsymbol{q}, \omega) = \langle \hat{M} \rangle \left[\frac{\delta(\omega - \omega_q)}{1 - \exp(-\hbar\omega_q / k_B T)} + \frac{\delta(\omega + \omega_q)}{\exp(\hbar\omega_q / k_B T) - 1} \right] \tag{4.157}$$

where $\langle \hat{M} \rangle$ is given by Eq. 4.156, ω_q by Eq. 3.72 (Sect. 3.2.1) for $\boldsymbol{q} \mathrel{\hat{=}} (\zeta, 0, 0)$ [83H4] and by $2zSJ[1 - \cos(2\pi\zeta)]$ for $\boldsymbol{q} \mathrel{\hat{=}} (\zeta, \zeta, 0)$ [76F]. For these low temperatures, we have $\hbar\omega_q >> k_B T$ and $\exp(\hbar\omega_q / k_B T) >> 1$ and may approximate Eq. 4.157 as follows

$$S(\boldsymbol{q}, \omega) \approx \langle \hat{M} \rangle \, \delta(\omega - \omega_q) \tag{4.157a}$$

The δ-function lineshape in Eq. 4.157 means that the experimentally observed lineshape depends on the resolution function of the neutron spectrometer employed in the experiment. In Eq. 4.157 or 4.157a, the prefactor $\langle \hat{M} \rangle$ (Eq. 4.156) becomes $\langle \hat{M} \rangle = 0.826\ S$ with the numerical values for K_2CuF_4 at 2 K (see Table 5 and [83H4]). For temperatures near T_C, e.g. $T = 6$ K for K_2CuF_4, the width of the measured neutron groups is much larger than at low temperatures so that $S(\boldsymbol{q}, \omega)$ can be approximated by the following smooth curve

$$S(\boldsymbol{q},\omega) = \left[\frac{1}{2} + \frac{1}{\exp\,(\hbar\omega_\mathrm{q}/k_\mathrm{B}T) - 1} \pm \frac{1}{2}\right] \frac{A_\mathrm{LS}}{(\omega \mp \omega_\mathrm{q})^{1-1/(4\pi\tilde{K})}} \tag{4.158}$$

where the upper sign corresponds to the creation of a magnon and the lower to the annihilation. In Eq. 4.158, A_LS is a constant factor. It is noteworthy that in this theory $\tilde{K}$ is used without any renormalization due the presence of vortices as in the theory for the 2D XY-model (cf. Eq. 4.48b in Sect. 4.1.8). For the comparison with the experimental data, the following approximation of Eq. 4.158 has been used [83H4]

$$S(\boldsymbol{q},\omega) \approx \frac{A_\mathrm{LS}}{(\omega - \omega_\mathrm{q})^{1-1/(4\pi\tilde{K})}} \tag{4.158a}$$

Finally, let us consider the experimental results above T_C in the 2D Heisenberg range ($\zeta > 0.1$) [76M3, 77M1, 83H4]. For $T > T_\times = 7.3$ K (cf. Sect. 4.1.9), the theoretical derivation of $S(\boldsymbol{q}, \omega)$ has to start from a different form of the correlation function which is governed by the correlation length ξ, the inverse κ of which has been determined by neutron scattering experiments above T_C [82H5, 82H6]. On this basis, Moussa and Villain [76M3] obtain the following expression for the scattering function for temperatures above $T_\times > T_\mathrm{C}$, e.g. $T = 9$ K and 12 K for K_2CuF_4,

$$S(\boldsymbol{q},\omega) = \left(\frac{1}{\Gamma_\mathrm{q}}\right)^{1-\eta/2} \left\{\frac{2\,(1-\eta/2)}{[1+(\hbar\omega-\hbar\omega_\mathrm{q})^2/\Gamma_\mathrm{q}^2]^{1-\eta/4}} + \frac{\pi\cdot\eta/2}{[1+(\hbar\omega-\hbar\omega_\mathrm{q})^2/\Gamma_\mathrm{q}^2]^{1/2-\eta/4}}\right\} \tag{4.159}$$

In Eq. 4.159, Γ_q is a special damping different from the usual magnon-magnon interactions:

$$\Gamma_\mathrm{q} = \Gamma(q) = \hbar(\partial\omega/\partial q_\mathrm{x})/(2\xi) \tag{4.159a}$$

which vanishes for $\zeta = 0$ and for $\zeta = 0.5$ because of $\partial\omega/\partial q_\mathrm{x} = 0$ at these points in the center and at the boundary of the Brillouin zone. And this damping is further proportional to the inverse of the correlation length $\kappa = \xi^{-1}$ which increases with increasing temperature above T_C. In their applications of Eq. 4.159, Moussa and Villain have treated ξ and η as fit parameters while Hirakawa et al. have taken the experimental values obtained by neutron scattering experiments [82H5, 82H6]. The good agreement of these theoretical results (Eqs. 4.157–4.159) with the experimental data confirms once more that K_2CuF_4 is a good realization of the 2D Heisenberg model in the considered range of large wavevectors ($\zeta > 0.1$). Finally, the theory explains the spin-wave lineshape quantitatively for temperatures from 2 K up to 9 K and qualitatively beyond 9 K.

9.12.4.2.4 2D XY-Model: Influence of Vortices on $S(\boldsymbol{q}, \omega)$

The static critical properties of the 2D XY-model have been dealt with in detail in Sect. 4.1.8. The particular properties of this model originate from the Kosterlitz-Thouless transition at T_KT to a topological long-range order which is formed by bound vortex-antivortex pairs. And this special kind of phase transition is mediated by the unbinding of the pairs into an ideal, dilute gas of free vortices. It is not the intention of this section to repeat the static critical properties of the ideal and the finite-size 2D XY-model. Here, we will discuss the influence of the vortices on the dynamical properties. Such an influence was already mentioned in Sect. 4.1.8. For example, the spin-stiffness, at low temperatures $2S^2J$ or $\tilde{K} = (2S^2J)/(k_\mathrm{B}T)$, is strongly renormalized to $2S^2J_\mathrm{eff}$ or $\tilde{K}_\mathrm{eff}$ at temperatures near T_KT (cf. Eqs. 4.48a and

4.48b) due to the presence of vortices. An analogous renormalization is found in the magnon energies for wavevectors which correspond to the 2D XY-range (cf. Eq. 4.51) which is also considered as a rounded universal jump of the 2D XY-model.

Let us focus our attention now to temperatures above T_C (or T^* or T_{KT}) where the vortices form a dilute gas. Theoretically, the motion of these free vortices has been studied [82H7] and the vortex velocity autocorrelation function been derived, also magnon bound states in the presence of a single vortex [92C1] and the motion of a second vortex in the presence of the first one [91V1]. Ouantum fluctuations and corrections to the energies of a vortex-antivortex pair may induce an interaction between the vortex and the antivortex [89R, 94P3]. For the response of the system to inelastic neutron scattering, i.e. the scattering function $S^{\alpha\beta}(\boldsymbol{q}, \omega)$, a central peak at $\omega = 0$ was predicted for the longitudinal spin components due to the influence of the unbound vortices [80H9, 89G4]. Its width is determined by the vortex velocity autocorrelation function. Monte Carlo molecular dynamics simulations [86K3] have confirmed the existence of such a central peak as shown in Fig. 4.54 for a representative function $S(\boldsymbol{q}, \omega)$ without specifying the coordinates α and β. At $\tilde{T} = 0.5$, the results exhibit the usual spin-wave peak at $\omega \approx 4$ (in reduced arbitrary units). As in Sect. 4.1.8, $\tilde{T} = (k_B T)/(2S^2 J)$ is the temperature relative to the spin-stiffness (cf. Eq. 4.43a). At $\tilde{T} = 0.80$ and $\tilde{T} = 0.82$, a central peak develops in the Monte Carlo results in Fig. 4.54, and at $\tilde{T} = 0.9$, the spin-wave peak has disappeared and only the central peak remains. The result of other theoretical calculations is also that a dilute gas of mobile solitons induces a central peak in $S(\boldsymbol{q}, \omega)$ [92P] as well as bound pairs of vortices at low temperatures [93P2]. Experimentally, central peaks have been observed for both easy-plane ferromagnets, K_2CuF_4 [92M2] and Rb_2CrCl_4 [88B2, 92B2]. Inelastic neutron scattering on Rb_2CrCl_4 with a neutron polarization analysis [88B2] has provided information about the contributions to the scattering functions $S^{yy}(\boldsymbol{q}, \omega)$ (non-spin-flip scattering), $S^{xx}(\boldsymbol{q}, \omega)$ (spin-flip scattering) and $S^{zz}(\boldsymbol{q}, \omega)$. Some of the experimental data for $T = 50$ K are displayed in Fig. 4.55. The scans were taken near $\boldsymbol{K} = (0, 0, -2.9c^*)$ in a vertical magnetic field of 0.2 T strong enough to prevent neutron depolarization by the sample but sufficiently weak not to suppress the critical scattering. The spin-flip data (SF $\hat{=}$ S^{xx}, open circles in Fig. 4.55) consist of two spin-wave peaks and a weak central peak. The non-spin-flip data (NSF $\hat{=}$ S^{yy}, filled circles) exhibit a strong central peak and its longitudinal polarization indicates its diffusive origin. The solid lines in Fig. 4.55 represent fits to the experimental data where both Lorentzians and squared Lorentzians gave equally good fits. Summarizing the experimental results, there are four sources for the dynamic critical scattering in Rb_2CrCl_4:

1) in-plane spin waves at the expected energy $\hbar\omega_q$
2) a strong central peak originating from in-plane longitudinal fluctuations
3) a weak central peak corresponding to in-plane transverse fluctuations
4) a weak central peak due to out-of-plane transverse fluctuations.

These features have been observed experimentally in the temperature range where Rb_2CrCl_4 shows 2D XY-behaviour and where vortices will strongly influence the spin fluctuations. The experimental data can be compared to detailed theoretical predictions for the scattering functions $S^{\alpha\beta}(\boldsymbol{q}, \omega)$. Assuming an ideal gas of freely moving vortices, the results exhibit central peaks for both, in-plane and out-of-plane fluctuations [87M2, 88M2, 89G4, 89M2, 92V]. The predicted lineshape is different for transverse in-plane fluctuations [$S^{xx}(\boldsymbol{q}, \omega)$] and for out-of-plane fluctuations [$S^{zz}(\boldsymbol{q}, \omega)$], a squared Lorentzian and a Gaussian, resp., because these central peaks are due to quite different mechanisms. Similar results have been obtained by high precision Monte Carlo simulation [92L1]. But the calculated widths of the central peaks show a significant deviation from the experimental data so that future theoretical work may have to include additional interactions [92V].

9.12.4.2.5 Critical Broadening of the NMR Linewidth

Another experimental access to the dynamics of the correlations and thus to the dynamical critical properties is provided by the investigation of the broadening of the linewidth in nuclear magnetic resonance in the paramagnetic regime ($T > T_N$) when approaching T_N. Let us describe again the linewidth as a width ΔH_{NMR} in magnetic field, i.e. full width at half maximum. This broadening is then usually expressed as a power law

$$\Delta H_{\mathrm{NMR}} = \Delta H_{\mathrm{NMR}}^{\infty} + C_{\mathrm{NMR}} \cdot t^{-\mathrm{w}} \tag{4.160}$$

The second term of the sum in Eq. 4.160 is the critical part and the first term $\Delta H_{\mathrm{NMR}}^{\infty}$ the noncritical one. Both, C_{NMR} and $\Delta H_{\mathrm{NMR}}^{\infty}$ can be assumed to be temperature-independent. The NMR linewidth is related to the spin-spin relaxation time T_2. It probes the two-spin correlation function as defined in Eq. 4.22 in Sect. 4.1.5 and therefore also the temporal spin fluctuations of the magnetic system near the critical temperature. A detailed derivation of ΔH_{NMR} has been presented in a review by Benner and Boucher [90B1] on the basis of this correlation function and the hyperfine coupling between electronic and nuclear spin. Here, only the basic steps of this derivation will be presented. The critical part of Eq. 4.160 can be elucidated by the following form

$$\Delta H_{\mathrm{NMR}} - \Delta H_{\mathrm{NMR}}^{\infty} \sim A_{\mathrm{NMR}} \cdot T \cdot \sum_{\mathrm{q} \le \kappa} \chi(q,t) / \Gamma(q,\kappa) \tag{4.161}$$

where $\chi(q, t)$ is the susceptibility and $\Gamma(q, \kappa)$ the characteristic frequency as defined in Eqs. 4.24, 4.27 (Sect. 4.1.5) and 4.131. For an antiferromagnet, we have to choose for $\boldsymbol{K} = \boldsymbol{Q}_0 + \boldsymbol{q}$ the $\boldsymbol{Q}_0$ on an antiferromagnetic rod and $\chi(q, t)$ is the staggered susceptibility. For a ferromagnet, on the other hand, $\boldsymbol{Q}_0$ will be located on a ferromagnetic rod and $\chi(q, t)$ is the ordinary susceptibility. In the Heisenberg model, $\chi(q, t)$ and $\Gamma(q, \kappa)$ will be isotropic, i.e. $\chi^{\mathrm{xx}} = \chi^{\mathrm{yy}} = \chi^{\mathrm{zz}} = \chi$ and $\Gamma^{\mathrm{xx}} = \Gamma^{\mathrm{yy}} = \Gamma^{\mathrm{zz}} = \Gamma$ while in the anisotropic Ising model, only $\chi^{\mathrm{zz}} = \chi_{\|}$ and $\Gamma^{\mathrm{zz}} = \Gamma_{\|}$ will contribute to ΔH_{NMR}. In Eq. 4.161, A_{NMR} is an abbreviation for the usual geometric factors associated with the hyperfine interaction and T is the temperature. In this way, ΔH_{NMR} is related to the correlation function and reflects thus the spin fluctuations near the critical temperature. For deducing a theoretical expression for the exponent w in Eq. 4.160, it is convenient to introduce the dimensionless variable $x = q/\kappa$, to convert the sum Σ_{q} to an integral and to express χ and Γ as functions of x

$$\sum_{\mathrm{q}} \to \kappa^{\mathrm{d}} \int_{x \le 1} \mathrm{d}x\, x^{\mathrm{d}-1} \qquad \chi(q,t) \to \kappa^{-2+\eta} \cdot \chi(x) \qquad \Gamma(q,\kappa) \to \kappa^{\mathrm{z}} \cdot \tilde{\Omega}^{+}(x)$$

which leads to the following form for the NMR linewidth

$$\Delta H_{\mathrm{NMR}} - \Delta H_{\mathrm{NMR}}^{\infty} = A_{\mathrm{NMR}} \cdot T \cdot \kappa^{\mathrm{d}-2+\eta-\mathrm{z}} \int \mathrm{d}x\, x^{\mathrm{d}-1} \chi(x) \big/ \tilde{\Omega}^{+}(x) \tag{4.162}$$

If the integral over x in Eq. 4.162 is well-behaved and finite and if the hyperfine factor A does not vanish, the term with κ is the leading term for $T \to T_N$ ($\kappa \to 0$) and the exponent w is obtained by means of $\kappa \sim t^{\nu}$ as the following scaling relation [74H3, 90B1]

$$\mathrm{w} = \nu(2 - \mathrm{d} - \eta + \mathrm{z}) \tag{4.163}$$

Values w calculated by means of Eq. 4.163 are compiled below in Table 8 for various systems. Please note that the values for z and w are different for ferro- and antiferromagnets [77H2] in contrast to the static critical exponents in Table 7. Experimental data are shown in Fig. 4.56 for the quasi-two-dimensional antiferromagnet K_2MnF_4. The results presented there illustrate that the critical broadening is observed only in $^{19}F_I$-NMR and not in $^{19}F_{II}$-NMR for the reasons discussed already in context with Fig. 3.6 in Sect. 3.1.3, that the F_I-ions probe the sublattice magnetization, the staggered susceptibility and thus the longitudinal spin fluctuations and that the F_{II}-ions are sensitive only to the net magnetization and the corresponding susceptibility (cf. insert to Fig. 4.56 and Fig. 3.7). The broadening of the F_I-NMR linewidth is observed for $\boldsymbol{H_0} \parallel \boldsymbol{c}$ and for $\boldsymbol{H_0} \perp \boldsymbol{c}$. The solid lines in Fig. 4.56 are the result of a fit to Eq. 4.160. The exponent w determined in this way, w = 1.5 for $\boldsymbol{H_0} \parallel \boldsymbol{c}$ and also for $\boldsymbol{H_0} \perp \boldsymbol{c}$, is in good agreement with the theoretical value for a 2D Ising system (cf. Table 8 below). The NMR linewidth of the F_{II}-ions in Fig. 4.56 is considerably smaller than that of the F_I-ions where we have to note the logarithmic scale for ΔH_{NMR}. Its temperature dependence reflects that of noncritical spin fluctuations which is governed by spin diffusion [74B4, 90B1].

9.12.4.2.6 Critical Broadening of the EPR Linewidth

Information about the time- or frequency-dependence of the spin correlations and the dynamic critical phenomena can also be obtained by measuring the EPR linewidth ΔH_{EPR} above T_N, usually as a function of temperature and in many cases also the angular dependence of ΔH_{EPR}. Investigations of this kind are usually performed not only for the relatively small critical range near T_N but also at much higher temperatures up to room temperature because of the interesting properties especially of low dimensional magnetic systems with respect to relaxation and temporal correlations at these temperatures. The EPR linewidth ΔH_{EPR} is presented as full width at half maximum if an EPR transmission spectrum is recorded and as peak-to-peak linewidth in case of an EPR derivative spectrum. Experimental results are shown in Fig. 4.57 for $(CH_3NH_3)_2MnCl_4$ as a function of temperature T for $\boldsymbol{H_0} \parallel \boldsymbol{c}$ ($\psi = 0°$) and for $\boldsymbol{H_0}$ at an angle of 55° to the c-axis ($\psi = 55°$) [72B6, 75B6]. The temperature range from slightly above $T_N = 45.3$ K to about 70 K shows the critical broadening of ΔH_{EPR} and the range from about 80 K to 300 K a linear increase of ΔH_{EPR} with T. This temperature dependence can be written as [68S3, 71C4, 73W6, 75B6]

$$\Delta H_{EPR} = A_{EPR} + B_{EPR} \cdot T + C_{EPR} \cdot t^{-p} \qquad (4.164)$$

The decrease of ΔH_{EPR} with decreasing temperature is known as "exchange narrowing". The linear T-dependence is the result of phonon modulation of the exchange interaction. This and other aspects of the EPR linewidth at temperatures far above T_N will be discussed below in Sect. 4.2.8. In this section, we will concentrate on the critical broadening which can also be expressed as a power law analogous to the NMR linewidth [72W2, 73H4, 77H3]

$$\Delta H_{EPR} = \Delta H_{EPR}^{\infty} + C_{EPR} \cdot t^{-p} \qquad (4.165)$$

where the second term is the critical part diverging at T_N for p > 0. In the noncritical part, the linear T-dependence can be neglected in the small critical range and the first two terms of Eq. 4.164 are comprised to a constant ΔH_{EPR}^{∞}. Also C_{EPR} is assumed temperature-independent analogous to Eq. 4.160. Theoretical considerations for ΔH_{EPR} are similar to those for ΔH_{NMR} [90B1] but more sophisticated since ΔH_{EPR} is related to four-spin correlation functions which are usually decoupled into products of two-spin correlation functions. Further the geometrical factors of the hyperfine coupling denoted as A in Eq. 4.161 have to be replaced for EPR by dipolar geometrical factors F since the relaxation of the fluctuations occurs in this case via the magnetic dipolar interactions [72H3, 73H4, 90B1]. Thus the factors F are the spatial Fourier transform of dipolar lattice sums [90B1] as discussed in context with the dipolar anisotropy field H_{AD} (cf. Eq. 3.12 in Sect. 3.1.2). A similar scaling analysis as for ΔH_{NMR} can also be performed in this case for obtaining a theoretical form for the exponent p. Unfortunately, the leading dipolar geometrical factor F vanishes in some cases, e.g. in uniaxial lattices and the Ising model for both, ferromagnets and antiferromagnets. Therefore, we will derive here no general form for p. Such derivation is presented in detail in [90B1]. Further, the reader finds the numerical results for various cases in Table 8. These data are mainly taken from Table I in [90B1]. Some of the data are also found in other sources [73R2, 74B4, 74H3]. The numerical values of z, w and p have been calculated with the values of ν and η compiled in Table 7. Since some experimental data refer also to the 2D Heisenberg model this has been included here although it exhibits no ordinary phase transition. In this case, the values $\nu = 0.93$ and $\eta = 0.11$ have been taken from a renormalization group analysis by Fisher [74F2]. For the Ising model, two cases a) and b) have been listed in Table 8. The entry a) refers to a nonvanishing dipolar geometrical factor in the theory for ΔH_{EPR} which happens, for example, in antiferromagnets with an orthorhombic lattice. The entry b) gives the values of the exponents if this dipolar factor vanishes as it does in uniaxial lattices, i.e. for most of the perovskite layer structures. This means that the EPR linewidth will not show a critical broadening near T_N for Ising model uniaxial antiferromagnets but will remain finite and uncritical at T_N which is indicated as z = 0 (const) in Table 8. This z = 0 (const.) must not be confused with a logarithmic singularity as for the specific heat of the 2D Ising model listed in Table 7 as $\alpha = 0$ (log).

Table 8. Theoretical values for the exponents z, w and p

	z	w	p
	Ferromagnets		
2D Ising	$4 - \eta = 3.50$	$\nu(4 - 2\eta) = 3.50$	a) $\nu(6 - 3\eta) = 5.25$ b) $\nu(2 - 3\eta) = 1.25$
2D Heisenb.	$0.5(d + 2 - \eta) = 1.90$	$\nu(2 - 1.5\eta) = 1.71$	$\nu(2 - 1.5\eta) = 1.71$
3D Ising	$4 - \eta = 3.97$	$\nu(3 - 2\eta) = 1.85$	a) $\nu(5 - 3\eta) = 3.09$ b) $\nu(1 - 3\eta) = 0.57$
3D Heisenb.	$0.5(d + 2 - \eta) = 2.48$	$1.5\nu(1 - \eta) = 1.02$	$1.5\nu(1 - \eta) = 1.02$
	Antiferromagnets		
2D Ising	$2 - \eta = 1.75$	$2\nu(1 - \eta) = 1.50$	a) $\nu(4 - 3\eta) = 3.25$ b) 0 (const.)
2D Heisenb.	$0.5d = 1.00$	$\nu(1 - \eta) = 0.83$	$\nu(3 - 2\eta) = 2.59$
3D Ising	$2 - \eta = 1.97$	$\nu(1 - 2\eta) = 0.59$	a) $3\nu(1 - \eta) = 1.83$ b) 0 (const.)
3D Heisenb.	$0.5d = 1.50$	$0.5\nu(1 - 2\eta) = 0.33$	$\nu(2.5 - 2\eta) = 1.72$

Several experimental studies have been performed on the temperature dependence of the EPR linewidth in the critical region above but close to T_N (see Table 6). The results of de Wijn et al. [72W2] for $\Delta H_{\text{EPR}}(T)$ in K_2MnF_4 are reproduced in Fig. 4.58. The same drastic increase of ΔH_{EPR} as in Fig. 4.56 for approaching T_N from above is shown here in more detail for $\boldsymbol{H_0} \parallel \boldsymbol{c}$ and for $\boldsymbol{H_0} \perp \boldsymbol{c}$. The fit of he experimental data to Eq. 4.165 (full lines in Fig. 4.58) yields exponents p = 2.5(2) for $\boldsymbol{H_0} \parallel \boldsymbol{c}$ and p = 2.4(2) for $\boldsymbol{H_0} \perp \boldsymbol{c}$. These values do not agree with the theoretical ones for 2D Ising antiferromagnets in Table 8 but agree quite well with those for the 2D isotropic Heisenberg model. It is astonishing that the experimental critical data of an easy-axis antiferromagnet like K_2MnF_4 do not exhibit the 2D Ising character as all other data discussed so far. The insert to Fig. 4.58 shows the angular dependence $\Delta H_{\text{EPR}}(\psi)$ of the EPR linewidth at 50.6 K ($\hat{=}\, t = 0.20$). In this experiment, the external field H_0 has been applied under various angles ψ with respect to the c-axis (cf. Eq. 3.43 in Sect. 3.1.6). The full line in the insert of Fig. 4.58 illustrates that $\Delta H_{\mathrm{EPR}}(\psi)$ fits well to the form [72W2]

$$\Delta H_{\mathrm{EPR}}(\psi) = \Delta H_1\,(3\cos^2\psi - 1) + \Delta H_2 \tag{4.166}$$

where ΔH_1 and ΔH_2 are constants. The experiments have further shown that there is no anisotropy of the EPR linewidth in the basal plane ($\Delta H_{\mathrm{EPR}} \neq f(\beta)$ where β is the angle between $\boldsymbol{H_0}$ and the a-axis, cf. Eq. 3.43 in Sect. 3.1.6). For these temperatures slightly above the critical temperature T_{N}, ΔH_{EPR} is dominated by processes which induce a $\cos^2\psi$ or $\sin^2\psi$ angular dependence. An alternate form to Eq. 4.166 is

$$\Delta H_{\mathrm{EPR}}(\psi) = \Delta H_1'\,(1 - 0.5\sin^2\psi) + \Delta H_2' \tag{4.166a}$$

Eqs. 4.166 and 4.166a are equivalent yielding both a maximum for $\boldsymbol{H_0} \parallel \boldsymbol{c}$ ($\psi = 0°$) and a minimum for $\boldsymbol{H_0} \parallel \boldsymbol{a}$ ($\psi = 90°$). The second form Eq. 4.166a was predicted for the angular dependence of ΔH_{EPR} in theoretical considerations for the critical broadening of ΔH_{EPR} [73H4] where one has to take account of the dominance of short-wavelength spin fluctuations of the dipolar field near $\boldsymbol{Q}_0$, the superlattice wavevector describing the antiferromagnetic order. This theory is based on a similar one developed for 3D antiferromagnets [72R3].

Our next example is the double-layer compound $K_3Mn_2F_7$. The experimental data in Fig. 4.59 present the log-log plot for the determination of the exponent p from $\Delta H_{\mathrm{EPR}}(T)$ for $\boldsymbol{H_0} \parallel \boldsymbol{c}$ and $\boldsymbol{H_0} \perp \boldsymbol{c}$. For the range $0.1 \leq t \leq 0.35$, a straight line is obtained and the exponents resulting from a fit are $p = 3.0(2)$ and $2.9(2)$ for $\boldsymbol{H_0} \parallel \boldsymbol{c}$ and $\boldsymbol{H_0} \perp \boldsymbol{c}$, resp., which are also explained as being due to a 2D Heisenberg model [80U, 81U] by using the experimental values $\nu = 1.1$ and $\eta = 0.20$ [78U, 79U] for the calculation of p. In the range $0.02 \leq t \leq 0.1$ however, the experimental data in Fig. 4.59 deviate considerably from the straight line to lower values which has been explained by an increased anisotropy near T_{N}, i.e. the system comes closer to the 2D anisotropic Ising model. Also in this case, the angular dependence $\Delta H_{\mathrm{EPR}}(\psi)$ has been determined at 64.1 K ($\hat{=}\, t = 0.099$) and successfully been fitted to Eq. 4.166a. The angular dependence of ΔH_{EPR} in $K_3Mn_2F_7$, specifically the EPR for $\psi = 0°$ ($\boldsymbol{H_0} \parallel \boldsymbol{c}$), for $\psi = 90°$ ($\boldsymbol{H_0} \perp \boldsymbol{c}$) and for $\psi = 55°$, was studied over a wider temperature range from 64 K up to 96 K [81U]. The results revealed a change-over from the form of Eq. 4.166a to the different angular dependence $\sim (3\cos^2\psi - 1)^2$, cf. Eq. 4.182 in Sect. 4.2.8 below, which will be shown to be a manifestation of spin diffusion there.

The final example of studying ΔH_{EPR} are the experimental data for Rb_2MnCl_4 which have been obtained by EPR at 35 GHz for $\boldsymbol{H_0} \parallel \boldsymbol{c}$ and $\boldsymbol{H_0} \perp \boldsymbol{c}$ [83P] and at several frequences between 61.6 and 152 GHz for $\boldsymbol{H_0} \parallel \boldsymbol{c}$ [88G3, 90G4]. The angular dependence ΔH_{EPR} (ψ) shows for Rb_2MnCl_4 a similar change-over from Eq. 4.166a to Eq. 4.182 [83P] as in $K_3Mn_2F_7$. The critical broadening of ΔH_{EPR} is presented as log-log plot in Fig. 4.60. The fit to a straight line results in $p = 2.4(5)$ for the range $0.15 \leq t \leq 0.5$, in good agreement with K_2MnF_4 and $K_3Mn_2F_7$. As in the latter, the data deviate from this line to smaller values in the range $0.007 \leq t \leq 0.07$, where a fit to Eq. 4.165 yields $p = 0.22(26)$, with lower accuracy due to the small number of data points and due to the difficulties in measuring such large linewidths. But the data in Fig. 4.60 seem to indicate near $t \approx 0.12$ a crossover from 2D Heisenberg behaviour to a 2D Ising one. It should be noted that it is necessary for the millimeter-wave frequencies in Fig. 4.60 with relatively large fields H_{res} at resonance to use $T_{\mathrm{N}}(H)$ from the (H_0, T) phase diagram (Fig. 3.18 in Sect. 3.1.6) instead of $T_{\mathrm{N}} = 55$ K for $H_0 = 0$. For $\nu = 127$ GHz and $H_{\mathrm{res}} = 4.54$ T as an example, $T_{\mathrm{N}}(H) = 52.5$ K was used for calculating t. For measurements at higher frequencies, e.g. $\nu \geq 160$ GHz, no critical broadening of ΔH_{EPR} occurs. At these frequencies, H_{res} is so large that not the antiferromagnetic Ising-like phase is entered from the paramagnetic one but the XY-like spin-flop phase in a magnetic resonance experiment by decreasing the temperature. This is illustrated for Rb_2MnCl_4 with four selected frequencies in Fig. 4.61. There, the dash-dot lines show the phase boundaries as determined with neutron scattering (cf. Fig. 3.18 in Sect. 3.1.6). The data in Fig. 4.61 are presented as magnetic field at resonance

H_{res} versus T for various frequencies, and the bars at the data points indicate the observed linewidth ΔH_{EPR} and are not error bars. The broken lines are guide to the eye. In the antiferromagnetic phase ($H_{\mathrm{res}} < 5.5$ T, $T < 50$ K), H_{res} can be expressed as

$$H_{\mathrm{res}} = (2\pi/\gamma)\,|\,\nu - \nu_{\mathrm{AFMR}}\,(T, H_{0z} = 0)\,| \tag{4.167}$$

Here, ν is the frequency of the millimeter wave source in the magnetic resonance experiment and γ again the gyromagnetic ratio. The temperature-dependent AFMR frequency ν_{AFMR} for $H_{0z} = 0$ is given for $T \approx 0$ by Eq. 3.9 (Sect. 3.1.2). With increasing temperature, ν_{AFMR} decreases approximately as the sublattice magnetization (cf. Eq. 3.17 in Sect. 3.1.2). For frequencies ν smaller than the zero-field AFMR frequency at $T = 0$, the decrease of ν_{AFMR} with increasing T leads to $\nu_{\mathrm{AFMR}} = \nu$ and $H_{\mathrm{res}} = 0$ at a certain temperature and then H_{res} rises again with further increase of T (see Fig. 4.61). The AFMR linewidth increases with T according to the T^4-law (Eq. 3.13 in Sect. 3.1.2). In the spin-flop phase ($H_{\mathrm{res}} > 5.5$ T, $T < 50$ K), H_{res} can be deduced from Eq. 3.51a ($\nu_{\mathrm{AFMR,out\text{-}of\text{-}pl.}}$) in Sect. 3.1.6 as follows

$$H_{\mathrm{res}} = [(2\pi\nu/\gamma)^2 + 2\,H_{\mathrm{E}}(H_{\mathrm{A}} + \widetilde{H}_{\mathrm{A}})]^{1/2} \tag{4.168}$$

where H_{E}, H_{A} and $\widetilde{H}_{\mathrm{A}}$ have the same meaning as in Eq. 3.51a. The decrease of H_{res} in the spin-flop phase reflects the decrease of $2H_{\mathrm{E}}(H_{\mathrm{A}} + \widetilde{H}_{\mathrm{A}})$ with T mentioned above for ν_{AFMR}. Finally, all internal fields are zero in the paramagnetic phase and H_{res} is simply proportional to the frequency ν

$$H_{\mathrm{res}} = 2\pi\nu/\gamma \tag{4.169}$$

For frequencies below 150 GHz, this constant H_{res} is observed until the boundary to the antiferromagnetic phase is reached (see Fig. 4.61). ΔH_{EPR} increases towards T_{N} as already shown in Fig. 4.60. For frequencies above 150 GHz however, H_{res} shifts to higher values already before the boundary to the spin-flop phase is reached [88G3, 90G4] indicating the influence of an internal field while the system is still in the paramagnetic phase. Here, ΔH_{EPR} remains finite in the transition and does not show a critical broadening and divergence at the phase boundary. It reaches merely a maximum near but not at this boundary (see Fig. 4.61). A theoretical explanation for this behaviour is not yet available.

9.12.4.2.7 Critical EPR Linewidth due to Solitons or due to Magnons?

Returning to the broadening of ΔH_{EPR} in the transition from the paramagnetic to the antiferromagnetic phase, the question arises whether Eq. 4.165 with a critical exponent p is really an adequate description of this broadening. Waldner proposed an alternate way for this description [83W4, 86W, 92W]. He found empirically an Arrhenius law for the temperature dependence of ΔH_{EPR}

$$(\,\Delta H_{\mathrm{EPR}} - \Delta H^{\infty}_{\mathrm{EPR}}\,) \sim \exp\,(E_{\mathrm{s}}/k_{\mathrm{B}}T) \tag{4.170}$$

where ΔH_{EPR} and $\Delta H^{\infty}_{\mathrm{EPR}}$ have been defined in Eq. 4.165. In the corresponding logarithmic plot

$$\ln\,(\Delta H_{\mathrm{EPR}} - \Delta H^{\infty}_{\mathrm{EPR}}\,) = (E_{\mathrm{s}}/k_{\mathrm{B}}T_{\mathrm{N}}) \cdot (T_{\mathrm{N}}/T) + \text{const.} \tag{4.170a}$$

Waldner [83W4] has obtained straight lines for a number of perovskite-type layer compounds: K_2MnF_4, Rb_2MnF_4, $K_3Mn_2F_7$, $(CH_3NH_3)_2MnC1_4$, $(C_2H_5NH_3)_2MnCl_4$ and $[NH_3(CH_2)_2NH_3]MnCl_4$. As an example, Fig. 4.62 shows Waldner's plot for the experimental data of K_2MnF_4 [72W2] for $\boldsymbol{H}_0 \parallel \boldsymbol{c}$ and $\boldsymbol{H}_0 \perp \boldsymbol{c}$. The question is what is the theoretical basis for the Arrhenius law in Eq. 4.170. Waldner has considered the broadening as being due to the influence of nonlinear excitations, namely solitons. And he identified the quantity E_s with the soliton excitation energy in analogy to quasi-one-dimensional magnets. For such magnetic systems, the influence of solitons on the magnetic properties has been observed experimentally as reviewed in several papers [81M4, 82J2, 83S5]. Also the theoretical description of solitons is well established [80M1, 81A, 81M4], and measurements of the Mössbauer linewidth in an Fe-compound [81T3] revealed a broadening ~ $\exp(E_s/k_BT)$ due to solitons in accordance with Mikeska's theory [80M1]. Magnetic resonance experiments [84B2, 87B3] have confirmed theoretical predictions [81A] that the magnon linewidth contains soliton contributions which are proportional to the number $n_s \sim \exp(-E_s/k_BT)$ of thermally excited solitons.

Also in quasi-2D magnetic systems, including the 2D Heisenberg model, there exist nonlinear topological excitations [86G1, 90G3], large meandering domain walls and smaller sized droplet solitons. They have a considerable effect on the thermodynamics and the magnetic phase transitions of these systems, as verified by a Monte Carlo simulation for the anisotropic 2D Heisenberg model [94C]. Therefore, not only the spin waves contribute to the time-dependent spin correlation functions but also the nonlinear excitations or solitons which have been discussed for isotropic and anisotropic Heisenberg models of 2D ferromagnets and antiferromagnets in a number of papers the details of which will not be discussed here [61S, 75B3, 79K9, 80T4, 81K10, 84V3, 89I4, 90K1]. All these soliton calculations employ the continuum approximation. For ferromagnets, it is relatively easy to obtain static solitons. But in anisotropic systems, a fourth order term due to Skyrme [61S] has to be added to the Hamiltonian [89B2]. The problems to obtain mobile solitons in ferromagnets have been discussed by Zaspel [93Z]. For antiferromagnets, mobile solitons can be derived from static solutions by a Lorentz transformation since the Langrangian is Lorentz-invariant even for systems with easy-plane anisotropy [94I2, 95I1]. Let us return now to Waldner's interpretation of the experimental data. He considered E_s in Eq. 4.170 as a soliton energy and the experimental values for E_s/k_BT_N agree quite well with $E_s = 4\pi\rho_s$ where ρ_s is the spin stiffness (cf. Eq. 4.43a) which is indeed the energy derived by Belavin and Polyakov [75B3] for a static 2D soliton in case of an isotropic Heisenberg model. Anisotropy will increase the soliton activation energy [86W] as follows

$$E_s = (4\pi + \varepsilon)\,\rho_s = (4\pi + \varepsilon)\,2S^2\,|J| \tag{4.171}$$

where ε is related to the anisotropy $h_A = H_A/H_E$. For weakly anisotropic Mn-compounds, it can usually be neglected. We recall that the EPR linewidth in the fluctuation range is related to the temporal correlations and the dynamical critical behaviour. And the problems with this interpretation of the temperature dependence of ΔH_{EPR} are:

a) the energy $E_s = 4\pi\rho_s$ is that of a static 2D soliton, and it is hard to see how this can contribute to the time-dependent spin correlation function

b) the Arrhenius behaviour resulting from Mikeska's theory [80M1] is based on the motion of 1D sine-Gordon solitons which is not appropriate for the 2D case.

Thus we have to look for a better founded theoretical description of ΔH_{EPR}. The influence of the solitons on ΔH_{EPR} will result from an interaction of the solitons with the spin waves [92C1, 95P3]. And Zaspel and Drumheller [95Z1, 96Z1] have derived theoretically the dynamical correlation function and the EPR linewidth on the basis of a static soliton-magnon interaction. They have calculated not only the soliton-magnon contribution to ΔH_{EPR} but also the magnon-magnon contribution. Their method of calculation applies the work of Kawasaki [68K] and of Huber [72H3]. In their result for the soliton contribution to the EPR linewidth, the leading term in the temperature dependence is

$$\Delta H_{EPR,sol} \sim (\xi/a_{nn})^2 \tag{4.172}$$

where ξ is the temperature-dependent correlation length and a_{nn} the nearest neighbour distance. In Eq. 4.172, all temperature-independent and weakly temperature-dependent factors have been omitted. The interested reader will find the complete expression for $\Delta H_{EPR,sol}$ in Eq. 5.5 of [96Z1]. The leading term in the temperature dependence of the spin-wave or magnon contribution to the EPR linewidth is, on the other hand

$$\Delta H_{\mathrm{EPR,sw}} \sim (\xi / a_{\mathrm{nn}})^3 \tag{4.173}$$

with the same notation and the same simplifications as in Eq. 4.172. The complete expression for $\Delta H_{\mathrm{EPR,\,sw}}$ can be found in Eq. 6.3 of [96Z1]. The correlation length ξ of a 2D antiferromagnet has been derived in a number of papers by various methods, by a modified spin-wave theory [89B1, 89T2, 92T2], by Schwinger boson mean-field theory [88A6], by a combination of hydrodynamics, scaling and renormalization-group [89C3, 89T3] and by Monte Carlo simulations [90D4]. Most of this work is devoted to the properties of a $S = \frac{1}{2}$ quantum antiferromagnet on a square lattice like La_2CuO_4 which is closely related to the high-T_C superconductors. The basic common result of all these different theoretical considerations is

$$\xi / a_{\mathrm{nn}} \sim \exp\,(2\pi\, \rho_s / k_B T) \tag{4.174}$$

which has also been applied to the problem of calculating ΔH_{EPR} for antiferromagnets with a more classical spin like Mn-compounds by Zaspel and Drumheller [96Z1]. In Eq. 4.174, we have omitted constant or weakly temperature-dependent prefactors which are also different in some of the above mentioned papers. Inserting Eq. 4.174 into Eqs. 4.172 and 4.173, we obtain for both cases an Arrhenius-type behaviour

$$\Delta H_{\mathrm{EPR,sol}} \sim \exp\,(E_s / k_B T) = \exp\,(4\pi \rho_s / k_B T) \tag{4.175a}$$

for the soliton contribution and

$$\Delta H_{\mathrm{EPR,sw}} \sim \exp\,(6\pi \rho_s / k_B T) \tag{4.175b}$$

for the magnon contribution. In Eqs. 4.174 and 4.175, the spin-stiffness ρ_s is used with its spin-wave value $2S^2\,|J|$ (cf. Eq. 4.43a) without any renormalization due to the presence of nonlinear excitations (cf. Sect. 4.1.8). Finally, the total EPR linewidth is the sum of both contributions. But the comparison with the experimental results for various Mn-compounds has shown that the soliton contribution to the EPR linewidth is dominant in this case for the critical range in accordance with the empirical form Eq. 4.170

$$\Delta H_{\mathrm{EPR}} - \Delta H^{\infty}_{\mathrm{EPR}} \approx \Delta H_{\mathrm{EPR,sol}} \sim \exp\,(E_s / k_B T) \sim (\xi / a_{\mathrm{nn}})^2 \tag{4.176}$$

and that the magnon contribution has a negligible effect on ΔH_{EPR}. Thus, Waldner's interpretation is confirmed on a better founded theoretical basis. The experimental values of E_s derived from the slope of the logarithmic plot Eq. 4.170a are compared with the calculated values $E_s = 8\pi S^2\,|J|$ for various compounds in Table 6. The experimental and the calculated data for E_s agree within 10% for all single-layer compounds listed in Table 6, except for the double-layer compound $K_3Mn_2F_7$ for which the theory presented here is not appropriate. When the single-layer Mn-compounds are doped with a small amount of nonmagnetic impurities, e.g. $(C_3H_7NH_3)_2Mn_{1-x}Cd_xCl_4$ ($0.001 \le x \le 0.08$) and $(C_3H_7NH_3)_2Mn_{1-x}Zn_xCl_4$ ($0.001 \le x \le 0.01$), the study of ΔH_{EPR} shows also the expected Arrhenius law but reveals a drastic decrease of E_s [93G, 96S1]. The results are depicted for Zn-doped samples in Fig. 4.63. For x = 0.0106, the experimental data yield $E_s = 375$ K in comparison to $E_s = 727$ K in pure $(C_3H_7NH_3)_2MnCl_4$. Susceptibility measurements on these samples show that such small amounts of impurities do not lead to a measurable decrease of J or T_N. Therefore, it is probably the effect of the impurities on the solitons which causes the decrease of E_s which is not accounted for in the theory of Zaspel and Drumheller [96Z1]. One limitation of it is the continuum approximation which breaks down in the core of a soliton. Thus a cut-off radius should be introduced inside of which the calculation is performed for the discrete lattice and outside in the continuum approximation [96Z2].

Eq. 4.175b shows that also an Arrhenius law is expected if the magnon contribution is dominant for the EPR linewidth. This seems to be the case for Cu-compounds. Unfortunately, most of the perovskite-type layered Cu-compounds exhibit a strong ferromagnetic intralayer exchange interaction which governs the spin correlations above T_C even if they are antiferromagnets due to the weaker interlayer coupling. Cu-compounds with antiferromagnetic intralayer coupling are La_2CuO_4 and related cuprates. But there, EPR experiments have not been successful [89M4]. Therefore, the only available example is the antiferromagnet $Cu(HCOO)_2 \cdot 4\,H_2O$. Castner and Seehra [93C3] have reanalysed its EPR linewidth in the critical fluctuation range with respect to Eq. 4.170a. Their result is shown in Fig. 4.64 as experimental data ${}_{10}\log(\Delta H_{EPR} - \Delta H^{\infty}_{EPR})$ versus T_N/T compared to $(\xi/a_{nn})^2$ and $(\xi/a_{nn})^3$ (cf. Eqs. 4.172–4.175). Obviously, the experimental data in Fig. 4.64 fit excellently to

$$\Delta H_{EPR} - \Delta H^{\infty}_{EPR} \approx \Delta H_{EPR,sw} \sim (\xi/a_{nn})^3 \tag{4.177}$$

indicating that the spin-wave contribution is the dominating one for the EPR linewidth of this Cu-antiferromagnet. This finding agrees in principle with the theoretical result of Chakravarty and Orbach [90C1] who calculated the EPR linewidth for quasi-2D $S = \frac{1}{2}$ antiferromagnets. Their result for ΔH_{EPR} contains also the exponential $\exp(6\pi\rho_s/k_B T)$ as in Eq. 4.175b but, in addition, a prefactor $(2\pi\rho_s/k_B T)^{-5/2}$ which causes a decrease of ΔH_{EPR} in comparison to the exponential without prefactor. Such lower values of ΔH_{EPR} do not agree so well with the experimental data. The conclusion of this section is that the EPR linewidth of 2D antiferromagnets with nearly classical spins (Mn-compounds) is dominated by the soliton contribution while it could well be that the linewidth of 2D quantum antiferromagnets (Cu-compounds) is dominated by the magnon contribution.

9.12.4.2.8 EPR Linewidth at High Temperatures – Spin Diffusion

In this section, we will focus our attention to the EPR linewidth in the high temperature range $1.5\,T_N \le T \le 300$ K which is outside the range of the critical fluctuations. But it is advisable to include this range into our considerations on dynamical properties and temporal correlations because of the interesting properties of 2D magnetic systems at these temperatures. There is the exchange narrowing of the EPR linewidth due to the exchange interaction [53A, 54K, 71B2, 74R1, 75R3, 77S6, 78C3] which can be expressed as the linewidth in frequency space [53A]

$$\Delta\omega_{EPR} \approx \omega_F^2 / \omega_E \tag{4.178}$$

where ω_F is the rms frequency of the dipolar contributions to the fluctuations and ω_E is the exchange frequency [90B1]

$$\omega_E = (J/\hbar)\sqrt{(8/3)zS\,(S+1)} \tag{4.178a}$$

Another point of interest in 2D systems is the spin diffusion [63K2, 65B, 90B1]. For the isotropic Heisenberg model, the magnetization $\boldsymbol{M} = \Sigma\ \boldsymbol{S}_i$ commutes with the Hamiltonian and is therefore a constant of motion. As an example, let us discuss the consequences for the two-spin correlation function $G^{\alpha\beta}(\boldsymbol{r}, t)$, cf. Eq. 4.22 in Sect. 4.1.5. In the high-temperature limit and in hydrodynamic description, its long-time or low-frequency behaviour is governed by a diffusion equation [65B]

$$\partial G^{\alpha\beta}(\boldsymbol{r}, t)/\partial t = D\nabla^2 G^{\alpha\beta}(\boldsymbol{r}, t) \tag{4.179}$$

with the spin diffusion constant D. In Eq. 4.179, t is the time, not to be confused with the reduced temperature t in another context. The solutions of Eq. 4.179 are

$$G(\boldsymbol{r}, t) = (4\pi D t)^{-d/2} \exp[-r^2/(4Dt)] \tag{4.180}$$

where d is the spatial dimension and where we have dropped the superscripts α and β (coordinate directions) in order to simplify our further discussion. The time dependence of $G(\boldsymbol{r}, t)$ is shown schematically in Fig. 4.65 on a time scale relative to $1/\omega_E$ (cf. Eq. 4.178a). The autocorrelation function ($\boldsymbol{r} = 0$) has a maximum for $\omega_E t = 0$ and can well be approximated for short times ($0 \le \omega_E t \lessapprox 1$) by a Gaussian $\exp(-\omega_E^2 t^2)$. The cross correlation function ($\boldsymbol{r} \neq 0$) vanishes at $\omega_E t = 0$, i.e. there are no static cross correlations, and has a maximum for $\omega_E t \approx 1$. For long times ($\omega_E t > 1$), the diffusive behaviour according to Eq. 4.180 is observed. In 3D systems, the long-time tail decays as $t^{-3/2}$ which is fast enough to lead to a finite value of $F(\omega)$ at $\omega = 0$, where $F(\omega)$ is the time Fourier transform of $G(\boldsymbol{r}, t)$. In 2D magnets, on the other hand, it decays slowlier as t^{-1} which causes a divergence of $F(\omega)$ for $\omega \to 0$ as [90B1]

$$F(\omega) \sim \ln[(4\pi D)/(\omega a^2)] \tag{4.181}$$

where a is the lattice constant. And in 1D magnets, the long-time decay of the correlations is with $t^{-1/2}$ even slower and leads also to a divergence of $F(\omega)$ for $\omega \to 0$. In Monte Carlo simulations, these exponents (0.5 for 1D, 1 for 2D) have been questioned [88M3], but they seem to be correct [89G8, 89M3]. The result of recent theoretical treatments is, on the other hand, that the exponent for the isotropic Heisenberg model is not simply d/2 but 2d/(4 + d) [94L], see also [96L]. Moreover, the correlation function shows according to this theory not a simple decrease but an oscillatory behaviour. But up to now, no experimental verfication is available for this theory. Returning to Fig. 4.65, the range of diffusive behaviour is marked as shaded area. The divergence according to Eq. 4.181 will occur only in an ideal Heisenberg model for which Eqs. 4.179 and 4.180 have been derived. And in real systems, the divergence will be truncated because there are always perturbations of the Heisenberg model, namely a possibly weak anisotropy, at least the magnetic dipolar interactions, and a small interlayer interaction. At this point, we will not enter into further theoretical details of these phenomena but will look more for their effects on the experimental results of EPR linewidth studies.

Several features in the experimental data are indications or evidence for diffusion in the four-spin correlation function responsible for the EPR linewidth:

1) The angular dependence $\Delta H_{EPR}(\psi)$ will be dominated by the secular part of the dipolar interactions in the spin diffusion range and have the following form [73S2, 74R1, 79B9, 81F2, 90B1]

$$\Delta H_{EPR}(\psi) = \Delta H_A + \Delta H_C\,(3\cos^2\psi - 1)^2 \tag{4.182}$$

where ΔH_A and ΔH_C are constants. At the high temperatures under consideration ($T >> T_N$), this angular dependence of the ΔH_{EPR} exhibits a minimum at the magic angle $\psi = 54.736°$ where the secular part of the dipolar interactions vanishes. Fig. 4.66 presents $\Delta H_{EPR}(\psi)$ of $(C_2H_5NH_3)_2MnCl_4$ as an example of such an angular dependence.

2) A more direct evidence of spin diffusion is the logarithmic dependence of the nonsecular resonances in 2D systems [79B9, 80L3]. This dependence can most easily be observed by studying the EPR linewidth at the magic angle where the secular part of the dipolar interactions vanishes and where the EPR lineshape is Lorentzian. In this geometry, the EPR linewidth is [90B1]

$$\Delta H_{EPR} = \text{const.} - \tilde{A}_{EPR}/(D\ln\omega) \tag{4.183}$$

The results of such an investigation on $(C_2H_5NH_3)_2MnCl_4$ are reproduced in Fig. 4.67 where the experimental points have been collected from two independent measurements. All data fit nicely to the expected straight line. From its slope, the diffusion constant can be evaluated: $D/a^2 = 13(2)$ K $\hat{=}$ 0.27(4) THz where a is the lattice constant.

3) In 1D and 2D magnetic systems, the diffusive behaviour of the four-spin correlation function is the origin of satellite lines in the EPR spectrum. Such satellites appear at 2ω, 3ω etc. on a frequency scale if the main line is at frequency ω. Since magnetic resonance is usually performed by sweeping the magnetic field at constant frequency of the micro- or millimeter wave source, the satellite lines are found at 0.5 H_{res} when the main line is observed at H_{res} (half-field EPR [77N2, 77Y1, 78B7, 80B10, 90B1]). As an example, the derivative EPR spectra of the satellite line and the main line are presented for $(C_2H_5NH_3)_2MnCl_4$ in Fig. 4.68.

4) A further direct evidence for spin diffusion can be obtained by an analysis of the lineshape of the main and of the satellite lines. Theory yields a logarithmic lineshape for both except for the main line at the magic angle which is simply a Lorentzian [78B7, 80B10, 90B1].

There are only few experimental investigations where all four criteria for spin diffusion have been studied in detail, see Table 6 where also the EPR linewidth data at high temperatures are listed although they are strictly not critical properties. But these data are strongly related to the fluctuations and correlations as we have seen in this and in the foregoing sections. In many studies, only criterion 1), i.e. the angular dependence of ΔH_{EPR}, has been measured. And very often, an optimum fit to the experimental data was not possible with Eq. 4.182 and a better fit was obtained with the following form [72B6, 75B6, 83K8]

$$\Delta H_{EPR}(\psi) = \Delta H_A + \Delta H_B \cos^2\psi + \Delta H_C\,(3\cos^2\psi - 1)^2 \qquad (4.184)$$

which reflects a mixture of long-time diffusive contributions in the third term (cf. Eq. 4.182) and of short-time contributions with a different angular dependence in the second term. Finally, there are magnetic systems, mostly Cu-compounds, where the angular dependence of ΔH_{EPR} consists only of short-time contributions. It is then analogous to Eqs. 4.166 or 4.166a which will here be written in the simpler form

$$\Delta H_{EPR}(\psi) = \Delta H_A + \Delta H_B \cos^2\psi \qquad (4.185)$$

with the constants ΔH_A and ΔH_B. All these considerations about the angular dependence of ΔH_{EPR} (Eqs. 4.182, 4.184 and 4.185) presume implicitly that the symmetry of the magnetic compounds is high enough to show no angular dependence of ΔH_{EPR} in the basal plane [$\Delta H_{EPR} \neq f(\beta)$]. This is actually the case for most of the perovskite-type layer structures. Only for a few compounds, also an in-plane anisotropy of ΔH_{EPR} has been observed experimentally. These are rather complex structures like $[COOH(CH_2)_2NH_3]_2CuX_4$ with X = Cl, Br [80W2, 81W2, 83W2], $(C_6H_5NH_3)_2CuCl_4$ [82W6] and $[C_6H_5(CH_2)_nNH_3]_2CuBr_4$ with n = 1,2 [92Z2]. Also the influence of the interlayer exchange J' has been the subject of an EPR study on $(C_nH_{2n+1}NH_3)_2CuCl_4$ with n = 1, 2, 3 [81W6].

With respect to the temperature dependence of ΔH_{EPR} in the high temperature range, we recall from Eq. 4.164 that this will be a linear function of temperature when the critical part has died away

$$\Delta H_{EPR} = A_{EPR} + B_{EPR} \cdot T \qquad (4.186)$$

with the constants A_{EPR} and B_{EPR}. This more empirical relation deduced from the experimental data in Fig. 4.57 needs a more profound theoretical basis. In accordance with the diffusive behaviour of the long-time fluctuations is the approach to explain the temperature dependence by phonon modulation of the symmetric exchange constant J in the Heisenberg model. Such calculations were performed by Richards and Salamon [74R1] and Lagendijk [79L] for K_2MnF_4 and by Zaspel and Drumheller [75Z, 77Z] for various Cu-compounds. An angular dependence of ΔH_{EPR} as in Eqs. 4.184 and 4.185 with a $\cos^2\psi$ term raises the question for the origin of the short-time contributions. Especially a dependence like Eq. 4.185

indicates that spin diffusion is negligible. That means there are interactions in the Hamiltonian which break the continuous symmetry of the Heisenberg model, namely anisotropic exchange (cf. Eq. 3.69 in Sect. 3.2.1 and Eq. 3.97 in Sect. 3.2.3) and antisymmetric exchange (cf. Eq. 3.52 in Sect. 3.1.7). Since mostly Cu-compounds show this behaviour, single-ion anisotropy is not of importance in this context. For explaining the EPR linewidth as resulting from phonon modulation of antisymmetric and anisotropic exchange, the symmetry of the crystal under consideration has to be sufficiently low that especially the requirements for antisymmetric exchange are met (cf. [77S6] and Sect. 3.1.7). Corresponding theoretical calculations yield for the contribution of antisymmetric exchange in Cu-compounds to B_{EPR} in Eq. 4.186 [68S3, 71C4, 81W5]

$$B_{\mathrm{EPR,antisymmetric\ exchange}} \sim (\Delta g/g)^2\, J^4 \approx |\boldsymbol{D}_{\mathrm{DM}}|^2\, J^2 \tag{4.187a}$$

where Eq. 3.52a in Sect. 3.1.7 has been used. A similar result has been obtained for the contribution of anisotropic exchange to B_{EPR} [81W5]

$$B_{\mathrm{EPR,anisotropic\ exchange}} \sim (\Delta g/g)^4\, J^4 \tag{4.187b}$$

A comparison of Eqs. 4.187a and 4.187b leads to the conclusion that the antisymmetric exchange is the dominant contribution to the temperature dependence of the EPR linewidth because of $(\Delta g/g)^2 << 1$. Willett and Wong [81W5] have compiled experimental data of B_{EPR} and J for a number of Cu-compounds, namely 6 chlorides and 3 bromides. A plot of the values of B_{EPR} versus J shows that B_{EPR} is nearly proportional to J^4, i.e. anisotropic exchange seems to dominate. The much larger values for B_{EPR} in bromides as compared to chlorides are not accounted for by Eqs. 4.187a and 4.187b. Willett and Wong [81W5] have proposed to take the spin-orbit coupling into account which is different for chlorine and bromine. They replace $(\Delta g/g)$ by $\lambda_{\mathrm{eff}} = 0.5\ (\lambda_{\mathrm{Cu}} + \lambda_{\mathrm{X}})$ with X = Cl or Br and so obtain a satisfactory result of the ratio $B_{\mathrm{EPR,\ bromide}}/B_{\mathrm{EPR,\ chloride}}$ for $[\mathrm{COOH(CH_2)_2NH_3}]_2\mathrm{CuX_4}$. But for $[\mathrm{NH_3(CH_2)_4NH_3}]\mathrm{CuX_4}$, on the other hand, this approach predicts a ratio too large by a factor of 10 [83K8]. Moreover, the angular dependence $\Delta H_{\mathrm{EPR}}(\psi)$ is different for $[\mathrm{COOH(CH_2)_2NH_3}]_2\mathrm{CuCl_4}$ (spin diffusion, Eq. 4.184) and for $[\mathrm{COOH(CH_2)_2NH_3}]_2\mathrm{CuBr_4}$ (no spin diffusion, Eq. 4.185) [80W2, 81W2, 83W2]. The conclusion from all these considerations is that there are a number of theoretical treatments for ΔH_{EPR} which do not predict all experimental findings properly and that, in view of the limited character of the experimental data, it is often hard to decide which is the dominant contribution to the EPR linewidth [82K5].

9.12.4.2.9 EPR Linewidth in Mixed Crystals

Also for mixed crystals or solid solutions, the EPR linewidth has been studied as a function of temperature and as a function of the polar angle ψ between H_0 and the c-axis. Let us first look at the results for diluted systems $\mathrm{A_2M_x\tilde{M}_{1-x}X_4}$ where $\mathrm{M^{2+}}$ is a paramagnetic ion and $\tilde{\mathrm{M}}^{2+}$ a diamagnetic one and which exhibit a long-range magnetic order for $\mathrm{x > x_p}$ (percolation limit $\mathrm{x_p} = 0.59$) and no ordering for $\mathrm{x < x_p}$. Most experimental data are available for the EPR linewidth in compounds with M = $\mathrm{Mn^{2+}}$

$\mathrm{K_2Mn_xMg_{1-x}F_4}$ with $0.35 \le \mathrm{x} \le 1.0$ [77T5, 78Y2, 78Y3, 79T2, 80T5]

$\mathrm{K_2Mn_xZn_{1-x}F_4}$, $\mathrm{K_2Mn_xCd_{1-x}F_4}$ with x near $\mathrm{x_p}$ [78Y2]

$\mathrm{Rb_2Mn_xMg_{1-x}F_4}$ with $0.3 \le \mathrm{x} \le 1.0$ [79W2]

$\mathrm{Rb_2Mn_xCd_{1-x}Cl_4}$ with $0.4 \le \mathrm{x} \le 1.0$ [82P1, 83P, 84E, 87G3, 89B4]

but also some for M = $\mathrm{Cu^{2+}}$

$\mathrm{K_2Cu_xZn_{1-x}F_4}$ with $0.1 \le \mathrm{x} \le 1.0$ [83Y1, 83Y2]

Also for these diluted systems, the EPR linewidth data are compiled in Table 6. At room temperature, i.e. far above the critical temperature for systems with $x > x_p$, ΔH_{EPR} shows the diffusive behaviour as discussed for pure crystals in the last section. The angular dependence $\Delta H_{EPR}(\psi)$ follows closely Eq. 4.182 where the term with $(3\cos^2\psi - 1)^2$ yields a minimum at the magic angle $\psi = 54.7°$ which is enhanced for diluted systems with $x < 1.0$, e.g. $K_2Mn_xMg_{1-x}F_4$, $Rb_2Mn_xMg_{1-x}F_4$, $Rb_2Mn_xCd_{1-x}Cl_4$ and $K_2Cu_xZn_{1-x}F_4$ [77T5, 78Y3, 79W2, 82P1, 83P, 83Y1, 83Y2]. For $K_2Cu_xZn_{1-x}F_4$ [83Y2], the minimum of ΔH_{EPR} is most enhanced for $x \approx 0.43$ and disappears for $x = 0.1$ where the angular dependence follows Eq. 4.185. On lowering the temperature, samples with a concentration $x > x_p$ show a change-over of the angular dependence $\Delta H_{EPR}(\psi)$ from Eq. 4.182 to Eq. 4.184 and finally to Eq. 4.185 [78Y3, 83P, 84E] in the region of the critical broadening of ΔH_{EPR} when the temperature approaches the critical temperature. In $Rb_2Mn_xMg_{1-x}F_4$, the angular dependence for x near the percolation limit (x = 0.57, 0.70) is found to follow a $\cos^4\psi$ law rather than the $\cos^2\psi$ law of Eq. 4.185 [79W2]

$$\Delta H_{EPR} = \Delta H'_A + \Delta H'_B \cos^4\psi \tag{4.188}$$

This behaviour seems to be characteristic for the EPR linewidth for $x \approx x_p$ regardless whether antiferromagnetic ordering occurs ($x = 0.70$, $T_N \approx 15$ K) or not ($x = 0.57 < x_p$) and it is considered to originate from short-range antiferromagnetic correlations. At very low temperature ($T = 1.6$ K), samples with x = 0.54 and 0.57 near x_p of the same system show a nine-line finestructure which is ascribed to the effect of isolated Mn^{2+} clusters. For x well below the percolation concentration x_p, the EPR stays in all diluted systems at $H_{res} = 2\pi\nu/\gamma$ (cf. Eq. 4.169) down to low temperatures reflecting the absence of magnetic order. The angular dependence $\Delta H_{EPR}(\psi)$ is observed according to Eq. 4.182 also at all temperatures [78Y3]. In $K_2Mn_{0.43}Mg_{0.57}F_4$, a shift ΔH_{res} of the magnetic field at resonance is observed that is dependent on the polar angle ψ, and which vanishes at the magic angle $\psi = 54.7°$ [80T5]. This shift is explained by taking into account the dominancy of the $q = 0$ mode and the effect of the long-time tails of the spin correlation function (cf. spin diffusion in the last section). A further evidence for the diffusive behaviour of the EPR linewidth in diluted magnets is the observation of sidebands in $K_2Mn_x\tilde{M}_{1-x}F_4$ ($\tilde{M}$ = Mg, Zn, Cd; $x \approx x_p$) at $H_{res}/2$ (2ν, half-field EPR) and $H_{res}/3$ (3ν) [78Y2]. The lineshape should be Lorentzian for EPR at the magic angle $\psi = 54.7°$. This is actually observed for small dilutions (x = 0.7, 0.9) as well as for x = 1.0 in $K_2Mn_xMg_{1-x}F_4$ [77T5] while the results for x = 0.55 show a deviation from the Lorentzian lineshape. This is explained as a change of the correlations from 2D to 1D character near x_p. And for $x \approx 0.35$ in the same system, the lineshape deviates from Lorentzian towards Gaussian. It can be described as originating from a 1D-system of broken chains with 30–50 Mn^{2+}-ions [79T2].

The critical broadening of the EPR linewidth may be analyzed for diluted systems as for pure systems by fitting the experimental data to the power law Eq. 4.165, repeated here from Sect. 4.2.6 for the convenience of the reader

$$\Delta H_{EPR} = \Delta H^{\infty}_{EPR} + C_{EPR} \cdot t^{-p}$$

with the exponent p or to the Arrhenius law Eq. 4.170 (Sect. 4.2.7), also repeated here

$$(\Delta H_{EPR} - \Delta H^{\infty}_{EPR}) \sim \exp\,(E_s / k_B T)$$

with $E_s = 4\pi\rho_s$ resulting from the soliton contribution to the EPR linewidth, cf. Eq. 4.175a. Such an analysis was performed along both lines for $Rb_2Mn_xCd_{1-x}Cl_4$ with x = 0.62 – 1.0 in the configurations $\boldsymbol{H_0} \parallel \boldsymbol{c}$ and $\boldsymbol{H_0} \perp \boldsymbol{c}$ [83P, 84E, 87G3, 89B4]. For all concentrations, the resulting values of p show a change-over from a smaller value for $t \le t_{CH}$ to larger values for $t \ge t_{CH}$. The latter are close to the expected universal value p = 2.5 (cf. Table 8) in many cases. However, the values for p are scattered over a relatively wide range and the uncertainties are large. Since the values for the change-over temperature t_{CH} range from 0.1 to 0.85 [84E] with some tendency to increase with Cd-concentration, this change of p is not a cross-over as discussed in Sect. 4.1.9 but probably impurity-induced. The analysis with respect to the Arrhenius law yields one straight line in the log-plot (cf. Eq. 4.170a) and thus one value for E_s/k_BT_N and for E_s except for x = 0.70 where two lines are obtained with values close to each other (see Table 6). The values of E_s decrease drastically for $\boldsymbol{H_0} \parallel \boldsymbol{c}$ from $E_s = 969$ K (x = 1.0) to $E_s = 5.6$ K (x = 0.62) and for $\boldsymbol{H_0} \perp \boldsymbol{c}$ from $E_s = 1094$ K (x = 1.0) to $E_s = 3.6$ K (x = 0.62). This behaviour is to be expected since a dilution diminishes the number of magnetic ions in the sample which probably diminishes the spin stiffness ρ_s. However, the decrease of E_s with decreasing x is larger than the corresponding decrease of T_N (cf. Table 5) so that also the ratio E_s/k_BT_N decreases with x. On the other hand, the spin stiffness ρ_s is among the response functions which were calculated by Harris and Kirkpatrick [77H5]. Their constant A equals $S^2|J| = 0.5\ \rho_s$ and their Fig. 3 presents the results for $A(x)/A(1)$. After correcting these data for the dependence of J on a ($J \sim a^{-12}$, see Sect. 3.1.1 and [75J]), we may compare the calculated values $E_s = 4\pi\rho_s$ with the experimental data in Table 6 and find satisfactory agreement within the limits of experimental error. Typical values (x = 0.80) are $E_{s,\mathrm{exp}} = 250$ K and 281 K for $\boldsymbol{H_0} \parallel \boldsymbol{c}$ and $\boldsymbol{H_0} \perp \boldsymbol{c}$, resp., in comparison to $E_{s,\mathrm{calc}} = 366$ K.

Secondly, our attention will be focussed on magnetic mixtures, i.e. solid solutions $\mathrm{A_2M_x\widetilde{M}_{1-x}X_4}$ where both, $\mathrm{M^{2+}}$ and $\mathrm{\widetilde{M}^{2+}}$, are paramagnetic ions. For the discussion of the EPR results, especially the EPR linewidth obtained at temperatures above the critical temperature, in this context the competing interactions in these compounds and their magnetic ordering are not relevant as outlined in Sect. 3.3.5 and 3.3.6. Experimental data are available for the following systems (cf. Table 6)

$\mathrm{K_2Mn_{1-x}Fe_xF_4}$ (x = 0.001, 0.007, 0.015, 0.18) [83A2, 84V4]

$\mathrm{K_2Mn_{1-x}CoF_4}$ (x = 0.008) [84V4]

$\mathrm{K_2Mn_{1-x}Ni_xF_4}$ (x = 0.02, 0.10, 0.125) [84V4]

$\mathrm{(C_2H_5NH_3)_2Mn_{1-x}Cu_xCl_4}$ (x = 0, 0.03, 0.08, 0.30) [88T1]

At room temperature ($T = 293$ K), the angular dependence of $\Delta H_{\mathrm{EPR}}(\psi)$ of all these compounds is well described by Eq. 4.182 and thus reflects the diffusive behaviour already discussed for pure $\mathrm{K_2MnF_4}$ and for diluted Mn-compounds. One exception are the mixed crystals $\mathrm{K_2Mn_{1-x}Co_xF_4}$ where Eq. 4.184 with an additional $\cos^2\psi$ term yields a better fit to the experimental data [84V4]. Thus, the spin diffusion is only slightly affected by the impurities $\mathrm{Fe^{2+}}$, $\mathrm{Co^{2+}}$ und $\mathrm{Ni^{2+}}$. However, the EPR lines are severely broadenend by $\mathrm{Fe^{2+}}$ and $\mathrm{Co^{2+}}$ and not so much by $\mathrm{Ni^{2+}}$. For $\mathrm{Fe^{2+}}$ and $\mathrm{Ni^{2+}}$ the linewidth for the magic angle $\psi = 54.7°$ at room temperature $T = 293$ K is naturally proportional to the impurity concentration x (see Fig. 4.69)

$$\Delta H_{\mathrm{EPR}}(\mathrm{x} \neq 0,\ \psi = 54.7°) - \Delta H_{\mathrm{EPR}}(\mathrm{x} = 0,\ \psi = 54.7°) = C_{\mathrm{broad}} \cdot \mathrm{x} \qquad (4.189)$$

where the factor C_{broad} is very different for $\mathrm{Fe^{2+}}$ and $\mathrm{Ni^{2+}}$ reflecting the strong broadening by $\mathrm{Fe^{2+}}$ in contrast to $\mathrm{Ni^{2+}}$ [84V4]. The data in Fig. 4.69 yield $C_{\mathrm{broad}} \approx 97.3$ T for $\mathrm{Fe^{2+}}$ and $C_{\mathrm{broad}} \approx 0.125$ T for $\mathrm{Ni^{2+}}$. This broadening for Fe-doped samples is observed not only at 293 K but over the whole temperature range (60 K $\leq T \leq$ 300 K) for both configurations, $\boldsymbol{H_0} \parallel \boldsymbol{c}$ and $\boldsymbol{H_0} \perp \boldsymbol{c}$ [83A2]. The extreme broadening of the EPR linewidth for relatively small impurity concentrations of $\mathrm{Fe^{2+}}$ and $\mathrm{Co^{2+}}$ was also found in the fluoride perovskite system $\mathrm{RbMn_{1-x}\widetilde{M}_xF_3}$ with $\mathrm{\widetilde{M}}$ = Fe, Co, Ni [72G2]. It is attributed to the dominance of the fast spin-lattice relaxation of $\mathrm{Fe^{2+}}$ and $\mathrm{Co^{2+}}$ in the damping of the spin fluctuations [75H4, 83A2, 84V4]. The EPR linewidth of the system $\mathrm{(C_2H_5NH_3)_2Mn_{1-x}Cu_xCl_4}$ [88T1] shows a linear temperature dependence in the range 60 K $\leq T \leq$ 300 K outlined and discussed in the last section for pure magnets (cf. Eq. 4.186: $\Delta H_{\mathrm{EPR}}(T) = A_{\mathrm{EPR}} + B_{\mathrm{EPR}} \cdot T$).

The critical broadening of the EPR linewidth in magnetic mixtures at temperatures approaching the Néel temperature from above was also studied for the system $K_2Mn_{1-x}\tilde{M}_xF_4$ with $\tilde{M}$ = Fe, Co, Ni [83A2, 84V4]. The results were analyzed by means of the power law (Eq. 4.165). Except for $K_2Mn_{1-x}Ni_xF_4$ with the smaller Ni- concentrations x = 0.02 and 0.10, the log-log plot yields for all samples two straight line regimes as discussed above for $Rb_2Mn_xCd_{1-x}Cl_4$ separated by a change-over at the reduced temperature t_{CH} which increases with impurity concentration, e.g. for $K_2Mn_{1-x}Fe_xF_4$ from $t_{CH} \approx 0.2$ for x = 0.001 to $t_{CH} \approx 0.8$ for x = 0.015 (cf. Fig. 4.70), similar to the results in the diluted Mn^{2+}-system. The resulting values of the exponent p are listed for all these samples and for both configurations, $\boldsymbol{H_0} \parallel \boldsymbol{c}$ and $\boldsymbol{H_0} \perp \boldsymbol{c}$, in Table 6. For $t \geq t_{CH}$, they are generally close to the value found in pure K_2MnF_4 and thus to the theorectically expected value

$$p \approx p(x = 0) \approx 2.5 \tag{4.190a}$$

and smaller by about unity for the range closer to T_N, i.e. for $t \leq t_{CH}$

$$p \approx p(x = 0) - 1 \approx 1.5 \tag{4.190b}$$

where the fit to the experimental data is extended mostly over the range $0.2 \leq t \leq 0.7$ (sec Fig. 4.70) except for samples with $t_{CH} \approx 0.2$ where it was extended down to about $t = 0.08$. The values of p according to Eqs. 4.190a and 4.190b do not vary perceptibly with impurity concentration. The differences of p for $\boldsymbol{H_0} \parallel \boldsymbol{c}$ and $\boldsymbol{H_0} \perp \boldsymbol{c}$ are also within the limits of experimental error. In the range of critical broadening, the experimentally determined angular dependence of ΔH_{EPR} is well described by Eq. 4.166a, repeated here for convenience

$$\Delta H_{EPR}(\psi) = \Delta H_1'(1 - 0.5 \sin^2\psi) + \Delta H_2'$$

as predicted theoretically for this range (cf. Sect. 4.2.6) or, equivalently, by Eqs. 4.166 and 4.185. For the evaluation of t, the value of T_N is needed for the doped samples which was determined for each sample by observing the temperature below which the EPR absorption disappears and, for some samples, by measuring the magnetic susceptibility χ separately. The values in Table 6 show that T_N increases for the samples doped with Ni^{2+} and Co^{2+} while it decreases for Fe-doped samples as compared to pure K_2MnF_4. The reduction of p in the range closer to T_N means a reduction of the line broadening towards T_N. This effect is more pronounced for Fe^{2+} and Co^{2+} impurities than for Ni^{2+} ones. It is considered to be caused by the fast spin-lattice relaxation observed for the former two ions which is only weakly temperature-dependent and does therefore not contribute to the sharp increase of the linewidth near T_N.

9.12.4.3 Figures for 9.12.4 and Table 6

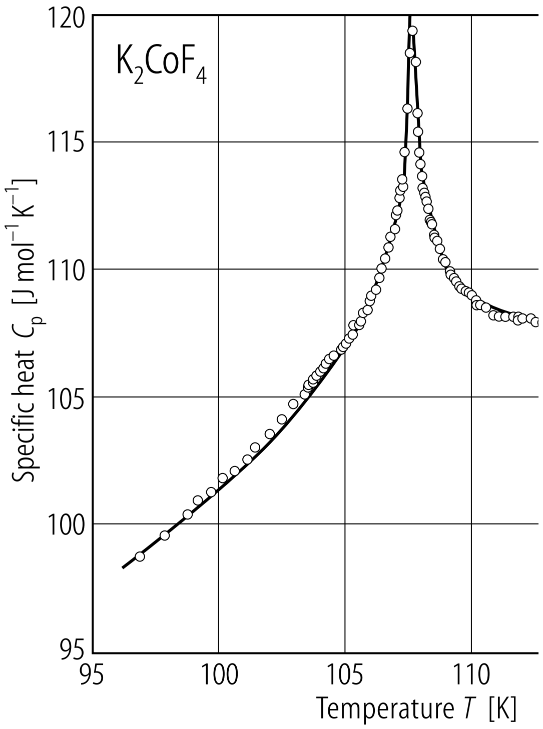

Fig. 4.1. K$_2$CoF$_4$. Specific heat C_p as a function of temperature T in the vicinity of the magnetic phase transition, experimental points and solid curve representing a fit to Eq. 4.16 with $\alpha^+ = \alpha^-$ and $D^+ = D^-$ (taken from [75I1]).

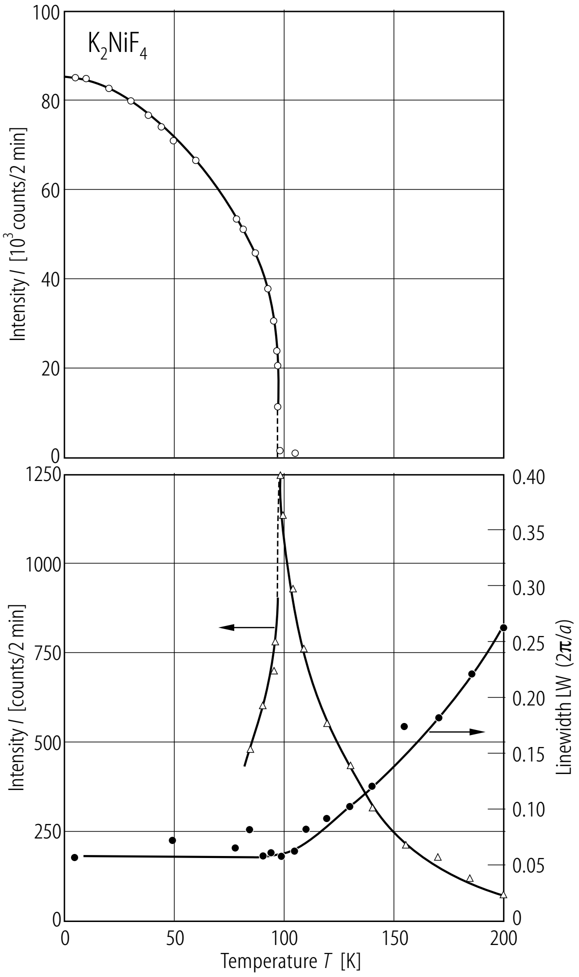

Fig. 4.3. K$_2$NiF$_4$. Neutron scattering intensity I as a function of temperature T near the magnetic phase transition for the afm. Bragg peak $\boldsymbol{Q}_0 \hat{=} (1, 0, 0)$ (top) and for the afm. Bragg rod $\boldsymbol{Q}_0 \hat{=} (1, 0, 0.25)$ (bottom), for the latter also the linewidth LW (full width at half-maximum), taken from [69B2, 70B3].

For Fig. 4.2 see next page.

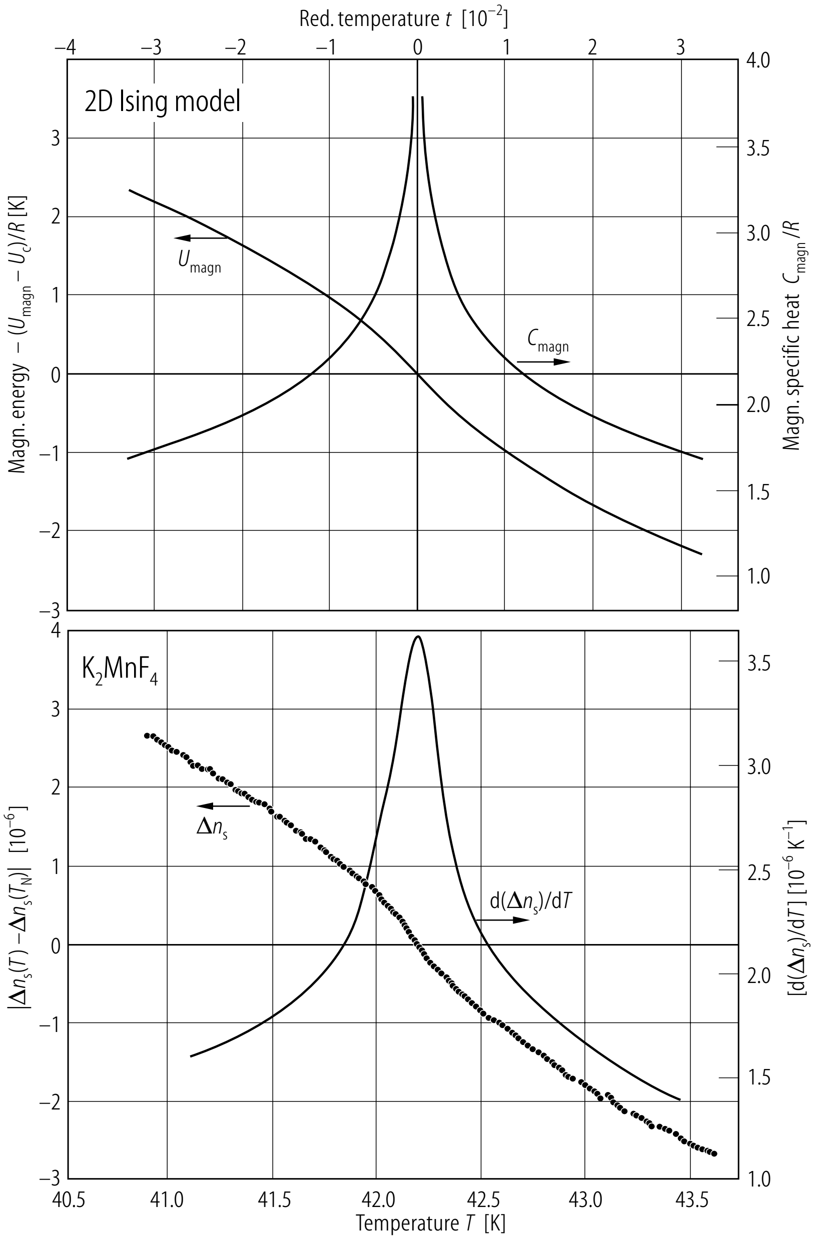

Fig. 4.2. K_2MnF_4. Linear magnetic birefringence (LMB), singular part of Δn near T_N: $\Delta n_s(T) - \Delta n_s(T_N)$ and $d(\Delta n_s)/dT$ versus temperature T (lower part), compared to the exact results for $-(U_{magn} - U_C)/R$ and C_{magn}/R of the 2D Ising model (upper part), after [79J, 84F1].

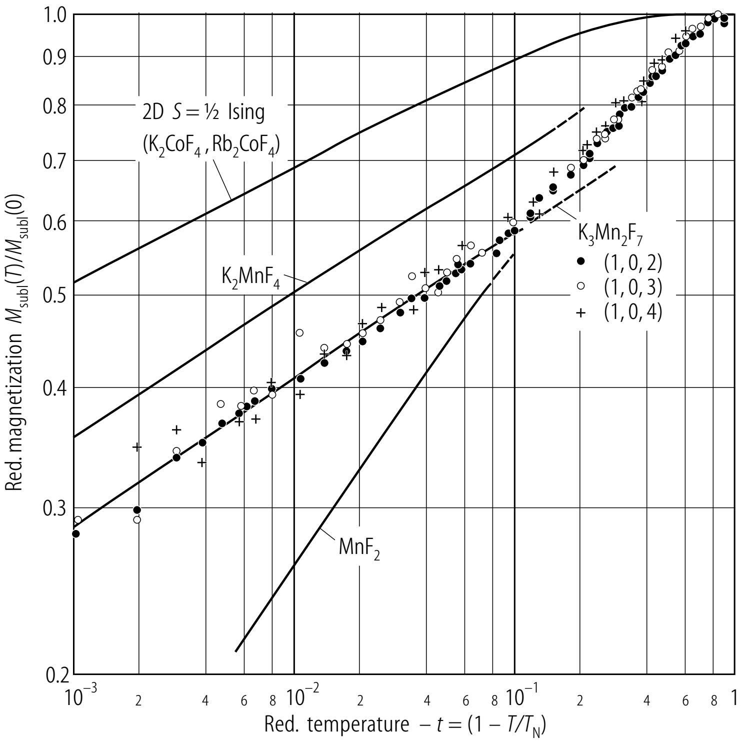

Fig. 4.4. $K_3Mn_2F_7$. Reduced sublattice magnetization $M_{subl}(T)/M_{subl}(0)$ versus reduced temperature $t = T/T_N - 1$ (log-log plot) as deduced from three magnetic Bragg reflections, yielding the critical exponent $\beta = 0.154$. For comparison, experimental data are shown for MnF_2 (3D afm.: $\beta = 0.335$), K_2MnF_4 (single-layer 2D afm.: $\beta = 0.150$) and the exact result for the 2D Ising model ($\beta = 0.125$) which is identical with the experimental data for K_2CoF_4 and Rb_2CoF_4 (taken from [79U]).

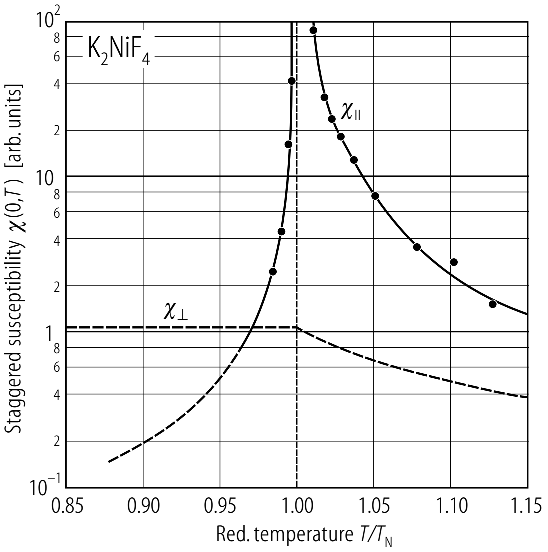

Fig. 4.5. K_2NiF_4. Staggered susceptibility $\chi(q = 0, T) = \chi(0, T)$ on a log-scale, longitudinal and transverse part, $\chi_\parallel$ and $\chi_\perp$, resp., versus reduced temperature T/T_N. The experimental points are deduced from scans across a Bragg ridge ($q = 0$ means on top of the ridge). The solid and broken lines refer to the analysis of $\chi(0, T)$ as explained in the text (taken from [77B2]).

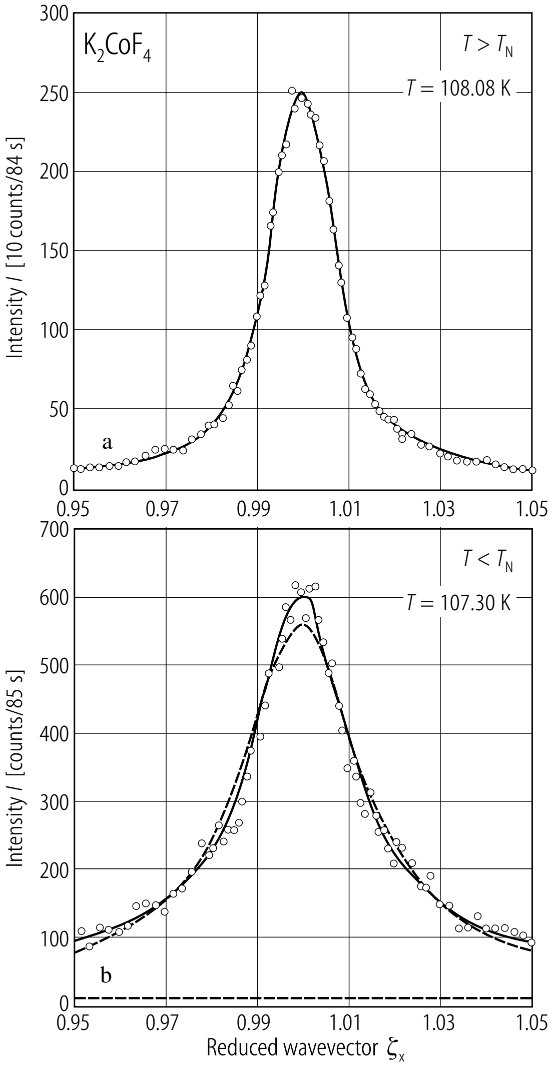

Fig. 4.6. K_2CoF_4. Intensity I of critical neutron scattering, scans across the Bragg ridge with $\boldsymbol{Q}_0 \mathrel{\hat{=}} (\zeta_x, 0, 0.45)$ for **(a)** $T > T_N$ and **(b)** $T < T_N$, experimental points and curves calculated by means of a fit to a theoretical form for $\chi(q, t)$ and a convolution with the resolution function. The broken horizontal line shows the background. For $T > T_N$: fits to Eq. 4.28 [$\chi_{OZ}(q, t)$]; and for $T < T_N$: fit to Eq. 4.31 [$\chi_{TF}(q, t)$, full line] and to 4.28 [χ_{OZ}, broken line] resp., taken from [84C1].

For Fig. 4.7 see next page.

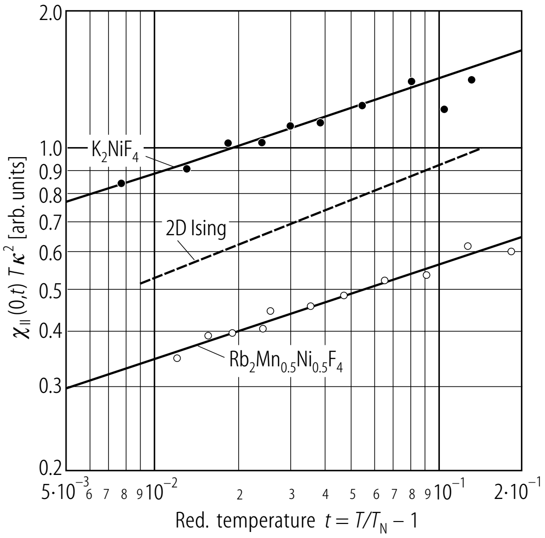

Fig. 4.8. K_2NiF_4, $Rb_2Mn_{0.5}Ni_{0.5}F_4$. log-log plot of $\chi_{\parallel}(0, t) \cdot T \cdot \kappa^2 \sim t^{\eta\nu^+}$ as a function of $t = T/T_N - 1$ where $\chi_{\parallel}(0, t)$ and κ are the longitudinal susceptibility on top of the ridge ($q = 0$) and the inverse correlation length, respectively. The product of the critical exponents ν^+ and η is determined from the slope of the solid lines averaging the experimental data. The broken line shows the exact result of the 2D Ising model with $\nu^{\pm}\eta = 0.25$ (taken from [77B2]).

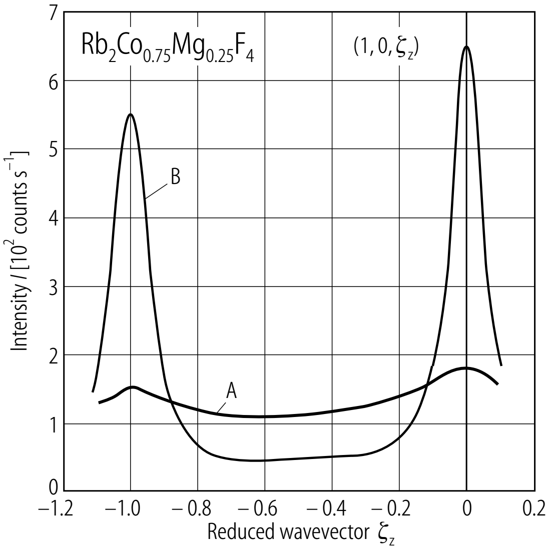

Fig. 4.9. $Rb_2Co_{0.75}Mg_{0.25}F_4$. Neutron scattering intensity I, scans along the antiferromagnetic rod with $\boldsymbol{Q} \mathrel{\hat{=}} (1, 0, \zeta_z)$ where $\zeta_z = 0$ and -1 mean antiferromagnetic superreflections from domain 1 and 2, resp., A) rapid cooling from 80 K to 4.2 K in a few seconds and B) slow cooling from about 70 K to about 30 K in 15 min (after [79I2]).

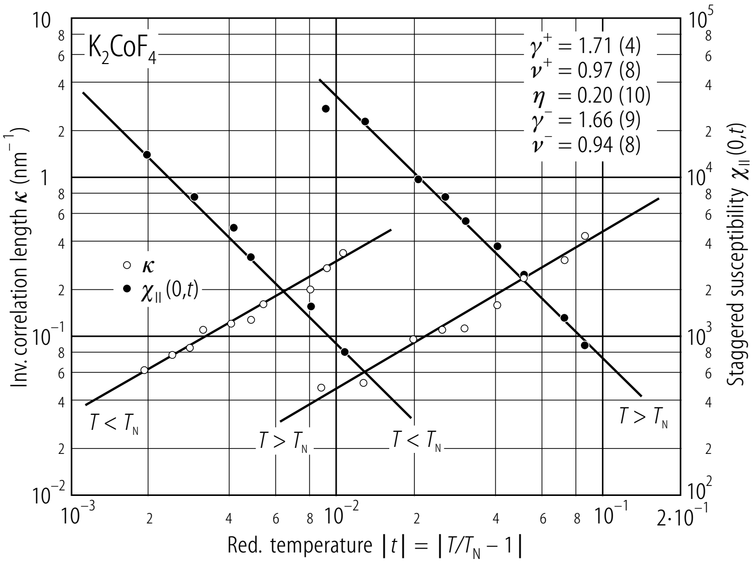

Fig. 4.7. K$_2$CoF$_4$. log-log plot of the staggered susceptibility $\chi(q = 0, t)$ (full circles) and the inverse correlation length κ (open circles) for $T > T_N$ and $T < T_N$ as a function of the reduced temperature $|t| = |T/T_N - 1|$. Optimum fits of the experimental data to Eq. 4.29 [$\chi_F(q, t)$] yield the critical exponents γ^+, ν^+, γ^-, ν^- and η. The straight lines demonstrate single power-law behaviour (after [74I1]).

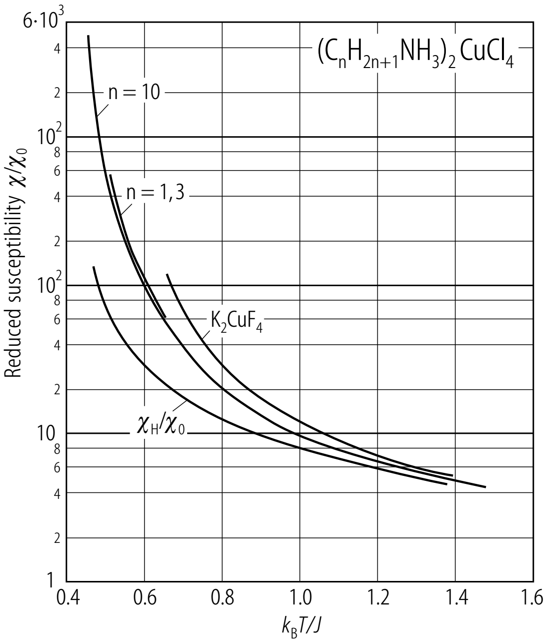

Fig. 4.10. K$_2$CuF$_4$, $(C_nH_{2n+1}NH_3)_2CuCl_4$ with n = 1, 3, 10. Experimental zero-field reduced susceptibilities χ/χ_0 ($\chi_0 = C/T$, cf. Eq. 4.8) as a function of k_BT/J in the 2D region of each compound. The curve χ_H/χ_0 denotes the reduced susceptibility of the 2D Heisenberg model, extrapolated from the experimental data (taken from [76N2]).

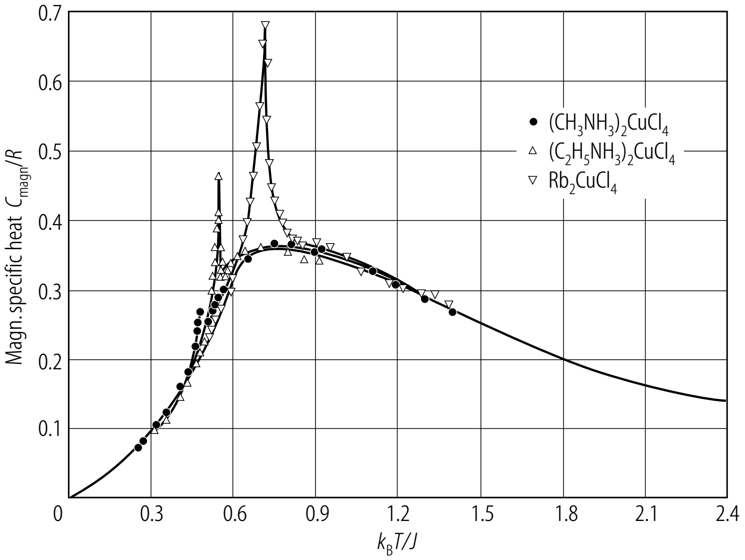

Fig. 4.11. Rb_2CuCl_4, $(CH_3NH_3)_2CuCl_4$, $(C_2H_5NH_3)_2CuCl_4$. Magnetic contribution to the specific heat C_{magn} (in units of R) as a function of k_BT/J, sharp spikes (singular part) at the critical temperature T_C and common broad maximum which is considered C_{magn} of the 2D Heisenberg model and which is extended to lower and higher temperatures by spin-wave calculations (Eq. 3.79(a) and high temperature series expansions (Eq. 4.39), after [77B3].

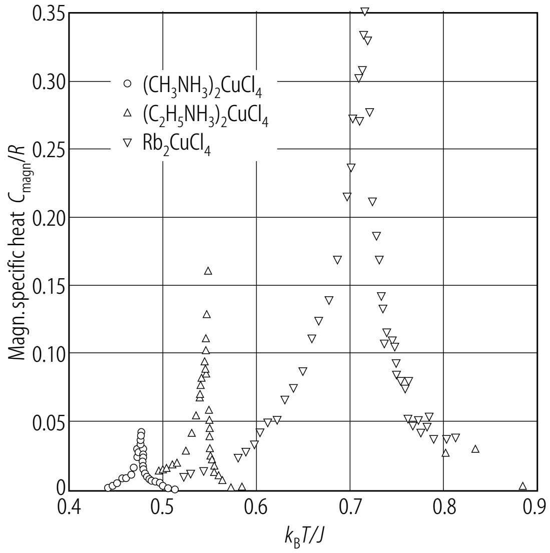

Fig. 4.12. Rb_2CuCl_4, $(CH_3NH_3)_2CuCl_4$, $(C_2H_5NH_3)_2CuCl_4$. Singular part of the magnetic specific heat C_{magn} (in units of R) as a function of k_BT/J. Even on the reduced temperature scale, the spikes appear at different positions since the critical temperature T_C depends not only on J but also on J_A and J' (after [77B3]).

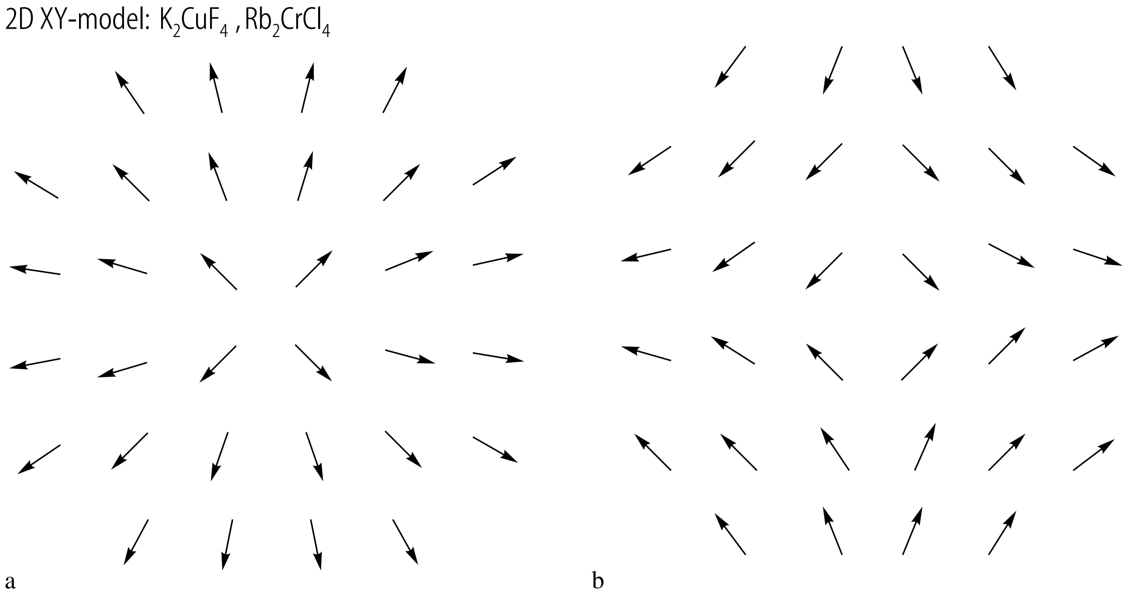

Fig. 4.13. 2D XY-model: K_2CuF_4, Rb_2CrCl_4. Two examples of spin orientations in vortices, **(a)** with vorticity $Q = +1$ and **(b)** with $Q = -1$ (after [90P]).

For Fig. 4.14 see next page.

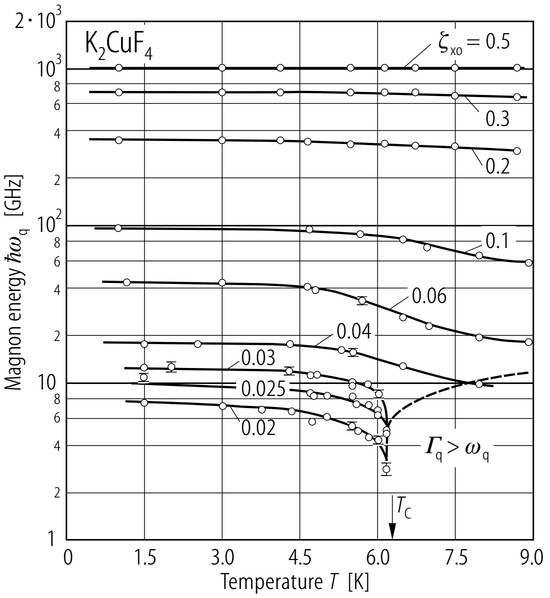

Fig. 4.15. K_2CuF_4. Temperature dependence of the magnon energy $\hbar\omega_q$ for wavevector $\boldsymbol{q} \mathrel{\hat{=}} (\zeta_{x0}, 0, 0)$. For $0.04 \le \zeta_{x0} \le 0.5$, the temperature renormalization of $\hbar\omega_q$ is moderate while a drastic decrease of $\hbar\omega_q$ is observed near T_C for $0 \le \zeta_{x0} \le 0.03$. The broken line marks the boundary beyond which the magnons are overdamped (damping $\Gamma_q > \omega_q$), after [83H4, 90H].

2D XY-model: K_2CuF_4, Rb_2CrCl_4

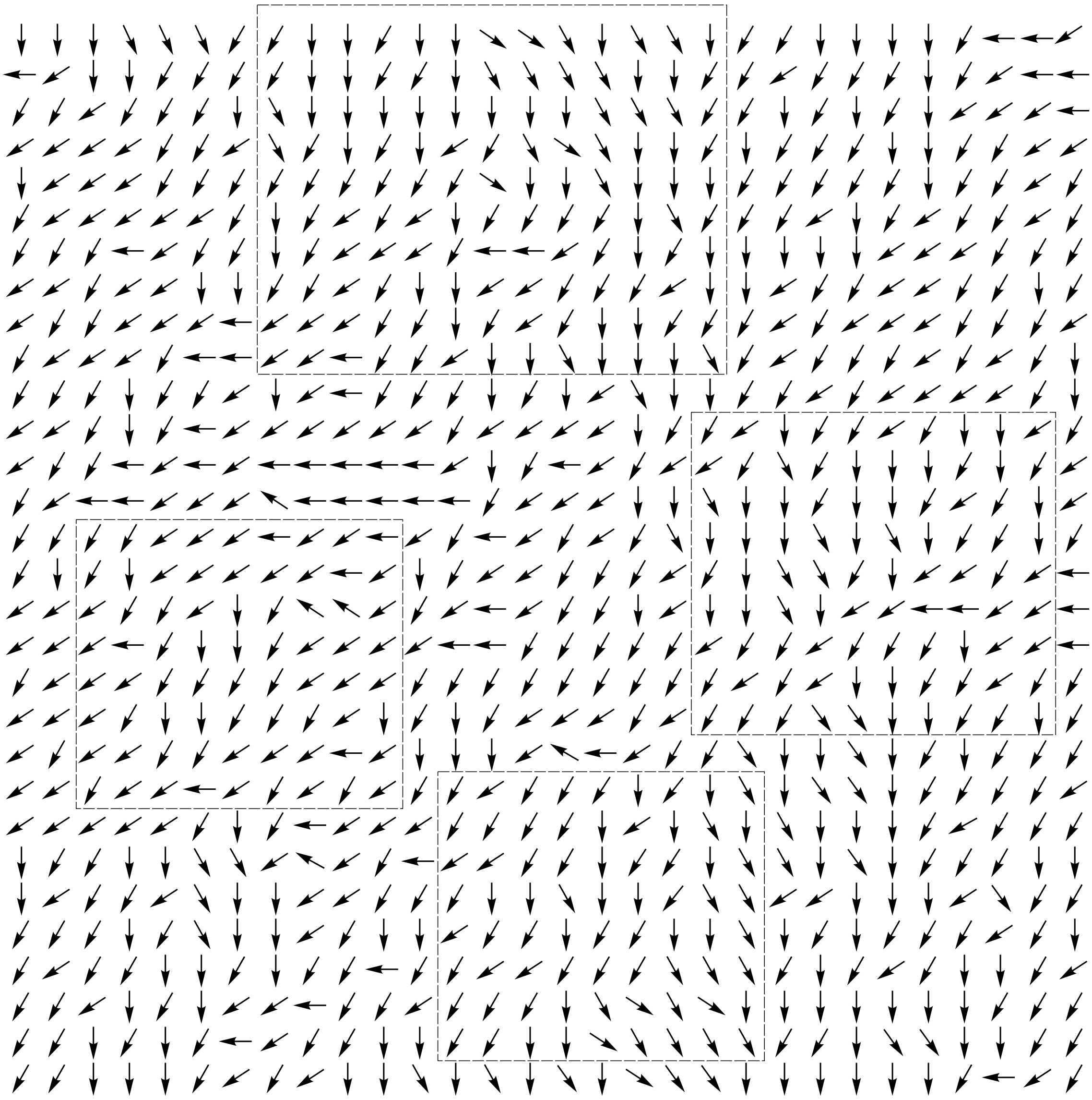

Fig. 4.14. 2D XY-model: K_2CuF_4, Rb_2CrCl_4. Typical equilibrium spin configuration in the vortex-antivortex pair region $k_BT = 0.5(2S^2J)$ obtained in a Monte Carlo simulation (2000 Monte Carlo steps). The vortex pairs are enclosed by broken lines (taken from [78M3]).

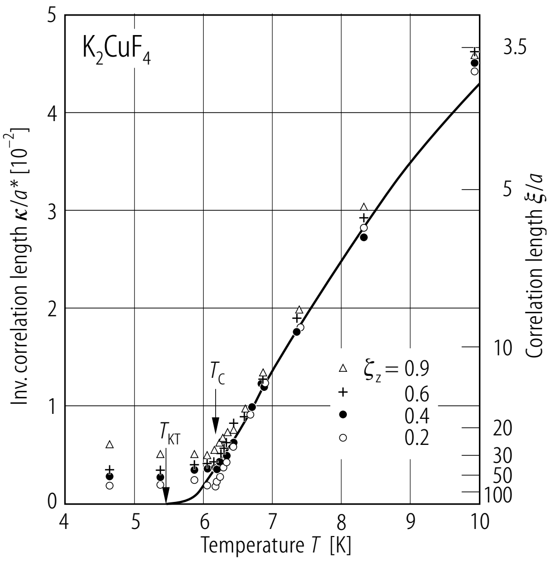

Fig. 4.16. K_2CuF_4. Correlation length ξ/a and its inverse κ/a^* versus temperature T, obtained by quasi-elastic neutron scattering with $\boldsymbol{Q}_0 \hat{=} (0, 0, 2 - \zeta_z)$ for various ζ_z and by fitting the experimental data to Eq. 4.29 [$\chi_F(q, T)$]. The solid curve is calculated using Eq. 4.43 (Kosterlitz-Thouless theory). The characteristic temperatures T_{KT} and T_C are indicated (after [82H5, 82H6]).

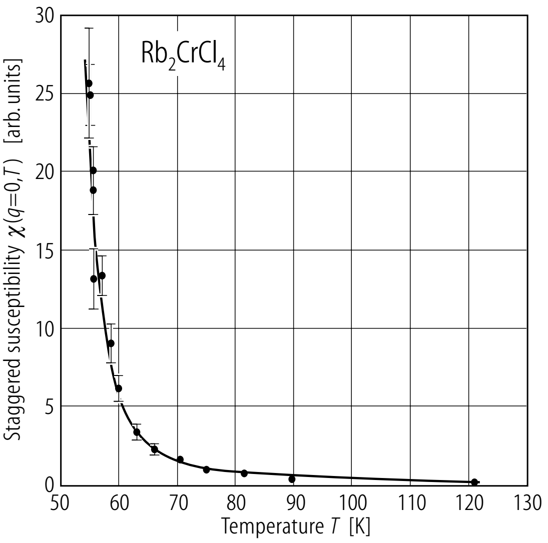

Fig. 4.17. Rb_2CrCl_4. Staggered susceptibility $\chi(q = 0, T)$ as a function of temperature T in the 2D region ($T > 55$ K), obtained by quasi-elastic neutron scattering with $\boldsymbol{Q}_0 \hat{=} (0, 0, 2 + \zeta_z)$ and by fitting the experimental data to Eq. 4.28 [$\chi_{OZ}(q, T)$] or Eq. 4.29 [$\chi_F(q, T)$]. The curve is calculated using Eq. 4.44 (Kosterlitz-Thouless theory), taken from [93A].

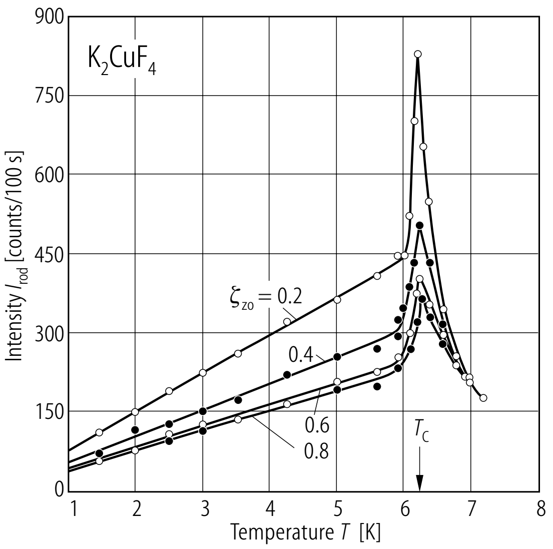

Fig. 4.18. K_2CuF_4. Temperature variation of the neutron scattering intensity I_{rod} of scans across the ferromagnetic rod with $\boldsymbol{Q}_0 \hat{=} (0, 0, 2 - \zeta_{z0})$ for various values of ζ_{z0}. For the interpretation of these data, see text (after [82H5, 82H6]).

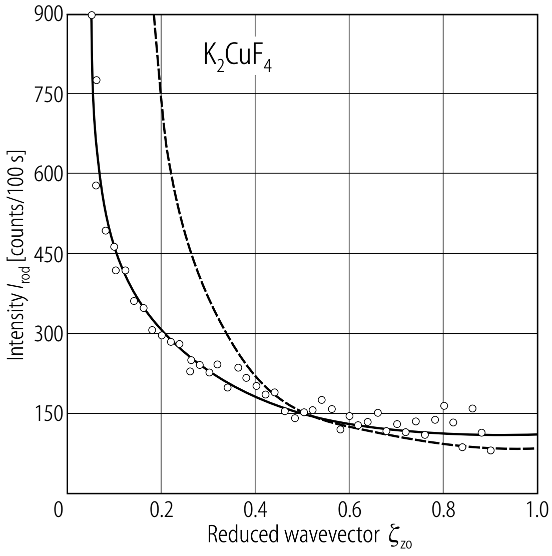

Fig. 4.19. K$_2$CuF$_4$. Neutron scattering intensity I_{rod} for scans across the ferromagnetic rod with $\boldsymbol{Q}_0 \hat{=} (0, 0, 2 - \zeta_{z0})$ as a function of ζ_{z0} at $T = 4.21$ K, experimental points and curves calculated for the 2D XY-model (solid line) and for the 2D Heisenberg model (broken line), taken from [79H2].

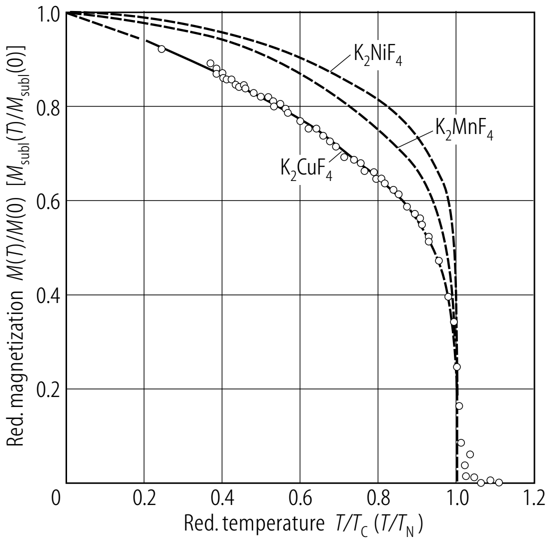

Fig. 4.20. K$_2$CuF$_4$. Reduced magnetization $M(T)/M(0)$ versus reduced temperature T/T_C, as determined by neutron diffraction (open circles) and by NMR (full line, after [73K2]). For comparison, the reduced sublattice magnetization $M_{subl}(T)/M_{subl}(0)$ versus T/T_N is shown for K$_2$MnF$_4$ and K$_2$NiF$_4$ (taken from [73H3]).

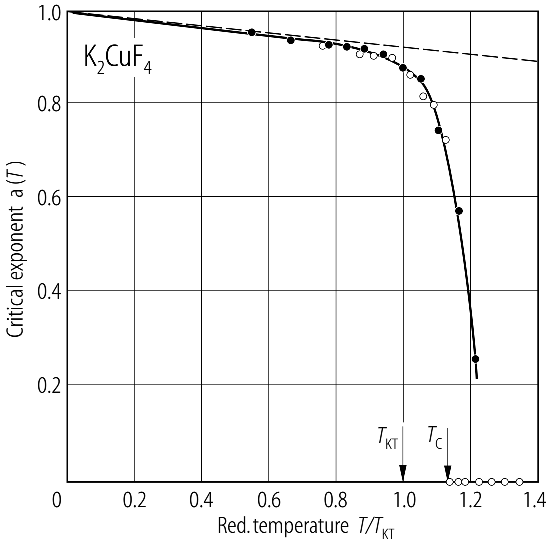

Fig. 4.21. K$_2$CuF$_4$. Critical exponent a(T) (cf. Eqs. 4.62 and 4.63) as a function of T/T_{KT}, derived from the susceptibility $\chi = \partial M/\partial H$, experimental points (open circles) and results of a Monte Carlo simulation (full circles). The broken line represents the spin-wave approximation, the full line is guide to the eye. Also indicated are the characteristic temperatures T_{KT} and T_C (taken from [81H2]).

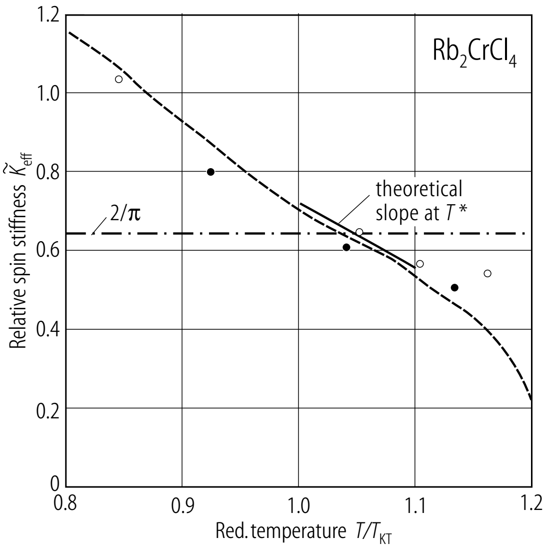

Fig. 4.22. Rb$_2$CrCl$_4$. Relative spin stiffness $\widetilde{K}_{\rm eff} = (2S^2J_{\rm eff})/(k_{\rm B}T)$ (cf. Eq. 4.48) as a function of $T/T_{\rm KT}$ in the vicinity of $T_{\rm KT} = 43.3$ K, determined by neutron inelastic scattering (full circles, after [81H4, 86H2]), by magnetization measurements (open circles, after [86C1]) and by neutron diffraction (dashed line, after [93A]). The horizontal line represents the universal value $\widetilde{K}_{\rm eff} = 2/\pi$ at $T = T^* = 1.051\ T_{\rm KT}$. Further indicated is the theoretical slope at T^* (taken from [94B1]).

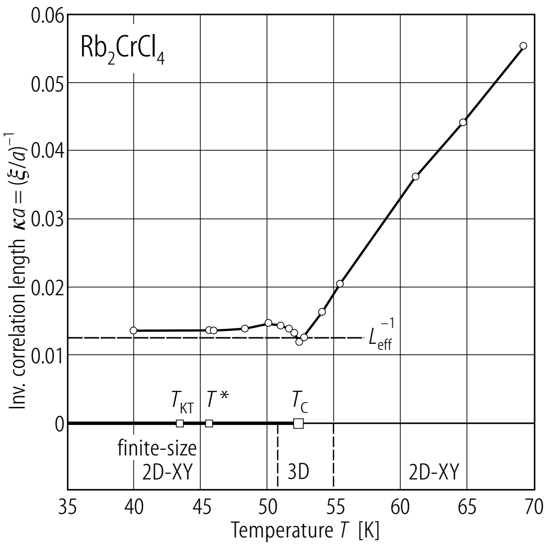

Fig. 4.23. Rb$_2$CrCl$_4$. Inverse correlation length $\kappa a = (\xi/a)^{-1}$ versus temperature, experimental data after [93A]. The broken line marks the minimum value of κa which is identified with the effective size $L_{\rm eff}^{-1}$ of the system in the finite-size 2D XY-model. The lower part of the figure illustrates the various critical regions and the characteristic temperatures as explained in the text (taken from [95B1]).

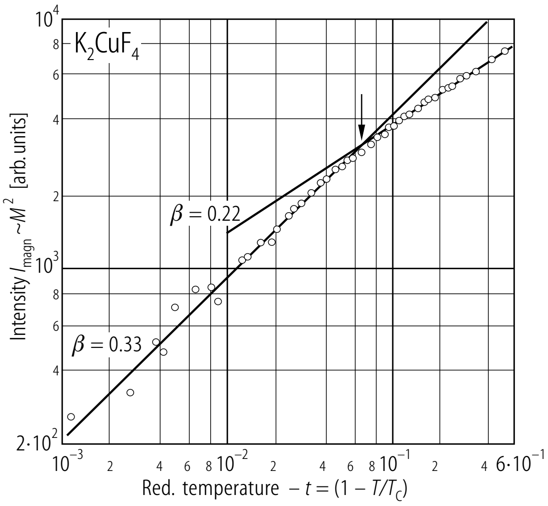

Fig. 4.24. K$_2$CuF$_4$. Example of a 2D ↔ 3D lattice dimensionality crossover in the critical behaviour of the magnetization M as obtained from neutron diffraction (after [73H3]), presented as log-log plot of the magnetic neutron diffraction intensity $I_{\rm magn} \sim M^2$ versus $(-t)$. The values of the critical exponents β are close to those for the 3D and 2D XY-model, resp. (taken from [90J1]).

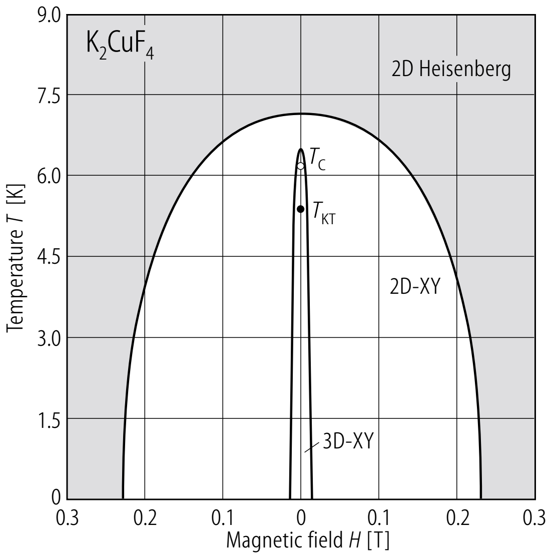

Fig. 4.25. K_2CuF_4. Schematic (T, H)-phase diagram illustrating the various critical regions and the crossover lines as explained in the text. Also indicated are the characteristic temperatures T_{KT} and T_C (after [82H5, 82H6, 90H]).

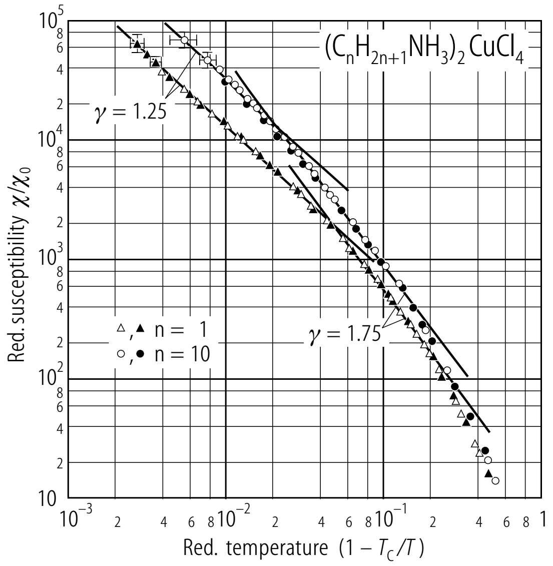

Fig. 4.27. $(C_nH_{2n+1}NH_3)_2CuCl_4$ (n = 1, 10). Lattice dimensionality crossover in the critical behaviour of the susceptibility, presented as log-log plot χ/χ_0 versus $(1 - T_C/T)$ ($\chi_0 = C/T$ (Eq. 4.8)). The open and closed experimental points refer to two independent measurements. The values of γ are close to those of the 3D and 2D Ising model (taken from [76J1, 78J]).

For Fig. 4.26 see next page.

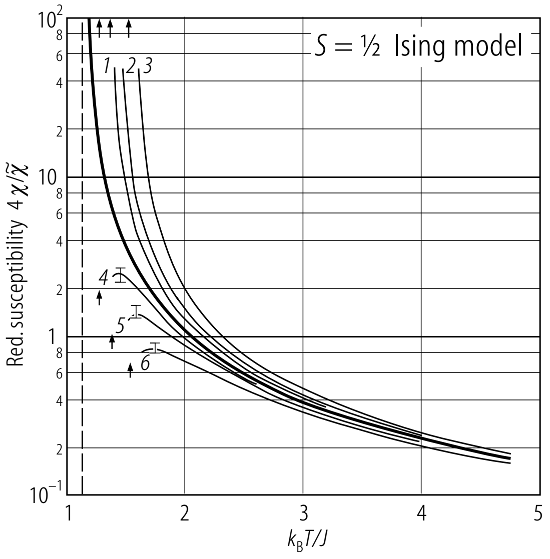

Fig. 4.28. $S = 1/2$ Ising model, theoretical calculation ($J > 0$, $J' > 0$ and/or $J' < 0$) of the 2D ↔ 3D crossover in the susceptibility, plotted as reduced susceptibility $4\chi/\tilde{\chi}$ versus k_BT/J. The heavy curve and the dashed vertical line represent $4\chi/\tilde{\chi}$ and k_BT_C/J, resp., for the 2D Ising model. The light curves and the corresponding arrows show $4\chi/\tilde{\chi}$ and k_BT_C/J for $J'/J = +0.05$, $= +0.1$, $= +0.2$ (curves 1–3), and $J'/J = -0.05$, $= -0.1$, $= -0.2$ (curves 4–6), taken from [78N2].

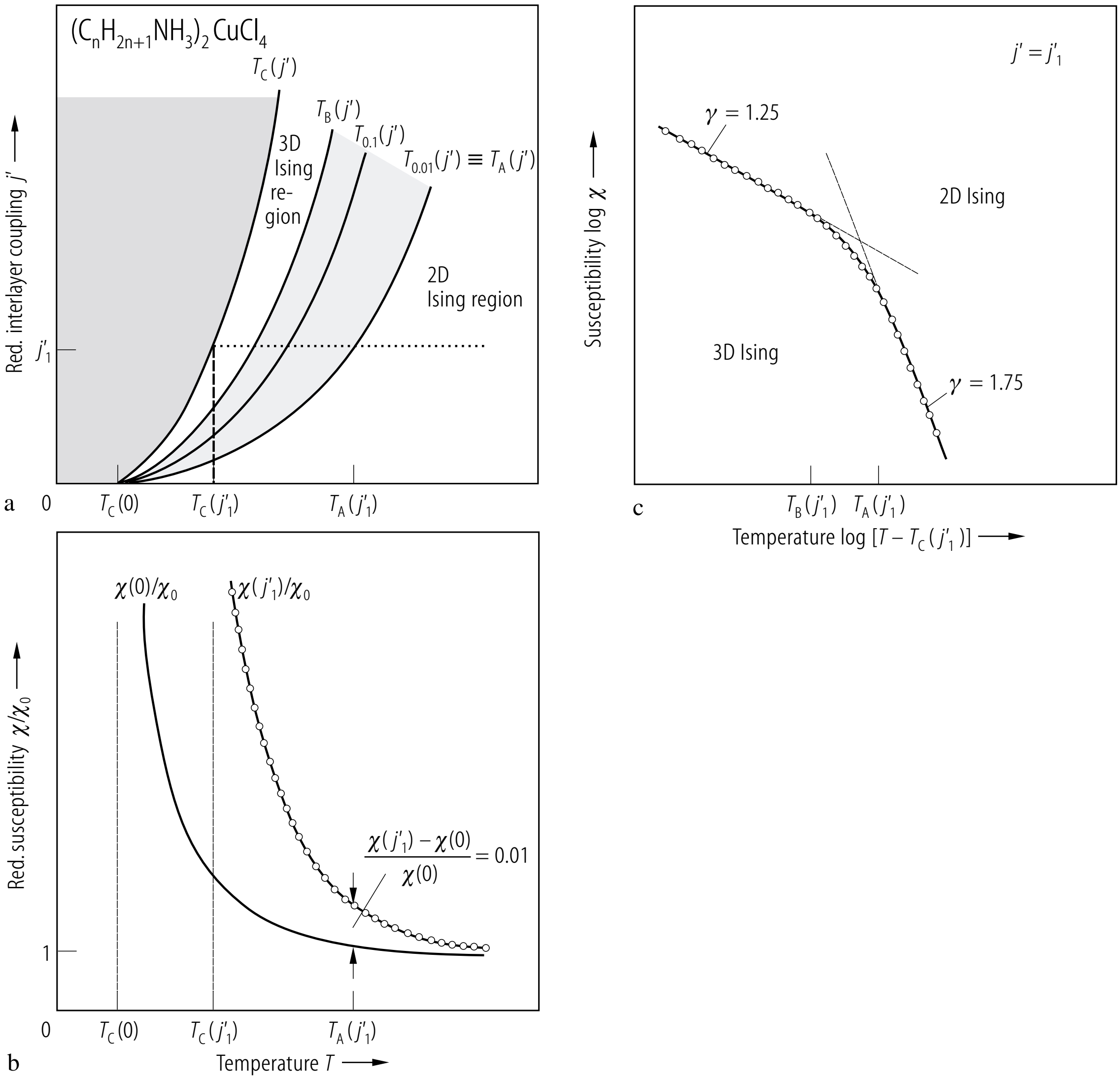

Fig. 4.26. (C$_n$H$_{2n+1}$NH$_3$)$_2$CuCl$_4$. **(a)** Analysis and illustration of the crossover from the 2D to the 3D Ising model ($T_C(j')$ is the critical temperature and the slightly shaded area the ×-over region), **(b)** ×-over phenomena in the susceptibility, (χ/χ_0 with $\chi_0 = C/T$ (Eq. 4.8)), and **(c)** critical exponent γ in the 3D, ×-over and 2D regions (taken from [72L1, 73L4]). Further details see text.

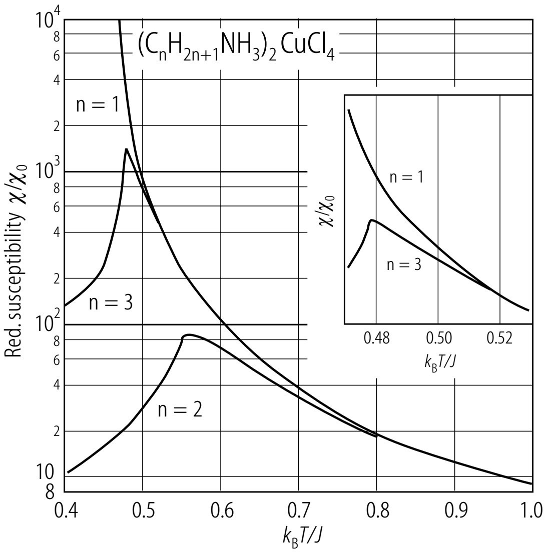

Fig. 4.29. $(C_nH_{2n+1}NH_3)_2CuCl_4$ (n = 1, 2, 3). Magnetic susceptibility, presented as χ/χ_0 versus k_BT/J. The susceptibility for the compounds with n = 2, 3 deviate from that for n = 1 to lower values because of $J' < 0$, i.e. antiferromagnetic interlayer coupling (taken from [76J1, 78J]).

For Fig. 4.31 see next page.

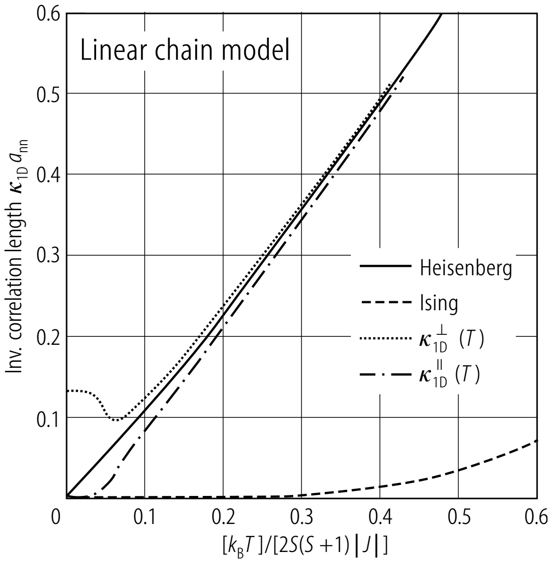

Fig. 4.32. Linear chain model, one-dimensional inverse correlation length $\kappa_{1D}a_{nn}$ versus $[k_BT]/[2S(S+1)|J|]$ for the 1D Heisenberg model, the 1D Ising model and a 1D Heisenberg antiferromagnet with uniaxial anisotropy ($H_A/H_E = 0.0073$) where $\kappa_{1D}^{\parallel}$ and $\kappa_{1D}^{\perp}$ are the inverse correlation lengths parallel and perpendicular to the anisotropy axis (taken from [80B1]).

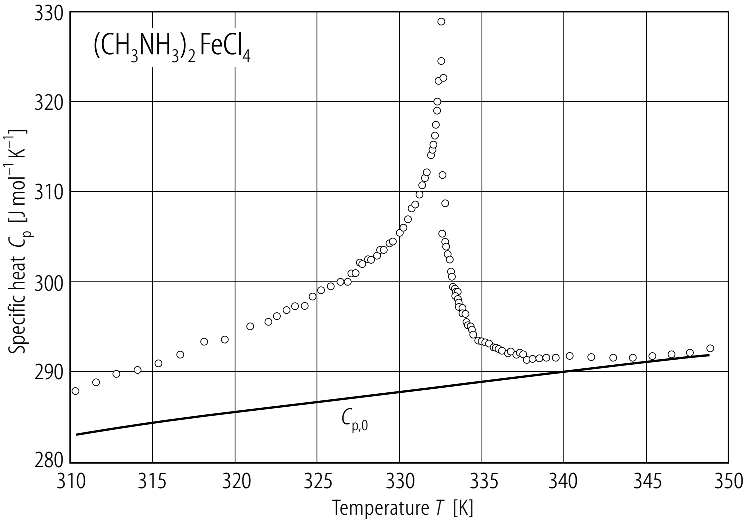

Fig. 4.30. $(CH_3NH_3)_2FeCl_4$. λ-type anomaly of the specific heat C_p near T_{C1}, the transition point between THT-phase and ORT-phase (experimental points). The full curve shows the noncritical background $C_{p,0}$ of C_p due to lattice vibrations (taken from [82G1]).

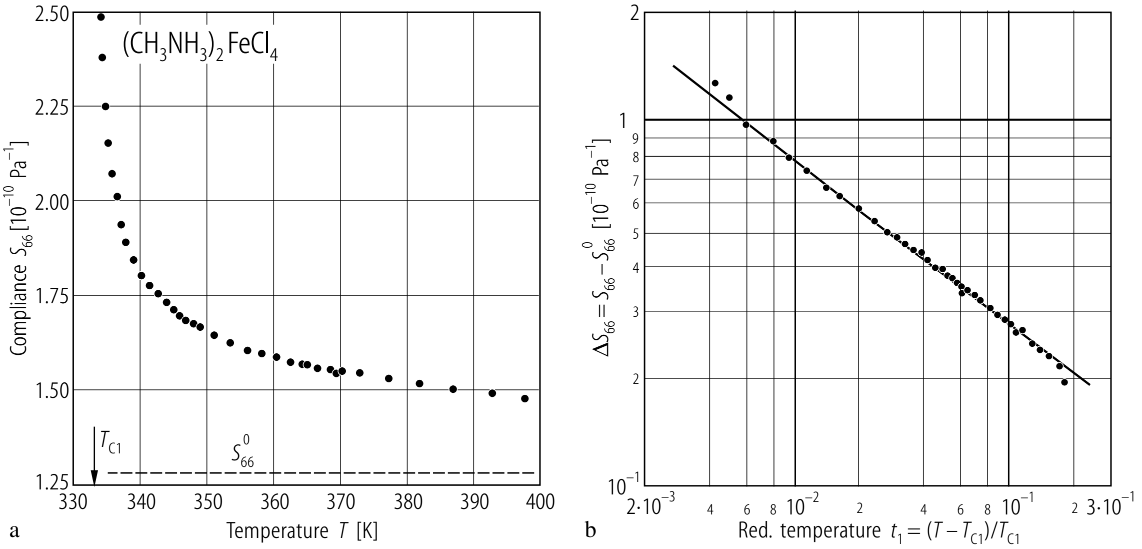

Fig. 4.31. $(CH_3NH_3)_2FeCl_4$. **(a)** Critical divergence of the elastic compliance S_{66} in the THT-phase above the critical temperature T_{C1}; and **(b)** a log-log plot of the anomalous part $\Delta S_{66} = S_{66} - S_{66}^0$ versus reduced temperature $t_1 = (T - T_{C1})/T_{C1}$ where S_{66}^0 is the part of the compliance not coupling to the phase transition (cf. Eqs. 4.78 and 4.86). The straight line represents the fit to Eq. 4.86 for the determination of the exponent ρ (taken from [82G1]).

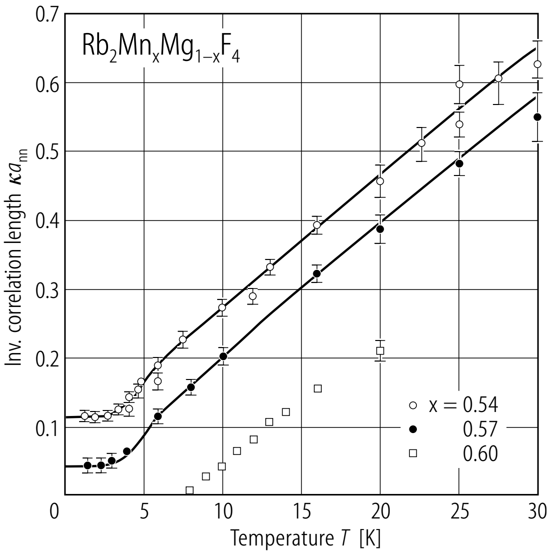

Fig. 4.33. $Rb_2Mn_xMg_{1-x}F_4$ with x = 0.54, 0.57, 0.60. Inverse correlation length κa_{nn} versus temperature, experimental points from neutron scattering data and, for x = 0.54 and 0.57, solid lines that result from a fit to Eq. 4.110a derived within the percolation multicritical theory (taken from [80B1]).

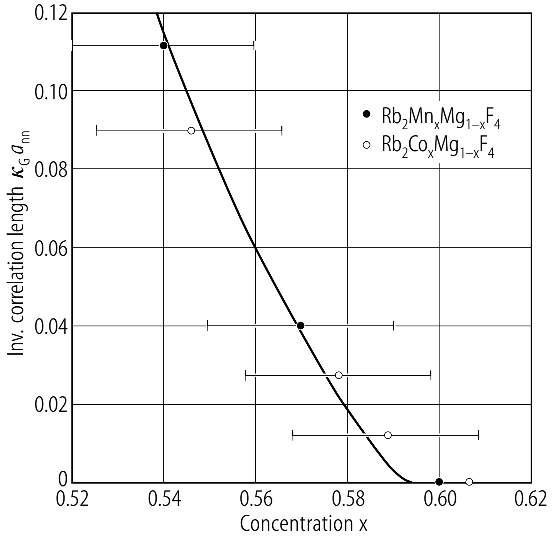

Fig. 4.34. $Rb_2Mn_xMg_{1-x}F_4$, $Rb_2Co_xMg_{1-x}F_4$. Inverse geometrical correlation length κ_G, i.e. the experimentally observed κ for $T \to 0$, versus concentration x. The curve represents a fit to Eq. 4.107 (see also Eqs. 4.110a and 4.110b). The error bars mark the uncertainties from the chemical analysis, taken from [80B1, 80C1] where further information about uncertainties in the concentrations is also found.

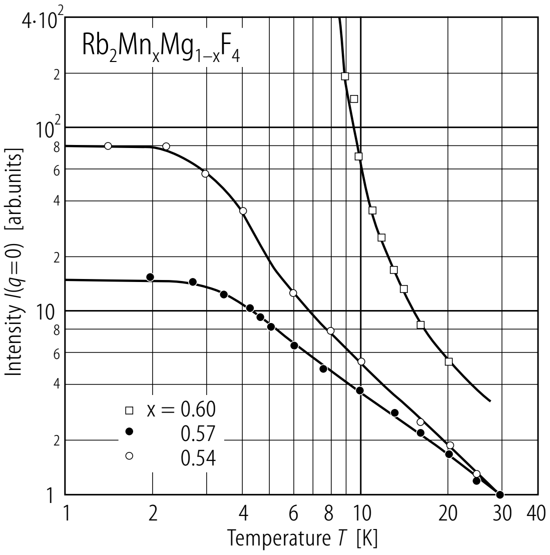

Fig. 4.35. $Rb_2Mn_xMg_{1-x}F_4$ with x = 0.54, 0.57, 0.60. Neutron scattering peak intensity $I(q = 0)$ on top of the 2D magnetic ridge versus temperature. The solid lines represent a fit to Eq. 4.111, i.e. $I(q = 0) \sim \kappa^{-(2-\eta)}$, with the experimentally measured values of κ (taken from [80B1]).

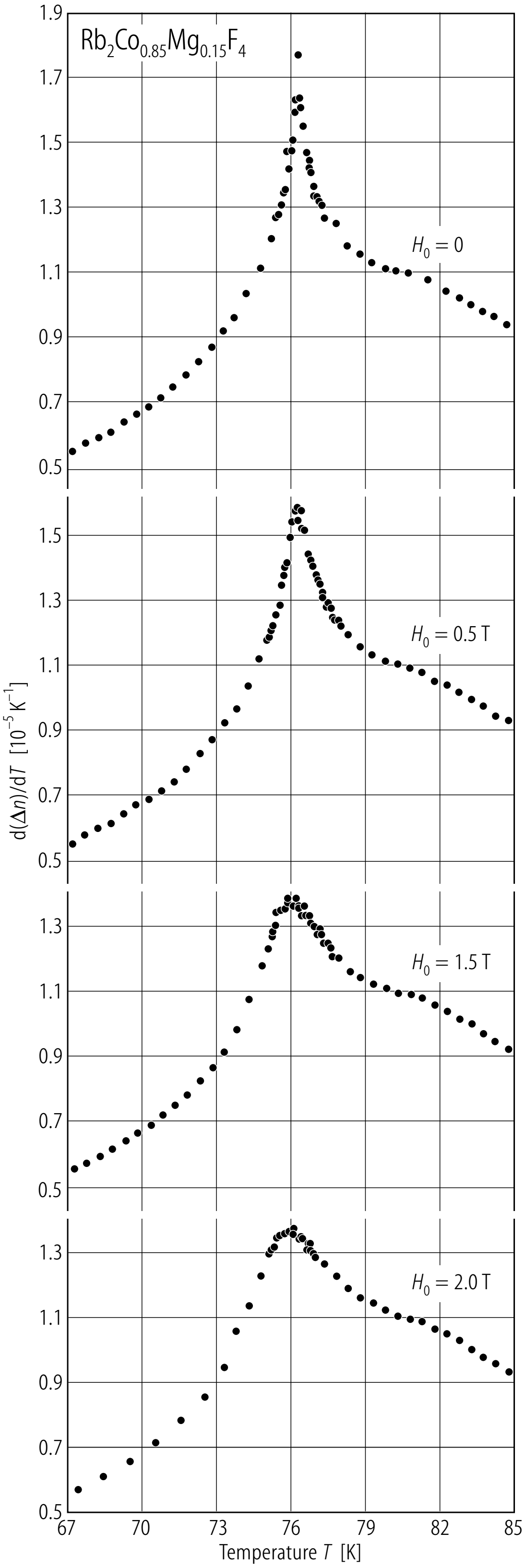

→

Fig. 4.36. $Rb_2Co_{0.85}Mg_{0.15}F_4$. LMB data $d(\Delta n)/dT$ versus temperature in external magnetic fields H_0 as indicated, applied parallel to the c-axis. The points represent the differences between successive data points Δn, divided by the temperature interval ΔT, plotted at the average temperature (after [83F3]).

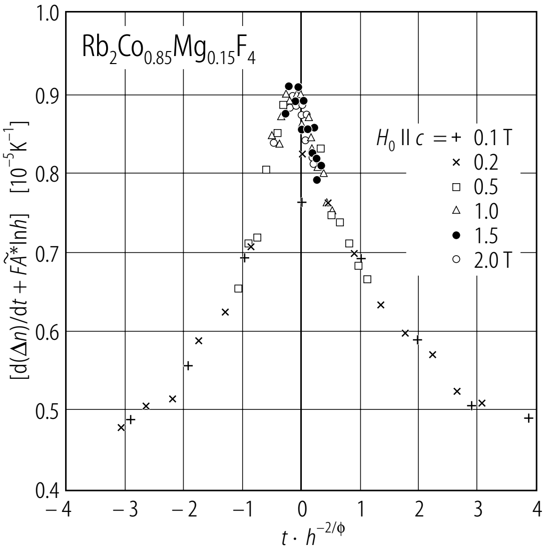

Fig. 4.37. $Rb_2Co_{0.85}Mg_{0.15}F_4$. Scaling plot $[d(\Delta n)/dT + F\tilde{A}^* \ln h]$ versus $t \cdot h^{-2/\phi}$ in applied fields ($0.1\ T \le H_0 \le 2.0\ T$) and for reduced temperatures ($10^{-3} \le |t| \le 10^{-2}$). The data collapse for all H_0 on a single curve, the scaling function $\tilde{g}(x)$ in Eq. 4.117b. For further details, see text (after [83F3]).

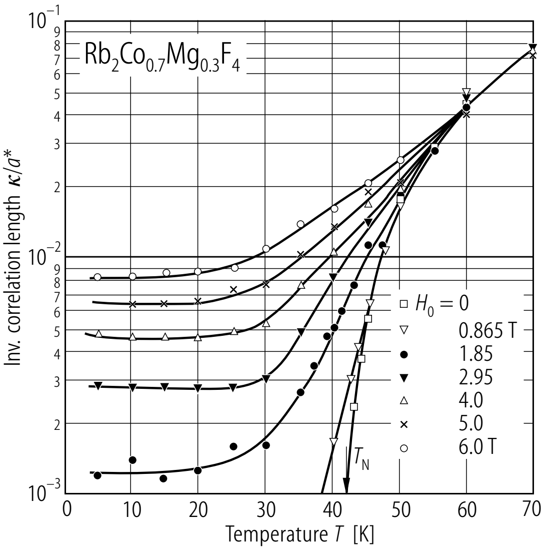

Fig. 4.38. $Rb_2Co_{0.7}Mg_{0.3}F_4$. Resolution-corrected inverse correlation length κ/a^* versus temperature T for $H_0 = 0$ (open squares) and at various fields H_0 ($\boldsymbol{H_0} \parallel \boldsymbol{c}$), determined from neutron scattering data in field-cooling (FC) experiments. The solid lines are guide to the eye (taken from [83B4]).

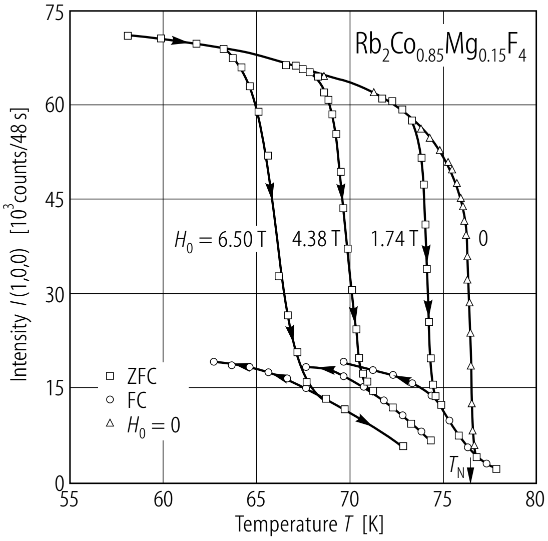

Fig. 4.39. $Rb_2Co_{0.85}Mg_{0.15}F_4$. Peak intensity $I(1, 0, 0)$ of the antiferromagnetic (1, 0, 0) Bragg reflection versus T at $H_0 = 0$, for zero-field cooling (ZFC) and for field cooling (FC) at $H_0 = 1.74$, 4.38 and 6.50 T. The arrows indicate the direction in which the data were taken (taken from [85B3, 85B4]).

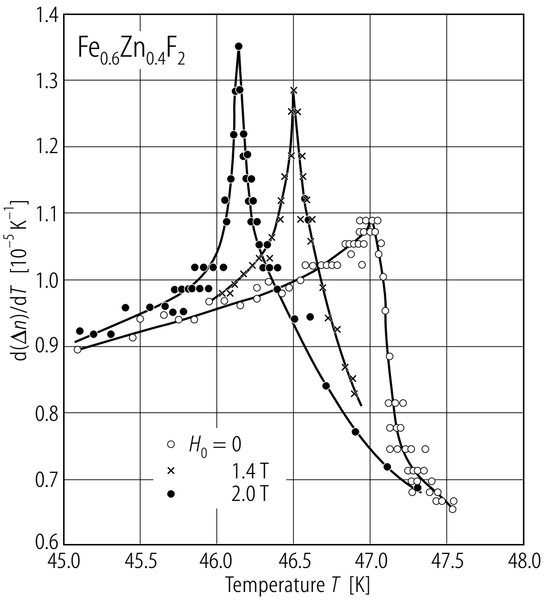

Fig. 4.40. Fe$_{0.6}$Zn$_{0.4}$F$_2$. LMB data d(Δn)/dT versus temperature in external magnetic fields H_0 as indicated, applied parallel to the c-axis. The points represent the differences between successive data points Δn, divided by the temperature interval ΔT, plotted at the average temperature. The horizontal groups of points in the data result from the finite resolution in Δn (≈10^{-8}), taken from [83B5].

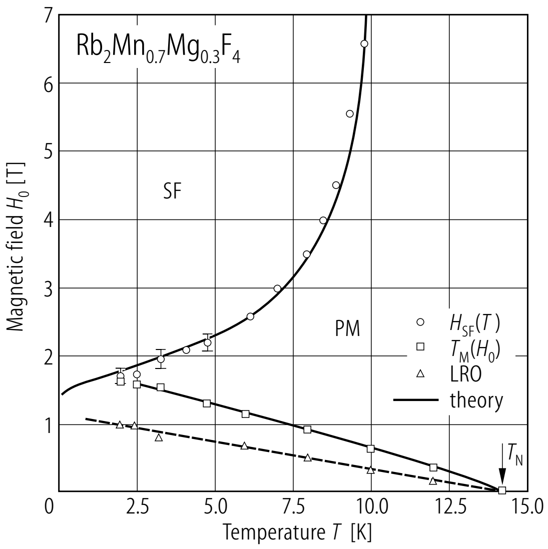

Fig. 4.41. Rb$_2$Mn$_{0.7}$Mg$_{0.3}$F$_4$. Magnetic (H_0, T) phase diagram with the boundary $H_{SF}(T)$ between spin-flop (SF) and paramagnetic (PM) phase and the metastability boundary $T_M(H_0)$, experimental points determined by neutron diffraction and calculated curves. Further is shown the line of reduction of LRO for increasing H_0 with the broken line as guide to the eye. For further explanations, especially with respect to the theoretical curves, see text (after [91B2, 93C2]).

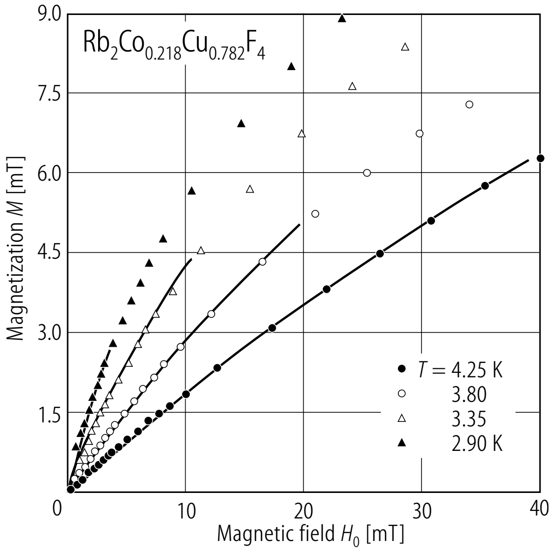

Fig. 4.42. Rb$_2$Co$_{0.218}$Cu$_{0.782}$F$_4$. Magnetization M versus magnetic field H_0, applied parallel to the c-axis, at various temperatures T, corrected for demagnetization effects. The solid lines represent fits to Eq. 4.124 (taken from [88D8]). For further details see text.

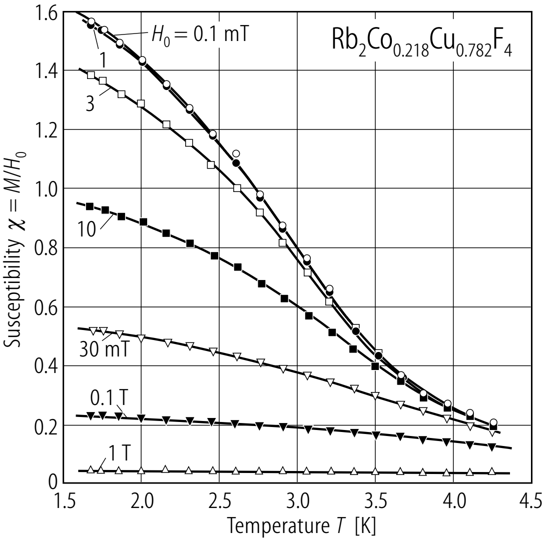

Fig. 4.43. Rb$_2$Co$_{0.218}$Cu$_{0.782}$F$_4$. Static susceptibility $\chi = M/H_0$ versus temperature T for various external fields H_0, applied parallel to the c-axis and ranging from 0.1 mT to 1 T. The data were corrected for demagnetization effects. Solid lines are guides to the eye (after [88D10]).

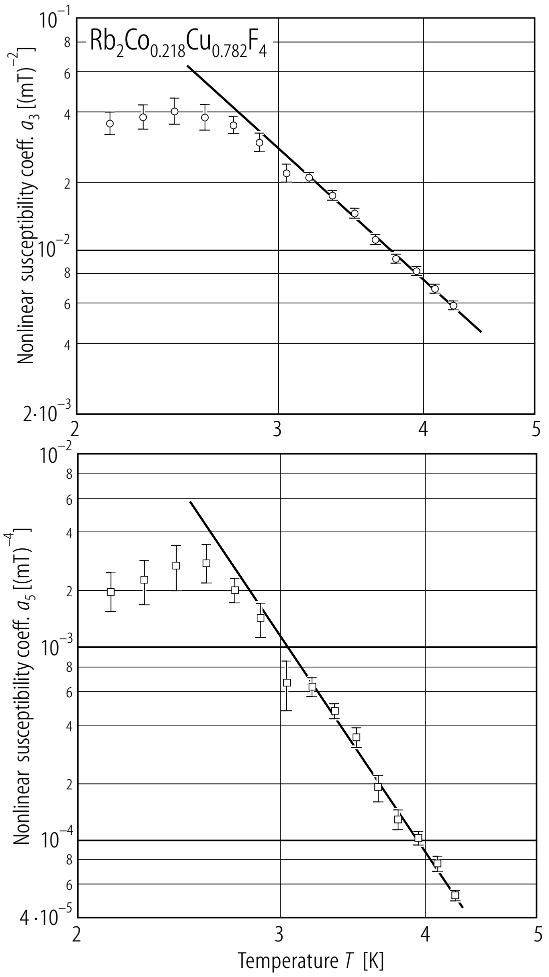

Fig. 4.44. Rb$_2$Co$_{0.218}$Cu$_{0.782}$F$_4$. log-log plot of the nonlinear susceptibility coefficients a_3 and a_5 versus temperature T, in the upper and lower part, respectively. The solid lines represent power law divergences towards $T_C = 0$ according to Eq. 4.125 (taken from [88D10]).

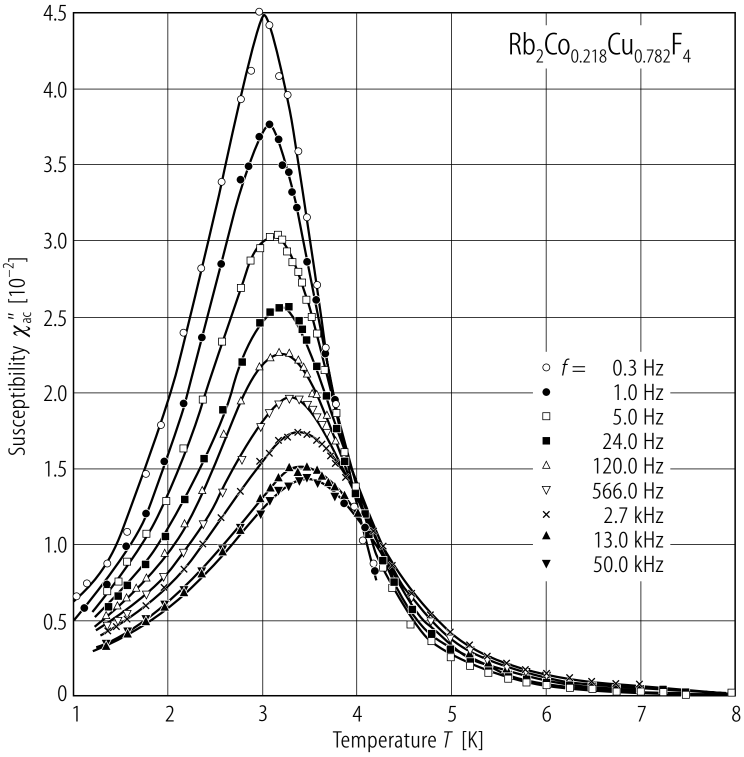

Fig. 4.45. $Rb_2Co_{0.218}Cu_{0.782}F_4$. Temperature dependence of the imaginary part χ''_{ac} of the linear ac susceptibility χ_{ac}, taken at various frequencies $f = \omega/2\pi$ ranging from 0.3 Hz to 50 kHz (after [88D11, 89D3]). Solid lines are guide to the eye.

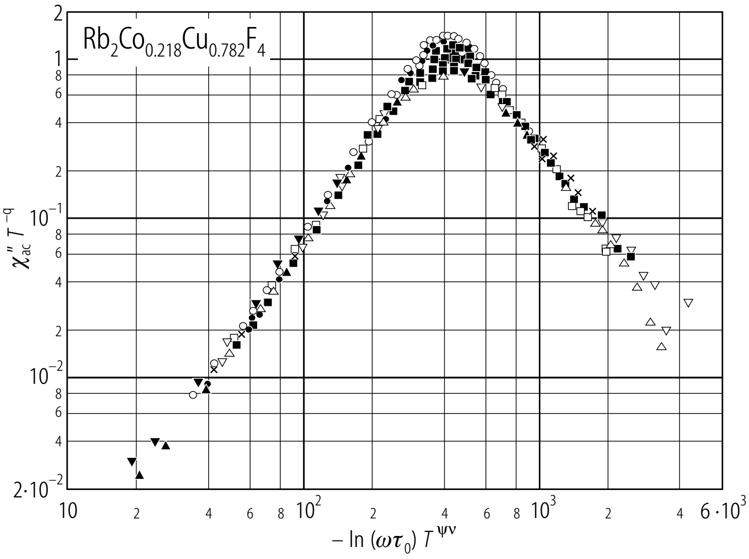

Fig. 4.46. $Rb_2Co_{0.218}Cu_{0.782}F_4$. Activated dynamic scaling plot $\chi''_{ac}(\omega, T) \cdot T^{-q}$ vs. $-\ln(\omega\tau_0) \cdot T^{\psi\nu}$ for temperatures from 1 to 7 K and frequencies from 0.3 Hz to 50 kHz. Symbols correspond to the frequencies in Fig. 4.45 (after [88D8, 88D9, 89D3]).

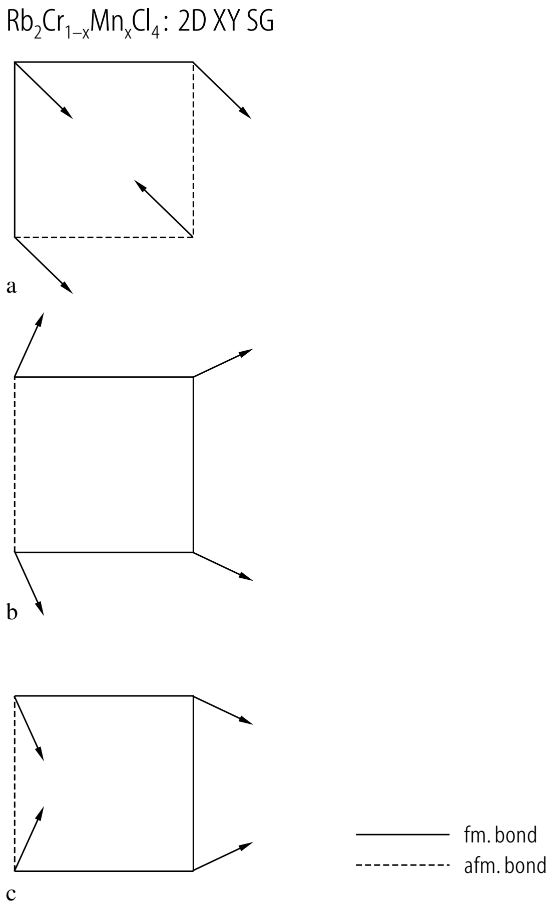

Fig. 4.47. $Rb_2Cr_{1-x}Mn_xCl_4$, a 2D XY spin glass at intermediate concentrations x. Classical ground state configuration of a set of four spins with ferromagnetic (solid lines) and antiferromagnetic (broken lines) exchange interactions. **(a)** nonfrustrated plaquette; **(b)** frustrated plaquette with chirality $\kappa = +1$; **(c)** frustrated plaquette with $\kappa = -1$ (after [77V2, 88K8]).

For Fig. 4.48 see next page.

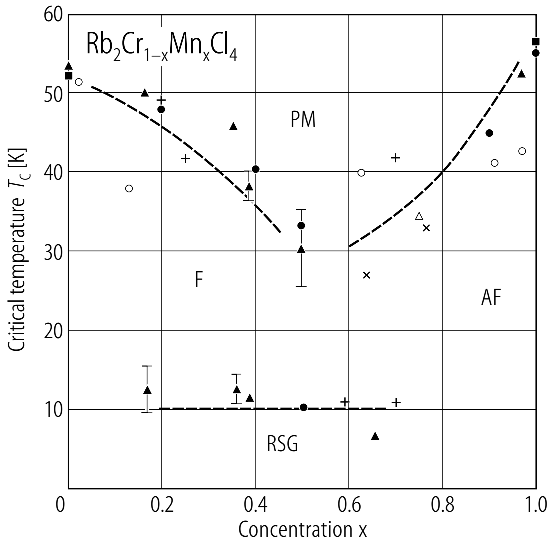

Fig. 4.49. $Rb_2Cr_{1-x}Mn_xCl_4$. (T_C, x) phase diagram mostly derived from neutron scattering studies: [84M1] (open circles), [86N3] (crosses), [88H4] (open triangles), [88K8] (full circles), [88S7, 88T2, 89S1, 92S7] (plusses), but also from susceptibility measurements: [88K8] (full triangles). Broken lines indicate the approximate boundaries between the paramagnetic phase (PM) and the ranges with ferromagnetic (F) or antiferromagnetic (AF) ordering. Below 10 K, the system behaves as a reentrant spin glass (RSG), after [88K8]. For x = 0 and x = 1, also the critical temperatures of pure Rb_2CrCl_4 and Rb_2MnCl_4 (full squares), resp., are indicated.

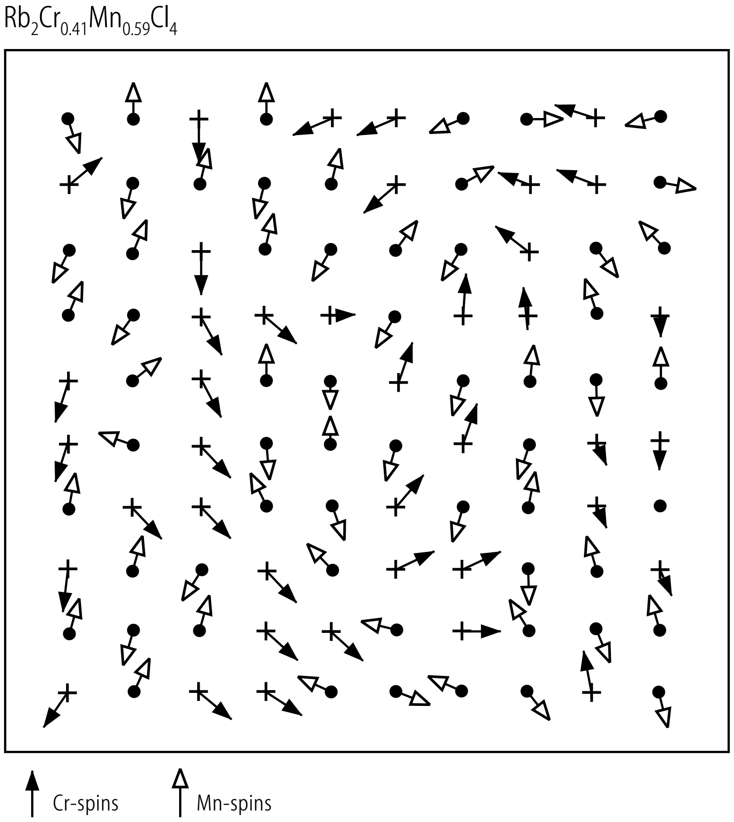

Fig. 4.48. $Rb_2Cr_{0.41}Mn_{0.59}Cl_4$. Ground state of an array of 10 × 10 spins which are part of a greater array of 40 × 40 spins. The ground state was calculated by Ching and Huber [88C6] for this sample with spin-glass behaviour as described in their paper. Crosses denote the Cr- and solid circles the Mn-positions (taken from [88S9]). For further explanations see text.

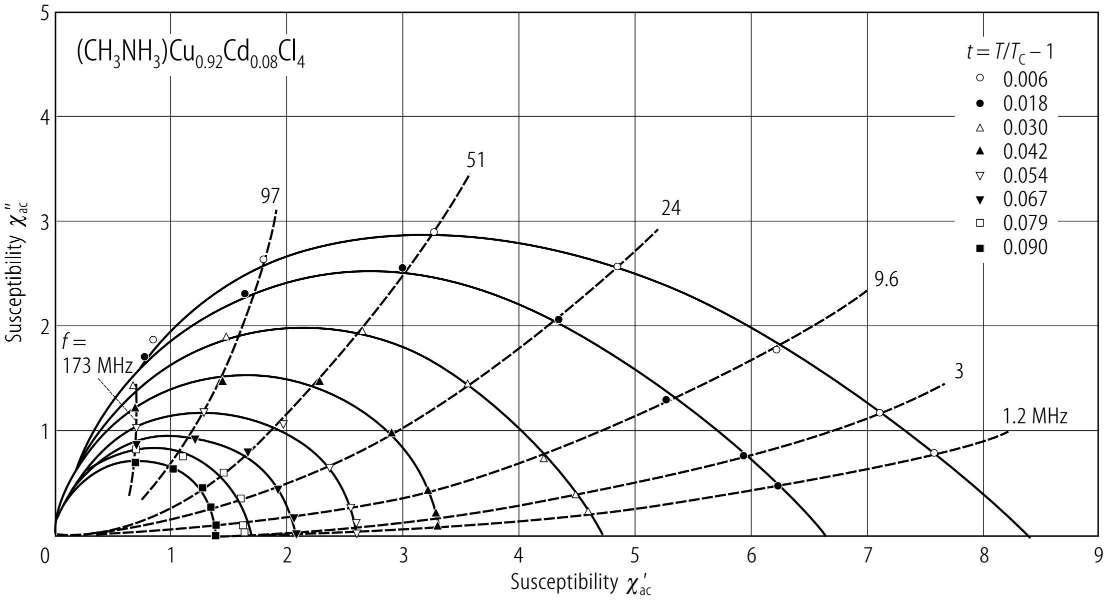

Fig. 4.50. $(CH_3NH_3)_2Cu_{0.92}Cd_{0.08}Cl_4$. Cole-Cole plot $\chi''_{ac}(\omega, T)$ versus $\chi'_{ac}(\omega, T)$ (cf. Eq. 4.143) for various reduced temperatures $t = T/T_C - 1$ ranging from 0.006 to 0.090. The data points correspond to frequencies between 1.2 MHz and 173 MHz (taken from [80O1]). For the interpretation of the data see text.

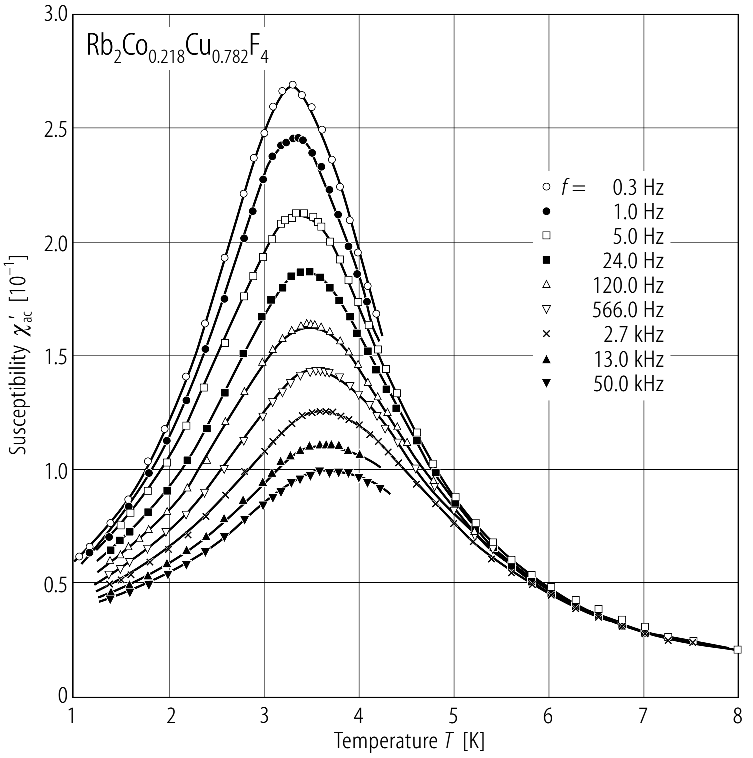

Fig. 4.51. $Rb_2Co_{0.218}Cu_{0.782}F_4$. Temperature dependence of the real part χ'_{ac} of the linear ac susceptibility χ_{ac}, taken at various frequencies $f = \omega/2\pi$ ranging from 0.3 Hz to 50 kHz (after [88D11, 89D3]). Solid lines are guide to the eye.

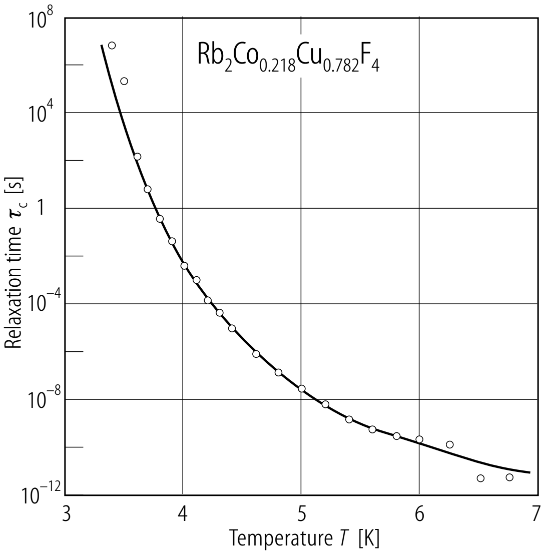

Fig. 4.52. $Rb_2Co_{0.218}Cu_{0.782}F_4$. Mean relaxation time τ_c versus temperature T, derived from the analysis of the experimental data by means of Eqs. 4.144a, 4.144b and 4.145 (Cole-Cole analysis). The solid line results from a fit of the data to Eq. 4.147 (taken from [88D11, 89D3]).

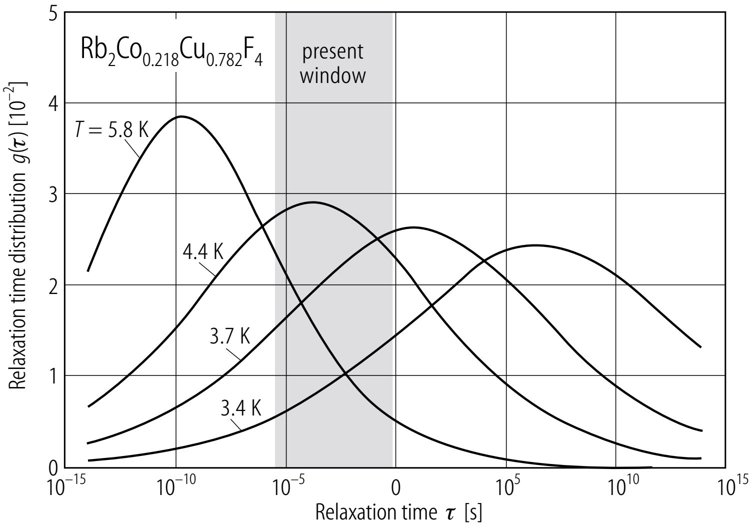

Fig. 4.53. $Rb_2Co_{0.218}Cu_{0.782}F_4$. Distribution of relaxation times $g(\tau)$ versus $_{10}\log(\tau)$ with τ in s, according to Eq. 4.148, for some selected temperatures. Note that $g(\tau)$ is symmetric about τ_c on this logarithmic scale (after [88D11, 89D3]).

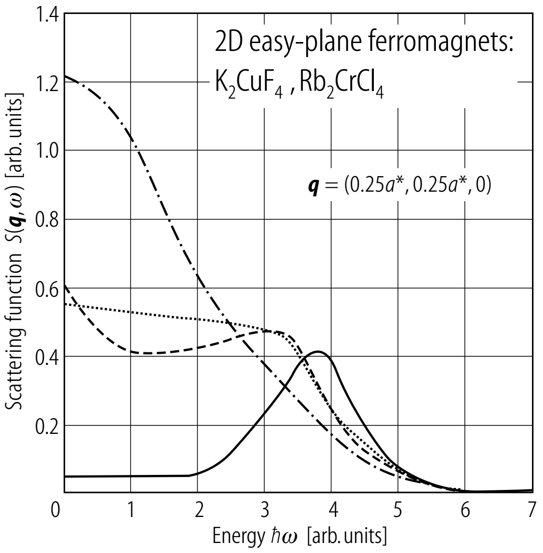

Fig. 4.54. K_2CuF_4, Rb_2CrCl_4 (2D easy-plane ferromagnets). Simulation of the scattering function $S(\boldsymbol{q}, \omega)$ for the 2D XY-model by a Monte-Carlo molecular dynamiques technique for $\boldsymbol{q} = (0.25a^*, 0.25a^*, 0)$ and for reduced temperatures $\tilde{T} = (k_BT)/(2S^2J) = 0.50$ (full line), 0.80 (broken line), 0.82 (dotted line) and 0.90 (dash-dot line), $S(\boldsymbol{q}, \omega)$ and $\hbar\omega$ in arbitrary units (taken from [86K3]).

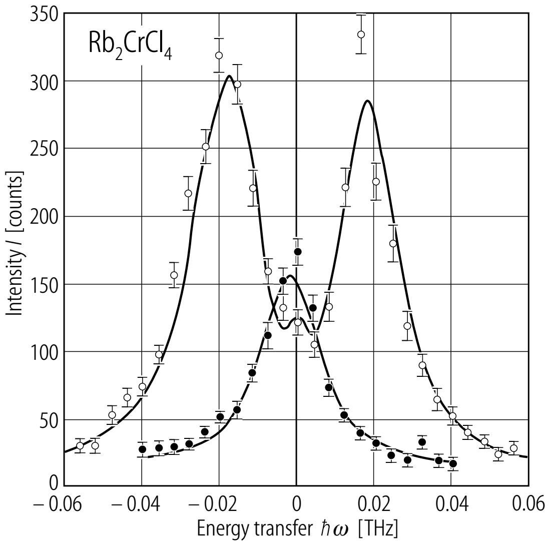

Fig. 4.55. Rb_2CrCl_4. Neutron inelastic scattering with polarization analysis, SF = spin-flip (open circles) and NSF = non-spin-flip (full circles) scattering observed at $\boldsymbol{Q} \mathrel{\hat{=}} (0, 0, 0.29)$ with $H_0 = 0.2$ T, taken from [88B2]. Typical counting times are 21 min per point. The solid lines are optimum fits of contributions described in [88B2].

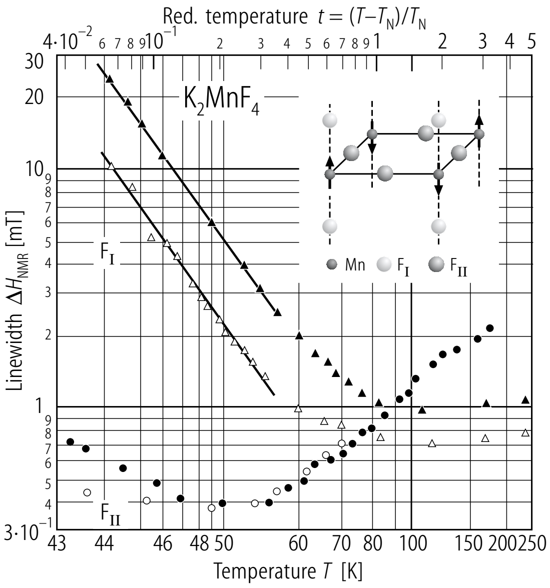

Fig. 4.56. K_2MnF_4. Critical behaviour of the NMR linewidth ΔH_{NMR} for $^{19}F_I$ and $^{19}F_{II}$ resonances with $\boldsymbol{H_0} \parallel \boldsymbol{c}$ (full triangles, full circles) and $\boldsymbol{H_0} \perp \boldsymbol{c}$ (open triangles, open circles). The solid lines represent a fit to Eq. 4.160 for describing the critical broadening of the $^{19}F_I$-NMR (after [90B1]). The experimental data are taken from [74B4]. Note that the t-scale is a logarithmic one and therefore the scale of $T = T_N(1 + t)$ a complicated nonlinear one.

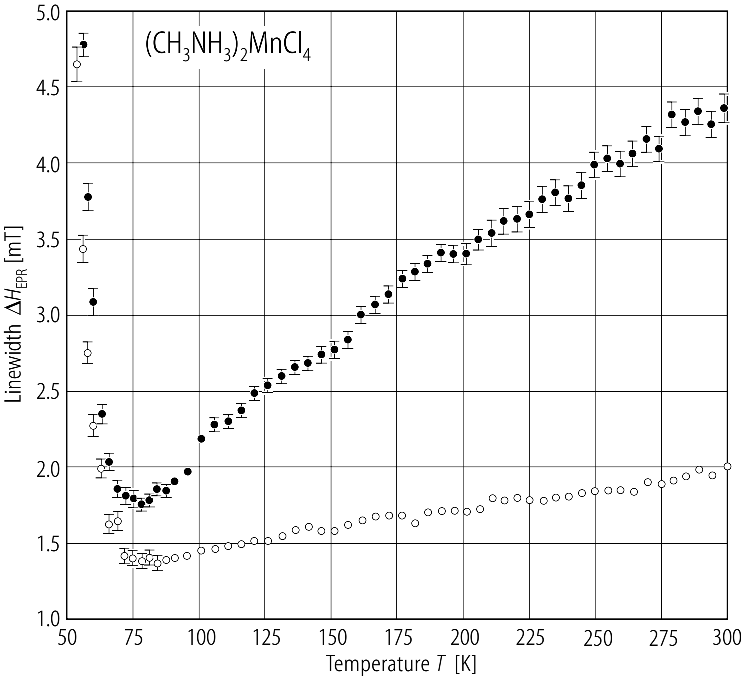

Fig. 4.57. $(CH_3NH_3)_2MnCl_4$. EPR linewidth ΔH_{EPR} versus temperature for $\psi = 0°$ (full circles) and $\psi = 55°$ (open circles) with the critical broadening towards $T_N = 45.3$ K and a linear increase towards room temperature (taken from [72B6, 75B6]).

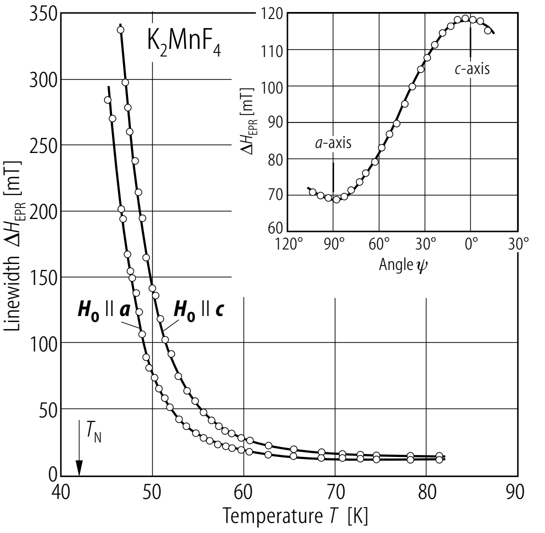

Fig. 4.58. K$_2$MnF$_4$. Temperature dependence of the EPR linewidth ΔH_{EPR} at $\nu = 24$ GHz for $H_0 \parallel a$ and $H_0 \parallel c$ with the critical broadening towards T_N. The insert shows $\Delta H_{EPR}(\psi)$ at 50.6 K with a $(3\cos^2\psi - 1)$ dependence (after [72W2]).

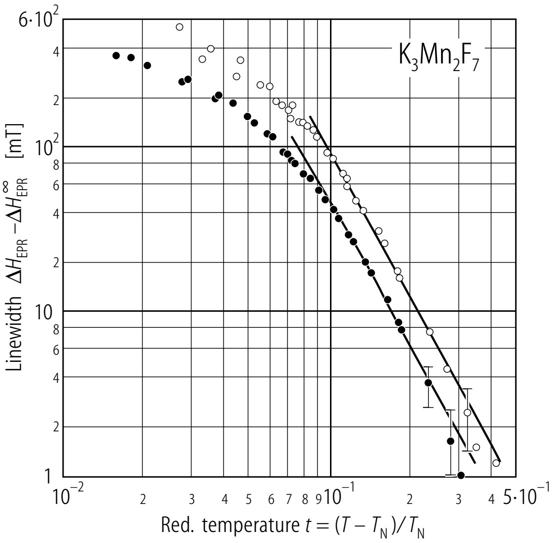

Fig. 4.59. K$_3$Mn$_2$F$_7$. log-log plot of $\Delta H_{EPR} - \Delta H_{EPR}^{\infty}$ ($\nu \approx 25$ GHz) versus reduced temperature t for $H_0 \parallel c$ (open circles) and $H_0 \perp c$ (full circles). Straight lines represent fits to the power law Eq. 4.165. For further explanations see text (taken from [81U]).

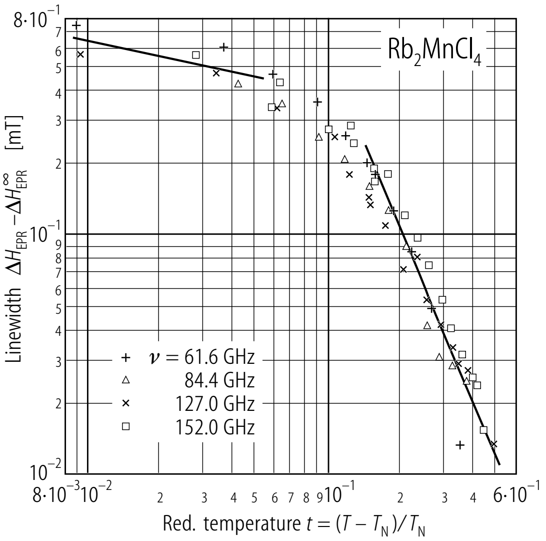

Fig. 4.60. Rb$_2$MnCl$_4$. log-log plot of $\Delta H_{EPR} - \Delta H_{EPR}^{\infty}$ versus reduced temperature t for $H_0 \parallel c$. The data were taken at various frequencies ν from 61.6 to 152 GHz. Straight lines are fits to the power law Eq. 4.165 (after [88G3, 90G4]).

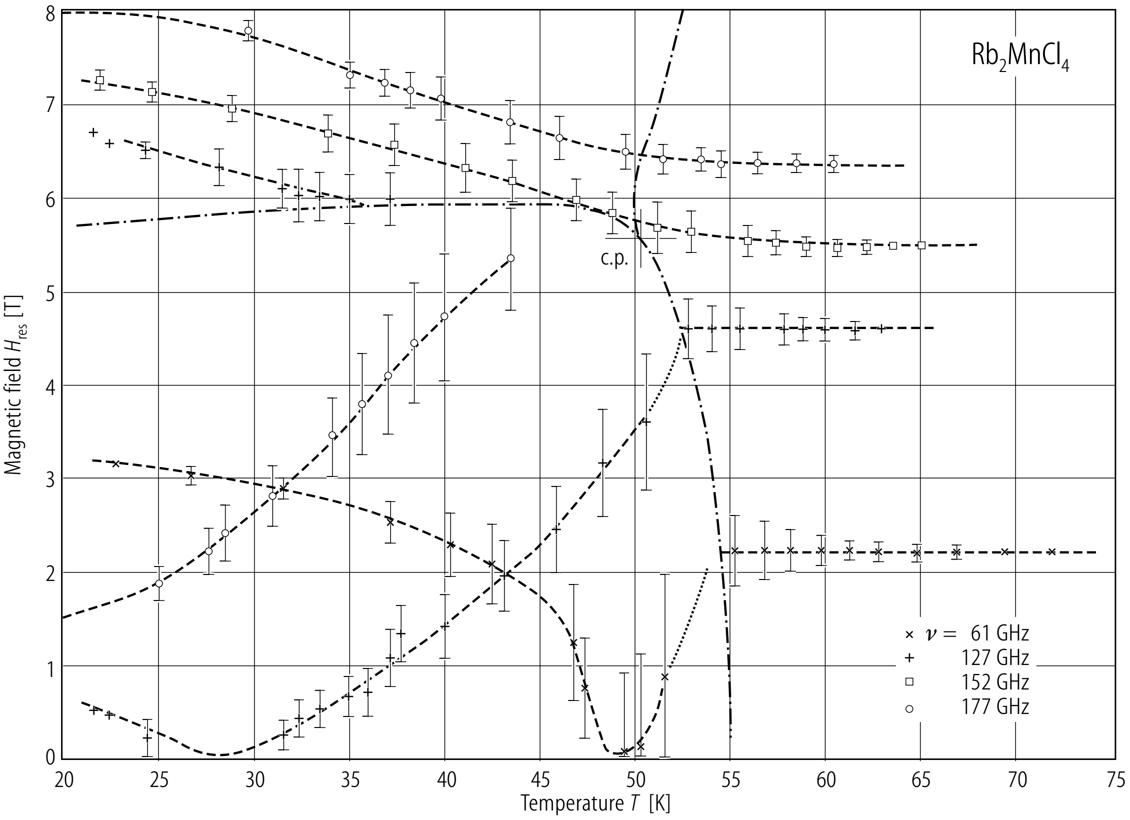

Fig. 4.61. Rb$_2$MnCl$_4$. Magnetic resonance at some frequencies from 61 to 177 GHz in the antiferromagnetic, the spin-flop and the paramagnetic regime. The data are presented as magnetic field at resonance H_{res} versus temperature T. The bars denote the resonance linewidth and not errors. Dash-dot lines mark the phase boundaries and CP the critical point (after [88G3, 90G4]).

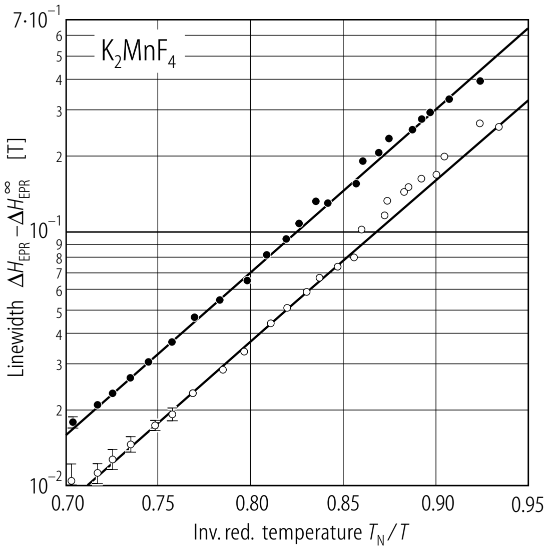

Fig. 4.62. K$_2$MnF$_4$. Analysis of ΔH_{EPR} with respect to soliton contributions (cf. Eq. 4.170), presented as $_{10}\log(\Delta H_{EPR} - \Delta H^{\infty}_{EPR})$ versus T_N/T (T_N = 42.1 K) for $\boldsymbol{H_0} \parallel \boldsymbol{c}$ (full circles) and $\boldsymbol{H_0} \perp \boldsymbol{c}$ (open circles). The slope of the straight line corresponds to E_s/k_BT_N (after [83W4]). The experimental data are taken from [72W2].

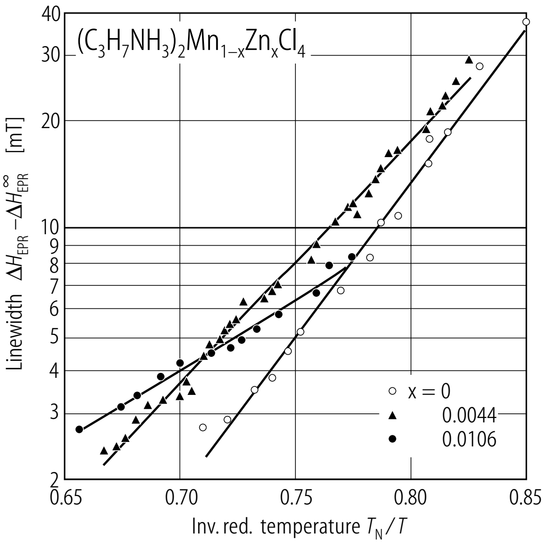

Fig. 4.63. $(C_3H_7NH_3)_2Mn_{1-x}Zn_xCl_4$ with x = 0, 0.0044, 0.0106. Straight-line fits to the experimental data $_{10}\log(\Delta H_{EPR} - \Delta H^{\infty}_{EPR})$ versus T_N/T for determining the soliton excitation energy E_s (cf. Eqs. 4.170), taken from [96S1].

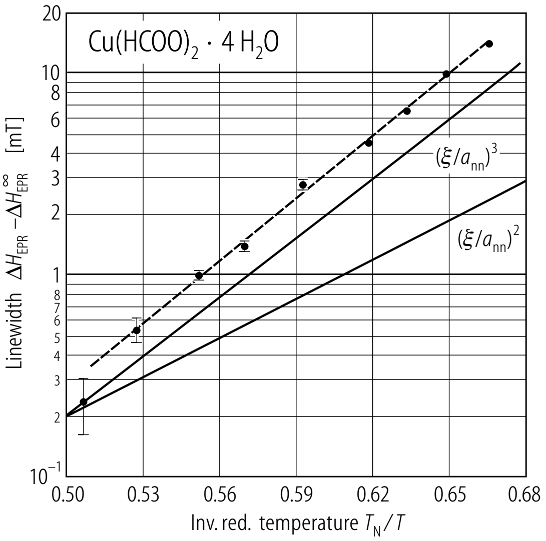

Fig. 4.64. $Cu(HCOO)_2 \cdot 4H_2O$. $_{10}\log(\Delta H_{EPR} - \Delta H^{\infty}_{EPR})$ versus T_N/T, experimental data for $\boldsymbol{H_0} \parallel \boldsymbol{b}$ (full circles) and theoretical calculations [95Z1, 96Z1] according to Eq. 4.172, soliton contribution $\Delta H_{EPR} \sim (\xi/a_{nn})^2$, and to Eq. 4.173, spin-wave contribution $\Delta H_{EPR} \sim (\xi/a_{nn})^3$. The calculated data were arbitrarily normalized to 0.2 mT at $T_N/T = 0.50$ (taken from [93C3]).

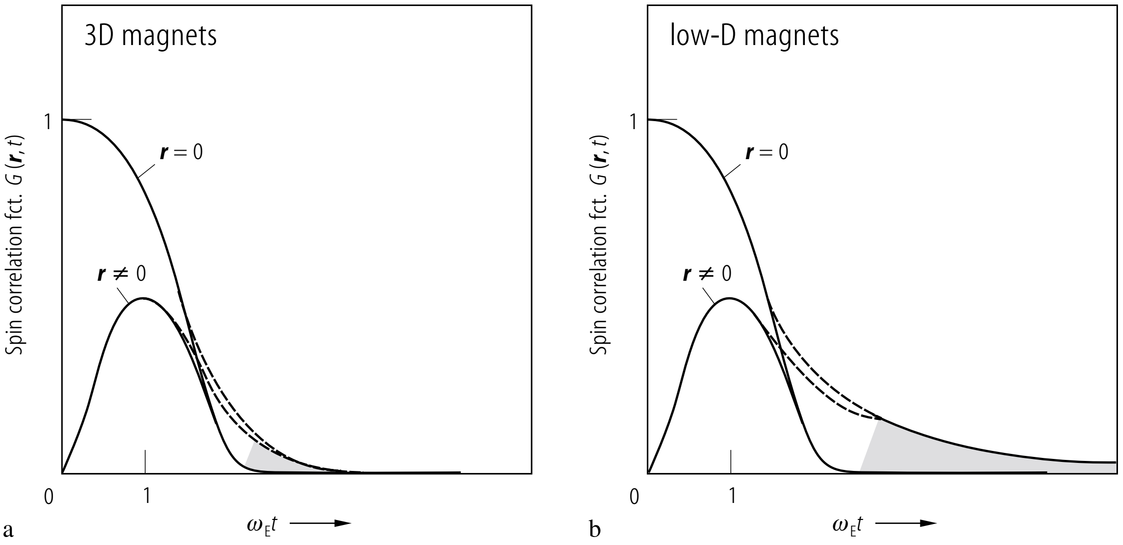

Fig. 4.65. **(a)** 3D magnets and **(b)** low-D magnets, two-spin correlation function $G(\boldsymbol{r}, t)$ versus $\omega_E t$, time t and exchange frequency ω_E (Eq. 4.178a), for $\boldsymbol{r} = 0$ and $\boldsymbol{r} \neq 0$. The shaded parts correspond to the long-time part with diffusive behaviour (taken from [90B1]).

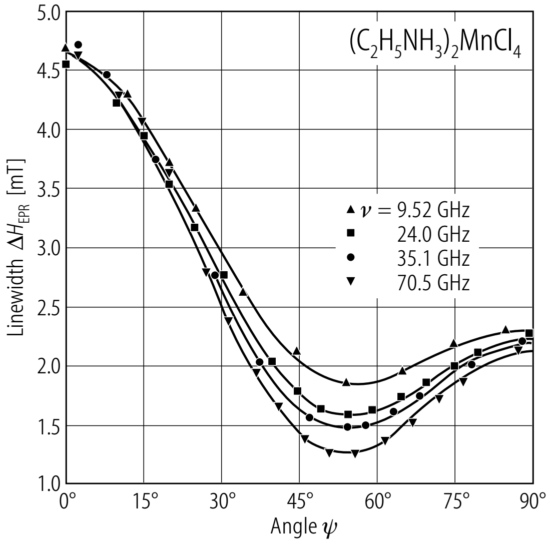

Fig. 4.66. $(C_2H_5NH_3)_2MnCl_4$. EPR linewidth ΔH_{EPR} versus polar angle ψ between H_0 and the c-axis for different frequencies. The solid curves represent theoretical calculations with a dominating $(3\cos^2\psi - 1)^2$ dependence (after [79B9, 90B1]).

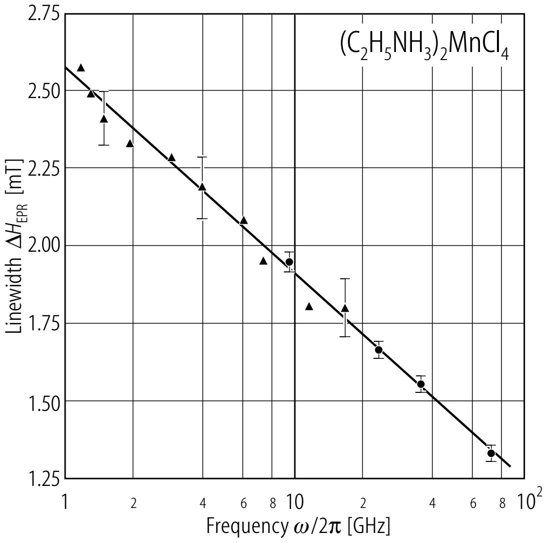

Fig. 4.67. $(C_2H_5NH_3)_2MnCl_4$. Dependence on $_{10}\log \nu$ (EPR-frequency ν) of ΔH_{EPR} at the "magic angle" $\psi = 54.7°$ and 300 K. The straight line as a fit to the experimental data allows the determination of the diffusion constant D (cf. Eq. 4.183, after [90B1], experimental data taken from [79B9] (full circles) and from [80L3] (full triangles).

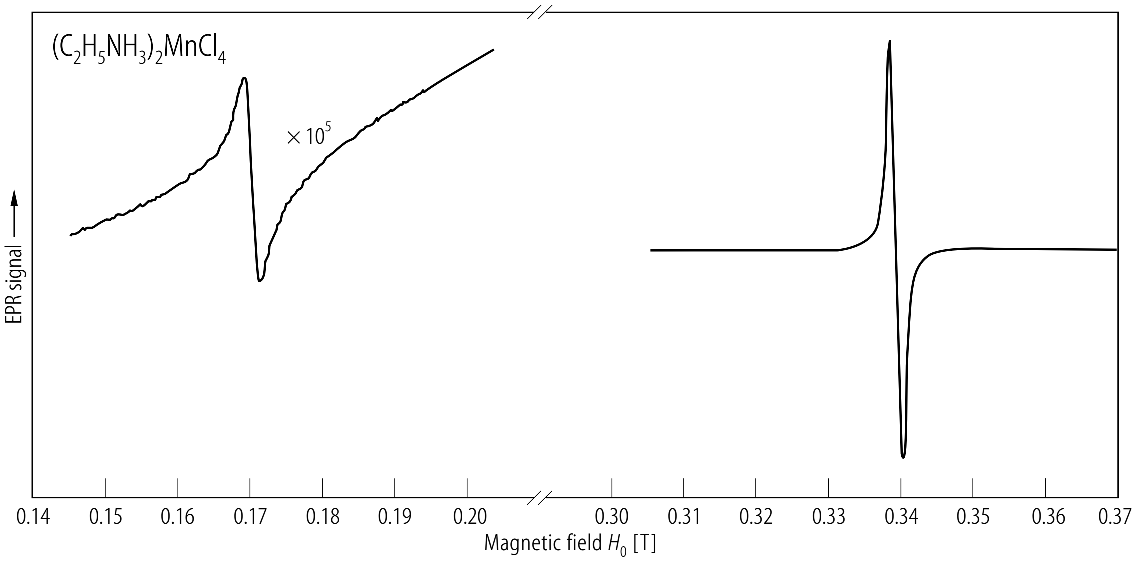

Fig. 4.68. $(C_2H_5NH_3)_2MnCl_4$. Derivative EPR spectra, i.e. signal versus magnetic field H_0 for $\psi = 50°$ and $\boldsymbol{h} \perp \boldsymbol{H_0}$, consisting of main line ($H_0 \approx 0.34$ T) and much weaker satellite line ($H_0 \approx 0.17$ T, half-field EPR), taken from [90B1].

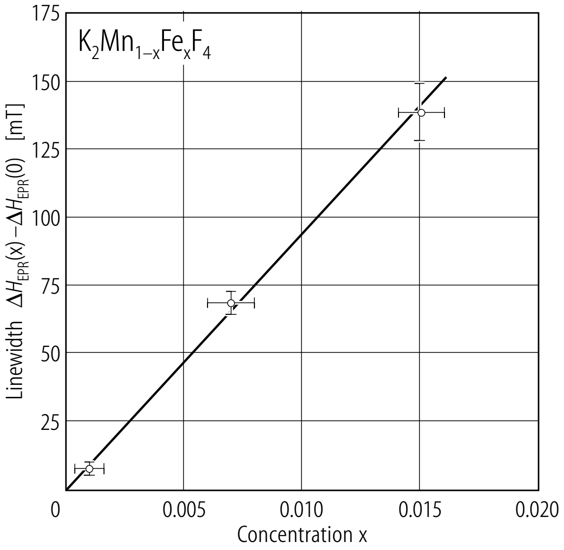

Fig. 4.69. $K_2Mn_{1-x}M_xF_4$ (M = Fe, Ni). Concentration dependence of the EPR linewidth, i.e. $\Delta H_{EPR}(x) - \Delta H_{EPR}(0)$ at $\psi = 54.7°$ and $T = 293$ K versus concentration x, for M = Fe and for M = Ni. The straight lines correspond to Eq. 4.189. Note the different x-scales for Fe and Ni (taken from [84V4]).

→

Fig. 4.70. $K_2Mn_{1-x}Fe_xF_4$ with x = 0.001, 0.007, 0.015. log-log plot of $\Delta H_{EPR} - \Delta H_{EPR}^{\infty}$ ($\nu \approx 24$ GHz) versus reduced temperature t for $\boldsymbol{H_0} \parallel \boldsymbol{c}$ (||) and $\boldsymbol{H_0} \perp \boldsymbol{c}$ (⊥), showing the different slopes for $t < t_{CH}$ and $t > t_{CH}$ (see Eqs. 4.190a and 4.189b), taken from [84V4].

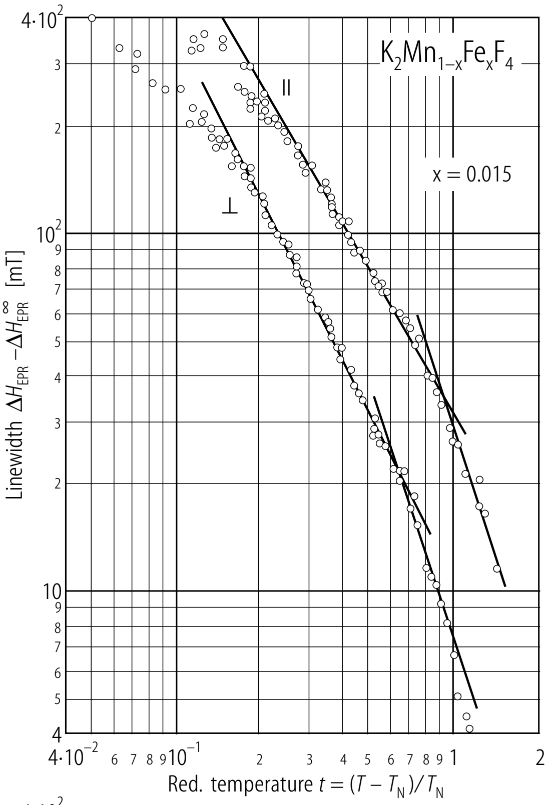
$K_2Mn_{1-x}Fe_xF_4$
x = 0.015
∥
⊥
Linewidth $\Delta H_{EPR} - \Delta H_{EPR}^{\infty}$ [mT]
$4\cdot10^2$
3
2
10^2
9
8
7
6
5
4
3
2
10
9
8
7
6
5
4
$4\cdot10^{-2}$
6
7
8
9
10^{-1}
2
3
4
5
6
7
8
9
1
2
Red. temperature $t = (T - T_N)/T_N$

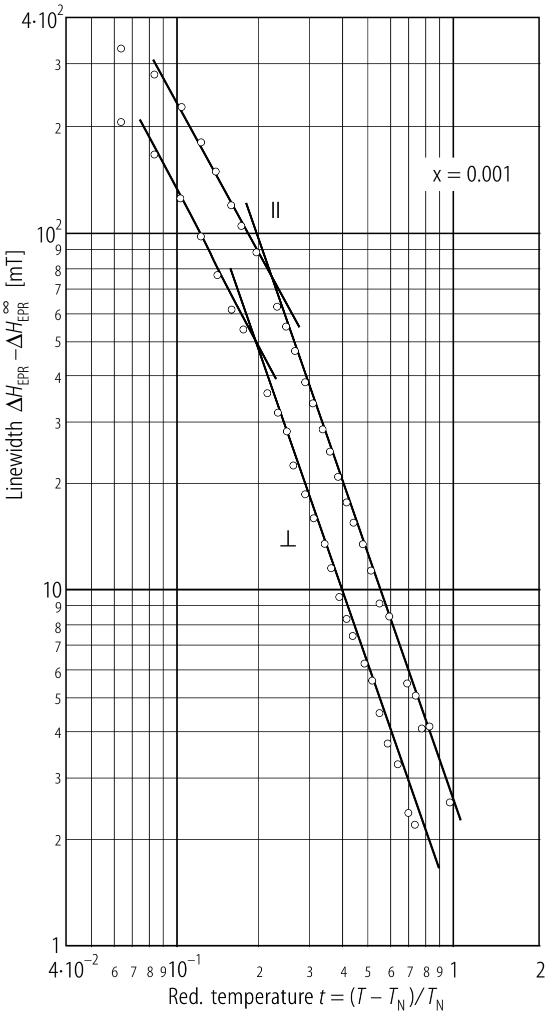
x = 0.001
∥
⊥
Linewidth $\Delta H_{EPR} - \Delta H_{EPR}^{\infty}$ [mT]
$4\cdot10^2$
3
2
10^2
9
8
7
6
5
4
3
2
10
9
8
7
6
5
4
3
2
1
$4\cdot10^{-2}$
6
7
8
9
10^{-1}
2
3
4
5
6
7
8
9
1
2
Red. temperature $t = (T - T_N)/T_N$

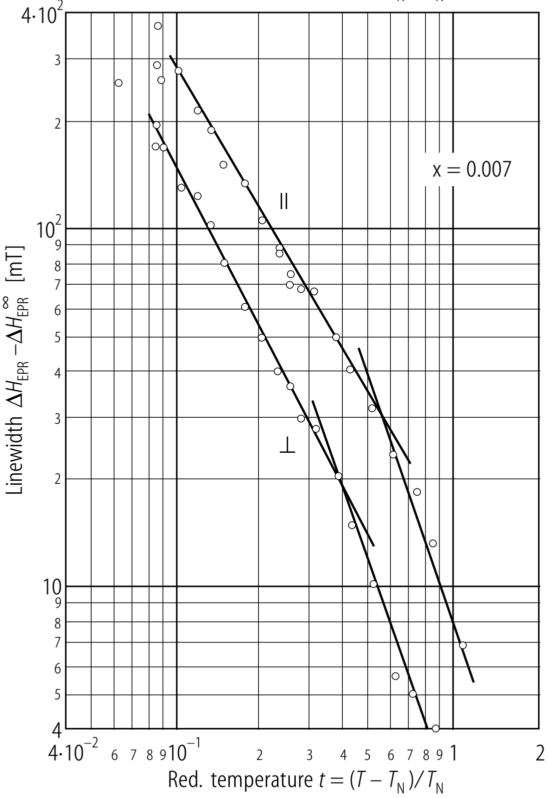
x = 0.007
∥
⊥
Linewidth $\Delta H_{EPR} - \Delta H_{EPR}^{\infty}$ [mT]
$4\cdot10^2$
3
2
10^2
9
8
7
6
5
4
3
2
10
9
8
7
6
5
4
$4\cdot10^{-2}$
6
7
8
9
10^{-1}
2
3
4
5
6
7
8
9
1
2
Red. temperature $t = (T - T_N)/T_N$

Table 6. Data about Critical Behaviour

Compound	Critical exponents, critical amplitudes etc.	References, remarks
I. Magnetic Phase Transitions		
a) Fluorides		
K_2MnF_4	Antiferromagnet, $\boldsymbol{M}_{\mathbf{subl}} \parallel \boldsymbol{c}$ (magn. order see Fig. 2.2)	
1) el. + quasi-el. n-scatt	afm. Bragg refl. (1, 0, 0): $I(\mathrm{T}) \sim M_{\mathrm{subl}}^{2}(T)$ $\rightarrow \beta = 0.15(1)$, $B_0 = 1.00(3)$ $[6 \cdot 10^{-4} \le \lvert t \rvert \le 0.3]$	[73B1] ($T_N = 42.14$ K), see also [72I, 73I, 74I1] β, B_0: Eq. 4.20
	afm. Bragg rod (1, 0, 0.4): $[0.008 \le t \le 0.15] \rightarrow \gamma = 1.65(15)$ $\nu = 0.9(1)$, $\eta = 0.20(5)$, $\kappa_0^+ / a^* = 0.106$, $\kappa_\perp^- / a^* = 0.024$	[76A3, 77B2, 77S1] ($T_N = 42.17$ K), see also [73I, 74I1] γ, ν, η, κ_0^+, $\kappa_\perp^-$: Eqs. 4.26, 4.28, 4.32, 4.32a, 4.33, 4.35
2) LMB	broad max. at $T > T_N$ and sharp spike at $T_N = 42.17$ K; singular part: $\Delta n_s(T) - \Delta n_s(T_N) \sim U_{\mathrm{magn}} - U_C$: $A^+/A^- = 0.98(4)$ and $\mathrm{d}(\Delta n_s)/\mathrm{d}T \sim C_{\mathrm{magn}}$ (symm. log. singularity at T_N)	[73J, 79J, 84F1] exp. data $\Delta n_s(T) - \Delta n_s(T_N)$ and $\mathrm{d}(\Delta n_s)/\mathrm{d}T$ fit well to 2D Ising ($U_{\mathrm{magn}} - U_C$) (Eq. 4.4a) and C_{magn} (Eq. 4.6)
3) C_{magn}	symm. log. sing. at T_N $[0.001 \le \lvert t \rvert \le 0.02]$ a) $\alpha^+ = \alpha^- = 0.011$, $A^+ = 0.030$, $A^- = 0.029$ b) $A^+ = 0.032$, $A^- = 0.030$; $A_{\mathrm{theory}} = 0.077$	C_p by ac cal. [80H4] ($T_N = 42.48$ K), see also [73S3] exp. data fitted: a) to Eq. 4.16 with $\alpha^+ = \alpha^-$, and b) to Eq. 4.17, both fits with $D^+ = D^-$; c) A_{theory}: Eq. 4.19
4) NMR LW	$T > T_N$: ${}^{19}F_I$-NMR, ΔH_{NMR} $[0.03 \le t \le 0.5]$ $\Delta H_{\mathrm{NMR}} \rightarrow$ w = 1.5 for $\boldsymbol{H_0} \parallel \boldsymbol{c}$ and $\boldsymbol{H_0} \perp \boldsymbol{c}$	[74B4, 90B1], ($T_N = 41.5$ K); $\Delta H_{\mathrm{NMR}}(T)$: Eq. 4.160
5) EPR LW	$T > T_N$: $\Delta H_{\mathrm{EPR}}(T)$ $[0.1 \le t \le 0.9]$, $\Delta H_{\mathrm{EPR}}(\psi)$ at 50.6 K	EPR at 24 GHz [72W2], see also [71Y1, 77N4]
	$\boldsymbol{H_0} \parallel \boldsymbol{c}$: p = 2.5(2), $\Delta H_{\mathrm{EPR}}^{\infty} = 11(1)$ mT, $C_{\mathrm{EPR}} = 2.1(4)$ mT $\boldsymbol{H_0} \perp \boldsymbol{c}$: p = 2.4(2), $\Delta H_{\mathrm{EPR}}^{\infty} = 9(1)$ mT, $C_{\mathrm{EPR}} = 1.4(3)$ mT	fit of exp. $\Delta H_{\mathrm{EPR}}(T)$ to Eq. 4.165 ($T_N = 42.1$ K); $\Delta H_{\mathrm{EPR}}(\psi)$ in accordance with Eq. 4.166
	alternatively: exam. of soliton contribution to EPR LW exp.: $E_s = 620(60)$ K, calc.: $E_s = 682$ K ($J = -4.34$ K)	[83W4, 96Z1]: reanalysis of the exp. data of [72W2] with respect to Eq. 4.170a; calc. E_s: Eq. 4.176
	h.t.: $\Delta H_{\mathrm{EPR}}(T)$ $[100\ \mathrm{K} \le T \le 300\ \mathrm{K}]$ and $\Delta H_{\mathrm{EPR}}(\psi)$ at 77 K and 300 K	EPR [73S2, 74R1]; $\Delta H_{\mathrm{EPR}}(T)$ approx. in accordance with Eq. 4.186; $\Delta H_{\mathrm{EPR}}(\psi)$ in accordance with Eq. 4.182
	satellite line at 2ν (half-field EPR)	[77N2, 77Y1], evidence for spin diffusion

Table 6. Data about Critical Behaviour *(continued)*

Compound	Critical exponents, critical amplitudes etc.	References, remarks
K$_3$Mn$_2$F$_7$	Antiferromagnet, $\boldsymbol{M}_{\mathbf{subl}} \parallel \boldsymbol{c}$ (magn. order see Fig. 2.4)	
1) el. + quasi-el. n-scatt.	several afm. Bragg reflections: $I(T) \sim M^2_{\mathrm{subl}}(T)$ $\rightarrow \beta = 0.154(6)$ $[10^{-3} \le \lvert t \rvert \le 10^{-1}]$	[78U, 79U] ($T_\mathrm{N} = 58.3(2)$ K); β: Eq. 4.20
	afm. Bragg rod (1, 0, 1.46): $[1.7 \cdot 10^{-2} \le t \le 0.35]$ $\rightarrow \gamma = 1.9(3)$, $\nu = 1.1(2)$, $\eta = 0.20(5)$	[78U, 79U], ($T_\mathrm{N} = 58.3(2)$ K); γ, ν: Eq. 4.26, 4.29, 4.32, 4.32a; η: $\nu(2 - \eta) = \gamma$ (cf. Eq. 4.13)
2) EPR LW	$T > T_\mathrm{N}$: $\Delta H_\mathrm{EPR}(T)$ $[0.1 \le t \le 0.35]$, $\Delta H_\mathrm{EPR}(\psi)$ at 64.1 K	EPR at 25 GHz [80U, 81U]
	$\boldsymbol{H_0} \parallel \boldsymbol{c}$: p = 3.0(2), $\Delta H^\infty_\mathrm{EPR}$ = 10.2(5) mT, C_EPR = 0.10(3) mT $\boldsymbol{H_0} \perp \boldsymbol{c}$: p = 2.9(2), $\Delta H^\infty_\mathrm{EPR}$ = 9.9(5) mT, C_EPR = 0.06(4) mT	fit of $\Delta H_\mathrm{EPR}(T)$ to Eq. 4.165 (T_N = 58.3 K); $\Delta H_\mathrm{EPR}(\psi)$ in accordance with Eq. 4.166a
	alternatively: exam. of soliton contribution to EPR LW exp.: E_s = 1550(100) K, calc.: no theory for E_s available	[83W4, 96Z1]: reanalysis of the exp. data of [80U, 81U] with respect to Eq. 4.170a
	h.t.: $\Delta H_\mathrm{EPR}(\psi)$ for $[64\ \mathrm{K} \le T \le 96\ \mathrm{K}]$	[81U]; $\Delta H_\mathrm{EPR}(\psi)$: Eq. 4.166a (64 K), Eq. 4.182 (95K)
Rb$_2$MnF$_4$	Antiferromagnet, $\boldsymbol{M}_{\mathbf{subl}} \parallel \boldsymbol{c}$ (magn. order see Fig. 2.3)	
1) el. + quasi-el. n-scatt.	several afm. Bragg reflections $[0.002 \le \lvert t \rvert \le 0.1]$:	[70B1]
	K$_2$NiF$_4$-type ordering: (1, 0, 0), (1, 0, 2) etc. $\rightarrow \beta = 0.18(1)$ Ca$_2$MnO$_4$-type ordering: (1, 0, $\frac{1}{2}$), (1, 0, $\frac{3}{2}$) etc. $\rightarrow \beta = 0.18(1)$	(T_N = 38.37 K) (T_N = 38.41 K) β: Eq. 4.20
2) EPR LW	$T > T_\mathrm{N}$: $\Delta H_\mathrm{EPR}(T)$ $[0.1 \le t \le 0.9]$	EPR at 24 GHz [72W2]
	$\boldsymbol{H_0} \parallel \boldsymbol{c}$: $\Delta H^\infty_\mathrm{EPR}$ = 11(1) mT, C_EPR = 2.1(4) mT, p = 2.5(2) $\boldsymbol{H_0} \perp \boldsymbol{c}$: $\Delta H^\infty_\mathrm{EPR}$ = 9(1) mT, C_EPR = 1.4(3) mT, p = 2.4(2)	fit of exp. $\Delta H_\mathrm{EPR}(T)$ to Eq. 4.165 (T_N = 38.4 K); no measurement of $\Delta H_\mathrm{EPR}(\psi)$
	alternatively: exam. of soliton contribution to EPR LW exp.: E_s = 650(60) K, calc.: E_s = 598 K (J = –3.81 K)	[83W4, 96Z1]: reanalysis of the exp. data of [72W2] with respect to Eq. 4.170a; calc. E_s: Eq. 4.176
K$_2$FeF$_4$	Antiferromagnet, $\boldsymbol{M}_{\mathbf{subl}} \perp \boldsymbol{c}$ (magn. order see Fig. 2.6)	
1) el. + quasi-el. n-scatt	afm. Bragg reflections (1, 0, 0), (1, 0, 3): $I(T) \sim M^2_{\mathrm{subl}}(T)$ $\rightarrow \beta = 0.15(1)$ $[0.01 \le \lvert t \rvert \le 0.25]$, T_N = 63.0(3) K	[82T1], see also Mössbauer study [78T2]; β: Eq. 4.20
	afm. Bragg rod (1, 0, 0.3): $\rightarrow \gamma^+ = 1.5(5)$, $\nu^+ = 0.9(2)$	[82T1] (T_N = 63.0 K); γ, ν: Eqs. 4.26, 4.28, 4.32, 4.32a
2) LMB	$\mathrm{d}(\Delta n)/\mathrm{d}T \sim C_\mathrm{magn}$: broad max. at $T > T_\mathrm{N}$ and symm. log. sing. at T_N = 63.0(3) K	[81K4]

Table 6. Data about Critical Behaviour *(continued)*

Compound	Critical exponents, critical amplitudes etc.	References, remarks
K_2CoF_4	Antiferromagnet, $\boldsymbol{M}_{\mathbf{subl}} \parallel \boldsymbol{c}$ (magn. order see Fig. 2.2)	
1) LMB	$\mathrm{d}(\Delta n)/\mathrm{d}T \sim C_{\mathrm{magn}}$: symm. log. sing. at $T_N = 107.42(2)$ K	[77I2, 78I1, 80I2, 80N1]
2) el. + quasi-el. n-scatt.	afm. Bragg reflections (1, 0, 0), (3, 0, 0): $I(T) \sim M^2_{\mathrm{subl}}(T)$ $\rightarrow \beta = 0.123(8)$ $[8 \cdot 10^{-3} \le \lvert t \rvert \le 0.1]$	[74I1, 74I2] ($T_N = 107.85$ K), see also [74S1, 74S3, 77S1]; β: Eq. 4.20
	$M_{\mathrm{subl}} \sim [1 - \sinh^{-4}(J_{\parallel}/k_BT)]^{1/8}$ for $[0.002 \le t \le 1]$	M_{subl}: Eqs. 3.66 and 4.1 (2D Ising model)
	afm. Bragg rod (1, 0, –0.24): $[-0.002 \le t \le -0.01,\ 0.01 \le t \le 0.1]$ $\gamma^+ = 1.71(4)$, $\gamma^- = 1.66(9)$, $\nu^+ = 0.97(5)$, $\nu^- = 0.94(8)$, $\eta = 0.2(1)$	[74I1, 74I2] ($T_N = 107.85$ K), see also [77S1] γ^+, γ^-, ν^+, ν^-, η: Eqs. 4.26, 4.29, 4.32, 4.32a
	afm. Bragg rod (1, 0, 0.45), $\nu^+ = \nu^- = 1.00$ fixed: $\kappa_0^+/a^* = 0.40(2)$, $\kappa_0^-/a^* = 0.74(8)$, $\kappa_0^-/\kappa_0^+ = 1.85(22)$, and $\gamma^+ = \gamma^- = 1.75$ fixed: $C_0^+/C_0^- = 32.6(37)$	[84C1]; $t > 0$: fit to Eq. 4.28 ($T_N = 107.47(2)$ K); $t < 0$: fit to Eq. 4.31 ($T_N = 107.70(3)$ K) κ_0^+, κ_0^-, C_0^+, C_0^-: Eqs. 4.8–4.11, 4.32, 4.32a
	$R_S = 0.0565(75)$	test of 2-scale-factor universality: Eq. 4.15
3) C_{magn}	symm. log. sing. at T_N $[0.001 \le \lvert t \rvert \le 0.02]$ a) $\alpha^+ = \alpha^- = -0.003(39)$, $A^+ = 0.411$, $A^- = 0.401$ b) $\alpha^+ = 0.021(47)$, $\alpha^- = -0.024(56)$, $A^+/A^- = 0.84(19)$ c) $A^+ = 0.384$, $A^- = 0.417$; d) $A_{\mathrm{theory}} = 0.346$	C_p by ac cal. [75I1, 76I2, 80H4] ($T_N = 107.71(3)$ K) exp. data fitted a) to Eq. 4.16 with $\alpha^+ = \alpha^-$, b) to Eq. 4.16 with $\alpha^+ \ne \alpha^-$, and c) to Eq. 4.17; all three fits with $D^+ = D^-$; d) A_{theory}: Eq. 4.19
Rb_2CoF_4	Antiferromagnet, $\boldsymbol{M}_{\mathbf{subl}} \parallel \boldsymbol{c}$ (magn. order see Fig. 2.2)	
1) el. + quasi-el. n-scatt.	afm. Bragg reflections (1, 0, 0), (1, 0, 1), (1, 0, 3): $I \sim M^2_{\mathrm{subl}}$ $\rightarrow \beta = 0.119(8)$, $B_0 = 1.16(3)$ $[0.003 \le \lvert t \rvert \le 0.3]$	[73S4, 74S1, 74S3] ($T_N = 103.025(10)$ K) β: Eq. 4.20
	$M_{\mathrm{subl}} \sim [1 - \sinh^{-4}(J_{\parallel}/k_BT)]^{1/8}$ for $[0.002 \le t \le 1]$	M_{subl}: Eqs. 3.66 and 4.1 (2D Ising model)
	afm. Bragg rod (1, 0, –0.53): $[0.01 \le t \le 0.3]$ $\rightarrow \gamma = 1.67(9)$, $\nu = 0.99(4)$, $\eta = 0.2(1)$, $\kappa_0^+/a^* = 0.263$	[74S1, 79I1] ($T_N = 102.06$ K), see also [73S4, 74S3] γ, ν, η, κ_0^+/a^*: Eqs. 4.26, 4.29, 4.32, 4.32a
	$T < T_N$: study of afm. Bragg reflections (1, 0, 1), (1, 0, 2) $T > T_N$: study of afm. Bragg rod (1, 0, 1.5)	[83H2, 84H1] ($T_N = 102.6(1)$ K)
	$\rightarrow$ exp. value $R_S = 0.043(2)$ $[0.005 \le \lvert t \rvert \le 0.045]$	test of 2-scale-factor universality: Eqs. 4.15, 4.36, 4.37
	$\kappa/a^* \sim \{\ln[\coth(J_{\parallel}/2k_BT)] - J_{\parallel}/k_BT\}$ $[0.004 \le t \le 0.09]$	$\kappa/a^* \sim \kappa a_{\mathrm{nn}}$: Eq. 4.10 (2D Ising model)
2) n-scatt, diff. cooling pr.	scans along afm. Bragg rod (1, 0, ζ) $[-1 \le \zeta \le 0]$: $\rightarrow \xi/c = 3.6$ at 77.5 K after rapid cooling through T_N $\rightarrow \xi/c = 10.3$ at 77.5 K after annealing at T_N	[78I3] ($T_N = 102.15$ K), see also [73S4, 74S1] 3D ordering depends on cooling rate! $\kappa = \xi^{-1}$ from width $\parallel$ (0, 0, 1) of (1, 0, 0) afm. Bragg refl.

Table 6. Data about Critical Behaviour *(continued)*

Compound	Critical exponents, critical amplitudes etc.	References, remarks
Rb_2CoF_4 (cont.)		
3) NMR LW	$T > T_N$, $\boldsymbol{H_0} \parallel \boldsymbol{c}$: $^{19}F_I$-NMR $\rightarrow$ w = 1.52(3) ^{87}Rb-NMR $\rightarrow$ w = 1.40(5) $[0.02 \le t \le 0.3]$	[72B3] (T_N = 99.8 K) $\Delta H_{NMR}(T)$: Eq. 4.160
4) LMB	$d(\Delta n)/dT \sim C_{magn}$: symm. log. sing. at T_N = 100.97 K a) $[5 \cdot 10^{-4} \le \lvert t \rvert \le 0.05]$: $\alpha = -0.002(13)$, $A^+/A^- = 1.010(8)$ b) $[5 \cdot 10^{-4} \le \lvert t \rvert \le 0.1]$: $\alpha = -0.003(10)$, $A^+/A^- = 1.020(7)$	[83N2] exp. data fitted to Eq. 4.18 with $D^+ = D^-$, fixed for the two ranges of t: data sets a) and b)
5) C_{magn}	symm. log. sing. at T_N $[0.001 \le \lvert t \rvert \le 0.02]$ a) $\alpha^+ = 0.027(71)$ $\alpha^- = 0.004(87)$, $A^+/A^- = 0.97(7)$ b) $\alpha^+ = \alpha^- = 0.016(51)$, $A^+/A^- = 1.05(9)$, $D^+/D^- = 1.00(3)$	C_p by ac cal. [76I2] (T_N = 102.5(1) K), see also [78S4] exp. data fitted a) to Eq. 4.16 with $\alpha^+ \ne \alpha^-$, $D^+ = D^-$, and b) to Eq. 4.16 with $\alpha^+ = \alpha^-$, $D^+ \ne D^-$
6) diffuse n-scatt.	study of afm. Bragg rods (1, 0, 0.1), (1, 0, 0.3), (1, 0, 2.3) $\Gamma_{\parallel}(0, \kappa) = 0.325(13) \cdot t^{1.69(2)} = 1.84(27) \cdot \kappa^{1.71(7)}$ $[0.03 \le t \le 0.4]$ $\Gamma_{\parallel}(q, 0) = 3.6(12) \cdot q^{1.67(8)}$ $[t = 0.0000(3)] \rightarrow z_{av} = 1.69(5)$	[82H4] (T_N = 102.96(1) K) $\Gamma_{\parallel}(q, \kappa) \hat{=}$ characteristic frequency (THz) of the critical longitudinal spin fluctuations, cf. Eqs. 4.133–4.135
7) ultrason. study	ultrason. attenuation: α_{sound} for f = 10–250 MHz $T > T_N$; $\alpha_{sound}(t) \rightarrow z = 1.21(10)$	[80S1] (T_N = 103.20(2) K) details of derivation of z from α_{sound} see [80S1]
K_2NiF_4	Antiferromagnet, $\boldsymbol{M_{subl}} \parallel \boldsymbol{c}$ (magn. order see Fig. 2.2)	
1) el. + quasi-el. n-scatt.	afm. Bragg refl. (1, 0, 0): $I(T) \sim M_{subl}^2(T)$ $\rightarrow \beta = 0.138(4)$, $B_0 = 1.00(3)$ $[3 \cdot 10^{-4} \le \lvert t \rvert \le 0.2]$	[70B3] (T_N = 97.23 K), see also [69B2, 70B1] β, B_0: Eq. 4.20
	afm. Bragg rod (1, 0, 0.4): $[0.008 \le t \le 0.15] \rightarrow \gamma = 1.65(15)$, $\nu = 0.9(1)$, $\eta = 0.20(5)$, $\kappa_0^+ / a^* = 0.056$, $\kappa_{\perp}^- / a^* = 0.017$	[76A3, 77B2] (T_N = 97.23), s. also [69B2, 71B1, 74I1] γ, ν, η, κ_0^+, $\kappa_{\perp}^-$: Eqs. 4.26, 4.28, 4.32, 4.32a, 4.33, 4.35
	comp. of exp. data for ξ / a and for struct. factor $S(\boldsymbol{q} = 0)$ to the theory for the 2D $S = \frac{1}{2}$ Heisenberg afm.	[90B3], using exp. data of [71B1]; for details of the theory see [88C4, 89C3]
2) LMB	$d(\Delta n)/dT \sim C_{magn}$: broad max. at $T > T_N$ and symm. log. sing. at T_N = 98.3(1) K	[74K2, 77I2, 78I1]
3) C_{magn}	symm. log. sing. at T_N $[0.001 \le \lvert t \rvert \le 0.01]$ a) $\alpha^+ = \alpha^- = 0.005$, $A^+ = 0.029$, $A^- = 0.030$ b) $A^+ = 0.030$, $A^- = 0.031$; c) $A_{theory} = 0.0345$	C_p by ac cal. [80H4] (T_N = 99.05 K), see also [71S2, 73S3] exp. data fitted a) to Eq. 4.16 with $\alpha^+ = \alpha^-$, and b) to Eq. 4.17 both fits with $D^+ = D^-$; c) A_{theory}: Eq. 4.19
4) NMR LW	$T > T_N$, $\boldsymbol{H_0} \parallel \boldsymbol{c}$: $^{19}F_I$-NMR, $\Delta H_{NMR} \rightarrow$ w = 0.54 $[0.003 \le t \le 0.7]$	[69M3] (T_N = 100.5 K); [74B6]: w > 0.54; $\Delta H_{NMR}(T)$: Eq. 4.160

Table 6. Data about Critical Behaviour *(continued)*

Compound	Critical exponents, critical amplitudes etc.	References, remarks
Rb_2NiF_4	Antiferromagnet, $\boldsymbol{M}_{\mathbf{subl}} \parallel \boldsymbol{c}$ (magn. order see Fig. 2.2)	
1) LMB	$d(\Delta n)/dT \sim C_{magn}$: broad max. at $T > T_N$ and symm. log. sing. at $T_N = 94.5(2)$ K	} [77I2, 78I1]
2) C_{magn}	symm. log. sing. at T_N $[7 \cdot 10^{-4} \leq \lvert t \rvert \leq 0.02]$ a) $\alpha^+ = \alpha^- = 0.001$, $A^+ = 0.079$, $A^- = 0.072$ b) $A^+ = 0.081$, $A^- = 0.073$; c) $A_{theory} = 0.072$	C_p by ac cal. [80H4] ($T_N = 97.03$ K), }{ exp. data fitted: a) to Eq. 4.16 with $\alpha^+ = \alpha^-$, and b) to Eq. 4.17, both fits with $D^+ = D^-$; c) A_{theory}: Eq. 4.19
K_2CuF_4	Ferromagnet, $\boldsymbol{M} \perp \boldsymbol{c}$ (magn. order see Fig. 3.27)	
1) meas. χ	$T > T_C$: $\chi_{\parallel}(T)$ $(\boldsymbol{H_0} \parallel \boldsymbol{a})$ and $\chi_{\perp}(T)$ $(\boldsymbol{H_0} \parallel \boldsymbol{c})$, $T_C = 6.28$ K anal. of $\chi_{\parallel}$: $[10^{-4} \leq t \leq 2 \cdot 10^{-3}] \rightarrow \gamma = 1.00(5)$ $[2 \cdot 10^{-3} \leq t \leq 0.8] \rightarrow 1.0 \leq \gamma \leq 2.0$	inductance bridge at $f = 70$ Hz [75D2, 76D5] }{ ×-over behaviour: no straight line in log-log plot γ: Eq. 4.32
	$5.5\text{ K} \leq T \leq 9\text{ K}$: $\chi_{ac}^{aa}(H_0, T)$ $(\boldsymbol{H_0} \parallel \boldsymbol{a})$ $[3\text{ mT} \leq H_0 \leq 90\text{ mT}]$ $\rightarrow \beta = 0.22(5)$, $\gamma = 0.99(5)$, $\Delta = \beta + \gamma = 1.21(5)$	}{ ac meas. at $f = 430$ Hz [81S1] ($T_C = 6.25$ K); scaling anal. using Eq. 4.12 b ($t > 0$): $\chi = H_{int}^{-\gamma/\Delta} \cdot \hat{\Psi}_+ (H_{int} / t^{\Delta})$
	$4.2\text{ K} \leq T \leq 7\text{ K}$: $\chi_{ac}(\omega)$ $[1\text{ MHz} \leq f \leq 200\text{ MHz}]$, $T_C = 6.25$ K $[5 \cdot 10^{-2} \leq t \leq 0.1]$ $\chi_{ac}(\omega = 0) \sim t^{-\gamma} \rightarrow 1.0 \leq \gamma \leq 1.7$ $\tau \sim t^{-\Lambda} \rightarrow 0.85 \leq \Lambda \leq 1.15$	ω-dependent meas. [80H6], see also [75H2] }{ ×-over behaviour: no straight line in log-log plot; $\chi_{ac}(\omega)$: Eqs. 4.139–4.140b; τ: Eqs. 4.141, 4.142
	$5.17\text{ K} \leq T \leq 7.70\text{ K}$: χ_{ac}^{aa} for $\boldsymbol{h} \parallel \boldsymbol{a}$ and $\boldsymbol{H_0} \parallel \boldsymbol{c}$,	ac meas. at $f = 570$ Hz [82S4]
	kinks of χ_{ac}^{aa} at $H_k = (T_g - T)^{1.0(1)}$, $T_g = 7.5$ K	2D XY-regime, at T_g ×-over to 2D Heisenberg
	$5.97\text{ K} \leq T \leq 6.67\text{ K}$: χ_{ac}^{cc} for $\boldsymbol{h} \parallel \boldsymbol{c}$ and $\boldsymbol{H_0} \parallel \boldsymbol{c}$,	ac meas. at $f = 570$ Hz [82S4]
	sharp peak of χ_{ac}^{cc} at $H_C(T) = \rightarrow T_C(H_0)$	$T_C(H_0)$ derived from H_C(T)
2) meas. M	$4.2\text{ K} \leq T \leq 11.0\text{ K}$: $M(H_0, T)$ for $\boldsymbol{H_0} \parallel \boldsymbol{a}$ $[2.5\text{ mT} \leq H_0 \leq 85\text{ mT}]$ $T > T_C$: $\chi = \partial M/\partial H \rightarrow B = b(2 - \eta) = 2.63$, $T_{KT} = 5.50$ K $T < T_C$: $\chi = \partial M/\partial H \rightarrow a(T)$, $\delta(T)$, $a(T_{KT}) = 0.875$	meas. magnetometer [81H2] }{ 2D XY-model: χ for $6.6\text{ K} \leq T \leq 7.3\text{ K}$ (Eq. 4.44, $b = 1.5$) χ for $T < T_C \rightarrow k_B T \chi \sim N^{a(T)}$ (Eq. 4.62)
	$4.2\text{ K} \leq T \leq 8.6\text{ K}$: $M(H_0, T)$ for $\boldsymbol{H_0} \parallel \boldsymbol{c}$ $[5\text{ mT} \leq H_0 \leq 80\text{ mT}]$ meas. of field-induced $\boldsymbol{M} \parallel \boldsymbol{c}$, derivation of $T_C(H_0)$	} meas. magnetometer [81H2]
3) C_{magn}	broad max. at $T > T_C$ and symm. log. sing. at $T_C = 6.25$ K; analysis of singular part $[10^{-3} \leq \lvert t \rvert \leq 10^{-1}]$: $A^+ = A^- = 0.0494$, $D^+ = -0.0797$, $D^- = -0.0530$	C_p by ad. cal., ac m. [72Y2, 76Y1], see also [74B2, 77B3] } [76Y1]: exp. data fitted to Eq. 4.17 with $E = 0$

Table 6. Data about Critical Behaviour *(continued)*

Compound	Critical exponents, critical amplitudes etc.	References, remarks
K_2CuF_4 (cont.)		
4) EPR LW	$\Delta H_{EPR}(T)$ [$4\ K \le T \le 300\ K$], $\Delta H_{EPR}(\psi)$ at several T satellite lines at 2ν and 3ν, lineshape analysis	[78N3, 83Y3], see also [72Y3, 81R1]; $T < 100$ K: evidence for spin diffusion, $\Delta H_{EPR}(\psi)$: Eq. 4.182
5) LMB	Δn_{ac}: $d\|\Delta n_{ac}\|/dT \sim C_{magn} \rightarrow$ broad max. at $T \approx 9.3$ K and sharp spike at $T_C = 6.189\ K \rightarrow \alpha^+ = \alpha^- = 0.07$	[80K2]; theory LMB see [81K6]; broad C_{magn}–max.: for low T spin-w. th. (Eq. 3.79), for high T h.t.s. (Eq. 4.39)
	$T < T_C$: $I_{ac}(T) \sim M^2(T) \rightarrow \beta = 0.33(1)$ [$10^{-3} \le \|t\| \le 0.05$], and $\beta = 0.24$ [$0.07 \le \|t\| \le 0.3$]	[80K2]; ×-over 3D XY ↔ 2D XY near $t = -0.055$ ($T = 5.9$ K), $T_C = 6.189$ K
	$\Delta n_{ac}(H_0, T)$, $\Delta n_{aa}(H_0, T)$ [$4.5\ K \le T \le 7\ K$, $0 \le H_0 \le 30\ mT$] scaled plot: $\sqrt{\Delta n} / H_{int}^{1/\delta}$ vs. $t / H_{int}^{1/\Delta} \rightarrow \beta = 0.345$, $\delta = 4.81$	[80K2], $T_C = 6.30$ K, scaled plot [83K4]; Eq. 4.12c: $M / H_{int}^{1/\delta} = \tilde{\Psi}_{\pm}(\|t\| / H_{int}^{1/\Delta})$
	fm. stripe domains: 1st order Bragg peak with $I_1(T) \sim M^2(T) \rightarrow \beta = 0.33(3)$ [$0.002 \le \|t\| \le 0.05$]	[82N1, 82N2]
6) el. + quasi-el. n-scatt.	magn. contribution to (0, 0, 4) Bragg refl.: $I(T) \sim M^2(T)$ $\rightarrow \beta = 0.33(3)$ [$10^{-3} \le \|t\| \le 0.05$], $\beta = 0.22$ [$0.07 \le \|t\| \le 0.3$]	[72H2, 73H3, 90J1], ×-over 3D XY ↔ 2D XY near $t = -0.064$ ($T = 5.85$ K), $T_C = 6.25$ K
	fm. Bragg rods (0, 0, 1.6), (0, 0, 1.8) [$4.5\ K \le T \le 10\ K$]	[82H5, 82H6], see also [72H2, 79H2, 81H3]
	$\rightarrow \kappa(T)$: $b = 1.5$, $T_{KT} = 5.5(1)$ K; observed ×-over: 3D XY – $T_x = 6.6$ K – 2D XY – $T_x = 7.3$ K – 2D Heisenberg	2D XY-model (cf. Eq. 4.43): $\kappa \sim \exp[-b\,\tilde{t}^{-1/2}]$ for $6.6\ K \le T \le 7.3\ K$
7) inel. n-scatt.	×-over in $\hbar\omega(q)$: 3D XY ↔ 2D XY ↔ 2D Heisenb. spin-wave lineshape: comparison to theory	[76M3, 77M1, 78M2, 83H4]; theory for the spin-wave lineshape of a 2D Heisenberg fm.: see [76M3, 77M1]
	$T > T_C$: central peak (dynamics of free spin vortices)	[92M2]; theory: [86K3, 87M2, 89M2]
Rb_2CuF_4	Ferromagnet, $\boldsymbol{M} \perp \boldsymbol{c}$ (magn. order see Fig. 3.27)	
meas. χ	$\chi_{\parallel}(T)$ for $\boldsymbol{H_0} \perp \boldsymbol{c}$, $\chi_{\perp}(T)$ for $\boldsymbol{H_0} \parallel \boldsymbol{c}$ [$0.5\ K \le T \le 8\ K$]	vibrating sample magnetometer [88D1]
	$T > T_C$: anal. $\chi_{\parallel} \rightarrow b = 1.5$, $\eta = 0.25$, $T_{KT} = 5.6(1)$ K	2D XY-model: χ (cf. Eq. 4.44) for $6.5\ K \le T \le 10\ K$
	$\chi'_{ac}(H_0, T)$ for $\boldsymbol{H_0} \perp \boldsymbol{c}$ [$3\ K \le T \le 8\ K$, $0 \le H_0 \le 0.1\ T$] $T > T_C$: $\gamma = 1.24(13)$, $\Delta = 1.32(12)$, $T_C = 6.05(9)$ K	ac meas. at $f = 530$ Hz [88D1]; scaling analysis using Eq. 4.12b ($t > 0$): $\chi = H_{int}^{-\gamma/\Delta} \cdot \hat{\Psi}_{+}(H_{int} / t^{\Delta})$

Table 6. Data about Critical Behaviour *(continued)*

Compound	Critical exponents, critical amplitudes etc.	References, remarks
b) Chlorides, Bromides, Iodides with inorganic A^+-ions		
Rb_2CrCl_4	Ferromagnet, $\boldsymbol{M} \perp \boldsymbol{c}$ (magn. order see Fig. 3.34)	
1) meas. χ	$\chi(T)$ for $\boldsymbol{H_0} \parallel (1, 1, 0) \rightarrow 0$ [$52\ \mathrm{K} \le T \le 55\ \mathrm{K}$], $T_C = 52.07$ K $T > T_C$: $\gamma = 1.35(2)$ [$0.003 \le t \le 0.01$], $1.4 \le \gamma \le 1.86$ [$0.01 \le t \le 0.05$]	[86K2] 3D XY-regime ×-over behaviour: no straight line in log-log plot
2) meas. M	$M(H_0, T)$ for $\boldsymbol{H_0} \parallel (1, 1, 0)$ [$0 \le H_0 \le 7$ T, $5\ \mathrm{K} \le T \le 160$ K]	[86C1], meas. of $\sigma \sim M$ (magn. moment per unit mass)
	$T < T_C$: $M(H_0, T) \longrightarrow a(T), \delta(T)$, $T_C = 52.4$ K	2D XY-model: $\langle M(T)\rangle = H_{\mathrm{int}}^{1/\delta(T)}$ (cf. Eq. 4.46)
	$T > T_C$: $\chi = \partial M/\partial H \rightarrow B = 4.07(10)$, $T_{KT} = 45.5$ K	2D XY-model: $\chi \sim \exp\,[B\,\tilde{t}^{\,-1/2}\,]$ (cf. Eq. 4.44)
3) LMB	$\Delta n_{xy}(H_0, T)$ for $\boldsymbol{H_0} \parallel \boldsymbol{X}$ [$0 \le H_0 \le 53$ mT, $40\ \mathrm{K} \le T \le 60$ K] $\Delta n(T) \rightarrow M(T) \rightarrow \beta = 0.28(2)$, $M(0) = 0.222(20)$ T $\Delta n(H_{\mathrm{int}}) \sim M^2(H_{\mathrm{int}})$, scaled plot: $\sqrt{\Delta n}\,/\,H_{\mathrm{int}}^{1/\delta}$ vs. $t\,/\,H_{\mathrm{int}}^{1/\Delta}$	[82K2]; definitions of the directions X and Y: [82K2] [82K2], $T_C = 52.71$ K; scaled plot [83K4]; Eq. 4.12c: $M\,/\,H_{\mathrm{int}}^{1/\delta} = \tilde{\Psi}_{\pm}(\lvert t\rvert\,/\,H_{\mathrm{int}}^{1/\Delta})$
4) el. + quasi-el. n-scatt.	magn. contribution to (0, 0, 4) Bragg refl.: $I(T) \sim M^2(T)$ $\rightarrow \beta = 0.333(19)$ [$6 \cdot 10^{-4} \le \lvert t\rvert \le 0.015$] $\beta = 0.230(2)$ [$0.015 \le \lvert t\rvert \le 0.12$]	[93A], see also [77F2, 79D3]; $T_C = 52.403$ K ×-over 3D XY ↔ 2D XY near $t = -0.015$ ($\hat{=}\ T = 51.6$ K); β: Eq. 4.20
	fm. Bragg rods $(0, 0, 3 + \zeta_{zo})$ [$5 \cdot 10^{-4} \le t \le 2$], $T_C \le T \le 55$ K: $\kappa \rightarrow \nu = 0.825(25)$, $T_C = 52.403(16)$ K, $\kappa_0^+\,/\,a^* = 0.123(6)$, $\kappa_z\,/\,a^* = 7.3(1) \cdot 10^{-3}$	[93A] 3D XY–regime, power law, cf. Eqs. 4.32a and 4.56
	$T \ge 55$ K: $\kappa, \chi \rightarrow b = 2.12(57)$, $B = 4.36(8)$, $T_{KT} = 43.4(27)$ K	2D XY-model: $\kappa(\tilde{t}\,)$ Eq. 4.43 and $\chi(\tilde{t}\,)$ Eq. 4.44
	neutron depolarization study of magn. critical fluctuations	[95T1]
5) inel. n-scatt.	T-dependence of $\hbar\omega(q)$ for $(\zeta, \zeta, 0)$ [$0.007 \le \zeta \le 0.028$]	[86H2], rapid drop of $\hbar\omega$ near T_C, esp. for $\zeta < 0.025$
	$T > T_C$: sharp magnons and central peak due to free vortices dynamics	[88B2, 92B2], inel. n-scatt, with polarized neutrons: spin-flip and non-spin-flip cross sections
Rb_2CrCl_3Br	Ferromagnet, $\boldsymbol{M} \perp \boldsymbol{c}$ (magn. order see Fig. 3.34)	
el. + quasi-el. n-scatt.	magn. contribution to (0, 0, 4) Bragg refl.: $I(T) \sim M^2(T)$ $\rightarrow \beta = 0.258(5)$ [$3.5 \cdot 10^{-3} \le \lvert t\rvert \le 0.9$]	[86B3], $T_C = 55$ K; value of β close to that of the 2D XY-model; β: Eq. 4.20

Table 6. Data about Critical Behaviour *(continued)*

Compound	Critical exponents, critical amplitudes etc.	References, remarks
$Rb_2CrCl_2Br_2$	Ferromagnet, $\boldsymbol{M} \perp \boldsymbol{c}$ (magn. order see Fig. 3.34)	
el. + quasi-el. n-scatt.	magn. contribution to (0, 0, 4) Bragg refl.: $I(T) \sim M^2(T)$ $\rightarrow \beta = 0.41(3)$ $[5.5 \cdot 10^{-3} \leq \lvert t \rvert \leq 0.037]$ $\beta = 0.265(5)$ $[0.037 \leq \lvert t \rvert \leq 0.9]$	[86B3], $T_C = 57$ K ×-over 3D XY ↔ 2D XY near $t = -0.015$ ($\hat{=}$ $T = 51.6$ K); β: Eq. 4.20
Rb_2MnCl_4	Antiferromagnet, $\boldsymbol{M}_{\mathbf{subl}} \parallel \boldsymbol{c}$ (magn. order see Fig. 2.2)	
1) el. + quasi-el. n-scatt.	afm. Bragg refl. (1, 0, 0): $I(T) \sim M^2_{\text{subl}}(T)$, $T_N = 55.842(6)$ K	[96K, 98K1]
	$\rightarrow H_0 < H_{SF}$: $\beta = 0.15(1)$ $H_0 > H_{SF}$: $\beta = 0.26(1)$ $[2 \cdot 10^{-3} \leq \lvert t \rvert \leq 0.08]$	$\boldsymbol{H}_\mathbf{0} \parallel \boldsymbol{c}$, H_{SF}: Eqs. 3.38, 3.39; β: Eq. 4.20; $H_0 < H_{SF}$: afm. Ising-like phase, $H_0 > H_{SF}$: XY-like spin-flop phase
2) el. + inel. n-scatt.	T-dependence of LW in q and ω for afm. Bragg rods and afm. Bragg refl. at $H_0 = 8$ T ($\boldsymbol{H}_\mathbf{0} \parallel \boldsymbol{c}$)	[92T1]; limited LRO: $\kappa > R_q$, $\Gamma_q > R_\omega$ (R_q, R_ω:resolution widths); competition between 2D and 3D order
3) LMB	$d(\Delta n)/dT \sim C_{magn}$: broad max. at $T > T_N$ and a sharp spike at $T_N = 54.83$ K	[80N1, 80P4]
	$T > 60$ K: exp. data comp. to h.t.s. calculation	[80P4]; h.t.s.: Eq. 4.39; coeff. see [67B2, 73Y3, 90N]
4) LMB, CMB	dependence on H_0 $[0 \leq H_0 \leq 10$ T] and T [4.2 K $\leq T \leq$ 60 K] $\rightarrow J = -5.6(1)$ K, $T_N = 55$ K, $H_{SF} = 5.6$ T	[80P3, 80P4], see also [78P]; H_{SF}: Eqs. 3.38, 3.39
5) EPR LW	$T > T_N$: $\Delta H_{EPR}(T)$ [55.4 K $\leq T \leq$ 83 K], $T_N(H_0 = 0) = 55$ K	EPR (61.1–152 GHz) [88G3, 90G4], see also [83P];
	$\boldsymbol{H}_\mathbf{0} \parallel \boldsymbol{c}$: p = 0.22(26) $[0.007 \leq t \leq 0.05]$, p = 2.4(5) $[0.1 \leq t \leq 0.5]$	ΔH_{EPR}: Eq. 4.165; $T_N(H_0)$, $\Delta H^{\infty}_{EPR} = f(\nu)$, $C_{EPR} = f(t\text{-range})$
	alternatively: exam. of soliton contribution to EPR LW exp.: $E_s = 850(70)$ K, calc.: $E_s = 919$ K ($J = -5.85$ K)	[88G3, 90G4], see also [83P]; reanalysis of the exp. data with respect to Eq. 4.170a; E_s: Eq. 4.176, [96Z1]
	h.t.: $\Delta H_{EPR}(\psi)$ at 300 K and at T below 70 K, change of $\Delta H_{EPR}(\psi)$: Eq. 4.182 (300 K) → Eq. 4.166 (< 70 K)	[82P1, 83P], EPR at 9.2, 35 GHz; 300 K: evidence for spin diffusion ($\Delta H_{EPR}(\psi)$, lineshape analysis)
Rb_2CuCl_4	Antiferromagnet, $\boldsymbol{M}_{\mathbf{subl}} \perp \boldsymbol{c}$ (magn. order see Fig. 3.27)	
C_{magn}	broad max. at $T > T_N$, sharp spike at $T = T_N = 13.8$ K	heat-pulse method [74B2, 77B3], see also [74W3]

Table 6. Data about Critical Behaviour *(continued)*

Compound	Critical exponents, critical amplitudes etc.	References, remarks
c) Chlorides and Bromides with organic A$^+$-ions		
$(C_6H_5CH_2NH_3)_2CrCl_4$	Ferromagnet, $\boldsymbol{M} \perp \boldsymbol{c}$	
meas. χ	χ'_{ac} at f = 198 Hz [5 K ≤ T ≤ 65 K], T_C = 37 K	[86B1]
	$T > T_C$: $\chi'_{ac}/\chi_0 \rightarrow \gamma = 1.87$ [0.05 ≤ t ≤ 0.22] $\gamma = 2.2$ [0.22 ≤ t ≤ 0.75]	×-over behaviour, unfortunately data not analysed with respect to the 2D XY-model (cf. Eq. 4.44)
$(C_6H_5CH_2NH_3)_2CrBr_4$	Ferromagnet, $\boldsymbol{M} \perp \boldsymbol{c}$	
meas. M	$M(T)/M(0)$ [10 K ≤ T ≤ 72 K], T_C = 52.0 K	[87B1]
	$T < T_C$: $\beta \approx 0.5$ [0.07 ≤ $\lvert t \rvert$ ≤ 0.15], $\beta = 0.23$ [0.25 ≤ $\lvert t \rvert$ ≤ 0.85]	β: 1st value 3D XY??, 2nd value 2D XY (Eq. 4.66)
$(CH_3NH_3)_2MnCl_4$	Antiferromagnet, $\boldsymbol{M}_{\mathbf{subl}} \parallel \boldsymbol{c}$ (spin canting, weak fm.: $\boldsymbol{M} \perp \boldsymbol{c}$)	details see [90A1], weak fm. due to DMI (Eq. 3.52)
1) el. + quasi-el. n-scatt.	afm. Bragg refl. (0, 1, 0): $I(T) \sim M^2_{subl}(T)$ $\rightarrow \beta = 0.195(10)$ [0.0013 ≤ $\lvert t \rvert$ ≤ 0.067], T_N = 44.63(10) K	[96K], see also [90A1]; β: Eq. 4.20
2) meas. M	weak fm. $M(T) \rightarrow \beta = 0.183(7)$, T_N = 44.79(1) K	SQUID magnetometer [96K]
3) C_{magn}	broad max. at $T > T_N$, not resolved: sharp spike at T_N	$C_{magn} = C_p$(Mn-comp.) – C_p(Cd-comp.) by ad. cal. [82W2]
4) meas. χ	χ [78 ≤ T ≤ 305 K]; χ'_{ac}, χ''_{ac} at f = 33 Hz [4.2 K ≤ T ≤ 140 K]	[74G2]
	$\rightarrow \gamma^+ = 2.90(13)$, $\gamma^- = 2.39(7)$; T_N = 45.3(5) K	γ^+, γ^-: Eq. 4.32
5) EPR LW	$T > T_N$: $\Delta H_{EPR}(T)$ [46.5 K ≤ T ≤ 77 K], T_N = 45.3 K	[71B4, 72B6, 75B6]: ν = 9.3 GHz, [80S4]: ν = 64.0 GHz
	$\boldsymbol{H}_{\mathbf{0}} \parallel \boldsymbol{c}$: p ≈ 0.6 [0.03 ≤ t ≤ 0.1], p = 2.6(2) [0.1 ≤ t ≤ 0.75]	ΔH_{EPR}: Eq. 4.165; $\Delta H^{\infty}_{EPR} = f(\nu)$, $C_{EPR} = f(t\text{-range})$
	alternatively: exam. of soliton contribution to EPR LW exp.: E_s = 760(60) K, calc.: E_s = 754 K (J = –4.80 K)	[83W4, 96Z1]: reanalysis of the exp. data of [75B6] with respect to Eq. 4.170a; calc. E_s: Eq. 4.176
	h.t.: $\Delta H_{EPR}(\psi, T)$ [50 ≤ T ≤ 300 K], $\Delta H_{EPR}(T)$ almost linear (cf. Eq. 4.186), fit of $\Delta H_{EPR}(\psi)$ to Eq. 4.184 at 300 K	[71B4, 72B6, 75B6]; evidence of spin diffusion; at all T > 70 K: $\Delta H_{EPR}(\psi)$ follows closely Eq. 4.182
$(C_2H_5NH_3)_2MnCl_4$	Antiferromagnet, $\boldsymbol{M}_{\mathbf{subl}} \parallel \boldsymbol{c}$ (spin canting, weak fm.: $\boldsymbol{M} \perp \boldsymbol{c}$)	details see [90A1], weak fm. due to DMI (Eq. 3.52)
1) el. + quasi-el. n-scatt.	afm. Bragg refl. (1, 0, 0): $I(T) \sim M^2_{subl}(T)$ $\rightarrow \beta = 0.18(4)$ [4.2 K ≤ T ≤ 41 K]; T_N = 42.1(2) K	[86A1, 90A1]; β: Eq. 4.20

Table 6. Data about Critical Behaviour *(continued)*

Compound	Critical exponents, critical amplitudes etc.	References, remarks
$(C_2H_5NH_3)_2MnCl_4$ (cont.)		
2) EPR LW	$T > T_N$: $\Delta H_{EPR}(T)$ [$46.5\ K \le T \le 70\ K$], ($T_N = 42.1\ K$)	EPR at 9.3 GHz [71B4]
	$\Delta H_{EPR}(T)$: exam. of soliton contribution to EPR LW exp.: $E_s = 770(80)\ K$, calc.: $E_s = 723\ K$ ($J = -4.60\ K$)	[83W4, 96Z1]: reanalysis of the exp. data of [71B4] with respect to Eq. 4.170a; calc. E_s: Eq. 4.176
	h.t.: $\Delta H_{EPR}(\psi, T)$ [$50 \le T \le 300\ K$], $\Delta H_{EPR}(T)$ almost linear (cf. Eq. 4.186), fit of $\Delta H_{EPR}(\psi)$ to Eq. 4.184 at 300 K satellite line at 2ν (half-field EPR), lineshape analysis	[72B6, 75B6, 78B7, 79B9, 80B10, 80L3], see also [71B4]; spin diffusion: a) $\Delta H_{EPR}(\psi)$: Eq. 4.182, b) satellite line c) lineshape d) $\Delta H_{EPR} \sim -\ln \omega \rightarrow D/a^2 = 271(40)$ GHz
$(C_3H_7NH_3)_2MnCl_4$	Antiferromagnet, $\boldsymbol{M}_{\mathbf{subl}} \parallel \boldsymbol{c}$ (spin canting, weak fm.: $\boldsymbol{M} \perp \boldsymbol{c}$)	details see [90A1], weak fm. due to DMI (Eq. 3.52)
1) el. + quasi-el. n-scatt.	afm. Bragg refl. (1, 0, 1): $I(T) \sim M^2_{subl}(T)$ $\rightarrow \beta = 0.229(5)$ [$4.2\ K \le T \le 38\ K$]; $T_N = 39.3(1)\ K$	[90A1]; β: Eq. 4.20
2) meas. M	weak ferromagnetic $M(T) \rightarrow \beta = 0.25(2)$	SQUID magnetometer [90A1]; β: Eq. 4.20
3) C_{magn}	broad max. at $T > T_N$, not resolved: sharp spike at T_N	$C_{magn} = C_p$(Mn-comp.) – C_p(Cd-comp.) by ad. cal. [81W3]
4) EPR LW	$T > T_N$: $\Delta H_{EPR}(T)$ [$0.17\ K \le t \le 0.41\ K$], ($T_N = 39.3\ K$)	EPR: [93G, 95Z1] ($\nu \approx 10$ GHz)
	$\Delta H_{EPR}(T)$: exam. of soliton contribution to EPR LW exp.: $E_s = 727(10)\ K$, calc.: $E_s = 699\ K$ ($J = -4.45\ K$)	analysis of the exp. data with respect to Eq. 4.170a; calc. E_s: Eq. 4.176; theory: [96Z1]
	h.t.: $\Delta H_{EPR}(\psi, T)$ [$50 \le T \le 300\ K$], $\Delta H_{EPR}(T)$ almost linear (cf. Eq. 4.186), fit of $\Delta H_{EPR}(\psi)$ to Eq. 4.184 at 300 K	[72B6, 75B6]; evidence for spin diffusion; at all $T > 70$ K: ΔH_{EPR} follows closely Eq. 4.182
$(CH_3NH_3)_2FeCl_4$	Antiferromagnet, $\boldsymbol{M}_{\mathbf{subl}} \perp \boldsymbol{c}$ (spin canting, weak fm.: $\boldsymbol{M} \parallel \boldsymbol{c}$)	details see [83N4], weak fm. due to DMI (Eq. 3.52)
1) C_{magn}	symm. log. sing. in C_p at $T_N = 90.90\ K$ $A^+ = A^- = 0.168$, $D^+ = 20.62$, $D^- = 20.69$, $E = 14.87$	[84Y1], C_p by high resolution ac calorimetry exp. data fitted to Eq. 4.17
2) Mössbauer study	hyperfine field $H(T)/H(0) = M_{subl}(T)/M_{subl}(0)$ $\rightarrow \beta = 0.146(5)$ [$2 \cdot 10^{-4} \le \lvert t \rvert \le 10^{-1}$]; $T_N = 94.46(2)\ K$	[77K8], see also [71M1, 74S6]; β: Eq. 4.20
3) meas. χ	$\chi(T)$ [$65\ K \le T \le 165\ K$], sharp peak at $T_N = 94.9\ K$ $\rightarrow \gamma^+ = 1.67(3)$, $\gamma^- = 1.60(10)$	[73W5], see also [71M1]; sharp peak at T_N resulting from spin canting and weak ferromagnetism

Table 6. Data about Critical Behaviour *(continued)*

Compound	Critical exponents, critical amplitudes etc.	References, remarks
$(C_2H_5NH_3)_2FeCl_4$	Antiferromagnet, $\boldsymbol{M}_{\mathbf{subl}} \perp \boldsymbol{c}$ (spin canting, weak fm.: $\boldsymbol{M} \parallel \boldsymbol{c}$)	details see [83N4]; weak fm. due to DMI (Eq. 3.52)
1) C_{magn}	nearly symm. log. sing. in C_p at $T_N = 98.36$ K $A^+ = 0.349$, $A^- = 0.411$, $D^+ = 20.40$, $D^- = 20.13$, $E = 12.30$	[84Y1], C_p by high resolution ac calorimetry exp. data fitted to Eq. 4.17
2) Mössbauer study	hyperfine field $H(T) \sim M_{subl}(T) \to \beta = 0.129$	measured by T. Suzuki, quoted in [84Y1]; β: Eq. 4.20
$(CH_3NH_3)_2CuCl_4$	Ferromagnet, $\boldsymbol{M}_{\mathbf{subl}} \parallel \boldsymbol{a}$ (covert spin canting, $\boldsymbol{c}$: hard axis)	details see [72J4, 84S4, 88D3, 89D2]; struct.: $P2_1/b11$
1) magn. fluctuations	magn. noise [0.01 Hz $\leq f \leq$ 10 Hz, 8 K $\leq T \leq$ 10 K] $\to$ noise max. near $T = 9.3$ K $\approx T_\times = 9.35$ K	[89T1, 92L2]; SQUID magnetometer $T_\times$: ×-over 3D Ising → 2D Ising, cf. [75A2, 76J1, 79O2]
2) meas. χ	$\chi(T)$ for $\boldsymbol{H_0} \parallel \boldsymbol{a}$ [8.5 K $\leq T \leq$ 10.5 K], $T_C = 8.903$ K $\to \gamma = 1.2$ [$0.002 \leq t \leq 0.04$], $\gamma = 1.73$ [$0.06 \leq t \leq 0.5$]	[76J1, 78J, 79O2, 80O1], see also [75A2, 75D2, 76D5] ×-over 3D Ising → 2D Ising at $t_\times = 0.05$ ($T_\times = 9.35$ K)
	$\chi_{ac}(\omega, T)$ [1.2 MHz $\leq f \leq$ 62 MHz, 8.5 K $\leq T \leq$ 10 K] $\tau \sim t^{-\Lambda} \to \Lambda = 1.05(3)$ [$0.003 \leq t \leq 0.1$]	[79O2, 80O1]; $\chi_{ac}(\omega)$: Eqs. 4.139–4.140b; τ: Eqs. 4.141, 4.142
3) optical studies	Faraday rotation 8000–25000 cm^{-1}, $H_0 = 0.125$ T $\sim \chi_\parallel$ for $T > T_C \to \gamma = 1.35(10)$ [$0.008 \leq t \leq 0.024$], ($T_C = 8.9$ K) $\gamma = 1.73(5)$ [$0.024 \leq t \leq 0.1$]	[75A3], see also [77H1] γ: Eq. 4.32; ×-over 3D Ising → 2D Ising behaviour at $t_\times = 0.024$ ($T_\times = 9.12$ K), see also [76J1, 76J2, 78J]
4) C_{magn}	broad max. at $T > T_C$, small sharp spike at $T_C = 8.895$ K	[71B5, 74B2, 74M2, 77B3], see also [67K2, 68V]
5) EPR LW	h.t.: $\Delta H_{EPR}(T)$ [100 K $\leq T \leq$ 300 K], → (Eq. 4.186), $B_{EPR} \sim J^4$	EPR: [72D]; theory for $\Delta H_{EPR}(T)$: [71C4, 81W5]
$(CD_3ND_3)_2CuCl_4$	Ferromagnet, weak afm., preferred spin direction in adjacent layers at ±23° from *b*-axis in *bc*-plane	details see [79S2, 83S2]; struct.: $A2_1/b11$
1) el. + quasi-el. n-scatt.	magn. contribution to (0, 0, 2) Bragg refl.: $I(T) \sim M^2(T)$ $\to \beta = 0.242(2)$ [$0.009 \leq \lvert t \rvert \leq 0.3$], $T_C = 8.84(1)$ K	[83S2, 84S4], β: Eq. 4.20
2) meas. χ	$\chi'_{ac}(T)$, $\chi''_{ac}(T)$ at $f = 20.7$ Hz [4 K $\leq T \leq$ 20 K] $\to \gamma = 1.24$ [$0.01 \leq t \leq 0.08$], $\gamma = 1.75$ [$0.08 \leq t \leq 0.26$]	[84S4]: γ: Eq. 4.32; ×-over 3D Ising → 2D Ising behaviour at $t_\times = 0.08$ ($T_\times = 9.55$ K)
$(C_2H_5NH_3)_2CuCl_4$	Antiferromagnet, $\boldsymbol{M}_{\mathbf{subl}} \parallel \boldsymbol{a}$ (covert spin canting, $\boldsymbol{c}$: hard axis)	details see [71J3, 72B5, 72J4, 73B5, 84V1]; struct.: Pbca
1) C_{magn}	broad max. at $T > T_N$, small sharp spike at $T_N = 10.20$ K	[71B5, 74B2, 74M2, 77B3], see also [67K2, 68V]
2) EPR LW	h.t.: $\Delta H_{EPR}(T)$ [100 K $\leq T \leq$ 300 K], → (Eq. 4.186), $B_{EPR} \sim J^4$	EPR: [72D], see also [73A6]; theory $\Delta H_{EPR}(T)$: [81W5]
	influence of radiation reaction damping on EPR lineshape	[77B5]; EPR ($\nu \approx 10.35$ GHz) [4.2 K $\leq T \leq$ 20 K]

Table 6. Data about Critical Behaviour *(continued)*

Compound	Critical exponents, critical amplitudes etc.	References, remarks
$(C_{10}H_{21}NH_3)_2CuCl_4$	Ferromagnet	$J' > 0$, see [72J4]
meas. χ	$\chi_{\parallel}(T)$ [$8.0\ K \le T \le 9.0\ K$], $T_C = 7.92$ K → $\gamma = 1.25$ [$0.015 \le t \le 0.03$], $\gamma = 1.75$ [$0.03 \le t \le 0.14$]	[76J1, 76J2, 78J]; γ: Eq. 4.32; ×-over 3D-Ising → 2D-Ising behaviour at $t_\times = 0.03$ ($T_\times = 8.15$ K)
$[C_6H_5(CH_2)_2NH_3]_2CuCl_4$	Ferromagnet $\boldsymbol{M} \parallel \boldsymbol{a}$ ($\boldsymbol{c}$: hard axis)	$J' > 0$, details see [76D2, 76Y3]; struct.: presumably Pbca
meas. χ	$\chi_{\parallel}(T)$ for $\boldsymbol{H_0} \parallel \boldsymbol{a}$, $H_0 \to 0$ [$4.2\ K \le T \le 13\ K$] → $\gamma = 1.7$ [$0.002 \le t \le 0.04$], $T_C = 9.439$ K	[78R2]; γ: Eq. 4.32; for $t < 0.002$ possibly ×-over 2D Ising → 3D Ising behaviour
$(CH_3NH_3)_2CuBr_4$	Four-sublattice antiferromagnet with hidden spin canting	details see [80K6, 81S5]
C_{magn}	sharp spike in C_p at $T_N = 15.8$ K	C_p by ad. cal. [80K6], see also [74B2, 74M2]
$(C_2H_5NH_3)_2CuBr_4$	Antiferromagnet, $\boldsymbol{M}_{subl} \parallel \boldsymbol{b}$ (spin canting, $\boldsymbol{c}$: hard axis)	details see [80K7, 81S5]; struct.: presumably Pbca
EPR LW	h.t.: $\Delta H_{EPR}(T)$ [$75\ K \le T \le 300\ K$], → (Eq. 4.186), $B_{EPR} \sim J^4$ 77 K: $\Delta H_{EPR}(\psi)$ in accordance with Eq. 4.185 (4.166)	EPR: [73W6], theory for $\Delta H_{EPR}(T)$: [71C4, 81W5]; B_{EPR}: antisymmetric, anisotropic exchange (Eqs. 4.187)
$(C_3H_7NH_3)_2CuBr_4$	Antiferromagnet (spin canting, weak ferromagnet)	details see [77K2]; struct.: Pbca
EPR LW	h.t.: $\Delta H_{EPR}(T)$ [$75\ K \le T \le 300\ K$], → (Eq. 4.186), $B_{EPR} \sim J^4$ 77K: $\Delta H_{EPR}(\psi)$ in accordance with Eq. 4.185 (4.166)	EPR: [73W6], theory for $\Delta H_{EPR}(T)$: [71C4, 81W5]; B_{EPR}: antisymmetric, anisotropic exchange (Eqs. 4.187)
d) Diammonium Compounds with $X = Cl^-, Br^-$		
$[NH_3(CH_2)_2NH_3]MnCl_4$	Antiferromagnet, $\boldsymbol{M}_{subl} \parallel \boldsymbol{c}$ (spin canting, weak fm. $\boldsymbol{M} \perp \boldsymbol{c}$)	details see [76A1, 81K9]; weak fm. due to DMI (Eq. 3.52)
EPR LW	295 K: $\Delta H_{EPR}(\psi)$ in accordance with Eq. 4.182 satellite line at 2ν (half-field EPR)	EPR: [75L10, 81K9]; evidence for spin diffusion: a) $\Delta H_{EPR}(\psi)$, b) satellite line
$[NH_3(CH_2)_4NH_3]MnCl_4$	Four-sublattice antiferromagnet, $\boldsymbol{M}_{subl} \parallel (\pm \sin\theta, 0, \cos\theta)$ with $\theta = 16°$; spin canting, weak fm.	details see [88S5]; spin canting due to DMI (see Eq. 3.52); struct.: $P2_1/b\ 11$
EPR LW	$T > T_N$: $\Delta H_{EPR}(T)$ for $\boldsymbol{H_0} \parallel \boldsymbol{c}$, $\boldsymbol{H_0} \perp \boldsymbol{c}$ [$0.03 \le t \le 0.35$]: $t > 0.1$ → $p \approx 2.7$, $t < 0.1$ → ×-over behaviour	[77H3], see also [75H3]; $T_N = 41$ K; fit of exp. data $\Delta H_{EPR}(T)$ to Eq. 4.165
	alternatively: exam. of soliton contribution to EPR LW exp.: $E_s = 850(50)$ K, calc.: J unknown	[83W4, 96Z1]: reanalysis of the exp. data of [77H3] with respect to Eq. 4.170a; calc. E_s: Eq. 4.176

Table 6. Data about Critical Behaviour *(continued)*

Compound	Critical exponents, critical amplitudes etc.	References, remarks
$[NH_3(CH_2)_6NH_3]FeCl_4$	Antiferromagnet (spin canting, weak fm.)	details see [82M2, 83S8, 95M1]
meas. M induced by H_0	$M(H_0, T)$ [$0 \le H_0 \le 3.2$ mT, 99 K $\le T \le$ 103.5 K] $\chi = \partial M/\partial H \to \gamma^+ = 1.63(4)$, $\gamma^- = 1.51(5)$	[95M2]; vibrating sample magnetometer γ^+, γ^-: Eq. 4.32
$[NH_3(CH_2)_2NH_3]CuCl_4$	Antiferromagnet, $\boldsymbol{M}_{\mathbf{subl}} \parallel \boldsymbol{b}$ ($\boldsymbol{c}$: hard axis, ($\lvert J'/J \rvert = 0.60$)	details see [77K4, 78A4, 79K8, 79S5]; struct.: $P12_1/a1$
1) LMB	$\Delta n(T)$ at 632.8 nm [4 K $\le T \le$ 290 K] $d(\Delta n)/dT \sim C_{magn}$: large peak at $T_N = 34.24(5)$ K	[78A4, 79K8]; sample: crystal section ∥ layers, ⊥ $\boldsymbol{b}$-axis sharp peak at T_N: typical 3D behaviour
2) NMR	^{2}D-NMR, -NQR: $\Delta f(T) \sim M_{subl}(T)$ [4 K $\le T \le$ 40 K] $\to \beta = 0.337(10)$ [$0.04 \le \lvert t \rvert \le 0.2$]	[77K4], see also [75K1, 76K4]; sample: $[ND_3(CH_2)_2ND_3]CuCl_4$: $\beta \mathrel{\hat{=}}$ 3D system (cf. Table 7)
3) EPR LW	h.t.: $\Delta H_{EPR}(T)$ [93 K $\le T \le$ 333 K], linear (cf. Eq. 4.186) 295 K: $\Delta H_{EPR}(\psi)$ in accordance with Eq. 4.185	EPR: [77Z, 82K5, 83K8]; B_{EPR}: short-time contributions dominating; theory B_{EPR}: [71C4, 77Z, 81W5]
$[NH_3(CH_2)_3NH_3]CuCl_4$	Antiferromagnet, $\boldsymbol{M}_{\mathbf{subl}} \parallel \boldsymbol{b}$ ($\boldsymbol{c}$: hard axis, ($\lvert J'/J \rvert = 0.10$)	details see [79K8]; struct.: Pnam
EPR LW	h.t.: $\Delta H_{EPR}(T)$ [60 K $\le T \le$ 300 K], $\to$ (Eq. 4.186), $B_{EPR} \sim J^4$ 295 K: $\Delta H_{EPR}(\psi)$ in accordance with Eq. 4.185	EPR: [77S6, 82K5, 83K8]; theory $\Delta H_{EPR}(T)$: [81W5] B_{EPR}: antisymmetic, anisotropic exchange (Eqs. 4.187)
$[NH_3(CH_2)_4NH_3]CuCl_4$	Antiferromagnet, $\boldsymbol{M}_{\mathbf{subl}} \parallel \boldsymbol{b}$ ($\boldsymbol{c}$: hard axis, ($\lvert J'/J \rvert = 0.012$)	details see [81S7]; struct.: $P12_1/a1$
EPR LW	h.t.: $\Delta H_{EPR}(T)$ [75 K $\le T \le$ 300 K], linear (cf. Eq. 4.186) 295K: $\Delta H_{EPR}(\psi)$ in accordance with Eq. 4.184	EPR: [82K5, 83K8]; some evidence for spin diffusion, but also short-time contributions to ΔH_{EPR}
$[NH_3(CH_2)_5NH_3]CuCl_4$	Antiferromagnet, $\boldsymbol{M}_{\mathbf{subl}} \parallel \boldsymbol{b}$ ($\boldsymbol{c}$: hard axis, ($\lvert J'/J \rvert = 0.003$)	details see [79K8]; struct.: $P12_1/n1$
LMB	$\Delta n(T)$ at 632.8 nm [4 K $\le T \le$ 290 K] $d(\Delta n)dT \sim C_{magn}$: broad max. for $T > T_N$	[79K8] broad max.: typical 2D behaviour
$[NH_3(CH_2)_2NH_3]CuBr_4$	Four-sublattice afm. with hidden spin canting ($\lvert J'/J \rvert = 1.8$)	details see [85R2]; struct.: $P12_1/a1$
EPR LW	h.t.: $\Delta H_{EPR}(T)$ [93 K $\le T \le$ 333 K], linear (cf. Eq. 4.186) 100 and 300 K: $\Delta H_{EPR}(\psi)$ fits well to Eq. 4.184	EPR: [83K8]; theory $\Delta H_{EPR}(T)$: [71C4, 77S6, 81W5]; B_{EPR}: antisymmetric, anisotropic exchange (Eqs. 4.187)
$[NH_3(CH_2)_3NH_3]CuBr_4$	Antiferromagnet ($\lvert J'/J \rvert = 1.0$)	details see [82S5, 84R6]; struct.: $P12_1/n\ 1$
EPR LW	h.t.: $\Delta H_{EPR}(T)$ [93 K $\le T \le$ 333 K], linear (cf. Eq. 4.186) 113 and 296 K: $\Delta H_{EPR}(\psi)$ fits well to Eq. 4.185	EPR: [83K8]; theory $\Delta H_{EPR}(T)$: [71C4, 77S6, 81W5]; B_{EPR}: antisymmetric, anisotropic exchange (Eqs. 4.187)

Table 6. Data about Critical Behaviour *(continued)*

Compound	Critical exponents, critical amplitudes etc.	References, remarks
$[NH_3(CH_2)_4NH_3]CuBr_4$	Antiferromagnet ($\lvert J'/J \rvert = 0.17$)	details see [82S5, 84R6]; struct.: $P12_1/a\ 1$
EPR LW	h.t.: $\Delta H_{EPR}(T)$ [$93\ K \le T \le 333\ K$], linear (cf. Eq. 4.186) 100 and 300 K: $\Delta H_{EPR}(\psi)$ fits well to Eq. 4.185	EPR: [83K8]; theory $\Delta H_{EPR}(T)$: [71C4, 77S6, 81W5]; B_{EPR}: antisymmetric, anisotropic exchange (Eqs. 4.187)
e) diluted magnets		
$K_2Mn_xMg_{1-x}F_4$	$x > x_p$: Antiferromagnet, $\boldsymbol{M}_{subl} \parallel \boldsymbol{c}$ (magn. order see Fig. 2.2)	
EPR LW	$x = 0.35, 0.86$: $\Delta H_{EPR}(T)$ for $\psi = 0°, 55°, 90°$ [$0 \le T \le 80\ K$]; various x [$0.35 \le x \le 1.0$]: $\Delta H_{EPR}(\psi)$ at 300 K; $x = 0.52$: satellite lines at 2ν, 3ν (half-field EPR, 1-third field EPR)	EPR at 9 GHz [78Y2, 78Y3], s. also [77T5, 80T5]; $\Delta H_{EPR}(T) \hat{=}$ Eq. 4.165 ($x > x_p$) and Eq. 4.186 ($x < x_p$); spin diffusion: $\Delta H_{EPR}(\psi)$ [Eq. 4.182], satellite lines
$Rb_2Mn_xMg_{1-x}Cl_4$	$x > x_p$: Antiferromagnet, $\boldsymbol{M}_{subl} \parallel \boldsymbol{c}$ (magn. order see Fig. 2.2)	
1) el + quasi-el. n-scatt.	$x = 0.54, 0.57, 0.60$: Heisenberg percolation; various afm. Bragg rods $\to I(q) \to \kappa(T) = \kappa_T + \kappa_G$	[76B7, 77C7, 80B1]; theory: [76K7, 76S7, 81C3]
	$\kappa_T \to D_{DS} = 1.00(5)$, $\nu_T = 0.90(5)$, $\gamma_T = 1.50(15)$ $\kappa_G \to \kappa_G^0 = 3.0$, $\nu_p = 1.354(15)$, $\gamma_p = 2.43(3)$ $I(q = 0) \to \eta = 0.34(8)$; $\phi = \nu_p / \nu_T = 1.48(15)$	$\kappa(T)$: Eq. 4.106, 4.110a; κ_T : Eq. 4.109a κ_G : Eq.4.107; $I(q)$: Eq. 4.105; theory for ν_p, γ_p : Eq. 4.102
2) (H_0, T) phase diagram	$x = 0.7$: $T_N = 14.2(3)$ K for $H_0 = 0$; influence of random fields, metastability boundary (cf. Fig. 4.41)	[88C3, 91B2, 93C2], n-scattering; review on random field effects: see [84B4]
3) EPR LW	$x = 0.30, 0.57, 0.70$: $\Delta H_{EPR}(\psi)$ at 295 K (all x) and at 70 K ($x = 0.30$), at 20 K ($x = 0.57$) and at 23 K ($x = 0.70$); $x = 0.54, 0.61, 0.70$: $\Delta H_{EPR}(T)$ at $\psi = 0°, 55°, 90°$	EPR at 12, 17.4, 35 GHz [79W2]; $\Delta H_{EPR}(\psi) \hat{=}$ Eq. 4.182 (295 K, all x; 70 K, $x = 0.30$) and Eq. 4.188 (20 K, $x = 0.57$; 23 K, $x = 0.70$)
$K_2Mn_xZn_{1-x}F_4$	$x > x_p$: Antiferromagnet, $\boldsymbol{M}_{subl} \parallel \boldsymbol{c}$ (magn. order see Fig. 2.2)	
n-diffraction	$x = 0.66, 0.74, 0.78, 0.91$: scans through afm. Bragg refl. along c at low T ($H_0 = 0$) $\to \kappa_z$ increasing for $x \to x_p$	[87D2, 88D11]; breakup of 3D LRO due to site-random fields from dilution, 2D order remains
$(C_3H_7NH_3)_2Mn_{1-x}Zn_xCl_4$	$(1-x) > x_p$: Antiferromagnet, $\boldsymbol{M}_{subl} \parallel \boldsymbol{c}$ (spin canting, weak fm.)	
1) meas. χ_{ac}	$0.001 < x < 0.05$: $T_N = 39.2$ K independent of these small x	[96S1]
2) EPR LW	$x = 0, 0.0044, 0.0106$: $\Delta H_{EPR}(T)$ [$45\ K \le T \le 60\ K$], exam. of soliton contribution to the EPR linewidth	[96S1]; E_s (Eq. 4.170) from slopes in Fig. 4.63, see also Fig. 1 of [96S1], $x = 0$: $E_s = 727$ K [95 Z1]

Table 6. Data about Critical Behaviour *(continued)*

Compound	Critical exponents, critical amplitudes etc.	References, remarks
$Rb_2Mn_xCd_{1-x}Cl_4$	x > x_p: Antiferromagnet, $\boldsymbol{M}_{subl} \parallel \boldsymbol{c}$ (magn. order see Fig. 2.2)	
1) EPR LW	$\Delta H_{EPR}(T)$: exam. of soliton contribution to EPR LW	analysis of $\Delta H_{EPR}(T)$ with respect to Eq. 4.170a; theory: [96Z1], see also [83W4]
	x = 1.0 $\boldsymbol{H}_0 \parallel \boldsymbol{c}$: E_s = 969(56) K, E_s/k_BT_N = 17.0(10)	T_N = 57 K, [83P, 84E]
	$\boldsymbol{H}_0 \perp \boldsymbol{c}$: E_s = 1094(56) K, E_s/k_BT_N = 19.2(10)	
	x = 0.91 $\boldsymbol{H}_0 \parallel \boldsymbol{c}$: E_s = 578(61) K, E_s/k_BT_N = 12.3(13)	T_N = 47 K, [87G3]
	x = 0.90 $\boldsymbol{H}_0 \parallel \boldsymbol{c}$: E_s = 507(43) K, E_s/k_BT_N = 11.8(10)	T_N = 43 K, [84E]
	$\boldsymbol{H}_0 \perp \boldsymbol{c}$: E_s = 585(43) K, E_s/k_BT_N = 13.6(10)	
	x = 0.80 $\boldsymbol{H}_0 \parallel \boldsymbol{c}$: E_s = 266(31) K, E_s/k_BT_N = 8.6(10)	T_N = 31 K, [89B4]
	x = 0.80 $\boldsymbol{H}_0 \parallel \boldsymbol{c}$: E_s = 250(26) K, E_s/k_BT_N = 9.6(10)	T_N = 26 K, [83P, 84E]
	$\boldsymbol{H}_0 \perp \boldsymbol{c}$: E_s = 281(26) K, E_s/k_BT_N = 10.8(10)	
	x = 0.74 $\boldsymbol{H}_0 \parallel \boldsymbol{c}$: E_s = 208(29) K, E_s/k_BT_N = 8.0(11)	T_N = 26 K, [89B4]
	x = 0.70 $\boldsymbol{H}_0 \parallel \boldsymbol{c}$: $t \le 0.9$: E_s = 90(5) K, E_s/k_BT_N = 6.0(3)	T_N = 15 K, [84E]
	$t \ge 0.9$: E_s = 167(5) K, E_s/k_BT_N = 11.1(3)	
	$\boldsymbol{H}_0 \perp \boldsymbol{c}$: $t \le 0.9$: E_s = 92(5) K, E_s/k_BT_N = 6.1(3)	
	$t \ge 0.9$: E_s = 159(5) K, E_s/k_BT_N = 10.6(3)	
	x = 0.62 $\boldsymbol{H}_0 \parallel \boldsymbol{c}$: E_s = 5.6(4) K, E_s/k_BT_N = 1.6(1)	T_N = 3.5 K, [84E]
	$\boldsymbol{H}_0 \perp \boldsymbol{c}$: E_s = 3.6(5) K, E_s/k_BT_N = 1.04(14)	
2) EPR LW h.t.	x = 0.4, 0.5, 0.62, 0.7, 0.8, 0.9, 1.0: $\Delta H_{EPR}(\psi)$ at 300 K, x = 0.8, 1.0: $\Delta H_{EPR}(\psi)$ at T below 70 K, lineshape analysis: change from 2D to 1D behaviour for x < 0.62	EPR at 9.2 and 35 GHz [82P1, 83P] 300 K: fit of $\Delta H_{EPR}(\psi)$ to Eq. 4.182 70 K: $\Delta H_{EPR}(\psi)$ changes Eq. 4.182 → Eq. 4.165
$(C_3H_7NH_3)_2Mn_{1-x}Cd_xCl_4$	(1–x) > x_p: Antiferromagnet, $\boldsymbol{M}_{subl} \parallel \boldsymbol{c}$ (spin canting, weak fm.)	
1) meas. χ_{ac}	$0.001 < x < 0.05$: T_N = 39.2 K independent of these small x	[96S1]
2) EPR LW	x = 0, 0.0019, 0.0115: $\Delta H_{EPR}(T)$ [41 K ≤ T ≤ 60 K], exam. of soliton contribution to the EPR linewidth	[96S1]; E_s (Eq. 4.170) from slopes in Fig. 4.63, see also Fig. 1 of [96S1]; x = 0: E_s = 727 K [95Z1]

Table 6. Data about Critical Behaviour *(continued)*

Compound	Critical exponents, critical amplitudes etc.	References, remarks
$K_2Fe_xZn_{1-x}F_4$	$x > x_p$: Antiferromgnet, $\boldsymbol{M}_{\mathbf{subl}} \perp \boldsymbol{c}$ (magn. order see Fig. 2.6)	
1) Mössbauer study	$T_N(x)/T_N(1)$ for various x: see Fig. 4 of [85D1]	$T_N(1) = 63.0(3)$ K
2) el. + quasi-el. n-scatt.	x = 0.74: afm. Bragg rod (1, 0, 0.4) → $I(q, T)$: [$4\text{ K} \le T \le 65\text{ K}$]	[85D1, 86D5]
	$I(q, T)$ shows broad maximum from $T_N = 22.6(10)$ K down to 11 K, its width Δq decreasing from 65 K to 23 K, then const. ($\Delta q \mathrel{\hat{=}} \xi_x / a_{nn} = 14.6$)	the magn. pt. is not sharp, onset of 3D order smeared over 23 → 11 K (see Fig. 8 of [85D1]; accordingly $I_{Bragg}(T)$ of (1, 0, 0) refl. gradually rising
$Rb_2Co_xMg_{1-x}F_4$	$x > x_p$: Antiferromgnet, $\boldsymbol{M}_{\mathbf{subl}} \parallel \boldsymbol{c}$ (magn. order see Fig. 2.2)	
1) el. + quasi-el. n-scatt.	afm. Bragg reflections (1, 0, 0), (1, 0, 3): $I(T) \sim M^2_{subl}(T)$	x = 0.65–1.0: very carefully grown samples, very slowly cooled
	and scans across afm. Bragg rod (1, 0, –0.51) → ν, η, κ_0^+ / a^*	through T_N: 3D LRO; $H_0 = 0$: REIM (Sect. 4.1.12)
	x = 1.00: $T_N = 103.0$ K $\beta = 0.115(16)$, $\nu = 0.99(4)$, $\eta = 0.2(1)$, $\kappa_0^+ / a^* = 0.35(8)$	[79I1, 81I2]; β: Eq. 4.20; ν, η, κ_0^+ / a^* : Eqs. 4.26, 4.29, 4.32a
	x = 0.91: $T_N = 85.5$ K $\beta = 0.125(5)$, $\nu = 1.00(5)$, $\eta = 0.2(1)$, $\kappa_0^+ / a^* = 0.30(2)$	[79I1, 81I2]; β: Eq. 4.20; ν, η, κ_0^+ / a^* : Eqs. 4.26, 4.29, 4.32a
	x = 0.82: $T_N = 67.2$ K $\beta = 0.125(5)$, $\nu = 1.00(5)$, $\eta = 0.2(1)$, $\kappa_0^+ / a^* = 0.18(2)$	[79I1, 81I2]; β: Eq. 4.20; ν, η, κ_0^+ / a^* : Eqs. 4.26, 4.29, 4.32a
	x = 0.70: $T_N = 40.8$ K $\beta = 0.13(2)$, $\nu = 1.08(6)$, $\gamma = 1.75(7)$, $\kappa_0^+ / a^* = 0.086(8)$	[87H2, 92C2]; β: Eq. 4.20; ν, γ, κ_0^+ / a^* : Eqs. 4.26, 4.29, 4.32a
	x = 0.70 with $\nu = 1.00$ and $\gamma = 1.75$ fixed: $\kappa_0^+ / a^* = 0.76(2)$, $\kappa_0^- / a^* = 0.148(8)$, $C_0^+ = 190(22)$, $C_0^- = 5.33(48)$, $\kappa_0^- / \kappa_0^+ = 1.95(11)$, $C_0^+ / C_0^- = 36(5)$, $R_S = 0.062(10)$	$t > 0$: fit to Eq. 4.28, $t < 0$: fit to Eq. 4.31 [$\lambda = 1.0(1)$, $\phi^2 = 0.40(16)$]; κ_0^+, κ_0^-, C_0^+, C_0^- : Eqs. 4.8 – 4.11, 4.32, 4.32a; R_S: Eq. 4.15 (2-scale-factor universality)
	x = 0.65: $T_N = 30.8$ K	[79I1, 81I2]

Table 6. Data about Critical Behaviour *(continued)*

Compound	Critical exponents, critical amplitudes etc.	References, remarks
$Rb_2Co_xMg_{1-x}F_4$ (cont.)		
2) n-scatt. ($x \approx x_p$)	x = 0.55, 0.575, 0.583, 0.595: Ising percolation afm. Bragg rod (1, 0, 0.4) $\rightarrow I(q) \rightarrow \kappa(T) = \kappa_T + \kappa_G$	[80B1, 80C1]; theory: [81C3]
	$\kappa_T \rightarrow D_{DS} = 0.96(6)$, $\nu_T = 1.32(4)$, $\gamma_T = 2.4(1)$ $\kappa_G \rightarrow \kappa_G^0 = 3.0$, $\nu_p = 1.354(15)$, $\gamma_p = 2.43(3)$ $I(q = 0) \rightarrow \eta = 0.32(8)$; $\phi = \nu_p/\nu_T = 1.03$	$\kappa(T)$: Eqs. 4.106, 4.110a; κ_T: Eq. 4.109a κ_G: Eq. 4.107; $I(q)$: Eq. 4.105; theory for ν_p and γ_p : Eq. 4.102
3) LMB	x = 0.85, $d(\Delta n)/dt \sim C_{magn}$: symm. log. sing. at $T_N = 76.35$ K $[5 \cdot 10^{-4} \leq \lvert t \rvert \leq 0.01]$: $\alpha = 0$, $A^+/A^- = 0.95(10)$	[83F3, 84B5]; $H_0 = 0$: REIM (cf. Sect. 4.1.12); exp. data fitted to Eq. 4.112 with $D^+ = D^-$
4) n-scatt., diff. cooling pr.	scans along afm. Bragg rod $(1, 0, \zeta)$ $[-1 \leq \zeta \leq 0] \rightarrow \xi \parallel c$	[78I3], see also [79I2, 83I2];
	a) after rapid cooling through T_N x = 1.0: $\xi/c = 3.6$ at 77.5 K x = 0.89: $\xi/c = 3.2$ at 11.8 K x = 0.85: $\xi/c = 2.1$ at 10.9 K x = 0.70: $\xi/c = 0.6$ at 9.4 K	rapid cooling: 2D LRO dominating, less 3D LRO $\kappa = \xi^{-1}$ from width $\parallel$ (0, 0, 1) of (1, 0, 0) afm. Bragg refl.
	b) after annealing at T_N for some time x = 1.0: $\xi/c = 10.3$ at 77.5 K x = 0.89: $\xi/c = 5.2$ at 20.7 K x = 0.85: $\xi/c = 5.9$ at 14.2 K x = 0.70: $\xi/c = 1.5$ at 14.0 K	annealing or very slow cooling: better 3D ordering $\kappa = \xi^{-1}$ from width $\parallel$ (0, 0, 1) of (1, 0, 0) afm. Bragg refl.
5) several methods	random field effects; $H_0 \neq 0$: RFIM (cf. Sect. 4.1.12); $\boldsymbol{H} \parallel \boldsymbol{c}$ $[0 \leq H_0 \leq 6\ \mathrm{T}] \rightarrow$ random field H_{RF} (Eq. 4.115b)	results indicate: magn. phase transition destroyed by H_{RF}; reviews: [84B4, 86K8, 88B5, 90J2, 91B1]
	x = 0.85, LMB: $d(\Delta n)/dT \sim C_{magn} \rightarrow$ rounded peak at $T_C(H_0) < T_N$ for $H_0 = 0$ (cf. Fig. 4.36); see also scaling plot $[d(\Delta n)/dT + F \cdot \widetilde{A}^* \ln h]$ versus $t \cdot h^{-2/\phi}$	[83F3, 84B5]; rounded peak due to random field; scaling plot Fig. 4.37 according to Eq. 4.117b, single curve obtained with $\phi = 1.75$, $F \cdot \widetilde{A}^* = 1.64 \cdot 10^{-6}\ K^{-1}$
	$0.6 \leq x \leq 1.0$, magn. meas.: $\chi_{\parallel}(H_0)$, $M(H_0)$ for $\boldsymbol{H_0} \parallel \boldsymbol{c}$	[83I3, 83I4]; FC, ZFC exp.; x = 0.6, $H_0 \approx 0$: $T_N = 19$ K
	x = 0.7, n-scatt.: fit of $I(q)$ to Eq. 4.118 $\rightarrow \kappa(H_0, T)$	[82Y3, 83B4, 83C4]; $\kappa(H_0, T)$: Eq. 4.119 (cf. Fig. 4.38)
	x = 0.85, n-scatt.: $I_{Bragg}(H_0, T)$, ZFC and FC exp. $\rightarrow$ metastability boundary $T_M(H_0)$ [Eq. 4.120];	[85B3, 85B4, 85J2]; $T_M(H_0) < T_C(H_0)$, cf. Fig. 5 of [85B3]; $t_M(H_0) = -(c_M h_{RF}^2)^{1/\phi}$ $[c_M = 29(1), \phi = 1.74(2)]$
	$0.30 \leq x \leq 0.91$, pulsed h.m.f. exp. $[0 \leq H_0 \leq 50\ \mathrm{T}]$	[84M4, 85K1]; different $T_M(H_0) \mathrel{\hat{=}}$ different time scale

Table 6. Data about Critical Behaviour *(continued)*

Compound	Critical exponents, critical amplitudes etc.	References, remarks
$Rb_2Co_xMg_{1-x}F_4$ (cont.)		
6) n-diffraction	x = 0.60, 0.65, 0.70: T_N = 20, 30.8, 42.8 K, resp.; afm. Bragg refl. (1, 0, 0): $I(q)$ according to Eq. 4.101 $\rightarrow q > \kappa_G$: $I(q) \sim q^{-D_f} \rightarrow D_f$ = 1.95(7) at T = 4.5 K	[93I3, 94I4, 95I2]; fractal structure of a percolating network, fractal dimension D_f (Eq. 4.100), theoretical value: D_f = 91/48 = 1.89583 (cf. Eq. 4.102)
7) meas. M and n-diffraction	x = 0.60: ordering kinetics, $M(t)$ and $I_{Bragg}(t)$ [$t \,\hat{=}\,$ time] → domain size $R(t) \sim [\ln t]^{3.5}$ at T = 15 K	[90I1, 94I4], see also [83I4, 85B3, 85B4]; magn. meas.: M; n-diffraction: $I_{Bragg} = I(1, 0, 0)$
8) el. + inel. n-scatt.	afm. Bragg rod (1, 0, 0.4): $I(q) \rightarrow \kappa(T)$, $I(\omega) \rightarrow \Gamma_{\parallel}$	[80C1, 84A, 86A5]; $I(q)$: Eq. 4.105; $I(\omega) \sim F_{\parallel}(\boldsymbol{K}, \omega)$
	x = 0.58: T = 45 K, κa = 0.19, $\Gamma_{\parallel}$ = 0.5 GHz T = 65 K, κa = 0.43, $\Gamma_{\parallel}$ = 3.9 GHz T = 75 K, κa = 0.55, $\Gamma_{\parallel}$ = 9.2 GHz	$F_{\parallel}(\boldsymbol{K}, \omega)$: Eq. 4.131; $\Gamma_{\parallel} \sim (\kappa a)^z$ [cf. Eq. 4.134]; analysis yields z = 2.4(1) agreeing well with theory z = 2.47 for a percolating network
	x = 0.6 (T_N = 17 K): additional term $B_S \cdot \omega^{-0.35(6)}$ in scattering function $S(\omega) \sim I(\omega)$ [cf. Eq. 4.151]	[95I3]; the additional term is ascribed to anomalous spin diffusion
$\mathbf{K_2Ni_xZn_{1-x}F_4}$	x > x_p: Antiferromagnet, $\boldsymbol{M}_{\mathbf{subl}} \parallel \boldsymbol{c}$ (magn. order see Fig. 2.2)	
n-diffracion	x = 0.75, 0.85, 0.96: T_N = 62, 77, 92 K, resp.; FC scans through afm. Bragg refl. (0, 1, 0) at 4.5 K with $\boldsymbol{H}_{\mathbf{0}} \parallel \boldsymbol{c}$:	[84D2]; FC scans lead to a frozen-in nonequilibrium domain structure (random field effect)
	$I(\zeta_x, 1, 0)$ [$0 \le H_0 \le 9.8$ T] → order in the layers	$\zeta_x = q_x / a^*$; this order unexpectedly long-range
	$I(0, 1, \zeta_z)$ [$0 \le H_0 \le 0.7$ T] → order between the layers $\left.\begin{array}{lll} x = 0.85 & \nu = 0.73(2) & \kappa_{0z}^{-1} = 0.49(2)\ \text{nm} \\ x = 0.96 & \nu = 0.71(3) & \kappa_{0z}^{-1} = 1.14(16)\ \text{nm} \end{array}\right\}$ H_0 in T	$\zeta_z = q_z / c^*$; I fitted to Eq. 4.123 → $\kappa_z = \kappa_{0z} H_0^{\nu}$ (Eq. 2 of [84D2]); order along c broken up by H_{RF} (cf. Eq. 4.115b) and for H_0 = 0 by site-random fields (dilution)
$\mathbf{K_2Cu_xZn_{1-x}F_4}$	x > x_p: Ferromagnet, $\boldsymbol{M} \perp \boldsymbol{c}$ (magn. order see Fig. 3.27)	
1) el. + quasi-el. n-scatt.	x = 0.60: no magn. intensity at Bragg reflection (0, 0, 4); fm. Bragg rod (0, 0, 4.5) → $\kappa(T)$ [1 K ≤ T ≤ 4 K]	[79W3]; fit of $I(q)$ to Eq. 4.28; analysis of κ analogous to Eq. 4.109, see also [76B7]
2) meas. χ	x = 0.75 (T_C = 2.3 K): χ_{ac} [1 MHz ≤ f ≤ 200 MHz], [2.0 K ≤ T ≤ 3.5 K] → Cole-Cole plot (Eq. 4.143)	see Fig. 2 of [80H10}: two types of nearly semicircles, type 1: 2.05–2.65 K, type 2: 2.05–2.45 K
	x = 0.8 (T_C = 3.90 K): χ''_{ac} for f = 7 Hz [2.2 K ≤ T ≤ 6.5 K] and f = 300 Hz [4.5 K ≤ T ≤ 9 K]	[95B2]: evidence for a dilution-induced Griffiths instability in the temperature range $T_C(x) \le T \le T_C$ (x = 1)
3) EPR LW h.t.	0.1 ≤ x ≤ 1.0: $\Delta H_{EPR}(\psi)$ at 295 K; $\Delta H_{EPR}(x)$ for ψ = 0°, 55°, 90°; satellite line at 2ν (half-field EPR)	EPR at 10 GHz [83Y1, 83Y2]; $\Delta H_{EPR}(\psi)$ in accordance with Eq. 4.182 (x ≥ 0.26) and with Eq. 4.185 (x = 0.10); evidence for spin diffusion

Table 6. Data about Critical Behaviour *(continued)*

Compound	Critical exponents, critical amplitudes etc.	References, remarks
$(CH_3NH_3)_2Cu_{0.92}Cd_{0.08}Cl_4$	Ferromagnet, $\boldsymbol{M} \perp \boldsymbol{c}$ (magn. order see Fig. 3.27)	
meas. χ_{ac}	$\chi_{ac}(T)$ [1.2 MHz $\le f \le$ 173 MHz, $0 \le (T/T_C - 1) \le 0.09$] → Cole-Cole plot (Eq. 4.143)	[80O1]; Fif. 4.50: semicircle for $T/T_C > 1.08$, strong deviation from it closer to T_C (distribution of τ)
f) mixed magnets		
$Rb_2Cr_{1-x}Mn_xCl_4$	Mixed system with competing exchange interactions	
1) el. + quasi-el. n-scatt. and meas. χ	$T_C(x)$, $T_N(x)$ for various x: see Fig. 4.49 where the different types of magn. order are indicated; data widely scattered, probably because of a high degree of disorder	Fig. 4.49: n-scatt. [84M1, 86N3, 88H4, 88K8, 88S7, 88T2, 89S1, 92S7], meas. χ [88K8]; additional information: see [81M1, 82K6, 84K8, 86K12, 91S1]
2) el. + quasi-el. n-scatt.	x = 0.20: (easy-plane fm.): magnetic contribution to (0, 0, 4) Bragg refl. $\to I(T) \sim M^2(T) \to T_C = 45.3$ K, $\beta = 0.223$	[91S1]; analysis of exp. data with a 4D integration technique in $(\boldsymbol{q}, \omega)$ space [92S9]
	x = 0.75 (easy-plane afm.): afm. Bragg refl. (1, 0, 0) → $I(T) \sim M^2_{\text{subl}}(T) \to T_N = 34.3(5)$ K, $\beta = 0.52(10)$;	[88H4]; β close to the mean field value 0.5
	x = 0.75: afm. Bragg rod (1, 0, –0.392) $\to I(q) \to \kappa(T) \to$ fit $\kappa = \kappa_0 e^{-b/T} \to \kappa_0 / a^* = 0.48(4)$, $b = 132(10)$ K	fit of $I(q)$ to Eq. 4.28; $\kappa(T)$: see Fig. 3 of [88H4]; analysis and fit of κ: Eq.2 of [88H4]
3) el. + inel. n-scatt.	x = 0.20 (easy-plane fm.): fm. Bragg rod (0, 0, 1.4) → $I(\omega, q)$ → considerable widths $\Delta\omega$ and Δq below T_C (cf. Fig. 2 of [92S7])	[92S7]; analysis of the exp. data with a 4D integration technique [92S9]; results indicate: magn. order not long-ranged but limited in space and time
	x = 0.59 (spin glass behaviour): magn. Bragg rod (1, 0, 0.25) $\to I(\omega, q) \to \kappa(T), \Gamma(T) \to T_f = 11$ K	[86N3, 88S7]; $\Gamma \to 0 \mathrel{\hat=} T_f$ (spin glass freezing)
	x = 0.70 (easy-plan afm.): afm. Bragg refl. (1, 0, 0) → $I(T) \sim M^2_{\text{subl}}(T) \to T_N = 45$ K, $\beta = 0.5$	[88T2, 89S1]; β equal to the mean field value
	x = 0.70: afm. Bragg rod (1, 0, 0.28) $\to I(\omega, q) \to$ considerable widths $\Delta\omega$ and Δq below T_N (cf.Fig. 2 of [88T2])	below T_N: $\Delta\omega$ and Δq indicate a magn. order not long-ranged but limited in space and time
4) EPR LW	x = 0.5: $H_{\text{res}}(T)$, $\Delta H_{\text{EPR}}(T)$ [35 K $\le T \le$ 80 K], ZFC FC exp.	EPR at 9.008 GHz [83T7]; the results indicate spin glass behaviour
	x = 0.7, 0.9: $T_N = 45.2$ K for x = 0.9; $\Delta H_{\text{EPR}}(T)$ [45 K $\le T \le$ 90 K] for $\boldsymbol{H_0} \parallel \boldsymbol{c}$ and $\boldsymbol{H} \perp \boldsymbol{c}$	EPR at 9.008 GHz [84K6]; critical broadening of ΔH_{EPR} is for x = 0.7 less drastic than for x = 0.9

Table 6. Data about Critical Behaviour *(continued)*

Compound	Critical exponents, critical amplitudes etc.	References, remarks
$K_2Mn_{1-x}Fe_xF_4$	Mixed antiferromagnets with competing anisotropies	
1) el. + quasi-el. n-scatt. + meas. χ	several afm. Bragg refl.: $I(T) \sim M^2_{\text{subl}}(T) \rightarrow \beta$;	definitions → β: Eq. 4.20; θ_{Mn}, θ_{Fe}: Eq. 3.149b
	χ studied with respect to magnetic ordering	
	x = 0: $T_N = 42.14(2)$ K, $\beta = 0.15(2)$, $\theta_{\text{Mn}} = 0°$	[73B1]
	x = 0.008: $T_N = 41.5(10)$ K, $\theta_{\text{Mn}} = \theta_{\text{Fe}} = 0°$	[78B4]
	x = 0.019 $T_N = 40(1)$ K, $\theta_{\text{Mn}} = \theta_{\text{Fe}} = 0°$	[78B4]
	x = 0.022: $T_N = 40.5(1)$ K, $T_R = 16(2)$ K, $\beta = 0.19(1)$, $T > T_R$: $\theta_{\text{Mn}} = \theta_{\text{Fe}} = 0°$, $T < T_R$: $0° \le \theta_{\text{Mn}}, \theta_{\text{Fe}} \le 90°$, $\theta_{\text{Mn}} \neq \theta_{\text{Fe}}$	[77B8, 78B4, 78B10, 79B2, 86F5]
	multicritical point: $x_{\text{C.P.}} = 0.026$, $T_{\text{C.P.}} = 36$ K	[86F5]
	x = 0.028: $T_N = 36.91(5)$ K, $T_R = 19(2)$ K, $\beta = 0.27(2)$, $T > T_R$: $\theta_{\text{Mn}} = \theta_{\text{Fe}} = 90°$, $T < T_R$: $0° \le \theta_{\text{Mn}}, \theta_{\text{Fe}} \le 90°$, $\theta_{\text{Mn}} \neq \theta_{\text{Fe}}$	[77B8, 78B4, 78B10]
	x = 0.061: $T_N = 42.30(5)$ K, $\beta = 0.26(2)$, $\theta_{\text{Mn}} = \theta_{\text{Fe}} = 90°$	[77B8, 78B4, 78B10]
	x = 0.125: $T_N = 44.0(1)$ K, $\beta = 0.21(2)$, $\theta_{\text{Mn}} = \theta_{\text{Fe}} = 90°$	[77B8, 78B4, 78B10]
	x = 1.0: $T_N = 63.0(3)$ K, $\beta = 0.15(2)$, $\theta_{\text{Fe}} = 90°$	[82T1]
2) n-diffraction	x = 0.022: afm. Bragg refl. (0, 1, 0) → $I(T)$, ZFC and FC exp. → history-dependent magn. order	[79B2, 86F5]; random field effects due to the disorder in this mixed antiferromagnetic system
3) EPR LW	$T > T_N$: $\Delta H_{\text{EPR}}(T) \rightarrow$ power law (Eq. 4.165)	EPR at 24 GHz [84V4]; fit of $\Delta H_{\text{EPR}}(T)$ to Eq. 4.165
	x = 0.001 $\boldsymbol{H_0} \parallel \boldsymbol{c}$: p = 2.3(2), p = 1.4(3) $\boldsymbol{H_0} \perp \boldsymbol{c}$: p = 2.2(2), p = 1.5(3) $\}$ $t_{\text{CH}} \approx 0.2$	$T_N = 41.0(5)$ K; 1st value of p: $t > t_{\text{CH}}$, 2nd value of p: $t < t_{\text{CH}}$ (cf. Eqs. 4.190a, 4.190b)
	x = 0.007 $\boldsymbol{H_0} \parallel \boldsymbol{c}$: p = 2.2(3), p = 1.3(2) $\boldsymbol{H_0} \perp \boldsymbol{c}$: p = 2.2(3), p = 1.5(2) $\}$ $t_{\text{CH}} \approx 0.5$	$T_N = 40.5(5)$ K; further explanations see above
	x = 0.015 $\boldsymbol{H_0} \parallel \boldsymbol{c}$: p = 2.4(3), p = 1.3(2) $\boldsymbol{H_0} \perp \boldsymbol{c}$: p = 2.4(3), p = 1.4(2) $\}$ $t_{\text{CH}} \approx 0.8$	$T_N = 34(2)$ K; further explanations see above
	x = 0.018 $\boldsymbol{H_0} \parallel \boldsymbol{c}$: p = 1.4(2) $\boldsymbol{H_0} \perp \boldsymbol{c}$: p = 1.4(2) $\}$ $t < 0.75$	$T_N = 34(1)$ K; further explanations see above
	x = 0.001, 0.007, 0.015; $T = 293$ K (h.t.): $\Delta H_{\text{EPR}}(\psi)$ and $\Delta H_{\text{EPR}}(x)$ for $\psi = 54.7°$, see Fig. 4.69 or Fig. 2 of [84V4]	EPR at 24 GHz [84V4]; fit of $\Delta H_{\text{EPR}}(\psi)$ to Eq. 4.182, $\Delta H_{\text{EPR}}(x)$ is in accordance with Eq. 4.189

Table 6. Data about Critical Behaviour *(continued)*

Compound	Critical exponents, critical amplitudes etc.	References, remarks
$K_2Mn_xCo_{1-x}F_4$	Mixed antiferromagnets, $\boldsymbol{M}_{\mathbf{subl}} \parallel \boldsymbol{c}$ (magn. order see Fig. 2.2)	
1) el. + quasi-el. n-scatt.	x = 0.98: several afm. Bragg refl.: $I(T) \sim M^2_{\mathrm{subl}}(T)$ $\rightarrow T_N = 44$ K, $\beta = 0.16(2)$; preferred spin direction: $\parallel c$	[78B4]; β: Eq. 4.20
2) EPR LW	$T > T_N$: $\Delta H_{\mathrm{EPR}}(T) \rightarrow$ power law (Eq. 4.165)	EPR at 24 GHz [84V4]; fit of $\Delta H_{\mathrm{EPR}}(T)$ to Eq. 4.165
	x = 0.992 $\boldsymbol{H_0} \parallel \boldsymbol{c}$: p = 2.4(3), p = 1.4(2) $\boldsymbol{H_0} \perp \boldsymbol{c}$: p = 3.0(3), p = 1.5(3) } $t_{\mathrm{CH}} \approx 0.8$	$T_N = 45(1)$ K; 1st value of p: $t > t_{\mathrm{CH}}$, 2nd value of p: $t < t_{\mathrm{CH}}$ (cf. Eqs. 4.190a, 4.190b)
$K_2Mn_xNi_{1-x}F_4$	Mixed antiferromagnets, $\boldsymbol{M}_{\mathbf{subl}} \parallel \boldsymbol{c}$ (magn. order see Fig. 2.2)	
1) NMR	x ≈ 0.01, x ≈ 0.99: $^{19}F_I$-NMR $\rightarrow T_1^{\mathrm{Ni}}(T)$ in K_2NiF_4 [$2\ \mathrm{K} \le T \le 30\ \mathrm{K}$] and $T_1^{\mathrm{Ni}}(T)$ in K_2MnF_4 [$2\ \mathrm{K} \le T \le 20\ \mathrm{K}$]	[83V1]; study of T_1 of the impurities yields information about their spin autocorrelation
2) EPR LW	$T > T_N$: $\Delta H_{\mathrm{EPR}}(T) \rightarrow$ power law (Eq. 4.165)	EPR at 24 GHz [84V4]; fit of $\Delta H_{\mathrm{EPR}}(T)$ to Eq. 4.165
	x = 0.98 $\boldsymbol{H_0} \parallel \boldsymbol{c}$: p = 2.5(2), $\boldsymbol{H_0} \perp \boldsymbol{c}$: p = 2.5(2) } no change of slope in the log-log plot	$T_N = 44(1)$ K; 1st value of p: $t > t_{\mathrm{CH}}$, 2nd value of p: $t < t_{\mathrm{CH}}$ (cf. Eqs. 4.190a, 4.190b)
	x = 0.90 $\boldsymbol{H_0} \parallel \boldsymbol{c}$: p = 2.5(2), $\boldsymbol{H_0} \perp \boldsymbol{c}$: p = 2.5(2) } no change of slope in the log-log plot	$T_N = 47(1)$ K; further explanations see above
	x = 0.875 $\boldsymbol{H_0} \parallel \boldsymbol{c}$: p = 2.5(2), p = 1.5(3) $\boldsymbol{H_0} \perp \boldsymbol{c}$: p = 2.5(2), p = 1.5(3) } $t_{\mathrm{CH}} \approx 0.2$	$T_N = 49(1)$ K; further explanations see above
	x = 0.875, 0.90, 0.98; $T = 293$ K (h.t.): $\Delta H_{\mathrm{EPR}}(\psi)$ and $\Delta H_{\mathrm{EPR}}(\mathrm{x})$ for $\psi = 54.7°$, see Fig. 6 of [84V4]	EPR at 24 GHz [84V4]; fit of $\Delta H_{\mathrm{EPR}}(\psi)$ to Eq. 4.182, $\Delta H_{\mathrm{EPR}}(\mathrm{x})$ is in accordance with Eq. 4.189
$Rb_2Mn_{0.5}Ni_{0.5}F_4$	Mixed antiferromagnets, $\boldsymbol{M}_{\mathbf{subl}} \parallel \boldsymbol{c}$ (magn. order see Fig. 2.2)	
el. + quasi-el. n-scatt.	afm. Bragg refl. (1, 0, 0.5): $I(T) \sim M^2_{\mathrm{subl}}(T)$ $\rightarrow T_N = 68.72$ K, $\beta = 0.16(1)$ [$34.4\ \mathrm{K} \le T \le T_N$]	[76A3, 77B2, 77S1]; β: Eq. 4.20
	scans across afm. Bragg rod (1, 0, 0.4) $\rightarrow \gamma = 1.60(15)$, $\nu = 0.9(1)$, $\eta = 0.20(5)$, $\kappa_0^+ / a^* = 0.126$, $\kappa_\perp^- / a^* = 0.035$	[77B2, 77S1]; γ, ν, η, κ_0^+, $\kappa_\perp^-$: Eqs. 4.26, 4.28, 4.32, 4.32a, 4.35; separation of $\chi_\parallel$ and $\chi_\perp$: see Sect. 4.1.5

Table 6. Data about Critical Behaviour *(continued)*

Compound	Critical exponents, critical amplitudes etc.	References, remarks
$K_2Mn_xCu_{1-x}F_4$	Mixed system with competing exchange interactions	
LMB	$d(\Delta n)/dT$: contributions from Mn-Mn, Cu-Cu, Mn-Cu pairs	[88J2]
	$x \le 0.23$, at low T: anomaly of $d(\Delta n)/dT \rightarrow T_C$	mainly contributions from Cu-Cu pairs
	$x \ge 0.23$: broad maximum of $d(\Delta n)/dT$ near 85 K	Schottky anomaly, mostly contributions from Mn-Cu pairs
	$x \ge 0.62$: sharp peak of $d(\Delta n)/dT \rightarrow T_N$	mainly contributions from Mn-Mn pairs
$(C_2H_5NH_3)_2Mn_{1-x}Cu_xCl_4$	Mixed antiferromagnets	
EPR LW	$x = 0, 0.03, 0.08, 0.30$: $\Delta H_{EPR}(T)$ for $\psi = 0°$, $\psi = 55°$ $[30\text{ K} \le T \le 295\text{ K}]$ and $\Delta H_{EPR}(\psi)$ at $T = 295$ K	EPR at 10 GHz [88T1]; $\Delta H_{EPR}(T)$ and $\Delta H_{EPR}(\psi)$ are in accordance with Eqs. 4.164 and 4.182, resp.
$K_2Fe_{1-x}Co_xF_4$	Mixed antiferromagnets with competing anisotropies	
1) el. + quasi-el. n-scatt	afm. Bragg refl. (1, 0, 0): $I(T) \sim M_{subl}^2(T)$	definitions → β: Eq. 4.20; θ_{Fe}, θ_{Co}: Eq. 3.149b
and also	afm. Bragg rod (1, 0, 0.4): $I(q) \rightarrow \chi(q)$	γ, ν: Eqs. 4.26, 4.28, 4.32, 4.32a
Mössbauer study, ^{19}F-NMR	$H_{hf}(T) \sim M_{subl}(T)$, $f_{NMR}(T) \sim M_{subl}(T)$	determination of $\theta_{Fe} = \angle(\boldsymbol{H}_{\mathbf{hf}}, c\text{-axis})$
	$x = 0$: $T_N = 63.0(3)$ K, $\beta = 0.15(1)$, $\theta_{Fe} = 90°$	[82T1]: n-scattering; [78T2]: Mössbauer study
	$x = 0.12$: $T_N = 60.6(5)$ K, $\beta = 0.16$, $\theta_{Fe} = \theta_{Co} = 90°$	[86V1]: n-scattering; [88V2]: ^{19}F-NMR study
	$x = 0.18$: $T_N = 57(2)$ K, $\theta_{Fe} = \theta_{Co} = 90°$	[86V2, 88V2]: ^{19}F-NMR study
	multicritical point: $x_{C.P.} = 0.22$, $T_{C.P.} = 57$ K	[86V1]: n-scattering
	$x = 0.27$: $T_N = 64.4(6)$ K, $T_R = 27(2)$ K, $\beta = 0.25(2)$, $T > T_R$: $\theta_{Fe} = \theta_{Co} = 0°$, $T < T_R$: $0° \le \theta_{Fe}, \theta_{Co} \le 90°$, $\theta_{Fe} \ne \theta_{Co}$	[83V3, 86V1]: n-scattering; [85V3]: Mössbauer study; $x \approx 0.2$ data of [84H3] are similar to the $x = 0.27$ data
	$x = 0.55$: $T_N = 89.6(1)$ K, $\beta = 0.13(2)$ $\theta_{Fe} = \theta_{Co} = 0°$ from rod scans: $\gamma = 1.5(3)$, $\nu = 0.7(2)$	[86V1]: n–scattering; [85V3]: Mössbauer study
	$x = 0.60$: $T_N = 92.2(1)$ K, $\theta_{Fe} = \theta_{Co} = 0°$	[84H3]: n-scattering
	$x = 0.70$: $T_N = 97(1)$ K, $\theta_{Fe} = \theta_{Co} = 0°$	[85V3]: Mössbauer study
	$x = 1.0$: $T_N = 107.85(5)$ K, $\beta = 0.123(8)$, $\theta_{Co} = 0°$	[74I1, 74I2]: n-scattering
2) n-diffraction	$x = 0.27$: FC scans through afm. Bragg refl. (1, 0, 0) at 5 K and 45 K with $\boldsymbol{H_0} \parallel \boldsymbol{c}$ $[0 \le H_0 \le 3\text{ T}]$	[84V7]; FC scans lead to frozen-in nonequilibrium domain structure (random field effects)
	$I(1, 0, \zeta_z) \rightarrow$ order between the layers $\rightarrow I \sim (q_z^2 + \kappa_z^2)^{-1}$ $\sim H_0^{-\gamma} \rightarrow \gamma = 1.3(2)$, $\kappa_z \sim H_0^{\nu} \rightarrow \nu = 0.7(2)$	$\zeta_z = q_z / c^*$; order along c broken up by H_{RF} (cf. Eq. 4.115b); details of the analysis in [84V7]

Table 6. Data about Critical Behaviour *(continued)*

Compound	Critical exponents, critical amplitudes etc.	References, remarks
$Rb_2Fe_xCo_{1-x}F_4$	Mixed antiferromagnets with competing anisotropies	
1) Mössbauer study	$H_{hf}(T) \sim M_{subl}(T) \to T_N(x)$, $\theta_{Fe}(x)$	[84H4]; $\theta_{Fe} = \angle(\boldsymbol{H}_{\mathbf{hf}}, c\text{-axis})$
	x = 0.02 $T_N = 102$ K $\theta_{Fe} = 0°$ x = 0.35 $T_N = 85$ K $\theta_{Fe} = 10(1)°$	these data provide the (T_N, x) phase diagram, see Fig. 6 of [84H4]
	x = 0.58 $T_N = 74$ K $\theta_{Fe} = 12(1)°$	
	x = 0.81 $T_N = 53$ K $\theta_{Fe} = —$	broad distribution of θ_{Fe}, see Fig. 2 of [84H4]
	x = 0.89 $T_N = 50$ K $\theta_{Fe} = 86(1)°$	
	x = 0.93 $T_N = 53$ K $\theta_{Fe} = 90(1)°$	
	x = 1.00 $T_N = 57$ K $\theta_{Fe} = 90°$	
2) (T_N, x) phase diagram	model calculation, datails see Table 5	[77M5, 78O3, 84H4]; modal results: see Fig. 7 of [84H4]
$Rb_2Co_xNi_{1-x}F_4$	Mixed antiferromagnets, $\boldsymbol{M}_{\mathbf{subl}} \parallel \boldsymbol{c}$ (magn. order see Fig. 2.2)	
1) C_{magn}	symm. log. singularity at T_N	sharp phase transition
	x = 0.50: $T_N = 114.8$ K, $A^+ = 2.10$, $A^- = 2.04$ x = 0.65: $T_N = 112.9$ K, $A^+ = 1.53$, $A^- = 1.68$ x = 0.80: $T_N = 111.9$ K, $A^+ = 2.06$, $A^- = 2.12$	C_p by ac cal. [81I3]; fit of the experimental data for C_p to Eq. 4.17 with the constraint $D^+ = D^-$
2) el. + quasi-el. n-scatt.	x = 0.5: afm. Bragg refl. (1, 0, 0) with $I(T) \sim M^2_{subl}(T)$ $\to \beta = 0.125(5)$ [$0.03 \le t \le 0.1$]	[81I3]; $T_N = 114.8$ K; β: Eq. 4.20
	afm. Bragg rod (1, 0, –0.51): [$0.01 \le t \le 0.25$] $\to \gamma = 1.67(13)$, $\nu = 0.98(6)$, $\eta = 0.2(1)$, $\kappa_0^+ / a^* = 0.35(2)$	[81I3]; γ, ν, η, κ_0^+ : Eqs. 4.26, 4.28, 4.32, 4.32a
$Rb_2Co_xCu_{1-x}F_4$	Mixed system with competing exchange interactions	
1) el. + quasi-el. n-scatt. and meas. χ	$T_C(x)$, $T_N(x)$ for various x: see Fig. 3.72 in Sect. 3.3.6, where the different types of magn. order are indicated	[88D1, 88D11, 92S1, 92S8], datails of magn. phase diagram in Table 5 and Sect. 3.3.6
2) meas. M	x = 0.218 (spin glass): $M(H_0, T)$ for $\boldsymbol{H}_{\mathbf{0}} \parallel \boldsymbol{c}$, FC exp., [$1.5\ \text{K} \le T \le 4.5$ K, $0.1\ \text{mT} \le H_0 \le 1$ T], cf. Fig. 4.42	[88D7, 88D8, 88D10]; vibrating sample magnetometer, all data corrected for demagnetization
	$\chi = M/H_0$ (Fig. 4.43) $\to \chi_{nl} \to a_3(T)$, $a_5(T)$ [Fig. 4.44] $\to \gamma + \beta = 9.0(5)$, $\gamma = 4.5(2)$ $\beta = 0.0(7)$ ($T_C \equiv 0$)	analysis for M, χ and χ_{nl} by means of Eqs. 4.124–4.126, scaling relation Eq. 4.127 (Fig. 3 of [88D7])

Table 6. Data about Critical Behaviour *(continued)*

Compound	Critical exponents, critical amplitudes etc.	References, remarks
$Rb_2Co_xCu_{1-x}F_4$ (cont.)		
3) meas. χ_{ac}	x = 0.110 (easy-axis fm.):	
	$\chi'_{ac}(T)$ [$2\ K \le T \le 8\ K, f = 3.53$ kHz], in a dc-field $\boldsymbol{H_0} \parallel \boldsymbol{c}$ [$0 \le H_0 \le 0.2$ T] superimposed to the ac-field → $T_C = 4.95(5)$ K , $\beta = 0.1(5)$, $\gamma = 1.5(3)$	[88D1, 88D11]; determ. β and γ from scaling plot $\chi'_{ac} \cdot H_0^{\gamma/\Delta}$ versus $H_0/\lvert t\rvert^{\Delta}$ (Eq. 4.12b) so that all data collapse on a single curve
	x = 0.218 (spin glass): $\chi'_{ac}(\omega,T)$, $\chi''_{ac}(\omega,T)$ [$1\ K \le T \le 7$ K, 0.3 Hz $\le f \le$ 50 kHz] (cf. Figs. 4.45, 4.51), corrected for demagnetization	[88D9, 88D11, 89D3, 90M]; $\omega = 2\pi f$; demagnetization correction: Eq. 3.94b; maximum of $\chi'_{ac}(\omega)\ \hat{=}\ T_f(\omega)$
	Cole-Cole equation: $\alpha = 0.900(2)$ at 3.50 K, $\alpha = 0.848(5)$ at 6.00 K → $\tau_c(T)$: see Fig. 4.52	Cole-Cole equ.: Eq. 4.144; Cole-Cole plot: Eq. 4.145 $\alpha \approx 0.9\ \hat{=}$ wide-spread distribution $g(\tau)$ [Fig. 4.53]
	$\tau_c \to \psi\nu = 2.2(2)$, $\tau_0 = (2 \pm 1)\cdot 10^{-13}$ s, $b = 10.8(6)$ K with $\nu = 2.3(4) \to \psi = 0.9(2)$, $\theta = -\nu^{-1} = -0.43(7)$	fit of τ_c to Eq. 4.147 in the range $3.7\ K \le T \le 6.8$ K; activated dynamics: Eqs. 4.146 and 4.147
	scaling plot $\chi''_{ac} \cdot T^{-q}$ vs. $[-\ln(\omega\tau_0) \cdot T^{\psi\nu}] \to \tau_0 = 10^{-13(1)}$ s $q = -3.0(5)$, $\psi\nu = 2.2(3) \to \gamma = 4.2(6)$, $\nu = 2.3(4)$, $\psi = 0.9(2)$	[88D8], activated dynamics scaling relation Eq. 4.128; scaling plot: Fig. 4.46; analysis with $\eta = 0.2(2)$
4) time evolution	x = 0.11 (fm.), x = 0.22, 0.33 (spin glass): $\chi'_{ac}(\omega,\ t)$, $\chi''_{ac}(\omega,\ t)$ [0.01 Hz $\le f \le$ 56 Hz], rapid cooling:	[93S2, 93S3, 95V]; ordering kinetics, aging; $\omega = 2\pi f$
	$\left.\begin{array}{ll} x = 0.11 & T \approx 9\ K \to T = 3.9\ K\ (< T_C) \\ x = 0.22 & T \approx 9\ K \to T = 3.2\ K\ (< T_f) \\ x = 0.33 & T \approx 9\ K \to T = 3.7\ K\ (< T_f) \end{array}\right\}$ within ≈ 45 s both, $\chi'_{ac}(\omega,\ t)$, $\chi''_{ac}(\omega,\ t)$, yield	$t\ \hat{=}$ time after the quench [$10\ s \le t \le 10^4$ s]; long relaxation times correspond to a domain growth $R(t) \sim [T \ln(t/\tau_0)]^{1/\psi}$ (Eq. 4.149)
	for x = 0.11 $(d-\theta)/\psi = 5.0(9)$ and $\psi = 0.20(5)$ x = 0.22 $(d-\theta)/\psi = 2.4(2)$ and $\psi = 0.93(10)$ x = 0.33 $(d-\theta)/\psi = 2.1(2)$ and $\psi = 1.06(10)$	exp. data of χ'_{ac} and χ''_{ac} fitted to Eq. 4.150 for various f $(\tau_0 = 1/\omega_0 = 2\cdot 10^{-13}$ s) → $((d-\theta)/\psi$; $\theta = 1$ for fm. and $\theta = -0.25$ for spin glass

Table 6. Data about Critical Behaviour *(continued)*

Compound	Critical exponents, critical amplitudes etc.	References, remarks
Rb$_2$Co$_x$Cu$_{1-x}$F$_4$ (cont.) 5) el. + quasi-el. n-scatt.	x = 0.037 (oblique fm.): fm. Bragg rod (0, 0, 1.7) $I(q) \rightarrow \chi_\perp(q, T) \rightarrow \kappa(T)$ [2 K ≤ T ≤ 11 K], → KT-theory [5 K ≤ T ≤ 11 K], const. [T < 3.3 K], $\kappa / a^* = 0.03$	[92S8]; $\chi_\perp(T)$ and $\kappa(T)$: see Fig. 2 of [92S8]; KT-theory = Kosterlitz-Thouless theory: χ (Eq. 4.44) $\xi = \kappa^{-1}$ (Eq. 4.43); fit result: b = 2.20(25)
	x = 0.88 (easy-axis afm.): afm. Bragg refl. (1, 0, 1) $I(T) \sim M^2_{\text{subl}}(T) \rightarrow T_N = 88.1(1)$ K, β = 0.16(4)	[94S4, 95S2], see also [92S1]: β: Eq. 4.20
	x = 0.88: several afm. Bragg rods → $I(q) \rightarrow \kappa \rightarrow \gamma = 1.5(2)$, $\nu = 1.02(4)$, $\kappa_0^+ / a^* = 0.34(3)$, $\kappa_1 / a^* = 0.011(2)$	fit of $I(q)$ to Eq. 4.29; γ, ν, κ_0^+, κ_1: Eq. 4.129 and 4.130 (κ_1 results from disorder phenomena)
	x = 0.88: afm. Bragg refl. (1, 0, l) [l = 0. 1, 2] → $I(1, 0, \zeta_z)$ $\rightarrow \kappa_z / c^* = 0.06 \mathrel{\hat{=}} \xi_z / c = 2.65$ at T = 13 K	$I(1, 0, \zeta_z) \mathrel{\hat{=}} I(q_z)$ to Eq. 4.123 → κ_z; predominantly 2D order: $\xi_{\text{in-plane}} >> \xi_z$
II. Structural Phase Transitions		
a) Fluorides no data about critical properties at structural phase transitions		
b) Chlorides, Bromides, Iodides with inorganic A$^+$-ions no data about critical properties at structural phase transitions		
c) Chlorides and Bromides with organic A$^+$-ions		
(CH$_3$NH$_3$)$_2$MnCl$_4$	THT ← T_{Cl} (cont. pt.) → ORT	complete sequence of struct. phase transitions: Table 4
linear birefringence	Δn, T_{C1} = 394.81 K → β = 0.337(5) [0.001 ≤ | t | ≤ 0.02]	[81K1], see also [74K1]; exp. data fitted to Eq. 4.84
(CD$_3$ND$_3$)$_2$MnCl$_4$	THT ← T_{Cl} (cont. pt.) → ORT	complete sequence of struct. phase transitions: Table 4
el. + quasi-el. n-scatt.	superreflection (3, 0, 2): $I \sim (-t_1)^{2\beta}$, T_{C1} = 389.6 K → β = 0.33(6) [0.002 ≤ | t_1 | ≤ 0.13]	[78L1]; exp. data below T_{C1} fitted to Eq. 4.83
(C$_2$H$_5$NH$_3$)$_2$MnCl$_4$	THT ← T_{C1} (cont. pt.) → ORT ← T_{C2} (disc. pt.) → OLT	complete sequence of struct. phase transitions: Table 4
linear birefringence	Δn, T_{C1} = 424.39 K → β = 0.283(5) [0.001 ≤ | t_1 | ≤ 0.02] T_{C2} = 226.4 K → β = 0.303(10) [0.0008 ≤ | t_2 | ≤ 0.006]	[81K1], see also n-scattering data in [86A1]; exp. data below T_{C1} and below T_{C2} fitted to Eq. 4.84

Table 6. Data about Critical Behaviour *(continued)*

Compound	Critical exponents, critical amplitudes etc.	References, remarks
$(CH_3NH_3)_2FeCl_4$	THT ← T_{C1} (cont. pt.) → ORT	complete sequence of struct. phase transitions: Table 4
1) specific heat anomaly	ΔC_p, $T_{C1} = 332.45$ K $[-0.1 \le t_1 \le -0.0003,\ 0.00035 \le t_1 \le 0.01]$ $\rightarrow A^+ = 0.675,\ A^- = 0.670,\ A^+/A^- = 1.008,$ $D^+ = 3.45,\ D^- = 5.03$	[82G1], C_p by high-resolution ac cal. exp. data $\Delta C_p = C_p - C_{p,0}$ (background subtracted) above and below T_{C1} fitted to Eq. 4.81
2) linear birefringence	Δn, $T_{C1} = 328$ K $\rightarrow \beta = 0.318(6)$ $[0.0045 \le \lvert t_1 \rvert \le 0.26]$	[74K1]; exp. data below T_{C1} fitted to Eq. 4.84
3) elastic compliance	S_{66}, $T_{C1} = 332.65$ K $\rightarrow \rho = 0.42,\ \phi = 1.21$ $[0.003 \le t_1 \le 0.2]$ $S_{66}^0 = 1.28 \cdot 10^{-10}$ Pa^{-1}, $S_{66}^+ = 1.068 \cdot 10^{-11}$ Pa^{-1}	[82G1], S_{66} from sound velocity measurements; exp. data above T_{C1} fitted to Eq. 4.86; ϕ: Eq. 4.87a ($\alpha = 0$)
4) sound attenuation	α measured for $[5\ \text{MHz} \le (\omega/2\pi) \le 70\ \text{MHz}]$, $T_{C1} = 332.6(2)$ K $\rightarrow \tilde{\rho} = 1.82(10)$ $[0.001 \le t_1 \le 0.5]$ $\tau \rightarrow z\nu = 1.40$ $[0.001 \le t_1 \le 0.5]$, $\tau_0^+ = 9.21 \cdot 10^{-15}$ s	[82Y2] exp. data above T_{C1} fitted to Eq. 4.137 τ: Eq. 4.136; exp. data above T_{C1} fitted to Eq. 4.138
$(C_2H_5NH_3)_2FeCl_4$	THT ← T_{C1} (cont. pt.) → ORT ← T_{C2} (cont. pt.) → OLT	complete sequence of struct. phase transitions: Table 4
1) specific heat anomaly	C_p, $T_{C1} = 377.49$ K $[-0.03 \le t_1 \le -0.0015,\ 0.002 \le t_1 \le 0.007]$ $\rightarrow A^+ = 0.705,\ A^- = 0.740,\ A^+/A^- = 0.95,$ $D^+ = 43.59,\ D^- = 45.01,\ E = 34.68$	[84Y1], C_p by high-resolution ac cal. exp. data above and below T_{C1} fitted to Eq. 4.82a
	C_p, $T_{C2} = 203.35$ K $[-0.05 \le t_2 \le -0.005,\ 0.003 \le t_2 \le 0.4]$ $\rightarrow A^+ = 0.399,\ A^- = 1.720,\ A^+/A^- = 0.232,$ $D^+ = 34.36,\ D^- = 33.16,\ E = 15.36$	[84Y1], C_p by high-resolution ac cal. exp. data above and below T_{C2} fitted to Eq. 4.82a
	C_p, $T_{C2} = 203.75$ K $[-0.3 \le t_1 \le 0.04,\ 0.003 \le t_1 \le 0.4]$ $\rightarrow \alpha^+ = 0.068,\ \alpha^- = 0.26;\ A^+ = 0.325,\ A^- = 0.945,$ $A^+/A^- = 0.344,\ D^+ = 29.58,\ D^- = 28.38,\ E = 15.39$	[84Y1], C_p by high-resolution ac cal. exp. data above and below T_{C2} fitted to Eq. 4.82b
2) elastic compliance	S_{66}, $T_{C1} = 379.0$ K $\rightarrow \rho = 0.38,\ \phi = 1.19$ $[0.025 \le t_1 \le 0.15]$ $S_{66}^0 = 2.0 \cdot 10^{-10}$ Pa^{-1}, $S_{66}^+ = 1.28 \cdot 10^{-11}$ Pa^{-1}	[83S1], S_{66} from sound velocity measurements; exp. data above T_{C1} fitted to Eq. 4.86; ϕ: Eq. 4.87a ($\alpha = 0$)
3) sound attenuation	α measured for $(\omega/2\pi) = 10, 30, 80$ MHz, $T_{C1} = 379.0$ K $\rightarrow \tilde{\rho} = 1.74(3)$ $[0.003 \le t_1 \le 0.05]$ $\tau \rightarrow z\nu = 1.33$ $[0.003 \le t_1 \le 0.05]$, $\tau_0^+ = 1.04 \cdot 10^{-13}$ s	[83S1] exp. data above T_{C1} fitted to Eq. 4.137 τ: Eq. 4.136; exp. data above T_{C1} fitted to Eq. 4.138

Table 6. Data about Critical Behaviour *(continued)*

Compound	Critical exponents, critical amplitudes etc.	References, remarks
$(CH_3NH_3)_2CuCl_4$ linear birefringence	Bbcm ← $T_{\rm C}$ (cont. pt.) → $P12_1/c1$ $T_{\rm C} = 348.50$ K, pt. slightly 1st order: $\Delta n(T_{\rm C}) = 1.09 \cdot 10^{-3}$ $\Delta n \sim \lvert t \rvert^{2\beta}$: $T_{\rm C} = 349.16$ K, $\beta = 0.173(5)$ $[0.001 \le \lvert t \rvert \le 0.015]$	complete sequence of struct. phase transitions: Table 4 [79K3], see also [77H1]; exp. data below $T_{\rm C}$ fitted to Eq. 4.84; diminution of β due to vicinity of TCP
$(C_2H_5NH_3)_2CuCl_4$ linear birefringence	Bbcm ← $T_{\rm C1}$ (cont. pt.) → $P\ 12_1/c1$ $T_{\rm C1} = 364.05$ K, pt. slightly 1st order: $\Delta n(T_{\rm C1}) = 7.5 \cdot 10^{-4}$ $\Delta n \sim \lvert t \rvert^{2\beta}$: $T_{\rm C1} = 365.23$ K, $\beta = 0.186(8)$ $[0.001 \le \lvert t \rvert \le 0.015]$	complete sequence of struct. phase transitions: Table 4 [79K3], see also [77H1]; exp. data below $T_{\rm C1}$ fitted to Eq. 4.84; diminution of β due to vicinity of TCP
d) Diammonium Compounds with X = Cl^-, Br^-		
$[NH_3(CH_2)_4NH_3]MnCl_4$ linear berefringence	OHT ← $T_{\rm C}$ (cont. pt.) → MRT Δn, $T_{\rm C} = 381.9(1)$ K → $\beta = 0.325$ $[0.0005 \le \lvert t \rvert \le 0.05]$	complete sequence of struct. phase transitions: Table 4 [81K3]; exp. data below $T_{\rm C}$ fitted to Eq. 4.84
$[ND_3(CH_2)_4ND_3]MnCl_4$ ^{2}D-NMR-NQR	same phase sequence as above, slightly different $T_{\rm C}$ $T_{\rm C} = 377$ K → $\beta = 0.34(2)$ $[0.006 \le \lvert t \rvert \le 0.03]$	[81K3]; exp. data below $T_{\rm C}$ fitted to Eq. 4.85
$[NH_3(CH_2)_3NH_3]CdCl_4$	OHT ← $T_{\rm C}$ (cont. pt.) → ORT $T_{\rm C} = 375$ K, no data about critical behaviour	complete sequence of struct. phase transitions: Table 4 [81K3]
$[ND_3(CH_2)_3ND_3]CdCl_4$ ^{2}D-NMR-NQR	same phase sequence as above, slightly different $T_{\rm C}$ $T_{\rm C} = 368.7(3)$ K → $\beta = 0.21(2)$ $[0.002 \le \lvert t \rvert \le 0.05]$	[81K3]; exp. data below $T_{\rm C}$ fitted to Eq. 4.85
$[NH_3(CH_2)_5NH_3]CdCl_4$	OHT ← $T_{\rm C2}$ (cont. pt.) → ORT $T_{\rm C} = 340$ K, no data about cririal behaviour	complete sequence of struct. phase transitions: Table 4 [81K3]
$[ND_3(CH_2)_5ND_3]CdCl_4$ ^{2}D-NMR-NQR	same phase sequence as above, slightly different $T_{\rm C2}$ $T_{\rm C} = 332.7(1)$ K → $\beta = 0.26$ $[0.001 \le \lvert t \rvert \le 0.1]$	[81K3]; exp. data below $T_{\rm C}$ fitted to Eq. 4.85

9.12.4.4 References for 9.12.4

30B Bloch, F.: Z. Phys. 61 (1930) 206.
44O Onsager, L.: Phys. Rev. 65 (1944) 117.
52Y Yang, C.N.: Phys. Rev. 85 (1952) 808.
53A Anderson, P.W., Weiss, P.R.: Rev. Mod. Phys. 25 (1953) 269.
54K Kubo, R., Tomita, K.: J. Phys. Soc. Jpn. 9 (1954) 888.
55N Nagamiya, T., Yosida, K., Kubo, R.: Adv. Phys. 4 (1955) 1.
58R3 Rushbrooke, G.S., Wood, P.J.: Mol. Phys. 1 (1958) 257.
61S Skyrme, T.H.R.: Proc. R. Soc. London 262 (1961) 237.
62L3 Lifshitz, I.M.: Sov. Phys. JETP 15 (1962) 939.
63K2 Kadanoff, L.P., Martin, P.C.: Ann. Phys. (N.Y.) 24 (1963) 419.
64F1 Fisher, M.E.: J. Math. Phys. 5 (1964) 944.
64F2 Fisher, M.E.: Am. J. Phys. 32 (1964) 343.
65B Bennett, H.S., Martin, P.C.: Phys. Rev. 138 (1965) A608.
66H1 Heller, P.: Phys. Rev. 146 (1966) 403.
66K Keffer, F.: Spin waves, in: Encyclopedia of Physics, Flügge, S. (ed.), Berlin: Springer-Verlag, 1966, Vol. XVIII/2, p. 249.
66M1 Mermin, N.D., Wagner, H.: Phys. Rev. Lett. 17 (1966) 1133.
66S2 Stanley, H.E., Kaplan, T.A.: Phys. Rev. Lett. 17 (1966) 913.
66W Wannier, G.H.: Statistical Physics, New York/London: John Wiley & Sons, 1966.
67B2 Baker, G.A., Gilbert, H.E., Eve, J., Rushbrooke, G.S.: Phys. Lett. 25A (1967) 207.
67D Dalton, N.W., Wood, D.W.: Proc. Phys. Soc. 90 (1967) 459.
67F1 Fisher, M.E.: Rep. Prog. Phys. 30 (1967) 615.
67F2 Fisher, M.E., Burford, R.J.: Phys. Rev. 156 (1967) 583.
67H1 Hohenberg, P.C.: Phys. Rev. 158 (1967) 383.
67H2 Heller, P.: Rep. Prog. Phys. 30 (1967) 731.
67K1 Kadanoff, L.P., Götze, W., Hamblen, D., Hecht, R., Lewis, E.A.S., Palciauskas, V.V., Rayl, M., Swift, J., Aspnes, D., Kane, J.: Rev. Mod. Phys. 35 (1967) 395.
67K2 Koppen, J., Hamersma, R., Lebesque, J.V., Miedema, A.R.: Phys. Lett. 25A (1967) 376.
68K Kawasaki, K.: Progr. Theor. Phys. 39 (1968) 285.
68M2 Marshall, W., Lowde, R.D.: Rep. Prog. Phys. 31 (1968) 705.
68M3 Mermin, N.D.: Phys. Rev. 176 (1968) 250.
68S2 Stanley, H.E.: Phys. Rev. Lett. 20 (1968) 589.
68S3 Seehra, M.S., Castner, T.G.: Phys. Condens. Mater. 7 (1968) 185.
68V de Vries, G., Breed, D.J., Maarschall, E.P., Miedema, A.R.: J. Appl. Phys. 39 (1968) 1207.
69B2 Birgeneau, R.J., Guggenheim, H.J., Shirane, G.: Phys. Rev. Lett. 22 (1969) 720.
69G2 Griffiths, R.B.: Phys. Rev. Lett. 23 (1969) 17.
69H1 Halperin, B.I., Hohenberg, P.C.: Phys. Rev. 177 (1969) 952.
69H2 Halperin, B.I., Hohenberg, P.C.: Phys. Rev. 188 (1969) 898.
69L3 Larkin, A.I., Pikin, S.A.: Sov. Phys. JETP 29 (1969) 891.
69M3 Maarschall, E.P., Botterman, A.C., Vega, S., Miedema, A.R.: Physica 41 (1969) 473.
70B1 Birgeneau, R.J., Guggenheim, H.J., Shirane, G.: Phys. Rev. B 1 (1970) 2211.
70B3 Birgeneau, R.J., Skalyo, J., Shirane, G.: J. Appl. Phys. 41 (1970) 1303.
71B1 Birgeneau, R.J., Skalyo, J., Shirane, G.: Phys. Rev. B 3 (1971) 1736.
71B2 Boucher, J.P.: Phys. Rev. B 4 (1971) 3819.
71B3 Berezinskii, V.L.: Sov. Phys. JETP 32 (1971) 493.
71B4 Boesch, H.R., Schmocker, U., Waldner, F., Emerson, K.: Phys. Lett. 36A (1971) 461.
71B5 Bloembergen P., Tan, K.G., Lefevre, F.H.J., Bleyendaal, A.H.M.: J. Phys. (France) 32 (1971) C1-878.
71C4 Castner, T.G., Seehra, M.S.: Phys. Rev. B 4 (1971) 38.

71J3 de Jongh, L.J., van Amstel, W.D., Miedema, A.R.: 1st European Conf. on Condensed Matter, Geneva 1971, Summaries p. 44.
71M1 Mostafa, M.F., Willett, R.D.: Phys. Rev. B 4 (1971) 2213.
71M2 Marshall, W., Lovesey, S.W.: Theory of Thermal Neutron Scattering, Oxford: Clarendon Press, 1971.
71S1 Stanley, H.E.: Introduction to Phase Transitions and Critical Phenomena, Oxford: Clarendon Press, 1971.
71S2 Salamon, M.B., Hatta, I.: Phys. Lett. 36A (1971) 85.
71S3 Shante, V.K.S., Kirkpatrick, S.: Adv. Phys. 20 (1971) 325.
71Y1 Yokozawa, Y.: J. Phys. Soc. Jpn. 31 (1971) 1590.
72B3 Bucci, C., Guidi, G., Vignali, C.: Solid State Commun. 10 (1972) 803.
72B4 Berezinskii, V.L.: Sov. Phys. JETP 34 (1972) 610.
72B5 Bloembergen, P., Franse, J.J.M.: Solid State Commun. 10 (1972) 325.
72B6 Boesch, H.: Ph.D. Thesis, University of Zürich (Switzerland) 1972.
72D Drumheller, J.E., Dickey, D.H., Reklis, R.P., Zaspel, C.E., Glass, S.J.: Phys. Rev. B 5 (1972) 4631.
72E Essam, J.W.: Percolation and cluster size, in: Phase Transitions and Critical Phenomena, Domb, C., Green, M.S. (eds.), London/New York: Academic Press, 1972, Vol. 2, p. 197.
72G2 Gulley, J.E., Jaccarino, V.: Phys. Rev. B 6 (1972) 58.
72H2 Hirakawa, K., Ikeda, H.: J. Phys. Soc. Jpn. 33 (1972) 1483.
72H3 Huber, D.L.: Phys. Rev. B 6 (1972) 3180.
72I Ikeda, H., Hirakawa, K.: J. Phys. Soc. Jpn. 33 (1972) 393.
72J4 de Jongh, L.J., van Amstel, W.D., Miedema, A.R.: Physica 58 (1972) 277.
72K Krasnow, R., Harbus, F., Liu, L.L., Stanley, H.E.: Phys. Rev. B 7 (1972) 370.
72L1 Liu, L., Stanley, H.E.: Phys. Rev. Lett. 29 (1972) 927.
72L2 Liu, L., Stanley, H.E.: Phys. Lett. 40A (1972) 272.
72S1 Stauffer, D., Ferer, M., Wortis, M.: Phys. Rev. Lett. 29 (1972) 345.
72T2 Temperly, H.V.N.: Two-dimensional Ising models, in: Phase Transitions and Critical Phenomena, Domb, C. Green, M.S. (eds.), London/New York: Academic Press, 1972, Vol. 1, p. 227.
72W2 de Wijn, H.W., Walker, L.R., Davis, J.L., Guggenheim, H.J.: Solid State Commun. 11 (1972) 803.
72W3 Wilson, K.G.: Phys. Rev. Lett. 28 (1972) 548.
72Y2 Yamada, I.: J. Phys. Soc. Jpn. 33 (1972) 979.
72Y3 Yamada, I, Ikebe, M.: J. Phys. Soc. Jpn. 33 (1972) 1334.
73A2 Aharony, A., Fisher, M.E.: Phys. Rev. B 8 (1973) 3323.
73A3 Aharony, A.: Phys. Rev. B 8 (1973) 3349.
73A4 Aharony, A.: Phys. Rev. B 8 (1973) 3358.
73A5 Aharony, A.: Phys. Rev. B 8 (1973) 3363. Erratum: Phys. Rev. B 9 (1974) 3946.
73A6 Ajiro, Y., Miura, M.: J. Phys. Soc. Jpn. 35 (1973) 1787.
73B1 Birgeneau, R.J., Guggenheim, H.J., Shirane, G.: Phys. Rev. B 8 (1973) 304.
73B3 Barouch, E., McCoy, B.M., Wu, T.T.: Phys. Rev. Lett. 31 (1973) 1409.
73B4 Berezinskii, V.L., Blank, A.Ya.: Sov. Phys. JETP 37 (1973) 369.
73B5 Bloembergen, P., Berkhout, P.J., Franse, J.J.M.: Int. J. Magnetism 4 (1973) 219.
73H3 Hirakawa, K., Ikeda, H.: J. Phys. Soc. Jpn. 35 (1973) 1328.
73H4 Huber, D.L., Seehra, M.S.: Phys. Lett. 43A (1973) 311.
73I Ikeda, H., Hirakawa, K.: J. Phys. Soc. Jpn. 35 (1973) 617.
73J1 Jahn, I.R., Bittermann, K.: Solid State Commun. 13 (1973) 1897.
73J2 Jahn, I.R.: Phys. Status Solidi (b) 57 (1973) 681.
73J4 Jou, D.C., Chen, H.H.: J. Phys. C: Solid State Phys. 6 (1983) 2713.
73K2 Kubo, H., Shimohigashi, K., Yamada, I.: J. Phys. Soc. Jpn. 34 (1973) 1687.
73K3 Kosterlitz, J.M., Thouless, D.J.: J. Phys. C: Solid State Phys. 6 (1973) 1181.
73L4 Liu, L., Stanley, H.E.: Phys. Rev. B 8 (1973) 2279.

73M Mikeska, H.J.: Z. Phys. 261 (1973) 437.

73P2 Pokrovskii, V.L., Uimin, G.V.: Phys. Lett. 45A (1973) 467.

73R1 Rehwald, W.: Adv. Phys. 22 (1973) 721.

73R2 Richards, P.M.: Solid State Commun. 13 (1973) 253.

73R3 Ritchie, D.S., Fisher, M.E.: Phys. Rev. B 7 (1973) 480.

73S2 Salamon, M.B., Richards, P.M.: AIP Conf. Proc. 10 (1973) 187.

73S3 Salamon, M.B., Ikeda, H.: Phys. Rev. B 7 (1973) 2017.

73S4 Samuelsen, E.J.: Phys. Rev. Lett. 31 (1973) 936.

73W2 de Wijn, H.W., Walker, L.R., Walstedt, R.E.: Phys. Rev. B 8 (1973) 285. Erratum: Phys. Rev. B 9 (1974) 2419.

73W5 Willett, R.D., Gerstein, B.G.: Phys. Lett. 44A (1973) 153.

73W6 Willett, R.D., Extine, M.: Chem. Phys. Lett. 23 (1973) 281.

73Y1 Yamaji, K., Kondo, J.: Phys. Lett. 45A (1973) 317.

73Y3 Yamaji, K., Kondo, J.: J. Phys. Soc. Jpn. 35 (1973) 25.

74A2 Aharony, A., Bruce, A.: Phys. Rev. Lett. 33 (1974) 427.

74B2 Bloembergen, P., Miedema, A.R.: Physica 75 (1974) 205.

74B4 Bucci, C., Guidi, G.: Phys. Rev. B 9 (1974) 3053.

74B5 Brezin, E., le Guillou, J.C., Zinn-Justin, J.: Phys. Lett. 47A (1974) 285.

74B6 Bucci, C., Guidi, G.: Phys. Lett. 48A (1974) 233.

74B7 Betts, D.D.: X-Y Model, in: Phase Transitions and Critical Phenomena, Domb, C., Green, M.S. (eds.), London/New York: Academic Press, 1974, Vol. 3, p. 570.

74D1 Domb, C.: Ising Model, in: Phase Transitions and Critical Phenomena, Domb, C., Green, M.S. (eds.), London/New York: Academic Press, 1974, Vol. 3, p. 357.

74F2 Fisher, M.E.: Rev. Mod. Phys. 46 (1974) 597.

74G1 Guttmann, A.J.: Phys. Rev. B 9 (1974) 4991.

74G2 Gerstein, B.C., Chang, K., Willett, R.D.: J. Chem. Phys. 60 (1974) 3454.

74H3 Halperin, B.I., Hohenberg, P.C., Shang-keng, Ma: Phys. Rev. B 10 (1974) 139.

74H5 Harris, A.B.: J. Phys. C: Solid State Phys. 7 (1974) 1671.

74H9 Harris, A.B., Lubensky, T.C.: Phys. Rev. Lett. 33 (1974) 1540.

74I1 Ikeda, H.: J. Phys. Soc. Jpn. 37 (1974) 660.

74I2 Ikeda, H., Hirakawa, K.: Solid State Commun. 14 (1974) 529.

74J1 de Jongh, L.J., Miedema, A.R.: Adv. Phys. 23 (1974) 1.

74K1 Knorr, K., Jahn, I.R., Heger, G.: Solid State Commun. 15 (1974) 231.

74K2 Kleemann, W., Pommier, J.: Phys. Status Solidi (b) 66 (1974) 747.

74K5 Kosterlitz, J.M.: J. Phys. C: Solid State Phys. 7 (1974) 1046.

74M2 Miedema, A.R., Bloembergen, P., Colpa, J.H.P., Gorter, F.W., de Jongh, L.J., Noordermeer, L.: AIP Conf. Proc. 18 (1974) part 2, 806.

74P2 Pokrovskii, V.L., Uimin, G.V.: Sov. Phys. JETP 38 (1974) 847.

74R1 Richards, P.M., Salamon, M.B.: Phys. Rev. B 9 (1974) 32.

74R2 Rushbrooke, G.S., Baker jr., G.A., Wood, P.J.: Heisenberg Model, in: Phase Transitions and Critical Phenomena, Domb, C., Green, M.S. (eds.), London/New York: Academic Press, 1974, Vol. 3, p. 246.

74S1 Samuelsen, E.J.: J. Phys. Chem. Solids 35 (1974) 785.

74S3 Samuelsen, E.J.: Proc. Int. Conf. Magnetism Moscow 1973, publ. 1974 by Academy of Sciences of the USSR, Vol. IV, p. 276.

74S5 Stanley, H.E.: D-vector model or "universality Hamiltonian": Properties of isotropically-interacting D-dimensional classical spins, in: Phase Transitions and Critical Phenomena, Domb, C., Green, M.S. (eds.), London/New York: Academic Press, 1974, Vol. 3, p. 486.

74S6 Schurter, J.L.: Ph.D. Thesis, Iowa State University, Ames/Iowa (USA) 1974.

74V4 Villain, J.: J. Phys. (France) 35 (1974) 27.

74W3 Witteveen, H.T.: Physica 71 (1974) 204.

74Y1 Yamazaki, H.: J. Phys. Soc. Jpn. 37 (1974) 667.

75A2 Ain, M., Hammann, J.: AIP Conf. Proc. 24 (1975) 309.

75A3 Arend, H., Schoenes, J., Wachter, P.: Phys. Status Solidi (b) 69 (1975) 105.
75B3 Belavin, A.A., Polyakov, A.M.: JETP Lett. 22 (1975) 245.
75B5 Bloembergen, P.: Physica 79B (1975) 467.
75B6 Boesch, H.R., Waldner, F.: Proc. Varenna LIX Summer Course Local Properties at Phase Transitions, Müller, K.A. (ed.), Amsterdam: North-Holland, 1975, p. 642.
75B7 Bruce, A., Aharony, A.: Phys. Rev. B 11 (1975) 478.
75B8 Blume, M., Heller, P., Lurié, N.A.: Phys. Rev. B 11 (1975) 4483.
75C2 Camp, W.J., van Dyke, J.P.: J. Phys. C: Solid State Phys. 8 (1975) 336.
75D2 Dupas, A., Renard, J.P.: Phys. Lett. 53A (1975) 141.
75D4 Dunn, A.G., Essam, J.W., Loveluck, J.M.: J. Phys. C: Solid State Phys. 8 (1975) 743.
75D5 Dunn, A.G., Essam, J.W., Ritchie, D.S.: J. Phys. C: Solid State Phys. 8 (1975) 4219.
75E2 Edwards, S.F., Anderson, P.W.: J. Phys. F: Metal Phys. 5 (1975) 965.
75G3 Guttmann, A.J.: J. Phys. A: Math. Gen. 8 (1975) 1236.
75H2 Hashimoto, T., Sato, A.: J. Phys. Soc. Jpn. 38 (1975) 345.
75H3 Hagen, H., Reimann, H., Waldner, F., Arend, H.: Helv. Phys. Acta 48 (1975) 441.
75H4 Huber, D.L., Seehra, M.S.: J. Phys. Chem. Solids 36 (1975) 723.
75H5 Harris, A.B., Lubensky, T.C., Holcomb, W.K., Dasgupta, C.: Phys. Rev. Lett. 35 (1975) 327. Erratum: Phys. Rev. Lett. 35 (1975) 1397.
75I1 Ikeda, H., Hatta, I., Ikushima, A., Hirakawa, K.: J. Phys. Soc. Jpn. 39 (1975) 827.
75I2 Imry, Y., Ma, S.: Phys. Rev. Lett. 35 (1975) 1399.
75J de Jongh, L.J., Block, R.: Physica 79B (1975) 568.
75K1 Kammer, H.: Helv. Phys. Acta 47 (1975) 442.
75L4 Landau, L.D., Lifschitz, E.M.: Lehrbuch der theoretischen Physik. Band V: Statistische Physik, 4. Auflage, Berlin: Akademie-Verlag, 1975.
75L10 Losee, D.B., Hall, J.W., Hatfield, W.E.: Solid State Commun. 16 (1975) 389.
75L11 Lubensky, T.C.: Phys. Rev. B 11 (1975) 3573.
75P2 Polyakov, A.M.: Phys. Lett. 59B (1975) 79.
75R3 Reiter, G.F., Boucher, J.P.: Phys. Rev. B 11 (1975) 1823.
75S1 Smolenskii, G.A., Pisarev, R.V., Sinii, I.G.: Sov. Phys. Usp. 18 (1975) 410.
75S3 Stauffer, D.: Z. Phys. B 22 (1975) 161.
75S5 Sherrington, D., Kirkpatrick, S.: Phys. Rev. Lett. 35 (1975) 1792.
75T2 Tarko, H.B., Fisher, M.E.: Phys. Rev. B 11 (1975) 1217.
75T3 Tracy, C., McCoy, B.: Phys. Rev. B 12 (1975) 368.
75T4 Thorpe, M.F.: J. Phys. (France) 36 (1975) 1117.
75V Villain, J.: J. Phys. (France) 36 (1975) 581.
75Y Yamaji, K., Kondo, J.: J. Phys. Soc. Jpn. 39 (1975) 1239.
75Z Zaspel, C.E., Drumheller, J.E.: Solid State Commun. 17 (1975) 1107.
76A1 Arend, H., Tichy, K., Baberschke, K., Rys, F.: Solid State Commun. 18 (1976) 999.
76A3 Als-Nielsen, J., Birgeneau, R.J., Guggenheim, H.J., Shirane, G.: J. Phys. C: Solid State Phys. 9 (1976) L121.
76A4 Aharony, A., Hohenberg, P.C.: Phys. Rev. B 13 (1976) 3081.
76A5 Als-Nielsen, J.: Neutron scattering and spatial correlation near the critical point, in: Phase Transitions and Critical Phenomena, Domb, C., Green, M.S. (eds.), London/New York: Academic Press, 1976, Vol. 5A, p. 88.
76A6 Akimitsu, J., Ito, Y.: J. Phys. Soc. Jpn. 40 (1976) 1621.
76A8 Aharony, A.: Dependence of universal critical behaviour on symmetry and range of interaction, in: Phase Transitions and Critical Phenomena, Domb, C., Green, M.S. (eds.), London/New York: Academic Press, 1976, Vol. 6, p. 357.
76A10 Aharony, A., Imry, Y., Shang-keng Ma: Phys. Rev. B 13 (1976) 466.
76A11 Aharony, A., Imry, Y., Ma, S.: Phys. Rev. Lett. 37 (1976) 1364.
76A13 Aharony, A., Imry, Y.: Solid State Commun. 20 (1976) 899.
76B4 Binder, K., Landau, D.P.: Phys. Rev. B 13 (1976) 1140.
76B5 Bloembergen, P.: Physica 81B (1976) 205.

76B6 Bervillier, C.: Phys. Rev. B 14 (1976) 4964.
76B7 Birgeneau, R.J., Cowley, R.A., Shirane, G., Guggenheim, H.J.: Phys. Rev. Lett. 37 (1976) 940.
76D2 Dupas, A., Le Dang, K., Renard, J.P., Veillet, P., Daoud, A., Perret, R.: J. Chem. Phys. 65 (1976) 4099.
76D5 Dupas, A., Renard, J.P.: J. Phys. (France) 37 (1976) C1-213.
76F Funahashi, S., Moussa, F., Steiner, M.: Solid State Commun. 18 (1976) 433.
76G5 Grinstein, G., Luther, A.: Phys. Rev. B 13 (1976) 1329.
76G6 Grinstein, G.: Phys. Rev. Lett. 37 (1976) 944.
76H3 Hohenberg, P.C., Aharony, A., Halperin, B.I., Siggia, E.D.: Phys. Rev. B 13 (1976) 2986.
76H4 Hutchings, M.T., Fair, M.J., Day, P., Walker, P.J.: J. Phys. C: Solid State Phys. 9 (1976) L55.
76I2 Ikeda, H., Hatta, I., Tanaka, M.: J. Phys. Soc. Jpn. 40 (1976) 334.
76I4 Imry, Y.: Phys. Rev. B 13 (1976) 3018.
76J1 de Jongh, L.J.: Physica 82B (1976) 247.
76J2 de Jongh, L.J., Stanley, H.E.: Phys. Rev. Lett. 36 (1976) 817.
76K4 Kammer, H.: Helv. Phys. Acta 49 (1976) 727.
76K5 Kadanoff, L.P.: Scaling, universality and operator algebra, in: Phase Transitions and Critical Phenomena, Domb, C., Green, M.S. (eds.), London/New York: Academic Press, 1976, Vol. 5A, p. 1.
76K7 Kirkpatrick, S.: Phys. Rev. Lett. 36 (1976) 69.
76K8 Kötzler, J., Kamleiter, G., Weber, G.: J. Phys. C: Solid State Phys. 9 (1976) L361.
76K9 Khokhlachev, S.: Sov. Phys. JETP 43 (1976) 137.
76L5 Leath, P.L.: Phys. Rev. B 14 (1976) 5046.
76M3 Moussa, F., Villain, J.: J. Phys. C: Solid State Phys. 9 (1976) 4433.
76M4 Migdal, A.A.: Sov. Phys. JETP 42 (1976) 743.
76M5 Murata, K.K.: Phys. Rev. B 13 (1976) 4015.
76N2 Navarro, R., de Jongh, L.J.: Physica 84B (1976) 229.
76O Oguchi, T., Ueno, Y.: J. Phys. Soc. Jpn. 41 (1976) 1123.
76S5 Steiner, M., Villain, J., Windsor, C.G.: Adv. Phys. 25 (1976) 87.
76S7 Stanley, H.E., Birgeneau, R.J., Reynolds, P.J., Nicoll, J.F.: J. Phys. C: Solid State Phys. 9 (1976) L553.
76S8 Sykes, M.F., Gaunt, D.S., Glen, M.: J. Phys. A: Math. Gen. 9 (1976) 97.
76S10 Sykes, M.F., Gaunt, D.S., Glen, M.: J. Phys. A: Math. Gen. 9 (1976) 725.
76W3 Wu, T.T., McCoy, B.M., Tracy, C.A., Barouch, E.: Phys. Rev. B 13 (1976) 316.
76Y1 Yamada, I., Suzuki, H.: Solid State Commun. 18 (1976) 237.
76Y2 Yamazaki, H., Tanaka, M.: J. Phys. Soc. Jpn. 41 (1976) 1540.
76Y3 Yamazaki, H.: J. Phys. Soc. Jpn. 41 (1976) 1911.
77A6 Aharony, A., Hohenberg, P.C.: Physica 86-88B (1977) 611.
77B2 Birgeneau, R.J., Als-Nielsen, J., Shirane, G.: Phys. Rev. B 16 (1977) 280.
77B3 Bloembergen, P.: Physica 85B (1977) 51.
77B4 Betts, D.D.: Physica 86-88B (1977) 556.
77B5 Benner, H.: Appl. Phys. 13 (1977) 141.
77B8 Bevaart, L., Lebesque, J.V., Frikkee, E., de Jongh, L.J.: Physica 86-88B (1977) 729.
77C7 Cowley, R.A., Shirane, G., Birgeneau, R.J., Guggenheim, H.J.: Physica 86-88B (1977) 727.
77C8 Chalupa, J.: Solid State Commun. 22 (1977) 315.
77F2 Fair, M.J., Gregson, A.K., Day, P., Hutchings, M.T.: Physica 86-88B (1977) 657.
77G4 le Guillou, J.C., Zinn-Justin, J.: Phys. Rev. Lett. 39 (1977) 95.
77H1 Heygster, G., Kleemann, W.: Physica 89B (1977) 165.
77H2 Hohenberg, P.C., Halperin, B.I.: Rev. Mod. Phys. 49 (1977) 435.
77H3 Hagen, H., Reimann, H., Schmocker, U., Waldner, F.: Physica 86-88B (1977) 1287.
77H5 Harris, A.B., Kirkpatrick, S.: Phys. Rev. B 16 (1977) 542.
77I2 Iio, K., Sakatani, M., Nagata, K.: J. Phys. Soc. Jpn. 43 (1977) 709.
77J2 José, J.V., Kadanoff, L.P., Kirkpatrick, S., Nelson, D.R.: Phys. Rev. B 16 (1977)
77J3 Jayaprakash, C., Katz, H.J.: Phys. Rev. B 16 (1977) 3987.

77K2 van Kempen, H., Mischgofsky, F.H., Wyder, P.: Phys. Rev. B 15 (1977) 4386.
77K4 Kammer, J.W.: Ph.D. Thesis, ETH Zürich (Switzerland) 1977.
77K6 Kawabata, C., Binder, K.: Solid State Commun. 22 (1977) 705.
77K8 Keller, H., Kündig, W., Arend, H.: Physica 86-88B (1977) 683.
77K10 Kinzel, W., Fischer, K.H.: Solid State Commun. 23 (1977) 687.
77L4 Lubensky, T.C.: Phys. Rev. B 15 (1977) 311.
77M1 Moussa, F., Villain, J.: Physica 86-88B (1977) 696.
77M4 Mandelbrot, B.B.: Fractals: Form, Chance and Dimension, San Francisco: Freeman, 1977.
77M5 Matsubara, F., Inawashiro, S.: J. Phys. Soc. Jpn. 42 (1977) 1529.
77N2 Nagata, K., Yamada, I., Komatsubara, T., Nishizaki, T.: J. Phys. Soc. Jpn. 43 (1977) 707.
77N3 Nelson, D.R., Kosterlitz, J.M.: Phys. Rev. Lett. 39 (1977) 1201.
77N4 Nagata, K., Yamamoto, I., Takano, H., Yokozawa, Y.: J. Phys. Soc. Jpn. 43 (1977) 857.
77P3 Petit, R.H., Ferré, J., Nouet, J.: Physica 86-88B (1977) 1213.
77R Reynolds, P.J., Stanley, H.E., Klein, W.: J. Phys. A: Math. Gen. 10 (1977) L203.
77S1 Shirane, G., Birgeneau, R.J.: Physica 86-88B (1977) 639.
77S5 Suzuki, M., Miyashita, S., Kuroda, A., Kawabata, C.: Phys. Lett. 60A (1977) 478.
77S6 Soos, Z.G., McGregor, K.T., Cheung, T.T.P., Silverstein, A.J.: Phys. Rev. B 16 (1977) 3037.
77S7 Stanley, H.E.: J. Phys. A: Math. Gen. 10 (1977) L211.
77S8 Stephen, M.J., Grest, G.S.: Phys. Rev. Lett. 38 (1977) 567.
77S9 Suzuki, M.: Prog. Theor. Phys. 58 (1977) 1151.
77T5 Takano, H., Yokozawa, Y.: J. Phys. Soc. Jpn. 42 (1977) 1059.
77V2 Villain, J.: J. Phys. C: Solid State Phys. 10 (1977) 4793.
77Y1 Yamada, I., Nishizaki, T.: J. Phys. Soc. Jpn. 43 (1977) 2093.
77Y4 Young, A.P.: J. Phys. C: Solid State Phys. 10 (1977) L257.
77Z Zaspel, C.E., Drumheller, J.E.: Phys. Rev. B 16 (1977) 1771.
78A4 Arend, H., v. Känel, H., Wachter, P.: J. Appl. Phys. 49 (1978) 2206.
78A5 Aharony, A.: Phys. Rev. B 18 (1978) 3328.
78B2 Blinc, R., Zeks, B., Kind, R.: Phys. Rev. B 17 (1978) 3409.
78B4 Bevaart, L., Frikkee, E., Lebesque, J.V., de Jongh, L.J.: Phys. Rev. B 18 (1978) 3376.
78B5 Betsuyaku, H.: Solid State Commun. 25 (1978) 185.
78B7 Benner, H.: Phys. Rev. B 18 (1978) 319.
78B8 Bruce, A.D., Cowley, R.A., Murray, A.F.: J. Phys. C: Solid State Phys. 11 (1978) 3591.
78B9 Blease, J., Essam, J.W., Place, C.M.: J. Phys. C: Solid State Phys.11 (1978) 4009.
78B10 Bevaart, L., Frikkee, E., Lebesque, J.V., de Jongh, L.J.: Solid State Commun. 25 (1978) 539.
78C3 Cheung, T.T.P., Soos, Z.G.: J. Chem. Phys. 69 (1978) 3845.
78C4 Cowley, R.A., Bruce, A.D.: J. Phys. C: Solid State Phys. 11 (1978) 3577.
78I1 Iio, K., Sakatani, M., Nagata, K.: J. Phys. Soc. Jpn. 45 (1978) 1567.
78I3 Ikeda, H., Hutchings, M.T., Suzuki, M.: J. Phys. C: Solid State Phys. 11 (1978) L359.
78J de Jongh, L.J.: J. Appl. Phys. 49 (1978) 1305.
78K2 Kosterlitz, J.M., Thouless, D.J.: Two-dimensional physics, in: Progress in Low Temperature Physics, Brewer, D.F. (ed.), Amsterdam: North Holland, 1978, Vol. VII B, Chapter 5, p. 371.
78K3 Kosterlitz, J.M., Santos, M.A.: J. Phys. C: Solid State Phys. 11 (1978) 2835.
78K10 Klein, W., Stanley, H.E., Reynolds, P.J., Coniglio, A.: Phys. Rev. Lett. 41 (1978) 1145.
78K11 Kawasaki, K., Yalabik, M.C., Gunton, J.D.: Phys. Rev. A 17 (1978) 455.
78L1 Lehner, N.: Progr. Rep. KfK 2720, Karlsruhe 1978.
78L5 Lindgård, P.A.: Phase transitions and critical phenomena, in: Neutron Diffraction, Dachs, H. (ed.), Topics in Current Physics, Berlin: Springer-Verlag, 1978, Vol. 6, Chapter 6, p.197.
78M2 Moussa, F., Hennion, B., Mons, J., Pepy, G.: Solid State Commun. 27 (1978) 141.
78M3 Miyashita, S., Nishimori, H., Kuroda, A., Suzuki, M.: Progr. Theor. Phys. 60 (1978) 1669.
78N2 Navarro, R., de Jongh, L.J.: Physica 94B (1978) 67.
78N3 Nishizaka, T., Yamada, I.: Solid State Commun. 28 (1978) 195.
78N4 Nattermann, Th.: Phys. Status Solidi (b) 85 (1978) 291.
78O3 Oguchi, T., Ishikawa, T.: J. Phys. Soc. Jpn. 45 (1978) 1213.

78P Popov, E.A., Beznosikov, B.V.: Sov. Phys. Solid State 20 (1978) 1991.
78R2 Renard, J.P., Corbel, G., Dupas, A.: unpublished results 1978, private communication.
78R3 Reynolds, P.J., Stanley, H.E., Klein, W.: J. Phys. A: Math. Gen. 11 (1978) L199.
78S4 Suzuki, M., Ikeda, H.: J. Phys. C: Solid State Phys. 11 (1978) 3679.
78S6 Savit, R.: Phys. Rev. B 17 (1978) 1340.
78T2 Thurlings, M.P.H., Hendriks, E.M., de Wijn, H.W.: Solid State Commun. 27 (1978) 1289.
78U van Uijen, C.M.J., de Wijn, H.W., Frikkee, E.: J. Phys. (France) 39 (1978) C6-755.
78W3 Wallace, D.J., Young, A.P.: Phys. Rev. B 17 (1978) 2384.
78Y2 Yokozawa, Y., Tanimoto, M.: J. Phys. Soc. Jpn. 44 (1978) 1741.
78Y3 Yokozawa, Y., Tanimoto, M., Takano, H.: J. Phys. Soc. Jpn. 45 (1978) 67.
78Y4 Yeomans, J.M., Stinchcombe, R.B.: J. Phys. C: Solid State Phys. 11 (1978) L525.
79A Aharony, A., Bruce, A.D.: Phys. Rev. Lett. 42 (1979) 462.
79B2 Bevaart, L., Frikkee, E., de Jongh, L.J.: Phys. Rev. B 19 (1979) 4741.
79B7 Berker, A.N., Nelson, D.N.: Phys. Rev. B 19 (1979) 2488.
79B8 Binder, K.: Theory and "technical" aspects of Monte Carlo simulations, in: Monte Carlo Methods in Statistical Physics, Binder, K. (ed.), Topics in Current Physics, Berlin: Springer-Verlag, 1979, Vol. 7, p. 1.
79B9 Benner, H.: Phys. Lett. 70A (1979) 225.
79B11 Buzaré, J.Y., Fayet, J.C., Berlinger, W., Müller, K.A.: Phys. Rev. Lett. 42 (1979) 465.
79D3 Day, P.: Accounts of Chemical Research 12 (1979) 236.
79F2 Fishman, S., Aharony, A.: J. Phys. C: Solid State Phys. 12 (1979) L729.
79F4 Feigelman, M.V., Tsvelik, A.M.: Sov. Phys. JETP 49 (1979) 1136.
79H2 Hirakawa, K., Yoshizawa, H.: J. Phys. Soc. Jpn. 47 (1979) 368.
79H3 Herrmann, H.J.: Z. Phys. B 32 (1979) 335.
79I1 Ikeda, H., Suzuki, M., Hutchings, M.T.: J. Phys. Soc. Jpn. 46 (1979) 1153.
79I2 Ikeda, H., Suzuki, M., Hutchings, M.T.: J. Magn. Magn. Mater. 14 (1979) 163.
79J Jahn, I.R.: Int. Conf. Magnetism, Munich 1979 (Abstract), unpublished results, presented in the review by J. Ferré et al. [84F1].
79K3 Kleemann, W., Schäfer, F.J., Nouet, J.: Physica 97B (1979) 145.
79K5 Kind, R., Blinc, R., Zeks, B.: Phys. Rev. B 19 (1979) 3743.
79K8 v. Känel, H.: Physica 96B (1979) 167.
79K9 Kovalev, A.S., Kosevich, A.M., Maslov, K.V.: JETP Lett. 30 (1979) 296.
79L Lagendijk, A.: Solid State Commun. 29 (1979) 593.
79M3 Morgenstern, I., Binder, K.: Phys. Rev. Lett. 43 (1979) 1615.
79N den Nijs, M.P.M.: J. Phys. A: Math. Gen. 12 (1979) 1857.
79O2 Okuda, Y., Matsuura, M., Haseda, T.: J. Phys. Soc. Jpn. 47 (1979) 773.
79P3 Pokrovsky, V.L., Uimin, G.V.: Adv. Phys. 28 (1979) 595.
79P5 Parisi, G., Sourlas, N.: Phys. Rev. Lett. 43 (1979) 744.
79S2 Steijger, J.J.M., Frikkee, E., de Jongh, L.J.: J. Magn. Magn. Mater. 14 (1979) 152.
79S5 Snively, L.O., Seifert, P.L., Emerson, K., Drumheller, J.E.: Phys. Rev. B 20 (1979) 2101.
79S6 Stinchcombe, R.B.: J. Phys. Soc. C: Solid State Phys. 12 (1979) 4533.
79S7 Stauffer, D.: Phys. Rep. 54 (1979) 1.
79T1 Tobochnik, J., Chester, G.V.: Phys. Rev. B 20 (1979) 3761.
79T2 Tanimoto, M.: J. Phys. Soc. Jpn. 47 (1979) 476.
79U van Uijen, C.M.J., Frikkee, E., de Wijn, H.J.: Phys. Rev. B 19 (1979) 509.
79W2 Walsh Jr., W.M., Birgeneau, R.J., Rupp, L.W., Guggenheim, H.J.: Phys. Rev. B 20 (1979) 4645.
79W3 Wagner, V., Krey, U.: J. Magn. Magn. Mater. 14 (1979) 169.
80B1 Birgeneau, R.J., Cowley, R.A., Shirane, G., Tarvin, J.A., Guggenheim, H.J.: Phys. Rev. B 21 (1980) 317.
80B9 Barber, M.N.: Phys. Rep. 59 (1980) 376.
80B10 Benner, H.: J. Magn. Magn. Mater. 15-18 (1980) 727.

80C1 Cowley, R.A., Birgeneau, R.J., Shirane, G., Guggenheim, H.J., Ikeda, H.: Phys. Rev. B 21 (1980) 4038.
80C2 Cowley, R.A.: Adv. Phys. 29 (1980) 1.
80E3 Essam, J.W.: Rep. Progr. Phys. 43 (1980) 833.
80G4 Gebhardt, W., Krey, U.: Phasenübergänge und kritische Phänomene, Braunschweig/Wiesbaden: Friedrich Vieweg & Sohn, 1980.
80G5 le Guillou, J.C., Zinn-Justin, J.: Phys. Rev. B 21 (1980) 3976.
80H4 Hatta, I., Ikeda, H.: J. Phys. Soc. Jpn. 48 (1980) 77.
80H5 Hatta, I., Ikeda, H.: J. Phys. Soc. Jpn. 49 (1980) 25.
80H6 Hashimoto, T., Kojima, Y., Ikegami, T.: J. Magn. Magn. Mater. 15-18 (1980) 1025.
80H7 Hikami, S., Tsuneto, T.: Progr. Theor. Phys. 63 (1980) 387.
80H8 Hirakawa, K., Yoshizawa, H.: J. Magn. Magn. Mater. 15-18 (1980) 417.
80H9 Huber, D.L.: Phys. Lett. 76A (1980) 406.
80H10 Hashimoto, T., Kojima, Y., Ikegami, T., Yamada, I.: J. Magn. Magn. Mater. 15-18 (1980) 227.
80I2 Iio, K., Hyodo, H., Nagata, K.: J. Magn. Magn. Mater. 15-18 (1980) 793.
80K2 Kleemann, W., Schäfer, F.J.: J. Magn. Magn. Mater. 21 (1980) 143.
80K6 Kimishima, Y.: J. Phys. Soc. Jpn. 49 (1980) 62.
80K7 Kubo, H., Suzuki, Y., Akitomi, T., Tsuru, K., Kimishima, Y.: J. Phys. Soc. Jpn. 48 (1980) 1387.
80L2 Lindgard, P.A., Als-Nielsen, J., Hutchings, M.T.: J. Magn. Magn. Mater. 15-18 (1980) 343.
80L3 Lagendijk, A., Siegel, E.: J. Magn. Magn. Mater. 15-18 (1980) 714.
80M1 Mikeska, H.J.: J. Phys. C: Solid State Phys. 13 (1980) 2913.
80M8 Morgenstern, I., Binder, K.: Phys. Rev. B 22 (1980) 288.
80M9 Miyashita, S.: Progr. Theor. Phys. 63 (1980) 797.
80N1 Nishino, T., Iio, K., Nagata, K.: J. Spectrosc. Soc. Jpn. 29 (1980) 263.
80N2 Nienhuis, B., Riedel, E.K., Schick, M.: J. Phys. A: Math. Gen. 13 (1980) L189.
80O1 Okuda, Y., Matsuura, M., Haseda, T.: J. Magn. Magn. Mater. 15-18 (1980) 1027.
80P3 Popov, E.A., Kotlyarski, M.M.: J. Magn. Magn. Mater. 15-18 (1980) 785.
80P4 Popov, E.A., Kotlyarski, M.M.: Sov. Phys. Solid State 22 (1980) 1763.
80P5 Phani, M.K., Lebowitz, J.L., Kalos, M.H., Penrose, O.: Phys. Rev. Lett. 45 (1980) 366.
80P6 Pearson, R.B.: Phys. Rev. B 22 (1980) 2579.
80R Reynolds, P.J., Stanley, H.E., Klein, W.: Phys. Rev. B 21 (1980) 1223.
80S1 Suzuki, M., Kato, K., Ikeda, H.: J. Phys. Soc. Jpn. 49 (1980) 514.
80S3 Shenker, S.H., Tobochnik, J.: Phys. Rev. B 22 (1980) 4462.
80S4 Strobel, K., Frank, J., Rosshirt, K., Geick, R.: Int. J. Millim. Waves 1 (1980) 295.
80S5 Stinchcombe, R.B.: J. Phys. C: Solid State Phys. 13 (1980) 3723.
80T4 Takeno, S., Honma, S.: Progr. Theor. Phys. 64 (1980) 1193.
80T5 Tanimoto, M., Yokozawa, Y.: J. Phys. Soc. Jpn. 49 (1980) 67.
80U van Uijen, C.M.J., de Wijn, H.W.: J. Magn. Magn. Mater. 15-18 (1980) 1023.
80W2 Willett, R.D., Wong, R., Numata, M.: J. Magn. Magn. Mater. 15-18 (1980) 717.
81A Allroth, E., Mikeska, H.J.: Z. Phys. B 43 (1981) 209.
81B4 Bruce, A.D.: J. Phys. C: Solid State Phys. 14 (1981) 193.
81B6 Blöte, H.W.J., Nightingale, M.P., Derrida, B.: J. Phys. A: Math. Gen. 14 (1981) L45.
81B7 Binder, K., Imry, Y., Pytte, E.: Phys. Rev. B 24 (1981) 6736.
81B9 Barbara, B., Malozemoff, A.P., Imry, Y.: Phys. Rev. Lett. 47 (1981) 1852.
81C3 Coniglio, A.: Phys. Rev. Lett. 46 (1981) 250.
81E Eschbach, P.D., Stauffer, D., Herrmann, H.J.: Phys. Rev. B 23 (1981) 422.
81F2 Ferrieu, F., Pomerantz, M.: Solid State Commun. 39 (1981) 707.
81H2 Hirakawa, K., Ubukoshi, K.: J. Phys. Soc. Jpn. 50 (1981) 1909.
81H3 Hirakawa, K., Shirane, G., Axe, J.D.: J. Phys. Soc. Jpn. 50 (1981) 787.
81H4 Hutchings, M.T., Als-Nielsen, Lindgard, P.A., Walker; P.J.: J. Phys. C: Solid State Phys. 14 (1981) 5327.
81I2 Ikeda, H.: J. Phys. Soc. Jpn. 50 (1981) 3215.

81I3 Ikeda, H., Abe, T., Hatta, I.: J. Phys. Soc. Jpn. 50 (1981) 1488.

81K1 Käräjämäki, E., Laiho, R., Levola, T., Kleemann, W., Schäfer, F.J.: Physica 111B (1981) 24.

81K3 Kind, R., Plesko, S., Günter, P., Roos, J., Fousek, J.: Phys. Rev. B 23 (1981) 5301. Erratum: Phys. Rev. B 24 (1981) 4910.

81K4 Krüger, W., Lammers, R., Merkel, J., Weber, H., Jahn, I.R.: Z. Kristallogr. 154 (1981) 305.

81K6 Kleemann, W., Ferré, J., Schäfer, F.J.: J. Phys. C: Solid State Phys. 14 (1981) 4463.

81K9 Kobets, M.I., Stepanov, A.A., Zvyagin, A.I.: Physica 108B (1981) 843.

81K10 Kosevich, A.M., Ivanov, B.A., Kovalev, A.S.: Physica 3D (1981) 363.

81K13 Kogon, H.S., Wallace, D.J.: J. Phys. A: Math. Gen. 14 (1981) L527. '

81K14 Kawabata, C., José, J.V., Kirkpatrick, S.: J. Phys. C: Solid State Phys. 14 (1981) L633.

81L Lüthi, B., Rehwald, W.: Ultrsonic Studies near Structural Phase Transitions, in: Structural Phase Transitions I, Topics in Current Physics, Müller, K.A., Thomas, H. (eds.), Berlin: Springer-Verlag, 1981, Vol. 23, p. 131.

81M1 Münninghoff, G., Kurtz, W., Treutmann, W., Hellner, E., Heger, G., Lehner, N., Reinen, D.: Solid State Commun. 40 (1981) 571.

81M3 Mazenko, G.F., Valls, O.T.: Phys. Rev. B 24 (1981) 1419.

81M4 Mikeska, H.J.: J. Appl. Phys. 52 (1981) 1950.

81P2 Pytte, E., Imry, Y., Mukamel, D.: Phys. Rev. Lett. 46 (1981) 1173.

81R1 Reinen, D., Krause, S.: Inorg. Chem. 20 (1981) 2750.

81S1 Suzuki, M., Ikeda, H.: J. Phys. Soc. Jpn. 50 (1981) 1133.

81S2 Solla, S.A., Riedel, E.K.: Phys. Rev. B 23 (1981) 6008.

81S5 Suzuki, Y., Tsuru, K., Kimishima, Y., Kubo, H.: J. Phys. Soc. Jpn. 50 (1981) 1479.

81S7 Snively, L.O., Drumheller, J.E., Emerson, K.: Phys. Rev. B 23 (1981) 6013.

81T2 Takeda, K., Okuda, Y., Yamada, I., Haseda, T.: J. Phys. Soc. Jpn. 50 (1981) 1917.

81T3 Thiel, R.C., de Graaf, H., de Jongh, L.J.: Phys. Rev. Lett. 47 (1981) 1415.

81U van Uijen, C.M.J., de Wijn, H.W.: Phys. Rev. B 24 (1981) 5368.

81W2 Willett, R.D., Jardine, F.H., Wong, R.J., Landee, C.P., Numata, M.: Phys. Rev. B 24 (1981) 5372.

81W3 White, M.A., Granville, N.W., Davies, N.J., Staveley, L.A.K.: J. Phys. Chem. Solids 42 (1981) 953.

81W4 van der Wal, A.J., de Wijn, H.W.: Phys. Rev. B 23 (1981) 5950.

81W5 Willett, R.D., Wong, R.J.: J. Magn. Reson. 42 (1981) 446.

81W6 Wong, R.J.H., Willett, R.D., Drumheller, J.E.: J. Chem. Phys. 74 (1981) 6018.

82A Alexander, S., Orbach, R.: J. Phys. Lett. (France) 43 (1982) L625.

82B5 Binder, K.: Z. Phys. B 48 (1982) 319.

82D2 Dotsenko, Vik.S., Dotsenko, Vl.S.: J. Phys. C: Solid State Phys. 15 (1982) 495.

82D3 Dotsenko, Vik.S., Dotsenko, Vl.S.: J. Phys. C: Solid State Phys. 15 (1982) L557.

82G1 Goto, T., Yoshizawa, M., Tamaki, A., Fujimura, T.: J. Phys. C: Solid State Phys. 15 (1982) 3041.

82G3 Grinstein, G., Ma, S.: Phys. Rev. Lett. 49 (1982) 685.

82H4 Hutchings, M.T., Ikeda, H., Janke, E.: Phys. Rev. Lett. 49 (1982) 386.

82H5 Hirakawa, K., Yoshizawa, H., Ubukoshi, K.: J. Phys. Soc. Jpn. 51 (1982) 2151.

82H6 Hirakawa, K.: J. Appl. Phys. 53 (1982) 1893.

82H7 Huber, D.L.: Phys. Rev. B 26 (1982) 3758.

82J2 de Jongh, L.J.: J. Appl. Phys. 53 (1982) 8018.

82K2 Kleemann, W., Schäfer, F.J., Day, P.: J. Phys. C: Solid State Phys. 15 (1982) 3987.

82K3 Kawabata, C., Bishop, A.R.: Solid State Commun. 42 (1982) 595.

82K5 Kite, T.M., Drumheller, J.E., Emerson, K.: J. Magn. Reson. 48 (1982) 20.

82K6 Kurtz, W.: Solid State Commun. 42 (1982) 875.

82M2 Mostafa, M.F., Semary, M.A., Abdel-Kader, M.M.: Physica 112B (1982) 197.

82M7 Mandelbrot, B.B.: The Fractal Geometry of Nature, San Francisco: Freeman, 1982.

82N1 Nitsche, W., Kleemann, W.: Opt. Commun. 41 (1982) 1.

82N2 Nitsche, W., Kleemann, W.: J. Magn. Magn. Mater. 28 (1982) 163.

82N4 Nienhuis, B.: J. Phys. A: Math. Gen. 15 (1982) 199.
82N5 Newman, K.E., Riedel, E.K.: Phys. Rev. B 25 (1982) 264.
82P1 Petrakovskii, G.A., Emel'yanova, L.S., Kokov, I.T., Bondarenko, G.V., Baranov, A.V.: Sov. Phys. JETP 56 (1982) 1260.
82S4 Suzuki, M.: J. Phys. Soc. Jpn. 51 (1982) 2772.
82S5 Snively, L.O., Haines, D.N., Emerson, K., Drumheller, J.E.: Phys. Rev. B 26 (1982) 5245.
82T1 Thurlings, M.P.H., Frikkee, E., de Wijn, H.J.: Phys. Rev. B 25 (1982) 4750.
82V Villain, J.: J. Phys. Lett. (France) 43 (1982) L551.
82W2 White, M.A., Granville, N.W., Staveley, L.A.K.: J. Phys. Chem. Solids 43 (1982) 341.
82W6 Willett, R.D., Waldner, F.: J. Appl. Phys. 53 (1982) 2680.
82W7 Wong, P., von Molnar, S., Dimon, P.: J. Appl. Phys. 53 (1982) 7954.
82Y2 Yoshizawa, M., Goto, T., Fujimura, T.: Phys. Rev. B 26 (1982) 1499.
82Y3 Yoshizawa, H., Cowley, R.A., Shirane, G., Birgeneau, R.J., Guggenheim, H.J., Ikeda, H.: Phys. Rev. Lett. 48 (1982) 438.
83A2 Arts, A.F.M., van der Vlist, H., van Miltenburg, J.G.M., van Uijen, C.M.J., de Wijn, H.W.: J. Magn. Magn. Mater. 31-34 (1983) 1181.
83A3 Aharony, A., Pytte, E.: Phys. Rev. B 27 (1983) 5872.
83B4 Birgeneau, R.J., Yoshizawa, H., Cowley, R.A., Shirane, G., Ikeda, H.: Phys. Rev. B 28 (1983) 1438.
83B5 Belanger, D.P., King, A.R., Jaccarino, V., Cardy, J.L.: Phys. Rev. B 28 (1983) 2522.
83B6 Belanger, D.P., Nordblad, P., King, A.R., Jaccarino, V., Lundgren, L., Beckman, O.: J. Magn. Magn. Mater. 31-34 (1983) 1095.
83B7 Birgeneau, R.J., Cowley, R.A., Shirane, G., Yoshizawa, H., Belanger, D.P., King, A.R., Jaccarino, V.: Phys. Rev. B 27 (1983) 6747. Erratum: Phys. Rev. B 28 (1983) 4028.
83C4 Cowley, R.A.: J. Magn. Magn. Mater. 31-34 (1983) 1439.
83C5 Cheung, H., McMillan, W.L.: J. Phys. C: Solid State Phys. 16 (1983) 7027.
83D3 Dotsenko, Vik.S., Dotsenko, Vl.S.: Adv. Phys. 32 (1983) 129.
83F3 Ferreira, I.B., King, A.R., Jaccarino, V., Cardy, J.L., Guggenheim, H.J.: Phys. Rev. B 28 (1983) 5192.
83G3 Gefen, Y., Aharony, A., Alexander, S.: Phys. Rev. Lett. 50 (1983) 77.
83H2 Hagen, M.: Ph.D. Thesis, University of Edinburgh (Great Britain) 1983.
83H4 Hirakawa, K., Yoshizawa, H., Axe, J.D., Shirane, G.: J. Phys. Soc. Jpn. 52 (1983) 4220.
83H6 Haldane, F.D.M.: Phys. Rev. Lett. 50 (1983) 1153.
83H7 Haldane, F.D.M.: Phys. Lett. 93A (1983) 464.
83I2 Ikeda, H.: J. Phys. C: Solid State Phys. 16 (1983) 3563.
83I3 Ikeda, H.: J. Phys. C: Solid State Phys. 16 (1983) L21.
83I4 Ikeda, H.: J. Phys. C: Solid State Phys. 16 (1983) L1033.
83J2 Jug, G.: Phys. Rev. B 27 (1983) 609.
83J3 Jug, G.: Phys. Rev. B 27 (1983) 4518.
83K4 Kleemann, W., Schäfer, F.J.: J. Magn. Magn. Mater. 31-34 (1983) 565.
83K8 Kite, T.M., Drumheller, J.E.: J. Magn. Reson. 54 (1983) 253.
83K9 Kapitulnik, A., Aharony, A., Deutscher, G., Stauffer, D.: J. Phys. A: Math. Gen. 16 (1984) L269.
83L Landau, D.P.: J. Magn. Magn. Mater. 31-34 (1983) 1115.
83M5 Margolina, A., Herrmann, H.J., Stauffer, D.: Phys. Lett. 93A (1983) 73.
83M6 McMillan, W.L.: Phys. Rev. B 28 (1983) 5216.
83N2 Nordblad, P., Belanger, D.P., King, A.R., Jaccarino, V., Ikeda, H.: Phys. Rev. B 28 (1983) 278.
83N4 Nakajima, T., Yamauchi, H., Goto, T., Yoshizawa, M., Suzuki, T., Fujimura, T.: J. Magn. Magn. Mater. 31-34 (1983) 1189.
83N5 Newlove, S.A.: J. Phys. C: Solid State Phys. 16 (1983) L423.
83P Petrakovskii, G.A., Yemelyanova, L.S., Velichko,V.V.: Solid State Commun. 48 (1983) 647.
83S1 Suzuki, T., Yoshizawa, M., Goto, T., Yamakami, T., Takahashi, M., Fujimura, T.: J. Phys. Soc. Jpn. 52 (1983) 1669.

83S2 Steijger, J.J.M., Frikkee, E., de Jongh, L.J., Huiskamp, W.J.: Physica 120B (1983) 202.

83S5 Steiner, M.: J. Magn. Magn. Mater. 31-34 (1983) 1277.

83S8 Semary, M.A., Abdel-Kader, M.M., Mostafa, M.F.: Chem. Phys. Lett. 96 (1983) 641.

83S10 Stinchcombe, R.B.: Dilute magnetism, in: Phase Transitions and Critical Phenomena, Domb, C., Lebowitz, J.L. (eds.), London/New York: Academic Press, 1983, Vol. 7, p. 152.

83T7 Tanimoto, M., Katsumata, K.: J. Magn. Magn. Mater. 31-34 (1983) 1389.

83T8 Teitel, S., Jayaprakash, C.: Phys. Rev. B 27 (1983) 598.

83V1 van der Vlist, H., Claassen, W.C.M., Arts, A.F.M., de Wijn, H.W.: J. Magn. Magn. Mater. 31-34 (1983) 1183.

83V3 Vlak, W.A.H.M., Frikkee, E., Arts, A.F.M., de Wijn, H.W.: J. Phys. C: Solid State Phys. 16 (1983) L1015.

83W2 Willett, R.D., Wong, R.J., Numata, M.: Inorg. Chem. 22 (1983) 3189.

83W4 Waldner, F.: J. Magn. Magn. Mater. 31-34 (1983) 1203.

83W5 Wong, P., von Molnar, S., Dimon, P.: Solid State Commun. 48 (1983) 573.

83Y1 Yamada, I., Shimoda, S., Nagano, S.: J. Magn. Magn. Mater. 31-34 (1983) 645.

83Y2 Yamada, I., Shimoda, S., Nagano, S.: Physica 121B (1983) 127.

83Y3 Yamada, I., Morishita, I., Tokuyama, T.: Physica 115B (1983) 179.

84A Aeppli, G., Guggenheim, H.J., Uemura, Y.J.: Phys. Rev. Lett. 52 (1984) 942.

84B2 Benner, H., Seitz, H., Wiese, J., Boucher, J.P.: J. Magn. Magn. Mater. 45 (1984) 354.

84B4 Birgeneau, R.J., Cowley, R.A., Shirane, G., Yoshizawa, H.: J. Stat. Phys. 34 (1984) 817.

84B5 Belanger, D.P., King, A.R., Jaccarino, V.: J. Appl. Phys. 55 (1984) 2383.

84B6 Binder, K.: Phys. Rev. B 29 (1984) 5184.

84B7 Bray, A.J., Moore, M.A.: J. Phys. C: Solid State Phys. 17 (1984) L463.

84C1 Cowley, R.A., Hagen, M., Belanger, D.P.: J. Phys. C: Solid State Phys. 17 (1984) 3763.

84C2 Cardy, J.L.: Phys. Rev. B 29 (1984) 505.

84D2 Dikken, B.J., Arts, A.F.M., de Wijn, H.W., Kjems, J.K.: Phys. Rev. B 30 (1984) 2970.

84E Emel'yanova, L.S.: Preprint No. 281F, Akademiya Nauk SSSR, Institut Fiziki im. L.V. Kirenskogo, Krasnoyarsk 1984 (in Russian).

84F1 Ferré, J., Gehring, G.A.: Rep. Prog. Phys. 47 (1984) 513.

84G4 Gerling, R.W., Landau, D.P.: Nonlinear exccitations in the classical XY-model, in: Magnetic Excitations and Fluctuations, Lovesey, S.W., Balucani, U., Borsa, F., Tognetti, V. (eds.), Springer Series in Solid State Sciences, Berlin: Springer-Verlag, 1984, Vol. 54, p. 61.

84G5 Grinstein, G.: J. Appl. Phys. 55 (1984) 2371.

84H1 Hagen, M., Paul, D.McK.: J. Phys. C: Solid State Phys. 17 (1984) 5605.

84H3 Higgins, S.A., Cowley, R.A., Hagen, M., Kjems, J., Dürr, U., Fendler, K.: J. Phys. C: Solid State Phys. 17 (1984) 3235.

84H4 Hiraoka, Y., Ito, A.: J. Phys. Soc. Jpn. 53 (1984) 3957.

84I2 Imry, Y.: J. Stat. Phys. 34 (1984) 849.

84I3 Imbrie, J.Z.: Phys. Rev. Lett. 53 (1984) 1747.

84K6 Katsumata, K., Tuchendler, J., Tanimoto, M.: Solid State Commun. 50 (1984) 193.

84K8 Katsumata, K., Tanimoto, M., Mitsuda, S., Endoh, Y.: J. Phys. Soc. Jpn. 53 (1984) 3315.

84K9 Kinzel, W., Binder, K.: Phys. Rev. B 29 (1984) 1300.

84L2 Lovesey, S.W.: J. Phys. C: Solid State Phys. 17 (1984) L213.

84M1 Münninghoff, G., Hellner, E., Treutmann, W., Lehner, N., Heger, G.: J. Phys. C: Solid State Physics 17 (1984) 1281.

84M4 Motokawa, M., Harada, T., Sakakibara, T., Date, M., Ikeda, H., King, A.R.: J. Phys. Soc. Jpn. 53 (1984) 2710.

84M5 Mandelbrot, B.B.: J. Stat. Phys. 34 (1984) 895.

84M6 Mandelbrot, B.B., Given, J.A.: Phys. Rev. Lett. 52 (1984) 1853.

84M8 McMillan, W.L.: J. Phys. C: Solid State Phys. 17 (1984) 3179.

84M9 McMillan, W.L.: Phys. Rev. B 29 (1984) 4026.

84R4 de Raedt, H., de Raedt, B., Firez, J., Lagendijk, A.: Monte Carlo study of the 2-dimensional spin-1/2 XY model, in: Magnetic Excitations and Fluctuations, Lovesey, S.W., Balucani, U., Borsa, F., Tognetti, V. (eds.), Springer Series in Solid State Sciences, Berlin: Springer-Verlag, 1984, Vol. 54, p. 172.

84R5 de Raedt, H., de Raedt, B., Lagendijk, A.: Z. Phys. B 57 (1984) 209.

84R6 Rubenacker, G.V., Haines, D.N., Drumheller, J.E., Emerson, K.: J. Magn. Magn. Mater. 43 (1984) 238.

84R7 Richards, P.M.: Phys. Rev. B 30 (1984) 2955.

84S4 Steijger, J.J.M., Frikkee, E., de Jongh, L.J., Huiskamp, W.J.: Physica 123B (1984) 271.

84S6 Shalaev, B.N.: Sov. Phys. Solid State 26 (1984) 1811.

84V1 Vasyukov, V.N., Zhuravlev, A.V., Lukin, S.N., Pashkevich, Yu.G.: Sov. Phys. Solid State 26 (1984) 790.

84V3 Voronov, V.P., Ivanov, B.A., Kosevich, A.M.: Sov. Phys. JETP 57 (1984) 1303.

84V4 van der Vlist, H., Arts, A.F.M., de Wijn, H.W.: Phys. Rev. B 30 (1984) 5000.

84V5 Villain, J.: The random field Ising model. Equillibrium and non-equilibrium properties, in: Magnetic Excitations and Fluctuations, Lovesey, S.W., Balucani, U., Borsa, F., Tognetti, V. (eds.), Springer Series in Solid State Sciences, Berlin: Springer-Verlag, 1984, Vol. 54, p. 143.

84V7 Vlak, V.A.H.M., Frikkee, E., Arts, A.F.M., de Wijn, H.W.: J. Phys. C: Solid State Phys. 17 (1984) L621.

84Y1 Yoshizawa, M., Suzuki, T., Goto, T., Yamakami, T., Fujimura, T., Nakajima, T., Yamauchi, H.: J. Phys. Soc. Jpn. 53 (1984) 261.

84Y3 Yoshizawa, H., Belanger, D.P.: Phys. Rev. B 30 (1984) 5220.

85B3 Belanger, D.P., King, A.R., Jaccarino, V.: Phys. Rev. Lett. 54 (1985) 577.

85B4 Belanger, D.P., Rezende, S.M., King, A.R., Jaccarino, V.: J. Appl. Phys. 57 (1985) 3294.

85B5 Belanger, D.P., King, A.R., Jaccarino, V.: Solid State Commun. 54 (1985) 79.

85B6 Belanger, D.P., King, A.R., Jaccarino, V.: Phys. Rev. B 31 (1985) 4538.

85B7 Bray, A.T., Moore, M.A.: J. Phys. C: Solid State Phys. 18 (1985) L927.

85D1 Dikken, B.J., Arts, A.F.M., de Wijn, H.J., Vlak, W.A.H.M., Frikkee, E.: Phys. Rev. B 32 (1985) 5600.

85D3 Dekker, C., Dikken, B.J., Arts, A.F.M.: Solid State Commun. 54 (1985) 887.

85H2 Haldane, F.D.M.: J. Appl. Phys. 57 (1985) 3359.

85H3 Henley, C.: Phys. Rev. Lett. 54 (1985) 2030.

85H5 Huse, D.A., Henley, C.L.: Phys. Rev. Lett. 54 (1985) 2708.

85H6 Huse, D.A., Morgenstern, I.: Phys. Rev. B 32 (1985) 3032.

85J2 Jaccarino, V., King, A.R., Belanger, D.P.: J. Appl. Phys. 57 (1985) 3291.

85K1 King, A.R., Jaccarino, V., Motokawa, M., Sugiyama, K., Date, M.: J. Appl. Phys. 57 (1985) 3297.

85K2 Kawamura, H., Tanemura, M.: J. Phys. Soc. Jpn. 54 (1985) 4479.

85L Loh, E. Jr., Scalapino, D.J., Grant, P.M.: Phys. Rev. B 31 (1985) 4712.

85P Pelcovits, R.A., Aharony, A.: Phys. Rev. B 31 (1985) 350.

85R2 Rubenacker, G.V., Waplak, S., Hutton, S.L., Haines, D.N., Drumheller, J.E.: J. Appl. Phys. 57 (1985) 3341.

85R4 Randeria, M., Sethna, J.P., Palmer, R.G.: Phys. Rev. Lett. 54 (1985) 1321.

85R5 Rammal, R., Benoit, A.: Phys. Rev. Lett. 55 (1985) 649.

85S2 Stauffer, D.: Introduction to Percolation Theory, London/Philadelphia: Taylor & Francis, 1985.

85S3 Shapir, Y.: Phys. Rev. Lett. 54 (1985) 154.

85S4 Schwartz, M., Soffer, A.: Phys. Rev. Lett. 55 (1985) 2499.

85V1 Vilfan, I., Cowley, R.A.: J. Phys. C: Solid State Phys. 18 (1985) 5055.

85V2 Villain, J.: J. Phys. (France) 46 (1985) 1843.

85V3 Vlak, W.A.H.M., Dikken, B.J., Arts, A.F.M., de Wijn, H.W.: Phys. Rev. B 31 (1985) 4496.

85Y3 Young, A.P., Nauenberg, M.: Phys. Rev. Lett. 54 (1985) 2429.

86A1 Achiwa, N., Yoshinari, T., Matsuyama, T., Kawano, S., Aoyagi, K.: Annu. Rep. Res. React. Inst. Kyoto Univ. 19 (1986) 31.

86A3 Affleck, I.: Phys. Rev. Lett. 56 (1986) 408.
86A5 Aeppli, G.: Physica 136B (1986) 301.
86A6 Aharony, A.: Europhys. Lett. 1 (1986) 617.
86B1 Bellitto, C., Day, P., Wood, T.E.: J. Chem. Soc. Dalton Trans. (1986) 847.
86B3 Bramwell, S.T., Day, P., Hutchings, M.T., Thorne, J.R.G., Visser, D.: Inorg. Chem. 25 (1986) 417.
86B4 Binder, K., Stauffer, D.: A simple introduction to Monte Carlo simulations and some specialized topics, in: Applications of the Monte Carlo Method in Statistical Physics, Binder, K. (ed.), Topics in Current Physics, Berlin: Springer-Verlag, 1986, Vol. 36 (2nd edition), p. 1.
86B6 Belanger, D.P., King, A.R., Jaccarino, V.: Phys. Rev. B 34 (1986) 452.
86C1 Cornelius, C.A., Day, P., Fyne, P.J., Hutchings, M.T., Walker, P.J.: J. Phys. C: Solid State Phys. 19 (1986) 909.
86D3 Day, P.: Proc. Indian Natl. Sci. Acad. 52A (1986) 117.
86D5 Dikken, B.J., Arts, A.F.M., de Wijn, H.W., Vlak, W.A.H.M., Frikkee, E.: J. Magn. Magn. Mater. 54-57 (1986) 30.
86F2 Fernandez, J.F., Ferreira, M.F., Stankiewicz, J.: Phys. Rev. B 34 (1986) 292.
86F4 Fisher, D.S.: Phys. Rev. Lett. 56 (1986) 416.
86F5 Frikkee, E., Bevaart, L., de Jongh, L.J.: private communication 1986.
86F6 Fisher, D.S., Huse, D.A.: Phys. Rev. Lett. 56 (1986) 1601.
86G1 de Groot, H.J.M., de Jongh, L.J.: Physica 141B (1986) 1.
86H2 Hutchings, M.T., Day, P., Janke, E., Pynn, R.: J. Magn. Magn. Mater. 54-57 (1986) 673.
86J3 Jain, S., Young, A.P.: J. Phys. C: Solid State Phys. 19 (1986) 3913.
86K2 Kleemann, W., Otte, D., Usadel, K.D., Brieskorn, G.: J. Phys. C: Solid State Phys. 19 (1986) 395.
86K3 Kawabata, C., Takeuchi, M., Bishop, A.R.: J. Magn. Magn. Mater. 54-57 (1986) 871.
86K4 Kawabata, C., Bishop, A.R.: Solid State Commun. 60 (1986) 169.
86K5 Kawabata, C., Bishop, A.R.: Z. Phys. B 65 (1986) 225.
86K7 Kertész, J.: J. Phys. A: Math. Gen. 19 (1986) 599.
86K8 King, A.R., Belanger, D.P.: J. Magn. Magn. Mater. 54-57 (1986) 19.
86K9 Kleemann, W., King, A.R., Jaccarino, V.: Phys. Rev. B 34 (1986) 479.
86K12 Kubo, H., Hamasaki, T., Tanimoto, M., Katsumata, K.: J. Phys. Soc. Jpn. 55 (1986) 3301.
86M4 Mydosh, J.A., King, A.R., Jaccarino, V.: J. Magn. Magn. Mater. 54-57 (1986) 47.
86N1 Neves, E.J., Perez, J.F.: Phys. Lett. 114A (1986) 331.
86N2 Nagatani, T.: J. Phys. A: Math. Gen. 19 (1986) L275.
86N3 Naumann, E.: Ph.D. Thesis, University of Marburg (Germany) 1986.
86O1 Ogielski, A.T.: Phys. Rev. Lett. 57 (1986) 1251.
86O2 Ogielski, A.T., Huse, D.A.: Phys. Rev. Lett. 56 (1986) 1298.
86O3 Olive, J.A., Young, A.P., Sherrington, D.: Phys. Rev. B 34 (1986) 6341.
86R2 Rauh, H., Erkelens, W.A.C., Regnault, L.P., Rossat-Mignod, J., Kullmann, W., Geick, R.: J. Phys. C: Solid State Phys. 19 (1986) 4503.
86S4 Sokolov, I.M.: Sov. Phys. Usp. 29 (1986) 924.
86S6 Singh, R.R.P., Chakravarty, S.: Phys. Rev. Lett. 57 (1986) 245.
86V1 Vlak, W.A.H.M., Frikkee, E., Arts, A.F.M., de Wijn, H.W.: Phys. Rev. B 33 (1986) 6470.
86V2 Vlak, W.A.H.M., van Dort, M.J., Arts, A.F.M., de Wijn, H.W.: J. Magn. Magn. Mater. 54-57 (1986) 41.
86W Waldner, F.: J. Magn. Magn. Mater. 54-57 (1986) 873.
86Y2 Young, A.P., Nauenberg, M.: J. Magn. Magn. Mater. 54-57 (1986) 63.
87A4 Ain, J. Phys. (France) 48 (1987) 2103.
87B1 Bellitto, C., Filaci, P., Patrizio, S.: Inorg. Chem. 26 (1987) 191.
87B3 Benner, H., Wiese, J., Geick, R., Sauer, H.: Europhys. Lett. 3 (987) 1135.
87B6 Bray, A.J.: Phys. Rev. Lett. 59 (1987) 586.
87B7 Bricmont, J., Kupiainen, A.: Phys. Rev. Lett. 59 (1987) 1829.
87B8 Belanger, D.P., Yoshizawa, H.: Phys. Rev. B 35 (1987) 4823.

87D2 Dekker, C., Arts, A.F.M., de Wijn, H.W., Kjems, J.K.: Phys. Rev. B 35 (1987) 7157.
87F1 Fisher, D.S.: J. Appl. Phys. 61 (1987) 3672.
87F2 Fisher, D.S., Huse, D.A.: Phys. Rev. B 36 (1987) 8937.
87G3 Greiner, P.: Diploma Thesis, University of Würzburg (Germany) 1987.
87H1 Hagen, M., Cowley, R.A., Nicklow, R.M., Ikeda, H.: Phys. Rev. B 36 (1987) 401.
87H3 Havlin, S., Ben-Avraham, D.: Adv. Phys. 36 (1987) 695.
87H5 Huse, D.A., Fisher, D.S.: Phys. Rev. B 35 (1987) 6841.
87K3 Kawamura, H., Tanemura, M.: Phys. Rev. B 36 (1987) 7177.
87L2 Larssen, T.A.: J. Phys. A: Math. Gen. 20 (1987) L291.
87M2 Mertens, F.G., Bishop, A.R., Wysin, G.M., Kawabata, C.: Phys. Rev. Lett. 59 (1987) 117.
87N3 Nienhuis, B.: Coulomb gas formulation of two-dimensional phase transitions, in: Phase Transitions and Critical Phenomena, Domb, C., Lebowitz, J.L. (eds.), London/New York: Academic Press, 1987, Vol. 11, p. 1.
87O1 Orbach, R., Kin-Wah Yu: J. Appl. Phys. 61 (1987) 3689.
87O2 Ozeki, Y., Nishimori, H.: J. Phys. Soc. Jpn. 56 (1987) 1568. Addendum: J. Phys. Soc. Jpn. 56 (1987) 2992.
87S1 Shankar, R.: Phys. Rev. Lett. 58 (1987) 2466.
88A3 Affleck, I., Kennedy, T., Lieb, E.H., Tasaki, H.: Commun. Math. Phys. 115 (1988) 477.
88A6 Auerbach, A., Arovas, D.P.: Phys. Rev. Lett. 61 (1988) 617.
88A7 Affleck, I.: Phys. Rev. B 37 (1988) 5186.
88B2 Bramwell, S.T., Hutchings, M.T., Norman, J., Pynn, R., Day, P.: J. Phys. (France) 49 (1988) C8-1435.
88B4 Bray, A.J.: Phys. Rev. Lett. 60 (1988) 720.
88B5 Belanger, D.P.: Phase Transitions 11 (1988) 53.
88B6 Belanger, D.P., King, A.R., Ferreira, I.B., Jaccarino, V.: Phys. Rev. B 37 (1988) 226.
88B7 Bhatt, R.N., Young, A.P.: Phys. Rev. B 37 (1988) 5606.
88C3 Cowley, R.A., Birgeneau, R.J., Thurston, T., Shirane, G.: J. Phys. (France) 49 (1988) C8-1221.
88C4 Chakravarty, S., Halperin, B.I., Nelson, D.R.: Phys. Rev. Lett. 60 (1988) 1057.
88C5 Cecatto, H.E., Naon, C.: Phys. Rev. Lett. 61 (1988) 2389.
88C6 Ching, W.Y., Huber, D.L.: Solid State Commun. 68 (1988) 723.
88D1 Dekker, C., Arts, A.F.M., de Wijn, H.W.: Phys. Rev. B 38 (1988) 11512.
88D3 Demokritov, S.O., Kreines, N.M., Kudinov, V.I., Petrov, S.V., Chubukov, A.V.: Sov. Phys. JETP 67 (1988) 2552.
88D4 Dzyaloshinskii, I.E., Polyakov, A.M., Wiegmann, P.B.: Phys. Lett. A 127 (1988) 112.
88D5 Dombre, T., Read, N.: Phys. Rev. B 38 (1988) 7181.
88D6 Dahr, D., Randeria, M., Sethna, J.P.: Europhys. Lett. 5 (1988) 485.
88D7 Dekker, C., Arts, A.F.M., de Wijn, H.W.: J. Appl. Phys. 63 (1988) 4334.
88D8 Dekker, C., Arts, A.F.M., de Wijn, H.W.: J. Phys. (France) 49 (1988) C8-1013.
88D9 Dekker, C., Arts, A.F.M., de Wijn, H.W., van Duyneveldt, A.J., Mydosh, J.A.: Phys. Rev. Lett. 61 (1988) 1780.
88D10 Dekker, C., Arts, A.F.M., de Wijn, H.W.: Phys. Rev. B 38 (1988) 8985.
88D11 Dekker, C.: Ph.D. Thesis, University of Utrecht (Netherlands) 1988.
88F1 Frey, E., Schwabl, F.: Z. Phys. B 71 (1988) 355. Erratum: Z. Phys. B 76 (1989) 139.
88F2 Fisher, D.S., Grinstein, G.M., Khurana, A.: Phys. Today 41 (December 1988) 56.
88F3 Fisher, D.S., Huse, D.A.: Phys. Rev. B 38 (1988) 373.
88F4 Fisher, D.S., Huse, D.A.: Phys. Rev. B 38 (1988) 386.
88G1 Gartenhaus, S., McCullough, W.S.: Phys. Lett. A 127 (1988) 315.
88G2 Gartenhaus, S., McCullough, W.S.: Phys. Rev. B 38 (1988) 11688.
88G3 Greb, H., Greiner, P., Sauer, H., Strobel, K.H., Geick, R.: J. Phys. (France) 49 (1988) C8-1487.
88G4 Gupta, R., de Lapp, J., Batrouni, G.G., Fox, G.C., Baillie, C.F., Apostolakis, J.: Phys. Rev. Lett. 61 (1988) 1996.
88H2 Haldane, F.D.M.: Phys. Rev. Lett. 61 (1988) 1029.
88H4 Higgins, S., Cowley, R.A.: J. Phys. C: Solid State Phys. 21 (1988) 2215.

88J2 Jamet, J.P., Ferré, J., Yamada, I., Itoh, M.: J. Phys. (France) 49 (1988) C8-1501.
88K3 Kubo, T., Kishi, T.: Phys. Rev. Lett. 61 (1988) 2585.
88K4 Kennedy, T., Lieb, E.H., Shastry, B.S.: J. Stat. Phys. 53 (1988) 1019.
88K5 Kennedy, T., Lieb, E., Shastry, B.S.: Phys. Rev. Lett. 61 (1988) 2582.
88K7 King, A.R., Ferreira, I.B., Jaccarino, V., Belanger, D.P.: Phys. Rev. B 37 (1988) 219.
88K8 Katsumata, K., Tuchendler, J., Uemura, Y.J., Yoshizawa, H.: Phys. Rev B 37 (1988) 356.
88L1 Ludwig, W.W.: Phys. Rev. Lett. 61 (1988) 2388.
88L2 Lai, Z.W., Mazenko, G.F., Valls, O.T.: Phys. Rev. B 37 (1988) 9481.
88M2 Mertens, F.G., Bishop, A.R., Gouvêa, M.E., Wysin, G.M.: J. Phys. (France) 49 (1988) C8-1385.
88M3 Müller, G.: Phys. Rev. Lett. 60 (1988) 2785.
88N Nattermann, T., Villain, J.: Phase Transitions 11 (1988) 5.
88O Okabe, Y., Kikuchi, M.: J. Phys. Soc. Jpn. 57 (1988) 4351.
88P Patrascioiu, A., Seiler, E.: Phys. Rev. Lett. 60 (1988) 875.
88R3 Ramos, C.A., King, A.R., Jaccarino, V., Rezende, S.M.: J. Phys. (France) 49 (1988) C8-1241.
88R4 Rosov, N., Kleinhammes, A., Lidbjörk, P., Hohenemser, C., Eibschütz, M.: Phys. Rev. B 37 (1988) 3265.
88R5 Reger, J.D., Young, A.P.: Phys. Rev. B 37 (1988) 5978.
88S3 Schwabl, F.: J. Appl. Phys. 64 (1988) 5867.
88S5 Stepanov, A.A., Pashchenko, V.A., Kobets, M.I.: Sov. J. Low Temp. Phys. 14 (1988) 304.
88S6 Shankar, R.: Phys. Rev. Lett. 61 (1988) 2390.
88S7 Sieger, D., Tietze, H., Geick, R., Schweiss, P., Heger, G., Treutmann, W.: J. Appl. Phys. 63 (1988) 3729.
88S9 Sieger, D., Ching, W.Y., Huber, D.L., Geick, R.: J. Phys. (France) 49 (1988) C8-1021.
88T1 Tien, C., Karra, J.S., Kemmerer, G.: Phys. Rev. B 37 (1988) 9564.
88T2 Tietze, H., Sieger, D., Schweiss, P., Geick,R., Treutmann, W.: J. Phys. (France) 49 (1988) C8-1253.
88V2 Vlak, W.A.H.M., van Dort, M.J., Arts, A.F.M., de Wijn, H.W.: Phys. Rev. B 38 (1988) 11659.
88W2 Weber, H., Minnhagen, P.: Phys. Rev. B 37 (1988) 5986.
88W3 Wen, X.G., Zee, A.: Phys. Rev. Lett. 61 (1988) 1025.
89B1 Becker, T., Reiter, G.: Phys. Rev. Lett. 63 (1989) 1004.
89B2 Bogolubskaya, A.A., Bogolubsky, I.L.: Phys. Lett. A 136 (1989) 485.
89B4 Brotzeller, C.: Diploma Thesis, University of Würzburg (Germany) 1989.
89B5 Bray, A.J.: J. Phys. A: Math. Gen. 22 (1989) L81.
89C3 Chakravarty, S., Halperin, B.I., Nelson, D.R.: Phys. Rev. B 39 (1989) 2344.
89C4 Colborne, S.G.W., Bray, A.J.: J. Phys. A: Math. Gen. 22 (1989) 2505.
89D2 Demokritov, S.O., Kreines, N.M., Kudinov, V.I.; Petrov, S.V.: Sov. Phys. JETP 68 (1989) 1277.
89D3 Dekker, C., Arts, A.F.M., de Wijn, H.W., van Duyneveldt, A.J., Mydosh, J.A.: Phys. Rev. B 40 (1989) 11243.
89F2 Falo, F., Floria, L.M., Navarro, R.: J. Phys.: Condens. Matter 1 (1989) 5139.
89G3 Gouvêa, M.E., Wysin, G.M., Bishop, A.R., Mertens, F.G.: J. Phys.: Condens. Matter 1 (1989) 4387.
89G4 Gouvêa, M.E., Wysin, G.M., Bishop, A.R., Mertens, F.G.: Phys. Rev. B 39 (1989) 11840.
89G8 Gerling, R.W., Landau, D.P.: Phys. Rev. Lett. 63 (1989) 812.
89I4 Ivanov, B.A., Stephanovich, V.A.: Phys. Lett. A 141 (1989) 89.
89M2 Mertens, F.G., Bishop, A.R., Wysin, G.M., Kawabata, C.: Phys. Rev. B 39 (1989) 591.
89M3 Müller, G.: Phys. Rev. Lett. 63 (1989) 813.
89M4 Mehran, F., Anderson, P.W.: Solid State Commun. 71 (1989) 29.
89M5 Mandelbrot, B.B.: Les Objects Fractals: Forme, Hasard et Dimension, Paris: Flammarion, 1989.
89M6 Mayer, I.O.: J. Phys. A: Math. Gen. 22 (1989) 2815.
89N2 Nishimori, H., Ozeki, Y.: J. Phys. Soc. Jpn. 58 (1989) 1027.

89O Ozeki, Y., Nishimori, H., Tomita, Y.: J. Phys. Soc. Jpn. 58 (1989) 82.
89R Rodriguez, J.P.: Phys. Rev. B 39 (1989) 2906.
89S1 Sieger, D.: Ph.D. Thesis, University of Würzburg (Germany) 1989.
89T1 Tsipenyuk, Yu.M., Yanev, V.P.: JETP Lett. 49 (1989) 458.
89T2 Takahashi, M.: Phys. Rev. B 40 (1989) 2494.
89T3 Tyc, S., Halperin, B.I., Chakravarty, S.: Phys. Rev. Lett. 62 (1989) 835.
89V Vannimenus, J., Kirkpatrick, S., Haldane, F.D.M., Jayaprakash, C.: Phys. Rev. B 39 (1989) 4634.
89Y5 Yonezawa, F., Sakamoto, S., Hori, M.: Phys. Rev. B 40 (1989) 650.
90A1 Achiwa, N., Matsuyama, T., Yoshinari, T.: Phase Transitions 28 (1990) 79.
90A3 Arts, A.F.M., de Wijn, H.W.: Spin waves in two-dimensional magnetic systems, theory and applications, in: Magnetic Properties of Layered Transition Metal Compounds, de Jongh, L.J. (ed.), Dordrecht: Kluwer Academic, 1990, p. 191.
90B1 Benner, H., Boucher, J.P.: Spin dynamics in the paramagnetic regime, NMR and EPR in two-dimensional magnets, in: Magnetic Properties of Layered Transition Metal Compounds, de Jongh, L.J. (ed.), Dordrecht: Kluwer Academic, 1990, p. 323.
90B3 Birgeneau, R.J.: Phys. Rev. B 41 (1990) 2514.
90B5 Bouchard, J.P., Georges, A.: Phys. Rep. 195 (1990) 127.
90C1 Chakravarty, S., Orbach, R.: Phys. Rev. Lett. 64 (1990) 224.
90C2 Clerc, J.P., Giraud, G., Langier, J.M., Luck, J.M.: Adv. Phys. 39 (1990) 191.
90D3 Demokritov, S.O., Kreines, N.M., Kudinov, V.I., Petrov, S.V.: J. Magn. Magn. Mater. 90&91 (1990) 305.
90D4 Ding, H.-Q., Makivić, M.S.: Phys. Rev. Lett. 64 (1990) 1449.
90D5 Ding, H.-Q., Makivić, M.S.: Phys. Rev. B 42 (1990) 6827.
90F3 Feder, J., Aharony, A.: Fractals, Amsterdam: North Holland, 1990.
90G3 de Groot, H.J.M., de Jongh, L.J.: Field-induced phenomena in two-dimensional weakly anisotropic Heisenberg antiferromagnets, in: Magnetic Properties of Layered Transition Metal Compounds, de Jongh, L.J. (ed.), Dordrecht: Kluwer Academic, 1990, p. 379.
90G4 Greb, H.: Ph.D. Thesis, University of Würzburg (Germany) 1990.
90H Hirakawa, K., Ikeda, H.: Neutron scattering experiments on two-dimensional Heisenberg and Ising magnets, in: Magnetic Properties of Layered Transition Metal Compounds, de Jongh, L.J. (ed.), Dordrecht: Kluwer Academic, 1990, p. 231.
90I1 Ikeda, H., Endoh, Y., Itoh, S.: Phys. Rev. Lett. 64 (1990) 1266.
90J1 de Jongh, L.J.: Introduction to low-dimensional magnetic systems, in: Magnetic Properties of Layered Transition Metal Compounds, de Jongh, L.J. (ed.), Dordrecht: Kluwer Academic, 1990, p. 1.
90J2 Jaccarino, V., King, A.R.: Physica A 163 (1990) 291.
90K1 Kosevich, A.M., Ivanov, B.A., Kovalev, A.S.: Phys. Rep. 194 (1990) 119.
90M Mydosh, J.A.: J. Magn. Magn. Mater. 90&91 (1990) 318.
90N Navarro, R.: Application of high- and low-temperature series expansions to two-dimensional magnetic systems, in: Magnetic Properties of Layered Transition Metal Compounds, de Jongh, L.J. (ed.), Dordrecht: Kluwer Academic, 1990, p. 105.
90P Pokrovsky, V.L., Uimin, G.V.: Theory of two-dimensional magnets, in: Magnetic Properties of Layered Transition Metal Compounds, de Jongh, L.J. (ed.), Dordrecht: Kluwer Academic, 1990, p. 53.
90R1 Regnault, L.P., Rossat-Mognod, J.: Phase transitions in quasi two-dimensional planar magnets, in: Magnetic Properties of Layered Transition Metal Compounds, de Jongh, L.J. (ed.), Dordrecht: Kluwer Academic, 1990, p. 271.
90S Shirakura, T., Matsubara, F., Inawashiro, S.: J. Phys. Soc. Jpn. 59 (1990) 2285.
90W2 Wang, J.S., Selke, W., Dotsenko, Vl.S., Andreichenko, V.B.: Europhys. Lett. 11 (1990) 301.
90W3 Wang, J.S., Selke, W., Dotsenko, Vl.S., Andreichenko, V.B.: Physica A 164 (1990) 221.
91B1 Belanger, D.P., Young, A.P.: J. Magn. Magn. Mater. 100 (1991) 272.

91B2 Birgeneau, R.J., Hill, J.P., Aharony, A., Cowley, R.A., Shirane, G., Thurston, T.R., Pelcovits, R.A.: Physica A 177 (1991) 58.
91F3 Ferrenberg, A.M., Landau, D.P.: Phys. Rev. B 44 (1991) 5081.
91F4 Ferreira, I.B., King, A.R., Jaccarino, V.: J. Appl. Phys. 69 (1991) 5246.
91F5 Ferreira, I.B., King, A.R., Jaccarino, V.: Phys. Rev. B 43 (1991) 10797.
91F6 Ferreira, I.B., Cardy, J.L., King, A.R., Jaccarino, V.: J. Appl. Phys. 69 (1991) 5075.
91G3 Gawron, T.R., Cieplak, M., Banavar, J.R.: J. Phys. A: Math. Gen. 24 (1991) L127.
91J2 Janke, W., Nather, K.: Phys. Lett. A 157 (1991) 11.
91S1 Schmidt, W.: Ph.D. Thesis, University of Würzburg (Germany) 1991.
91S2 Schins, A.G., Arts, A.F.M., de Wijn, H.W., Leylekian, L., Vincent, E., Paulsen, C., Hammann, J.: J. Appl. Phys. 69 (1991) 5237.
91V1 Völkel, A.R., Mertens, F.G., Bishop, A.R., Wysin, G.M.: Phys. Rev. B 43 (1991) 5992.
91W2 Wischmann, H.A., Müller-Hartmann, E.: J. Phys. I 1 (1991) 647.
92A2 Andreichenko, V.B., Selke, W., Talapov, A.L.: J. Phys. A: Math. Gen. 25 (1992) L283.
92B2 Bramwell, S.T., Hutchings, M.T., Fak, B.: Physica B 180&181 (1992) 259.
92B3 Baillie, C.F., Gupta, R., Hawick, K.A., Pawley, G.S.: Phys. Rev. B 45 (1992) 10438.
92C1 Costa, B.V., Gouvêa, M.E., Pires, A.S.T.: Phys. Lett. A 165 (1992) 179.
92C2 Cowley, R.A.: Physica B 180&181 (1992) 25.
92D1 Ding, H.-Q.: Phys. Rev. B 45 (1992) 230.
92D2 Ding, H.-Q.: Phys. Rev. Lett. 68 (1992) 1927.
92F1 Fischer, T.M., Frey, E., Schwabl, F.: J. Magn. Magn. Mater. 104-107 (1992) 201.
92F2 Frey, E., Schwabl, F.: J. Magn. Magn. Mater. 104-107 (1992) 204.
92G2 Gupta, R., Baillie, C.F.: Phys. Rev. B 45 (1992) 2883.
92H1 Halperin, B.I.: J. Magn. Magn. Mater. 104-107 (1992) 761.
92I1 Isichenko, M.B.: Rev. Mod. Phys. 64 (1992) 961.
92K2 Kawamura, H.: J. Phys. Soc. Jpn. 61 (1992) 1299.
92L1 Landau, D.P., Gerling, R.W.: J. Magn. Magn. Mater. 104-107 (1992) 843.
92L2 Leylekian, L., Tsipenyuk, Yu.M., Ocio, M., Hammann, J.: J. Magn. Magn. Mater. 104-107 (1992) 775.
92M2 Moussa, F., Ain, M., Hennion, B.: Physica B 180&181 (1992) 241.
92M4 Menezes, S.L., Gouvêa, M.E., Pires, A.S.T.: Phys. Lett. A 166 (1992) 330.
92M5 Menezes, S.L., Pires, A.S.T., Gouvêa, M.E.: Phys. Rev. B 45 (1992) 10454.
92M7 Makivić, M.S.: Phys. Rev. B 46 (1992) 3167.
92N Nifle, M., Hilhorst, H.J.: Phys. Rev. Lett. 68 (1992) 2992.
92P Pereira, A.R., Pires, A.S.T., Gouvêa, M.E., Costa, B.V.: Z. Phys. B 89 (1992) 109.
92S1 Schins, A.G., Nielsen, M., Arts, A.F.M., de Wijn, H.J.: Physica B 180&181 (1992) 161.
92S6 Stauffer, D, Aharony, A.: Introduction to Percolation Theory, London/Philadelphia: Taylor & Francis, 1992, 2nd edition.
92S7 Sieger, D., Schmidt, W., Tietze-Jaensch, H., Geick, R., Schweiss, P., Treutmann, W., Godfrin, H.: J. Magn. Magn. Mater. 104-107 (1992) 895.
92S8 Schins, A.G., Arts, A.F.M., de Wijn, H.W., Nielsen, M.: J. Magn. Magn. Mater. 104-107 (1992) 931.
92S9 Schmidt, W., Sieger, D., Tietze-Jaensch, H., Geick, R.: Nucl. Instrum. Methods Phys. Res. A316 (1992) 364.
92T1 Tietze-Jaensch, H., Sieger, D., Jaitner, H., Geick, R., Schweiss, P., Treutmann, W., Regnault, L.P., Fak, B.: J. Magn. Magn. Mater. 104-107 (1992) 897.
92T2 Takahashi, M.: J. Magn. Magn. Mater. 104-107 (1992) 845.
92V Völkel, A.R., Wysin, G.M., Bishop, A.R., Mertens, F.G.: J. Phys.: Condens. Matter 4 (1992) 9411.
92W Waldner, F.: J. Magn. Magn. Mater. 104-107 (1992) 793.
92Z2 Zhou, P., Drumheller, J.E., Patyal, B., Willett, R.D.: Phys. Rev. B 45 (1992) 12365.
93A Als-Nielsen, J., Bramwell, S.T., Hutchings, M.T., McIntyre, G.J., Visser, D.: J. Phys.: Condens. Matter 5 (1993) 7871

93B1 Bramwell, S.T., Holdsworth, P.C.W.: J. Phys.: Condens. Matter 5 (1993) L53.
93B2 Bramwell, S.T., Holdsworth, P.C.W.: J. Appl. Phys. 73 (1993) 6096.
93B3 Butera, P., Comi, M.: Phys. Rev. B 47 (1993) 11969.
93C2 Cowley, R.A., Aharony, A., Birgeneau, R.J., Pelcovits, R.A., Shirane, G., Thurston, T.: Z. Phys. B 93 (1993) 5.
93C3 Castner, T.G., Seehra, M.S.: Phys. Rev. B 47 (1993) 578.
93G Grigereit, T.E., Drumheller, J.E., Zaspel, C.E.: J. Appl. Phys. 73 (1993) 7010.
93I Ikeda, H., Iwasa, K., Anderson, K.H.: J. Phys. Soc. Jpn. 62 (1993) 3832.
93J Janke, W., Nather, K.: Phys. Rev. B 48 (1993) 7419.
93M2 Menezes, S.L., Pires, A.S.T., Gouvêa, M.E.: Phys. Rev. B 47 (1993) 12280.
93M3 Mydosh, J.A.: Spin Glasses: An Experimental Introduction, London: Taylor & Francis, 1993.
93P1 Pich, C., Schwabl., F.: Phys. Rev. B 47 (1993) 7957.
93P2 Pires, A.S.T., Gouvêa, M.E.: Phys. Rev. B 48 (1993) 12698.
93R2 Rieger, H., Young, A.P.: J. Phys. A: Math. Gen. 26 (1993) 5279.
93S2 Schins, A.G., Arts, A.F.M., de Wijn, H.W.: Phys. Rev. Lett. 70 (1993) 2340.
93S3 Schins, A.G., Dons, E.M., Arts, A.F.M., de Wijn, H.W., Vincent, E., Leylekian, L., Hammann, J.: Phys. Rev. B 48 (1993) 16524.
93V Visser, D., Bramwell, S.T.: J. Appl. Phys. 73 (1993) 5345.
93Z Zaspel, C.E.: Phys. Rev. B 48 (1993) 926.
94B1 Bramwell, S.T., Holdsworth, P.C.W.: J. Appl. Phys. 75 (1994) 5955.
94B2 Bramwell, S.T., Holdsworth, P.C.W.: Phys. Rev. B 49 (1994) 8811.
94C Costa, B.V., Pires, A.S.T., Gouvêa, M.E.: Phys. Rev. B 50 (1994) 3828.
94I2 Ivanov, B.A., Sheka, D.D.: Phys. Rev. Lett.: 72 (1994) 404.
94I4 Ikeda, H.: Physica A 204 (1994) 328.
94K Karszewski, M., Kushauer, J., Binek, Ch., Kleemann, W., Bertrand, D.: J. Phys.: Condens. Matter 6 (1994) L75.
94L Lovesey, S.W., Engdahl, E., Cuccoli, A., Tognetti, V., Balcar, E.: J. Phys.: Condens. Matter 6 (1994) L521.
94N Nakayama, T., Yakubo, K., Orbach, R.L.: Rev. Mod. Phys. 66 (1994) 381.
94P1 Pich, C., Schwabl, F.: Phys. Rev. B 49 (19994) 413.
94P2 Pires, A.S.T., Pereira, A.R., Gouvêa, M.E.: Phys. Rev. B 49 (1994) 9663.
94P3 Pereira, A.R., Pires, A.S.T., Gouvêa, M.E.: J. Magn. Magn. Mater. 134 (1994) 121.
94R Rieger, H., Steckemetz, B., Schreckenberg, M.: Europhys.Lett. 27 (1994) 485.
94S2 Schultka, N., Manousakis, E.: Phys. Rev. B 49 (1994) 12071.
94S4 Schins, A.G., Nielsen, M., Arts, A.F.M., de Wijn, H.W.: Phys. Rev. B 49 (1994) 8911.
94W Wysin, G.M.: Phys. Rev. B 49 (1994) 8780.
95B1 Bramwell, S.T., Holdsworth, P.C.W., Hutchings, M.T.: J. Phys. Soc. Jpn. 64 (1995) 3066.
95B2 Binek, C., Kleemannn, W.: Phys. Rev. B 51 (1995) 12888.
95C1 Curély, J.: Europhys. Lett. 32 (1995) 529.
95C2 Cuccoli, A., Tognetti, V., Verrucchi, P.: Phys. Rev. B 51 (1995) 12840.
95C3 Cuccoli, A., Tognetti, V., Vaia, R.: Phys. Rev. B 52 (1995) 10221.
95I1 Ivanov, B.A., Sheka, D.D.: JETP 80 (1995) 907.
95I2 Ikeda, H., Iwasa, K., Fernandez-Baca, J.A., Nicklow, R.M.: Physica B 213&214 (1995) 146.
95I3 Ikeda, H., Itoh, S., Adams, M.A.: Phys. Rev. Lett. 75 (1995) 4440.
95L v. Löhneysen, H., Beckmann, D., Wosnitza, J., Visser, D.: J. Magn. Magn. Mater. 140-144 (1995) 1469.
95M1 Mostafa, M.F., Emrick, R.M.: Physica B 210 (1995) 67.
95M2 Mostafa, M.F., El-Essawi, M., Vuillemin, V.V.: Phys. Status Solidi (b) 189 (1995) K61.
95O1 Olsson, P.: Phys. Rev. B 52 (1995) 4511.
95O2 Olsson, P.: Phys. Rev. B 52 (1995) 4526.
95P1 Pich, C., Schwabl, F.: J. Magn. Magn. Mater. 140-144 (1995) 1709.
95P2 Pires, A.S.T.: Solid State Commun. 96 (1995) 915.
95P3 Pereira, A.R., Pires, A.S.T., Gouvêa, M.E.: Phys. Rev. B 51 (1995) 15974.

95R4	Rieger, H.: Phys. Rev. B 52 (1995) 6659.
95R5	Ramirez, A.P., Schins, A.G., Arts, A.F.M., de Wijn, H.W.: J. Magn. Magn. Mater. 140-144 (1995) 1713.
95S2	Schins, A.G., Nielsen, M., Arts, A.F.M., de Wijn, H.W.: J. Magn. Magn. Mater. 140-144 (1995) 1715.
95T1	Takahashi, M., Itoh, S., Takeda, M.: J. Phys. Soc. Jpn. 64 (1995) 268.
95V	Valkonet, J.P.G., Schins, A.G., Arts, A.F.M., de Wijn, H.W.: J. Magn. Magn. Mater. 140-144 (1995) 1707.
95Z1	Zaspel, C.E., Grigereit, T.E., Drumheller, D.E.: Phys. Rev. Lett. 74 (1995) 4539.
96B	Biagini, C., Cuccoli, A., Tognetti, V., Vaia, R., Verrucchi, P.: J. Appl. Phys. 79 (1996) 4638.
96K	van de Kamp, R.: Ph.D. Thesis, Technical University of Berlin (Germany) 1996.
96L	Lovesey, S.W.: J. Phys.: Condens. Matter 8 (1996) L307.
96M	Mydosh, J.A.: J. Magn. Magn. Mater. 157&158 (1996) 606.
96R	Rieger, H., Santen, L., Blasum, U., Diehl, M., Jünger, M., Rinaldi, G.: J. Phys. A: Math. Gen. 29 (1996) 3939.
96S1	Subbaraman, K., Zaspel, C.E., Drumheller, J.E.: J. Appl. Phys. 79 (1996) 5368.
96T	Talapov, A.L., Blöte, H.W.J.: J. Phys. A: Math. Gen. 29 (1996) 5727.
96Z1	Zaspel, C.E., Drumheller, J.E.: Int. J. Mod. Phys. B 10 (1996) 3649.
96Z2	Zaspel, C.E., Godinez, D.: J. Magn. Magn. Mater. 162 (1996) 91.
98K1	van de Kamp, R., Steiner, M., Tietze-Jaensch, H.: Physica B 241-243 (1998) 570.
98K2	Kobe, S.: Phys. Bl. 54 (1998) 917.